PROCEEDINGS

SPIE—The International Society for Optical Engineering

# XIII International Symposium on Gas Flow and Chemical Lasers and High-Power Laser Conference

**Antonio Lapucci**
**Marco Ciofini**
*Editors*

**18–22 September 2000**
**Florence, Italy**

*Organized by*
INOA—Italian National Institute of Applied Optics
ENEA—Ente per le Nuove Tecnologie, l'Energia e l'Ambiente (Italy)
CNR—National Research Council (Italy)

*Sponsored by*
European Office of Aerospace Research and Development, Air Force Office of Scientific Research, U.S. Air Force Research Laboratory
SPIE—The International Society for Optical Engineering
El.En. SpA (Italy)
Consorzio CEO—Centro di Eccellenza Optronica (Italy)



SPIE P PROCEEDINGS SERIES

**Volume 4184**

# REPORT DOCUMENTATION PAGE

Form Approved OMB No. 0704-0188



| 1. AGENCY USE ONLY (Leave blank) | 2. REPORT DATE | 3. REPORT TYPE AND DATES COVERED |
|---|---|---|
| | 2000 | Conference Proceedings |

| 4. TITLE AND SUBTITLE | 5. FUNDING NUMBERS |
|---|---|
| XIII Int'l Symposium on Gas Flow & Chemical Lasers and High Power Laser Conference | F61775-00-WF038 |
| 6. AUTHOR(S) | |
| Conference Committee | |
| 7. PERFORMING ORGANIZATION NAME(S) AND ADDRESS(ES) | 8. PERFORMING ORGANIZATION REPORT NUMBER |
| Qbit Srl<br>c/o Instituto Nazionale de Ottica<br>Largo E. Fermi 6<br>Firenze I-5015<br>Italy | N/A |
| 9. SPONSORING/MONITORING AGENCY NAME(S) AND ADDRESS(ES) | 10. SPONSORING/MONITORING AGENCY REPORT NUMBER |
| EOARD<br>PSC 802 BOX 14<br>FPO 09499-0200 | CSP 00-5038 |

11. SUPPLEMENTARY NOTES

| 12a. DISTRIBUTION/AVAILABILITY STATEMENT | 12b. DISTRIBUTION CODE |
|---|---|
| Approved for public release; distribution is unlimited. | A |

13. ABSTRACT (Maximum 200 words)

The Final Proceedings for XIII Int'l Symposium on Gas Flow & Chemical Lasers and High Power Laser Conference, 18 September 2000 - 22 September 2000

This is an interdisciplinary conference. Topics include CO2 and CO lasers, metal vapor lasers, chemical lasers, solid state lasers, diode lasers, VUV/XUV lasers, new laser media, laser physics modeling, laser resonators, beam delivery, adaptive optics, fiber lasers, diffractive optics, and applications.

| 14. SUBJECT TERMS | 15. NUMBER OF PAGES |
|---|---|
| EOARD, Diode lasers, Solid state lasers, Chemical lasers, Laser beam control | 638 |
| | 16. PRICE CODE<br>N/A |

| 17. SECURITY CLASSIFICATION OF REPORT | 18. SECURITY CLASSIFICATION OF THIS PAGE | 19, SECURITY CLASSIFICATION OF ABSTRACT | 20. LIMITATION OF ABSTRACT |
|---|---|---|---|
| UNCLASSIFIED | UNCLASSIFIED | UNCLASSIFIED | UL |

NSN 7540-01-280-5500

Standard Form 298 (Rev. 2-89)
Prescribed by ANSI Std. 239-18
298-102

PROCEEDINGS

# XIII International Symposium on Gas Flow and Chemical Lasers and High-Power Laser Conference

**Antonio Lapucci**
**Marco Ciofini**
*Editors*

**18–22 September 2000**
**Florence, Italy**

*Organized by*
INOA—Italian National Institute of Applied Optics
ENEA—Ente per le Nuove tecnologie, l'Energia e l'Ambiente (Italy)
CNR—National Research Council (Italy)

*Sponsored by*
European Office of Aerospace Research and Development, Air Force Office of Scientific Research, U.S. Air Force Research Laboratory
SPIE—The International Society for Optical Engineering
El.En. SpA (Italy)
Consorzio CEO—Centro di Eccellenza Optronica (Italy)

*Supported by*
EOS—European Optical Society
SIOF—Italian Optical and Photonics Society
Department of Physics, University of Florence (Italy)
Municipality and Provincial Administration of Florence (Italy)



SPIE P PROCEEDINGS SERIES
**Volume 4184**

SPIE is an international technical society dedicated to advancing engineering and scientific applications of optical, photonic, imaging, electronic, and optoelectronic technologies.

The papers appearing in this book compose the proceedings of the technical conference cited on the cover and title page of this volume. They reflect the authors' opinions and are published as presented, in the interests of timely dissemination. Their inclusion in this publication does not necessarily constitute endorsement by the editors or by SPIE. Papers were selected by the conference program committee to be presented in oral or poster format, and were subject to review by volume editors or program committees.

Please use the following format to cite material from this book:

Author(s), "Title of paper," in *XIII International Symposium on Gas Flow and Chemical Lasers and High-Power Laser Conference*, Antonio Lapucci, Marco Ciofini, Editors, Proceedings of SPIE Vol. 4184, page numbers (2001).

ISSN 0277-786X
ISBN 0-8194-3847-2

Published by
**SPIE—The International Society for Optical Engineering**
P.O. Box 10, Bellingham, Washington 98227-0010 USA
Telephone 1 360/676-3290 (Pacific Time) • Fax 1 360/647-1445
http://www.spie.org/



Printed in the United States of America.

# Contents

## CHEMICAL LASERS: IODINE PHOTODISSOCIATION LASERS



## CHEMICAL LASERS: HF/DF



## HIGH-POWER SOLID STATE AND DIODE LASERS

## GAS LASERS: METAL VAPOR



## GAS LASERS: CO

## GAS LASERS: $CO_2$

## UV-VUV EXCIMER LASERS

## NEW LASER MEDIA

## LASER PROCESS MODELING



## GAS FLOW IN LASERS



## LASER RESONATORS AND BEAM OPTICAL QUALITY

## BEAM DELIVERY AND PROPAGATION

## HIGH-POWER LASER APPLICATIONS

# Conference Committees

*Conference Chair*

**Antonio Lapucci,** Istituto Nazionale di Ottica Applicata (Italy)

*Program Chair*

**Tommaso Letardi,** Ente per le Nuove tecnologie, l'Energia e l'Ambiente (Italy)

*International Advisory Committee*

**A. Lapucci** *Chair* (Italy)
**K. M. Abramski** (Poland)
**V. V. Apollonov** (Russia)
**P. Atanasov** (Bulgaria)
**M. L. Autric** (France)
**H. J. Baker** (UK)
**V. Y. Baranov** (Russia)
**N. G. Basov** (Russia)
**W. L. Bohn** (Germany)
**A. S. Boreysho** (Russia)
**H. Brunet** (France)
**C. Creput** (France)
**J. Eichler** (Germany)
**C. Fotakis** (Greece)
**T. Fujioka** (Japan)
**D. R. Hall** (UK)
**H. Hügel** (Germany)
**R. Jalin** (France)
**K. Kasuya** (Japan)
**J. Kodymova** (Czech Republic)
**P. G. Kryukov** (Russia)
**M. Kudriatsev** (Russia)
**T. Letardi** (Italy)
**P. Loosen** (Germany)
**K. Maeno** (Japan)
**N. Oraevsky** (Russia)
**P. J. M. Peters** (Netherlands)
**D. Pigache** (France)
**J. P. Reilly** (USA)
**S. Rosenwaks** (Israel)
**D. Schuöcker** (Austria)
**L. H. Sentman** (USA)
**F. K. Tittel** (USA)
**K. Truesdell** (USA)
**J. Tulip** (Canada)
**R. F. Walter** (USA)
**W. S. Watt** (USA)
**W. J. Witteman** (Netherlands)
**D. Xianwan** (China)
**H. X. Yan** (China)
**C. Zhang** (China)

*Program Committee*

**T. Letardi,** *Chair*, Ente per le Nuove tecnologie, l'Energia e l'Ambiente (Italy)
**M. L. Autric,** University of Marseille (France)
**H. J. Baker,** Heriot-Watt University (UK)
**W. L. Bohn,** DLR (Germany)
**A. S. Boreysho,** Baltic State Technical University (Russia)
**P. Burlamacchi,** Università degli Studi di Firenze (Italy)
**P. Di Lazzaro,** Ente per le Nuove tecnologie, l'Energia e l'Ambiente (Italy)
**H. Hügel,** Universität Stuttgart (Germany)
**K. Kasuya,** Tokyo Institute of Technology (Japan)
**A. Lapucci,** Istituto Nazionale di Ottica Applicata (Italy)
**K. Maeno,** Chiba University (Japan)
**P. Mazzinghi,** Istituto Nazionale di Ottica Applicata (Italy)

**A. P. Napartovich,** Troitsk Institute for Innovation and Fusion Research (Russia)
**J. Reilly,** Northeast Science and Technology, Inc. (USA)
**S. Rosenwaks,** Ben-Gurion University of the Negev (Israel)
**S. Solimeno,** Università degli Studi di Napoli (Italy)
**A. Sona,** Università degli Studi dell'Insubria (Italy)
**O. Svelto,** Politecnico di Milano (Italy)
**M. Vannini,** Istituto di Elettronica Quantistica (Italy)
**W. S. Watt,** WSW Consulting (USA)

*Local Organizing Committee*

**Antonio Lapucci,** *Conference Chair*
**Tommaso Letardi,** *Program Chair*
**Cristina Pescucci,** *Operational Organization General Manager*
**Marco Ciofini,** *Information Systems, Proceedings Book Edition*
**Paolo Di Lazzaro,** *Author Assitance*
**Silvia Guidotti,** *Secretariat*
**Daniela Fubiani,** *Secretariat*
**Maria Teresa Civale,** *Logistic Organization*
**Luca Morelli,** *Accomodation and Side Events*
**Silvano Mascalchi,** *Audio/Visual Equipment*

*Session Chairs*

Chemical Lasers
**A. Lapucci,** Istituto Nazionale di Ottica Applicata (Italy)
**W. L. Bohn,** DLR (Germany)
**J. Kodymova,** Institute of Physics (Czech Republic)
**S. Rosenwaks,** Ben-Gurion University of the Negev (Israel)
**A. S. Boreysho,** Baltic State Technical University (Russia)

Solid State and Diode Lasers
**H. Hügel,** Universität Stuttgart (Germany)
**H. J. Baker,** Heriot-Watt University (UK)

UV-VUV Lasers
**T. Letardi,** Ente per le Nuove tecnologie, l'Energia e l'Ambiente (Italy)
**P. Di Lazzaro,** Ente per le Nuove tecnologie, l'Energia e l'Ambiente (Italy)

Gas Lasers
**R. Salimbeni,** Istituto di Elettronica Quantistica (Italy)
**D. R. Hall,** Heriot-Watt University (UK)

Laser Resonators
**J. Tulip,** University of Alberta (Canada)

Gas Flow in Lasers
**T. Fujioka,** Tokai University (Japan)

Beam Delivery and Propagation
**A. S. Boreysho,** Baltic State Technical University (Russia)

New Laser Media
**W. S. Watt,** WSW Consulting (USA)

High-Power Laser Applications
**K. Kasuya,** Tokyo Institute of Technology (Japan)
**T. Letardi,** Ente per le Nuove tecnologie, l'Energia e l'Ambiente (Italy)
**M. L. Autric,** University of Marseille (France)
**A. Lapucci,** Istituto Nazionale di Ottica Applicata (Italy)

# Introduction

GCL-HPL 2000, the XIII International Symposium on Gas Flow and Chemical Lasers and High-Power Laser Conference, took place at the Demidoff Hotel, in Pratolino, Florence, Italy, 18–22 September 2000. The meeting dealt with all the aspects of basic and applied research in high-power lasers, high-power beam characteristics and manipulation techniques, and laser/material interaction processes. It saw significant participation of attendees as well as submission of contributed papers. This was probably due to the coincidental occurrence of a few particular conditions. First of all, most laser-related large conferences have relegated gas and chemical lasers to a secondary role, considering these technologies to be already mature. This gives the GCL-HPL conference series a unique character. Furthermore, large efforts were made by the organizing and program committees to make the meeting as interesting and up-to-date as possible. Finally, the many places of interest in and around the city of Florence played a considerable role. The local organizers and tour operators did their best to make the social activities pleasant and attractive, maintaining the traditional high level of this symposium. In spite of this, the technical sessions benefitted from continuous and active participation of attendees, giving the feeling of general appreciation of the scientific program.

I personally went through the experience of more than one year of full immersion in the study and review of the different themes touched by the conference program, and I received the impression that there are numerous and quite active researchers in these fields. However, because of my organizing duties, I had very little time to exchange ideas during the conference. I did get in contact with most of the members of the community and it seems that for most of them fruitful and friendly exchanges were possible during the conference. It was a great honor for me to hear the same impressions of success from the international advisory committee members who attended all the previous GCL and GCL-HPL conferences.

My thanks go to all the attendees for their high-quality participation, and to the international advisory committee and program committee members who helped in manuscript review, selection work, and session chairing. A special thanks for the inestimable contribution to the conference series goes to the two members who decided to resign from the international advisory committee after this event: William Watt and Tommaso Letardi. The greatest acknowledgment goes to my colleagues Marco Ciofini and Cristina Pescucci, who made the event possible with their continuous and unlimited work. Lastly, tender thanks go to my little Tommaso and Valentina who had to leave me out of their games for some time, given the extra work I had.

At the final IAC meeting, which traditionally takes place at the end of the conference, we decided the venues of the two successive GCL-HPL events. The XIV Symposium will take place in Wrocław, Poland, 25–30 August 2002. Professor Krzysztof Abramski will be the next chair. It was also decided that the 2004 event will take place in Prague, Czech Republic, and will be chaired by Professor Jarmilá Kodymova. My best wishes to Krzysztof and Jarmilá for their upcoming work.

**Antonio Lapucci**

**Editor's Note**

The final section of this book is a paper presented during the 1998 GCL-HPL event. This paper was inadvertantly missing from the corresponding proceedings volume. Below is a message from the GCL-HPL'98 chairperson:

> The paper "Influence of x-ray preionization on the performance of a hf phototriggered laser," by S. Pasquiers, C. Postel, and V. Puech, was presented by the authors during the GCL-HPL'98 symposium in St. Petersburg. Unfortunately, the manuscript was lost. On behalf of the GCL-HPL'98 Organizing Committee, I ask the authors to accept our sincere apologies. At the same time, I appreciate Dr. Antonio Lapucci's help in resolving this matter.
> *Anatoly Boreysho, Chair of GCL-HPL'98, St. Petersburg*

Invited Paper

# The Airborne Laser

Steven E. Lamberson

Airborne Laser System Program Office
USAF Space & Missile Systems Center
Kirtland AFB, New Mexico

## ABSTRACT

The US Air Force Airborne Laser (ABL) is a major weapon system development by the United States Air Force to provide an airborne, multi-megawatt laser system with a state-of-the-art atmospheric compensation system to destroy enemy theater ballistic missiles at long ranges. This system will provide both deterrence and defense against the use of such weapons during regional conflicts. This paper provides an overview of the ABL weapon system including: the notional operational concept, the development approach and schedule, the overall aircraft configuration, the technologies being incorporated in the ABL, and the risk reduction approach being utilized to ensure program success.

Keywords: ABL, Beam Control, Fire Control, high energy lasers, illuminator lasers, ATP

## 1. INTRODUCTION

The US Air Force is developing the first ever directed energy weapon system for defense against theater ballistic missiles. This revolutionary weapon system will consist of a multi-megawatt chemical oxygen iodine laser integrated into a Boeing commercial 747-400 freighter. The primary mission of the ABL is to kill theater ballistic missiles in the boost phase of flight. The ABL also brings a number of other capabilities to the battlefield commander. The ABL will detect missiles shortly after cloud break and can provide near real time launch warning to the rest of the forces. In addition, the ABL will quickly and precisely locate the launch point, providing this information to attack operations. The ABL will pass trajectory information on to the subsequent tiers of the Theater Missile Defense (TMD) architecture. Finally, the ABL will provide accurate impact point predictions, shortly after burnout.

In addition to these inherent capabilities, the ABL's potential performance in a number of adjunct missions is being evaluated. As the ABL enters the Engineering Manufacturing and Development (EMD) phase, the Air Force will determine which if any of these capabilities to incorporate into the operational ABL weapon system. These include protection of High Value Assets from enemy surface-to-air and air-to-air missile systems, battlefield imaging using the large aperture telescope, battlefield command and control, cruise missile defense, and suppression of enemy air defenses.

## 2. SYSTEM OVERVIEW

The ABL is not intended to fight alone. It is an integral part of the overall TMD family of systems as shown in Fig. 1. It is being developed to provide depth to the TMD architecture. By killing missiles during the boost phase of flight, the ABL dramatically reduces the stress on midcourse and terminal systems, increasing their effectiveness and reducing their inventory requirements. In addition, some of the debris will fall on enemy territory.

XIII International Symposium on Gas Flow and Chemical Lasers and High-Power Laser Conference,
Antonio Lapucci, Marco Ciofini, Editors, Proceedings of SPIE Vol. 4184 (2001)

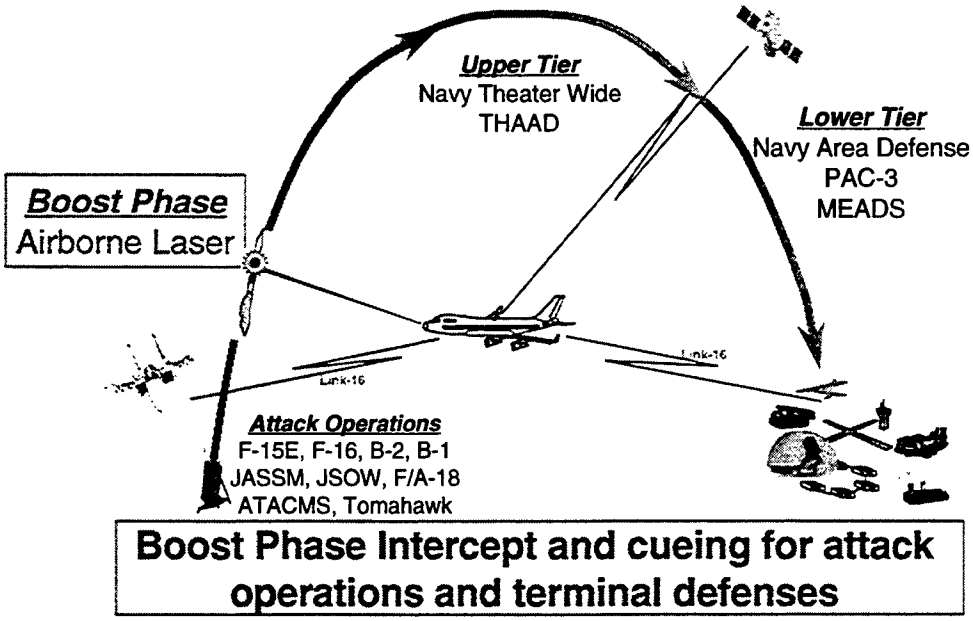


Figure 1. Theater Missile Defense Family of Systems

The ABL loiters above the clouds as shown in Fig. 2. As a ballistic missile exits the cloud layer, it is detected by the surveillance IR sensors surrounding the fuselage of the aircraft. The information from these sensors as well as the active ranger is used to quickly establish the trajectory(ies) of the target(s). The battle manager then selects the target to be engaged and passes the engagement off to the fire control subsystem. The fire control subsystem points the nose mounted turret toward the rnissile to be engaged, and acquires it in a boresighted IR camera mounted on the main gimbal of the turret.

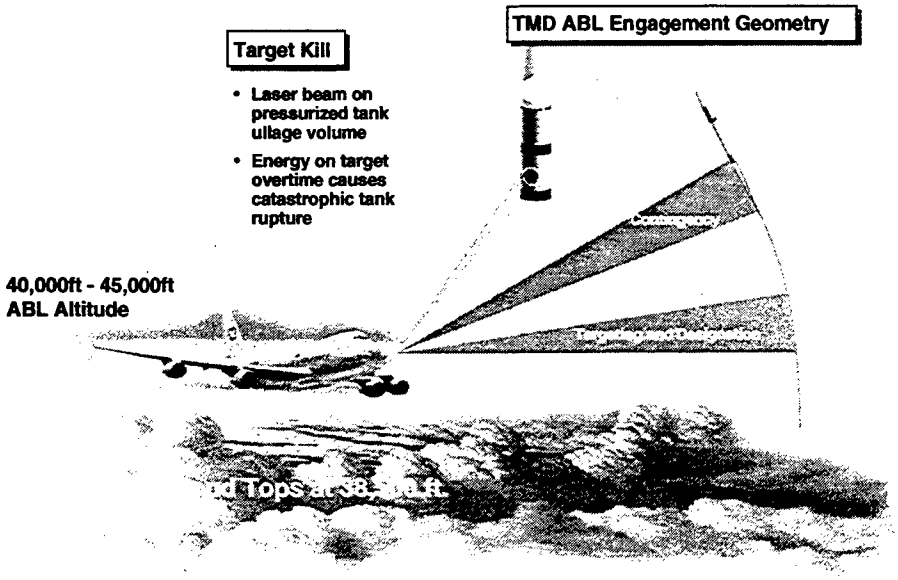


Figure 2. Typical ABL Engagement

The surveillance sensors surrounding the fuselage of the aircraft can detect launches at any azimuth as shown in Fig. 3. The high-energy laser has a large field of view, but cannot shoot out the back of the aircraft. Normally loitering is done such that the back is not turned to the expected launch area.

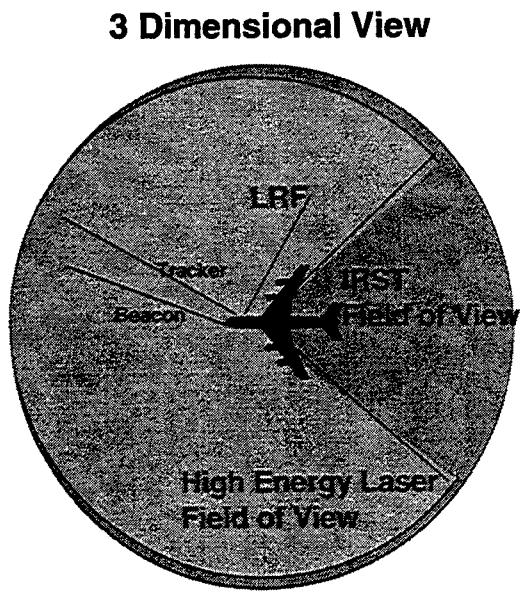


Figure 3. ABL Field of View

The ABL would typically be orbiting in friendly territory as shown in Fig. 4, supported by fighter CAP like other High Value Assets such as AWACS and JSTARS. The ABL is, however, an integrated part of the Air Battle and the location of the orbits will be flexible. The battlefield commander has the capability to locate the ABL when and where it is required depending on the air superiority picture.

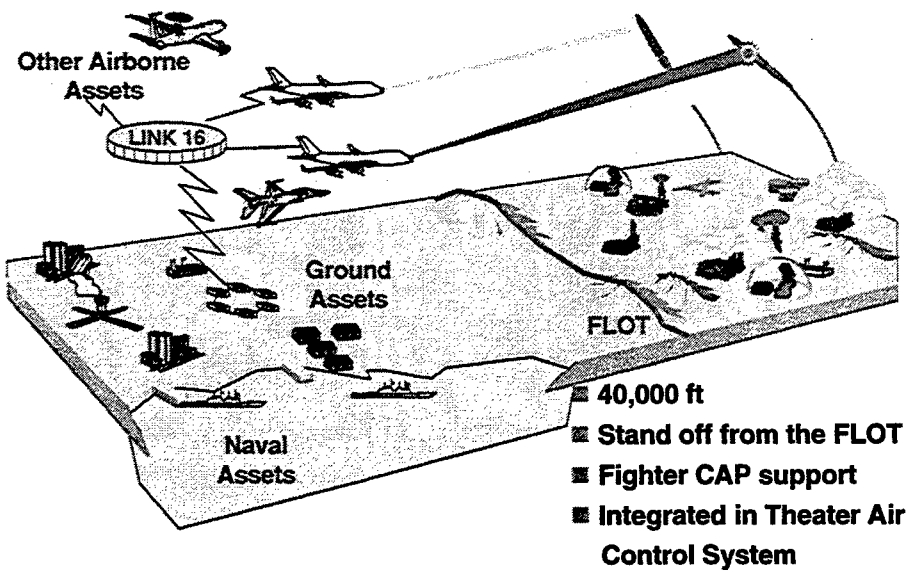


Figure 4. ABL Employment

The ABL is currently in the Program Definition and Risk Reduction (PDRR) phase. This phase culminates in the shoot down of a missile in 2003. The current plans are to build seven ABL aircraft. At most, two of those would be in maintenance at any one time. Therefore, five of the seven ABLs will be available at all times to rapidly deploy to theaters of potential conflict and maintain two orbits. The ABL arrives in theater fully loaded with laser fuel and ready for combat. A minimal resupply tail, airlifted in using cargo aircraft, maintains the ABL's ability to stay on orbit.

The PDRR ABL is a scaleable and traceable demonstration system. It is essentially identical to the EMD ABL except that it has a reduced number of modules in the laser systems as shown in Fig. 5. The PDRR ABL therefore gives a very high confidence demonstration of the ability of the operational ABL weapon system.

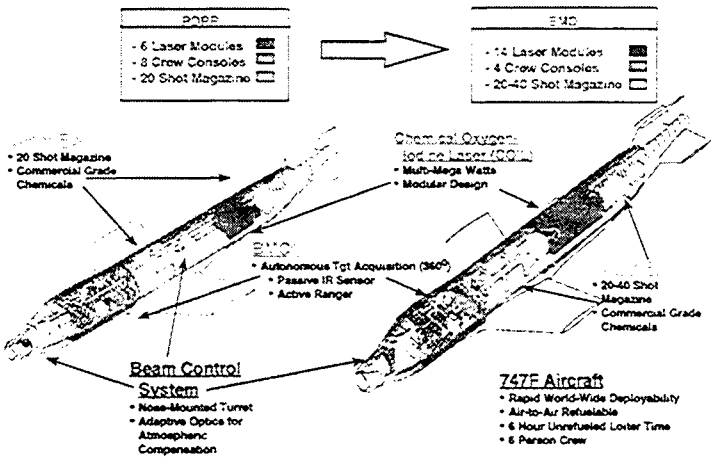


Figure 5. ABL Configuration

## 3. ABL ENGAGEMENT SEQUENCE

The engagement sequence is shown in Fig. 6. First, we pick up the missile in the surveillance sensor. The bright missile plume is easily detected as it breaks through the clouds. Next we hand off to the acquisition IR sensor mounted on the telescope gimbal. This relatively large field-of-view camera ensures that the gimbal is in fact pointed at the target and allows the target to be centered in the telescope aperture. Then we hand off to a shared aperture plume tracker. A hardbody handover algorithm is used based on information from the plume tracker to offset the telescope from the plume. Finally, we illuminate the missile hardbody with our target illuminator laser and establish fine track on the missile.

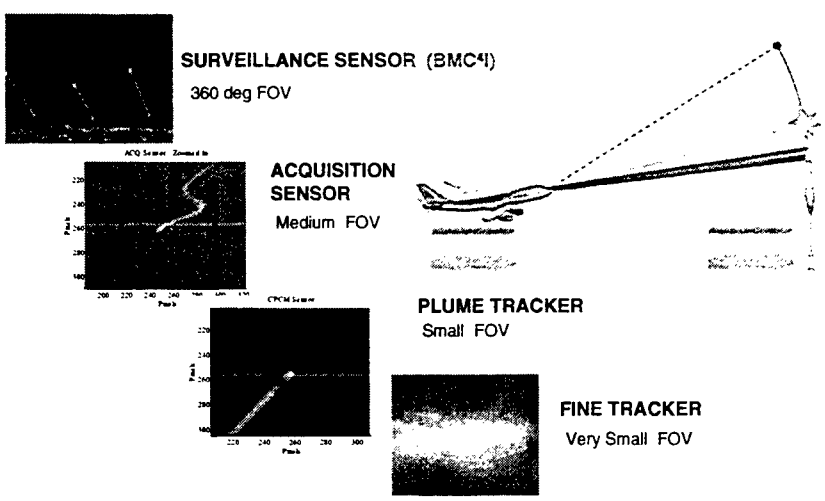


Figure 6. Engagement Sequence

To achieve performance over long ranges through the atmosphere, atmospheric compensation is used to partially correct the distortions imparted to the high-power laser beam by atmospheric turbulence as shown in Fig. 7. A beacon illuminator laser is used to illuminate a small spot on the target. The reflected light from the missile is distorted by the atmosphere as it travels to the aircraft. Wavefront sensors on the aircraft measure the phase distortions imparted to this reflected light beam as it

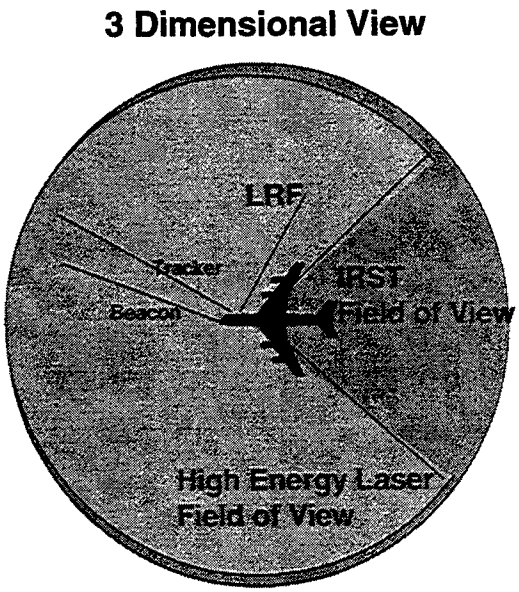


Figure 3. ABL Field of View

The ABL would typically be orbiting in friendly territory as shown in Fig. 4, supported by fighter CAP like other High Value Assets such as AWACS and JSTARS. The ABL is, however, an integrated part of the Air Battle and the location of the orbits will be flexible. The battlefield commander has the capability to locate the ABL when and where it is required depending on the air superiority picture.

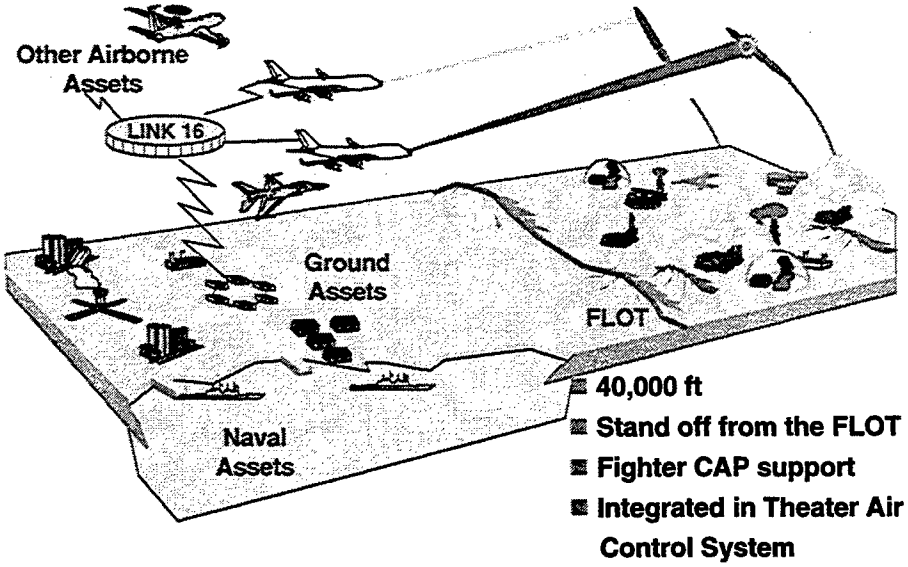


Figure 4. ABL Employment

The ABL is currently in the Program Definition and Risk Reduction (PDRR) phase. This phase culminates in the shoot down of a missile in 2003. The current plans are to build seven ABL aircraft. At most, two of those would be in maintenance at any one time. Therefore, five of the seven ABLs will be available at all times to rapidly deploy to theaters of potential conflict and maintain two orbits. The ABL arrives in theater fully loaded with laser fuel and ready for combat. A minimal resupply tail, airlifted in using cargo aircraft, maintains the ABL's ability to stay on orbit.

The PDRR ABL is a scaleable and traceable demonstration system. It is essentially identical to the EMD ABL except that it has a reduced number of modules in the laser systems as shown in Fig. 5. The PDRR ABL therefore gives a very high confidence demonstration of the ability of the operational ABL weapon system.

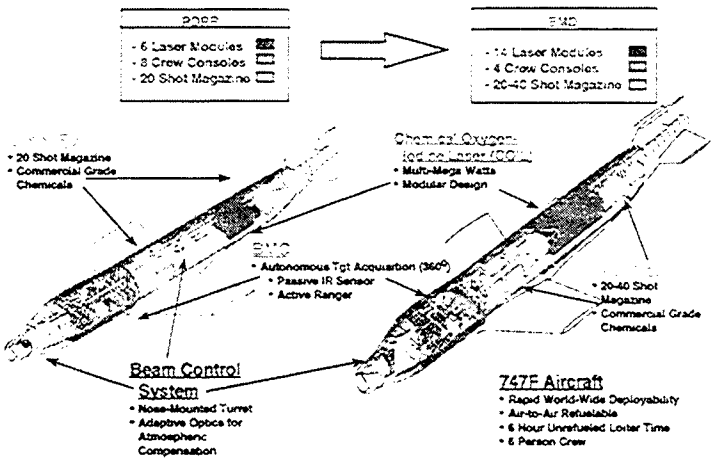


Figure 5. ABL Configuration

## 3. ABL ENGAGEMENT SEQUENCE

The engagement sequence is shown in Fig. 6. First, we pick up the missile in the surveillance sensor. The bright missile plume is easily detected as it breaks through the clouds. Next we hand off to the acquisition IR sensor mounted on the telescope gimbal. This relatively large field-of-view camera ensures that the gimbal is in fact pointed at the target and allows the target to be centered in the telescope aperture. Then we hand off to a shared aperture plume tracker. A hardbody handover algorithm is used based on information from the plume tracker to offset the telescope from the plume. Finally, we illuminate the missile hardbody with our target illuminator laser and establish fine track on the missile.

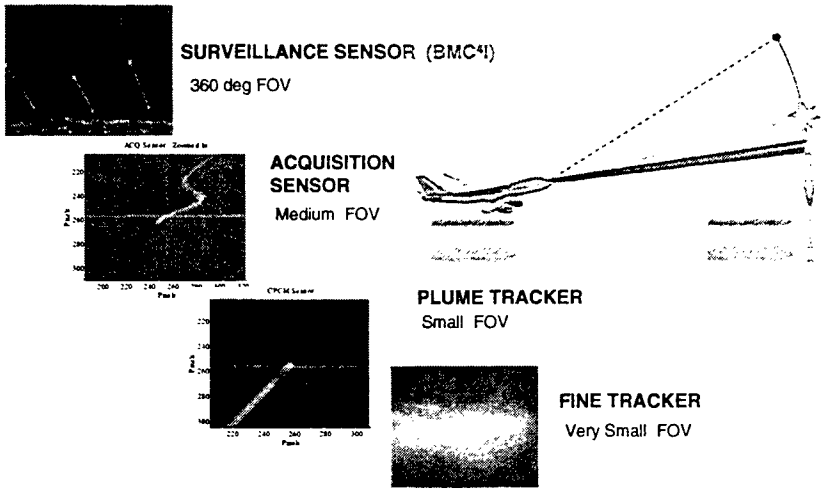


Figure 6. Engagement Sequence

To achieve performance over long ranges through the atmosphere, atmospheric compensation is used to partially correct the distortions imparted to the high-power laser beam by atmospheric turbulence as shown in Fig. 7. A beacon illuminator laser is used to illuminate a small spot on the target. The reflected light from the missile is distorted by the atmosphere as it travels to the aircraft. Wavefront sensors on the aircraft measure the phase distortions imparted to this reflected light beam as it

propagates from the target to the aircraft. The conjugate is placed on the outgoing laser beam using a deformable mirror, partially compensating for the effects of the atmosphere.

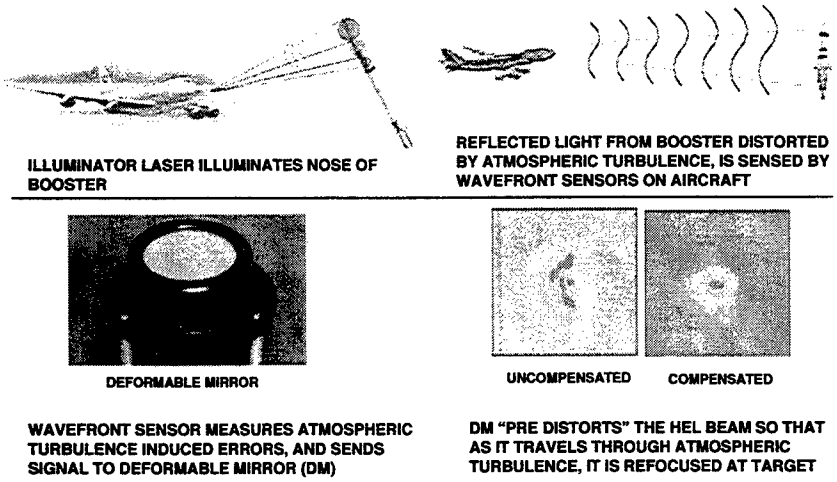


Figure 7. Atmospheric Compensation

## 4. ABL LASER AND BEAM CONTROL TECHNOLOGY

The ABL is enabled by over 20 years of laser technology development. The Airborne Laser Laboratory demonstrated the ability to integrate all the necessary subsystems to successfully destroy missiles in flight from an airborne platform in the late seventies and early eighties. More recent developments shown in Fig. 8 include the Chemical Oxygen Iodine Laser, allowing long range propagation due to its short wavelength (1.3 microns); adaptive optics, allowing extended range in the presence of atmospheric turbulence; and active tracking, allowing precise aimpoint maintenance on the target. In addition, lethality demonstrations demonstrated the ability to destroy missile targets using laser energy.

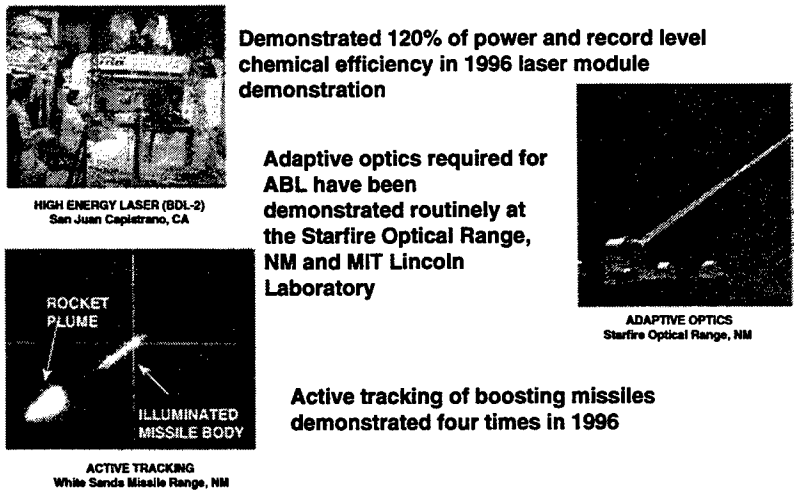


Figure 8. Enabling Technology

The ABL is built around a high power Chemical Oxygen Iodine Laser as shown in Fig. 9. The laser uses a single unstable resonator with a number of laser gain modules in series (6 for PDRR and 14 for EMD). Basic Hydrogen Peroxide (BHP) is sprayed through a large number of holes in an injector plate forming a droplet field. The helium-chlorine gas mixture is forced through this droplet field. At the surface of each droplet, the chlorine reacts with the OH ions, liberating singlet delta oxygen and the chlorine is trapped in the liquid as dissolved salt. The BHP is recirculated through a thermal management system, removing the heat generated during this process. The helium-singlet delta oxygen mixture is accelerated through a supersonic nozzle with iodine molecules injected in the flow immediately upstream of the nozzle throats. The singlet delta oxygen first dissociates the iodine molecules into iodine atoms, then excites the iodine atoms into the I* excited state, The 1.3-micron light beam is extracted using a standard unstable resonator. The drawing on the right is an isometric view of one of the laser modules.

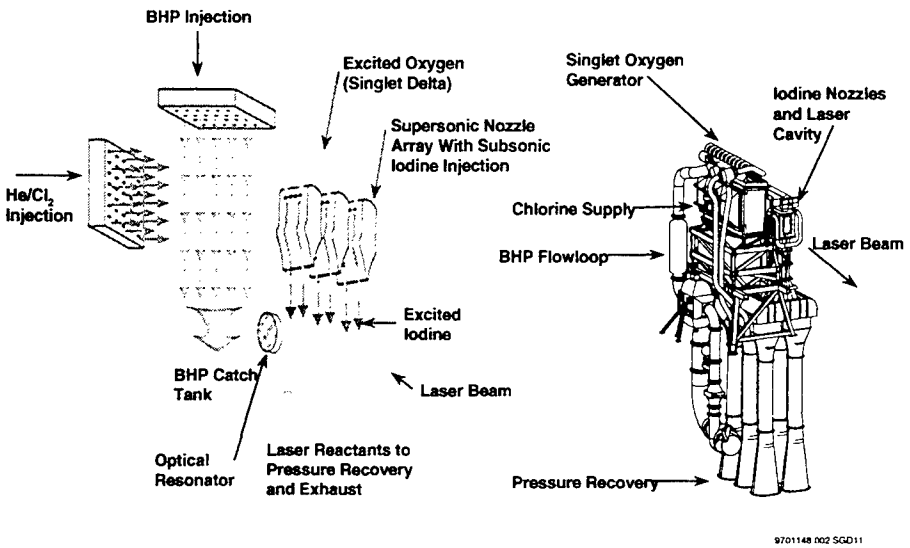


Figure 9. Chemical Oxygen Iodine Laser

The risk of the ABL laser development is being systematically bought down with a "build a little, test a little" approach. Prior to contract award in November 1996, the contractor had conducted laboratory and brassboard experiments to demonstrate the feasibility of producing the performance necessary for the ABL. This culminated with a demonstration from the brassboard, BDL2, of 120% of the ABL design power for a single module. The STET single injector tube tests, testing one of six ejectors to be used for each module, were completed, demonstrating the ability to operate the ejector systems necessary to provide pressure recovery on the aircraft. The flight weight laser module tests, demonstrating the ability to package the laser module to fit on the aircraft, were next. Future tests include an airworthiness test of a laser module, including the ejector system, and operation of six modules on the ground prior to installation on the aircraft.

The Airborne Laser will bring destruction at the speed of light to the battlefield, revolutionizing warfare. The ABL is a robust and flexible addition to the air battle, providing both deterrence and defense against the launch of theater ballistic missiles.

## ACKNOWLEDGEMENTS

This work is funded by the US Government, Department of Defense, and constitutes the contributions of the USAF Space and Missile Center, the Air Force Research Laboratory, and their contractors. Specific recognition is given to all the members of Team ABL for the design progress and risk reduction on the Airborne Laser Program.

Invited Paper

# Chemical Oxygen Iodine Laser (COIL) kinetics and mechanisms

Anatoly V. Komissarov, Vasily Goncharov, and Michael C. Heaven
Department of Chemistry, Emory University, Atlanta, GA 30322, USA

## ABSTRACT

The dissociation of $I_2$ by $O_2(a^1\Delta)$ is a critical process for the chemical oxygen iodine laser. Despite many years of study the dissociation mechanism is not properly understood. Currently accepted models assume that vibrationally excited $I_2$ is the immediate precursor to atomic I. However, studies of $I_2$ vibrational relaxation kinetics cast doubt on this assignment. New measurements of quenching rate constants for $I_2(A')$ indicate that electronically excited $I_2$ is a more likely precursor. A revised kinetic model for the dissociation process is proposed, based on the active participation of electronically excited $I_2$. Vibrationally excited $I_2$ remains an important species in this model as the $I_2$ must be vibrationally excited before the electronically excited states can be accessed. A preliminary rate constant package for the new model is presented.

## 1. INTRODUCTION

Chemiluminescence from flowing mixtures of $O_2(a^1\Delta)$ and $I_2$ was first examined by Arnold et al. [1] Intense emissions were observed from electronically excited $I_2$ and the $^2P_{1/2}$-$^2P_{3/2}$ transition of atomic iodine. Subsequent investigations of this system[2-5] led to the development of the chemical oxygen iodine laser (COIL)[6-8]. After thirty years of study a great deal is known about the kinetics that occur within the laser. However, the mechanism by which $I_2$ is dissociated by $O_2(a^1\Delta)$ remains poorly understood[9-13]. This represents an important gap in our knowledge as the dissociation process significantly impacts the efficiency of the laser. There are two mechanisms by which this occurs. First, it is known from empirical studies that an average of 4 to 6 $O_2(a^1\Delta)$ molecules are needed to dissociate one $I_2$ molecule[10,14-16]. Hence, the dissociation process consumes an appreciable amount of energy. Second, the time scale of the dissociation process influences energy extraction as it determines the downstream position at which the maximum concentration of $I(^2P_{1/2})$ (denoted as I* in the following) will occur. If the dissociation process takes place too slowly the maximum I* concentration is achieved after the gas has left the optical cavity. Alternatively, if high concentrations of I* are formed before reaching the optical cavity, energy is lost during transport (mostly due to quenching by $H_2O$ from the $O_2(a)$ generator). This leads to a curious situation where the conditions that give maximum power from the laser do not correspond to complete dissociation of $I_2$[16,17].

The efficiency and time scale of the dissociation process depend on concentration ratios, mixing dynamics and total pressure. At present our ability to design new types of mixing nozzles and/or develop systems that operate at higher pressures is limited, in part, by our poor understanding of the dissociation kinetics. In the following we briefly review the currently accepted mechanism for the dissociation process and draw attention to some of the ambiguities that are inherent in the model. Recent experimental studies of key reactions are described, and a revised kinetic model of the dissociation process is proposed. This model resolves some of the ambiguities and it is characterized by a family of physically reasonable rate constants. It should provide a better description of the dissociation process for conditions that are significantly different from those used in conventional COIL devices.

## 2. PREVIOUSLY PROPOSED MECHANISMS FOR DISSOCIATION OF $I_2$ BY $O_2(a^1\Delta)$

At least two $O_2(a^1\Delta)$ molecules are needed to dissociate $I_2$. Arnold et al.[1] proposed two plausible dissociation mechanisms. The first involved direct dissociation by energy transfer from $O_2(b^1\Sigma^+)$, the latter being

XIII International Symposium on Gas Flow and Chemical Lasers and High-Power Laser Conference,
Antonio Lapucci, Marco Ciofini, Editors, Proceedings of SPIE Vol. 4184 (2001)

produced by the energy pooling process $O_2(a^1\Delta)+O_2(a^1\Delta)\rightarrow O_2(b^1\Sigma^+)+O_2(X^3\Sigma^-)$ {1}[a]. In the second model $I_2$ was excited by the energy transfer process $O_2(a^1\Delta)+I_2\rightarrow O_2(X^3\Sigma^-)+I_2^\dagger$ {32}. The excited intermediate was then dissociated by the step $O_2(a^1\Delta)+I_2^\dagger\rightarrow O_2(X^3\Sigma^-)+2I$ {34}. Arnold et al.[1] did not specifically identify $I_2^\dagger$, but they speculated that it could be an electronically excited state ($I_2(A')$ and/or $I_2(A)$) or vibrationally excited $I_2(X)$. The idea that $I_2$ could be electronically excited by collision with a single $O_2(a^1\Delta)$ molecule was discounted when it was discovered that the lowest lying excited state ($I_2(A')$) was energetically inaccessible. Derwent and Thrush[5] found that dissociation by $O_2(b^1\Sigma^+)$ could fit their dissociation rate data, provided that the rate constant for this process was near the gas kinetic limit ($\approx 2\times10^{-10}$ cm$^3$ s$^{-1}$). This model was set aside when it was found[18,19] that the rate constant for quenching of $O_2(b^1\Sigma^+)$ by $I_2$ was no more than $2\times10^{-11}$ cm$^3$ s$^{-1}$.

The most careful and exhaustive study of the dissociation mechanism was carried out by Heidner et al.[9] They obtained conclusive evidence that an excited state of $I_2$ was involved. They also found that the dissociation rate increased dramatically as atomic I was liberated. This acceleration was attributed to the chain branching reactions

$$O_2(a^1\Delta)+I\rightarrow O_2(X^3\Sigma^-)+I^* \qquad \{40\}$$

$$I^*+I_2\rightarrow I+I_2^\dagger \qquad \{33\}$$

Hiedner et al.[9] were unable to resolve the uncertainty concerning the identity of $I_2^\dagger$. Based on the fact that Hall and Huston[20] observed vibrationally excited $I_2$ resulting from reaction 33 they favored the notion that $I_2^\dagger$ was the vibrationally excited species. Subsequently, Van Bentham and Davis[10] showed that vibrationally excited $I_2$ ($I_2(X, v>33)$) was present in flowing $O_2(a^1\Delta)/I_2$ mixtures.

Despite the circumstantial evidence there are problems with the assumption that $I_2^\dagger$ is the vibrationally excited species. Heidner et al.[9] found that relatively high pressures of the Ar buffer gas used in their experiments did not influence the $I_2$ dissociation rate. This was unexpected as $I_2^\dagger$ should be vibrationally relaxed by collisions with Ar[20]. Problems were encounterd in attempts to model the dissociation rate data. The mechanism assumed by Heidner et al.[9] has strong correlations between several sets of rate constants, so they were unable to find a unique solution. Two sets of rate constants, representative of viable limiting cases, were proposed. Some of the rate constants differ by more than an order of magnitude between the two models. The one parameter that was well defined in both models, the rate constant for deactivation of $I_2^\dagger$ by $H_2O$, was gas kinetic ($k_{36}=3\times10^{-10}$ cm$^3$ s$^{-1}$). This is an unusually large value for vibrational relaxation.

Heidner et al.[9] reported that neither of their kinetic models provided an adequate representation of all of the kinetic data. Unfortunately they could not delve into this problem any further. Their model 1 rate constants were adopted in the standard kinetics package[21,22] that is used for most computational simulations of COIL devices.

## 3. PROBING THE IDENTITY OF $I_2^\dagger$

Although the kinetic properties of $I_2^\dagger$ did not appear to fit with conventional notions of vibrational relaxation processes, this was not sufficient grounds for dismissing the assignment to $I_2(X, v>20)$. Perhaps the relaxation dynamics of these highly excited vibrational levels was markedly different from the behavior observed for the lower levels. To examine this possibility Heaven and co-workers[23-26] measured ro-vibrational relaxation rate constants for $I_2(X)$ vibrational levels in the range $23\leq v\leq 42$ (i.e. the levels populated by energy transfer from I* and $O_2(a^1\Delta)$). In these experiments pulsed lasers were used to excited isolated ro-vibrational levels of $I_2(X)$. Delayed probe laser pulses were used to monitor the range of ro-vibrational levels populated by collisions with a variety of energy transfer agents (He, Ar, $O_2$, $N_2$, $Cl_2$, and $H_2O$). The primary findings were that vibrational relaxation of $I_2(X,v\geq 23)$ followed the trends predicted by

[a] The numbering of reactions is chosen to be consistent with the standard package[21,22]. The number for each reaction is given in curly brackets.

well-established theoretical models[26]. Vibrational relaxation was five to ten times slower than rotational energy relaxation, and was dominated by single quantum transfer events ($\Delta v=-1$). Kinetic modeling was needed to relate these measurements to $I_2^\dagger$ removal rate constants. Energy transfer from I* and $O_2(a^1\Delta)$ populates $I_2(X)$ levels around v=40, whereas levels with v>20 have enough energy to be dissociated by $O_2(a^1\Delta)$. Models for descending the vibrational ladder from v=40 to 20 by successive $\Delta v=-1$ steps were used to predict the vibrational deactivation rate constants (denoted here by $k_M^\dagger$). For $H_2O$ this procedure yielded $k_{H_2O}^\dagger=5\times10^{-12}$ cm$^3$ s$^{-1}$, which is a factor of 60 smaller than the value required by the models of Heidner et al.[9] Vibrational deactivation rate constants for $O_2(X)$ and Ar were $3\times10^{-12}$ and $2\times10^{-12}$ cm$^3$ s$^{-1}$ respectively. The most informative way to compare these results with the rate constants used in the models of Heidner et al.[9] is to compare ratios, as this removes some of the correlation problems. Vibrational relaxation measurements yielded the ratios $k_{H_2O}^\dagger / k_{O_2}^\dagger=1.7$ and $k_{O_2}^\dagger / k_{Ar}^\dagger=2.5$, whereas the corresponding ratios for Heidner's model 1 (model 2) were 5.0 (50) and 12.5 (500).

The large disparities between vibrational relaxation parameters and rate constants derived from the models of Heidner et al.[9] indicate that either $I_2^\dagger$ is not vibrationally excited $I_2$ or that the kinetic model has enough flexibility to accommodate the experimental values for the vibrational deactivation rate constants. The latter possibility was explored by Paschkewitz and Heaven[13], who re-analyzed the data of Heidner et al.[9] An attempt was made to improve the definition of some of the poorly known rate constants by performing constrained least squares fits to the dissociation rate data. The results of this exercise gave a slightly improved representation of the data, as compared to the original models 1 and 2. However, the most troubling problems could not be resolved. The value for $k_{H_2O}^\dagger$ could not be reduced below $4.8\times10^{-11}$cm$^3$s$^{-1}$, which was still too fast, and the upper bound for deactivation by Ar, $k_{Ar}^\dagger<2\times10^{-14}$ cm$^3$ s$^{-1}$ was much too low.

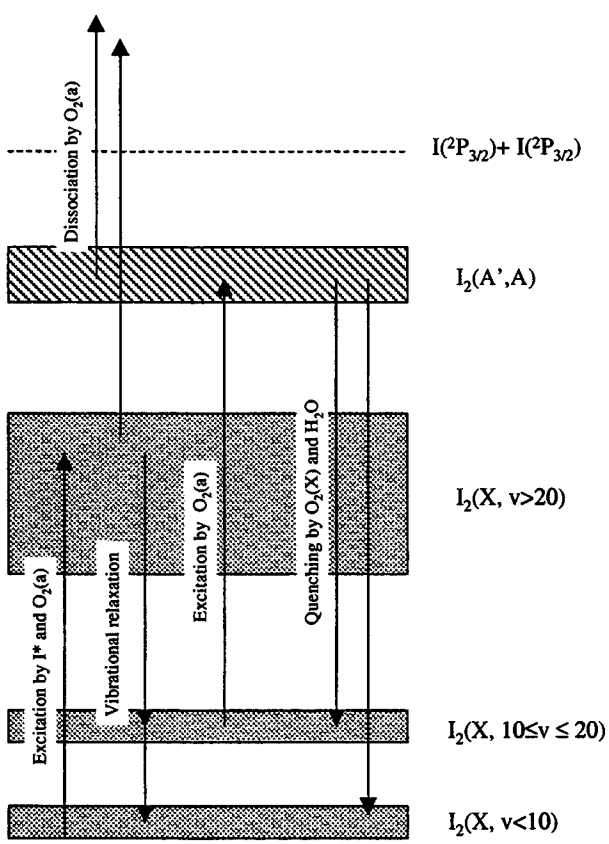

Figure 1. Schematic of the proposed dissociation mechanism

Several previous investigators have noted that deactivation of $I_2^\dagger$ is more reminiscent of electronic quenching than vibrational relaxation. It is known that both $I_2(A')$ and $I_2(A)$ are present in flowing mixtures of $O_2(a^1\Delta)$ and $I_2$. Drawing on these observations Bacis and co-workers[11,12,27] proposed multi-step dissociation mechanisms that included electronically excited $I_2$ as an important intermediate. The specific scheme that is relevant to the present discussion is illustrated in Fig. 1. In this model it is assumed that electronic excitation of $I_2(A',A)$ by $O_2(a^1\Delta)$ is governed by the Franck-Condon principle. This predicts that $I_2(X)$ levels in the range $10\leq v\leq15$ will be most receptive for electronic energy transfer. Experimental evidence supporting this assumption was obtained by Barnault et al.[27] The kinetic implications of the scheme outlined in Fig.1 were explored most recently by

Paschkewitz and Heaven[13]. Channels involving electronically excited $I_2$ were added to the standard COIL model and attempts were made to re-optimize the rate constant package by fitting the $I_2$ dissociation rate data. In this initial study the rate constant for the reaction

$$I_2(X, v>20) + O_2(a^1\Delta) \rightarrow 2I + O_2(X^3\Sigma^-) \qquad \{34\}$$

was not reduced below $k_{34}=1.5\times10^{-11}$ $cm^3$ $s^{-1}$ (1/20 the value used in the standard package). With such rapid dissociation of $I_2(X, v>20)$ the channel through the electronically excited states could not make a significant contribution. The preliminary indications were that the deficiencies of the standard model could not be overcome by including the participation electronically excited $I_2$.

Restricting the range of values considered for $k_{34}$ is somewhat arbitrary as there are no direct experimental data for this process. Further reduction of $k_{34}$ forces the dissociation process to proceed via electronic excitation of $I_2$. Under these conditions the kinetics become sensitive to electronic quenching of $I_2(A',A)$. A model of this form has the potential to give a good representation of the dissociation rate data, provided that quenching by Ar is very slow and that $H_2O$ is more effective than $O_2(X)$ in dissipating energy from $I_2(A',A)$. It is probable that both the A' and A states of $I_2$ exhibit similar quenching kinetics. Hence, for simplicity the remainder of this discussion is focused on $I_2(A')$ (in addition, this species is appreciably more metastable than $I_2(A)$). Tellinghuisen and Phillips[28] have shown that quenching of $I_2(A')$ by Ar is slow ($k=2.8\times10^{-14}$ $cm^3$ $s^{-1}$) and that the primary mechanism of this process is collision induced dissociation. This is encouraging, but data for quenching by $O_2(X)$ and $H_2O$ were needed to further examine the role of $I_2(A')$ in the dissociation process.

## 4. STUDIES OF THE QUENCHING OF $I_2(A')$ BY $O_2(X)$ AND $H_2O$

As the required rate constants for quenching of $I_2(A')$ by $O_2$ and $H_2O$ were not available we measured these parameters using pulsed laser pump-probe techniques. To populate the A' state a mixture of $I_2$ in Ar was excited by 193 nm pulses from an ArF laser.[28] This initially promotes $I_2$ to the $D(0_u^+)$ state. Collisions with Ar rapidly induce transfer to the $D(2_g)$ state, which then radiates down to $A'^3\Pi(2_u)$. This sequence occurs within the radiative lifetimes of the D and D' states (approximately 10 ns). The population in the A' state was monitored by probe laser excitation of the D'←A' transition[29]. Loss of population from A' was followed by varying the delay between the pump and probe lasers. For low concentrations of $I_2$ in 20 Torr of pure Ar the A' state decayed with a lifetime of about 30 μs. This was consistent with the earlier study by Tellinghuisen and Phillips[28]. Metered quantities of $O_2$ or $H_2O$ were added to the $I_2$/Ar mixtures to observe quenching by these collision partners. The quenching rate constants were found to be $(6.3\pm0.6)\times10^{-12}$ and $(3.4\pm0.4)\times10^{-12}$ $cm^3$ $s^{-1}$ for $O_2(X)$ and $H_2O$, respectively.

These measurements showed that both $O_2$ and $H_2O$ are much more effective quenchers of $I_2(A')$ than Ar. However, Heidner et al.'s[9] models require $H_2O$ to be a better deactivator of $I_2^\dagger$ than $O_2$ whereas the present measurements indicate the opposite trend. This apparent disagreement can be resolved if quenching by $O_2$ is dominated by the Franck-Condon favored transfer process

$$I_2(A') + O_2(X^3\Sigma^-) \rightarrow I_2(X, v>10) + O_2(a^1\Delta) \qquad \{28\}$$

Data for matrix isolated $I_2/O_2$ mixtures shows that this is, indeed, a facile transfer process[30].

## 5. REVISED KINETIC MODEL FOR THE DISSOCIATION OF $I_2$ BY $O_2(a^1\Delta)$.

To further test the hypothesis that $I_2(A')$ is a significant dissociation intermediate, a new kinetic model of the dissociation process has been examined. This model is based on the standard reaction set with the addition of reactions involving $I_2(X, 10<v<20)$ and $I_2(A')$, and modification of some of the standard package rate constants. The full set of reactions and rate constants is listed in Table 1. Numerical integration of the coupled rate equations was used to predict $I_2(X)$ removal kinetics[13]. Several rate constants were manually adjusted to achieve reasonable agreement with the dissociation rate data of Heidner et al.[9] The revised model gives a significantly better fit to the experimental data than the standard package. From a chemical physics perspective the most appealing aspect of the model is that the rate constants all have magnitudes that are appropriate for the types of process that they are associated with. Note that the specific values for the rate

constants in Table 1 are not unique and they are not fully optimized. Further improvements could be achieved by coupling the differential equation solver with a non-linear least squares fitting routine.

Table 1. Kinetic scheme used to simulate the experimental data of Heidner et al.[9]

| Reaction # | Reaction | Rate Constant/ $cm^3\ s^{-1}$ |
|---|---|---|
| | | |
| 1 | $O_2(a)+O_2(a)\rightarrow O_2(b)+O_2(X)$ | $2.7\times10^{-17}$ |
| 21 | $O_2(b)+I_2\rightarrow O_2(X)+2I$ | $4.0\times10^{-12}$ |
| 40 | $O_2(a)+I\rightarrow O_2(X)+I^*$ | $7.6\times10^{-11}$ |
| 41 | $O_2(X)+I^*\rightarrow O_2(a)+I$ | $2.6\times10^{-11}$ |
| 44 | $O_2(a)+I^*\rightarrow O_2(b)+I$ | $1.1\times10^{-13}$ |
| 32 | $O_2(a)+I_2\rightarrow O_2(X)+I_2^{**}$ | $\mathbf{2.0\times10^{-14}}$ |
| 34 | $O_2(a)+I_2^{**}\rightarrow O_2(X)+2I$ | $\mathbf{1\times10^{-13}}$ |
| **27** | $\mathbf{O_2(X)+I_2^{**}\rightarrow O_2(X)+I_2^*}$ | $\mathbf{3\times10^{-12}}$ |
| **39** | $\mathbf{H_2O+I_2^{**}\rightarrow H_2O+I_2^*}$ | $\mathbf{5\times10^{-12}}$ |
| **38** | $\mathbf{I_2^*+O_2(a)\rightarrow I_2(A')+O_2(X)}$ | $\mathbf{6\times10^{-12}}$ |
| 25 | $I_2(A')+O_2(a)\rightarrow 2I+O_2(X)$ | $\mathbf{2\times10^{-10}}$ |
| **28** | $\mathbf{I_2(A')+O_2(X)\rightarrow I_2^*+O_2(a)}$ | $\mathbf{6.3\times10^{-12}}$ |
| **29** | $\mathbf{I_2(A')+H_2O\rightarrow I_2+H_2O}$ | $\mathbf{3.4\times10^{-12}}$ |
| **63** | $\mathbf{I_2^*+H_2O\rightarrow I_2+H_2O}$ | $\mathbf{1.2\times10^{-12}}$ |
| **64** | $\mathbf{I_2^*+O_2(X)\rightarrow I_2+O_2(X)}$ | $\mathbf{1.5\times10^{-12}}$ |
| **65** | $\mathbf{I_2^{**}+Ar\rightarrow I_2^*+Ar}$ | $\mathbf{2.0\times10^{-12}}$ |
| **66** | $\mathbf{I_2^*+Ar\rightarrow I_2+Ar}$ | $\mathbf{2.0\times10^{-13}}$ |
| 33 | $I^*+I_2\rightarrow I+I_2^{**}$ | $3.5\times10^{-11}$ |
| 5 | $O_2(b)+H_2O\rightarrow O_2(X)+H_2O$ | $5.5\times10^{-12}$ |
| 48 | $I^*+H_2O\rightarrow I+H_2O$ | $2.0\times10^{-12}$ |
| **67** | $\mathbf{O_2(b)+I_2^*\rightarrow O_2(X)+2I}$ | $\mathbf{3.0\times10^{-12}}$ |

Boldface type is used to indicate reactions that are not part of the standard package and rate constants that have been assigned values that are different to those used in the standard package. The reaction numbering scheme is chosen to be consistent with Table 1 of reference 22. $I_2^{**}$ is $I_2(X,v>20)$ and $I_2^*$ is $I_2(X,\ 10\leq v<20)$.

## 6. CONCLUSION

The currently accepted model for the dissociation of $I_2$ by $O_2(a^1\Delta)$ assumes that vibrationally excited $I_2$ is the immediate precursor for atomic iodine. However, kinetic models based on this assumption lead to predictions of physically unreasonable rate constants for deactivation of $I_2^\dagger$ by $H_2O$ and Ar. New measurements for the quenching of $I_2(A')$ by $H_2O$ and $O_2(X)$ support the idea that electronically excited $I_2$ may be the dominant I atom precursor. A kinetic model of the dissociation process that includes electronically excited $I_2$ gives a better fit to dissociation rate data than the standard model. Although we have not developed a unique set of rate constants for the new model, a physically reasonable solution is presented. The primary finding is that dissociation via an electronically excited $I_2$ intermediate provides an improved description of the dissociation process.

## ACKNOWLEDGMENT

The authors are grateful to AFOSR for the support of this work under grant AFOSR F49620-98-1-0054

## REFERENCES


1 S. J. Arnold, N. Finlayson, and E. A. Ogryzlo, *J. Chem. Phys.* **44,** 2529 (1966).

2 R. G. Derwent, D. R. Kearns, and B. A. Thrush, *Chem. Phys. Lett.* **6,** 115-16 (1970).

3 R. G. Derwent and B. A. Thrush, *Chem. Phys. Lett.* **9,** 591-2 (1971).

4 R. G. Derwent and B. A. Thrush, *Faraday Discuss. Chem. Soc.* **No. 53,** 162-7 (1972).

5 R. G. Derwent and B. A. Thrush, *J. Chem. Soc., Faraday Trans. 2* **68,** 720-8 (1972).

6 W. E. McDermott, N. R. Pchelkin, D. J. Benard, and R. R. Bousek, *Appl. Phys. Lett.* **32,** 469-70 (1978).

7 D. J. Benard, W. E. McDermott, N. R. Pchelkin, and R. R. Bousek, *Appl. Phys. Lett.* **34,** 40-1 (1979).

8 K. A. Truesdell, C. A. Helms, and G. D. Hager, *Proc. SPIE-Int. Soc. Opt. Eng.* **2502,** 217-37 (1995).

9 R. F. Heidner, III, C. E. Gardner, G. I. Segal, and T. M. El-Sayed, *J. Phys. Chem.* **87,** 2348-60 (1983).

10 M. H. Van Benthem and S. J. Davis, *J. Phys. Chem.* **90,** 902-5 (1986).

11 D. Cerny, R. Bacis, A. J. Bouvier, S. Poulat, A. Topouzkhanian, and J. Verges, *J. Quant. Spectrosc. Radiat. Transfer* **47,** 9-18 (1992).

12 A. J. Bouvier, R. Bacis, A. Bouvier, D. Cerny, S. Churassy, P. Crozet, and M. Nota, *J. Quant. Spectrosc. Radiat. Transfer* **49,** 311-23 (1993).

13 J. S. Paschkewitz and M. C. Heaven, *Proc. SPIE-Int. Soc. Opt. Eng.* **3931A,** 169-178 (2000).

14 G. D. Hager, C. A. Helms, K. A. Truesdell, D. Plummer, J. Erkkila, and P. Crowell, *Proc. Int. Conf. Lasers* **18th,** 219-224 (1996).

15 B. D. Barmashenko, A. Elior, E. Lebiush, and S. Rosenwaks, *Proc. SPIE-Int. Soc. Opt. Eng.* **1810,** 513-16 (1993).

16 B. D. Barmashenko and S. Rosenwaks, *AIAA J.* **34,** 2569-2574 (1996).

17 C. A. Helms, J. Shaw, G. D. Hager, K. A. Truesdell, D. Plummer, and J. Copland, *Proc. SPIE-Int. Soc. Opt. Eng.* **2502,** 250-7 (1995).

18 R. G. Aviles, D. R. Muller, and P. L. Houston, *Appl. Phys. Lett.* **37,** 358 (1980).

19 D. F. Muller, R. H. Young, P. L. Houston, and J. R. Wiesenfeld, *Appl. Phys. Lett.* **38,** 404-6 (1981).

20 G. E. Hall, W. J. Marinelli, and P. L. Houston, *J. Phys. Chem.* **87,** 2153-61 (1983).

21 G. P. Perram and G. D. Hager, (Air Force Weapons Lab.,Kirkland AFB,NM,USA., (1988), pp. 33

22 G. P. Perram, *Int. J. Chem. Kinet.* **27,** 817-28 (1995).

23 M. L. Nowlin and M. C. Heaven, *J. Phys. IV* **4,** C4/729-C4/737 (1994).

24 W. G. Lawrence, T. A. VanMarter, M. L. Nowlin, and M. C. Heaven, *Proc. SPIE-Int. Soc. Opt. Eng.* **2702,** 214-225 (1996).

25 M. L. Nowlin and M. C. Heaven, *J. Chem. Phys.* **99,** 5654-60 (1993).

26 W. G. Lawrence, T. A. Van Marter, M. L. Nowlin, and M. C. Heaven, *J. Chem. Phys.* **106,** 127-141 (1997).

27 B. Barnault, A. J. Bouvier, D. Pigache, and R. Bacis, *J. Phys. IV* **1,** C7/647-C7/650 (1991).

28 J. Tellinghuisen and L. F. Phillips, *J. Phys. Chem.* **90,** 5108 (1986).

29 X. Zheng, S. Fei, M. C. Heaven, and J. Tellinghuisen, *J. Chem. Phys.* **96,** 4877-83 (1992).

30 M. Macler, J. P. Nicolai, and M. C. Heaven, *J. Chem. Phys.* **91,** 674-82 (1989).

Invited Paper

# Review of the US Air Force Research Laboratory's 10-kW RADICL laser

Charles A. Helms*
Directed Energy Directorate, US Air Force Research Laboratory
3550 Aberdeen Ave SE, Kirtland Air Force Base, NM 87117

## ABSTRACT

The US Air Force Research Laboratory has actively pursued the development of the Chemical Oxygen-Iodine Laser (COIL) since its invention in 1977[1]. The power scaling potential of the COIL was verified in the late 1980's on the RotoCOIL device, which was later decommissioned. A smaller COIL teststand (ReCOIL) was then upgraded with a rotating-disk oxygen generator and a variable-height slit nozzle to become the principal testbed for continued COIL development. The modified device was named the Research Assessment Device Iodine Chemical Laser (RADICL). RADICL has supported several major test campaigns during the past 9 years, many of which have been published. These include 2-D gain maps[2], iodine dissociation studies[3], magnetic gain-switching demonstrations[4], mode-locking[5], metal cutting/fiber delivery demonstrations, and more recently measurements of water concentration and oxygen yield[6]. A review of the major results of these test programs and previously unpublished data are presented.

**Keywords:** chemical oxygen-iodine laser, RADICL, COIL, oxygen-iodine laser research

## 1. INTRODUCTION

Since the first demonstration of the laser, military use of this technology has been pursued. One military application of lasers involves the use of high power lasers at long ranges within the earth's atmosphere. This type of mission carries with it a number of requirements for the laser system: high power, good beam quality, and good atmospheric propagation. It is also desirable to operate at a relatively short wavelength to permit the use of reasonably sized optics.

The United States Air Force has conducted a vigorous research program to develop candidate laser systems for high power laser missions. This effort spawned the first demonstration of the chemical oxygen-iodine laser (COIL) in 1977. The COIL is driven by a chemical reaction between gaseous chlorine and an aqueous basic hydrogen peroxide solution (BHP) that yields electronically-excited oxygen ($O_2(a^1\Delta)$) as one of the reaction products. The singlet-delta oxygen in turn transfers energy via collisions to atomic iodine which lases at 1.315 microns.

COIL technology has matured over the past 23 years from the initial demonstration to enabling major military programs such as the Air Force's Airborne Laser (ABL). The High Power Gas Lasers Branch of the Air Force Research Laboratory has played a significant role in the development of COIL. Perhaps the most significant COIL demonstration was the RotoCOIL test program conducted in the late 1980's where scaling to 25 kW was verified. Following the deactivation of RotoCOIL, the ReCOIL laser, a 1-2 kW sparger driven COIL, was upgraded and renamed RADICL. The upgrades included replacing the sparger oxygen generator with a rotating disk oxygen generator similar to the generators used on the RotoCOIL program. The 25-cm by 0.89-cm slit nozzle was replaced with a variable-slit nozzle adjustable from 0.38 cm to 2.16 cm. The ability to mix BHP external to the generator and flow BHP through the generator while lasing were also added. The upgrade from a sparger type oxygen generator to a rotating disk generator allowed the nominal chlorine flowrate to be increased from 0.15 mol/s to 0.5 mol/s.

* Correspondence: Email: charles.helms@kirtland.af.mil; Telephone: 505 846-0718; Fax: 505 853-0485

XIII International Symposium on Gas Flow and Chemical Lasers and High-Power Laser Conference,
Antonio Lapucci, Marco Ciofini, Editors, Proceedings of SPIE Vol. 4184 (2001)

## 2. HARDWARE CONFIGURATIONS

RADICL has had several configurations during its 9 year existence. The initial (nominal) configuration consisted of: 38 cm-diameter rotating disk generator, a transition duct to mate the generator exit dimensions of 20 cm by 20 cm to 25 cm wide by 7.6 cm high, an adjustable height slit nozzle set at 25 cm by 0.89 cm, and a cavity total ramp expansion angle of 6 degrees (fig 1). Iodine and helium were injected approximately 1 cm upstream of the slit nozzle through 2 rows of holes on each of the upper and lower walls of the main flow duct (fig 2). Each upstream row contained 115 holes of 0.81 mm diameter and each downstream row contained 232 holes of 0.406 mm diameter. The expansion section of the nozzle was designed by the method of characteristics to provide relatively shock-free expansion using standard COIL gas flow and provided a factor of 2 area increase at the nominal throat height of 0.89 cm. The original configuration did not include mirror boxes or bank blowers, and used 50 mm optics to outcouple power. The initial configuration also had the capability to flow BHP through the generator during lasing using a Viking gear pump with a capacity of 2.2 l/sec (fig 3). The gas flow was pumped using a combination of blowers and mechanical rotary pumps which provided a total pump capacity of approximately 40,000 CFM at pressures up to 20 torr.

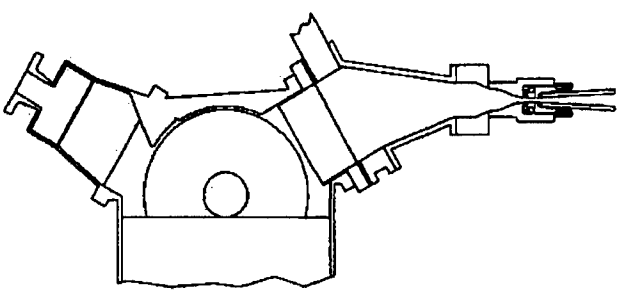

Figure 1. The original RADICL configuration showing the rotating-disk generator, liquid separator, transition duct, diagnostic duct, and nozzle/cavity.

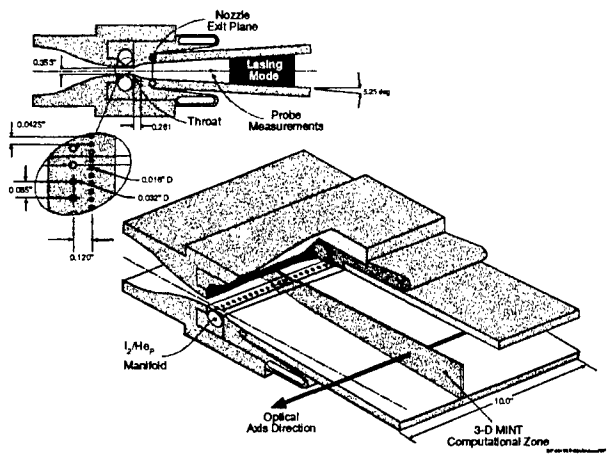


Figure 2. Detailed view of the RADICL nozzle and cavity showing iodine injection location.

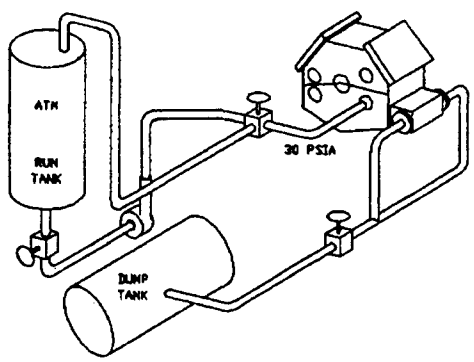


Figure 3. BHP flowloop system for the RADICL device.

During 1993, advantage was taken of the ability to adjust the height of the slit nozzle. Since the nozzle expansion was fixed at a total change of 0.89 cm in height (to provide a factor of 2 increase at the nominal 0.89 cm throat height), changing the throat height also changed the MACH number in the cavity region. The throat height was tested at heights ranging from 0.38 cm to 2.16 cm.

In late 1993, the volume of the transition duct between the oxygen generator and the diagnostic duct was outfitted with a set of plastic blocks to reduce volume and therefore reduce the quenching of singlet-delta oxygen in transport to the nozzle. The transport volume (defined as the volume from the exit of the diskpack to the choked throat) was reduced from 13 liters to 5.6 liters.

In order to increase the chlorine throughput of the device (and presumably power), an 45.7-cm diameter diskpack was designed and built for the RADICL generator housing. The generator housing was a "clamshell" type design, with a seam between the two halves running horizontally across the middle of the housing, bisecting the shaft mounts for the diskpack. The larger diskpack was able to use the same lower section, but required a somewhat larger upper section. A spacer was also required to provide clearance between the 45.7-cm disks and the liquid separator.

## 2. RESULTS OF MAJOR TEST PROGRAMS

### 2.1. Iodine Dissociation Experiments

In 1993, the Air Force became interested in high-pressure COIL operation. As part of an experimental test program to study high-pressure operation, a diagnostic to monitor molecular iodine absorption at 488 nm in the RADICL cavity was used. The subsonic pressure in RADICL was varied from roughly 60 to 130 torr by adjusting the helium flowrate through the generator. The chlorine flowrate was fixed at 0.5 mol/sec and the helium to chlorine ratio through the generator was varied from $He:Cl_2 = 2:1$ to $He:Cl_2 = 10:1$. Both the power and cavity iodine dissociation were affected strongly and (at that time) unexpectedly by the changes in generator helium, secondary helium, and iodine flowrates (fig 4). A simple model was conceived[3] to

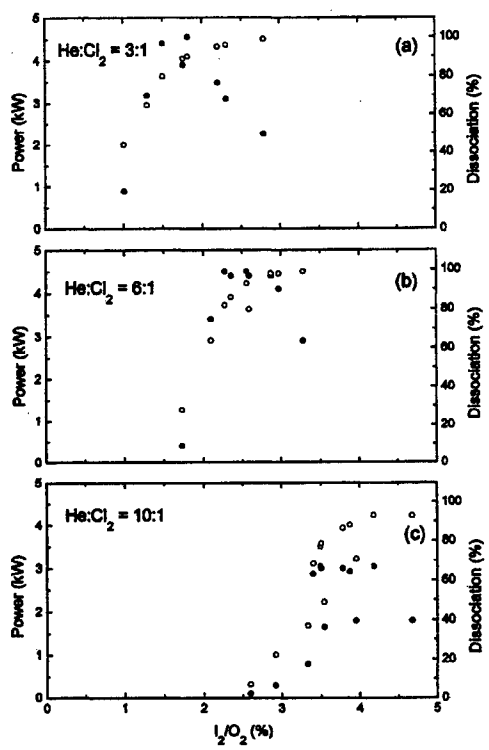


Figure 4. Iodine dissociation and power as a function of $I_2:O_2$ ratio and $He:Cl_2$ ratio.

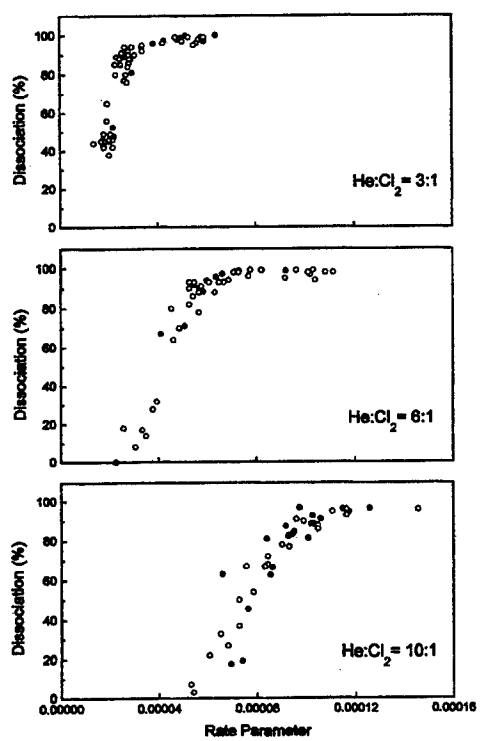


Figure 5. Correlation between observed iodine dissociation and a computed initial rate of reaction for the slow step in the dissociation process.

rationalize the results which focused on the initial slow step in the dissociation process as described by Heidner. Essentially, the model assumes that the first step in the dissociation is the pumping of ground-state molecular iodine to vibrationally-excited iodine by $O_2(a^1\Delta)$. This reaction was assumed to occur at the surface of the iodine jets, where oxygen and iodine first combine. An initial number density for singlet-delta oxygen and iodine at the interface can be derived using flowrates and

pressures. This very simple picture was able to predict all the observed trends (fig 5). Later, in 1994-1995, the dissociation experiments were repeated using RADICL in the "reduced transport volume" configuration discussed in section 2.2.

### 2.2. Effect Of Transport Volume On Chemical Efficiency

In the spring of 1994, an effort was made to eliminate as much volume as possible from the transport region between the oxygen generator and the sonic throat. A set of plastic ramps was installed to reduce volume while maintaining a smooth internal duct (fig 6). Power was measured as a function of chlorine flowrate under typical flow conditions for both the original volume configuration and the reduced volume configuration. These experiments were performed using both 38 cm- and 45.7-cm diameter generator diskpacks. The sonic throat height was opened to 1.42 cm to further reduce transport loss of $O_2(a^1\Delta)$ relative to the nominal 0.89-cm throat. A summary of the results for the 45.7-cm diskpack tests at a $He:Cl_2$ ratio of 3:1 and with a penetration parameter[7] maintained at 0.14 is shown in Figure 7. For the large volume original configuration, the power achieved did not exceed 11 kW regardless of the chlorine flowrate. This is due to increased loss of excited oxygen at the higher oxygen pressures produced by higher chlorine flowrate. When the volume was decreased, higher oxygen partial pressures could be effectively transported to the cavity. Similar trends were observed at other throat height settings.

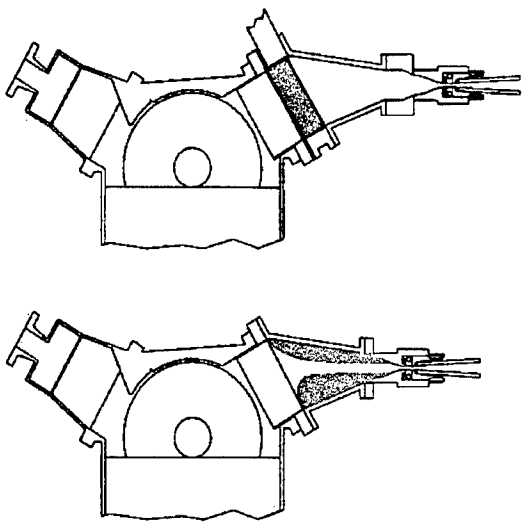

Figure 6. Cross-sectional view of RADICL with and without volume reducing inserts.

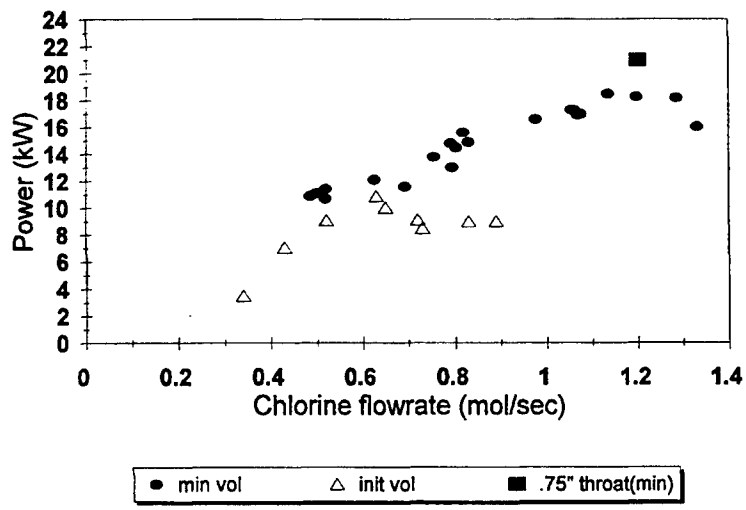


Figure 7. Power as a function of chlorine flowrate for the original volume and reduced volume configurations.

### 2.3. Optical Diagnostics

Starting in 1993, the US Air Force Research Laboratory has focussed on using room-temperature narrow-band diode laser technology to develop improved diagnostics for COIL research. Through a partnership with Physical Sciences Inc. (PSI), AFRL has acquired fairly mature diagnostic systems to measure water vapor, ground-state oxygen, and iodine atom absorption/gain in environments typically encountered in COIL devices. A sampling of measurements using these diagnostics is presented in this section.

#### 2.3.1. Excited-oxygen fraction

Historically, the accurate determination of the fraction of singlet-delta oxygen in the flow of a COIL (oxygen yield) has proven very difficult. Approximately five years ago PSI began development of a diagnostic system that permits an accurate determination of the number density of $O_2(^3\Sigma, v=0)$, from which the yield can be derived using a few reasonable assumptions. This method has been applied to determine the oxygen yield in the RADICL device. The yield was determined to be Y=0.41 in the diagnostic duct using a 38-cm diskpack, 0.5 mol/s $Cl_2$ mixed with 1.5 mol/s He, and a throat height of 0.89 cm. The transport volume was 8 liters. When the transport volume was decreased to 5.6 liters and the slit nozzle set to 1.42 cm, the yield was determined to be Y = 0.52 for $He:Cl_2 = 3:1$ and Y = 0.56 for $He:Cl_2 = 4:1$[6].

### 2.3.2. Water condensation in the COIL cavity

A diode-laser-based probe has been designed and built by PSI that allows convenient measurement of water vapor in the gas flow of the RADICL device. The diagnostic was originally designed to operate in the subsonic diagnostic duct, but has also been used to observe water vapor in the supersonic cavity of RADICL. The question of whether water vapor condenses in the supersonic expansion in a typical MACH 2 COIL has been raised by several workers, and the water probe was used to study this issue. In order to determine the fraction of water condensed, water number density was measured in the subsonic diagnostic duct and in the cavity under the same flow conditions. The number densities were then converted to water flowrates and compared to compute the fraction condensed. This approach assumes that the water is evenly distributed in the flow, and that the condensation is uniform from the top ramp to the bottom ramp. Under nominal conditions (0.5 mol/s $Cl_2$, 1.5 mol/s $He_{pri}$ [Helium flowing through the generator], 0.89-cm throat), little condensation was observed. However, by cooling the gas by any of several methods, such as increasing the primary diluent ratio or not heating the secondary flow, significant condensation was observed (figure 8). By lowering the gas temperature, a greater supersaturation exists which results in increased condensation.

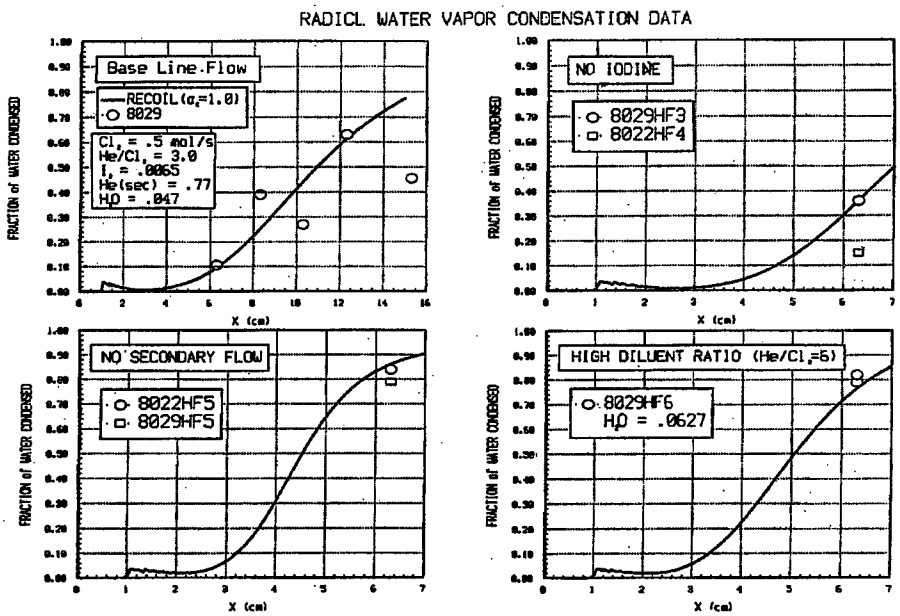


Figure 8. Water condensation in the RADICL cavity and 1-d model prediction.

### 2.4. Diagnostics Coupled to 3-D Modeling

The optical diagnostics were used to test the capability of the 3-D MINT code to predict the performance of RADICL under variable laser operating conditions. Information about the flowfield determined from the diagnostics was used both as input to the model (e.g. water flowrate and oxygen yield) and to evaluate model results (e.g. small signal gain and dissociation). A set of 7 run conditions were selected that were designed to stress the ability of the MINT code to predict laser performance and cavity conditions. The selected case are shown in Table 1.

Table 1. Description of modeled RADICL tests

| Condition | Effect on Performance |
|---|---|
| Nominal condition | Establish baseline performance and conditions |
| Low iodine flowrate | Poor iodine dissociation |
| Elevated iodine flowrate | Excess singlet oxygen consumed in dissociation |
| Low iodine jet penetration | Poor mixing and use of singlet oxygen |
| Elevated iodine jet penetration | Poor iodine dissociation |
| Elevated primary diluent ratio ($He:Cl_2$=6:1) | Poor iodine dissociation |
| Elevated water content | Excess deactivation of excited iodine by water |

As seen from the table, several cases were designed to test the model's ability to predict the level of iodine dissociation in the RADICL cavity by changing each of several flowrates. This is perhaps the most critical and difficult event to model adequately. The agreement between experimentally-determined iodine dissociation and the computed dissociation at the same location are shown in figure 9.

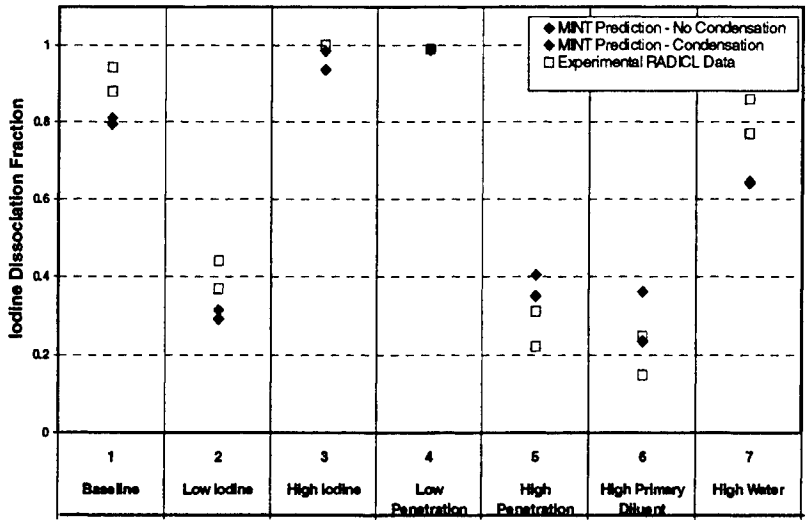


Figure 9. Comparison of measured and predicted iodine dissociation for the 7 RADICL test cases using the 3-D MINT code.

## 3. SUMMARY

The RADICL device has been a very useful learning and development tool that has served the US Air Force well, resulting in a number of publications. We look forward to the development of the next generation device as we continue to advance the state-of-the-art of COIL technology.

## ACKNOWLEDGMENTS

A sizable team is required to test a relatively large device such as RADICL. Also, since many test programs spanning 9 years were discussed in this paper, many people played significant roles in RADICL's successes over the years. Although everyone involved cannot be named, the author wishes to recognize Gordon Hager, Keith Truesdell, Keith Healey, Roman Martinez, Vincent Valdez, James Copland, Kip Kendrick, and Glenn Bingham as key personnel that contributed greatly to the RADICL system.

## REFERENCES

1. W. E. McDermott, N. R. Pchelkin, D. J. Benard, and R. R. Bousek, "An Electronic Transition Chemical Laser," *Appl. Phys. Lett.* **32,** pp 469-470, 1978.
2. R. F. Tate, B. S. Hunt, C. A. Helms, K. A. Truesdell, and G. D. Hager, "Spatial gain measurements in a chemical oxygen-iodine laser (COIL)," *J. Quant. Elec.* **31**, no. 9, pp 1632-1636, 1995.
3. C. A. Helms, J. Shaw, G. D. Hager, and K. A. Truesdell, "Iodine Dissociation in COILS", in *Proc. of X Int. Symp. on Gas flow and Chemical Lasers*, SPIE vol. 2502, pp 250-257, 1994.
4. G. D. Hager, D. Kopf, D. Plummer, T. Salsich, and P. Crowell, "Demonstration of a Repetitively-Pulsed Magnetically Gain–Switched Chemical Oxygen-Iodine Laser," *Chem. Phys. Lett.* **204**, No. 5, 1993.
5. S. P. Phipps, C. A. Helms, J. Copland, W. Rudolph, K. A. Truesdell, and G. D. Hager, "Mode-Locking a CW Supersonic Chemical Oxygen-Iodine Laser," *J. Quant. Elec.* **32**, no. 12, pp 2045-2050, 1996.
6. K. R. Kendrick, B. G. Quillen, and C. A. Helms, "Determination of Singlet-Oxygen Generator Efficiency on a 10-kW Class Supersonic Chemical Oxygen-Iodine Laser (RADICL)," *J. Quant. Elec.* **35**, no. 12, pp 1759-1764, 1999.
7. T. L. Rittenhouse, S. P. Phipps, and C. A. Helms, "Performance of a High-Efficiency 5-cm Gain Length Supersonic Chemical Oxygen-Iodine Laser," *J. Quan. Elec.* **35**, pp.857-866, 1999.

# Supersonic COIL with iodine injection in transonic and supersonic sections of the nozzle

S. Rosenwaks, E. Bruins, D. Furman, V. Rybalkin and B. D. Barmashenko

Department of Physics, Ben-Gurion University of the Negev, Beer-Sheva 84105, Israel

## ABSTRACT

We report on a detailed experimental study of the gain and temperature in the cavity of a supersonic chemical oxygen-iodine laser operating without primary buffer gas and on preliminary power measurements in this laser. In particular, a study is carried out to find optimal values of the flow parameters corresponding to the maximum gain. The measurements are performed for slit nozzles with different numbers and positions of iodine injection holes. Using a diode laser based diagnostic, the gain and temperature in the cavity are studied. Maximum gain of 0.73%/cm is obtained at chlorine and secondary nitrogen flow rates of 15 mmole/s and 7 mmole/s, respectively, for a slit nozzle with transonic injection of iodine. Preliminary power measurements are performed. For slit nozzle with iodine injection in the diverging part of the nozzle output power of 287 W with chemical efficiency of 21% was measured at 15.1 mmole/s of $Cl_2$ with no primary buffer gas. This is the highest reported chemical efficiency of a supersonic COIL operating without primary buffer gas.

**Keywords:** chemical lasers, oxygen, iodine, power lasers.

## 1. INTRODUCTION

Recently in [1,2] we reported on an efficient supersonic COIL applying simple grid nozzle geometry and transonic mixing of iodine and oxygen. This scheme of transonic mixing made it possible to obtain output power of 190 W at 11.8 mmole/s of $Cl_2$ with no primary buffer gas and very small secondary $N_2$ flow rate (~ 1 mmole/s). In the present paper we report on measurements of the gain and temperature in the cavity of a slit nozzle, supersonic COIL operating without primary buffer gas and using different schemes of iodine injection. Just as in [3] the measurements are performed using diode laser-based diagnostic. Both the gain and the temperature are measured as functions of the iodine flow rate, chlorine and secondary buffer gas flow rates, optical axis position along and across the flow and Mach number in the cavity. The results are compared with those obtained in [4] for a grid nozzle. Preliminary power measurements are done for some of the nozzles.

## 2. EXPERIMENTAL SETUP

The experimental setup, including a jet-type singlet oxygen generator (JSOG), is similar to that used in [2] and [5]. The oxygen produced in the generator flows to a diagnostic cell with a flow cross section of 1 x 5 $cm^2$, which serves as an interface between the generator and iodine injectors housing. The $O_2(^1\Delta)$ yield, water vapor fraction, $Cl_2$ utilization and the temperature of the subsonic flow are simultaneously measured in the diagnostic cell as described in [5]. The iodine-oxygen mixing system is located downstream of the diagnostic cell and uses slit supersonic nozzle. In this paper we study slit nozzles with iodine injection in transonic and supersonic sections of the nozzle and different numbers and diameters of the injection holes. The results are compared with those obtained using grid supersonic nozzle with transonic iodine injection described in [4]. The slit nozzles (Fig. 1) have the same critical cross sections of 2.5 $cm^2$ as the grid nozzle described in [5]. They have two rows of injection holes in each wall (top and bottom). In slit nozzles No. 1 and 2 iodine is injected at the nozzle throat and in nozzle No. 3 – in the diverging section of the nozzle. The first row of nozzle No.1 has 24, 0.6-mm diameter holes and the second row (lying 1 mm downstream of the first one) has 25, 0.4-mm diameter holes. The total cross section of the injection holes of nozzle No. 1 is close to that of the grid nozzle. The first row of nozzle No.2 has 31, 0.6-mm diameter holes and the second row 62, 0.4 mm diameter holes. Thus, slit nozzle No.2 has a smaller mixing scale but higher total cross section of the injection holes than nozzle No. 1. The first row of nozzle No.3 is located 3 mm downstream of the critical cross section and has 49, 0.5-mm diameter holes and the second row has 50, 0.4-mm diameter holes. The total cross sections of the injection holes for nozzles No.2 and 3 are larger than for nozzle No. 1. The laser section starts at the nozzle

XIII International Symposium on Gas Flow and Chemical Lasers and High-Power Laser Conference,
Antonio Lapucci, Marco Ciofini, Editors, Proceedings of SPIE Vol. 4184 (2001)

exit plane (flow cross section of 5 x 1 $cm^2$) from where the floor and the ceiling diverge at an angle of 8°. The optical cavity has 5 cm gain length and consists of a flat mirror and a mirror of 2 m curvature. In most experiments the gain was measured at the optical axis of the cavity, i.e., at the centerline of the flow. Two optical axis positions are available: 4.5 and 8 cm downstream of the nozzle exit-plane. The pumps provide a volumetric pumping rate of 1400 L/s, which is 3 times higher than the pumping rate in our previous experiments [1] and [3].

The iodine diagnostic system used in the present work was developed by Physical Sciences Inc. It is based on sensitive absorption spectroscopy by tunable near infrared diode laser monitoring gain $g$ for the $I^*(5p^5\ ^2P_{1/2}, F=3) \rightarrow I(5p^5\ ^2P_{3/2}, F = 4)$ transition at 1315 nm. The laser frequency is scanned over the I transition in a single pass configuration through the gain region in the cavity. The temperature $T$ of the gas in the cavity is found from the width of the Doppler profile of the I transition.

## 3. RESULTS AND DISCUSSION

### 3.1. Measurements of the gain and temperature

In our experiments the pumping rate and hence the pressure $p$ in the cavity are controlled by opening a leak downstream of the cavity. Some experiments are carried out with opened leak and hence smaller pumping rate and Mach number in the cavity. It is done to compare our present results with the results of experiments with grid nozzle [4] performed with old pumps having smaller volumetric flow rate of 450 L/s. The opening of the leak is chosen to get the same $p$ (about 1.5 Torr) as in experiments [4] with the grid nozzle at chlorine flow rate $nCl_2 \cong$ 11.7 mmole/s. The maximum gain $g$ = 0.53 %/cm, optimized for iodine ($nI_2$) and nitrogen ($nN_2$) flow rates, at $nCl_2$ = 11.7 mmole/s is obtained for slit nozzle No. 1 (with smaller number of the injection holes). For slit nozzles Nos. 2 (with transonic injection and larger number of holes) and 3 (with iodine injection in the diverging section) the maximum values of $g$ are 0.45 %/cm and 0.4%/cm, respectively. The maximum gain for slit nozzles Nos. 1, 2 and 3 under the present conditions is higher than that for the grid nozzle (0.34 %/cm, see [4]). This is probably because the gain measurement in a grid nozzle averages over high and low gain areas, whereas in a slit nozzle the measurement stays in a high gain region.

The maximum gain decreases as the optical axis is moved downstream from the first to the second position located 4.5 and 8 cm downstream of the nozzle exit, respectively. For the optical axis located 8 cm downstream of the nozzle exit, maximum $g$ of 0.44 %/cm is obtained for nozzle No. 3 at $nCl_2$ = 20 mmole/s. This value of $g$ is smaller than 0.48 %/cm measured for the optical axis located 4.5 cm downstream of the nozzle exit plane at the same $nCl_2$. A possible reason is quenching of $I^*$ and $I_2^*$ (mainly by $H_2O$) and $O_2(^1\Delta)$ losses with distance. This result is in agreement with the conclusion of [2] that maximum power is achieved when the distance between the optical axis and the supersonic nozzle exit plane is minimal (4.5 cm). That is why all the experiments described below are carried out for the optical axis located 4.5 cm downstream of the nozzle exit.

To obtain maximum pumping rate and Mach number the rest of the experiments are carried out with closed leak downstream of the cavity. For high pumping rate the gain measured at 11.7 mmole/s of chlorine is higher than that measured for low pumping rate. For nozzles No. 2 and 3 the maximum values of the gain, 0.65 and 0.55 %/cm, respectively, are higher than the values of $g$ (0.45 and 0.4%/cm, respectively) obtained for the same nozzles with opened leak. Figs. 2 shows dependencies of $g$ and $T$ on $nI_2$ for the slit nozzles No. 2 at $nCl_2$ = 11.7 mmole/s. Just as in [4] $g$ is a non-monotonous function of $nI_2$. Unlike the gain, $T$ increases monotonously with iodine flow rate. The value of $T$ corresponding to the maximum gain is rather high (~250 K). This is due to the large heat release in the iodine dissociation reaction and the absence of primary buffer gas. Increase of $nCl_2$ from ~12 mmole/s to ~20 mmole/s results in a very small rise of the gain. For example, for nozzle No. 2 the gain increases from 0.65%/cm to 0.67 %/cm which is within our error limits.

To check the mixing efficiency for closed leak, we measured the gain at $nCl_2$ =20 mmole/s at a point located 0.2 cm down of the centerline of the flow at equal distances from the centerline and the floor of the supersonic section. The maximum gain of 0.44%/cm obtained for very high $nI_2$, 0.43 mmole/s, is smaller than that obtained in the centerline (0.67%/cm). For $nI_2$ = 0.33 mmole/s (corresponding to the maximum value of $g$ at the centerline), the gain is 0.34%/cm, i.e., only about half

of the gain at the centerline, whereas T is only 220 K, i.e., lower than the temperature at the centerline (250 K). That means that for $nN_2$, corresponding to the maximum gain at the centerline of the flow, the elemental iodine is concentrated near the centerline, and the mixing is slow.

To optimize the gain, $nCl_2$ was varied in the range between 12 and 20 mmole/s. The maximum gain of 0.73%/cm was obtained in run No. 9 at $nCl_2$ of 15 mmole/s.

### 3.4. Measurements of laser power

Preliminary measurements of the power were performed for slit nozzles No. 1 and 3, with iodine injection in the sonic and diverging part of the nozzles, respectively. The total mirror transmission was about 0.6%. For Nozzle No. 1 the flow conditions were close to the conditions corresponding to the maximum gain at $nCl_2$ of 11.7 mmole/s: no primary buffer gas, $nN_2$ of 2.5 mmole/s. The maximum power was $W = 210$ W. The chemical efficiency, defined as $W/(91 \times nCl_2)$, is 20%. This value is a little higher than the 18% efficiency obtained under similar conditions in our grid nozzle (Ref. 2). For nozzle No. 3 output power of 202 W with chemical efficiency of 15% was measured at 15.1 mmole/s of $Cl_2$ ,no primary buffer gas and secondary $N_2$ flow rate of 12.8 mmole/s. However, when the diagnostic cell was replaced by a short adapter, reducing the transport volume between the generator exit and the iodine injection location from 95 $cm^3$ to 25 $cm^3$, the power was substantially increased to 287 W, corresponding to chemical efficiency of 21%. The reason for the power increase is the rise in yield and decrease of stagnation temperature due to smaller losses of $O_2(^1\Delta)$. For both Nozzle 1 and 3 the power and chemical efficiency did not change as the leak downstream of the cavity was closed. 21% efficiency is the highest reported chemical efficiency of a supersonic COIL operating without primary buffer gas.

## 4. SUMMARY

A parametric study of the gain and temperature in a supersonic COIL operating without buffer gas makes it possible to find optimal values of the flow parameters corresponding to the maximum gain. Maximum gain is achieved when the distance between the optical axis and the supersonic nozzle exit plane is minimal (4.5 cm). For this position of the optical axis maximum gain of 0.73%/cm is obtained at chlorine and secondary nitrogen flow rates of 15 mmole/s and 7 mmole/s, respectively, for a slit nozzle with transonic injection of iodine. For higher chlorine flow rate of 20 mmole/s the maximum gain is a little smaller, 0.67 %/cm. The value of the maximum gain is almost the same for two slit nozzles (Nos. 1 and 2) with transonic injection and different numbers of injection holes, which means that mixing in the direction of the optical axis is good. However, measurements at a point located down of the flow centerline show that the gain is strongly non-uniform in direction perpendicular to both the flow direction and optical axis, which means that the overall mixing is poor. For slit nozzle No. 3 with iodine injection in the diverging part of the nozzle the values of the maximum gain are smaller than for the nozzles with transonic injection. Opening a leak downstream of the cavity in order to decrease the Mach number and increase the cavity pressure results in the decrease of the gain. Maximum values of the gain obtained using the slit nozzles are much higher than the values measured in [4] for a grid nozzle where the maximum gain was only 0.34%/cm. Preliminary power measurements were performed. For slit nozzle with iodine injection in the diverging part of the nozzle output power of 287 W with chemical efficiency of 21% was measured at 15.1 mmole/s of $Cl_2$ with no primary buffer gas and secondary $N_2$ flow rate of 12.8 mmole/s. This is the highest reported chemical efficiency of a supersonic COIL operating without primary buffer gas.

## REFERENCES


1. D. Furman, B. D. Barmashenko and S. Rosenwaks, "An efficient supersonic chemical oxygen-iodine laser operating without buffer gas and with simple nozzle geometry," *Appl. Phys. Lett.*, vol. 70, pp. 2341-2343, 1997.
2. D. Furman, B. D. Barmashenko and S. Rosenwaks, "Parametric study of an efficient supersonic chemical oxygen-iodine laser/jet generator system operating without buffer gas," *IEEE J. Quantum Electronics*, vol. 34, pp. 1068 -1074, 1998.
3. E. Lebiush, B. D. Barmashenko, A. Elior and S. Rosenwaks, "Parametric study of the gain in a small scale, grid nozzle supersonic chemical oxygen-iodine laser," *IEEE J. Quantum Electronics*, vol.31, pp. 903-909, 1995.

4. D. Furman, E. Bruins, B. D. Barmashenko and S. Rosenwaks, "Small signal gain and iodine dissociation in a supersonic chemical oxygen-iodine laser with transonic injection of iodine," *Appl. Phys. Lett.*, vol. 74, pp. 3093-3095, 1999.
5. D. Furman, B. D. Barmashenko and S. Rosenwaks, "Diode-laser based absorption spectroscopy diagnostics of a jet-type generator for chemical oxygen-iodine lasers," *IEEE J. Quantum Electronics*, vol. 35, pp. 540-547, 1999.

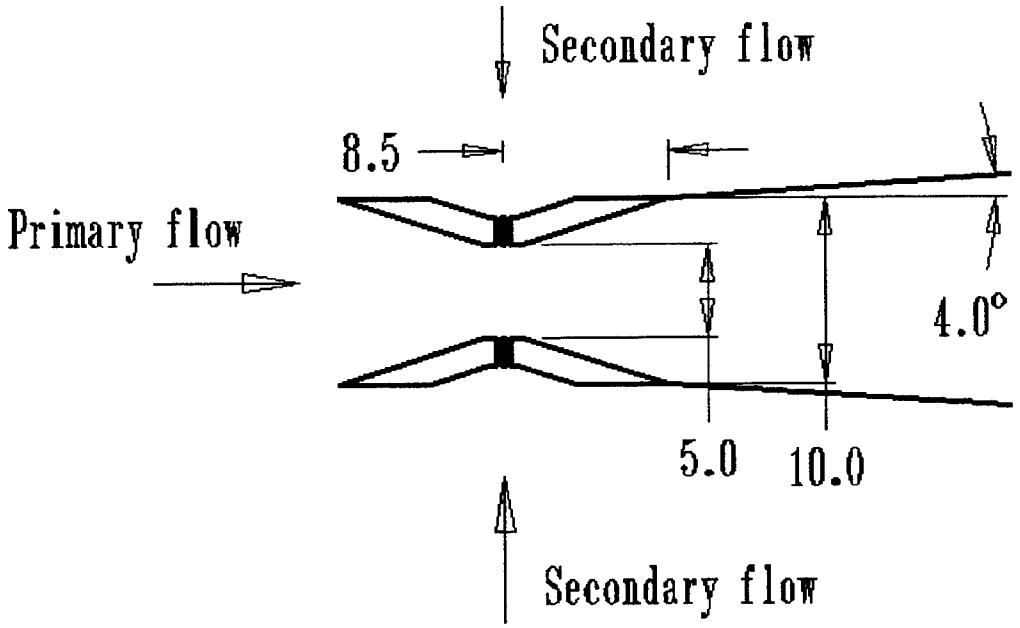


Fig. 1. Schematics of the slit nozzle. All measures are in millimeters.

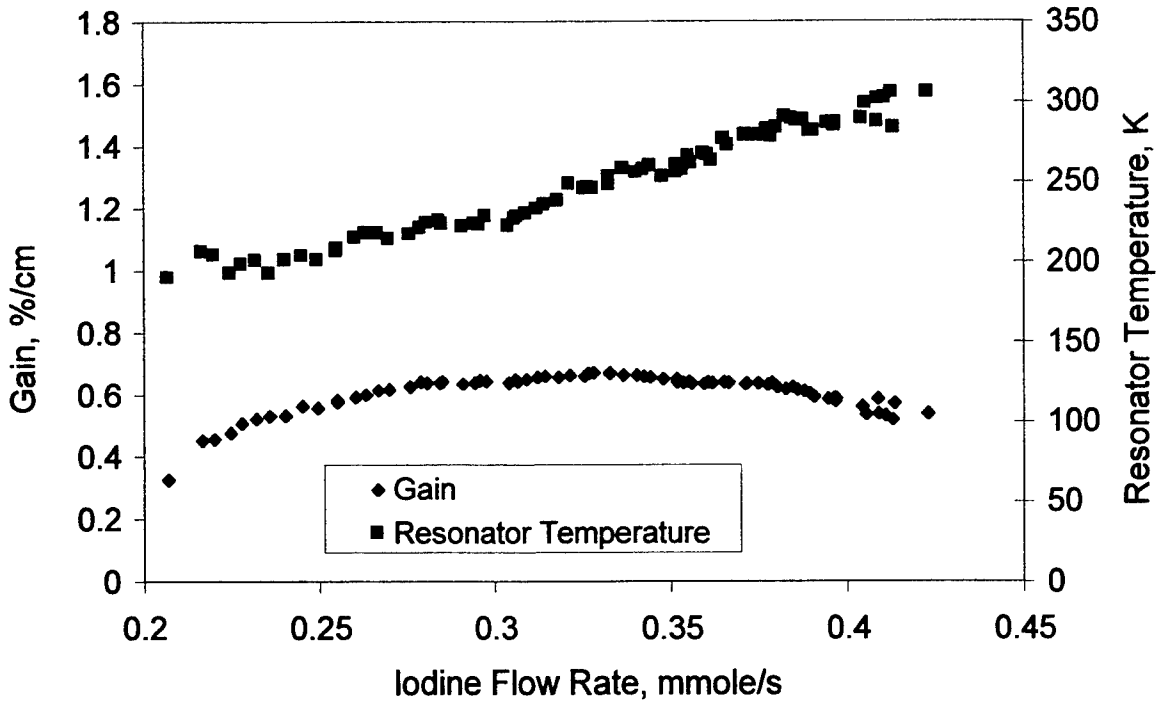


Fig. 2. The gain and temperature at the cavity optical axis for slit nozzle No. 2 as a function of the iodine flow rate. The chlorine and secondary nitrogen flow rates are 20.1 and 8.7 mmole/s, respectively, the leak downstream of the cavity is closed.

# Development of a prototype COIL for decommissioning and dismantlement

Masamori Endo[♦A], Kazuyoku Tei[A], Daichi Sugimoto[A], Kenzo Nanri[A], Taro Uchiyama[B], and Tomoo Fujioka[A]

[A]Department of Physics, Tokai University, 1117 Kita-Kaname, Hiratsuka City,259-1292, Japan.
[B]Department of System Design Engineering, Keio University, 3-14-1, Hiyoshi, Kohoku-ku, Yokohama, 223-8522, Japan.

## ABSTRACT

A study of chemical oxygen-iodine laser (COIL) for the use of decommissioning and dismantlement of nuclear facilities is conducted. A scaled-down model was developed as a prototype. Laser duct and optical cavity were designed so that it can be operated in both supersonic mode and high-pressure subsonic mode for the comparative study. A 1.34kW output with chemical efficiency of 24.6% was obtained in the supersonic mode. In the high-pressure subsonic mode, output power was 1.12kW with chemical efficiency of 20.6%. A subsonic operation at 12Torr was demonstrated for the first time. A preliminary experiment of thick steel cutting was demonstrated by the developed system. The obtained data was in good agreement with published data.

**Keywords:** iodine, laser, decommissioning, industrial laser, COIL, subsonic

## 1. INTRODUCTION

Chemical oxygen-iodine laser (COIL) has several unique characteristics that are suitable for industrial applications, such as high power (up to megawatts), good beam quality, and optical fiber availability.
Among the possible applications of COIL such as automotive industries,[1)] or heavy industries, the decommissioning and dismantlement (D&D) of the nuclear reactors is the most promising one. It can be said that there is no other practical candidate for the D&D application, since no laser can operate at >10kW output at a wavelength where optical fiber delivery is available.
There are two more facts that make COIL as a promising candidate of D&D laser. Firstly, since this specific application does not require a 24-hours-a-day operation, the existing COIL technology is ready for a practical solution. Secondly, since COIL is a chemical laser, it does not require an electric input in principle. That means COIL can be constructed as a mobile laser system.
Last year, we proposed three operational modes of industrial COILs.[2)] Among them, what we call Mode II was devoted for D&D application. Figure 1 shows the schematic drawing of the Mode II COIL. Initially, a sufficient amount of BHP for designed operational period is supplied. After the operation, the worn BHP is taken away and refreshed at a plant placed where electricity and resources are easily available. From the experience in the Kawasaki Heavy Industries, 220 liter of BHP is required for 1kWh operation without BHP refreshment. Based on our previous studies, we have proposed a conceptual design of a 30kW COIL system operating in Mode II.[3)] It was estimated that such a system could be contained in five train-containers.

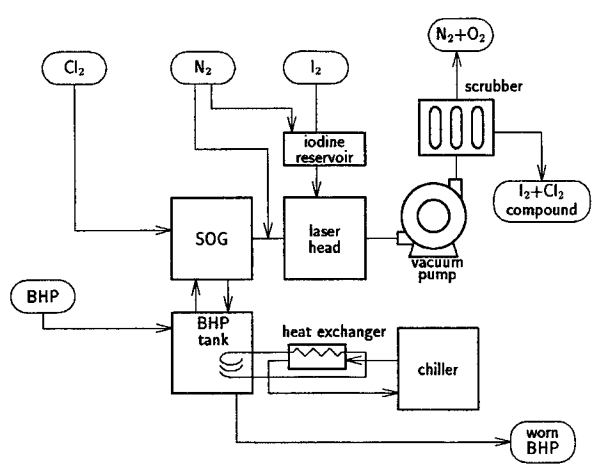


Fig. 1: Block diagram of the Mode II COIL

♦ Correspondence: Email: masamori@keyaki.cc.u-tokai.ac.jp; Telephone: +81-463-58-1211 Ext. 3721;

XIII International Symposium on Gas Flow and Chemical Lasers and High-Power Laser Conference,
Antonio Lapucci, Marco Ciofini, Editors, Proceedings of SPIE Vol. 4184 (2001)

In this study, we develop a scaled-down model of a D&D COIL system operating in Mode II. The output power was decided to be 1kW owing to the available vacuum pump system. The operational characteristics of the developed system, and the results of the preliminary D&D experiments are presented in this paper.

## 2. EXPERIMENTAL SETUP

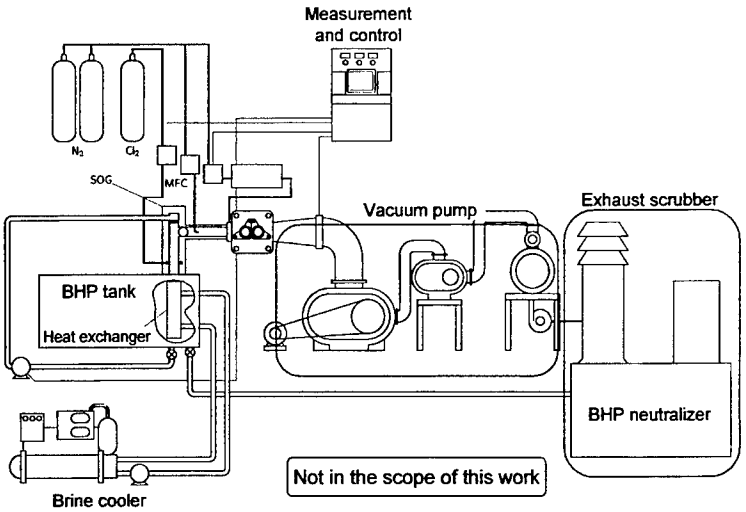


Fig. 2: Schematic drawing of the experimental setup.

Figure 2 shows the experimental facility. It consists of a large BHP tank (500liter max.), counter-flow type liquid jet SOG, laser cavity, vacuum pump, gas and liquid neutralizer, gas supply system, and measurement/control subsystems. Although the mode II system must be designed to be mobile, the limitation of the research fund did not allow us redesign the vacuum pump and gas/liquid neutralizer. Therefore, they were same as the one we used in the previous studies, and therefore, not in the scope of this study.

Laser duct and optical cavity were designed so that it can switch the operation mode from supersonic to subsonic quickly, by changing the detachable supersonic nozzle and shifting the position of the optical cavity. When we operate the system in the high-pressure subsonic mode, the capacity of the present vacuum system was too large. Therefore, a choke valve was used to adjust the effective vacuum capacity.

A BHP recirculation system consists of the LH-640 lobe pump (ITT Jabsco), synchronous motor and variable frequency inverter is devised. The pump is operated at low revolution (200~250 rpm typ.) to prevent cavitation of the BHP. Photo 1 shows the experimental facility viewed from the upstream.

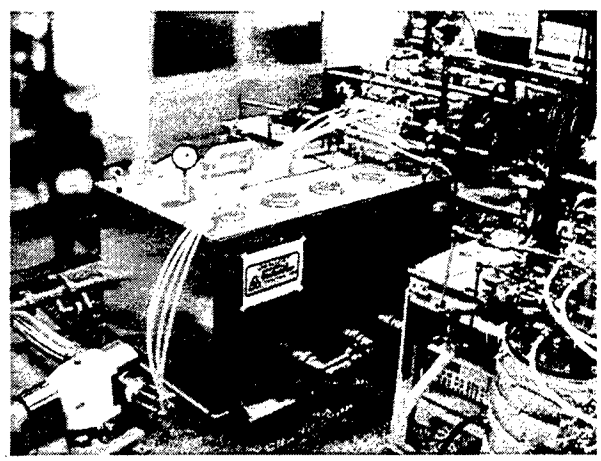

Photo 1: Experimental setup.

## 3. EXPERIMENTAL RESULTS

### 3.1. Full-power operation

The developed COIL system was operated in supersonic mode and high-pressure subsonic mode. After the optimization of the operational conditions, we have obtained the maximum output power in supersonic and subsonic mode as Table 1. Note that we did not apply the primary-buffer cooling technique in this study.

Table 1: Maximum output power and operational conditions

| Op. mode | $Cl_2$ [mmol/s] | Primary buf. [mmol/s] | Secondary buf. [mmol/s] | Output [kW] | Flow velocity [m/s] | Chemical eff. [%] | Spec. energy [J/l] |
|---|---|---|---|---|---|---|---|
| Supersonic | 60 | 40 | 60 | 1.34 | 400 | 24.6 | 1.12 |
| Subsonic | 60 | 30 | 60 | 1.12 | 110 | 20.6 | 2.18 |

In the supersonic mode, we have successfully reduced the buffer gas flow rate at a half of our previous studies.[4] The flow duct was originally designed for $Cl_2$:$N_2$=1:2, the try-and-error basis optimization enabled us to operate the device in a very low buffer gas flow. As a result, the specific energy was doubled compared to the previous operations in supersonic mode. This result reminded us that the supersonic mode operation might be still attractive.

In the high-pressure subsonic mode operation, we have operated the device at 6 Torr. The obtained output was lower than the supersonic mode. Nevertheless, it exceeded the design criteria. The specific energy resulted in much lower than our record.[5] The reason is still unknown. More detailed comparison of the flow parameters (pressure, velocity, etc...) to the previous device is now being conducted.

### 3.2. High-pressure operation

We increased the operation pressure of the system in the subsonic mode further to obtain the higher specific energy. The result is shown in Fig. 3. The specific energy increases in proportion to the operation pressure. However, that was obtained only with the degradation of the chemical efficiency and output power.
The highest specific energy was obtained in the operation at 12Torr. As far as we know, it was the highest static pressure of subsonic COIL ever obtained.

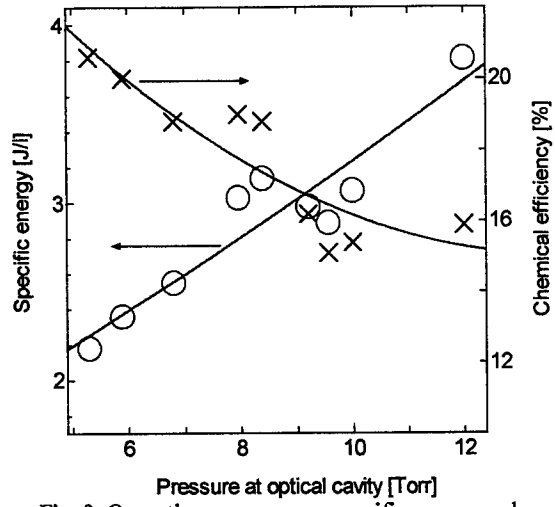

Fig. 3: Operation pressure vs. specific energy and chemical efficiency.

### 3.3. Long-term operation

Although one of the primary goals of this work is the long-term stable operation, it has not been possible so far due to the unacceptable rise of the BHP temperature. Two to three minutes is the current limit of operation at 1kW output. This was due to the improperly designed heat exchanger, which is immersed in the BHP tank. The long-term operation was tried at a reduced chlorine flow rate (40 mmol/s). Up to 40 minutes of operation was demonstrated, however, it was terminated because the BHP temperature exceeded 0 °C.

### 3.4. Thick steel cutting experiment

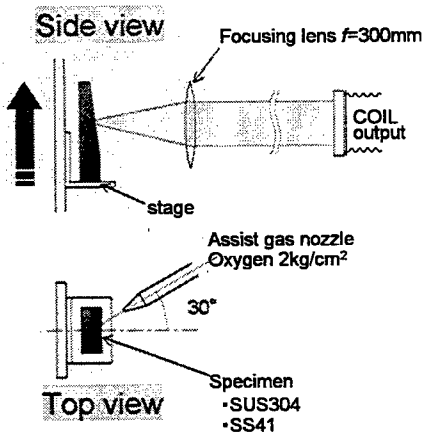

Fig. 4: Schematic drawing of the thick steel cutting experiment

Followed by the successful operation at a 1kW output power, we conducted a preliminary D&D experiment. The prepared materials were mild steel (SS41) and stainless steel (SUS304). Figure 4 shows the experimental setup.
Figure 5 shows the cutting capability as a function of the thickness. As the thickness increased, the cutting capability decreased further than the first-order approximation, namely, $dv$=const, where $d$ is the material thickness, and $v$ is the cutting speed. This can be explained by the heat loss through the kerf.
Two models are known for the thick metal cutting by laser. One was proposed by the group of Kawasaki Heavy Industries as[6]

$$\frac{d}{P} = \frac{\alpha}{vw_k + \beta}, \tag{1}$$

where $d$ is the cut depth, $P$ the laser power, $v$ the cutting speed, $w_k$ the width of the kerf (to be exact, they used the beam diameter instead of the kerf width), $\alpha$ and $\beta$ are empirical constants derived by the thermal property of the materials and laser wavelength. The other model was proposed by the Phillips Laboratory as[7]

$$\frac{d}{P} = \frac{\alpha'}{vw_k + \beta'\sqrt{vw_k}}, \tag{2}$$

where $\alpha'$ and $\beta'$ are empirical constants similar to Kawasaki model. Note that the $\alpha$s and $\beta$s have slightly different meaning in both models.
Figure 6 shows the published data of thick steel cutting by COIL in the Philips Laboratory.[7] The cutting capability per unit output power is plotted as a function of the (kerf width)·(cutting speed). Open plots show the results of Ref. 7, while filled

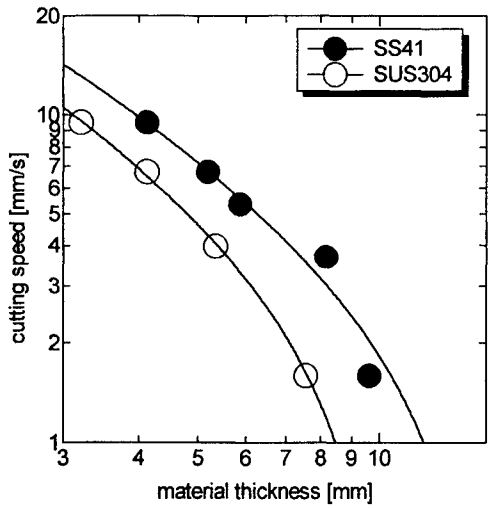

Fig. 5: Cutting speed as a function of material thickness.

plots show our results. The dashed line and the solid line represent the theoretical prediction by Eq. (1) and Eq. (2), respectively.

It is seen that our results were slightly better than the one of Ref. 7. It can be explained by the difference in the assist gas species. They used He or $N_2$ while we used $O_2$ as an assist gas.

Both theories predict the experimental results correctly in the range of the experimental data. However, the predictions of both models differ considerably in the case of slow cut of very thick material. Now we are capable of conducting D&D experiments, our next goal is the verification of the model and prediction of the performance of the real D&D COIL, using the current device as a simulator.

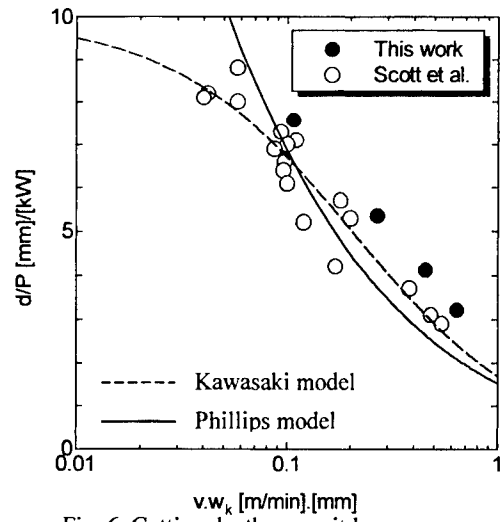

Fig. 6: Cutting depth per unit laser power as a function of (cutting speed)·(kerf width).

The cutting capability of a 300mm stainless steel was calculated using Eq. (1) and Eq. (2). The output power, beam quality, and the focal length of the lens were assumed to be 30kW, $M^2$=40, and 1500mm, respectively. While Phillips model predicts the cutting speed of 12mm/min, Kawasaki model predicts the cut off is impossible. The need for the model verification is highlighted by this estimation.

## 4. CONCLUSIONS

A scaled-down model of COIL for D&D applications has been developed. Laser duct and optical cavity were designed so that it can be operated in both supersonic mode and high-pressure subsonic mode for the comparative study. A 1.34kW with chemical efficiency of 24.6% was obtained in the supersonic mode. In the high-pressure subsonic mode, output power was 1.12kW with chemical efficiency of 20.6%. A subsonic operation at 12Torr was demonstrated for the first time. As a result, specific energy of 3.8J/liter was obtained. Long-term operation has not been proven yet because of the temperature rise of basic hydrogen peroxide (BHP). A preliminary experiment of thick steel cutting was demonstrated by the developed system. The obtained data was in good agreement with published data. It was shown that the predictions of the D&D COIL performance was quite different depended on the model used.

## ACKNOWLEDGEMENTS

This work was done as one of the research programs of the New Energy and Industrial Technology Development Organization (NEDO), and it was partly supported by Ministry of Education, Science and Culture.

## REFERENCES

1. M. Endo, S. Takeda, F. Wani, D. Sugimoto and T. Fujioka, 32nd ISATA, 99NM025 (Vienna, June 1999).
2. M. Endo, D. Sugimoto, S. Takeda, K. Nanri and T. Fujioka, *Proc. SPIE* **3931**, pp. 110-115, 2000.
3. K. Tei, D. Sugimoto, M. Endo, S. Takeda and T. Fujioka, *Proc. SPIE* **3887**, pp.162-169, 1999.
4. M. Endo, S. Nagatomo, S. Takeda, M. V. Zagidullin, V. D. Nikolaev, H. Fujii, F. Wani,D. Sugimoto, K. Sunako, K. Nanri, and T. Fujioka, *IEEE J. Quant. Electron.* **34**, pp.393-398, 1998.
5. F. Wani, M. Endo, and T. Fujioka, *Appl. Phys. Lett.* **75**, pp.3081-3083, 1999.
6. J. Adachi, N. Takahashi, K. Yasuda, and T. Atsuta, *Progress in Nuclear Energy* **32**, pp. 517-523, 1988.
7. J. E. Scott, J. A. Rothenflue, W. P. Latham, and A. Kar, *Proc. SPIE* **2702**, pp.339-348, 1996.

# Chemical Oxygen-Iodine Laser Research in Dalian

Sang Fengting, Yang Bailing, Zhaung Qi

Dalian Institute of Chemical Physics, Chinese Academy of Sciences
P.O.Box 110 - 7, Dalian 116023, China
Tel:+86-411-4696034, email:sft@ms.dicp.ac.cn

## ABSTRACT

A multi-kilowatt supersonic chemical oxygen iodine laser (COIL) has been constructed. Two types of jet singlet oxygen generator (SOG) such as tube-array and plate have been tested. An output power of 8.8KW with chemical efficiency of 21.4% was obtained at the chlorine flow rate of 450mmole/s. The influence of BHP (basic hydrogen peroxide) temperature on the output power of COIL has been studied. And the absolute concentration of $O_2(^1\Delta)$ in the jet SOG was measured using the Piston-source method.

**Keywords:** Chemical oxygen iodine laser (COIL), singlet oxygen generator (SOG), chemical efficiency

## 1. INTRODUCTION

The chemical oxygen iodine laser (COIL) is the first chemical laser of electronic transition[1]. It has a lot of attractive features including shot-wavelength, high efficiency, high energy density, low operational temperature, and high scalability. Its wavelength of 1.315μm is ideal for optical fiber delivery. In addition, a high–quality output beam is expected owing to its low-pressure gain medium. Because of these unique characteristics, COIL has the potential applications in industry and military.

The lasing of COIL is based on a transition in the hyperfine structure of the iodine atom:

$$I(^2P_{1/2}) + nh\nu \rightarrow I(^2P_{3/2}) + (n+1)h\nu \tag{1}$$

Where $h\nu=1.51\times10^{-11}$J. In the COIL, the I $(^2P_{1/2})$ level of the iodine atom is excited by energy transfer from the first electronically excited state $O_2$ $(^1\Delta)$:

$$O_2(^1\Delta) + I(^2P_{3/2}) \rightarrow O_2(^3\Sigma) + I(^2P_{1/2}) \tag{2}$$

The singlet oxygen is obtained in a generator via a chemical reaction between chlorine and basic hydrogen peroxide (BHP):

$$2KOH + H_2O_2 + Cl_2 \rightarrow O_2(^1\Delta) + 2H_2O + 2KCl \tag{3}$$

The reaction includes several steps[2] actually:

$$\left.\begin{aligned} &OH^- + H_2O_2 \rightarrow H_2O + HO_2^- \\ &HO_2^- + Cl_2 \rightarrow HOOCl + Cl^- \\ &HO_2^- + HOOCl \rightarrow H_2O_2 + ClO_2^- \\ &ClO_2^- \rightarrow O_2(^1\Delta) + Cl^- \end{aligned}\right\} \tag{4}$$

In the COIL, prior to lasing $O_2$ $(^1\Delta)$ dissociates the molecular iodine, which is one of the most complicated and least understood processes. The iodine atoms are obtained via autonomous dissociation of iodine molecules in the presence of singlet oxygen, This process is considered as a two-step reaction process[3] as follow:

$$\left.\begin{aligned} &O_2(^1\Delta) + I_2 \rightarrow O_2(^3\Sigma) + I_2(v) \\ &I_2(v) + O_2(^1\Delta) \rightarrow O_2(^3\Sigma) + 2I(^2P_{3/2}) \end{aligned}\right\} \tag{5}$$

XIII International Symposium on Gas Flow and Chemical Lasers and High-Power Laser Conference,
Antonio Lapucci, Marco Ciofini, Editors, Proceedings of SPIE Vol. 4184 (2001)

According to these chemical processes, we have constructed our CW supersonic COIL system with a jet SOG, an electrically heated iodine generator, an array-nozzle bank, and an unstable resonator as well as a vacuum pumping system[4].

## 2. EXPERIMENT

### 2.1. The tube-type jet SOG

The generation of $O_2$ ($^1\Delta$) at high pressure in the jet SOG created new possibilities for preparing active medium of a supersonic COIL. The high-pressure jet SOG is based on the reaction of the $Cl_2$ flow with the counter-flowing jet of the BHP.

The plate injector-shower is used generally in the jet SOG, and the plate-thick is 4~6mm but the pressure drop through the plate is higher, so the liquid pressure before the plate is more then 1.5-2.0 atm. Therefore, a heavy BHP pumping system is needed for COIL with plate-type jet SOG. The rigidity of the tube is better than the plate; the tube is ideal material for the jet-shower. The setup of COIL with the tube-type jet SOG is shown in Fig.1.

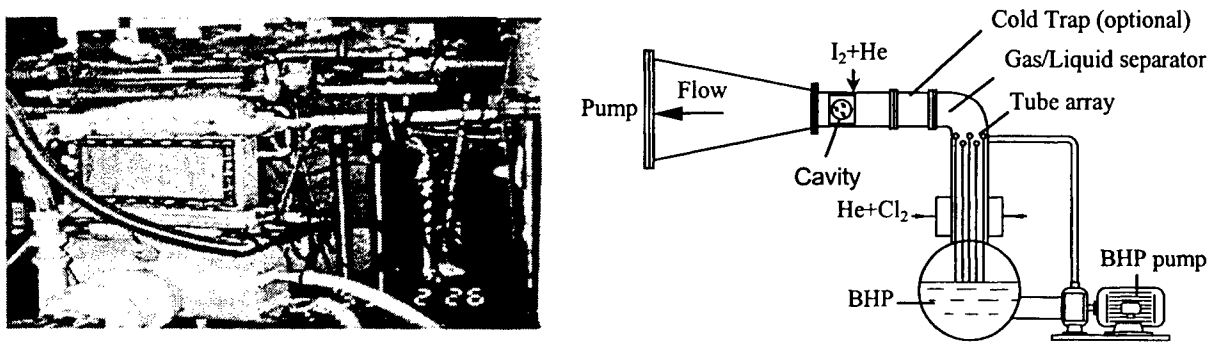


Fig.1 The experimental setup of COIL with a tube-type jet SOG

There are forty tubes of 10 cm length and 4 mm i.d. in the SOG, and twenty-five liquid jet holes, 0.7 mm i.d. on each tube. The arrangement of the tubes is shown in Fig.2. In our experiments, the BHP feeding pressure in the tubes is between 0.6-0.7 atm.

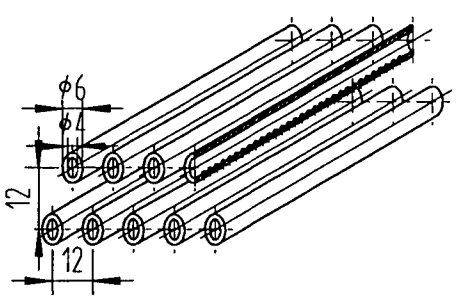


Fig.2 Schematic of the tube array

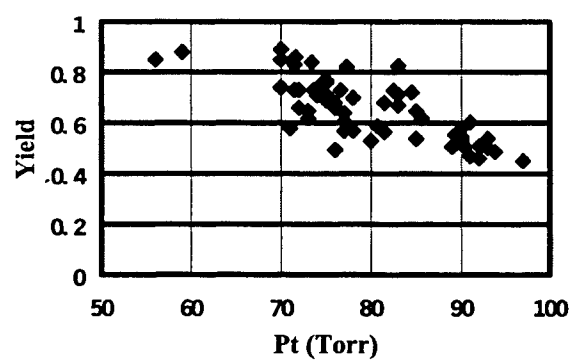


Fig.3 The variation of $O_2(^1\Delta)$ yield with the SOG pressure

Due to the main path of gas quenching of $O_2$ ($^1\Delta$) is the energy pooling process:

$$O_2(^1\Delta)+O_2(^1\Delta)\rightarrow O_2(^1\Sigma)+O_2(^3\Sigma),\qquad K=2.7\times10^{-17}cm/molec\cdot\sec \tag{6}$$

So the concentration of $O_2$ ($^1\Delta$) which measured by the Piston source method[5] will be decreased with the pressure increase in the jet SOG and has been proved experimentally as shown in the Fig.3.

The parameters of the tube-type SOG are summarized in Table 1.

**Table 1 The tube-type SOG parameters**

| | |
|---|---|
| *$Cl_2$ flow rate* | *450 mmol/s* |
| *He flow rate* | *1800 mmol/s* |
| *JSOG volume* | *8.0 L* |
| *JSOG pressure* | *50-100 torr* |
| *Specific surface area of BHP jet* | *~3.5-4.0 $cm^{-1}$* |
| *Initial concentration of $HO_2^-$* | *6.7 mol/l* |
| *Velocity of BHP jet* | *10 m/s* |
| *Velocity of gas flow* | *20-40 m/s* |
| *Coefficient of mass transfer in liquid phase* | *12.3 cm/s* |
| *$T_{BHP}$* | *250-263 K* |

The results of the experiments are that the output power of the COIL increases with the temperature of BHP of the COIL using water vapor trap (Fig.4). Because $U_{Cl2}$ and $Y_\Delta$ increase with the temperature of BHP, the output power of the COIL will be increased.

The process of $O_2$ ($^1\Delta$) generation can be regarded as a surface reaction in BHP jet:

$$Cl_2 + HO_2^- \rightarrow O_2(^1\Delta) + 2Cl^- + H^+, \quad k = 1.15\times10^{34}\exp(-15816/T_w)^6 \tag{7}$$

And there is an empirical formula for k where $T_w$ is the average surface temperature of the BHP jet. The calculated results[7] show the relation of the $U_{Cl2}$ and $Y_\Delta$ with given $T_w$ and found that the results agreed closely with the experiments in Fig.5. The $T_W$ is usually about *10~20°K* higher then $T_{BHP}$ due to the exothermic reaction[7].

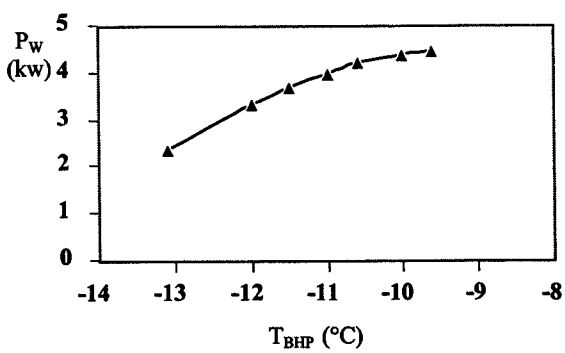


Fig.4 The relation of output power with $T_{BHP}$

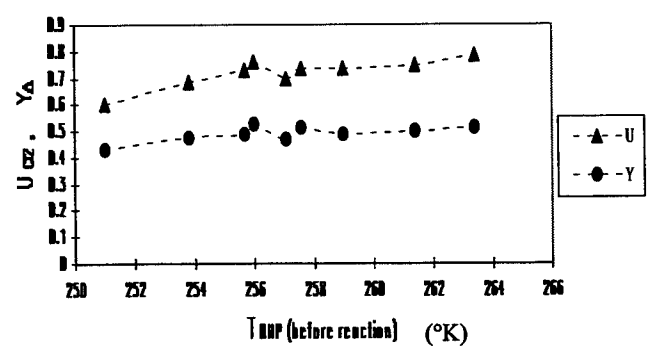


Fig.5 Experimental results of $U_{Cl2}$, $Y_\Delta$ with $T_{BHP}$

An output power of 8.8 KW and chemical efficiency 21.4% has been achieved at chlorine flow rate as 450 mmol/sec by using the tube-type jet SOG.

### 2.2 The U-shaped folded unstable resonator and UR-90 outputting annular beam

For a high power COIL system, an unstable resonator suitable for lager mode volume is critical important. It cannot only get a large controllable mode volume, but also has good transverse mode and better beam quality. In general, confocal unstable resonator is used in the COIL system.

Due to the gain region of the COIL is longer, we designed and used a U-shaped folded unstable resonator as shown in Fig.6. Experimental results show that the output power of the COIL with the U-shaped folded unstable resonator has been increased one and half times compared with the conventional unstable resonator. And the beam quality β as 4-5 is achieved. These experiments is completed on the COIL with rotating disk SOG[4]

It is very important that how to obtain good beam quality in the supersonic transversely flowing medium. The conventional confocal unstable resonator has some advantages such as large controllable mode volume, good transverse mode discrimination and efficient coupling output, but it is very difficult to obtain a near diffraction limit beam because its sensitive to the medium heterogeneity and cavity misalignment.[8] The configuration and experimental results of UR-90 with filled-in output beam were previously reported.[9]

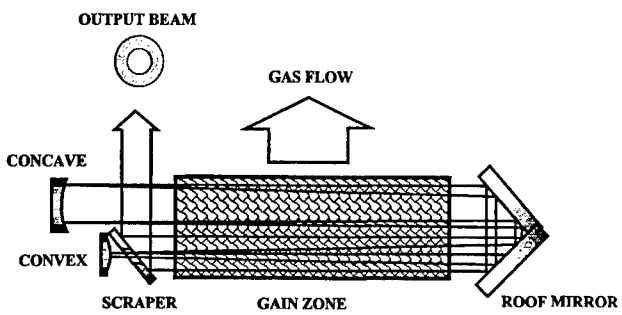


Fig.6 Schematic of the U-shaped folded unstable resonator

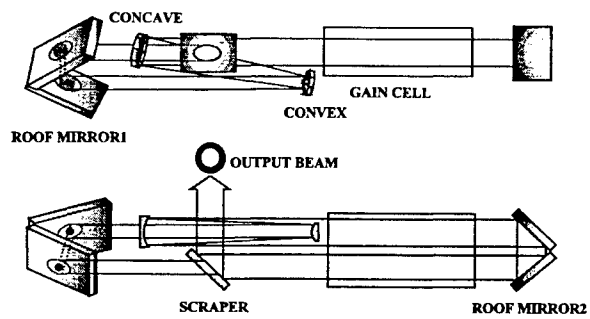


Fig.7 Schematic of UR90 with annular output beam

The schematic configuration of UR-90 with annular output beam is illustrated in Fig.7. The greatest difference between UR90 with annular output beam and filled-in output beam is the shape and position of the output scraper where the former is placed on-axis and later is located off-axis. The actual parameters of the UR90 with annular output beam are listed in Table 2.

**Table 2 UR-90 with annular output beam parameters**

| | | | |
|---|---|---|---|
| Magnification | 1.69 | Diameter of beam | 38 |
| Concave radius/mm | 6000 | $L_a$/mm | 3208 |
| Convex radius/mm | 3540 | $L_b$/mm | 1230 |
| Equivalent Fresnel number | 5.4 | $L_c$/mm | 5390 |
| Hole radius of scraper mirror/mm | 11.2 | Cavity length/mm | 9828 |

The far field intensity distribution of the UR90 with annular output beam is shown in Fig.8 in case of magnification of 1.69 and average output power of 4kw.

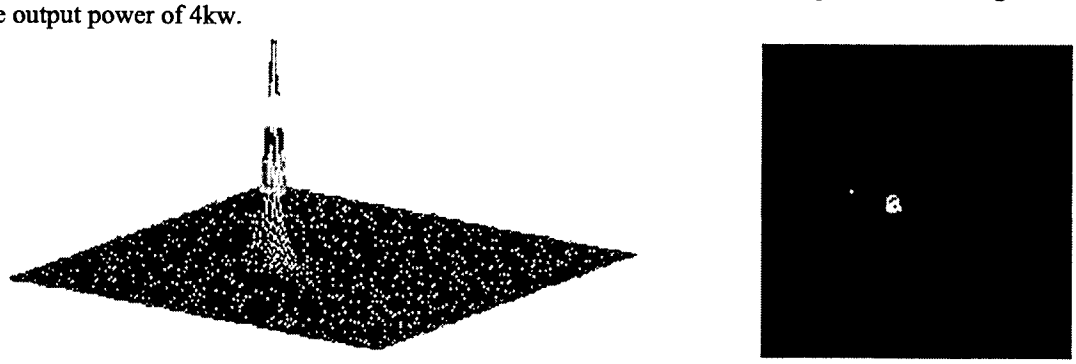

Fig.8 Plot of the far field intensity profile pattern of the UR90 with annular output beam in case of magnification of 1.69. The focusing lens has a 5-m focal length.

The measured beam divergence is 0.27mrad, and the beam quality of β=3.2 has been achieved, where β is define as

$$\beta = \frac{\theta_{experiment}}{\theta_{theory}} \tag{8}$$

Where $\theta_{experiment}$ is the measured beam divergence and $\theta_{theory}$ is the divergence of a filled-in beam with uniform amplitude and phase at the same beam dimension.

## 3. CONCLUSION

The COIL is a most attractive short wavelength chemical laser system with very good scalable ability, excellent beam quality and good transfer performance in optical fiber.

Although the performance of the tube-type jet SOG is same as the plate-type jet SOG, but the BHP feeding pressure needed is only 0.6-0.7 atm. Sequent BHP pumping system will be not heavy. This is very important for the application.

The U-shaped folded unstable resonator is really effective for increase chemical efficiency and improving beam quality

.The UR-90 with annular output beam is useful for COIL to obtain the near diffraction limit beam quality.


## ACKNOWLEDGEMENTS

The authors thank Prof. Lu Wenfa, Jin Yuqi, Duo Lioing Chen Fang, Sun Yishu , Sun Long, and Han Xinmin for their helpfully discuss and invaluable help with the optical alignment, the optical diagnostic, and operation of the COIL system.


## REFERENCES


[1] W.E. McDermott, N.R.Pchelkin et al. *Appl.Phys.Lett.*.**32** pp469-470, 1978.

[2] K.A.Truesdell ,S.E. Lamberson, "Phillps lab.COIL technology overview", *SPIE.* **1810**, pp489.

[3] T.T.Yang, D.A.Copeland et al. *AIAA* 97-2384, pp4.

[4] Yang Bailing,, "Latest advances in COIL at Dalian", *SPIE.* **3574**, pp281-289.

[5] Duo Liping, "Measurements of absolute $O_2$ ($^1\Delta$) concentration in SOG by using the piston source method", *SPIE* 3931, pp92.

[6] Zhaung Qi, Sang Fengting, Zhou Dazheng. "*Short wavelength chemical laser*", chapter 2, pp45, Defense industry press of China, Beijing, 1997.

[7] Liu Wenfa,Han Xinmin, Chen Fang, Sang Fengting, "Influence of the Temperature of Basic Hydrogen Peroxide on the Utilization of Chlorine and the Yield of Singlet Oxygen in a Jet Generator", to be published.

[8] Jin Yuqi,Sun Yishu, Sang Fengting et al," Experimental investigation of unstable resonator for a cw supersonic COIL",*High Power Laser and Particle Beam,***9**(2),pp227-232 ,1997.

[9] Zhou Dazheng,Han Xinmin, "Desigh method of unstable resonator with 90-deg. Beam rotation" , *High Power Laser and Particle Beam*, **7**(4), pp528-534,1995.

# RF plasma jet generator of singlet delta oxygen for oxygen-iodine laser

Josef Schmiedberger*[a], Shinichi Hirahara[a], Yasuhiro Ichinohe[a], Masataro Suzuki[a], Wataru Masuda[a], Yoshihumi Kihara[b], Eiji Yoshitani[c] and Hiroo Fujii[b]

[a]Nagaoka Univ. of Technology, Dept. of Mech. Eng., 1603-1 Kamitomioka, Nagaoka, 940-2188 Japan

[b]Anan Col. of Technology, Fac. of Advanced Eng., 265 Aoki, Minobayashi, Anan, 774-0017 Japan

[c]Fujisaki Electric Co., 1-38 Tatsumi, Anan, 774-0001 Japan

## ABSTRACT

An RF plasma jet generator of singlet delta oxygen has been developed for use in an oxygen-iodine laser. The plasma jet was produced in an Al cylindrical nozzle, having the inner diameter of 3 mm and the length of 8 mm. The discharge was done in the gas mixture $O_2$:$N_2$:NO=200:20:10 sccm and then it was chilled reactively by the mixture Ar:$NO_2$=200:10 sccm, which was injected into the plasma jet at the nozzle exit. The RF frequency was 99.9 MHz and the RF power was 200 W. The $O_2(a^1\Delta_g)$ relative yield of 32 % was achieved at the pressure of 0.43 Torr. The current device DSOG-3 was tested in a discharge oxygen-iodine laser (DOIL). The reaction scheme of DOIL is the same as in COIL, except of the generator of singlet delta oxygen. The pressure inside the laser was 0.6-0.9 Torr and the mixtures $O_2$:NO=200:100 sccm and Ar:$NO_2$=100:100 sccm were used. The iodine flow rate was 0.3 mmol/min. Both types axial and transverse subsonic flow lasers were examined. The latter had better performance. The CW output power was 3 nW at the laser wavelength of 1315 nm, when the yield of $O_2(a^1\Delta_g)$ was 25 %. The RF DOIL has been demonstrated experimentally.

**Key words:** radio-frequency plasma, plasma jet, plasma chilling, hollow cathode, molecular singlet delta oxygen, chemical oxygen-iodine laser, discharge oxygen-iodine laser, axial flow, transverse flow.

## 1. INTRODUCTION

The chemical oxygen-iodine laser (COIL) works on the $^2P_{1/2}\rightarrow{}^2P_{3/2}$ transition of the iodine atom by energy transfer from molecular singlet delta oxygen $O_2(a^1\Delta_g)$. Since the first experimental demonstration of COIL[1], excited oxygen has been usually produced by the chemical reaction of $Cl_2$ with basic solution of $H_2O_2$ in a chemical singlet oxygen generator. Previous attempts to make an alternative generator of $O_2(a^1\Delta_g)$ for use in an oxygen-iodine laser suffered either from a low relative yield of singlet delta oxygen $[O_2(a^1\Delta_g)]/[O_2]_{total}$ or from a low pressure of oxygen. The population inversion in COIL at the room temperature is achieved at the relative yield of about 17 %. Taking into account laser resonator losses, it is desirable to achieve a yield of around 30 % at an oxygen pressure of around 0.5 Torr. In this paper we report an RF plasma jet generator of $O_2(a^1\Delta_g)$, which has been developed for a discharge oxygen-iodine laser (DOIL). The reaction scheme of DOIL is the same as in COIL, except of the generator of singlet delta oxygen.

## 2. RF PLASMA JET GENERATOR OF SINGLET DELTA OXYGEN

The generator labeled as DSOG-3 is schematically shown in Fig. 1. The current device DSOG-3 is an improved version of DSOG-2, which was used in our experiments previously[2]. The discharge chamber consisted of two electrodes with insulation in coaxial arrangement. The outer-grounded electrode and the RF nozzle were made of pure Al and they were water-cooled. Gas was fed into the nozzle. High purity gases were used. The RF power was supplied via an impedance matching network. A typical pressure upstream the nozzle was about 6-9 Torr and 0.1-0.9 Torr downstream. The RF frequency was 99.9 MHz and the RF power was up to 200 W. The pumping velocity was up to 600 $m^3/h$ and it could be changed by a throttling valve.

* Permanent Address: Institute of Physics, Dept. of Gas Lasers, Na Slovance 2, 180 40 Praha 8, Czech Republic, e-mail schmiedb@fzu.cz



XIII International Symposium on Gas Flow and Chemical Lasers and High-Power Laser Conference,
Antonio Lapucci, Marco Ciofini, Editors, Proceedings of SPIE Vol. 4184 (2001)

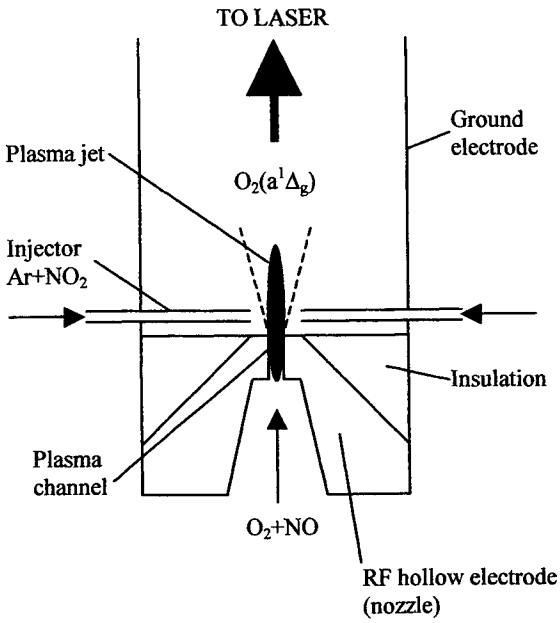


Fig. 1 RF plasma jet generator of $O_2(a^1\Delta_g)$ (DSOG-3)

During the development stage the gas mixture $O_2$:$N_2$:NO=200:20:10 sccm appeared to be the best one. The basic production channel of $O_2(a^1\Delta_g)$ is the electron impact on a ground state molecule of oxygen. However, this way can produce only 10-13 % yield of $O_2(a^1\Delta_g)$, if only pure $O_2$ is used. The enhancement due to $N_2$, described in DSOG-2 experiments[2], increases the yield slightly by 2-3 %. NO is used in order to add another production channel of $O_2(a^1\Delta_g)$ generation. Such enhancement is caused by energy transfer from electronically excited state of NO molecule to oxygen molecule[2]

$$NO(a^4\Pi_i) + O_2 \rightarrow O_2^* + NO \qquad (1)$$

where the star in superscript denotes singlet states. It is assumed that a subsequent depopulation to $O_2(a^1\Delta_g)$ occurs. Then the relative yield of $O_2(a^1\Delta_g)$ exceeds 20 %. The electronically excited state $a^4\Pi_i$ of NO molecule has the energy of 4.71 eV and it is metastable, the lifetime is 160 ms[3].

The plasma jet was produced in the Al cylindrical nozzle, having the inner diameter of 3 mm and the length of 8 mm. The best performance of DSOG-3 was achieved when the plasma jet was chilled reactively by the gas mixture Ar:$NO_2$=200:10 sccm, which was injected into the plasma jet 5 mm downstream the nozzle exit. Six quartz injectors were used symmetrically at the mutual angle 60°, lying in a plane perpendicular to the axis of the plasma jet. The exit of injectors was 5 mm off the plasma jet axis. The $NO_2$ injection was the necessary step to achieve a higher-pressure operation of DSOG-3. This scheme is based on the well-known homogeneous catalytic recombination of atomic oxygen and ozone destruction by NO. Both O and $O_3$ are strong quenchers of $O_2(a^1\Delta_g)$. $NO_2$ reactions are a part of this scheme. The basic processes of NO-catalyzed recombination of O atoms[4,5,6,7] are:

$$O + NO \rightarrow NO_2 + h\nu \qquad (2)$$

$$O + NO + M \rightarrow NO_2 + M \qquad (3)$$

$$O + NO_2 \rightarrow NO + O_2 \qquad (4)$$

The equation (2) represents the well-known process used as a standard for chemiluminescent reactions with the rate constant $6.4\times10^{-17}$ $cm^3\cdot molecule^{-1}\cdot s^{-1}$ [4]. The equation (3) is the nonluminescent analogy of the previous one using a third body M. The reaction (4) is very much faster than reactions (2) and (3). It implies a possibility to boost the initial rate of O and $O_3$ removal by starting the reaction scheme with the process (4) (i.e. injecting $NO_2$ into DSOG-3 instead of NO downstream the plasma channel). The plasma channel produces oxygen atoms nonuniformly, mainly near the nozzle wall. This is caused by "U" profile of electric field transverse distribution inside the nozzle. Most of oxygen atoms are thus contained in the outer layer of the plasma jet. The basic processes of $O_3$ destruction by NO are following[8]:

$$NO + O_3 \rightarrow NO_2^* + O_2 \qquad (5)$$

$$NO + O_3 \rightarrow NO_2 + O_2 \qquad (6)$$

$$NO_2^* \rightarrow NO_2 + h\nu \qquad (7)$$

$$M + NO_2^* \rightarrow NO_2 + M \qquad (8)$$

where the star denotes electronically excited state and M is another body. The rate constants of the primary processes are $k_{(5)}=(7.6\pm1.5)\times10^{11}\cdot\exp(-4180\pm300/RT)$ and $k_{(6)}=(4.3\pm1.0)\times10^{11}\cdot\exp(-2330\pm150/RT)$ $cm^3\cdot mole^{-1}\cdot s^{-1}$. When O and $O_3$ occurrence is reduced, the pressure can be increased substantially. During preliminary experiments without a laser, the singlet delta oxygen yield of 32 % was achieved at the elevated output pressure of 0.43 Torr. The efficiency of DSOG-3 was 2.2 %. This efficiency is defined as a ratio of the power in $O_2(a^1\Delta_g)$ and the RF power. The dependence of $O_2(a^1\Delta_g)$ yield on the RF power and pressure are in Fig. 3 and 4. Both the dependencies were measured 50 cm downstream the nozzle.

The diagnostics of $O_2(a^1\Delta_g)$ was based on the fundamental emission band at 1268 nm. The emission from the diagnostic chamber (Pyrex pipe connecting DSOG-3 and DOIL) was coupled into the step index optical fiber with a core

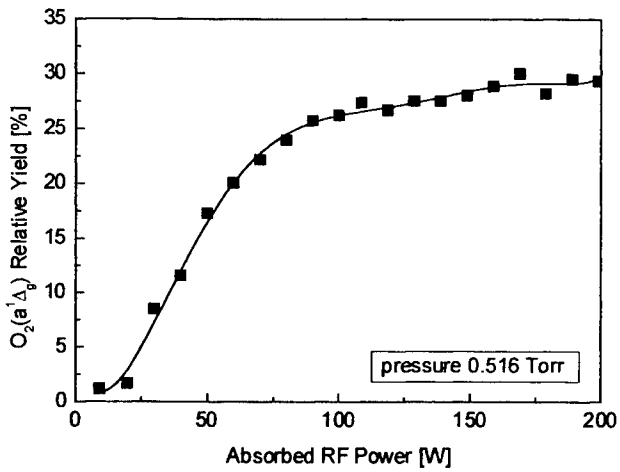


Fig. 2 $O_2(a^1\Delta_g)$ relative yield vs. RF power

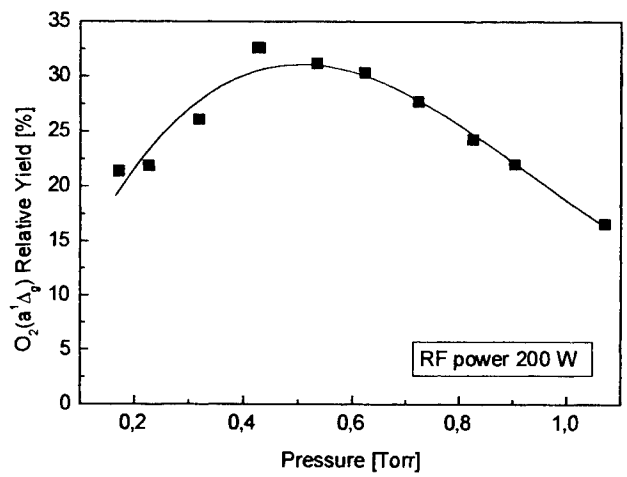


Fig. 3 $O_2(a^1\Delta_g)$ relative yield vs. pressure

diameter of 0.8 mm. The fibers were 2 m long and guided the radiation to the optical spectrum analyzer. Usually, only a narrow part of the infrared spectra, surrounding the fundamental emission band was monitored – the range 1.22-1.32 μm. Some optical noise was detected as a consequence of the reactions (2) and (7). This noise originated from the airglow chemiluminescent reaction of NO with O and $O_3$. A personal computer integrated only the true fundamental emission band. These data together with pressure and temperature data measured in the diagnostic chamber were used to determine the yield of $O_2(a^1\Delta_g)$.

## 3. LASER TESTS OF DSOG-3

The effluent of DSOG-3 was mixed with molecular iodine in the far afterglow region 60-100 cm downstream the nozzle. Both axial and transverse subsonic flow DOIL types were examined (see Fig. 4), using the plan-concave stable resonator, which was formed by two dielectric mirrors. The output flat mirror had the transmission T=0.5 % and the rear concave mirror had the reflectivity R>99.9 %. The radius of curvature was 2 m.

The laser resonator length was 100 cm in case of axial flow DOIL. The axial flow DOIL had the active medium length of 50 cm and its diameter was 17 mm. The laser tube was made of Pyrex glass. Iodine vapor was injected near the rear mirror by a hollow Al ring with 3 holes symmetrically. The diameter of holes was 0.5 mm. The flow rate of iodine was 0.3-0.6 mmol/min. Ar was used as the iodine carrier gas and the mirror purging gas. The flow rate of Ar was 28 sccm for mirror purging and 14-28 sccm for iodine injection. Such usage of Ar and some pressure losses in the axial laser tube elevated the pressure to 0.9 Torr and the yield of $O_2(a^1\Delta_g)$ decreased to around 20 %. Consequently the gas mixtures composition was modified. The discharge mixture $O_2$:NO=200:100 and the chilling mixture Ar:$NO_2$=100:100 were used. $N_2$ was deleted because its positive effect disappeared at higher pressure, probably due to $O_2(a^1\Delta_g)$ quenching by atomic oxygen. The yield of $O_2(a^1\Delta_g)$ was only 25 % because the total concentration of $O_2$ molecules increased by the factor of 1.32, which was measured by a mass analyzer. The increase of $O_2$ pressure was caused by NO and $NO_2$ decomposition and subsequent formation of $O_2$ and $N_2$ molecules. The laser output power was around 1 nW and the wavelength was 1315 nm.

The laser resonator length was 67 cm in case of transverse flow DOIL. The transverse flow DOIL had the active medium length of 15 cm and its height was 1.1 cm. The laser body was made of acryl. Iodine was injected by 30 holes, which were equidistantly distributed in a row on a stainless steel pipe. This pipe had the outer diameter of 6.2 mm and it served as the injector. The diameter of holes was 0.5 mm. The flow rates were the same as in the axial flow case. The pressure inside the laser was 0.65 Torr. The laser output power was about 3 nW.

The laser output power was estimated from spectral measurements. Atomic iodine emission at 1315 nm was coupled into the optical fiber at the laser output mirror. The fiber guided the radiation to the optical spectrum analyzer. Both the lasers were tested in the same way. Typical examples of spectra are shown in Table 1. In case of misaligned resonators the spectral line corresponds to a spontaneous emission on the optical axis. A primary alignment of the laser resonator was done with He-Ne laser and the final adjustment was done maximizing the spectral line height. The spectral lines obtained with aligned resonators are significantly higher than that with misaligned resonators. The intensity ratio of aligned and

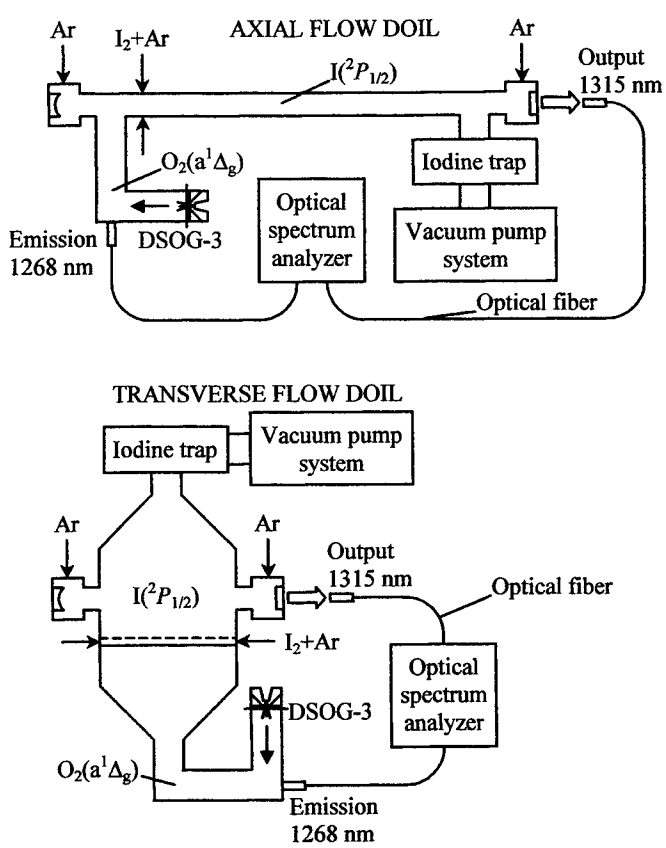


| DOIL | Aligned resonator | Misaligned resonator | Intensity ratio | Output power |
|---|---|---|---|---|
| Axial flow | 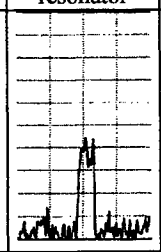 | 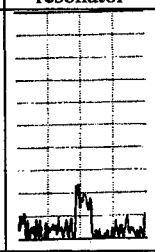 | 2.3 | ~1 nW |
| Transverse flow | 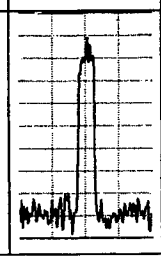 | 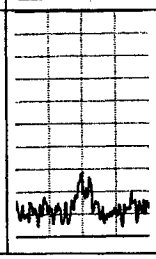 | 6.1 | ~3 nW |

Table 1 Spectral pattern of atomic iodine emission at 1315 nm with aligned and misaligned laser resonators of DOIL. The full range of vertical scale in spectra is 1 pW and the horizontal scale is 10 nm/D. The line center is at the wavelength of 1315 nm.

Fig. 4 Discharge Oxygen-Iodine Laser (DOIL) axial and transverse flow configuration

misaligned resonators was 2.3 in case of the axial flow DOIL and 6.1 in case of the transverse flow DOIL. The comparison of axial and transverse flow lasers shows that the laser effect was more significant in case of the transverse DOIL. Under these conditions the CW DOIL has been demonstrated experimentally. The overall performance of DOIL is still far from optimum, namely due to DSOG-3 parameters. The generator of $O_2(a^1\Delta_g)$ requires significant improvements, however, it is already sufficient for weak laser oscillations near the laser threshold. Comparing to COIL, DOIL exhibits the ability of long term and very stable performance.

## 4. CONCLUSION

The experimental demonstration of CW laser action in the subsonic discharge oxygen-iodine laser confirms the feasibility of $O_2(a^1\Delta_g)$ plasma generation as the alternative way to the chemical generation.

## 5. ACKOWLEDGEMENT

The authors wish to acknowledge the support of Anan College of Technology, Fujisaki Electric Company, Kawasaki Heavy Industries, Ltd. and Nagaoka University of Technology.

## 6. REFERENCES

1. W.E. McDermott, N.R. Pchelkin, D.J. Benard, R.R. Bousek, Appl. Phys. Lett. **32**, 469 (1978).
2. J. Schmiedberger, S. Takahashi, H. Fujii, *XI. GCL/HPL*, 25-30 Aug. 1996, Edinburgh, UK, Proc. SPIE **3092**, 694.
3. A.A. Radzig, B.M. Smirnov, „Reference Data on Atoms, Molecules, and Ions", Springer-Verlag, 1985.
4. A. Fontijn, C.B. Meyer, H.I. Schiff, J. Chem. Phys., **40**, 1, 1 January 1964, 64.
5. G.A. Woolsey, P.H. Lee, W.D. Slafer, J. Chem. Phys., **67**, 3, 1 August 1977, 1220.
6. M. Sutoh, Y. Morioka, M. Nakamura, J. Chem. Phys., **72**, 1, 1 January 1980, 20.
7. M. Venugopalan, „*REACTIONS UNDER PLASMA CONDITIONS*", Wiley-Interscience, II, New York, 1971.
8. P.N. Clough, B.A. Thrush, Trans. Faraday Soc., P. 4, V. 63, No. 532, April 1967, 915.

# A new chemically pumped I ($^2P_{1/2} \rightarrow {}^2P_{3/2}$) laser at 1.315 μm

Thomas L. Henshaw*, Gerald C. Manke II, Timothy J. Madden and Gordon D. Hager

Air Force Research Laboratory

High Power Gas Lasers Directorate

Kirtland AFB, NM, USA 87117-5776

Michael R. Berman

Air Force Office of Scientific Research/NL

801 North Randolph St, Room 732

Arlington, VA 22203-1977

## ABSTRACT

CW laser action has been demonstrated on the electronic I* ($^2P_{1/2}$) → I ($^2P_{3/2}$) transition of atomic iodine at 1.315 μm from the NCl ($a^1\Delta$) + I ($^2P_{3/2}$) energy transfer reaction. The stimulated emission was generated in a transverse subsonic flow device when hydrogen azide, $HN_3$, was injected into a flow of iodine and chlorine atoms. The measured laser output power was 180 mW.

**Keywords:** chemical laser, iodine laser, energy transfer laser, NCl ($a^1\Delta$) metastables, azides

## 1. INTRODUCTION

In view of their generally efficient conversion of chemical potential into laser radiation, chemical lasers have been sought out for numerous applications in which lightweight, self-contained lasers are utilized. It was not until 1978 that McDermott and co-workers demonstrated the first chemically pumped electronic transition laser. [1,2] Continuous wave (cw) laser oscillation was achieved on the I* ($^2P_{1/2}$) - I ($^2P_{3/2}$) transition of atomic iodine via the energy transfer reaction between the oxygen metastable, $O_2$ ($a^1\Delta$), and a ground state iodine atom, I ($^2P_{3/2}$). This chemistry forms the basis of the high-powered Chemical Oxygen Iodine Laser, or COIL, which operates in the near-infrared at 1.315 μm with cw power up to 40 kW. Recently, this laboratory reported for the first time a direct and quantitative measurement of the population inversion between the I ($^2P_{3/2}$) and I*($^2P_{1/2}$) states of atomic iodine produced by energy transfer from NCl ($a^1\Delta$).[3] This effort represented a significant milestone in the development of a chemically pumped, all gas phase iodine laser. In continuing our investigation into the NCl ($a^1\Delta$) / I*($^2P_{1/2}$) energy transfer system, we report for the first time an example of continuous wave I* ($^2P_{1/2}$) - I ($^2P_{3/2}$) laser oscillation resulting from entirely gas phase chemical generation.

## 2. EXPERIMENTAL

* Correspondence: Email: Thomas.Henshaw@kirtland.af.mil; Telephone:505-853-0574; Fax: 505-846-4807



XIII International Symposium on Gas Flow and Chemical Lasers and High-Power Laser Conference,
Antonio Lapucci, Marco Ciofini, Editors, Proceedings of SPIE Vol. 4184 (2001)

The demonstration of I* ($^2P_{1/2}$) - I ($^2P_{3/2}$) laser action was performed in a transverse subsonic flow reactor shown in Figure 1. The essential features of this apparatus are a DC discharge for F atom production, an axial injector for DCl injection, and two side-wall transverse injectors for HI and $HN_3$ admission into the flow stream. In addition, the apparatus is equipped with sensitive optical diagnostics for measuring optical gain between the I ($^2P_{3/2}$) – I* ($^2P_{1/2}$) states and chemiluminescent I* ($^2P_{1/2}$) emissions. Experimental details of the gain measurement and methodology have been described elsewhere [4-6] and only a brief discussion is presented here.

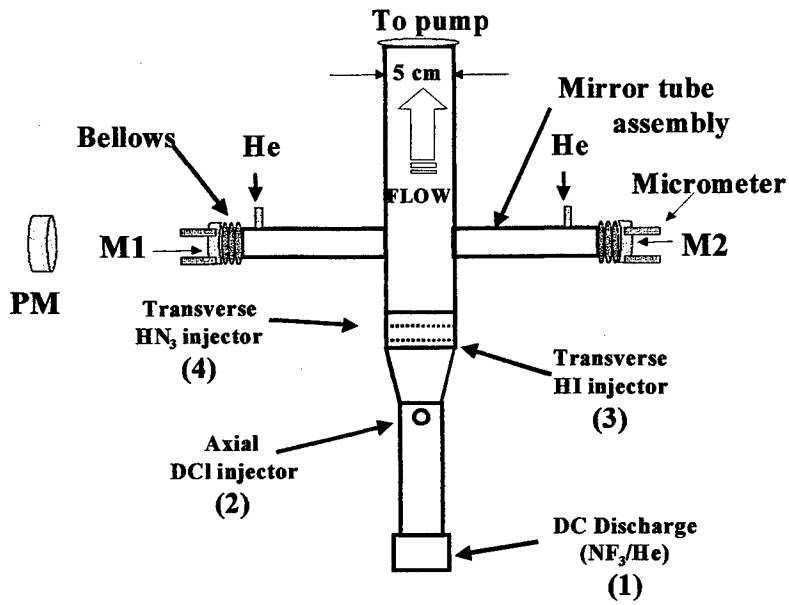


Figure 1. Schematic representation of the subsonic flow device and optical resonator showing (1) D.C. discharge, (2) axial injector (DCl), (3) first set of transverse wall injectors (HI), (4) second set of transverse wall injectors ($HN_3$). The optical cavity, consisting of mirrors M1 (outcoupler) and M2, is joined to the flow tube by two tubes containing mirror mounts, bellows and micrometers for alignment. Each tube is purged with He and the out-coupled laser power measured with a power meter, PM.

The laser cavity consisted of 5 cm wide x 2 cm high stainless steel duct (cross sectional area = 10 $cm^2$) whose inner surfaces were lined with Teflon ramps and flow shrouds to minimize wall deactivation and help confine the active gain zone to a nominal 5 cm in length. The resonator mirrors, M1 and M2 in Figure 1, were 2.54 cm in diameter and were mounted on two 2.54-cm (o.d.) vacuum tubes with mirror bellows and micrometers for alignment. The mirrors were separated by 1.15 m and purged with He during laser operation. The reactor wall height (2 cm) and the inside diameter of the mirror mount (2 cm) adjoining the mirrors to the vacuum tubes defined the minimum aperture of the cavity. Laser power measurements were conducted under a variety of optical resonator conditions. However, owing to the potentially small zero power of the system, the initial resonator was fitted with two symmetric 5 m concave ultra-high finesse cavity mirrors (Research Electro Optics Corp) that were primarily used to confirm the presence of stimulated emission. These high finesse mirrors were characterized by Cavity Ringdown Spectroscopy (Los Gatos Research, Los Gatos, CA) and revealed a high reflectivity of 99.998% at 1.32 μm; however, measurement of transmission and substrate absorption / scattering losses were not performed. Subsequent to the initial laser demonstration, additional power extraction experiments were conducted using various output couplers listed at a nominal 99.8% and 99.9% reflectivity (CVI, Inc.) and the high finesse back reflector of 99.998% reflectivity. The laser power output was measured with an Ophir power meter (Model PD 300-IR Nova) for tests in the 0-30 mW range and a Coherent meter (Model 210) for powers above 30 mW.

Fluorine atoms are generated using a 10 kW DC discharge (1.75 kW actual power load when running) of $F_2$ or $NF_3$ in helium. Flow reactor pressures were measured with calibrated absolute capacitance manometers. Reagents introduced into the flow stream were measured with either calibrated mass flow controllers or sonic orifices. Hydrogen azide was synthesized by the reaction of molten stearic acid ($CH_3(CH_2)_{16}COOH$) with sodium azide ($NaN_3$,) under vacuum at 110 °C. A 10:1 molar excess of stearic acid over sodium azide was used. The gaseous $HN_3$ was stored as a 10% mixture in helium.

Helium diluent (Matheson, 99.995%), $NF_3$ (Spectra Gas, 99%), DCl (Cambridge Isotopes, 99 %), HI (Matheson, 99%) was used without further purification.

## 3. RESULTS AND DISCUSSION

The chemical generation of $I^*(^2P_{1/2})$ and subsequent lasing is based on a sequential process in which Cl and I atoms are produced,

$$F + DCl \rightarrow DF + Cl,\ k_{300\,K} = 1 \times 10^{-11}\ cm^3/s\ ^{(7)} \quad (1)$$
$$Cl + HI \rightarrow HCl + I(^2P_{3/2}),\ k_{300\,K} = 1.0 \times 10^{-10}\ cm^3/s,\ ^{(8)} \quad (2)$$

followed by NCl ($a^1\Delta$) production,

$$Cl + HN_3 \rightarrow HCl(v) + N_3,\ k_{300\,K} = 1 \times 10^{-12}\ cm^3/s\ ^{(9)} \quad (3)$$
$$Cl + N_3 \rightarrow NCl(a^1\Delta, b^1\Sigma, X^3\Sigma) + N_2(X^1\Sigma),\ k_{300\,K} = 2 \times 10^{-11}\ cm^3/s\ ^{(10,11)} \quad (4)$$

and finally the energy transfer reaction between NCl ($a^1\Delta$) and I ($^2P_{3/2}$) to generate $I^*(^2P_{1/2})$: [10,12]

$$NCl(a^1\Delta) + I(^2P_{3/2}) \rightarrow NCl(X^3\Sigma) + I^*(^2P_{1/2}),\ k_{300\,K} = 2 \times 10^{-11}\ cm^3/s \quad (5)$$
$$I^*(^2P_{1/2}) + h\nu \rightarrow I(^2P_{3/2}) + nh\nu\ (1.315\ \mu m) \quad (6)$$

The magnitude of these room temperature rate coefficients indicate a rapid mechanism for the generation of NCl ($a^1\Delta$) and $I^*(^2P_{1/2})$. Furthermore, since both the branching fractions for NCl ($a^1\Delta$) and $I^*(^2P_{1/2})$ in reactions (4) and (5) are reported to exceed 50%, the mechanism described here depicts an efficient gas phase chemical process for the production of NCl ($a^1\Delta$) and $I^*(^2P_{1/2})$. [10-12]

The observation of small signal gain on the I ($^2P_{3/2}$) – I* ($^2P_{1/2}$) transition was measured with a continuously tunable, single-mode 1.315 μm diode laser with a spectral line width of less than 500 kHz (FWHM) over 30 GHz from 7602.4 to 7603.5 $cm^{-1}$. This performance allows the laser to scan across the entire I ($^2P_{3/2}$) – I* ($^2P_{1/2}$) transition with complete hyperfine resolution. In these studies, the F(3,4) transition was used to monitor the I ($^2P_{3/2}$) → I* ($^2P_{1/2}$) gain. Under the flow condidtions provided in Table 1, the I ($^2P_{3/2}$) – I* ($^2P_{1/2}$) absorption curve was inverted to the positive direction when $HN_3$ is added to a flow of chlorine and iodine atoms. The magnitude of the peak gain was measured to be 0.025%/cm. Due to the small signal gain of the system, the initial resonator was fitted with two symmetric 5 m concave ultra-high finesse cavity mirrors ( 0.99998 reflectivity at 1.32 μm) to overcome cavity losses and confirm the presence of stimulated emission. The relevant flow and resonator conditions for establishing lasing are tabulated as Trial 1 in Table 1. Evidence of laser action was demonstrated by measuring the output power on a calibrated power meter. Thus, upon adding $HN_3$ to a steady stream of Cl and I atoms, 3mW of power was measured per mirror port for a total of 6 mW. In addition, the mode pattern of the laser was easily observed on a near- IR phospor card (1.3 μm) at a distance of two meters from the output coupler (M1). In contrast, upon misaligning the cavity or turning off any of the fuels, the laser power signal was immediately extinguished and returned to baseline. The laser run time is typically 20 - 30 seconds, however, this period of operation simply was performed only to conserve the $HN_3$ fuel. Longer run times of up to several minutes are possible and are only limited by the storage volume and pressure of our $HN_3$ reservoir (300 L). Attempts at extracting more power from the cavity was performed by replacing the output coupler (M1) with more transmissive mirrors. In this vein, two vendor quoted mirrors with nominal reflectance values of 0.998 R (2 m cc) and 0.999 R (2 m cc) were tested for output power. No attempt at specifying the mirror scattering or absorption was performed. For purposes of identification, the 0.998 R and 0.999 R mirrors were labeled OC I and OC II, respectively. Trial 2 in Table 1 shows the effect of substituting the high finesse outcoupler with OC I, R = 0.998. For near identical flow conditions, the output power more than triples. Indeed, using OCI under the enhaced $NF_3$, $HN_3$ and HI flow conditions shown in Trial 3 the power increases considerably to 110mW. The highest powers were obtained in Trial 4 with OC II, R = 0.999, as an extracted power of 180 mW was observed.

Table 1. Flow reactor conditions for achieving laser action on the $I^*(^2P_{1/2})$ - I ($^2P_{3/2}$) transition.

| Flow Reactor Conditions | | | | | | | | Resonator Conditions | | |
|---|---|---|---|---|---|---|---|---|---|---|
| Trial | He (mmol/s) | $NF_3$ (mmol/s) | DCl (mmol/s) | $HN_3$ (mmol/s) | HI (mmol/s) | P (torr) | Zone (cm) | HR | OC | Power (mW) |
| 1 | 128.80 | 1.08 | 2.11 | 3.16 | 0.04 | 15.73 | 15 | 0.99998 | 0.99998 | 6 |
| 2 | 127.86 | 1.02 | 2.20 | 3.03 | 0.04 | 15.61 | 15 | 0.99998 | 0.998 (I) | 19 |
| 3 | 149.78 | 1.53 | 2.22 | 4.36 | 0.07 | 14.67 | 15 | 0.99998 | 0.998 (I) | 110 |
| 4 | 141.73 | 1.51 | 2.40 | 4.59 | 0.07 | 14.95 | 15 | 0.99998 | 0.999 (II) | 180 |

## ACKNOWLEDGMENTS

The authors wish to acknowledge Brian Anderson, Ralph Tate, John Herbelin, Vaughn Halford, Richard Hagenloh and Shiv Dass for their technical assistance in these studies.

## REFERENCES

1. W. E. McDermott, N. R. Pchelkin, D. J. Benard, R. R. Bousek, " An Electronic Transition Chemical Laser," Appl. Phys. Lett. **32**, pp.469- 470, 1978.
2. D. J. Benard, W. E. McDermott, N. R. Pchelkin, R. R. Bousek, "Efficient Operation of a 100-W Transverse Flow Oxygen-Iodine Chemical Laser," Appl. Phys. Lett. **34**, pp. 40-41, 1979.
3. J. M. Herbelin, T. L. Henshaw, B. D. Rafferty, B. T. Anderson, R. F. Tate, T. J. Madden, G. C. Manke II, G. D. Hager, "The Measurement of Gain on the 1.315 μm Transition of Atomic Iodine in a Subsonic Flow of Chemically Generated NCl ($a^1\Delta$)," *Chem. Phys. Lett.* **299**, pp. 583-588, 1999.
4. R.F. Tate, B.T. Anderson, P.B. Keating, G.D. Hager, "Zeeman Spectra of Atomic Iodine in a 0 – 400 Gauss B-Field," Proc. SPIE, Gas and Chemical Lasers and Intense Beam Applications, 3268, pp. 115-124, (1998).
5. B. D. Rafferty, B.T. Anderson, T. L. Henshaw, J.M. Herbelin, G.D. Hager, "Titration of Fluorine Atoms by Laser Absorption of Iodine Atoms," Lasers 97, pp. 23-28, (1997).
6. T. L. Henshaw, T. J. Madden, J. M. Herbelin, G. C. Manke II, B. T. Anderson, R. F. Tate, and G. D. Hager, "Measurement of gain on the 1.315 μm transition of atomic iodine produced from the NCl ($a^1\Delta$) + I ($^2P_{3/2}$) energy transfer reaction," Paper 3612-24, SPIE Conference on Gas and Chemical Lasers and Intense Beam Applications II, San Jose, CA, January 1999.
7. M.A.A. Clyne, W.S. Nip, "Kinetics of Fluorine Atom Reactions Using Resonance Absorption Spectrometry in the Far Vacuum Ultraviolet, Reactions F + HCl, $CH_4$, $CHCl_3$, $CHCl_2F$, and $CHClF_2$," Int. J. Chem. Kinet. **10**, pp. 367-387, 1978.
8. F. J. Wodarczyk, C. B. More, "Laser Initiated Chemical Reactions: Total Absolute Reaction Rate Constants for Cl + HBr and Cl + HI," Chem. Phys. Lett. **26**, pp. 484-488, 1974.
9. G.C. Manke II, T. L. Henshaw, T. J. Madden, G. D. Hager, "Temperature dependence of the Cl + $HN_3$ reaction from 300 to 480K," Chem. Phys. Lett. **310**, pp. 111-120, 1999.
10. T. L. Henshaw, S. D. Herrera, and L. A. Schlie, "Temperature Dependence of the NCl ($a^1\Delta$) + I ($^2P_{3/2}$) Reaction from 300-482 K," J. Phys. Chem. **102**, pp. 6239-6246, 1998.
11. G. C. Manke II, D. W. Setser, " Kinetics of NCl ($a^1\Delta$ and $b^1\Sigma$+) Generation: The Cl + $N_3$ Rate Constant, the NCl ($a^1\Delta$) Product Branching Fraction, and Quenching of NCl ($a^1\Delta$) by F and Cl Atoms," J. Phys. Chem. **102**, pp. 153 – 163, 1998.
12. A. J. Ray, R. D. Coombe, "Energy Transfer from NCl ($a^1\Delta$) to Iodine Atoms," J. Phys. Chem. **97**, pp. 3475-3479, (1993).

# ElectriCOIL: An Advanced Chemical Iodine Laser Concept

David L. Carroll and Wayne C. Solomon
*CU Aersopace, Urbana, IL 61802*
and
*University of Illinois at Urbana-Champaign, Urbana, IL 61801*

## ABSTRACT

Advanced chemical iodine laser technology will logically include novel all gas phase generation techniques for an iodine energy donor and the injection of atomic rather than molecular iodine. Candidate methods are discussed for the creation of an all gas phase energy donor as well as for injecting atomic iodine. This research will lead directly to designs that will be fabricated and tested extensively with detailed diagnostics to evaluate the chosen design's performance attributes. Preliminary analysis and modeling of the ElectriCOIL system concept is presented. ElectriCOIL will reduce weight and simplify both military and commercial chemical iodine laser systems. Potential cost and weight savings are also envisioned as the massive quantities of liquid chemicals will be completely eliminated from the device operation.

Keywords: ElectriCOIL, COIL, chemical oxygen iodine laser, iodine laser, electrical singlet oxygen generation, iodine dissociation.

## 1. INTRODUCTION

Several dramatic changes to gain generator technologies are needed to allow chemical oxygen-iodine laser (COIL) systems to achieve their full potential as efficient producers of 1.3 μm laser beams. These include: 1) Highly improved nozzle mixing efficiencies; 2) Carefully designed media and beam quality properties; 3) Higher pressure recovery potential; and 4) Radically new the $O_2(^1\Delta)$ generator subsystems. This paper addresses the fourth issue, innovative improvements in generation of excited states of both oxygen and iodine. The development of gas phase $O_2(^1\Delta)$ generator subsystems will also have a direct impact on technological improvements needed in under items 1 and 3.

The Chemical Oxygen-Iodine Laser (COIL) was developed first by the United States Air Force in 1978 [McDermott, 1978]. Since that initial demonstration COIL technology has undergone numerous improvements [Truesdell, 1992] and chemical efficiencies as high as 27-30% using helium diluent have been demonstrated [Rittenhouse, 1999; Yang, 1997]. Much of the COIL technology development to date has focused on the singlet-oxygen generator (SOG) and the liquid SOG technology has developed to a fairly mature state; major improvements to the aqueous system are less likely to occur, especially in terms of efficiency as expressed by power to weight ratios. The basic COIL design has changed little over the past decade. However, an all gas phase system offers a new exciting pathway. One approach is to exploit the recent findings at the Air Force Research Laboratory (AFRL) with the NCl $(^1\Delta)$ all gas phase chemical system [Henshaw, 2000]; a second is to provide the necessary atomic Iodine and $O_2(^1\Delta)$ purely by electrical means.

AFRL has recently demonstrated that significant quantities of excited iodine atoms can be produced using an all gas phase generator [Henshaw, 2000]. The excited species which transfers to Iodine atoms, in this case, $NCl(^1\Delta)$, can be produced without a liquid phase generator. This is the first major breakthrough in energy donor generator technology in ten years. This Air Force research provides a roadmap for future work in the field. The Air Force Research Laboratory at Albuquerque demonstrated lasing with this concept [Henshaw, 2000]. As their research proceeds, a number of opportunities subsequently open up. The potential which intrigues CU Aerospace and the University of Illinois is presented in this paper. We believe that it is possible to construct a highly efficient electric generation scheme to provide the precursor energy donor species, $O_2(^1\Delta)$. A new kind of cw COIL laser which is an Electrically assisted Chemical Oxygen Iodine Laser, (**ElectriCOIL**) would subsequently be achievable, see Figure 1. Workers in Japan [Itami, 1999; Fujii, 2000] and Russia [Ivanov, 1999] have shown that flowing discharge tubes containing ground state oxygen can produce significant quantities of the desired, $O_2(^1\Delta)$ precursor molecules. This paper suggests how one can transform such research into a practical all gas phase system. Atomic iodine injection is also an integral part of the proposed program. Figure 1 illustrates the limitations of existing COIL technology as well as the possible improvement from the implementation of ElectriCOIL technology. Such an


XIII International Symposium on Gas Flow and Chemical Lasers and High-Power Laser Conference,
Antonio Lapucci, Marco Ciofini, Editors, Proceedings of SPIE Vol. 4184 (2001)

electronically produced $O_2(^1\Delta)$ generator could be even more effective if implemented simultaneously with an atomic iodine augmentation technique.

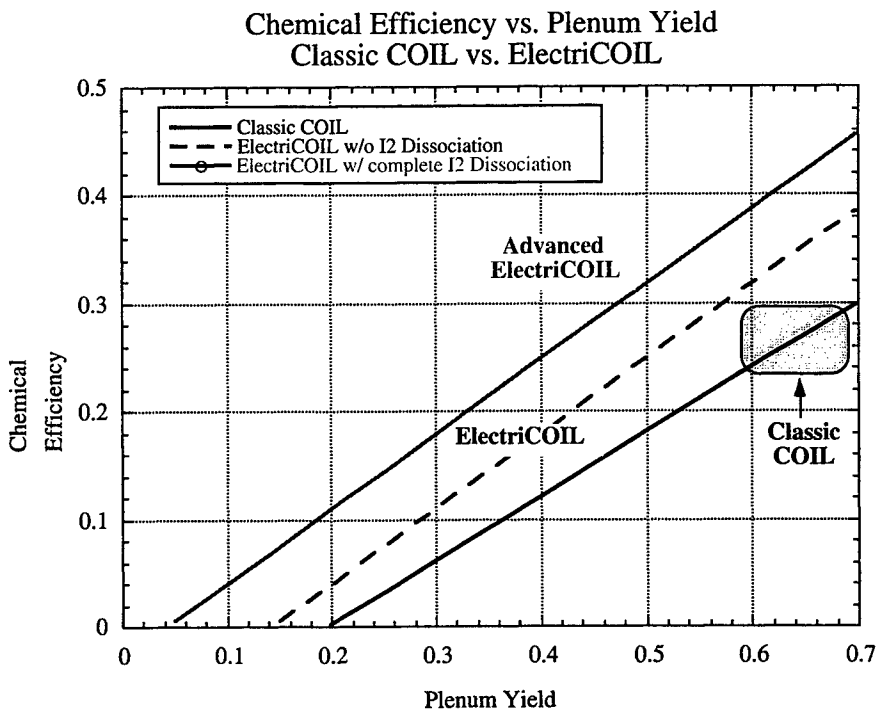


Fig. 1. Using a heuristic equation, a comparison between classic COIL technology and the performance possibilities for an ElectriCOIL device are illustrated. While ElectriCOIL may not be able to match the plenum yield of today's COIL system, significantly smaller yields are capable of matching current chemical efficiencies.

We believe the ElectriCOIL concept will be a major breakthrough in high power laser technology. The impact of this technology is summarized below:

- ***Dramatically reduce the overall energy donor and gain generator tankage requirements by eliminating the aqueous chemicals needed for generation of $O_2(^1\Delta)$ in today's COIL systems.***
- ***Eliminate the need to constantly re-supply an advanced version of a military or commercial COIL system with exotic aqueous fluids which are inherently difficult to handle. Advanced laser support hardware will largely consist of power conditioning equipment and a small tank of liquid oxygen.***
- ***Take advantage of research in aircraft power generation systems to provide the necessary power to supply an airborne ElectriCOIL laser system.***

## 2. BACKGROUND

Low pressure discharges in electronegative gases are the basis for plasma processing in micro electronics. The plasma of the dc low pressure discharge in a long cylindrical tube with the electric field directed along the axis is convenient for experimental study. A high degree of both non-equilibrium and non-uniformity with the radius along the axis is an important feature of these discharges. In pure oxygen the major active particles are atomic oxygen and the oxygen metastable $O_2(^1\Delta)$. Modeling of the electric discharge phenomena has shown that oxygen atoms and $O_2(^1\Delta)$ account for the volume processes within the discharge [Ivanov, 1999]. It has also been found experimentally that excitation of molecular oxygen in a glow discharge at around 1 torr provides significant quantities of $O_2(^1\Delta)$ [Ivanov, 1999]. Concentrations of $O_2(^1\Delta)$ on the order of $2\times10^{15}$ molecules/cc were observed [Ivanov, 1999] employing emission spectroscopy of the 1268 nm band for the transition $O_2(^1\Delta, \nu=0) \rightarrow O_2(^3\Sigma, \nu=0)$.

Fujii [Fujii, 1994] reported good success, 17% yield of $O_2(^1\Delta)$, with a small RF generator. More recently, workers in Japan provided evidence that they could produce 21% $O_2(^1\Delta)$ in a microwave discharge [Itami,1999] and 32% using an RF discharge [Fujii, 2000]. They studied the yield sensitivity of $O_2(^1\Delta)$ in the presence of various compositions of $O_2$, $N_2$, NO, and $NO_2$ and showed added gases gave improved results. The experiments were carried out in subsonic axial flow at 2 torr in

a 30 cm long tube with window attachments for observation. Their paper leads one to believe that they are expecting to conduct lasing experiments in the near future employing an upgraded system with a more efficient discharge.

## 3. PRELIMINARY ANALYSIS

To investigate important technology issues related to the COIL lasers, it is useful to employ the COIL heuristic equation developed by Hon *et al.* [Hon, 1996], which is given by,

$$\eta_{chem} = U_{Cl2}\,(Y_{plen} - Y_{diss} - Y_{th} - Y_{deact})\,\eta_{mix}\,\eta_{geom}\,\eta_{ext}\,\eta_{res} \qquad (1)$$

where $\eta_{chem}$ is the chemical efficiency, $U_{Cl2}$ is the utilization of chlorine in the singlet oxygen generator (SOG), $Y_{plen}$ is the yield in the plenum region just upstream of iodine injection, $Y_{diss}$ is the loss of singlet delta oxygen due to dissociation of the iodine molecules, $Y_{th}$ is the threshold yield representing the minimum $O_2(^1\Delta)$ fraction necessary for positive gain, $Y_{deact}$ is the loss of yield due to deactivation reactions, $\eta_{mix}$ is the mixing efficiency defined as the ratio of the accessed $O_2(^1\Delta)$ to the total $O_2(^1\Delta)$ in the flow, $\eta_{geom}$ represents the fraction of the flow interrogated by the resonator, $\eta_{ext}$ is the optical extraction efficiency, and $\eta_{res}$ is the flow residence time efficiency. The yield is defined as the ratio of excited $O_2(^1\Delta)$ to total oxygen in the flow.

Table 1 and Figure 1 present a preliminary examination of the implementation of an ElectriCOIL concept using the heuristic equation [Hon, 1996]. The classic COIL case compared with is the baseline RADICL condition with helium diluent, 0.50 moles/s of $Cl_2$, 4:1 diluent ratio, and a titration ratio of 1.7%; there is a substantial amount of reported data for this condition [Helms, 1994; Tate, 1995]. For ElectriCOIL preliminary estimates it is assumed that the $\eta_{mix}$, $\eta_{geom}$, $\eta_{ext}$ and $\eta_{res}$ terms remain the same as with classic COIL [Truesdell, 1996], that the $Y_{deact}$ term is zero, and $Y_{th}$ has a 150K cavity temperature ($Y_{th}$ =0.044); with these assumptions, Eq. (1) reduces to:

$$\eta_{chem} = 0.6962\,(Y_{plen} - Y_{diss} - 0.044) \qquad (2)$$

Table 1. Estimated effects of different conditions on RADICL performance.

| | Classic COIL | Early ElectriCOIL w/ I2 Injection | Early ElectriCOIL w/ I atom Injection | Mid-stage ElectriCOIL w/ I atom Injection | Advanced ElectriCOIL w/ I atom Injection |
|---|---|---|---|---|---|
| Conditions | $Y_{plen}$ =0.60<br>$Y_{diss}$ =0.10<br>$H_2O$<br>$T_{cav}$=170K | **$Y_{plen}$ =0.20**<br>$Y_{diss}$ =0.10<br>**No $H_2O$**<br>**$T_{cav}$=150K** | $Y_{plen}$ =0.20<br>**$Y_{diss}$ =0.0**<br>No $H_2O$<br>$T_{cav}$=150K | **$Y_{plen}$ =0.30**<br>$Y_{diss}$ =0.0<br>No $H_2O$<br>$T_{cav}$=150K | **$Y_{plen}$ =0.40**<br>$Y_{diss}$ =0.0<br>No $H_2O$<br>$T_{cav}$=150K |
| Heuristic Equation | 24.1% | 3.9% | 10.9% | 17.8% | 24.8% |

Table 1 shows that the heuristic equation predicts a nominal chemical efficiency of 24.1% for the given classic COIL RADICL case. Switching to an early stage ElectriCOIL in which it is assumed that a 20% yield can be obtained (as demonstrated by Japanese researchers [Itami, 1999]), all of the water is removed from the flow, the expected performance is a mere 3.9% chemical efficiency.

Discussed above was the possibility of injecting atomic, rather than molecular, iodine. For this situation $Y_{diss}$ =0. The heuristic equation indicates that this alone results in a significant performance improvement when the dissociation term is zero, Eq. (2), Table 1. Because of the large potential performance enhancement, we feel the investigation of iodine pre-dissociation schemes is an important issue. Conceptually, the ideal ElectriCOIL design appears to be one that injects atomic iodine into a waterless primary flow with singlet delta oxygen generated electrically, provides complete mixing by the end of the optical extraction region, and gives a low cavity temperature of around 150 K. The heuristic equation indicates that such an advanced ElectriCOIL concept could realistically provide chemical efficiencies of around 25%, comparable to today's classic COIL, Table 1, and potentially provide even higher chemical efficiencies if the plenum yield can be increased above roughly 40%, Fig. 1. Even an ElectriCOIL that provides 24% chemical efficiency is an enormous improvement to the classic COIL design because it will lead to a significant reduction of weight per kW of the Airborne Laser (ABL) and simpler operation procedures.

Preliminary calculations using the Blaze II chemical laser model [Sentman, 1977; Carroll, 1995; Carroll, 1996] support the qualitative conclusions drawn from the heuristic equation. Fig. 2 illustrates Blaze II results that are comparable to those shown in Fig. 1, which was based upon the heuristic equation. The advantage of the ElectriCOIL concept is

immediately realized when examining the gain curve with and without molecular iodine pre-dissociation, Fig. 3. The gain curve, with a 20% yield and no pre-dissociation, is very low and would not make a useful laser. However, when the molecular iodine is completely pre-dissociated, then the gain curve, even with a 20% yield, compares very favorably with the classic COIL type gain curve having a 67% yield. Note that the classic COIL curve is for a VertiCOIL case that was baselined to power data, not gain data; historically, when Blaze is baselined to power data the gain curve underpredicts gain data.

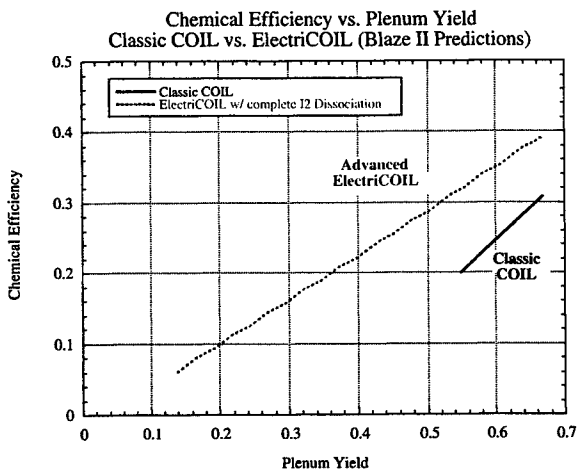


Figure 2. Blaze predictions comparing classic COIL technology and the performance possibilities for an ElectriCOIL device are illustrated. While ElectriCOIL may not be able to match the plenum yield of today's COIL system, significantly smaller yields are capable of matching current chemical efficiencies.

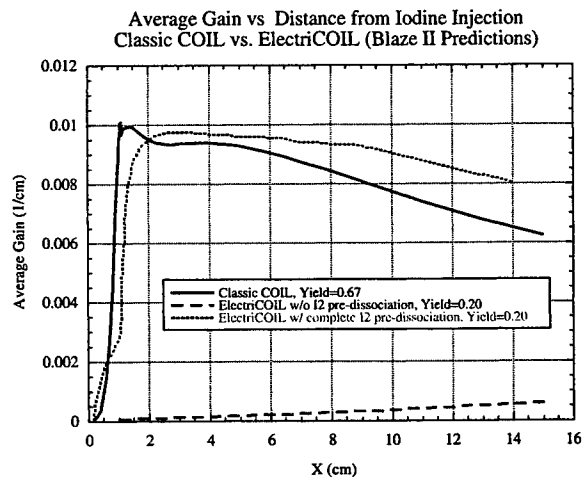


Fig. 3. Blaze predictions of the average gain as a function of distance from the iodine injection position for classic COIL with a yield of 0.67, ElectriCOIL with and without molecular iodine pre-dissociation. Helium diluent was used for these calculations.

Figures 2 and 3 illustrate the innovative concept of combining both electrically produced singlet delta oxygen and pre-dissociated iodine. Each of these concepts have been demonstrated individually, but not in combination; when both ideas are implemented together it is possible to obtain significant gain and laser power with a mere 20% yield; this yield has already been generated in experiments conducted by Itami [Itami, 1999]. More recently, Fujii [Fujii,2000] obtained 32% yield using an RF discharge; this result is particularly encouraging. Experimental work in the area of iodine pre-dissociation has been conducted by Endo and Fujioka's group in Japan [Endo, 1999]. They reported nearly total dissociation from interaction of an Iodine/$N_2$ stream within the microwave cavity. Experiments with subsonic injection, sonic injection and supersonic injection of the atomic iodine stream were conducted. Due to experimental difficulties, only the transonic injection mixing nozzle showed the expected increase in laser efficiency. In this case, about a 10% increase in laser efficiency was noted by Endo. This is probably a lower bound on the efficiency increase since it was difficult to insure that recombination in the injectors was negligible. Iodine pre-dissociation has also been investigated using three-dimensional CFD computations by Madden *et al.* [Madden, 1998]; Madden's results indicated that the injection of atomic iodine slightly downstream of the throat would enhance the power output. Thus it should be possible to demonstrate a 10-15% chemical efficiency with today's electrical generation technology. Improved methods of generating higher yields should lead to even higher chemical efficiencies.

## 4. CONCLUDING REMARKS

We believe that the key performance enhancements to COIL technology are the combination of electrically generated $O_2(^1\Delta)$ and the injection of pre-dissociated iodine with an appropriately redesigned nozzle [Carroll, 2000] that uses the atomic iodine efficiently in the laser region. The principle candidate being considered for creating excited oxygen in the primary flow is an RF discharge. For the ElectriCOIL concept we are focused on either RF discharge [Vagin, 1995], microwave discharge [Sugimoto, 1999] or photolytic pumping for creating atomic iodine to inject into the primary flow. Based upon experimental results of Fujii [Fujii, 2000] that obtained a 32% yield of $O_2(^1\Delta)$, analysis predicts that the ElectriCOIL concept should be able to obtain a chemical efficiency of at least 18%; assuming further enhancements the RF generator would enable a yield of 40%, analysis predicts that a chemical efficiency of around 25% should be achievable.

## ACKNOWLEDGEMENTS

This work was supported by the Air Force Research Laboratory SBIR contract F29601-00-C-0086.

## REFERENCES

Carroll, D. (1995). *AIAA Journal*, **33**, 8, pp.1454-1462.

Carroll, D. (1996). "Optimizing High Pressure Chemical Oxygen-Iodine Laser," Proc. of the Int. Conf. on Lasers'95, eds. V. Corcoran and T. Goldman, STS Press, McLean VA, 225.

Carroll, D., King, D., Fockler, L., Stromberg, D., Solomon, W., Sentman, L., and Fisher, C. (2000), *IEEE J. of Quant. Electronics*, **36**, 1, 40.

Endo, M., Sugimoto, D., Okamoto, H., Takeda, S., and Fujioka, T. (1999). "Performance characteristics of the microwave assisted chemical Iodine oxygen laser", AHPLA'99 SPIE conference, Osaka, November 1999.

Fujii, H. (1994). "COIL in Japan," AIAA Paper 94-2419, Colorado Springs, CO, June 1994.

Fujii, H., Itami, S., Kihara, Y., Fufisaki, K., Okamura, M., Yoshitani, E., Yano, K., Miyatake, T., Schmiedberger, J. (2000). "Hybrid oxygen iodine laser with a discharge singlet oxygen generator," Laser Ablation Conference, Santa Fe, 2000.

Helms, C., Shaw, J., Hager, G., and Truesdell, K. (1994). AIAA Paper 94-2437.

Henshaw, T.L., Madden, T.J., Manke, G.C., Anderson, B.T., Tate, R.F., Berman, M.R., and Hager, G.D. (2000). AIAA Paper 2000-2424.

Hon, J., Hager, G., Helms, C., and Truesdell, K. (1996). *AIAA Journal*, **34**, 8, 1595.

Itami, S., Nakamura, Y., Nakamura, A., Shinagawa, K., Okamura M., and Fujii, H. (1999). AHPLA '99, Osaka, Nov 1999.

Ivanov, V.V., Klopovsky, K..S., Lopaev, D.V., Rakhimov, A.T., and Rakhimova, T.T. (1999). "Experimental and Theoretical Investigation of Oxygen Glow Discharge Structure at Low Pressures", *IEEE Trans. on Plasma Science*, **27**, p. 1279.

Madden, T., Hager, G., Lampson, A., and Crowell, P. (1998). "Computational Fluid Dynamic Investigation of Supersonic Mixing Mechanisms for the Chemical Oxygen-Iodine Laser (COIL)," presented at the Int. Conf. on Lasers'98, Tucson, AZ, Dec. 7-11, 1998.

McDermott, W., Pchelkin, N., Benard, D., and Bousek, R. (1978). *Appl. Phys. Lett.* **32**, 8, 469.

Rittenhouse, T, Phipps, S., and Helms, C. (1999). *IEEE J. of Quant. Elec.*, **35**, 6, p. 857.

Sentman, L., Subbiah, M., and Zelazny, S. (1977). "Blaze II: A Chemical Laser Simulation Computer Program," Bell Aerospace Textron, Buffalo, NY, T.R. H-CR-77-8.

Sugimoto, D., Okamoto, H., Wani, F., Endo, M., Takeda, S., and Fujioka, T. (1999). AIAA Paper 99-3426.

Tate, R., Hunt, Helms, C., Truesdell, and Hager, G. (1995). *IEEE J. of Quant. Elec.*, **31**, 9, 1632.

Truesdell, K., Lamberson, S., and Hager, G. (1992). AIAA Paper 92-3003.

Truesdell, K., Helms, C., Frerking, S., Hager, G., Plummer, D., and Copland, R. (1996). "COIL performance modeling and recent advances in diagnostic measurements," *XI Int. Symp. on Gas Flow and Chemical Lasers and High Power Lasers Conf.*, SPIE, Vol. 3092, 676.

Vagin, N., Pazyuk, V., and Yuryshev, N. (1995). *Kvantovaya Elektronika* (in Russian), **22**, 776.

Yang, T., Copeland, D., Bauer, A., Quan, V., McDermott, W., Cover, R., and Smith, D. (1997). AIAA Paper 97-2384.

# Comparative studies on small signal gain and output power for COIL systems

Jürgen Handke, Karin M. Grünewald, Frank Duschek
DLR - Institute of Technical Physics*

## ABSTRACT

In the 10-kW chemical oxygen-iodine laser (COIL) of DLR, the small signal gain and the laser output power were measured for identical gas flow conditions. The comparison of both results is used to elaborate the expressiveness of small signal gain for COIL laser design.

For these investigations the temporal and spatial dependencies of small signal gain and laser power are measured along the flow axis of the cavity. The measurement of small signal gain is performed by a commercial diagnostic system of PSI with a software package upgraded by the Air Force Research Lab of Kirtland, U.S.A. [1,2,3,4] The laser power is extracted in a stable resonator configuration. In case of spatially resolved investigations, slit apertures of 6 mm width in flow direction are integrated in the cavity.

KEYWORDS: Supersonic COIL, small signal gain, spatial power extraction, slit resonator

## 1. INTRODUCTION

In general, small signal gain (ssg) data describe the laser-relevant properties of the active medium. Therefore, for many types of lasers this information is used to figure out the optimum flow conditions for the active medium and to locate the position of the resonator axis for maximum power extraction. Applying this procedure to a COIL device may result in misleading conclusions.

The chemical oxygen iodine laser is not homogeneously excited within the cavity: All energy that may be converted to optical energy is produced in the oxygen generator and carried along by $O_2(^1\Delta)$ molecules. The lasing species, that is atomic iodine, is admixed to the oxygen flow in general as molecular iodine and must be dissociated first. The atomic iodine is pumped from the ground state $I(^2P_{3/2})$ (referred to as I) into the upper laser level $I(^2P_{1/2})$ (referred to as I*) by energy transfer from $O_2(^1\Delta)$ molecules according to

$$[O_2(^1\Delta)] + [I(^2P_{3/2})] \xleftrightarrow{k_{eq}} [O_2(^3\Sigma)] + [I(^2P_{1/2})] \tag{1}$$

where $O_2(^3\Sigma)$ denotes the oxygen ground state and $k_{eq}$ is the equilibrium constant given by $k_{eq} = 0.75 \exp(401/T)$. The ssg $g_0$ is given by the equation

$$g_0(\nu) = \frac{7}{12}\frac{A\cdot\lambda^2}{8\pi} f(\nu)\cdot\{[I(^2P_{1/2})] - \frac{1}{2}[I(^2P_{3/2})]\} \tag{2}$$

with the Einstein coefficient A, the temperature dependent line shape function $f(\nu)$, and the wavelength $\lambda = 1.315$ µm. The ssg mainly depends on the inversion density. Taking into account eq. (1) and denoting the sum of [I*] and [I] by $[I_{at}]$, the density of total atomic iodine, eq. (2) can be rearranged to

$$g_0(\nu) = \frac{7}{12}\frac{A\cdot\lambda^2}{8\pi}\frac{1}{2} f(\nu)\cdot[I_{at}]\cdot \mathrm{fct}(Y_{Cav,E}), \quad \mathrm{fct}(Y_{Cav,E}) = \frac{Y_{Cav,E}[2\cdot k_{eq}(T)+1]-1}{Y_{Cav,E}[k_{eq}(T)+1]+1}\ . \tag{3}$$

$Y_{Cav,E}$ denotes the yield (ratio of excited to total oxygen) at the cavity entrance. For typical COIL operating conditions $\mathrm{fct}(Y_{Cav,E})$ comes up to a slowly varying value at the order of 1. Within this regime $[I_{at}]$ is of predominant importance for the magnitude of ssg.

* Correspondence: Langer Grund, D-74239 Hardthausen, Germany, Tel. +496298 28-230, Fax +496298 28-582, e-mail: juergen.handke@dlr.de

XIII International Symposium on Gas Flow and Chemical Lasers and High-Power Laser Conference,
Antonio Lapucci, Marco Ciofini, Editors, Proceedings of SPIE Vol. 4184 (2001)

In terms of a simplified analytic expression the output power of a COIL is given by a heuristic equation [5]

$$P_{OUT} = 91 \cdot \frac{kJ}{mol} \cdot \dot{n}_{Cl_2} \cdot U \cdot [Y_{plen} - Y_{th} - Y_{diss} - Y_{deact}] \cdot \eta_{mix} \cdot \eta_{geo} \cdot \eta_{ext} \quad (4)$$

$\dot{n}_{Cl_2}$ denotes the chlorine flow rate to the generator and U the utilization, that is the fraction of reacted to total chlorine. The equation takes into account the available energy produced in the oxygen generator and stored in the flow of singlet delta oxygen ($Y_{plen}$), various loss terms due to threshold ($Y_{th}$), iodine dissociation ($Y_{diss}$), and deactivation processes ($Y_{deact}$), and additionally efficiencies due to gas flow mixing ($\eta_{mix}$) and resonator coupling ($\eta_{geom}$, $\eta_{ext}$). As far as the interest is focussed on the laser power emitted from the respective COIL device with fixed energy input, the predominant parameter for power output is the difference between the oxygen yield at the cavity entrance and threshold condition, expressed by the simplified relationship

$$P_{OUT} \propto [Y_{Cav,E} - Y_{th}] \quad (5)$$

For typical gas flow conditions in a COIL, the concentration of the lasing species $I^*$ is very low compared to the concentration of excited oxygen. Therefore, the COIL output power by far exceeds the energy stored in the upper laser level. This is managed by the fact that after deexcitation of $I^*$ by the radiation field the atomic iodine may be repumped again until the amount of $O_2(^1\Delta)$ falls below the threshold yield. Thus, each iodine atom may contribute for many times to the total output power by emitting stimulated radiation and being repumped again [6].

In summary, within a simplified comparison ssg is mainly dependent on the density of total atomic iodine while output power is dominated by the available excited oxygen.

## 2. EXPERIMENTAL

In order to demonstrate the different dependencies of ssg and power on flow conditions and outcoupling position experiments were performed on the 10 kW COIL device at the DLR Lampoldshausen test site [6, 7]. At base line conditions a primary flow of 500 mmol/s of chlorine is established at a He dilution ratio of 3. The iodine is admixed in the subsonic part of a 2-dimensional nozzle array. For the comparative studies the secondary flow is varied from 3 to 13 mmol/s of iodine at He dilution ratios between 40 to 100. Detailed parametric studies on the device revealed a flow ratio of iodine to oxygen of 1.75% at a He diluent ratio of 70 for maximum power extraction [8]. These conditions are referred to as "optimum conditions" within this paper. The flow within the cavity is supersonic at about M=1.7. The gain length amounts to 200 mm. The coupling geometry is depicted in Fig. 1. The resonator consists of 2 circular mirrors of 2" in diameter. For maximum power output the reflectivities are near 100% for the total reflector and 92% for the coupling mirror. The resonator axis is located 17 mm downstream of the nozzle exit plane (NEP). For the comparative studies the same set-up is applied. Additionally a slit aperture of 6 mm width is integrated directly on the inside of the coupling mirror. The resonator axis is located at different z-positions. For each position an adjusted slit aperture is used. The coaxial alignment of slit and resonator axis is controlled by imaging the output power distribution in black lucite while the power itself is monitored by fast detectors coupled to an Ulbricht sphere.

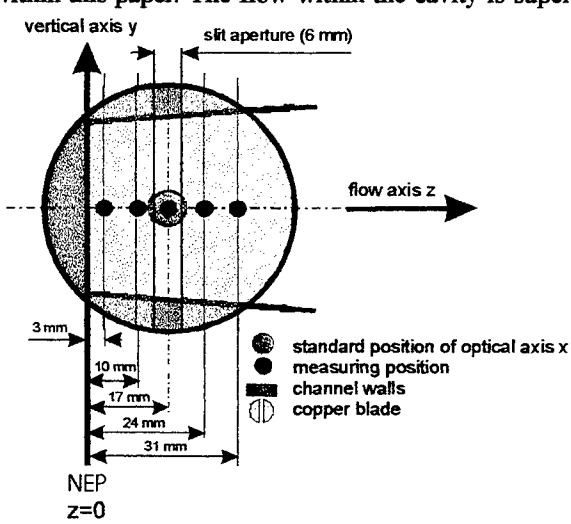


**Fig. 1: Investigated outcoupling configuration.**

Ssg and power measurements were performed for identical flow conditions and at the same local positions. The experimental set-up for ssg measurements and the results of the 2-dimensional ssg and temperature mapping are presented in a separate paper at this conference [9] while only special topics concerning the comparison of ssg and output power are reported within this paper.

## 3. COMPARISON OF OUTPUT POWER AND SMALL SIGNAL GAIN DATA

In a first approach, the output power is studied without any additional slit aperture (i.e. full resonator width, optical axis at 17 mm). Fig. 2 reveals ssg and power data at the position of the resonator axis for maximum power output. Primary flow

and iodine flow are kept constant. Only the secondary dilution ratio is varied. The ssg comes up to about 1.2 % $cm^{-1}$ at maximum. This value fits well with those data derived from Rigrod type measurements carried out earlier[7]. Comparing the fitted curves for output power and ssg it is obvious that both shapes are similar and both curves maximize at the same dilution ratio of about 70. Therefore, at first glance it seems straight forward to optimize a COIL for maximum power output by analyzing the ssg behaviour.

The results are quite different as soon as local scans are considered. In Fig. 3 measured data for ssg and laser power, coupled out by the slit aperture, are plotted versus the position along the flow axis. Again primary and iodine flow are kept constant. Only the amount of secondary He is varied. For optimum and low amount of secondary helium the ssg is nearly constant or slightly decreasing throughout the whole cavity. From ssg and intracavity temperature one can infer that the maximum concentration of atomic iodine is already obtained at the NEP and thereby the $I_2$ dissociation is mainly completed.

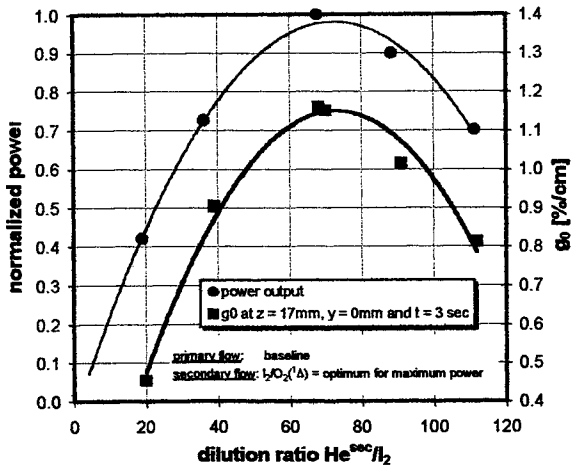


**Fig. 2: Correlation of small signal gain and power output at standard resonator position at a variation of the secondary helium flow rate.**

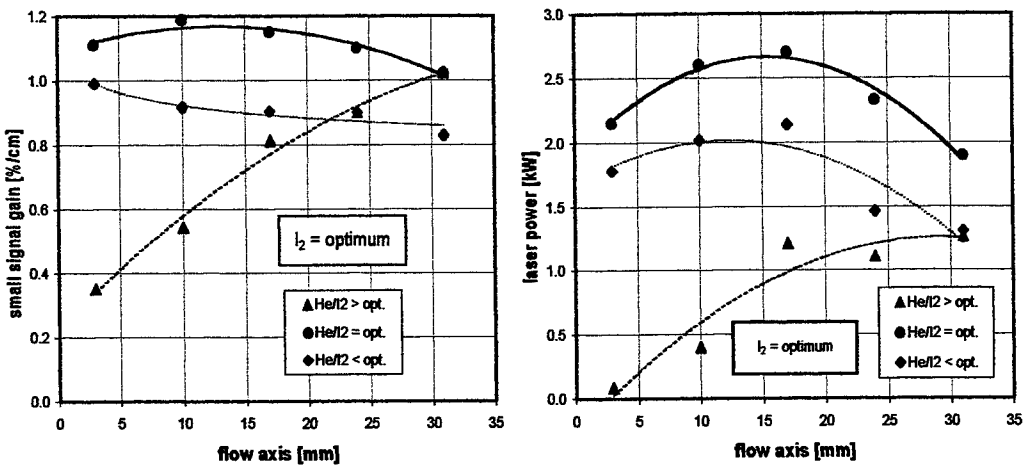


**Fig. 3: Effect of helium flow rates on small signal gain and power profiles.**

The data in Fig. 3 concerning higher helium admixing are of special interest. In this regime the ssg increases throughout the cavity up to the most downstream position. This is explained by a continuously increasing density of atomic iodine. The dissociation is not completed when the flow enters the NEP. However, there is an important difference comparing gain and power data: In spite of bad mixing conditions the ssg comes up to values as high as for best mixing conditions. On the other hand, the output power is by far lower than for optimum conditions. The elongated dissociation path length results in increased losses of excited oxygen and additionally the threshold comes up due to heating effects. In consequence, there is less available singlet delta oxygen and therefore less output power.

Ssg and output power are not only dependent on the

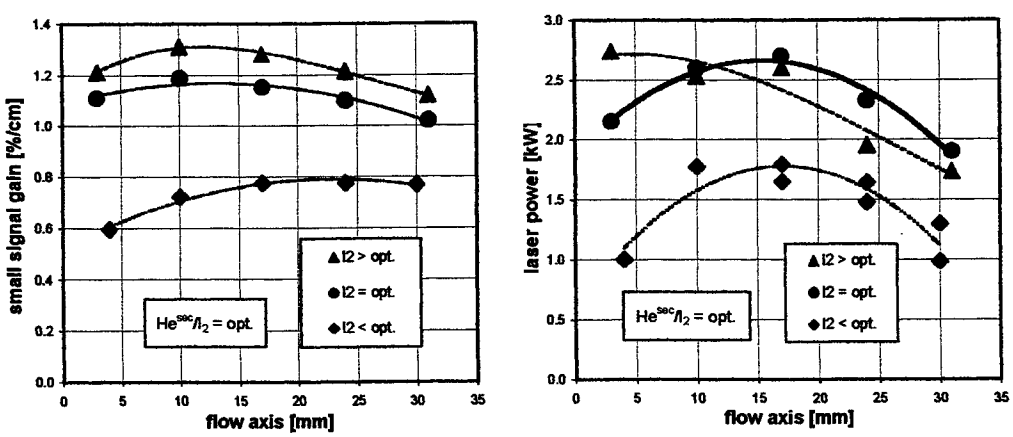


**Fig. 4: Effect of iodine flow rates on small signal gain and power profiles.**

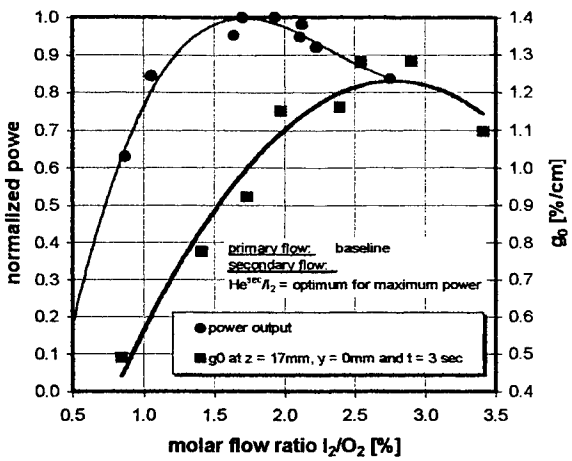


**Fig. 5: Correlation of small signal gain and power output at standard resonator position at a variation of iodine flow rate.**

secondary diluent ratio but also on the iodine flow itself as shown in Fig. 4 . The iodine flow rate is varied whereas the admixed He flow is always adjusted to the optimum ratio of He:$I_2$ [8]. As far as ssg is concerned, an increase of the iodine flow rate results in higher ssg values. That is as expected from theory: higher iodine flow rates result in higher densities of atomic iodine – and thereby in higher inversion densities - as long as the degree of dissociation remains high and/or there still is enough excited oxygen. However, concerning high iodine flow rates, an increase in ssg does not result in higher output power. Only the spatial shape of the power data is changed: The power maximum is shifted towards the NEP.

Similar to Fig. 2, power data for full resonator width and ssg readings are plotted in Fig. 5. While again the primary flow is kept constant, the molar ratio of iodine to total oxygen is varied at optimum admixing of secondary He. The maximum ssg is measured between 2.5 and 3% of iodine. The peak value of power occurs at about 1.7% of iodine. For these conditions, only 2/3 of the maximum ssg is achieved. Obviously, operating conditions for maximum power output are significantly different from those for maximum ssg.

## 4. CONCLUSION

Small signal gain measurements are informative for analyzing the active medium of a COIL. The densities of I and $I^*$ can be derived from ssg data achieving valuable information on the dissociation process. Moreover ssg measurements are an excellent tool for the determination of temperature in the supersonic flow. They will also provide some first hint concerning operating conditions for high output power. But in detail, there are different optima of operating conditions concerning maximum power output and maximum amplification. This does not only concern the gas composition but also the local position of power extraction. Therefore, in order to achieve efficient laser operation it is essential to attach a resonator to the COIL device and to maximize the laser power directly. Only this way the optimum gas flow conditions as well as the optimum local outcoupling position can be determined reliably.

## REFERENCES


[1] S.J.Davis, W.J.Kessler, M.Bachmann, "Collisional broadening of absorption lines in water vapor and atomic iodine relevant to COIL diagnostics", Gas and Chemical Lasers and Intense Beam Applications II, Vol 3612, pp. 157-166, San José, 1999.

[2] P.B.Keating, C.A.Helms, G.T.Anderson, T.L.Rittenhouse, K.A.Truesdell, G.D.Hager, "Two-dimensional gain and cavity temperature maps of a small-scale supersonic COIL", Lasers, pp. 1996.

[3] R. Highland, L.Hanko, G.Hager, K. Truesdell, "Spectral and Saturation Characteristics of COIL", 25th AIAA Plasmadynamics & Lasers Conference, 94-2438, Colorado Springs, 1994.

[4] R.F.Tate, B.S.Hunt, C.A.Helms, K.A.Truesdell, G.D.Hager, "Spatial Gain Measurements in a Chemical Oxygen Iodine Laser (COIL)", IEEE Journal of Quantum Electronics, Vol. 31, No. 9, pp. 1632-1636, 1995.

[5] J.F.Hon, D.N.Plummer, P.G.Corwell, J.Erkkila, G.D.Hager, C.A.Helms, K.A.Truesdell, "A Heuristic Method for Evaluating COIL Performance", 25th AIAA Plasmadynamics & Lasers Conference, 94-2422, Colorado Springs, 1994.

[6] L.H.von Entreß-Fürsteneck, J.Handke, K.M.Grünewald, W.L.Bohn, W.O.Schall, "Supersonic COIL Operation at DLR Germany", 11th Int. Symposium on Gas Flow and Chemical Lasers and High Power Laser Conference, H.J.Baker, ed., Proc. SPIE 3092, pp.553-556,1996.

[7] J.Handke, K.M.Grünewald, W.O.Schall, L.H.von Entreß-Fürsteneck, "Power Extraction Investigations for a 10 kW-Class Supersonic COIL", 12th Int. Symposium on Gas Flow and Chemical Lasers and High Power Laser Conference, A.S.Boreisho and G.A.Baranov, ed., Proc. SPIE 3574, pp.309-314,1998.

[8] K.M.Grünewald, J.Handke, L.H.von Entreß-Fürsteneck, W.O.Schall, "Effects of the Gas Mixing on COIL Performance", 12th Int. Symposium on Gas Flow and Chemical Lasers and High Power Laser Conference, A.S.Boreisho and G.A.Baranov, ed., Proc. SPIE 3574, pp.315-320,1998.

[9] K.M. Grünewald, J.Handke, F.Duschek, "Small signal gain and temperature profiles in supersonic COIL", presented at the 13th Int. Symposium on Gas Flow and Chemical Lasers and High Power Laser Conference, Florence, 2000.

# COMPUTATIONAL MODELING FOR SUPERSONIC OXYGEN-IODINE LASER WITH VARIOUS FLOW MIXING SYSTEMS

Yu. N. Deryugin, E. A. Kudryashov, B. A. Vyskubenko, D. K. Zelenski, Yu. V. Kolobyanin
Russian Federal Nuclear Center - VNIIEF, 607190, Sarov, Nizhni Novgorod Region, Russia

## ABSTRACT

A mathematical model of oxygen-iodine laser is described. A numerical analysis of three alternatives of mixing is performed.

**Key words:** mathematical model, supersonic mixing, gain factor, dissociation

## INTRODUCTION

Among the most promising directions in developing industrial cw lasers, one is associated with the oxygen-iodine machine which active medium is forced through the resonator at supersonic velocity[1]. Constructionally, lasers of this kind consist of a singlet oxygen generator (SOG), transition channel to connect SOG with nozzle generating supersonic flow, and resonator where the conditions of quantum oscillator self-excitation become feasible. Active medium of those lasers is generated due to turbulent mixing between energy carrier gas containing singlet oxygen and working gas with iodine molecules. Working gas is injected either through nozzle walls or with the aid of a central skew-field under the conditions of sub- or supersonic flow. Perfection and tests of mixing device constructions to provide for the least loss in available energy is one of the most important mission of COIL development which will require computational modeling methods.

For investigating non-equilibrium flow structure in mixing COIL devices and determining laser performance in the current work we have formulated and created a mathematical model. The model engages a set of equations for multicomponent gas motion, kinetics of chemical reactions, turbulent viscosity, and stationary lasing.

A numerical procedure used to determine active medium gasdynamics and kinetics throughout the COIL duct is built in terms of principles of spatial decomposition, split into physical processes, and difference scheme of the second accuracy order. The procedure was supported by software in FORTRAN-90. For all the models of interest we have developed a 2D code. For computations of subsonic and supersonic mixing also was created a 3D code.

The paper reports the results of the computation for particular mixing devices and energy performance of the laser.

## MATEHMATICAL MODEL

A set of equations used for flow simulations in gasdynamic channel of COIL can be expressed in vectorial form as[2]:

$$\frac{\partial \rho}{\partial t} + div\rho\bar{u} = 0\,, \qquad \frac{\partial \rho\bar{u}}{\partial t} + Div\rho(\bar{u}\bar{u}) = -gradp + Div\sigma\,, \qquad (1)$$

$$\frac{\partial \rho E}{\partial t} + div\rho\bar{u}H = Div\left(\frac{\mu}{\Pr}gradh\right) + div\sigma\bar{u}\,, \qquad \frac{\partial \rho c_i}{\partial t} + div\rho\bar{u}c_i = div\left(\frac{\mu}{D_S}\right)gradc_i + \omega_i\,,\ i = 1,2,\ldots,N.$$

where ρ is the density, $\bar{u}$ is the velocity vector, P is the pressure, E is the total energy, $c_i$ is the weight concentration of the i-th component, the term $\omega_i$ describes the concentration changes of the i-th component due to the chemical reactions in a gas mixture composed of the following components: oxygen molecule $c_1$-$O_2(X^3\,\Sigma_g)$ in ground electronic state, electronically excited oxygen molecule $c_2$-$O_2(a^1\Delta_g)$, electronically excited oxygen molecule $c_3$-$O_2(b^1\,\Sigma_g)$, iodine molecule $c_4$-$J_2$ in ground state, excited iodine molecule $c_5$-$J_2$, electronically excited iodine atom $c_6$-$J(^2P_{3/2})$, electronically excited iodine atom $c_7$-$J(^2P_{1/2})$, chlorine atom $c_8$-Cl, chlorine molecule $c_9$- $Cl_2$, $c_{10}$-JCl, $c_{11}$-$H_2O$, $c_{12}$- $N_2$ , $c_{13}$- Ar, $c_{14}$- He.

Equations (1) are closed up with thermal and caloric equations of state: $T = \frac{mp}{R\rho}$; $h = \sum_{i=1}^{N} c_{P_i}\frac{c_i}{m_i}m(T - T_0) + \Delta h_i\frac{c_i}{m_i}m$ , expressions for components of viscous strain tensor $\sigma_{ij}$, and relations for laminar and turbulent viscosity. Laminar viscosity is determined by Satterland formula, and turbulent viscosity - using two-parameter differential model described by Potankar and Spolding (see for instance ref.[6]) and based on differential relations for the turbulent kinetic energy $k_t$ and its dissipation rate $d_t$

XIII International Symposium on Gas Flow and Chemical Lasers and High-Power Laser Conference,
Antonio Lapucci, Marco Ciofini, Editors, Proceedings of SPIE Vol. 4184 (2001)

$$\frac{\partial \rho k_t}{\partial t} + div(\rho u k_t) = div(\rho \frac{\upsilon_t}{\tau_k} grad k_t) + \rho \upsilon_t \left[ \left( \frac{\partial u}{\partial y} \right)^2 + \left( \frac{\partial u}{\partial z} \right)^2 \right] - \rho d_t$$

$$\frac{\partial \rho d_t}{\partial t} + div(\rho u d_t) = div(\rho \frac{\upsilon_t}{\tau_d} grad d_t) + c_1 \rho k_t \left[ \left( \frac{\partial u}{\partial y} \right)^2 + \left( \frac{\partial u}{\partial z} \right)^2 \right] - c_2 \frac{\rho d_t^2}{k_t}$$

Effective turbulent viscosity is determined in the present model according to the expression $\upsilon_t = c_\upsilon \frac{k_t^2}{d_t}$, and universal constants have the following values: $c_\upsilon = 0.09$; $c_1 = 0.13$; $c_2 = 1.92$; $c_k = 1$; $\tau_d = 1.13$.

Computations of COIL lasing power employ the model in which the shape of the intensity distribution over the flow is assumed known (from experiments, for instance) while its amplitude is fitted to the condition of stationary lasing like the case of the constant-intensity model (see for instance [7]). Threshold condition allowing for inconstancy of the kinetic parameters along resonator axis is written as:

$$P(A) = \int_S J(x)\bar{k} \frac{r_1 r_2 \bar{k}}{\left(r_1 e^{\bar{k}L} + 1\right)\left(e^{\bar{k}L} - 1\right)} dS = 0,$$

where S is the mirror area; $\bar{k}$ is the gain factor; $J$ is the intensity; $r_1$, $r_2$ are the reflection factors of the mirrors; $L$ is the length of the optical axis of the resonator. The emission intensity $J(x)$ is given in the form: $J=AJ_0(x)$, where $J_0(x)$ is a known function of intensity distribution with the amplitude $A$.

## SOLUTION PROCEDURE

The mathematical model describing non-equilibrium flows of gaseous mixtures in COIL ducts is supported with software. The multidimensional flow throughout the gasdynamic channel is determined by consecutive solution of a set of tasks. Each of the tasks is solved for the flow field values in one of the regions of the gasdynamic channel. Obtained solutions are used then to set source data for the next task. The way of computation geometry regionalization and order of tasks solution depends on the laser design of interest, flow type, and a set of equations used to describe the latter.

Simulations of sub- and transonic flows are based on the equations of either non-viscous gas in case of homogeneous gas mixture or Navier-Stokes allowing for turbulent mixing in flow of interest. Numerical solutions are found following the pseudoviscosity method. Non-stationary equations are approximated with difference scheme: explicit for gasdynamics and implicit for kinetics. The difference approach used to calculate hydrodynamic equations was developed following difference methods of Godunov[8] and Lax-Wendroff[9]. In order to determine the convection streams, this approach first solves the discontinuity decomposition problem on each of the edges. Then it determines what is the zone accommodating the edge. If the edge is occurred in a shock-wave area, the convection streams are determined from solutions of the discontinuity decomposition problem. Otherwise, the parameters are recalculated following Lax scheme. The scheme calculates the turbulent flows per the bottom layer. The kinetics of the chemical reactions is calculated using the explicit scheme with weights. The equations of the differential models of turbulence are integrated on a time- and space – shifted mesh using one-sided difference scheme to calculate convection streams.

The second task is computation of supersonic flows. The flow field parameters are determined either by integrating stationary equations of non-viscous gas or from approximate Navier-Stokes equations. For numerical procedure development the differential equations are re-arranged for variables related to the streamlines and that are analogues of Lagrangian variables:

$$dt = dx,\ dm_1 = \rho u dy - \rho v dx,\ dm_1 = \rho u dz - \rho w dx$$

Approximate Navier-Stokes equations for these variables are:

$$\frac{\partial}{\partial t}\left(\frac{1}{\rho u}\right) - \frac{\partial}{\partial m_1}\left(\frac{v}{u}\right) - \frac{\partial}{\partial m_2}\left(\frac{w}{u}\right) = 0;$$

$$\frac{\partial}{\partial t}\left(\frac{P}{\rho u} + u\right) - \frac{\partial}{\partial m_1}\left(\frac{v}{u}P - q_u\right) + \frac{\partial}{\partial m_2}\left(\frac{w}{u}P - q_u\right) = \frac{\partial}{\partial m_1}\left(\kappa_t \frac{\partial u}{\partial m_1}\right) + \frac{\partial}{\partial m_1}\left(\kappa_t \left(\frac{\partial v}{\partial m_1} + \frac{\partial w}{\partial m_2}\right)\right) + \frac{\partial}{\partial m_1}\left(\kappa_t \left(\frac{\partial v}{\partial m_1} + \frac{\partial w}{\partial m_2}\right)\right);$$

$$\frac{\partial v}{\partial t} + \frac{\partial (P - q_v)}{\partial m_1} = \frac{\partial}{\partial m_1}\left(\kappa_t \frac{\partial u}{\partial m_1}\right) + \frac{\partial}{\partial m_2}\left(\kappa_t \left(\frac{4}{3}\frac{\partial w}{\partial m_2} - \frac{2}{3}\frac{\partial v}{\partial m_1}\right)\right)$$

$$\frac{\partial w}{\partial t}+\frac{\partial(P-q_w)}{\partial m_2}=\frac{\partial}{\partial m_1}\left(\kappa_t\frac{\partial u}{\partial m_2}\right)+\frac{\partial}{\partial m_2}\left(\kappa_t(\frac{4}{3}\frac{\partial w}{\partial m_2}-\frac{2}{3}\frac{\partial v}{\partial m_1})\right)$$

$$\frac{\partial H}{\partial t}=\frac{\partial}{\partial m_1}\left(\frac{\kappa_t}{P_{rt}}\frac{\partial h}{\partial m_1}\right)+\frac{\partial}{\partial m_2}\left(\frac{\kappa_t}{P_{rt}}\frac{\partial h}{\partial m_2}\right)+\frac{\partial}{\partial m_1}\left[\kappa_t\left(\frac{1}{P_{rt}}-\frac{1}{S_{ct}}\right)\sum_i h_i\frac{\partial c_i}{\partial m_1}\right]+$$

$$+\frac{\partial}{\partial m_2}\left[\kappa_t\left(\frac{1}{P_{rt}}-\frac{1}{S_{ct}}\right)\sum_i h_i\frac{\partial c_i}{\partial m_2}\right]+\frac{\partial}{\partial m_1}(uq_u+vq_v)+\frac{\partial}{\partial m_2}(uq_u+wq_w)+$$

$$+\frac{\partial}{\partial m_1}\left[\kappa_t\left(u\frac{\partial u}{\partial m_1}+\frac{4}{3}v\frac{\partial v}{\partial m_2}\right)\right]+\frac{\partial}{\partial m_2}\left[\kappa_t\left(u\frac{\partial u}{\partial m_2}+\frac{4}{3}v\frac{\partial w}{\partial m_1}\right)\right]-\frac{E_{изл}}{\rho u};$$

$$\frac{\partial C_i}{\partial t}=\frac{\partial}{\partial m_1}\left(\frac{\kappa_t}{S_{ct}}\frac{\partial C_i}{\partial m_1}\right)+\frac{\partial}{\partial m_2}\left(\frac{\kappa_t}{S_{ct}}\frac{\partial C_i}{\partial m_2}\right)+\frac{w_i}{\rho},\quad \kappa_t=\rho u\mu_t.$$

Regularizing the problem with strong oblique shock waves, we artificially added viscous terms $q_u$, $q_v$, and $q_w$ taken in the form suggested by J. Neumann and R. Richtmayer[9].

Equations for turbulent values are written as:

$$\frac{\partial k_t}{\partial t}=\frac{\partial}{\partial m_1}\left(\frac{\kappa_t}{\sigma_k}\frac{\partial k_t}{\partial m_1}\right)+\frac{\partial}{\partial m_1}\left(\frac{\kappa_t}{\sigma_k}\frac{\partial k_t}{\partial m_1}\right)+\rho^2 uv_t\left[\left(\frac{\partial u}{\partial m_1}\right)^2+\left(\frac{\partial u}{\partial m_2}\right)^2\right]-\frac{d_t}{u};$$

$$\frac{\partial d_t}{\partial t}=\frac{\partial}{\partial m_1}\left(\frac{\kappa_t}{\sigma_d}\frac{\partial d_t}{\partial m_1}\right)+\frac{\partial}{\partial m_2}\left(\frac{\kappa_t}{\sigma_d}\frac{\partial d_t}{\partial m_2}\right)+c_1\rho^2 uk_t\left[\left(\frac{\partial u}{\partial m_1}\right)^2+\left(\frac{\partial u}{\partial m_2}\right)^2\right]-c_2\frac{d_t}{k_t u}.$$

The scope of equations is solved following finite-difference procedure from ref.[9], that was created for 2D-flows and extended for 3D-case. Calculations are made on a chequerwise mesh. Such parameters as density, velocity components, pressure, enthalpy, concentrations, and kinetic parameters are determined at the points of the difference mesh having integer indexes ($t^n$, $m_{1i}$, $m_{2j}$), and parameters characteristic of turbulence ($v_t$, $\mu_t$, $k_t$, and $d_t$) – at the points with half-integer indexes ($t^{n+1/2}$, $m_{1i+1/2}$, $m_{2j+1/2}$). Layer-to layer transition is made in two stages. In the first stage, a new meaning of the turbulent viscosity is found on the mesh with half-integer indexes. The equations of the turbulence model are approximated using difference scheme of the second accuracy order. The second stage concerns with integration of the motion equations on the mesh with integer indexes. Numerical integration of the equations in this stage uses difference scheme of the predictor-corrector type.

The final task is determination of energy performance. The intensity value is obtained under the stationary oscillation condition by shooting method. The workflow of iteration cycle is as follows. The amplitude $A$ is predicted for the given shape of the intensity distribution $J_0(x)$. The flow field values are calculated in the resonator region. The threshold value $P(A)$ that suits the given intensity is determined. This is the essence of one iteration cycle. If $|P(A)|>\varepsilon$ ($\varepsilon$ is the prescribed accuracy), the program proceed with the next iteration. The amplitude value in iterations is determined subject to the following algorithm. First iteration calculates the flow in the "idle" resonator, i.e. $A'$ is assumed null. With condition $P(A')>0$ being observed, that indicates possibility of stationary oscillation, the intensity value in second iteration is defined on the assumption that all energy available at vibrational levels is transferred to emission. At this value of the amplitude the solution appears to be confined within the "fork" $P(A')>0$; $P(A^2)<0$. In the following iterations the value $A^r$ is determined first from linear and then quadratic interpolations.

## COMPUTATION RESULTS

The above computational procedure was used to study the process of active mixture generation in supersonic COIL with flat nozzle. The supersonic partition of the nozzle was calculated using the method of characteristics for Mach number 2.4. The subsonic partition consists of a straight channel and conic one with a half-angle $45^{\circ}$. The critical section of the nozzle is 0.33 cm. A gaseous mixture 0.07 $O_2$ + 0.17 $O_2(^1\Delta)$ + 0.01 $Cl_2$ + 0.02 $H_2O$ + 0.73 $N_2$ having initial parameters $P_0$ = 100 Torr and $T_0$ = 300 K is delivered at the nozzle entrance. Injection of the working gas $I_2$ together with buffer gas $N_2$ into the energy carrier is performed using a central skew-field under the conditions of subsonic flow in the vicinity of the critical section. We investigated numerically three alternatives of mixing of energy carrier and working flows.

First alternative concerns with flat flow mixing. In this case injection takes place in the axis plane. Fig. 1 shows a schematic diagram of the mixing device and computed flow fields. As seen from the figure, flow mixing isn't sufficiently intensive. A major part of the energy carrier flow doesn't participate in active mixture generation. The average gain factor at the

resonator entrance situated at 4 cm of the critical section amounts to 0.0053 $cm^{-1}$. Computations of the energy values give the value 51J/g.

In the second alternative the working gas was injected with the aid of pipes running out of the central skew-field along the axis plane and uniformly distributed relative to X- and Y- coordinates. A schematic diagram of the mixing device is shown in fig.2. Also shown in the same figure are the computed concentration fields of molecule $I_2$ in the planes passing through the jets centers. In this version mixing is more intensive than in the first case. However, similar to the previous case, a major part of the energy carrier flow doesn't also participate in active mixture generation. In this version the average gain factor at the resonator entrance has the value 0.0061$cm^{-1}$. The extracted energy is 94 J/g.

In the third version the working gas was also injected through pipes, as was previously, but accommodated chequerwise. A schematic diagram of the mixing device is shown in fig.3. Also shown in the same figure are the computed concentrations of molecule $I_2$ across the flow and in the planes passing through the jets centers. In this version mixing is the most intensive. The average gain factor at the resonator entrance is 0.0074 $cm^{-1}$. The extracted energy is 171J/g.

## CONCLUSION

3D procedures to calculate oxygen-iodine laser performance have been developed. A numerical analysis of three mixing alternatives has been carried out.

## REFERENCES


1. Basov N.G., Zagidullin M.V., Igoshin V.I., Katullin V.A., Kupriyanov N.L.. Theoretical analysis of chemical oxygen-iodine lasers (rus)// Trudy FIAN (1986), vol 171, pp. 30-53.
2. Loytzyansky L.G. Liquid and gas mechanics. Moscow: Nauka, 1970, 904.
3. Launder B.B., Spolding O.B. Lectures 1л mathematical modela of turbulence. London-New-Jorlc: Acad..Press., 1972.
4. Bredshow P.: Turbulence. Moscow: Mashinostroenie, 1980.
5. Abramovich G.N., Krashennikov S.Yu., Secundov A.N. Turbulent flows under the effect of volumetric forces and non-availability for automatic simulations. Moscow: Mashinostroenie, 1975.
6. Forst U., Moulden T. Turbulence. Principles and applications. Moscow: Mir,1980.
7. Vyskubenko B.A., Deryugin Yu.N., Kirillov G.A. etc. Comparison between 2D calculations of mix SOG and experimental data (rus)// Voprosy atomnoy nauki i tekhniki. Ser. Metodiki i programmy... 1983. Is. 3(4). pp. 18-21.
8. Godunov S.K., Zabrodin A.V., Ivanov M.Ya., etc. Numerical solution of multidimension gasdynamic problems. Moscow: Nauka, 1976.
9. Richtmayer R., Morton K. Difference methods for boundary problems. Moscow: Mir, 1972.
10. Bulkin Yu.N., Vyskubenko B.A., Deryugin Yu.N., Kolobyanin Yu.V., Kudryashov E.A. Computational modelling of turbulent flow in mix gasdynamic lasers (rus)// VANT. Ser. Matematicheskoe modelirovanie fizicheskikh processov. 1991, is.1, pp.17-22.

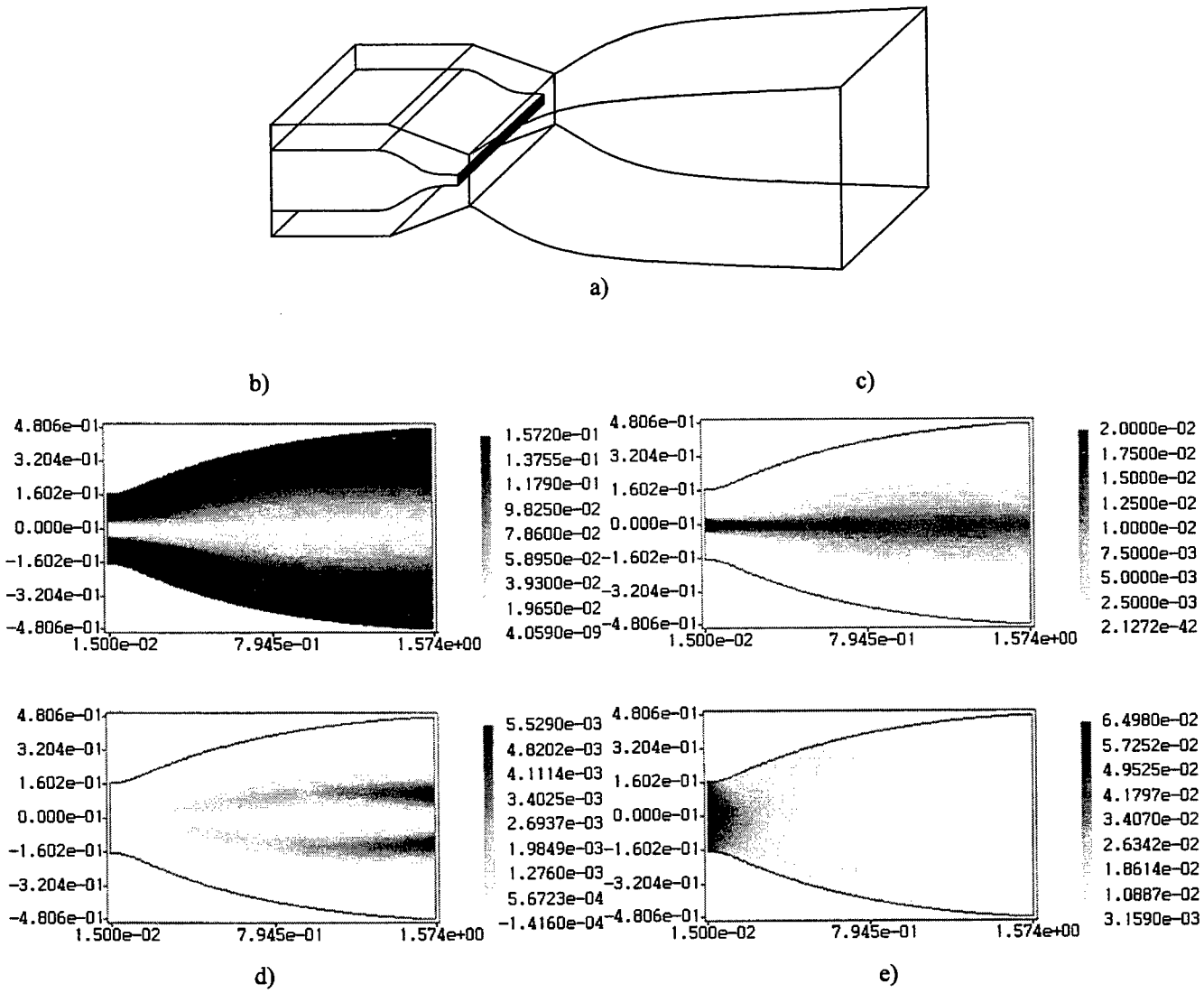


a) schematic diagram of mixing device;
b) singlet oxygen concentration;
c) iodine molecule concentration;
d) gain factor;
e) pressure.

Fig.1.

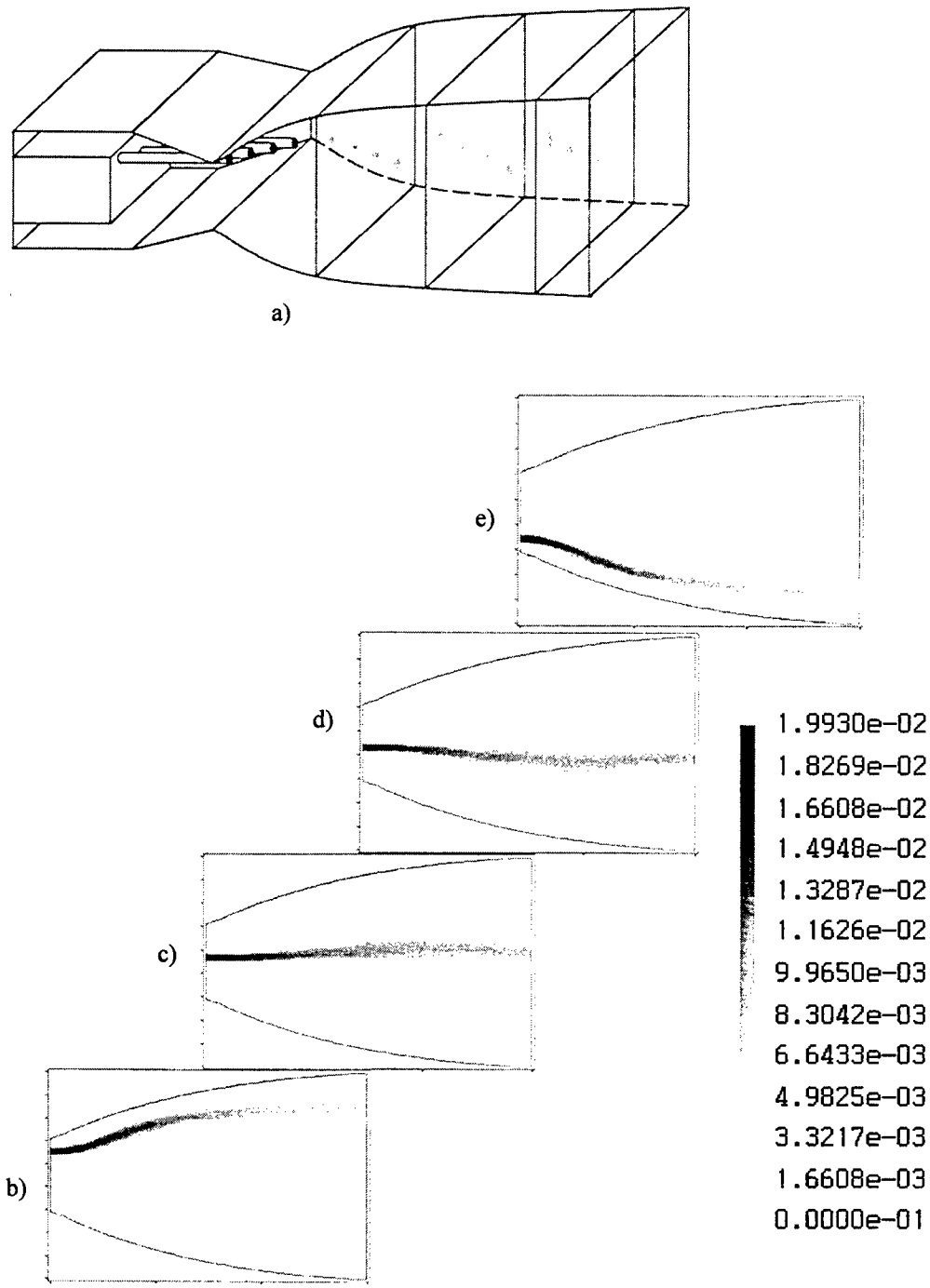


a) schamatic diagram of mixing device;
b-e) iodine molecule concentartion.

Fig.2.

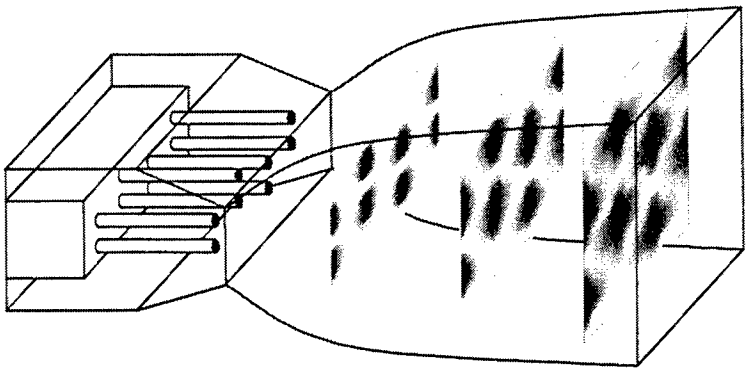

a)

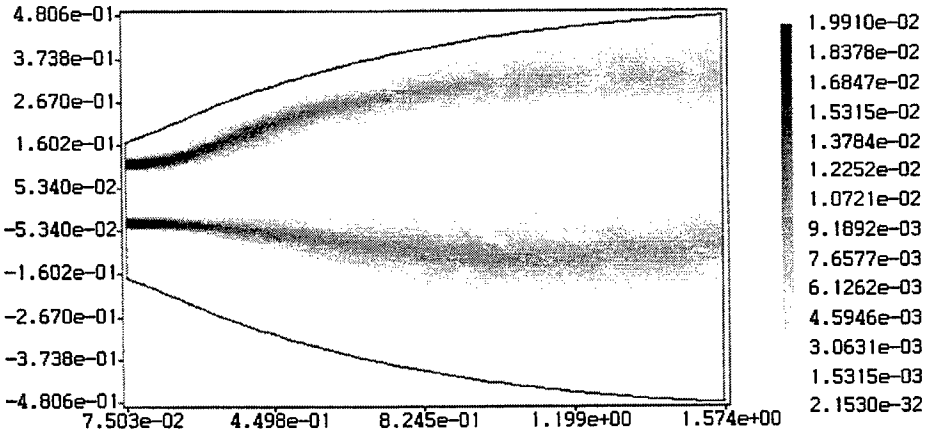


c)

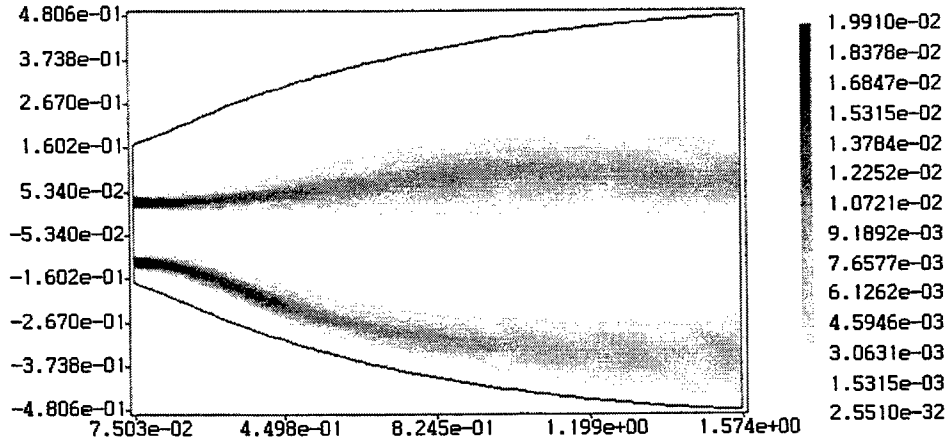


b)

a) schematic diagram of mixing device;
b-c) iodine molecule concentration

Fig.3

# Supersonic Oxygen-Iodine Laser Evolution at Russian Federal Nuclear Center - VNIIEF

B. A. Vyskubenko, A. A. Adamenkov, Yu. N. Deryugin, S. P. Il'in, Yu. V. Kolobyanin, I.M. Krukovski, E. A. Kudryashov
Russian Federal Nuclear Center - VNIIEF
Mira prosp. 37, Sarov, 607190, Nizhni Novgorod region, Russia
Fax: (831) 30 45646
Tel: (831) 30 41303
E-mail: vyskubenko@otd13.vniief.ru

## ABSTRACT

The results of experimental and numerical-theoretical supersonic COIL study carried out at RFNC-VNIIEF in 1998-2000 are performed. The novel data concern our research into the twisted-flow SOG (TA SOG) performance. The experimental investigations of gas-dynamic and energy performance, chemical efficiency, and optical quality are reported and discussed for the supersonic COIL with the parallel-flow system of gaseous iodine and singlet oxygen mixing. Application of TA-SOG together with the parallel-flow mixing system was shown to allow high values of COIL operation.
The peculiarities of numerical-theoretical model developed at RFNC-VNIIEF are discussed.

## 1. INTRODUCTION

Industrial applications of the Oxygen – Iodine Laser (COIL) have been under active consideration in the last 5-7 years [1-4]. The interest in development of industrial COIL is stipulated by a number of its advantageous peculiarities such as: first, high emission power at good beam quality; second, possibility for powerful emission of COIL to reach remote workplaces via virtually loss-less fiber-silica beam delivery, which opens new technological areas of application. Due to the purely chemical pumping method, an independent powerful industrial laser facility wouldn't have too high demand in electric energy. Together with other unique features, all the above properties give COIL a definite priority over other industrial lasers, especially in such applications as dismantling of outserved nuclear plants or accident response operations [3-5].
COIL development for industrial purposes faces a set of difficulties, the most serious of them being as follows: i) keeping of the working vacuum inside the laser cavity; ii) safety and ecological problems related to the presence of chlorine, iodine, and corrosive solutions; iii) effective procedures of hydrogen peroxide alkali solution (BHP) preparation and re-circulation. These and other problems refer to the tasks that will be solved in the course of industrial COIL development in VNIIEF. The principal problem at which the developers are currently focusing their efforts is pressure recovery at the exit COIL duct. The highest singlet oxygen pressure that may ensure high laser efficiency is supposed to be determined experimentally. Increasing the singlet oxygen pressure one can obtain higher output power with the same size of a facility; and increase in the total pressure at the same gas flowrate reduces energy inputs for evacuation. There is no doubt that the approach demonstrated by the Samara scientific team, when the pressure is elevated by buffer gas ejection [5], is worthy of note. However, this setup needs optimization to decrease the buffer gas flowrate. Our approach combines the buffer gas ejection and production of singlet oxygen at the maximal pressure [6, 7]. Then, the paper reports on the present state of the problem according to the results of our investigations in VNIIEF.

## 2. SINGLET OXYGEN GENERATOR

A key device of COIL governing available laser energy flux is a singlet oxygen generator (SOG) where chemical energy changes into the one stored with electronic levels of oxygen molecules. Singlet oxygen transportation from SOG to the area of mixing with iodine is accompanied with small loss in available energy but sufficient increase in gas temperature. The last effect leads to additional available energy loss in mixing of oxygen with iodine. Loss reduction requires the transportation volume between the reaction zone of SOG and nozzle inlet to be as small as possible. The problem of coordination between SOG and nozzle can be readily handled if the gas velocity values at the SOG outlet and nozzle inlet are close to each other. In this case SOG is coordinated with the nozzle through a minimal intermediate volume ensuring the least transport loss. That means that in-SOG the gas velocity should be not less than 50 – 60 m/s. We assume here the areas of sub- and supersonic parts of the nozzle to be equal to each other as is desirable for modular design. Proceeding on available SOG publications, the highest gas velocity, at which – according to the authors – the output flow is aerosol-free , was achieved in a jet-type SOG as 37 m/s [8]. Further velocity increase was hindered with liquid fraction entrainment out of the reactor. Just the same reason limits the pressure at the jet-SOG output with a value about 100 Torr. We understand here that SOG operates without any buffer gas. [1]. At the same time, elevated total pressure inside COIL gas channel brings about a


XIII International Symposium on Gas Flow and Chemical Lasers and High-Power Laser Conference,
Antonio Lapucci, Marco Ciofini, Editors, Proceedings of SPIE Vol. 4184 (2001)

number of unquestionable advantages [3-5]. For today, as is known from COIL publications, the main unit limiting singlet oxygen pressure inside the COIL channel is SOG.
Issuing from the requirements of high output pressure and, at the same time, high velocity, we, in VNIIEF, have proposed a SOG design with twisted aerosol flow (TA SOG) [11] which schematic and general view are shown accordingly in Figs.1 and 2.

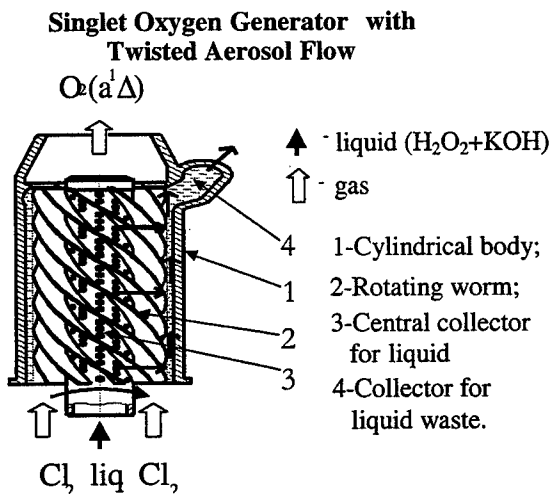


**Fig. 1**

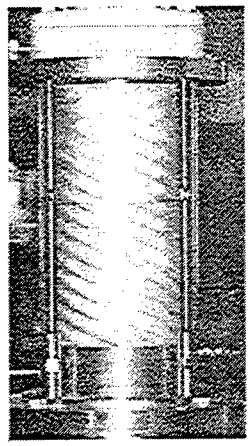

**Fig. 2** TA-SOG model Photo

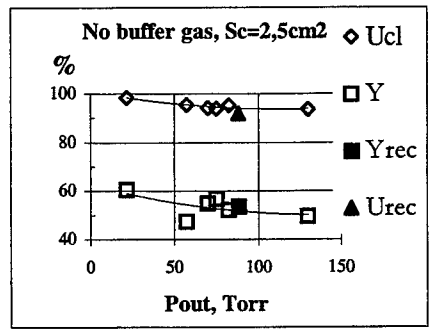


**Fig. 3**
TA SOG values measured without buffer gas at gas velocity $V_{out}$=50 m/s.
Measurement point at 10 cm of outlet.

Our investigations performed with measurements of singlet oxygen concentrations have demonstrated the efficiency of the proposed system. As was shown in ref. [12], TA SOG is able to provide, without chlorine dilution with indifferent gas, an output pressure up to 150 Torr at more than 50 %- yield of singlet oxygen. With chlorine dilution, the pressure was successfully increased up to 250 Torr at the in-reactor gas velocity 75 m/s, singlet oxygen yield above 60%, and partial pressure of singlet oxygen at the reactor outlet of about 50 Torr. The highest gas velocity in the reaction zone was up to 100 m/s, electron flux density exceeded 1.7 kW/cm$^2$. All these parameters were provided at steady operation of the reactor and output flow free of aerosol at the chlorine utilization above 90%. Fig. 3 shows the pressure dependence of TA-SOG output values at gas velocity 50 m/sec.

The TA SOG reactor can be connected directly to the nozzle without choking the flow between SOG and nozzle and without any extra measures to provide dry gas flow that is ensured by steady SOG operation conditioned with the design on its own. Aside from the listed values, TA SOG construction can also provide an increase in the waste solution pressure at the reactor outlet to above atmospheric values, thus simplifying essentially the fashion of solution re-circulation. To this end, it will be sufficiently to connect, through a manifold, the delivery tank containing atmospheric-pressure BHP with the input and output solution branch pipes of SOG. One should emphasize that this requires no additional pumps. The above fashion has been implemented successfully. SOG operated steadily for three minutes. This time limitation was a result of ability of our evacuating system. Fig. 3 demonstrates TA SOG output parameters in BHP-recycle mode of operation. It is seen that both the singlet oxygen yield and chlorine utilization don't noticeably differ from those in the case of one-pass BHP flow.

## 3. MIXING SYSTEM

The data performed demonstrate that stable-operating elevated-pressure SOG does exist in reality. The next step towards high-pressure COIL is the development of proper laser ensuring high efficiency under conditions of elevated singlet oxygen concentrations. Nowadays the urgent question to answer is: is it possible for the laser to use a flow with high singlet oxygen (SO) concentration without noticeable loss in efficiency? The primary task here is the development and optimization of a system for SO mixing with iodine. The investigations launched in VNIIEF for supersonic COIL model are oriented towards handling this problem. Our estimates conducted with the COIL simulations using the code developed at VNIIEF have showed that it will be possible to keep high laser efficiency at a partial SO pressure of at least 60 Torr. For today, among all generators we know it is only TA SOG that can approach so high SO pressure. Therefore, laser experiments with TA SOG allow us to determine a tolerant pressure of SO inside COIL duct that may permit high laser efficiency. Below we shall give the first results of lasing studies with TA SOG application. As a first step on the present stage, we needed confirmation in lasing experiments the TA SOG performance obtained earlier in measurements of SO concentration and making sure of

sufficient effectiveness of the mixing system we used. Therefore, our experiments were performed with SO pressure at the nozzle inlet of 20 to 30 Torr as it was in the early papers, reported on the highest COIL efficiency attained so far [9,10,15]. Fig. 4 shows a photo of the laser facility that represents a COIL model with twisted aerosol flow SOG (TA SOG) connected with supersonic nozzle. We have successfully implemented the approach of active gas media mixing in supersonic flows developed earlier in VNIIEF for mix-type gasdynamic laser (GDL) [13, 14]. As it was proposed in our early papers [6, 7], iodine admixed together with carrier gas was introduced into SO as jets moving in parallel with the main flow. Along with this the point of iodine injection shifts from sub- to supersonic region in different experiments. As we think, it is the approach to iodine mixing that can provide low loss at a high pressure of singlet oxygen. Another specific feature of our experiments was application of a resonator extended in flow direction. Like in our early GDL works, the overall length of the tree-sectional resonator was 12 cm in flow direction. This resonator allows stored laser energy extraction at low iodine concentration thus reducing losses in mixing singlet oxygen with iodine at high pressure. The results of laser experiments are represented in Fig. 5. Fig. 6 demonstrates that each of three resonator sections contribute

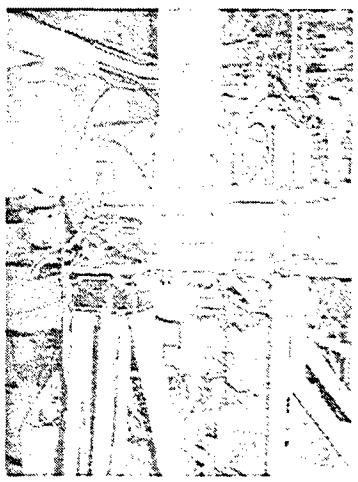

**Fig. 4.**
Facility view during laser experiments.

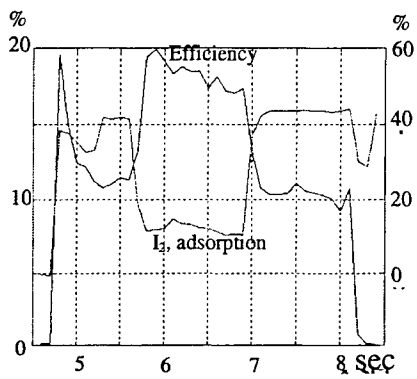


**Fig.5.** Typical experimental records

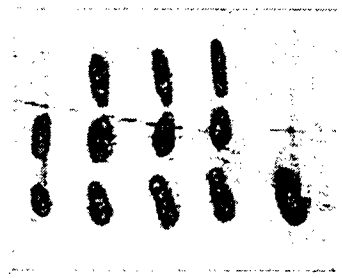

**Fig. 6.** Beam patterns with three resonator sections in some experiments

to total laser output power. A more detailed information on the results of our study is given in the related report presented by my colleagues at this conference. After preliminary optimization of the mixing system and mirrors, the attained overall chemical efficiency of the laser has achieved 20%. Below some values of one of the experiments are presented. Designations are: $G_{cl}$ – chlorine flowrate (mmol/s); $G_{bufl}$– buffer gas 1 (nitrogen delivered together with chlorine) flowrate (mmol/s); $G_{buf2}$ – buffer gas 2 (nitrogen delivered after SOG procedures) flowrate (mmol/s); $G_{car}$- iodine carrier (helium) flowrate (mmol/s); $P_0$ – pressure in front of the nozzle (Torr); Eff – chemical efficiency of the laser.

| $G_{cl}$ | $G_{bufl}$ | $G_{buf2}$ | $G_{car}$ | $P_0$ | Eff (%) |
|---|---|---|---|---|---|
| 55.8 | 112 | 37.7 | 22.5 | 56.9 | 20 |

As it was suggested, the system of parallel flow mixing appeared to be rather steady with regard to the pressure difference occurred between the main flow and injected jets. The values of lasing won't change strongly if the point of injection shifts from the subsonic flow into the supersonic region. As well, the laser power keeps virtually the same value during injection point placing in the supersonic region if helium is changed by nitrogen as a buffer gas. As was shown, with the elementary estimates using conservation laws, mixing in parallel flows takes place at lower loss in total pressure and is accompanied with less reduction of Mach number and less temperature increase. This allows us to hope for high efficiency keeping under the conditions of pressure increase. Iodine injection together with a carrier gas is evidently superior with respect to total pressure increase.

Thus, the preliminary laser experiments using TA SOG and parallel-flow mixing system have demonstrated:

- High stability of TA SOG operation: TA SOG outlet was dry in all laser experiments
- High TA SOG efficiency confirmed with high laser efficiency at low iodine concentrations
- Necessity of resonator extended in flow direction – each resonator section contributed essentially into the overall lased power

Investigations into the laser performance and its optimization at high singlet oxygen pressure are expected as the next step in the supersonic COIL study program.

## 4. NUMERICAL COIL MODEL

Simultaneously with the experimental study of the laser emission values we were conducting a numerical COIL simulations. This allowed us to catch the processes occurred in the COIL flow more entirely and to conceive the effect of various parameters upon the laser efficiency. The developed theoretical models determine the gas parameters in-SOG flow and during transportation towards iodine injection plane, as well as mixing SO with iodine, interaction with laser emission in the resonator. The SOG model calculates kinetic equations allowing for SO production and relaxation, heat exchange in interaction with BHP surface and equations of one-dimensional gasdynamics allowing for pressure loss in friction between the liquid phase and channel walls. The models of the laser itself describe singlet oxygen transportation taking into account drag and heat transfer inside the COIL subsonic channel, and calculate together kinetic equations, as is written for the corresponding chemical reactions accompanying the processes of iodine mixing and dissociation, and 2- or 3-D turbulent equations of Navier-Stokes allowing for component mixing. Inside the resonator the energy equations were added with the terms allowing for interaction with emission and energy outcoupling during lasing. More detailed numerical models descriptions are summarized in special reports, presented by my colleagues at this conference.

Detailed comparison the simulation and experimental results still lies ahead, but the first numerical calculations give the reasonable results.

It follows from numerical simulations that:

- Mixing in parallel flows ensures high lasing efficiency up to SO pressure in front of the nozzle of at least 60 Torr.
- Displacement of iodine dissociation into supersonic flow region at high SO pressure would reduce stored energy loss.
- Decrease in iodine concentration would allow reduction of loss in mixing and more homogeneous distribution of the gain in flow direction.
- Due to using a resonator extended in flow direction, homogeneous inversion distribution would allow an increase in lasing efficiency. In this case, the mirrors load gets lower. Lowered mirrors load and homogeneous of the gain over the resonator are preferable for getting high quality of output emission.

## 5. CONCLUSION AND AKNOWLEDGEMENT

The work is financially supported by the International Scientific and Technology Center (Moscow), ISTC Project #1118. The authors are most grateful to Drs. V.D. Nickolaev (elder) and M. V. Zagidullin for very useful advises and friendly discussions.

## REFERENCES

1. K.A.Truesdell, C.A.Helms and G.D.Hager, "A history of Coil Development in the USA", Proceedings to the 25th AIAA Plasmadynamics and Lasers Conference, paper number AIAA 94-2421
2. K.Yasuda, T.Atsuta, T.Sakurai, H.Okado, A.Hayakawa, and J.Adachi, "Study on material processing of Chemical Iodine Laser", Proceedings of International Conference on Nuclear Engineering, S504-3, pp.1769-1773.
3. H.Fujii and T.Atsuta, "Industrial Chemical Oxygen Iodine Laser", Proceedings of XI International Symposium in Gas Flow and Chemical Lasers and High-Power Laser Conference, 1996, SPIE, Vol.3092, pp. 700-705.
4. H.v.Bulow and W.O.Schall, "Oxygen Iodine Laser for industrial applications", Proceedings of X International Symposium in Gas Flow and Chemical, 1994, SPIE.
5. M.R.Hallada, S.L. Seiffert, R.F. Walter, J. Vetrovec. "Chemical Oxigen Iodine Laser (COIL) for the dismantlement of nuclear facilities", Gas, Chemical, and Electrical Lasers and Intense Beam Control and Applications, 24 – 25 January 2000, Proceedings of SPIE Vol. 3931, p.p. 149-155.
6. A.A. Adamenkov, B.A. Vyskubenko, N.N. Gerasimenko, V.A. Eroshenko, Yu.N. Derjugin, D.K. Zelensky, S.P. Ilyin, I.M. Krukovsky, E.A. Kudriashov. "High Pressure COIL Problem", Proc. Forth International Workshop on Iodine Lasers and Applications", Prague, SPIE Vol. 2767, p.209, 1995.
7. A.A. Adamenkov, B.A. Vyskubenko, N.N. Gerasimenko, Yu.N. Derjugin, D.K. Zelensky, S.P. Ilyin, I.M. Krukovsky, E.A. Kudriashov. " Oxygen-Iodine Laser Capacity at the Elevated Pressure", XI International Symposium on Gas Flow Chemical Lasers, SPIE Vol. 3092, pp.581-584, 1996.
8. V.N. Azjazov, M.V. Zagidullin, V.D. Nikolaev, M.I. Svistun, N.A. Hvatov. "• $_2(^1\Delta)$ - Jet Generator with an Oxygen Pressure to 13,3 • P• ", Sov. Quantum Electronics, **21**, pp.129 – 132, 1994.
9. M.V. Zagidullin, V.D. Nikolaev, M.I. Svistun, N.A. Hvatov, N.I. Ufimtsev. "High Efficiency Supersonic Chemical Oxygen-Iodine Laser with Chlorine Flow Rate 10 mmol/s ", Sov. Quantum Electronics, **24**, pp.201 – 205, 1997.

10. W.E. McDermott, J.C. Stephens, J. Vetrovec, and R.A. Dickerson. "Operating Experience With a High Throughput Jet Generator", 28th Plasmadinamics and Lasers Conference, AIAA 97-2385, June 23-25, 1997.
11. B.A. Vyskubenko, V.F. Gerasimenko, I.M. Krukovsky. "Method of singlet oxygen production and device for it realization" ("Metod polucheniya singletnnogo kisloroda i ustroistvo dlya polucheniya"), Rus. Invention application No 95115631 of Sept.15, 1995.
12. I.M.Krukovsky, A.A.Adamenkov, B.A.Vyskubenko, Yu.N.Deryugin, S.P.Ilyin, E.A.Kudryashov, "Investigation of the Singlet Oxygen Generator with the Twisted Flow", Proceedings of SPIE, Gas, Chemical, and Electrical Lasers and Intense Beam Control and Applications, San Jose, Vol. 3931, pp.99-108, (2000).
13. B.A.Vyskubenko, E.T.Demenyuk, G.A.Kirillov, Yu.V.Kolobyanin, S.B.Kormer, N.A.Nitochkin., Gasdynamic laser experimental investigation. Doklady Akademii Nauk SSSR, V 248, ¹ 1. (1979).
14. V.V. Buzoverya, Yu. N. Bulkin, B.A. Vyskubenko, S.P. Il'in, G.A.Kirillov, Yu.V.Kolobyanin, E.A. Kudryashov, Yu.V.Savin. "Experimental Device to Study Energy Characteristics of Gasdynamic Lasers and Basic Results", Proceedings of International conference "Lasers-96" (Portland, USA, December 2 - 6, 1996).
15. Phipps S.P.,Helms C.A., Truesdell K.A., Healcy K.P. Compact CW Supersonic Chemical Oxygen-Iodine Laser. - Presented at the 25th Plasmadynamics and Lasers Conferens, AIAA Paper 94-2453, Colorado Springs, CO, 1994.

# Numerical Study of Nozzle Scale Effect upon High - Pressure Oxygen - Iodine Laser Performance

E.A. Kudryashov, Yu. N. Deryugin, B.A. Vyskubenko, S.P. Il'in, Yu. V. Kolobyanin E.A.
Russian Federal Nuclear Center (VNIIEPh), Sarov, Nizhni Novgorod Region, Russia, 607190

## Abstract

The numerical calculations of the gain and dissociation degree of molecular iodine in a supersonic COIL channel are reported for supersonic mixing of flows and 0.2-, 0.3-, 0.4- mm- height critical sections of nozzles profiled for Mach number 2.5 to 4.0.

**Key words:** supersonic mixing, gain (factor), dissociation.

## Introduction

In attempts to attain high efficiency (25% and more) of oxygen-iodine laser one must keep a whole series of conditions. First, it is required for a singlet oxygen generator to have accordingly the least utilization and oxygen excitation degree (yield) of 95 % and 50 % at its outlet. The second condition is minimal transport loss of singlet oxygen occurred in propagation of generator gas inside a subsonic channel (from SOG outlet to supersonic nozzle). Third, a prepared active medium must have rather good characteristics inside the laser cavity, i.e. high gain, low temperature, and homogeneous distribution of gasdynamic values.

The present report is dwelled on the third point and gives the results of our numerical research into the effect of the geometry of supersonic nozzle region upon the active medium performance of COIL. Along with this we shall consider different versions with high working gas pressure at the nozzle inlet. The high pressure of working gas is requested for easier removing of waste mixture through a neutralization system into the atmosphere. For obtaining high pressure values it is possible to employ a generator gas strongly diluted with a buffer one. The dilution degree depends on the type of SOG in use. As is known, the oxygen pressure at the outlets of the widely used currently jet- and disk- type generators doesn't exceed 20 – 30 Torr [1,2,3,4,5]. At the same time, the worm-type SOG (TA SOG) developed at RFNC-VNIIEF allows between 80 and 100 Torr of oxygen with a high excitation degree[6,7,8]. In this case getting of about 200 Torr pressure at the nozzle inlet requires noticeably smaller degree of dilution with buffer gas. It is obvious that when the gas in use contains more singlet oxygen the value of stored specific energy will be higher.

## Mathematical Model

For calculations of the SOG performance and investigation into the structure on non-equilibrium flow we at RFNC-VNIIEF have developed a model that was realized as a program code that includes four groups of equations.

The first group contains gas motion equations of Eiler, boundary layer, parabolic and complete Navier-Stokes for compressible gas. Based on the Eiler equations it is possible to calculate subsonic, transonic, and supersonic frictionless flows. Turbulent supersonic flow mixing processes in mix chemical lasers are calculated from parabolic Navier-Stokes equations. Complete Navier-Stokes equations allow simulations of turbulent mixing of subsonic flows and streams behind the nozzle pallet.

The second group of equations was composed of equations for various turbulence approaches. The models utilized in numerical experiments are both simple algebraic turbulence approach, Prandtl's for instance, and multiparameter differential turbulence approaches such as Secundov's or bi-parameter (k-e)-model developed later by Launder, Potankar, and Spolding.

The third group calculates the chemical kinetic equations that includes the following elementary processes:

1. $O_2(a^1\Delta_g) + I(^2P_{3/2}) \leftrightarrow O_2(X^3\Sigma_g) + I\,(^2P_{1/2})$
2. $O_2(a^1\Delta_g) + O_2(a^1\Delta_g) \rightarrow O_2(b^1\Sigma_g) + O_2(X^3\Sigma_g)$
3. $O_2(a^1\Delta_g) + O_2(a^1\Delta_g) \rightarrow O_2(X^3\Sigma_g) + O_2(X^3\Sigma_g)$
4. $O_2(a^1\Delta_g) + I(^2P_{1/2}) \rightarrow O_2(b^1\Sigma_g) + I(^2P_{3/2})$
5. $O_2(b^1\Sigma_g) + M \rightarrow O_2(a^1\Delta_g) + M$
6. $O_2(a^1\Delta_g) + M \rightarrow O_2(X^3\Sigma_g) + M$
7. $I(^2P_{1/2}) + M \rightarrow I(^2P_{3/2}) + M$
8. $O_2(b^1\Sigma_g) + I_2 \rightarrow O_2(X^3\Sigma_g) + I\,(^2P_{3/2}) + I\,(^2P_{3/2})$
9. $O_2(a^1\Delta_g) + I_2 \rightarrow O_2(X^3\Sigma_g) + I_2^*$
10. $I(^2P_{1/2}) + I_2 \rightarrow I(^2P_{3/2}) + I_2^*$
11. $O_2(a^1\Delta_g) + I_2^* \rightarrow O_2(X^3\Sigma_g) + I(^2P_{3/2}) + I(^2P_{3/2})$
12. $I(^2P_{1/2}) + I_2^* \rightarrow I(^2P_{3/2}) + I(^2P_{3/2}) + I(^2P_{3/2})$

XIII International Symposium on Gas Flow and Chemical Lasers and High-Power Laser Conference,
Antonio Lapucci, Marco Ciofini, Editors, Proceedings of SPIE Vol. 4184 (2001)

13. $I(^2P_{3/2}) + I(^2P_{3/2}) + M \rightarrow I_2 + M$
14. $I(^2P_{1/2}) + W \rightarrow I(^2P_{3/2}) + W$
15. $I_2^* + O_2(X^3\Sigma_g) \rightarrow I_2 + O_2(X^3\Sigma_g)$
16. $I_2^* + H_2O \rightarrow I_2 + H_2O$
17. $I_2^* + N_2 \rightarrow I_2 + N_2$

where M designates any of the particles participating in the reactions, and $I_2^*$ designates excited molecular iodine.
Lastly, the fourth group consists of lasing equations.
The calculus problem to determine gas-dynamic and kinetic values of the active medium throughout the COIL duct is reduced to consecutive solutions of simpler tasks. Each of the task concerns with flow-field values in one of the regions into which the gas-dynamic channel is divided, while each task solution is then used to set initial data for next problem.
The in-resonator flow calculations were conducted with non-equilibrium flow procedures linked with the modules of emission power determination for various resonator types.
The numerical procedures were realized in the program codes written in FORTRAN-90. The three-dimensional code (3D) has been developed for all of the considered models.

## Results of calculations

In this paragraph we shall perform the results of our COIL calculations carried out for the temperature and pressure of the working gas in front of the nozzle accordingly 300 K and 200 Torr. It was assumed that in terms of molar flowrate one half of the working gas was performed with the buffer gas, i.e. nitrogen, and another half – with the gas at the outlet of TA SOG with the chlorine utilization 94%, oxygen yield 60%, and water vapor pressure 1.9 Torr. Molecular iodine vapors were supplied together with the carrier gas – nitrogen – into the vicinity of the critical nozzle section (supersonic mixing version). Along with this, the molar flowrates of the admixed and working gases relate as 1:4. Our choice of supersonic mixing version was stipulated by the following factors. First, in distinction from the version with gas mixing in subsonic region, no special matching are required for the distance between the point of gas admixing and critical nozzle section at variation of the working gas values. Second, as it will be shown below, by changing the iodine concentration in carrier gas composition and nozzle scale it is possible to control the length of the lasing region in flow direction.
In case of subsonic mixing one tends, as a rule, to have virtually complete interflow and molecular iodine dissociation. The fact that atomic iodine is present in the working medium provides for enhanced relaxation of the stored energy into heat. This results in warming the flow inside both subsonic and supersonic nozzle regions. Being heated, the supersonic flow will become stagnated. At the same time, the rapid growth of the boundary layer on the nozzle walls leads to additional stagnation of the flow. For operations with high-pressure working gas all these factors impose rather strict limitations upon selection of supersonic nozzle: it must be extremely short and expanded at a large angle.
However, the supersonic mixing version hasn't so severe limitations in this aspect. The main requirement here follows from the general physics consideration as the demand of the velocities of the carrier gas (together with iodine vapors) and gas containing singlet oxygen to differ by 20 – 30 % at least. Then, the process of mixing and generation of active medium will develop rather intensively. In this case the principal factor influencing on dissociation of molecular iodine is the nozzle length in flow direction that governs the mixing degree. Let's illustrate now this fact with the example of supersonic nozzles (profile with corner point) profiled for Mach numbers from 2.5 to 4.0 and having various scales. It's worth to note that profiled nozzles are more preferable for better gasdynamic (and consequently, optical) quality of in-resonator flow. Figs. 1-4 show the relative concentration of molecular iodine and gain factor calculated for the critical section height of the nozzle $h^* = 0.2, 0.3, 0.4$ cm and $M = 2.5$ (fig. 1), 4.0 (fig. 2) as functions of the distance taken in flow direction from the critic. The molar iodine concentration in admixed gas was let to vary from 0.4% to 1.6%.
As follows from the results performed in figs.1-2 (curves b, d, f), virtually all iodine dissociates at the distance equal to $2 \div 10$ lengths of the profiled part of the nozzle and measured in flow direction from the critical section ($L \approx 20$ cm). It's worth to note that the rate of dissociation of molecular iodine goes up with increase in its concentration. The character of changes in the relative iodine concentration occurred with variations in the distance of the critical section has its own peculiarities. It is possible to choose conditionally three main sections. First section: value $\chi = I_2/I_{20}$ increases to the level 0.9; second section: $0.1 \le \chi \le 0.9$; third section: $\chi \le 0.1$. As is seen from figs.1-2 (b, d, e), the first section has the low dissociation rate. This property is explained with the fact that the dissociation and mixing processes develop concurrently. The rate of the mixing of the energy-carrier gas flow with the iodine carrier depends mainly on two factors: mixing geometry and rate difference. The length of this section $L_1$ is a function of the nozzle's profile and scale as well as of the initial iodine concentration: $L_1$ goes up with increase in Mach number and goes down with increase in initial iodine concentration. The second section is characterized by the rapid reduction in concentration of $I_2$, the rate of dissociation decreasing with increase in number M. This circumstance can readily be explained with the gas density decrease occurred with higher M. Lastly, the remained portion of iodine undergoes slow decay in the third section. Thus, variations in initial molecular iodine concentration would allow us to change the distance at which complete (or partial) dissociation takes place.

The most actual fact for laser cavity operation is the gain behavior in supersonic channel. As is seen in figs. 1-2 (a, c, e), the gain reaches its maximum value at the distance corresponding to $\chi$ somewhere between 0.2 and 0.3. It's worth to note that with increase in the initial iodine concentration the maximum became sharper and shifts towards the critical section. The knowledge of the gain value along the flow would allow us to select, in the most optimal way, the resonator position corresponding to the highest efficiency. If the resonator in use is short along the flow, the more preferable initial concentrations of $I_2$ are high. Increase in resonator length in flow direction leads to reduction of optimal iodine concentration.

## Conclusions and Acknowledgement

With supersonic mixing application one will be able to:

- use nozzles with a small expansion ratio even at a rather high pressure at nozzle inlet;
- control the length of lasing region in flow direction by changing the scale, nozzle profile, and iodine concentration.

The work was supported financially by the International Science and Technology Center, Moscow (ISTC Project #1118).

## References

1. Harpole G.M., English W.D., Berg J.G., and Miller D.J., "Rotating disk oxygen generator", AIAA 23rd Plasmadynamics & Lasers Conference, July 6-8, 1992, Nashville TN, USA, paper AIAA 92-3006.
2. Grunewald K., Handke J., Bohn W.L., Schall W.O., "Investigations on the efficiency of a rotating disk oxygen generator", XI International Symposium on Gas Flow and Chemical Lasers and High-Power Laser Conference, H.J. Baker ed., Proc. SPIE 3092 (1997), p.553.
3. Aziazov V.N., Zagidullin M.V., Nikolaev V.D., Khvatov N.A., Svustun M.I., "$O_2(^1\Delta)$ stream generator with oxygen pressure up to 13.3 kPa", *Quantum Electronics*, **21**, 129 (1994).
4. Zagidullin M.V., Nikolaev V.D., Khvatov N.A., Svustun M.I., "The sub- and supersonic COILs driven by jet tipe singlet oxygen generator", XII International Symposium on Gas Flow and Chemical Lasers and High-Power Laser Conference, 31 August-5 September 1998, St. Petersburg, Russia, p.246.
5. Zagidullin M.V., "The study and development of jet type singlet oxygen generator for COIL", XII International Symposium on Gas Flow and Chemical Lasers and High-Power Laser Conference, 31 August-5 September 1998, St. Petersburg, Russia, p.569.
6. Vyskubenko B.A., Krukovsky I.M., Adamenkov A.A., Deryugin Yu.N., Il'yin S.P., Kudryashov E.A., "Investigation of the Singlet Oxygen Generator with the Twisted Flow", Conference on Lasers and Electro-Optics Europe, CLEO®/Europe, 14-18 September 1998, p.271.
7. Ivan M. Krukovsky, Anatoly A. Adamenkov, Boris A. Vyskubenko, Yuriy N. Deryugin, Sergey P. Ilyin, Eugeny A. Kudryashov, "Investigation of the Singlet Oxygen Generator with the Twisted Flow" / in Gas, Chemical, and Electrical Lasers and Intense Beam Control and Applications, Santanu Basu, Steven J. Davis, Ernest A. Dorko, Editors, Proceeding of SPIE Vol. 3931, 99-108 (2000).
8. F. Wani, M. Endo, B.A. Vyskubenko, S. Takeda, T. Fujioka, H. Fujii, "Experimental Study of Singlet Oxygen Generator for the COIL", 29th Plasmadynamics and Lasers Conference, June 15-18, 1998, Albuquerque, NM, AIAA 98-2990.

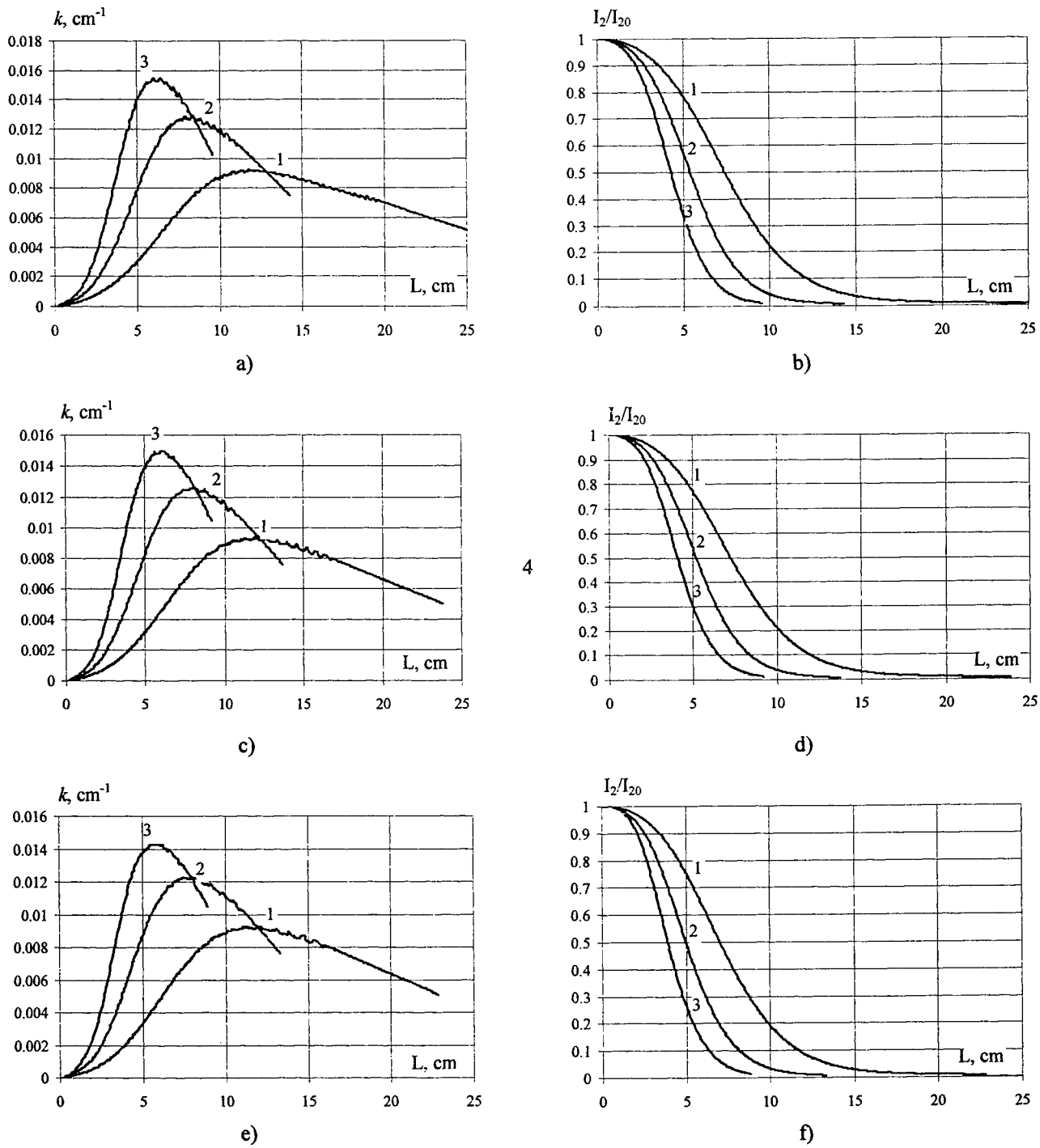


Fig.1

Gain factor $k$ (a, c, e) and relative molecular iodine concentration $I_2/I_{20}$ (b, d, f) calculated as functions of distance L of nozzle critical section. Nozzle profile corresponds to Mach number M = 2.5, adiabatic exponent $\gamma = 1.4$.
(a, b) – nozzle critical section height h* = 0.2 cm, profiled part length $l_{noz}$ = 1 cm; (c, d) – h* = 0.3 cm, $l_{noz}$ = 1.5 cm; (e, f) – h* = 0.4 cm, $l_{noz}$ = 2.0 cm. Molar iodine concentration in admixed gas $\alpha_I$ = 0.4 % (1), 0.6 % (2), 0.8 % (3).

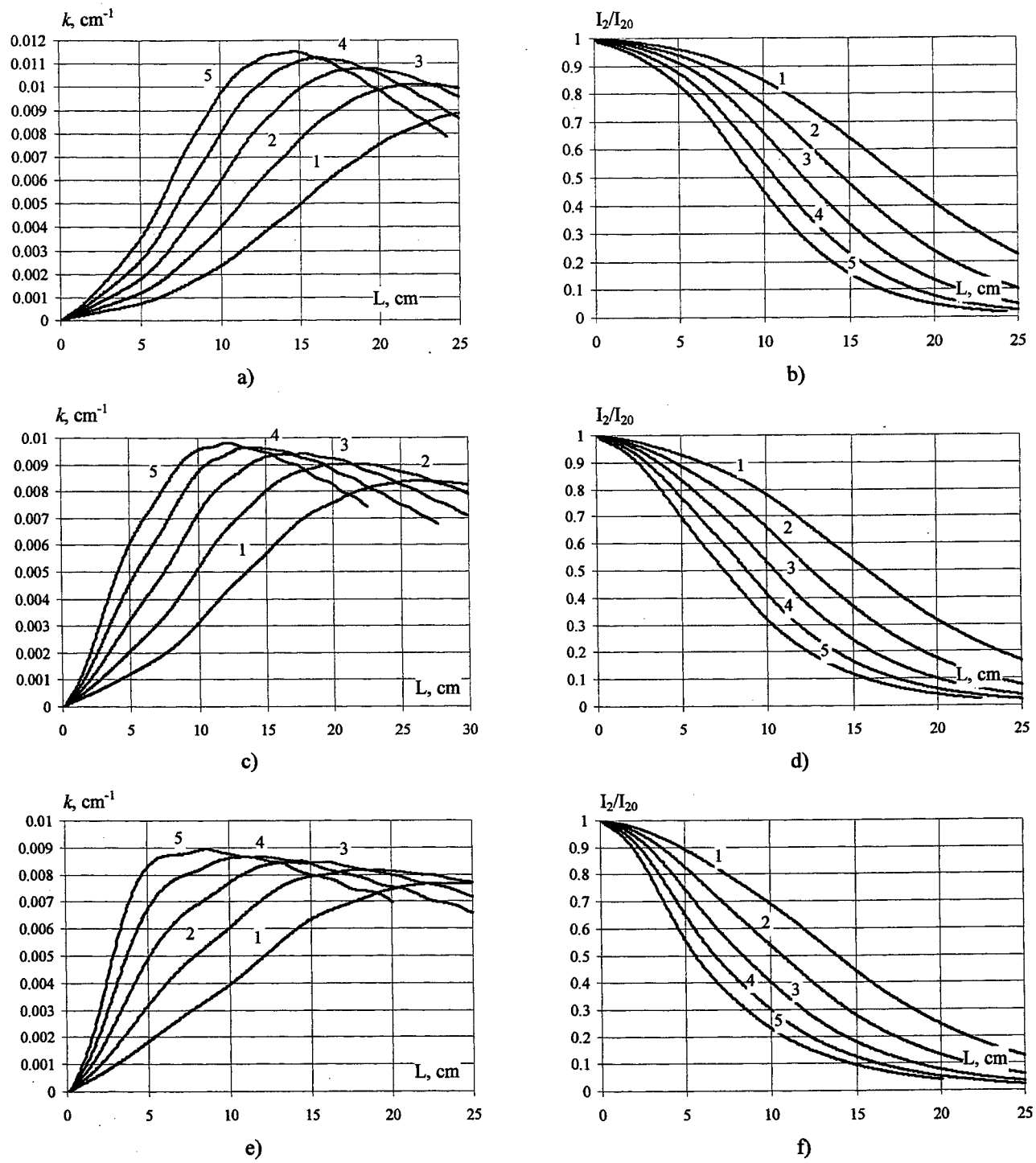


Fig.2

Gain factor $k$ (a, c, e) and relative molecular iodine concentration $I_2/I_{20}$ (b, d, f) calculated as functions of distance L of nozzle critical section. Nozzle profile corresponds to Mach number M = 4.0, adiabatic exponent $\gamma = 1.4$.
(a, b) – nozzle critical section height h* = 0.2 cm, profiled part length $l_{noz}$ = 5.25 cm; (c, d) – h* = 0.3 cm, $l_{noz}$ = 7.9 cm; (e, f) – h* = 0.4 cm, $l_{noz}$ = 10.5 cm. Molar iodine concentration in admixed gas $\alpha_I$ = 0.8 % (1), 1.0 % (2), 1.2 % (3), 1.4% (4), 1.6% (5).

# Iodine dissociation in supersonic COILs with different schemes of iodine mixing

B. D. Barmashenko, E. Bruins, D. Furman, V. Rybalkin and S. Rosenwaks

Department of Physics, Ben-Gurion University of the Negev, Beer-Sheva 84105, Israel

## ABSTRACT

An analytical model is developed for calculating the iodine dissociation fraction $F$ and the number $N$ of $O_2(^1\Delta)$ molecules lost in the region of iodine dissociation per $I_2$ molecule in slit nozzles. The model is applied to results obtained for different mixing schemes.

**Keywords:** chemical lasers, oxygen, iodine, dissociation.

## 1. INTRODUCTION

To understand the kinetic and mixing processes in supersonic COILs operating without primary buffer gas and different mixing schemes and optimize the output power it is necessary to get information on the small signal gain and iodine dissociation fraction. The gain can be easily measured using diode laser based diagnostic [1-3]. However, it is difficult to measure the dissociation fraction of iodine because the absorption of $I_2$ molecules in the supersonic portion of the flow is very small, in particular when the gain length is short, as in our laser [4]. The only experimental measurement of the dissociation fraction was carried out in [5] for the RADICL, where the gain length is 25 cm, i. e. 5 times longer than in our laser. An analytical method was developed in [3] for calculation of the iodine dissociation fraction $F$ and the number $N$ of $O_2(^1\Delta)$ molecules lost in the region of iodine dissociation per $I_2$ molecule. In this paper this method is modified to be applicable to the slit nozzles and applied to results obtained for different mixing schemes.

## 2. MODEL FOR CALCULATION OF *F* AND *N* FOR SLIT NOZZLE

The model for calculation of $F$ and $N$ for grid nozzle was presented in [3]. Here this model is modified to be applicable to the slit nozzle. Using the dependencies of $g$ and $T$ on $nI_2$ we can calculate the $I_2$ dissociation fraction $F$ at the resonator optical axis. To take into account final mixing rate of iodine, assume that total number density of iodine atoms is non-uniform in direction y perpendicular to both the flow direction and resonator optical axis:

$$[\mathrm{I}]+[\mathrm{I}^*]=\frac{p}{kT}\frac{n\mathrm{I}_2}{n}Ff(y), \qquad (1)$$

where $n$ is the total flow rate, $f(y)$ a normalized form-factor and $H$ is the height of the flow duct. Therefore the iodine mixing parameter can be defined as

$$\eta=1/f(0). \qquad (2)$$

For uniform iodine distribution both $f(0)$ and $\eta$ are equal to unity. If the mixing is slow and iodine is concentrated near the centerline one has $f(0)>>1$ and $\eta<<1$, which means that mixing parameter is small. The relation between the local gain $g$, $F$ and the $O_2(^1\Delta)$ yield $Y$ at the optical axis is [3]



XIII International Symposium on Gas Flow and Chemical Lasers and High-Power Laser Conference, Antonio Lapucci, Marco Ciofini, Editors, Proceedings of SPIE Vol. 4184 (2001)

$$g = \sigma_0 \left(\frac{300}{T}\right)^{1/2} \frac{p}{kT} \frac{nI_2}{n\eta} F \frac{(2K_e+1)Y-1}{(K_e-1)Y+1}, \tag{3}$$

where $K_e = 0.75 \exp(402/T)$ is the equilibrium constant of reaction $O_2(^1\Delta) + I(^2P_{3/2}) \rightarrow O_2(^3\Sigma) + I(^2P_{1/2})$. The following relation connects $Y$ with the yield $Y_i$ before the iodine injection:

$$Y = Y_i - \frac{nI_2 F}{nO_2} N, \tag{4}$$

where $nO_2 = (nCl_2)_0 U$ is the oxygen flow rate and $U$ the chlorine utilization in the $O_2(^1\Delta)$ generator. Eq. (4) assumes fast diffusion of oxygen molecules, i. e., the oxygen is distributed uniformly over $y$. $N$ can be found from the energy conservation equation:

$$c_p[(n_p + n_s)T_0 - n_p(T_{0i})_p - n_s(T_{0i})_s] = q_\Delta nI_2 FN - q_{I_2} nI_2 F$$
$$- q_{I^*} nI_2 F \frac{2K_e Y}{(K_e-1)Y+1}, \tag{5}$$

where $c_p = 7/2\ k$ is the specific heat capacity of diatomic gas, $n_p = (nCl_2)_0 + nH2O$ and $n_s = nN_2 + nI_2$ are the primary and secondary flow rates, $T_0$ the stagnation temperature of the flow in the reaction zone, $(T_{0i})_p$ and $(T_{0i})_s$ the stagnation temperatures of the primary and secondary flow, respectively and $q_\Delta = 11{,}340$ K, $q_{I_2} = 18{,}400$ K and $q_{I^*} = 10{,}954$ K are the energy of $O_2(^1\Delta)$, dissociation energy of $I_2$ and the energy of $I^*(^2P_{1/2})$, respectively. The first term in the right-hand-side of Eq. (5) corresponds to the energy lost by $O_2(^1\Delta)$ in the region of $I_2$ dissociation, the second term to the energy of $I_2$ dissociation, and the third to the energy of excitation of the iodine atoms produced via the iodine dissociation.
Just as in [3], $T_0$ is given by:

$$T_0 = T_{0c} \frac{\mu}{\mu_c} + T - T_c \frac{\mu}{\mu_c}, \tag{6}$$

where $T_c$ and $\mu_c$ are the static temperature and molecular weight in the "cold" runs without adding $I_2$ to secondary $N_2$. The value of $T_c$ was found by linear extrapolation of $T(nI_2)$ to $nI_2$, corresponding to zero gain.

$$T_{0c} = \frac{n_p(T_{0i})_p + nN_2(T_{0i})_s}{n_p + nN_2} \tag{7}$$

is the stagnation temperature in the cold runs.

Solving the system of equations (3) – (5), with $T_0$ given by Eqs. (6) and (7), we find dependencies of $F$, $N$ and $Y$ on $nI_2$. The mixing parameter $\eta$ is an unknown parameter. To determine the value of $\eta$ we compared the dependence $N(nI_2)$ with the theoretical value of the number $N$ (indicated below as $N_{th}$) as described in [3].

## 3. APPLICATION OF THE MODEL TO DIFFERENT MIXING SCHEMES

The model is applied to the results of experimental measurements of $g$ and $T$ for nozzles with iodine injection in transonic and supersonic sections of the nozzle described in detail in [5]. Fig. 1 shows dependencies of $g$, $T$ and on $nI_2$ for slit nozzle

No. 1 [5] at $nCl_2$ = 11.7 mmole/s and opened leak downstream of the resonator (see Ref. 5). The maximum value of $F$ is about 0.6 for Nozzle No. 1. The dissociation fraction $F$ for nozzles No. 1 and 2 is higher than for the grid nozzle, which is due to above-mentioned higher mixing parameter in the slit nozzle. For nozzle No. 3 (iodine injection in the diverging section), $F$ is about 0.3, i. e., much smaller than for nozzles Nos. 1 and 2. This is because of the short residence time of the gas in the volume between the iodine injectors and the resonator optical axis, due to the high jet velocity caused by both high $nN_2$ and the fact that iodine is injected in the divergent section of the flow. To determine the values of the mixing parameter $\eta$ we compared the dependence $N(nI_2)$ with $N_{th}$ as described above. Good agreement between $N$ and $N_{th}$ is obtained for $\eta$ equal to unity. As shown in [3] for the grid nozzle, the best agreement between $N$ and $N_{th}$ is obtained for mixing parameter of ~ 0.5. Hence the mixing parameter for slit nozzle No. 1 is higher than for the grid nozzle. The values of $\eta$ for other nozzles are found the same way and are close to unity.

Calculated values of $F$ for closed leak are higher than for opened leak. Fig. 2 shows dependencies of $g$, $T$ and $F$ on $nI_2$ for nozzle No. 2 at $nCl_2$ = 20.1 mmole/s. It is seen that the maximum value of $F$ is close to unity. The same is correct for all other runs with closed leak except the run for Nozzle No. 3 (iodine injection in the diverging section), where $F$ is about 0.6. To obtain that the calculated $F < 1$ for any $nI_2$ one should assume that the mixing parameter $\eta$ is about 0.7 or even smaller, i.e., that mixing is poor. For larger $\eta$ (close to unity), calculated maximum values of $F$ are larger than 1, which is obviously incorrect. The value $\eta = 0.7$ corresponds to the best agreement between $N$ and $N_{th}$. Closing of the leak has two opposite effects on iodine dissociation. On the one hand, for closed leak the mixing efficiency $\eta$ is smaller, hence the local number density of iodine atoms near the flow centerline is higher than for opened leak, which results in higher rate of iodine dissociation and larger $F$. On the other hand, the flow velocity for closed leak is larger than for opened leak. As a result, the residence time of the gas between the injection location and optical axis and hence the value of $F$ should decrease. The effect of small mixing efficiency is probably stronger than the effect of the shorter residence time, which results in the higher values of $F$ for closed leak.

## 4. SUMMARY

Measured values of the gain and temperature in the cavity of a slit nozzle, supersonic COIL are used to calculate the iodine dissociation fraction $F$ using a very simple model. Maximum calculated values of $F$ are close to unity for slit nozzles with transonic injection of iodine, however, in this case mixing is poor. Opening a leak downstream of the cavity in order to decrease the Mach number and increase the cavity pressure results in the decrease of the dissociation fraction. However, the mixing parameter in this case is close to unity. Naturally, the calculated values of $F$ should be regarded as rough estimates, however, we believe that qualitatively our simple model predicts the correct behavior of $F$ as a function of different flow parameters. To find the exact values of $F$ experimental measurements of iodine molecule absorption in the cavity should be carried out.

## REFERENCES


1. E. Lebiush, B. D. Barmashenko, A. Elior and S. Rosenwaks, "Parametric study of the gain in a small scale, grid nozzle supersonic chemical oxygen-iodine laser," *IEEE J. Quantum Electronics*, vol.31, pp. 903-909, 1995.
2. D. Furman, E. Bruins, B. D. Barmashenko and S. Rosenwaks, "Small signal gain and iodine dissociation in a supersonic chemical oxygen-iodine laser with transonic injection of iodine," *Appl. Phys. Lett.*, vol. 74, pp. 3093-3095, 1999.
3. D. Furman, B. D. Barmashenko and S. Rosenwaks, "Parametric study of an efficient supersonic chemical oxygen-iodine laser/jet generator system operating without buffer gas," *IEEE J. Quantum Electronics*, vol. 34, pp. 1068 -1074, 1998.
4. C. A. Helms, J. Shaw, G. D. Hager and K. A. Truesdell, "Iodine dissociation in COILs," *SPIE*, vol. 2502, pp. 250 – 257, 1996.
5. S. Rosenwaks, E. Bruins, D. Furman, V. Rybalkin and B. D. Barmashenko, "Supersonic COIL with iodine injection in transonic and supersonic sections of the nozzle," paper presented in GCL-HPL 2000.

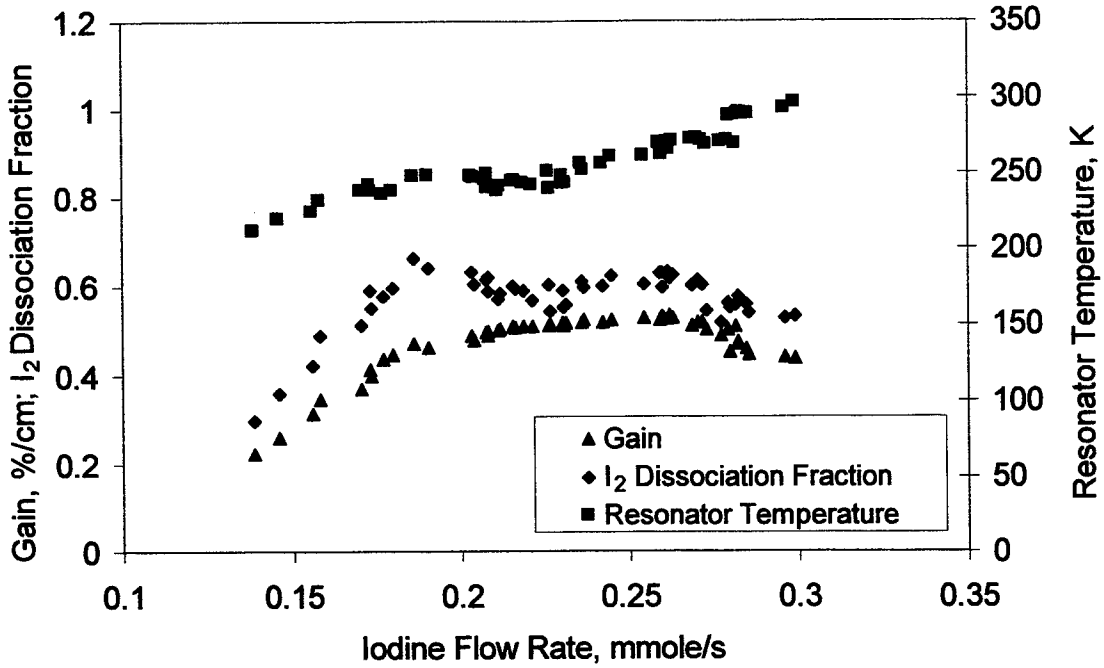


Fig. 1. The gain, temperature and iodine dissociation fraction at the resonator optical axis for slit nozzle No. 1 as a function of the iodine flow rate. The chlorine and secondary nitrogen flow rates are 11.7 and 2.5 mmole/s, respectively, the leak downstream of the resonator is opened.

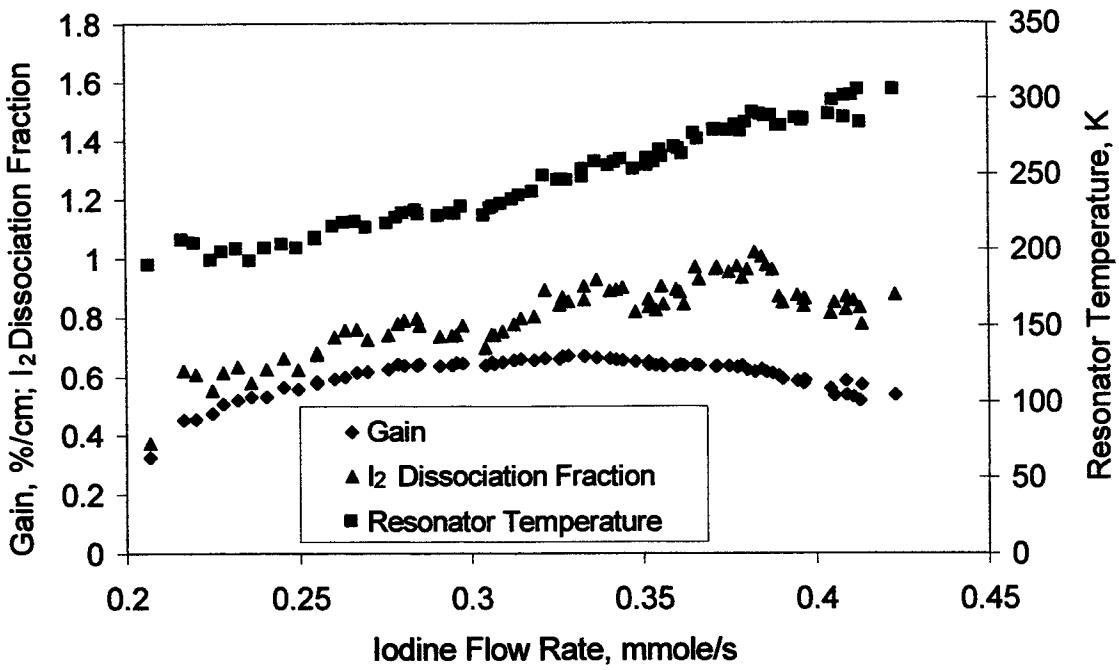


Fig. 2. The gain, temperature and iodine dissociation fraction at the resonator optical axis for slit nozzle No. 2 as a function of the iodine flow rate. The chlorine and secondary nitrogen flow rates are 20.1 and 8.7 mmole/s, respectively, the leak downstream of the resonator is closed.

# Investigation of UR90 Outputting Annular Beam for a Chemical Oxygen Iodine Laser

Yuqi Jin, Fengting Sang, Bailing Yang, and Qi Zhuang

Dalian Institute of Chemical Physics, Chinese Academy of Sciences
457 Zhong Shan Road, Dalian 116023, P.R.China
Tel: +86-411-4671991, email: yqjin@ms.dicp.ac.cn

## ABSTRACT

In this paper, we mainly describe the structure of an unstable resonator with 90-deg beam rotation(UR90) outputting annular beam for a chemical oxygen iodine laser(COIL) and the geometry mode of the beam. A beam quality of 3.2 times diffraction limit was achieved in the experiment while the COIL average output power was approximately 4kw in the case of magnification of 1.69, as well as the property of the annular beam was analyzed.

**Keywords:** chemical oxygen iodine laser, beam quality, unstable resonator, UR90, annular beam

## 1. INTRODUCTION

The chemical oxygen iodine laser(COIL) is a chemical laser with high efficiency, high power and a short wavelength. In recent year development of the COIL has been remarkable. Beam quality is also an important characteristic for COIL, however, experimental investigation for improvement of the COIL beam quality has scarcely been reported.

It is very important that how to obtain good beam quality in the supersonic transversely flowing medium. A conventional confocal unstable resonator has some advantages of large controllable mode volume, good transverse mode discrimination, and efficient coupling output, but it is very difficult to obtain a near diffraction limit beam because of its sensitive to the medium heterogeneity and cavity misalignment.[1]

For the supersonic flowing medium of the COIL, singlet oxygen $O_2(^1\Delta)$ that is the energy reservoir ties to the following relation.

$$Y = (Y_0 - B/A)e^{-Ax/u} + B/A \tag{1}$$

where $Y$ is yield of $O_2(^1\Delta)$, $Y_0$ is initial yield of $O_2(^1\Delta)$, $A=K_F[I]+K_R[I^*]$, $B=K_R[O_2]_0[I^*]$

The yield of singlet oxygen $O_2(^1\Delta)$ based upon Eq. 1 drops down exponentially and the gain decreases along the direction of the gas flowing. Therefore, due to obtain the good beam quality, it is necessary to have a novel optical resonator which can average the optical aberrations, thermal distortion and heterogeneity of the supersonic flow.

The concept of beam rotation was first presented by Yu. A.Anan'ev[2] at St. Petersburg University, Russia in 1979. Paxton and Latham Jr.[3] at Air Force Weapons Laboratory USA successfully demonstrated in $CO_2$ laser using UR90 with filled in beam output in 1986. A good beam quality was achieved by means of beam rotation averaging the optical aberrations, thermal distortion and heterogeneity of the supersonic flow. We obtained the result of 5kw average output power and beam quality of less than 2 times diffraction limit by using the UR90 resonator on COIL in 1996.[4] The magnification of the cavity is enlarged as the gain is increased, and then the efficient mode volume can not be fully used in the UR90 with a filled in output beam by using beam expanding spherical mirrors. However, in this case, the UR90 having annular output beam was used to avoid above disadvantage.

In this paper, we report the experimental results of the UR90 with annular output beam for the COIL including output power and beam quality, the comparison with the filled in beam is also given.



XIII International Symposium on Gas Flow and Chemical Lasers and High-Power Laser Conference,
Antonio Lapucci, Marco Ciofini, Editors, Proceedings of SPIE Vol. 4184 (2001)

## 2. EXPERIMENTAL APPARATUS

### 2.1 Chemical Oxygen Iodine Laser Experimental setup

The schematic drawing of the COIL experimental setup is shown in Fig. 1.

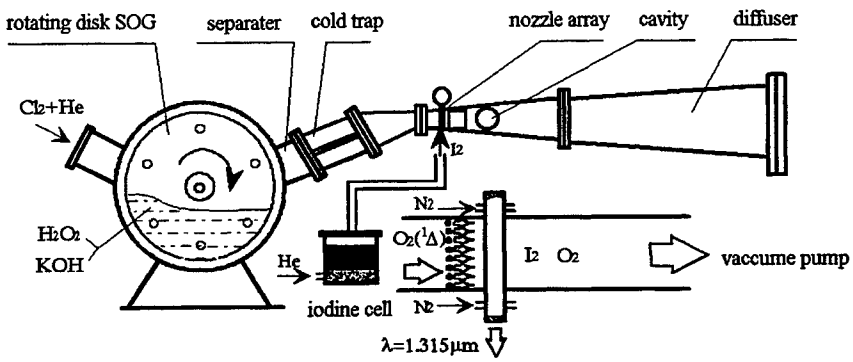


Fig. 1 The schematic drawing of the COIL setup

The basic composition of the supersonic COIL system consists mainly of a gas supply system, a basic hydrogen peroxide(BHP) premixing system, a rotating disk singlet oxygen generator(SOG), a gas-liquid separator, a water vapor cold trap, an iodine vapor generator, a supersonic oxygen iodine mixing nozzle array, a gain cell with an optical resonator, and a vacuum system with roots and mechanical pumps.

The device is driven by a rotating disk singlet oxygen generator. A mixture of chlorine and helium is introduced into SOG where it contacts basic hydrogen peroxide. The gas flow including excited oxygen, ground state oxygen chemically produced in SOG, some residual chlorine , few water vapor and lots of helium passes through a gas-liquid separator and cold trap to reduce the water content. The flow is ducted to the subsonic entrance channel of the nozzle. Gaseous iodine is injected in front of the nozzle throat and mixed with the singlet oxygen. The nozzle array provides a $M$=2 active flow in the cavity. After leaving cavity, the exhausted gas flow is eliminated by roots and mechanical pumps.

### 2.2 The Description of UR90 with Annular Output Beam

The configuration and experimental result of UR90 with filled-in output beam were previously reported.[5] The greatest difference between UR90 with annular output beam and filled-in output beam is the shape and position of the output scraper where the former is placed on-axis and the latter is located off-axis. The schematic configuration of UR90 with annular output beam is illustrated in Fig.2.

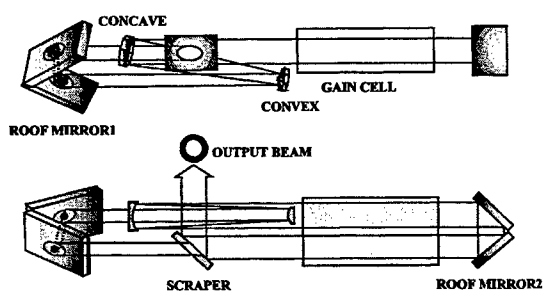


Fig. 2 Schematic of UR90 with annular output beam

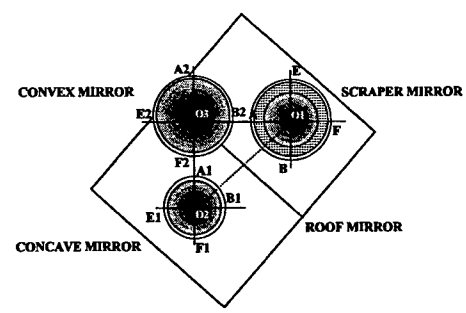


Fig. 3 The left side view of UR90 with annular output beam

The UR90 with annular output beam is composed of two rooftop mirrors, an off-axis expanding telescope, and a output scraper. The No.1 rooftop mirror that consists of two orthogonal reflecting plates glued together has 45 degrees to horizon and provides beam rotation. While a light beam passes a round trip in the cavity, the beam cross section will rotate 90 degrees around the axis clockwise and be expanded $M$ times, where $M$ is cavity magnification. The left side view of UR90

with annular beam is shown in Fig.3. As shown the beam cross section inside the cavity on each mirror, it is evidently that we can derive $O_1O_2O_3$ which is an isosceles right triangle. That will provide the reference calibration point for alignment of the resonator.

For the UR90 with filled-in output beam, the beam cross section on the output scraper is shown in Fig.4. Where O is the point of optical axis position, $M$ is the cavity magnification, the shadow "CDEF" is the size of the output beam, $a$ is the distance from the edge of the scraper to the optical axis. To ensure that the rectangle beam emerges itself while oscillating, the geometric beam size is established proper ratio between the length of the beam and the width. The proportion is expressed as follow:

$$l = (M^2 + M^4)a; h = (M + M^3)a; l/h = M \tag{2}$$

Which is equal to the optical magnification. For the COIL, as the length of the gain medium along the gas flow is definite, in case of lower gain, the magnification is selected lower, the shape of the beam is close to square and the volume of the mode is lager. However, the magnification is enlarged as the gain increased, then the shape of the beam is being changed to prolate and the mode volume decreases. That will make against the efficient use of the gain medium.

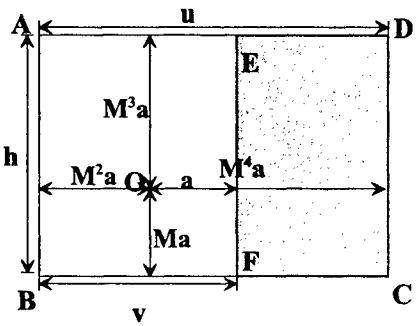


Fig. 4 Beam cross-section of UR90 with filled in beam on the scraper mirror position

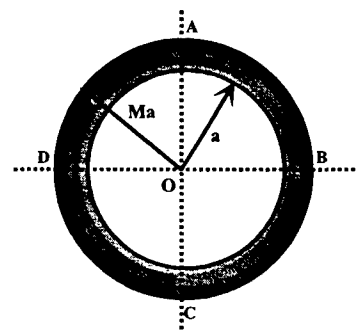


Fig. 5 Beam cross-section of UR90 with annular beam on the scraper mirror position

For the UR90 with annular output beam, the output beam section is shown in Fig.5. Where $O$, $M$, and the shadow are defined as above. $a$ is the radius of the aperture on the scraper. To ensure that the beam emerges itself while it rotates 90 degrees, the shape of the beam is square and circle, and the geometric shape of the beam is no longer related to the magnification. When the different magnification is selected, the beam section is not changed by means of corresponding size of the aperture on the scraper.

## 3. EXPERIMANTAL RESULTS AND ANALYSIS

We used a magnification of 1.69. The equivalent length is given by[6]

$$L_{eq} = (1 + \frac{1}{M^2})(L_a + \frac{L_b}{M} + \frac{L_c}{M^2}) \tag{3}$$

Where $M$ is the magnification, $L_a$ is the distance in the forward direction from the scraper to the convex mirror, $L_b$ is the distance from the convex mirror to the concave mirror, and $L_c$ is the distance from the concave mirror to the scraper. The equivalent Fresnel number $N_{eq}$=5.4 is calculated from

$$N_{eq} = \frac{a^2(M^4 - 1)}{2\lambda M^4 L_{eq}} = \frac{a^2(M^2 - 1)}{2\lambda(M^2 L_a + M L_b + L_c)} \tag{4}$$

Where $a$ is the aperture radius of the scraper, $\lambda$ is the laser wavelength. The actual parameters of the UR90 with annular output beam are listed in Table 1.

**Table 1 UR90 with annular output beam parameters**

| | | | |
|---|---|---|---|
| Magnification | 1.69 | Diameter of beam | 38 |
| Concave radius/mm | 6000 | $L_a$/mm | 3208 |
| Convex radius/mm | 3540 | $L_b$/mm | 1230 |
| Equivalent Fresnel number | 5.4 | $L_c$/mm | 5390 |
| Hole radius of scraper mirror/mm | 11.2 | Cavity length/mm | 9828 |

The far field intensity distribution of the UR90 with annular output beam is shown in Fig.6 in case of magnification of 1.69 and average output power of 4kw.

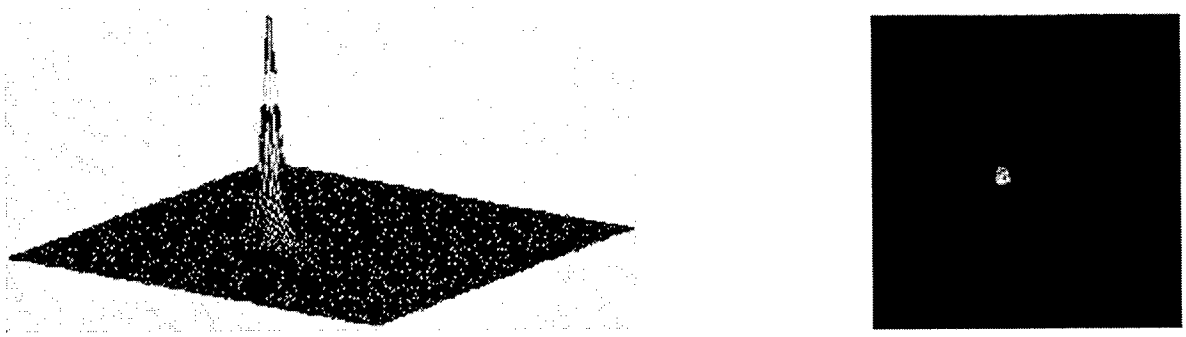

Fig.6 Plot of the far field intensity profile pattern of the UR90 with annular output beam in case of magnification of 1.69. The focusing lens has a 5-m focal length.

By using the Model LBA-100A laser beam quality analyzer made by Spiricon, Inc., the measured beam divergence is 0.27mrad, and the beam quality of β=3.2 has been achieved, where β is defined as

$$\beta = \frac{\theta_{experiment}}{\theta_{theory}} \tag{5}$$

where $\theta_{experiment}$ is the measured beam divergence and $\theta_{theory}$ is the divergence of a filled-in beam with uniform amplitude and phase at the same beam dimension.

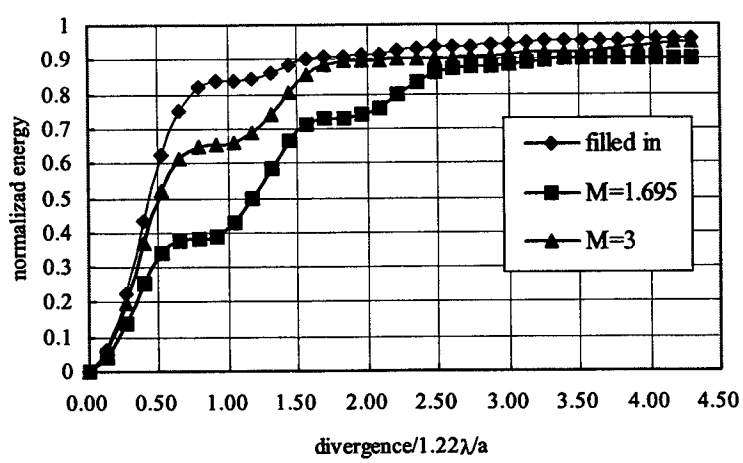


Fig.7 The relation of diffraction limit vs magnification

For a ideal annular beam, the far field energy distribution is expressed as

$$E(z)=\frac{1}{2(1-\varepsilon^2)}\int_0^z[\frac{2J_1(z)}{z}-\varepsilon^2\frac{2J_1(\varepsilon z)}{\varepsilon z}]^2 zdz \tag{6}$$

where ε is the shelter ratio of the aperture and is equal to the reciprocal of magnification.

Figure 6 gives the theoretic curve of the far field energy integral vs diffraction limit in case of different magnification, from the view of the curve of $M$=1.69, the beam quality of the annular beam is equal to 2.6 times diffraction limit. Hence the experimental result of β=3.2 quietly approaches to the theoretic value of β=2.6, in the other word, the actual beam quality was mainly affected by the shelter of the annular beam, but the affection of the shelter is decreased as the magnification is increased, foe example, a magnification of M=3 is selected, the ideal beam quality of β=1.4 can be achieved.

The experimental result proved that the aberrations, thermal distortion, and heterogeneity of the gain medium in the UR90 with annular output beam can also be mitigated by beam rotation compared with the UR90 with filled-in output beam , the near theoretic beam quality can be obtained. As the high gain medium and high magnification are used, the influence of the shelter is reduced, then the near diffraction limit beam quality can be achieved.

## ACKNOWLEDGEMENTS

The authors thank Zhao Tong, Xu Wengang, Wang Ke, Guo Jingwei, and Cong Ziqiang for their invaluable help with the optical alignment, the optical diagnostic, and operation of the COIL system.

## REFERENCES

1. Jin Yuqi, Sun Yishu, Sang Fengting, Yang Bailing, and Zhuang Qi, "Experimental investigation of unstable resonator for a cw supersonic COIL", *High Power Laser and Particle Beams*, **9**(2), pp. 227-232 , 1997.
2. Yu A. Anan'ev, "Properties of unstable resonator with field rotation", *Sov. J. Quantum Electron*, **9**, pp. 1105-1114, 1979.
3. Paxton A H and Latham Jr. W P, "Unstable resonator with 90° beam rotation", *Applied Optics*, **25**(7), pp. 2939-2946, 1986.
4. Jin Yuqi, Yang Bailing, Sang Fengting, Zhou Dazheng, Duo Liping, and Zhuang Qi, "Experimental investigation of an unstable resonator with 90-deg beam rotation for a chemical oxygen iodine laser", *Applied Optics*, **38**(15), pp. 3249-3252, 1999.
5. Zhou Dazheng, Jin Yuqi, Zhao Tong, Sun Long, Xu Wengang, "Experimental investigation of kilowatts class COIL UR90", *High Power Laser and Particle Beams*, **9**(2), pp. 215-220, 1997.
6. Zhou Dazheng, Han Xinmin, "Design method of unstable resonator with 90–deg beam rotation", *High Power Laser and Particle Beams*, **7**(4), pp. 528-534, 1995.

# Small signal gain and temperature profiles in supersonic COIL

Karin M. Grünewald, Jürgen Handke, Frank Duschek
DLR - Institute of Technical Physics*

## ABSTRACT

In the cavity of the supersonic COIL of DLR, the time dependence and the spatial dependence of small signal gain (ssg) and intra-cavity temperature (ict) are investigated for a broad range of operating conditions.

The ssg is measured by a commercial diagnostic system of PSI with a software package upgraded by the Air Force Research Lab of Kirtland, U.S.A.[1,2,3,4,5] The line-shape of the COIL gain profile is scanned in frequency by a diode laser of narrow linewidth operating in the region of the COIL transition frequency. The ict is derived from the full bandwidth at half maximum of the inscribed Gaussian profile.

The experiments are performed for different combinations of secondary gas flow at unchanged primary baseline conditions. The results are interpreted with regard to the ssg and the temperature distribution for optimized COIL operation.

KEYWORDS: Supersonic COIL, small signal gain, intra-cavity temperature, optimized laser operation

## 1. INTRODUCTION

The lasing transition of COIL takes place between the first excited electronic state of atomic iodine $I(^2P_{1/2})$ and its ground state $I(^2P_{3/2})$ at a wave length of $\lambda = 1.315$ µm. The equation for the stimulated emission is given by

$$I(^2P_{1/2}) + h\nu_0 \rightarrow I(^2P_{3/2}) + 2\cdot h\nu_0,$$

with Planck's constant h and the resonating frequency of the lasing transition $\nu_0 = 2.28\cdot 10^{14}$ Hz. In present COIL-systems, the energy for the excitation of atomic iodine is stored in molecular oxygen of the singlet delta state $O_2(^1\Delta)$. The excited oxygen is also used to dissociate the molecular iodine vapor before entering the laser cavity. By both processes, dissociation and excitation, the oxygen is de-excited into its ground state.

When the beam of a probe laser with infinitesimally small intensity $\Im_0$ and the resonant frequency $\nu_0$ interrogates the COIL–active medium, the amplification can be described by the following expression:

$$\frac{\Im(\nu_0)}{\Im_0(\nu_0)} = e^{(g_0\cdot L)},$$

where $\Im$ symbolizes the amplified intensity. The gain length is denoted by L. The ssg $g_0$ is given by the equation

$$g_0(\nu) = \frac{7}{12}\frac{A\lambda^2}{8\pi} f(\nu)\left([I(^2P_{1/2})] - \frac{1}{2}[I(^2P_{3/2})]\right),$$

with the Einstein coefficient A and the line-shape function f(ν). Since the ict T has to be measured in a non-contact way to avoid disturbances of the supersonic gas flow, it is derived from the full width at half maximum of the Gaussian profile

$$\Delta\nu_D(T) = \frac{2\cdot\nu_0}{c}\sqrt{\frac{2\cdot k\cdot T}{M}\cdot \ln 2},$$

that is inscribed in the Voigt profile of the gain line-shape. The full width at half maximum of the Gaussian profile is given by $\Delta\nu_D$, and the Boltzmann's constant is denoted by k. The velocity of light within the medium is represented by c and M symbolizes the mass of the particles.

## 2. EXPERIMENTAL

For the investigation of ssg in DLR COIL, the beam of the probe laser passes the gain medium parallel to the optical axis.

* Correspondence: Langer Grund, D-74239 Hardthausen, Germany, Tel. +496298 28-241, Fax +496298 28-582, e-mail: karin.gruenewald@dlr.de

XIII International Symposium on Gas Flow and Chemical Lasers and High-Power Laser Conference,
Antonio Lapucci, Marco Ciofini, Editors, Proceedings of SPIE Vol. 4184 (2001)

The measurements were performed for hot runs of 10 sec. duration.

As shown in fig. 1, the set-up consists of the probe beam emitter/detector unit of the gain diagnostics and a mirror system for beam alignment, both mounted on an assembly of motorized linear stages. The stages allow fast and precise movements in two perpendicular directions. This special arrangement enables a two-pass scan of the probe through the COIL medium. The divergence of the probe beam was roughly determined to a value of 2.3 mm·mrad.

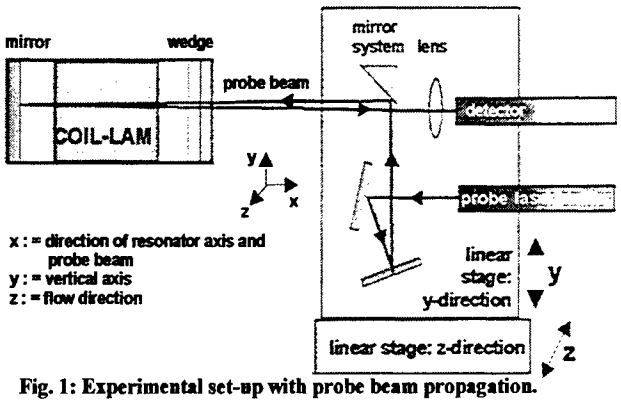


**Fig. 1: Experimental set-up with probe beam propagation.**

The temporal dependencies of ssg and of ict are measured for 5 positions along the flow axis at different heights of the flow channel. In a second scheme, the spatial dependencies of ssg and temperature are recorded. The resulting grid of measuring positions is presented in fig. 2.

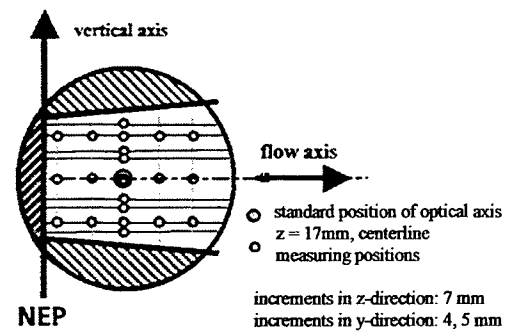


**Fig. 2: Cavity aperture with measuring positions for 2D small signal gain and temperature detection.**

During the progressing hot run, scans are performed in flow direction as well as in vertical direction of the flow channel. Temporal effects due to the increasing water vapor evaporation in the progressing hot run have to be de-convoluted from the local gain readings to achieve the pure spatial dependencies of ssg and temperature.

In DLR COIL, the iodine flow is perpendicularly admixed to the flow of excited oxygen in the subsonic region of a laval nozzle array. Helium is chosen as buffer gas for both flows. For such mixing conditions, the dissociation of iodine starts before the gas flow enters the nozzle throat and is expected to be fairly finished at the nozzle exit plane (NEP). For the whole test series, the primary gas flow remains unchanged at baseline conditions with a chlorine molar flow rate of 500 mmol/s and a dilution ratio of $He:Cl_2 = 3:1$.

In former investigations[6] the optimum adaptation of secondary gas flow to the primary baseline conditions was found to be $I_2/O_2 \approx 1.75$ % and $He^{sec}/I_2 \approx 70$. The optimization of gas mixing was performed with the intention to achieve maximum power output from a stable resonator. For the investigations on ssg, the secondary gas flow is varied from the optimized conditions in two different manners: First, the molar flow ratio $He^{sec}/I_2$ is changed while keeping the iodine molar flow rate optimum, and second, by changing the iodine molar flow rate, while the $He^{sec}/I_2$ ratio is kept at the optimum value. The results of the measurements are interpreted in comparison to the ssg and temperature distribution for optimized COIL operation.

## 3. PROFILS OF SMALL SIGNAL GAIN AND TEMPERATURE

### 3.1 Development of small signal gain and intra-cavity temperature during progressing hot run

Fig. 3 presents the histories of ssg and ict for a variation of the secondary helium flow at optimum iodine flow rate.

The achievable ssg strongly depends on the gas mixing. The optimum operating conditions yield the maximum ssg for the whole hot run duration at a range of 1 %/cm to 1.2 %/cm. While a deficiency of secondary helium leads to a strong reduction of ssg, a surplus of secondary helium shows only a slight effect. The de-

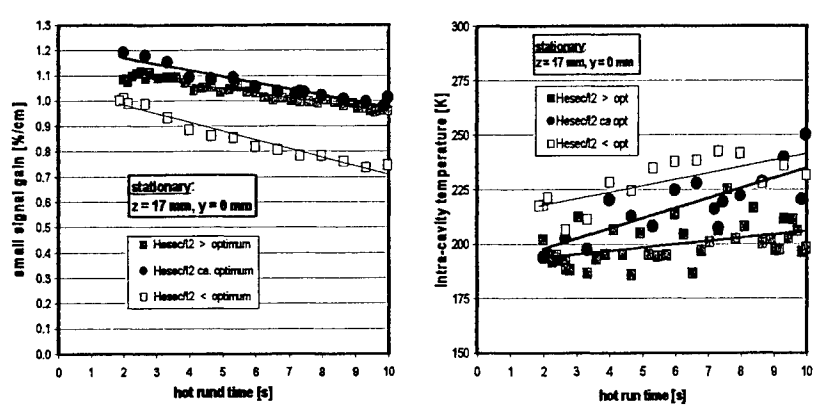


**Fig. 3: Time dependent small signal gain (left diagram) and intra-cavity temperature (right diagram) for a variation of secondary helium flow rate (z = 17mm, y= 0).**

crease of ssg along the time scale can be approximated by straight lines. The shape of ssg follows from increasing quenching of atomic iodine due to the temporal increase of water vapor evaporation. Thus, the temporal profiles of ssg strongly depend on the operating conditions, but are independent of the local position within the cavity. This fact is used in the following to eliminate the superimposed temporal effects from the spatial readings.

The evaluation of the temperature readings is complicated by the scattering of the results (mainly in the case of small values of ssg due to the low signal–to-noise ratio). Therefore, in a first approach, the temperature readings, fig. 3, are also fitted by straight lines. This simple approximation enables a survey on the temporal dependence of temperature in a cavity with supersonic flow. The ict starts at 200 K ± 10% and increases by a value up to 25 % during the 10 seconds of hot run.

### 3.2 Spatial dependencies of small signal gain for different operating conditions

Fig. 4 shows profiles of ssg along the flow axis for a variation of secondary helium and iodine, respectively. Due to the high dilution ratio of $I_2$ for high helium flow rates, the ssg profiles follow from the inefficient iodine dissociation. The dissociation extends into the cavity region. When the dilution ratio of iodine is small, the iodine concentration in the secondary jets is higher and the flow velocity is smaller. Consequently, the dissociation rate at the cavity entrance is higher but accompanied by a high consumption of $O_2(^1\Delta)$ and a high energy release into the flow.

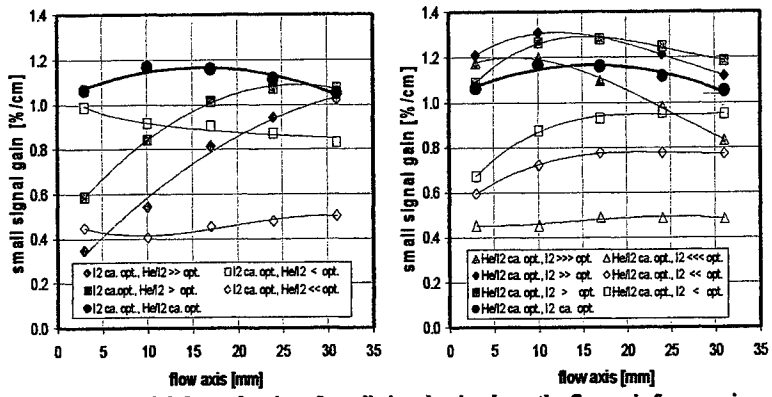


**Fig. 4: Spatial dependencies of small signal gain along the flow axis for a variation of the secondary helium flow rate (left diagram) and a variation of the iodine flow rate (right diagram): t = 3 sec.**

A raise of the iodine flow rate higher than optimum leads to an increase of ssg and a shift of the local maximum towards the NEP. At a further increase of iodine, the local ssg-maximum "moves" into the area of the nozzle grid, and the ssg-values monitored in the cavity only present the inclined branch beyond the maximum. Generally, the effects of a variation of iodine flow rate on ssg do also depend on the respectively chosen combination of secondary helium and iodine flow[7].

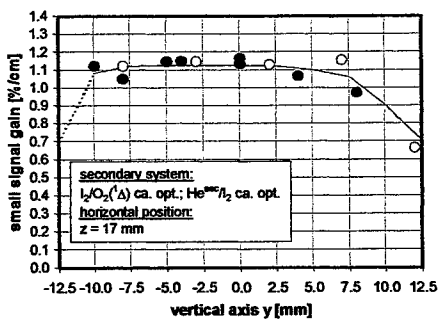


**Fig. 5: Vertical scan of ssg at 3 sec after hot run start.**

As presented in fig. 5 for optimum operating conditions, the profile of ssg in vertical direction shows a broad core flow with almost constant ssg. Taking into account that the spatial resolution for the recording of ssg amounts to 7 mm, this core flow reaches from –10 mm up to +10 mm The behavior of ssg within the boundary layers could not be detected in detail, because of the unfavorable ratio of layer thickness to beam diameter.

### 3.3 Spatial dependencies of intra-cavity temperature for different operating conditions

The spatially dependent temperatures corresponding to the above presented ssg measurements are shown in fig. 6. In each of the test runs, the temperature increases along the flow axis due to the heat release in the loss processes. The increase of the temperature continuously raises the threshold yield in flow direction.

As to be seen in the left diagram of fig. 6, the temperature achieved at the cavity entrance is highest for small ratios of $He/I_2$. This behavior points out both, high $O_2(^1\Delta)$–losses due to the dissociation of iodine and a weak heat dissipation due to the small amount of secon-

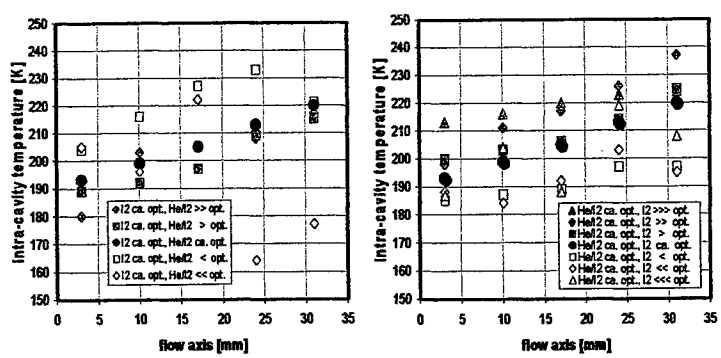


**Fig. 6: Spatial dependencies of ict along the flow axis) for a variation of the secondary helium flow rate (left diagram) and a variation of the iodine flow rate (right diagram at t = 3 sec.**

dary helium. With increasing helium flow rate, the ict decreases. The highest ratio of $He/I_2$ leads to the smallest ict, even smaller than for optimized conditions. The still lower ssg at the cavity entrance, directly confirms the assumption of an incomplete dissociation for high helium flow rates.

The right diagram of fig. 6 shows the results for a variation of the iodine flow rate. At small flow rates, a comparatively small part of $O_2(^1\Delta)$ is lost in dissociation and the gas flow is not yet strongly heated up at the entrance of the cavity. High iodine molar flow rates cause high $O_2(^1\Delta)$-consumption in dissociation and the ict starts at values above the temperature for optimized conditions. Consequently, the fact that the highest values of ssg are achieved with high iodine flow rates, despite of the high threshold yield, demonstrates the effect of the large number of iodine atoms on the amplification properties.

## 4. CONCLUSION

The stationary ssg decreases almost linearly with time during the hot flow. The gradient is independent of the local position within the cavity, but depends on the operating conditions. At operating conditions that induce small values of ssg, the temperature measurements show a strong scattering of the values.

For optimum operating conditions, the spatially scanned ssg is nearly constant along the flow axis at about 1.2 %/cm The corresponding ict increases from 190 K to 240 K during a hot flow of 10 seconds.

For non-optimum operating conditions, the ssg varies along the flow axis. Generally, the spatial dependence of ssg is determined by the combination of dissociation, excitation and quenching loss due to the respective gas mixing. For most operating conditions, the resulting ssg is smaller than the ssg achieved by optimized mixing conditions. The only exception is found for high iodine flow rates. The corresponding ssg can exceed the values achieved for optimized laser operation, mainly in the fore part of the cavity. Thus, the ssg is essentially determined by the number of iodine atoms in the flow and by the temperature of the active medium. In vertical direction, there exists a broad core flow with almost constant ssg.

A temperature range of 200 K ± 10 % and above is found to be typical for the whole test series. Smaller values of temperature were measured only for extreme operating conditions, that are not usable with regard to an efficient laser operation.

The ssg presented in this paper is an average value in the direction of the probe laser path. Due to the nozzle grid configuration, the ssg actually varies according to the different layers across the flow field. Experiments on the spatial dependence of ssg in the direction of the optical axis will complete the present investigation.

## ACKNOWLEDGEMENTS

The authors like to thank the people of the AFRL of Kirtland for the supply of the iodine diagnostics and for their kind support during the initial operation.

## REFERENCES

[1] S.J.Davis, W.J.Kessler, M.Bachmann, "Collisional broadening of absorption lines in water vapor and atomic iodine relevant to COIL diagnostics", Gas and Chemical Lasers and Intense Beam Applications II, Vol 3612, pp. 157-166, San José, 1999.

[2] P.B.Keating, C.A.Helms, G.T.Anderson, T.L.Rittenhouse, K.A.Truesdell, G.D.Hager, "Two-Dimaensional Gain and cavity temperature maps of a small-scale supersonic COIL", Lasers, pp. 1996.

[3] R. Highland, L.Hanko, G.Hager, K. Truesdell, "Spectral and Saturation Characteristics of COIL", 25th AIAA Plasmadynamics & Lasers Conference, 94-2438, Colorado Springs, 1994.

[4] R.F.Tate, B.S.Hunt, C.A.Helms, K.A.Truesdell, G.D.Hager, "Spatial Gain Measurements in a Chemical Oxygen Iodine Laser (COIL)", IEEE Journal of Quantum Electronics, Vol. 31, No. 9, pp. 1632-1636, 1995.

[5] B.D.Barmashenko, A.Elior, E. Lebiush, S.Rosenwaks, "Gain and Power in COILs – Theory and Experiment", 25th AIAA Plasmadynamics & Lasers Conference, 94-2438, Colorado Springs, 1994.

[6] K.Grünewald, J.Handke, W.O.Schall, L.v.Entress-Fürsteneck," Effects of gas mixing on COIL performance", [3574-41], 12th International Symposium on Gas Flow and Chemical Lasers and High Power Lasers GCL/HPL, SPIE, Vol. 3574, pp. 315 – 320, St. Petersburg, 1998.

[7] R.F.Tate, B.S.Hunt, C.A.Helms, G.D.Hager, K.A.Truesdell, "2-D Gain Measurements in a COIL device", 25th AIAA Plasmadynamics & Lasers Conference, 94-2438, Colorado Springs, 1994.

# Frequency conversion of high power iodine lasers radiation

Viktor I. Bespalov[*a], Stanislav A. Sukharev[b], Karel Rohlena[*c]

[a]Institute of Applied Physics, Russian Academy of Sciences, Nizhniy Novgorod, Russian Federation

[b]Russian Federal Nuclear CenterVNIIEF, Sarov, Nizhniy Novgorod Region, Russian Federation

[c]Institute of Physics, Academy of Sciences of the Czech Republic, Prague, Czech Republic

## ABSTRACT

A frequency conversion technique applied to iodine laser beams is described in detail for the ISKRA-4 and PERUN as representatives of wide and narrow aperture systems. The conversion efficiency was measured and predicted theoretically for both the 2nd and 3rd harmonics. The performance of conventionally grown conversion DKDP crystals is compared with that grown by the accelerated and the directional method. Examples are given of physical target experiments using the converted beams.

**Keywords:** Lasers, Frequency conversion, Harmonics, Non-linear optics

## 1. INTRODUCTION

Frequency conversion of high power infrared laser radiation (wavelength 1-1.3 μm, diameter of the beam ~50 cm, fluency several joules per square centimeter) into the visible or ultraviolet spectral region imposes specific requirements on the parameters of both the radiation and the converter. At present, a considerable experience exists of frequency conversion of Nd:glass solid state lasers and of the iodine photodissociation gas lasers.[1-4]

A key problem of the frequency conversion development of wide aperture converters is the choice and manufacture of high quality non-linear medium and of phase synchronization type. Owing to the requirements of transparency, high optical breakdown threshold and necessity to grow large aperture crystals the only reasonable candidate up to now has been the crystal of KDP (DKDP). The most popular phase synchronization type used on the majority of present systems for the 2nd harmonic generation is the second type (oee) scheme and for the 3rd harmonics generation the favorite scheme is type II - type II. The same scheme of conversion in the 3rd harmonics suffered from certain difficulties on the system NOVA caused by a depolarization of the radiation. Even with a small proportion of depolarized radiation in the ~74 cm beam the conversion efficiency approaches ~50 % at the intensity 1.25 $GWcm^{-2}$ falling rapidly with the rising intensity.[5] As the next scheme on the NOVA and the new systems NIF and MEGAJOULE the type I - type II was chosen as less sensitive to the depolarization.

Well known are the results of frequency conversion in the 2nd and 3rd harmonics on the iodine laser system ASTERIX.[3] DKDP crystals were used together with the second type synchronization. The conversion efficiency was better than 60 %.

In the present report the results are presented of the frequency conversion of high power iodine lasers on the systems ISKRA-4 (Russia) and PERUN (Czech Republic).

## 2. FREQUENCY DOUBLING AND TRIPLING

The ISKRA-4 system is a large single channel iodine photodissociation laser having several amplifier stages. It consists of an oscillator, four intermediate amplifiers and two power amplifiers. The beam diameter at the output is 41 cm. The pulse energy is ~ 1 kJ, the length of the pulse is $\tau_{0.5}$ = 0.3-0.5 ns with the beam divergence $\Theta_{0.8E} \sim 1\times10^{-4}$ rad.[4]

The first experimental results of the conversion in the 2nd harmonics of the iodine laser radiation (λ=1.315 μm) on the ISKRA-4 system are presented in.[6] With a 4 cm beam a technical conversion efficiency of 40 % was reached at the mean intensity 2 $GWcm^{-2}$. Conventionally grown DKDP crystal were used (scheme oee) 1.5-2.5 cm thick. For the next experiments with iodine laser frequency conversion the DKDP crystals were used, which were grow by one of the two fast

* Corresponding author phone +420 2 6605 2792, fax +420 2 6880729, rohlena@fzu.cz

XIII International Symposium on Gas Flow and Chemical Lasers and High-Power Laser Conference,
Antonio Lapucci, Marco Ciofini, Editors, Proceedings of SPIE Vol. 4184 (2001)

growth methods, which were developed in the Institute of Applied Physics of the Russian Academy of Sciences in Nizhny Novgorod (IAP).

The crystals of required dimensions and orientations are grown directly. The growth is taking place in a vessel, the dimensions of which correspond to the size of the crystal to be grown. The fast growth of the oriented crystal slabs is enforced by placing in the vessel a suitable seed. The growth then proceeds from a natural crystal face, which is either a face of the prism (101) or of the pyramid (101).

Studies were done to compare the converter performances based on the conventionally grown crystals and the crystals grown by the technology of the fast and of the directional growth. For that purpose an ISKRA-4 beam with an improved spatial profile was used, with the conventional crystal element of dimensions 10×10×2 cm and an oblique element with the aperture 15×15 cm.[6] The laser pulse, which had the length 0.2-0.3 ns and the divergence $1.2\times10^{-4}$ rad, was characterized by an inhomogeneity of radial intensity distribution $\Delta I/I_{mean} \sim 0.1$. Its diameter was 8 cm. It was linearly polarized. The measured conversion efficiency at the intensity 3 $GWcm^{-2}$ exceeded 80 %, see fig. 1. The experimental points belonging to the conventional and the oblique elements were lying on a single experimental curve. In the same figure computational curves are shown calculated for the beam divergence $1\times10^{-4}$ rad and a varying deviation from the exact direction of phase synchronization. All calculation were done in the approximation of plane monochromatic waves. The results were integrated over the radial dependence, divergence angle and time. The time profile of the laser pulse was supposed to be a hyperbolic secans. The following absorption coefficients for various wavelenghts propagating inside the crystals were used $\alpha_{1o} = 0.05\ cm^{-1}$, $\alpha_{2o} = 0.03\ cm^{-1}$, $\alpha_{2e} = 0.005\ cm^{-1}$, $\alpha_{3e} = 0.01\ cm^{-1}$.

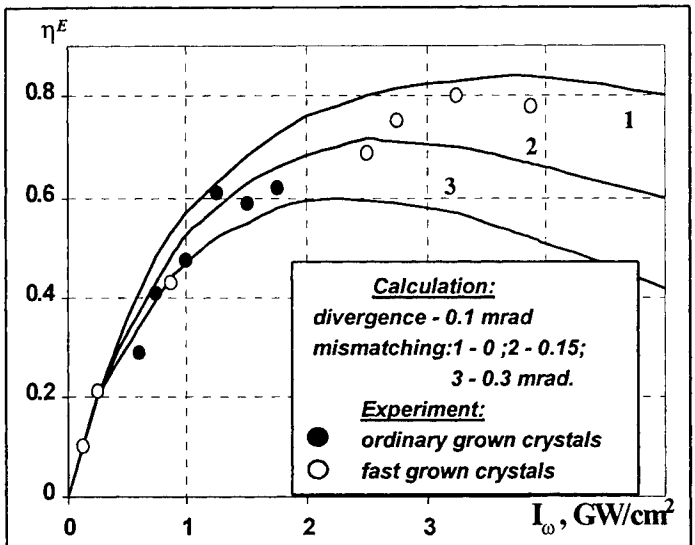


Figure 1. 2ω conversion efficiency as a function of the average incident power density

In the first experiments with the conversion into the 3rd harmonics the efficiency did not exceed 40 %.[16] Oblique DKDP crystals grown by the accelerated and directional method were used of deuterization degree 85 % and each was 1.7 cm thick. The used scheme was type II - type II. The beam diameter was 8 cm. The pulse energy was ~20 J with the time lengths 0.3-0.5 ns. The radiation was linearly polarized, its divergence was $3\times10^{-4}$ rad. The maximum efficiency was attained for 1.2 $GWcm^{-2}$.

On the system PERUN a conversion to the 2nd (0.657 μm) and 3rd harmonics (0.438 μm) was successfully implemented.[7,8] One of the important features distinguishing the system PERUN from the other iodine lasers ASTERIX[3] and ISKRA-4[4] is a long pumping time (270 μs) long. As a consequence, owing to the long pumping pulse inhomogeneities of the refraction index of the amplifying medium develop. This is influencing both the energy distribution in the near zone and also the beam divergence is increased. The final amplifier A4 with the diameter 8.4 cm gives on its output ~40 J, pulse length $\tau_{0.5}$ = 0.3-0.5 ns and the divergence $\Theta_{0.8E} \sim 4\times10^{-4}$ rad. For the conversion to the 2nd harmonics a monocrystal DKDP of the fast growth was used with the deuterization degree 87 % and dimensions 10×10×2.4 cm. The converter element was cut for the oee scheme. The conversion efficiency to 2ω of ~60 % is attained, the energy of the red radiation ≥20 J.

For the 3rd harmonics conversion there was using the scheme type II - type II (oee-eoe). A pair of DKDP crystals with the deuterization degree 84 % and dimensions 10×10×1.5 cm and 10×10×1.6 cm were used as a doubler and mixer. The experimental points indicate the obtained conversion efficiency 60 %, pulse energy was 20 J. At the intensity ≈2 $GWcm^{-2}$ the dependence of conversion efficiency in the 3rd harmonics on the deviation from the exact phase synchronization angle of the second crystal was measured. The results are seen in fig. 2. The width of this curve at half magnitude is ~3 angular minutes.

For the frequency doubling on the ISKRA-4 system, since for the beam diameter ~40 cm no crystals of comparable dimensions are available, crystal mosaic converter composed of four smaller elements 15×15×1.8 cm and 21×21×1.8 cm were applied.

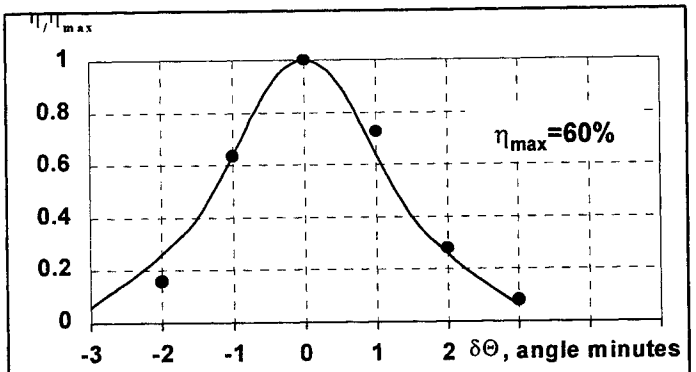


*Line - calculation*
*Θ=0.3 mrad, $\Delta\Theta_1$=1.5 mrad, I=2 GW/cm²*
*points - experiment*
*I=(1.8-2.3) GW/cm², $L_1$=15 mm, $L_2$=16 mm*

Figure 2. 3ω conversion efficiency as a function of mixer matching angle

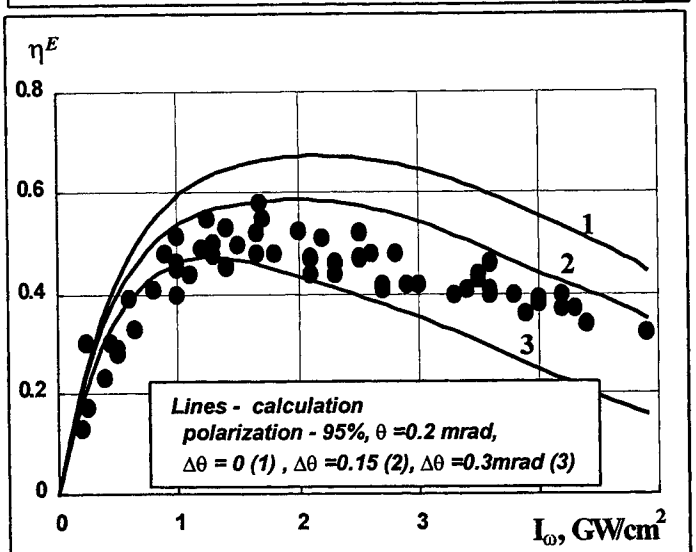


Figure 3. Doubling efficiency of the mosaic converter as a function of the average intensity of radiation

On the ISKRA-4 system with the converter mosaic with the technical conversion efficiency ~50-55 % the converted pulse energy was up to 600 J and the beam divergence $\Theta_{0.8E}$ ~ $1.5\times10^{-4}$ rad, the power ~3TW. The dependence of the conversion efficiency on the intensity is shown in fig. 3.

## 3. EXPERIMENTS WITH THE CONVERTED BEAMS

A number of target experiments was perfomed to investigate the laser-matter interaction using the converted radiation. These experiments were directed at laser light 2nd harmonics (λ=0.657 μm) conversion in x-ray laser plasma emission on a plane gold targets with the focused heating radiation intensity $3\times10^{13}$-$10^{14}$Wcm$^{-2}$, see.[9] The laser light absorption efficiency in the plasma was ~80 %, conversion efficiency in x-ray reached ~45 %, which is twice as high as if working with the 1st harmonics λ=1.315 μm. The energy of the soft x-ray radiation (hν~1 keV) was ~100 J, the length of the x-ray pulse was ~1 ns.

Similarly a series of compression experiments with the spherical target of high aspect ration $A_s \geq 300$ was performed.[10] Within that experimental series a record neutron output $N = 6\times10^7$ ever achieved on ISKRA-4 using coated glass shell targets was recorded.

Also experiments with turbulent mixing of thin layers of Al and Au using the layered plane targets illuminated by the 2nd and 3rd harmonics were done. The results of the first experiments devised to investigate the mixing of thin layers of Al and Au during the laser acceleration of flat three-layer targets of Si (5 μm), Al (2 μm), and Au (0.05-0.26 μm) by radiation converted to the second harmonic from the ISKRA-4 laser with an intensity of $4\times10^{13}$-$7\times10^{13}$ W/cm² ($\tau_{0.5}$~1 ns), which acts on the Si side of the target.[11]

On the system PERUN with a flexible arrangement of the beam conversion it was possible to test the idea of beam smoothing by applying a target illumination by a two-colour double pulse.[12] Equally, the efficiency of highly charged ion production of heavy elements, such as needed for injectors into large ion accelerators, was examined by using converted higher harmonics beams.[13]

## 4. CONCLUSIONS

The successful transformation of powerful iodine lasers PERUN and ISKRA - 4 in the mode of operation on II and III harmonics is conducted by conversion of a laser radiation in large-aperture DKDP crystals of accelerated growth. A number of experimental investigations on interaction of converted radiation with matter were carried out.

## ACKNOWLEDGMENTS

A support by the grants nos. 202/98/1274 and 202/00/1217 of the Grant agency of the Czech Republic for K.R. and International Science and Technology Center grants #223-95 and #1185-99 is gratefully acknowledged.

## REFERENCES

1. E. M. Campbell, J. T. Hunt, E. S. Bliss D. R. Speck, and R. P. Drake, "Nova Experimental Facility (Invited)", *Rev. Sci. Instr.* **57**, pp. 2101-2106, 1986.
2. C. Yamanaka, S. Nakai, T. Yamanaka, Y. Izava, Y. Kato, K. Mima, K. Nishihara, T. Mochizuki, M. Yamanaka, M. Nakatsuka, T. Sasaki, T. Yabe, K. Yoshida, H. Azechi, H. Nishimura, T. Harimatsu, S. Ido, N. Nizanaga, S. Sakabe, H. Takabe, J. Jitsuno and M. Takagi, "High Thermonuclear neutron yield by shock multiplexing implosion with GEKKO XII green laser" *Nucl. Fusion* **2**, pp. 19-30, 1987.
3. A. G. Maaswinkel, K. Eidmann, and S. Witkowsky, "Comparative Study of Laser Acceleration of Thin Foils at Wavelength 0.44 μm and 1.3 μm", *Optics Comm.* **51**, pp. 255-259, 1984.
4. A. I. Zaretskiy, G. A. Kirillov, S. B. Kormer, G. G. Kochemasov, V. M. Murugov, and S. A. Sukarev, "Investigation of microtargets irradiated with a laser pulses of iodine laser of 1-3 TW power"*Kvantovaya Elektr.*, **10**, pp.756-766, 1983 (in Russian).
5. M. A. Henesian, R. D. Boyd, J. K. Lawson, and P. J. Werner, "Beam Depolarization Effects on Nova Frequency Conversion," Laser Program Annual Report 1986 UCRL-50021-86, Livermore National Laboratory, Livermore, Calif., pp. 6-42 to 6-47, 1987.
6. A. I. Zaretskiy, G. A. Kirillov, S. B. Kormer, G. G. Kochemasov, V. M. Murugov, and S. A. Sukharev, "Experiments on ISKRA-4," *Izv. Akad. Nauk., Seria fizicheskaya*, **48**, pp. 1611-1618, 1984 (in Russian).
7. V. I. Bespalov, V. I. Bredichin, M. Chvojka, B. Králiková, L. Láska, K. Mašek, A. V. Ryadov, K. Rohlena, J. Skála, S. A. Sukharev, O. Štirand, I. N. Voronich, A. I. Zareckij, "Conversion to the second harmonic of high power iodine photodissociation laser system PERUN," *Czech. J. Phys*, **45**, pp. 757-760, 1995.
8. V. I. Bespalov, V. I. Bredichin, D. G. Efimov, V. I. Katsman, B. Králiková, L. Láska, K. Mašek, K. Rohlena, J. Skála, S. A. Sukharev, P. Trenda, I. N. Voronich, A. I. Zareckij, "Conversion to the third harmonic of the iodine photodissociation laser system PERUN," *Czech. J. Phys.* **45**, pp. 761-765, 1995.
9. S. A. Bel'kov, A. V. Besserab, G. V. Dolgoleva, N. V. Zhidkov, A. I. Zaretski, G. A. Kirillov, G. G. Kochemasov, A. V. Kunin, N. N. Rukavishnikov, N. A. Suslov, and S. A. Sukharev, "Investigation of laser energy conversion into plasma X-rays in the system Iskra-4", Czechoslovak Journal of Physics, v. **42**, pp. 969-973, 1992.
10. S. A. Bel'kov, A. V. Besserab, I. N. Voronich, S. G. Garanin, G. V. Dolgoleva, A. I. Zaretskii, V. M. Izgorodin, B. N. Ilyushechkin, G. G. Kochemasov, A. V. Kunin, S. G. Merkulov, N. N. Rukavishnikov, A. V. Ryadov, N. A. Suslov, and A. A. Sukharev "Investigation of the compression of high aspect targets irradiated with a laser pulse of the second harmonic of the Iskra-4 iodine laser", *ZhETF* **101**, pp. 80-88, 1992 (in Russian), Sov.Phys. JETP **74**, (1), pp. 43-47, 1992.
11. V. A. Andronov, S. A. Bel'kov, A. V. Besserab, I. N. Voronich, S. G. Garanin, A. A. Gorbunov, V. N. Derkach, G. V. Dolgoleva, A. I. Zaretsky,, V. M. Igodin, B. N. Ilyushechkin, G. A. Kirillov, G. G. Kochemasov, Yu. V. Kuratov, V. P. Lazarchuk, V. A. Lebeďev, V. M. Murugov, L. S. Mkhitar'yan, A. V. Okutin, S. I. Petrov, A. V. Pinegin, N. N. Rukavishnikov, A. N. Razin, A. V. Ryadov, A. V. Senik, N. A. Suslov, S. A. Sukharev, and V. A. Tokarev, "Investigation of the turbulent mixing of thin layers of materials of different density during the laser acceleration of flat multilayer targets in the Iskra-4 facility," *ZhETF* **111**, pp.882-888, 1997, [Sov.Phys. JETP **84**, pp. 485-488, 1997].
12. K. Mašek, B. Králiková, L. Láska, S. Přeučil, K. Rohlena, J. Skála, P. Straka, A. V. Besserab, S. G. Garanin, Yu. F. Kiryanov, G. G. Kochemasov, L. V. Lvov, A. B. Ryadov, S. A. Sukharev, A. A. Suslov, O. A. Vinokurov, A. I. Zaretskiy, "Self-smoothing effect of double-pulse laser plasma," Proc. 4th Int. Workshop on Iodine Lasers and Applications, 18-22 September 1995, Třešť Castle, Czech Republic, SPIE **2767**, pp. 91-96.
13. L.Laska, J.Krasa, M.P.Pfeifer, P.Trenda, B.Kralikova, J.Skala, K.Rohlena, E.Woryna, J.Farny, P.Parys, J.Wolowski, W.Mroz, A.Shumshurov, B.Sharkov, K.Langbein, H.Haseroth, "Multiply charged ion generation from NIR and visible laser-produced plasma", REV.Sci.Instr. **67**, pp.950-952, 1996.

# Chemical Oxygen-Iodine Laser with a Closed Gas Cycle

**John Vetrovec**
The Boeing Company, Rocketdyne Propulsion & Power
6633 Canoga Avenue, Canoga Park, CA 91309, U.S.A.
tel. (818) 586-3101, fax (818) 586-3074
jan.vetrovec@boeing.com

## ABSTRACT

This work describes a conceptual design of a chemical oxygen-iodine laser (COIL) where diluent gas is continuously recirculated in a closed cycle. Scaling laws, component design, and expected performance are discussed.

**Keywords:** COIL, iodine laser, vacuum pump, cryosorption

## 1. INTRODUCTION

In a chemical oxygen-iodine laser (COIL), chemically prepared, gaseous gain medium at 3-10 Torr pressure is drawn through the laser cavity by vacuum suction. Multiple-stage vacuum pumps such as Roots blowers or steam ejectors are typically used to receive and compress the gas flowing from the laser and exhaust it to the atmosphere. The size and weight of such vacuum pumps present a significant challenge to engineering a transportable COIL system needed for special industrial applications [1,2]. Our recent publication [3] describes two COIL systems that use a cryosorption vacuum pump to provide vacuum and safely contain laser exhaust gas: (1) COIL with $N_2$ diluent where the cryosorption pump adsorbs all the cavity flow in real time, and (2) COIL where non-sorbable diluent (e.g., He or Ne) is circulated between COIL and the cryosorption pump in a closed-loop arrangement. The present work further elaborates on the closed gas cycle COIL, which offers the advantages of compact hardware, higher efficiency, continuous operation, and low consumption of refrigerant.

## 2. CRYOSORPTION VACUUM PUMPS FOR COIL

Sorption pumps function by the physical adsorption of gases at the surface of molecular sieves (zeolites) or other sorption material [4]. Such materials have an extraordinarily large specific surface area per unit of mass (~1000 $m^2$/gram), which enables considerable gas adsorption capacity. Figure 1 shows that at the temperature of liquid nitrogen and 10 Torr partial pressure ~19 grams of $N_2$ or $O_2$ can be adsorbed onto 100 grams of Linde 4A synthetic zeolite. Sorption capacity of zeolites is highly dependent on zeolite temperature and pressure of gas above the sorption surface. For example, at an equilibrium pressure of 10 Torr, changing the temperature from 293 to 77 K increases the capacity of zeolite Linde 4A to sorb $N_2$ more than 200 times. The sorption capacity of zeolites is also highly dependent on the gas to be pumped. In general, light inert gases are hardly pumped at all. As seen in Figure 2, the capability of synthetic zeolite Linde 13X to pump He or Ne at a temperature of 78 K is several orders of magnitude lower than for $N_2$.

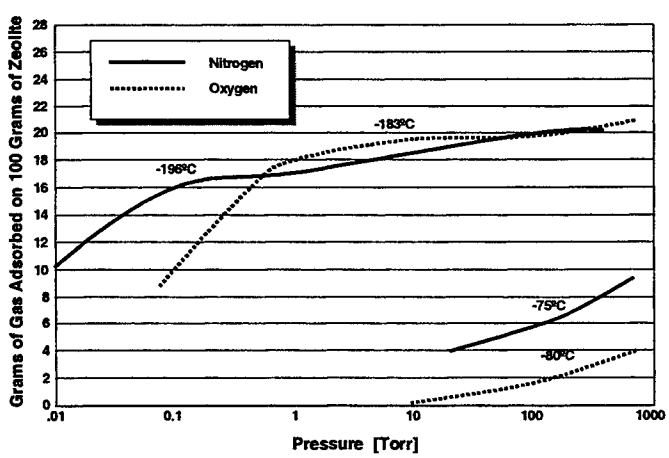


*Figure 1: Isotherms for absorption of $O_2$ and $N_2$ on Linde 4A zeolite (after [5])*

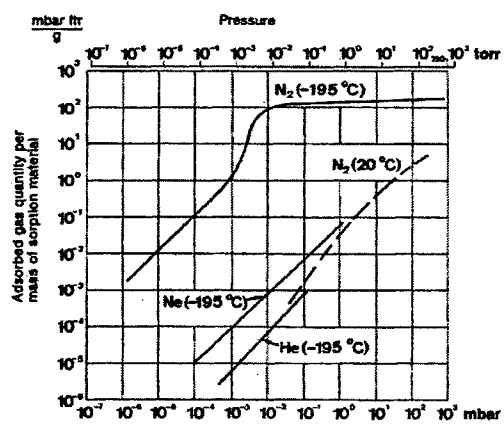


*Figure 2: Adsorption isotherms of zeolite 13X for $N_2$, He, and Ne at various temperatures [6]*

XIII International Symposium on Gas Flow and Chemical Lasers and High-Power Laser Conference,
Antonio Lapucci, Marco Ciofini, Editors, Proceedings of SPIE Vol. 4184 (2001)

A COIL using $N_2$ or other diluent gas efficiently sorbed by zeolites permits easy integration with a cryosorption vacuum pump. An integrated system of this type is shown in Figure 3. During laser operation, decelerated flow from the diffuser is directed into the gas chiller/condenser where it is chilled to approximately 100 K and condensable vapors ($Cl_2$, $I_2$, and $H_2O$) are trapped onto condenser surfaces. Cold and dry gas containing only $N_2$ and $O_2$ flows from the gas chiller into the zeolite bed cooled to a temperature of ~80 K and is trapped by cryosorption. Operation of a large scale COIL with $N_2$ diluent and cryosorption pump such as shown in Figure 3 was successfully tested at Boeing-Rocketdyne Propusion & Power in March 1999 [7]. Design, operation, and scaling of this type of pump were previously described by us elsewhere [3,8].

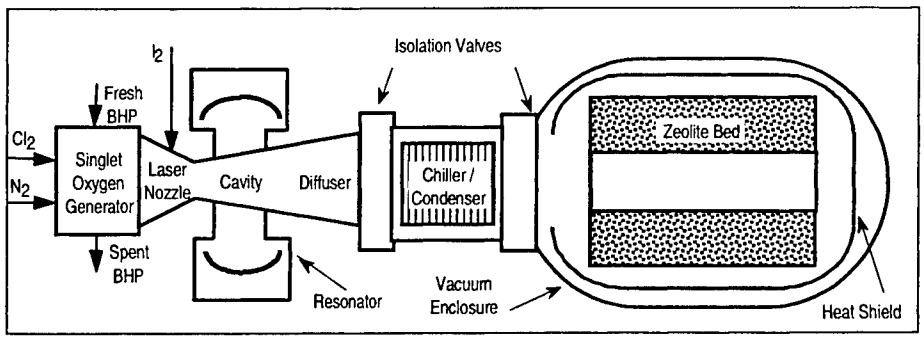


*Figure 3: COIL with cryosorption pump [3]*

One challenge that this type of system must overcome is rejection of heat released in the pumping process, namely: (1) change in gas enthalpy as the gas is cooled to the sorption temperature and (2) release of the heat of sorption. For example, chilling of $N_2$ from 300 to 77 K reduces its enthalpy by 13.3 kJ/mol and its sorption on zeolite releases on the average about 13.1 kJ/mol [4]. The heat of adsorption is particularly problematic as it is deposited into the zeolite, causes it to warm-up, and reduces its sorption capacity. To maintain sorption capacity, removal of the adsorption heat may be handled in two distinct ways. In the first approach, the zeolite bed can be operated in an inertial (heat capacity) mode. Here, the amount of zeolite is increased to allow it to soak up the heat of adsorption with only a modest temperature rise and with some tolerable loss of sorption capacity. In the second approach, heat of adsorption is removed from the zeolite in real-time by using an imbedded heat exchanger [3]. However, low thermal conductivity of zeolites requires a large heat exchanger to sustain reasonable heat transfer rates. Thus, either approach leads to increased size and weight of the zeolite pump.

## 3. CLOSED GAS CYCLE (CGC) COIL

The limitations of the system in Figure 3 can be avoided if a non-sorbable diluent gas (such as He or Ne) is recirculated between COIL and a zeolite, and $O_2$ is continuously removed from the flow. In such a system, shown in Figure 4, flow from COIL cavity is first made free of $Cl_2$, $I_2$ and $H_2O$ vapors, and cooled to improve the volumetric efficiency of the compressor. Compressed mixture of $O_2$ and diluent is cooled in a recuperative heat exchanger to about 200 K followed by chilling to ~80 K. Cold and dry gas is then directed into a separator where $O_2$ is removed from the flow by adsorption onto zeolite. Heat released by adsorption of $O_2$ is rejected into diluent flowing through the separator. Diluent, which is not significantly adsorbed onto zeolite is passed through the second branch of the recuperative heat exchanger where it is warmed to above 250 K and returned back to the COIL. Excess diluent that cannot be used by COIL can be returned to the compressor inlet through a bypass line.

Design of the $O_2$ separator is very simple and effective. The separator contains a porous packed bed of zeolite granules, typically 1 mm in size, which are held in place by screens. As the mixture of diluent and $O_2$ flows through the spaces between zeolite granules, $O_2$ is adsorbed onto the zeolite and the granules are convectively cooled by the diluent. The bed may be layered (with gaps between layers) to provide a more uniform removal of $O_2$ with only a small pressure loss across the oxygen separator. Since only $O_2$ is adsorbed in this concept, the amount of zeolite can be quite modest. Correspondingly, heat released by absorption is also reduced. In addition, diluent flowing through the separator efficiently cooles the zeolite. Continuous operation of the laser in industrial environment could be realized with two separators where one unit is removing $O_2$ from the flow while the other is being regenerated.

The amount of diluent flowing through the separator must be sufficient to carry away the heat of adsorption while keeping the zeolite at a low temperature. Minimum molar ratio of diluent/$O_2$ ($\equiv\Re$) that enters the separator and meets this criterion can be estimated as $\Re \cong \langle H_a \rangle/(c_p\ \Delta T)$, where $\langle H_a \rangle$ is the average heat of $O_2$ sorption, $c_p$ is the specific heat of diluent gas and $\Delta T$ is the overall temperature rise in the diluent. This estimate ignores the thermal inertia of the separator and complex thermal and absorption processes in the zeolite bed [9]. Most of these processes occur in a narrow zone which gradually

travels downstream from the leading end of the bed. Since zeolite sorption capacity is a strong function temperature, one may conduct trades between $\Re$, the amount of zeolite, and compressor size. Conventional COIL systems operate with total cavity exit flow having $\Re$ between 3 and 8. To ensure proper cooling of zeolite, the CGC COIL should operate with $\Re > 10$ at the separator inlet. Because operating COIL cavity at such high dilution ratio is undesirable, most of the diluent is returned to the compressor inlet on a by-pass line and may be used to operate an ejector to boost the inlet pressure.

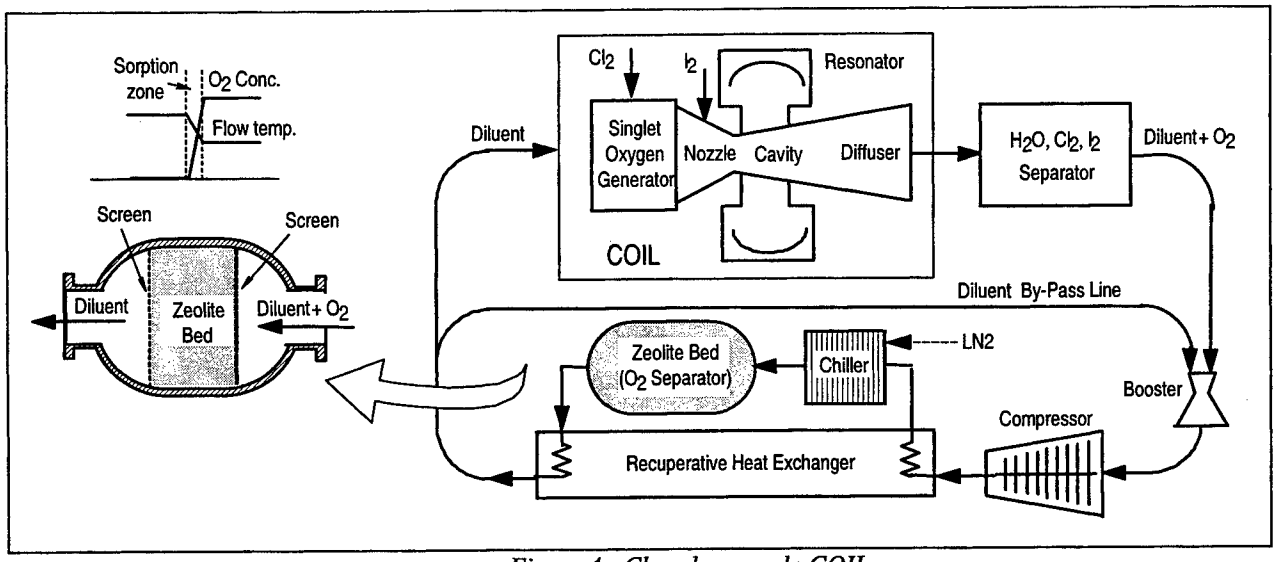


*Figure 4: Closed gas cycle COIL*

## 4. DILUENT AND COMPRESSOR

The choice of diluent for the CGC-COIL is driven by operational considerations. Obvious candidates are the light noble gases: He and Ne. COIL with He diluent has obtained a chemical efficiency of ~30% [10]. However, He is difficult to compress which, in CGC COIL, may limit its usefulness to subsonic systems. While no experimental data exists on using Ne diluent in COIL, its performance can be expected to fall somewhere between that of He and $N_2$. We estimate a chemical efficiency of 28% for a supersonic COIL with Ne diluent. Compressing the Ne is comparable to that of air, which permits using a variety of commercially available blowers and compressors. A supersonic COIL requires a high a compressor with a high compression ratio $r_c = 6\text{-}12$. This in combination with low suction pressure and high throughput requirements makes the choice of a compressor more difficult. Fortunately, required compression ratio can be greatly reduced if the high pressure diluent on the by-pass line is used to operate an ejector that boosts the compressor inlet gas pressure. For intermittent laser operation the compressor can be off-loaded by recirculating all the diluent flow on the by-pass line and shunting the booster.

Adiabatic work done by the compressor scales as $\gamma/(\gamma -1)\ T_1\ \Re\ (1-r_c^{\ (\gamma -1)/\gamma})$, where $\gamma$ is the specific heat ratio of the gas mixture and $T_1$ is the inlet gas temperature. Clearly, reducing $T_1$ and $r_c$ are important to keeping the compressor power within reasonable limits. We have developed a computer model to analyze the performance of the CGC-COIL flow loop. The model includes the compression and booster processes, heat transfer, refrigeration, and pressure drops along the loop. Parametric studies using this model have revealed that as $\Re$ was increased to improve cooling of the $O_2$ separator, the adiabatic work done by the compressor remained relatively flat. This can be directly attributed to an improved performance of the booster, which receives incerased flow of high pressure diluent from the by-pass line. At higher $\Re$, the booster significantly increases the compressor inlet pressure and reduces the required compression ratio. Such an effect becomes even more pronounced if another compressor is installed on the by-pass line.

## 5. SYSTEM IMPLICATIONS

We identified an attractive configuration of a supersonic CGC COIL with high $\Re$ and moderate compressor requirements. Figure 5 shows typical temperature and pressure parameters in the compressor-separator section of this concept. The compressor inlet flow has been boosted from COIL exhaust pressure to 60 Torr and cooled to 160K to reduce the compressor load. Cooling for this is provided by cold GN2 boil-off from the chiller. Figure 6 compares this concept to the

system in Figure 3. Note that CGC COIL uses 5 times less zeolite and about half of the refrigeration than COIL with $N_2$ diluent. However, this apparent advantage is at least in-part offset by its mechanical complexity and more intricate control.

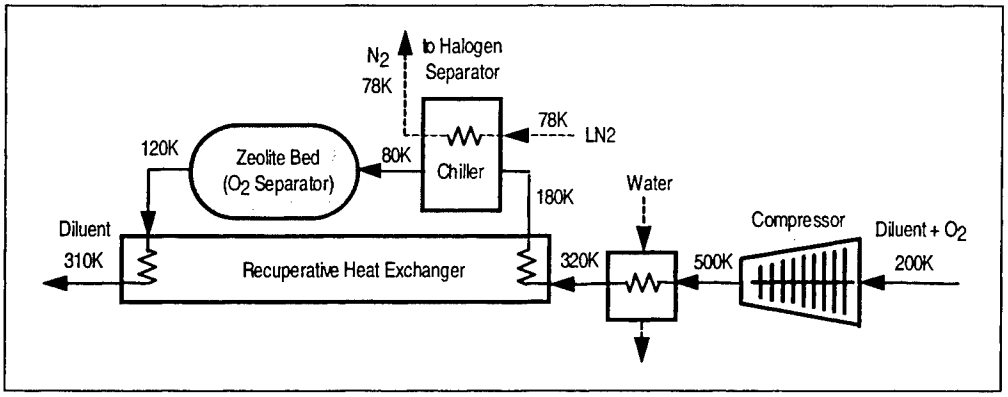


*Figure 5: Temperatures and heat flow in supersonic CGC COIL*

| Parameter | COIL with $N_2$ Diluent (Figure 3) | Supersonic CGC COIL (Figure 4) |
|---|---|---|
| Chlorine flow [mol/s] | 1 | 1 |
| Oxygen flow [mol/s] | 0.95 | 0.95 |
| Diluent | Nitrogen | Neon |
| Diluent & $I_2$ Carrier Cavity Flow [mol/s] | 4 | 4 [3] |
| Dilution ratio at sorption pump ($\Re$) | 4 | 15 |
| Compression ratio ($r_c$) | — | 8 |
| Compressor power (mechanical) [kW] [5] | — | 70 |
| Chemical Efficiency [%] | 26 | 28 |
| Laser Power [kW] | 23.7 | 25.5 |
| Amount of zeolite / kWh of laser power [1] | 114 | 23 |
| LN2 consumption / kWh of laser power [4] | 55 | 27 |
| Amount of Zeolite [kg] [1] | 2,698 | 576 |
| LN2 Consumption (incl. Regen) [kg] [1,2,4] | 1,306 | 252 |

[1]for 1 hour operation @ 190g/kg max coverage; [2]excluding regeneration; [3]excluding bypass; [4]assuming $\langle H_a \rangle$=14 kJ/kg; [5]adiabatic effic. = 85%

*Figure 6: Comparison of parameters for COIL with various cryosorption pump systems*

## 6. CONCLUSION

Principles of CGC COIL were presented and key considerations discussed. In CGC COIL, only the $O_2$ working gas is sorbed which allows major reduction in size and weight of the cryosorption pump (i.e., $O_2$ separator) and consumption of refrigerant. The $O_2$ separator construction is very simple and allows highly efficient real-time cooling of the zeolite by diluent flowing through the bed. This permits the laser to operate continuously for long periods of time. Use of Ne diluent is also expected to provide higher chemical efficiency than $N_2$ diluent.

## 7. REFERENCES


1. J. Vetrovec et al., "Chemical oxygen-iodine laser for dismantlement of nucl. facilities," proc. ICALEO'99, p. 124, 1999
2. D.G. O'Brien, "Star Wars laser technology for gas drilling and completion of 21st century," paper no. 56625, proc. Society of Petroleum Engineers Annual Technical Conference & Exhibition, Houston, TX, Oct. 3-6, 1999
3. J. Vetrovec, "Chemical oxygen-iodine laser with a cryosorption pump," SPIE Vol. 3931, p. 60, 2000
4. Rene A. Haefer, *Cryopumping Theory and Practice*, Chapter 5, Claredon Press, Oxford, UK, 1989
5. *Union Carbide's Molecular Sieves*, product brochure of UOP, Inc., Des Plaines, IL, USA
6. *Product and Vacuum Technology Reference Book*, Leybolt Heraus, Export, PA, USA (1990)
7. "Boeing completes testing of high-energy laser," Boeing News Now, April 29, 1999
8. J. Vetrovec, "COIL with a cryosorption vacuum pump system," US Patent Application No. 09/107,251
9. R.T. Yang, "Separation of gases by adsorption processes," Butterworth Publ., Stoneham, MA, 1987
10. W.E. McDermott, J.C. Stephens, J. Vetrovec, and R.A. Dickerson, "Operating experience with high throughput jet generator," SPIE Proc. Vol. 2987, 1997

# Study of Multi-Guideplate Singlet Oxygen Generator

Satoshi Shinoda and Taro Uchiyama
Department of Electrical Engineering, Keio University, 3-14-1 Hiyoshi, Kohoku-Ward, Yokohama-City, Kanagawa Prefecture 223-0061, Japan

## ABSTRACT

The most important part of chemical oxygen-iodine laser (COIL) is the singlet oxygen generator (SOG) that produces pumping energy source of the laser system. A new prototype high pressure SOG, which has possibility to overcome the problems existing several types of SOG have, was developed. This SOG, we call multi-guideplate SOG, is based on jet-type one. The jets of basic hydrogen peroxide (BHP) are spread and fixed on the surfaces of some guide plates attached to the nozzle plate. In this study, it was shown that multi-guide plate-SOG could produce higher $O_2(^1\Delta)$ pressure and make the jet flow stabler than jet-type SOG in the high flow rate of the gas stream.

**Keywords:** chemical oxygen-iodine laser, COIL, singlet oxygen generator, SOG, guide plate, BHP

## 1. INTRODUCTION

Chemical oxygen-iodine laser (COIL) was demonstrated in 1978 for the first time[1], and has been studied by many research institutes. COIL has many excellent characteristics, such as high power, high efficiency, good beam quality, and applicability of transmission through optical silica fiber. Hence COIL is expected for a next-generation industrial laser.[2,3]

COIL operates for transition between excited level and ground state level of atomic iodine. The excited level of atomic iodine is produced by energy transfer from $O_2(^1\Delta)$

$$I + O_2(^1\Delta) \rightarrow I^* + O_2(^3\Sigma) \tag{1}$$

$$I^* \rightarrow I + h\nu\ (1.315\mu m) \tag{2}$$

$O_2(^1\Delta)$ is generated in the bulk of BHP by according reaction

$$H_2O_2 + 2KOH + Cl_2 \rightarrow 2H_2O + 2KCl + O_2(^1\Delta) \tag{3}$$

However $O_2(^1\Delta)$ loses energy quickly in the liquid solution. The reaction proceeds only on the surface of BHP solution, therefore it is very important to make large surface area of BHP and to separate $O_2(^1\Delta)$ from BHP smoothly.

On the other hand, $O_2(^1\Delta)$ released from BHP is quenched in the gas stream

$$O_2(^1\Delta) + O_2(^1\Delta) \xrightarrow{k_1} O_2(^3\Sigma) + O_2(^1\Sigma) \qquad k_1 = 5.7\times10^{-4}T^{3.8}\exp(700/T)\ [cm^3/mol\cdot s] \tag{4}$$

$$O_2(^1\Sigma) + H_2O \xrightarrow{k_2} O_2(^3\Sigma) + H_2O \qquad k_2 = 4.0\times10^{12}\ [cm^3/mol\cdot s] \tag{5}$$

Since $k_2$ is much faster than $k_1$, these equations can be expressed as the following self-quenching equation

$$O_2(^1\Delta) + O_2(^1\Delta) \xrightarrow{k_2} O_2(^1\Delta) + O_2(^3\Sigma) \tag{6}$$

The equation shows that the deactivation of $O_2(^1\Delta)$ in the gas stream increases fast with an increase in the gas pressure squared. Therefore, generated $O_2(^1\Delta)$ should be transferred to the outlet of SOG as soon as possible.

Although there are several types in SOG, jet-type SOG[4,5,6] and rotating-disk-type SOG[7] are vigorously studied today. Depending on the operating condition, jet-type SOG may suffer from break up of BHP-jets and from spraying. As a result, jet-type SOG is sometimes unstable, if it works long time. Rotating-disk-type SOG has great characteristics, such as the stability of operation and the rapid separation of singlet delta oxygen from basic hydrogen peroxide (BHP). But it has also several problems, for example, dilution of $Cl_2$, lower speed of refreshing BHP, larger size of the device than jet-type SOG.

Multi-guide plate SOG has possibility to get over the problems. This SOG is based on jet-type one. The difference is that some guide plates are attached to the jet nozzle plate. We can make BHP films very easily, because the jets of BHP become spread and fixed on the surfaces of guide plates. $Cl_2$ flows through the narrow spaces between the guide plates. Hence the jets become stable and we can make large surface area of BHP. In addition, the multi-guideplate-SOG can realize rapid separation of singlet delta oxygen from BHP as easily as rotating-disk-type one, and can refresh exhausted BHP as fast as

XIII International Symposium on Gas Flow and Chemical Lasers and High-Power Laser Conference,
Antonio Lapucci, Marco Ciofini, Editors, Proceedings of SPIE Vol. 4184 (2001)

jet-type one.

## 2. EXPERIMENTAL SETUP

The schematic diagram of the experimental setup is shown in Fig.1. It consists of reaction chamber, nozzle plate with guide plates, BHP solution reservoir, BHP solution tank, $Cl_2$ injector, cooling system and vacuum pump.

The reaction chamber made of scleroid PVC resin has 70mm inside diameter, 80mm outside diameter, and the height of reaction zone of 120mm. The BHP solution (15~20% $H_2O_2$ and 25~35% $KOH$ ) kept under −10℃ by refrigerant of ethylene glycol is injected downward from the solution reservoir located at upper part of the chamber through the jet nozzle plate into the reaction chamber. The jet speed was ~2m/s. $Cl_2$ flows transversely into the reaction chamber through many orifices of 2mm diameter. The $O_2(^1\Delta)$ concentration is monitored at the outlet of SOG by detecting the spontaneous emission (1270nm), using Ge photodiode with a narrow-band filter. The residual BHP solution is collected at the BHP tank and pumped to upper reservoir by circulating pump.

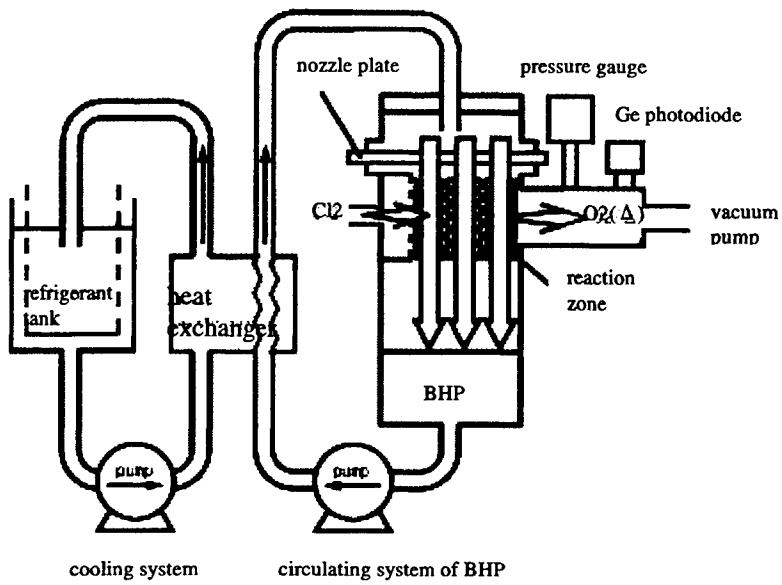


**Fig.1 The schematic diagram of experimental setup**

Fig.2 shows the schematic diagram of the nozzle plate of jet-type SOG. The nozzle plate has 80 holes, and the diameter of the hole is 1mm. The schematic diagram of multi-guideplate SOG is shown in Fig.3. Three guide plates made of plastic (12cm height, 5.5cm width, 0.5cm thick, interval between guide plates-1.3cm) are attached to the nozzle plate which has also 80 orifices. The specific surface areas of multi-guideplate SOG and jet-type one are respectively 1.17cm$^{-1}$ and 0.96cm$^{-1}$. The specific surface area of multi-guideplate SOG is about 1.27 times larger than that of jet-type SOG.

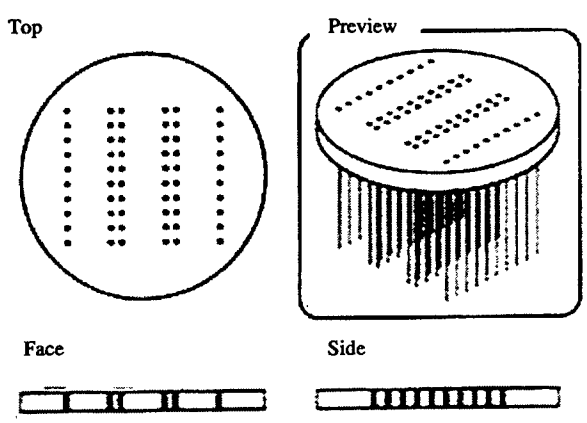


**Fig.2 nozzle plate of jet-type SOG**

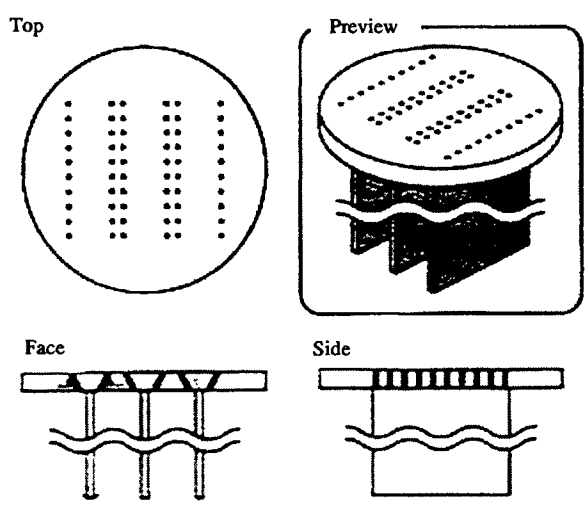


**Fig.3 nozzle plate with guide plates**

## 3. RESULTS AND DISCUSSION

In the tests, the multi-guideplate SOG was compared with a jet-type SOG. Fig.4 shows $O_2(^1\Delta)$ pressure variation with the flow rate of $Cl_2$. It shows that multi-guideplate SOG generated higher $O_2(^1\Delta)$ than jet-type SOG, and the result was beyond our expectation. It was about 20% higher than our prediction. The reason is considered as follows. Because the gas flows through the narrow space partitioned by the guide plates in multi-guideplate SOG, Reynolds number gets larger and laminar flow is generated. As a result the gas flow becomes very smooth. Rapid separation of $O_2(^1\Delta)$ from BHP solution and quick transfer of $O_2(^1\Delta)$ are realized, which reduce deactivation of singlet delta oxygen.

$O_2(^1\Delta)$ pressure vs time characteristics of the jet-type SOG and the multi-guideplate SOG are shown respectively in Fig.5 and Fig.6. These are typical results of the tests in our system. In the high flow rate of $Cl_2$, the difference is obvious. While the jet-type SOG didn't work stably, the operation of multi-guideplate one was very stable. The each average of square is respectively 0.59 and 0.39. This is because the laminar gas flow fixed the jets of BHP solution to the guide plates. These results show that the multi-guideplate SOG succeeded in making stable BHP film.

At the last, we describe chlorine utilization and $O_2(^1\Delta)$ yield that are very important parameters of SOG.

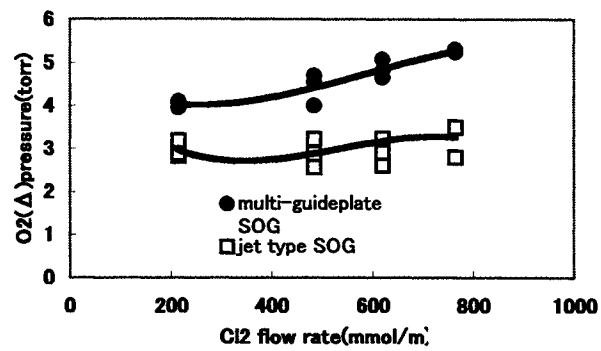


**Fig.4 $Cl_2$ flow rate-$O_2(\Delta)$ characteristic**

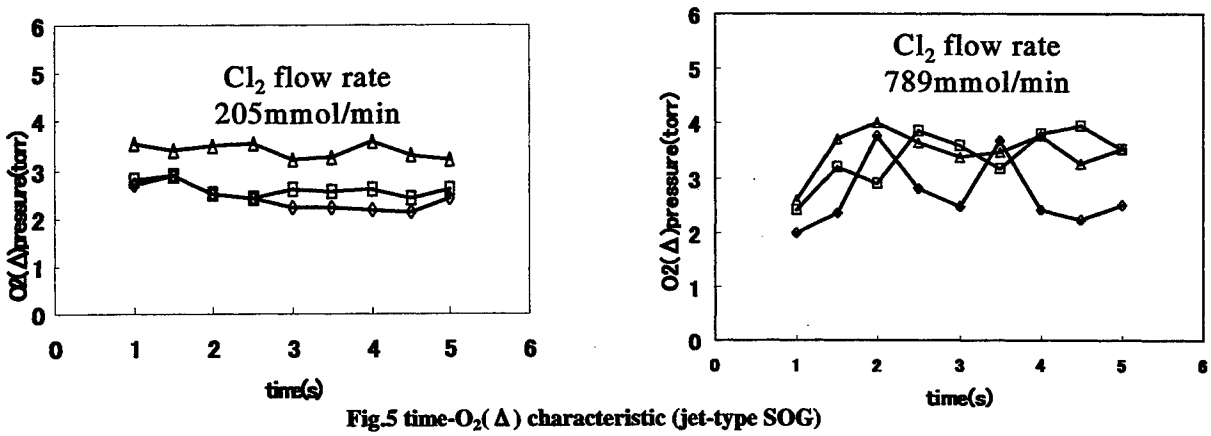


**Fig.5 time-$O_2(\Delta)$ characteristic (jet-type SOG)**

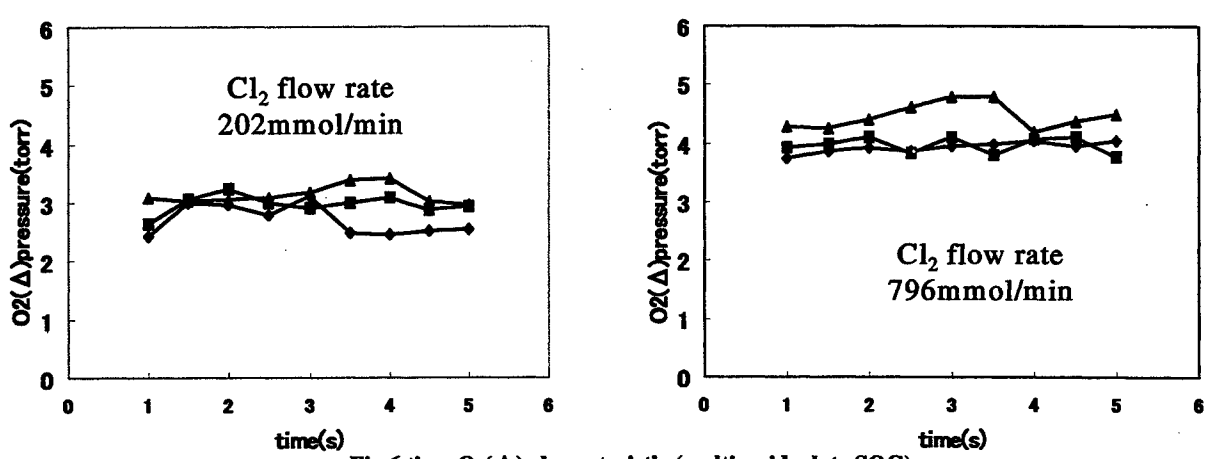


**Fig.6 time-$O_2(\Delta)$ characteristic (multi-guideplate SOG)**

These parameters were estimated by calculation, for we have no system to measure residual $Cl_2$ . We calculated $Cl_2$ utilization and $O_2(^1\Delta)$ yield of the multii-guideplate SOG by using one-dimensional code[8,9,10]. The results of calculation were ~70% $Cl_2$ utilization, ~65 % $O_2(^1\Delta)$ yield . Though there are uncertain elements, estimated value is not enough high for a high pressure SOG. In the multi-guideplate SOG the interval between guide plates isn't enough short, so $Cl_2$ does not react effectively. Hence the specific surface area should be larger or buffer gas to dilute chlorine gas might be required.

## 4.CONCLUSION

A new prototype SOG-multi-guideplate SOG-was developed. Although it has very simple structure, it could make the film of BHP solution very easily. The specific surface area was 1.17cm$^{-1}$, which was 1.27 times larger than our jet-type SOG. In the typical condition, multi-guideplate SOG generated about 1.52 times higher pressure of $O_2(^1\Delta)$ than jet-type one. In the high flow rate of $Cl_2$ multi-guideplate SOG operated more stably than jet-type one. These results, we consider, were because the laminar gas flow realized rapid separation of $O_2(^1\Delta)$ from BHP solution, quick transfer of $O_2(^1\Delta)$ ,and fixation of jets of BHP. Consequently the deactivation of generated $O_2(^1\Delta)$ decreased and stability of operation was improved. $Cl_2$ utilization and $O_2(^1\Delta)$ yield of the multii-guideplate SOG were respectively ~70% and ~65%, which were calculated by using one-dimensional code.

## 5.REFERENCES


1. W.E.McDermott, N.R. Pchelkin, D.J.Bernard, and R.R.Bousek, " An electronic transition chemical laser," Air Force Weapons Laboratory, Appl. Phys. Lett. 32 (8), pp.469-470, 1978
2. Masamori Endo, Syoji Nagatomo, Syuzaburo Takeda, Fumio Wani, Kenzo Nanri, and Tomoo Fujioka," Advanced technologies in chemical oxygen-iodine laser for industrial applications," Tokai University and Kawasaki Heavy Industries, SPIE vol.3268, pp.106-114, 1998
3. Yuko Hoshino, Shunsuke Takahashi, Tomoyuki Sekiguchi and Taro Uchiyama, "Slit nozzle jet $O_2(^1\Delta)$ generator," Keio University, SPIE vol.1996, pp. 549-552, 1996
4. William P. Latham, James A.Rothenflue, and Charles A. Helms,"Cutting Performance of a Chemical Oxygen-Iodine Laser," Air Force Research Laboratory, SPIE vol.3268, pp. 130-136, 1998
5. Jamila KODYMOVA and Otomar SPALEK," Performance Characteristics of Jet-type Generator of Singlet Oxygen for Supersonic Chemical Oxygen-Iodine Laser," Institute of Physics, Academy of Sciences of the Czech Republic, Jpp. J. Appl. Phys. Vol. 37,pp. 117-121, 1998
6. William E. McDermott," Performance characteristics of a high pressure jet generator, " Rocketdyne Division, Boeing North American, SPIE vol.3268, pp.88-98, 1998
7. Wolfgang O.Schall and Frank Duschek, "A new type of rotating disk singlet oxygen generator," DLR, SPIE vol. 3092, pp. 686-689, 1996
8. M.V.Zagidullin, V.D.Nikolaev, M.I.Svistun, N.I.Ufimtsev "Predicted and measured output of high pressure jet SOG," P.N.Lebedev Physical Institute, SPIE vol.2767, pp. 221-228, 1996
9. Fumio Wani, Masamori Endo, Boris A. Vyskubenko, Sergey P. Ilyin, Ivan M. Krukovsky, Shuzaburo Takeda, and Tomoo Fujioka, "Parametric Study of a Twisted Aerosol-Type Singlet Oxygen Generator," Tokai University, Russioan Federal Nuclear Center, IEEE JOURNAL OF QUANTUM ELECTRONICS, vol. 34, no.11, pp. 2130-2137, 1998
10. M.V.Zagisullin, A.Yu.Kurov, N.L.Kuriyanov, V.D.Nikolaev, M.I.Svistun, and N.V.Erasov," Higly efficient jet $O_2(^1\Delta)$ generator," P.N.Lebedev Physical Institute, Sov.J.Quantum Electron.21 (7), pp. 747-753, 1991

# Parametric Study of a Mist Singlet Oxygen Generator

Shigeki Muto*[a], Takanori Kawano[b], Shoji Takeishi[a], Masamori Endo[a],
Kenzo Nanri[a], Shuzaburo Takeda[b] and Tomoo Fujioka[a]
[a]Department of Physics, School of Science, Tokai University
[b]Department of Electro-Photo Optics, School of Engineering, Tokai University
1117 Kitakaname, Hiratsuka, Kanagawa, 259-1292, Japan.

## ABSTRACT

New type mist singlet oxygen generator (Mist-SOG) for the chemical oxygen-iodine laser (COIL) has been developed. This SOG is devoted to make the liquid recirculation unnecessary with the complete reaction through a single pass of basic hydrogen peroxide (BHP). 75% of $Cl_2$ utilization and 76% of $O_2(^1\Delta)$ yield were obtained with $Cl_2$ molar flow rate of 3.0 mmol/s. $H_2O_2$ utilization in the BHP was achieved as high as 12.3%. This value is about 24 times larger than that obtained by the liquid-jet SOG.

**Keywords:** mist, singlet oxygen generator, SOG, chemical oxygen-iodine laser, COIL

## 1. INTRODUCTION

Chemical Oxygen-Iodine Laser (COIL), which is capable of producing a high power and good quality beam, is expected to be utilized as a new laser source for industrial applications. Developments of the industrial COIL have been vigorously carried out in Tokai University group in the past several years.[1]

In the COIL, the lasing process is described by the following chemical reactions:

Singlet oxygen $O_2(^1\Delta)$ generation

$$H_2O_2 + 2KOH + Cl_2 \rightarrow O_2(^1\Delta) + 2KCl + H_2O \quad (1)$$

Iodine injection and dissociation

$$n\ O_2(^1\Delta) + I_2 \rightarrow n\ O_2 + 2I \quad (2)$$

Energy transfer

$$O_2(^1\Delta) + I \rightarrow O_2 + I^* \quad (3)$$

Stimulated emission

$$I^* + h\nu \rightarrow I + 2h\nu \quad (4)$$

The COIL oscillates from excited iodine atoms pumped through a near-resonant energy transfer process with chemically generated singlet oxygen as mentioned above. So, one of the key issues to achieve efficient operation in the COIL depends on the characteristics of the singlet oxygen generator (SOG) device. Singlet oxygen acting as an energy donor of the COIL is commonly generated via reactions with basic hydrogen peroxide (BHP) and $Cl_2$ in the SOG. However, recirculation device is necessary for the efficient use of the stored energy in BHP, since the $H_2O_2$ utilization/pass is limited less than 1% in the liquid-jet SOGs that are commonly used for industrial COIL prototypes.[2] And a reduction of the dimensions and weight of the COIL device is required for a practical COIL system, in particular, for a mobile system such as field applications.

In order to improve the $H_2O_2$ utilization and to get rid of the recirculation system of the BHP, a new type SOG, Mist-SOG has been developed. This paper describes the first successful operation of this Mist-SOG, which will be beneficial for compact industrial COILs.

*Correspondence: Shigeki Muto: E-mail: 0aspm017@keyaki.cc.u-tokai.ac.jp; Fax: +81-463-50-2013

XIII International Symposium on Gas Flow and Chemical Lasers and High-Power Laser Conference,
Antonio Lapucci, Marco Ciofini, Editors, Proceedings of SPIE Vol. 4184 (2001)

## 2. EXPERIMENTAL SETUP

A schematic drawing of the experimental setup of the Mist-SOG system is shown in Fig.1. A reaction chamber is made of lucite vessel having an inner diameter and a height, 40 mm and 120 mm, respectively. BHP is made from one volume part of 45% wt. $H_2O_2$ and one volume part of 48% wt. KOH. BHP is prepared in a stainless-steel mixing tank, and the temperature is kept at 253 K. The Mist-SOG system is made of two conical nozzles vertically countered each faces to separate BHP from $O_2(^1\Delta)$ by the inertial force as shown in Photo 1. The pressurized liquid BHP is atomized to the mist by the hollow cone spray nozzle (IKEUCHI KB-22) whose cone angle is 60 degrees and sprayed from the upper part to downward. And $Cl_2$ flows upward from the lower part in the reaction chamber. Since this specific nozzle produces quite uniform droplets (65 ± 10μm), that ensures the complete separation of BHP from the gas flow.

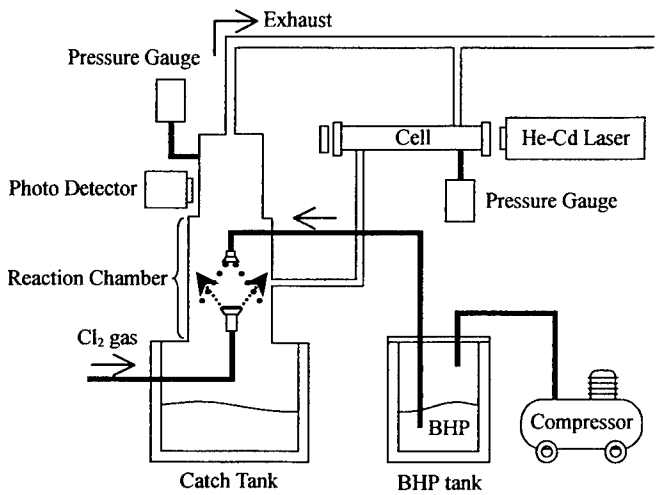


Fig.1: Experimental setup

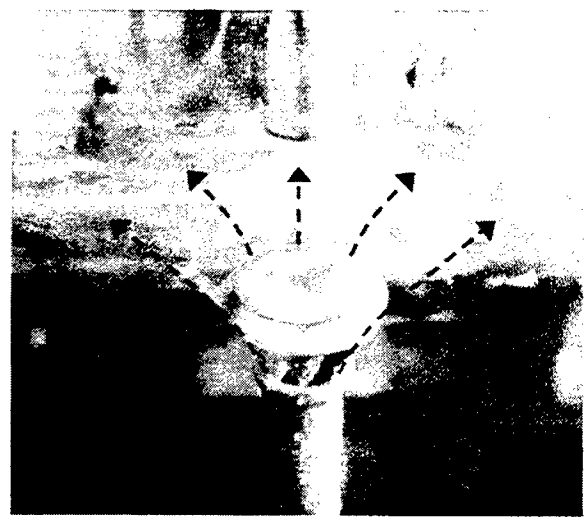

Photo 1: Mist-SOG system

The total pressure is measured by the capacitance manometer (KMS BARATRON 122A), and the excited oxygen concentration is monitored by detecting the spontaneous emission (1.27μm) by the Ge photodiode with narrow-band interference filter.[3] The $Cl_2$ flow rate is controlled and monitored by a digital mass flow controller (Aera FC-782). The unreacted $Cl_2$ concentration is measured by the absorptiometry method by using a He-Cd laser (λ=325nm). To obtain the $Cl_2$ utilization and the $O_2(^1\Delta)$ yield, it is necessary to know the partial pressure of oxygen. It is calculated by subtracting the $Cl_2$ and water vapor partial pressures from the total pressure, the latter is deduced with the measurement of the BHP temperature in the catch tank, assuming the saturation condition. All measured values are collected by a data logger, and displayed on a PC.

## 3. RESULTS AND DISCUSSIONS

Fig.2(a) shows the time history of total pressure and singlet oxygen partial pressure measured with the method mentioned above. In this experiment, $Cl_2$ gas molar flow rate was varied from 1.0 to 10.0 mmol/s under constant BHP flow rate of 2.4 ml/s at a nozzle pressure of 8.0 atm. While total pressure increased as $Cl_2$ molar flow did, singlet oxygen partial pressure did not so. Fig.2(b) shows the time history of $Cl_2$ utilization and $O_2(^1\Delta)$ yield. The $Cl_2$ utilization has the tendency of decreasing with increasing the $Cl_2$ molar flow rate. However, the $O_2(^1\Delta)$ yield seems to have the maximum value in this operation.

From these experimental results, the $Cl_2$ utilization, the $O_2(^1\Delta)$ yield and the $H_2O_2$ utilization are shown in Fig.3 as a function of the $Cl_2$ molar flow rate.

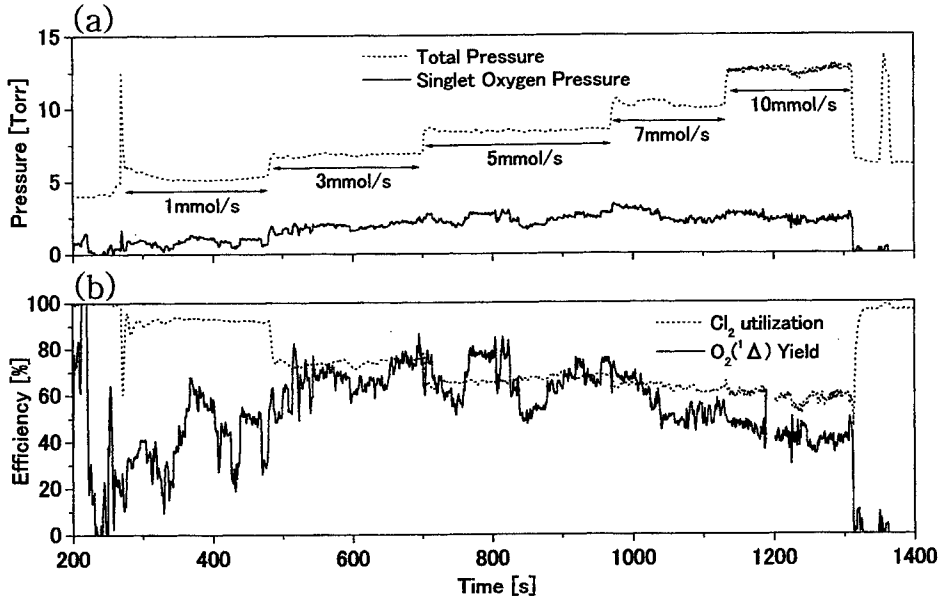


Fig.2(a): Time history of total pressure and singlet oxygen pressure
(b): Time history of $Cl_2$ utilization and $O_2(^1\Delta)$ yield

$H_2O_2$ utilization is defined by the following equation:

$$H_2O_2 \text{ utilization } [\%] = \frac{H_2O_2 \text{ reaction rate } [\text{mmol/s}]}{H_2O_2 \text{ flow rate } [\text{mmol/s}]} \times 100 \tag{5}$$

In this figure, the $O_2(^1\Delta)$ yield has the maximum value at 4 mmol/s of the $Cl_2$ molar flow rate. It seems to be weird that the $O_2(^1\Delta)$ yield is lower at the $Cl_2$ flow of 1mmol/s. We believe that is due to the inaccuracy of the $O_2$ partial pressure estimation, especially in the low $Cl_2$ flow region. On the other hand, the $Cl_2$ utilization monotonically decreases with increasing the $Cl_2$ molar flow rate. The optimum operation of the SOG can be achieved at the $Cl_2$ molar flow rate of 3 mmol/s taking account a balance between the $Cl_2$ utilization and the $O_2(^1\Delta)$ yield. At this value of the $Cl_2$ molar flow rate, the $H_2O_2$ utilization in the BHP was achieved as high as 12.3%.

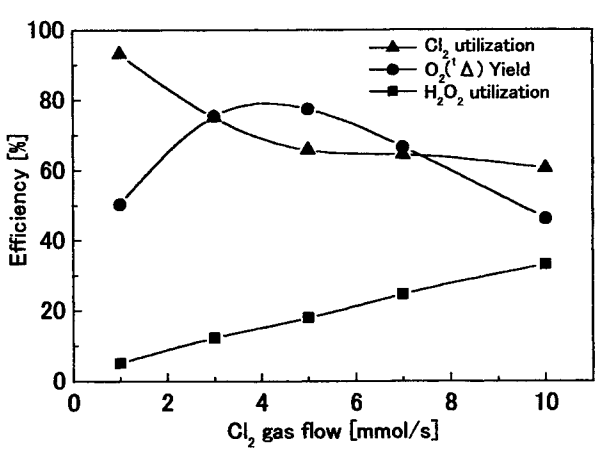


Fig.3: Efficiency as a function of $Cl_2$ flow rate

## 4. CONCLUSIONS

The maximum value of 75% for $Cl_2$ utilization and 76% for $O_2(^1\Delta)$ yield were obtained at $Cl_2$ molar flow rate of 3.0 mmol/s. The $H_2O_2$ utilization in the BHP was achieved as high as 12.3%. This value is about 24 times larger than that obtained in the liquid-jet SOG.[2] These results show the prospect of the Mist-SOG for the COIL without BHP recirculation.

In this study, however, the $Cl_2$ utilization is less than that of Jet-SOG. Specific surface area might be small because of a large diameter of the mist. Thus, short contact time in gas-liquid phase results in inefficient reaction.

In this experiment, the water vapor pressure was deduced by the saturation pressure of the BHP catch tank to obtain the $Cl_2$ utilization and the $O_2(^1\Delta)$ yield, that resulted in the uncertainty of the oxygen partial pressure. We are preparing the measurement system of the water vapor pressure for more precise characterization.

## ACKNOWLEDGEMENT

The authors wish to express their gratitude for the financial support from Grant-in-Aid for General Scientific Research (B), the Ministry of Education, Science and Culture.

## REFERENCES

1. M. Endo, D. Sugimoto, S. Takeda, K. Nanri and T. Fujioka, "Industrial chemical oxygen-iodine laser at Tokai University", *Proc. SPIE* **3889**, pp.438-446, 1999.
2. M. V. Zagidullin, A. Yu. Kurov, N. L. Kupriyanov, V. D. Nikolaev, M. I. Svistun and N. V. Erasov, "Highly efficient jet singlet oxygen generator", *Sov. J. Quantum Elecron.* **21**, pp.747-753, 1991.
3. M. Endo, K. Kodama, Y. Handa and Y. Uchiyama, "Performance characteristics of a high-pressure pulsed singlet oxygen generator", *J. Appl. Phys.* **71**, pp.5760-5767, 1992.

# Study of Chemical Oxygen Iodine Laser for high power utilizing RF discharge dissociation of $I_2$

Shinji Ide, Tsuyoshi Wakazono, Takahiro Takemoto, and Taro Uchiyama,

## 1. ABSTRACT

We suggest pre-dissociation iodine molecule utilizing RF-discharge (Radio Frequency discharge) dissociation of $I_2$ for chemical oxygen iodine laser (COIL). The object of the study is to make clear that RF discharge is effective on our experiment. We focus chemical reaction of COIL itself, and especially consider a scheme of dissociation of $I_2$. So following chemical reaction is a process of dissociate iodine molecule into iodine atom by $O_2(^1\Delta)$.

$$I_2 + nO_2(^1\Delta) \rightarrow 2I + n\,O_2(^3\Sigma) \quad n=4\sim6 \tag{1}$$

This chemical reaction indicates that to dissociate iodine molecule into iodine atom needs a lot of $O_2(^1\Delta)$. In our experiments we could prove that RF was effective in this term. Approximately 60% of iodine molecular, which is dissociated by RF discharge, is carried to laser cavity. It is estimated that the other 40% of iodine atom is recombination in our COIL system. As the results, we can obtain higher power, higher gain by using RF discharge dissociation than normal COIL.

**Key words:** COIL, chemical laser, oxygen, iodine, radio frequency, RF discharge, dissociation

## 2. INTRODUCTION

Iodine molecule is dissociated by only singlet delta oxygen in a chemical reaction of COIL until now. New type of COIL[1], which is utilizing RF-discharge dissociation of $I_2$, was suggested at Uchiyama Lab, 1996, for the first time in the world. Shimizu report, 1996,at Uchiyama Lab, reported that Output power of RF-COIL recorded 4-5 times higher power than that of normal COIL. This result was far much higher power than estimated calculation results. Loss in a resonator , existing of water vapor, an amount of $O_2(^1\Delta)$, operating time of COIL caused a different measurement output power of COIL. Especially, electromagnetic wave that was generated by RF-discharge affected the measuring devices. The object of the study is to make clear that RF discharge is effective for chemical oxygen iodine laser (COIL) at the condition of eliminating a bad influence of some electromagnetic wave. Recent study often reports the highest record of chemical efficiency at COIL. In general the generation of excited oxygen is recorded 50～60%, but the chemical efficiency is achieved only around 20～25%.If the loss exists only on a experimental setup or physical factor, the chemical efficiency comes up to the near value of generated excited oxygen. But it doesn't come true. The reasons exist in a loss of mirror, a process in a dissociation of $I_2$, excitation, quenching, and so on. So we suggest pre-dissociation iodine molecule utilizing RF-discharge dissociation of $I_2$ for chemical oxygen iodine laser in order to use $O_2(^1\Delta)$ more efficiently, and prove that RF discharge is effective at COIL.

### 2・1 Characteristics of COIL

COIL is a potentially high power laser, which is applied for industry and other practical use. The characteristic of COIL is to operate using only the chemical reaction and a good character of transferring optical fiber because the wavelength of COIL is a range of the lowest loss. COIL is operated utilizing the energy of $O_2(^1\Delta)$ which is produced from chemical reaction with $Cl_2$ gas and basic-$H_2O_2$. The excited iodine atom is produced by the energy transfer reaction between the excited molecular $O_2(^1\Delta)$ and iodine atom. Then COIL is lasing by the energy transition between the excited level and the ground state level of iodine

### 2・2 Basic chemical reaction scheme in general COIL Operation

COIL operates for transition between the exited level and the ground state of atomic iodine. Following reaction equation is last step of chemical reaction of COIL.

$$I(P_{1/2}) \rightarrow I(P_{3/2}) + 1.315\,\mu\,m \tag{2}$$

The exited level of atomic iodine is produced by energy transfer from singlet states of molecular oxygen, $O_2(^1\Delta)$.

XIII International Symposium on Gas Flow and Chemical Lasers and High-Power Laser Conference,
Antonio Lapucci, Marco Ciofini, Editors, Proceedings of SPIE Vol. 4184 (2001)

$$O_2(^1\Delta) + I(P_{3/2}) \rightarrow O_2(^3\Sigma) + I(P_{1/2}) \quad (3)$$

$O_2(^1\Delta)$ is produced by chemical reaction between basic hydrogen peroxide solution and chlorine gas.

$$H_2O_2+2KOH+Cl_2 \rightarrow . O_2(^1\Delta) +2H_2O+2KCl \quad (4)$$

In normal COIL, $O_2(^1\Delta)$ is also utilizing to dissociate molecular iodine.

$$I_2+ nO_2(^1\Delta) \rightarrow 2I+nO_2(^3\Sigma) \quad n=4\sim6 \quad (5)$$

Eq(5) shows much energy is needed to dissociate molecular iodine.

### 2·3 Merit of utilizing RF-discharge

The number of $O_2(^1\Delta)$ ,n, is very important parameter which affects the output power. While excess existence of $I_2$ in the reaction zone results in reducing the inversion density of iodine by quenching the exited substance. Atomic iodine is recombined by collision with molecular iodine as follow reaction.

$$2I+ I_2 \rightarrow 2I_2 \quad (6)$$

The excited state of atomic iodine is dropped to the ground state.

$$I^*+ I_2 \rightarrow I + I_2 \quad (7)$$

As a results, to dissociate $I_2$ need much more $O_2(^1\Delta)$ through these quenching reaction as Eq(5). In this study we suggest a new type of COIL named "RF-COIL" utilizing a radio frequency discharge to dissociate $I_2$ in stead of $O_2(^1\Delta)$. The dissociation reaction is modified following reaction.

$$I_2 + h\nu \rightarrow 2I \quad (8)$$

The advantage of RF-discharge for setup is that electrical rods and other optical parts are not damaged because RF can easily discharge not to contact to iodine. It is necessary to increase the gain of COIL because of achieving high efficiency and high power. Through this improvement, it is possible to get high density of iodine atom and we can use much of $O_2(^1\Delta)$ for exciting iodine atoms instead of dissociating $I_2$.

## 3. EXPERIMEMTAL SETUP

### 3.1 General transonic COIL system

Fig.1 shows the experimental setup. The COIL apparatus consists of solution tank, singlet delta oxygen generator (SOG), water vapor trap, laser cavity and RF discharge equipment. To product initial solution basic-$H_2O_2$(basic hydrogen peroxide $H_2O_2$), 35% $H_2O_2$ and 50% KOH are mixed in the ratio of 10:1 in the solution tank. Then evaporating cooling function by 3000l/min vacuum pump cools the solution about -5℃. The BHP solution is transferred to SOG. In the SOG, $O_2(^1\Delta)$ is generated by passing $Cl_2$ gas through liquid mixture. Babbler type of SOG is used in order to obtain the stable $O_2(^1\Delta)$ yield constantly. The $O_2(^1\Delta)$ generated in the SOG is carried to laser cavity through water vapor trap to remove water vapor which quench I* in the resonator. And then the gas is mixed with $I_2$ from iodine injector. The laser body is made from Lucite. Its flow duct has 3cm in height and 37cm in width and connects to vacuum pump with capacity of 15000L/min. Iodine injector is made of 8mm in diameter, 30cm long stainless tube perforated 0.5mm holes leaving 3mm spaces.

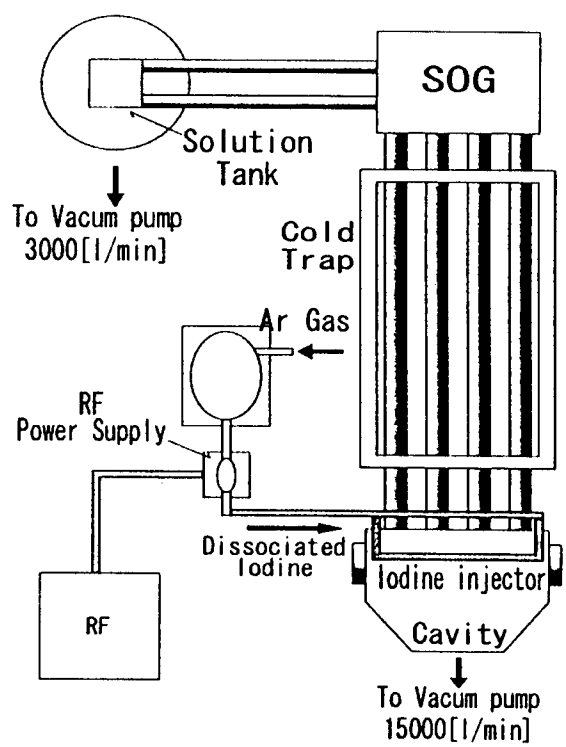


Fig.1 Schematic diagram of the COIL apparatus

### 3.2 RF-discharge system

Fig.2 shows the setup of RF-discharge system. To dissociate iodine molecule, RF-discharge power supply machine that generates electromagnetic wave in a radio frequency is settled. The RF discharge machine supplies 50.3Mhz at 50W－200W power, and operates the reflecting volume to maintain discharging. RF discharge machine supplies iodine molecules with electrical energy, and dissociated iodine molecules into iodine atoms.

3.2.1 RF-power-supply machine

RF-power-supply (PEARL corporation) consists of matching box and main power supply machine. The main machine can control both input power and reflect power with the controllers, in addition to control frequency from 100[kHz] to 99.9[MHz]. We adjust reflect power around 10% in order to stabilize an electric discharge on our experiment.

3.2.2 Electrode and electrical rod

Electrical rod is made of Pyrex glass, 120[mm] of length 15[mm] of diameter. An electrode, which shapes semicircle, is arranged around electrical rod. It is made of aluminum, 2[mm] thick, 50[mm] lengths and 16[mm] radius of curve.

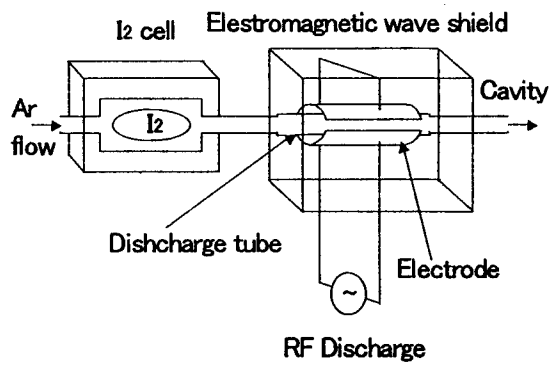


Fig.2 RF-discharge system

## 4. RESULT and DISCUSSION

### 4.1 Iodine molecule dissociation rate

Dissociation of iodine molecule is measured by using the absorption of $I_2$. To estimate dissociation rate, a green He-Ne laser (wavelength: 543.5nm) is used since $I_2$ has a strong absorption of light whose wavelength is about 500nm. Approximately 60% of iodine molecular, which is dissociated by RF discharge in our laboratory, is carried to laser cavity. It is estimated that the other 40% of iodine atom is recombination in this COIL system. Recombination reaction is so complicated that recombination scheme is not exactly appeared.

### 4.2 Laser power measurement

The dependence of the output power on $Cl_2$ flow rate is shown in Fig.3. Power enhancement could be recognized every $Cl_2$ flow rate. The output power of RF-COIL (60W discharge) was attained 10% higher than that of normal COIL at 600[mmol/min] $Cl_2$ flow rate. It conducts that RF discharge could promote the power enhancement. But in our COIL apparatus output power is smaller generally reported papers. As a result, our apparatus achieves power enhancement in the case of using RF-discharge, but this case means efficiency of a low $O_2(^1\Delta)$ pressure. Recent results of reports are the case of high pressure. It is significant to work at high pressure, for example supersonic COIL.[3]

Chemical efficiency shown at Fig.1 indicates that using RF-discharge is efficient to increase chemical efficiency at this apparatus. Chemical efficiency is related to output power, it can be said about the same consideration. We try to work the case of high power, high efficiency next time.

### 4.3 Small signal gain measurement

Fig.4 shows the experimental result of the measurement of small signal gain. RF-COIL gain is superior to normal-COIL gain as $Cl_2$. flow rate increasing. When $Cl_2$ flow rate is low, though it means $O_2(^1\Delta)$ flow is low, the difference between RF-COIL gain and COIL gain is wide. We can consider two reasons. The reason is that $O_2(^1\Delta)$ is used for exiting iodine

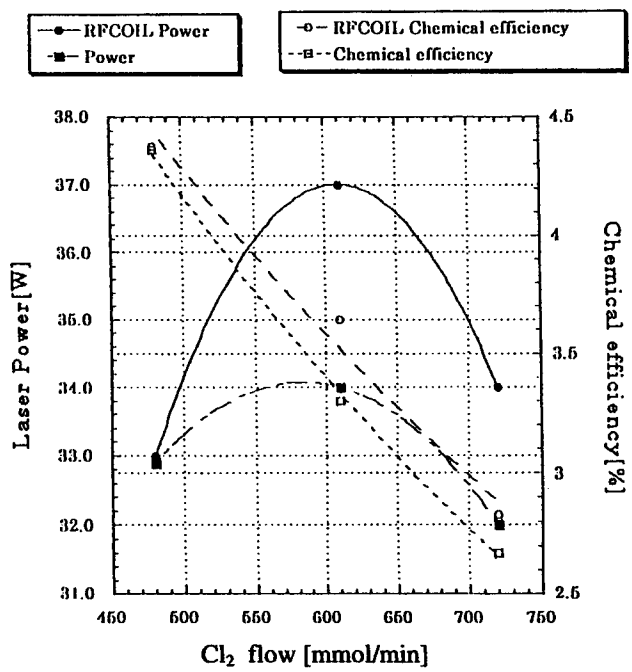


Fig.3 Output power and Chemical efficiency

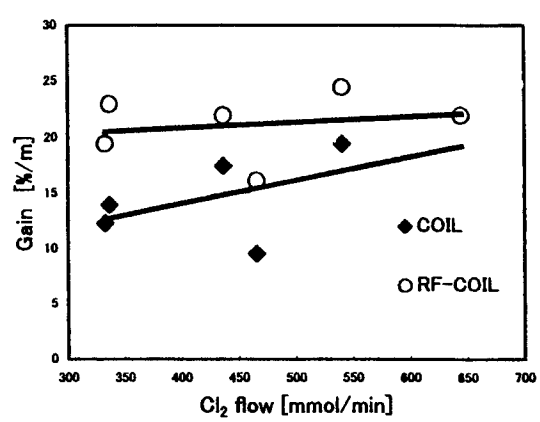


Fig.4 Small signal gain measurement

atoms instead of dissociating $I_2$ compared with normal COIL. If we use RF-discharge, we can obtain higher gain at a low $Cl_2$. flow rate and high gain stability even if $Cl_2$. flow rate change.

**4.4 Dependence of gain as a function of RF-discharge power**

Small signal gain as a function of RF-discharge power is shown in Fig.5. Though RF-discharge power has changed through 95[w]—155[w], gain doesn't change drastically. The more a power is supplied, the higher the small signal gain increases. We can consider that only low power of RF-discharge can dissociate iodine molecule enough. As a result, inversion of excited iodine atom, built up.

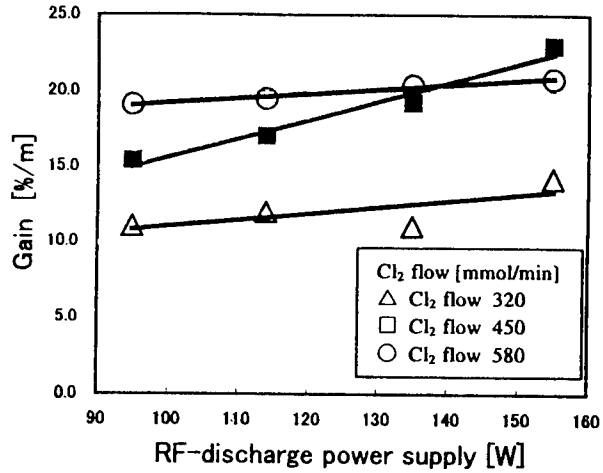


Fig.5 Dependence of gain as a function of RF-discharge power

## 5.CONCLUSION

On the term of this experiments, the output power of RF-COIL was attained 37.5W and chemical efficiency was 3.6% while 34.0W, 3.3% in normal COIL at chlorine flow rate 600mmol/min. The maximum enhancement of power output power is 10% at chlorine flow rate 600mmol/min. The small signal gain of this apparatus is achieved at 25[%/m] at RF-COIL. The maximum enhancement of gain is 21% at chlorine flow rate 330mmol/min. On our experimental apparatus, Iodine molecule is dissociated 60% into iodine atom. These results mean that utilizing the RF discharge dissociation of $I_2$ was useful to get high power, and high gain.

## 6. REFERENCE

[1] Tuyoshi Wakazono, Katuki Hashimoto, Tomohiro Takemoto, Taro Uchiyama, Mikio Muro "The Study of Chemical Oxygen-Iodine Laser using RF discharge dissociation of $I_2$ " SPIE Vol.3574 p290-p294

[2] Hideki Yoshimoto, Hideo Yamakoshi, Yukio Shibukawa, and Taro Uchiyama "A highly efficient, compact chemical oxygen-iodine laser" Journal of APPLIED PHYSICS, Vol59, Number12,15 June 1986

[3] Daichi Sugimoto, Hideo Okamaoto, Fumio Wani, Masamori Endo, Shuzaburo Takeda, and Tomoo Fujioka "Output Power Enhancement by pre-dissociation of Iodine in Supersonic Chemical Oxygen-Iodine Laser " AIAA-99-3426

# Numerical Simulation of Throat-mixing System for Supersonic Flow Chemical Oxygen-Iodine Laser

Masataro Suzuki*, Takanori Suzuki, and Wataru Masuda

Nagaoka University of Technology, 1603-1 Kamitomioka, Nagaoka, Niigata 940-2188 JAPAN

## ABSTRACT

Throat-mixing systems for the supersonic flow chemical oxygen-iodine laser (SCOIL) are proposed and assessed in the present study. Three-dimensional, numerical simulation solving compressible gas dynamics together with chemical kinetics has been made for investigating the characteristics of the mixing condition and chemical reactions. The compressible Navier-Stokes equations and a chemical kinetic model encompassing 21 chemical reactions and 10 chemical species are solved by means of full-implicit finite difference method. Two types of nozzles, a Laval nozzle and cylinder nozzle are adopted. The results show satisfactorily high values of the small signal gain coefficient (SSG). The SSG value increases along the flow in the nozzle in relatively short distance of $x$, reaches to the maximum at the position of 25 ~ 47 mm distant from the throat, and decreases slightly downstream the flow. The proposed throat-mixing system shows higher efficiency than the supersonic parallel-mixing system. The Laval nozzle is found to give the peak SSG value of 40 % higher than that of the parallel-mixing system. It is also noted that the cylinder nozzle has superior ability than the parallel-mixing system, in spite of its exceedingly simple structure.

**Keywords:** Supersonic Flow, Chemical Laser, Throat Mixing, Oxygen, Iodine, Numerical Simulation

## 1. INTRODUCTION

The supersonic flow chemical oxygen-iodine laser (SCOIL) has been investigated in order to increase the efficiency and power of the COIL by gas cooling through supersonic expansion. The COIL basically works on the energy transfer from the excited oxygen molecule to the iodine atom and the light emission from the excited iodine atom. Those reactions can be expressed as follows:

$$O_2\,(^1\Delta) + I\,(^2P_{3/2}) \rightarrow O_2\,(^3\Sigma) + I\,(^2P_{1/2}), \tag{1}$$

$$I\,(^2P_{1/2}) \rightarrow I\,(^2P_{3/2}) + h\nu, \tag{2}$$

where $O_2\,(^1\Delta)$, $O_2\,(^3\Sigma)$, $I\,(^2P_{3/2})$, and $I\,(^2P_{1/2})$ are the oxygen molecule in the excited state, that in the ground state, the iodine atom in the ground state, and that in the excited state, respectively. In reality the reactions shown above consist of numerous elementary reactions, which includes $I\,(^2P_{1/2})$ consumption without contributing to the emission of laser light. It has been found that the balance of the rates of gas mixing and chemical reactions is of significant importance for the performance of the laser. If the iodine gas is injected into the gas flow of $O_2\,(^1\Delta)$ at subsonic region upstream the throat of the expansion nozzle, mixing and chemical reactions may occur too quickly so that the gas in the resonating region no longer contains sufficient amount of $I\,(^2P_{1/2})$. On the other hand, if the iodine gas is introduced in the supersonic flow region downstream the nozzle, the mixing rate of the reacting gas species would be slow since the flow becomes laminar, and dominates the reaction (1), accordingly.

In the previous study, a parallel-mixing system, in which iodine gas is introduced in the supersonic flow region, was found to give good performance if ramp nozzle arrays are adopted and strong vortices are given in the flow. However, this system needs complex nozzle arrays. In the practical point of view, simple nozzle is desirable. A throat-mixing system, a system in which the iodine gas is introduced into the $O_2\,(^1\Delta)$ flow at the throat of the expansion nozzle, is expected to give good performance for both the mixing condition and the simple nozzle-shape. Thus, in this study, throat-mixing systems for the SCOIL are examined adopting two types of nozzles, a Laval nozzle and simple cylinder nozzle.

* Correspondence: Email: szk@nagaokaut.ac.jp; Telephone: +81 (258) 47-9738; Fax: +81 (258) 47-9770

XIII International Symposium on Gas Flow and Chemical Lasers and High-Power Laser Conference,
Antonio Lapucci, Marco Ciofini, Editors, Proceedings of SPIE Vol. 4184 (2001)

## 2. NUMERICAL MODEL

In order to investigate the characteristics of the mixing condition and chemical reactions in the throat-mixing and parallel-mixing systems, three-dimensional, compressible Navier-Stokes equations and a chemical kinetic model are solved by means of full-implicit finite difference method.

The chemical kinetic model encompassing 21 chemical reactions and 10 chemical species are shown in Table 1. Since the chemical model is revised after the publication of the previous paper, the calculation for the ramp nozzle is done again in this work. However, there is insignificant change in the results.

Figure 1 shows the nozzle geometries and the calculating domains for parallel-mixing and throat-mixing systems. The geometry and boundary condition of the ramp nozzle in the parallel mixing system, shown in Fig. 1 (a), is same to those adopted in the previous work. The Laval and cylinder nozzles are shown in Fig. 1 (b) and (c), respectively. Both of the nozzles are lined along the throat with iodine-injecting orifices of 0.5 mm in diameter. The gas mixture of 0.010 molar fraction of $I_2$ and 0.99 of He at 370 torr in pressure and 400 K in temperature is injected perpendicular into the main gas flow. The gas, provided at the plenum of the main flow, is at 100 torr in pressure and 273 K in temperature, and assumed to consist of $O_2$ ($^1\Sigma$), $O_2$ ($^1\Delta$), $O_2$ ($^3\Sigma$), $H_2O$, $Cl_2$, and He, the molar fraction of those are $2.1 \times 10^{-5}$, 0.075, 0.075, 0.010, 0.020, and 0.820, respectively. In order to save computing time, symmetric conditions are applied.

## 3. RESULTS AND DISCUSSION

### 3.1. Mixing of the Flow

Figure 2 shows the streamlines of the gas flow. As it is seen in Fig. 2 (a), the gas flow in the parallel-mixing system has a strong vortex along the streamline passing beneath the rim of the ramp nozzle. It would be no doubt that the zigzag structure of the ramp nozzle causes rotating motion in the flow in the boundary layer between the two gas flows. The vortex significantly grows in the region of $0 \le x \le 70$ mm, although its extent spreads insignificant downstream the flow in $x > 70$ mm. Since the vortex does not spread over the whole extent of the flow region, a certain amount of the two gasses is supposed to flow away unmixed.

On the other hand, the gas flow of the iodine mixture injected from the orifice at the throat spreads widely in the flow field in the case of the throat mixing system obeying the Laval nozzle, as it is shown in Fig. 2 (b). It is observed that the gas flow injected from the orifice is stretched widely in $y$-direction, the direction of the injection. It should be noted that the $y$-$z$ plane, normal plane to the direction of the main flow, has notably thin area of 0.75 mm × 7.5 mm. The injected gas spreads mainly in the expanding region of the Laval nozzle. It is suggested from this expanding behavior that the friction between two perpendicular flows causes a vortex near the center of the calculating $y$-$z$ plane at the throat. Since the injecting orifice of 0.25 mm in radius is centered at $z = 0$, the center of the vortex is assumed at $z = 0.25$ mm. Though the cylinder nozzle causes similar flow behavior as shown in Fig. 2 (c), the extent area of the vortex seem to be smaller

Table 1. Chemical kinetic model.

| No. | Reaction | Rate coefficient $k_f$ ($m^3$/kmol s) |
|---|---|---|
| 1 | $O_2(^1\Delta) + O_2(^1\Delta) \rightarrow O_2(^1\Sigma) + O_2(^3\Sigma)$ | $1.62 \times 10^4$ |
| 2 | $O_2(^1\Sigma) + H_2O \rightarrow O_2(^3\Sigma) + H_2O$ | $4.03 \times 10^9$ |
| 3 | $O_2(^1\Delta) + O_2(^3\Sigma) \rightarrow O_2(^3\Sigma) + O_2(^3\Sigma)$ | $9.63 \times 10^2$ |
| 4 | $O_2(^1\Delta) + H_2O \rightarrow O_2(^3\Sigma) + H_2O$ | $2.41 \times 10^3$ |
| 5 | $O_2(^1\Delta) + Cl_2 \rightarrow O_2(^3\Sigma) + Cl_2$ | $3.61 \times 10^3$ |
| 6 | $O_2(^1\Delta) + He \rightarrow O_2(^3\Sigma) + He$ | $4.82 \times 10^0$ |
| 7 | $I_2(^1\Sigma) + O_2(^1\Sigma) \rightarrow 2I(^2P_{3/2}) + O_2(^3\Sigma)$ | $2.41 \times 10^9$ |
| 8 | $I_2(^1\Sigma) + O_2(^1\Sigma) \rightarrow I_2(^1\Sigma) + O_2(^1\Delta)$ | $9.63 \times 10^9$ |
| 9 | $I_2(^1\Sigma) + O_2(^1\Delta) \rightarrow I_2^* + O_2(^3\Sigma)$ | $4.21 \times 10^6$ |
| 10 | $I_2(^1\Sigma) + I(^2P_{1/2}) \rightarrow I_2^* + I(^2P_{3/2})$ | $2.28 \times 10^{10}$ |
| 11 | $I_2^* + O_2(^1\Delta) \rightarrow 2I(^2P_{3/2}) + O_2(^3\Sigma)$ | $1.81 \times 10^{11}$ |
| 12 | $I_2^* + O_2(^3\Sigma) \rightarrow I_2(^1\Sigma) + O_2(^3\Sigma)$ | $3.01 \times 10^{10}$ |
| 13 | $I_2^* + H_2O \rightarrow I_2(^1\Sigma) + H_2O$ | $1.81 \times 10^{11}$ |
| 14 | $I_2^* + He \rightarrow I_2(^1\Sigma) + He$ | $1.92 \times 10^{10}$ |
| 15 | $I(^2P_{3/2}) + O_2(^1\Delta) \rightarrow I(^2P_{1/2}) + O_2(^3\Sigma)$ | $1.40 \times 10^{13} T^{-1}$ |
| 16 | $I(^2P_{1/2}) + O_2(^3\Sigma) \rightarrow I(^2P_{3/2}) + O_2(^1\Delta)$ | $1.87 \times 10^{13} T^{-1} \exp(-401.4\, T^{-1})$ |
| 17 | $I(^2P_{3/2}) + O_2(^1\Delta) \rightarrow I(^2P_{3/2}) + O_2(^3\Sigma)$ | $6.02 \times 10^5$ |
| 18 | $I(^2P_{1/2}) + O_2(^1\Delta) \rightarrow I(^2P_{3/2}) + O_2(^1\Sigma)$ | $6.60 \times 10^7$ |
| 19 | $I(^2P_{1/2}) + O_2(^1\Delta) \rightarrow I(^2P_{3/2}) + O_2(^3\Sigma)$ | $3.00 \times 10^7$ |
| 20 | $I(^2P_{1/2}) + I(^2P_{3/2}) \rightarrow I(^2P_{3/2}) + I(^2P_{3/2})$ | $9.63 \times 10^6$ |
| 21 | $I(^2P_{1/2}) + H_2O \rightarrow I(^2P_{3/2}) + H_2O$ | $1.20 \times 10^9$ |

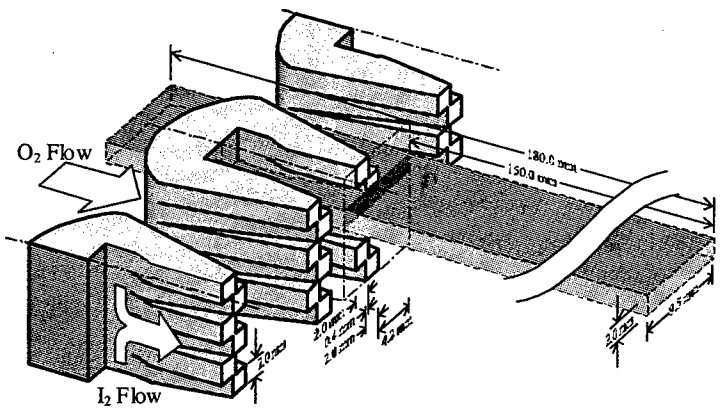


(a) Parallel-mixing system (Ramp nozzle)

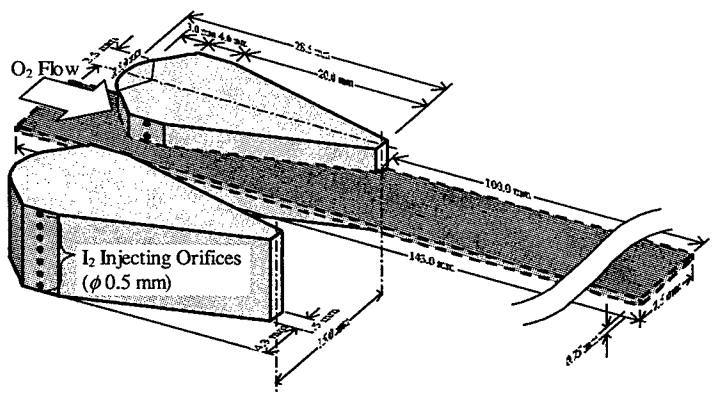


(b) Throat-mixing system (Laval nozzle)

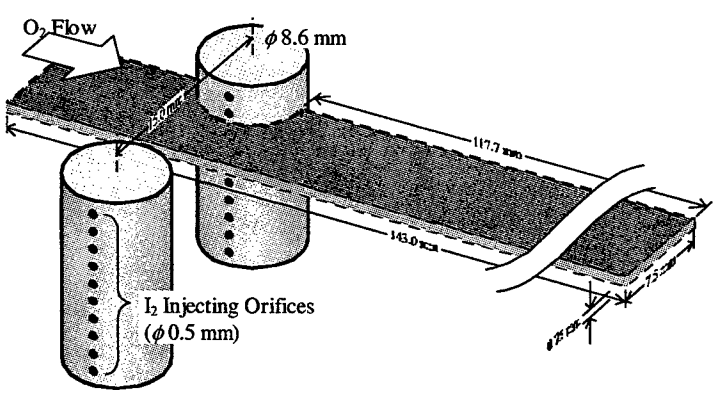


(c) Throat-mixing system (Cylinder nozzle)

Figure 1. The nozzle geometries and the calculating domains.

than that in the case of Laval nozzle. Since the cylinder nozzle has short path length for the supersonic expansion, only 4.3 mm, in contrast to the Laval nozzle of 20 mm, it is plausible that the vortex expands narrower area than that of Laval nozzle.

### 3.2. Small Signal Gain (SSG)

Small signal gain (SSG), $G$, is regarded as an index of the efficiency of the laser. Higher density of I ($^2P_{1/2}$) and lower density of I ($^2P_{3/2}$) gives higher value of $G$. Since the computation is done for three-dimensional flow field, SSG is distributed in the $y$-$z$ plane. Thus, average of SSG in the $y$-$z$ plane, $\overline{G}$, is calculated as follows:

$$\overline{G}(x) = \frac{1}{A}\iint G dydz, \qquad (3)$$

where $A$ is the area of the flow region on the $y$-$z$ plane at the location of $x$.

Figure 3 shows the distribution of $\overline{G}$ along the $x$ direction. The values of $\overline{G}$ for both of the Laval and cylinder nozzles increase in relatively short distance of $x$, reach to the maximum at $x = 47$ mm for the Laval nozzle and $x = 25$ mm for the cylinder nozzle, and decreases slightly downstream the flow. Comparing with them, the SSG value for the ramp nozzle in the parallel-mixing system increases at a slower speed, and reach to the lower peak of 0.5 $m^{-1}$. It is interesting to note that the strong vortex, as shown in Fig. 2 (a), does not always give high efficiency of the laser power.

It is seen that all SSG data trace uneven lines on the graph. Since the unevenness seemed to be of periodic, it is inferred that static waves are established in the flow region.

It is obviously seen that the throat mixing system of the Laval nozzle gives the highest $\overline{G}$, the peak value of which is 0.72 $m^{-1}$ at $x = 47$ mm. This peak value is 40 % higher than that of ramp nozzle adopted in the parallel mixing system. Though the efficiency of the cylinder nozzle is less than the Laval nozzle, it still has superior ability than the parallel-mixing system. Since this nozzle has great advantage in its exceedingly simple structure, it is one of the most promising systems in a practical use.

## 4. CONCLUSIONS

Throat-mixing systems for the supersonic flow chemical oxygen-iodine laser (SCOIL) are investigated by computing three-dimensional, numerical simulation. In the case of the throat-mixing system, the gas flow of the iodine mixture injected from the orifice at the throat spreads widely in the flow compared to the parallel-mixing system. The gas flow injected from the orifice is stretched widely in $y$-direction in the thin flowing area. The friction between two perpendicular flows is supposed to cause a vortex near the center of the calculating $y$-$z$ plane at the throat.

The SSG values for the throat-mixing system increase in shorter distance of $x$ compared to that of parallel mixing system. The Laval nozzle gives the highest SSG value, the peak value of which is $0.72\ \mathrm{m}^{-1}$ at $x = 47$ mm. This peak value is 40 % higher than that of ramp nozzle adopted in the parallel mixing system. It is also noted that the cylinder nozzle has superior ability than the parallel-mixing system. Since this nozzle has great advantage in its exceedingly simple structure, it is one of the most promising systems in a practical use.

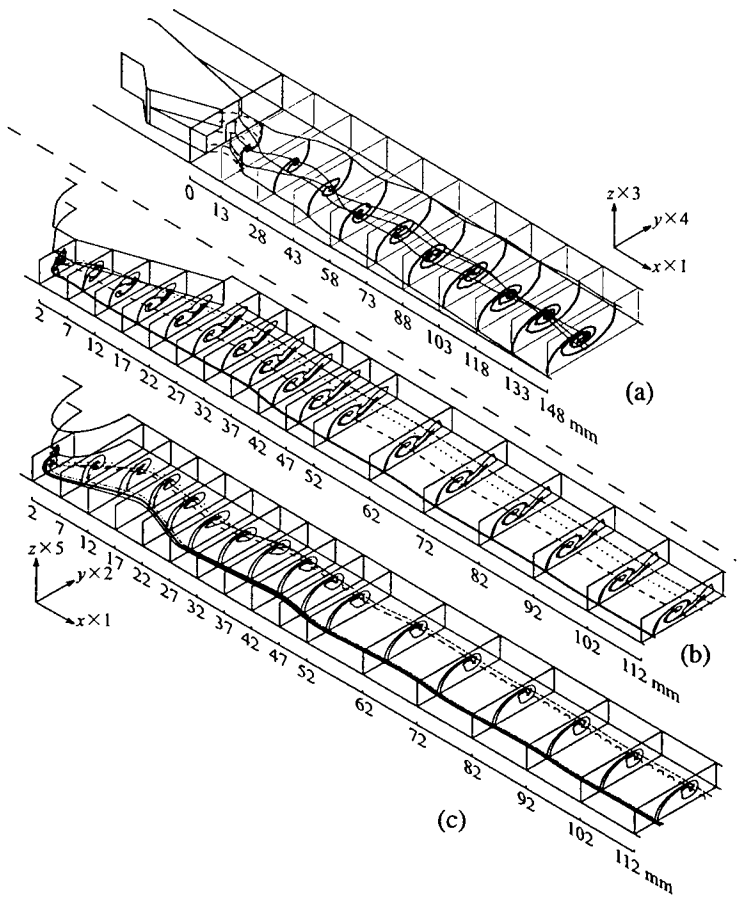


Figure 2. Stream lines of injecting flow.

(a) Parallel-mixing system (Ramp nozzle)
(b) Throat-mixing system (Laval nozzle)
(c) Throat-mixing system (Cylinder nozzle)

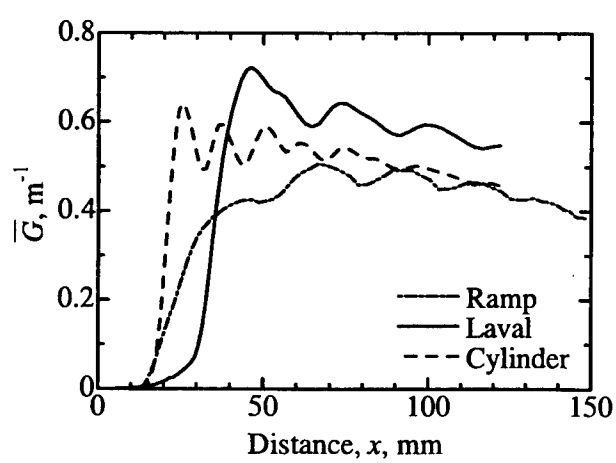


Figure 3. Distribution of the small signal gain $\overline{G}$ along the main flow.

## REFERENCES


1. W. Masuda, M. Hishida, S. Hirooka, N. Azami, and H. Yamada, "Three-Dimensional Mixing/Reacting Zone Structure in a Supersonic Flow Chemical Oxygen-Iodine Laser," JSME Int. J. **B40-2**, p209, 1997.
2. W. Masuda, M. Satoh, H. Fujii, T. Atsuta, "Numerical Simulation of a Supersonic Flow Chemical Oxygen-Iodine Laser Solving Navier-Stokes Equations," JSME Int. J. **B40-1**, p. 87, 1997.
3. W. Masuda, M. Hishida, and N. Azami, "Effects of Wall Catalysis on the Reacting Zone Structure of a Supersonic Flow Chemical Oxygen-Iodine Laser", JSME Int. J., **B40-3**, p. 674, 1998.
4. R. J. Driscoll, "Mixing Enhancement in Chemical Lasers, Part I: Experiments," AIAA J. **24-7**, p. 1120, 1986.
5. R. J. Driscoll, "Mixing Enhancement in Chemical Lasers, Part II: Theory," AIAA J. **25-7**, p. 965, 1987.

# Modeling of chemical generation of atomic iodine for chemical oxygen-iodine laser

Vít Jirásek*, Otomar Špalek, Jarmila Kodymová
Institute of Physics, Academy of Sciences of the Czech Republic
Na Slovance 2, 182 21, Prague 8, Czech Republic

## ABSTRACT

A purely chemical method was suggested for generation of atomic iodine from gaseous reactants for the use in a COIL. In this method, fluorine or chlorine atoms are produced and subsequently react with hydrogen iodide forming atomic iodine. Both reaction systems were modeled for different reaction conditions. A yield of atomic iodine up to 80 % was achieved in the optimum case for the system leading via chlorine.

Keywords: atomic iodine, chemical oxygen-iodine laser, modeling

## 1. INTRODUCTION

In a conventional COIL operation, a part of the energy stored in singlet oxygen is consumed for the dissociation of iodine molecules used as a precursor of atomic iodine. Therefore, an injection of atomic iodine into the laser mixing zone can significantly increase the extracted power at the same input parameters. By using generation of atomic iodine from gaseous reactants only, some technical problems connected with the evaporation process of solid or liquid molecular iodine can be also avoided.

An effort was devoted recently to work out a method for the direct generation of atomic iodine. For instance, electrical discharge technique using alkyliodides for a pulsed COIL has been investigated in Lebedev Physical Institute[1], and a microwave discharge technique of pre-dissociation of molecular iodine was reported by the Japanese group.[2] A chemical generation of atomic iodine by reaction of atomic chlorine with hydrogen iodide has been used in the system similar to a COIL where the energy transfer from $NCl(a^1\Delta)$ to the ground state I atoms has been investigated.[3]

We have started recently with the study of the chemical generation of atomic iodine by reaction of mixed commercially available gases in order to achieve a cw COIL operation.

## 2. CHEMISTRY OF ATOMIC IODINE PRODUCTION

A principle of the method is based on the reaction between atomic fluorine or atomic chlorine with hydrogen iodide

$$F(Cl) + HI \rightarrow HF^* (HCl^*) + I(^2P_{3/2}) \qquad (1a,b)$$

forming atomic iodine in a fast exothermic process

$k_{1a} = 6.3 \times 10^{-12}\ cm^3s^{-1}$ ($\Delta H^o_{298} = -216.7$ kJ/mol)
$k_{1b} = 1.64 \times 10^{-10}\ cm^3s^{-1}$ ($\Delta H^o_{298} = -132.5$ kJ/mol),

where some part of liberated energy is stored in vibrationally excited HX molecules.[4]
Mechanisms proposed for both fluorine and chlorine atoms generation follow.

### 2.1 Generation of atomic fluorine

The reaction of molecular fluorine with nitrogen oxide[5]

$$NO + F_2 \rightarrow NOF^* + F \qquad k_2 = 7 \times 10^{-13}\, e^{-1150/T}\ cm^3s^{-1} \qquad (2)$$

* e-mail address: jirasek@fzu.cz

XIII International Symposium on Gas Flow and Chemical Lasers and High-Power Laser Conference,
Antonio Lapucci, Marco Ciofini, Editors, Proceedings of SPIE Vol. 4184 (2001)

is a fast exothermic process ($\Delta H^0_{298}$ = -77 kJ/mol).[6] The F atoms are lost by reaction with NO and recombination processes[7]

| | | |
|---|---|---|
| $F + NO + NO \rightarrow NOF + NO$ | $k_3 = 1.7 \times 10^{-31}$ cm$^6$ molec$^{-2}$ s$^{-1}$ | (3) |
| $F + NO + He \rightarrow NOF + He$ | $k_4 = 1.1 \times 10^{-31}$ cm$^6$ molec$^{-2}$ s$^{-1}$ | (4) |
| $F + wall \rightarrow products$ | $k_5 = 12 \pm 19$ s$^{-1}$ | (5) |
| $F + F + M \rightarrow F_2 + M$ | $k_6 = 5.3 \times 10^{-34}$ cm$^6$ molec$^{-2}$ s$^{-1}$ | (6) |
| $NOF^* \rightarrow NO + F$ | $k_7 = 3.3 \times 10^{-14}$ cm$^3$ s$^{-1}$. | (7) |

where electronically excited $NOF^*$ molecules decay to the ground state by both radiative and non-radiative processes. Kinetics of this system may be also complicated by very reactive molecular fluorine, which is always presented in the reaction system.[8] The atomic fluorine production predicted by Helms et al[7] corresponds to the measured efficiency of 20-30%, and a percentage dissociation of $F_2$ molecule to F atoms of 18%.[7,9]

### 2.2 Generation of atomic chlorine

A proposed mechanism is based upon the reaction of chlorine dioxide with nitrogen oxide running through the chain-branching reaction mechanism applied successfully in chemical HCl and HCl/$CO_2$ transfer lasers [10]

| | | |
|---|---|---|
| $ClO_2 + NO \rightarrow NO_2 + ClO + 60.6$ kJ/mol | $k_8 = 3.4 \times 10^{-13}$ cm$^3$ s$^{-1}$ | (8) |
| $ClO + NO \rightarrow NO_2 + Cl + 37.2$ kJ/mol | $k_9 = 1.7 \times 10^{-11} e^{(\pm 120/T)}$ cm$^3$ s$^{-1}$ | (9) |
| $Cl + ClO_2 \rightarrow 2\ ClO + 23$ kJ/mol | $k_{10} = 5.9 \times 10^{-11}$ cm$^3$ s$^{-1}$ | (10) |
| $Cl + NO_2 + He \rightarrow NO_2Cl + He$ | $k_{11} = 7.2 \times 10^{-31}$ cm$^6$ molec$^{-2}$ s$^{-1}$ | (11) |
| $Cl + ClNO_2 \rightarrow Cl_2 + NO_2$ | $k_{12} = 3.0 \times 10^{-11}$ cm$^3$ s$^{-1}$ | (12) |
| $ClO + NO_2 + He \rightarrow NO_3Cl + He$ | $k_{13} = 1.0 \times 10^{-31}$ cm$^6$ molec$^{-2}$ s$^{-1}$ | (13) |
| $Cl + Cl + M \rightarrow Cl_2 + M$ | $k_{14} = 6.4 \times 10^{-33}$ cm$^6$ molec$^{-2}$ s$^{-1}$ | (14) |

The reaction (8) initiates the chain while reactions (9) and (10) propagate the chain with Cl and ClO acting as chain carriers. The termolecular reactions (11) and (13) and the reaction (12) act conversely, representing the principal loss mechanism for Cl atoms and ClO radicals. It was shown by the Arnold et al's[10] numerical calculations that the chain carriers Cl and ClO must not be excessively depleted by the loss processes if the reaction system $ClO_2$/NO has to be efficient.

### 2.3 Loss processes of atomic iodine

The ground state atomic iodine is lost mainly in three-body recombination reactions

| | | |
|---|---|---|
| $I + I + M \rightarrow I_2 + M$ | $k_{15} = 4.2 \times 10^{-33}$ cm$^6$ molec$^{-2}$ s$^{-1}$ | (15) |
| $I + NO_2 + M \rightarrow INO_2 + M$ | $k_{16} = 1.68 \pm 0.38 \times 10^{-31}$ cm$^6$ molec$^{-2}$ s$^{-1}$ | (16) |
| $I + INO_2 \rightarrow I_2 + NO_2$ | $k_{17} = 8.3 \times 10^{-11}$ cm$^3$ s$^{-1}$ | (17) |
| $I + Cl + M \rightarrow ICl + M$ | $k_{18} = 1.0 \times 10^{-32}$ cm$^6$ molec$^{-2}$ s$^{-1}$, | (18) |

where the last three reactions occur in the system leading via chlorine.
For a direct production of atomic iodine in the COIL, the deactivation of $O_2(^1\Delta_g)$ and $I^*(^2P_{1/2})$ by reaction mixture components must be considered. HX molecules are only weak quenchers of $O_2(^1\Delta_g)$[11]

| | | |
|---|---|---|
| $O_2(^1\Delta_g) + HI \rightarrow O_2(^3\Sigma_g) + HI$ | $k_{19} \leq 2 \times 10^{-17}$ cm$^3$ s$^{-1}$ | (19) |
| $O_2(^1\Delta_g) + HCl \rightarrow O_2(^3\Sigma_g) + HCl$ | $k_{20} = 4 \times 10^{-18}$ cm$^3$ s$^{-1}$ | (20) |

as well as $ClO_2$ and NO.
A quenching of excited iodine by hydrogen halides is somewhat faster[12]

| | | |
|---|---|---|
| $HI + I^* \rightarrow HI + I$ | $k_{21} = 5.7 \times 10^{-14}$ cm$^3$ s$^{-1}$ | (21) |
| $HCl + I^* \rightarrow HCl + I$ | $k_{22} = (0.32\text{-}1.5) \times 10^{-14}$ cm$^3$ s$^{-1}$. | (22) |

## 3. MODELING OF REACTION SYSTEMS

To understand more the above kinetics of chemical generation of atomic iodine, and to assess an appropriateness of suggested reaction systems for the COIL conditions, a numerical modeling of both systems was accomplished. A simple one-dimensional, constant pressure numerical model was developed with the following assumptions: an instantaneous mixing of reactants, neglecting heat transport to the walls and considering an adiabatic process. The mass and enthalpy balance equations were solved by using a fourth-order Runge-Kutta routine. A time course of concentrations of all reaction components and intermediates, and system temperature was obtained. The calculations were accomplished for the flow and pressure conditions typical for the mixing region of supersonic COIL in our laboratory: 40 mmol/s of $Cl_2$, 80 mmol/s of primary He, and 40 mmol/s of secondary He, total pressure in subsonic channel of 4 kPa, and $O_2(^1\Delta_g)$ partial pressure of 580 Pa (with the excitation efficiency of 60%). A gas flow velocity in reactor was considered to be 100 m/s.

Both reaction systems suggested for atomic iodine generation can be generally solved for two different experimental configurations. In the first arrangement, the gaseous reactants for chemical generation of atomic iodine are introduced directly into the main (primary) flow containing singlet oxygen, residual chlorine and water vapor. This procedure looks very simple and convenient but one has to take into account the fact that the primary gas components can react with reactants and products included in atomic iodine synthesis. In the second experimental arrangement, atomic iodine could be generated in a separate reactor from which a gas containing atomic iodine is injected into the primary flow. In this case, a total pressure of reactants can be significantly higher than in the first configuration, providing a higher rate of reactions of atomic iodine generation.

## 4. RESULTS AND DISCUSSION

### 4.1 Reaction system with atomic fluorine as intermediate reactant

The modeling of system leading via fluorine included reactions (1a), (2)-(6) and (15). The highest F atoms yield was obtained for the concentration ratio $[F_2]$:[NO] = 1:2. Due to the significant loss processes, the optimum injection for the HI was found simultaneously with $F_2$ and NO. Results are illustrated in Figure 1. A moderate iodine yield of 45% was achieved at the reaction path of 50 cm. The reaction path can be reduced by the decreasing in helium dilution, as is shown in Figure 2. This is, however, accompanied by a significant increase in temperature.

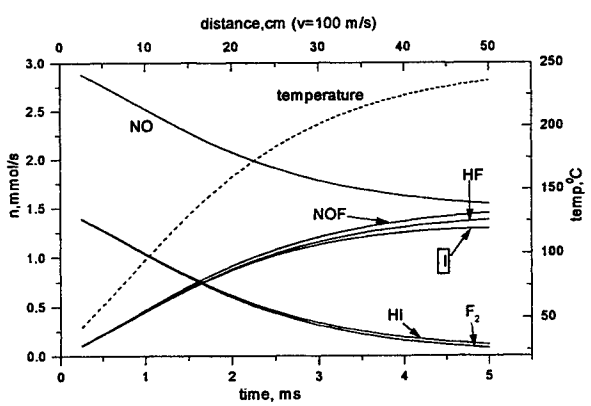


Fig.1: Molar flowrates of reactants for system with atomic fluorine. The upper X-coordinate denotes the distance from the point of gases injection.

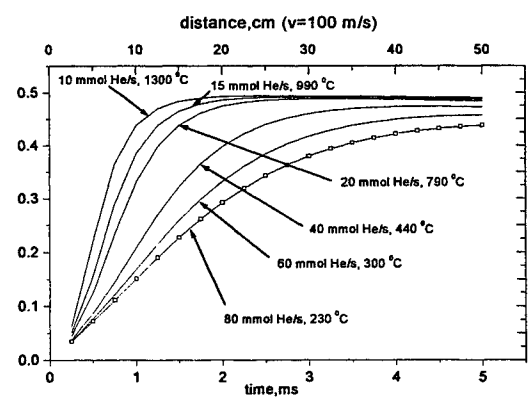


Fig.2: Atomic iodine yield as a function of distance for different helium dilution and temperature at the distance of 30 cm.

### 4.2 Reaction system with atomic chlorine as intermediate reactant

The modeling of system going via chlorine included reactions (1b), (8)-(13), (15)-(17). It was shown[10] that an effective production of atomic chlorine requires the concentration ratio $[ClO_2]$:[NO] = 1:2. If the ratio is 1:1, ClO radical is predominantly formed, which was confirmed by our modeling (see Figure 3). Due to the chain-branching reaction

mechanism, the ClO radical should not be significantly depleted by reaction (9). The modeling was therefore performed for

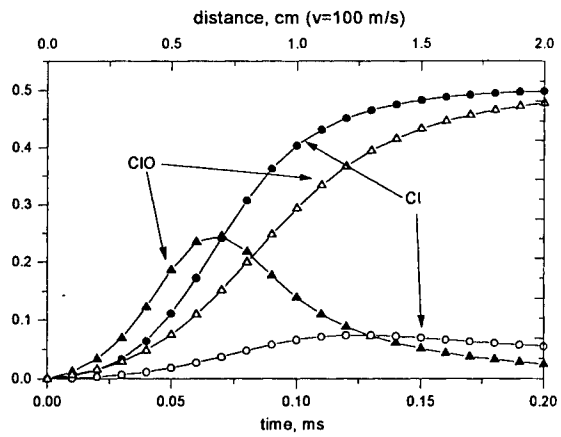


Fig.3: Relative concentrations (to $ClO_2$) of Cl and ClO radicals. Open symbols denote concentration ratio $[ClO_2]$:[NO] = 1:1, solid symbols the ratio 1:2.

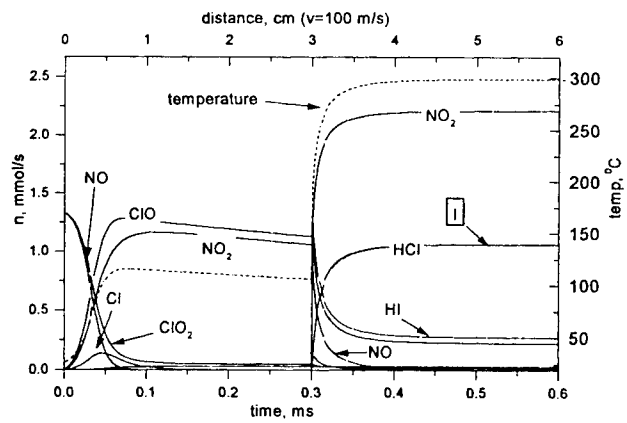


Fig.4: Molar flowrates of reactants for system with atomic chlorine. HI and second part of NO are injected 3 cm downstream.

a such reaction arrangement, in which first $ClO_2$ and NO are injected in concentration ratio 1:1 and the second part of NO is injected together with HI 3 cm downstream. The results are shown in Figure 4. In this case, the atomic iodine yield is nearly 80% at the distance of 4 cm, while the concentrations of ClO and $ClO_2$ are already negligible at this distance. The temperature comes to 300 $^0$C.

## 5. Conclusions

The concentration and temperature profiles in the reaction systems for atomic iodine generation were calculated by using the simple one-dimensional model. In the optimum conditions, the system going via atomic chlorine resulted in the 80% yield of atomic iodine at the reaction path of 4 cm. It would suit for the COIL operation quite well. The way including atomic fluorine would require probably using a separate reactor working at higher pressure, and a cooling device.

## 6. Acknowledgment

This work was supported by the USAF European Office for Research and Development (EOARD), the Contract F6177-99-WE059. The authors thank to Dr. G. Hager from the USAFRL for his encouragement in this work.

## 7. References

1. V.S. Pazyuk, N.P. Vagin, N.N. Yuryshev, *Proc. SPIE* Vol. **2767**, p. 206, 1995
2. M. Endo, M. Kawakami, S. Takeda, F. Wani, T. Fujioka, *Proc. SPIE* Vol. **3612**, p. 56, 1999
3. T.L. Hanshaw, T.J. Madden, J.M. Herbelin, G.C. Manke, B.T. Anderson, R.T. Tate, G.D. Hager, *Proc. SPIE* Vol. **3612**, p. 147, 1999
4. N. Jonathan, C.M. Melliar-Smith, S. Okuda, D.H. Slater, D. Timlin, *Mol.Phys.* **22**, p. 561, 1971
5. C.E. Kolb, *J. Chem.Phys.* **64**, p. 3087 (1976)
6. S. Johnston, H. J. Bertin, *J. Amer.Chem.Soc.* **81**, p. 6402, 1959
7. C.A. Helms, L. Hanko, K. Healey, G. Hager, G.P. Perram, *J. Appl.Phys.* **66**, p. 6093, 1989
8. M.A.A. Clyne, D.J. McKenney, R.F. Walker, *Can. J. Chem.* **51**, p. 3596, 1973
9. J.M. Hoell, F. Allario, O. Jarrett, R.K. Seals, *J. Chem.Phys.* **38**, p. 2896, 1973
10. S.J. Arnold, K.D. Foster, D.R. Snelling, R.D. Suart, *IEEE J. Quant.Electr.* **QE-14**, p. 293, 1978
11. J.B. Koffend, C.E. Gardner, R.F. Heidner, *J. Chem.Phys.* **80**, p. 1861, 1984
12. Yu.A. Kulagin, L.A. Shelepin, V.N. Yarygina, *Trudy FIAN* **218**, p. 166, 1994

# BHP jet stabilization of COIL

Sung-Ok Kwon, Taek-Soo Kim, Seong-Hoon Kim, Yun-Dong Choi,
Yun-Sig Lee*,Young-Soo Park*, Hyung-Shik Kim* and Cheol-Jung Kim,

Korea Atomic Energy Research Institute, P.O. Box 105, Yusong, Taejon, Korea 305-600
Tel; +82-42-868-2913,Fax; +82-42-861-9602,e-mail; chjkim@kaeri.re.kr
*Industrial Research Institute, Hyundai Heavy Industry
1, Cheonha-Dong, Dong-Ku, Ulsan, Korea 682-060

## ABSTRACT

A COIL (Chemical Oxygen-Iodine Laser) of 2.2 kW output power has been developed in Korea. The effects of stability and uniformity of the BHP(Basic Hydrogen Peroxide) jet columns on the operation of the COIL are reported. In this paper, the uniform jet speed distribution of jet SOG (JSOG) in a supersonic COIL is achieved by using the centrifugal pump. And the vane plate in front of BHP jet plate is installed to suppress the turbulent BHP flow generated by the centrifugal pump. The stability and uniformity of BHP jet columns are increased by installing the vane plates. Substantially, the chemical efficiency is increased up to 21.7 %.

**Keywords:** COIL, SOG, jet stabilization, centrifugal pump

## 1. INTRODUCTION

The COIL is an efficient source of high output power. At present, JSOG is frequently used as a source of high-energy singlet oxygen in COIL. In JSOG, the fast flowing BHP jet is injected into reaction region to react with a flow of chlorine. The inherent instability of BHP jet leads to jet breakup and produce the unwanted aerosol. This aerosol that is swept into the supersonic nozzle contributes the increase of water vapor content and degrade the chemical efficiency. The improvement of the chemical efficiency is one of the most important for the high output power of COIL. Since the COIL was discovered in 1977, many researchers have investigated to achieve higher chemical efficiency.[1]-[5] It is well known that the chemical efficiency is dependent upon the utilization of chlorine gas, singlet oxygen yield and the reaction of energy transfer between singlet oxygen and iodine, etc. [2] So, in order to improve the chemical efficiency, the stabilization of BHP jet column in SOG has need to be increased. This work introduces the use of centrifugal pump as a BHP circulation. The centrifugal pump generally has a characteristic of large flow rate and no cavitations. But the bubble in BHP is easily generated by shearing stress of pump impellers, and the BHP flow is highly turbulent. A BHP flow is guided by the vane plates in front of BHP jet plate to minimize the turbulent effect. Using this approach, relatively stable jets have been produced. A test of JSOG with the use of centrifugal pump is described and the results of COIL operation are discussed.

XIII International Symposium on Gas Flow and Chemical Lasers and High-Power Laser Conference,
Antonio Lapucci, Marco Ciofini, Editors, Proceedings of SPIE Vol. 4184 (2001)

## 2. EXPERIMENTAL SETUP

The experimental setup for the COIL experiments is shown schematically in Fig. 1. The apparatus consists of three parts: the singlet oxygen generator (SOG) and basic hydrogen peroxide (BHP) circulation system, the laser cavity with supersonic nozzle, and the vacuum pump system.

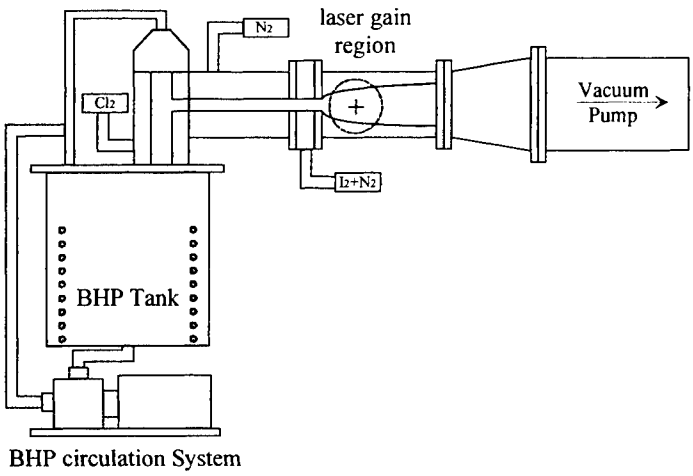


**Fig. 1. Experimental setup.**

**Table 1. Run conditions for the 2kW COIL.**

| | | |
|---|---|---|
| Gas Flows | $Cl_2$ flow rate | ~ 110 mmole/s |
| | $I_2$ flow rate | ~ 1.4 mmole/s |
| | Pri. $N_2$ flow rate | ~ 110 mmole/s |
| | Sec. $N_2$ flow rate | ~ 110 mmole/s |
| Jet SOG | SOG reaction volume | 0.375 ℓ |
| | a | 4.8 $cm^{-1}$ |
| | SOG pressure | 37 torr |
| | BHP flow rate | 132 ℓ /min. |
| | BHP molarity | 6.1 M |
| | Jet speed | 6.3 m/s |
| | Gas speed | 16 m/s |
| Laser Cavity | Gain length | 15 cm |
| | Static pressure | 3 torr |
| | Plenum pressure | 27 torr |

JSOG was designed and developed from samara. The jet plate has 720 holes with diameter 0.8 mm in the Teflon jet plate. BHP/$Cl_2$ reaction region was 100 mm reaction length with a 25 x 150 $mm^2$ cross section. The BHP solution was prepared from 20 liters of 50 % $H_2O_2$ and 20 liters of 91 % KOH in a mixing tank, and cooled down to -10 ~ -20 °C by heat exchanger using ethanol as refrigerant. The BHP solution was delivered into SOG by a three stage centrifugal pump. The vane plates in front of BHP jet plate were installed to generate the uniform BHP jet columns. Chlorine was supplied into the reaction region through two tubes mounted on the bottom of the SOG at a distance 10 cm below a singlet oxygen exit. The operation conditions of COIL are presented in Table 1. The maximum chlorine flow rate was limited up to 110 mmole/s because the pooling reaction was dominant due to the high SOG pressure. The primary buffer gas and the iodine carrier gas were set to same flow rate with chlorine flow rate. BHP flow rate was controlled by changing the motor speed of centrifugal pump. The BHP flow rate was 132 liters/min and the jet speed is 6.3 m/s. Singlet oxygen was passed through the slit valve and was transported along a channel of 10 x 150 $mm^2$ cross section to a molecular iodine injector unit. The primary $N_2$ injector was mounted in wall of the gas channel at a distance of 20 mm from the slit valve. The iodine injector was a slit type with an internal cross section 10 x 150 $mm^2$ for a gas flow and has the injector holes in the upper and lower wall of the aperture. The iodine molecules were evaporated by halogen lamp in the iodine vessel and then carried by $N_2$ gas to the iodine injector. The distance between the supersonic nozzle throat and the optical axis was 6.5 cm. The supersonic nozzle was designed to M=2 and the measured gas speed in the cavity was M= 1.76. The gain length and the supersonic nozzle throat height were 150 mm and 10 mm, respectively. The optical resonator was 760 mm length and consisted of a flat mirror and a concave mirror with 5-m curvature. The vacuum pump speed was about 2200 liter/sec.

## 3. RESULTS AND DISCUSSION

The behavior of BHP jet stability under the use of centrifugal pump and guided vane plate was investigated experimentally to optimize the COIL operating condition. The centrifugal pump generated a highly turbulent BHP flow so that the fluid pressure was not constant over the jet plate. And, the aerosol was easily generated because the fluid has a lot of bubbles. Fig.2 (a) and (b) show BHP was delivered directly to jet plate without a guided vane plate. In this case BHP jet speed was not uniform in the SOG reaction volume and the aerosol was generated by a highly turbulent BHP flow. This aerosol became entrained in the gas flowing out the JSOG and was swept into the supersonic nozzle. The aerosol contributes the quenching of excited iodine leads to the decrease of the chemical efficiency. To remedy this problem, a guided vane plate was placed on the jet plate to suppress the fluid turbulence so that the BHP flow could be directed vertically downward (Fig. 2(c)). The uniform jet speed resulting from uniform pressure distribution over the jet plate was observed, and BHP carryover was significantly reduced with some tolerance.

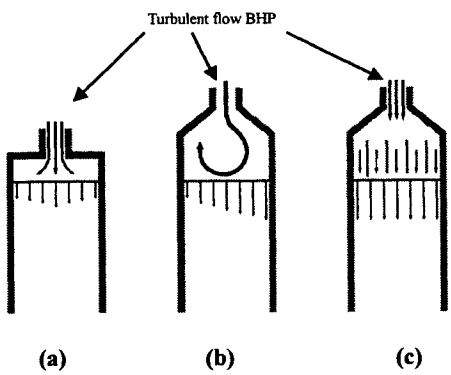


**Fig 2. Dependence on spatial distribution of the BHP jet**

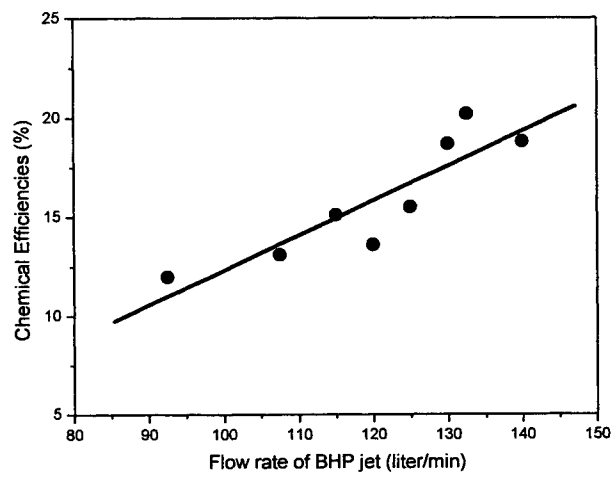


**Fig.3. Chemical efficiencies vs. BHP flow rate**

Fig.3 shows the dependence of the chemical efficiency on the BHP flow rates. It is shown that the chemical efficiency was increased up to 21.7% with the increase of BHP flow rate under the use of the vane plate. It can be deduced that the pressure distribution over the jet plate is tend to uniform over the jet plate as the flow rate and the fluid pressure increase. Also, the momentum of BHP jet that has a lot of bubbles in the fluid should be high enough to overcome a BHP carryover. Although the fluid pressure was changed as the SOG pressure due to the centrifugal pump characteristics, the fluid pressure was about 1.5 kg/cm$^2$ at the optimum SOG pressure of 37 torr.

**Table 2. Experimental results at optimum output power of COIL**

| | |
|---|---|
| $M_c$ | ~110 mmole/s |
| $m_c$ | 2.93 mmole/s.cm$^2$ |
| $P_{sog} \cdot t_{sog}$ | 0.22 torr·sec |
| Utilization | 92 % |
| Yield | 60 % |
| Mirror transmittance | 2 % |
| Laser power | 2.2 kW |
| Chemical efficiency | 21.7 % |

The dependences of output power on the iodine flow rate are plotted in Fig. 4 for comparing the effect of BHP jet stabilization. The laser power was diminished after several second because of BHP carryover in the case of Fig. 2 (b), but, after jet stabilization, the output power was stable within 30 second and then gradually decreased due to BHP temperature rise and consequently the increase of water vapor content. Some of optimum experimental results are shown in Table 2.

The centrifugal pump showed a rather good performance for a long time operation up to several ten minutes with chlorine flow rate of less than 30 mmole/s.

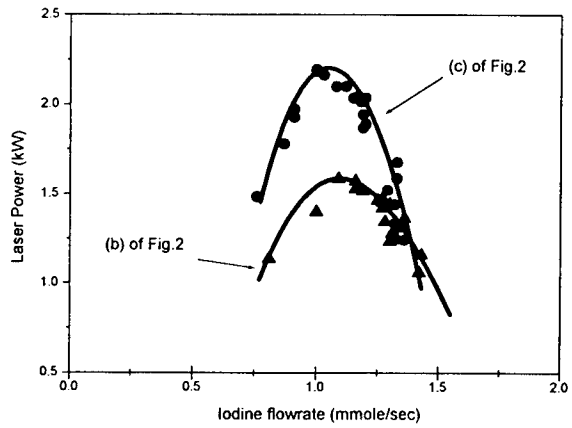


**Fig 4. Comparison of output power vs. iodine flow rate at chlorine flow rate of 110 mmole/s**

## 4. CONCLUSIONS

The effects of stability and uniformity of the BHP jet columns on the operation of the COIL were reported. The centrifugal pump was used for the circulation of BHP, and the BHP was guided by vane to suppress the effect of turbulent BHP flow. The high values of chlorine utilization and singlet oxygen yield were obtained with a reduced BHP carryover after jet stabilization. The highest power was 2.2 kW with 21.7% chemical efficiency. And the centrifugal pump that has a large flow capacity and nearly no cavitations can be successfully used for COIL operation.

## REFERENCES

1. M.V.Zaggidullin, V.D.Nikolaev, M.I.Svistun, N.A.Khvatov, N.I.Ufimtsev, "High efficient supersonic chemical Oxygen iodine laser with a chlorine flow rate of 10 mmol s-1" Quantum Electronics 27(3) 195-199 (1997)
2. K.R.Kendrick, C.A.Helms, B.G.Quillen, "Determination of singlet-oxygen generator efficiency on a 10-kW class supersonic chemical oxygen-iodine laser(RADICL)". IEEE J. Quantum Electron., 35(12), 1759-1764(1999)
3. M. V. Zagidullin, A.Yu. Kurov, N. L. Kupriyanov, V. D. Nikolaev, M. I. Svistun, and N. V. Erasov, "Highly efficient jet $O_2$ ($^1$□) generator," *Sov. J. Quantum Electron.* **21**, pp. 747-753, 1991
4. M. V. Zagidullin, N. V. Erasov, A.Yu. Kurov, V. D. Nikolaev, M. I. Svistun, and N. A. Khvatov, "An oxygen-iodine laser utilizing a high-pressure $O_2$($^1$□) generator," *Sov. J. Quantum Electron.* **21**, pp. 1303-1304, 1991
5. J. Schmiedberger, J. Kodymova, O. Spalek, and J. Kovar, "Experimental study of gain and output coupling characteristics of a cw chemical oxygen-iodine laser ", *IEEE. J. Quantum Electron.* **27**, pp. 1265-1270, 1991

# Preliminary experimental results on chemical generation of atomic iodine for a COIL

Otomar Špalek[**,1,2], Vít Jirásek[1,2], Jarmila Kodymová[1], Ivo Jakubec[2], Miroslav Čenský[1]
[1]Institute of Physics, Academy of Sciences of the Czech Republic
Na Slovance 2, 182 21 Prague 8, Czech Republic
[2]Institute of Inorganic Chemistry, Academy of Sciences of the Czech Republic
250 68 Řež by Prague, Czech Republic

**ABSTRACT**

A chemical method of atomic iodine generation with a potential application in chemical oxygen-iodine laser (COIL) was investigated experimentally. The process consists in a fast reaction of gaseous hydrogen iodide with chlorine atoms produced in reaction of gaseous chlorine dioxide with nitrogen oxide. In conditions characteristic for a subsonic mixing region of COIL, atomic iodine was produced with a yield of 20-50 %. This is in a fair agreement with results of mathematical modeling of this complex reaction system.

**Keywords:** atomic iodine, COIL, oxygen-iodine laser

## 1. INTRODUCTION

A direct generation of atomic iodine instead of molecular iodine dissociation by singlet oxygen in a COIL can increase significantly the laser gain. It can save a part of singlet oxygen energy consumed for iodine dissociation and avoid the very fast quenching of excited iodine atoms by iodine molecules. Recently, some physical methods of atomic iodine production for COIL have been proposed and tested (electrical discharge in alkyliodides vapours,[1] mw discharge in iodine vapours[2]). A chemical generation of atomic iodine through reaction of hydrogen iodide with atomic chlorine has been applied in the laser system based on $NCl(a^1\Delta) + I(^2P_{3/2})$ energy transfer reaction. Chlorine atoms were produced in this system in the reaction of DCl with F atoms arising from a dc discharge in $F_2$+He mixture.[3]
In search for a method of atomic iodine generation which could be appropriate for COIL, two fast reactions have been chosen

$$F + HI \rightarrow I(^2P_{3/2}) + HF \qquad k_{1a} = 6.3 \times 10^{-12}\ cm^3s^{-1} \qquad (1a)$$

and

$$Cl + HI \rightarrow I(^2P_{3/2}) + HCl \qquad k_{1b} = 1.64 \times 10^{-10}\ cm^3s^{-1} \qquad (1b)$$

where some part of liberated energy is stored in vibrationally excited HX molecules. The fast reaction of nitrogen oxide with molecular fluorine has been suggested to produce fluorine atoms

$$NO + F_2 \rightarrow NOF + F \qquad k_2 = 7 \times 10^{-13} e^{-1150/T}\ cm^3s^{-1} \qquad (2)$$

Chlorine atoms can be generated efficiently in a chain-branching reaction

$$ClO_2 + NO \rightarrow ClO + NO_2 \qquad k_3 = 3.4 \times 10^{-13}\ cm^3s^{-1} \qquad (3)$$
$$ClO + NO \rightarrow Cl + NO_2 \qquad k_4 = 1.7 \times 10^{-11} e^{-120/T}\ cm^3s^{-1} \qquad (4)$$
$$Cl + ClO_2 \rightarrow 2\,ClO \qquad k_5 = 5.9 \times 10^{-11}\ cm^3s^{-1} \qquad (5)$$

Both reaction systems are accompanied by a number of loss processes, which are summarized in our paper.[4] According to a detailed analysis based on published reaction rates of possible reactions of these reactants and products with components of the COIL medium (singlet oxygen, excited I atoms), the atomic iodine production by the proposed methods directly in COIL was not precluded. A mathematical modeling of the both reaction

* E-mail:spaleko@fzu.cz

XIII International Symposium on Gas Flow and Chemical Lasers and High-Power Laser Conference,
Antonio Lapucci, Marco Ciofini, Editors, Proceedings of SPIE Vol. 4184 (2001)

systems for conditions typical in a subsonic stream of singlet oxygen in the supersonic COIL has been performed.[4] According to results of the modeling atomic chlorine is more appropriate precursor than atomic fluorine. Reactions leading to the atomic iodine production via chlorine are accomplished on a shorter reaction path (several centimeters at gas velocity of 100 m $s^{-1}$) than via fluorine, and with I yield up to 80 % in optimum conditions (assuming an instantaneous mixing of reactants). The promising results of modeling brought us to an experimental verification of the proposed generation of atomic iodine for flow and pressure conditions similar to a subsonic region of COIL, i.e., a gas velocity of 100 m $s^{-1}$, and atomic iodine partial pressure of several tens of Pascal.

## 2. EXPERIMENTAL

Fig. 1 shows a scheme of the small scale experimental device constructed for testing a principle possibility to generate atomic iodine in COIL-similar conditions. Chlorine dioxide diluted with nitrogen (1:40) is introduced into the through-flow chemical reactor 1 as a primary gas. Nitrogen oxide mixed with nitrogen (1:9) is injected in two streams by injectors I#1 and I#2, and last, hydrogen iodide diluted with nitrogen (1:8.5) is admixed by injector I#3. Nitrogen oxide is injected consecutively in two streams because the ClO radical, the reaction product of $ClO_2$ with the first NO molecule (eq. (3)), has longer lifetime than atomic chlorine (the product of the second step - eq.(4)). A design of the reactor allows to vary distances between injectors and so to optimize a time span between injection of reactants. A flow rate of each secondary gas is controlled by a stainless steel needle valve and evaluated from a pressure measured before a diaphragm orifice (in flowmeters 6, 7, and 8), in which the sonic speed is fulfilled. The reactor is made of stainless steel tube of 10 mm in inner diameter, the gas injectors I are made of stainless steel tube of 5 mm in outer diameter. Gases are injected through openings drilled perpendicularly to the injector axis at the end of each injector. A diameter and number of openings of each injector were calculated to attain both a full penetration of each secondary flow into the primary flow, and a needed pressure downstream the measuring diaphragm orifice in each gas flowmeter. Gaseous chlorine dioxide used as a precursor of atomic chlorine, is produced in the column 2 by reaction of gaseous chlorine with solid sodium chlorite[5]

$$2\ NaClO_2(s) + Cl_2(g) \rightarrow 2\ ClO_2(g) + 2\ NaCl(s) \qquad (6)$$

Chlorine was diluted by nitrogen in the ratio 1:50 to assure, for safety reasons, a partial pressure of $ClO_2$ lower then 4 kPa (30 Torr). A flow rate of both gases was measured by rotameters 3 and 4. Operating pressure in the column 2 was controlled by valve 5 and maintained at about 100 kPa. For analysis, the exiting gas was absorbed in 2 % KI, and this solution titrated with 0.05 M $Na_2S_2O_3$, first in neutral, and then in acidic medium. A flow rate of both $ClO_2$ and residual chlorine were evaluated from these analyses.

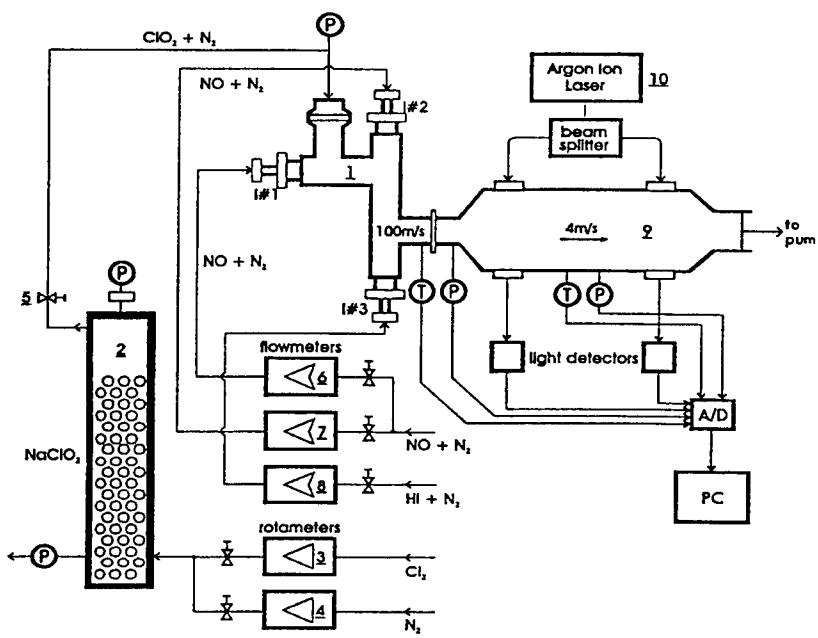


Fig.1: Scheme of a small scale device for atomic iodine generation

The rate of atomic iodine production was determined indirectly from a concentration of molecular iodine formed by I atoms recombination. A designed diagnostic cell **9** allowed to measure $I_2$ concentration in two locations, in which a different degree of I recombination is expected issuing from the rate of termolecular reaction

$$I + I + M \rightarrow I_2 + M \qquad k_7 = 4.2 \times 10^{-32}\ cm^6\,molec^{-2}\,s^{-1}\ (M = N_2) \qquad (7)$$

For a pumping rate of the rotary pump used (25 $m^3\ h^{-1}$), a time interval between the HI injection and the first detection cell is 7 ms, or 120 ms for the second detection cell, respectively. Molecular iodine concentration was measured from the light absorption at 488 nm using the split beam of Ar ion laser **10** and Si diodes for detection. The amplified electric signals of the diodes, the gas flowmeters, and the Ni-NiCr thermocouple monitoring gas temperature were processed by AD converter and PC on-line. A gas velocity in the reactor was 100 m $s^{-1}$, and 4.7 m $s^{-1}$ in the diagnostic cell at the full pumping rate. The gas mixture is exhausted from the diagnostic cell through a scrubber (with sodium hydroxide) and liquid nitrogen trap by a rotary pump.

## 3. RESULTS AND DISCUSSION

### 3.1 $ClO_2$ generator operation

The $ClO_2$ generator containing approx. 3 l $NaClO_2$ produced in average from 60 to 80 μmol $ClO_2$ $s^{-1}$ with 80 % yield. The $ClO_2$ production could be increased even up to 120 μmol $s^{-1}$ at a higher chlorine flow rate but with the 70 % yield only. The production rate with the same filling of $NaClO_2$ was by 10 % lower after two months of intermittent operation (though the chemical conversion of $NaClO_2$ by reaction (6) was insignificant).

### 3.2 Molecular iodine production

Simultaneously with the I atoms production and their successive recombination, molecular iodine may be formed also by the reaction of residual molecular chlorine with hydrogen iodide

$$Cl_2 + 2\,HI \rightarrow 2\,HCl + I_2 \qquad (8)$$

As the rate constant of reaction (8) has not been found in literature, we evaluated $k_8$ experimentally in order to estimate the effect of this reaction on the total $I_2$ concentration measured in the detection cells. For this purpose, $Cl_2$+$N_2$ mixture was introduced directly into the reactor **1**, gas mixture HI+$N_2$ into the injector **#3**, and $I_2$ concentration was measured in both detection cells. The rate constant $k_8 = (3.4 \pm 1.7) \times 10^{-33}\ cm^6\,molec^{-2}\,s^{-1}$ was obtained from six experiments performed at different $ClO_2$ and HI flowrate.

### 3.3 Atomic iodine production

An example of the measured time course of molecular iodine flow rate in the first and second detection cells for different flowrate of HI is shown in Fig. 2. These data together with other results are summarized in Tab.1.

Tab l.

Flowrate of reactants and molecular iodine, *n*, yield of atomic iodine, *Y*, and total pressure in the reactor, $P_{tot}$

| $n_{ClO2}$, μmol $s^{-1}$ | $n_{Cl2}^{resid.}$, μmol $s^{-1}$ | $n_{NO}(1),(2)$ μmol $s^{-1}$ | $n_{HI}$, μmol $s^{-1}$ | $n_{I2}(a)$, μmol $s^{-1}$ | $n_{I2}(b)$, μmol $s^{-1}$ | $n_{I2}'(a)$, μmol $s^{-1}$ | $n_{I2}'(b)$, μmol $s^{-1}$ | $Y_I(a)$, % | $Y_I(b)$, % | $P_{tot}$, kPa |
|---|---|---|---|---|---|---|---|---|---|---|
| 60 | 7.3 | 60 | 55 | 6.0 | 6.6 | 0.005 | 0.09 | 20 | 22 | 1.92 |
| 60 | 7.3 | 60 | 116 | 10.6 | 14.4 | 0.024 | 0.40 | 35 | 47 | 2.10 |
| 60 | 7.3 | 60 | 55 | 5.0 | 6.0 | 0.005 | 0.09 | 17 | 20 | 1.92 |
| 60 | 7.3 | 60 | 70 | 8.8 | 10.3 | 0.075 | 1.14 | 29 | 31 | 4.06 |
| 78.7 | 10.8 | 60 | 53 | 9.5 | 12.7 | 0.007 | 0.12 | 32 | 42 | 1.92 |
| 78.7 | 10.8 | 60 | 69 | 7.8 | 10.8 | 0.180 | 2.53 | 25 | 28 | 4.93 |

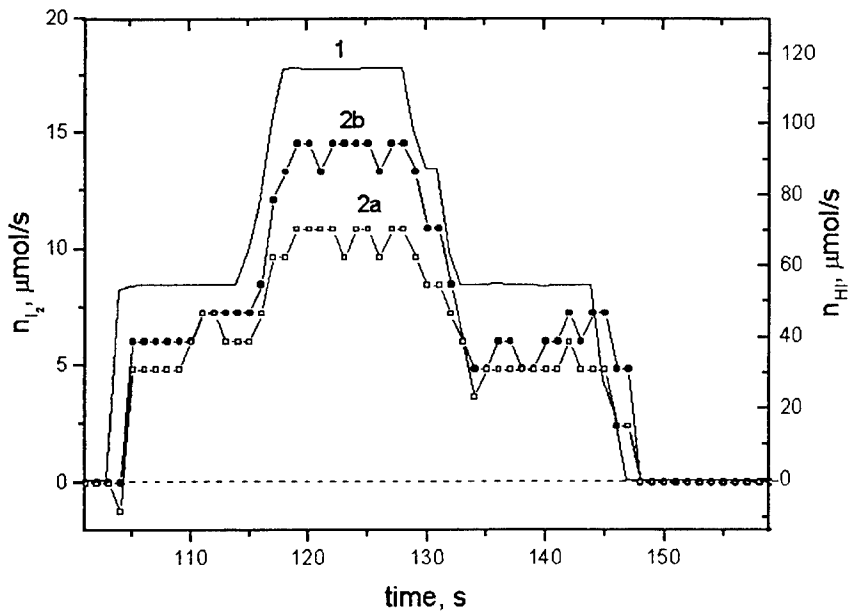


Fig. 2: Time course of HI flowrate (1), and $I_2$ flowrate through the first (2a), and second (2b) detection cell. Primary flow: 60 µmol $ClO_2$ $s^{-1}$, 1st injector: 60 µmol NO $s^{-1}$, 2nd injector: 60 µmol NO $s^{-1}$

In these experiments, a distance between the first and second injector openings was adjusted to 2.8 cm, between the second and third injector openings to 0.37 cm. The HI flowrate was varied while NO and $ClO_2$ flowrate remained constant, so that the concentration of nitrogen dioxide (the by-product of reactions (3) and (4)) and also $NO_2$ contribution to the light absorption remained constant being included into a baseline of photodiodes.
Table 1 presents flow rates of reactants, and molecular iodine through the first, $n_{I2}(a)$, and the second detection cell, $n_{I2}(b)$, evaluated from the measured light absorption. A flow rate of molecular iodine formed by the reaction (8), $n_{I2}'$, was calculated using the estimated rate constant $k_8$ and the flow rate of HI and residual chlorine. This calculation does not consider hydrogen iodide consumed in much faster simultaneous reaction (1b), so that $n_{I2}'$ represents the highest estimate of the $I_2$ production rate by eq. (8). As a consequence, the difference ($n_{I2}$-$n_{I2}'$) denotes the minimum estimate of the flow rate of molecular iodine formed by recombination of iodine atoms. The yield of atomic iodine was calculated as the ratio $2(n_{I2}-n_{I2}')/n_{NO}(1)$. In the performed measurements, gas temperature in the first detection cell was in the range of 70 to 85 °C. The yield of atomic iodine became higher with increasing HI flowrate, and was between 20 and 50 %.
In accordance with the rate of the reaction (7), the measured $I_2$ flowrate in the first detection cell, $n_{I2}(a)$, is lower than in the second cell, $n_{I2}(b)$. Assuming this kinetics, the recombination of atomic iodine is not fully accomplished in the second cell, so that the actual yield of iodine atoms may exceed the data presented in Tab.1 and Fig. 2. These conclusions, however, do not meet the results issuing from relatively faster reactions of iodine atoms with nitrogen dioxide published by Buben[7]

$$I + NO_2 + M \rightarrow INO_2 + M \qquad k_9 = 1.68 \pm 0.38 \times 10^{-31}\ cm^6 molec^{-2} s^{-1} \qquad (9)$$
$$I + INO_2 \rightarrow I_2 + NO_2 \qquad k_{10} = 8.3 \times 10^{-11}\ cm^3 s^{-1} \qquad (10)$$

Using the rate constants $k_9$ and $k_{10}$, the recombination of iodine atoms should be accomplished in the first detection cell, and consequently, $I_2$ flowrate in both cells should be equal. It is expected that a final answer will be given when the planned direct atomic iodine detection using the diode probe laser diagnostics[7] is used.
In comparison with results of modeling of the reaction system,[4] the experimentally obtained yield of atomic iodine is somewhat lower. This can be explained by the assumption of instantaneous mixing of reactants in the mathematical model and/or eventual not full recombination of iodine atoms in the detection cells. The temperatures determined in the measurements are substantially lower than the calculated values.[4] The most probable reason is a substantial part of liberated reaction energy stored in vibrationally excited HCl molecules.[8]

## 4. CONCLUSION

Preliminary experiments were performed that verified a possibility to generate atomic iodine by chemical reactions of gaseous reactants in conditions suitable to COIL. Atomic iodine was generated with a yield up to 50 % in reaction of hydrogen iodide with atomic chlorine, which was produced by a reaction of chlorine dioxide with nitrogen oxide. A more reliable results are expected from a direct atomic iodine detection using the diode probe laser diagnostics, which is planned in a near future.

## 5. ACKNOWLEDGMENT

This work was supported by the USAF European Office for Research and Development (EOARD), the Contract F6177-99-WE059. The authors thank to Dr. G. Hager from the USAFRL for his advice in this work.

## 6. REFERENCES

1. V.S. Pazyuk, N.P. Vagin, N.N. Yuryshev, *Proc. SPIE* Vol. **2767**, p. 206, 1995
2. M. Endo, M. Kawakami, S. Takeda, F. Wani, T. Fujioka, *Proc. SPIE* Vol. **3612**, p. 56, 1999
3. T.L. Hanshaw, T.J. Madden, J.M. Herbelin, G.C. Manke, B.T. Anderson, R.T. Tate, G.D. Hager, *Proc. SPIE* Vol. **3612**, p. 147, 1999
4. V. Jirasek, O. Špalek, J. Kodymová, *Proc. of this conference* (contribution P1.15)
5. R.D. Suart, D.R. Snelling, K.D. Foster, R. Lambert, DREV Report 1005-76, Defense Research Establishment, Valcartier, Quebec, Canada.
6. S.N. Buben, I.K. Larin, N.A. Messineva, E.F. Trofi,ova, Kinetika i Kataliz **31**, p.. 973, 1990 (in Russian)
7. S.J. Davis, M.G. Allen, W.J. Kessler, K.R. McManus, M.F. Miller, P.A. Mulhall, *Proc. SPIE* Vol. **2702**, p. 195, 1996
8. N. Jonathan, C.M. Melliar-Smith, S. Okuda, D.H. Slater, D. Timlin, *Mol.Phys.* **22,** p. 561, 1971

# Study of Energy Performances of Supersonic COIL Operating with Twisted–Aerosol SOG

Anatoly A. Adamenkov, Victor V. Bakshin, Valentin I. Efremov, Sergey P. Ilyin, Yuri V. Kolobyanin, Ivan M. Krukovski, Eugeny A. Kudryashov, Vladimir B. Moiseev, Boris A. Vyskubenko
Russin Federal Nuclear Center - VNIIEF
Mira prosp. 37, Sarov, 607190, Nizhni Novgorod region, Russia

## ABSTRACT

An experimental study of energy performances and chemical efficiency of supersonic COIL with twisted aerosol SOG and the parallel-flow system was made. An experimental supersonic COIL setup is present.

**Keywords:** Chemical Oxygen Iodine Laser (COIL), supersonic nozzle, gases mixing, chemical efficiency.

## 1. INTRODUCTION

The source idea of the mixing device for oxygen-iodine laser (COIL), that was generated around the phenomenon of molecular iodine dissociation during its mixing with singlet oxygen in subsonic flow with subsequent expanding and cooling of laser active mixture inside subsonic nozzle /1/, has allowed a high chemical efficiency of COIL demonstrated as about 27 %. This result was obtained applying a large amount of buffer helium ($Cl_2$:He=1:4) in singlet oxygen generator (SOG) to reduce singlet oxygen transport loss and in-resonator working mixture temperature. After changing helium with nitrogen, the COIL chemical efficiency went down to about 16 % level /2/. These-days' publications discuss extensively various conceptions of more advanced mixing nozzles for COIL /3-5/. The essence of those concepts is that while creating any modern mixing device one must at the same time provide for high chemical efficiency of COIL and high stagnation pressure (recovery) of working gas. This will lower the inputs for spent gas exhaust and is essential for laser industrial facilities. We suggest the increase of singlet oxygen pressure at the nozzle unit inlet be by far more promising. In this case it will be possible to decrease essentially the ratio of concentrations of water vapor and singlet oxygen as well as the relative singlet oxygen loss in molecular iodine dissociation. This consideration underlies the concept of the state-of-the-art high-pressure COIL suggested previously by us in refs. /6-8/ and developed around the combination of a parallel gaseous iodine – singlet oxygen flow mixing system and high-pressure singlet oxygen generator.
The present paper reports on the first step on the way of testing the concept. Namely, under the low-pressure conditions (about 10 Torr) of singlet oxygen we have obtained the experimental results for verifying over the data of various publications. The work primary objective was experimental research into the energy performance of the supersonic COIL using the parallel-flow mixing system suggested earlier by us in ref. /6-8/ as well as testing of the twisted aerosol singlet oxygen generator (TA SOG) /9-11/ operating into the supersonic COIL.

## 2. EXPERIMENTAL SETUP

A photo of the experimental setup is shown in Fig. 1. The experimental setup utilizes a twisted aerosol singlet oxygen generator (TA SOG) /9-11/. The TA SOG provides for two-stage delivery of buffer gases (nitrogen) into the reactor: jointly with chlorine and through a special ejector device at the reaction zone outlet. The gas velocity at the reactor outlet is up to $V_{out} \approx 85$ m/s when chlorine and buffer gases are portioned as $Cl_2$:Buff.1:Buff.2=1:2:1. These are the major reactor values:

- gas pressure at the reactor outlet – 70-75 Torr;
- singlet oxygen yield - 70 % at least;
- chlorine utilization - above 95 %.

The system of BHP making is intended to prepare for TA-SOG any predetermined ratio of the working solution ($KOH+H_2O_2+H_2O$) components and cool this down to a working temperature about -20°C.
A nozzle unit made currently by us for experimental setup activity represents a mononozzle which critical section height $h^*$ was let to range from 2 to 4 mm at the respective opening ratio $h/h^*$. The Mach number calculated for 2-mm critical section


XIII International Symposium on Gas Flow and Chemical Lasers and High-Power Laser Conference,
Antonio Lapucci, Marco Ciofini, Editors, Proceedings of SPIE Vol. 4184 (2001)

and adiabatic exponent $\gamma$=1.4 is M≈3. The supersonic nozzle profile was shaped as the seventh flow line that is continued as a straight line sloped at $\alpha=2.5^0$. The active length of the nozzle was 150 mm across the flow.

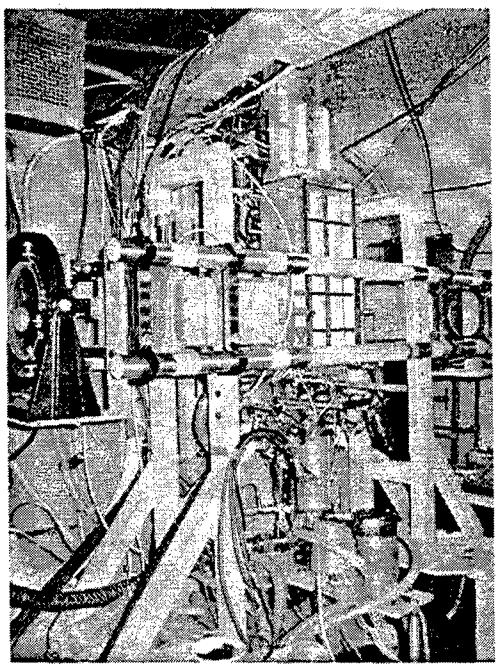

**Fig. 1.** Experimental COIL setup.

Gaseous iodine and a carrier gas (nitrogen or helium) are delivered into singlet oxygen flow with the aid of a tube injector. The injector is composed of 149 tubes, outer diameter 1 mm and inner diameter 0.65 mm, distributed in two rows with 2-mm spacing on the exit edge of the wing-shaped central body.The tubes of the injector are oriented in the singlet-oxygen flow direction thus allowing us – by moving the injector - to vary and optimize the position of the iodine injection plane with respect to the critical section of the supersonic nozzle and within the wide limits from 20 mm in subsonic to 3 mm in supersonic regions. The same nozzle construction (Fig. 2) were also used in our previous gas-dynamic laser (GDL) investigations when this allowed us to reach the record-breaking specific energy values /6/.

The laser resonator built around matrix mirrors and also well showing itself during the GDL study was described earlier in ref. /6/ and is shown in Fig. 3. For gas-flow effect protection, the resonator mirrors were placed into special "pockets", 360 mm depth, pressurized with pure helium. The mirror separation is about 870 mm. The "pockets" were isolated from the supersonic channel with operated shutters. The cavity end mirror is composed of three square mirrors 40×40 mm$^2$ accommodated on a common support so that their axes are parallel to each other. The radius of curvature of each mirror is R=10 m.

The reflection factor of the dielectric covering of the cavity end mirrors is 0.993. The flat outcoupler was commonly used by all three resonators and had a rectangular shape 40×120 mm$^2$. The outcoupler transmittance could be varied from 0.01 to 0.04.

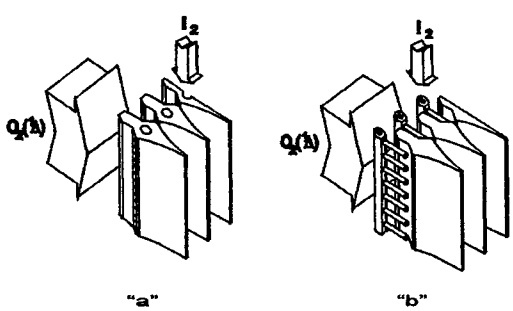


**Fig. 2.** Supersonic COIL's mixing systems:
"a" – traditional mixing system with transverse iodine injection into singlet oxygen flow through holes in the nozzle's walls, "b" – mixing system with iodine injection in parallel to singlet oxygen flow through thin tube injector.

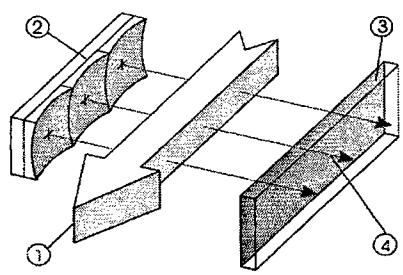


**Fig. 3.** Small-scale COIL resonator's scheme with matrix mirror: 1 – gas flow, 2 – matrix nontransmitting mirror, 3 – output half-transmitting mirror, 4 – laser emission.

The optical axes of the first, second and third resonators are accordingly at about 60, 100, and 140 mm distance of the critical nozzle section. The resonator design had the possibility to travel along the flow within a distance up to 250 mm of the critical section. A supersonic diffuser is intended to change the supersonic COIL flow into the subsonic and to decouple gasdynamically between the optical laser cavity and vacuum tank.

Gaseous iodine delivery system function is to produce gaseous iodine and deliver it into the injector of the nozzle unit to mix with singlet oxygen. Gaseous iodine is generated in a vaporizer-type system. Crystalline iodine is heated in a self-contained vessel up to a predetermined level of saturated vapor and via a sonic nozzle flows into a duct delivering warmed

carrier (helium or nitrogen) and further into the injector of the nozzle unit. The iodine flowrate was adjusted by changing the nozzle diameter and in-tank pressure, and the carrier flowrate – by changing sizes of a delivery orifice and the pressure in front of it. To prevent condensation, the iodine delivery duct is maintained at about 100 $^0$C. An assistant gases delivery system includes subsystems to deliver buffer gases (nitrogen) into the reactor, a subsystem to deliver carrier into the iodine system duct, a subsystem to deliver a gas to purge the mirrors, chlorine displacement subsystems, and liquid (BHP) displacement subsystems for the reactor. The assistant gases flowrates are determined from the pressure drop readings on calibrated delivery orifices. All the subsystems are equipped with filters. An evacuating system consists of a vacuum tank, volume of 5 m$^3$, pumps to remove gases, and a neutralization system to detoxify chlorine and iodine. The residual pressure of the evacuating system doesn't exceed $10^{-1}$ Torr. COIL experimental setup measurements are being performed with a computerized control system. This complex was implemented around a personal computer, type IBM PC, and is divided functionally into two systems – monitoring and logging. Both systems are closely interconnected by sharing the same hardware and software. The facility control as well as data acquisition and processing were fully automated with the development of this complex.

## 3. EXPERIMENTAL RESULTS AND DISCUSSION

The experiments were performed with nitrogen used as a buffer gas in the proportion $O_2$:Buff.1:Buff.2=1:2:1 at the total gas pressure 70 to 75 Torr at the SOG outlet. The molar flowrate of the iodine carrier (Buff.3) was approximately equal to the molar flowrate of oxygen ($O_2$:Buff.3=1:1). Thus, the oxygen to buffer nitrogen molar ratio was in our experiments equal to $O_2$:$N_2$=1:4 and the singlet oxygen pressure at the nozzle inlet was about 10 Torr.

Varying the position of the gaseous iodine injection plane from 15 mm in subsonic to 0.5 mm in supersonic regions with respect to the critical section of the supersonic nozzle, we were able to measure the experimental relative emission power of COIL as shown in Fig. 4. It is seen from the figure that under the conditions of the reported experiments the optimal distance constituted about 1.5 mm of the critical section in subsonic region. Variation of the outcoupler transmittance at the optimal iodine injection plane positioning has shown that the optimal - for getting the highest chemical efficiency - value of this factor was ~ 1 %.

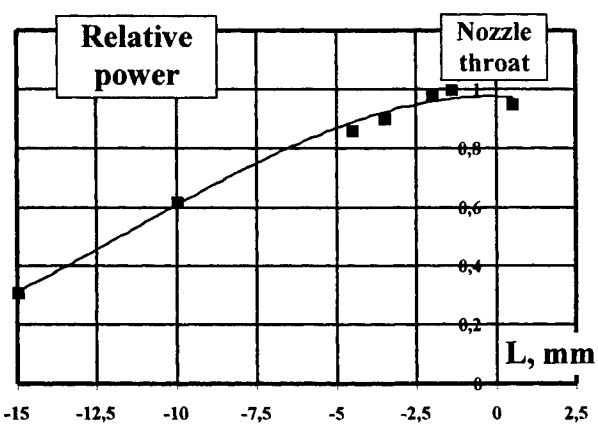


**Fig.4.** Relative COIL power vs. situation of iodine injection plane with respect to critical nozzle section.

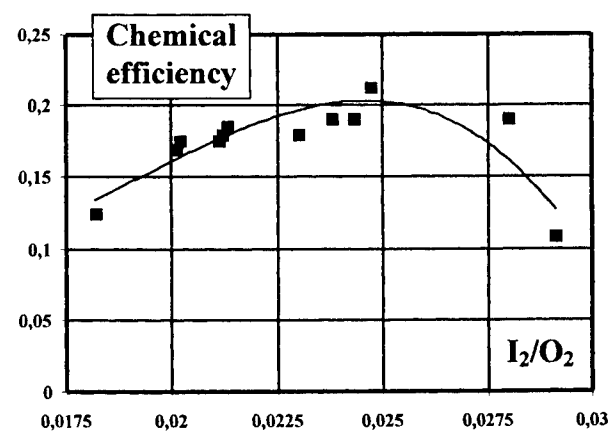


**Fig.5.** Chemical efficiency of COIL vs. ratio of iodine and oxygen concentrations for the optimal position of iodine injection plane.

Fig. 5 gives the chemical efficiency of COIL as functions of the ratio of iodine and oxygen concentrations measured for the optimal iodine injection plane position. As seen from the figure, the optimal iodine-to-oxygen ratio was about 0.025 in our experiments. This ratio is somewhat higher than in most reported works, which relates, possibly, to the lower dissociation degree of molecular iodine occurred with the mixing system in use and under the low pressure of singlet oxygen. It should be noted that in case of the optimal iodine concentration only two first mirrors of the matrix resonator are equipped. When the iodine concentration goes down, all three matrix resonator mirrors start to steadily act providing pickup of the inversion from the active medium 120 mm long in flow direction. This allows us to hope for getting higher energy performances of COIL after optimization of iodine concentration and position of optical resonator. The highest chemical efficiency of the laser reached for the emission arriving from the outcoupler direction was about 17 % at the 1.1 %- transmittance of the last. Allowing for the transmittance value of the "non-transmitting" mirror (~0.3 %), we estimated the total chemical efficiency

of the laser as 21 %, which is in a good agreement with the data reported by other authors /2, 12/. One may expect that an increase in the singlet oxygen pressure at the nozzle inlet would increase the dissociation degree of molecular iodine giving a possibility to reduce the relative iodine concentration, loss in the energy stored in singlet oxygen, and gas-flow temperature inside the laser cavity and to raise the chemical efficiency of the laser.

## 4. CONCLUSIONS AND ACKNOWLEDGEMENT

1. An experimental facility has been created to investigate into the energy performance of COIL for broadly ranged values of interest.
2. A supersonic COIL model has been developed realizing mixing of parallel flows of gaseous iodine and singlet oxygen; and its high efficiency has been successfully demonstrated.
3. The twisted aerosol singlet oxygen generator (TA SOG) operation together with the supersonic COIL has been tested and its high efficiency and reliability have been demonstrated.
4. An experimental study has been conducted of the specific energy performances and chemical efficiency of the supersonic COIL for a singlet oxygen pressure about 10 Torr at various positioning of the injection plane, iodine concentration, and output mirror transmittance.
5. Chemical efficiency of COIL above 20 % has been reached with nitrogen used as a buffer gas.

The authors consider it as their pleasant duty to thank the scientists of the Samara Division of the Lebedev Physics Institute – V.D. Nickolaev and M.V. Zagidullin – for useful discussions of the work.
The work was supported financially by the International Science and Technology Center, Moscow (ISTC Project #1118).

## REFERENCES

1. P. V. Avizonis, G. Hasen, K. A. Truesdell, **"The Chemically Pumped Oxygen - Iodine Laser"**, Proceeding of SPIE, Vol. 1225, pp. 448 - 477 (1990).
2. T.L. Rittenhouse, S.P. Phipps, and C.A. Helms, **"Performance of a High-Efficiency 5 cm Gain Length Chemical Oxygen-Iodine Laser"**, IEEE J. Quantum Electron., vol. 35, June 1999, pp.857-866.
3. Valeri D. Nikolaev, **"Comparative analysis of the different methods of preparing active medium in supersonic COIL"**, Proceeding of SPIE Vol. 3268, 157-162 (1998).
4. D.L. Carroll and W.C. Solomon, D. King, L. Fockler, D. Stromberg, M. Sexauer, A. Milmoe and L.H. Sentman, **"Advanced Mixing Nozzle Concepts for COIL"**, Proceedings of International Conference on «Lasers'99», V.J. Corcoran and T.A. Goldman, Editors, STS PRESS, McLean, VA, 1999, pages 69 –77.
5. T.T. Yang, Y.C. Hsia, L.F. Moon, and R.A. Dickerson, **"Advanced Mixing Nozzle Concepts for COIL"**, Proceeding of SPIE Vol. 3931, pp. 116-130 (2000).
6. Yu.V. Kolobyanin, B.A. Vyskubenko, A.A. Adamenkov, V.V. Buzoverya, Yu.N. Bulkin, S.P. Ilyin, G.A. Kirillov, E.A. Kudryashov and Yu.V. Savin. **"Selection of the Optimum Mixing System for Supersonic Gas Flow Laser"**, Proceedings of International Conference on «Lasers'96», V.J. Corcoran and T.A. Goldman, Editors, STS PRESS, McLean, VA, 1997, pages 175-181.
7. A.A. Adamenkov, B.A. Vyskubenko, N.N. Gerasimenko, V.A. Eroshenko, Yu.V. Derjugin, D.K. Zelensky, I.M. Krukovsky, E.A. Kudryashov, **"High Pressure Iodine-Oxygen Laser Problem"**, Proceeding of SPIE Vol. 2767, pages 209-215, (1996).
8. A.A. Adamenkov, B.A. Vyskubenko, N.N. Gerasimenko, Yu.V. Derjugin, D.K. Zelensky, S.P. Ilyin, I.M. Krukovsky, E.A. Kudryashov, **"Oxygen – iodine laser capacity at the elevated pressure"**, Proceeding of SPIE Vol. 3092, pages 581-584 (1997).
9. F. Wani, M. Endo, B.A. Vyskubenko, S. Takeda, T. Fujioka, H. Fujii, **"Experimental Study of Singlet Oxygen Generator for the COIL"**, 29th Plasmadynamics and Lasers Conference, June 15-18, 1998, Albuquerque, NM, AIAA 98-2990.
10. F. Wani, M. Endo, B.A. Vyskubenko, S.P. Ilyin, I.M. Krukovsky, S. Takeda, T. Fujioka, **"Parametric Study of a Twisted Aerosol-Type Singlet Oxygen Generator"**, IEEE J. Quantum Electron., vol.34, NOV. 1998, pp. 2130-2137.
11. Ivan M. Krukovsky, Anatoly A. Adamenkov, Boris A. Vyskubenko, Yuriy N. Deryugin, Sergey P. Ilyin, Eugeny A. Kudryashov, **"Investigation of the Singlet Oxygen Generator with the Twisted Flow"**, Proceeding of SPIE Vol. 3931, 99-108 (2000).
12. V.D. Nickolaev, M.V. Zagidullin, **"Completely Scaleable 1 kW Class COIL with Verti-JSOG and Nitrogen Buffer Gases"**, AIAA-99-3815, 1999.

# Production of Gas-Phase Singlet Oxygen from Organic Ozonides

**John Vetrovec**
The Boeing Company, Rocketdyne Propulsion & Power,
6633 Canoga Avenue, Canoga Park, Calif. 91309, U.S.A.
tel. (818) 586-3101, fax (818) 586-3074
jan.vetrovec@boeing.com

## ABSTRACT

This work examines the prospects of generating gas-phase $O_2(^1\Delta)$ from thermal decomposition of $(C_6H_5O)_3PO_3$ for use in the oxygen-iodine laser. The process promises major advantages over the traditional production of $O_2(^1\Delta)$ from the reaction of $Cl_2$ with basic hydrogen peroxide, namely (1) producing $O_2(^1\Delta)$ from a single liquid fuel (as opposed to reacting liquid fuel and oxidant gas), (2) fuel with a long storage life, (3) up to four times lower heat release which greatly reduces needs for refrigeration, and (4) simple hardware.

## INTRODUCTION AND BACKGROUND

The atomic iodine laser operating on the transition I $(^2P_{1/2}) \rightarrow$ I $(^2P_{3/2})$ + hν (1.315 μm) was discovered over 35 years ago [1]. It was subsequently recognized that iodine can be dissociated and pumped to the I $(^2P_{1/2})$ state by energy transfer from singlet oxygen ($O_2(^1\Delta)$) [2]. The only technique successful in producing gaseous $O_2(^1\Delta)$ in concentrations sufficient to operate the oxygen-iodine laser uses the reaction of $Cl_2$ with an aqueous solution of basic hydrogen peroxide (BHP) [3]. The laser using this process is known as the chemical oxygen-iodine laser (COIL) and continues to be a subject of intense research [4]. However, the $Cl_2$-BHP reaction for generating $O_2(^1\Delta)$ has significant operational drawbacks, which includes corrosiveness and limited storage life of the reactants, and the need for complex reactant feed system involving pumps, tanks, and heat exchangers.

Numerous other processes have been shown to produce $O_2(^1\Delta)$ [5]. Some of these hold a promise of producing gas-phase $O_2(^1\Delta)$ in concentrations suitable for oxygen-iodine laser and replace the $Cl_2$-BHP reaction. One of the more promising schemes that has received significant attention involves an electric discharge in a flow of $O_2$, $O_2$ carrying gas, or oxygen-rich gaseous compound, see e.g., [6,7]. However, this method has not been successful attempts at producing $O_2(^1\Delta)$ in concentrations sufficient to operate the oxygen-iodine lasers. Another promising, but thus far unsuccessful process for producing $O_2(^1\Delta)$ for the oxygen-iodine laser involves a photolytic decomposition of ozone ($O_3$) by ultraviolet light [8,9].

## $O_2(^1\Delta)$ FROM DECOMPOSITION OF OZONIDES

A variety of organic compounds including some from the triaryl phosphite family, certain phosphines, sulfides, sulfones, benzaldehyde, and methyl isopropyl ether, have been shown to form stable ozone adducts or endoperoxides, which can be thermally decomposed to yield $O_2(^1\Delta)$ [5]. To take advantage of the high reactivity of $O_2(^1\Delta)$ some of these processes have been commercially utilized for in-liquid oxidation of chemicals. For example, triphenyl phosphite-ozone adduct $(C_6H_5O)_3PO_3$ (TPPO3) can be formed by introducing $O_3$ into a solution of triphenyl phosphite $(C_6H_5O)_3P$ (TPP) in methylene chloride ($CH_2Cl_2$) solvent at about –78°C as

$$(C_6H_5O)_3P + O_3 \xrightarrow[CH_2Cl_2]{-78°C} (C_6H_5O)_3PO_3 \qquad \text{(Eq. 1)}$$

When the ozone adduct (also called ozonide) is allowed to warm up, triphenyl phosphate $(C_6H_5O)_3PO$ (TPPO) is produced and $O_2(^1\Delta)$ is evolved in liquid as

$$(C_6H_5O)_3PO_3 \xrightarrow[CH_2Cl_2]{>-35°C} (C_6H_5O)_3PO + O_2(^1\Delta) \qquad \text{(Eq. 2)}$$

This reaction has been reported to produce $O_2(^1\Delta)$ with the yield approaching 100% in liquid [10]. Figure 1 illustrates the basic steps of this process. Our analysis shows that producing gas-phase $O_2(^1\Delta)$ with a yield over 50% appears possible .


XIII International Symposium on Gas Flow and Chemical Lasers and High-Power Laser Conference,
Antonio Lapucci, Marco Ciofini, Editors, Proceedings of SPIE Vol. 4184 (2001)

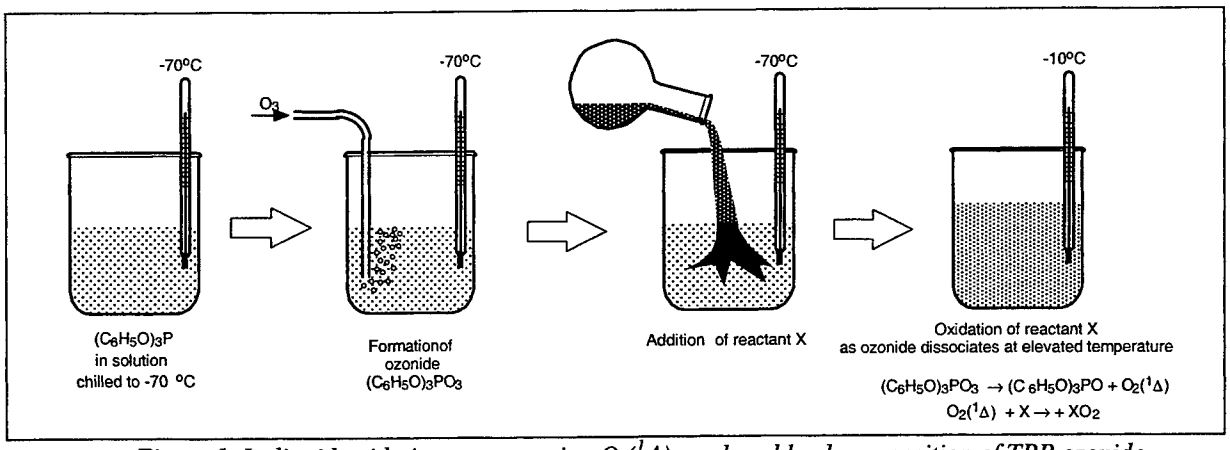


*Figure 1. In-liquid oxidation process using $O_2(^1\Delta)$ produced by decomposition of TPP ozonide*

## PROCESS CONSIDERATIONS FOR GAS-PHASE PRODUCTION OF $O_2(^1\Delta)$

Design of a process for gas-phase production of $O_2(^1\Delta)$ for use in the oxygen-iodine laser must consider factors such as ozonide storage life, triggering of ozonide decomposition, heat release, properties of suitable solvents, compatibility with laser processes, and $O_2(^1\Delta)$ quenching in liquid. In the process shown in Figure 1, $O_2(^1\Delta)$ generated by the decomposition of TPPO3 is consumed in liquid solution rather than being extracted to the gas phase. Extracting $O_2(^1\Delta)$ into the gas-phase requires diffusion of liquid-borne $O_2(^1\Delta)$ molecules to liquid surface. During the diffusion, however, a significant fraction of $O_2(^1\Delta)$ can be lost by deactivation to ground state via $O_2(^1\Delta) \rightarrow O_2\,(^3\Sigma) + h\nu$.

One of the critical steps is selecting a suitable solvent. Such a solvent should have a sufficiently low melting point, preferably well below –80°C, be resistant to oxidation, cause little or no ozonide decomposition, and exhibit low quenching of $O_2(^1\Delta)$ and $I(^2P_{1/2})$. Examples of suitable solvents include $CH_2Cl_2$, lower alcohols, and selected members of the Freon® family. Solvents in which hydrogen (protium) atoms have been replaced by deuterium are known to exhibit particularly low quenching of $O_2(^1\Delta)$. For example, $O_2(^1\Delta)$ lifetime in $CD_2Cl_2$ is 120 μs versus 59 μs in $CH_2Cl_2$ [11]. (Note that $O_2(^1\Delta)$ life time in BHP is only ~4 μs.) Concentrations of the TPP solution may range from 1 mol per liter to several moles per liter.

Solution of TPPO3 produced by reaction (1) can be stored at low temperature, typically around –100°C, until ready for use. The decomposition rate of TPPO3 depends primarily on the solvents and storage temperature. In particular, storage time $t_f$ at which a fraction $f$ of TPPO3 becomes decomposed can be estimated as

$$t_f = -ln\,(1-f)/(A\,e^{-E/(RT)}) \qquad \text{(Eq. 3)}$$

where $E$ is activation energy, $R$ is gas constant, $T$ is storage temperature, and $A$ is a constant specific to TPPO3 solvent. Under favorable conditions, a solution of TPPO3 can be stored for a considerable time. For example, TPPO3 in $CH_2Cl_2$ solvent ($E$ = 14.1 kcal/mol, $A = 1.57\times10^9$ sec$^{-1}$ [10]) can be stored at –100°C for about 2 years. This is a major improvement over the 1 to 10 day shelf life of BHP used in COIL.

## SINGLET OXYGEN GENERATOR (SOG) CONCEPT

Properly designed SOG will decompose most of the supplied TPPO3 fuel and extract a large fraction of produced $O_2(^1\Delta)$ into gas phase. For this purpose the SOG must be able to (1) rapidly heat the TPPO3 fuel to well above -35°C and (2) reduce the path length for $O_2(^1\Delta)$ diffusion to liquid surface. A possible approach is shown in Figure 2. TPPO3 solution from a pressurized cryogenic storage tank is first preheated to about -35°C and then supplied to the SOG atomizing nozzle. Atomized TPPO3 solution is then mixed into a flow of warm diluent gas and further heated. Heating rapidly decomposes the ozonide and produces $O_2(^1\Delta)$ according to Eq. (2). For example, 90% of TPPO3 in $CH_2Cl_2$ solvent heated to 100°C will decompose in about 100 milliseconds. Gaseous $O_2(^1\Delta)$ produced in this manner is separated from spent fuel (solution of TPPO) and provided to laser nozzle. If desirable, solvent vapors can be condensed from the flow.

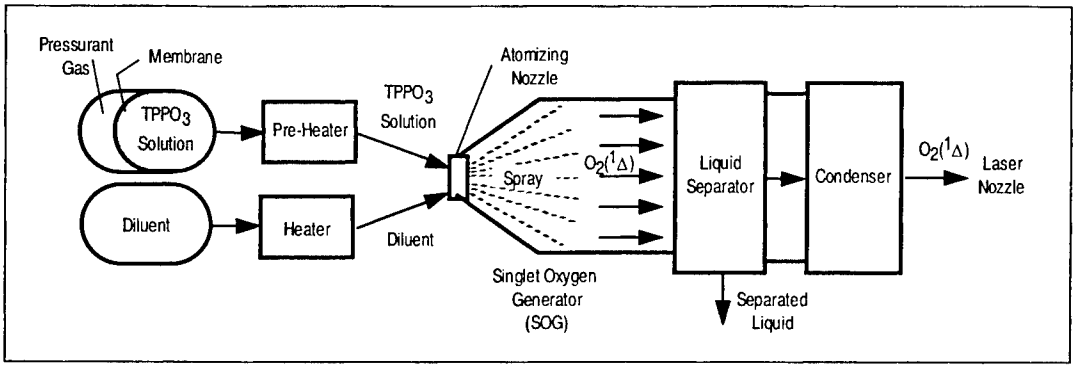


*Figure 2: Singlet oxygen generator and feed system for production of $O_2(^1\Delta)$ by decomposition of TPP ozonide*

Producing small droplet size is critical to obtaining a high $O_2(^1\Delta)$ yield. Reducing droplet size reduces diffusion path that $O_2(^1\Delta)$ molecule has to travel in the solvent from its point of origin to the liquid surface. Such a diffusion path should be on the order of the diffusion scale length defined as $x_s \sim (D\tau)^{1/2}$ where $\tau$ is $O_2(^1\Delta)$ lifetime in solvent and $D$ is a solvent-specific diffusion coefficient. For example, for TPPO3 in $CD_2Cl_2$ solvent with $\tau$ = 120 μs and D = 2.4 x $10^{-5}$ $cm^2/s$, $x_s$ is about 0.5 μm. For TPPO3 in $CCl_3F$ (Freon 11), $x_s$ is about 1.5 μm. The lifetime of $O_2(^1\Delta)$ in Freon 113 is particularly long (15,800 μs), resulting in $x_s$ of about 6 μm. Dependence of estimated $O_2(^1\Delta)$ yield on relative droplet size is shown in Figure 3.

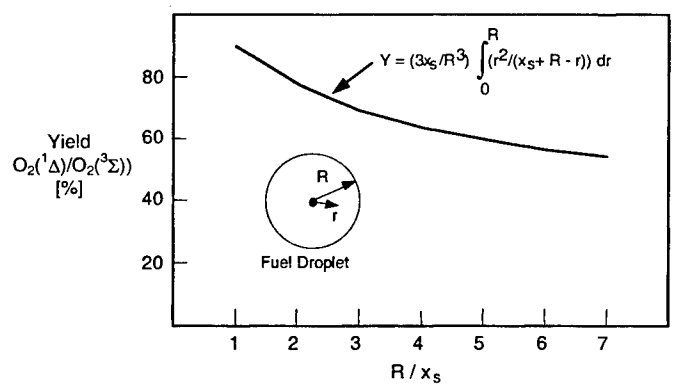


*Figure 3: Estimated $O_2(^1\Delta)$ yield versus droplet size relative to $x_s$ (R is assumed constant inside SOG)*

Besides using warm diluent, other techniques can be used to heat TPPO3 spray, namely high-intensity light, and ultrasonic or dielectric heating. The amount of supplied heat can be quite small as the decomposition is quite exothermic, releasing about 14 kcal/mol of TPPO3. Thus, the heat input is only required to decompose the outer layer of a fuel droplet. Once the decomposition is triggered, self-generated heat feeds the process. As seen in Figure 4, initial surface heating of a droplet establishes a "reaction zone," which then propagates into the bulk of the liquid, locally heating and decomposing the ozonite. Temperature rise of the surface layer will cause some solvent to evaporate, thus shrinking the droplet and reducing the $O_2(^1\Delta)$ diffusion pathlength. Evaporation of the solvent also carries away excess heat of reaction. It is theoretically possible to prepare a TPPO3 solution in which the heat of decomposition is sufficient to vaporize all the solvent.

## SYSTEM ATRIBUTES OF OZONE-OXYGEN-IODINE LASER (XOIL)

Ozone oxygen-iodine laser (XOIL) promises a substantial technical improvement over the chemical oxygen-iodine laser (COIL) and other chemical lasers. In XOIL, $O_2(^1\Delta)$ is produced from mono-fuel, as opposed to reacting fuel and oxidant. Furthermore, TPPO3 fuel becomes completely expended in a single pass through the SOG. As a result, the fuel system could use simple, compact, light-weight hardware. TPP is an inexpensive commercial chemical commonly used as an oil additive and stabilizer for PVC [12]. TPPO3 fuel is non-reactive and has a storage life of at least several years. Expended fuel is nonreactive, and nonflammable. TPPO contained in expended fuel is also a common industrial substance used as a flame-retardant plasticizer [ibid]. Heat release during $O_2(^1\Delta)$ production is 3-4 times less than in COIL. Real-time cooling could be conveniently provided by evaporation of fuel solvent and the resulting vapor may be used as diluent. XOIL system would have no recirculating liquid, pumps, rotating machinery, refrigeration equipment, or large heat exchangers. Figure 5 compares essential elements of COIL and XOIL systems.

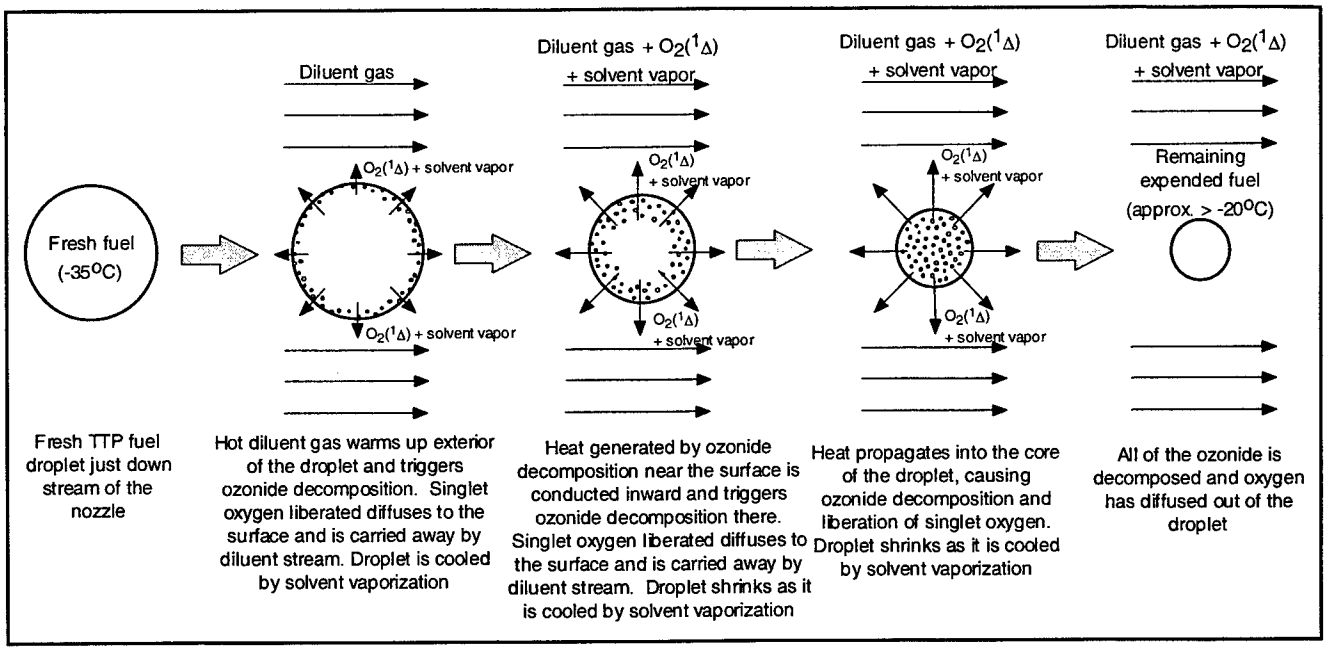


*Figure 4. Process for extraction of $O_2(^1\Delta)$ from droplet of ozonide solution*

| Fuel Parameter | XOIL | COIL |
|---|---|---|
| Type | Single fuel, liquid | 2 reactants, liquid + gas |
| Storage life | ~700 days | 1-10 days (BHP) |
| Storage temp. | -100° C | -20° C |
| Feed system | Atomizing injector + heater | Liquid jet injector, pump, heat exchanger, holding tanks, real time refrigeration |
| Reactivity | Fresh fuel is non-reactive at storage temperature, spent fuel is non-reactive | Significant |
| Heat released in reaction | ~60 kJ/mol | 150-200 kJ/mol |
| Specific energy in fuel | 25-50 kJ/kg | ~30 kJ/kg |
| $H_2O$ content in $O_2(^1\Delta)$ | None | Significant |

*Figure 5. Comparison of fuels for XOIL and COIL systems*

## CONCLUSION AND ACKNOWLEDGEMENTS

Our investigation shows that organic ozonides, especially TPPO3, are a potential source of gaseous $O_2(^1\Delta)$ for the oxygen-iodine laser. Using TPPO3 promises significant system advantages over the Cl2-BHP production of $O_2(^1\Delta)$ in COIL namely (1) producing $O_2(^1\Delta)$ from a single liquid fuel (as opposed to reacting liquid fuel and oxidant gas), (2) fuel with a long storage life, (3) up to four times lower heat release which greatly reduces needs for refrigeration, and (4) simple hardware. We thank Dr. George Schneider and Harry Arbit of Boeing for many useful discussions.

## REFERENCES


1. J.V.V. Kasper et al., *Appl. Phys. Lett.*, 5, 231-233 (1964)
2. R. Derwent et al., *Chem. Phys. Lett.*, 6, 115 (1970)
3. A.U. Khan and M. Kasha, , *J. Am. Chem. Soc.*, 92, 3293 (1970)
4. W.E. McDermott et al., *Appl. Phys. Lett.*, 32, 469-470 (1978)
5. A.A. Frimer, "Singlet O2," vol. 1, ch. 2, CRC Press, Inc., Boca Raton, FL (1985)
6. G. Gousset et al., Plasma Chemistry and Plasma Processing, 9 (2), 198 (1989)
7. J. Schmiedberger and H. Fujii, SPIE vol. 2502, 338 (1994)
8. A.I. Didyukov et al., Sov. J. of Quant. Electr. 12 (4), 451 (1982)
9. V.A. Zootarev et al., Sov. J. of Quant. Electr. 19 (6) (1989)
10. R. W. Murray and M. L. Kaplan, *J. Am. Chem. Soc.*, 91, 5358 (1969)
11. C.S. Foote, Ch. 3 in "Active oxygen in chemistry," ed. by C.S. Foote et al., Blackie Acad. And Prof., NY (1995)

# High pressure pulsed COIL assisted with an instantaneous production of atomic iodine

Kenji Suzuki*, Kozo Minoshima[a], Daichi Sugimoto, Kazuyoku Tei, Masamori Endo, Taro Uchiyama[b], Kenzo Nanri, Shuzaburo Takeda[a], and Tomoo Fujioka

Department of Physics, School of Science, Tokai University
1117 Kitakaname, Hiratsuka-City, Kanagawa, Japan
[a]Department of Electro-photo optics, School of engineering, Tokai University
[b]Department of System Design Engineering, Keio University

## ABSTRACT

A new strategy for pulse oscillation of chemical oxygen–iodine laser based on a combination of a porous pipe SOG with an instantaneous atomic iodine generation, has been developed to seek the potential of COIL as an amplifier of the nuclear fusion driver. This new scheme allows one to produce a large aperture high pressure laser medium, which is favorable to the laser amplifier, while maintaining a minimum degradation of stored energy by water vapor. The experimental apparatus consists of the porous pipe SOG, an iodine donor ($CH_3I$) injector, a flash lamp for the iodine dissociation, and an optical resonator. Operational characteristics of the apparatus including dependence of output energy on an iodine concentration was studied. As the result, the maximum output energy of 800mJ was obtained. It was also found that the $CH_3I$ was dissociated through unidentified chemical reaction associated with the $O_2(^1\Delta)$.

**Keywords:** laser fusion, chemical laser, COIL, oxygen iodine laser

## 1. INTRODUCTION

Establishment of a new energy source for the 21st century is a most important task for the human being. The inertial confinement fusion (ICF) is well known as one of the promising candidates. Several types of lasers have been extensively studied for this application. Chemical oxygen iodine laser (COIL) can be counted among those candidates. The basic pumping mechanism of the COIL is as follows. An excited–state oxygen $O_2(^1\Delta)$, which is an energy source of the COIL, is produced by a chemical reaction between an aqueous solution of $H_2O_2$ and a gaseous $Cl_2$. Then an iodine atom $I(^2P_{3/2})$ in a ground state is excited to the upper state $I(^2P_{1/2})$ by the $O_2(^1\Delta)$ through a near resonant energy transfer, creating the population inversion.

The COIL has several characteristics suitable for high energy pulse amplification. First, the chemical efficiency is very high because of its unique pumping mechanism. Second, there are no thermal problems to the laser medium, because it consists of gaseous medium, which can be easily replaced with the new one right after the laser oscillation. Therefore, higher repetition rate and relatively good beam quality can be realized at the same time. Third, the wavelength of this laser is 1.315 μm, which happens to be at the lowest optical loss region of the silica glass and is close to the wavelength of glass lasers (1.06 μm). Thus, the direct application of the existing wavelength conversion technology can be possible.

In the early 90's Endo *et al.* had studied an instantaneous production of high pressure $O_2(^1\Delta)$ using a porous pipe SOG as a basic study for the application written above[1, 2]. The partial pressure of $O_2(^1\Delta)$ generated with the porous pipe SOG reaches up to 38 Torr [3]. A laser medium based on such a high pressure $O_2(^1\Delta)$ allows one to realize efficient energy extraction by virtue of the increased energy density. A drawback for a practical use, however, has been a limited scalability of the active medium in the cross sectional direction, associated with the $I^*$ deactivation due to the water vapor. The deactivation process is so rapid that the significant part of stored energy in $O_2(^1\Delta)$ can dissipates (through the near resonant energy transfer between $O_2(^1\Delta)$ and I) faster than the filling time of large aperture active medium.

* Correspondence: Email: 9jspm014@keyaki.cc.u-tokai.ac.jp; Telephone: +81–463–58–1211 (Ex.3721); Fax: +81–463–50–2013



XIII International Symposium on Gas Flow and Chemical Lasers and High-Power Laser Conference, Antonio Lapucci, Marco Ciofini, Editors, Proceedings of SPIE Vol. 4184 (2001)

According to the research done by Yuryshev *et al.*, a hybrid pulsed COIL based on an instantaneous iodine atom generation avoids the unfavorable deactivation [4]. We consider this approach may also be applied for the fusion driver system and enable us to produce the large aperture laser medium. In this study, a new strategy for pulse oscillation based on a combination of a porous pipe SOG with an instantaneous atomic iodine generation, has been developed. The pulse oscillation experiment was conducted for the basic study of this new scheme.

## 2. LIMITATION OF THE CONVENTIONAL APPROACH

Suppose that the pulse energy is 100 kJ and a damage threshold of silica glass is 20 J/cm$^2$ [5]. The required diameter of the laser medium cross section then becomes ~1 m to prevent the damage onto the optics. The gas velocity of the porous pipe SOG can be increased up to 300 m/sec, because of its unique $O_2(^1\Delta)$ generation mechanism. Therefore, assuming 0.5 m of gas transportation distance, the gas filling time in the laser chamber $T$ is estimated to be 1.7 msec.

In the conventional COIL medium, the following two reactions are dominant for its energy quenching process,

$$I^* + H_2O \rightarrow I + H_2O \tag{1}$$
$$O_2(^1\Delta) + I \rightarrow O_2 + I^* \tag{2}$$

Assuming the near resonant energy transfer between $O_2(^1\Delta)$ and $I^*$, stored energy lifetime $\tau$ is given by,

$$\tau = \frac{4}{3}\frac{1}{k[H_2O]}\frac{[O_2]}{[I_2]} \tag{3}$$

where $k$ is rate a constant of the reaction (1). It is obvious from the eq.(3) that the stored energy lifetime is inversely proportional to the $I_2/O_2$ ratio. Therefore, $I_2$ concentration must be kept small enough to maintain the longer lifetime. Assuming $k = 1.9\times10^{-12}$ cm$^3$/s and 1 Torr of $H_2O$, the $I_2/O_2$ ratio satisfying the condition of $T<\tau$ would be

$$I_2/O_2 < \sim 0.01 \tag{4}$$

From the above estimation, the part of the stored energy which can be extracted per one–pass of the light pulse, is limited to only 1 % of all the stored energy, since the COIL is the $O_2(^1\Delta)$–I energy transfer laser. As the result, more than a hundred of round trips may be required to extract all the stored energy from the laser medium. Such a large number of round trips may cause a large optical loss, which makes the application of COIL unpractical.

In this study, a new strategy for pulse oscillation based on a combination of a porous pipe SOG with an instantaneous atomic iodine generation, has been developed. Iodine donors used in this approach (such as $CH_3I$, $CF_3I$ and etc.) are chemically stable to $O_2(^1\Delta)$, causing no quenching during the mixing process. As the result, number of optical passes can be reduced by increasing the $I/O_2$ ratio, which, in this approach, is independent from the stored energy lifetime. Therefore, this new scheme allows one to produce a large aperture–high pressure laser medium, while maintaining a minimum degradation of stored energy due to the water vapor.

## 3. EXPERIMENTAL SETUP

Figure 1 shows the schematic drawing of the experimental apparatus. It consists of a singlet oxygen generator (SOG), $CH_3I$ injectors, a cavity arms with laser mirrors, a Xe flash lamp, and measurement devices.

The SOG consists of a solution tank, a chlorine tank, and a porous pipe on whose surface $O_2(^1\Delta)$ generation occurs. The dimension of the SOG is 1200 mm long, 90 mm wide, and 150 mm in height. The solution, consists of 48% $H_2O_2$ and 45% KOH is fed to SOG before the experiment. In the SOG, a porous pipe of 1000 mm long, 70 mm o.d., and 110 mm average pore is supported by a perforated inner tube and is rotated by a motor (90 rpm) to wet its surface uniformly. There is an $CH_3I$ injector just above the SOG. A pre-chamber which contains mixture of $CH_3I$ and nitrogen gas is connected to the injector designed to provide the mixture into the laser cavity. The laser cavity, 1900 mm long and 30 mmϕ in diameter is directly connected to the SOG. The entire system is evacuated and kept under 0.5 Torr by a vacuum pump. The flash lamp, 400 mm long, 5 mmϕ i. d. and made of silica glass, is used for the $CH_3I$ photodissociation. Xe gas is filled at 60 Torr in the tube.

The operation is conducted as follows: first, V2 is kept open, V1 and V3 are kept closed, the $Cl_2$ tank contains 1–3.5 kg/cm$^2$ of pure chlorine gas, and the pre-chamber contains mixture of $CH_3I$ and nitrogen gas. Immediately after the V2 was closed, the V1 and the V3 are opened simultaneously. The $Cl_2$ gas is injected into the inside of the porous pipe at a blast through the perforated inner tube, causing the reaction on the surface of the pipe allowing singlet oxygen to fill the upper volume of the system. Since V1 and V3 are the pneumatic high-speed butterfly valve, these are opened within 50ms. As the mixture of $O_2$ and $CH_3I$ fills the upper volume of the system, Xe lamp emits intense UV radiation to dissociate the $CH_3I$. The V1, the V3, and the Xe lamp are synchronized and controlled by a delay circuit to optimize the laser oscillation. After the operation, the pressure of the system reaches the constant value and V2 is opened to evacuate the whole system again.

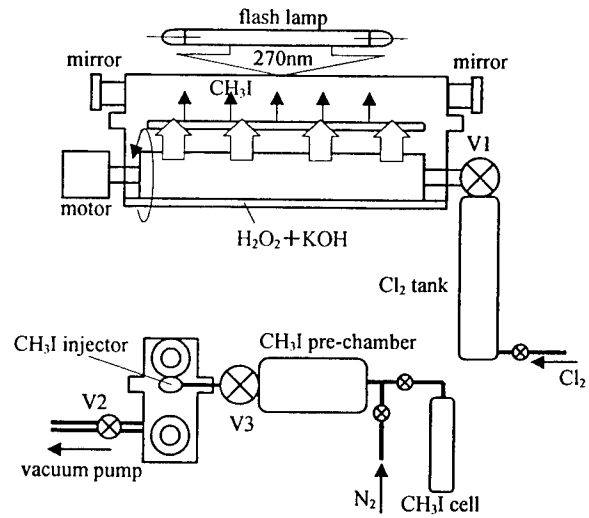

Fig. 1 Schematic drawing of the experimental apparatus

The laser output energy is measured using a joule-meter. The pulse waveform is monitored using Ge photodiode with 1.315μm bandpass filter and ND filters. The Spontaneous emission of the $O_2(^1\Delta)$ is detected using Ge photodiode with 1.27μm bandpass filter. I* fluorescence is also detected by Ge photodiode with the 1.315μm bandpass filter. Each of the detected signals is monitored with oscilloscope and recorded by a PC.

## 4. RESULTS AND DISSCUSSIONS

Figure 2 shows the observed pulse waveform. Maximum output energy of 800 mJ was obtained and the pulse duration was approximately 2 msec.

Figure 3 shows the laser output energy as a function of $CH_3I$ pressure. It was observed that the output energy increases as the $CH_3I$ partial pressure. However, above the certain level of $CH_3I$ pressure, output energy went into decline. In addition, surprisingly, the laser oscillation was not triggered by the flash lamp ignition, but started spontaneously. From these observed facts, it is hypothesized that laser oscillation is not achieved by instantaneous iodine generation based on the UV photodissociation, but some unknown chemical reaction processes. If the laser oscillation is triggered by UV photodissociation, the laser output energy should not decrease at the higher $CH_3I$ pressure region as long as the complete photodissociation is assumed.

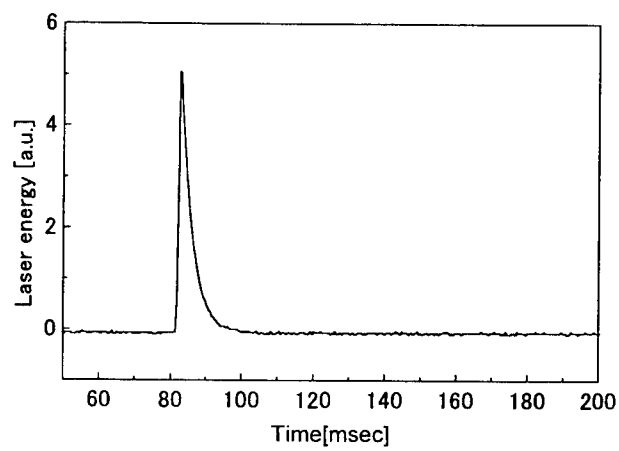

Fig. 2 Laser pulse waveform

Spontaneous emission of $O_2(^1\Delta)$ was observed both in the absence and the presence of $CH_3I$, in order to identify the above hypothesis. The result is shown in Fig. 4. In the presence of $CH_3I$, strong fluorescence was observed even in the absence of the flash lamp ignition. We presumed that the spontaneous emission of I* is generated by some chemical reactions. It was also observed that the rapid quenching of stored energy occurred after the strong fluoresce. According to this fluorescence measurement, it was revealed that the $CH_3I$ was dissociated through unidentified chemical reaction.

At this moment, two possible dissociation processes may be considered. The first one is associated with the three-body reaction including the chlorine [6]. The second one would be the direct $CH_3I$ dissociation by the $O_2(^1\Delta)$.

$$O_2(^1\Delta)+Cl_2+CH_3I \rightarrow I(I^*)+\text{products} \quad (5)$$

$$nO_2(^1\Delta)+CH_3I \rightarrow I(I^*)+\text{products} \quad (6)$$

According to the Yuryshev's papers [6], the $CH_3I$ is chemically inert with respect to $O_2(^1\Delta)$ and, therefore, no indication of $CH_3I$ dissociation by $O_2(^1\Delta)$ has been reported within our knowledge. In our experimental condition, on the other hand, partial pressure of the $O_2(^1\Delta)$ is approximately ten times higher and that might cause a significant difference in the dissociation processes.

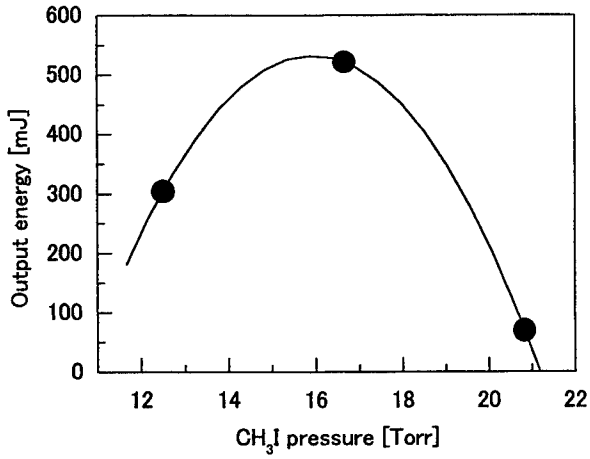


Fig. 3 Laser output energy as a function of the $CH_3I$ pressure

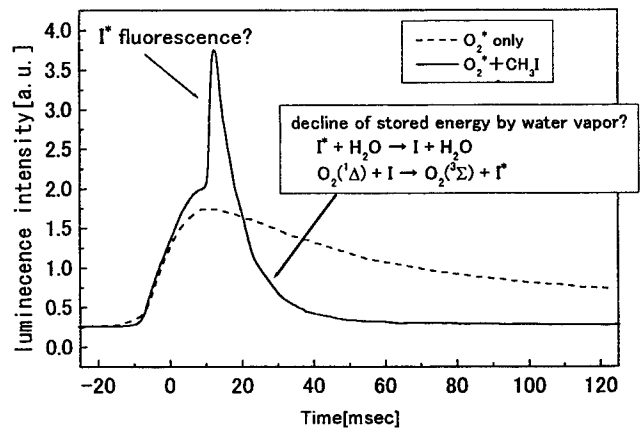


Fig. 4 $O_2(^1\Delta)$ fluorescence measurement

## 5. CONCLUSIONS

Research on a high pressure photodissociation COIL was conducted. The first laser apparatus was developed and tested for a laser oscillation. The laser oscillation using alkyl iodine ($CH_3I$) as an iodine donor was achieved. The output energy was 800 mJ and the pulse duration was 2 ms. According to the $I^*$ fluorescence measurement, it was found that the $CH_3I$ was dissociated through unidentified chemical reaction. We assumed that the $O_2(^1\Delta)$ played an important role in the dissociation process. In order to check the above assumption, it is necessary to improve the utilization to examine whether chlorine contributes to the dissociation reaction or not. In addition, use of other iodine donors may prevent the chemical reaction-based iodine generation.

## ACKNOWLEDGEMENT

Authors would like to express their sincere thanks to Prof. Kanno of Tokai University for his beneficial consultation in fabricating the Xe flash lamp.

## REFERENCES

1. M. Endo, K. Kodama, Y. Hanada, and T. Uchiyama, "Theoretical Study of a New Energy Extraction Scheme of a Chemically Pumped Pulsed Iodine Laser Amplifier", *Appl. Phys.* **B 56**, pp.379-384, 1993.
2. M. Endo, K. Shiroki, and T. Uchiyama, "Chemically pumped atomic iodine pulse laser", *Appl. Phys. Lett.*, **59**, pp.891-892, 1991.
3. M. Endo, K. Kodama, Y. Hanada, and T. Uchiyama, "Performance characteristics of a high-pressure pulsed singlet oxygen generator", *J. Appl. Phys.* **71**, pp.5760-5767, 1992.N. G. Basov, N. P. Vagin, P. G. Kryukov, D. Kh. Nurligareev, V. S. Pazyuk, and N. N. Yuryshev, "Molecules of $CH_3I$ and $n$-$C_3F_7I$ as iodine atom donors in a pulsed chemical oxygen–iodine laser" *Sov. J. Quantum Electron.* **14**, pp.1275-1276, 1984.
5. X. Liu, D. Du, and G. Mourou, "Laser Ablation and Micromachining with Ultrashort Laser Pulses",*IEEE J. Quant. Electron.*, **33**, p1706, 1997.
6. N. P. Vagin, P. G. Kryukov, V. S. Pazyuk, and N. N. Yuryshev "Influence of chlorine on the energy stored in the active medium of a pulsed oxygen-iodine chemical laser" *Sov. J. Quantum Electron.* **18**, pp.1114-1117, 1988.

# Experimental Investigation on COIL with Pipe-array Jet-type $O_2(^1\Delta)$ Generator

Liu Wan-fa, Chen Fang, Han Xin-min, Sang Feng-ting

Dalian Institute of Chemical Physics, Chinese Academy of Sciences
P.O.Box 110 - 7, Dalian 116023, China

## ABSTRACT

A series of experiments were done on COIL with a pipe-array jet-type $O_2(^1\Delta)$ generator. The investigation emphasized on the performance, parameters and relative techniques of the generator. A chemical efficiency of 20.6% was obtained.

**Keywords:** COIL (Chemical Oxygen-Iodine Laser), Jet-type Singlet Oxygen Generator (JSOG), Pipe-array

## 1. INTRODUCTION

Acting as an energy-source, the singlet oxygen generator (SOG) perhaps is the most important (and most difficult) part for a chemical oxygen-iodine laser (COIL). Several generations of the SOG have been developed since its debut [1]. Gradually, the jet-type singlet oxygen generator (JSOG) becomes one of the highlights of the COIL in recent years [2,3].

We have theoretically investigated the JSOG with experimental validation [4,5]. Generally, the dominant parameters in the generator are the utilization of chlorine ($U_{Cl2}$) and the yield of delta oxygen ($Y_\Delta$) which can be expressed as follows:

$$U_{Cl_2} = 1 - c_{1g} \tag{1}$$

where $c_{1g}$ is the normalized average concentration of the residual $Cl_2$ in the gas-phase near the exit of the generator. In a cylindrical coordinate system [4], $c_{1g}$ can be written as

$$c_{1g} = \sum_{n=1}^{\infty} A_n \exp(-a^2 \omega_n{}^2 l) \cos(\omega_n r) \tag{2}$$

where

$$a^2 = \frac{D_g}{v_g} \tag{3}$$

$D_g$ — the diffusion coefficient in the gas-phase [5]

$v_g$ — the velocity of the gas flow ($Cl_2$+$He$)

The eigenvalue $\beta_n$ of equation (2) complies with

$$\beta_n tg(\beta_n) = \frac{k_q d}{m_H D_g} \tag{4}$$

in which $k_q$ — the mass transfer coefficient in the liquid-phase

$d$ — the equivalent distance from the gas-liquid(jet) interface to the center of the gas-phase (i.e. the center of the adjacent BHP columns in a unit volume considered.)

$m_H$ — Henry's constant

And

$$\omega_n = \frac{\beta_n}{d} \tag{5}$$

$$A_n = \frac{2}{d} \int_0^d \cos(\omega_n r) dr$$

$$Y_\Delta = \frac{1}{1 + \frac{k_4}{k_1 c^{(0)}_{HO_2}} \frac{U_{Cl_2}}{1 - U_{Cl_2}} + U_{Cl_2} k_p P_{Cl_2} \frac{d}{k_g}} \tag{6}$$

where

$k_1 = 3.07\times10^6\ cm^3/mole\text{-}s$



XIII International Symposium on Gas Flow and Chemical Lasers and High-Power Laser Conference,
Antonio Lapucci, Marco Ciofini, Editors, Proceedings of SPIE Vol. 4184 (2001)

$k_4 = 5.5\times10^5\ s^{-1}$

$c^{(0)}{}_{HO_2}$ — the initial concentration of $HO_2^-$

$k_p$ — the equivalent quenching rate [6,7]

$k_g$ — the mass transfer coefficient in the gas-phase

$P_{Cl2}$ — the partial pressure of residual $Cl_2$

Although the JSOG features high efficiency, small volume and no cold-trap, etc., we found that the JSOG has some shortcoming — in order to get ideal BHP (basic hydrogen peroxide) jet, rigorous manufacture is required for the plate with BHP inlet orifice; the driving pressure of the BHP jet (before the inlet) is rather high (several atm), therefore few type of pump can meet the needs of the BHP circulation (from tens of torr to several atm); and the utilization of the BHP is not high in the unit time, indicating a large amount of BHP liquid needed for a circulation (due to a far-thin-surface reaction between BHP and $Cl_2$).

To avoid these difficulties, we developed another type of JSOG using pipe-array (PJSOG) to replace the plate-type "shower-head". A series of experiments were performed on the COIL with this PJSOG.

## 2. EXPERIMENT

### 2.1. Experimental setup

In Fig.1, (a) and (b) are the right-view and side-view of the layout of COIL with PJSOG respectively.

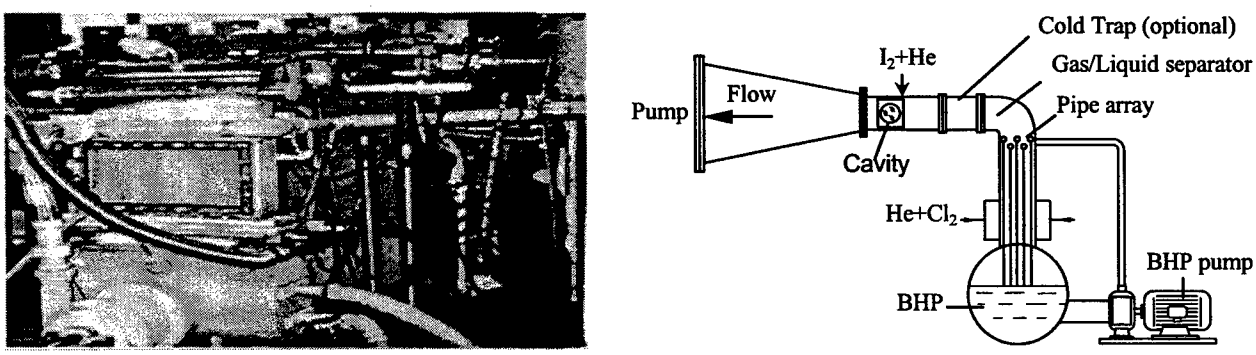


(a) (b)

Fig.1 The experimental setup of COIL with a PJSOG

Fig.2 shows the arrangement of the pipe-array. The outer-diameter of each pipe is 6mm with the thickness of 1mm of the pipe-wall. There is a raw of small holes (ϕ 0.7mm) in each pipe to form the BHP jet. The BHP driving pressure is 0.6-0.7atm. The operating parameters of the PJSOG are listed below.

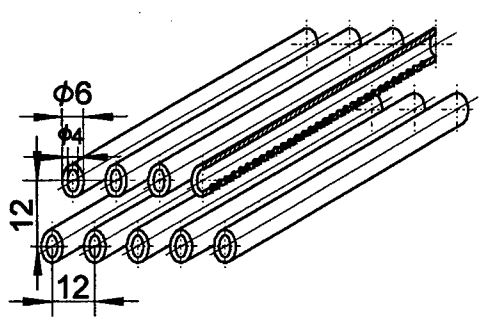


Fig.2 Arrangement of the pipe-array

| | |
|---|---|
| *$Cl_2$ flow rate* | *250 mmol/s* |
| *He flow rate* | *1000 mmol/s* |
| *PJSOG volume* | *4 L* |
| *PJSOG total pressure* | *30-50 torr* |
| *Specific surface area of BHP jet* | *1.5-3.0 $cm^{-1}$* |
| *Initial concentration of $HO_2^-$* | *6.7 mol/L* |
| *Velocity of BHP jet* | *5-7 m/s* |
| *Velocity of gas flow* | *20-40 m/s* |
| *Coefficient of mass transfer in liquid phase* | *12.3 cm/s* |
| *Initial BHP temperature* | *250-263 K* |
| *Utilization of $Cl_2$* | *60% - 96%* |
| *Yield of $O_2(^1\Delta)$* | *35% - 57%* |

## 2.2. Experimental results

A series of experiments were performed on the COIL with the PJSOG. Several parameters were optimized gradually to improve the entire chemical efficiency of the system. The variation of some parameters vs time were monitored using various sensors and data collectors (Fig.3 ~ Fig. 8).

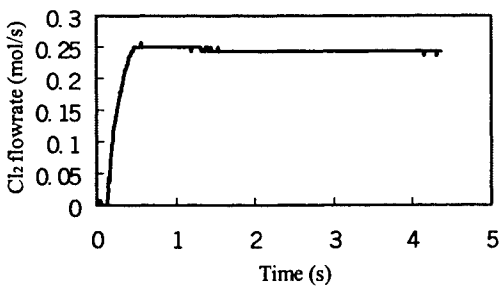


Fig. 3 The variation of $Cl_2$ flowrate

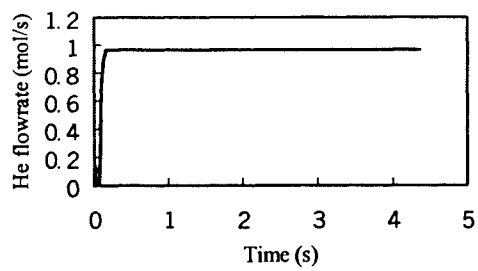


Fig. 4 The variation of primary He flowrate

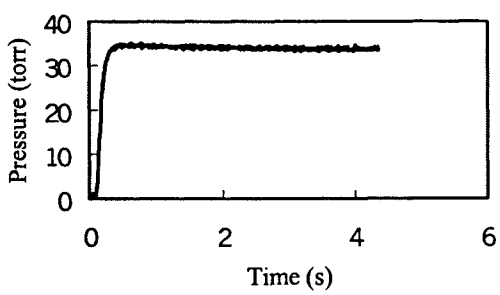


Fig. 5 The variation of PJSOG total pressure

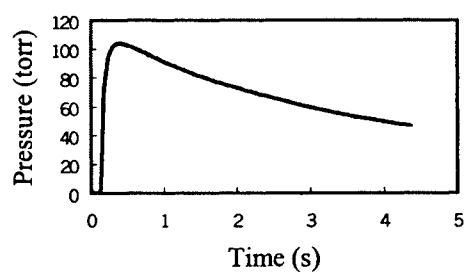


Fig. 6 The variation of the pressure inside iodine injector

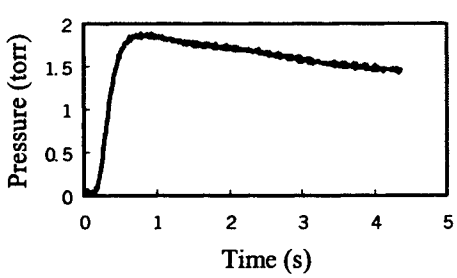


Fig. 7 The variation of cavity static pressure

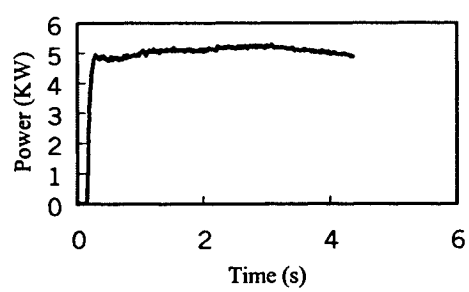


Fig. 8 The variation of output power

For a set of optimized parameters of the COIL with the PJSOG, the corresponding output laser energy was 19.5KJ (4 seconds), the average laser power was 4.875KW, and the chemical efficiency was 20.6%. The experiments were repeatable.

## 3. CONCLUSION

The PJSOG can avoid several difficulties of the conventional JSOG — it is easy to manufacture due to the simple structure; the driving pressure of the BHP jet is rather low (less than 1atm); the utilization of the BHP is high in the unit time.

The condition to achieve the chemical efficiency of 20.6% was not perfect for the whole COIL system. We believe that the efficiency can be improved further by optimizing the supersonic nozzle, the injection of iodine and the optical resonator, etc.


## ACKNOWLEDGEMENTS

The authors thank the persons who contributed to the experiment, including Xu Wen-gang, Wang Ke, Zhao Tong, Xu Zeng-he, Cong Zhi-qiang, Zhou Da-zheng, Wang Cheng-dong, Jin Yu-qi, Zhuang Qi and the relevant workgroups, for their cooperation and suggestions.


## REFERENCES


1. W.E.McDermott, "The Generation of Singlet Delta Oxygen - A Technology Overview", *AIAA*-**92-3005**, 23rd Plasmadynamics and Lasers Conference, Nashville, TN, 1992.
2. M.V.Zagidullin, A.Yu.Kurov, N.L.Kupriyanov, V.D.Nikolaev, M.I.Svistun and D.V.Erasov, "High Efficient Jet $O_2(^1\Delta)$ Generator", *Sov. J. Quant. Elect.* Vol.**21**, No.**7**, pp.747-753, 1991.
3. W.E.McDermott, J.C.Stephens, J.Vetrovec, and R.A.Dickerson, "Operating Experience with a High Throughput Jet Generator", *AIAA*-**97-2385**, 28th Plasmadynamics and Lasers Conference, Atlanta, GA, 1997.
4. Liu Wan-fa, et al., "The Theoretical Modeling of Jet Singlet Oxygen Generator", *J. Quant. Elect. (Chinese)*, Vol.**24**, No.**9**, pp.298-301, 1999.
5. B.M.PAMM, *Gas Absorption* (Russian Edition), Translated into Chinese by Liu Feng-zhi, et al., Chemical industry press of China, 1985.
6. P.G.Crowell and D.N.Plummer, "Simplified Chemical Oxygen-Iodine Laser System Model", *SPIE* Vol.**1871**, Intense Laser Beams and Applications, pp.148-180, 1993.
7. T.T.Yang, D.A.Copeland, A.H.Bauer, V.Quan, W.E.McDermott, R.A.Cover and D.M.Smith, "Chemical Oxygen-Iodine Laser Performance Modeling," *AIAA*-**97-2384**, 28th Plasmadynamics and Lasers Conference, Atlanta, GA, 1997.

# Prague Asterix Laser System (PALS) and its upgrade

K. Rohlena*[a], B. Rus[a], L. Juha[a], J. Skála[a], B. Králiková[a],

K. Jungwirth[b], J. Ullschmied[b], K. J. Witte[c], and H. Baumhacker[c]

[a]Institute of Physics of the Academy of Sciences of the Czech Republic,

Na Slovance 2, 182 21 Prague 8-Libeň, Czech Republic,

[b]Institute of Plasma Physics of Academy of Sciences of the Czech Republic,

Za Slovankou 3, 182 21 Prague 8, Czech Republic

[c]Max-Planck-Institute für Quantenoptik,

Hans-Kopfermann-Straße 1, D-85748 Garching, Germany

## ABSTRACT

The PALS project is based on iodine photodissociation system ASTERIX transferred from the Max-Planck-Institute für Quantenoptik, Garching, Germany, to a dedicated experimental hall built at the Institute of Plasma Physics of Academy of Sciences of the Czech Republic. A novel feature of the system is a newly designed twin interaction chamber comprising several technical innovations. As a user facility the system was inaugurated in June 2000 and starting from October it will serve the users coming under the EU 5$^{th}$FP "Transnational access" scheme. A brief description of planned upgrades of the original system is given. These include (1) implementation of adaptive optics, (2) replacement of the iodine master oscillator by a more flexible solid state oscillator based on fiber optics, and (3) a fs extension of the laser output using the OPCPA method.

## 1. BRIEF HISTORY

The first notion of the PALS project emerged in 1995 when it became clear that the MPQ Garching large facility ASTERIX IV would become available. The first official offer from the Directoriat of MPQ came to the Institute of Physics of Academy of Sciences in spring 1996. In the autumn a joint research centre PALS with the Institute of Plasma Physics was formed and it was decided to built for the system a new dedicated hall. The last shot took place in Garching in spring 1997 and in June a contract concerning the laser transfer was signed, also endorsed by Euratom. The clean hall ensuring a mechanical and thermal stability was built throughout 1998 while parts of the system were being transported from Garching to Prague. Starting from 1999 the system was being re-assembled in the new laboratory and a new interaction chamber for the target area was designed and manufactured. In February 2000, while the first operational tests took place, a 5$^{th}$FP contract was signed with DGXII in Brussels about the access of European users to the PALS laboratory. The first full energy shot came in spring 2000 followed by the inauguration of the system. The first users are scheduled for October 2000.

## 2. CHARACTERISTICS OF THE SYSTEM

The PALS system (fig.1) as it is now implemented in Prague is a single beam (1 kJ, diameter 29 cm) iodine photodissociation laser chain delivering on the target in the vacuum interaction chamber the focused power density up to $10^{16}$Wcm$^{-2}$ in 400 ps at the fundamental wavelength 1.315 $\mu$m. A conversion by a pair of DKDP crystals to the 2$^{nd}$ or 3$^{rd}$ harmonics is possible with the efficiency of about 70%. An auxiliary beam (100 J, 15 cm) is derived from the main beam optical path after the 4$^{th}$ amplifier and it is introduced in the interaction area through a beam distribution system,[2] where it can be split into two beams each independently timed. Also, a possibility for the

*Corresponding author: e-mail: rohlena@fzu.cz, fax:+420 2 6880729



XIII International Symposium on Gas Flow and Chemical Lasers and High-Power Laser Conference,
Antonio Lapucci, Marco Ciofini, Editors, Proceedings of SPIE Vol. 4184 (2001)

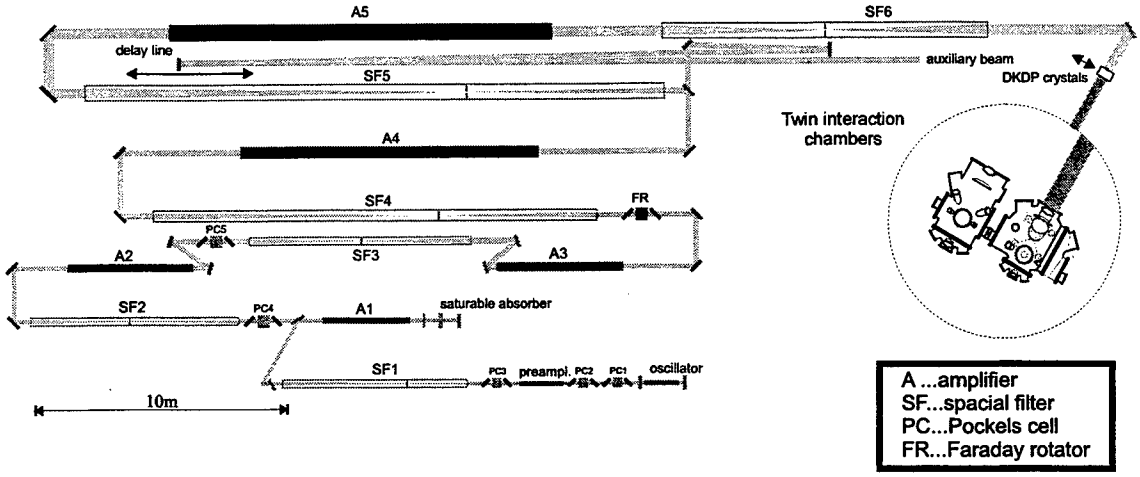


**Figure 1.** Scheme of the PALS system with the target area.

main pulse to be divided in two approximately equal pulses with a defined time delay is planned. The repetition time of full energy shots is about 20 min.

The interaction chamber (fig.2) for the new laboratory is an original design created in a cooperation between the PALS and the french LSAI (Université Paris-Sud) and LULI laboratories. It consists of two separate vacuum vessels, which can be either connected or used independently. The main chamber is a spherical one (diameter 1 m) with a pneumatically controlled gate to safeguard an easy access to the target optical bench. The auxiliary chamber is a cylinder 65 cm × 1 m, which is either connected with the main chamber through a vacuum tunnel, or it may be disjoint and moved within the target area. The principle technical innovation of both the chamber sections is a double bellow compensating system, which takes care of chamber body deformation during its evacuation and ensures an almost absolute mechanical stability of the internal optical benches.[2]

## 3. SCIENTIFIC GOALS

A single beam high power laser is a flexible and universal experimental tool, which by creating extreme conditions inside a tiny (typically 100 m$\mu$ focal spot on the target surface, generates a hot and dense laser plasma. In the following some typical topics concerning the laser plasma research to which the PALS system is immediately applicable will be mentioned.

Using the sufficient energy margin of the laser system PALS and, indeed, a plan to launch an x-ray laser beam in the main interaction chamber of the system the technique of x-ray back-lighting with a sufficient temporal resolution will be developed to image the phenomena close to the target surface under various regimes of laser illumination. A double pulse regime interaction with a defined time delay between the pulses, the amplitude ratio and also the colour ($1\omega$, $2\omega$, $3\omega$) of the illuminating laser light may be applied for the plasma generation. The aim will be a detailed understanding of processes which may control the smoothing of inhomogeneities induced by imperfections of the laser beam on the surface of directly illuminated target. This kind of work should elucidate the rôle of heat transport in the smoothing mechanism inside the dense regions of the plasma beyond the critical surface.

Laser plasma, especially that generated on a target with a high Z, if left to expand is a very high yield source of highly ionized ions. A laser ion source may be used as an accelerator injector, however, its field of application is broader, as the ion produced are at the same time accelerated. The laser produced ions can thus be used for an ion implantation either directly or with a subsequent acceleration. As substrate for the implantation metallic and polymer materials will be used with a careful tuning of the implantation regime to change the surface properties. The aim is controlling the resistance against surface wear and corrosion, coefficient of dry friction, affinity to water, chemical catalytic ability etc.

Laser plasma is also a very efficient source of very intense and very short burst in the soft x-ray region. The unique source of these properties offers itself for various applications. Moreover, the PALS beam can be focused in a line focus by a cylindrical lens, which makes an operation of x-ray laser possible with the plasma column

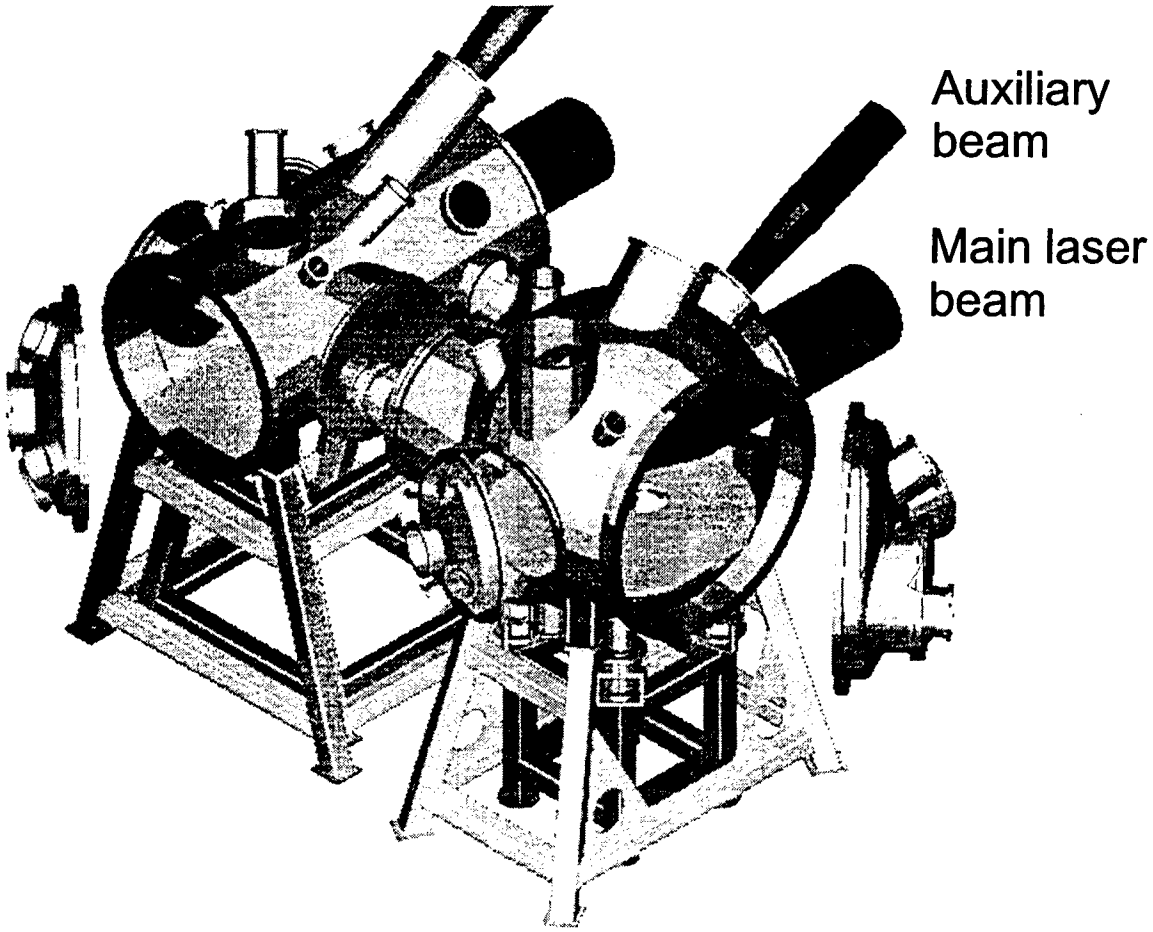


**Figure 2.** View of the twin interaction chamber with entering laser beams

serving as the amplifying laser medium. The beam of a soft x-ray laser has an unsurpassed brightness delivering a monochromatic and coherent x-ray beam to a secondary target. The dual interaction chamber of the PALS system has been designed for this kind of work. Among possible applications of both the kind of sources (coherent and incoherent) some exceed the field of pure physics and may be interdisciplinary in nature. As an illustration of usefulness of laser plasma x-ray sources a few examples will be mentioned. These are: (1) generation of laser plasma by the x-ray laser beam on a secondary target to model the plasma on the surface of cooling stellar (white dwarfs) and various other astrophysical objects for laboratory measurements of their fundamental properties; (2) experimental modelling of processes of significance for the molecular evolution in the outer space or also of the early Earth atmosphere; (3) radiography and interferometry of dense plasma (see above) and mapping of surfaces; (4) nanolithography and nanostructuring; (5) contact soft x-ray microscopy (imaging in vivo of biological objects), radiation damage biophysics; (6) material testing under a heavy radiation load, and many others.

The outward streaming plasma generates on the target surface a reactive pressure, which reaches safely $10^{11}$ Pa. This pressure pulse causes a shock wave to propagate through the target, which can be visualized and its velocity measured. From the known properties of the shock wave the equation of state of the target material in this pressure range can be determined. A part of the experimental time will thus be devoted to a study of materials under high pressure.

## 4. SYSTEM UPGRADES

Adaptive optics: the PALS system being a gas laser with a short pumping pulse, which leaves the optical homogeneity of the gaseous active medium largely untouched, low B-integral, and a spatial filter following each amplifier is not so much prone to wave front deformation as e.g. solid state lasers. Nonetheless, the instruments of addaptive optics

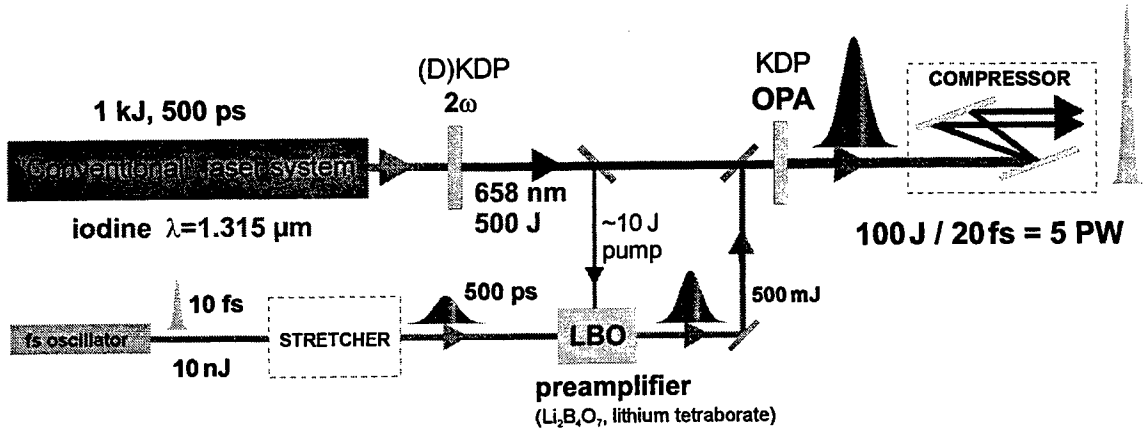


**Figure 3.** Scheme of a proposed OPCPA amplification chain to be implemented on PALS

may make the system less sensitive to operational error, such as insufficient pause between the shots and the like. It was proposed to use a deformable bimorph mirror (beam diameter 90 mm) at the output side of the third spatial filter combined with step motor powered tip-tilt mounts of the existing system mirrors and possibly of a gold coated membrane deformable mirror (37 actuators) replacing a tip-tilt mirror used with the double pass first amplifier. The elements of the adaptive optics will be computer controlled by using on-line date acquisition from several far-field monitors following each amplifier. In addition, a wave front monitor of Shack-Hartmann type will be placed at the end of the laser chain to control the bimorph mirror. The adaptive optics will take care of beam deformations caused by residual temperature gradients in the laser medium and improve the target illumination homogeneity.[3]

Solid state oscillator: the present iodine oscillator of the PALS system is using an active mode locking to generate the first seed pulse with an impressive stability of the output (better than 1.5 %). The expert solution required, however, a large amount of space (oscillator table is 7 m long) and neither the existing oscillator allows for any pulse shaping or a generation in the region of several nanosecods. The non-linearity of the pulse propagation due to early saturation effects causes a certain rigidity of the generation, with the resulting pulse length below 0.5 ns. To generate longer or shaped pulses requires an utmost care to be taken of the seed pulse shaping. It seems that a suitable tool for this fairly difficult task has been found in the form of optical fiber generator as proposed for NIF. Its viability was demonstrated within the PHELIX project in GSI Darmstadt, Germany.[4] The seed pulse is obtained by chopping a CW light of a diode pumped fibre laser by an acousto-optic modulator. After a preamplification it is arbitrarily and smoothly shaped in a modulator by applying a suitable variable voltage to obtain pulses in the $0.5 \div 20$ ns range. The resulting pulse of a very low energy must then be amplified in a regenerative ring fibre amplifier to a level of $\sim 10$ mJ. For the iodine laser a chain of conventional solid state amplifiers of a suitable material (forsterite) must follow to raise the energy to $\sim 1$ J before the entry to the first iodine amplifier. Other advantages of the fiber technique, beside a small size, is the availability of most of the key components on the telecommunications market.

Femtosecond upgrade of the PALS system: a way towards the generation and subsequent target experiments with an ultra short pulse in the femtosecond region was opened by the invention of the OPCPA (optical parametric chirped pulse amplification) method.[5] This method proved to be very promising for transferring energy from the spectrally narrow PALS pulse to a chirped pulse, with a sufficiently broad spectrum (generated by a minute Ti:Sapphire oscillator) by a process of three wave parametric interaction (fig.3). The non-linear crystal pseudo-amplifiers (LBO, KDP) of such a system, pumped by the red ($2\omega$) or blue ($3\omega$) converted PALS beam would amplify the chirped pulse to the level of 100 J. After a compression in a vacuum chamber by a pair of large aperture diffraction gratings the pulse should be compressed under 100 fs and the final power would lie in the PW range.[6] This is due to a wide transparency range of the non-linear crystals, which makes it possible for a broad frequency spectrum to be parametrically amplified. It is clear that if successful this upgrade of the PALS system would broaden the field of applications and, indeed, enter the field of new physics. Hence, it is our intention, to direct the future development and scientific programme of the PALS system towards this goal.

## 5. ACKNOWLEDGEMENTS

A support by the grants nos. 202/98/1274, 202/99/0623 and 202/00/1217 of the Grant agency of the Czech Republic for the Czech co-authors is gratefully acknowledged.

## REFERENCES

1. B. Rus, K. Rohlena, J. Skála, B. Králiková, K. Jungwirth, J. Ullschmied, K. J. Witte, and H. Baumhacker, "New high-power laser facility PALS - prospects for laser plasma research," *Laser and Particle Beams* **17**, pp. 179-194, 1999.
2. B. Rus, K. Rohlena, J. Skála, B. Králiková, K. Jungwirth, J. Ullschmied, K. J. Witte, and H. Baumhacker, *Proc. IFSA'99*, Bordeaux, September 13-17, 1999, pp. 32-39, Elsevier Paris, Amsterdam, Lausanne, New York, Oxford, Shannon, Tokyo, 2000.
3. "ADAPTOOL", 5$^{th}$FP RTD Contract No HPRI-1999-50010.
4. M. Roth M., B. Becker-de-Mos, R. Bock, S. Borneis, H. Brandt, C. Bruske, J. Caird, E. Devald, C. Haefner, D. H. H. Hoffmann, M. P. Kalachnikov, H.-J. Kluge, F. Krausz, T. Kühl, G. Logan, D. Marx, P. Neumayer, P. V. Nickles, M. P. Perry, K. Poppensieker, I. Reinhard, W. Sandner, R. Sauerbrey, A. Tauschwitz, and I. Willy, "PHELIX - a Petawatt High Energy Laser for Heavy Ion Experiments," *Proc. of ECLIM'2000*, Prague, Czech Republic, 12-16 June 2000.
5. I. N. Ross, P. Matoušek, M. Towrie, A. J. Langley, and J. L. Collier, "The prospects for ultrashort pulse duration and ultrahigh intensity using optical parametric chirped pulse amplifiers", *Optics Commun.* **144**, pp. 125-133, 1997.
6. P. Matoušek, B. Rus, and I. N. Ross, "Design of multi-petawatt optical parametric chirped pulse amplifier for the iodine laser ASTERIX IV," *IEEE J. Quant. Electron.* **36**, pp. 158-163, 2000.

Invited Paper

# Mechanisms of HF laser performance

Lee H. Sentman
Aeronautical and Astronautical Engineering Department
University of Illinois, Urbana, IL 61801

## ABSTRACT

The roles that rotational nonequilibrium, mixing and the optical resonator play in determining the power spectral performance of the cw HF laser are reviewed. Experiments and analyses that led to an understanding of these elements are summarized. The factors that influence the overtone performance of the HF laser are reviewed. The line selected performance is related to multiline performance.

**Keywords:** rotational nonequilibrium, fluid element stretching, optical resonators, overtone, line selection

## 1. INTRODUCTION

The continuous wave (cw) HF laser operates on several, generally 6 to 12, individual vibration-rotation transitions simultaneously. The lasing transitions occur in the $2 \rightarrow 1$ and $1 \rightarrow 0$ vibrational bands of the HF molecule. The performance of the HF laser is characterized by the total power, the power spectral distribution and the extent to which the outcoupled beam can be focussed to a spot in the far field. Since the population inversion is produced by a chemical reaction in a flowing fluid and the energy is extracted by an optical resonator, the role each of these elements plays in determining the performance of the HF laser will be examined.

The HF laser was first demonstrated in 1967 by Kompa and Pimentel[1]. The first cw HF laser was demonstrated in 1969 by Spencer, Mirels, Jacobs and Gross[2]. The potential for efficient generation of very high powers was apparent. However, there were several problems that had to be solved. The chemical reactions that produced the population inversion were very fast, on the order of $\mu$ sec. If the chemicals were premixed, the width of the laser beam would be on the order of millimeters with resulting very large intensities which windows and mirrors could not survive. The exothermicity of the pumping reactions raised the temperature which increased the rates of deactivation of the excited HF.

To solve the heat release and width of the lasing zone problems, the F atoms were produced in combustors and the flow was expanded through supersonic nozzles. The $H_2$ was injected into the flow at the exit of the supersonic nozzles. The HF was formed in a low pressure, low temperature, high speed flow which reduced the HF deactivation rates and extended the gain region sufficiently to obtain laser beams several cm in size. Work then focussed on the best ways to mix the $H_2$ with the F atoms. At the same time, extensive efforts were undertaken to understand the details of the formation and deactivation of the excited HF and to develop optical resonators to extract the laser beam from the flow. The fluid flow, the chemical kinetics and the optical resonator all interact nonlinearly. The role each of these elements play in determining HF laser performance will be illustrated.

## 2. POWER SPECTRAL DISTRIBUTION OF THE HF LASER

Experimental data showed that the HF laser operated on several (v,J) transitions (wave lengths) simultaneously, with the spectra generally peaked around J = 6, 7, 8 in both $v = 2 \rightarrow 1$ and $v = 1 \rightarrow 0$ vibrational bands. Since it was well known that rotational relaxation is the fastest collisional deactivation mechanism, the original models of laser performance, e.g., Refs. 3, 4, 5, assumed the HF was in rotational equilibrium. These models were capable of predicting the correct power in each vibrational band. However, they allowed only one (v,J) transition in each vibrational band to lase at a time. They predicted a sequential shift as lasing progressed from low J to high J lines. In the early '70's, J. C. Polanyi and his students performed a comprehensive set of experiments on the hydrogen halides, including HF, that measured the fraction of product molecules that were formed in each (v,J) state for both the cold[6] and hot[7] reactions:

$$F + H_2 \rightarrow HF(v,J) + H \qquad v = 1,2,3, \quad 34 \text{ Kcal/mole} \quad \text{"cold reaction"} \tag{1}$$

$$H + F_2 \rightarrow HF(v,J) + F \qquad v = 3,4,5,6, \quad 67 \text{ Kcal/mole} \quad \text{"hot reaction"} \tag{2}$$

The resulting distributions for the cold reaction are shown in Fig. 1. The data showed that the product molecules were produced in a decidedly nonequilibrium distribution over both rotational and vibrational states. At this time computer

XIII International Symposium on Gas Flow and Chemical Lasers and High-Power Laser Conference,
Antonio Lapucci, Marco Ciofini, Editors, Proceedings of SPIE Vol. 4184 (2001)

speeds had increased to the point where it was feasible to set up a kinetic model that treats each (v,J) state of the HF molecule as a separate species where the nacent distribution was that measured by Polanyi and coworkers. This approach was implemented by Hough and Kerber[8] for the pulsed laser and by Sentman[9] for the cw laser. For the cw case, 21 J states in v = 0, 1, 2, that is, 63 states for the lasing molecule, are followed. The results of these models were the prediction of simultaneous lasing on many (v,J) lines in each vibrational band, in agreement with experiment, Fig. 2. When the rotational relaxation rate constants in these models are increased by a factor of $10^6$ above the measured values, the rotational nonequilibrium models reproduce the results of the rotational equilibrium models. Since these models showed that it was necessary to follow the individual (v,J) states of HF, an extensive effort by many researchers to measure the J dependence of the deactivation rates for HF followed.

The computer models still predicted significant power in the higher vibrational bands that are populated by the hot reaction. Particularly in the cw case, under certain conditions some power is observed in the 3 → 2 band, but generally no power occurs in the 4 → 3, 5 → 4 or 6 → 5 bands. Polanyi and coworkers[10] performed a set of chemiluminescence depletion with mass spectrometry experiments that allowed them to measure the relative rates for the deactivation reactions:

$$HF(v,J) + D \rightarrow F + HD \text{ and } \rightarrow H + DF \quad \text{for } v = 3, 4, 5, 6 \tag{3}$$

These measured rates showed that these reactions deactivated the HF(v = 3 - 6) as fast or faster than the pumping reactions produced it. When these reactions were incorporated into the kinetic models, the predictions of which vibrational bands lased were in agreement with data. These collisional decomposition reactions are the reason it has not been possible to construct a cw HF laser that utilizes the hot reaction.

The essential rotational nonequilibrium kinetics required to model the HF laser are:

Pumping Reactions

$$F + H_2 \rightarrow HF(1,J) + H \tag{4}$$
$$F + H_2 \rightarrow HF(2,J') + H \tag{5}$$
$$F + H_2(0) \Leftrightarrow HF(3) + H \tag{6}$$
$$F + H_2(1) \rightarrow HF(3) + H \tag{7}$$
$$F_2 + H \rightarrow HF(3) + F \tag{8}$$

Collisional Deactivation Reactions

$$HF(1,J) + M \Leftrightarrow HF(0,J''') + M \tag{9}$$
$$HF(2,J') + M \Leftrightarrow HF(1,J) + M \tag{10}$$
$$HF(3) + M \Leftrightarrow HF(2,J') + M \tag{11}$$
$$H_2(1) + H \Leftrightarrow H_2(0) + H \tag{12}$$

where M = HF, F, H, $H_2$ and DF

Multiquantum Deactivation Reactions

$$HF(2,J') + M \rightarrow HF(0,J''') + M \tag{13}$$
$$HF(3) + M \rightarrow HF(1,J) + M \tag{14}$$
$$HF(3) + M \rightarrow HF(0,J''') + M \tag{15}$$

where M = HF, F, H and DF

Collisional Decomposition Reaction

$$H + HF(3) \rightarrow H_2 + F \tag{16}$$

VV Transfer Reactions

$$H_2(1) + HF(2,J') \Leftrightarrow H_2(0) + HF(3) \tag{17}$$
$$H_2(1) + HF(1,J) \Leftrightarrow H_2(0) + HF(2,J') \tag{18}$$
$$H_2(1) + HF(0,J''') \Leftrightarrow H_2(0) + HF(1,J) \tag{19}$$
$$HF(1,J) + HF(2,J') \Leftrightarrow HF(0,J''') + HF(3) \tag{20}$$
$$HF(2,J') + HF(2,J') \Leftrightarrow HF(1,J) + HF(3) \tag{21}$$
$$HF(1,J) + HF(1,J) \Leftrightarrow HF(0,J''') + HF(2,J') \tag{22}$$

Rotational Relaxation Reactions

$$HF(2,J') + M \Leftrightarrow HF(2,J) + M \tag{23}$$
$$HF(1,J) + M \Leftrightarrow HF(1,J'') + M \tag{24}$$
$$HF(0,J''') + M \Leftrightarrow HF(0,J^{V}) + M \tag{25}$$

where M = HF, F, H, $H_2$, $F_2$, DF, He, Ar

The $H_2$ in Eqs. (4) and (5) is $H_2(0) + H_2(1)$. The species denoted by Ar is included to take account of any other combustion or dissociation products that may be present in the mixture and which would contribute to the rotational relaxation but not the collisional deactivation of the lasing species.

## 3. MIXING MECHANISMS OF THE HF LASER

At the same time as the kinetic studies were underway, extensive efforts to determine the "best" ways to fluid dynamically mix the F and $H_2$ were under taken. The initial devices used alternating primary and secondary slit nozzles at the exits of which the two streams began mixing. In these devices the mixing was two dimensional, diffusive where the mixing layer grows ~ $\sqrt{x}$. Photography of the flow showed that the mixing was slow and that the primary and secondary streams were not fully mixed before the fluid exited the laser resonator, Fig. 3a. Various schemes were tried to increase the rate of mixing. One of the most successful schemes injected interleaved jets of He near the exits of the primary and secondary nozzles, Fig. 4. These jets, denoted trip jets, caused a rapid increase in the rate of mixing and about a factor of two increase in power. The mechanism by which this occurred was determined by Driscoll in a series of papers in the AIAA Journal[11, 12, 13]. Using laser induced fluorescence, Driscoll showed that the trip jets introduced fluid element stretching which dramatically increased the surface area of contact between the primary and secondary streams which increased the rate at which they mixed, Fig. 3b. Driscoll showed that the same effect could be obtained by putting alternating, interleaved solid ramps at the exits of adjacent nozzles, Fig. 5. The logical development of the trip jet concept lead to eliminating the secondary nozzle and injecting the $H_2$ directly into the primary flow near the exit of the nozzle. To shield the $H_2$ from the primary flow until it exited the nozzle, a He jet was placed immediately upstream of the $H_2$ jets. This is illustrated in the TRW HYLTE nozzle[14], Fig. 6.

Another scheme that mixed efficiently was called the double axisymmetric nozzle. This was a conical hole primary nozzle around the exit of which the $H_2$ was injected from a concentric circular slit. This is illustrated by the Bell Aerospace Textron BCL-13 nozzle[15], Fig. 7. These nozzles were excellent performers.

At this time system studies indicated that a cylindrical geometry for the gain generator was the best way to package a laser that was to be put into orbit. The manufacturing problems associated with constructing the double axisymmetric nozzles on the surface of a cylinder resulted in this technology not being persued. It was easier to construct slit nozzles with trip jets out of circular rings which could be stacked together to form the gain generator. The TRW hypersonic wedge nozzle used in the ALPHA laser is an example[16], Fig. 8.

## 4. OPTICAL RESONATORS FOR THE HF LASER

The three basic resonators that can be employed on the HF laser are the Fabry-Perot (plane parallel mirrors), the staple (two concave or concave and a flat) and the unstable ( a concave and a convex). In the Fabry-Perot resonator there is no upstream - downstream coupling of the gain medium. In the staple resonator, there is complete upstream – downstream coupling of the gain medium across the optical axis. In the unstable resonator, there is partial coupling of the gain medium, from the optical axis upstream and from the optical axis downstream, but not across the optical axis. These differences determine the degree of difficulty involved in including the resonator in the kinetic-fluid dynamic model of the laser.

The Fabry - Perot and stable resonators use partially transmitting mirrors to extract power from the laser. An unstable resonator uses a reflective optic, the scraper mirror, to extract power from the laser. Since transmissive optics are unable to survive at the 100's of kilowatt power level, unstable resonators are usually used to extract power from high power HF lasers. The outcoupled beam from an unstable resonator generally has a hole in it so that some of the radiation can be fed back into the resonator to keep the lasing process going. The problem is to design the unstable resonator to produce an outcoupled beam with a uniform phase so it can be focussed to a spot in the far field. Since diffraction effects play a major role in the performance of an unstable resonator, the resonator must be designed with a wave optics code. At a minimum, these models are two dimensional, and in most cases, a three dimensional wave optics model is used.

Coupling the rotational nonequilibrium kinetic – fluid dynamic model with the wave optics model of the unstable resonator or the geometric optics model of the stable resonator requires an iterative procedure. Since the flow and optical axes are perpendicular to each other, the computer models are coupled in an iterative fashion. An initial guess at the intensity distribution on each line is used to run the fluid dynamic- kinetic model to obtain the gain distribution on each line. Then the optics model propagates the initial guess of the intensity distribution on each line one round trip through the resonator. Each time the optical wave passes through the gain medium, the intensity distribution is modified by the gain distribution from the preceding fluid dynamics – kinetics calculation. After the round trip through the resonator, the new intensity

distribution is used in the fluid dynamic – kinetic model to recalculate the gain. When the changes in I and $\alpha$ are less than $\varepsilon$, the procedure has converged. The resulting power, spectra and intensity distributions agree very well with data.

It is posssible for a time dependent oscillation to occur on lines whose saturated gain does not fill the unstable resonator[17], Fig. 9. The period increases as the magnification of the resonator decreases and the amplitude increases as the fraction of the resonator filled by the line decreases[18]. The oscillations do not occur if the gain medium is strongly coupled to the optical fields diffractively ($N_F < 3$) or geometrically ($n_p > 3.8$).

With appropriate fluid dynamic, kinetic and optical models, it is possible, in theory at least, to predict laser performance as various aspects of the laser design are changed.

Prior to the development of the cylindrical gain generator, the lasers were rectangular and the optical resonators were developed to extract power from rectangular gain regions. The cylindrical gain region produced by the cylindrical gain generator required the development of an entirely new resonator to extract the power. This resulted in a class of resonators denoted High Extraction Efficiency Decentered Feedback Annular Ring Resonator[19] (HEXDARR), Fig. 10. Testing on the ALPHA laser has demonstrated good performance for the HEXDARR[20].

## 5. HF OVERTONE PERFORMANCE

The most recent development of the HF laser was the demonstration of lasing on the first overtone $\Delta v = 2$ ($v = 2 \rightarrow v = 0$) transitions between 1.3 – 1.4 $\mu$. The cw overtone was first demonstrated by W. Q. Jeffers[21] of Helios, Inc, which holds the patent[22] on the HF overtone laser. An extensive series of experiments by Helios[21], UIUC[23] and TRW[14] demonstrated that 60% - 90% of the fundamental power is obtainable on the overtone, the overtone is optimized by the same flow rates as the fundamental, overtone efficiency is independent of mode volume and whether the mixing is slow or fast. Since the overtone is a low gain system, $\alpha_{OT} \approx (1/80)\alpha_{FUND}$, to suppress fundamental lasing, mirror coatings must be less than 1% reflective over the fundamental wavelenghts and highly reflective (>99%) over the overtone wavelengths. Optimization of the output power[24] requires careful selection of the reflectivity of the resonator mirrors as a function of their absorption/scattering losses, Fig. 11. The overtone mirror design problem lead to the development of uncooled silicon optics. Measurements of the fundamental gain while lasing on the overtone[25] [$P_{20}(7)$, $P_{20}(8)$, $P_{20}(9)$, $P_{20}(10)$] showed that lasing on the overtone suppressed the gains of the low J lines $P_1(4\text{-}6)$ and $P_2(4\text{-}6)$ 41% - 96% and suppressed the gains of the high J lines $P_1(7\text{-}9)$ and $P_2(7\text{-}9)$ 3%-44% for a well saturated overtone laser. The high J lines are suppressed because their upper or lower levels are directly invoved in overtone lasing. The upper levels of the $P_2(7\text{-}9)$ lines are depopulated and the lower levels of the $P_1(7\text{-}9)$ lines are populated by overtone lasing, which decreases their gains. The low J $P_2$ lines are suppressed[26] because overtone lasing depopulates the high J $v = 2$ states which blocks the rotational relaxation that populates the low J $v = 2$ states which decreases the gains of the $P_2(4\text{-}6)$ lines. The low J $P_1$ lines are suppressed because overtone lasing populates the high J $v = 0$ states which increases the rotational relaxation that populates the $v = 0$ low J states which decreases the gains of the $P_1(4\text{-}6)$ lines.

## 6. LINE SELECTED PERFORMANCE

To operate the HF laser in a multiple line selected mode, a grating is incorporated into the resonator in the off-Littrow orientation[27]. In an unstable resonator, the feedback mirrors are placed at the locations of the positive first order diffraction of the desired lines. In a stable resonator, one line can be selected in the Littrow orientation and the remaining lines selected by placing mirrors at the locations of the positive first order diffractions of the desired lines. The possible line combinations are dictated by the grating equation. The grating characteristics, ruling and Blaze angle, are selected to permit only first order diffraction and to keep the grating incident angle < 57° for the wavelengths of interest. Experiments by Aerospace Corp.[28] and UIUC[29,30] have shown that 55% - 80% of the multiline power can be obtained by operating the HF laser in the line selected mode on two to four lines.

## 7. CONCLUDING REMARKS

The rotational nonequilibrium distribution produced by the pumping reaction is primarily responsible for the power sprctral distribution of the HF laser. The basic kinetic processes of the HF laser are fairly well understood. The rate constants for the major kinetic processes are known. Some of the energy transfer/redistribution rate constants are less well known.

Mixing is the mechanism that is primarily responsible for the power of the HF laser. The basic fluid dynamic mechanism that controls the mixing of the reactants is fluid element stretching. Laser design uses this understanding to optimize laser performance for the mission the laser is to perform.

Resonators that efficiently extract the energy from the gain medium in a beam that can be focussed to a spot in the far field have been demonstrated for cylindrical as well as rectangular gain media.

Effficient overtone lasing has been demonstrated. The processes responsible for the suppression of the fundamental gain while lasing on the overtone have been identified.

Efficient line selected operation of the HF laser has been demonstrated for both stable and unstable resonators. The grating characteristics required for efficient line selected operation have been identified.

The majority of the experimental test time on high power lasers has been devoted to demonstrating scalability to the very large powers required for the weapons application. Little time has been spent optimizing a given laser.

On the other hand, the HF probe laser has been developed and well engineered. This is illustrated by Helios which started with the initial designs of Hinchen (United Technologies) and Spencer (The Aerospace Corp). These were 15 cm gain length devices that produced ~ 5 watts multiline power. After some 10 years of engineering, the same 15 cm device produced ~ 40 watts mutiline power, an 8 fold increase.

## REFERENCES


1. K. L. Kompa and G. C. Pimentel, "Hydrofluoric Acid Chemical Laser," *J. Chem Phys.* **47**, pp. 857 - 858, 1967.
2. D. J. Spencer, T. A. Jacobs, H. Mirels and R. W. F. Gross, "Continuous-Wave Chemical Laser," *Int. J. Chem. Kinet.* **1**, pp. 493 - 494,1969.
3. G. Emanuel, "Analytical Model for a Continuous Chemical Laser," *J. Quant. Spectrosc. Radiat. Transfer* **11**, pp. 1481-1520, 1971.
4. H. Mirels, R. Hofland and W. S. King, "Simplified Model of CW Diffusion-Type Chemical Laser," *AIAA J.* **11**, pp. 156-164, 1973.
5. G. Emanuel, W. D. Adams and E. B. Turner, "RESALE-1: A Chemical Laser Computer Program," TR-0172(2776)-1, The Aerospace Corporation, July, 1971.
6. J. C. Polanyi and K. B. Woodall, "Energy Distribution Among Reaction Products, VI. $F+H_2$, $D_2$," *J. Chem. Phys.* **57**, pp. 1574-1586, 1972.
7. J. C. Polanyi and J. J. Sloan, "Energy Distribution Among Reaction Products, VII. $H+F_2$," J. Chem. Phys. **57**, pp. 4988-4998, 1972.
8. J. J. T. Hough and R. L. Kerber, "Effect of Cavity Transients and Rotational Relaxation on the Performance of Pulsed HF Chemical Lasers: A Theoretical Investigation," *Applied Optics* **14**, pp. 2960-2970, 1975.
9. L. H. Sentman, "Rotational Nonequilibrium in cw Chemical Lasers," *J. Chem. Phys.* **62**, pp. 3523-3537, 1975.
10. F. E. Bartoszek, D. M. Manos and J. C. Polanyi, "Effect of Changing Reagent Energy. X. Vibrational Threshold Energies for Alternative Reaction Paths $HF(v) + D \rightarrow F + HD$ and $\rightarrow H + DF$," *J. Chem. Phys.* **69**, pp. 933- 935, 1978.
11. R. J. Driscoll, "Effect of Reactant-Surface Stretching on Chemical Laser Performance," AIAA J. **22**, pp. 65-74, 1984.
12. R. J. Driscoll, "Mixing Enhancement in Chemical Lasers, Part I: Experiments," AIAA J. **24**, pp. 1120-1126, 1986.
13. R. J. Driscoll, "Mixing Enhancement in Chemical Lasers, Part II: Theory," AIAA J. **25**, pp. 965-971, 1987.
14. W. Duncan, S. Patterson, B. Graves and M. Holloman, "Recent Progress in Hydrogen Fluoride Overtone Chemical Lasers," *AIAA Preprint* 91-1480, AIAA 22nd Fluid Dynamics, Plasma Dynamics and Laser Conference, June 24-26, Honolulu, Hawaii, 1991.
15. "Proposal for Alpha I Design," Report No. 9294-953002, Bell Aerospace Textron, January, 1980.
16. J. A. Horkovich and P. J. Pomphrey, "Recent Advances in the Alpha High Power Chemical Laser Program," AIAA Preprint 97-2409, AIAA 28th Plasmadynamics and lasers Conference, June 23-25, Atlanta, GA, 1997.
17. L. H. Sentman, M. H. Nayfeh, S. W. Townsend, K. King, G. Tsioulos and J. Bichanich, "Time-dependent Oscillations in a cw Chemical Laser Unstable Resonator," *Applied Optics* **24**, pp. 3598-3609, 1985.
18. L. H. Sentman, J. Gilmore and D. Carroll, "Mechanism for Time-Dependent Oscillations in a cw HF Chemical Laser Unstable Resonator," *AIAA Preprint* 89-1897, AIAA 20th Fluid Dynamics, Plasma Dynamics and Laser Conference, June 12-14, Buffalo, NY, 1989.

19. R. C. Wade, "Chemical Lasers with Annular Gain Media," in *Optical Resonators-Science and Engineering*, edited by R. Kossowsky et al, pp. 211-223, Kluwer Academic Publishers, Netherlands, 1998.
20. J. A. Horkovich, C. L. Nefzger, B. C. Platt, G. A. Hyver, P. J. Pomphrey, J. L. Jacoby and D. N. Loomis, "Space-Based Laser Programs High Power Testing Progress," AIAA Preprint 98-2661, AIAA 29th Plasmadynamics and Lasers Conference, June 15-18, Albuquerque, NM, 1998.
21 W. Q. Jeffers, "Short Wavelength Chemical Lasers," *AIAA J.* **27**, pp. 64-66, 1989.
22. W. Q. Jeffers, United States patent 4,760,582, July 26, 1988.
23. D. L. Carroll, L. H. Sentman, P. T. Theodoropoulos, R. E. Waldo and S. J. Gordon, "Experimental Study of Continuous Wave Hydrogen-Fluoride Chemical Laser Overtone Performance," *AIAA J.* **31**, pp. 693-700, 1993.
24. D. L. Carroll and L. H. Sentman, "Maximizing Output Power of a Low-Gain Laser System," *Applid Optics* **32**, pp. 3930-3941, 1993.
25. P. T. Theodoropoulos, L. H. Sentman, D. L. Carroll, R. E. Waldo, S. J. Gordon and J. W. Otto, "Continuous Wave Hydrogen Fluoride Overtone Lasing Saturation Effects on Fundamental Gain Suppression," *AIAA J.* **34**, pp. 1216-1223, 1996.
26. P. T. Theodoropoulos and L. H. Sentman, "Fundamental Gain Suppression Mechanisms in a Continuous Wave Hydrogen Fluoride Overtone Laser," *AIAA J.* **34**, pp. 1589-1594, 1996.
27. R. A. Chodzko, "Multiple-Selected-Line Unstable Resonator," *Applied Optics* **13**, pp. 2321-2325, 1974.
28. R. A. Chodzko, "Multiple Line Selection in cw HF/DF Chemical Lasers," Report Number ATR-92(2732)-1, The Aerospace Corp., Los Angeles, CA, 1993.
29. S. J. Gordon, L. H. Sentman, D. S. Jenkins and A. J. Eyre, "A Study of Line Selection in cw HF Lasers," AAE TR 97-02, UIUL ENG 97-0502, Aeronautical and Astronautical Engineering Dept., University of Illinois, Urbana, IL, March, 1997.
30. L. H. Sentman, J. T. Cassibry, B. P. Wootton and A. J. Eyre, "Influence of Grating Design on cw HF Laser Line Selected Performance," AAE TR 99-08, UILU ENG 99-0508, Aeronautical and Astronautical Engineering Dept., University of Illinois, Urbana, IL, June, 1999.

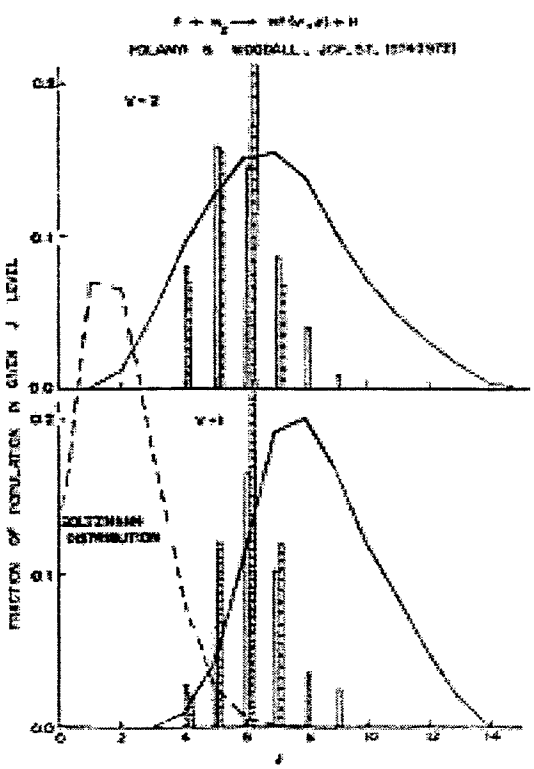

Figure 1. Comparison of the pumping distribution and the power spectral distributions of two cw HF lasers. The open bar is from an Aerospace laser; the hatched bar is the CL-XI laser.

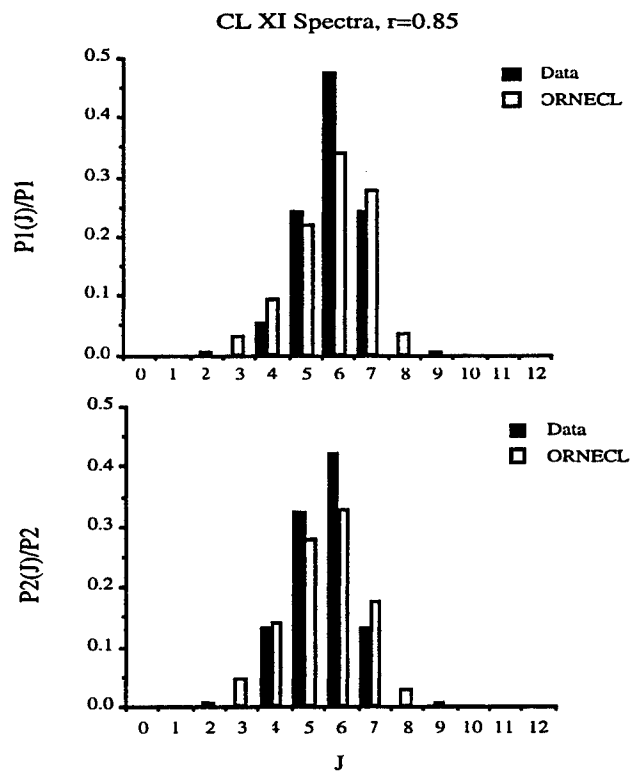


Figure 2. Comparison of data and ORNECL model spectra for the CLXI laser.

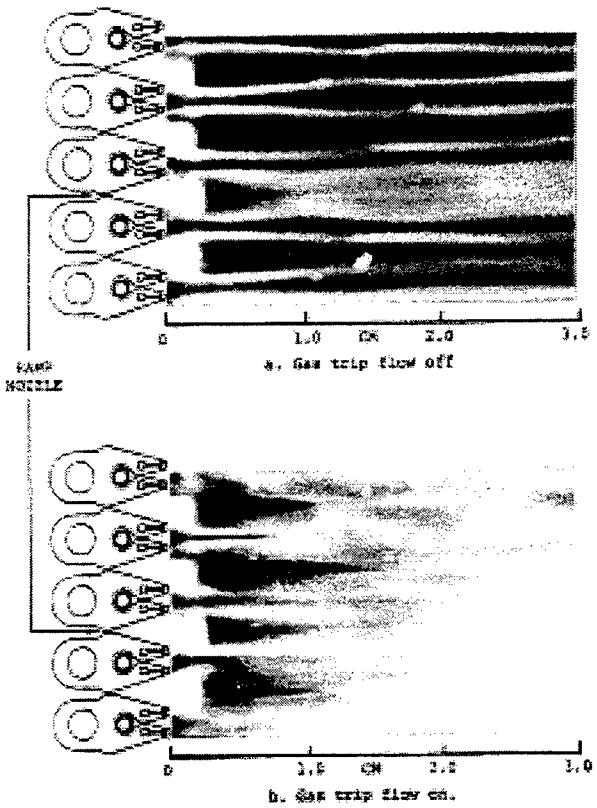

Figure 3. Flow visualization of effect of trip jets and ramps on mixing.[12]

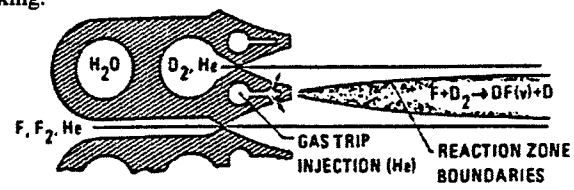


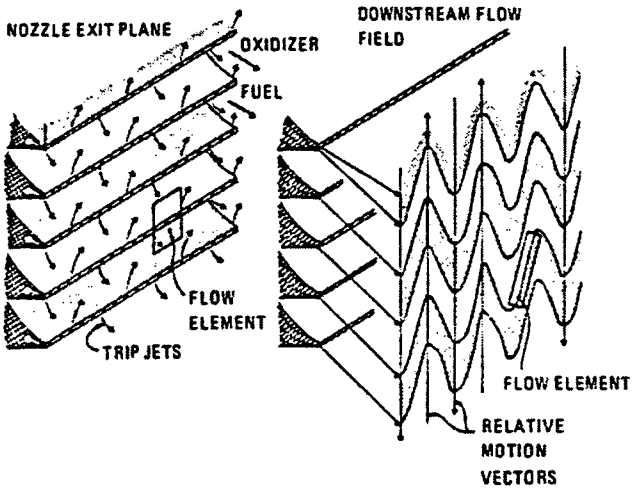


Figure 4. Trip nozzle flow field[13].

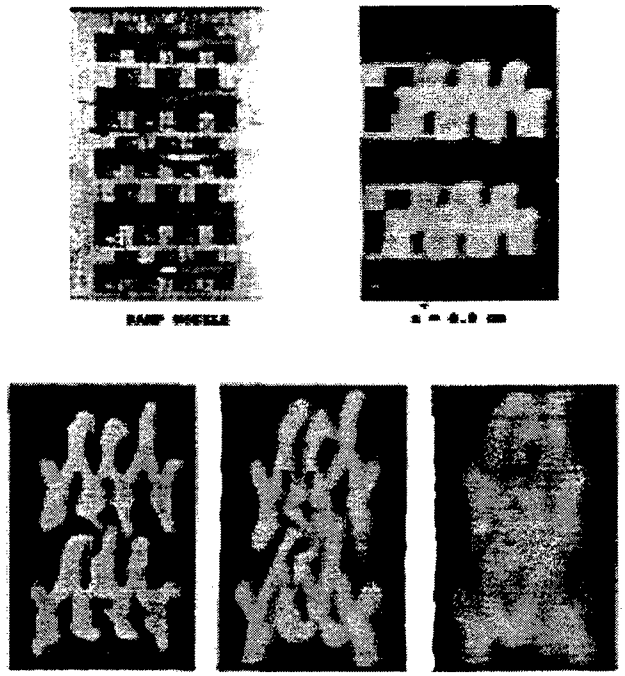

Figure 5. Laser induced fluorescence flow visualization of ramp nozzle flow[12], p=10 Torr, oxidizer nozzle seeded with $I_2$.

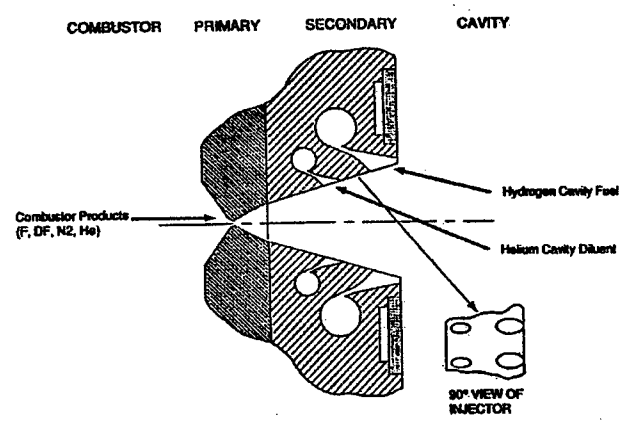


Figure 6. TRW hypersonic, low temperature (HYLTE) nozzle[14].

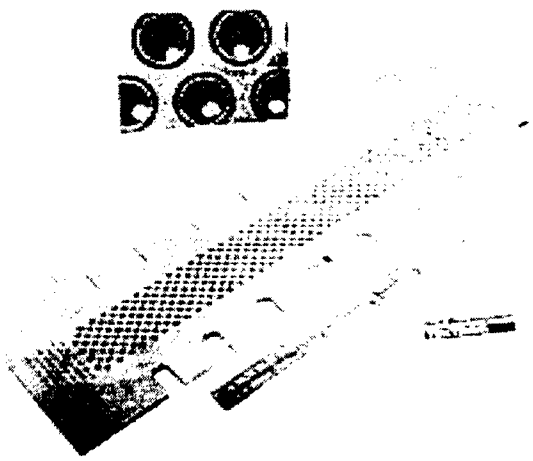

Figure 7. Bell Aerospace Textron BCL – 13 nozzle[15].

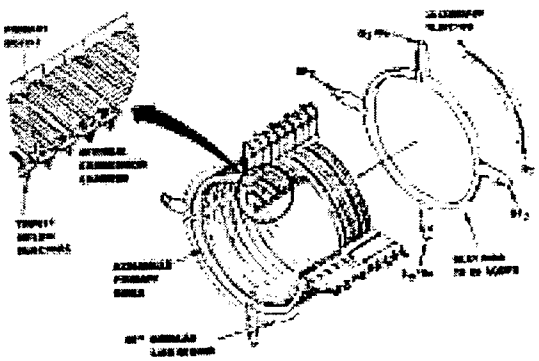

Figure 8. TRW hypersonic wedge nozzle used in the ALPHA laser gain generator[16].

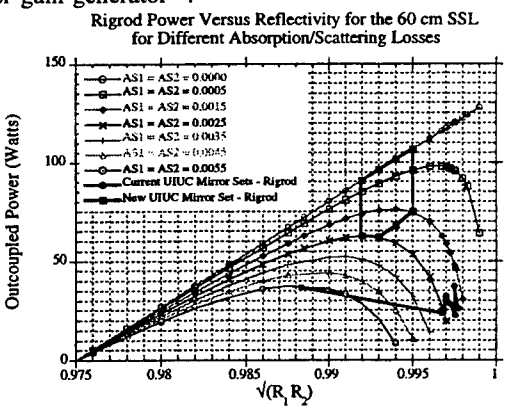


Figure 11. Predicted outcoupled overtone power for the old and the new overtone mirror sets for the UIUC 60 cm gain length supersonic laser.

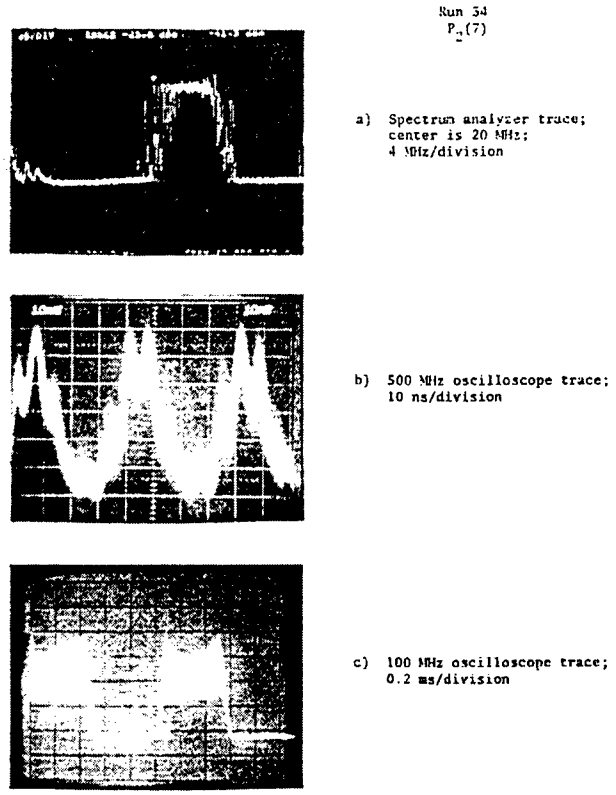


Figure 9. Typical oscilloscope[17] traces of the time dependent oscillations on the $P_2(7)$ line whose saturated gain did not fill the unstable resonator. The 7 ns mode beat superimposed on the 40 ns oscillation is clearly evident.

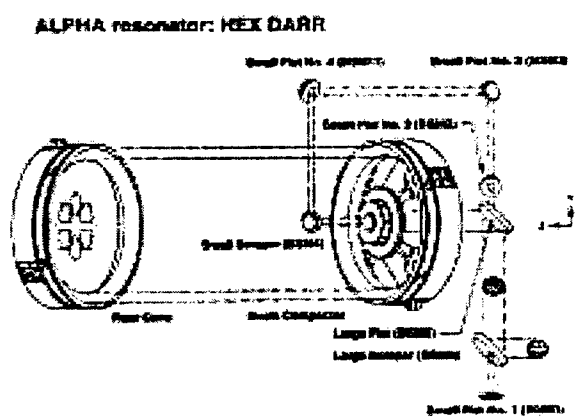


Figure 10. Schematic of the High Extraction Efficiency Decentered Feedback Annular Ring Resonator (HEXDARR)[20] employed on the ALPHA laser.

# Peculiarities of a e-beam pumped, non-chain, HF laser

N. G. Ivanov, B. Lacour* and V. F. Losev

* CILAS, route de Nozay, MARCOUSSIS, FRANCE

Gas Laser Laboratory, High Current Electronics Institute SB RAS,

4, Akademichesky ave., Tomsk, 634055, RUSSIA

Fax (382 2)259410, e-mail: losev@ogl.hcei.tsc.ru

## ABSTRACT

The results of experimental and theoretical investigations on a pulsed, chemical e-beam pumped, non-chain HF laser with a 25 l active volume are submitted. It is shown that there are conditions of anomalous behavior of the output radiation which could be explained by the existence of a space-charge effect in the plasma.

**Keywords:** non-chain HF laser, efficiency, laser energy, electron beam pump, radiation.

## 1. INTRODUCTION

Non-chain HF/DF chemical lasers are high efficient sources of coherent radiation in near infrared spectrum region ($\lambda$ = 2.6-5 μm). A large number of spectral lines covering the absorption spectrum of many atmospheric pollution and technological products makes such lasers as universal sources of radiation in systems for ecological and technological monitoring. For pumping these lasers are usually used electric discharges or electron beams. E-beam pumped chemical laser is more convenient for obtaining of a kilojoule level of output energy. In case of HF laser, $SF_6$-$H_2$ gas mixtures are typically used. In papers [1-2], anomalies of e-beam propagation in electronegative gases were found when the length run of electrons reduces leading to locking of the electron beam. In paper [3] it was shown that when the $SF_6$ is pumped by an e-beam, there is an anomalous behavior of the deposited energy. Namely when the gas pressure is increased more than $5.5 \times 10^4$ Pa, the excited region was found to be smaller than in calculations. The authors supposed that this anomaly was caused by the formation of a large volume charge in the plasma. This is due to the small conductivity in electronegative gas. As a result the e-beam is locked in by the space-charge and a large amount of the electron energy is lost in working against the space-charge electric field. In these conditions there should be some anomalous behavior of the output parameters of the e-beam pumped chemical laser.

In the present paper the peculiarities of a pulsed chemical, e-beam pumped, non-chain HF laser areas are investigated and the optimal conditions of the excitation of this laser are discussed.

## 2. EXPERIMENTAL APPARATUS

Experiments were carried out on the setup described in Ref. [4]. It consisted of a laser chamber, two vacuum diodes producing electron beams, and six high voltage ten-stages Marx generators. Each vacuum diode was powered from 3 Marx generators, having a stage capacitance of 0.1 μF and a charging voltage up to 80 kV. The diode explosive-emission cathode was made of graphite rods. Typical electron beam parameters for one diode were 450 keV maximum energy, 40 kA current for a pulse duration of 800 ns. Each e-beam was injected into the gas laser mixture through a 13 cm width, 150 cm length and 50 μm thickness titanium or kapton foil supported by a steel grid. The distance between the opposite foils in the cell was 12 cm. The laser cell had a total volume of 60 l. The laser resonator was formed by the two laser cell windows (20 cm in diameter, TlBr, transmissivity of 75%) and a flat outside Al-mirror. Laser mixture of $SF_6$-$H_2$ with 0.3-1 bar pressure was used in our experiments.

The output laser energy was measured with IKT-1N (active surface 1 $cm^2$) and TPI-2-7 (active surface 24 x 24 $cm^2$) calorimeters. The pulse shape was registered by a photoresistor FSG-22 on an oscilloscope S8-14. The energy deposited in the gas by the e-beam was determined by the pressure jump method in pure $SF_6$. Pressure jump was measured with a 6MD-

XIII International Symposium on Gas Flow and Chemical Lasers and High-Power Laser Conference,
Antonio Lapucci, Marco Ciofini, Editors, Proceedings of SPIE Vol. 4184 (2001)

X1B pressure transducer and an oscilloscopes S8-14. Laser parameters were registered for a fresh gas mixture and the first shot as the laser energy decreases from shot to shot (approximately in 1.5-2 times). Additionally a calculation of the deposited in gas energy was realized by Monte-Carlo method, without taking into account of the volume charge in plasma.

## 3. EXPERIMENTAL RESULTS AND DISCUSSION

First of all the optimal ratio between $SF_6$ and $H_2$ for the maximum efficiency and output laser energy was determined. This value did not essentially depend on the gas mixture pressure and the pump power. The optimal $SF_6$:$H_2$ ratio was approximately 50:1, so this ratio was used in all our experiments.

The first series of experiments was carried out with Ti foils. In these cases we compared the HF laser parameters for one side pumping and for two sides pumping. The diode voltage (electron energy) remained unchanged but the injected charges approximately increased twofold. The behavior of the total laser energy from mixture pressure for two sides and one side pump is shown in Fig.1. Dotted line is the calculated energy we could expect to obtain, adding the laser energies obtained from the first and second beams working separately. The behavior of the output energy in the case of two sides pumping was normal up to the pressure 0.7 bar, but beyond this value the behavior was essentially **nonnormal**, since the output energy became less than the sum of the energies obtained from separate pumping. The measurement of the energy deposited in the gas showed that its value increases up to 1 bar pressure, both for one e-beam and two e-beams pumping. Therefore a decrease of the output energy beyond 0.7 bar pressure for two sides pump is also **nonnormal** with respect to the deposited energy.

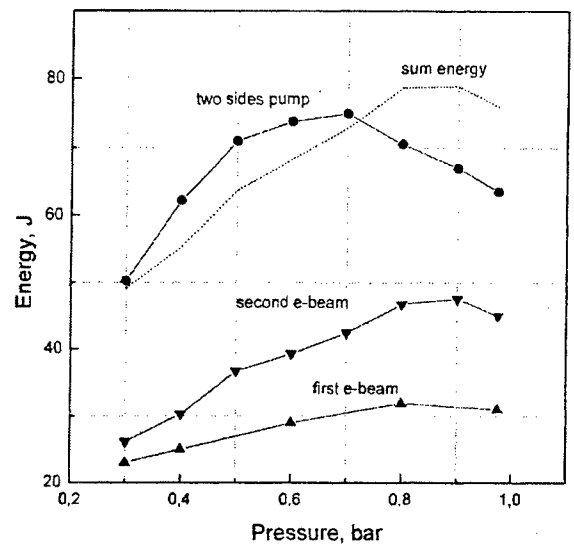


Fig.1. Laser radiation energy versus the mixture pressure (Ti - foil).

Registration of the laser beam pattern near the output window on thermal paper showed that the basic part of the laser energy was concentrated inside an area of 12x12 $cm^2$ (approximately) for mixture pressure up to 0.8 bar. At 1 bar pressure a decrease of the energy density in the central part has appeared. The structure of the beam pattern was found inhomogeneous with more dark and light zones. Nevertheless measurements of the energy density of the laser output beam showed a rather good uniformity between the foils when we used the two sides pumping (Fig.2). For one side pumping the laser energy density decreased sharply from the foil to the opposite side, however the sum of the laser energy (dotted lines) in the center was lager then for two sides pumping. A second interesting fact is the higher laser energy level at 0.7 bar pressure in a comparison with 0.9 bar for all measured points. Since the pump power is higher at 0.9 bar, this behavior of the laser energy can be considered also as a new **nonnormality** of the e-beam pumped HF laser.

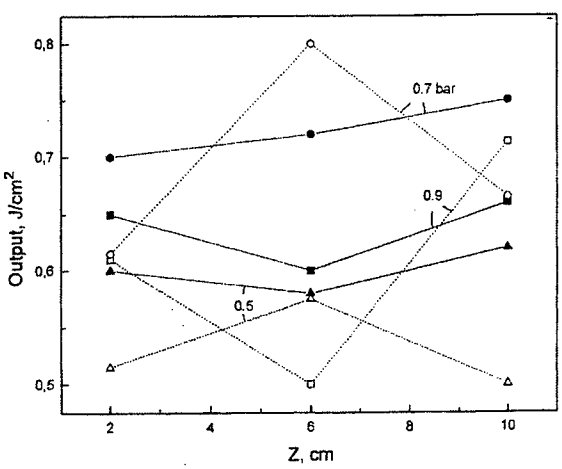


Fig.2. Laser radiation density versus the distance from the left foil at different mixture pressure. Solid line is two sides pump, dotted line – sum of densities in case of the first and second diodes working separately.

In Fig.3 is shown the behavior of the laser efficiency as a function of the mixture pressure for one side and two sides pumping. Main points are: efficiency increases when the mixture pressure decreases and second, efficiency for two sides pumping is lower than for one side pumping when the mixture pressure is higher than 0.7 bar and - vice versa - efficiency for two sides pumping is higher than for one side pumping when the pressure is lower than 0.7 bar.

In last series of experiments HF laser we increased the deposited pump energy (injected in gas charge) for one side pump and for two sides pump by changing the Ti foils with 50 μm thick aluminized kapton foils. Pumping energy in this case increased approximately in one and half times. In spite of this the laser output energy for two sides pumping (Fig.4) is practically the same as compared with Ti foils. This fact is the following **nonnormality** of the HF laser. Besides laser energy for two sides pumping became less than the sum of the energies obtained from each e-beam for all pressure values. Another difference is that fact that the decrease of the laser energy for the second e-beam pumping begun more early with respect to gas pressure

than in the case of Ti foils (0.7 bar instead of 0.9 bar). Laser efficiency for two sides pumping with kapton foils was less than with Ti foils (Fig.3).

We have investigated the temporal behavior of the laser pulse for different conditions. The pulse duration (FWHM) decreased with the rise of pressure from 900 ns (gas pressure 400 mb) up to 350-400 ns (1000 mb).

The simulation of e-beam pumping in $SF_6$ mixture (400 mb,700 mb and 1000 mb) by Monte-Carlo method has been carried out. A better agreement between the simulated and experimental values of the gas deposited energy has been obtained for lower pressure. While increasing the pressure from 400 mb up to 1000 mb the agreement was worse as the calculated deposited energy increased more quickly than the experimental one.

Finally we would like to discuss the **nonnormalities** of HF laser and try to explain them. Basic peculiarity of HF laser is the high attachment of electrons in the plasma by the $SF_6$ excited molecules. This leads to a decrease of the electron conductivity and appearance of the problem of compensation the space-charge brought in the gas by the e-beam. Due to this phenomenon appears in the plasma a high negative potential and a large amount of the electron beam energy is probably lost in the work against the electric space-charge field.

At the beginning of our research there was the question about high negative potential existence in HF laser plasma and its influence on laser output was. The results our experiments show, that HF laser has many **nonnormalities** which could be explained by taking into account the existence of large space charges.

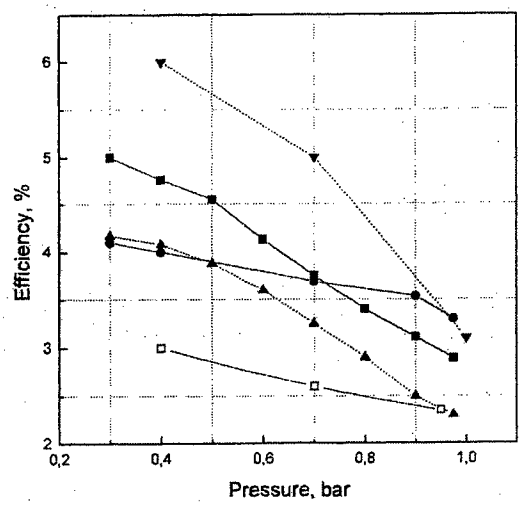


Fig.3. Laser efficiency as a function of the mixture pressure. Open squares – kapton foil, other – Ti foil; solid curves – experiment, dotted curves – calculation; squares and triangles – two sides pump, circles – one side pump; down triangles – calculation from specific energy.

The first fact is the decrease of the output laser energy (total and specific) with increase of the pump energy when working with Ti foil and two sides pumping (Fig.1 and Fig.2), and for mixture pressure higher than 0.7 bar. May we assume that at the point 0.7 bar (**critical point**) some critical deposited energy or critical charge is reached from which the laser output begins to decrease. The range of pressure where the laser output decreases can be named **critical range**. In case of one side pumping the critical deposited energy is reached at higher pressure 0.9 bar (Fig.1). Within the normal range of pressure (0.4 - 0.7 bar, for two sides pumping, Ti - foil) laser efficiency and output energy are larger than the efficiency and sum of energies derived from the first and second beams working separately. The more uniform pump may easily explain this fact. Within the critical range, these parameters are less since some part of the e-beam energy is lost in the work against the electric space-charge field.

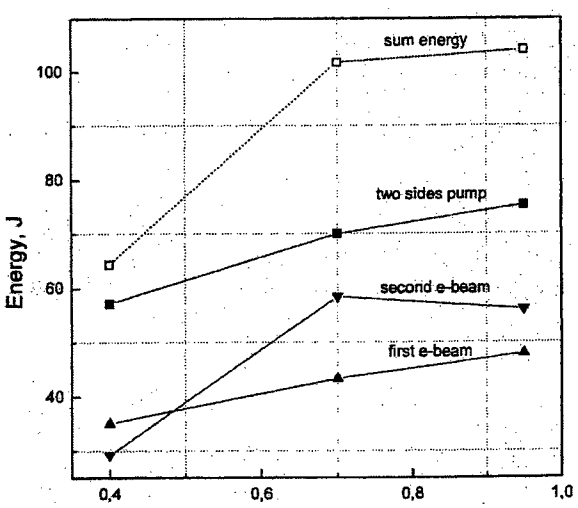


Fig.4. Laser radiation energy versus the mixture pressure in case kapton foil. Dotted line is sum of energy of the first and second diodes pump.

In order to obtain an additional information about the influence of the space charge on the laser output, we increased the deposited pump power by changing the Ti foils with kapton foils. In this case, for two sides pumping the whole range of pressure 0.4-0.95 bar became the critical range since for two sides pumping the output energy is less than the sum of energies due to the first and second beams working separately (Fig.4). As the electric space-charge field increased, the electrons began sooner to loss larger energy in working against this field and the laser efficiency (Fig.3) decreased in a comparison with Ti foils experiment. An important proof of the space-charge influence at the laser output is the shape of the laser pattern for two sides pump and one side pump. It appears that in case one side pumping, the area of the laser pattern from one e-beam is greater, thus indicating a lower space-charge field and a lower loss of e-beam energy in comparison with two sides pumping.

From our point of view the obtained results show that the space-charge field exists and influences the laser output. For our experimental conditions, with two sides pumping, the **critical point** corresponds to a specific deposited pump energy of 60-70 J/l. This specific pump energy corresponds to the **critical** charge value of $2x10^{-4}$ C/l.

Besides the experiments we carried out a simple estimation of the space-charge field for the following conditions: mixture pressure – 1 bar, quantity of e-beams – 2, foils – Ti, total e-beams current density through foils I = 20 A/cm$^2$, I = plasma electrons current density + plasma ions current density.

As a result we obtained: electron concentration in plasma – $10^{12}$ cm$^{-3}$, ions concentration – $5x10^{16}$ cm$^{-3}$. Electron drift velocity $10^7$ cm/c – current density is 3 A/cm$^2$ (E/p=17 kV/cm bar). Ion drift velocity $10^3$ cm/c – current density is 15 A/cm$^2$ (E/p=17 kV/cm bar). Electron and ion current density is 18 A/cm$^2$ (near to 20 A/cm$^2$). The space charge produces an electric field of about 17 kV/cm (potential in center of chamber is about 100 kV). In such a case an e-beam with energy of about 300 keV (our real beam) will lose about 30% of its energy in working against the electric space-charge field. If we look on the behavior of the output laser energy versus mixture pressure (Fig.1) it is possible to see that the output energy at 1 bar decreased approximately 30% (if we extrapolate the curve up to energy 90 J).

In spite of the influence of the space charge on the laser output in the critical range, HF laser could successfully work in the normal range. In our case this was realized with Ti foils and two sides pumping at mixture pressure less than 0.7 bar and for one side pumping at mixture pressure less than 0.9 bar. An efficiency of 4-5% and a specific laser energy of 4 J/l could be obtained. We suppose that the laser efficiency might be increased if we decrease a little the e-beam current density and increase a little the diode voltage and the active volume dimension (distance between the foils) with respect to our experimental conditions.

## 4. CONCLUSION

In the present paper experimental and theoretical research on a pulsed chemical e-beam pumped HF laser with 25 l active volume using the non-chain reaction have been carried out. Laser parameters as a function of the current density, the electrons energy, the mixture pressure and the mixture composition were investigated. The basic results of these research are the following.

1. It has been shown that space-charge could be formed in the active media of a e-beam pumped HF laser. The space-charge created electric field decreases the useful deposited pump energy. The basic proof of the space-charge existence and its influence on the laser output is as follows:

   - decrease of the laser energy and efficiency for two sides pumping with Ti foils (mixture pressure > 0.7 bar) and kapton foils (pressure 0.4-0.95 bar) in comparison with the sum of the energies obtained from the first and second beams working separately;

   - decrease of the specific laser energy and laser efficiency in case of deposited pump energy increase (change of the pressure with 0.7 bar on 0.9 bar, Ti foils, two sides pump);

   - decrease of the generation range with the increase of the deposited pump energy (case with kapton, one side pumping and two sides pumping).
2. A critical value of the deposited pump energy (injected charge) was found (corresponding to the beginning of the decrease of the laser energy). For our experimental conditions the **critical** deposited pump energy equals 60-70 J/l (**critical** injected charge equals $2x10^{-4}$ C/l).
3. On the basis of our results it can be concluded that for effective pumping a chemical HF laser by e-beam, using a non-chain reaction, it is necessary to have a pumping level lower than some **critical value**. In this case it is possible to excite large active volumes and to obtain kilojoule laser output energy.

## REFERENCES


1. Ramirez I.I., Prestwich K.R., J. Appl. Phys., **50**, p.4988-4995, 1979.
2. Grabovsky E.V., Denisenko V.P., Jivotov V.K. et al., Sov.JTF, **49**, №10, p. 2224-2226, 1979.
3. Bashurin V.P., Velikanov C.D., Dovgy A.Ya. et al., Sov. J. Papers of Academy Sciences USSR, **287**, №3, p. 614-618, 1986.
4. Yu. I. Bychkov, N. G. Ivanov, V. F. Losev et al., *Kvantovaya Elektron.* (Moscow) **17**, p. 300-303, 1990.

# Stabilization and effective generation laser on $SF_6$-$H_2$ mixture

Michail V. Erofeev, Victor M. Orlovskii, Victor S. Skakun,.
Edward A. Sosnin, Victor F. Tarasenko[1]

High Current Electronics Institute, 4, Akademichesky Ave.,
634055 Tomsk, Russia

## ABSTRACT

Energy, temporal and spectral characteristics of HF-laser pumped by non-chain chemical reaction initiated by radially converging e-beam, planar e-beam and non-self-sustained discharge have been investigated. The major channels of vibrationally excited HF molecules formation have been analysed. It has been confirmed that the high efficiency (~ 10 %) of non-chain HF laser can be reached only by simultaneous atomic and molecular fluorine formation under the action of e-beam and molecular fluorine participation in the inversion releasing process. It is shown that the laser pulse has a complex spectral-temporal structure caused by consecutive generation of the P-lines $P_2 \rightarrow P_1 \rightarrow P_3 \rightarrow P_4 \rightarrow P_5 \rightarrow P_6$ and overlapping of the rotary lines of the same oscillatory band and separate oscillatory lines during a pulse of radiation. With e-beam pumping of a 30 l active volume laser, the output energy as high as 115 J and efficiency with respect to e-beam energy deposited into gas mixture up to 8 % were demonstrated. The optimal gas mixture $SF_6 : H_2 = 8 : 1$ under pressure of 0.45 atm has been obtained. At pressure 1.1 atm and non-uniform output distribution, total laser energy and efficiency with respect to e-beam energy deposited into gas were found to be up to 200 J and 11 %, respectively. Use of e-beam initiated low pressure pulsed discharge for excitation HF molecules leads to increase of radiation energy in 2.8 times. Also investigations on zeolite-based different absorbents influence on energy stability of HF-laser are presented and radiation energy decay after $10^3$ shoots not more than 15-20 % is gained.

**Keywords:** HF-laser, spectrum, efficiency of generation, e-beam and discharge pumping

## 1. INTRODUCTION

Use of e-beam at chain and non-chain chemical reaction initiation in HF-lasers allows to excite large volumes of active media and obtain significant energies of radiation [1,2,3]. The most high efficiency values and radiation energies are being achieved in chain reaction pumped chemical lasers. With HF-lasers practical use one needs to have not only high energy parameters at single pulse mode but also safety and convenient conditions to work, and in some cases pulsed periodical laser mode. From this point of view, non-chain lasers operating on $SF_6$ with $H_2$ or $D_2$ mixtures or their complexes at the condition of achievement with them of sufficiently high efficiencies (10 % and higher).

The present paper reports the experimental results on investigation of the main factors which influence on efficiency of non-chain chemical HF-lasers initiated by radially convergent or planar e-beams. The investigations conducted in [4] where in particular it was shown that radiation efficiency achievement more than 9 % is possible only with e-beam produced molecular fluorine taking part in laser inversion, were continued by the present work.

## 2. EXPERIMENTAL SETUP AND MEASUREMENT METHODS

There were three set-ups used in the experiments. In the first set-up which had the volume of 30 l, the pumping was realized by a radially convergent e-beam; HF-laser energy and temporal parameters of radiation and also pumping pulse parameters obtained with this set-up were described in [3,4,11].

The experiments were performed on the second set-up which was earlier described in [5]. Accelerator provided to form e-beam with the following parameters: beam-current density was of 2.5 A/cm$^2$, cross section of electron stream 42×1.5 cm, the pulse duration of current amplitude at FWHM was 50 ns, electron energy downstream off the foil was 155 keV (maximum at the curve dependence of electron energy via its quantity). Initiation of chemical reaction was realized by

[1] Correspondence: E-mail: VFT@loi.hcei.tsc.ru; Telephone: (3822) 258-685; Fax: (3822) 259-410

XIII International Symposium on Gas Flow and Chemical Lasers and High-Power Laser Conference,
Antonio Lapucci, Marco Ciofini, Editors, Proceedings of SPIE Vol. 4184 (2001)

e-beam or in the process of e-beam initiated non-sustained discharge from the bank of capacitors of $3.9 \cdot 10^{-9}$ F. Anode-cathode gap was up to 2.3 cm. Laser's resonator was formed by spherical copper mirror with a radius of curvature of 2.5 m and plane-parallel plate made of KRS-5 with reflection of 33% in 3 μm spectral region. The laser output energy was registered by IMO-2N and IKT-1N calorimeters. Temporary characteristics of impulse were measured by FSG-22-3A2 photoresistor with 1.5-11 μm region spectral sensitivity. Spectral characteristics of radiation were measured with MDR-12 monochromator with 300 stroke/mm (inverse line dispersion 9.6 nm/mm).

Investigations on zeolite-based different absorbents influence on energy stability of HF-laser were performed on the third set-up (with $20 \times 1 \times 1 \approx 20$ cm$^3$ active volume) which was earlier described in [14].

## 3. EXPERIMENTAL RESULTS AND DISCUSSIONS

### 3.1. HF-laser pumped by planar e-beam

The mixture $SF_6$:$H_2$=7:1 was close to optimal in the range of pressures from 0.1 to 1 atm. Further increase of $H_2$ concentration led to insignificant increase of energy and then to its drop. The change in absorbed energy of e-beam in the gas media was calculated by the formula: $W_b = j_b \cdot (dE/dx) \cdot V \cdot t_b$. Here $j_b$ is a beam density, $dE/dx$ - average energy loss per unity of length, $V$- volume of active region of gas cell and $t_b$-e-beam duration. The value of 130 keV has been taken as an average energy distribution of electrons by velocities, e-beam flow average energy loss per unity of length were $1.8 \cdot 10^3$, $3.5 \cdot 10^3$, $6.48 \cdot 10^3$, $15.6 \cdot 10^3$, $19 \cdot 10^3$ eV/cm and corresponded to the pressures 0.096, 0.184, 0.344, 0.82, 1 atm for $SF_6$:$H_2$=7:1 [6]. The dynamics of the radiation energy change has tendency to saturation and is caused by energy e-beam spectra. Such dependences were observed in [7, 8, 9]. Maximal value of energy radiation is totally defined by chemical reaction rate increasing with laser pressure on one hand and collisional decontamination HF molecules rates rising on the other hand. This tends to the efficiency decrease with further increasing of pressure and radiation energy. The maximum of efficiency (~5.5%) was obtained at ~0.4 atm. It is noted that, secondary electrons spectrum depending on operating mixture composition and pressure [10] can influence optimal pressure with respect to obtaining of maximal radiation efficiency.

### 3.2. HF-laser pumped by planar e-beam initiated discharge

Aimed to investigate the additional electric field influence on efficiency, to the gas gap constant voltage was applied. In the process of pulsed non-sustained discharge, external electric field addition allows to increase average energy of secondary electrons and, by doing so, to provide more intensive fluorine accumulation [8]. Use of e-beam initiated low pressure pulsed discharge in $SF_6$:$H_2$=7:1, p=0.184 atm leads to increase of radiation energy in 2.8 times at electric field strength close to breakdown values. However, in this case energy diffused to gas in the process of discharge breakdown is higher than absorbed e-beam energy at an order. Correspondingly, laser efficiency decreases too. When voltage is higher than static breakdown voltage, increase of the total efficiency should be expected.

### 3.3. HF-laser pumped by radially converging e-beam

The main results are illustrated in Fig. 1. Fig. 1 gives dependences of energy (deduced from the pressure jump) in an active $SF_6$-$H_2$ mixture or in $SF_6$ when the pressure was increased to 1 atm. In the case of $SF_6$ the energy deposited in the gas ceased to rise beginning from ~0.6 atm (curve 2), whereas in an $SF_6$-$H_2$ mixture (curve 1), at the same pressure the input energy was higher and it continued to rise with increase of the pressure. The difference between the energies corresponding to curves 1 and 2 was the chemical reaction energy (curve 2). An increase in the pressure of the active mixture from 0.45 bar to 1 bar increased the chemical reaction energy deposited in the gas by a factor of ~2. However, the energy distribution over the output beam of the laser then became more nonuniform. At the mixture pressure of ~1.1 atm the total radiation energy was ~200 J.

### 3.4. HF non-chain chemical laser efficiency

In [4, 12] it was shown that e-beam pumped HF non-chain chemical laser efficiency is determined not only by atomic fluorine but molecular fluorine as well. The both particles are formed at e-beam injection into operating mixture at the expense of $SF_6$ molecules dissociation. In this case, derivation of HF vibrationally excited molecules can result from two main processes:

$$F + H_2 \rightarrow HF(v \leq 3) + H + Q_1 \text{ (31,8 kcal/mole)}, \quad (1)$$

$$F_2 + H \rightarrow HF(v \leq 6) + F + Q_2 \text{ (98 kcal/mole)}, \quad (2)$$

where $Q_1$ and $Q_2$ are energy released from chemical reaction. Here the inversion could be presented in the following way [4,12,13]. Since the specific reaction rate (1) is 5,5 times higher than in reaction (2), and the last takes place after sufficient hydrogen atoms appear, than at the first stage inverse HF molecules population is observed ($v \leq 3$). Just this leads to appearance of generation on these vibrational transitions with ($v \leq 3$). At the second stage the reaction (2) realizes the inverse HF molecules population has achieved, at higher vibrational transitions ($v \leq 6$) including. Besides that, atomic fluorine formed in the reaction (2) can participate once again in inversion development at transitions ($v \leq 3$), reaction (1). Thus, in operating mixture there can have place short chains which can lead to HF-laser efficiency increase, and in this case in spectra of generation vibrational transitions ($v$ = 4-6) must be presented. With this the radiation pulse duration must exceed e-beam pulse duration.

In Fig. 2 spectral energy distribution for laser mixture $SF_6$:$H_2$=7:1 is presented. For the three tested pressure values, generation was observed on transitions with $v > 3$. With much higher pressure values (0.82 and 0.344 atm) generation was registered at all the six transitions of P-branch ($P_1$,$P_2$,$P_3$,$P_4$,$P_5$,$P_6$), and the maximal energy value was on the transition • 2. Only on transitions $P_1$,$P_2$,,$P_3$,,$P_4$,$P_5$ pressure decrease up to 0,096 atm led to generation and displacement of maximum of generation to the transition $P_1$. Thus, spectral characteristics of radiation confirm participation of molecular fluorine in HF-laser inversion.

HF-laser temporal and spectral-temporal characteristics were investigated either for total laser signal or for separate lines at pressure range of 0.1-1 atm for laser mixture $SF_6$:$H_2$=7:1. Typical e-beam pulse oscilloscope traces (curve 1), total radiation at all lines (curve 2) and dependence of radiation duration at FWHM of intensity on pressure are shown in Fig. 3. The Fig. 3a presents e-beam current pulse and laser radiation pulse achieved at the set-up with radially convergent e-beam pumping. The generation threshold obtained since 40 ns after e-beam current injection, and radiation pulse duration significantly exceeds the pumping pulse duration and has a complicated spiking structure. Evidently, it may be related to the fact that in generation participate different vibrational transitions, including the case with $v > 3$, generation at which has big times of delay. In Fig. 3b are shown pulses of e-beam current and generation obtained at the set-up with planar e-beam pumping. It is clearly seen, that the radiation pulse has the similar structure. Dependence of radiation pulse duration at the FWHM via pressure is presented in Fig. 3c. Pressure growth increases specific inputs in operating mixtures and speeds up chemical reactions rates that just causes radiation pulse duration reduction, nevertheless also at the pressure of 1 atm radiation pulse duration exceeded the pumped pulse duration (50 ns at FWHM). So, laser radiation pulse duration changed from 150 to 600 ns with mixture pressure varying from 1 to 0,1 atm, and laser radiation time delay relatively to initial action on e-beam gas media varied with this from 20 ns at 1 atm to 97 ns at 0.1 atm.

According to [4,12] limit efficiency of non-chain HF-laser with only atomic fluorine participation in inversion development is defined by $\eta = 0{,}88 \cdot 10^{-2} \cdot h\nu$, where $h\nu$ = 10,2 kcal/mole, and can not exceed 9 %. In this work we have got generation efficiency at the set-up with radially convergent e-beam pumping over 10%. In papers [8,12] it was also reported about non-chain HF-laser radiation efficiency 10 % and more. Thus spectral-temporal characteristics and realization of high efficiencies strengthen the case for participation of molecular fluorine in non-chain HF-laser inversion development.

### 3.5. Stabilization characteristics of HF-laser

The quenching have an important bearing on the energy characteristics of HF- lasers. Quenching efficiency of various particles can have considerable differences. The most efficient quenching molecules have attraction forces between itself, which depends on hydrogen links and leads to formation of long-lived complexes. For example, $H_2O$ molecule deactivates any molecule after few collisions, and HF molecule deactivates HF* molecule after 60 collisions [12]. Therefore, as accumulation of HF molecules is in progress after a number of shots we have energy-decay. In the process of work, a row of wide-porosity synthetic zeolites such as NaA, NaX, CaA and others possessing high adsorbing characteristics relatively adsorption of water were used in order to define absorption efficiency of molecules $H_2O$ and HF. Zeolite CaA was obtained by ion exchange $Ca^{2+}$ for $Na^+$ from preliminarily decationized NaX by treatment of which with 25 % $NH_4Cl$ water solution at 90 $^0$C during two hours. Before use, the zeolite samples under study were calcinated at 500 $^0$C during 8 hours, after that a portion of 10 g (25 cm$^3$) was placed into the laser operating volume and tested.

Carried out studies have shown that the zeolites NaA, NaX, CaA, used as absorbents for $H_2O$ and HF absorption, efficiently absorb the molecules $H_2O$ and HF being formed during laser operation. Figures 4 and 5 give dependences of radiation energy on a number of shots for gas mixture $SF_6$:$H_2$=7:1 with use of the absorbent (curves 1, 2), and without one (curve 3). Zeolite-based absorbent was distributed uniformly over the entire titanium foil area, which is located along the length of the active volume. As it is seen from Fig. 4 and 5, absorbent presence allows to decrease relative radiation energy-decay from 40 to 13 % for HF-laser pumped by planar e-beam (repetition rate was approximately 1 shot a minute), from 60

to 15 % for electrodischarge HF-laser with UV ionization (repetition rate of shots was 1 Hz) and from 80 to 25 % (repetition rate of shots was 2 Hz) in the investigating interval of the shots.

## CONCLUSION

The present paper reports on investigations of spectral and temporal characteristics of HF-lasers with non-chain chemical pumping initiated by radially convergent and planar e-beams. Electric fields in the center and near the side wall of laser chamber, and also radiation energy density distribution in wide aperture laser output beam have been measured. The main channels of vibrationally excited HF molecules formation have being analyzed. Based on spectral and temporal investigations it has been confirmed that high efficiencies (~10 %) of non-chain HF-laser can be achieved only at the expense of simultaneous formation of atomic and molecular fluorine under e-beam influence on operating mixture. It was shown that the lasing pulse has a complicated spectral temporal structure determined by sequential generation of P-lines $P_2 \rightarrow P_1 \rightarrow P_3 \rightarrow P_4 \rightarrow P_5 \rightarrow P_6$ and overlapping during radiation pulse both of rotational lines of one and the same vibrational band and separate vibrational bands.

Under e-beam pumping of a laser with active volume of 30 l output energy as high as 115 J and efficiency with respect to e-beam energy deposited into gas mixture up to 8 % were demonstrated. Optimal gas mixture $SF_6 : H_2 = 8 : 1$ under pressure of 0.45 atm was chosen to provide no more than two-fold specific output power variations across the laser beam area. Total laser energy and efficiency with respect to e-beam energy deposited into gas were found to be up to 200 J and 11 %, respectively, at pressure 1.1 atm and with non-uniform output distribution.

Low pressure pulsed discharge initiated by e-beam flow for excitation HF molecules leads to increasing of radiation energy in 2.8 times. Also investigations on zeolite-based different absorbents influence on energy stability of HF-laser are presented and radiation energy decay after $10^3$ shots not more than 15 % is gained.

## REFERENCES


1. S.D. Velikanov, M.V. Sinitsyn, V.D. Urlin, "Pulsed chemical laser with an e-beam initiated reaction", *Kvant. Elektron.*,**23**, pp. 25-28, 1996.
2. M. Costaud, J. Boulsc, M. Autric, *SPIE Proc.*, **3092**, pp. 585, 1996.
3. V.F. Tarasenko, E.H. Baksht, M.I. Lomaev, A.N. Panchenko, V.M. Orlovskii, E.A. Sosnin, "Efficient non-chain chemical HF-lasers initiated by e-beam and self-sustained discharge", *SPIE Proc.*, **3268**, pp. 228-235, 1998.
4. V.F. Tarasenko, E.H. Baksht, M.I. Lomaev, A.N. Panchenko, V.M. Orlovskii, E.A. Sosnin, A.G. Ponomarenko, Yu.I. Hapov, "Powerfull non-chain chemical HF-lasers initiated by e-beam and self-sustained discharge", Lasers'97, STS Press, McLean, VA, pp. 695-702, 1998.
5. O.V. Sereda, V.F. Tarasenko, A.V. Fedenev, S.I. Yakovlenko, "Powerful IR lasers on XeI transitions", *Kvant. Elektron.*, **20**, 6, pp. 535-558, 1993.
6. A.P. Komar, S.P. Kruglov, N.V. Lopatin, *Total Energy Measurements of Breaking Radiation Beams from Electron Aaccelerators*, Nauka, Leningrad,1982.
7. V.M. Orlovskii, E.A. Sosnin, A.G. Ponomarenko, "Efficiency of chemical $SF_6$-$H_2$ laser pumped by e-beam", *Zh. Tekn. Fiz.*, **69**, 1, pp. 76-78, 1999.
8. A.S. Bashkin, A.N. Oraevskii, V.N. Tomashov, "Energy characteristics of chemical HF-laser pumped by e-beam", *Kvant. Elektron.*, **4**, 1, pp. 169-171, 1977.
9. N.G. Basov, *Chemical Lasers*, Nauka, Moscow, 1982.
10. V.F. Tarasenko, A.V. Fedenev, V.S. Skakun, "Efficiency of laser on Xe transitions pumped by e-beam", *Kvant. Elektron.*, **26**, 3, pp. 209-213, 1999.
11. E.N. Abdullin, A.M. Efremov, B.M. Kovalchuk, V.F. Tarasenko, A.N. Panchenko, V.M. Orlovskii, E.A. Sosnin, V.V. Ryzhov, I.Yu. Turchanovskii, "Laser on $SF_6$-$H_2$ mixture pumped by radially convergent e-beam", *Kvant. Elektron.*, **24**, pp. 781-785, 1997.
12. Yu.I. Hapov, *Energy Characteristic $SF_6$-$H_2$ Set-up Pumped by E-beam*, Dissertation of Ph.D (Tech.), Novosibirsk, 1982.
13. R. Gross, J. Bott, *Handbook of Chemical Lasers*, Wiley Interscience, New York, 1976.
14. F.G. Gorunov, K.V. Gurkov, M.I. Lomaev, E.A. Sosnin, V.F. Tarasenko, "Pulse chemical electrodischarge laser on $SF_6$-$H_2$ mixture", *Kvant. Elektron.*, **21**, pp. 1148-1150, 1994.

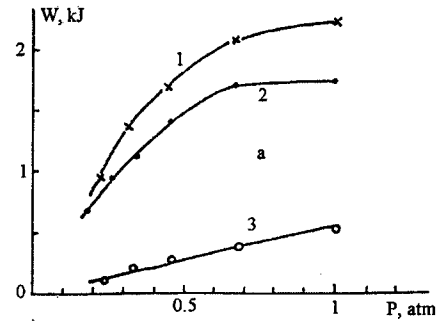


Fig. 1. Dependencies of the energy $W$ deposited to the gas, found experimentally from measurements of the pressure jump (1-3). The curves represent the total energy deposited by the e-beam and the chemical reaction (1), the energy deposited by the e-beam (2) and by the chemical reaction (3)

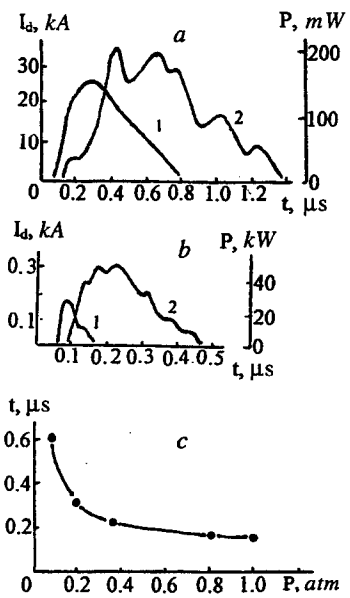


Fig. 3. Oscilloscope traces of current beam pulses (1) and generation (2) under radially convergent (a) and planar (b) beam pumping of $SF_6$-$H_2$ = 7:1 mixture at 0.45 atm and 0.344 atm correspondingly. Dependence of radiation pulse duration of the FWHM obtained at the set-up 2 on $SF_6$-$H_2$ = 7:1 pressure (c)

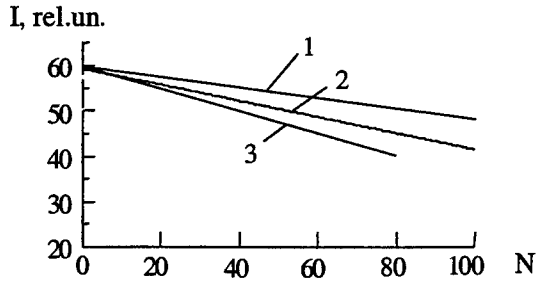


Fig. 4. Dependences of radiation energy in relative units on a number of shoots for gas mixture $SF_6$:• $_2$=7:1 with use of the absorbent. Volume of absorbent: 1- 4 $cm^3$ , 2- 6 $cm^3$ , 3- 0 $cm^3$

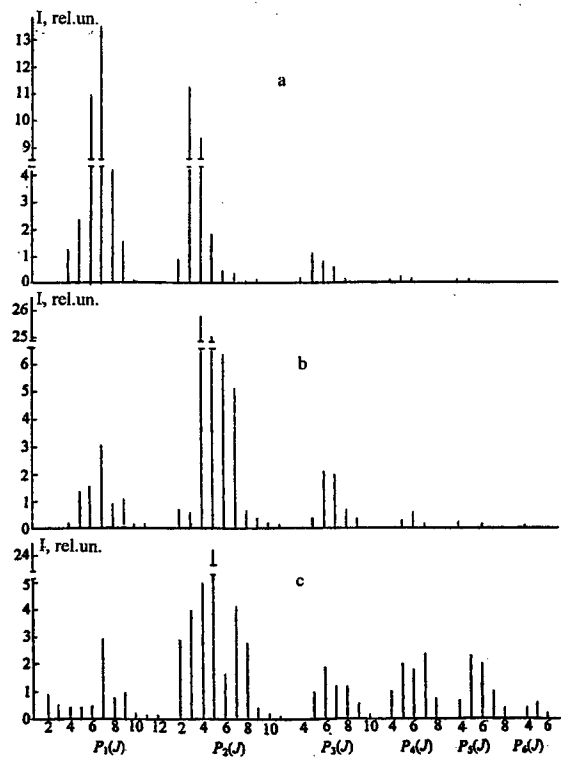


Fig. 2. Generation energy distribution over spectral components in laser mixture $SF_6$-$H_2$ = 7:1 at pressure 0.096 (a), 0.344 (b) and 0.82 atm (c), set-up 2

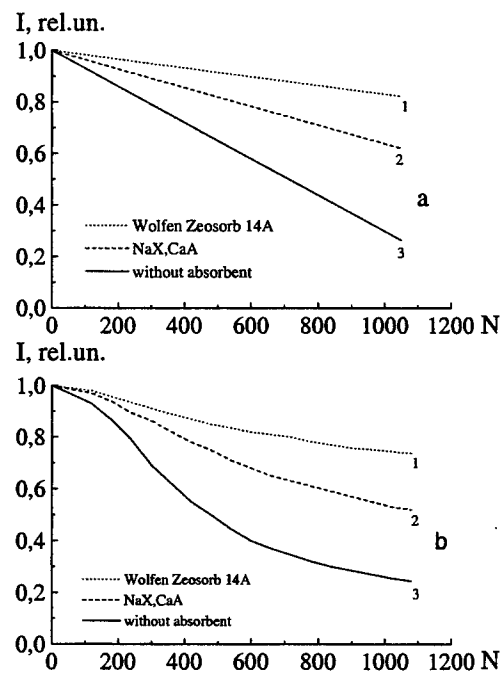


Fig. 5. Dependences of radiation energy in relative units on a number of shoots for gas mixture $SF_6$:• $_2$=7:1 with use of different absorbents at repetition rate of shorts 1 Hz (a) and 2 Hz (b)

# Cascade scheme "master generator - amplifier" of the photoinitiated pulsed chain chemical HF/DF-laser

B.S.Alexandrov, A.V.Arsenjev, M.A.Azarov, V.A.Drozdov, G.A.Troshchinenko

Russian Scientific Centre "Applied Chemistry"

14, Dobrolubov ave., St.Petersburg, 197198, Russia

## ABSTRACT

The cascade scheme "master generator – amplifier" of the photoinitiated pulsed chain chemical HF/DF-laser is investigated by numerical modelling and in experiment. The possibility to control the duration and spectrum of the laser pulse is shown, the efficiency of amplifier can exceed the efficiency of the equivalent generator.

**Keywords:** chemical pulsed HF/DF laser, chain reaction, amplifier, synchronisation of photoinitiation, spectrum, efficiency

## 1. INTRODUCTION

Pulsed chemical HF- and the DF-lasers are capable to generate with high efficiency the low divergent power radiation beams in wide spectrum range (from 2.6 μm up to 5 μm) with pulse duration, changed within the limits of one - two orders of magnitude.

Use of the cascade schema "master generator (MG) - amplifier (A)" expands capability to control the parameters of the power pulse of the laser radiation and provides achievement of its maximal brightness. Depending on the concrete technical applications the change of duration of an output pulse, its divergence and spectrum is realised as a result of variation of these MG parameters. It is possible to obtain the output radiation with higher optical characteristics and higher specific energy in comparison with the equivalent generator due to reduction of diffraction losses at single-pass propagation of the radiation pulse with small divergence through the wide aperture A. The laser distinguishing from A only by replacement of windows on the resonator mirrors is referred here as the equivalent generator (EG).

On the first stage of study of the cascade scheme the efficiency of the amplifier was obtained 3 - 10 times less in comparison with EG [1,2]. Further the amplifier efficiency on the level of 100% in relation to EG was achieved [3], however the energy characteristics of the DF-laser in this experiment did not exceed half of the HF-laser characteristics.

Here the theoretical and experimental study of conditions of co-ordination of the processes in active medium (AM) of MG and A, at which the energy efficiency of A is close the efficiency of EG, is carried out for the pulsed chemical laser. The dependence of the pulse energy of A on duration, energy and spectrum of MG pulse and on a time delay $\Delta t$ between the beginning of initiation of chemical reactions in MG and A is investigated. The connection between the shape and duration of pulses on input and on output from A is determined at various $\Delta t$.

## 2. RESULTS OF EXPERIMENTS AND NUMERICAL MODELLING

The experimental investigation is carried out on lasers of a multimodular cylindrical design with a central arrangement of a photolamp [4], with a total AM volume up to 100 l and an aperture of the laser beam of 60 mm (MG) and 130 mm (MG and A) and with an initiation energy from 0.1 kJ/l (MG, A) up to 1.2 kJ/l (MG). The pulsed chemical HF- and DF-lasers with the AM length of 1.9 m and 3.8 m were used as MGs. An external resonator of MG consists of round mirrors carried on distance up to 5 m. A copper mirror with reflection factor 0.98 serves as a total reflector. A parallel-plane plate or set of plates from $CaF_2$ with reflection factor ~ 0,06 are used as output coupler. A design of an operating chamber and the initiation system of A is the same as at MG. The only difference is that the windows of the operating chamber of A are inclined at angle of 15° to a resonator axis. Density of the MG radiation on input of A is changed by selection of a combination of periscope mirrors in a channel of optical connection between MG and A. The MG radiation spectrum is varied by change of AM length and selection of the resonator mirrors. The initiation energy is varied by change of voltage

Correspondence: Email: gtrosh@GT4631.spb.edu; Telephone: 812 238 9070; Fax: 812 238 9251



XIII International Symposium on Gas Flow and Chemical Lasers and High-Power Laser Conference, Antonio Lapucci, Marco Ciofini, Editors, Proceedings of SPIE Vol. 4184 (2001)

of discharge and capacity of the condensers. The channel of optical connection of special pressure-tight design for ensuring minimum distance (5 cm) for propagation of radiation from MG to A through atmosphere air is made.

For computational simulation the theoretical model combining the description of the longitudinal non-uniform radiation effects in A and of the chemical, vibrational and rotational kinetic processes is used. The method-of-characteristics is used for the solution of the partial differential equations describing passage of plane laser radiation waves in two counter directions. The similar model of radiation transport was offered in Ref.[5], where it was supposed, that the characteristics the AM are identical on whole volume. In the present study the longitudinal heterogeneity of chemical and kinetic processes is taken into account. It is essential, as the amplification of the input radiation at its propagation along an amplifier axis creates various conditions for laser processes in various points of reactor.

As a result of this study the conditions of achievement of maximal energy efficiency of A in HF- and DF-cascades are determined. These conditions are as follows.

**A. The time delay between the beginning of the chain chemical reaction initiation in MG and A should ensure the synchronisation of achievement of maxima of the chemical pumping rate in both reactors.**

The dependence of the specific output energy $E_{out}/V$ of A on the time delay $\Delta t = t_{ini}$ (MG) - $t_{ini}$ (A) between the beginning initiation of A $t_{ini}$ (A) and MG $t_{ini}$ (MG) is shown for HF- and DF-laser in Fig.1 (without including the input energy $E_{in}$). In this experiment the composition of AM, pressure and conditions of initiation in MG and A were identical, optimal value is $\Delta t$ = 0 - 0.3 μs, energy of the output radiation of A decreases 2 times at deviation from this value on ± 1 μs (the full pulse duration was 3 – 3.5 μs).

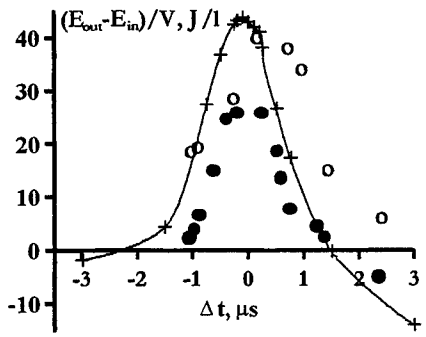


●○ - experiment
✚ - semiempirical model[4]
✚○ - MG (2 m, M = 38) - A (4 m), HF
● - MG (4 m, M = 42) - A (2 m), DF
Fig.1

The similar dependence is displayed in Fig.2a, b for experiment with the DF-laser, when the parameters of AM and initiation in MG and A were essentially various. In Fig.2a the dependence of the laser pulse duration (τ) of MG on energy in a discharge circuit ($E_{ini}$) of the photolamp is shown. A goal of this experience was amplification of the short MG signal with duration of 1 μs (at level of 0.1 of the maximal radiation intensity $I_{max}$). Such a shortening was achieved due to increase of pressure up to 1.5 atm and increase of the initiation energy contribution in AM as a result of increase of the discharge circuit energy and reduction of a diameter of the chemical reactor. The MG output radiation was expanded in the periscope system and passed to input of the wide aperture A (the input radiation density of 1 J/cm$^2$) with length of 4.8 m, where the AM pressure was 1.12 atm and the initiation energy was increased 2 times in comparison with conditions of experiment in Fig.1. The EG pulse duration was 2 μs, energy of 1.4 kJ, in experiment the pulse energies of A and EG were close each other. The optimal mode for this DF-cascade is advance in initiation of A on 1.4 μs (Fig.2b). The data of calculation for the same conditions, but for HF-cascade, are given in Fig.2b, in this case the optimal advance is 1.2 μs; the radiation intensity of the output A pulse, the MG and EG pulses are shown in Fig.2c, the point t = 0 corresponds to beginning the A initiation.

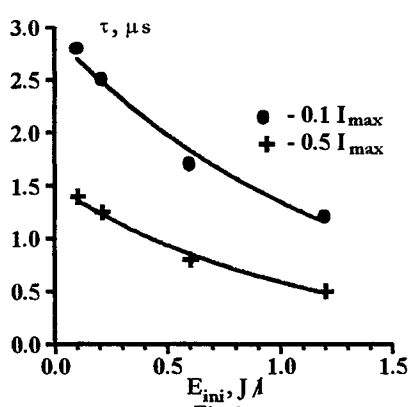


Fig.2a

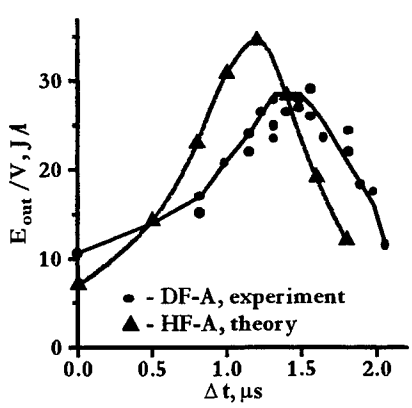


Fig.2b

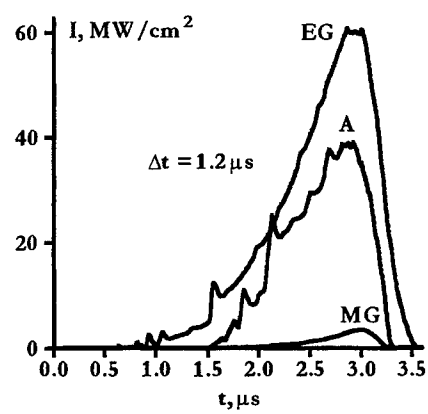


Fig.2c

Fig.3a, b, c illustrate the data of calculation of HF-cascade, the MG pulse with the radiation density of 0.1 J/cm$^2$ and duration of 160 ns is passed to A (length of 2 m, AM pressure of 1.4 atm, the initiation intensity is increased 5 times, duration of EG pulse of 1.45 μs). Such a short MG pulse was obtained due to reduction of duration and increase of initiation intensity. In Fig. 3a a series of the output A pulses is shown at various values of Δt. Optimal mode in this case is the delay of MG initiation relative to A of 2 μs (Fig. 3c). In Fig.3b the MG and A pulses are depicted at Δt = 1.8 μs; the forward and

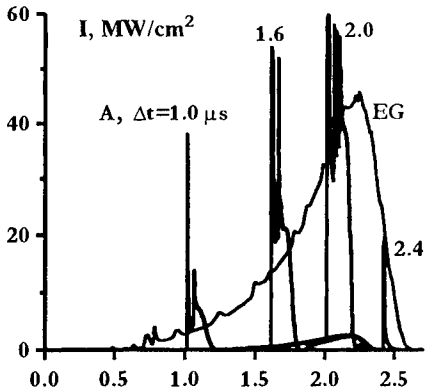

Fig.3a

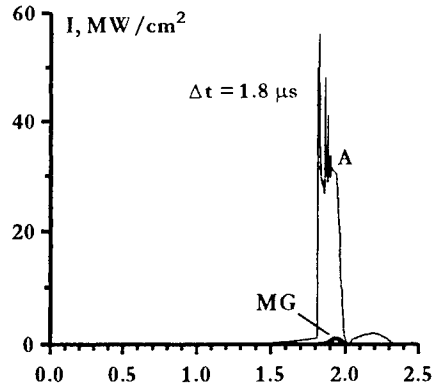

Fig.3b

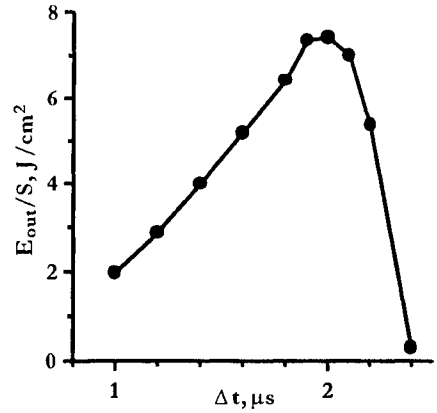

Fig.3c

back fronts of A pulse are more abrupt, than they are for MG pulse, owing to the large AM gain of A. The steepening the fronts enlarges the pulse duration up to ~200 ns (the same effect is visible in Fig.2c). The own A lasing in the superradiation mode is observed on time intervals of 1.4 - 1.8 μs and 2.05 - 2.35 μs.

For all considered cases the maximal energy of the A pulse is obtained at coincidence of the moments, when rates of the inverse population creation in AMs of MG and A achieve their maximal values.

### B.The radiation energy density on the input of A should provide the high degree of saturation of AM.

The experimental dependence of the A specific output energy $E_{out}$/V on the input energy density $E_{in}$/S is shown in Fig.4a. The data for HF- and DF-cascades with the various ratios of the reactor lengths of MG and A and with the various MG resonator qualities are given. The resonator quality is characterised here as factor M of excess of the maximal AM unsaturated gain above the lasing threshold. The results of calculation of similar dependence ($E_{out}$/S – the A output energy density) for conditions corresponding to Fig. 2c are shown in Fig. 4b.

These data demonstrate the weak sensitivity of the A specific energy to the input radiation density. At change of the input density 250 times the specific energy of A for HF- and DF-lasers changes 1.6 ÷3 times depending on the initiation intensity and the MG radiation spectrum. The low sensitivity of the

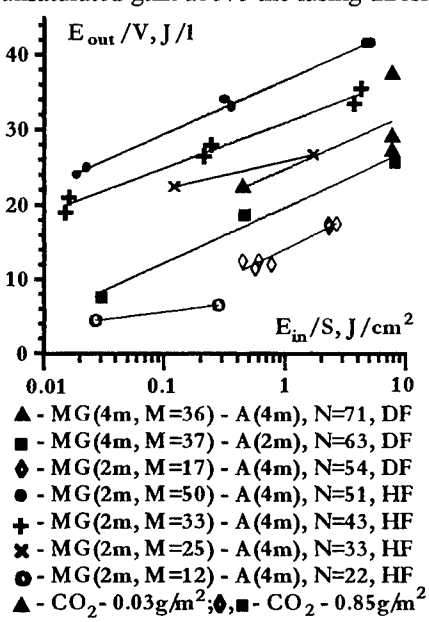

Fig.4a

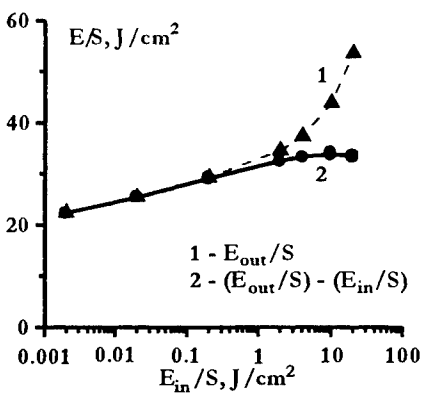

Fig.4b

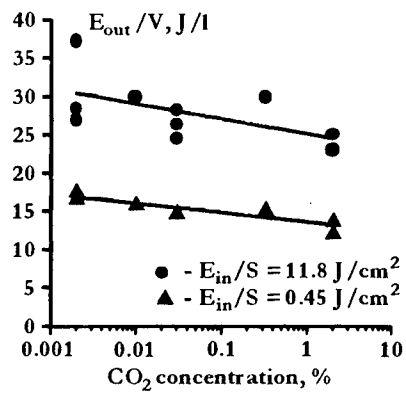

Fig.5

energy characteristics to input density is caused by the large length of A and the high gain for the large number of spectrum lines. Nevertheless, for achievement of

the specific energy, exceeding 90 % of the EG specific energy, the input density for HF amplifier with length of 4m should be more than 1 J/cm$^2$.

**C. The MG resonator should provide more than 50-multiple excess of the unsaturated maximal gain above the lasing threshold for initiation of the high band transitions up to 6-5, 7-6 for HF- and 9-8, 10-9 for DF-lasers.**

The number of the MG spectrum lines (N) was changed from 22 up to 51 for HF- and from 54 up to 71 for DF-laser in experiment due to change of the lasing threshold, at that the A pulse energy grew, correspondingly, ~4.5 and ~1.8 times (Fig. 4a). The change of spectrum of the HF- and DF-lasers depending on M is considered in Ref.[6]

**D. For achieving the DF-laser specific energy at the level of 90% of the HF-laser specific energy the content of the $CO_2$ impurity in AM of DF-laser and in the connection channel between MG and A should not exceed 0.05% and 0.03 g/m$^2$, respectively.**

The influence of impurity of $CO_2$ molecules inside the resonator on the radiation characteristics of HF- and DF-lasers is considered in detail in Ref.[7]; (see also Fig.4a where $CO_2$ concentration is noted in units of the thickness of the precipitated layer). Also a removal of the absorbing $CO_2$ impurity from the optical connection channel between MG and A is necessary. The dependence of the specific radiation energy for DF-A on $CO_2$ concentration in the optical connection channel is displayed in Fig.5.

## 3. CONCLUSIONS

The following energy characteristics of HF (DF) laser of the multimodular design were obtained in experiment as a result of realisation of the stated above conditions. The maximal technical efficiency of ~40 % (35 %) and the amplifier specific energy of 42 (37) J/l were measured at the maximal achieved energy density of the input signal of ~10 J/cm$^2$, most complete MG radiation spectrum consisting of 43 lines of six vibrational bands for HF-laser and ~80 lines of nine bands for DF-laser and the specific initiation energy of 105 J/l. The output pulse energy of the MG – A cascade was 3.4 (2.9) kJ and the A efficiency relative to EG exceeded 100 % in some experiments at the optimum time delay.

The control of the output pulse duration for the DF-laser from 1 μs up to 3.5 μs was realised in experiment at the constant A parameters as a result of the duration change of the MG pulse.

Application of MG with the small aperture (SAMG) in the MG - A cascade allows noticeably simplify and reduce the price of obtaining the required parameters of the laser beam, first, owing to reduction of the charges by manufacturing the optical elements of the SAMG resonator and, secondly, owing to the greater simplicity to control the SAMG initial parameters, such as total pressure and initiation intensity, which determine energy, spectrum and duration of the laser pulse.

## REFERENCES


1. N.G.Basov et all, "Investigation of system "HF masfer generator – amplifier" on chain fluorine-hydrogen reaction", *Kvantovaja electronica*, **5**, p.910, 1978 (in Russian).
2. G.C. Tisone, J.M. Hoffman, " Optical energy extraction from electron beam initiated $F_2$-$H_2$ mixture ", *J.Appl. Phys.*, **47**, p.3530, 1976.
3. V.P.Borisov, V.S.Burtsev, S.D.Velikanov, M.V.Sinitsyn, V.V.Shchurov, "Laser amplifier with initiation of chain chemical reaction by high-power light sources", in *XII International Symposium on Gas Flow and Chemical Lasers and High-Power Laser Conference*, Proc. SPIE Vol.3574, pp..361-367 (1998).
4. M.A.Azarov, B.S.Alexandrov, V.A.Drozdov, G.A.Troshchinenko, "Ways and conditions of achieving extreme characteristics of pulsed chemical DF and HF lasers", in *XI International Symposium on Gas Flow and Chemical Lasers and High-Power Laser Conference*, Proc. SPIE Vol.3092, pp.606-609 (1997).
5. J.B. Moreno, "Computer model for the H2-F2 super-radiant laser", AIAA-Paper 75-36, 1975.
6. M.A.Azarov, B.S.Alexandrov, V.A. Drozdov, G.A.Troshchinenko, "Influence of the cavity losses on the energy and spectral characteristics of a pulsed chemical chain-reaction HF(DF) laser", *Quantum Electronics*, **30**, pp.30-36, 2000.
7. M.A.Azarov, V.A.Drozdov, G.A.Troshchinenko, "Effects of absorption and relaxation on $CO_2$ impurities in pulsed DF/HF laser", in *XII International Symposium on Gas Flow and Chemical Lasers and High-Power Laser Conference*, Proc. SPIE Vol.3574, pp.606-611 (1998).

# Comparison of performance of chain and non-chain HF phototriggered lasers

B. Lacour, S. Pasquiers, C. Postel, V. Puech

Laboratoire de Physique des Gaz et des Plasmas (UMR 8578 du CNRS)
Bat 210, Université Paris-Sud, 91405 Orsay Cedex, France

## ABSTRACT

Results of the investigation of the discharge parameters, active medium homogeneity and stability, and laser performance are reported for a 2.5x2.5x50 $cm^3$ HF phototriggered laser working either in chain and non-chain mode. Using a $Ne/F_2/H_2/O_2$=93/5/1.5/0.5 mixture, a specific output laser energy of 9 J/l was obtained with an electrical efficiency of 38%. Compared to the performance of non-chain reaction HF lasers, these data correspond to an increase of the efficiency by a factor of 8. However, due to the development of discharge instabilities the output laser energy is not higher than that obtained with the non-chain laser mixtures.

## 1. INTRODUCTION

To date, the so-called phototriggered discharges allowed to reach the best laser performance for non-chain HF lasers. A specific output energy of about 10 J/l at an efficiency near 5 % was obtained in $Ne/SF_6/C_2H_6$ mixtures [1], and it was shown that this kind of excitation can be effectively used for the excitation of large aperture lasers [2]. On the other hand, Kutumov et al [3] recently reported that, in a pulsed chemical HF laser initiated by a dielectric barrier discharge, the substitution of $H_2/SF_6$ mixtures by $H_2/F_2$ ones, resulted in their device by an increase of the laser performance by more than one order of magnitude: specific output energy near 40 J/l at more than 60 % electrical efficiency. Those performances have been obtained with a specific electrode material not easily available in large dimensions, in such a way that the development of high energy lasers based on this technique may be rather difficult.

The goal of the present investigation was to perform a systematic study of a phototriggered discharge in $Ne/F_2/SF_6/H_2$ gas mixtures. The evolution of the electric parameters, the active medium homogeneity and stability, and the laser performance (output energy, efficiency and pulse shape) versus the partial pressure of $SF_6$ and $F_2$ have been studied. As a result, the physical processes involved in the limitation of the performance of the HF phototriggered laser using either chain or non-chain reactions are discussed.

## 2. EXPERIMENTAL SET-UP AND DIAGNOSTICS

In the phototriggered operating mode, the discharge electrodes are directly connected to an energy storage unit, which is pulsed charged up to a voltage higher than the sustaining voltage of the discharge. When this voltage is reached, the gas mixture is seeded with initial electrons which induce the discharge breakdown. The main feature is that there is no switch between the electrodes and the storage unit. A schematic cross-sectional view of the laser is shown in figure 1. This laser, named X525, comprised essentially three parts. The first one, the pre-ionisation unit, is an X ray generator composed of a cold cathode diode powered by a Marx generator. The X ray dose entering in the laser chamber is 10 mrad, which produces an initial electron density of about $2.10^9$ electrons per $cm^3$ in 100 mbar of $SF_6$. The second main element of the laser is the discharge chamber. The X-rays enter in this chamber through the plane bottom of the cell which acts as one electrode of the discharge. The other electrode is a profiled electrode calculated to provide a uniform electric field over 50 cm long and 2.5 cm width. The gap between the two electrodes is 2.5 cm, in such a way that the active volume is 312 $cm^3$. The optical cavity consists of a totally reflecting mirror and an output coupler made by an uncoated $CaF_2$ window. The third element of the laser is the energy storage unit. It is composed of ceramic capacitors used in two different configurations. In the first one, pure phototriggered operating mode, all the capacitors are directly connected to the upper electrode. In this configuration, the total capacitance can be up to 144 nF. The capacitors are pulsed charged up to the operating voltage with a rise time of 10 µs. However, for some gas mixtures, this rise time is too long and a discharge breakdown occurs before the firing of the X-rays, resulting in a very inhomogeneous discharge. A solution to avoid these spontaneous breakdowns, is



XIII International Symposium on Gas Flow and Chemical Lasers and High-Power Laser Conference,
Antonio Lapucci, Marco Ciofini, Editors, Proceedings of SPIE Vol. 4184 (2001)

to reduce the rise time of the voltage application to less than 1 µs. This is done through the use of a C-L-C circuit, represented in figure 1. A first capacitor bank is pulsed charged in 10 µs and the stored energy is transferred to the second capacitor bank, directly connected to the discharge electrode, in about 300 ns. In these experiments, we have used the same values for both capacitors banks, C=36 nF or C=72 nF. The voltage applied on the storage unit is measured with a resistive probe, while the current is measured with a Rogowsky coil. The laser energy is measured with a calibrated joulemeter and the shape of the laser pulse is recorded with a Ge-Au detector. In order to control the discharge homogeneity, the fluorescence of the plasma is measured with an intensified CCD camera allowing exposure time as low as 5 ns. As shown in Figure 2, the line of sight of the camera makes a small angle with the optical axis of the laser, in such a way that the discharge is seen in perspective on more than the three quarter of its length. Examples of the discharge quality for an homogeneous discharge and an inhomogeneous one are respectively given in figure 3a and figure 3 b.

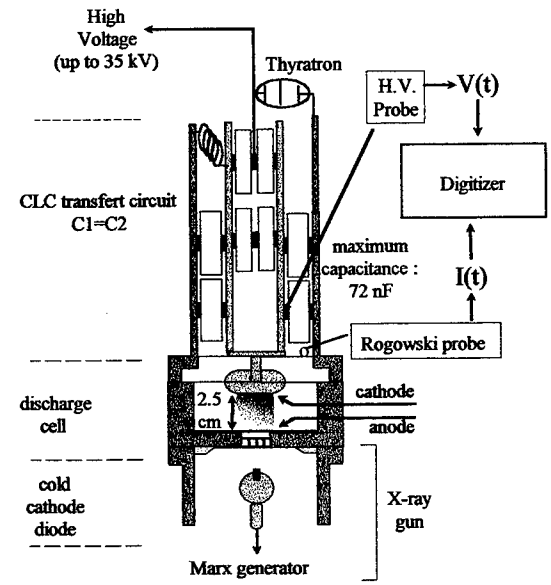


Figure 1: Schematic view of the X525 laser.

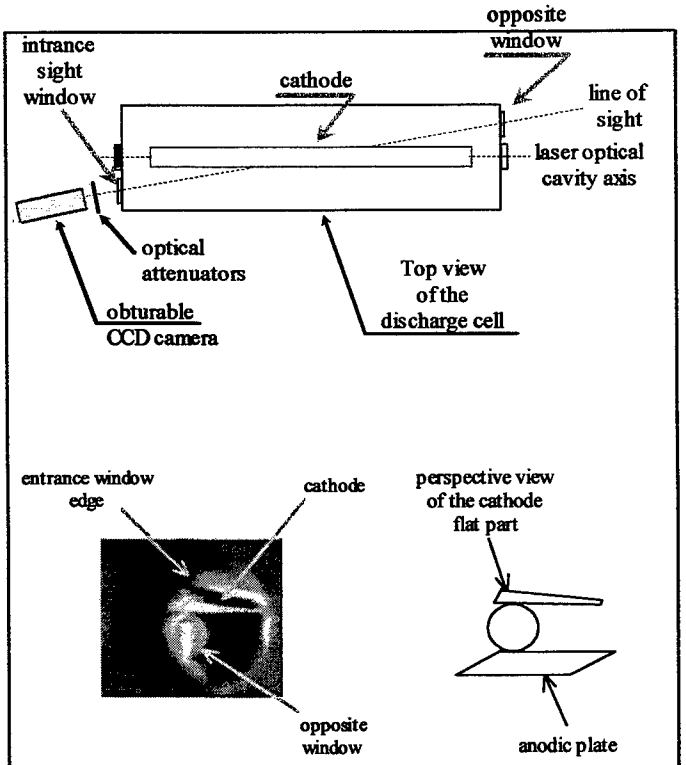


Figure 2: experimental set-up for the measurement of the discharge quality.

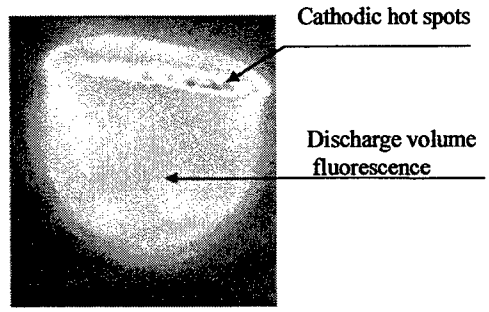


Figure 3a: homogeneous discharge in a $SF_6/C_2H_6$ mixture

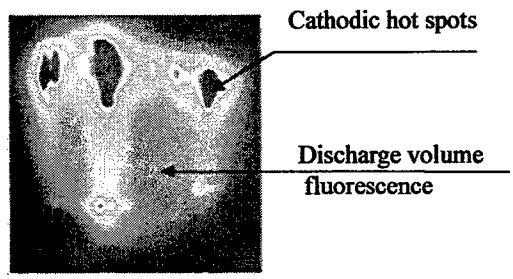


Figure 3b: inhomogeneous discharge in a $SF_6/H_2$ mixture.

## 3. RESULTS AND DISCUSSION

As the result of our investigation of the performance of the X525 laser working with non-chain mixtures has been previously published [1], we will just recall here the main features observed with these mixtures, to compare the results with those obtained with the chain-reaction mixtures on which we will focused the discussion. For non-chain mixtures ($Ne/SF_6/H_2$ or $Ne/SF_6/C_2H_6$) we have shown that the replacement of $H_2$ by $C_2H_6$ allowed to increase the laser performance by a factor of two, giving rise to a specific output energy of 10 J/l with an efficiency of 4.5 %. These performance were obtained with the pure phototriggered circuit (voltage rise time of about 10 µs) with 144 nF for the total capacitance of the storage unit. The investigation with the intensified CCD camera pointed out that the performance increase obtained with the use of $C_2H_6$ as H-atom donor was due to the stabilisation of the discharge which appears as a very homogeneous one (see figure 3a), while in $H_2$-based mixtures discharge instabilities rapidly grow up, leading to a very inhomogeneous medium (see figure 3b) producing large perturbation of the laser pulse. With ethane the specific output laser energy was only limited by the available maximum pumping energy (220 J/l) due to the maximum value of the X525 storage capacitance, 144 nF, and the maximum charging voltage, 31 kV.

In order to increase the laser performance we have investigated what kind of improvement could be reached through the use of chain mixture: $Ne/SF_6/F_2/H_2/O_2$. Most of the experiments were performed with the classical ratio $F_2/O_2$=10, which insures the stability of the $F_2/H_2$ gas mixture versus spontaneous burning, and with a ratio $F_2/H_2$=3. The $F_2$ molecules were handled in standard bottles containing 5 % of $F_2$ diluted in neon.

For a pure phototriggered circuit with a capacitance of 36 nF, charged to an initial voltage of 17 kV, the evolution, versus the $F_2$ partial pressure, of the specific output laser energy and electrical efficiency is shown in figure 4. This figure points out that the laser performance increases linearly with the $F_2$ partial pressure. For 35 mbar of $SF_6$, the addition of 8 mbar of $F_2$ allows to increase the laser performance by a factor of three. However, the specific output energy remains quite low, and it would be benefit to increase the $F_2$ partial pressure. But, a $F_2$ partial pressure higher than 8 mbar produces spontaneous discharge breakdowns before the firing of the preionisation, resulting in a very inhomogeneous discharge and poor laser performance. To overcome this problem, we have used a C-L-C phototriggered circuit providing a voltage rise time across the electrodes of 300 ns. With this circuit the spontaneous discharge breakdown was completely suppressed, allowing higher $F_2$ partial pressures and higher performance as shown in figures 5 and 6 which shown the evolution, versus the initial voltage, of the laser performance for different $F_2$ pressures.

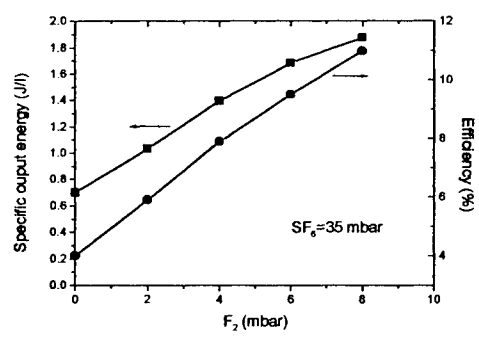


Figure 4: Evolution, versus the $F_2$ partial pressure, of the laser performance for a pure phototriggered discharge circuit.

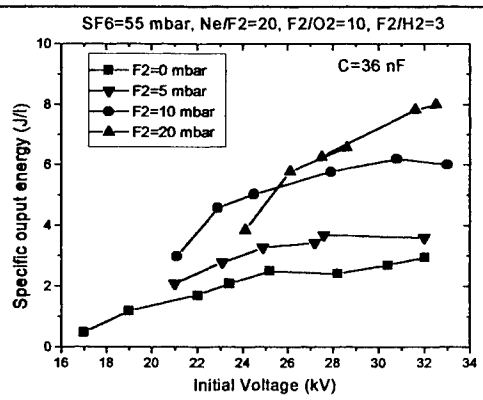


Figure 5: Evolution of the specific energy versus the initial applied voltage.

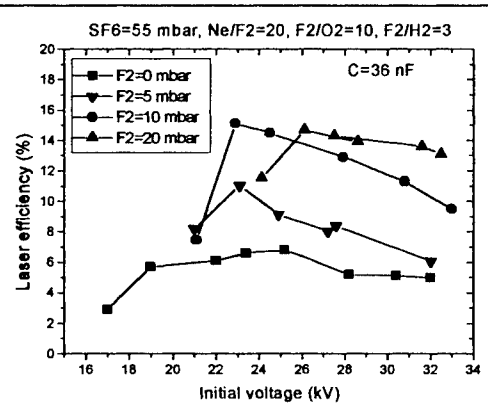


Figure 6: Evolution of the laser efficiency versus the initial applied voltage.

The data plotted in figures 5 and 6 were obtained for a storage capacitance of 36 nF and a $SF_6$ pressure of 55 mbar. Approximately the same specific output energy was achieved for a storage capacitance of 72 nF, giving an electrical efficiency divided by a factor of 2, and for any $SF_6$ pressure in the range 20-80 mbar. It was observed that, for a given gas mixture composition and a given capacitance, the best result is obtained for the highest voltage which can be applied without appearance of voltage and current oscillations during the discharge. These oscillations appear as a very sensitive indication of the development of discharge instabilities like the one shown in figure 3b. For mixtures comprising $SF_6$, the discharge quality becomes very poor for $F_2$ pressures higher than 20 mbar, resulting in deceptive laser performance.

On the other hand, removing $SF_6$ from the laser mixture allows to increase the $F_2$ partial pressure approximately by a factor of two. As shown in figure 7, the laser efficiency of $Ne/F_2/H_2/O_2$ mixtures is more than 30% for $F_2$ partial pressure in the range 20-40 mbar, with a maximum value of 38 % for $F_2$ partial pressure in the range 20-30 mbar. The specific output laser energy first increases linearly with the $F_2$ content, up to a pressure of 30 mbar, and then saturates. For higher $F_2$ pressure, the discharge appears very unstable and the specific laser output energy dramatically drops down. The increase of the storage capacitance from 36 nF to 72 nF does not allow to increase the output energy which is even lowered (6 J/l for $F_2$=40 mbar). This seems directly connected to a worse discharge quality. Thus, the highest specific output energy reaches in the X525 laser using the chain reaction is 9.4 J/l, which is almost the same than that obtained with non-chain reaction: 9.7 J/l. From that point of view, the use of chain reaction for the phototriggered HF laser appears quite disappointing, the only advantage being an increase of the electrical efficiency by a factor of 8. On the other hand, a drawback of the chain laser is the duration of the laser pulses which are in the microsecond range compared to those of the non-chain laser which, for the X525 laser, are less than 100 ns. As a result, for the same specific output energy, the peak power of the chain mixtures is reduced by a factor of 20 compared to the peak power extracted from a non-chain mixture.

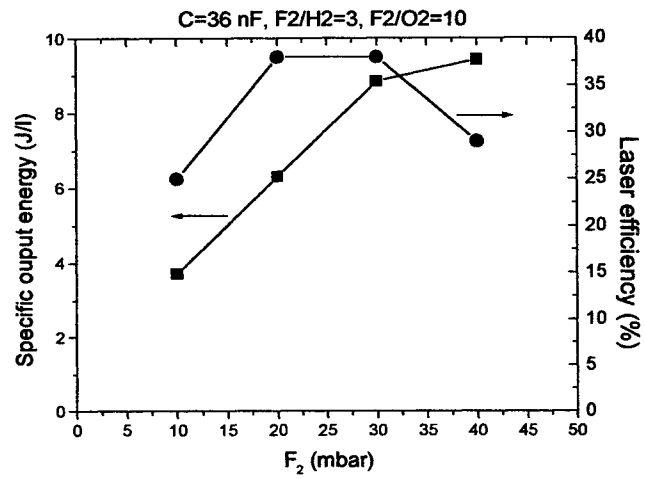


Figure 7: Evolution of the laser performance versus the $F_2$ partial pressure for mixtures without $SF_6$.

## ACKNOWLEDGMENTS

The authors wish to thank CILAS for its financial support.

## REFERENCES

[1] L. Richeboeuf, S. Pasquiers, F. Doussiet, M. Legentil, C. Postel , V. Puech: Appl. Phys. B68, 45-53 (1999)
[2] B. Lacour, C. Gagnol, P. Prigent, V. Puech: in XII° Gas Flow an Chemical Lasers, St Petersburg 1998, Proc. SPIE 3574, 334-340
[3] C. A. Kutumov, E. A. Klimuk, G.A. Troschchinenko: in XII° Gas Flow an Chemical Lasers, St Petersburg 1998, Proc. SPIE 3574 , 601-605

# Experimental Study of Pulse-Periodic DF Laser Operation with up to 1,200 Hz Repetition Rate and about 25 W Average Power

I.L. Butzykin, S.D. Velikanov, P.A. Evdokimov, A.F. Zapol'sky,
E.V. Kovalev, B.E. Kodola, I.N. Pegoev

Russian Federal Nuclear Center – All-Russian Scientific Research Institute of Experimental Physics
Mira prosp. 37, 607190 Sarov, Nizhni Novgorod region
Tel: (831 30) 5 66 30, Fax: (831 30) 5 45 65, E-mail: zapolsky@otd13.vniief.ru

## ABSTRACT

The study of DF laser generating average power 25 to 30 W at 1,200 Hz repetition rate is reported. Acoustic perturbation effect on the stability and homogeneity of discharges produced in the laser active medium and thus on output laser power is demonstrated.

## 1. INTRODUCTION

A strong emphasis made currently on the development of small-sizes pulse-periodic DF lasers is associated with the good-looking prospects for their application in medicine, ecology, etc. areas [1, 2]. Along with this, not-small-importance problem became their design optimization made for the purpose of getting elevated output power and its in-time constancy, technical efficiency, and other performances.

In attempts to acquire the highest Pulse-Periodic Chemical Laser (PPCL) performance one must not only develop a compact discharge chamber (DC), voltage pulse generator (VPG), and preionization methods to produce stable discharge, but also optimize active mixture (AM) pressure and composition and maintain its homogeneous flow between the electrodes of DC.

With the increase in frequency more and more severe requirements are imposed on the volumetric homogeneity of energy deposition in principal discharge and density homogeneity of AM in the laser active volume. As the interelectrode replacement ratio (number of mixture replacements between two consecutive pulses) is to be kept within the advisable limits [3], the width of the basic electrodes must be as small as possible. This leads to deterioration of discharge homogeneity and may be compensated only partially with special electrode profiles and DC construction. The AM density fluctuations are induced by both inhomogeneous energy deposition and acoustic perturbations (AP) sequent of pulse-periodic initiation, and they can reach the values with noticeable effect upon the homogeneity and stability of the volumetric discharge [4-6 ]

This work is a sequel to the studies reported in ref. [2-4, 7]. The description of conducted experiments, and analyzi of the results obtained are given.

## 2. EXPERIMENTAL SETUP

The present facility is destined to investigate into the DF laser operation performance in a pulse and pulse-periodic modes. The operating diagram and structure of the facility used in these studies have been described elsewhere [6], the differences being the facts that no heat exchanger and system for precipitating sulfur are required in our case.

The principal element of the system is a gasdynamic channel (GC) representing a hollow loop between inner and outer housings in which there are suited axial-flow fans to make the AM flow, a filter filled with a sorbent to purify the AM of the chemical reaction products, and dielectric flow-directors. In the channel bottle neck, the flow passes the interelectrode space (IS). The flow velocity in the IS can vary between 12 and 36 m/s subject to the type and number of the fans in use, the design of the electrodes mounted into the DC, and the distance between them.

The filter design and its situation place were chosen to provide the least gasdynamic drag. As was done in ref. [2-4], we used activated $Al_2O_3$ with 2-3 mm diameter granules as a sorbing material. The granules were bulked between two metal meshes accommodated in front of the fans. The DC is made as a unit module with arranged inside it the GC narrowing on both sides into the IS and which least cross-section is $(8\div10)$x280 mm$^2$. The main-discharge-formation electrodes – anode and cathode - as well as the preionization pair, connected to the cathode through blocking capacitors and high-voltage buses, were all mounted in the central partition of the DC.

The main electrodes were made of aluminum alloy with a Stappaerts profile [8] 18 mm width and with a smooth and flat or profiled surface representing a collection of blades (knife-edges). Peculiarities of discharge excitation between such electrodes were reported in ref [7] for one initiation event. The preionization electrodes were just the same as described in ref. [7].

The VPG was built according the schematic of a one-stage doubling Fitch circuit. By changing the number of capacitors, the VPG overall capacity was variable from 4.6 to 25 nF, thus modifying the stored energy $E_{st}$. The switching device (SD) was a controlled discharger or a thyratron.



XIII International Symposium on Gas Flow and Chemical Lasers and High-Power Laser Conference,
Antonio Lapucci, Marco Ciofini, Editors, Proceedings of SPIE Vol. 4184 (2001)

The charging voltage pulses $U$ from the VPG' capacitors and signals from the pyroelectric sensor used for measuring the amplitude and repetition rate of the emitted pulses were both recorded at the same time by oscilloscopes.
The total energy emitted in a pulse train was measured by thermocouple calorimeters, and the laser pulse shape was recorded by a photoresistance.
The pressure $P$ in the active mixture was variable in our experiments within 0.08÷0.75 bar region. Our experiments were carried out with mixtures of the same composition: $SF_6 : D_2 = 6 : 1$, regarded as optimal of such DF lasers in ref. [3].
The LU design allowed direct observation of a discharge between the main electrodes in the visible spectral range. The discharge was recorded with a camera through the transparent side window and, in some cases, through the outcoupling window.

## 3. EXPERIMENTAL INVESTIGATIONS

In the first pulse-periodic experiments we have investigated the potencies of the electrode pairs considered previously in ref. [7]: flat – flat electrodes, flat anode – knife-edge cathode, knife-edge – knife-edge electrodes, the IS being 8 mm in all cases. The pulse laser energy was measured as averaged over 0.1 sec interval value at the constant $U$ equal to 18 kV and $E_{st}$ about 1.44 J. The repetition rate $f$ was changed stepwise from experiment to experiment. The AM flow velocity inside the IS had 36 to 28 m/s value. As the AM wasn't able to make a full turnover in the GC within a 0.1 sec instant, its composition, density, and temperature may safely be thought as unvaried parameters.
The average energy $Eo$ in laser pulses is shown in fig. 1(a) as a function of the frequency $f$ for each electrode combination.

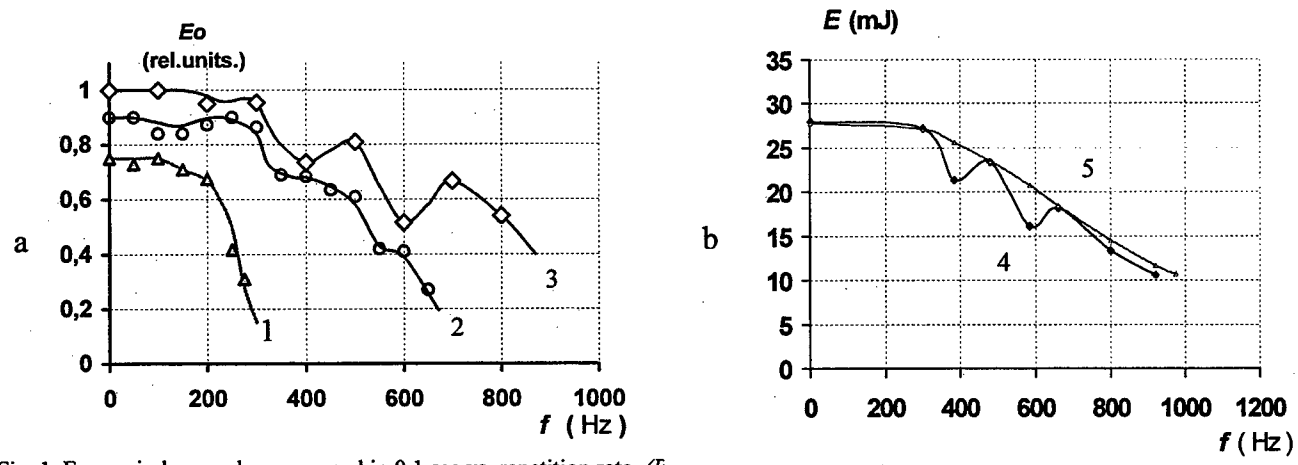


Fig. 1. Energy in laser pulses averaged in 0.1 sec vs. repetition rate. ($P$ – 0.16 bar ($SF_6 + D_2$))
a) experimental series with a switching element (discharger) of the РУ78- type, without lattices:
1 – flat-flat configuration, 2 – flat anode and knife-edge cathode, 3 – knife-edge – knife-edge configuration;
b) experimental series with a thyratron of the ТП-10к/25-type, flat anode and knife-edge cathode:
4 – without lattices, 5 – with additional lattices.

As was in ref. [7], the best configuration appeared to be the knife edge – knife edge in which oscillation was suppressed at the frequency $f_2 \sim 800$ Hz. For other two combinations this value was $f_2 \sim 650$ and 250 Hz, respectively. The use of the proposed double knife-edge design is equivalent to rising U and would improve the laser efficiency and discharge stability. The mean energy $Eo$ in pulses is virtually constant value up to the frequency $f_1$ equal to about 300 Hz if at least one electrode was knife-edged, and up to about 200 Hz if both electrodes were flat. Further increase in the $f_1$ led to a considerable reduction of the laser energy.
As was revealed in the further investigations, some resonance and stroboscopic phenomena may take place. Every consequent pulse discharge may coincide or not coincide in time and space with the unfavorable result of interaction between acoustic waves (AWs): in places where the AM is condensed considerably no discharge is occurred, but low AM density may even lead to streamer origination. Presence of many places where the discharge isn't effective or hasn't been excited at all reduces in fact the working volume, which in itself does lead to a decrease in the lased energy.
The curves shown in fig. 1(a) have the property that proves all the aforesaid. One can observe the wavelike character of the mean energy of the laser pulses as a function of the repetition rate $f$ in case when one of the electrodes is knife-edged. The energy local minimums are repeating with about 200 Hz period, corresponding to the time when the wave reflected by the mount plate of the funs would enter the IS for the given construction of Pulse-Periodic DF Laser.
Fig.2 (a), for various repetition rates, gives the discharge glow – integral over 0.1 sec - along the electrodes in visible light. An analysis of these photos allows us to make another suggestion on the effect of the AWs propagating across the gas flow along the radiation axis of the laser on the discharge initiation processes. The light intensity is higher in places with lower density,

and, as a rule, no light is on the contrary observed if the density is high. Estimates show that the distance between the centers of the dark (and light as well) regions corresponds to concurring fronts (low-density regions) of AWs coming to meet each other after being reflected by the side surfaces, i.e. by the places where the resonator mirrors are mounted. While the repetition rate goes up, the dark and light regions broaden and displace, wich is obviously indicative about the stroboscopic effect.
The effect of such waves can be weakened or eliminated fully by tilting the sidewalls of the chamber toward the active mixture axis (resonator axis), inclusive the case when optical mirrors tilted toward the resonator axis are introduced inside the resonator. The present LU design was made only with sidewalls tilting at the $30^0$ angle relative to the axis and towards each other.

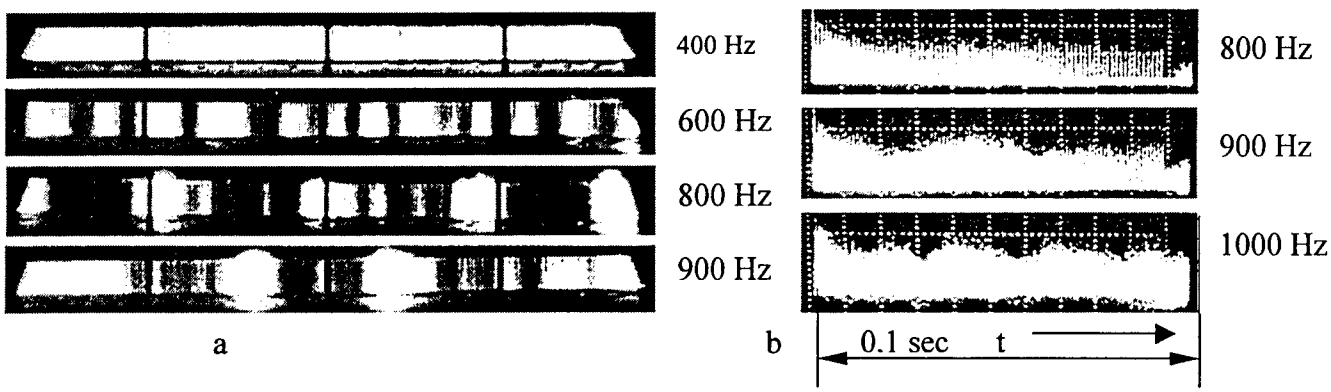


Fig.2.a) Discharge glow along the electrodes at various initiating frequencies. Three dark zones – shadows of return current wireways
b) Laser energy change in pulse train for various initiating frequencies. $P = 0.16$ bar ($SF_6 + D_2$), straight sidewalls.

The above consideration can be illustrated by the oscillograms in fig. 2b. In the case in question, the sidewalls weren't tilted. During the first 10-12 pulses the per-pulse energy goes down to 0.6-0.7 initial value and then fluctuates about this level. The starting energy drop refers seemingly to accumulation of a heated and ionized partially mixture between the edges of the electrodes. The following energy fluctuations are evidently a consequence of the interaction between the AWs in the AM. Quenching by all means of the last would attenuate the energy fluctuation in a train of laser pulses.
An efficient method to quench the AW inside the IS became the increase of the sound speed *Vs* by diluting the AM with a light gas, such as helium in particular. Sound speed increase inside the mixture facilitates the compensation for the density inhomogeneity during the time between consecutive pulses. Along with this and at the expense of changing the AM electric properties one may expect also advancement in homogeneity and stability of pulse discharges.
Fig. 3a shows the luminescence of the discharge in visible light in the experiments with different initiating frequencies in the AM containing 0.45 bar He. A comparison between these photos and figs. 2(a) is indicative about a remarkable improvement of discharge homogeneity in mixtures with helium additions, inclusive the case of up to 1,200 Hz and higher. As also were in all of the subsequent experiments, in these experiments the sidewalls were tilted and additional lattices were inserted across the AM flow.

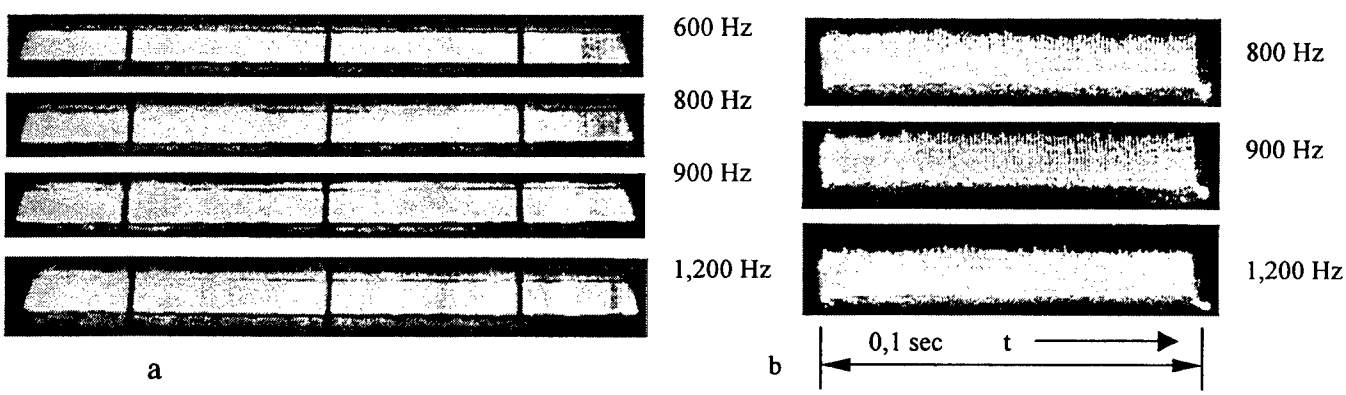


Fig 3 a) Discharge glow along the electrodes with 0.45 bar He addition for various initiating frequencies.
$P = 0.14$ bar ($SF_6 + D_2$) + 0.45 bar He; with additional lattices and tilted sidewalls;
b) Laser energy change in pulse train for various initiating frequencies.
$P = 0.14$ bar ($SF_6 + D_2$) + 0.45 bar He, sidewalls tilted bar $30^0$ relative the cavity axis

Fig. 3 shows oscillograms of laser pulses measured at different initiating frequencies in the AM containing 0.45 bar of He. It follows from the comparison of the oscillograms given in figs. 2a and 3b that the energy pulsation in a pulse train goes down considerably when the AM is diluted with helium. The energy drop that takes place in helium-less mixtures during a few first pulses has disappeared.

Fig. 4 shows the mean energy in the laser pulses as a function of the repetition rate for the AM with various content of helium and without it. In all the experiments we kept $U = 18$ kV and $Est \sim 1.44$ J.

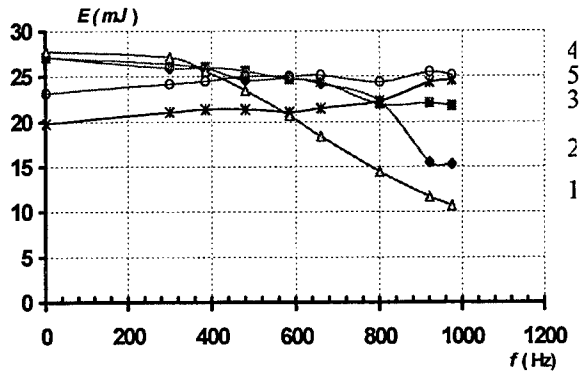


Fig. 4. Mean laser energy vs. initiating frequency and He content in active mixture

1 - $P$ = 0.16 bar ($SF_6 + D_2$), $Vs \sim 146$ m/sec;
2 - $P$ = 0.16 bar ($SF_6 + D_2$) + 0.15 bar He, $Vs \sim 207$ m/sec;
3 - $P$ = 0.14 bar ($SF_6 + D_2$) + 0.3 bar He, $Vs \sim 267$ m/sec;
4 - $P$ = 0.14 bar ($SF_6 + D_2$) + 0.45 bar He, $Vs \sim 331$ m/sec;
5 - $P$ = 0.14 bar ($SF_6 + D_2$) + 0.6 bar He, $Vs \sim 395$ m/sec.

The graphs given in fig. 4 indicate that the highest laser energy values reached at about 1,000 Hz frequencies correspond to a content of helium in the AM about 0.45 bar. The lowered $SF_6$ concentration and elevated buffer gas content as shown in figs 4 and 5 lead to a decrease in $E$ at low initiating frequencies but for high frequencies the mean energy goes up reaching - at $f$ = 1,000 Hz - about 0.9 of the value attainable at single-shot initiation without helium. The laser power acquired here is $E*f \sim 26 * 10^{-3}$ J * 1000 sec $^{-1} \sim 26$ W and the technical efficiency - $100*E/Est \sim 100*26*10^{-3}$ J/1.44 J ~ 1.8%.

The virtual constancy of the laser energy with growing $f$ up to about 1,000 Hz at high He content points to optimality of the initiating AM conditions that have been found out in the course of the present investigations.

## 4. CONCLUSION

The present study has eventuated in the laser facility of 25-30 W output power operating in the DF laser spectral range at the repetition rate up to 1,200 Hz and efficiency about 2%.

It was shown that the factor principal among those reducing the mean energy in laser pulses and leading even to suppression of oscillation before reaching the frequency limit of lasers like this is acoustic perturbations inside the active volume that are a product of pulse-periodic mixture initiation. Interaction between acoustic waves in the media results in non-uniformity in the mixture density in the interelectrode spacing and, so, it brings about such phenomena as local overheated areas, streamers, and decrease in laser pulse energy.

These are the technical solutions that contribute essentially to attainment of the highest possible performance of the laser:

- development of a system of electrodes with a flat smooth anode and knife-edge cathode;
- quenching of acoustic perturbations inside the active volume by tilting the sidewalls of the gas-dynamic channel in the cavity region and by placing two additional metal lattices in the way from the blowers to discharge chamber, which eliminates reflection of some part of acoustic waves by construction members;
- more than twofold dilution of the active mixture $SF_6 + D_2$ with helium; due to a considerable increase in the sound speed in so doing, the difference in the mixture density that hasn't been fully eliminated using the aforementioned design approaches was reduced during the pulse spacing time to the values having little effect upon the discharge quality and lasing properties of the active mixture.

## REFERENCES


1. Khinkly A.D (editor) *"Lazerny kontrol atmosphery"* ("Laser control in the atmosphere"), Moscow, Mir, 1979.
2. Velikanov S.D., Elutin A.S., Kudryashov E.A., etc. *Quantum Electronics*, 27, 3, 273-276 (1997).
3. Velikanov S.D., Zapol'sky A.F., Frolov Yu.N. *Quantum Electronics*, 27, 1, 9-12 (1997).
4. Borisov V.P., Burtzev V.V., Velikanov S.D., etc. *Quantum Electronics*, 25, 7, 617-620 (1995).
5. Baranov B.Yu., Malyuta D.D., etc. *Kvantovaya Elektronika (rus)*, 7, 12, 2589 (1980).
6. Rudko R.I., Drozdowicz Z., Linhares S., Bua D. Rev. Sci. Instrum., 53, № 4, p.452 (1982).
7. Velikanov S.D., Evdokimov P.A., Zapol'sky A.F.,etc. *Kvantovaya Elektronika (rus)*, 25, 10, 925 (1998).
8. Stappaerts E.A. Appl. Phys. Lett., 40, p.1018 (1982).
9. Bugayov S.P., Kreyndel Yu.B., Shchagin P.M. *"Elektronnie puchki bolshogo secheniya" ("Electron beams of large cross-section")*, Moscow, Energoatomizdat, 1984.

Invited Paper

# High power kW-range diode lasers for direct materials processing

Friedrich G. Bachmann*

ROFIN-SINAR Laser GmbH & MDS Project Mangement
Galileo-Galilei-Str. 10, D-55129 Mainz, Germany

## ABSTRACT

This paper provides information about the basic technology of high power diode lasers and their applications in a tutorial way. Each step from the milli-watt laser light generation in the pn-transition to the multi-kilo-watt laser system is explained. Typical applications of high power diode lasers, some of them already in industrial manufacturing, are described.

**Keywords:** High power diode lasers; materials processing; welding; brazing; hardening; surface treatment; hardening.

## 1. INTRODUCTION

Diode Lasers are widely used in communication, computer and consumer electronics technology. These applications are based on systems, which provide power in the milliwatt range. Since a few years high power diode laser systems are available, with a power range up to several kilowatts. Their basis, however, are in principle still the milliwatt lasers mentioned above, which are integrated into a compact system and combined by mechanical and optical micro-technology. This novel way to build a high power laser leads to a high power laser source, which is in fact not bigger than a shoe box. With these lasers classical laser materials processing becomes possible; moreover, the high efficiency, the small size, the modular design of high power diode lasers open up new applications, which have not been attractive or even not possible so far. In this paper we will explain the technology of the high power diode lasers as well as give examples for materials processing applications, which are partially even already introduced in industrial manufacturing.

## 2. HIGH POWER DIODE LASERS

From a traditional diode laser element typically only a few milliwatts can be extracted from a pn-transition; in fact a diode laser is a complex sequence of differently doped GaAlAs layers, which sometimes have only the thickness of a few atomic layers, as is schematically presented in fig. 1[1]. The light is actually emitted from a layer, which is less than a micron thick. The basic material for a laser diode are n-doped GaAs single crystals, which are grown with extremely low impurity levels in special furnaces (see Iga et.al.[2]); the crystals are sliced by special saws to wafers with a thickness of about 350 µm and a diameter of 2 or 3". The layer structure is then generated by CVD-processes and epitaxial growth. After the deposition and structuring of the contact layers, the wafer is scratched and carefully broken into the individual diodes. Multilayer mirrors are then deposited at the edges, so that a resonator is formed. A sketch of an individual diode laser element is shown in fig.2[3]. From such an element typically a few milliwatts of laser light can be extracted.

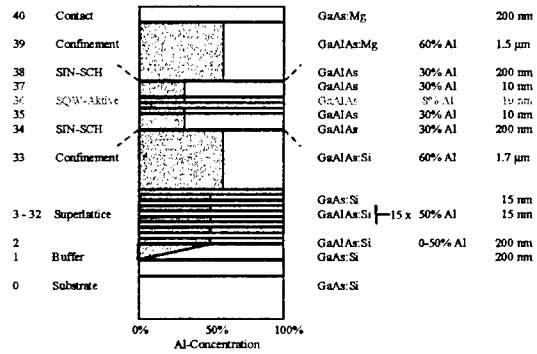


Fig. 1: Schematic layer structure of a laser diode: light is generated in a layer less than 1 µm (layer 34 to 38) (SIN-SCH = "Step Index Separate Confinement Hetrostructure"; SQW = "Single Quantum Well")[1]

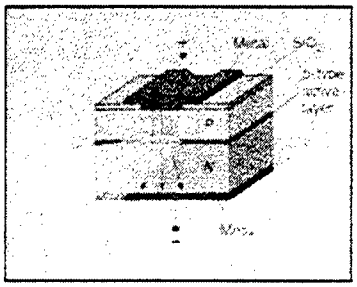

Fig. 2: scheme of light generation in a pn-transition of a laser

* Correspondence: e-mail: f_bachmann@compuserve.com; Tel.: +49 6131 9226-28; Fax +49 6131 9226-57



XIII International Symposium on Gas Flow and Chemical Lasers and High-Power Laser Conference,
Antonio Lapucci, Marco Ciofini, Editors, Proceedings of SPIE Vol. 4184 (2001)

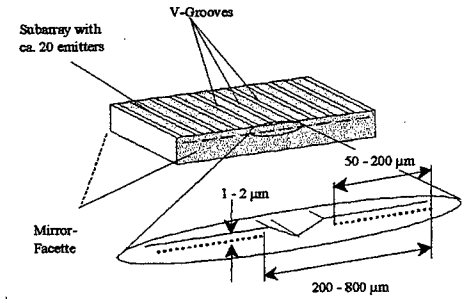


Fig. 3a: Integration of several individual diode lasers into one one semiconductor element: the laser bar

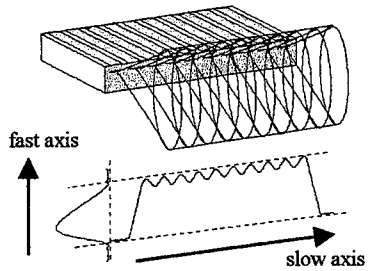


Fig. 3b: Beam propagation and intensity profile from a diode laser bar

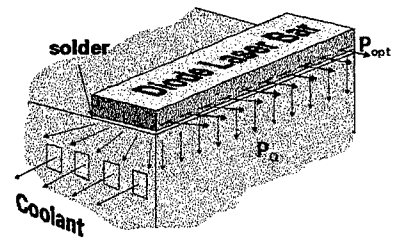


Fig. 4: Scheme of a micro-channel cooler; the bar is precision mounted by a special solder

To increase the power, several single elements are integrated into one semiconductor element, which has a size of about 10000 µm x 1000 µm x 115 µm (fig. 3a), where 1000 µm is a typical resonator length. This unit is called a "laser bar". The special shape of the light generation area leads to special light emitting characteristics, which shows a high divergence in the direction of the pn-transition ("fast axis"), and a lower divergence, but a wide emitting "stripe" in the other ("slow axis"), as represented in fig. 3b. Even if these laser bars show electrical to optical efficiencies of 40 to even above 50%, considerable amount of heat must be removed through the small footprint; therefore, the laser bar must be mounted onto a special water-cooled heat sink, which removes the excess heat and, thus, prevents the bar resp. the mirror facets from thermal destruction. The microchannel cooling technology was originally based on silicon anisotropic etching[4]; today these heat sinks are typically manufactured from copper. They contain a network of small channels, with a cross section of about 300 µm x 300 µm. Water is driven through these microchannels, which are located underneath the laser bar (fig. 4) for most efficient cooling. Typical flow rates through one cooler are in the order of 0,5 l/min; a typical heat resistance is in the range of 0,4 K/W. This cooling efficiency allows to use the laser at currents up to above 50 A, i.e. to create laser power up to 40 or 50W, or even higher without damage.

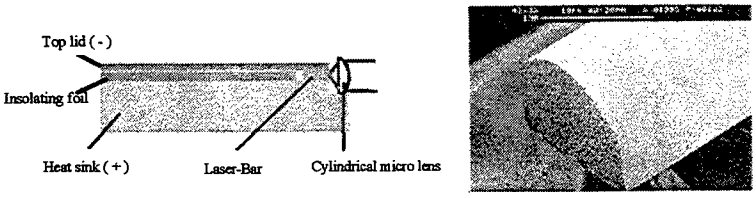


Fig. 5: Scheme of a laser bar mounted on a heat sink with a micro lens for fast axis collimation (FAC; left); REM picture of FAC microlens (right)

The fast axis light is collimated by cylindrical micro-lenses (fig. 5); these lenses, which are just a mm in height need not only to be manufactured very accurately, but also exact positioning (< ± 0.5 µm resp. <1°) is mandatory for a good beam quality. Of course in this context it becomes evident, that not only the accurate mounting of the lens is essential for maintaining the beam quality, but also the mounting and positioning of the diode laser bar itself onto the heat sink in the step before. The same accuracy applies as for the lens; additionally the bending of the bar over its length, the so called "smile" must be minimised.

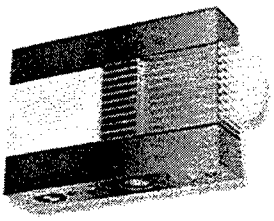

Fig. 6: stacked diode laser micro-channel heat sinks (ca. 500 W)

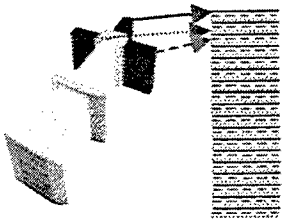

Fig. 7: Aperture fill with two or three stacks by use of stripe mirrors or prism stacks[5]

Several of these elements can be stacked on top of each other, so that finally up to 1 kW can be reached from this unit (fig. 6). For further power increase two or even three of such stacks can be combined by stripe mirrors (fig. 7) to fill in the aperture, so that the beam quality can be (theoretically) maintained; single or combined stacks can be further directed onto the same optical path by polarisation coupling (fig. 8) or wavelength coupling (fig. 9), so that up to 5 or 6 kW laser power can be delivered from a laser head, which is typically not greater in size than a shoe box.

For improvement of the brilliance and matching of the different divergencies, sophisticated beam rearrangement systems are applied, e.g. a step mirror[6] or a beam tilt unit[7]. Those special optical elements cut the wide beam of the diode laser bar into smaller pieces and re-arrange them on top of each other, so that the width and divergence are reduced in one direction at the expense of the other, where width and divergence are increased.

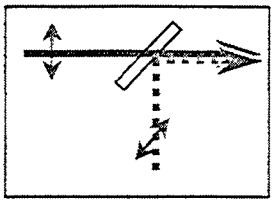

Fig. 8: Scheme of polarization coupling

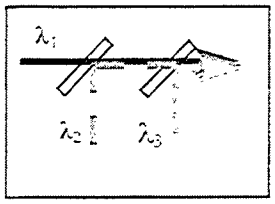

Fig. 9: Scheme of wavelength coupling

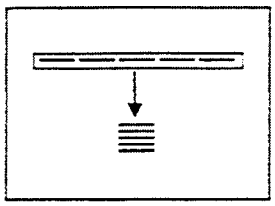

Fig. 10: Scheme of beam rearrangement

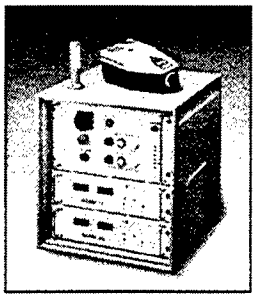

Fig. 11: High power diode laser, up to 3 kW, with power supply

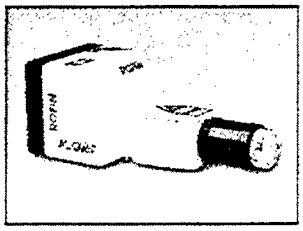

Fig. 12: High power diode laser with increased beam quality

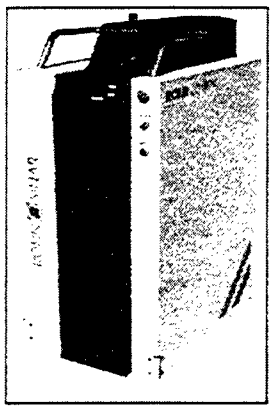

Fig.13 (right): Fibre coupled diode laser up to 2.2 kW

Using the technologies, which have been explained above, high power diode lasers up to 8 kW are available on the market place today. As an example, in fig. 11 a standard high power system with 1.5 kW is shown with focal spot size of 1.8 x 3.8 mm²♦) (with f = 50 mm working optics); the same system, with a slightly larger power supply, but the same size of the laser head is available up to 3 kW. Fig. 12 is a 1.5 kW system with an improved beam quality, which delivers a 1.3 x 1.3 mm² spot in the focus, with f = 63 mm optics; also this unit is available up to 3 kW with a slightly larger head than shown in the photograph. Nevertheless, the head size is just 500 mm x 180 mm x 160 mm (l x w x h) and the weight not more than 12 kg. In this system polarisation coupling (see fig. 8), wavelength coupling (see fig. 9) and a beam special beam rearrangement scheme (see fig. 10) are implemented. This kind of unit is also the basis for the fibre coupled unit shown in Fig. 13, which provides 2.2 kW out of an optical fibre with a core diameter of 1.5 mm. For many applications, the fibre coupling seems to be an essential step forward for the acceptance of this technology in a manufacturing environment.

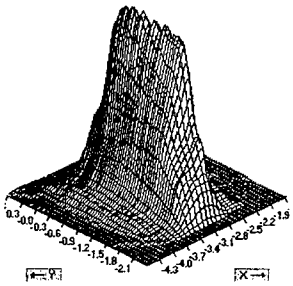

Fig. 14: typical energy distribution in the focal plane of a standard high power diode laser

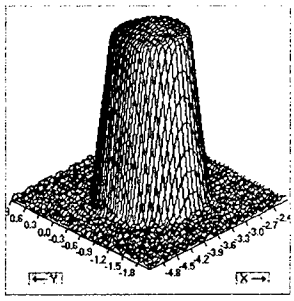

Fig. 15: typical energy distribu tion in the focal plane of a fibre coupled high power diode laser

The beam profile of high power diode lasers is typically a top hat profile in one direction (corresponding to the "slow axis" of the laser bars) and a Gaussian in the other, as presented in fig. 14; this is, however, only true in the focal plane: The beam forming and imaging optics are optimised for the best superposition of the individual beam sources in this plane; leaving the focal plane, considerable changes of the intensity distribution occur and, thus, defocussing is not recommended for high power diode lasers. If a fibre is used for the beam delivery of a high power diode laser, a round top hat profile can be reached in the focal plane (fig. 15); however, even if the circular symmetry is of course maintained, also here considerable changes in the beam profile have been measured if the focal plane is left.

## 3. APPLICATIONS OF HIGH POWER DIODE LASERS

As explained in section 2, high power diode lasers consist of a large number of single lasers, which are incoherently coupled together to deliver laser power in the kW range; as a consequence of this the quality of the beam is rather poor compared with conventional lasers. Today, dependent from power, a beam parameter product between 10 and 500 mm mrad is typical for these lasers, which for the time being excludes these lasers from traditional high power laser applications like cutting or precision marking (fig. 16[8]); deep penetration welding, however, has been demonstrated recently[9], which was possible by high absorption of diode laser wavelength and by use of a high beam quality 2.5 kW laser. The scheme in fig. 16 clearly shows, that in the high power range heat conduction welding, brazing, surface treatment and cladding can be performed. As mentioned above, the typical laser power is in the range of 3 kW (higher powers are available on request); the working

♦) All focus data are taken at 86% (i.e. according to $1/e^2$ criterion)

distance is about 45 mm to reach high intensity. In such an optical configuration a focal area of ca. 1.3 x 1.3 mm² can be illuminated, which finally leads to a maximum averaged power density of about 1,7 x $10^5$ W/cm². Despite the fact, that the power density is not as high, the high power diode laser offers advantages compared to conventional lasers, since its high efficiency (> 30% wall plug efficiency) leads to economic use and since its small size makes its integration into existing production systems simple; mounting of the laser head directly onto a robot is very simple (see fig. 18) and even portable systems can be easily realised.

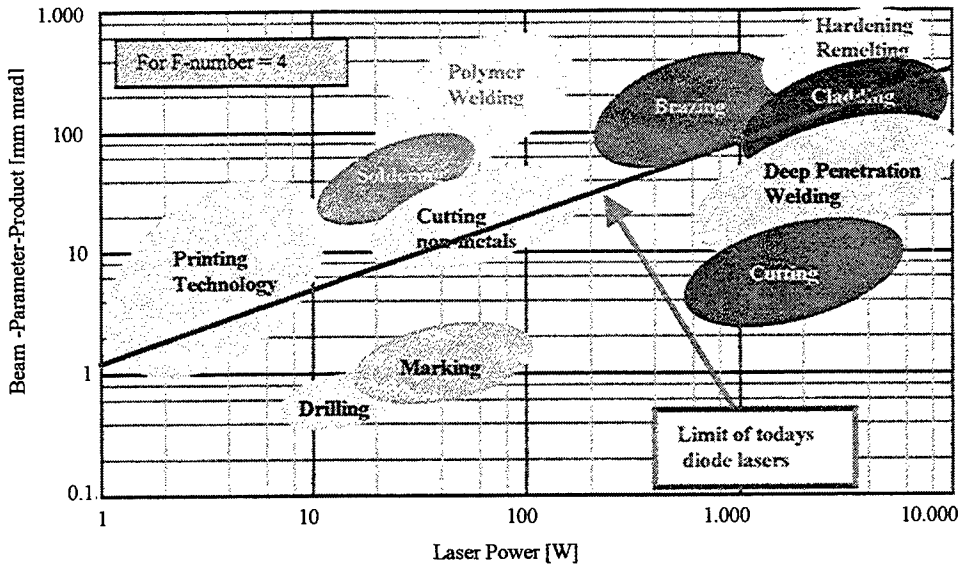


Fig. 16: Beam parameter field for the materials processing with lasers (after P.Loosen[8])

### 3.1 Welding of Metals

Even if from simple 3D-calculations, assuming a half infinite work piece rather low welding speeds for heat conduction welding are expected, thin sheet welding can show considerable speeds, since the three dimensional heat conduction creates a limited heat flow and an overheating at the bottom of the sheet. A 150 µm thick plate of a stainless steel could be welded with only 500 W laser power at a speed of 6 m/min. Care must be taken to avoid oxidation, even downstream the laser welding spot; furthermore, the technology of the clamping tool becomes essential, since larger heat load is created to the material and since the material is very thin and tends to move or bend under the influence of the heat. Of course, if thicker material (e.g. 1 mm thick stainless steel) is welded with a heat conduction welding technique, welding speed becomes rather slow, compared with conventional deep penetration welding: Fig. 17 shows a cross section of a fillet weld at a lap joint of 1 mm steel (1.4301), welded with a 2 kW diode laser with a speed of about 0.5 m/min. A key advantage of heat conduction welding with a diode laser beam, however, is the very smooth and nicely shaped welding seam, which can also be seen in fig. 17. This so called "cosmetic weld" led to one of the very first industrial manufacturing applications of diode lasers, the welding of kitchen sinks[10] (fig. 18). The diode laser weld led to a considerable reduction of finishing after the weld compared with the conventional method used so far; in fact, only polishing of the seam is necessary, which has to be done for the whole assembly anyway before shipment, but grinding and other surface treatment procedures can be completely avoided, which is the basis for considerable cost savings.

Fig. 17: Cross section of a fillet weld at a lap joint of 1 mm stainless steel (1.4301), performed with a 2 kW diode laser (0.5 m/min, Argon shield gas)

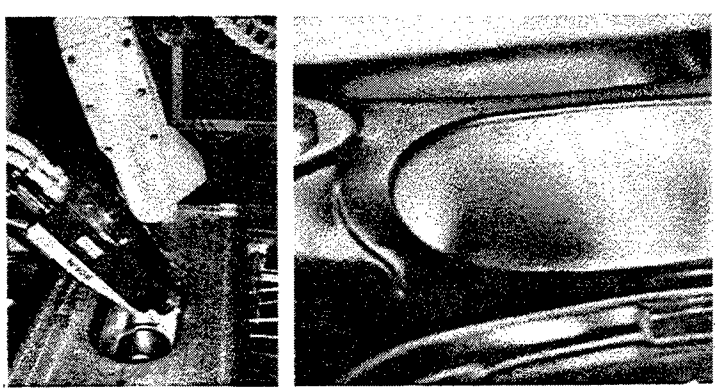

Fig. 18: Welding of kitchen sink with a diode laser[10];
Left: Positioning of the laser with a robot
Right: Kitchen sink after weld (before polishing)

As menioned above, just recently, even deep penetration welding has been demonstrated with high power diode laser[9]; a special model of a ROFIN DL025S diode laser, which provided 2.5 kW and a spot of 1.0 x 1.2 mm² was used to perform the full penetration bead-on-plate welds in stainless steel sheets of different thicknesses between 2 and 6 mm. As can be

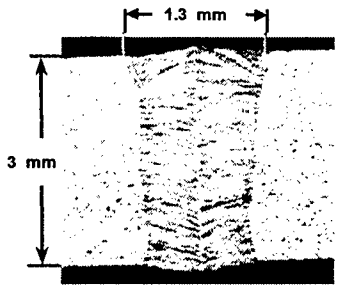


Fig. 19: Deep penetration welding of stainless steel with HPDL[9]

seen in fig. 19, a narrow seam (aspect ratio of > 2) and a horizontal dendritic weld structure are reached, which together with an intense vapour plume indicate the deep penetration process. Even if for the diode lasers, which are available today, the working distance is still too short (in the range of 30 to 80 mm) and the speed (in the range of 0.2 m/min for 6 mm thick to 1.4 m/min for 2 mm thick stainless steel) is still too low for most industrial applications, the results nevertheless show the enormous speed of improvement and development in this technology! This result looks contradictory with fig. 16 of this paper; this discrepancy is, however, a consequence of the higher absorption of the diode laser caused by its shorter wavelength and the smaller F-number applied with todays high power diode lasers.

### 3.2 Brazing

Brazing becomes more and more an attractive joining technology in automotive body manufacturing as well as in sealing RF tight shield housings for electronic components. Experiments in ROFIN-SINAR's application laboratories have shown the successful brazing of Zn coated steel (0.9 mm) with CuSi hard solder fed as a 1 mm diameter wire. The experiments led to very smooth seams (fig. 20). Brazing speed was 2-4 m/min with 2.5 kW power, but this depends strongly on the individual requirements of gap filling with the hard solder material. At least the same results as with a NdYAG laser can be obtained with a high power diode laser, but for considerably lower costs!

Fig 20: Hard soldering of Zn-coated steel with high power diode lasers

### 3.3 Hardening

Because of its rectangular shape, with a top hat profile in one direction ("slow axis") and a Gaussian like in the other ("fast axis") the high power diode laser beam is especially well suited for surface hardening applications. Additionally, in comparison to $CO_2$ laser the emission wavelength of these lasers (typically 808 nm or/and 940 nm) is short, which leads to higher absorption resp. less reflection and thus rules out the necessity of absorbing coating. The much higher efficiency of the diode lasers together with the advantages mentioned above, makes the high power diode laser a very efficient, reliable and cost efficient tool for hardening.

A very prominent example from a manufacturing application of high power diode lasers is the hardening of torsion springs, which are used at the angles of car doors. The high power diode laser does not only provide an ideal beam geometry and intensity distribution, but is also the most cost efficient way for the transformation hardening. The torsion springs, shown in fig. 21a have to be hardened over an angle of >170°, over a length of ca. 10 mm and to a depth of 0.2 to 0.4 mm. With a set-up, which uses two lasers under an angle of about 120°, this geometry can be hardened homogeneously (see fig. 21 c), if the lasers scan over the 10 mm length. An active process control, which uses two pyrometers for temperature recording assures the quality for each individual part[5,11].

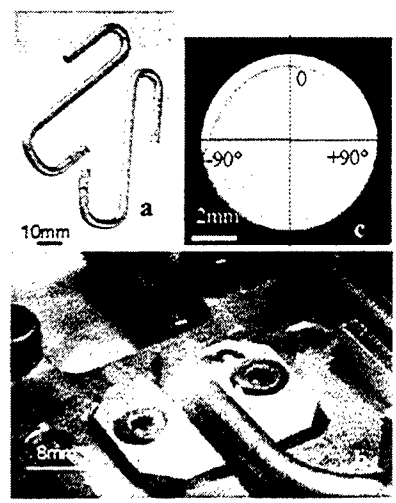


Fig. 21: Hardening of torsion springs by high power diode lasers[11, 12]; a: Torsion springs; b: process photograph; c: cross section of hardened torsion spring

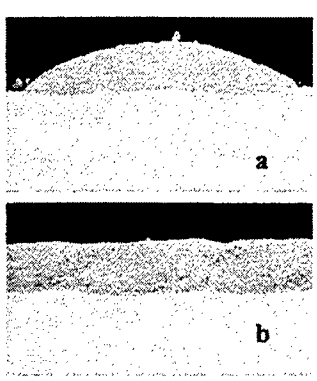


Fig. 22: Powder Deposition of Stellite F onto a steel substrate
a) deposition of a single track
b) overlapping tracks

### 3.4 Cladding

An important surface related application of high power lasers is also the deposition of wear resistant layers or deposition of layers for repair. A widely used and successful method is the deposition of e.g. Stellite from a powder, which is fed to the laser heated zone through a special nozzle. Also for this application, for which $CO_2$ high power lasers have been mainly used in the past, the high power diode laser provides an ideal tool. With a typical power density of ca. $2 \times 10^4$ W/cm² delivered in a spot of ca. 2 x 4 mm² layers with a thickness of more than 0.5 mm have been deposited with a speed of ca. 400 mm/min (fig. 22 a). Actually, this speed is more than twice as fast as in a comparable setup with a $CO_2$ laser[12], resp. the required laser power is half as much as in case of using a $CO_2$ laser; thus, also here the high

power diode laser provides a much more cost efficient way to run the process. The overlap region, if tracks are deposited in an overlapping way in parallel, looks very smooth and dense (fig. 22 b)[12].

### 3.5 Low power applications: Soldering and polymer welding[13]

Laser soldering (with Nd:YAG lasers) is well known since many years; it is attractive for soldering of sensible or hardly accessible electronic parts, since it is contactless, provides a good accessibility and the energy can be exactly controlled. However, only since diode lasers are available, this application became economically attractive, because of their high efficiency and long lifetime. Similarly to the soldering application, also polymer welding with $CO_2$ and Nd:YAG lasers is well known since many years, but the break through seems to come with the diode lasers as well. Contrary to soldering, a special, optimal configuration, namely a (for the laser) transparent layer on top of a (for the laser) absorbing layer is necessary; this technology is called transmission welding. First applications are already in manufacturing, however questions of polymer material itself, pigmentation and clamping have still to be investigated and answered for large market penetration. Details can be found elsevere[13].

## 4. SUMMARY AND CONCLUSION

High Power Diode Lasers up to several kilowatts are at the threshold to the large scale introduction in the industrial environment. Todays systems provide sufficient power for those applications which require moderate power density in the range of $10^4$ to $10^5$ W/cm² at an high wall plug efficiency of more than 30%. Their very small size makes them an ideal tool for integration into manufacturing machines and for portable systems. With increased beam quality, further increase of lifetime and further reduction of investment cost, these lasers look into a bright future with an enormous increase of market share. Ambitious research programs have been launched to reach this goal in a reasonable time[14].

## ACKNOWLEDGEMENT

I would like to express my great thanks to my colleagues (in alphabetic order) at Osram Semiconductors GmbH & Co. OHG in Regensburg, Germany, Dr.B.Acklin and J.Luft, the Fraunhofer Institut für Lasertechnik (ILT) in Aachen, Germany, Dr.P.Loosen, D.Hänsch, Dr.D.Petring, Prof.R.Poprawe, H.Pütz, U.-A.Russek and B.Schürmann, and also at the Fraunhofer Institut für Werkstoff- und Strahltechnik (IWS) in Dresden, Germany, Prof. E.Beyer, Prof. B.Brenner, Dr. S.Bonß, Dr. S.Nowotny, and A.Richter, who performed the experiments, permitted the use of their results, graphics and photographs..

## LITERATURE AND REFERENCES

1. J.Luft, OSRAM Opto Semiconductors GmbH & Co. OHG, personnel communicationm
2. K.Iga, et.al. in *Process technology for semiconductor lasers*, Springer Series in Materials Sciences Vol. 30, (1996)
3. B.R.Marx, "Homegrown diode lasers compete well against foreign counterparts", Laser Focus World, Sept 1998, pp. 104-120 (1998)
4. B.D.Tuckerman, "Heat transfer microstructures for integrated circuits", Thesis, Stanford University (1984)
5. By Courtesy of Fraunhofer Institut für Lasertechnik, Aachen, Germany
6. Patent No. DE 44 38 368 C2, Fraunhofer-Institut für Lasertechnik, Aachen, Germany
7. Patent No. DE 195 00 513 C1, Dilas Diodenlaser GmbH, Mainz, Germany
8. P.Loosen, Fraunhofer-Institut für Lasertechnik, Aachen, Germany, personal communication
9. D.Petring, Fraunhofer-Institut für Lasertechnik, Aachen, Germany, personal communication
10. C.Brettschneider, "Im Vordergrund steht die Ästhetik", Laser-Praxis 2/98 S.10 (1998)
11. B.Schürmann, F.Bachmann, "Potentiale des Umwandlungshärtens mit Dioden-Laserstrahlung in der industriellen Anwendung", Laser-Praxis 1/2000 pp. 14-16 (2000)
12. A. Richter, S. Novotny, T. Naumann, E. Beyer, "Cladding with high power diode lasers" LaserOpto 31, 3, pp. 63-?? (1999)
13. F.Bachmann, S.Fujishima, R.Takahashi, "Micro Materials Processing with High Power Diode Lasers"; Proc. of First International Symposium on Laser Precision Manufacturing, Omiya Sinic City, Omiya, Saitama, Japan June 14-16,2000, to be published
14. F. Bachmann, "Present status and future aspects of high power diode laser materials processing under the view of the German national research project", Proc. SPIE Vol. 3933, pp. 90-104 (2000)

Invited Paper

# High Power DPSSL for Laser Fusion and it's Application to Industry

Sadao Nakai*[a], Tadashi Kanabe[a], Toshiyuki Kawashima[b], Masanobu Yamanaka[a]
Yasukazu Izawa[a], Masahiro Nakatuka[a], Ranganathan Kandasamy[a], and L-Project Members[a]
Hirohumi Kan[b], Teruo Hiruma[b], Masayuki Niino[c], and ASPIC Members

[a] Institute of Laser Engineering, Osaka Univ. Suita, Osaka 565-0781 Japan
[b]Hamamatsu Photonics K.K. Hamakita, Shizuoka 434-8601 Japan
[c]Kakuta Research Center, National Aerospace Lab. ,Koganezawa 1, Kimigaya, Kakuda, Miyagi, 981-15 Japan

**keywords:** Laser fusion, laser propulsion, DPSSL, inertial fusion energy

## ABSTRACT

We are developing high average power diode pumped solid state laser DPSSL for laser fusion power plant, for space propulsion and for various applications in industry. The common features or requirements of our High Average-power Laser for Nuclear-fusion Application (HALNA) are large pulse energy with relatively low repetition of few tens Hz, good beam quality of order of diffraction limit and high efficiency more than 10%. We constructed HALNA 10 (10J×10Hz) and tested the performance to clarify the scalability to higher power system. We have obtained in a preliminary experiment a 8.5J output energy at 0.5Hz with bean quality of 2 times diffraction limited far-field pattern. We are also trying to extend the laser technology of high peak power with low repetition to that of high averge power laser with high repetition or CW operation. The progress of power laser technology is now opening new fields of applications in science and industry. The flexibility and variety of performance are needed.

## 1. INTRODUCTION

The technical and economical feasibility of DPSSL (Diode Pumped Solid State Laser) for laser fusion driver have been investigated through a conceptual design study of a laser fusion power plant KOYO, and also through a experimental investigation on a small scale DPSSL system. DPSSL seems to be feasible candidate for the driver of laser fusion power plant[1)2)3)]. The specification of laser fusion driver is close to that of laser for space propulsion application. They are large pulse energy and high peak power with good beam quality, and relatively low repetition frequency of few tens to hundreds Hz. Investigation on laser rocket propulsion and space debris clearing are being proceeded along with the laser fusion driver development. The industrial applications of high power laser are progressing with the development of DPSSL with the feature of high efficiency and expectation of low photon cost. Cooperative programs with industry are also proceeded to enhance the spin-off of power laser development on the way to achieve giant laser system of high peak intensity (MJ/ns) and high average power (MW) with high-efficiency (10%) and good beam quality for laser fusion driver.

High power laser diode is one of the key element of DPSSL. The development and improvement of laser diode and its stacking technique are being proceeded with attentions on efficiency, frequency control and suppression of chirping, life and manufacturing cost. A 100kW diode bar assembly has been fabricated and its performance is satisfactory for pumping. The cost reduction is the future technical issue which is most important figure for the application to laser fusion driver.

As a first step of the HALNA development, a small scale module, HALNA 10, which has a 10J×10Hz laser output at 1053 nm has been constructed. The module having water-cooled zig-zag path Nd: glass slab amplifier has a small but enough size to investigate the key issues of the laser fusion driver such as thermal effects, beam quality, energy flow and

* Correspondence: Email: nakai@ile.osaka-u.ac.jp; Telephone: +81-6-6879-8720, Fax: +81-6-6877-4799



XIII International Symposium on Gas Flow and Chemical Lasers and High-Power Laser Conference,
Antonio Lapucci, Marco Ciofini, Editors, Proceedings of SPIE Vol. 4184 (2001)

efficiency in the system, and to confirm our conceptual design[4]. Along with the HALNA development, high average power lasers with high repetition or CW operation are also developing. Direct use of LD, High rep-rate DPSSL, and laser produced plasma X-ray source are our scope to develop for industrial application.

## 2. INVESTIGATION TOWARD LASER DRIVEN IFE POWER PLANT

The establishment of gain scaling of implosion fusion with the evaluation of the tolerable conditions on driver and fuel pellet is the most important issue. The worldwide efforts to clarify the implosion physics have given us a feasible prospect toward the achievement of fusion ignition, burning and energy gain. It should be noticed that the validity of a simulation code to give the gain scaling is examined by implosion experiments and also physical modeling of each elementary process of implosion. Fig.1 shows a typical example of gain scaling.

The reactor technologies for IFE (Inertial Fusion Energy) power plant have been identified and evaluated through the conceptual design studies. KOYO was reported in 1992[5),6)], which was designed taking into account the newest gain scaling of direct drive at that time and, the progress and perspective of DPSSL technology. A wetted wall, which is formed with seeped out LiPb layer from guided flow in woven SiC pipes, is the key concept of the chamber. The feature of system design of KOYO is the arrangement of multiple chambers to one driver as shown in Fig. 2. This gives us wide flexibility in optimizing the system design. The most critical issue which affect the engineering feasibility of a laser fusion power plant is high power laser driver. The required specifications for the laser driver of KOYO are ( i ) pulse energy of 4MJ/pulse, ( ii ) repetition of 12Hz, (iii) overall efficiency of 12%, with(iv) low cost and long life with enough robustness. The development of this kind of super laser is very challenging for new technology. The progress of high power single shot laser and the prospect of the development of high average power laser for power plant are shown in Fig.3.

## 3. SPACE APPLICATION OF HIGH POWER LASER

The ASPIC (Advanced Space Propulsion Investigation Committee) has investigated non-chemical propulsion system and its mission plan working on a specific system concept for the construction of future space infrastructure. The technical main part of this concept is to use Laser Orbital Transfer Vehicle (LOTV) for carrying the payloads from LEO to GEO . The overall concept is shown in Fig.4. The LOTV catches pay loads on the LEO and are accelerated by receiving the laser power from Air Born Laser Platform (ABLP). The payloads are released on GEO and LOTV comes down to LEO for next mission. The conceptual design and mission analysis have been conducted at ASPIC working. The overall specifications are shown in Fig.4. The design of laser thruster and performance test with protomodel is urgently required to give the reasonable prospect of this concept.

The basic design of laser on ABLP is essentially same as the laser fusion driver. The unit module of laser output of 1kJ is identical with the fusion driver for power plant KOYO. We can share the technical developments each other. There are many technical issues, which must be developped to demonstrate the technical feasibility and also the economical merit of the new space system. They span over very wide fields of engineering including rocket propulsion, plasma physics,laser technology, precision measurement and control, and many high-tech engineering. Transparency and collaboration in the world are essential condition to proceed the research and development .

## 4. SCIENCE AND INDUSTRIAL APPLICATIONS OF HIGH POWER LASER

High power laser applications in science and industry are opening new fields of physical paramenters of materials, new interaction physics and new methodology in engineering. Some typical examples are shown in Fig.5 together with the prospect of laser fusion development. It should be noted that the specific features of industrical laser such as stability,

mentainability, robustness, low cost of facility and operation, conpactness, and flexibility and easy of operation are essentially important for the future expansion of the use of laser light. High power LD and DPSSL are the most feasible candidate in laser application.

## 5. DEVELOPMENT OF HIGH AVERAGE-POWER LASER FOR HUCLEAR-FUSION APPLICATION (HALNA)

We have newly designed a DPSSL driver HALNA (High Average-power Laser for Nuclear-fusion Application) based on a water cooled zig-zag path slab laser module, which can deliver 10kJ output energy at 350nm with 12Hz repetition[4].

Two typical schemes of assembly of solid state laser amplifier plate are shown in Fig.6 with pumping LD and flow of coolant. We have adapted the water-cooled zig-zag path concept mainly because of better cooling capability and efficient coupling of LD pump light with simpler configuration. In adapting this concept, we rely on progress of coating technology on laser slab and phase coupled combining of multiple beams. The schematic design of the module for KOYO driver is shown in Fig.7,which can deliver 10kJ output energy at 350mn with 12Hz repetition.

As a first step of development, 10J×10Hz module HALNA-10 has been constructed to investigate and confirm the technical key issues of this concept of DPSSL such as thermal effects, beam quality, energy flow and efficiency, and life of key elements such as cooling surface, laser slab, and diode. It can be scaled up as shown in Fig.7 to reach to a 10kJ×10Hz module which consists of 15 beamlets with phase coupled beam combining.

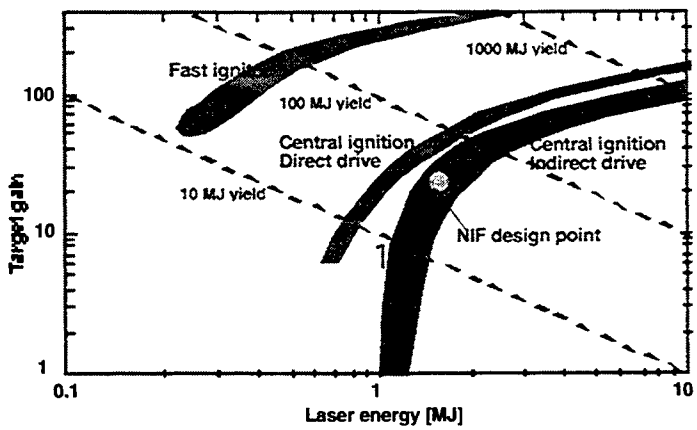


Fig.1 A typical example of gain scaling.

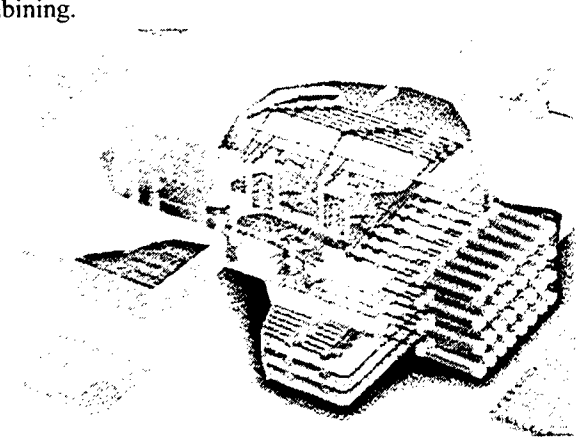

Fig.2. System design of laser fusion power plant KOYO

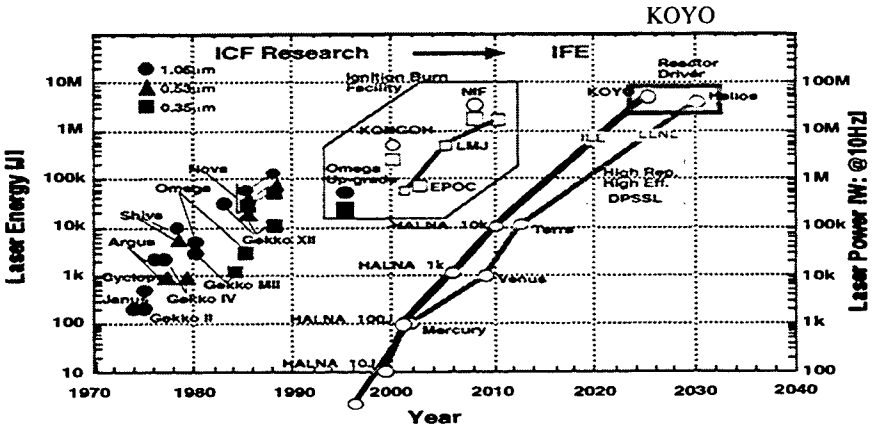


Fig.3. Progress of ICF and IFE laser drivers.

〔Specification of LOTV, ABLP and Mission〕

| | |
|---|---|
| 〔LOTV〕 | |
| weight of LOTV | 1000 (kg) |
| weight of propelant | 2900 (kg) |
| 〔LOTV Thrustor〕 | |
| thrust | 40.8 (N) |
| specific thrust | 1000 (sec) |
| 〔Trajectory〕 | |
| time from LEO to GEO | 10 (days) |
| circulation for one mission | 70 (turns) |
| 〔ABLP〕 | |
| laser power | 700 (kw at $\omega$) |
| | 500 (kw at $\omega$) |
| weight of laser on ABLP | <200 (ton) |
| operation mode at $\omega$ | 1kJ×700 Hz |
| | ~70kJ×10Hz |
| pulse width | 10~50 (ns) |
| beam divergence | 1~2TDL |

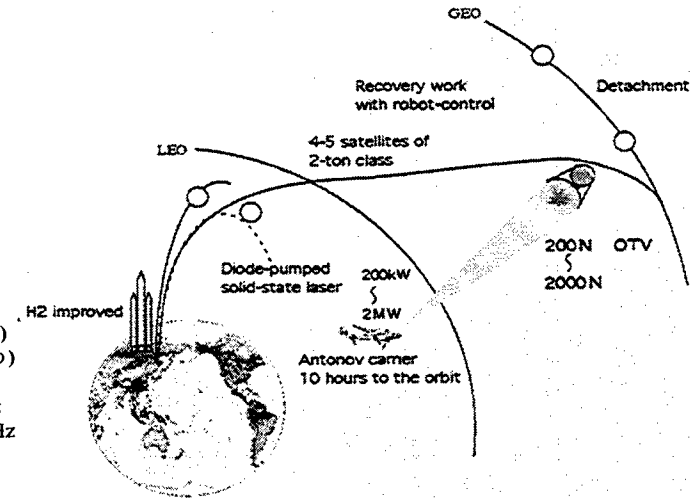


Fig.4. Concept of LOTV, ABLP and Mission.

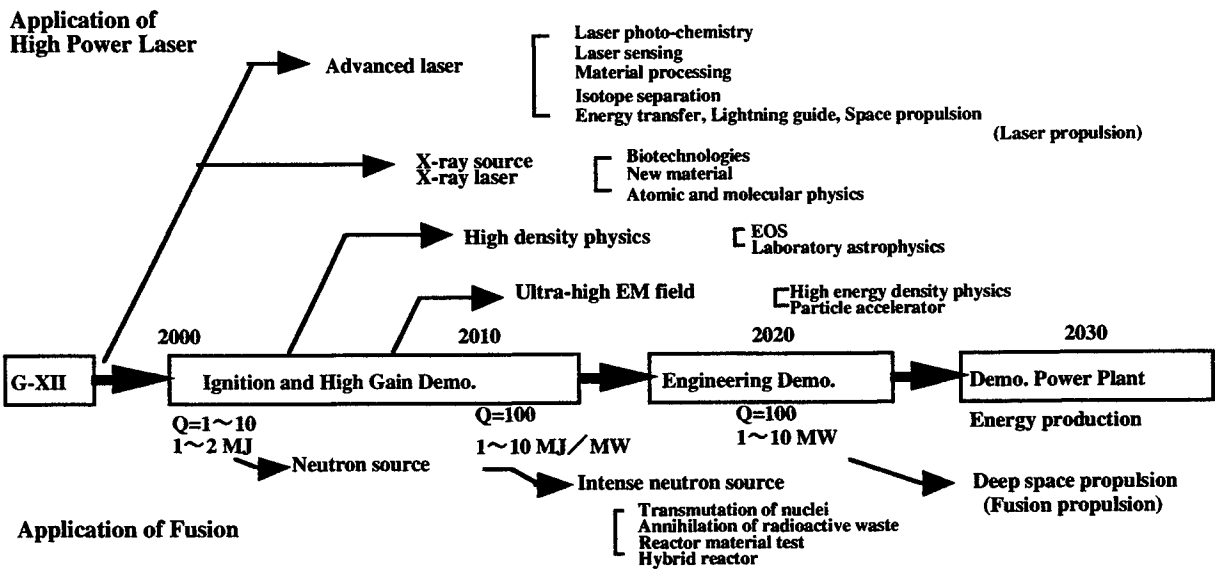


Fig.5. Application and Spin-off IFE Development

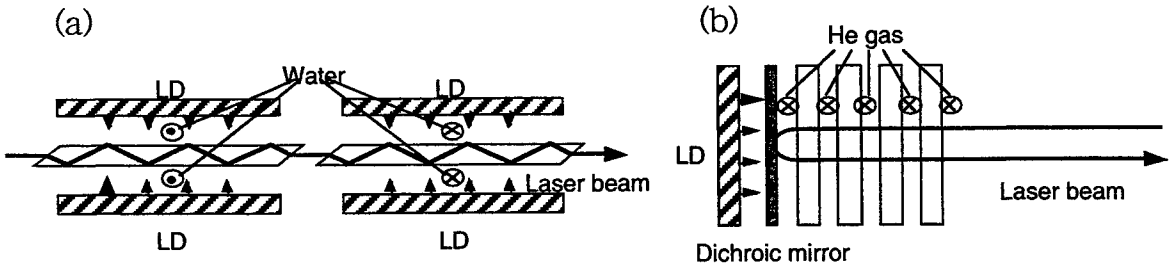


Fig.6. Typical layout of laser material, coolant flow, and pumping LD for high average power DPSSL. (a)zig-zag slub type with water cooling and (b) disk type with gas cooling.

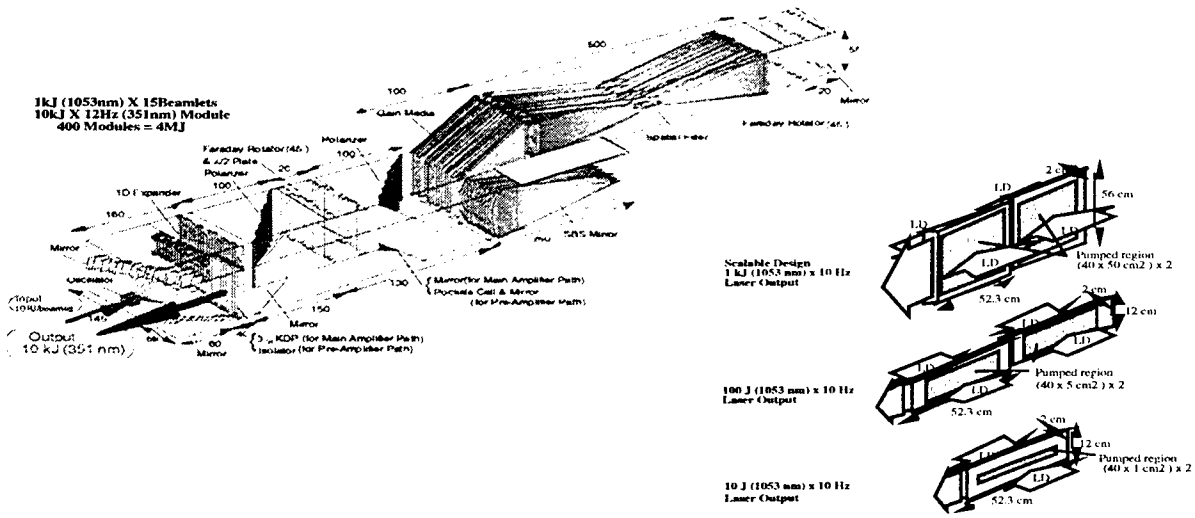


Fig.7. Development plan for reactor driver module of 10kJ×10Hz starting from equivalent mini-module of 10J×10Hz .

### 4.1. Experimental Setup

We constructed a 200-kW LD pumped 10J X 10Hz 1053nm Nd: glass zig-zag slab laser driver module HALNA 10. For the laser gain medium, we have adopted the glass host which can be produced in large sizes with good optical quality. The Nd: glass slab is cooled on both sides with flowing water having higher cooling capability than He-gas cooling. The Nd: glass slab thickness and the stored energy density were chosen to be same values as those of the 10kJ driver module. The 803nm AlGaAs laser diodes (Hamamatsu Photonics) to pump the Nd: glass slab amplifier have been successfully constructed, which generate in total over 200kW peak power with 2.6kW/cm$^2$ peak power intensity at duty cycle 0.2%(10Hz)(Fig.8). The 1053nm small sigmal gain of main amplifier was measured to be 15.9per pass with 0.35ms LD pumping, which is large enough to obtain the output over 10J. The stores energy (34J) and pumping efficiency (44%) of main amplifier at 1053 nm showing the design points are nearly attained.

### 4.2. Experimental Results and Discussion

The 8.5J X 0.5Hz 1053nm output energy was obtained in a preliminary experiment (Fig.9). The extraction efficiency was 24% in this case. The optical to optical conversion efficiency was 10.9%. The output pulse width was measured to be 20ns (FWHM). The near-field patern of 20mm X 10mm with a filling factor of 50% and two times diffraction limitted far-field pattern were observed. With increasing the system transmission to 55% in the multi-path amplification, the 10J X 10Hz output at 1053nm can be realized by compensating for simultaneously the thermal lens, thermal birefringence, and thermal aberration.

The resistivity of Nd: glass surface against flowing water versus time was evaluated by measuring the scattering loss at 632.8nm. After over one year, the scattering loss was as low as 1.3 % through 14 bounce path with HAP-4 Nd: glass, verified using the scattering loss measurement.

The performances of HALNA 10, except the output, extraction efficiency and optical to optical conversion efficiency, nearly confirmed our conceptual design. We have a confidence that a next 100J X 10Hz DPSSL module HALNA100 (Fig.8) can be constructed using 2 MW LD pumping, where the vertical thermal lensing, observed strongly (26cm focal length) with the 10J X 10Hz module, will become smaller (25m focal length) due to increased LD pump width from present 1cm to 5cm.

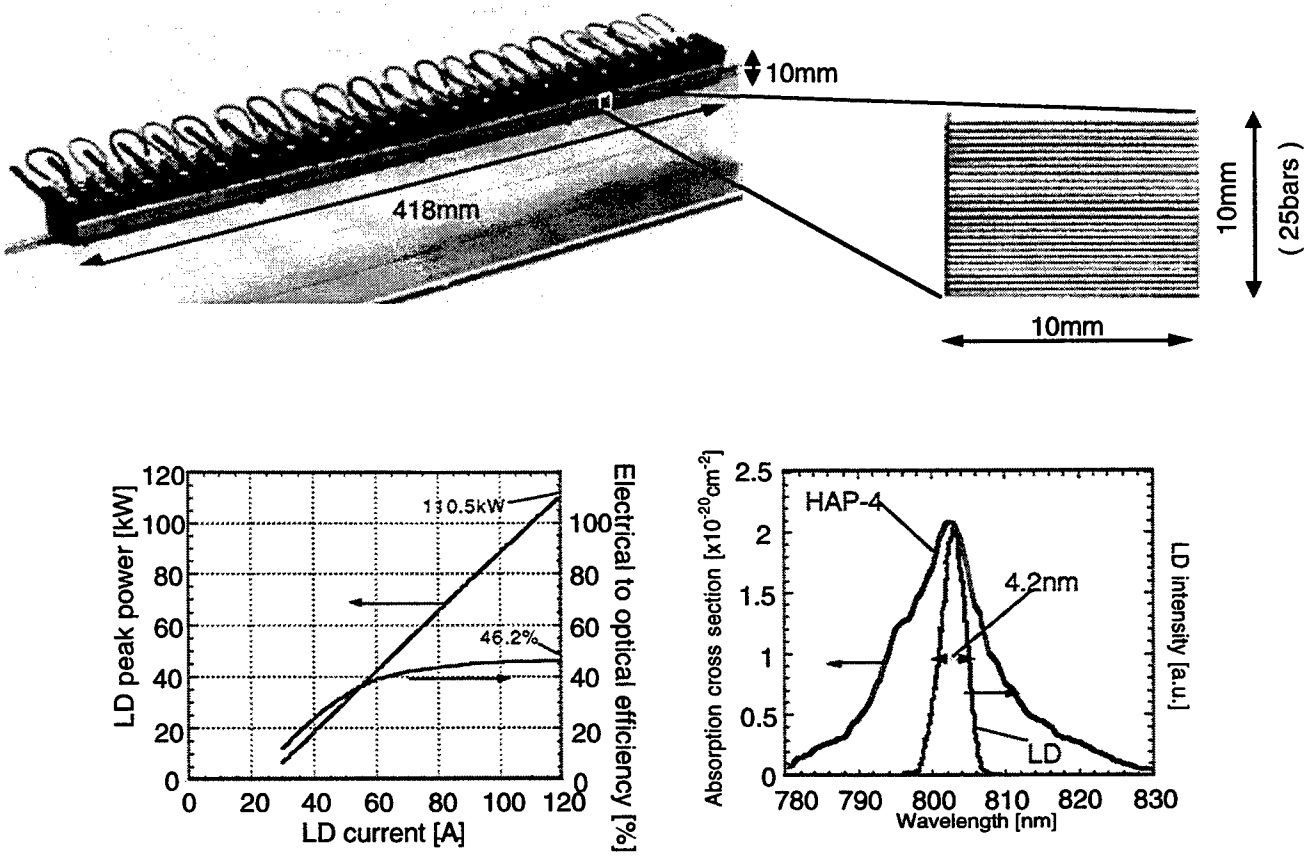


FIG.8. Photograph of quasi-CW 110 kW AlGaAs laser diode module (top), measured total peak power and electrical to optical efficiency (bottom left), and comparison between measured lasing wavelength of module and absorption line of HAP-4 Nd: glass (bottom right).

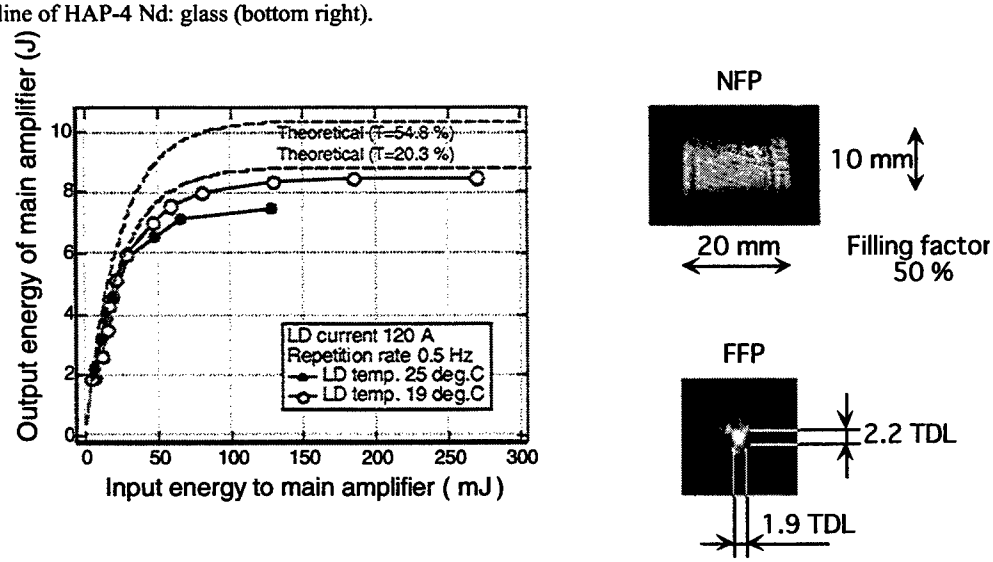


FIG. 9. 1053-nm output energy at 0.5 Hz versus input energy (left), and near field(NFP) and far-field (FFP) patterns at 8.5-J output energy at 0.5 Hz (right).

## 5. CONCLUSION

We are developing high average power laser of low rep-rate and large pulse energy with good beam quality for laser fusion and also for space application. The driver for laser fusion power plant requires output energy of ~MJ/pulse and tens MW average power with good beam quality of order of diffraction limit and high efficiency better than 10 %. These specifications are similar to the requirement for rocket propulsion and LOTV.

We have designed a DPSSL of water cooled zig-zag slab Nd:glass laser NALNA, which has 10 kJ output power as a module being consisted with 15 beamlets. Each beamlet has 1kJ output at 1.05 $\mu$m. This beamlet is the basic unit, which combined in different ways depending on applications. A small scale test module of 10 J $\times$ 10 Hz output power, HALNA-10 has been constructed and tested. Even the preliminary results have given us confidence to be able to scale up and to achieve the designed specification.

Various kind of operation mode from CW, high repetitive operation of kHz~MHz, and low rep-rate of order 10 Hz with large pulse energy can be designed in accordance with different applications. Industrial applications of laser power are being proceeded keeping the collaboration between university and industry with complimentary contributions which spans over fundamental physics of laser-matter interaction to machine development. We are now facing to exciting phase toward new era of engineering which utilizes more light.

## REFERENCES


1. Krupke, W.F. ,"Solid state laser driver for an ICF reactor", Fusion Technol. **15** ,pp. 377, 1989 .
2. Naito, K., et al., "Conceptual design studies of a laser diode pumped solid state laser system for the laser fusion reactor driver", Jpn. J. Appl. Phys. **31**,pp. 259,1992
3. Orth, C.D., et al., "A diode pumped solid laser driver for inertial fusion energy", Nuclear Fusion **44**,pp. 75, 1996
4. Matsui, H., et al., "Conceptual design of a laser-diode-pumped Nd: glass slab laser driver for inertial fusion energy" Fusion Engineering and Design **44**, ,pp. 401, 1999
5. Mima, K., et al., "Design of inertial confinement fusion reactor driven by laser diode pumped solid state laser" Plasma Physics and Controlled Nuclear Fusion Research, **3**, pp. 381, IAEA Vienna ,1993
6. Nakai, S, et al.,"Development of Laser Fusion Power Plant KOYO" 16th IAEA Fusion Energy Conference IAEA-CN-64/ GP-17, Montreal, Canada, 7-11 October 1996

# Continuously Pumped All-Solid-State Laser Systems with Fiber Phase Conjugate Mirror

Enrico Risse [*a], Oliver Mehl [a], Thomas Riesbeck [a], Anca Mocofanescu [b], and Hans J. Eichler [a]

[a] Technische Universität Berlin, Optisches Institut, P1-1,
Str. des 17. Juni 135, 10623 Berlin, Germany

[b] Institute of Atomic Physics, Dept. of Lasers,
P.O. Box MG-36, Bucharest 7600, Romania

## ABSTRACT

All-solid-state laser sources are required for numerous applications in industry and science. Scaling of average output power while preserving a diffraction limited beam quality results in high brightness operation. However, conventional laser systems suffer from thermally induced phase distortions in the active medium, which considerably reduce their beam quality. Advanced pumping geometry, diode pumping, as well as active media with high quantum efficiency can reduce the thermal load. But the remaining phase distortions result in a reduction of beam quality.

Optical phase conjugate mirrors are suitable to compensate for phase distortions in master oscillator power amplifier systems (MOPA). Stimulated Brillouin scattering in conventional, commercially available silica fibers facilitates reliable and stable phase conjugation. These all-solid state devices reveal an energy reflectivity of almost 90% and require low financial efforts. Moreover, the SBS threshold is determined by the appropriate fiber core diameter. Therefore fiber phase conjugators can be applied in continuously pumped, repetitively q-switched laser systems which usually exhibit smaller peak power in comparison with pulsed pumped systems.

A four-pass amplifier arrangement with birefringence compensation was developed. Nearly diffraction limited output with 32 W average power has been achieved at 10 kHz repetition rate. Power scaling up to 100 W seems to be possible.

**Keywords:** Phase Conjugate Mirror, Stimulated Brillouin Scattering, MOPA, High Brightness

## INTRODUCTION

Stimulated Brillouin Scattering (SBS) is the most attractive process to realize self pumped phase conjugate mirrors (PCM) for high power operation. To compensate for phase aberrations the beam passes the distorted active medium twice. After the first amplification pass the beam quality is reduced and the distorted beam enters the SBS mirror. Then the reflected phase conjugate beam propagates the same way through the active medium. Thereby the beam passes again the same phase distortion and the initial beam quality can be reproduced.

Liquid or gaseous SBS cells cannot be used in continuously pumped laser systems since their peak power thresholds are in excess of the available pulse peak power. In a waveguide geometry the SBS threshold depends on the waveguide medium as well as its dimensions. Therefore, the peak power threshold can be adapted to the available pulse peak power choosing adequate waveguide dimensions. Multimode silica step index fibers are suitable waveguides for this purpose. Moreover, they are easy to handle and harmless to the environment. An estimation of their SBS power threshold is given by

$$P_{thr} = \frac{21 \cdot A_{eff}}{L_{eff} \cdot g_B},$$

where $A_{eff}$ is the effective area inside the fiber core, and $g_B$ the Brillouin gain coefficient.[1] For silica fibers $g_B$ is about 2.4 cm /GW. The lower Brillouin gain coefficient of quartz glass compared to liquid or gaseous SBS media can be overcome by an increased interaction length. The effective interaction length $L_{eff}$ is approximated by min $\{L_{fiber}, L_{cohr}\}$, where $L_{fiber}$ is the length of the used fiber and $L_{cohr}$ the coherence length of the laser system. The effective interaction length as well as the Brillouin gain coefficient are affected by the longitudinal mode spectrum of the laser system. A more detailed discussion taking this into account is published elsewhere.[1]

XIII International Symposium on Gas Flow and Chemical Lasers and High-Power Laser Conference,
Antonio Lapucci, Marco Ciofini, Editors, Proceedings of SPIE Vol. 4184 (2001)

## MASTER OSCILLATOR

The developed master oscillator is depicted in Fig. 1. It consists of a diode pumping chamber, an acoustooptic modulator (AOM), an etalon, a thin-film polarizer (TFP), an output coupler and high reflectivity mirrors. The ring resonator is applied to avoid spatial hole burning. The external feedback mirror facilitates clockwise unidirectional operation. As active medium a Nd:YAG rod is used with a length of 56 mm and a diameter of 4 mm. An additional intracavity etalon with a thickness of 2 mm and a reflectivity of 50 % reduces the spectral bandwidth to increase the possible interaction length inside the fiber. A lens with a focal length of f = - 500 mm increases the fundamental mode diameter. Q-switching operation is obtained using an AOM with a repetition rate of 10 kHz and an RF driver power of 5 W. The oscillator provides an average output power of 10 W with a nearly diffraction limited beam quality. Pulse widths of 280 ns lead to pulse peak power of 3 kW.

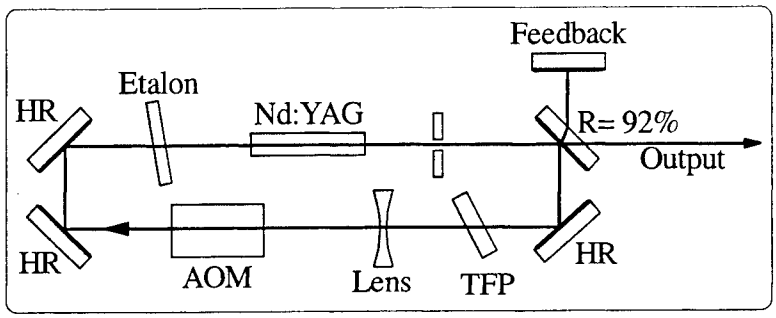


Fig. 1: Scheme of the developed diode pumped Nd:YAG master oscillator

## AMPLIFIER ARRANGEMENT

Two commercially available pumping chambers from an industrial laser system are used as amplifiers. The identical Nd:YAG rods with a diameter of 6.35 mm and a length of 178 mm are pumped by two arc lamps in specular cavities.
Assuming a maximum average oscillator power of 10 W and a repetition rate of 10 kHz the pulse energy cannot exceed 1 mJ. Therefore the energy density in front of the first amplifier can be estimated to be smaller than 10 mJ/cm² in case of a 4 mm beam diameter. Taking a saturation energy density of 500 mJ/cm² for Nd:YAG into account, the amplifiers would operate far below their saturation fluence resulting in a small extraction efficiency. However, the extraction efficiency can be improved by increasing the number of amplifier passes.
Therefore a four pass amplifier arrangement was applied, see Fig. 2. The oscillator beam passes an optical isolation and is amplified in a serial amplifier arrangement. To compensate for thermally induced stress birefringence in the active media the well known relay-imaging setup containing two lenses and a 90° quartz rotator is used.[2] Birefringence compensation results in depolarization losses below 2 % after passing both amplifiers. After the first amplification pass, the beam is collimated and reflected using a conventional curved HR-mirror.

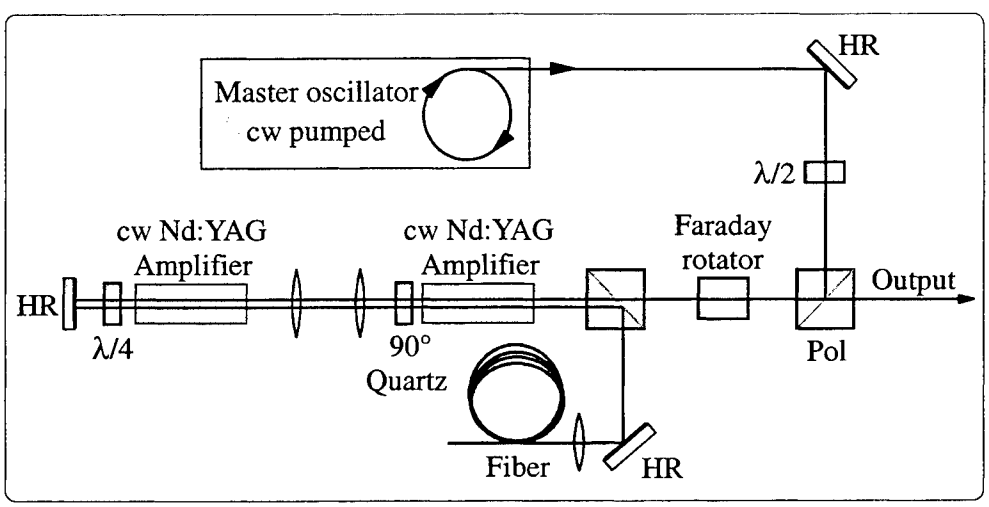


Fig. 2: Continuously pumped MOPA system with four pass amplifier arrangement and fiber phase conjugator

The polarization direction is rotated by 90° passing the quarter wave plate twice. During the second pass the beam is amplified again and coupled into the fiber phase conjugator. The beam is phase conjugated in a multimode silica step index fiber with a core diameter of 50 $\mu$m, a numerical aperture of 0.22, and a length of 5 m. After two additional amplifier passes the initial beam quality is reproduced and the beam is extracted with help of the optical isolation. Applying the four pass scheme to the serial amplifier arrangement an average output power up to 32 W has been achieved at 10 kHz repetition rate. Figure 3 shows the measured output power as a function of the oscillator power.

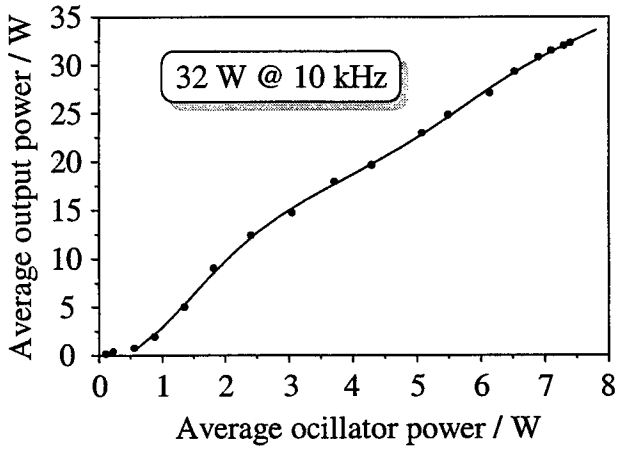


Fig. 3: Measured average output power as a function of the oscillator power.

Figure 4 shows the reflectivity of two different multimode silica fibers with a core diameter of 25 and 50 $\mu$m as a function of the incident pulse peak power. The given reflectivity is corrected for coupling losses and exceeds 85 % for both fiber phase conjugators. Their SBS power thresholds were extrapolated to be 0.3 kW, and 2.0 kW respectively. The often used SBS liquid carbon disulfide ($CS_2$) exhibits a 9-times higher SBS threshold, compared to the multimode silica fiber with 50 $\mu$m core diameter.

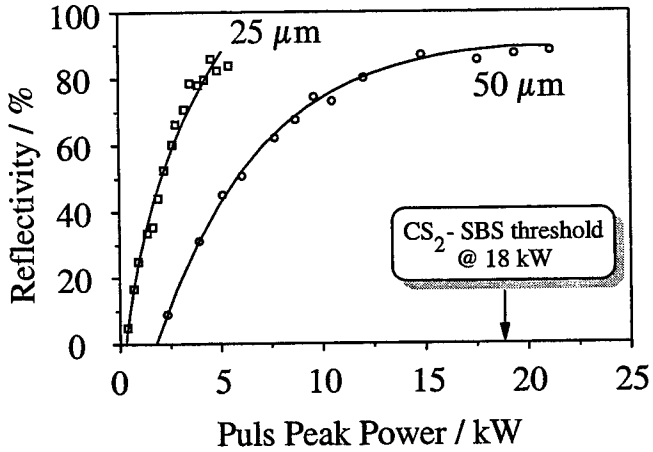


Fig. 4: Reflectivity of multimode silica fibers with a core diameter of 25$\mu$m and 50$\mu$m vs. pulse peak power.

## BEAM QUALITY

The beam quality measurements were carried out according to the international standard "Test methods for laser beam parameters", ISO/CD 11 146.[3] Hereby the beam radius is determined by the second moment of the intensity distribution. The setup shown in Fig. 5 was used for a simultaneous measurement of beam quality and average output power. Fresnel reflection at two uncoated wedge plates supplies an attenuated beam that is focused with a long focal length lens yielding an external beam waist. A 10-bit digital CCD camera was used to determine the beam diameter along the beam's caustic. The times diffraction limit factor $M^2$ was determined to be smaller than 1.3 for both directions in space, see Fig. 6.

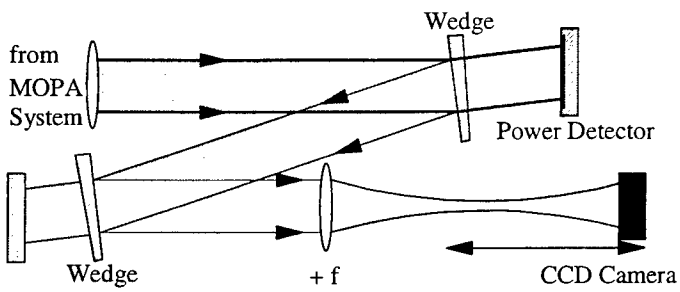


Fig. 5: Beam quality measurement setup.

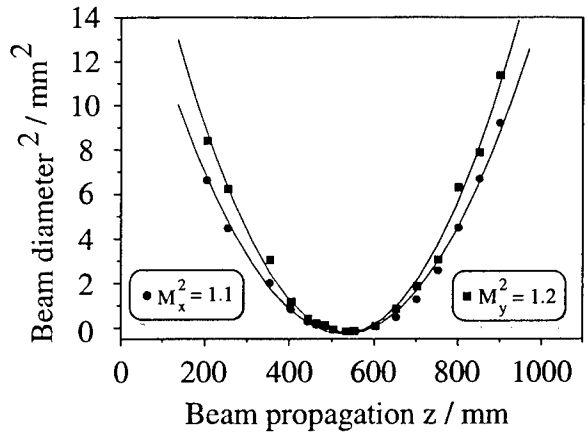


Fig. 6: Determination of the times diffraction limit factor $M^2$.

## CONCLUSION AND OUTLOOK

A continuously pumped all solid state Nd:YAG MOPA system with fiber phase conjugate mirror has been developed. Due to phase conjugation the initial beam quality of the master oscillator is reproduced after four pass amplification. Average output power up to 32 W with a times diffraction limit factor $M^2$ smaller than 1.3 has been obtained at 10 kHz repetition rate. Stimulated Brillouin scattering in a multimode silica fiber with a core diameter of 50 $\mu$m facilitates phase conjugation for pulse peak powers above 2 kW. The fiber phase conjugate mirror is self-pumped and reveal energy reflectivity up to 88 %.

Currently output power scaling up to 100 W is under development. Therefore an improvement of extraction efficiency in the serial amplifier arrangement is the main issue. Moreover, the pulse length of the master oscillator will be reduced, resulting in higher pulse peak power and increased energy reflectivity of the fiber phase conjugate mirror. To enhance the amplifier's extraction efficiency active media with smaller diameter are used to obtain an increased energy density. Additionally, diode pumping will be applied to improve the amplifier gain and the overall efficiency of the MOPA system.

## REFERENCES

1. G.P. Agrawal, "Nonlinear fiber optics", 2nd ed., Academic Press (1995)
2. Q. Lü, N. Kugler, H. Weber, S. Dong, N. Müller and U. Wittrock, "A novel approach for compensation of birefringence in cylindrical Nd:YAG rods", Opt. Quant. Electron., pp. 57-69, Vol. 28 (1996)
3. Document ISO/TC 172/SC 9/WG 1 N 56, ISO/CD 11 146, Optics and optical instruments – Lasers and laser related equipment – Test methods for laser beam parameters: Beam width, divergence angel and beam propagation factor, Nov. 26, 1993

*Phone: +49 (30) 314-22449, Fax: +49 (30) 314-21079, e-mail: enrico.risse@physik.tu-berlin.de

Invited Paper

# Metal Vapour Lasers: New Developments and Applications

Colin Webb

University of Oxford, Clarendon Laboratory, Parks Road, Oxford OX1 3PU, UK

## ABSTRACT

Copper vapour lasers are high repetition rate, pulsed devices with output at 511nm (green) and 578nm (yellow). In recent years, diagnostic studies have led to advances in power, efficiency and output beam quality. Originally developed for industrial scale isotope enrichment processes, new applications for these lasers include high-speed imaging, velocimetry and micro-machining of hard materials. By frequency doubling the 511nm green output, output powers of order 1W at 255nm in the UV can be obtained. This radiation is ideal for the manufacture of Fiber Bragg Gratings – essential components for modern optical telecommunications. Kinetic enhancement of the excitation mechanisms of the laser provides not only increases in output power of compact copper lasers but also dramatic improvements in laser brightness.

**Keywords:** metal vapour lasers, high speed imaging, velocimetry, micro-machining, fiber Bragg gratings, high power UV, kinetic enhancement of copper lasers

## 1. INTRODUCTION

The best known type of metal vapour laser is the copper vapour laser (CVL) which is representative of the class known as 'self-terminating' or 'cyclic' lasers whose amplifying medium is the vapour of a neutral atomic species, usually a metal.

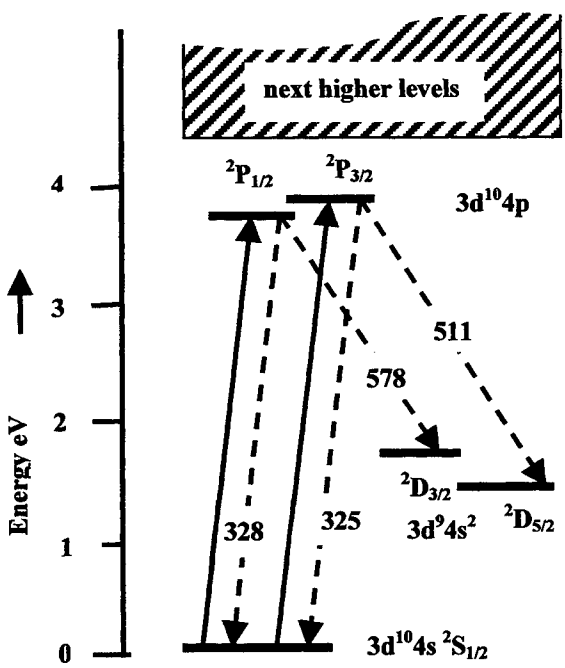


Figure 1 Low-lying energy levels of atomic copper

The CVL is characterised by its ability to produce high average powers in the form of pulses of 20–40ns duration on two visible transitions (511nm green, 578nm yellow) from units capable of round the clock operation. Typical efficiencies are of the order of 1–3% for the conversion of electrical input to laser power. CVLs can also be operated in the form of oscillator-amplifier chains.

The basic principles of operation can be understood from the atomic term diagram of the neutral copper atom shown in Figure1. In a fast rising, high current pulse in a discharge containing a buffer gas (neon) and ~ 0.3mbar of elemental copper vapour, electrons excite copper atoms preferentially to the $^2P$ upper laser levels. The population in these levels quickly exceeds (on a per statistical weight basis) that of the metastable $^2D$ lower levels and a short period of gain lasting up to 50–70ns ensues.

After the laser pulse the population has been transferred to the $^2D$ lower levels which are optically forbidden to decay back to the $^2S$ ground state by the strong parity selection rule. Fortunately, electron quenching in super-elastic collisions provides an effective route by which the $^2D$ population can decay on timescales of 10-100 μs. By the time of the next current excitation pulse, the residual lower laser level population is small.

XIII International Symposium on Gas Flow and Chemical Lasers and High-Power Laser Conference,
Antonio Lapucci, Marco Ciofini, Editors, Proceedings of SPIE Vol. 4184 (2001)

## 2. MILESTONES IN METAL VAPOUR LASER DEVELOPMENT

### 2.1. Elemental CVLs

The earliest report of self-terminating laser action was the demonstration of the atomic Pb laser in 1965 by Fowles and Silfvast[1]. This was followed in 1966 by the first demonstration of laser action in a furnace heated CVL by Walter *et al*[2]. Isaev *et al*[3] in 1972 made a major step forward with the demonstration that the heat of the discharge alone was sufficient to evaporate metallic copper and thus provide a self-heated CVL. Another important development was made by Smilansky *et al*[4] in 1978 who showed that uniform discharges in the neon/copper vapour mix were possible in wide bore discharge tubes, opening the way to volumetric scaling of CVL output.

Developments of elemental CVLs continued throughout the 1980's and in 1987 Warner *et al*[5] disclosed that amplifier units providing 775W each were incorporated into the master oscillator / power amplifier (MOPA) chains installed at Lawrence Livermore National Laboratories (LLNL).

### 2.2. Limitations to Elemental CVL Performance

One of the problems which limits the ability of the elemental CVL to operate at very high repetition rates is the fact that the electron density does not decay sufficiently fast between excitation current pulses. Experiments by Hogan[6] using a two-wavelength interferometric technique show that in a standard CVL (even one containing 0.5% $H_2$ in neon) decays to only about 30% of the peak value (~ 1 x $10^{14}cm^{-3}$) in the 150μs inter-pulse period.

The consequence of this is that the tube remains weakly conducting at the start of the next excitation pulse and a small dark current (the phantom current) flows before the gas in the tube undergoes breakdown. The presence of this remanent electron density is thus to decrease the excursion of electron temperature on the leading edge of each successive laser pulse with deleterious effects on the excitation of copper atoms.

### 2.3. Copper Halide Lasers

The high temperature (1500C) needed to provide an adequate vapour pressure of elemental copper for CVL operation was initially seen as a problem for CVL technology. In the 1973/74 period several groups[7, 8] experimented with copper halide vapours such as CuCl which have sufficient vapour levels in the 500–700C range. In these early experiments laser operation was obtained on the second pulse in a double-pulse pair, in which the first pulse served to dissociate the halide molecules into their atomic constituents. In 1974 Sabotinov *et al*[9] developed truly pulse-repetitive lasers in Ne–CuBr vapour mixtures showing that devices of average power several W could be obtained using the halide vapour approach.

### 2.4. Copper HyBrID Lasers

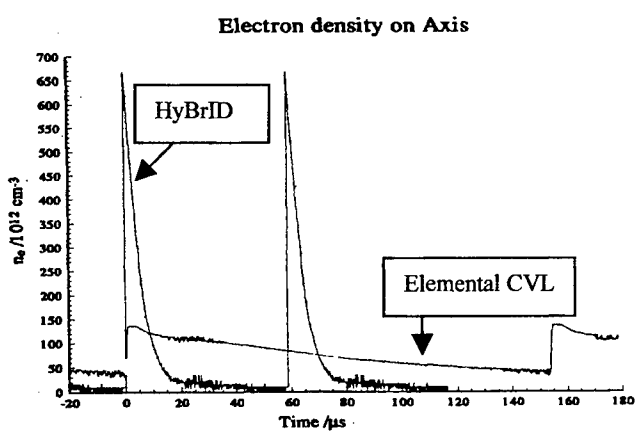


Figure 2. Time dependence of electron density in elemental and HyBrID CVLs[11]

A major advance in halide containing CVLs was made in 1990 by Maitland, Little, Jones and co-workers at St Andrews University[10] in the form of the Hydrogen Bromide In Discharge (HyBrID) laser concept. In this laser the copper vapour is obtained from metallic copper strips lining the discharge tube at intervals along its length by the action of HBr gas entrained in the flow of neon.

These devices which operate at temperatures of only 600C, like their copper halide predecessors, can be fabricated from silica tubing using glass-blowing techniques. This allows a greater degree of design flexibility than their high temperature elemental CVL counterparts.

As shown in Figure 2, the electron density in a HyBrID laser[11] reaches peak values some 30 times higher than that of a comparable elemental CVL and decays very much more rapidly before the next pulse is applied, allowing operation at much higher pulse repetition frequencies.

So far, HyBrID laser technology does not seem to have been commercialised. Perhaps this is associated with the problem of dendrites of metallic copper building up in the cold end-regions of HyBrID laser tubes. The dendrites can grow large enough to obstruct the beam path after the laser has been operating for some time. Nevertheless, excellent efficiencies (up to 3%) have been reported for such devices[12] with output powers of order 100–300W.

## 2.5. Evolution of High Beam Quality CVLs

One of the problems with early elemental CVLs was that in order to run efficiently they needed rather low buffer gas pressures (less than 50mbar). As shown in Figure 3, the beam profile at early stages develops from an annular profile of seed emission.[13] This is due to the large value of remanent electron density which constrains the radial penetration depth of electric fields of the applied excitation pulse via the so called 'skin effect' in conducting media.

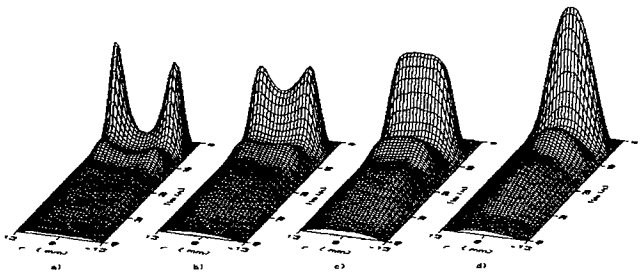

Figure 3. Time traces of laser intensity across aperture of Oxford Lasers LS20-10 for a) 30 b) 50 c) 80 d) 115mbar

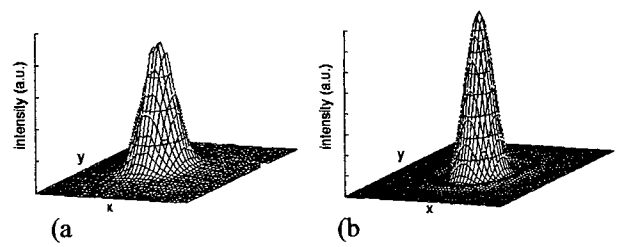


Figure 4. Far-field intensity profiles a) measured for LS20-10 laser with M=360 resonator b) diffraction limited Airy profile

Modifications to the electrical circuits have allowed efficient operation of the CVL at higher values of buffer pressure which give rise to gain profiles which are axially peaked (as shown in Figure 3). In early CVL oscillators it was necessary to use off-axis unstable resonators to take advantage of the early growth of gain at positions near the tube wall to provide a beam which could be used to seed the axial region of the same tube and thus extract low divergence output. However, the combination of new excitation circuits and a small admixture (0.5%) of $H_2$ in neon can give rise to a radial profile peaked on axis. This allows axial unstable resonator configurations to be employed, giving rise (as shown in Figure 4) to near diffraction limited beam quality with commercial single unit CVLs.[13]

## 2.6. CVLs in Isotope Separation

The main driving force behind the development of high power CVL chains throughout the 1980's was the requirement for an industrially qualified, high repetition rate, pulsed laser system to pump the dye oscillator amplifier laser chains employed in pilot plants investigating the commercial feasibility of laser techniques in uranium isotope enrichment.

At LLNL in the USA a demonstration facility was constructed using in-house technology to provide three beams of several kilowatts average power tuned to individual absorption lines of U235. The first of these beams selectively excites ground state U235 atoms to an excited configuration from which the second beam step-wise excites (also selectively) these atoms to an even higher configuration. The third beam ionizes the excited atoms which are then extracted as ions under the influence of electric and magnetic fields.

A similar but smaller test facility was constructed in the late 1980's by British Nuclear Fuels (later URENCO) at its centrifuge enrichment facility at Capenhurst in the UK. The CVLs for this installation and its precursors at Harwell and Culham Laboratories were designed and manufactured by Oxford Lasers Ltd.

In the early 1990's, following the demise of the former Soviet Union, quantities of enriched uranium from former weapons industries began to appear on the open market. The need for new and exotic means of enriching uranium fuel for the dwindling number of nuclear reactors then under construction effectively disappeared and Oxford Lasers Ltd was faced with the prospect of finding new applications for its expertise in CVL manufacture.

New applications have been successfully developed by the company and are described in the following sections.

## 3. NEW APPLICATIONS

### 3.1. High Speed Imaging

Because of its short pulse duration (less than 30ns) and high repetition rate capability (up to 30kHz in standard air cooled units) the CVL makes an ideal strobe lamp for illuminating very fast events in conjunction with film motion pictures or video cameras. A very important feature of CVL performance in this application is the low jitter (less than 2ns rms) in timing between the command pulse and the appearance of the laser pulse.

One of the many applications that could be mentioned in this context is the certification testing of new jet engines for the aero-industry in which a turbine blade is deliberately exploded. Clearly engine manufacturers wish to recover as much information as possible in the few 10's of milliseconds following the explosion and illumination of the engine with CVLs linked to high-speed cameras has provided unique insights.

At a more humble level, the ability of the high intensity of the CVL pulse has enabled the recording of excellent motion pictures showing the behaviour of molten metal in a weld-pool during electric arc welding. In this application, the narrow band nature and short duration of the laser pulse is essential for the rejection of the broad band emission from the arc plume since both spectral and temporal filtering are employed.

### 3.2. Velocimetry

For studies of fluid flow for example in internal combustion engines, the multi-pulse nature of the CVL output is extremely important. It allows multiple images of individual droplets of unburnt fuel or seeding particles to be recorded, revealing the direction and magnitude of velocity of the particle using lightsheet illumination. Using this technique, researchers have been able to record time resolved vector maps of the velocities of the fuel / air mixture in IC and diesel engines.

### 3.3. Micro-machining

#### 3.3.1. Drilling with CVLs

In recent literature there have been many publications which suggest that clean, dross and recast-free holes can only be drilled in metals and other hard materials using lasers whose pulse duration is less than 1 picosecond.[14] However, in techniques developed at Oxford Lasers Ltd, it has been demonstrated that clean, dross free holes with excellent internal finish and sharp edges *can* be drilled in such materials with CVLs at rates suitable for industrial production processes.

In the example shown in Figure 5 the 50 micron diameter holes were drilled with CVL beams of near diffraction limited beam quality. The technique employs a proprietary trepanning device to direct the focus spot (typically 5–10 microns diameter) in a circular path. In this way, a circular plug is removed from the surrounding metal leaving a slightly undersized hole which is then finished to the required dimensions by continuing the trepanning motion of the beam.

This technique is not necessarily restricted to the CVL. Technically it would be possible to use other pulsed, visible, nanosecond lasers but the CVL offers a unique combination of beam quality, average power and repetition rate, as well as round the clock performance required for an industrial system.

### 3.3.2. Characteristic time scales and diffusion lengths

Following Corkum *et al*[15] it is possible to characterise the laser-metal interaction into three different regimes according to whether the laser pulse duration $\tau_p$ is shorter than the characteristic time $\tau_e$ describing the thermalisation time of the electron gas or is intermediate between that and $\tau_i$ (the relaxation time of the lattice ions) or finally whether $\tau_p$ is longer than $\tau_i$.

Calculations due to Kapitan[13] of the magnitudes of these times and the associated diffusion lengths for heat transport in Al, Fe and Cu metals are listed in Table.1. From this table it is evident that the characteristic diffusion lengths for pulses of 10ns duration in these three metals are of order 1μm and that reducing the pulse duration by a factor of $10^4$ to 100fs reduces the diffusion scale length by only a factor of 5.

| regime | characteristic time-scales and diffusion lengths | Al | Fe | Cu |
|---|---|---|---|---|
| | $\tau_e = (8/\pi)^{1/4}\ (1/g)\ (c_e c_i T_{th})^{1/2}$ | 10.4 ps | 13.3 ps | 13.2 ps |
| | $\tau_i = (8/\pi)^{1/4}\ (1/g)\ (c_i^3/T_{th} c_e)^{1/2}$ | 90.9 ps | 149.6 ps | 141.5 ps |
| $\tau_p < \tau_e$ | $D_e = (128/\pi)^{1/8}\ (k/g)^{1/2}\ (c_i/T_{th} c_e)^{1/4}$ | 0.13 μm | 0.26 μm | 0.18 μm |
| $\tau_e < \tau_p < \tau_i$ | $D_e' = (\tau_p/\tau_e)^{1/5} D_e \cong (\tau_i/\tau_e)^{1/5} D_e$ | 0.20 μm | 0.42 μm | 0.29 μm |
| $\tau_i < \tau_p$ | $D_i = (\kappa\tau_p)^{1/2}$ for $\tau_p \cong 10$ns | 0.98 μm | 0.48 μm | 1.07 μm |

**Table 1.** Timescales and diffusion lengths from the two-temperature model.[15] The electron phonon coupling constant g and electron heat capacity $c_e$ are taken to be $10^{11}$ $Wcm^{-3}K^{-1}$ and $0.1Jcm^{-3}K^{-1}$ respectively for all metals. The threshold temperature $T_{th}$ is taken to be the boiling temperature of metal for the explosive ejection regime considered here.[13]

Analysis of a large volume of published data on laser / metal interaction[13] indicates that the key parameter in determining whether the interaction is below threshold or sufficient to cause evaporation or to cause explosive melt ejection is the value of energy absorbed per unit volume, rather than the fluence (energy per unit area). In calculating the appropriate volume, it is the cylinder defined by the area of the laser focal spot together with the appropriate diffusion length that is required. Since the diffusion length is independent of pulse duration for $\tau_p$ less than 10ps, in this regime the threshold fluence approaches a constant value and becomes independent of $\tau_p$. The value of absorbed energy density per pulse at which explosive melt ejection occurs is in the region $10^5$ to $10^6$ $Jcm^{-3}$. This marks the transition from a slow surface evaporation process to the melt explosion process required for successful drilling.

### 3.3.3. Industrial micro-machining systems

A photograph of an industrial micro-machining system including a five-axis work station and 45W CVL manufactured by Oxford Lasers Ltd is shown in Figure 6. Systems of this type have been delivered to manufacturers of automotive components for the drilling of diesel or gasoline fuel injector nozzles (see Figure 7) and to manufacturers of high precision inkjet printers. Table.2 lists the capability of such CVL drilling equipment.

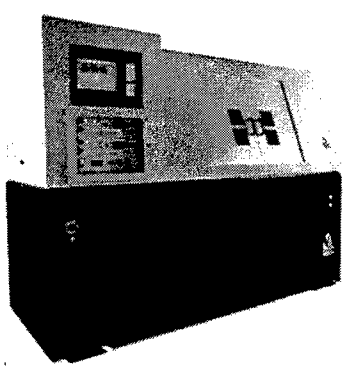

Figure 6. Five-axis workstation for micro-machining

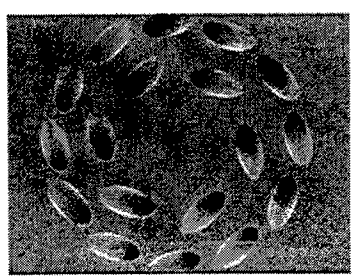

Figure 7. A swirl gasoline injector for use in racing car engines

| | |
|---|---|
| Hole diameters: | 20 – 500 μm |
| Hole roundness and diameter tolerance: | ± 3 μm |
| Hole taper: | Variable (+,0,-) |
| Hole depths: | 0.010 – 1.5 mm |
| Recast layer: | < 1 μm thick |
| Component heating: | Minimal |
| Hole angles: | Multi-axis drilling |
| Materials: | All hard materials |

Table 2. CVL drilling capability

### 3.4. Fiber Bragg Grating Manufacture

Efficient frequency conversion of the output from CVLs has been the subject of many studies in recent years, particularly since the introduction of β-barium borate (BBO) as the non-linear material. Coutts[16] obtained powers of 1.75W at 255nm (SHG of 511nm), 1.2W at 289nm (SHG of 578nm) and 1.5W at 271nm (sum frequency 511nm + 578nm) from a nominally 20W CVL. This work has been commercialised by Oxford Lasers Ltd in the design and production of a range of UV industrial CVLs whose properties are summarised in Table 3.

| | | FBG250 | FBG600 | FBG1000 |
|---|---|---|---|---|
| Average Power | @ 255 nm | 250 | 600 | 1000 |
| Options | @ 271 nm | 250 | 600 | 1000 |
| | @ 289 nm | 100 | 250 | 400 |
| Peak power (kW) | | 1.5 | 4 | 6 |
| Power stability (+/- % rms) over 8 hours | | 3 | 3 | 3 |
| Spatial coherence (mm) | | 2 | 2 | 1 |
| Beam diameter (mm) | | 3 | 4 | 4.5 |
| Divergence (mrad) | | 0.3 | 0.3 | 0.6 |
| Pointing stability (mrad) | | 0.05 | 0.05 | 0.05 |
| Power consumption (kW) | | 3.5 | 4 | 4 |

**Table 3.** Specification of Oxford Lasers UV CVLs for FBG manufacture

Fiber Bragg Gratings (FBGs) are an essential component for modern telecommunications systems in which dense wavelength division multiplexing (DWDM) is employed to increase the information transmission capacity of optical fiber networks by transmitting many (40–100) individual wavelength channels down a single optical fiber. To tune the semiconductor transmitter lasers to the specific wavelengths required and to split out individual channels at the receiving end requires the use of sharply tuned filters that employ Bragg gratings inscribed in the core.

The technique of inscribing FBGs in telecommunications fiber involves exposing the fiber to a striped pattern of UV light in the range 230–260nm where the germanium-oxygen bond has a characteristic absorption. The refractive index of the fiber core is permanently modified by exposure to the UV and, if the planes of alternating high and low refractive index are spaced at intervals of half integer values of the signal wavelength (in the fiber core medium), then strong and selective reflection of the signal occurs.

In the production of FBG's the pattern of bands of alternating high and low intensity of the UV radiation can be obtained by splitting the beam from the UV laser into two and recombining it so that interference fringes occur in the overlap region. A simple way of achieving this is to use a phase mask. This is a plane transmission diffraction grating specially designed to produce only two orders of diffraction, say +1 and –1. There is no need for the fiber to be held in close contact with the phase mask during FBG imprinting provided the UV laser has sufficient coherence length.

Three types of laser are used industrially for the production of FBGs. These are the frequency doubled argon ion laser, the KrF excimer laser and the frequency doubled (255nm) CVL. In choosing a laser for industrial FBG production, manufacturers look for a stable UV output power, good beam pointing stability, long coherence length and low running costs. Oxford Lasers experience with UV CVLs has shown that this laser satisfies all these requirements better than either of the alternatives. Its coherence length (40mm) is much longer than the excimer laser, its electrical efficiency in generating UV is 10 times greater than the argon ion laser and its running cost is less than $7 per hour.

## 4. KINETICALLY ENHANCED CVLs

Piper and co-workers[17] at Macquarie University have demonstrated that very substantial improvements both to output power and beam quality in elemental CVLs can be obtained by the addition of very small controlled quantities of HCl to the buffer gas mixture (neon + $H_2$) in an otherwise standard laser. The efficiency and power gain results from dissociative attachment of electrons to HCl in the inter-pulse period which acts to rapidly reduce the free electron density and has the same beneficial effect in controlling the electron density and conductivity of the afterglow plasma as in the HyBrID laser described above.

The presence of $Cl^-$ ions also aids in the quick recombination of $Cu^+$ ions increases the available density of Cu in the tube which would otherwise be cumulatively depleted by repetitive ionization. The performance benefits obtained by the

relatively simple modifications needed to upgrade standard CVLs are seen in terms of increased output power from a device of given volume. For example: in 1986 Oxford Lasers Model CU15 produced 10W output power on a plane/plane resonator with a 1m long discharge tube of 25mm diameter; the LS 20-10 standard water cooled laser introduced in 1994 produced 25W from a tube of the same dimensions; with kinetic enhancement this device (designated LM100X in 1999) can produce 60W from a tube of the same dimensions. There are also benefits in terms of the flexibility of operating frequency. Output powers in excess of 50W can be obtained from the LM100X for pulse repetition frequencies over the full range from 15 to 40 kHz. Experimental devices of this type have been operated over frequencies of 5 to 100 kHz.

Another feature of laser performance which is strongly influenced by kinetic enhancement is the duration of the gain pulse whose FWHM is not only noticeably increased but also achieves maximum gain later in the pulse.

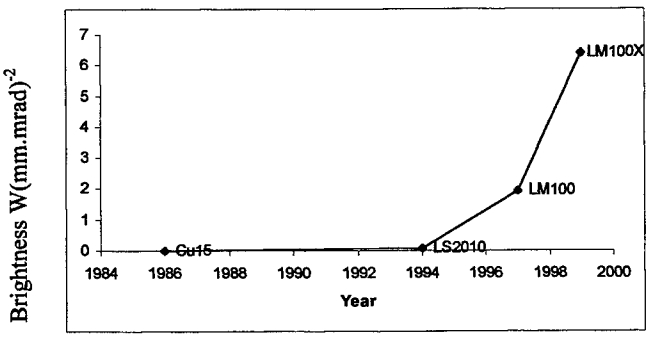


| | | | |
|---|---|---|---|
| Cu15 | - | 10W air cooled CVL | (1986) |
| LS2010 | - | 25W water cooled CVL | (1994) |
| LM100 | - | 20W water cooled CVL | (1997) |
| LM100X | - | 60W KE-CVL | (1999) |

Figure 8. Improvements to brightness performance of Oxford Lasers compact CVLs

This means that the gain period during which low divergence radiation can build up in an unstable resonator is significantly extended. However, the most dramatic improvements from kinetic enhancement are seen when we consider the combined effect of increased output power and beam quality in the form of brightness of the beam measured in Watts per (mm.mrad)$^2$ from a 1m long x 25mm laser tube as shown in Figure 8.

The patented technology of kinetic enhancement for CVLs has been exclusively licenced to Oxford Lasers Ltd for non-nuclear applications.

## 5. SUMMARY

Although improvements in solid state, high repetition rate, pulsed lasers are being made, continuing development of CVLs has enabled them to maintain their position at the forefront of laser technology for industrial applications.

CVLs can perform precision drilling in hard materials with little or no recast and minimal heat affected zones. Such laser systems are capable of round the clock operation in industrial environments for a variety of micro-machining manufacturing processes. With highly stable output power and beam pointing characteristics, 1000 hour routine service intervals and a cost of operation at only $7 per hour, they are winning widespread acceptance as industrial machine tools.

New applications include: micro-milling, micro-cutting, etching and, with UV capability, the direct writing of Fiber Bragg Gratings. The implementation of kinetic enhancement offers substantial further improvements in CVL performance which will ensure that they continue to out-perform competition from solid state lasers for some time to come.

## ACKNOWLEDGEMENTS

The author gratefully acknowledges his many colleagues for their skill in research and whose inventiveness is clear from the foregoing text. In particular he would like to thank:

D.W.Coutts, D.Kapitan, G.Marshall and G.P.Hogan, Clarendon Laboratory, University of Oxford

R.J.Carman, R.P. Mildren, M.J.Withford, D.J.W.Brown and J.A.Piper, Centre for Lasers and Applications, Macquarie University, NSW Australia

M.R.H.Knowles, H.Booth, G.Rutterford, A.J.Bell, A.J.Andrews, G.Foster-Turner, and A.J.Kearsley at Oxford Lasers Ltd.

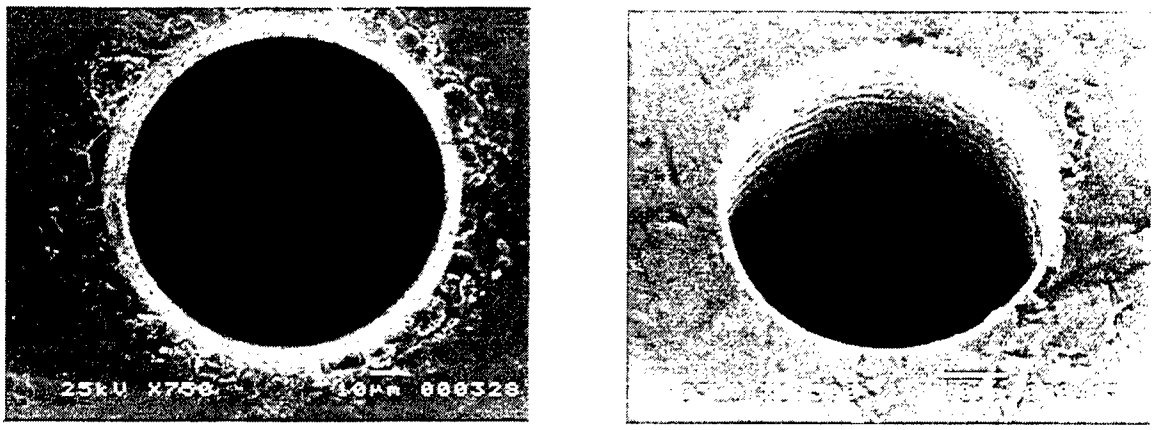

Figure 5. A 50μm diameter hole drilled in 100μm thick stainless steel. Left hand view- laser entry side. Right hand view - laser exit side. The hole is shown in its "as-drilled" condition, no post-drilling clean-up has been applied. Note absence of dross, good internal finish and sharpness of edge.

## REFERENCES


1. G.R Fowles and W.T Silfvast, "High-gain transition in lead vapor," *Appl. Phys. Lett,* **6,** pp.236-237,1965.
2. W.T Walter, M. Piltch, N. Solimene and G. Gould, "Pulsed laser action in atomic copper vapor," *Bull. Am. Phys. Soc,*.**11**, p.113, 1966.
3. A.A Isaev, M.A Karayan and G.G Petrash, "Effective pulsed copper-vapor laser with high average generation power," *JETP Lett,* **16**, pp.27-29, 1972.
4. I. Smilansky, A. Kerman, L.A Levin and G. Erez, "Scaling of discharge heated copper vapour laser," *Opt. Commun.* **25**, pp.79-82, 1978.
5. B.E Warner, "Status of copper vapor laser technology at Lawrence Livermore National Laboratory," *Paper CFH4 in CLEO 1991 Tech Digest*, pp.516-518, 1991.
6. G.P Hogan and C.E Webb, "Time- and spatially-resolved electron density measurements in an operating copper vapour laser," *Meas. Sci. Technol.* **8**, pp.1095-1104, 1997.
7. C.S Liu, E.W Sukov and L.A Weaver, "Copper super-radiant emission from pulsed discharges in copper iodide vapor,"*Appl. Phys. Lett.* **23**, pp.92-93, 1973.
8. C.J Chen, N.M Nerheim and G. Russell, "Double-discharge copper vapor laser with copper chloride as lasant," *Appl. Phys. Lett.* **23**, pp.514-515, 1973.
9. N.V Sabotinov, "Copper Bromide lasers," pp.113-124 in *Pulsed Metal Vapour Lasers*, C.E Little and N.V Sabotinov (eds), Kluver Academic Publishers, NATO ASI Series, 1996.
10. E.S Livingstone, D.R Jones, A. Maitland and C.E Little, "Charactersitics of a copper bromide laser with flowing Ne-HBr buffer gas,"*Opt.Quantum Electron.* **24**, pp.73-83, 1992.
11. C.E Webb and G.P Hogan, "Copper laser kinetics – a comparative study," pp.29-42 in *Pulsed Metal Vapour Lasers*, C.E Little and N.V Sabotinov (eds), Kluver Academic Publishers, NATO ASI Series, 1996.
12. E. Le Guyadec, P. Coutance, G. Bertrand and C. Peltier, "A 280W average power Cu-Ne-HBr laser amplifier," *IEEE Jour. Quantum. Electron.* **35**, pp.1616-1621, 1999.
13. D. Kapitan, "Laser ablation with copper vapour lasers," *D.Phil.Thesis*, University of Oxford, 1999.
14. C. Momma, B.N.Chichkov, S.Nolte, F.von Afvensleben, A.Tünnermann, H. Welling and B.Wellegehausen, "Short pulse laser ablation of solid targets," *Opt. Commun.* **129**, pp.134-142, 1996.
15. P.B Corkum, F Brunel, N.K Sherman and T Srinivasan-Rao, "Thermal response of metals to ultra-short laser excitation,"*Phys. Rev. Lett,* **25**, pp.2886-2889, 1988.
16. D.W Coutts, "Optimisation of line-focusing geometry for efficient nonlinear frequency conversion from copper vapour lasers,"*IEEE Jour. Quantum Electron.* **31**, pp.2208-2214, 1995.
17. M.J Withford, D.J.W Brown, R.J Carman and J.A Piper, "Enhanced performance of elemental copper-vapour lasers by use of $H_2$-HCl-Ne buffer gas mixtures," *Opt. Lett.* **23**, pp.706-708, 1998.

# Time Resolved H atom Density Measurements in a Cu HyBrID Laser

R.P. Mildren, R.J. Carman and J.A. Piper

Centre for Lasers and Applications, Department of Physics
Macquarie University, NSW 2109, Australia

## ABSTRACT

We are presently developing nonlinear spectroscopic techniques for measuring the spatio-temporal density behaviour of H and halogen atoms species to investigate the action of these species in halogen enhanced copper lasers. In this paper, we report time resolved measurements of ground-state H atom density in a Cu HyBrID laser obtained using two-photon allowed laser induced fluorescence. Ultraviolet probe radiation (205nm) was focussed through an end window to excite the n=3 level and the resultant Balmer fluorescence detected via a side window. The results indicate that the H atom density is depleted to less than half its prepulse value during the excitation pulse and then recovers almost fully during the first 20 microseconds of the interpulse period. By interrupting the discharge, we also have used the technique to investigate the H reassociation rate at the tube wall. The results suggest the technique, which may also be adapted to obtain halogen densities and gas temperature measurements, is a promising diagnostic for investigating halogen enhanced Cu laser vapor plasmas.

Keywords: copper vapour laser, discharge, kinetics, H atom, density measurements, two photon, laser induced fluorescence

## 1. INTRODUCTION

The presence of halogen and hydrogen additives in copper laser discharges is well known for bringing about major increases in the total power, pulse rate and particularly their high beam quality output. The kinetics of these 'halogen enhanced' devices (including the kinetically enhanced copper vapor laser, the Cu HyBrID laser and the CuBr laser with $H_2$ additive) are much more complex than the pure buffer gas systems owing to the increased number of plasma species, and the plasma processes which output performance are not well understood. Though experimental measurements of the spatio-temporal evolution of Cu species[1-3] and electron densities[2] have been performed to date, the key reactants such as H and X species (where X is Cl or Br) have not been measured. Such data is important for investigating the action of these species in the plasma directly and via computer modeling.

In this paper, we investigate the potential of the two-photon allowed laser induced fluorescence (TALIF) technique for measuring the density of ground-state atomic H in a Cu HyBrID laser discharge. H is expected to play an important role in the dissociative attachment reaction ($HX + e^- \Rightarrow X^- + H$) and also H is an effective electron cooler and third body reactant on account of its low mass. The TALIF technique relies on two photon absorption at 205.14nm to excite the n=3 level from the ground-state which subsequently decays by the fluorescence of $H_\alpha$ radiation. This technique has been previously used for measuring the H density in etching plasmas[4], rf discharges[5], arcs[6] and flames[7]. The fact that it is a nonlinear process (signal $\propto$ [probe intensity]$^2$) is a particular advantage in the present application since the quadratic dependence of the signal can be utilized to avoid the effects of populations in the cooler end-zones which are uncharacteristic of the active medium. This affects linear line-of-sight measurements, however, using a focussed probe beam in the TALIF scheme density information can be gained from a selected longitudinal location in the discharge.

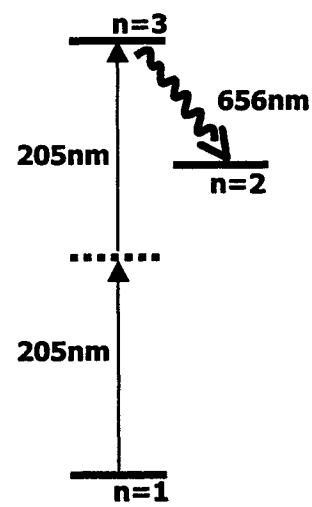


**Figure 1 Energy level diagram showing the pump and fluorescence transitions used in the TALIF scheme.**

XIII International Symposium on Gas Flow and Chemical Lasers and High-Power Laser Conference,
Antonio Lapucci, Marco Ciofini, Editors, Proceedings of SPIE Vol. 4184 (2001)

## 2. EXPERIMENT

The 205nm probe radiation was generated by frequency tripling the 615nm output of Lumonics HyperDye dye laser in a pair of BBO crystals (refer Figure 2). The output pulses, which were up to 0.4mJ in energy, ~10ns in duration and at 10Hz pulse repetition frequency, were focussed into the test medium using a plano-convex $CaF_2$ lens. The focal position was approximately 200mm from the anode and on the tube axis. The relative probe energy was monitored by measuring the energy of the back reflected beam from the flat face of the focussing lens with a photodiode. The fluorescence signal was collected at right angles to the probe beam and passed though a narrow bandpass filter and onto the photomultiplier detector. To minimise the background signal due to the discharge itself, the fluorescence was first spatially filtered by imaging the waist through a slit. The probe pulse and the fluorescence intensities were recorded on a digital oscilloscope.

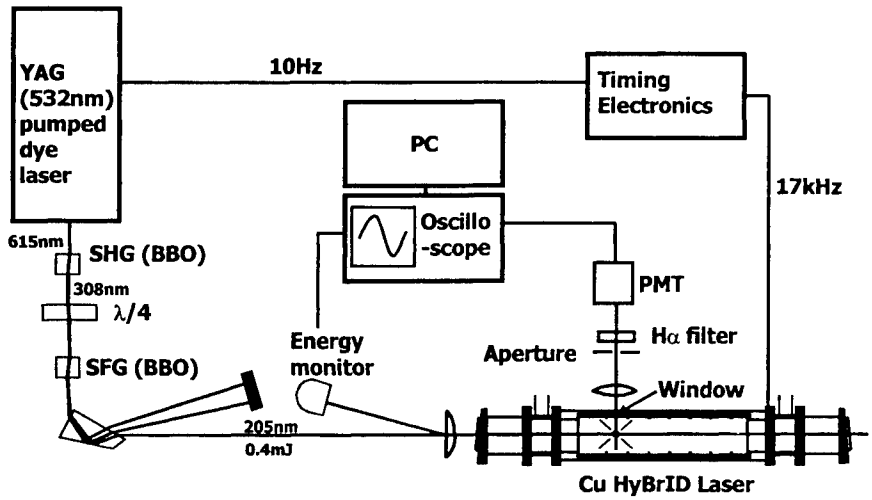


**Figure 2 Schematic of the experimental set-up used to detect ground-state H atoms.**

Preliminary tests were performed on a low pressure cell in which $H_2$ at low pressure (<10 torr) was dissociated using a microwave discharge. The plasma was displaced from the probed region to enable the alignment of the focal spot with the light collection optics to be optimized more easily in an environment with low $H_\alpha$ background. As shown in Figure 3, it was found that the lens focal length was a critical parameter influencing the level and the saturation characteristics of the signal. For short focal lengths (<100mm), the signal level increased quadratically with probe intensity for pulse energies <0.1mJ but signal saturation was noted at the higher intensities. Saturation was also observed by others[eg. 6], and is attributed to the photoionization of H. To avoid this saturation, a longer focal length lens was used ($f$=550mm); this provided adequate signal strength, however, note that the longer focal length also introduced more scatter in the signal.

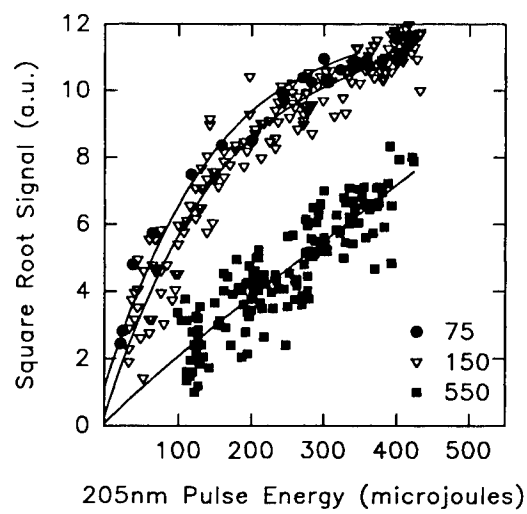


**Figure 3 Dependence of the square root of the TALIF signal on probe pulse energy for several lenses of different focal lengths (75, 150 & 550mm).**

Measurements were performed on a Cu HyBrID laser tube (in preference to the kinetically enhanced copper vapour lasers in our laboratory) as its lower operating temperature enabled the tube to be easily adapted to access the fluorescence signal from a side window. The HyBrID laser, which has been described in detail previously[8], was a 20W device operating at 17kHz pulse rate. A slot 3 × 20mm long was cut into the alumina discharge tube at the position adjacent the probe focus and a silica window inserted into the slot. In principle, it is possible to monitor the fluorescence exiting through the end windows, however, the sidelight configuration was chosen to maximize the ratio of the TALIF signal to the background plasma emission.

## 3. RESULTS

As shown in Figure 4, the TALIF signal appears on a significant background of $H_\alpha$ emission from the plasma, particularly in the early afterglow (ie. <2μs). For these early times, the TALIF signal (<5mV) is a small fraction of the background (>50mV) and thus the density cannot be accurately determined in this period. Due to the scatter in the TALIF signal, it was

necessary to average over many acquisitions. At the same time, it was important to minimise the measurement duration as there was signficant drift in the ambient H density. As a compromise, the TALIF signal was averaged over 60 acquisitions which measnt that each run of about 30 data points could be achieved within several minutes. Though some slight drift in the ambient H density was still observed, it was removed from the data by recording the prepulse value prior to each data point and then normalising each point to this value.

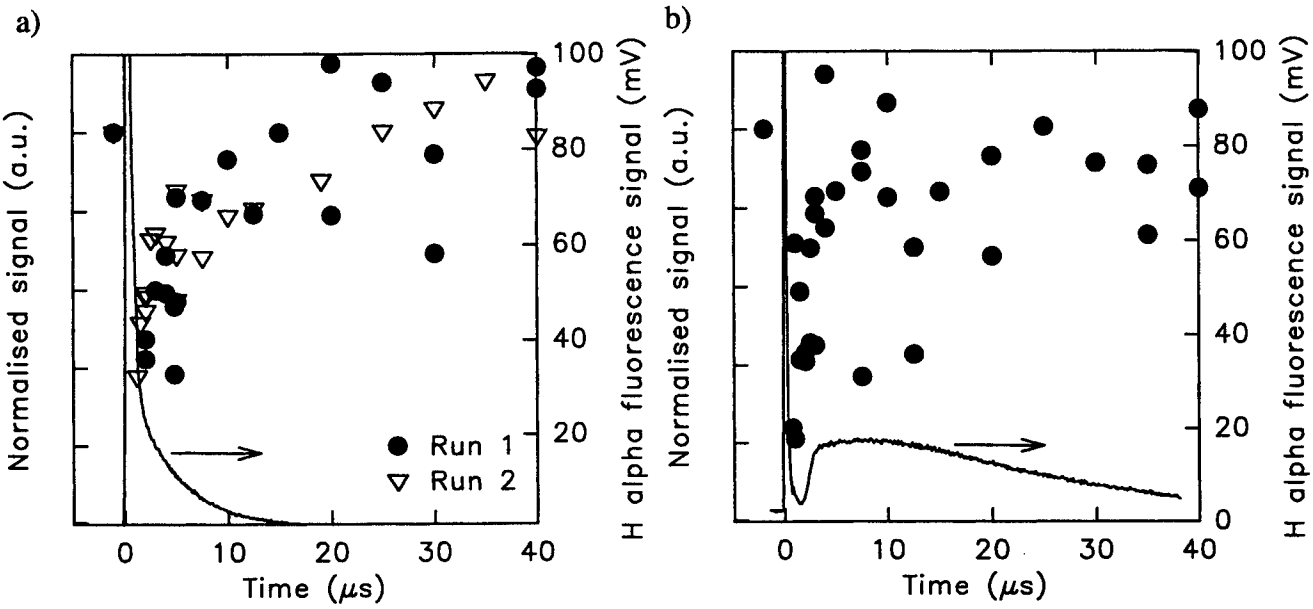


**Figure 4 The time dependence of the TALIF signal during the interpulse period for a) a discharge in Ne with H present as an impurity and b) for normal Cu HyBrID lasing conditions (ie. with 2-5% HBr additive). The time behavior of the background plasma induced emission $H_\alpha$ is also shown (solid curve).**

The temporal density behaviour was obtained for laser operation with HBr additive corresponding to near maximum output power, and for comparison for the laser operating with Ne buffer-gas only (ie. with H present as an impurity). The sources of scatter and proposed methods for improving the signal-to-noise are discussed in the next section. The results show that H atom density decreases markedly during the excitation phase (to <40% of the prepulse value) for both buffer gas conditions. Initial indications suggest that recovery occurs more quickly during the interpulse period for the discharge in Ne buffer gas (during the first 5-10μs) than for the Ne-HBr HyBrID discharge (10-20μs).

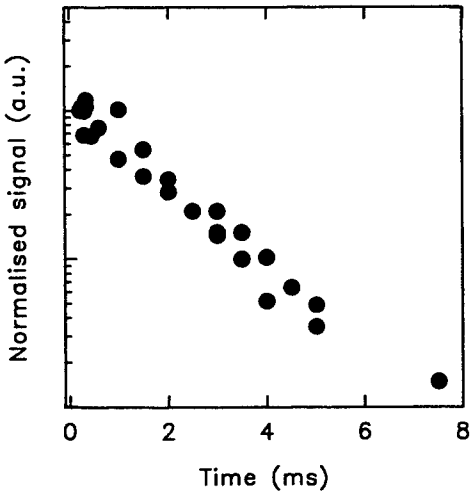


**Figure 5 The decay of H density upon interrupting the discharge.**

The H density evolution was also observed when interrupting the discharge to investigate the rate at which H atoms reassociate by non-discharge processes. Using the timing electronics, the discharge was interrupted for 8ms in phase with the 10Hz clock of the probe laser, and the probe delay scanned through this period. As shown in Figure 5, the decay is single exponential with time constant ~3ms. The single exponential suggests that a single process dominates the decay. Moreover, the time constant is much larger than that for radial diffusion to the tube wall (~100μs), which suggests that the coefficient for H reassociation at the wall is significantly less than unity.

## 4. DISCUSSION

The results of this study suggest that the TALIF technique is suitable for measuring the range of H atom densities in a Cu HyBrID laser discharge. Since other Cu lasers which use hydrogen as performance enhancing additive contain similar partial pressures of H species, it is expected that the technique is also applicable to these devices. The position of the measurement

is determined by the location of the probe focus and therefore the technique can also be extended to resolve radial and longitudinal H density information. Note that the density of halogen atoms may also be measured using a similar TALIF scheme[9].

We plan to perform a more detailed study of the spatio-temporal behaviour, however, it is important to first improve the measurement uncertainty present in the current experiment. Though the fluctuations in the integrated energy of the probe pulses were compensated for, the instantaneous intensity intensity at the focal point is expected to be sensitive to the details of spatio-temporal modulations in the probe pulse. The signal scatter is thus likely to be significantly improved with increased control of the spatial and temporal jitter in the probe beam amplitiude.

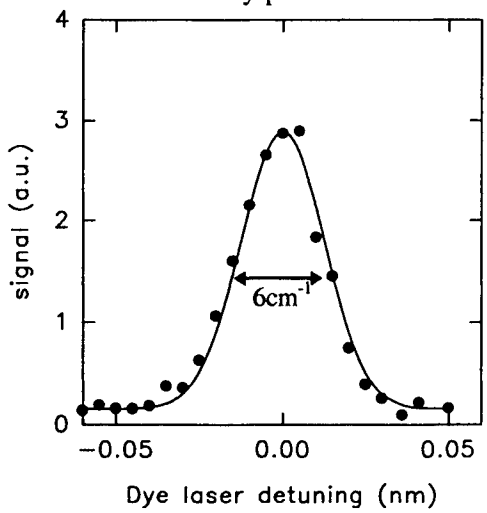


**Figure 6 TALIF signal as a function of probe laser detuning with Gaussian fit at the time just prior to the excitation pulse.**

Finally, it is interesting to note that the technique may also provide a useful method for obtaining gas temperature measurements[10]. Assuming that the Lyman β transition is predominantly Doppler broadened, then the TALIF signal dependence on probe wavelength reflects the velocity distribution of the H atoms in the focal region of the probe. This technique for determining the gas temperature avoids perturbations arising from the component of signal originating from the end-zones which may affect the previous linear methods of measurement (eg. by monitoring Balmer emission broadening). For the present system, the TALIF signal dependence on the probe wavelength (as shown in Figure 6) is consistent with the convolution of the measured probe bandwidth and the expected Doppler profile. The bandwidth of the dye laser, which was measured using a monitoring etalon, was 0.5cm$^{-1}$ corresponding to an effective bandwidth of the probe of 3cm$^{-1}$ (6 photons at 615nm are necessary to excite the two-photon transitions), and the Doppler width is also ~3cm$^{-1}$ for the estimated gas temperature of 2000K. By narrowing the probe bandwidth to a smaller fraction of the Doppler width (using an intracavity etalon for example), an accurate measurement technique for spatio-temporal resolved gas temperatures may be realised.

## REFERENCES


[1] R.P. Mildren, M.J. Withford, D.J.W. Brown, R.J. Carman and J.A. Piper, "Afterglow ground-state copper density behaviour in kinetically-enhanced copper vapour lasers", *IEEE J. Quantum Electron.* **34**, pp. 2275-2278, 1998.

[2] G.P. Hogan, C.E. Webb, C.G. Whyte and C.E. Little, "Experimental studies of CVL kinetics" in *Pulsed Metal Vapour Lasers,-Physics and Emerging Application in Industry, Medicine and Science*, (eds C.E. Little and N.V. Sabotinov) Kluwer Academic Publishers: Dordrecht, pp. 67-72, 1996.

[3] D.N. Astadjov, N.K. Vuchkov, G.G. Petrash, and N.V. Sabotinov, "Parametric study of the CuBr laser with hydrogen additives," *IEEE J. Quantum Electron.* **24**, pp. 1927-1935, 1988.

[4] P. Bletzinger and B.N. Ganguly, "High fractional dissociation efficiency in $H_2$ and $H_2$-$N_2$ gas mixtures in a helical resonator discharge", *Chem. Phys. Lett.* **247**, pp. 584-588, 1995.

[5] B.L. Preppernau, D.A. Dolson, R.A. Grottscho, and T.A. Miller, *Plasma Chem. Plasma Proc.* **9**, pp. 157-64, 1989.

[6] S.C. Snyder, A.B. Murphy, D.L. Hofeldt, and L.D. Reynolds, "Diffusion of atomic hydrogen in an atmospheric-pressure free-burning arc discharge," *Phys. Rev. E*, **52**, pp. 2999-3009, 1995.

[7] J.E.M. Goldsmith, "Photochemical effects in 205-nm, two-photon-excited fluorescence detection of atomic hydrogen", *Opt. Lett.* **11**, pp. 416-8, 1986.

[8] R.P. Mildren, "The role of buffer gas flow in Cu HyBrID lasers", *IEEE J. Quantum Electron.* **36**, pp. 1145-1150, 2000.

[9] G.S. Selwyn, L.D. Baston, and H.H. Sawin, "Detection of Cl and chlorine-containing negative ions in rf plasmas by two-photon lsaer-induced fluorescence", *Appl. Phys. Lett.* **51**, pp. 898-900, 1987.

[10] J.R. Dunlop, A.D. Tserepi, B.L. Preppernau, T.M. Cerny and T.A. Miller, "H atom plasma diagnostics: a sensitive probe of temperature and purity," *Plasma Chem. Plasma Proc.* **12**, pp. 89-101, 1992.

# High Power Copper Vapour Lasers driven by Solid State Power Supplies

E. Le Guyadec [a*], D. Chatroux [a], L. Garnier [b], F. Fourreau [c]
[a] CEA Valrhô DCC/DTE/SLC/LETC, BP 111, 26702 Pierrelatte cedex (France).
[*a] Tel/fax : 33 4 75504000 / 33 4 75504962, Email : erick.leguyadec@cea.fr
[b] ENERTRONIC, ZI Tharabie, rue du Ruisseau, 38290 S[t] Quentin Fallavier (France).
Tel : 33 4 74952946.
[c] CILAS, 8 Av. Buffon, La Source 45000 Orléans (France) Tel: 33 2 38641555.

## ABSTRACT

For 8 years, Copper Vapour Lasers (CVLs) driven by solid state power supplies have been experimented and used in French SILVA program development in co-operation with industrial partners. We present high performances and reliability obtained and applications to other laser systems.

**Keywords:** Copper Vapour Laser, all Solid State power supply, performance, reliability.

## 1. INTRODUCTION

The shape of repetitively pulsed electrical signals that excite CVLs is of first importance. It gives the suitable electron temperature and density that mainly control the dynamics of the copper excited state population and hence the optical gain. Depending of the Copper Laser size and nature, here are the main electrical parameters to be delivered by the power supplies: A voltage level on the laser head from 25 to 100 kilovolts, a repetition rate from 5 to 25 kHz and a average commuted power between 10 and 50 kW.
These parameters are now obtainable by power supplies using all solid state components such as IGBTs or MOSFETs in exchange of gas tubes like thyratrons.

## 2. SOLID STATE POWER SUPPLIES

Our experience in thyratron use for CVL's give us an operational life of the order of 1000 H or $1^{1/2}$month of continuous work. Their exchange induces a loss of time and money . The designed goal was to develop high power switches made from standard silicon components with the same or better technical characteristics but a far better reliability in the range of 20000 hours and a cost equivalent to the thyratron based device. An analysis of the technical and economical parameters has led us to study two solutions depending on a choice criterion relative to the switched energy per pulse.

### 2.1. High energies.

For switched energies of the order of 10 J, we have developed switching units based on a line of Isolated Gate Bipolar transistors (IGBTs). For example we use in parallel 32 IGBTs rated at 800 V to commute 10 J in few microseconds. They are followed by voltage transformers and magnetic switches in order to produce 100 kV – 5000 A pulses of 50 ns width at 5 kHz. These supplies are one of the basis of the ICL 400-500 , a 500 W optical rated CVL amplifier, manufactured by CILAS.

### 2.2. Low energies.

For power supplies with a switched energy up to 2 J, the preferred technology is an arrangement in arrays of power MOSFET transistors to sustain the voltage and pass the current with low losses. The basic structure is an array of 350 very standard MOSFETs ( see figure 1) which is able to switch 5 kV in 20 ns with a 800 A current pulse.

XIII International Symposium on Gas Flow and Chemical Lasers and High-Power Laser Conference,
Antonio Lapucci, Marco Ciofini, Editors, Proceedings of SPIE Vol. 4184 (2001)

**Figure 1**

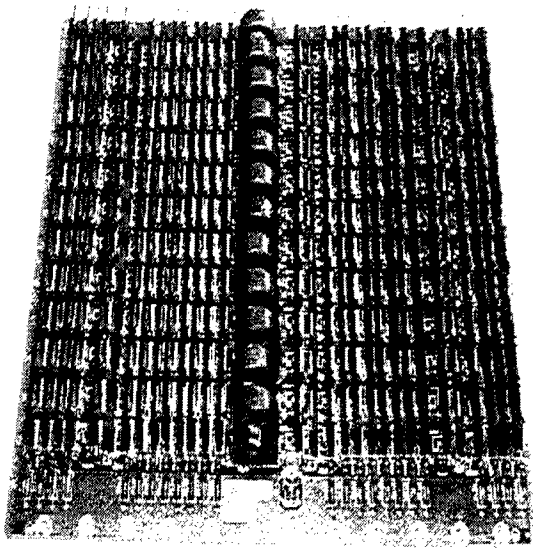

**The basic MOSFET array 5kV - 800A**

**Figure 2**

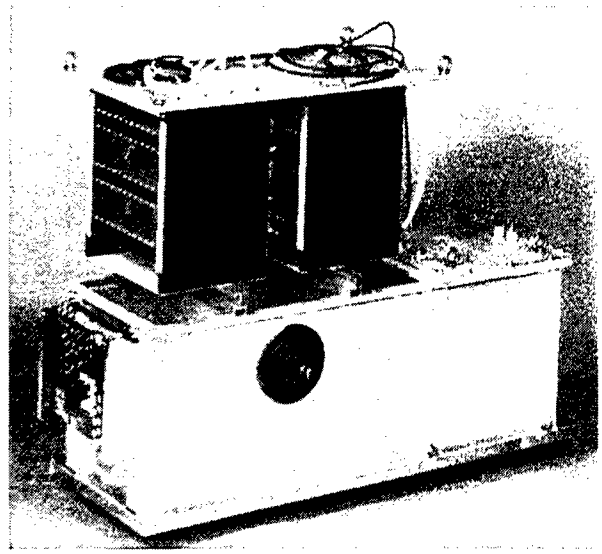

**The MOSFET based power supply, 25 kV – 1600**

These planar cards are easily connected with a low inductance and the standard switching unit comprises 10 cards. It is able to switch in 20 ns 25 kV with 1600 A pulses at repetition rates between 5 and more than 25 kHz (see figure 2) and a pulse to pulse jitter lower than 1 ns. These integrated power supplies are manufactured now by ENERTRONIC i.e. for the exchange of gas tubes in our CVLs.

**2.3. Reliability of MOSFETs Switches.**

The array adopted architecture which is tolerant to the failure of up to 8 MOS in different lines and the inherent reliability qualities due to the margins taken on the voltage and current specifications of MOSFETs (10 to 20 % beyond the nominal) render the switching unit particularly reliable.

Its failure rate $\lambda$ which is the inverse of the MTBF can be described by the following formula:

$$\lambda^{-1}(H) = \frac{3 \cdot 10^{8}}{z} \cdot \sum_{i=n-x}^{n} \frac{\exp - \frac{1.7 \cdot V}{i \cdot V_{max}}}{i}$$

with: z = the number of components in parallel = 54
n = the number of components in series = 65
x = the number of admitted defects = 8
V = the total applied voltage = 25000 V
$V_{max}$ = the max voltage on one MOSFET = 500 V

A numerical application for this formula gives a $\lambda < 10^{-5}$ (or a MTBF > 100,000 H). Effectively, we have accumulated more than 150,000 H without failure on these switches with 25,000 H (3 years) from one. Tests on MOSFETs cards could be included. They would permit to settle a preventive repair strategy that would further lower the failure rate.

## 3. RESULTS OBTAINED ON CVL's.

-With the IGBTs switched power supplies, more than 500 W [1] (on CVL lines at 510 and 578 nm) have been demonstrated by CILAS in an amplifier configuration and > 400 W in oscillator during long term

trials. The laser heads 'ICL 400-500' are 3 m long with a internal diameter of 80 mm , heated at ~ 1500°C by the 5 kHz discharge and the amplifying medium is a mixture of neon + 1% $H_2$ and vaporised copper ( figure 3 ).

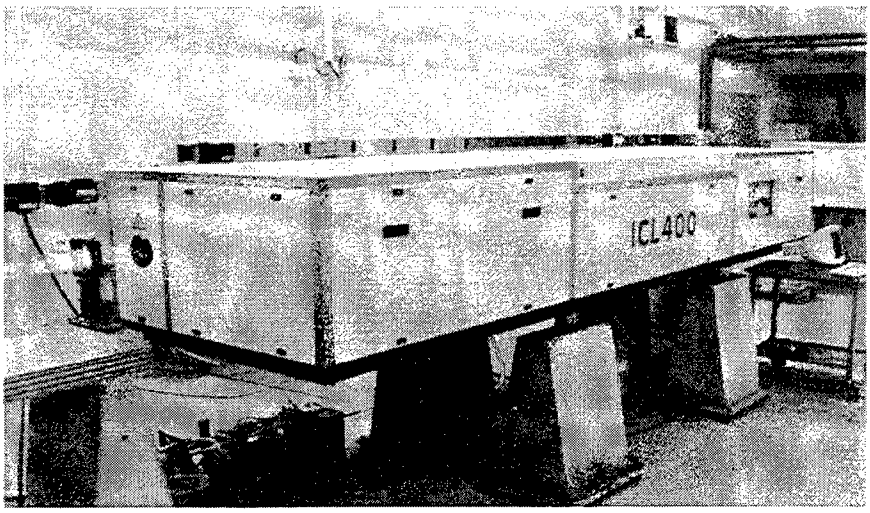


**Figure 3 : The ICL 400-500 laser.**

-With a standard 10 kW class MOSFET switched power supply, we obtain up to 110 W of optical power at a repetition rate of 5 kHz on CILAS 'MNT 100' laser heads[2] (Length = 3 m, dia. 50 mm). The gas mixture is vaporised copper (1500°C) and neon + 1% $H_2$.
We have paid a great attention on the power decrease due to the migration of copper in the tube. It has been extensively studied on this laser and lowered to the level of 0.02 W/H (Fig. 4), allowing a continuous use up to 1000 hours.

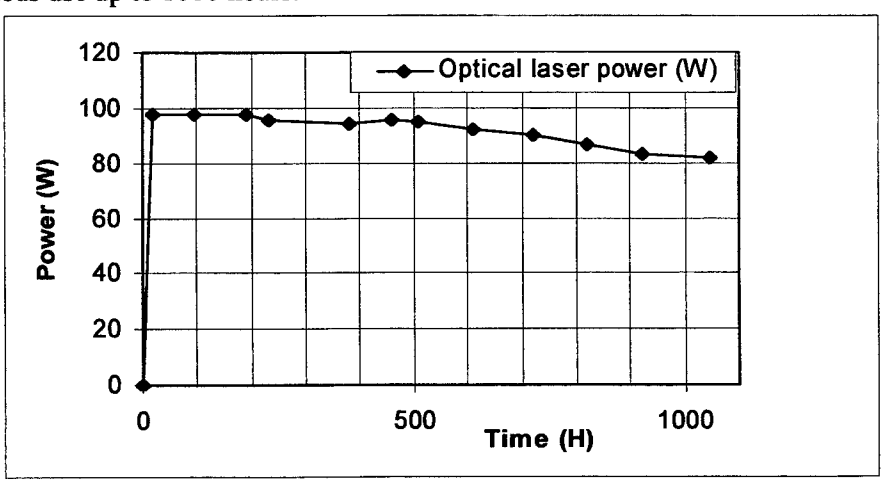


**Fig. 4 : Evolution of laser power with time with an MNT 100 oscillator.**

-With a special 50 kW class MOSFET driven power supply[3] we have obtained 280 W of optical power from a cold (650°C) laser head at 17 kHz from a Ne + 4.7% HBr gas mixture injected in the laser tube (dimensions: L = 3 m, dia. 80-108 mm, 19.5 litters of active volume). The deposited power in the head was 7.3 kW, leading to a head efficiency of 3.8% which is twice the best value we obtain on high temperature elemental CVL's. This progress is due to the very good shape of the excitation electrical pulses (Fig. 5) and to the 'HBr effect' which allow a high copper density on the axis but a low prepulse electron density. This last parameter is induced by the fast electrical charge recombination following the copper ionization by the discharge and is the result of the HBr dissociative attachment process and the associated reactions[4].

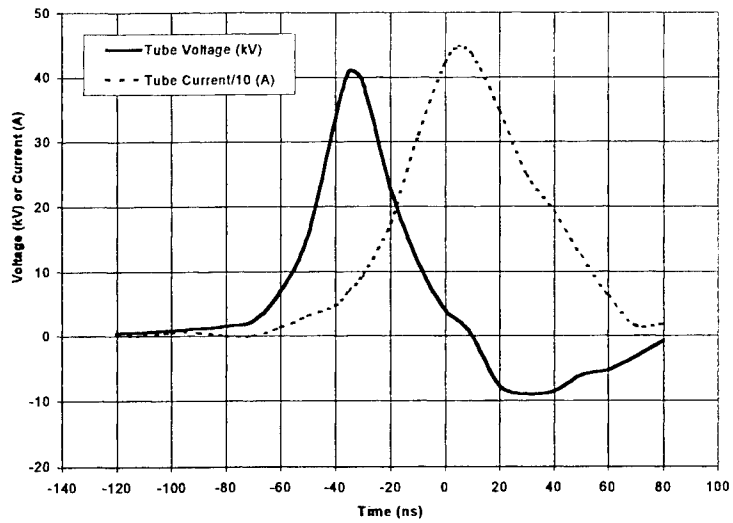


**Fig. 5 : Electrical signals on the laser head.**

| | |
|---|---|
| Cu + e- (fast) → Cu+ | (1: Copper ionization) |
| HBr + e- (slow) → H + Br- | (2: Dissociative Attachment) |
| Br- + Cu+ → Cu + Br | (3: Charge neutralization) |
| Br +H → HBr | (4: HBr reformation) |

From the same power supply we have also obtained 125 W from a hot (1500 °C) laser tube (L = 3 m, dia. = 50 mm) with a mixture of 0.5% $H_2$ + 1.5% HCl, neon and vaporised copper at 17 kHz with only 6.6 kW deposited in the laser head (1.9 % head efficiency).
At the same repetition rate and other operating conditions but without HCl, the optical power was negligible. For the same deposited power at 5 kHz, this head gives near 100 W of optical power, so we have obtained a 25% gain in power and efficiency with HCl.

## 4. CONCLUSION AND PERSPECTIVES

After the demonstration of the very good reliability of the developed CVL lasers, our goal is the reduction of their cost of ownership by pushing their MTBF until 10000 H and increasing the component integration.
The array architecture presented here for IGBTs and power MOSFETs can be extended to other components such as thyristors, fast MOSFETs and diodes. We are now testing systems for the switching of high energies (200 J ) at low repetition rate or the very fast (1 ns) power MOSFET commutation for applications in electro-optics.
Other applications where pulsed power is needed by optical systems, are in the scope of this technology:

-Supplies for high repetition rate excimer lasers (500 –1000 Hz) with the possibility of a better pulse stabilisation and the disappearance of the warm-up dead time.

-Supplies for soft X and Extreme UV lamps and lasers. Pulses ranging from 5000 to 30000 A with a voltage from few to tens of kV are needed for these devices.

## REFERENCES

1. A. Rosengard et al., *Optique et photonique*, n°4 dec. 1999, pp. 37-40, 1999.
2. D. Chatroux et al., *Optique et photonique*, n°4 dec. 1999, pp. 29-32, 1999.
3. E. Le Guyadec et al., *IEEE J. of Quant. Elect.*,.Vol **35**, n°11, pp. 1616-1622, 1999.
4. F. Girard, Thesis, Univ. Paris XI - ORSAY, 10 dec. 1999.

# High pulse repetition frequency CuBr-laser

Gennadiy S. Evtushenko*[a], Gueorgii G. Petrash[b], Viktor B. Sukhanov[a], Dmitriy V. Shijanov[a], Valeriy F. Fedorov[a]

[a] Institute of Atmospheric Optics, Siberian Branch of Russian Academy of Sciences, Tomsk, Russia
[b]Lebedev Physical Institute, Russian Academy of Sciences, Moscow, Russia

## ABSTRACT

In the paper, we present new results of CuBr-laser study in a regular pulse mode with a high PRF and in a mode of modified double pumping pulses with PRF = 30 kHz. It has been shown a stable PRF over 500 kHz can be obtained.

**Keywords:** Metal vapor laser (MVL), pulse repetition frequency (PRF)

## INTRODUCTION

There is a strong need for metal-vapor lasers (MVL) with a high pulse repetition frequency (PRF) for some practical applications, including atmospheric optics [1,2]. Typical values of PRF for MVL are from several kHz to several tens kHz, while the lasers with PRF more than 100 kHz were reported in only a few of papers (see [3-5]). Due to lower operating temperatures required to provide necessary density of metal atoms, there is less danger to overheat the active media of a metal-halide laser compared with a pure MVL at high PRF. Therefore, study of metal-halide pulse-periodic lasers is of a special interest. Moreover, the relaxation times of population density of metastable atoms and pre-pulse electron density for CuBr-laser's discharge are lower than for Cu-laser and range from $10^{-5}$ – $10^{-6}$ s [4]. By the above reasons, PRF 100-1000 kHz can be expected. In our previous paper[6], we mentioned CuBr-laser with PRF 300 kHz and noticed that the laser has better frequency features compared with a Cu-laser.

## EXPERIMENTAL RESULTS

In this paper, we study high frequency possibilities of CuBr-laser using a model pumping mode. The active media of CuBr-laser is pumped by double pulses with variable time delay between them. Pairs of pulses are generated with the regular PRF of 10-30 kHz. Such pumping mode more closely simulates a mode of regular pulses than a simple method of double pulses. Experimentally we use a quartz gas-discharge tube (GDT) for a CuBr-laser with bore diameter (*d*) from 0.6 to 3.0 cm and length (*l*) - 20-80 cm (Fig.1). As a buffer gas, we use pure neon at the pressure of 30-100 torr and record

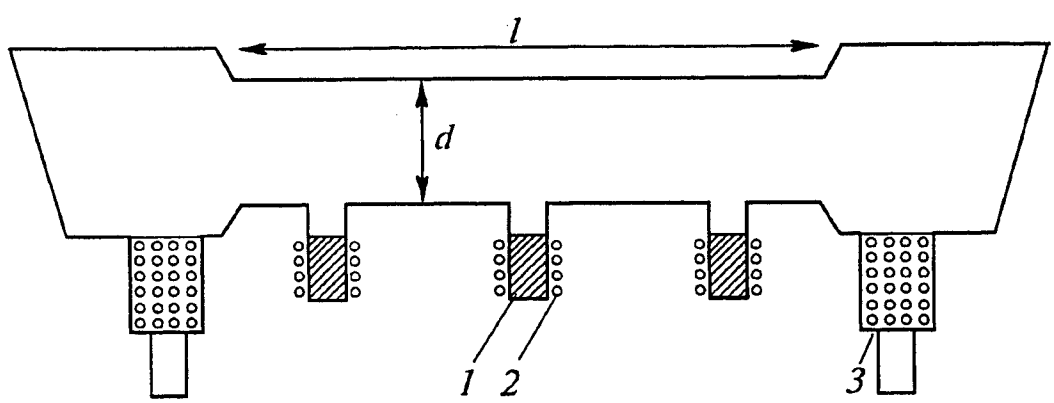


Fig. 1. Gas discharge tube. 1 – container with copper bromide; 2 – heater; 3 – electrode.

* Correspondence: E-mail: gel@asd.iao.tsc.ru; Phone: 3822 229989; Fax: 3822 259086

XIII International Symposium on Gas Flow and Chemical Lasers and High-Power Laser Conference,
Antonio Lapucci, Marco Ciofini, Editors, Proceedings of SPIE Vol. 4184 (2001)

current, voltage, and laser pulses as usual. The experimental setup is shown in Fig. 2. An active media is excited by double pulses with complete discharge of the storage capacitors $C_1$ and $C_2$ through the GDT and switches $T_1$ and $T_2$, respectively. A master oscillator allows to change time delay between pulses in the pair from 0.1 to 10 μs. At the first step, the laser is brought up to a stable lasing mode maintained by the first pulse. Then the second pulse is shifted with respect to the first one until second lasing pulse appears. Under these conditions, maximal PRF has been obtained for GDT with various diameters. The above circuit is also used for experiments in another pumping mode with regular pump pulses up to 50 kHz. Higher regular PRFs up to 300 kHz have been obtained using tasitron TGU 1-5/12 as a switch.

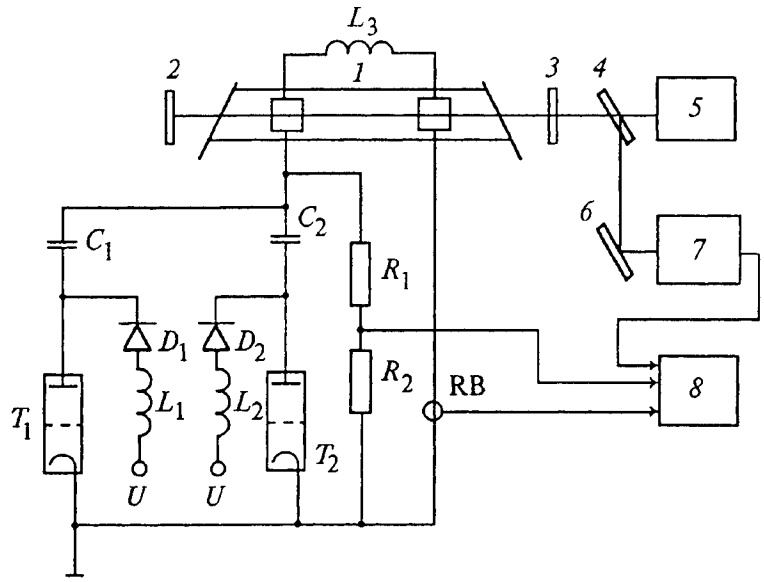


Fig. 2. Experimental setup: gas-discharge tube (*1*); mirrors of plane-parallel cavity (*2* and *3*); plane-parallel plates (*4* and *6*); IMO–2M calorimeter (*5*); FEK–19 coaxial photodiode (*7*); S1–122A oscilloscope (*8*); TGI 1–1000/25 thyratrons ($T_1$ and $T_2$); charging inductances and diodes $L_1 = L_2$, $D_1 = D_2$; by-pass inductance $L_3$; working capacitors $C_1$ and $C_2$; voltage divider $R_1$ and $R_2$; Rogowskii loop (RB).

Maximal values of model PRF and of PRF obtained in a regular pulsed mode[6] for several GDTs are shown in Fig.3 and Table 1.

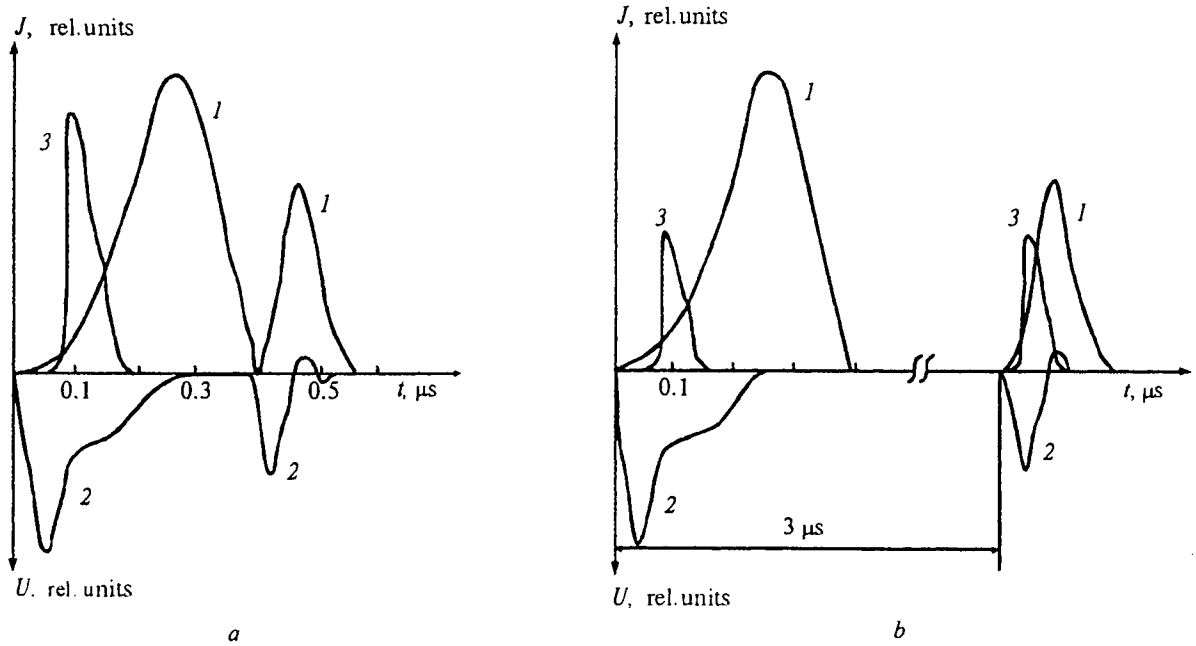


Fig. 3. Oscillograms of current (*1*), voltage (*2*), and lasing (*3*) pulses of a CuBr laser pumped by paired pulses. Gas-discharge tube was 1.6 cm in diameter and 40 cm in length, $p_{Ne}$ = 30 torr; repetition frequency of regular pulses was 10 kHz; time delay between the pulses in a pair τ = 0 (*a*) and 3 μs (*b*).

*Table 1*

| GDT $d$, cm and $l$, cm | | Model PFR, kHz | Regular PRF, kHz |
|---|---|---|---|
| 0.4 | 30 | 160 | |
| 0.6 | 20 | 160 | |
| 0.8 | 40 | | 270 |
| 1.0 | 35 | 200 | |
| 1.4 | 25 | | 300 |
| 1.6 | 40 | 333 | |

By direct inspection, one can assure maximal values of model PRF correlate well with those obtained in a regular pulsed mode.

Here we notice that a pumping source based on a thyratron does not allow to completely optimize parameters of excitation, dissociation, thermal conditions, etc. In particular, obtaining high PRFs requires to further shorten a pump pulse to the value close to lifetime of the population inversion. Using the vacuum lamp GMI-34 as a switch in a pumping circuit we succeed to shorten a pump pulse (at half of maximum) up to 40 ns. In this case, an operating capacitor partially discharges into the GDT. When lasing occurs in both pulses minimal time delay between two pulses is 1.5 μs in GDT with diameter 2.5 cm and length 80 cm at the 30 kHz PRF of pulse pairs (Fig. 4). The time delay corresponds to maximal PRF higher than 660 kHz.

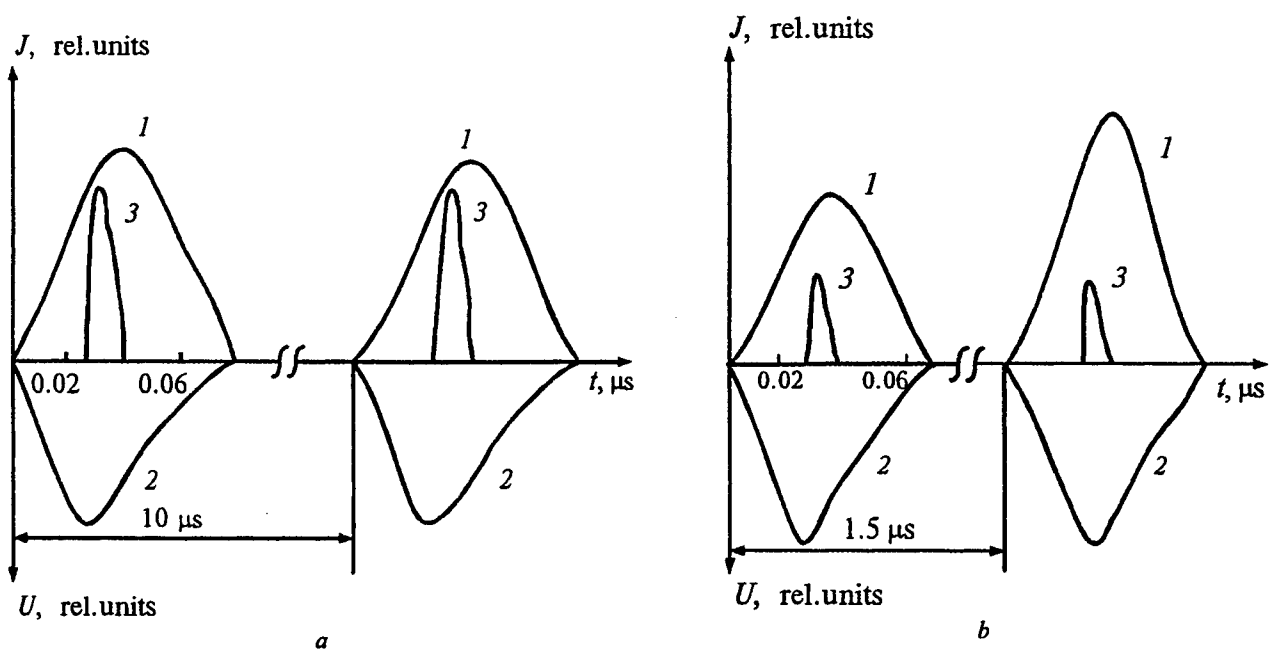


Fig. 4. Current (*1*), voltage (*2*), and lasing (*3*) pulses of a CuBr laser pumped via a modulator tube switch. Gas-discharge tube was 2.5 cm in diameter and 80 cm in length; $p_{Ne}$ = 30 torr; repetition frequency of regular pulses 30 kHz; time delay between the pulses in pair $\tau$ = 10 (*a*) and 1.5 μs (*b*).

In our opinion, higher maximal PRF can be expected for GDT with small diameter. Unfortunately, some technical problems associated with low input power didn't allow us to pump GDT with diameter smaller than 2.0 cm using GMI-34 vacuum lamp.

## CONCLUSION

In this paper, we discuss the experiments performed with CuBr-laser in a mode of modified double pumping pulses. The obtained results clearly show that regular PRF more than 500 kHz can be obtained for the laser.

## ACKNOWLEDGMENTS

The authors are thankful to Dr. Vladimir Klimkin for useful discussion. The work was partly supported by Russian Foundation for Basic Research (Grant No. 99-02-17016a).

## REFERENCES

1. G.S. Evtushenko, "Metal-Vapor Lasers for Atmospheric Optics", Izvestiya Vyssh. Uchebnykh Zavedenii, Fizika. **42**, pp. 89-96, 1999.
2. G.S. Evtushenko, V.M. Klimkin, "Metal-Vapor Lasers Application in Atmospheric Optics", Atmospheric and Ocean. Optics, **12**, pp. 840-848, 1999.
3. A.N. Soldatov, V.I. Solomonov, *Gas Discharge Lasers at Self-Terminating Transitions of Metal Vapors*, Nauka, Novosibirsk, 1985 (in Russian).
4. V.M. Batenin, V.V. Buchanov, M.A. Kazaryan, I.I. Klimovskii, and E.I. Molodykh, *Lasers at Self-Terminating Transitions of Metal Atoms*, Nauka, Moscow, 1998 (in Russian).
5. C.E. Little, *Metal Vapour Lasers. Physics, Engineering & Applications*, John Willey & Sons Ltd., Chichester, UK, 1998.
6. G.S. Evtushenko, G.G. Petrash, V.B. Sukhanov, and V.F. Fedorov . "CuBr laser with a pulse repetition rate up to 300 kHz", Quantum Electronics, **29**, pp. 775-777, 1999.

# A 50 - Watt copper bromide laser

Nikola V.Sabotinov*[a], Ivan K.Kostadinov[b], Hans W.Bergmann[c], Renzo Salimbeni[d], Jerzy Mizeraczyk[e]

[a]Institute of Solid State Physics, Blvd.Tzarigradsko Chaussee 72, 1784 Sofia, Bulgaria

[b]Pulssvet Co., Blvd.Tzarigradsko Chaussee 72, 1784 Sofia, Bulgaria

[c]Univ. of Bayreuth, Dept.Metallic Materials, Ludwig-Thoma-Str.36b, D-95440 Bayreuth, Germany

[d]Istituto di Eletronica Quantistica del CNR, Via Panciatichi 56/30, 50127 Firenze, Italy

[e]Institute of Fluid Flow Machinery, Polish Acad.of Sci., ul.J.Fiszera 14, 80 - 952 Gdansk, Poland

## ABSTRACT

A 50 W CuBr laser is reported. Characteristics of the major laser parameters are presented: output power, laser pulse repetition frequency, and laser beam quality. The laser has been designed for precision material processing in industry.

Keywords: MVL, CVL, CuBr Vapor Laser, Laser parameters

## 1.INTRODUCTION

In connection with the industrial precision materials processing there is a continuously growing interest in the high power lasers oscillating in the visible spectral region. At present, two types of lasers are competitive for applying in this area. In the last several years significant development has been achieved in the Nd:YAG lasers with diode pumping and second harmonic non-linear conversion. They oscillate in the green range at 532 nm wavelength. An output power of more than 100 W was obtained but the reliable commercial lasers operate at several 10s of Watts. The main problems with these lasers are related to the strength of the non-linear crystals, thermoeffects in the active region and achievement of high beam quality (BQ). Solid state laser systems of this type having high beam quality are very expensive which is an obstacle to their massive entering into industry.

Another powerful laser oscillating in the visible spectral region is the copper vapor laser (CVL). This laser with the use of unstable resonator provides high BQ reaching the diffraction limit and high average output powers of several 100s Watts. The main problem with this type of lasers is the high temperature of the active medium which leads to numerous problems in its industrial exploitation. This big problem of the CVL has been solved by its low temperature variant: the copper bromide laser CuBrVL [1].

CuBrVL has a temperature of the active medium by about 1000°C lower than the CVL [2]. The presence of bromide Br and hydrogen additives [3] enhances the laser performance. With the CuBrVL an output powers of > 100 W at the record high efficiency of 3.8% has been obtained [4]. The laser pulse duration under optimum conditions of oscillation is 2-3 times larger than in the CVL and the pulse repetition frequency PRF is 15-25 kHz. The laser radial distribution is close to the Gaussian and with the use of unstable resonator a BQ is achieved near the diffraction limit [5]. At present, the CuBrVL is a well developed laser that has begun to find successful employment in industry .[6,7]

In this paper a CuBrVL of an average output power of 50 W is described.

## 2.GENERAL DESCRIPTION OF CuBrVL

The 50 W CuBrVL is built in a common box including the laser tube, power supply unit and the necessary optics. The laser dimensions are 2500X400X320 mm$^3$, the total weight is 90 kg. The electrical power supply is from the electrical

*Correspondence: Email: n.sabotinov@main.issp.bas.bg; Telephone: +359 2 756 009; Fax: +359 2 756 009

XIII International Symposium on Gas Flow and Chemical Lasers and High-Power Laser Conference,
Antonio Lapucci, Marco Ciofini, Editors, Proceedings of SPIE Vol. 4184 (2001)

network, three phase, as the total consumed power is 4 kW. Water cooling is used for the power supply and the metal box in proximity to the laser tube.

## 2.1. The laser tube

The laser tube is given in Fig.1. It is made from quartz glass and has a diameter of 55 mm and a total length of 2 m. The active zone is between the two electrodes and has a length of 1.5 m and a diameter of 30 mm set by quartz diaphragms. The electrodes are made from porous copper with special reservoirs around them to capture Br and CuBr penetrating in them [2]. Along the tube length in the active zone there are reservoirs for CuBr. The cold zones of the tube between the electrodes and the quartz windows capture the worked off CuBr and the unnecessary free bromide.

The active zone with reservoirs is located in a metal envelope where the heaters are mounted (Fig.2). With their help on the basis of precise thermoregulation a stable steady temperature is maintained within ±1°C in the active zone. The optimum operating temperature is about 490°C. The laser tube is filled with neon having a partial pressure of about 20 Torr and hydrogen of 0.5 Torr. The described laser tube depending on the delivered input power may produce an output power of up to 72 W. This power can be maintained at a thyratron anode voltage of 16 kV, a pulsed current of 320 A, a capacity of 2 nF and a PRF of 17 kHz.

In Fig.3 is shown the laser output power as a function of the thyratron anode voltage.

The laser tubes operates in the sealed-off regime. The hydrogen pressure is maintained steady by means of a specially developed source of hydrogen. The construction developed for the laser tube permits to maintain a laser output of 50 W for 1000 h. In Fig.4 is shown the average laser output power as a function of the hydrogen pressure in the laser tube.

Fig.5 shows waveforms of the pulses of laser output, current and voltage at a laser output power of about 30 W during a 500 hour testing. These results show how stable the laser parameters are in time.

The optimum parameters for laser action at an output power of 50 W have been found to be as follows: neon pressure: 20 Torr, hydrogen pressure: 0.5 Torr, temperature of the reservoirs for CuBr: 490°C, voltage of the operating capacitor: 14 kV; capacity of the capacitor bank: 1.8 nF, pulse repetition frequency of the power supply: 18 kHz.

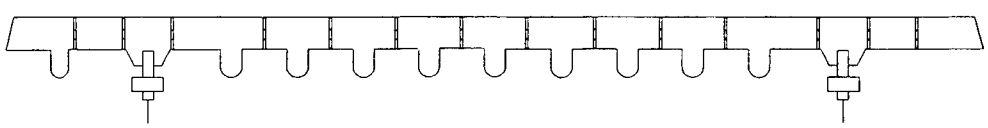

Fig. 1. Schematic diagram of the laser tube construction.

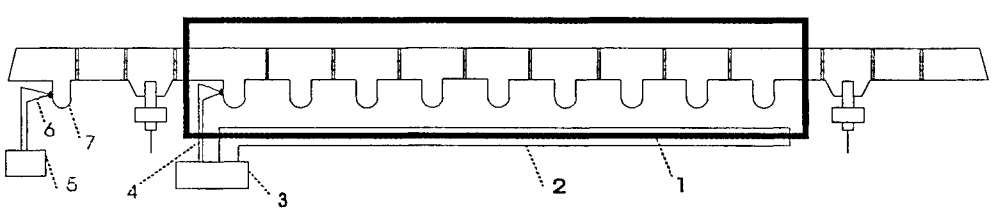


1- stainless steel enclosure
2- heaters
3- temperature controller
4- thermocouple
5- temperature controller
6- thermocouple
7- hydrogen generator

Fig. 2. Schematic diagram of the laser tube with its metal jacket.

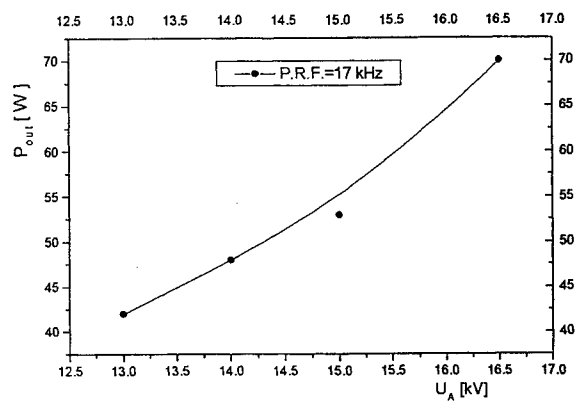


Fig. 3. Laser output power as a function of the thyratron anode voltage.

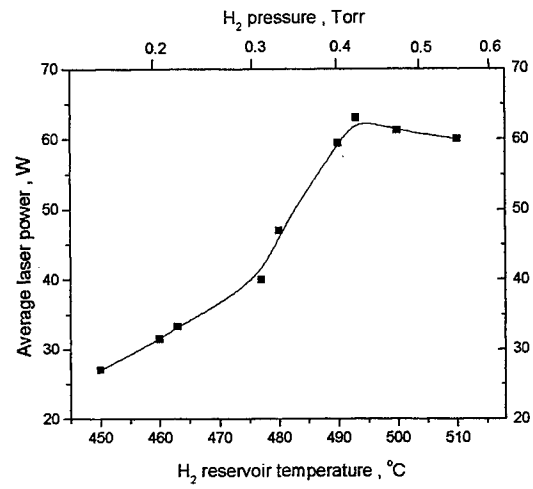


Fig. 4. Average laser output power as a function of the hydrogen pressure.

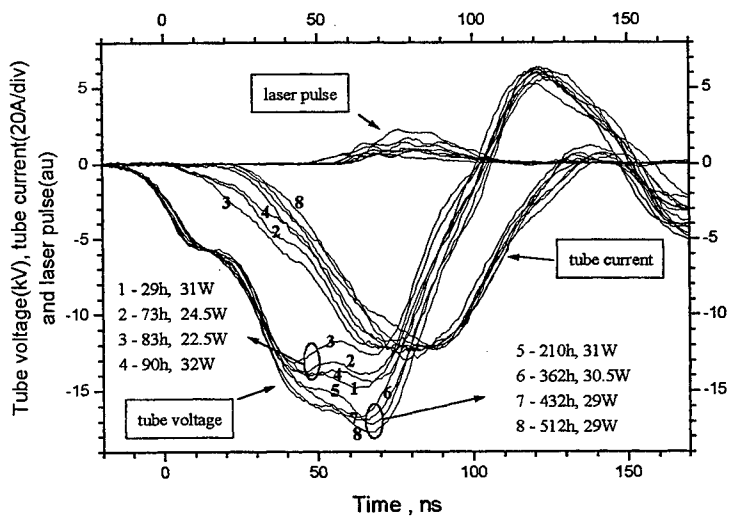


Fig. 5. Waveforms of the laser pulse, current and voltage at a laser output power of about 30 W during 500 hour testing.

## 2.2. Laser power supply

The power supply for the laser is a transistor pulse generator which does pulse charging of the capacitor bank of 1.8 nF to a voltage of 14 kV with a frequency of 17 kHz. High voltage pulses are formed on the tube of a thyratron EEV CX1835. The thyratron together with the pulse transformer of the inverter are cooled in a common oil tank. In the thyratron anode circuit there is a saturating inductor: magnetic assist. The simultaneous influence of the 4 factors described below makes exceptionally effective the power supply of the 50-W CuBr laser: 1) Comparatively low pulsed current of the discharge tube (no more than 200 A); 2) Delivery of high voltage pulses to the anode with a guaranteed pause of 30 microseconds for recovering the thyratron isolation after each pulse; 3) Use of a relevant magnetic assist with ~ 60 nanoseconds of hold-off time; 4) The use of a water-cooled oil-tank ensures an extremely long life time of the thyratron: ~ 3000 hours and more.

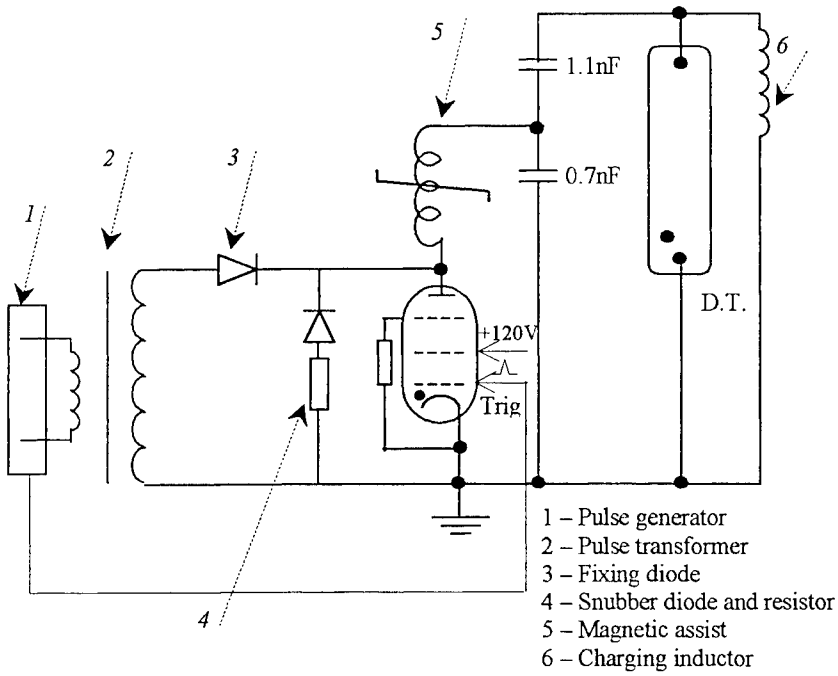


Fig. 6. Circuit diagram of the laser excitation set up.

## 3.CONCLUSIONS

The 50-W CuBr laser is a powerful source of visible laser light as produces the lines 510.6 and 578.2 nm with the intensity ratio 3:2. This laser has numerous advantages to the copper vapor laser (CVL) as a result of the low working temperatures. First of all, the CuBrVL has a fast start up time of 15-20 min., as well as high efficiencies 2-3 times exceeding those of the CVL. With reference to construction, the CuBrVL is considerably cheaper. The CuBrVL works in the sealed-off regime, the laser tubes are easily replaceable when needed. The CuBrVL can work in moving robotics systems at angles of up to 45° designed for industrial precision materials processing and high speed photography.

## ACKNOWLEDGEMENTS

This work has been funded by the scientific research project NATO SfP-972 685 (SfP- Copper Bromide Laser).

## REFERENCES

1. N.V.Sabotinov, P.K.Telbizov and S.D.Kalchev, Bulgarian patent No:28674, 1975.
2. N.V.Sabotinov, "Copper bromide lasers," Pulsed Metal Vapor Lasers–Physics and Emerging Applications in Industry, Medicine and Science, edited by C.E.Little and N.V.Sabotinov, 113-124 Kluwer Academic Publishers, 1996.
3. D.N.Astadjov, N.V.Sabotinov and N.K.Vuchkov, "Effect of hydrogen on CuBr laser power and efficiency," *Opt.Commun.* **vol.56(4)**, pp.279-282, 1985.
4. D.N.Astadjov, K.D.Dimitrov, D.R.Jones, V.Kirkov, C.E.Little, N.V.Sabotinov and N.K.Vuchkov, "Copper bromide laser of 120 W average output power," *IEEE J.Quantum Electron.* **QE-33(5)**, pp.705-709, 1997.
5. V.M.Stoilov, D.N.Astadjov, N.K.Vuchkov and N.V.sabotinov, "High spatial intensity diffraction-limited 10 W CuBr laser with hydrogen additives," *Optical and Quantum Electronics*, **v.32**, 2000.
6. Project "New generation lasers for high precision materials processing," No.CIPA-CT94-0214, Copernicus programme of the European Community, 1995-1998.
7. Project No. SfP-972 685 Copper Bromide Laser of NATO Science for Peace Programme, 1999-2002.

# Copper ion laser in He-CuBr, He-Cu and Ne-CuBr pulse longitudinal discharge

N. K. Vuchkov, K. A. Temelkov, N.V. Sabotinov, P. V. Zahariev, I. Kostadinov
Metal Vapor Lasers Laboratory
Institute of Solid State Physics, Bulgarian Academy of Sciences,
Tzarigradsko Chaussee 72, Sofia 1784, BULGARIA
e-mail: nvuchkov@issp.bas.bg

## ABSTRACT

In ns-pulsed longitudinal discharge-excited He-Cu and He-CuBr vapor ion lasers oscillation in the IR spectral range has been obtained. UV laser operation has been obtained only in Ne-CuBr vapor ion laser. An average output power of 210 mW has been measured on the laser line 248.6 nm and a 270 mW on multiline - 248.6, 252.9, 260.0 and 270.3 nm.

**Keyword:** metal vapor laser, copper bromine laser, UV copper ion laser.

## 1. INTRODUCTION

One of the main purposes in the metal vapor lasers development is the obtaining of a high-power and stable laser operation in the UV spectral range. Up till now UV laser oscillation has been successfully obtained in Ne-Cu (249 nm-270 nm) and He-Ag (224 nm-227 nm) [1-3] hollow cathode discharges, but it is a matter of serious difficulty to achieve continued and stable laser action in the hollow cathode laser system.

An opportunity for a metal vapor laser development is the investigation, started in [4] on the $Cu^+$ and $Ag^+$ laser oscillation in nanosecond pulse longitudinal Ne-CuBr, He-CuBr and He-AgI discharges.

In this paper a UV laser oscillation on four $Cu^+$ and four IR lines in Ne-CuBr and He-CuBr nanosecond pulsed longitudinal discharges, respectively is described. Laser action has been also obtained on seven $Cu^+$ transitions in the near IR spectral range, using a pulsed longitudinal He-Cu discharge as an active medium.

## 2. EXPERIMENTAL APPARATUS

The investigation has been carried out in three different laser tube constructions. In the first discharge tube T1 six quartz diaphragms were mounted along the tube with inside diameter of 26 mm, made of fused silica (similar discharge tube was used in [4]). The thin (1.5 mm) quartz diaphragms were with an aperture of 12 mm, which defined the active zone diameter. The distance between the electrodes was 80 cm. CuBr powder was placed in five quartz side-arm reservoirs, mounted symmetrically between the diaphragms and externally heated.

The active length of the second tube T2 was also 80 cm. In comparison with the first tube discharge confining quartz diaphragms were not used, and the inside diameter (12 mm) of the active zone was determined by the quartz tube itself. CuBr powder was placed in five quartz side-arm reservoirs, which were externally heated.

For the Cu vapor ion laser the active medium has been confined in a ceramic tube of sapphire with active length of 50 cm and i.d. of 12 mm. The ceramic tube was sleeved in a quartz tube with i.d. of 60 mm (T3). The space between ceramic and quartz tubes was filled by a fibrous insulation. Pieces of pure copper were spread along the floor of the ceramic tube. At each end of the ceramic tube porous copper electrodes were placed.

The investigated ion CuBr and Cu vapor lasers have been excited excitation scheme with interacting circuits (IC). The IC excitation of the CuBr lasers, operating on the self-terminating atom transitions, is described in details in [5].

Spectral investigation on the laser radiation and spontaneous emission has been made by Bentham M300 spectrometer, equipped with two 1800 groove/mm holographic gratings and DH-2 photo-multiplier. With studied lasers an additional spectral selection is necessary to prevent radiation (with average output power from 1 to 6 W depending on the discharge conditions) of the 510.6 nm and 578.2 nm self-terminating atom transitions from entering the spectrometer or

XIII International Symposium on Gas Flow and Chemical Lasers and High-Power Laser Conference,
Antonio Lapucci, Marco Ciofini, Editors, Proceedings of SPIE Vol. 4184 (2001)

the optical detector. For this purpose a quartz prism was used. The average output power was measured by a Scientech 362 and Scientech Vector power meters. The waveforms of the discharge current and the tube voltage were detected by a Rogowski-coil probe and a Tektronix P6015 HV probe. The laser pulses were observed by a Liconix Model 40D pulse detector. All pulses were displayed on a Tektronix 2455A oscilloscope with a 20 MHz cutoff filter.

## 3. EXPERIMENTAL RESULTS

Laser oscillation on four UV $Cu^+$ lines - 248.6, 252.9, 260.0 and 270.3 nm, has been obtained by laser tube T1. For Ne buffer-gas pressures 5.5 and 7 Torr, and pulse repetition frequencies 21 and 22 kHz the dependence of the 248.6 nm laser line intensity on the discharge current amplitude and average input power has been determined. An optimal value of the discharge current (input power respectively) was observed in the range 120-130 A, depending on the Ne pressure and pulse recurrence frequency.

The dependence of the 248.6 nm laser line intensity on the pulse repetition frequency has been investigated for the Ne buffer-gas pressures of 5.5 and 7 Torr. Laser oscillation was observed in a very narrow frequency band - from 20.5 to 22.5 kHz. Maximal radiation intensity was achieved about 21 kHz. Similar narrowing of the range, in which UV lasing occurred, was observed with respect to the reservoir temperature.

Maximal average output power, achieved on the 248.6 nm laser line by T1, was 5 mW.

A stable laser operation on the lines 248.6, 252.9, 260.0 and 270.3 nm was obtained by laser tube T2 in a wide range of the discharge parameters change - pulse repetition frequency from 9.5 to 28 kHz, Ne buffer-gas pressure from 6.5 to 14.5 Torr. An optimization of the four capacitors, forming capacitor bank of the excitation circuit, has been undertaken. The highest output characteristics were achieved by nominal values of the capacitors $C_1$ = 500 pF, $C_2 = C_3$ = 235 pF, $C_4$ = 2200 pF. Further investigation on the laser optimization was carried out by this tube, because of considerable higher output parameters.

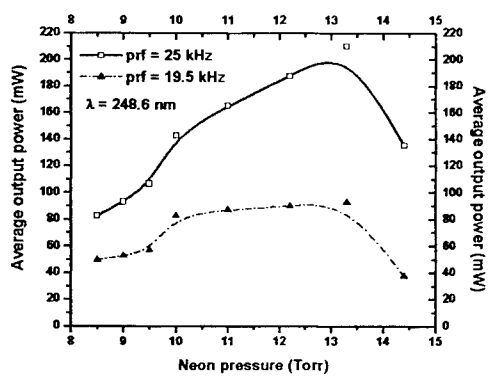


Fig.1. Average output power as a function of pulse recurrence frequency

The dependence of the average output power, measured on the laser line 248.6 nm, on the Ne buffer-gas pressure is given in Fig. 1. The optimal temperature of the reservoirs with CuBr is 560 $^0$C [4]. It can be seen, that the optimal Ne pressure (with regard to maximal output power achievement) is 13.5 Torr.

The average output power as a function of the pulse recurrence frequency (f) is shown in Fig. 2. A monotonous growth of the output power with the frequency increase up to 25 kHz has been observed. It is possible, that the decrease of the output power at frequencies above 25 kHz is due to some problems with the excitation generator operation at this frequencies.

Under optimal discharge conditions the average output power on the four UV $Cu^+$ laser lines is given in Table I. At a Ne buffer-gas pressure of 13.5 Torr, pulse repetition frequency of 25 kHz, average input power of 1440 W, an average output power of 210 mW has been measured on the laser line 248.6 nm. Under the same conditions a multiline average output power of 270 mW has been achieved by a 99.9 %-reflectivity mirror and an output coupler with the following transmission: 4 % (248.6 nm), 4.5 % (252.9 nm), 5.5% (260.0 nm) and 12.5 % (270.3 nm).

**Table I**: λ - wavelength of the corresponding laser line; p - optimal Ne buffer-gas pressure; $I_R$ - amplitude of the discharge current; prf - optimal pulse recurrence frequency; $T_r$ - operating temperature; $P_{out}$ - single-line average output power.

| λ, nm | 248.6 | 252.9, 260.0 and 270.3 |
|---|---|---|
| p, Torr | 13.5 | 13.5 |
| $I_R$, A | 90 | 90 |
| prf, kHz | 25 | 25 |
| $T_r$, $C^0$ | 560 | 560 |
| $P_{out}$, mW | 210 | 40 |

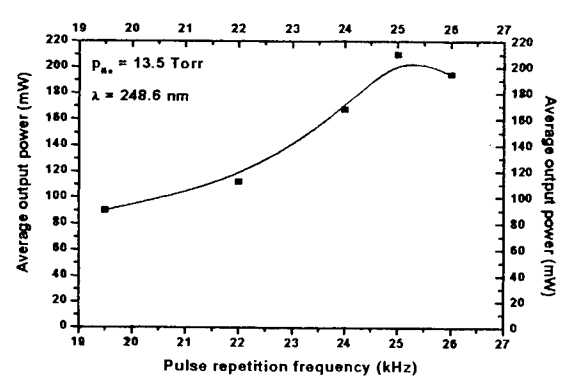


Fig. 2. Dependence of the average output power, on the pulse repetition frequency.

In Fig. 3 the waveform of the discharge current pulse and output power pulse on the llaser line 248.6 nm are shown. It can be seen peak pule power is about 1.7 W at a laser pulse duration (FWHM) of 5 μs.

Laser oscillation on four IR $Cu^+$ laser lines has been obtained in a He-CuBr discharge in laser tube T1. Pulse longitudinal discharge-excited He-Cu laser, operating on seven IR $Cu^+$ laser transition, has been also investigated in T3. The results, obtained via a 99.9 %-reflectivity mirror and an output coupler with a transmission of 2 %, are shown in Table II. A maximal multiline average output power of 430 mW and 765 mW has been achieved in He-CuBr and He-Cu discharge, respectively.

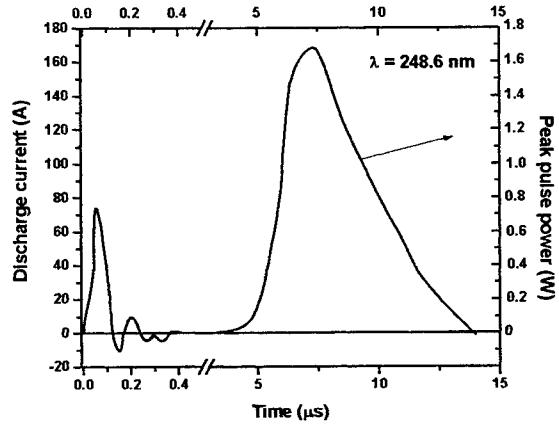


Fig. 3. Waveform of the discharge current pulse and output power pulse on the llaser line 248.6 nm.

**Table II**: λ - wavelength of the corresponding laser line; p - optimal helium buffer-gas pressure; prf - optimal pulse repetition frequency; $T_r$ - operating temperature; $P_{out}$ - average output power.

| Cu atoms source | λ, nm / parameters | 740.4 | 766.5 | 773.9 | 780.8 | 798.8, | 819.8 | 827.7 |
|---|---|---|---|---|---|---|---|---|
| CuBr | p, Torr | 10 | 10 | 10 | 10 | - | - | - |
| CuBr | prf, kHz | 14, 22 | 14, 22 | 14, 22 | 14, 22 | - | - | - |
| CuBr | $T_r$, $C^0$ | 530 | 530 | 530 | 530 | - | - | - |
| CuBr | $P_{out}$, mW | 35 | 37 | 15 | 345 | - | - | - |
| Cu | p, Torr | 18 | 18 | 18 | 18 | 18 | 18 | 18 |
| Cu | prf, kHz | 22 | 22 | 22 | 22 | 22 | 22 | 22 |
| Cu | $T_r$, $C^0$ | 1500 | 1500 | 1500 | 1500 | 1500 | 1500 | 1500 |
| Cu | $P_{out}$, mW | 10 | 10 | 5 | 725 | 5 | 5 | 5 |

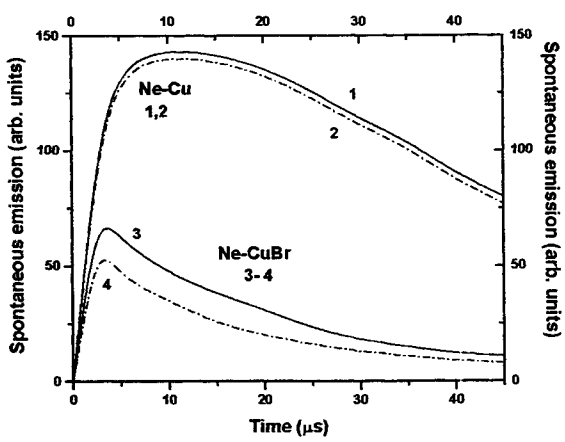


Fig. 4. Spontaneous emission of the 248.6 nm line in Ne-CuBr and Ne-Cu discharge.

In Ne-Cu pulsed longitudinal discharge laser oscillation in the UV spectral range has not be obtained. The spontaneous emission of the 248.6 nm line has been investigated in both lasers. The results are presented in Fig. 4. Curves 1 and 2 are waveforms of the spontaneous emission in Ne-Cu discharge with and without a high-reflective UV mirror, respectively. Curves 3 and 4 are waveforms in Ne-CuBr discharge with and without a high-reflective UV mirror, respectively. The intensity of this line is higher in the case of the pure copper laser but the influence of the mirror on the intensity was much higher for the Ne-CuBr.

## 4. DISCUSSION

The discharge conditions for obtaining of laser oscillation on the UV and IR $Cu^+$ lines in nanosecond pulse longitudinal discharge have been compared at the utilization of CuBr and Cu as a source of the Cu atoms.

The utilization of a laser tube without discharge confining diaphragms allows to: 1) extend considerably variation range of the discharge parameters - buffer-gas pressure, metal vapor pressure, excitation pulse repetition frequency, average input power (discharge current amplitude), and hence to carry out an optimization of the average output power at the indicated parameters variation; 2) obtaining of two order of magnitude increase of the average laser power.

An average output power of 270 mW has been achieved at multiline output on the four UV $Cu^+$ laser lines, which is considerably higher result in comparison with the 200 mW record multiline average output power for UV $Cu^+$ hollow cathode systems, measured in [2]. On the 248.6 nm laser line an average output power of 210 mW has been measured in our experiment (for example in [2] the average laser power has been 28 mW on that laser line). At a laser pulse duration (FWHM) 5 μs and excitation pulse recurrence frequency 25 kHz the peak pulse power on the 248.6 nm laser line is 1.7 W, exceeding two times the results, achieved via UV $Cu^+$ hollow cathode lasers (0.9 W [2]).

Till now it has been assumed, that the metal halide are not appropriate for active particle source in the ion metal lasers, because the halide atoms reduce the electron temperature and hence the output parameters decrease in comparison with the ion laser with pure metal vapor [6]. In [2] it has been supposed: 1) the Ne metastables affects considerably the lower UV laser line levels; 2) the Ne metastables can be quenched by argon admixture. With UV $Cu^+$ CuBr vapor laser copper atoms are produced by an electron impact dissociation of the CuBr molecule during the discharge period. As in fact the identical Cu and Br concentrations are produced after the dissociation. At a distance $3.5 \div 4.5$ eV below Ne metastable level three 4p $Br^+$ levels are located closely to the 4s $Cu^+$ metastable levels.We assume that a Ne metastable decay has been caused by Penning collisions with ground state Br atoms. The estimated cross section and rate constant for this reaction are considerably higher than those for Penning impacts between the Ne metastables and ground state Cu atoms. The record output powers, achieved in the present work support the assumption for a positive effect of the Br presence in the discharge on the formation of the inversion population.

## ACKNOWLEDGMENT

This work was supported by project NATO SfP 971989 "High beam quality UV lasers for microelectronics" and by Bulgarian Science Fund, Grant F-703.

## REFERENCES

1. J. R. McNeil, G. J. Collins, K. B. Persson, and D. L. Franzen, "Ultraviolet laser action from Cu II in the 2500-A region," Appl. Phys. Lett., vol. 28, No. 4, pp. 207-209, 1976.
2. H. J. Eichler, H. Koch, R. Molt, J. L. Qiu and W. Martin, "Optimization of the UV Cu II laser," Appl. Phys. B, vol. 26, pp. 49-56, 1981.
3. R. Solanki, W. M. Fairbank Jr., and G. J. Collins, "Multiwatt operation of Cu II and Ag II hollow cathode lasers," IEEE J. Quantum Electron., vol. QE-16, No. 12, pp. 1292-1294, 1980.
4. N. K. Vuchkov, K. A. Temelkov, N. V. Sabotinov, "UV lasing on $Cu^+$ in Ne-CuBr pulse longitudinal discharge," IEEE J. Quantum Electron., vol. 35, pp. 1799-1804, 1999.
5. N. K. Vuchkov, D. N. Astadjov, and N. V. Sabotinov, "Influence of the excitation circuits on the CuBr laser performance," IEEE J. Quantum Electron., vol. 30, No. 3, pp. 750-758, 1994.
6. I. G. Ivanov, E. L. Latush, and M. F. Sem, "Metal vapor ion lasers," John Wiley & Sons Ltd., West Sussex, England, 1996.

# UV He-Au ion laser excited by longitudinal ns discharge

Todor St. Petrov*[a], Nikola Sabotinov[a], Ivan Kostadinov[b]
[a]Institute of Solid State Physics, 72 Tzarigradsko Chaussee, 1784 Sofia, Bulgaria
[b]Pulssvet Co., 72 Tzarigradsko Chaussee, 1784 Sofia, Bulgaria

## ABSTRACT

We report laser characteristics of a gold ion laser radiating on the lines 282.3nm, 284.7nm, 289.3nm and 291.8nm. A longitudinal nanosecond discharge has been used for excitation. Quasi-cw lasing was obtained with ~33%/m small-signal gain and 110 mW average output power for the strongest line 282.3nm. This average output power corresponds to the record peak power of 1.7W. The investigated laser offers promising prospect for various scientific and technological applications.

**Keyword:** metal vapor laser, gold vapor laser, UV gold ion laser.

## 1. INTRODUCTION

The metal vapor ion lasers which generate on the ion transitions of copper, gold or silver in the spectral waveband 224 - 293 nm, are very attractive for applications in biology, photo technology, medicine, cw-quasi UV pumping of the dye lasers etc.

The gold metal vapor ion laser (GMVIL), is capable to emit seven ultraviolet (UV) lines 226.4 nm, 253.4 nm, 261.7 nm, 282.3 nm, 284.7 nm, 289.3 nm and 291.7 nm. Lasing on these transitions has been demonstrated in a hollow cathode discharge. An average output power of 19.2 mW in cw mode was reported for the lines 282.3 nm and 284.7 nm, and the pick output power of 600 mW in the case of simultaneous lasing of the lines 282.3 nm, 284.7 nm, 289.3 nm and 291.7 nm.[1, 2, 3] The strongest line in the mentioned papers had been 282.3 nm.

In the beginning of the nineties were reported significant increases in the average output power and small-signal gain of the GMVIL excited in the hollow cathode discharge. Rózsa, Adamowicz *et al.* have obtained 50% $m^{-1}$ small-signal gain and an average output power of 100mW.[4, 5, 6]

Recently it was shown that the efficiency of Duffendack reaction is quite good in a longitudinal nanosecond discharge (LND).[7] The efficiently working He-CuBr ion laser and Ne-CuBr ion laser were built. Record small-signal gain was measured for two copper ion UV lines - 19% for 248.6nm and 16% for 270.3nm.

Results described above have initiated the reported investigations. The investigations presented in this paper is aimed to determine conditions for UV lasing on gold ion lines in a He-Au pulsed longitudinal nanosecond discharge in a tube having the same parameters as the tube for commercial GVL.

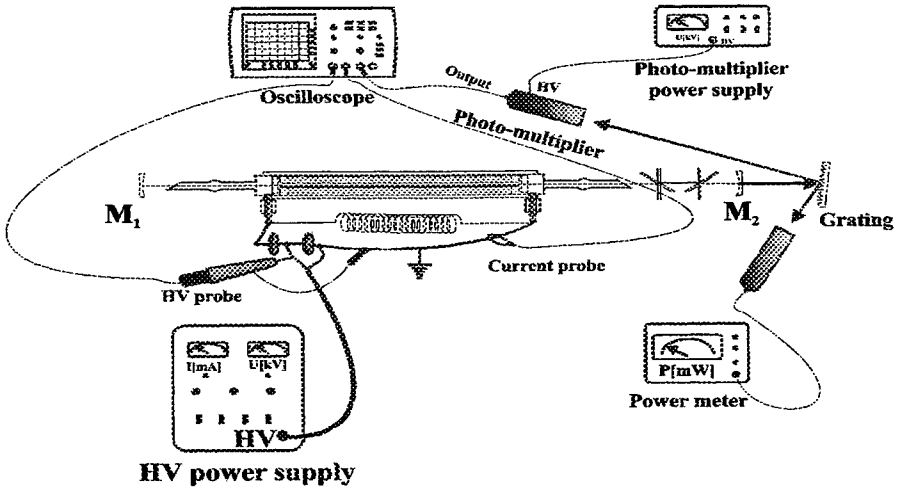


**Fig 1** The experimental setup

## 2. EXPERIMENTAL SETUP

The Fig. 1 illustrates the entire experimental setup.

The working temperature of the laser is higher than 1800°C. It is a reason that the laser tube is made from thermal resistive materials. The outside tube is a quartz tube having a diameter of 80mm (Fig. 2)

Correspondence: e-mail: tspetrov@issp.bas.bg; Tel./Fax: +359 2 756 009

XIII International Symposium on Gas Flow and Chemical Lasers and High-Power Laser Conference,
Antonio Lapucci, Marco Ciofini, Editors, Proceedings of SPIE Vol. 4184 (2001)

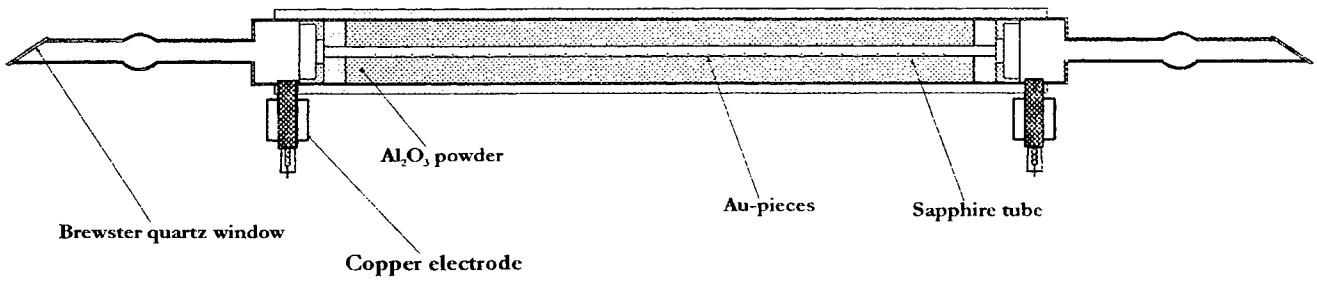


**Fig. 2** Main view of the investigated laser tube

and a 1000mm length. The discharge channel is limited by a sapphire tube. The sapphire tube has the dimensions, 700mm length and 10 mm inner diameter. The laser active zone is about 600 mm long. Small Au-pieces are placed along the sapphire tube. Two quartz rings fix the discharge tube. The volume between the sapphire tube and the outside quartz tube is filled with $Al_2O_3$ powder. Thus it is possible to protect the quartz tube from the discharge thermal radiation of the discharge. The electrodes were made of porous copper with special design.

The end parts of the laser tube are made from quartz too. They are cut at the Brewster angle for $\lambda = 282$nm and the quartz windows are stuck to them. The parameters of these tubes depend on the necessity to protect the quartz windows from contamination. Their inner diameter is 22mm and the length is 250mm.

The power supply high – voltage pulsed generator is based on a hydrogen thyratron – TGI 1000/25. The main parameters are: HV up to 12 kV and frequency from 4.5kHz to 12.5kHz. The Blumline scheme is used for excitation. Two low-inductance ceramic capacitors of the type KVI-3 are used. Typical capacity values for them are 1÷2nF. The charge inductance $L$ is about 0.8mH. These values are determined experimentally.

External mirrors are used in the investigated laser. $M_1$ is the back concave mirror with a reflectivity of 99.9% for the spectral range 265-300nm and radius of curvature 2m. When the gain measurements are carried out, the coupling mirror has the parameters of $M_1$, while for an optimization of the average output power the mirrors are different.

The small-signal gain measurements are carried out by inserting a calibrated loss element (high optical quality quartz plane-parallel plate) into the laser cavity – method of attenuator.[8]

The spectral monitoring has been done by a homemade holographic relief grating or a conventional monochromator. The parameters of the homemade grating are 2414 grove/mm and absolute reflection efficiency 78%. The monochromator is equipped with a 1800 grove/mm holographic grating and it is used for monitoring the spontaneous emissions.

The temporal behavior of the laser pulse has been studied by means of a UV sensible Photo-multiplier (18A) and a digital 200MHz oscilloscope Tektronix TDS 420A with a 20-MHz cutoff filter.

The waveforms of the discharge current and high voltage have been monitored by a Rogovski – coil and a Tektronix-P6015A HV probe. The pulses have been visualized by the mentioned oscilloscope.

A Scientech 360-power meter has been used for measurement of the average laser output power.

## 3. EXPERIMENTAL RESULTS AND COMMENTARY

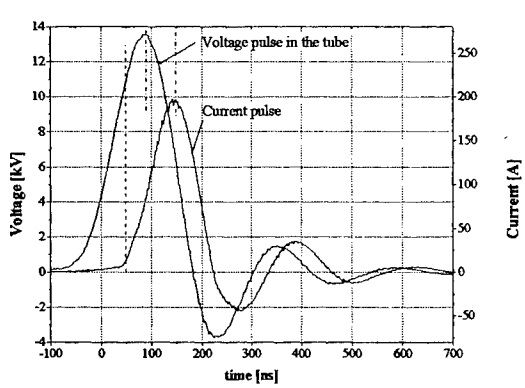


**Fig. 3** Typical current and voltage pulses

The typical working conditions for the reported investigations are pulse repetition frequency (PRF) in the range of 6 kHz to 12 kHz and He pressure from 9 torr to 30 torr. The construction of the laser tube enables achieving a quite high temperature on the wall of the discharge channel and delivering gold atoms to the active zone. The working dencyty of gold atoms is in the range $10^{14} \div 10^{15}$ cm$^{-3}$. [9] These parameters are very close to those of a gold atom vapor laser.

The required concentration of fast electrons for ionization of the helium ground state ions is generated within the time of very short powerful pulse (~200A and $\Delta\tau \approx 200$ ns (Fig. 3)). The number of the electrons during the pumping pulse is of about $10^{15}$cm$^{-3}$. [1, 9] The typical time delay of the current pulse to the voltage pulse is of about 65ns.

For the mentioned conditions lasing on four UV gold ion transitions has been obtained: 282.3 nm, 284.7 nm, 289.3 nm and 291.8 nm. The energy defect $\Delta E$ of Duffendack reaction for the upper laser levels of the presented transitions is lower than 0.4 eV. This fact determines high efficiency of the excitation process.

**Table 1** The main experimental results for the optimal conditions: He pressure of about 15 torr and PRF = 7.5 kHz.
$I_{dis}$ – the amplitude of the current pulse; $\Delta\tau$- laser pulse duration; $P_{out}$ – average output power; $E_{pulse}$- laser pulse energy; $P_{pulse}$ – laser pulse power.

| $\lambda$ [nm] | 282.3 | 284.7 | 289.3 | 291.7 |
|---|---|---|---|---|
| $I_{dis}$ [A] | ~ 180 | 160 | 160 | ~ 180 |
| gain [%/m] | 33 | ~ 15 | ~ 13 | ~ 17 |
| $\Delta\tau$[μs] | ~ 8.5 | ~ 5.5 | ~ 5.5 | ~ 5.5 |
| $P_{out}$ [mW] | ~ 110 | 1 | ~ 1 | ~ 20 |
| $E_{pulse}$[μJ] | ~ 14.6 | | | ~ 2.6 |
| $P_{pulse}$[W] | ~ 1.7 | | | ~ 0.48 |

### 3.1. Gain measurement:

The gain measurement were done by the method of attenuator. Two counter-rotating plate-parallel quartz plates are inserted into the cavity and turned slightly off the Brewster angle until the lasing is stopped (Fig.1). When oriented at the Brewster angle the plate does not introduce a significant loss into the resonator. The losses introduced by the tilting plates are calculated using the formulas, which are based on the Fresnel formula. The interference among the reflected beams is neglected. The plate normally used is thick enough (2mm) to render sufficient spatial separation between the beams for any appreciable interference to occur. The fluorescence of the Brewster windows, of the attenuator and coupling mirror provoked by the laser beam increases resonator losses. They are plainly visible. These losses become stronger for the high intensity of the optical field inside the laser cavity. In our measurement the losses due to fluorescence of the Brewster windows and the attenuator are not determined.

The gain measurements have been done for a different helium pressure. The optimal He pressure for lasing and for the highest gain is of about 15 torr. The pulse repetition frequency was 7.5 kHz. In Table 1 are shown the main experimental results. A gain of 33%/m for the strongest line 282.3nm in a quasi-cw mode of lasing is obtained. The results from the gain measurement give us an idea for the parameters of the reflection coefficient of the coupling mirror.

The laser pulses are shown in the Fig. 4. This oscillogram enables to evaluate the power distribution for the different lines. These pulses have been observed when the reflection coefficient of the $M_2$ was 99.5%. Normally the strongest line starts 1÷2 μs early than the others. This fact does not depend significantly on the discharge parameters.

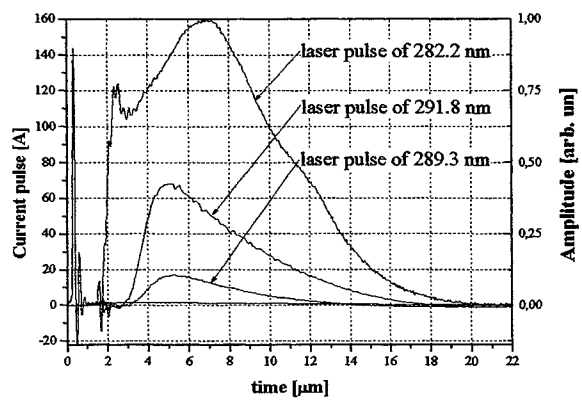


**Fig. 4** Laser pulses of the three of the radiating lines.

The most interesting line, because of its good lasing parameters, is 282.3 nm. On the Fig. 5 is shown the temporal behavior of the laser pulse, spontaneous emission and discharge current pulse at 282.3 nm. Lasing occurs 1.5μs after the end of the current pulse. This fact shows that excitation processes by electron impact-direct or stepwise-cannot be directly responsible for excitation of the upper laser level. The large duration of the laser pulse and pulse of spontaneous emission, confirms that the main excitation process is Duffendack between the long life species He ions and gold atoms. The same behavior has and other three lines (Fig. 4). The second pick in the laser pulse of 282.3 nm implies eventual influence of the following three-recombination process.

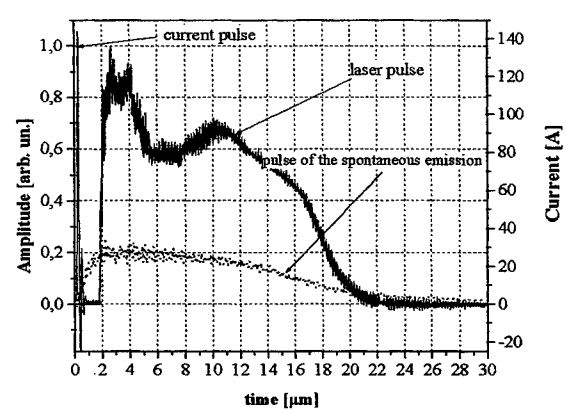


**Fig. 5** Pulses of the spontaneous emission and lasing of the strongest gold ion lines 282.3 nm

$$He + Au^{+*} + e^{-} \rightarrow He^{*} + Au$$

In this way it is possible to depopulate the low laser level. The difference between low laser levels of the transition 282.3 nm

and the metastable helium level - $2^3S_1$ is less than 0.01eV. Unfortunately we could not present the experimental arguments about this speculation.

An output power of 110 mW of the line 282.3 nm has been obtained. The optimal reflection coefficient for the coupling mirror $M_2$ has not been determined. The coupling mirror was 85%, but it is not an optimal value. Higher output power can be expected for a better geometry of the laser cavity. The entire volume of the laser active medium is not used.

The reported results show that the use of the pulsed longitudinal discharge at nanosecond duration and high repetition rate of the excitation pulse permits to obtain lasing with output characteristics comparable with those for the CW or pulsed HC laser. This fact shows that the HC laser can be replaced successfully with the described type of laser in cases where CW lasing is not necessary. A very important detail is that the laser tube and power supply are very similar (can say practically the same) to the conventional high-power gold vapor laser. It can be assumed that He-$Au^+$ laser system operating in the UV spectral range with an average output power of about 200mW and a lifetime ~1000 h could be produced.

## 4. CONCLUSIONS:

1. UV lasing on four gold ion lines in a He-Au pulsed longitudinal nanosecond discharge has been achieved.
2. Quasi-cw lasing is obtained in a longitudinal nanosecond discharge with ~33%/m-gain for the strongest line 282.3nm.
3. Lasing of 125mW on two lines 282.3nm and 291.8nm is monitored.
4. The record peak $P_{pulse}$ of 1.7 W was measured for the strongest line 282.3 nm.

## ACKNOWLEDGMENT

The reported laser is designed for an industrial laser system and has been developed under the project **NATO SfP-971989** *"High Beam Quality UV Lasers for Microelectronics"*.

## References:

1. R.D. Reid, J. R. McNeil and G.J. Collins, "New ion laser transitions in He-Au mixtures", *Appl. Phys. Lett* **29**, pp. 666-8, 1976.
2. K. Jain, "New ion laser transitions in cooper, silver and gold", *Appl. Phys. Lett* **34**, pp. 398-9, 1979.
3. K. Jain, "New UV and IR transitions in gold, cooper and hollow cathode lasers", *IEEE J.Quantum Electron.* **QE-16,** pp. 387-8, 1980.
4. K.A. Peard, R.C. Tobin, K. Rózsa, Z. Donkó, "A high-voltage hollow-cathode Au-II 282-nm laser", *IEEE J.Quantum Electron.* **QE-30,** pp. 1181-1186, 1994.
5. K. Jain and S.A. Newton, "Operating characteristics of UV and IR hollow cathode silver, gold and cooper ion lasers", *Appl. Phys. B* **26**, pp. 49-56, 1981.
6. R.C. Tobin, K.A. Peard, G.H. Bode, K. Rózsa, Z. Donkó and L. Szalai, "High-gain hollow-cathode metal ion lasers for the UV and VUV", *IEEE J. Selected Topics Quantum Electron.* **1**, pp. 805-10, 1995.
7. N.K.Vuchkov, K.A.Temelkov, N.V.Sabotinov, "UV lasing on Cu+ in a Ne-CuBr pulsed longitudinal discharge", *IEEE J. Quantum Electron.* **QE-35,** pp.1799-1804, 1999.
8. B. S. Patel, A. Mallik, and Shiv Charan, "Brewster window losses in 6328 a He-Ne lasers", *Journal of Physics E: Scientific Instruments,* **6**, pp. 1014-1016, 1973.
9. C.E. Little, *"Metal Vapor Lasers"*, pp. 51-54, John Wiley & Sons Ltd., 1999.

# Plasma kinetics issues for repetition rate scaling of kinetically enhanced copper vapour lasers

R J Carman*[a], R.P. Mildren[a], J A Piper[a], G D Marshall[b] and D W Coutts[b]

[a]Centre for Lasers and Applications, Macquarie University, Sydney, NSW 2109, Australia
[b]Dept. of Atomic and Laser Physics, Clarendon Laboratory, Oxford University, Parks Rd, Oxford, UK.

## ABSTRACT

The performance of a small-scale KE-CVL operating at a pulse repetition rate of 50kHz has been investigated by comparing modelling results and experimental data to understand the underlying plasma kinetics issues for pulse repetition rate scaling. Comparison between initial modelling predictions and experimental results relating to the laser output power and the population densities of the metastable lower laser levels ($Cu^*$ $4s^2$ $^2D_{3/2,5/2}$ ) suggests that there is an additional de-excitation mechanism for the metastables in the KE-CVL. The most likely de-excitation mechanism involves vibrationally-excited $H_2(v)$ molecules $Cu^{*2}D+H_2(v) \Rightarrow CuH+H$. A rate-coefficient of $2\times10^{-16}m^3s^{-1}$ is obtained by comparing modelling results with experimental data relating to the laser output power and the time-evolution of the axial $^2D_{3/2}$ metastable population density.

**Keywords**: copper laser, kinetic enhancement, KE-CVL, plasma kinetics, HCl.

## 1. INTRODUCTION

Halogen based gas additives such as $HCl+H_2$ have been used in elemental copper vapour lasers (CVLs) to modify the plasma kinetics and dramatically improve the laser performance in a technique known as kinetic enhancement[1]. The technique utilises the large dissociative attachment cross-sections of these molecules to directly remove free electrons from the plasma over the afterglow period to radically improve the plasma relaxation rate leading to more favourable "pre-pulse" conditions. With kinetic enhancement, the output power from a conventional CVL (25mm bore x 1m) is typically doubled, the high beam-quality extraction is increased by a factor of 3-4, and laser action is sustained at much higher pulse repetition frequencies (prf=20-40kHz). Recent studies[2] using a kinetically enhanced copper vapour laser (KE-CVL) of similar size have demonstrated that high output power (exceeding the maximum attainable from the laser operating as a conventional CVL) can be sustained up to 70kHz, with laser action occurring up to 120kHz. The ultimate limits for high prf operation of KE-CVLs will be determined by the fundamental plasma kinetics issues which have yet to be fully understood. In particular, the observed performance of small- and medium-scale KE-CVLs operating at high prf (>20kHz) appears to greatly exceed expectations and predictions from preliminary numerical modelling. In this paper, kinetics issues are investigated by comparing experimental data and modelling results for a small-scale KE-CVL operating at 50kHz where the laser output power (~35W) is close to optimum.

## 2. EXPERIMENTAL DETAILS AND NUMERICAL MODEL

The laser used in this study is a small-scale device with a 25mm diameter by 61cm long active region (volume $300cm^2$). The alumina ceramic plasma tube is surrounded by a fibrous style insulation inside a 70mm ID quartz vacuum envelope. Cold slotted copper electrodes are employed with the co-axial current return and brass end pieces water cooled. A 1%-2% hydrogen/neon buffer gas mix is flowed through an oven containing $ZrCl_4$ powder at ~100°C to generate the $HCl-Ne-H_2$ buffer gas additive. Optimum neon pressures are 35-40mb. A thyratron switched LC inversion circuit incorporating two stages of magnetic pulse compression is used to provide fast-risetime excitation pulses. Modelling simulations have been undertaken to match experimental conditions[2] corresponding to the "fast circuit" which was used to generate lasing at the highest prfs (20-80kHz). The computer model used in this study has been reported in detail elsewhere[3]. The model incorporates a detailed kinetics scheme for the $HCl-Ne-H_2-Cu$ mixture in the plasma encompassing 29 species populations and ~150 electronic, radiative and heavy-body reactions and processes. External circuit details are included. The species population densities and other plasma parameters are evaluated as a function of time and radial position. All the model results are calculated in a temporally self-consistent manner, with the long-term evolution plasma kinetics followed over multiple excitation/afterglow cycles.

* Correspondence Email: rcarman@physics.mq.edu.au; Fax: 612-9850-8983

XIII International Symposium on Gas Flow and Chemical Lasers and High-Power Laser Conference,
Antonio Lapucci, Marco Ciofini, Editors, Proceedings of SPIE Vol. 4184 (2001)

## 3. RESULTS AND DISCUSSIONS

For the KE-CVL operating at 50kHz, the measured I-V characteristics agree well with model calculations as shown in fig.1 (based on 0.5%HCl+2.5%$H_2$), particularly with respect to magnitude and duration of the "phantom current" around t=240ns. However, the model predicts no lasing action at 50kHz, whereas a laser output power of 35W is consistently observed experimentally. This disparity is surprising since close agreement between model results and a broad range of experimental data has been demonstrated for a medium-scale KE-CVL operating at a lower pulse repetition rate of 12kHz[3]. Further analysis of the model results at 50kHz reveal that lasing action is being inhibited principally by the high pre-pulse population density of the two metastable lower laser levels $Cu^*\ 4s^2\ ^2D_{3/2,5/2}$. If the pre-pulse densities are reduced (from those calculated self-consistently over multiple discharge cycles), the calculated laser output power (fig.2) in the subsequent excitation phase increases dramatically to reach the output power levels seen experimentally. Similar reductions of the pre-pulse electron density [e] (fig.2), another parameter known to strongly influence laser performance, do not lead to significant increases in the calculated laser output power.

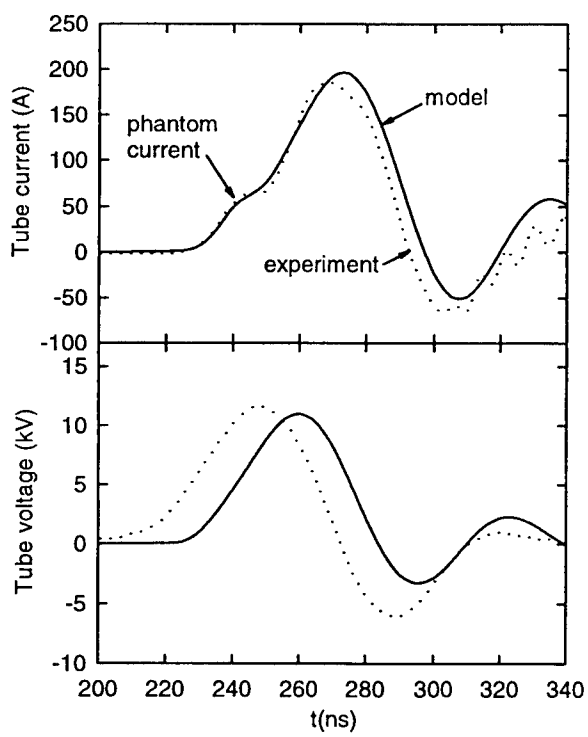


Fig.1. Calculated and experimental I-V waveforms for the small KE-CVL at 50kHz, 35mb, 2.5%$H_2$, 0.5%HCl.

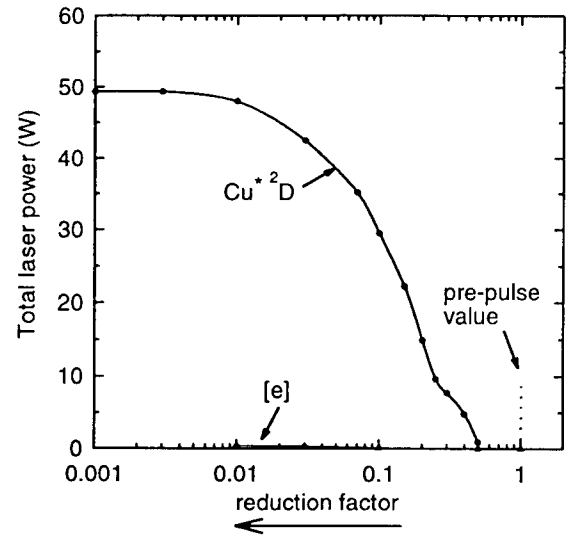


Fig.2. Calculated laser output power as a function of reduced pre-pulse $Cu^*\ ^2D_{3/2,5/2}$ metastable densities, and reduced pre-pulse electron density [e].

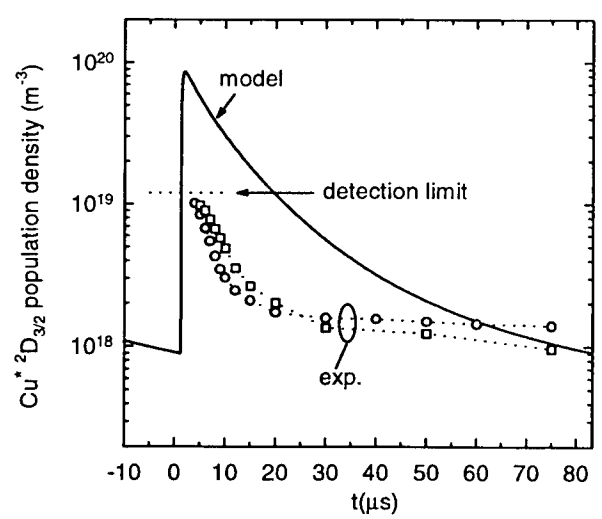


Fig.3. Time dependence of the axial $Cu^*\ ^2D_{3/2}$ density over one excitation/afterglow cycle for a medium-scale KE-CVL[3] at 12kHz comparing model results and experimental (absorption) measurements.

These results suggest that there may be an additional de-excitation mechanism of the metastable $4s^2\ ^2D_{3/2,5/2}$ levels manifesting in the KE-CVL which results in significantly lower pre-pulse densities of the lower laser levels. Inconclusive evidence of an additional de-excitation mechanism for the $^2D_{3/2,5/2}$ metastables has been reported previously[3] for a medium scale KE-CVL device operating at 12kHz. Population density (absorption) measurements of the $^2D_{3/2}$ level during the afterglow (fig.3) appear to indicate a very rapid decay in the first 10μs, in disagreement with model results. In this case,

lasing action was not inhibited in the model because the predicted pre-pulse metastable densities were consistent with experimental measurements. In the KE-CVL, fast e-HCl attachment reactions facilitate the rapid removal of free electrons during the afterglow period. The model calculations[3] at 12kHz suggest that electronic de-excitation rates of the $^2D_{3/2,5/2}$ metastables during the afterglow period would in fact be *reduced* in the KE-CVL (where there are fewer electrons) compared to a conventional CVL.

### 3.1 De-excitation mechanisms for $Cu^* 4s^2\ ^2D_{3/2,5/2}$ states

Collision processes leading to de-excitation of the $^2D_{3/2,5/2}$ metastables may be summarised as follows:

(a) processes currently included in the model[3] (with known rate-coefficients):

Elemental (Ne-Cu) CVLs:

$Cu^*4s^2\,^2D + Ne \Rightarrow Cu\ ^2S_{1/2}$ (ground) $+ Ne + \Delta E$ (1)

$Cu^*4s^2\,^2D + Cu^2S_{1/2} \Rightarrow Cu^2S_{1/2} + Cu\ ^2S_{1/2} + \Delta E$ (2)

with $H_2$ additive:

$Cu^*4s^2\,^2D + H \Rightarrow Cu\ ^2S_{1/2} + H + \Delta E$ (3)

$Cu^*4s^2\,^2D + H_2(v=0) \Rightarrow Cu^2S_{1/2} + H_2(v=0) + \Delta E$ (4)

$Cu^*4s^2\,^2D + H^- \Rightarrow CuH + [e] + \Delta E$ (5)

with HCl additive:

$Cu^*4s^2\,^2D + Cl \Rightarrow Cu^2S_{1/2} + Cl + \Delta E$ (6)

$Cu^*4s^2\,^2D + Cl^- \Rightarrow CuCl + [e] + \Delta E$ (7)

(b) additional processes under evaluation (with unknown rate-coefficients):

$Cu^*4s^2\,^2D + H_2(v) \Rightarrow Cu\ ^2S_{1/2} + H_2(v+3) + \Delta E$ (8)

$Cu^*4s^2\,^2D + H_2(v) \Rightarrow CuH + H + \Delta E$ (9)

$\Rightarrow Cu\ ^2S_{1/2} + H_2(v+3) + \Delta E$

$Cu^*4s^2\,^2D + HCl(v=0) \Rightarrow Cu^2S_{1/2} + HCl(v=0) + \Delta E$ (10)

$Cu^*4s^2\,^2D + HCl(v) \Rightarrow Cu^2S_{1/2} + HCl(v+3) + \Delta E$ (11)

$Cu^*4s^2\,^2D + HCl(v) \Rightarrow CuCl + H + \Delta E$ (12)

$\Rightarrow Cu^2S_{1/2} + HCl(v+3) + \Delta E$

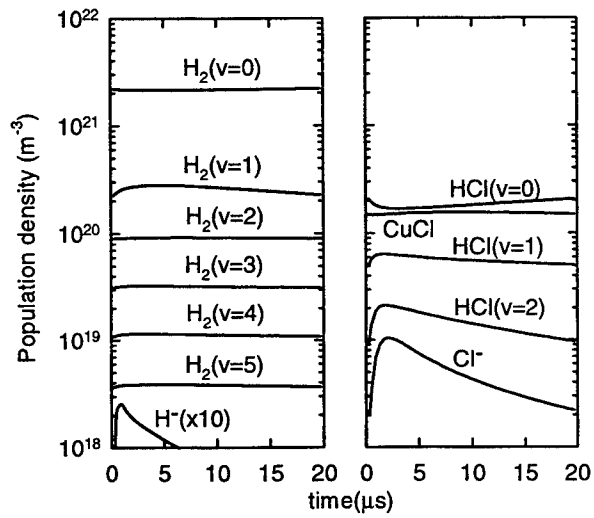


Fig.4. Time evolution of species population densities (axial) over one excitation/afterglow cycle in the small-scale KE-CVL at 50kHz.

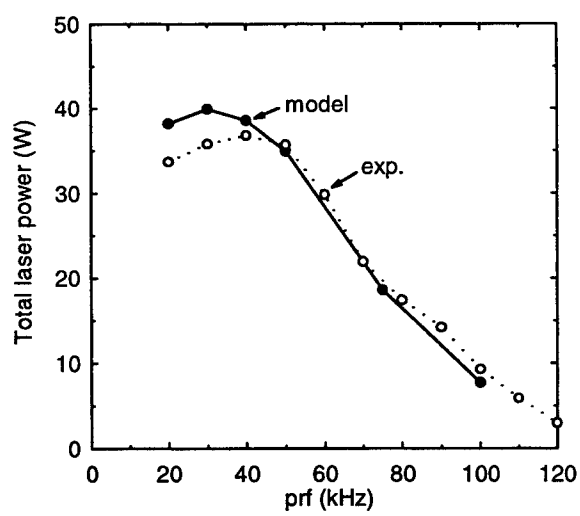


Fig.5. Laser output power from the small-scale KE-CVL for different repetition rates comparing experimental data and model calculations (with $^2D_{3/2,5/2}$ de-excitation via process (9))

None of the mechanisms (1)-(7) have rate-coefficients large enough to account for the rapid decay of the metastable density on the timescale of the afterglow (10-20μs at 50kHz). Reactions (8) and (11) are unlikely to have large rate-coefficients since the molecular vibrational energy levels spacings are not closely matched (resonant) with the $^2D_{3/2,5/2}$ excitation energies. De-excitation of both $^2D_{3/2,5/2}$ metastable levels by $H_2(v>0)$ and HCl(v) via the formation of CuH and CuCl molecules are exothermic reactions. Model results at 50kHz indicate that $H_2(v)$ is the most abundant molecular species (on axis) in the afterglow plasma (fig.4). De-excitation of the $^2D_{3/2,5/2}$ metastables by collisions with $H_2(v)$ (forming CuH) has been investigated previously[4] although the rate-coefficient is not known. (Note: process (9) for v=0 is discounted because the formation of CuH from $Cu^{*2}D_{3/2,5/2}$ states would be endothermic). Since the HCl(v) density is significantly lower than $H_2(v)$ (although not negligible), processes (10) and (12) are not considered further. By comparing model results and experimental data for the KE-CVL at 50kHz, we estimated the rate-coefficient for reaction (9) with $H_2(v>0)$ is $k_9=2.0\times10^{-16}m^{-3}s^{-1}$. This is not atypical for known abstraction (exchange) reaction rates[3]. With the inclusion of (9) in the KE-CVL kinetics scheme (and assuming $k_9$ is the same for all vibrational levels of $H_2$), the predicted laser output power is brought into close agreement with experimental results (fig.5).

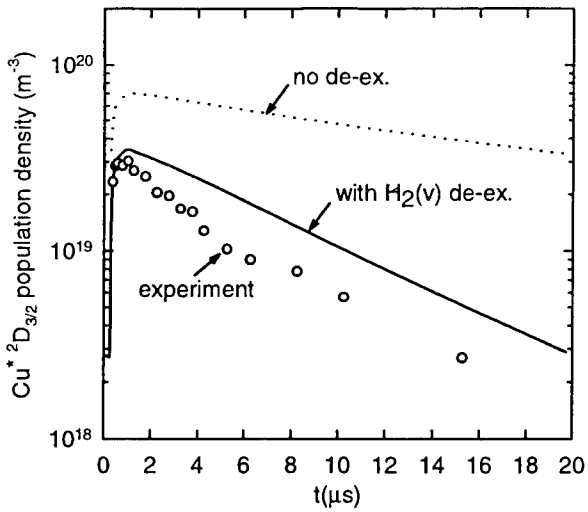


Fig. 6. Time dependence of the $Cu^*$ $^2D_{3/2}$ density (on axis) over one excitation/afterglow cycle for the small-scale KE-CVL at 50kHz comparing model calculations and experimental hook measurements.

The calculated decay-rate of the $^2D_{3/2}$ metastable density is increased significantly (fig.6) with the inclusion of de-excitation via $H_2(v)$ and follows more closely the temporal evolution seen in experimental (hook) population measurements. (note: modelling shows that this effect is obscured in conventional CVLs with $H_2$ because the metastable decay rates are more strongly regulated by electron impact collisions). For the KE-CVL operating conditions at 50kHz, the calculated decay time for (9) is ~8μs. In fact, it is important to realise that the pre-pulse metastable densities reach a steady-state over many excitation/afterglow cycles as shown in fig.7. This result illustrates the importance of calculating the long-term evolution of the plasma kinetics self-consistently.

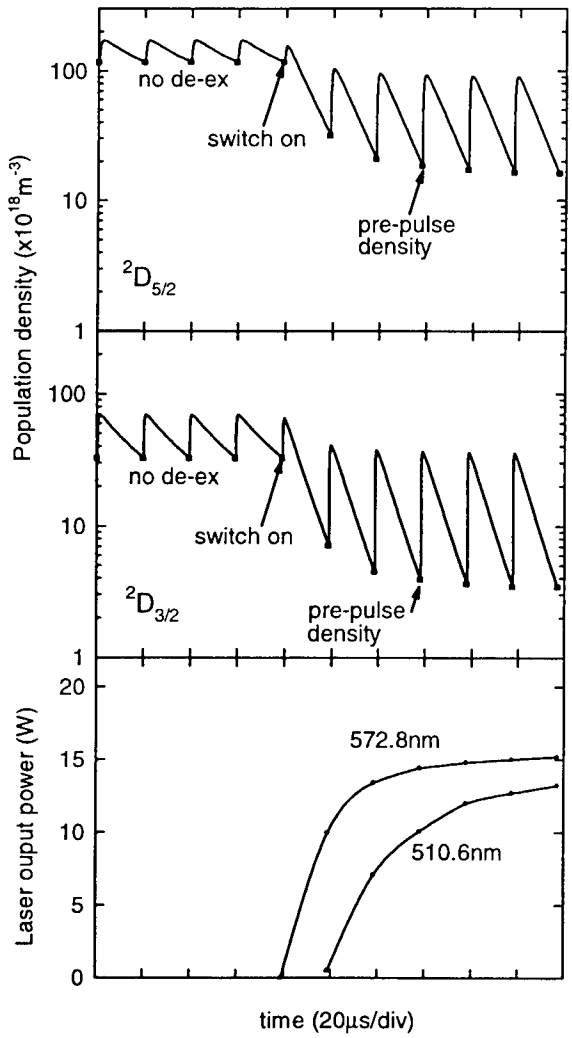


Fig.7. Time-evolution of the $Cu^*$ $^2D_{3/2,5/2}$ densities (on axis) and laser power over several excitation/afterglow cycles (for the small-scale KE-CVL at 50kHz) as the metastable de-excitation via process (9) is switched-on.

## 4. CONCLUSION

Plasma kinetics issues in a small-scale KE-CVL operating at an elevated prf of 50kHz have been investigated by comparing modelling results and experimental data. Comparisons between modelling and experimental results in relation to the laser output power and population densities of the metastable lower laser levels suggests that there is an additional de-excitation mechanism for the metastables viz: $Cu^{*2}D+H_2(v)$=>CuH+H. A rate-coefficient $k_9=2x10^{-16}m^3s^{-1}$ for this reaction is proposed.

## REFERENCES


1. M.J. Withford, D.J.W. Brown, R.J. Carman and J.A. Piper, "Kinetically enhanced copper vapour lasers employing $H_2$-HCl-Ne buffer gas mixtures", *Optics Comm.*, **154**, pp.160-166, 1998.
2. G.D. Marshall and D.W. Coutts, "Pulse repetition rate scaling of a small scale (50W) kinetically enhanced copper vapour laser (KE-CVL), in: *Proc. Conf. on Lasers and Electro-Optics*, OSA Technical Digest, Optical Society of America, Washington DC, 1999, paper CThK1.
3. R.J. Carman, R.P. Mildren, M.J. Withford, D.J.W. Brown and J.A. Piper, "Modelling the plasma kinetics in a kinetically enhanced copper vapour laser utilising HCl + $H_2$ admixtures, *IEEE J. Quantum Electron.*, **QE-36**, pp.438-449, 2000.
4. J. Garcia-Prieto, M.E. Ruiz, E. Poulain, G.A. Ozin and O. Novaro, "Theoretical studies of the photoexcited state Cu atom reactions. II. The $Cu^*+H_2$ =>CuH+H photochemical reaction", *J.Chem.Phys.*, **81**, pp.5920-5927, 1984.

# Maintaining efficiency of a Cu-HyBrID laser while changing laser parameters

R. Riva*, J. T. Watanuki, C. L. dos Santos, N. A. S. Rodrigues and C. Schwab.

IEAv /CTA, Rod. Tamoios, km 5, 12231-970 - São José dos Campos, SP, Brazil

## ABSTRACT

The pulse parameters of a Cu-HyBrID laser were measured in a large range of discharge conditions. It was shown that the laser efficiency is determined by an adequate pre-pulse electron density. Almost constant laser average power and efficiency can be obtained in very different pulse repetition rates provided other discharge parameters were adjusted in order to maintain the optimal pre-pulse electron density. We observed that the pulse width depends mainly on the HBr concentration while the pulse energy is mainly dependent on the absolute HBr pressure and repetition rate.

**Keywords:** copper lasers, HyBrID lasers, HBr, visible lasers, laser efficiency

## 1. INTRODUCTION

The most striking features of the Cu-HyBrID lasers are their ability to operate at high pulse repetition rates, low operation temperatures and very short warm-up times. It has been observed that almost constant laser average power and efficiency are obtained in very different pulse repetition rates. Consequently, the laser pulse energy, width or peak power can be varied while maintaining laser efficiency at high levels. The controlling of laser pulse parameters can be very important in several applications. For instance, laser beam divergence depends on the number of round trips in the cavity and therefore it is desirable to have a lengthened laser pulse [1]. In the same way, to preserve the laser beam quality in oscillator/amplifier systems the laser pulse width of the oscillator must be larger than the gain duration time of the amplifier. For laser material processing, the ablation regime is controlled by laser intensity while the ablation depth is controlled by laser fluency [2].

Many of the observed characteristics of the copper HyBrID lasers can be attributed to a reduced pre-pulse electron density between electrical excitation pulses. However it has been shown[3] that, whether pre-pulse electron density is too low, the laser efficiency decreases and instabilities takes place in the discharge. The pre-pulse electron density depends on many different parameters, such as repetition rate, absolute and relative gas mixture, discharge input power and so on, and it might be possible to have the same pre-pulse electron density for many combination of values of the different parameters. In other words, the same laser efficiency (hopefully, the maximum one) could be obtained for a large range of pulse repetition rate, pulse peak power and pulse energy. Therefore the purpose of the present paper is to investigate the dependence of the laser pulse parameters on the operational characteristics of the laser discharge in order to control them in a large range maintaining laser efficiency at the best values.

## 2. EXPERIMENTAL DETAILS

The Cu-HyBrID laser investigated in this work was a small size one, with a 25 mm bore and 700 mm long discharge tube. The details of the laser construction can be found elsewhere[4]. With this laser we obtained typically an average output power of 16 W and an efficiency of 1 % using an external plane-plane resonator. The gas enters at the anode end of the laser, and is evacuated through an activated charcoal filter to a rotary vacuum pump from the cathode end. Mixture of Neon (99.99% purity) and HBr (99.8% purity) was carefully controlled by using independent mass-flow controllers (MKS). The gas lines were connected together just after the controllers where a Baratron (MKS) measured the gas mixture pressure. The total gas (Ne + HBr) flow rate was fixed at 30 sccm. The excitation circuit was a standard resonant-charging, capacitor

* Correspondence: Email: riva@ieav.cta.br; Telephone: (55) 12 347 5432, Fax: (55) 12 344 1177

XIII International Symposium on Gas Flow and Chemical Lasers and High-Power Laser Conference,
Antonio Lapucci, Marco Ciofini, Editors, Proceedings of SPIE Vol. 4184 (2001)

transfer type switched by an E.E.V. CX 1535 thyratron. Storage (1.2 nF) and peaking (0.6 nF) ceramic capacitors (TDK) were mounted directly on the laser head to minimize circuit inductance.

Laser discharge conditions were followed by measuring the storage and peaking capacitor voltages with two high voltage probes P6015 (Tektronix). The laser current and voltage values were obtained by processing the voltage waveforms acquired with a digitizing oscilloscope TDS540 (Tektronix) as described in [5]. The laser average power was measured with a calorimeter (OPHIR 30 A - SH). A fast photodiode (EGG 3602) measured the laser pulse. The typical temporal evolution of principal laser and discharge parameters are shown in Figure 1. The laser discharge voltage is different from the storage capacitor voltage due to the influence of the circuit inductance.

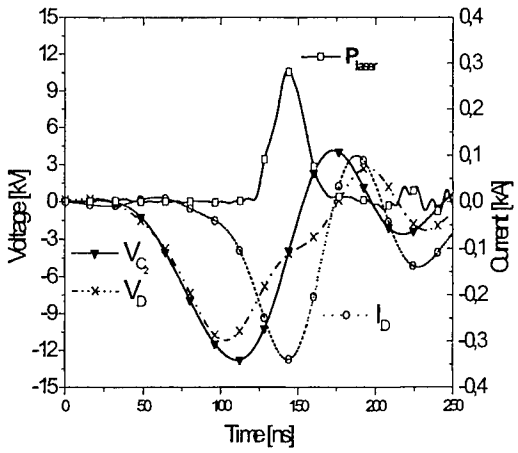


*Fig.1 – Temporal evolution of laser discharge voltage ($V_D$), laser discharge current ($I_D$), storage capacitor voltage ($V_{C2}$) and laser pulse power.*

The actual discharge breakdown is coincident with the maximum of the laser discharge voltage. The initial current that appears before breakdown is due to free electrons that rest after the end of the afterglow period[6]. Considering that this initial current is essentially due to free electrons prior to the true avalanche, the pre-pulse electron density is estimated by integrating that current from the start of the pulse voltage up to the breakdown time $T_B$ (the time when pulse voltage is maximum). The result of this integral is proportional to the residual electrical charge. Taking into account the active volume of the laser, the pre-pulse electron density $n_{e0}$ can be estimated by:

$$n_{e0} \propto \frac{1}{V_L} \int_0^{T_B} I_L(t)dt \qquad (1)$$

## 3. RESULTS AND DISCUSSION

The main consequence of a lower pre-pulse electron density on laser discharge is a higher voltage breakdown. The first effect of an increased breakdown voltage on laser performance is a better transfer of the energy accumulated on storage capacitor C1 to the peaking capacitor C2. The laser discharge current is much higher, and much more electrical power is injected into discharge leading to an increase of laser power. Thus, we estimated the pre-pulse electron density for different laser conditions, and observed the way this quantity affects the laser performance. Figures 2 and 3 show the main parameters that affect pre-pulse electron density.

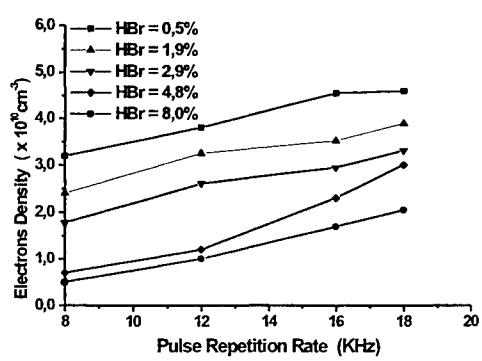


*Fig. 2 -Pre-pulse electron density as a function of pulse repetition rate for different HBr concentrations. The total laser gas pressure was 32 mbar and charging voltage was 12 kV.*

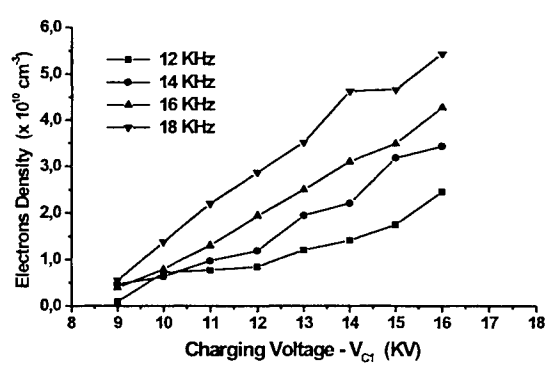


*Fig. 3 - Pre-pulse electrons density as function of charging voltage for different discharge pulse repetition rates for fixed HBr concentration (5%).*

It is clear from these figures that the strong reduction on pre-pulse electron density is mainly due to the HBr concentration. However, both pulse repetition rate and capacitor charging voltage can be also varied in order to control the pre-pulse electron density. This is particularly true for intermediate values of HBr concentration (5 %) as is shown in Figure 3. These results indicate that the reaction time for electron capture during the post-discharge is of the same order of the time between discharge pulses. Figures 4 and 5 show the laser peak current and breakdown voltage as function of charging voltage for HBr concentration fixed at 5 %. The laser current depends mainly on the charging voltage and is practically independent of pulse repetition rate. These results explain the almost linear increasing of pre-pulse electron density with charging voltage, assuming the maximum electron density is proportional to the laser current and that the reaction time for electron capture is almost constant for fixed HBr concentration.

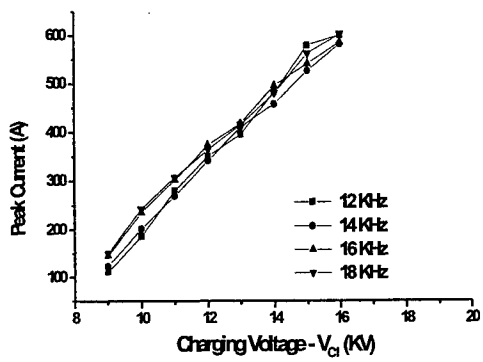


*Fig. 4 - Laser peak current as function of charging voltage for fixed HBr concentration (5%).*

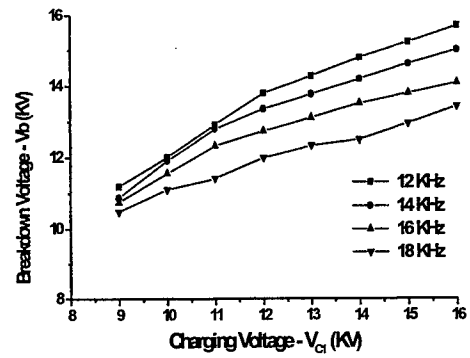


*Fig. 5 - Breakdown voltage versus charging voltage for different pulse repetition rates for fixed HBr concentration (5%).*

We measured the laser efficiency for different pulse repetition rates and charging voltages. The results are shown in Figure 6. We observe that the best laser efficiency occurs for different charging voltages for each pulse repetition rate. The optimal charging voltage diminishes with increasing of pulse repetition rate. However no matter the working conditions of the laser we find that this optimal values are obtained when the pre-pulse electron density is between 1 x $10^{10}$ and 2 x $10^{10}$ electrons/cm$^3$. Expressing these results as function of the discharge average input power, defined by the product:

$$P_D = \tfrac{1}{2} C_1 . f . V^2$$

where $C_1$ is the 1.2 nF storage capacitor, $f$ is the pulse repetition frequency and $V$ is the charging voltage, we observe that the laser efficiency remains at the maximum for every pulse repetition rate if the power dissipated into the discharge lies between 1500 and 1700 W. In this case the laser pulse energy can be varied from 0.7 to 1.4 mJ maintaining optimal laser efficiency. In a recent work[7], it was shown that, due to the thermal dissociation of HBr, the actual HBr density present in the active medium depends strongly from the discharge input power.

We observed too, that for this fixed discharge input power, the laser pulse width is almost constant (30 ns) and, consequently, the laser peak power decreases with pulse repetition rate. It is an interesting result because the discharge voltage and current for each pulse repetition rate are very different. One possible explanation is as follows. The discharge breakdown voltage is related with the initial electron energy and the peak discharge current is associated with the maximum electron density. It is well known that there is an optimal range of electron energy for efficiently excite upper laser level. The transfer of electrical circuit energy to laser discharge is improved with low pre-pulse electron density and, consequently, with high voltage breakdown. However, high values of electron energy favors the ionization or excitation to higher energy levels, decreasing the ground state population. In addition, we observed that for a fixed HBr concentration the laser emission always starts when the discharge voltage is about 8 kV (see Figure 1), no matter the pulse repetition rate, indicating probably that the electron energy achieved at this point an appropriate value to excite the upper laser level. Thus, for lower pulse repetition rates, the voltage breakdown is higher than for higher pulse repetition rates and, it takes a longer time to laser emission start. A similar thing happens with the laser discharge current: at the laser start voltage (8 kV), the lower pulse repetition rate, the higher the discharge current. Consequently the excitation rate to the upper laser level is higher for lower pulse repetition rates. This can explain the almost constant laser pulse width for different pulse repetition rate and the dependence of the laser peak power on breakdown voltage.

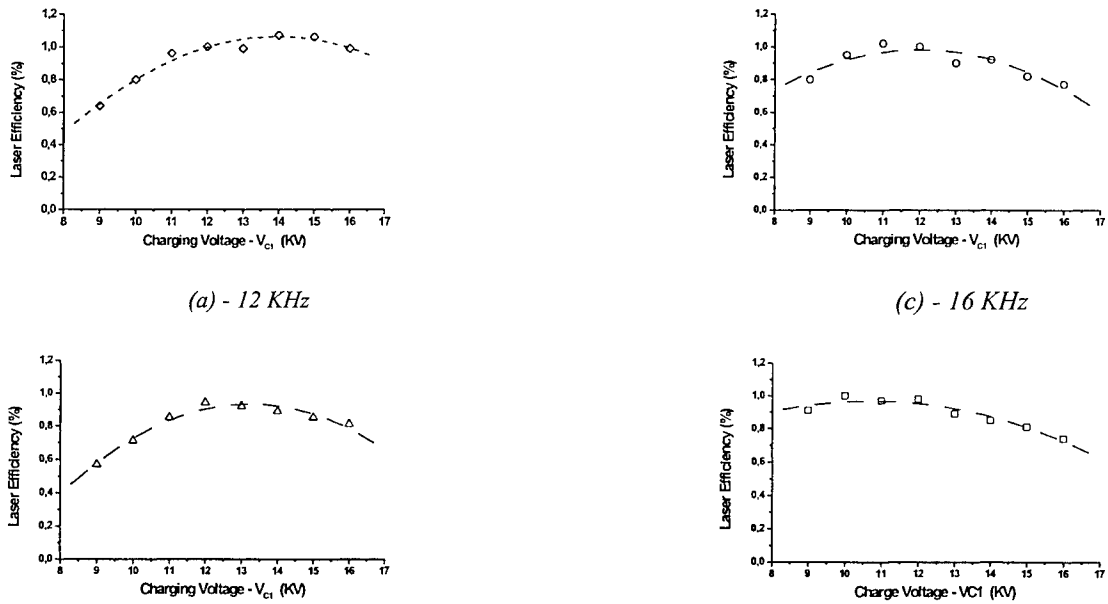


*(a) - 12 KHz*

*(c) - 16 KHz*

*(b) - 14 KHz*

*(d) - 18 KHz*

***Fig. 6** - Energy conversion efficiency as function of charging voltage for different pulse repetition frequencies.*

When the HBr concentration was varied, however, we observed significant changes in the laser pulse width. Figure 7 shows the behavior of the laser pulse width ( Fig. 7-a) and laser peak power (Fig. 7-b) as the HBr concentration is varied for different values of the charging voltage. In these figures, the pulse repetition frequency was fixed at 18 kHz. The point here is the possibility of obtaining the same energy for pulses with very different widths and peak powers, for a given pulse repetition frequency.

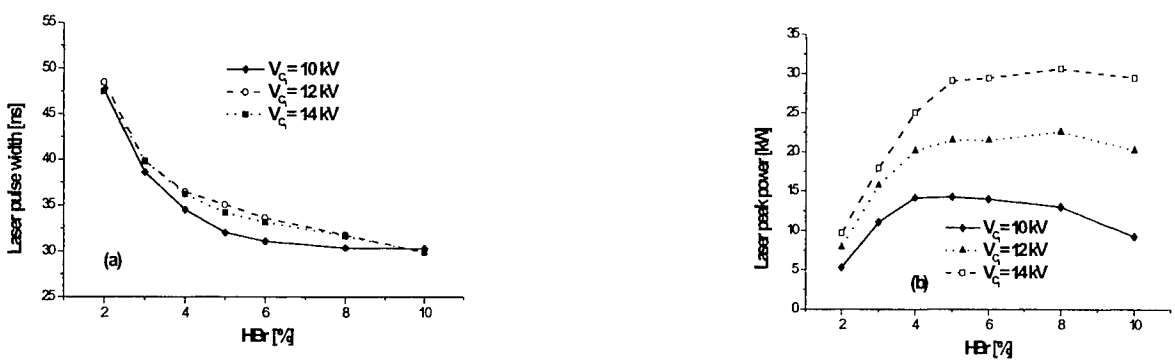


***Fig.** 7 –Laser pulse width (a) and laser peak power (b) as function of HBr concentration for different charging voltages.*

Finally, we examined the laser behavior as the total gas pressure ( Ne + HBr) was varied. Figure 8 shows the laser pulse energy as function of HBr pressure (at different concentrations). The pulse repetition rate was 18 kHz and the charging voltage was 13 kV. The best results for the laser pulse energy were for an absolute HBr pressure of ~ 2 mbar. Again, for this optimal value of HBr pressure, and independently of total gas pressure, we observed that laser emission starts when the discharge voltage is at 8 kV. Therefore the absolute quantity of HBr determines the electron energy. In these conditions the

laser pulse width depends mainly on the HBr concentration and not on the HBr pressure. This is another way to control laser pulse width while maintaining constant the laser pulse energy.

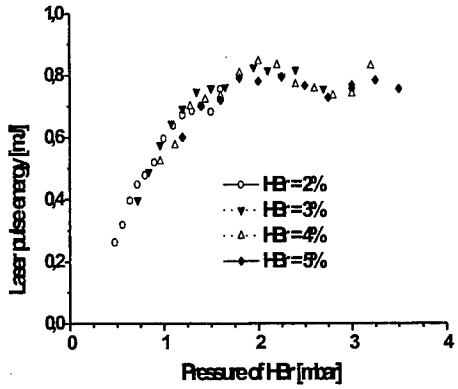


*Fig. 8 –Laser pulse energy as function of HBr pressure for different HBr concentrations.*

## 5. CONCLUSIONS

There is not a unique set of discharge parameters for the Cu-HyBrID work efficiently provided the pre-pulse electron density is maintained at the optimal range. We have shown that the pre-pulse electron density depends on several discharge parameters that can be controlled independently. As a consequence the laser pulse parameters can be varied in a wide without affecting the laser performance.


## ACKNOWLEDGMENTS

We wish to thanks FAPESP and PADCT for financial support.


## REFERENCES


1. D.W. Coutts, *IEEE J Quantum Electron*, **31**, pp 330-342, 1995
2. R. Riva, N.A.S. Rodrigues, J.T. Watanuki, B. Christ, C.Schwab, *Proceedings of Symposium on Laser and their Applications,* H.L. Fragnito, Ed, Campinas, SP, pp. 90-93, 1997.
3. D. R. Jones, S. N. Halliwell, C. E. Little, *Opt. Comm.,* **111**, pp. 394-402, 1994
4. R. Riva, J.T. Watanuki, N.A.S. Rodrigues, C.Schwab, in *Separation Phenomena in Liquids and Gases, Fifth Workshop Proc.,* C. Schwab, N.A.S. Rodrigues, and H.G. Woods, eds.,,pp. 241-243, 1996.
5. P. Persephonis, V. Gianettas, A. Ioannou, J. Parthenios, C. Georgiades, *IEEE J Quantum Electron,* **31**, pp 1779-1784, 1995.
6. G.P. Hogan, C.E. Webb, *Opt. Comm.,* **117**, pp-570-579, 1995
7. E. Le Guyadec, P. Coutance, G. Bertrand, C.Peltier, *IEEE J Quantum Electron,* **35**, pp 1616-1622, 1999.

Invited Paper

# CO Overtone Transition Lasers

Andrei A. Ionin*

P.N.Lebedev Physics Institute of Russian Academy of Sciences, Leninsky pr.53, 117924 Moscow, Russia

## ABSTRACT

A survey of experimental and theoretical results on physics of a CO laser operating on first-overtone (FO) vibrational transitions V+2→V is presented. A special attention is paid to quite new results recently obtained at the Lebedev Physics Institute (Russia), TRINITI (Russia) and Air Force Research Lab (USA). Efficient multiwavelength pulsed FO CO lasing with output efficiency up to 11% and specific output energy up to 50 J/l Amagat is observed within the spectral range of 2.5-4.1 μm corresponding to the vibrational transitions V+2→V from 6→4 up to 37→35. Single-line frequency tunable FO CO lasing on the wavelengths from ~2.7 up to 4.2 μm with the maximum output efficiency up to ~1% is also observed. Multiline and single-line lasing on 430 ro-vibrational lines is obtained. Theoretical calculations based on the experimental data predict that multiline FO CO laser efficiency can be enhanced up to 20%. The effect of "spectrum alternation", i.e. an alternation of strong and weak vibrational bands, in pulsed FO CO laser spectrum, which is determined by two sets of cascade transitions, is experimentally observed for the first time. An influence of nitrogen on spectral characteristics of a single-line FO CO laser operating on very high vibrational transitions up to 38→36, which is related to quasy-resonance overlapping of the transition with 0→1 transition of nitrogen molecule, is discussed. High efficiency and high specific output energy places the FO CO laser amongst other high-power lasers such as $CO_2$ laser, fundamental band CO laser and HF(DF) laser.

Key words: CO laser, overtone transition, vibrational-vibrational exchange, output efficiency

## 1. INTRODUCTION

Carbon monoxide laser is very attractive both for practical applications and for fundamental research[1-3]. From the practical point of view its high output efficiency and the possibility of achieving very high overage power are very important. Just because of the basic properties of the anharmonic oscillator[4,5], an inversion population between vibrational-rotational levels of the CO molecule is created by vibration-vibration exchange and lasing itself is possible not only in the fundamental band (FB) (V+1→V;λ≅4.63-8.23 μm [6,7] but also in the first-overtone (FO) (V+2→V, λ≅2.5-4.2 μm [8-10]) spectral band (Fig.1). The very opportunity of FO CO lasing is due to rather high probability of two-vibrational quantum transition V+2→V for anharmonic CO molecule, because Einstein coefficient $A_{v+2,v}$ for the FO transition V+2→V depends on the number of vibrational level V, the ratio $A_{v+2,v}/A_{v+1,v}$ increasing with the number V and even being higher than 1 for highly excited CO molecule transitions [11-13] (Fig.2). FO lasing on vibrational-rotational transition V+2→V; J→J+1 takes place with a frequency $\omega^{J\to J+1}_{V+2\to V}$ determined from the simple equation: $\hbar\omega^{J\to J+1}_{V+2\to V} = \hbar\omega^{J\to J+1}_{V+2\to V+1} + \hbar\omega^{J\to J+1}_{V+1\to V} + \Delta E_{rot}$ (Fig.3). The spectral range of FO CO laser covers that of well-known chemical HF-and DF-lasers, ro-vibrational lines spacing being several times less than that of those lasers. FO CO laser spectral lines coincide with a lot of absorption lines of numerous organic and nonorganic substances such as $H_2O$, $CO_2$, $CH_4$, $H_2O$, $NO_2$, NO, acetone, benzene, methanol, etc., etc[14](Fig.4). FO CO laser running on these wavelengths can be successfully used for resonance influence upon various media in nonlinear spectroscopy, atmosphere monitoring, laser chemistry, etc., long wavelength-range spectrum of FO CO laser coinciding with atmospheric "transparency window" and short wavelength-range radiation being effectively absorbed by water (Fig.4), which can be used in medical applications, for instance. The paper is a review of researches on FO CO laser, the main attention being paid to the quite new experimental and theoretical results jointly obtained by scientific team of the Lebedev Physics Institute (Russia), Troitsk Institute for Innovation and Fusion Research (TRINITI) (Russia) and Air Force Research Lab (USA). Theoretical calculations were performed by theoretical group of TRINITI headed by Prof.A.Napartovich.

## 2. FO CO LASER'S HISTORY

For the first time FO CO lasing was observed in chemical carbon monoxide laser[15]. FO CO laser characteristics were very poor: output power ~100 μW was ~1% of total chemical CO laser power. For electric discharge CO laser cw FO CO lasing was observed for the first time in[16], where supersonic expansion and cooling of pre-excited CO:He:$O_2$ mixture was used. Gas mixture CO:He:$O_2$= 78:92:1 at intracavity gas pressure 2.75 Torr and gas temperature ~40 K (Mach number 4.2) was used. The active gain path was 20 cm at the optical axis. The output mirror provided ~1% transmission and 99% reflectivity over a 2.6 - 3.1 μm band pass, the reflectivity being 30% in the 4.8 - 6.0 μm range of FB CO lasing. The rear cavity mirror was a 4-m radius-of-curvature total reflector with 99% reflectivity. FO CO lasing took place on 25

* Correspondence: E-mail: aion@sci.lebedev.ru; Phone/fax: 7(095)132 0425



XIII International Symposium on Gas Flow and Chemical Lasers and High-Power Laser Conference, Antonio Lapucci, Marco Ciofini, Editors, Proceedings of SPIE Vol. 4184 (2001)

ro-vibrational lines, ranging from P(5) line of V+2→V = 12→10 vibrational band at λ = 2.688 μm to the P(6) line of 21→19 at 3.066 μm. FO CO laser power and output efficiency was 20 W and 0.6%, respectively, total output power (FO+FB) being 88 W. Half a year later FO CO lasing was observed in pulsed e-beam controlled discharge (EBCD) CO laser[17] with active volume of ~5 l. A laser resonator was used with output mirror with reflectivity of ~84% for 2.8 - 3.2 μm spectral range and ~14% for 5.0 - 5.6 μm range. Laser mixture $CO:N_2:He$ = 1:9:10 at gas density 0.5 Amagat (Amagat is a reduced density unit corresponding to the number of moles in the one mole volume 22.4 l). Pump pulse length was 50 μs. The output energy was 9 J at specific output energy (SOE) 3.5 J/l Amagat and output efficiency 3.1%. The total (FO+FB) efficiency was 30%. FO CO lasing was observed within 2.7 - 3.0 μm spectral range corresponding to the vibrational bands V+2→V from 13→11 up to 16→14.

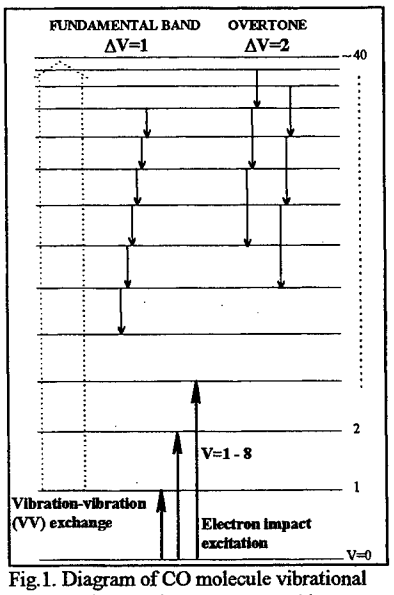

Fig.1. Diagram of CO molecule vibrational levels, main pumping processes and laser transitions

An optimization of pump conditions and output mirrors enabled authors of[18, 19] to extend FO CO lasing range up to 2.7 - 3.3 μm and to enhance SOE and output efficiency up to 10 J/l Amagat and 5%, respectively. FB CO lasing was not suppressed yet. Although the authors of[18, 19] carried out detailed parametric study of the FO CO laser, they failed in further increase of output efficiency and extension of lasing spectrum, which seemed to be due to poor characteristics of cavity mirrors. The maximum output energy of ~50 J at output efficiency of 5% and SOE 10 J/l Amagat was obtained in[20] for the FO CO laser with active volume of 10 liters. A lack of interest in such a laser emitting radiation strongly absorbed by water vapor and having low efficiency prevented from further progress in R&D of high-power FO CO laser in the 80's.

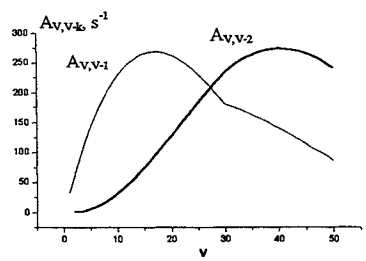

Fig.2. Einstein coefficients for fundamental and first-overtone transitions[13]

However, the interest in low-power FO CO laser, that could be used for spectroscopy, still existed. Single-line low pressure cw FO CO laser was developed in[21, 22], which operated on 330 ro-vibrational lines (150 lines in[21]) and was frequency tuned within spectral range of 2.62 - 4.07 μm corresponding to overtone transitions from 10→8 up to 37→35. The laser tube of 90 cm length and 13 mm in diameter was cooled by liquid nitrogen. The laser mixture $CO:N_2:He:Ar$ at gas pressure 17 mbar was pumped by a dc discharge. The laser cavity consisted of gold coated concave (R=10m) mirror and a reflection grating in Littrow configuration (450 grooves/mm). This laser having low output power of ~0.55 W (no data about output efficiency at all) quite recently was used for spectroscopic applications[23], which do not need high output power and output efficiency.

Theoretically the opportunity of achieving FO CO lasing in electric discharge laser was predicted in[24]. Numerical studies on characteristics of FO CO laser were performed also in[25]. Analytical theory of the steady state operation of FO CO laser was developed in[26]. Numerical calculations were performed in[27] on simultaneous FB and FO lasing. Because of the lack of experimental data on vibrational-vibrational exchange rates for highly excited levels of CO molecule, normally they use extrapolation of low-level kinetic constants for modeling lasing on high vibrational transitions[24-30]. For instance, basing on an agreement between the theory and experiment for FB CO laser operating on vibrational transitions from 5→4 up to 16→15, the authors of[30] used the same set of kinetic constants for an estimation of potential characteristics of supersonic FO CO laser operating on vibrational transitions up to 44→42 with output power up to 20 MW and output efficiency up to 34%. However, for such high vibrational levels the very applicability of the extrapolation method is questionable and has to be verified by a comparison of experimental and theoretical data.

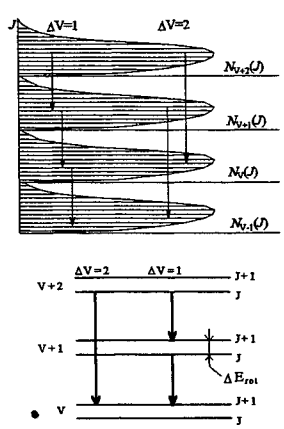


$$\hbar\omega_{V+2\to V}^{J\to J+1} = \hbar\omega_{V+2\to V+1}^{J\to J+1} + \hbar\omega_{V+1\to V}^{J\to J+1} + \Delta E_{rot}$$

Fig.3. Diagram of rotational distribution of population within vibrational levels of CO molecule and laser transitions

Such a comparison was done in[29], where multiline FO CO laser pumped by short (~1.5 μs) electric discharge pump pulse was researched both experimentally and theoretically. The authors of[29] observed rather good agreement between the theory and experiment, but FO CO laser spectrum range was rather narrow (11 lines on rather low vibrational transitions from 14→12 up to 19→17) and output

efficiency was rather low 1.2% at SOE 12 J/l Amagat.

Therefore, there had not been a FO CO laser, which had high efficiency, high SOE and spectrum overlapping with atmospheric "transparency window" until a scientific team of the Lebedev Physics Institute, TRINITI and the US AF Research Lab started their joint activity three years ago.

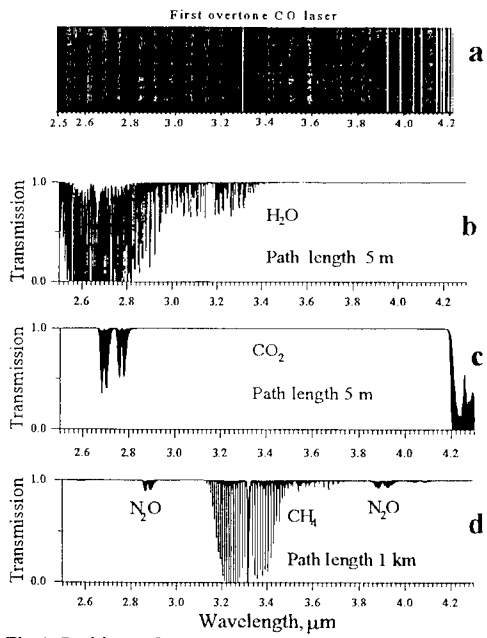


Fig.4. Positions of FO CO laser spectral lines (a). Linear transmission spectra of atmospheric water vapor (b), carbon dioxide (c), methane and nitric oxide (d) within 2.5-4.2 μm spectral region[14]

## 3. MULTILINE FO CO LASER

The experiments were carried out on cryogenically cooled EBCD laser facility with active length of 1.2 m. The active volume of the laser was determined by diameter of intracavity diaphragm and optics used in the experiments. The maximum e-beam current density was 20 mA/cm$^2$, with electron energy being 150 keV. The pump pulse length could be varied from 25 μs up to several ms, being 25 μs in most of the experiments. Specific input energy (SIE) changed from ~50 up to ~1000 J/l Amagat. Gas density varied within 0.05-0.5 Amagat. For obtaining multiline FO CO lasing we used both intracavity spectral filter and multilayer dielectric mirrors. To exclude an influence of FB CO lasing on FO CO laser characteristics and to make a comparison between the theory and experiment easier, intracavity spectral filters was used[13, 31-33]. The filters were made of fused silica of 2 mm (thick) and 0.5 mm (thin) thickness. The laser resonator consisted of two totally reflected copper mirrors (plane and concave). Laser radiation was extracted out of the resonator due to Fresnel reflection from both sides of the filter. By using the thin filter we extended FO CO laser spectrum up to 3.6 μm. Lasing took place an vibrational transitions from 13→11 up to 25→23 (λ=2.7- 3.6 μm). When using the thin filter, output efficiency was 5.5% at SOE 20 J/l Amagat. FB lasing was totally suppressed. Knowing all intracavity optical losses, theory using the experimental data, predicted for FO CO laser efficiency to be up to 20%[31-33].

When using dielectric mirrors, the 2.2 m laser resonator consisted of two spherical concave multilayer mirrors with radius of curvature of 10.0 (15.0) m or of spherical and flat mirrors situated on the laser chamber. Therefore, we excluded the influence of atmospheric air upon the laser characteristics, which can be considerably strong[13, 31-33]. Various sets of mirrors made in Russia (M1+M2, M2+M2) and made in the United States (M92+M92, M98+M98, M92+M99) were used (two laser mirrors in one set). The effective reflectivity $R=(R_iR_j)^{1/2}$ (i, j=1, 2) for the mirror of the equivalent laser resonator is presented in Fig.5. To suppress FB lasing, special attention was paid to the reduction of a mirrors' reflectivity for wavelengths longer than 4.8 μm, which corresponded to the FB spectral region. Just for the suppression of FB lasing, two dielectric mirrors were used instead of one together with a metal mirror used in earlier papers[17-20]. The active laser volume determined by mirror size and intracavity diaphragms was 2.3 l for the Russian mirrors and 0.85 l for US mirrors. Taking into account a high feasibility of destruction of dielectric mirrors in a high Q-factor laser resonator at relatively low output laser intensities, and our previous results[31-33] demonstrating that the best FO CO laser efficiency was obtained at a gas density of 0.1 - 0.2 Amagat, the experiments were carried out at a low density 0.12 Amagat of gas mixture $CO:N_2:He$ = 1:9:10 at an initial temperature 100 K. Output spectra of the FO CO laser using various resonators consisting of sets of mirrors (M1+M2, M2+M2) and (M92+M92, M98+M98) are presented in Fig.5 together with spectral characteristics of the mirrors (a vertical scale for each lasing band (FO and FB) is different). FB lasing was suppressed only for the laser with the resonator consisting of the mirror set M2+M2. When using other mirror sets, despite FB lasing, the FO CO laser operated on high vibrational transitions with wavelengths up to ~ 4.1 μm (M92+M92 set) and on lower transitions down to ~ 2.5 μm (M1+M2 set). When the M1+M2 set was used, the short-wave spectrum boundary

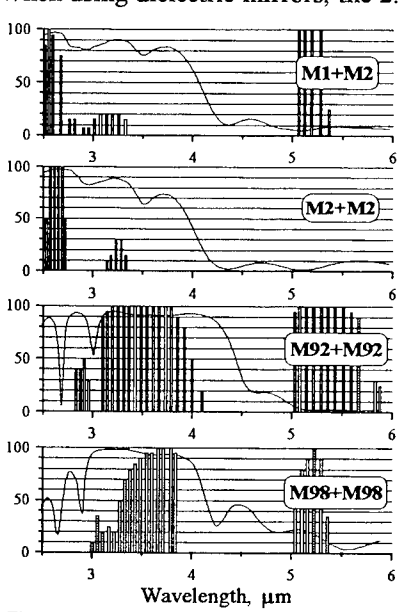


Fig.5. Spectral dependence of effective reflectivity for different mirror sets and corresponding CO laser spectrum (overtone and fundamental band) for four laser resonators consisting of mirrors M1, M2, M92 and M98. $CO:N_2:He$ = 1:9:10; N = 0.12 Amagat; T = 100 K; SIE is 300 J/l Amagat[8, 9]

corresponded to vibrational transition 6→4 with wavelength 2.51 μm. A very weak laser line, corresponding to the 37→35 vibrational transition at the longer wavelength of 4.09 μm, was observed when the M92+M92 set of mirrors was used (Fig.5). Thus, the multiline pulsed FO CO laser operates in the wavelength region 2.5 - 4.1 μm, with the laser spectrum contents being determined by the spectral characteristics of the equivalent mirror. The SOE of ~25 J/l Amagat for the FO CO laser was obtained when using the M98+M98 set of mirrors. For the same set, FB CO laser SOE reached ~20 J/l Amagat. Output efficiency came up to 11% for the FO CO laser (Fig.6), with the FB CO laser efficiency reaching up to 9%. Therefore, the total CO laser efficiency (FO+FB) was 20%. The SIE growth up to ~700 J/l Amagat (M92+M99 mirror set) resulted in a SOE of ~50 J/l Amagat. For the M98+M98 mirror set, we limited SIE because of the danger of multilayer laser mirrors damaging due to a high total (FO+FB) energy density.

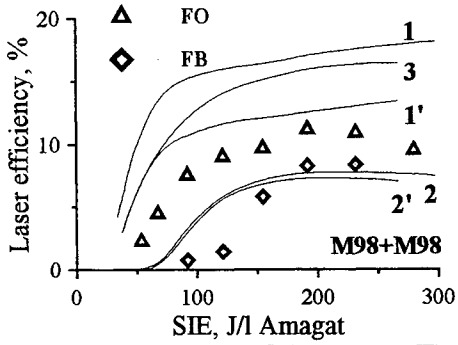


Fig.6. Laser efficiency vs. specific input energy (SIE) for mirror set M98+M98 (experiment -points; theory - curves) Theoretical results: 1, 1', 3 - first-overtone (FO) lasing; 2, 2' - fundamental band (FB) lasing 1, 2 - base model; 1', 2' - additional nonselective optical losses are included (0.5% per single pass); 3 - FB lasing is assumed to be suppressed, additional optical losses are the same $CO:N_2:He=1:9:10$; N=0.12 Amagat; SIE=300 J/l Amagat; T=100 K [9]

Theoretical modeling of the FO CO laser for conditions corresponding to the experiments involving the US mirrors was performed for the mirror set M98+M98. Experimentally measured cavity parameters were included in the model, which essentially coincide with the earlier published model [13, 29, 31-33]. The only difference was that, at present, in this model the laser transitions in the fundamental band were also included. Therefore, it was possible to simulate simultaneous lasing in both bands (first-overtone and fundamental). High values of the reflection coefficient for the mirrors made laser characteristics more sensitive to an exact magnitude of additional intracavity optical losses not included in the model, i.e. diffraction loss and optical loss depending on gas refractive index gradients. In Fig.6, calculated laser efficiency for FO (curve 1) and FB (curve 2) lasing is compared with the experimental data for the mirror set M98+M98. The FO laser efficiency predicted is about 1.5 times higher than measured in the experiments, while the efficiency for the FB lasing is described more or less satisfactorily. To evaluate the sensitivity of calculations to the exact value of the intracavity loss, additional optical losses were introduced equal to 0.5% per single pass. The result of the theoretical predictions is shown in Fig.6 (curve 1' for the FO and curve 2' for the FB efficiency, respectively). It can be seen that the FO curve came closer to experimental points while the FB efficiency is insensitive to the variation of losses. Calculations of the FO laser efficiency for the same cavity, assuming that FB lasing is totally suppressed, yielded curve 3 in Fig.6. This means that additional absorption of radiation in the fundamental band can lead to further increase of the FO laser efficiency up to 15-17%. Application of optimal laser mirrors (no spectral holes within 2.5-3.0 μm region) will increase the output efficiency up to 20% [13, 31-33].

## 4. SINGLE-LINE PULSED FO CO LASER

The FO CO laser resonator consisted of a diffraction grating operating in Littrow configuration and concave (r=10 m) copper mirror, the former being located at a distance of 0.4 m from Brewster window made of $CaF_2$ and the latter being installed at the laser chamber. Polarization plane of intracavity radiation was perpendicular to grating grooves (S-polarization). The laser resonator length was 2.5 m. There were two diaphragms inside the laser resonator with diameter 50 mm near the copper mirror and ~30 mm near the grating. The optical volume was 0.85 *l*. FO CO laser radiation was extracted through the zero diffraction order of the grating. The different diffraction gratings were used for spectral selection and tuning of FO CO laser radiation. The gratings were made of Al coated glass and had 200 grooves per mm. When using one of the grating (G1), FO CO laser radiation was frequency tuned within spectral range of 2.7 - 4.1 μm corresponding to the overtone vibrational transitions from 12→10 up to 37→35. Maximum output efficiency was ~0.1% for the wavelength 3.34 μm (ro-vibrational transition 28→26 P(11)). Nitrogen free laser mixture CO:He = 1:4 was used at gas density 0.12 Amagat (SIE was 320 J/l Amagat).

Fig.7 demonstrates FO CO laser efficiency for another grating (G2) versus wavelength when using gas mixtures CO:He=1:4 (Fig.7a) and $CO:N_2=1:6$ (Fig.7b) at gas density 0.12 Amagat. When using $CO:N_2$ gas mixture, laser efficiency came up to ~ 0.6% (Fig.7b) at the wavelength 3.8 μm. For CO:He mixture laser efficiency was ~ 0.1%. However, for lasing on higher vibrational band helium free laser mixture was not so good. For example, lasing on 38→36 vibrational transition was not observed at all, when using $CO:N_2$ mixture. It should be noted that addition nitrogen with concentration more than 10% to the helium mixture CO:He=1:4 suppressed lasing on that vibrational transition. Thus, with the grating G2 the longest wavelength obtained for gas mixture CO:He=1:4 was 4.16 μm (Fig.7a) (38→36 transition) and 4.03 μm (Fig.7b) (37→35 transition) for $CO:N_2=1:6$ gas mixture. The phenomenon is related to V-V exchange resonance between

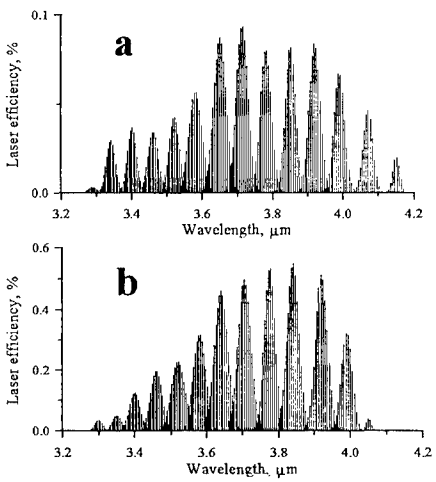


Fig.7. Output laser efficiency for two different gas mixtures (a, b) vs. wavelength. Diffraction grating G2 Gas density 0.12 Amagat CO:He=1:4; SIE = 320 J/l Amagat (a); $CO:N_2$=1:6; SIE = 500 J/l Amagat (b) [10]

40→38 overtone vibrational transition of CO molecule and 0→1 fundamental vibrational transition of $N_2$ molecule (see below).

By using the gratings frequency tunable single-line FO CO lasing was observed within spectral region 2.71-4.17 μm on 413 ro-vibrational lines. The lack of lasing at wavelength shorter than ~2.7 μm can be related to atmosphere water vapor being in laser resonator between Brewster window and a grating over the distance of 0.4 m. Taking into account ro-vibrational lines observed for multiline lasing on lower vibrational transition, altogether 430 ro-vibrational lines were detected in the experiments. It should be noted that single-line pulsed FO CO lasing was obtained on highly excited CO molecule transitions. Small signal gain measured for these transitions by introducing calibrated intracavity optical losses came up to ~0.3-0.4 $cm^{-1}$.

## 5. FO CO LASER SPECTRUM FORMATION

Quite interesting effects of spectrum formation are experimentally observed for FO CO laser operating both in multiline and single-line mode of operation. The effect of "spectrum alternation" (i.e. an alternation of strong and weak vibrational bands) in multiline pulsed FO CO laser spectrum was experimentally observed [34](Fig.8). The effect was theoretically predicted in Ref.[35], however has never been observed before our experimental research. The "spectrum alternation" is caused by two sets of cascade transitions (Fig.1) operating independently, which can happen if the rate of radiative transitions is much higher than that of vibrational-vibrational exchange.

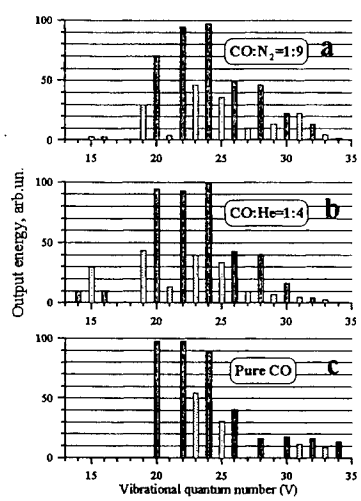


Fig. 8. "Zebra-like" spectra for FO CO laser operating on various laser mixtures $CO:N_2$=1:9 (a), CO:He=1:4 (b) and pure CO (c). N=0.12 Amagat, T=100 K [34]

An alternation of FO CO laser output energy over vibrational bands ("zebra-like" spectrum) was observed for a laser mixture of $CO:N_2:He$=1:9:10 at gas density of 0.12 Amagat in[34]. Although, there was mentioned in Ref.[35] that the "spectrum alternation" took place in nitrogen containing laser mixture only, the effect was also experimentally observed for various gas mixtures $CO:N_2$=1:9, CO:He=1:4 and pure CO (Fig.8a-c). Two sets of vibrational bands corresponding to two different lasing cascades are designated by gray and black bars. The "spectrum alternation" was observed for different gas density varying within 0.02-0.3 Amagat.

Another effect of FO CO laser spectrum formation is suppression of single-line lasing on the highest vibrational transition 38→36 when adding a small amount of nitrogen (Fig.7, see above). The change of single-line FO CO laser spectrum seems to be related to specific kind of intermolecular V-V exchange - two vibrational quantum for one: $CO(V)+N_2(0)\rightarrow CO(V-2)+N_2(1)$. The result of numerical calculations[36], which confirms the idea, is presented in Fig.9.

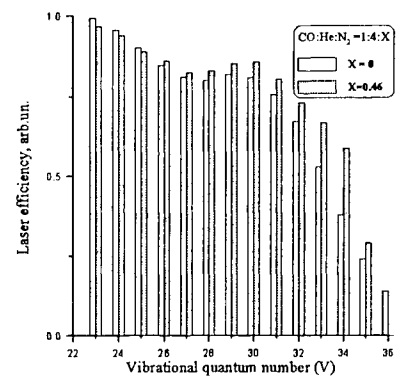


Fig.9. Output laser efficiency vs. vibrational quantum number V (V+2→V) for two different laser mixture $CO:He:N_2$=1:4:X, where X = 0; 0.46[36].

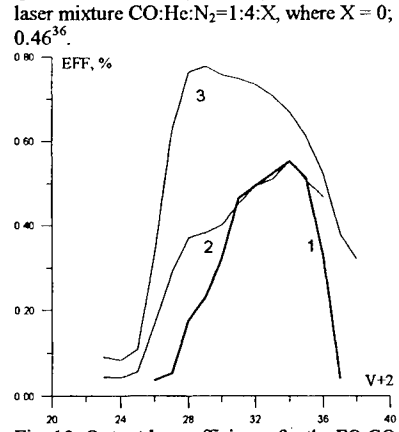


Fig. 10. Output laser efficiency for the FO CO laser [36] vs. vibrational transition V+2→V. 1 - experiment; 2, 3 - results of simulation by multi- and single-quantum models (2 - multiquantum, 3 - single-quantum).

It should be noted that so-called multiquantum vibration exchange model was used for above calculations, which took into consideration multiquantum exchange processes: $CO(V)+CO(U)\rightarrow CO(V-n)+CO(U+n)$ (n>1) in addition to single-quantum exchange process (n=1). An application of multiquantum model is extremely important for a description of kinetics of highly excited vibrational levels of CO molecule[37], i.e. just for levels on which FO CO laser runs. Single-line FO CO laser spectrum (so-called tuning curve) was calculated by using multi- and

single-quantum models (Fig.10) and compared with experimental results. It can be clearly seen that the multiquantum model produces much better agreement with the experimental data than the single-quantum one.

## 6. CONCLUSIONS

Pulsed FO CO laser operates in the wide IR spectral region from 2.5 up to 4.1 μm, on vibrational transitions from 6→4 up to 37→35 as broad band dielectric mirrors are used for a laser resonator. FO CO laser spectrum (vibrational bands position) is strongly depends on spectral characteristics of laser mirrors. Using dielectric mirrors with high reflectivity within extended spectral range and with low useless optical losses enabled us to enhance pulsed FO CO laser efficiency up to 11%. The results of the theoretical calculations are in a good agreement with the experimental ones. Basing on these results the theory predicts, that FO CO laser efficiency can be as 15 - 20%. Tunable FO CO lasing on wavelength from 2.7 up to 4.2 μm corresponding to overtone vibrational transitions from 13→11 up to 38→36 was obtained. The maximum SOE came up to ~ 3 J/l Amagat, with single-line output efficiency being up to 0.6%. Multiline and single-line lasing was observed on 430 ro-vibrational lines. Although these results were obtained for cryogenically cooled FO CO laser, theoretical calculations predict that the laser can successfully operate at room temperature with output efficiency 1-3% (SIE=530 J/l Amagat, $T_0$=278K, p=413 Torr, $CO:N_2:He$=12.5:37.5:50, E/N=1.5 $10^{-16}$ V $cm^2$)[36]. The prediction was quite recently confirmed in Ref.[38], in which 2% output efficiency was experimentally obtained for repulsed FO CO laser operating at room temperature within ~2.8-3.3 μm spectral region by using EBCD laser facility operating before as fundamental band CO laser[38, 39]. High efficiency and high specific output energy obtained just places the FO CO laser amongst other high-power lasers such as $CO_2$ laser, FB CO laser, HF(DF) laser, its spectrum region covering that of HF and DF lasers and the number of spectral lines, many of which coincide with absorption lines of many substances, being much higher. FO CO laser can be considered as a new efficient source of high-power IR radiation which can be used for different applications.

## REFERENCES


1 A. Ionin and I. Spalding "CO-lasers - state of the art and potential of applications" in Gas Lasers - Recent Developments and Future Prospects, Ed. by W.J. Witteman and V.N. Ochkin (NATO ASI Series, 3. High Technology - Vol. **10**, pp. 279-289, 1996).
2 A.P.Napartovich, "Physics of high-power CO laser", *ibid*, pp. 11-22.
3 A.A.Ionin, Proc. SPIE, **3889**, p.424, 2000
4 C.E. Treanor, J.W. Rich, R.G. Rehm, J.Chem.Phys. **48**, p.1798, 1968
5 J.W. Rich, J. Appl. Phys. **42**, p.2719, 1971
6 J.Yardley, *J.Mol. Spectr.*, **35**, p.314, 1970
7 J.E.McCord, A.A.Ionin, S.P.Phipps et al, Proc. SPIE, **3889**, p.691, 2000
8 A.A. Ionin, A.A. Kotkov, A.K. Kurnosov, A.P. Napartovich et al, *Opt. Comm.* **160**, p.255, 1999
9 N.Basov, G.Hager, A.Ionin, A.Kotkov et al, *Opt.Comm.*, **171**, p.107, 1999
10 N.Basov, G.Hager, A.Ionin, A.Kotkov et al, Proc. SPIE, **3889**, p.482, 2000
11 N.N.Sobolev and V.V.Sokovikov, *Uspekchi Fizicheskikch Nauk*, **110**, #2, p.191, 1971 (in Russian)
12 S.D.Rockwood, J.E.Brau, W.A.Proctor et al, IEEE J.Quantum Electronics, **QE-9**, p.120, 1973
13 A.Ionin, Yu.Klimachev, A.Kotkov, A.Kurnosov, A.Napartovich et al, Preprint #11 of Lebedev Physics Institute, pp. 1-55, 1998
14 O.G.Buzykin, A.A.Ionin, S.V.Ivanov et al, Preprint #12 of the P.N.Lebedev Physics Institute, pp.1-31, 2000,
15 F.G.Sadie, P.A.Buger and O.G.Malan, *J.Appl.Phys.*, **43**, p.2906, 1972
16. R.C.Bergman, J.W.Rich, *Appl.Phys.Lett.* **31**, p.597, 1977
17 N.G.Basov, V.A.Danilychev, A.A.Ionin et al, *Kvantovaya Electronika*, **5**, p.1855, 1978 (in Russian)
18. N.G.Basov, V.S.Kazakevich, I.B.Kovsh, *Kvantovaya Electronika*, **7**, p.1966, 1980 (in Russian)
19. N.G.Basov, V.S.Kazakevich, I.B.Kovsh, *Kvantovaya Electronika*, **7**, p.1973, 1980 (in Russian)
20. N.G.Basov, A.A.Ionin, I.B.Kovsh, *Infrared Physics*, **25**, p.47 (1985)
21. M. Gromoll-Bohle, W. Bohle and W. Urban, *Opt. Comm.*, **69**, p.409, 1989
22. E.Bachem, A.Dax, T.Fink et al., *Appl. Phys.* **B57**, p. 185, 1993
23. M.Murtz, B.Frech, P.Palm et al., *Optics Lett.*, **23**, p.58, 1998
24. Yu.B.Konev, I.V.Kochetov, A.K.Kurnosov, V.G.Pevgov, *Pis'ma v ZhTF*, **3**, p.1267, 1977 (in Russian)
25. A.F.Suchkov, Y.N.Shebeko, *Kvantovaya Electronika*, **6**, p.960, 1979 (in Russian)
26. S.A.Zhdanok, I.V.Kochetov et al, *Inzhenerno Fizicheskii Zhurnal*, **38**, p.273, 1980 (in Russian)
27. Yu.B.Konev, I.V.Kochetov et al, *Inzhenerno Fizicheskii Zhurnal*, **41**, p.514, 1981 (in Russian)
28. V.I.Dolinina, I.B.Kovsh et al,. *Kvantovaya Electronika*, **10**, 6, p.1228, 1983 (in Russian)
29. A.D.Belykh, V.A.Gurashvili, A.P.Napartovich et al, *Kvantovaya Electronika*, **22**, p.333, 1995 (in Russian)
30. B.S.Aleksandrov, V.A.Belavin, B.M.Dymshyts et al,. *Kvantovaya Electronika*, **24**, 7, p.601, 1997 (in Russian)
31. A.Ionin, A.Kotkov, A.Kurnosov, A.Napartovich et al, Proc. Int. Conf.LASERS'97, Dec 1997, New Orleans, LA, USA, STS Press, p.92, 1998
32. A.Ionin, A.Kotkov, A.Kurnosov, A.Napartovich et al, Int. Conf. Photonics West'98, Jan 1998, San Jose, CA, USA, Proc. SPIE, **3268**, 1998
33 A.Ionin, A.Kotkov, A.Kurnosov, A.Napartovich et al, *Opt. Comm.* **155**, p.197, 1998
34 A.Ionin, A.Kotkov, A.Kurnosov, A.Napartovich et al, *Opt. Comm.* **178**, p.377, 2000
35 A.F.Suchkov and Yu.N.Shebeko, Sov.J.Quantum Electron., **9**, p.565, 1979
36 N.Basov, A.Ionin, A.Kotkov, A.K.Kurnosov et al, Preprint #17 of the P.N.Lebedev Physics Institute, p.1-55, 2000 (in Russian)
37 A.A.Ionin, Yu.M.Klimachev, Yu.B.Konev et al, Preprint #70 of the P.N.Lebedev Physics Institute, p.1-45, 1999
38 W.L.Bohn, Int.Symp. "High-Power Laser Ablation 2000", 23-28 Apr. 2000, Santa Fe, NM, USA, Adv.Tech.Program, paper 4065-58
39 A.Ionin, W.Mayerhofer, S.Walter, E.Zeyfang, Proc.SPIE, **2502**, p.44, 1995

# Room-temperature repetitively pulsed CO overtone laser

E. Zeyfang, W. Mayerhofer, S. Walther

DLR Stuttgart, Institut für Technische Physik
Pfaffenwaldring 38-40, D-70569 Stuttgart, Germany

## ABSTRACT

Experimental results on a pulsed e-beam sustained discharge CO laser are reported. The gas was cooled down to a temperature of 5° C, the active volume was 1.5 l. Optimizing gas composition, gas pressure, and output mirror reflectivity, pulse energies up to 8 J corresponding to a specific value of 16 J / lbar could be demonstrated. The spectrum of the laser radiation was analyzed, lines between 2.8 and 3.3 µm were found. In burst mode operation, up to 100 pulses at pulse frequencies up to 30 Hz have been achieved, resulting in an average laser power of 60 W.

**Keywords:** CO overtone laser, repetitively pulsed, room-temperature operation

## 1. INTRODUCTION

Operating a CO laser in the first overtone regime, a great number of laser lines in the very interesting wavelength range between 2 µm and 5 µm can be produced. Up to now only results from experiments at cryogenic gas temperatures have been published [1,2]. Based on experiments running as a fundamental mode CO laser at room temperature [3], investigations on the multispectral laser of the Institut für Technische Physik operating as first overtone CO laser ( gas temperature ≈ 5° C ) have been carried out ( $\lambda = 2.5 - 3.5$ µm ).

## 2. EXPERIMENTAL SET-UP

The Institute's multispectral laser has been developed from a pulsed $CO_2$ laser towards a reliable and powerful test bed for different laser gases [4]. Fig. 1 shows a schematic cross section , Fig. 2 the beam exit side of the laser. The laser gas is excited in a volume of 12 l ( 10x10x120 $cm^3$ ) by means of an e-beam sustained pulsed discharge. To exchange the gas in the discharge region and to remove loss energy, the laser gas is circulated by three axial blowers and cooled in a heat exchanger

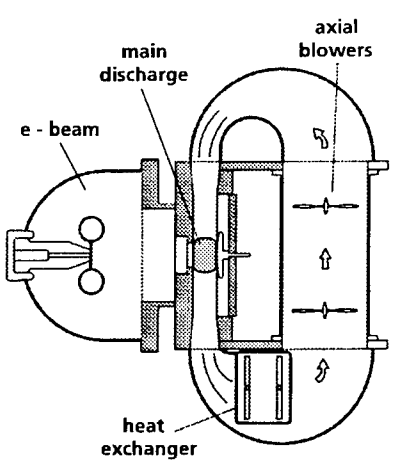


Fig. 1. Multispectral laser test-bed, schematic.

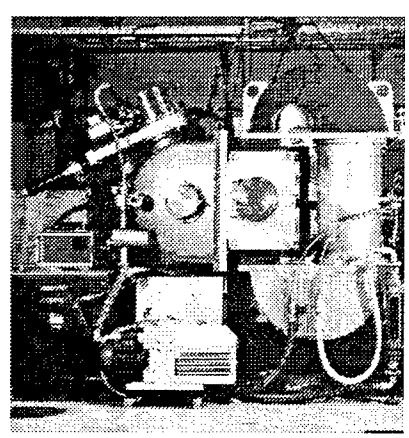

Fig. 2. Multispectral laser with stable resonator, beam exit side.



XIII International Symposium on Gas Flow and Chemical Lasers and High-Power Laser Conference,
Antonio Lapucci, Marco Ciofini, Editors, Proceedings of SPIE Vol. 4184 (2001)

down to a minimum of 5° C. The laser gas was a mixture of CO, $N_2$, and He which was purified during filling by means of a liquid Nitrogen cooled Zeolith filter.
To reduce costs, ZnSe output mirrors of 2" diameter have been chosen, resulting in a beam diameter of 4 cm and a reduced active volume of 1.5 l. The concave Cu end mirror had a radius of curvature of 13 m.

## 3. SINGLE PULSE OPERATION

### 3.1 Optimization of output mirror transmission and gas mixture

To determine the optimal operation parameters of the overtone laser, three different output mirrors with a transmission of T=1%, T=2%, and T=3% resp. at $\lambda = 2.7 - 3.3$ µm and T > 90% at $\lambda = 4.8 - 6$ µm have been investigated at different gas mixtures. Gas pressure was 400 mbar, gas temperature between 5° C and 7° C. The Helium fraction was held constant at 50%, the CO and $N_2$ fraction was varied between 5% CO / 45% $N_2$ and 20% CO / 30% $N_2$ respectively. The results are shown in Fig. 3. The maximum pulse energy was measured at a CO fraction of 12.5% for all three mirrors. If not mentioned otherwise, all the following experiments have been performed using this optimal gas mixture and the output mirror with a transmission of T=3%.

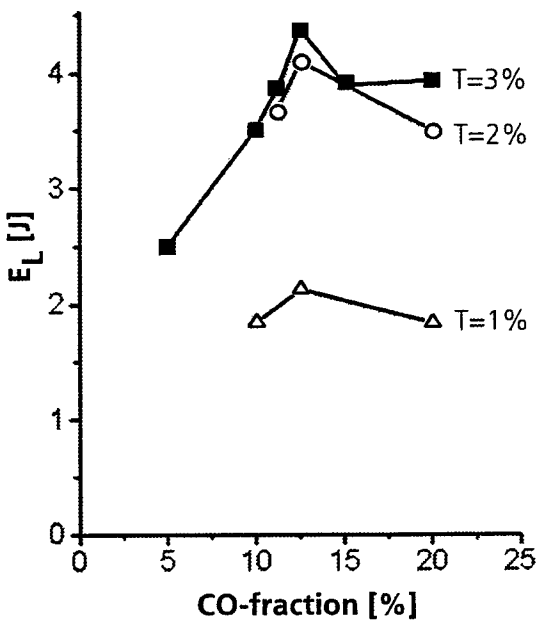


Fig.3. Influence of gas mixture and output mirror transmission T on pulse energy, main discharge loading voltage 44 kV

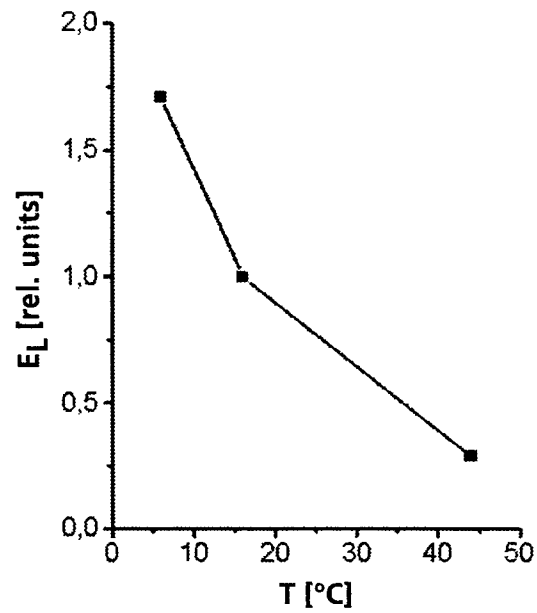


Fig. 4. Laser pulse energy as a function of gas temperature T; $E_L$=1 J at T=16° C

### 3.2 Influence of gas temperature and gas pressure

The influence of the gas temperature on the laser performance is shown in Fig. 4. The laser pulse energy was about 1J (100%) at T=16° C, it rises to 170% at T=6° C and falls to about 30% at T=44° C. These results are preliminary because the experiment was carried out before optimizing the laser parameters.
Fig. 5 shows the dependence of the pulse energy on the gas pressure. A maximum of 7 J was measured at a pressure of 325 mbar. At lower pressures the laser pulse energy decreases rapidly caused by the growing instability of the main discharge.

### 3.3. Laser pulse energy as a function of the discharge energy

Varying the main discharge loading voltage up to 48 kV, corresponding to a discharge energy of 346 J in 1.5 l active volume, the laser output energy was measured at gas pressures of 400 mbar and 325 mbar ( Fig. 6 ). The maximum pulse energy achieved was 8.2 J for 325 mbar. This corresponds to a specific pulse energy of 16.8 J/lbar and a electrical efficiency of 2.4%. For comparison, a typical result for fundamental operation is also given in Fig. 6.

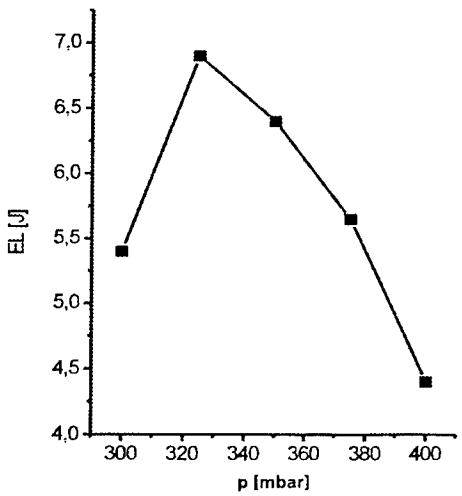


Fig. 5. Laser pulse energy vs. gas pressure, loading voltage 46 kV

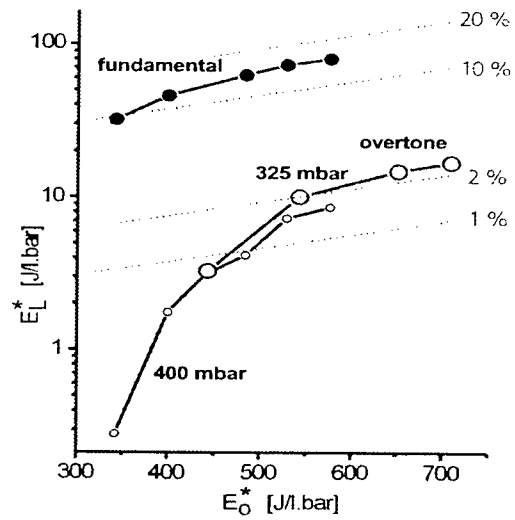


Fig. 6. Spec. laser pulse energy vs. spec. discharge energy, ----- electrical efficiency

### 3.4. Laser pulse form

To determine the laser pulse form, measurements of the laser output power as a function of time have been carried out using an Ulbricht integrating sphere and a fast photoelectromagnetic detector. An example of the results is given in Fig.7 for a laser pulse energy of 4.4 J. Typical for a CO laser is the delay between the discharge pulse at t=0 ( duration 8 μs ) and the onset of the laser pulse, as well as the long pulse duration of more than 100 μs. Both the delay and the length of the pulse are varying with the discharge energy.

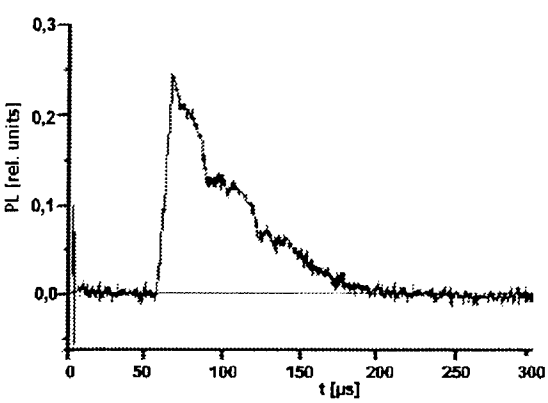


Fig. 7. Laser pulse form, laser energy 4.4 J

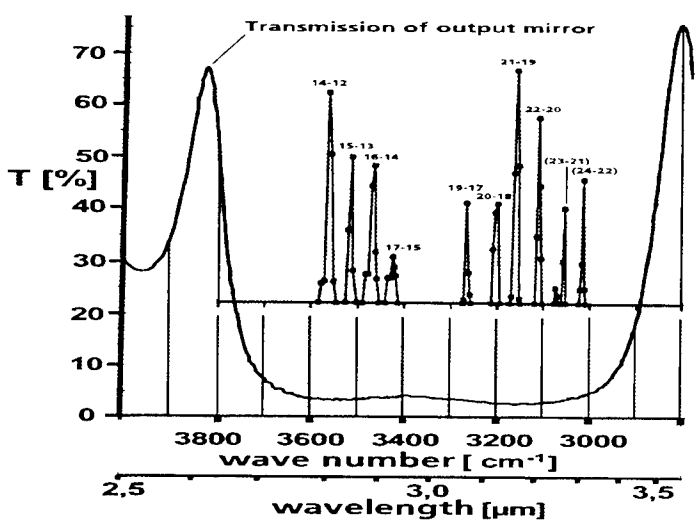


Fig. 8. Spectrum of CO overtone laser together with transmittance curve of the output mirror

### 3.5. Spectrum of the CO overtone laser

Using one of the laser mirrors as a filter with T<1% at 2.7 – 3.3μm and T=99% at 4.8 – 6 μm it could be verified that the CO laser was operating in the overtone regime only. To check the wavelength distribution, a very sensitive Joulemeter with a detector surface of 1x1 $mm^2$ was moved along the exit slit of a spectrum analyzer. The resulting spectrum together with the transmissivity of the output mirror is shown in Fig. 8. Each "spectral line" includes a multitude of rotational transitions, which could not be resolved by the measuring arrangement. The numbers of the vibrational bands are depicted at the corresponding spectral peaks.

## 4. REPETITIVE OPERATION

To investigate the laser performance in the repetitive mode, bursts of up to 200 pulses at pulse frequencies of up to 30 Hz have been run. The pulse energy was 2 J, resulting in a mean output power of 60 W. After 100 pulses at 20 Hz ( Fig. 9 ) no degradation of the pulse energy could be observed. The laser gas temperature remained constant at 5° C at the entrance of the discharge region.

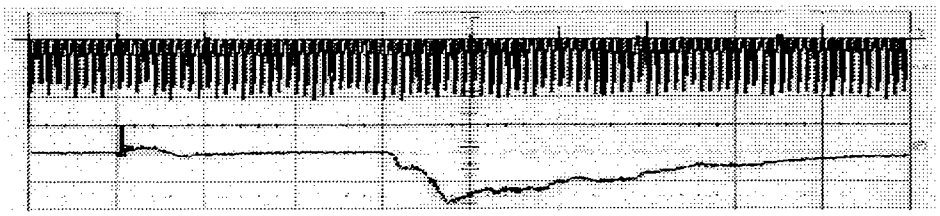

Fig. 9.
Top:
burst of 100 pulses at 20 Hz pulse frequency, pulse energy 2 J
Bottom:
single pulse ( zoomed ), time scale 20 µs/div

## 5. SUMMARY

The DLR multispectral laser can be operated reliably and reproducibly near room temperature in the CO first overtone regime at wavelengths between 2.8 and 3.3 µm. In table 1 the optimal results obtained at a gas temperature of 5° C are summarized, the potential for the total discharge volume of 12 l and typical results of the fundamental mode operation are added for comparison.

| | | Overtone | | Fundamental | |
|---|---|---|---|---|---|
| | Active volume [ l ] | **1.5** | 12 | **1.5** | 12 |
| Single pulse | max. pulse energy [ J ] | **8** | 64 | **42** | 335 |
| | electr. efficiency [ % ] | **2.4** | | **15** | |
| Repetitive | pulse energy [ J ] | **2** | 16 | **24** | 190 |
| | pulse frequency [ Hz ] | **30** | | **30** | |
| | number of pulses | **100** | | **100** | |
| | mean laser power [ W ] | **60** | 480 | **720** | 5800 |

Table 1. Experimental results of the CO laser ( **1.5 l active volume**, overtone and fundamental operation ) and extrapolation to the full active volume of 12 l

Concerning long term operation, the damage resistance of the mirror coatings must be increased and the problem of gas degradation has to be solved. Carbon dioxide produced in the discharge can be removed by means of a Zeolith filtering system which has been demonstrated successfully in cw CO laser operation. More critical is the outgasing of impurities from laser structural components. This problem has to be investigated thoroughly and can be avoided by the selection of suitable materials.

## 6. REFERENCES


1. A. Ionin et al., "Experimental and theoretical study on first overtone carbon monoxide laser physics", Lebedev Physical Institute Preprint No. 11, Moskow 1998.
2. N. G. Basov et al., "Efficient Pulsed First-Overtone CO Laser Operating Within the Spectral Range of 2.5-4.2 µm", *J. Quantum Electronics*, **36,** No. 7, pp. 810-823, 2000.
3. A. Ionin, W. Mayerhofer, S. Walther, E. Zeyfang, "Roomtemperature repetively pulsed e-beam sustained carbon monoxide laser", 10th Int. Symp. Gas Flow and Chem. Lasers, Proc. SPIE 2502, pp. 44-49, 1995.
4. W. Mayerhofer, E. Zeyfang, W. Riede, "Design data of a repetitively pulsed 50 kW multigas laser and recent experimental results", 12th Int. Symp. GCL/HPL, Proc. SPIE 3574, p. 644, 1998.

# MULTIQUANTUM VIBRATIONAL EXCHANGE IN VIBRATION EXCITED CO MOLECULES

A.A.Ionin, Yu.M.Klimachev, Yu.B.Konev*, A.A.Kotkov, A.K.Kurnosov**, A.P.Napartovich**, L.V.Seleznev, D.V.Sinitsyn, Yu.V.Terekhov

P.N.Lebedev Physics Institute, 53, Leninsky Prosp., 117924, Moscow, Russia
* Institute of High Temperatures, 13/19, Izghorskaya Str., 127412, Moscow, Russia
** Troitsk Institute for Innovation and Fusion Research, Troitsk, 142092, Moscow Region, Russia

## ABSTRACT

Studies of vibration-vibration exchange in CO molecules excited up to vibration quantum numbers v=20 are performed both theoretically and experimentally. New kinetic model taking into account multi-quantum VV exchange in temperature range T=100÷300K is described for the first time. Description of the experimental methodology allowing for studies of effects of relaxation of the vibrational distribution after a sudden disturbance is given. The disturbance of the vibrational distribution is produced by Q-switched short pulse of single line radiation in fundamental band. The relaxation is studied by measuring laser pulse energy of the second pulse initiated by resonator Q-switching produced with variable time delay relative to the first pulse. A set of kinetic rate constants accepted in the model for various gas temperatures, vibration level numbers and number of exchanged vibration quanta from 1 to 4 is presented. Good agreement between experimental data and results of the advanced theory is the first direct evidence in support of multi-quantum exchange model.

**Keywords:** vibration exchange, kinetic model, multi-quantum exchange, rate constants, CO molecules

The formation of inverse population in CO laser is grounded on fine peculiarities of VV exchange of molecules excited in high vibration levels[1]. This fact was important practical reason, strongly stimulated the studies of VV exchange kinetics. Historically, the first, as the most simple, single-quantum exchange (SQE)[2-5]model. This model has no strong physical background and was never verified for calculations of VV-exchange rates of highly excited CO molecules. Nevertheless, SQE model was widely used in practical calculations. Its justification was based on rather satisfactory agreement between calculated and measured steady state vibrational distribution function (VDF)[6].

Multi-quantum exchange (MQE) processes in CO were calculated later[7-10]. A set of rate constants (RC) from Ref. 10, given at low temperature T≈100 K for vibrational levels v>5, was incorporated in CO vibrational kinetics model[11,12]. The results were a satisfactory agreement with measured of steady state VDF. The calculations[11,12] also demonstrated that transient behavior of the VDF after frequency selective perturbation is quite different in both models for high vibrational levels (v=20÷25), but very similar for lower levels. The main objective of the paper is to verify MQE model of CO laser active medium kinetics. Previously[11,12], MQE model was formulated only for constant T≈100 K gas temperature. This restriction prevented to compare in details the results of calculations and real experiments. More general MQE model, taking into consideration time variation of gas temperature in the range ~ 100÷300 K, is presented below. To verify model, experimental data were used on the second pulse energy restoration in resonator double Q switching CO laser with line selection in high vibration v number transitions[13-15].

Kinetic model of $CO:N_2$:He laser was published in Ref. 4. Revised model was presented in Ref. 16. It includes detailed information on all important processes, that is, VV and VV' exchange rates, rates of excitation of molecules by electron impact, VT relaxation, processes of spontaneous and induced radiation, spectroscopic data and the equation for gas temperature. Except VV exchange rates, in MQE model this information is used without changes. Only those aspects of kinetic model are considered below, which concern VV exchange rates.

Schematically, the system of kinetic equations, describing a time evolution of CO molecule population on vibrational level v, has the form:

$$\frac{dn_v}{dt} = R^v_{e-V} + R^v_{VV} + R^v_{VV'} + R^v_{VT} + R^v_{SP} + R^v_{IND} \ , \qquad (1)$$

Here $R^v_{e-V}$, $R^v_{VV}$ $R^v_{VV'}$, $R^v_{VT}$, $R^v_{SP}$, $R^v_{IND}$ are the rates of electron-molecule excitation, intra- and inter-molecular vibration-vibration exchange, vibration relaxation, spontaneous and induced radiative transitions. The description of these rates can be found elsewhere[16,17] and is not presented here. The rates of multi-quantum VV exchange has a form:

$$R^v_{VV} = \sum_{m\geq 1}(W_{v+m,v}n_{v+m} + W_{v-m,v}n_{v-m} - (W_{v,v+m} + W_{v,v-m})n_v) \ , \qquad (2)$$



XIII International Symposium on Gas Flow and Chemical Lasers and High-Power Laser Conference, Antonio Lapucci, Marco Ciofini, Editors, Proceedings of SPIE Vol. 4184 (2001)

Here $W_{v+m,v}$ is the frequency of transitions from level v+m to level v and $W_{v-m,v}$ is the frequency of transitions from level v-m to level v, expressed as follows:

$$W_{v+m,v} = \sum_{i \geq m} Q_{v+m,v}^{i-m,i} \cdot n_{i-m}, \quad W_{v-m,v} = \sum_{i \geq m} Q_{i,i-m}^{v-m,v} \cdot n_i, \tag{3}$$

$Q_{v+m,v}^{i-m,i}$ are RC of m-quantum exchange. One may conclude from Ref. 10 that processes with m>4 are not important for v< 30-35 and are not considered.

For low vibrational levels effects of anharmonicity and, hence, effects of multi-quantum exchange play a negligible role. Therefore, for v-numbers v<5 rate constants were taken in accordance with recommendations of Ref. 16, i.e. within the framework of the SQE model. Analysis of data in Ref. 10 allows to select for any exchanged quanta m the range of vibration quantum number v, where the probabilities of multi-quantum transitions are of the order of unity. One can consider these processes as near-resonant, processes out this range – as non-resonant. All quantum numbers v, u, for $|v-u| \geq 6$ proved to fall into non-resonant range. For near-resonant exothermic single quantum and two quantum exchange processes RC were presented in the form:

$$Q_{v-k,v-k-1}^{v-1,v} = Q_{v-1,v-2}^{v-1,v} \cdot \Phi(v,k), \tag{4}$$

Data from Ref. 10 allowed to determine function $\Phi(v, k)$ only for a few selected v numbers. At intermediate v numbers $\Phi(v, k)$ function was interpolated linearly. For v>16 it was considered as constant, $\Phi(v, k)=\Phi(16, k)$. RC calculated in this manner were called as modified rate constants (MRC). MRC were used in the model for v≥10. Finally, in the range 10≥v≥5 RC were calculated as a linear superposition of MRC and those from Ref.16.

For non-resonant processes transition probabilities are small and supposed to follow SSH perturbation theory [18]. The perturbation theory gives the following dependence of rate constants on initial and final quantum numbers v and u and the number of exchanged quanta m:

$$Q_{v,v-m}^{u,u+m} \sim \left|\frac{q_{v,v-m}}{q_{m,0}}\right|^2 \left|\frac{q_{u,u+m}}{q_{0,m}}\right|^2 F(\Delta E_{u,u+m}^{v,v-m}), \tag{5}$$

where F(ΔE) is an adiabaticity function for non-resonant processes, which has a universal form in the SSH theory (see, for example Ref 4, 17), $\Delta E_{u,u+m}^{v,v-m}$ is energy defect of process, $q_{v,v-m}$ is the matrix element of the lowest order interaction term giving rise to a process of m quantum exchange. These matrix elements can be calculated using relative value of appropriate Einstein coefficients $A$ and frequency $\nu$ of transitions. Einstein coefficients $A$ for transitions in CO molecule are presented, for example, in Ref. 3, 4, 16. The procedure described was used to determine RC for temperatures T=100 K, 200 K, 300 K. At intermediate temperatures RC were calculated by means of linear logarithmic interpolation. For endothermic processes RC were found using detailed balance principle. RC at T=100 K are shown in Fig. 1.

Double Q-switching technique for frequency selective mode of CO laser operation was used to study effects of vibration dynamics induced by the first short laser pulse perturbation of VDF on selected vibrational-rotational transition of CO molecule. The second laser pulse on the same transition served as an indicator of relaxation rate of this perturbation. To compare calculations and measurements the ratio $\mathbf{Q_2/Q_1=R}$ of the second laser pulse energy to the energy of the first one as a function of the delay time $\tau_{1-2}$ was taken as a quantitative measure of VDF recovering.

Measurements of **R** dependencies on $\tau_{1-2}$ were carried out for variable experimental conditions: different selected vibrational-rotational transitions; different laser mixture density **N** and temperature **T**; specific input energy (SIE) deposited into electric discharge; time delay $\tau_d$ between beginning of the pump discharge pulse and the first Q-switched laser pulse.

Experimental setup and method of measurements were described in details previously[13-15] and are not presented. The conditions of experiments were as follows: laser gas mixture $CO:N_2$=1:1, laser gas density **N**=0.047 Amagat, initial gas temperature **T**=100±3 K, specific input energy (SIE) varied in the range 200-600 J/l.Amagat with relative uncertainty 5%. Measured parameters of active media (specific energy input, initial gas temperature, gas density and composition etc.) and laser action (selected lines and resonator loss, $\tau$, $\tau_d$, $\tau_{1-2}$) were used as input parameters to calculate the process of double pulse Q switched laser action. MQE kinetic model was used to calculate ratio R as function of time delay $\tau_{1-2}$.

Representative results of calculations are presented in Fig. 2. Experimental data are presented by points with estimated uncertainty of measurements. Also presented the results of calculations using SQE model.

One can see that MQE model describes experimental data rather well. SQE does not correlate with measurements. Taking in mind that maximum value of R was in the range 0.8-0.9, the interval $\tau_{1\text{-}2}$ to reach R=0.8 was used as measure of time constant of population restoration process and labeled as $\tau_{0.8}$. One can see that measured values of $\tau_{0.8}$ in selected transitions are in the range 3.6-6.3 μs. Table 1 shows $\tau_{0.8}$ obtained from measurements and calculations using both models.

Table 1.

| Transition V→V-1 P(J) | SIE J/l.Amagat | $\tau_d$, μs | $\tau_{0.8}$, μs SQE | MQE | experiment. |
|---|---|---|---|---|---|
| 13→12 P(11) | 250 | 590 | 2.30 | 5.80 | 6.3 |
| 13→12 P(11) | 290 | 590 | 2.30 | 5.30 | 4.2 |
| 15→14 P(13) | 330 | 590 | 1.70 | 5.45 | 4.0 |
| 15→14 P(13) | 375 | 590 | 1.50 | 5.00 | 3.6 |
| 19→18 P(15) | 330 | 590 | 1.45 | 5.80 | 5.5 |
| 20→19 P(14) | 560 | 590 | 1.30 | 3.60 | 3.7 |

After instant perturbation of population $n_v$ in vibration level v the process of restoration op population follows approximately the equation

$$\frac{d(\Delta n_v)}{dt} = R_v - \frac{\Delta n_v}{\tau_{vv}} \tag{7}$$

where $R_v$ is the pumping rate of level v from all other levels and $\tau_{vv}$ is time constant of relaxation process. It is easily follows from (2) and (3) that

$$1/\tau_{vv} = \sum_{m\geq 1}\Big( \sum_{i\geq 0} n_i \cdot Q_{v,v-m}^{i,i+m} + \sum_{i\geq m} n_i \, Q_{i,i-m}^{v,v+m} \Big). \tag{8}$$

Fig. 3 shows v number dependencies of $\tau_{vv}^{-1}$ calculated for typical conditions of experiments. One can see that frequencies $\tau_{vv}^{-1}$ given by MQE model (curve 1) exceed those given by SQE (curve 2). Differences increase with v number and reach 5-fold at v>30. Curve 3 shows $\tau_{vv}^{-1}$ given by SQE processes in MQE model. MQE processes are very important, as one can conclude comparing curves 1 and 3. Time constants $\tau_{vv}$ are important parameters in line selective CO laser kinetics. In particular, gain saturation intensities can be easily evaluated as $I_s \approx h\nu/\sigma\tau_{vv}$ ($h\nu$ - quanta of radiation, $\sigma$ - cross section for induced transitions).

In conclusion, theoretical and experimental study of vibrational exchange kinetics of highly excited CO molecules has been performed using double pulse Q-switching CO laser. MQE model of CO kinetics[11,12] is generalized to take into consideration time varying temperature in the range T=100-300K. Calculations of double pulse Q switching line selective CO laser using MQE model correlate reasonably well with measurements for transitions in the range of v numbers from v=13 to v=20. The same calculations using SQE model differ considerably from measurements. This is the first direct experimental evidence in support of MQE in comparison with SQE model.

This research was supported by Russian Foundation for Basic Research (Grant N 99-02-17553), European Office of Aerospace Research and Development (USA), AF Research Lab (USA).

## REFERENCES


1. Treanor C.H., Rich J.W., Rehm R.G. *J.Chem.Phys.*, 48, №4, 1798 (1968).
2. Jeffers W.Q., Kelley J.D. *J.Chem.Phys.*, 55, 4433 (1971)
3. Lacina W.B., Mann M.M., McAllister G.H. *IEEE J.*, QE-9, 588 (1973)
4. Yu.B.Konev, I.V.Kochetov, V.G.Pevgov, V.F.Sharkov. *The Analisys of kinetical processes of importance for CO laser.* I.V.Kurchatov Atomic Energy Institute. Preprint 2821, Moscow (in Russian) (1977). Yu.B.Konev, I.V.Kochetov, V.S.Marchenko, V.G.Pevgov, V.F.Sharkov. *The main characteristics of CO laser gas discharge plasma.* I.V.Kurchatov Atomic Energy Institute. Preprint 2810, Moscow, 1977 (in Russian).
5. Smith N.S., Hassan H.A. *AIAA Journ.*, 14, 374 (1976)
6. R.Farrenq, C.Rossetti, G.Guelashvili, W.Urban. *Chem. Phys.*, 1985, v. 92, p. 389.
7. Dillon T.A., Stephenson J.C. *Phys. Rev.A*, 6, 1460 (1972)
8. Cacciatore M, Billing G.D. *Chemical Physics*, 58, 395, (1981)
9. Cacciatore M, Billing G.D. *Chem. Phys. Lett.*, 94, 218, (1983)
10. G.D.Billing.. In: *Non-equilibrium vibration kinetics.* Ed. by M.Capitelli. Springer, Berlin, 1986, Ch.4.
11. Yu.B.Konev, I.V.Kochetov, A.K.Kurnosov, B.A.Mirzakarimov. *J. Phys. D:Appl. Phys.*, v. 27, pp. 2054-2059 (1994).
12. Yu.B.Konev, I.V.Kochetov, A.K.Kurnosov, B.A.Mirzakarimov. *Quant. Electr.* v. 24, pp. 124-127 (1994)
13. Ionin A.A., Klimachev Yu.M., Sinitsyn D.V. et al. *Multi-quantum VV-exchange modeling of the pulsed Q-switched frequency selected CO laser* (XI International Symposium on Gas Flow and Chem. Lasers and High Power Laser Conf., Edinburgh, UK, 1996, Proc. SPIE 3092, 1996, p. 301).
14. Ionin A.A., Klimachev Yu.M., Konev Yu.B. et al. *Double pulse lasing in single line Q-switched CO laser.* (Proceedings of the International Conf. on LASERS'97. Ed. J. J. Carroll & T. A. Goldman. STS Press/McLean, VA, 1998, pp. 88-91).
15. Ionin A.A., Klimachev Yu.M., Konev Yu.B. et al. *Izvestiya of Russian Academy of Sciences, Series Physics*, v. 63, 676 (1999).

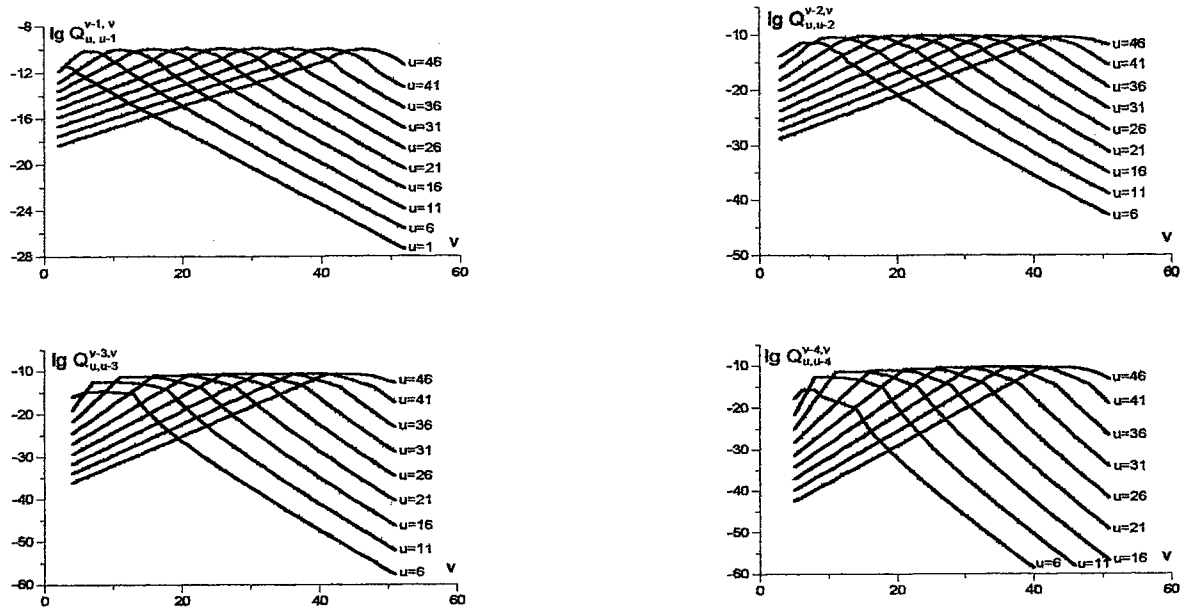


Fig. 1.Rate constants of multi-quantum exchange at T=100K

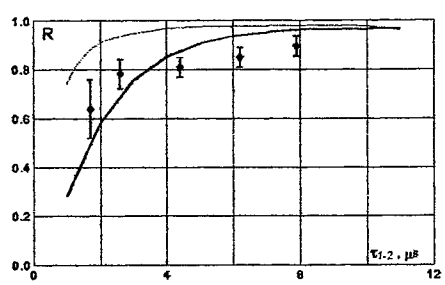


Fig. 2. Energy recovering vs. pulse time delay $\tau_{1-2}$, MQE calculation (solid line), SQE calculations (dashed line), experiment (points): $\tau_d$=590 μs, SIE=560 J/l•Amagat, transition 20→19P(14).

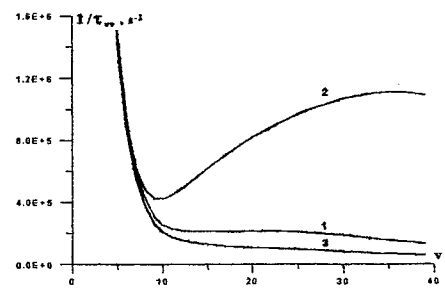


Fig. 3. frequency $1/\tau_{vv}$ vs. vibration number v: curve 1-MQE, curve 2-SQE, curve 3 - SQE in MQE model.

# The influence of plasma-chemistry products on CO vibrational distribution in a carbon monoxide laser medium.

G.Grigorian* and A.Cenian #
*Institute of Physics, St.Petersburg State University, 198904 St.Petersburg, Petrodvoretz , Ulianovskaya 1; e-mail:galina.grigorian@usa.net
#Institute of Fluid-Flow Machinery, Polish Academy of Sciences, 80-952 Gdansk, Fiszera 14
e-mail:cenian@imp.pg.gda.pl

## ABSTRACT

The vibrational distribution function (VDF) of CO molecules in the mixture with helium decreases rapidly for vibrational levels higher than 11. The VDF plateau may be significantly increased by addition of nitrogen or Xe. There is a strong correlation between VDF and concentrations of plasma-chemical products in the mixture.

**Keywords:** CO lasers

## 1. INTRODUCTION

The CO lasers are of a great interest for the industrial applications. There are no alternatives for devices generating radiation in the $5 < \lambda < 6$ μm range. Although, there are already some CO lasers available on the market but the laser plasma-chemistry has not been thoroughly studied and understood.

This paper presents results of the experimental and numerical investigations of the plasma-chemical processes in the DC discharge of CO lasers. The special attention is paid to the generation of species containing carbon, like: $C_2$ or $C_2O$, which may play an active role in the vibrational de-excitation of CO molecules.

## 2. EXPERIMENTAL SET-UP AND PROCEDURE

The measurements have been performed in sealed off and slow-flow set-ups, using various compositions of $CO:N_2:He:Xe$ mixtures at pressures ranging from 3 to 15 Torr. All experiments were carried out in a discharge tube of the internal diameter of ~ 15 mm and a length of ~ 50 cm. The tube was cooled with water flowing in an outer jacket. The experimental set-up is schematically shown in Fig.1. The discharge current was in the range 20-100 mA. The special care

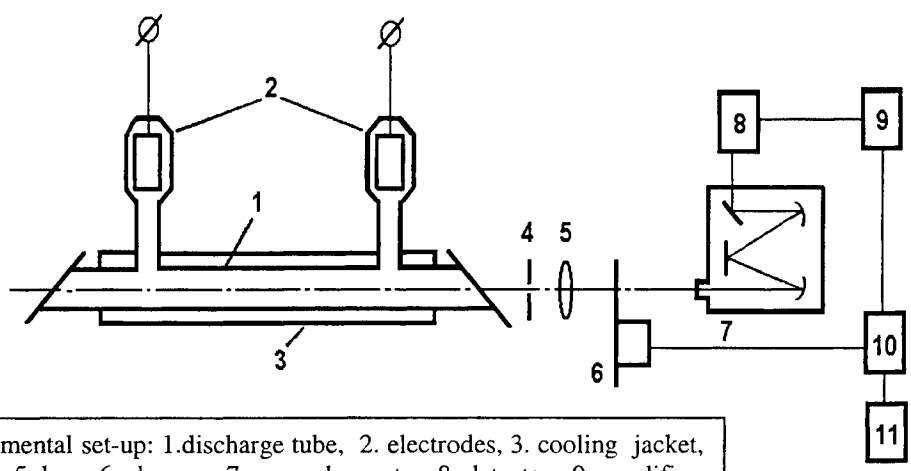


Fig.1. Experimental set-up: 1.discharge tube, 2. electrodes, 3. cooling jacket, 4. diaphragm, 5. lens, 6. chopper, 7. monochromator, 8. detector, 9. amplifier, 10. synchronizer, 11. X-Y recorder



XIII International Symposium on Gas Flow and Chemical Lasers and High-Power Laser Conference, Antonio Lapucci, Marco Ciofini, Editors, Proceedings of SPIE Vol. 4184 (2001)

was undertaken to minimize all the possible impurities in the working gas mixture.

The vibrational distributions of the CO molecules were determined from the infrared emission spectra of CO (first and second overtones) using a standard procedure based on the least squares fitting [1].

The concentration of carbon atoms was determined from the C(2p3s $^1P^0$) electronic-state emission, considering wavelength $\lambda$ = 247.8 nm, i.e. transition 2p3s $^1P^0 \rightarrow$ 2p2 $^1S_0$. This estimation procedure is reasonable, because the considered electronic state is excited by collisions of the carbon atoms (in the ground state) with electrons.

The aim of our experimental work was to determine concentrations of vibrationally excited CO molecules as well as various plasma-chemical products and to study possible correlation.

The rate constants of various processes were calculated using EEDF determined for various mixtures from the Boltzmann equation in the two-term spherical harmonics approximation. The cross sections for collision processes with participation of electrons, published in ref. 2 were used in the work.

## 3. RESULTS AND DISCUSSION

Figure 2 presents the vibrational populations of CO molecules at different experimental conditions. The populations of CO(v) levels in He-CO mixture are smaller than in the mixtures containing nitrogen or xenon. They fall also rapidly in the region of vibrational levels, v >11. The addition of $N_2$ or Xe leads to an increase of vibrational level population, more significant for higher vibrational levels. Usually, in the case of the Xe addition, this phenomenon is related to the E/N decrease and the resulting growth of the vibrational excitation efficiency.

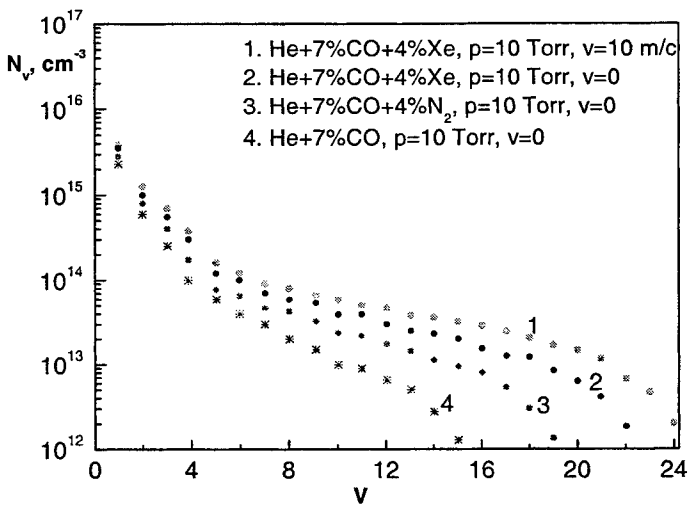


Fig. 2. Vibrational distribution of CO molecules in the discharge

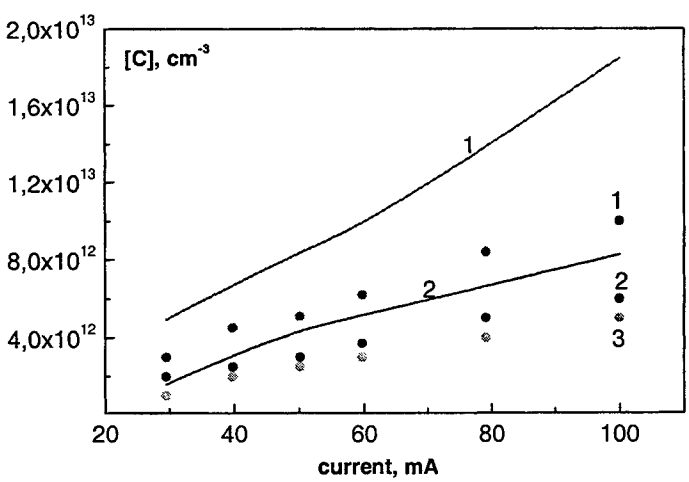


Fig. 3.Concentration of carbon atoms vs discharge current; points – experiment, lines – calculations; p = 10 Torr;
(1) He +7%CO; 2- He +7%CO +4% Xe; 3- He +7%CO +4%$N_2$

On the other hand, the carbon containing species like: $C_2$ and $C_2O$ - produced during plasma-chemical reactions, may also influence the vibrational distribution function (VDF) through several energy loss mechanisms including: the VT, VV and VE relaxation. Unfortunately the rate constants for those processes are not well known.

However, the VT relaxation, usually less efficient than the VV one, probably does not contribute significantly to the loss of the vibrational energy. Even if the rates for the VT relaxation on C, $C_2$, and $C_2O$ are as large as for He, the respective concentrations are much smaller than that of He.

The second mechanism, the VV' transfer (usually a near resonant process) may be significant-ly more efficient. The $C_2O$ molecule in the ground electronic state has three characteristic frequencies [3]: $\omega_1$ = 2046 (1841) cm$^{-1}$, $\omega_2$ = 608 (580) cm$^{-1}$, $\omega_3$ = 1270 (1097) cm$^{-1}$ (in the parenthesis the theoretical values [] are presented). They are close to the frequencies of the CO molecule for the vibra-tional transitions in the Treanor and VDF plateau regions (energy regions where vibrational distribution function is far from Boltzmann equilibrium). The $C_2$ molecules may contribute to VV′ transfer even more significantly than $C_2O$, because the frequency of the v = 0 $\rightarrow$ v = 1 transition of $C_2(X\ ^1\Sigma)$ is almost in resonance with the frequency of v = 13 $\rightarrow$ v=12 transition of the CO molecules. The discussed resonance processes may markedly decrease the CO(v) populations in the VDF plateau region.

The vibrational-electronic, VE, processes must also be considered as a possible mechanism of

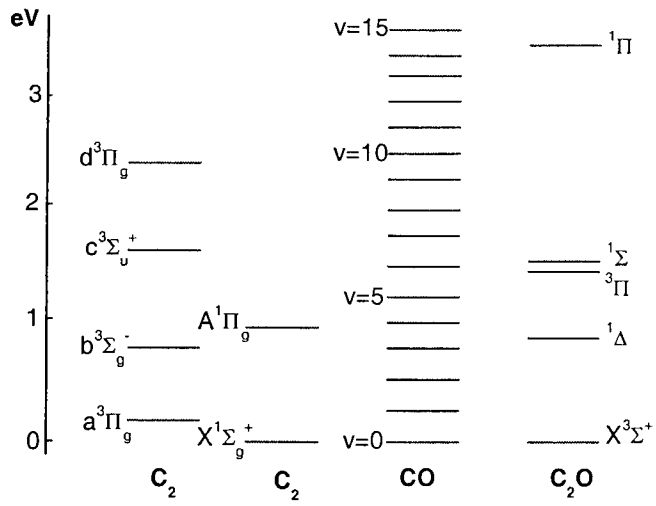


Fig. 4. Energy diagram of vibrational levels of CO and electronic states of $C_2$ and $C_2O$.

Under considered conditions process (2) prevails in the C formation (~70%); diffusion is the main loss mechanism of atomic carbon. The measured and calculated concentrations of the carbon atoms, [C], are presented in Fig.3. It is clear that the concentration of C atoms significantly decreases when nitrogen or xenon is added to the gas mixture. The rate constants for the reactions of C with $N_2$ and N are small [4,5] and cannot explain the observed phenomenon. However, the NO molecules may appear in the discharge plasma, when nitrogen is added to the He-CO mixture. These molecules efficiently decrease concentrations of all carbon-containing species and particularly the concentration of carbon atoms due to the reaction

$$C + NO \rightarrow \text{products}, \qquad (3)$$

with the rate $k_3 \sim 10^{-10}$ $cm^3/s$ [5,6]. This reaction may explain the observed fall of [C] (after $N_2$ addition) but only when [NO] > $10^{12}$ $/cm^3$. It is worth to note that the NO emission was observed in the $N_2$ containing mixtures but concentration of NO molecules was not determined.

Furthermore, the intense emission from $C_2(d^3\Pi)$ was observed showing a significant overpopulation of the sixth vibrational level (in the discharge spectrum one may see the so-called "high pressure bands") – see Fig. 5. The population of the level v=6 was by 8 -15 times larger than populations of lower levels. When some percent of Xe is added to the He-CO mixture – see Fig. 5(b), the intensity of radiation from the [$C_2(d^3\Pi$, v<6)] levels decreases by factor 2. At the same time the transition from [$C_2(d^3\Pi$, v=6)] falls more than 1 order of magnitude. The mechanisms responsible for the $C_2(d^3\Pi$, v=6) formation are not clearly understood, but it was suggested that the level is populated due to the process of $C_2O$ decomposition [7-9]:

$$C + C_2O \rightarrow C_2(d^3\Pi, v=6) + CO, \qquad (4)$$

with the rate constant $k_4 = 3\times10^{-10} cm^3/c$ [10]. The $C_2O$ molecules appear in the discharge plasma due to the process [5,7]

$$C + CO + M \rightarrow C_2O + M. \qquad (5)$$

Taking into account the measured concentrations of carbon atoms and $C_2(d^3\Pi$, v=6) – see Fig. 6, the estimation of [$C_2O$] may be performed - results are presented in Fig. 7. The [$C_2O$] decrease after $N_2$ addition may be explained both by smaller

CO(v) relaxation. There are several excited electronic states of $C_2$ and $C_2O$ molecules, even in the vicinity of CO lowest vibrational levels, v < 10 – see Fig.4.

The above considerations gave stimulus to measure (and calculate) the concentrations of these species in various discharge conditions.

The initial stage of production of mentioned species is generation of carbon atoms, through the main two processes

$$CO + e \rightarrow C + O + e, \qquad (1)$$

$$CO + CO(a^3\Pi) \rightarrow CO_2 + C. \qquad (2)$$

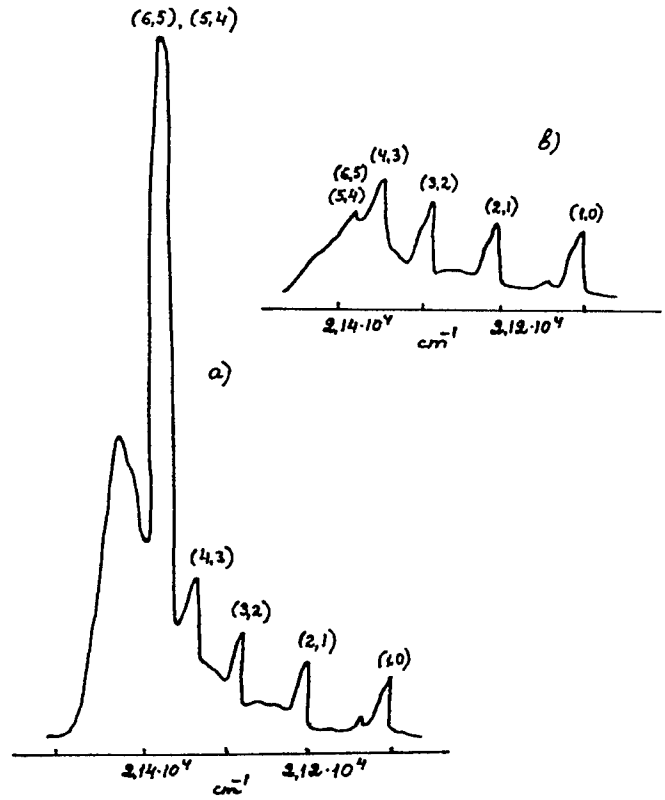


Fig.5. The spectrum of Swan bands of $C_2(d^3\Pi \rightarrow a^3\Pi, \Delta v = 1)$:
(a) He+7%CO, p=5 Torr, I=20 mA;
(b) He+7%CO+4%Xe, p=5 Torr, I=20 mA – the intensity mulitiplied by 2.

concentration of [C] as well as by fast reaction with NO created in the discharge. Rate constant for this process is again high ~ $10^{-10}$ $cm^3/s$ [11,12].

The $C_2O$ concentration significantly falls also when Xe is added into the mixture. This may be explain by the $C_2O$ decomposition (the dissociation energy for $C_2O$ is equal to 2.3 eV) in collisions with the excited metastable xenon:

$$C_2O + Xe^* \rightarrow Xe + CO + C\,. \qquad (6)$$

Estimations show that the rate constant for this process must be ~ $10^{-10}$ $cm^3/s$.

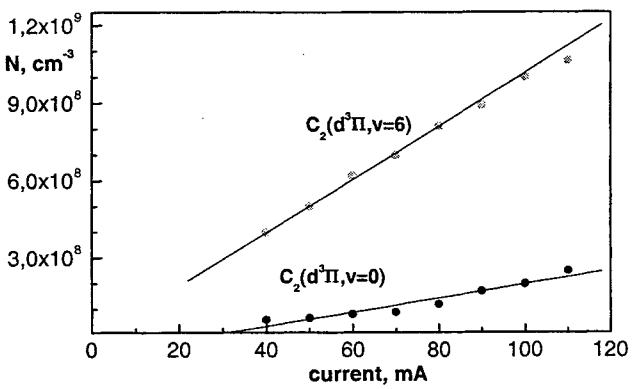


Fig.6. Concentration of $C_2(d^3\Pi$, v=0) and $C_2(d^3\Pi$, v=6) vs discharge current He+12%CO, p=15 Torr

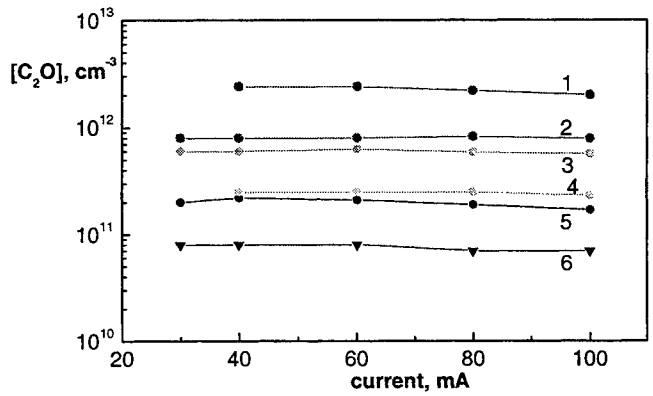


Fig.7. Concentration of $C_2O$ molecules vs discharge current; (1)- He+12% CO, p =15 Torr; (2)- He+7% CO, p=12 Torr; (3)- He+7% CO, p = 10 Torr; (4)- He+12% CO+10% Xe, p=15 Torr; (5)- He+7% CO+4%$N_2$, p=10 Torr; (6) He +7%CO +4%Xe, p = 10 Torr

## 4. CONCLUSIONS

The analysis of the presented experimental data shows that the highest vibrational excitation of CO molecules is obtained under conditions when the concentration of carbon-contained species is low. This is consistent with the results of previous works [13,14], where concentrations of these particles were measured in He-CO and He-CO-$O_2$ mixtures.

Therefore, we conclude that $C_2$ and $C_2O$ molecules should be considered as the important catalyst of CO vibrational relaxation as well as the serious pollutants of the CO laser mixture.

## REFERENCES


1. Horn K.R. and Oettinger P.E., *J.Chem.Phys.*, **54,** pp. 3040- , 1971.
2. A.V.Phelps et al., Joint Institute for Laboratory Astrophysics (JILA) Information Center Report No.26, 1985. (to be found on ftp://jila.colorado.edu/collision_data/).
3. Walch S.P. J.Chem.Phys.,**72,** 5679- , 1980.
4. Washida N., Kley D., et al., *J.Chem.Phys.*, **63,** pp. 4230, 1975.
5. Husain D., Kirsch L.J., *Trans.Farad.Soc.*, **67,** pp. 2025- , 1971.
6. Braun V., Rosi A., et al., *Proc. Roy.Soc.*, **312,** pp. 417- , 1969.
7. Goss F., Sadeghi N. et al., *Chem.Phys.Lett.*, **13,** pp. 557- , 1972.
8. Kunz C., Harteck P. et al., *J.Chem.Phys.*, **46,** 4157- , 1967.
9. Vann B.N., *J.Chem.Phys.*, **97,** pp. 3137- , 1992.
10. Ionikh Y.Z., Kostiukevich I.N., et al., *Optika i spektroskopija*, **76,** 406- , 1994, (in Russian).
11. Williamson D.G., Bayes K.D., *J.Am.Chem.Soc.* ,**89,** 3390- , 1967.
12. Donnelly V., Pitts W., McDonald J., *Chem.Phys.*, **49,** pp. 289- , 1980.
13. Grigorian G.M.,Dymshitz B.M. and Ionikh Y.Z., *Opt.Spectrosc.*, **65,** pp. 686- , 1988.
14. Grigorian G.M.,Dymshitz B.M. and Ionikh Y.Z., *Sov.J.Quant.Electron.*, **19,** pp. 889- , 1989.

# Microwave excited cw CO laser at room temperature

J. H. Schäfer, J. Uhlenbusch und M. Wierich
Institut für Laser- und Plasmaphysik, Heinrich-Heine-Universität Düsseldorf, Universitätsstraße 1
D-40225 Düsseldorf

## ABSTRACT

The laser gas of a 700 W CO laser is excited by microwaves and cooled down to room temperature. A mass spectrometer controls the supply of $O_2$ and CO and the adsorption of $CO_2$ in zeolithe traps.

## 1. INTRODUCTION

The low power CO laser with its high quantum efficiency and the manifold of laser lines is an important coherent light source for laser spectroscopy in the mid-infrared spectral range. There are also reports on the studies of industrial applications of high power CO lasers. Some advantages in material processing have been shown for the CO laser due to its relatively short wavelengths compared with that of the $CO_2$ laser. One difficulty for high power CO lasers to be practically applied, however, seems to be the necessity of cooling down the laser gas to cryogenic temperature by heat conduction or fast expansion. Nevertheless, high power operation of the CO laser at room temperature with reasonable efficiency is possible, too. But the optimum working gas mixture is not easy to keep under control with a constant laser power level. The aim of the work therefore is to recieve high constant laser power output. The results presented here are gained with a CO laser excited by microwaves and cooled by fast axial gas flow in a closed loop.

## 2. EXPERIMENTAL SETUP

### 2.1. Principle description

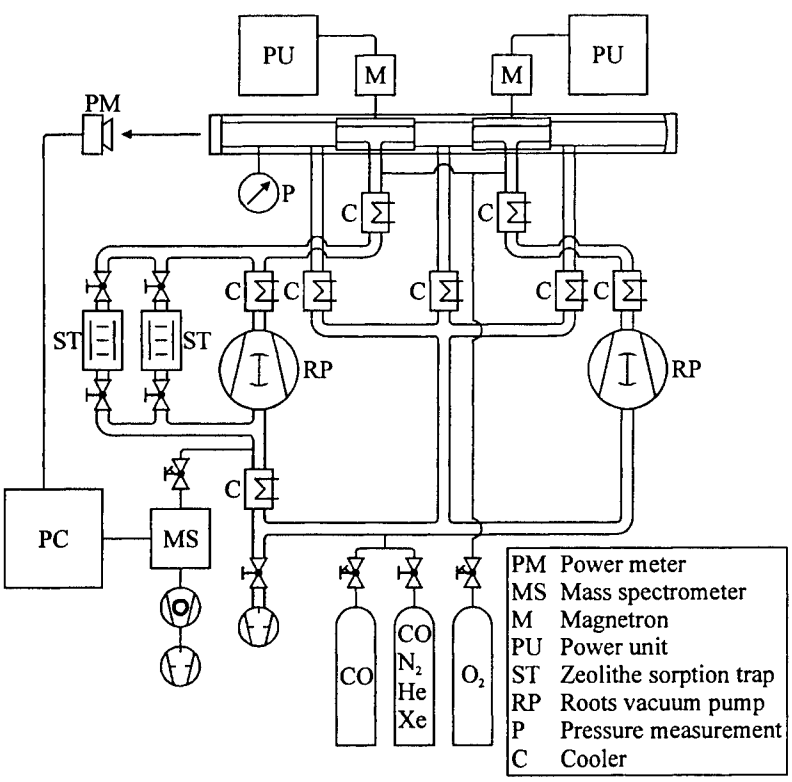


Resonator length: L = 2240 mm

Curve radius of the reflector: R = 20 m

Transmission of the output mirror: t = 0,2

Gas rate of the roots vacuum pumps:

$$\dot{V} = 2 \cdot 4000\ m^3/h$$

Gas inlet temperature: $T_{In}$ = 279 K – 281 K

Gas outlet temperature: $T_{Out}$ = 373 K – 393 K

Operating pressure: p = 35 mbar – 48 mbar

Gas volume: V = 200 l

Mass spectrometer:
Quadruvac PGA 100 (Leybold)



XIII International Symposium on Gas Flow and Chemical Lasers and High-Power Laser Conference,
Antonio Lapucci, Marco Ciofini, Editors, Proceedings of SPIE Vol. 4184 (2001)

### 2.2. Sight of the experiment

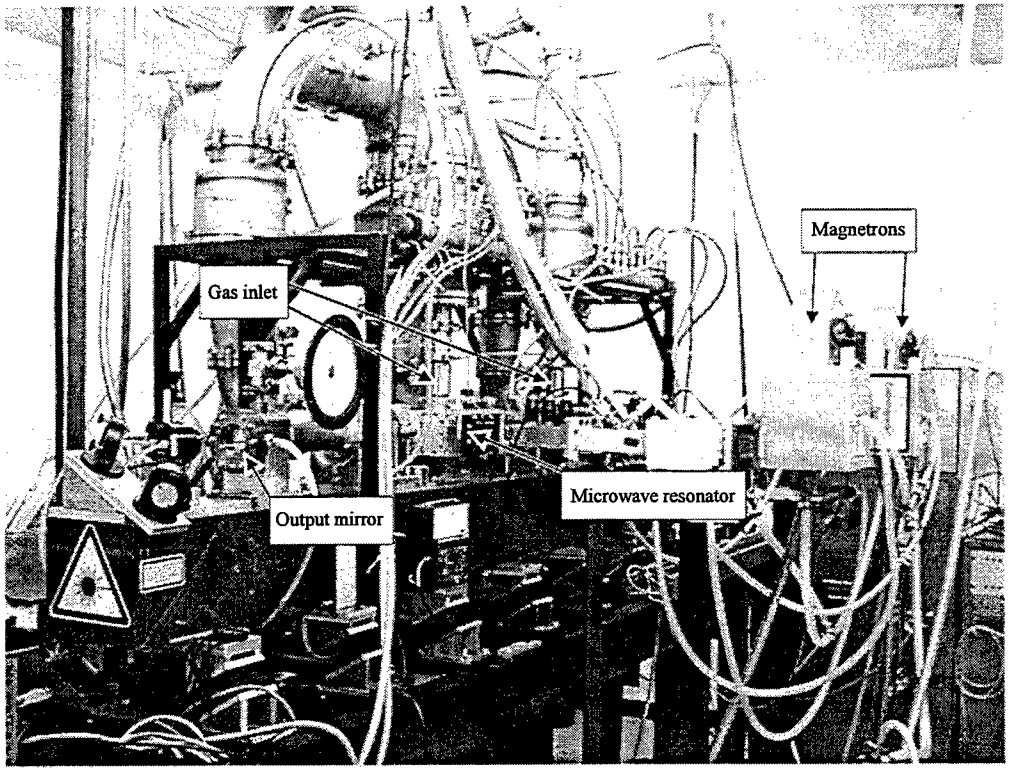


### 2.3. The microwave resonator

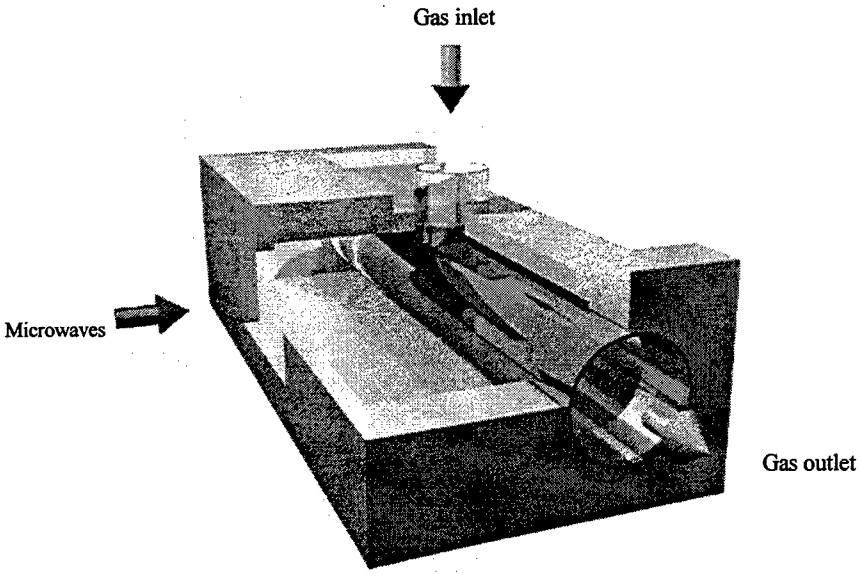


Dimensions of the microwave resonators:
125 mm · 60 mm · 300 mm

Diameter of the glass tube:
$d_L = 51$ mm

Diameter at the gas inlet:
$d_E = 36$ mm

Length of the glass tube:
$l = 370$ mm

Magnetron:
Type YJ1600, 6 kW,
$\nu = 2{,}46$ GHz

## 3. PROBLEMS

Laser output power decays after starting the experiment using a gas mixure with following components: 8,5 % CO, 7,5 % $N_2$, 4,5 % Xe, 79,5 % He. The concentration of $CO_2$ constantly rises in the closed system.

## 4. SOLUTION OF THE PROBLEMS

- Measuring absolute gas concentrations with a mass spectrometer over time
- Small, constant input of oxygen
- Regulation of the CO concentration
- Adsorption of CO2 in zeolithe traps

## 5. EXPERIMENTAL RESULTS

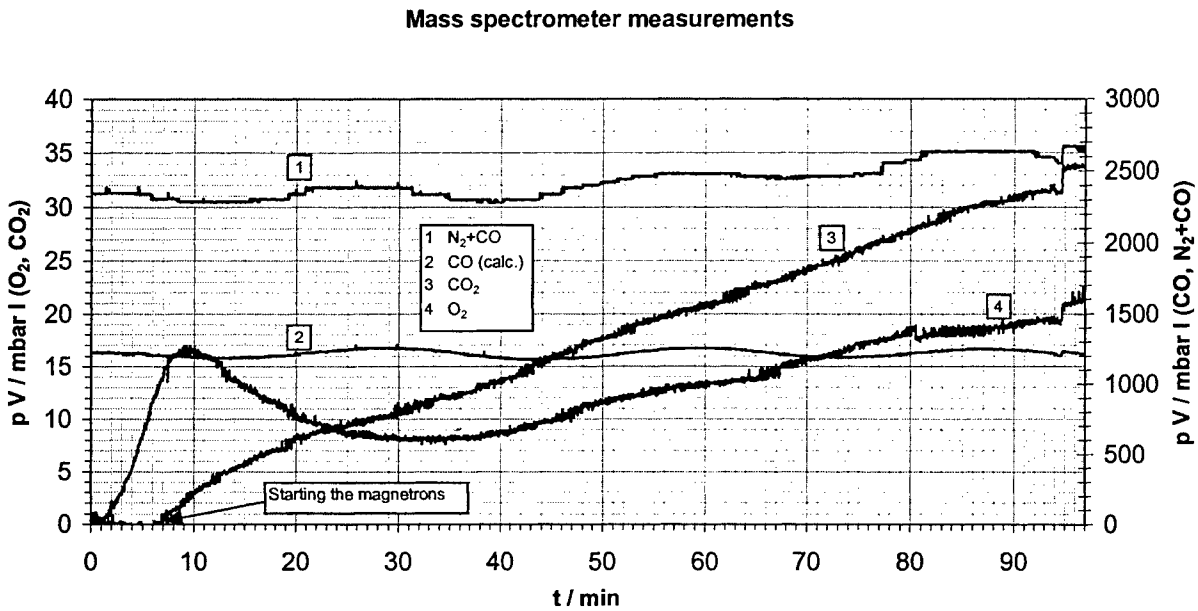


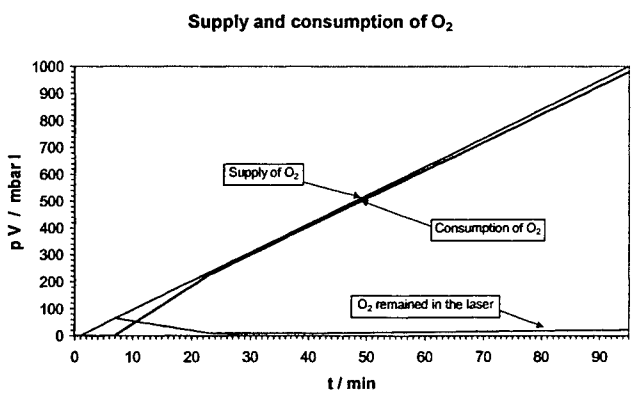


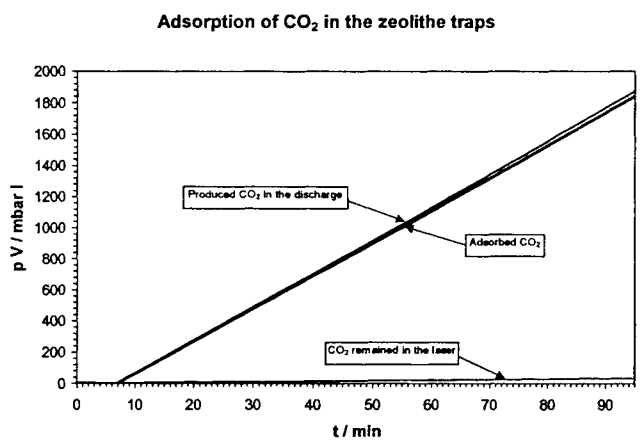


The mass spectra of $CO_2$, O2, CO+$N_2$ and C, latter as an indication for the CO concentration are monitored. In the laser active medium a small amount of the CO is dissociated or oxydized, so it has to be replaced. The C peak in the mass spectrum is used to regulate the CO concentration. The presence of oxygen is crucial for the laser action and is therefore refilled with a constant rate. With an optimized rate the mass spectra shows only a very small amount of remained oxygen in the laser. $CO_2$ produced in the discharge hampers laser action and must be adsorbed in the zeolithe traps. The mass spectrum shows the small amount of $CO_2$ in the laser.

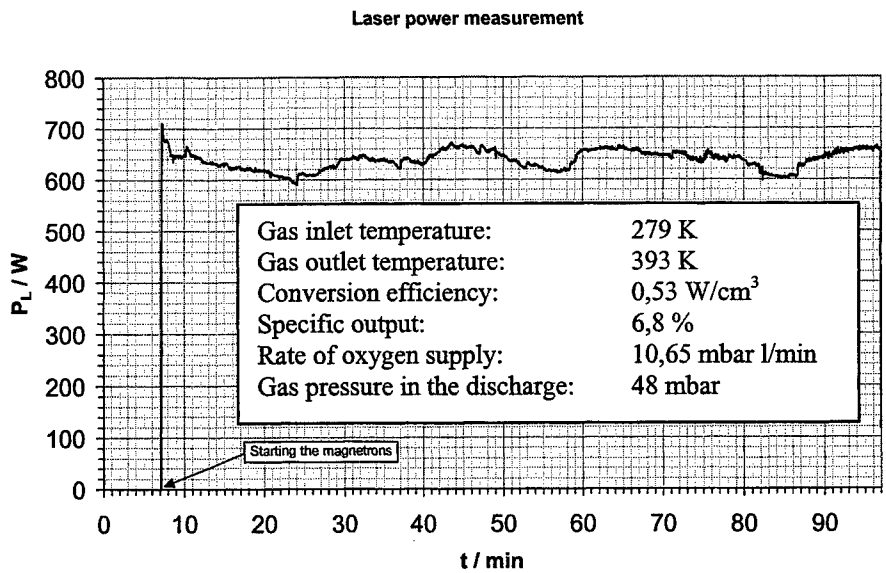


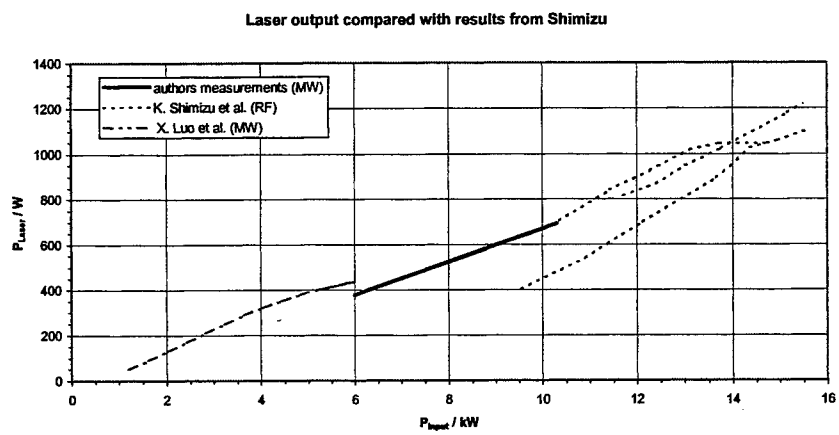


## 6. SUMMARY

High power operation of microwave excited CO lasers at room temperature is possible. Only water cooled heat exchangers are necessary. The discharge section is composed of two T shaped discharge tubes with an inner diameter of 51 mm and a length of 300 mm. Microwave power is supplied from two 6 kW, 2,46 GHz magnetrons. The laser gas (79,5 % He, 7,5 % $N_2$, 8,5 % CO, 4,5 % Xe) circulates driven by two roots pumps in a closed loop. The optical cavity of optical length of 2240 mm consists of a total reflecting gold coated copper mirror and an $CaF_2$ outcoupler with 20 % transmission. The laser output is monitored together with the mass spectra of $CO_2$, $O_2$, $CO+N_2$ and C, latter as an indication for the CO concentration. Temperature in the entrance and outlet region of the laser tubes, as well as current and voltage of the magnetrons, are monitored. The CO concentration is controlled and kept on a constant level. Results show that the optimized supply of $O_2$ together with adsorption of $CO_2$ in the zeolithe traps yields a constant laser output.

## REFERENCES


1. Konki Shimizu, Manabu Taniwaki and Shunichi Sato, "1-kW, room temperature, fast-axial-flow CO laser excited by a radio-frequency discharge", Vol. **21**, No. 2, *Optics letters*, pp. 125- 127, January 15, 1996
2. X. Luo, J.H. Schäfer and J. Uhlenbusch, "High power room temperature operating cw CO laser excited by microwave discharge", *10th International Symposium on Gas Flow and Chemical Lasers*, SPIE Vol. **2502**, pp. 69-74, 05.-09. September, 1994

# Numerical simulation of gas discharge CO laser

Rafail Safioulline*

Kazan State Academy of Architecture and Building Construction, Kazan

## ABSTRACT

A mathematical model for gas discharge CO lasers includes vibrational kinetics of CO and $N_2$ molecular species as well as the equation for electron energy distribution and gas dynamic equations. The effective method for numerical simulation of powerful CO lasers is proposed.

**Keywords:** Gas discharge, CO laser, anharmonic oscillators, vibrational levels, numerical simulation

## 1. INTRODUCTION

The numerical simulation of gas discharge CO lasers is of current interest till now. The development of the efficient numerical schemes properly describing the processes in CO lasers allows one to search for the optimal conditions for laser operating. A mathematical model for gas discharge CO lasers includes vibrational kinetics of CO and $N_2$ molecular species and the equation for electron energy distribution function (EEDF). One must also deal with gas dynamic, electric field and induced radiative equations. In the present paper the method for numerical simulation of electric CO lasers first proposed in paper[1] has been developed.

## 2. THEORETICAL PART

The anharmonic oscillator model for vibrational levels $E_n^{(1)}$ and $E_n^{(2)}$ of CO and $N_2$ molecular species has been used:

$$E_n^{(j)} = E_1^{(j)} \cdot n - \Delta E^{(j)} \cdot n(n-1),\ j = 1,2,$$

$$E_1^{(1)} = 3084K,\ \Delta E^{(1)} = 18.7K,\ E_1^{(2)} = 3353K,\ \Delta E^{(2)} = 21.1K \tag{1}$$

For about 60 vibrational levels of CO and 50 vibrational levels of $N_2$ molecular species have been considered in calculations. The following vibration-vibration (V-V) and vibration-to-translation (V-T) processes were treated for CO-$N_2$ gas mixtures:

$$CO(n) + CO(m) \Leftrightarrow CO(n-1) + CO(m+1), \tag{2}$$

$$N_2(n) + N_2(m) \Leftrightarrow N_2(n-1) + N_2(m+1), \tag{3}$$

$$CO(n) + N_2(m) \Leftrightarrow CO(n-1) + N_2(m+1), \tag{4}$$

$$CO(n) + CO \Leftrightarrow CO(n-1) + CO, \tag{5}$$

$$CO(n) + N_2 \Leftrightarrow CO(n-1) + N_2, \tag{6}$$

$$N_2(n) + CO \Leftrightarrow N_2(n-1) + CO, \tag{7}$$

$$N_2(n) + N_2 \Leftrightarrow N_2(n-1) + N_2. \tag{8}$$



XIII International Symposium on Gas Flow and Chemical Lasers and High-Power Laser Conference,
Antonio Lapucci, Marco Ciofini, Editors, Proceedings of SPIE Vol. 4184 (2001)

In addition also He and Ar components were taken into account. It's convenient to define the following vibration distribution functions:

$$f_n = N_n^{(1)}/N^{(1)},\ g_n = N_n^{(2)}/N^{(2)} \tag{9}$$

Then the vibration relaxation in CO-$N_2$ gas mixtures including the induced radiative processes may be described by following set of equations:

$$df_n/dt = F_n + (\alpha_{n+1}I_{n+1}/\Delta_n - \alpha_n I_n/\Delta_{n-1}) \cdot T/(\xi_1 P) = F_n + \varphi_n\ ,\ dg_n/dt = G_n\ . \tag{10}$$

Here $F_n$ and $G_n$ include the V-V and V-T processes, in addition $F_n$ contains the spontaneous radiative terms. T, P are the absolute temperature and pressure of gas mixture, whereas $\xi_1$ is the CO mole fraction in mixture. The parameters $I_n$, $\alpha_n$ are the intensity and the amplification factor for $n \Rightarrow n-1$ carbon monoxide radiative transition, $\Delta_n = E_{n+1}^{(1)} - E_n^{(1)}$.

One-dimensional vibration not in equilibrium flow of non-viscous CO-$N_2$ gas mixture in plane channel with varying section has been treated. In that case one may write the gas dynamic equations as follows:

$$\rho US = G = \text{const.}, \tag{11}$$

$$\rho U dU/dx + dP/dx = 0, \tag{12}$$

$$\rho U \frac{d}{dx}(C_pT + U^2/2 + e) = \delta W - \sum_{\nu=1}^{\nu 1} \xi_1 \rho R E_\nu^{(1)} A_{\nu,\nu-1} f_\nu - \sum_{\nu=1}^{\nu 1} \alpha_\nu I_\nu = \phi, \tag{13}$$

$$e = R(\xi_1 \sum_{\nu=1}^{\nu 1} E_\nu^{(1)} f_\nu + \xi_2 \sum_{\nu=1}^{\nu 2} E_\nu^{(2)} g_\nu), \tag{14}$$

$$P = \rho RT. \tag{15}$$

The designations used here are: $\rho$ the gas density, U the flow velocity, R the gas constant for mixture under consideration, S the area of the channel section, G the mass flow, $C_p$ the translation-rotational specific heat capacity at constant pressure, $\delta$ the part of electric field power W, which enters to translational, rotational and vibrational degrees of freedom of molecular species, e the specific vibrational energy.

The radiative emission equations are written as

$$AI_{n+1} - BI_n + CI_{n-1} + D = 0 \tag{16}$$

with coefficients A, B, C depending on n and D depending on $F_n$. If laser generation takes place at ($n \Rightarrow n-1$) transitions, $l < n < m$ (natural numbers l, m are determined in calculations) then the set of eq. (16) is solved by scalar sweep method under zero boundary conditions.

## 3. NUMERICAL SCHEME

In general, eq. (10) - (16) must be solved simultaneously. The proposed method of solution actually is a splitting method with respect to physical processes. It's reduced to sequential solution of vibrational kinetic, gas dynamic and induced radiative emission equations.

Thus the calculations at arbitrary section of resonator are reduced to the following iterative processes. Each global iteration includes: 1) determination of vibrational distribution functions $f_n$, $g_n$ (at known U,T,P,$I_n$); 2) determination of U,T,P (at known $f_n$,$g_n$,$I_n$); 3) determination of $I_n$ (at known $f_n$,$g_n$,U,T,P) .

The stages of solution are briefly described below. The semi-implicit difference scheme[2] to eq. (10) is applied:

$$f_n^{m+1} - f_n^m = \Delta x[0.6(F_n/U)^{m+1} + 0.4(F_n/U)^m] + \varphi_n, \quad (17)$$

$$g_n^{m+1} - g_n^m = \Delta x[0.6(G_n/U)^{m+1} + 0.4(G_n/U)^m] \quad (18)$$

It must be taken into account that

$$F_n = A_n f_{n+1} + B_n f_n + C_n f_{n-1} + D_n, \quad (19)$$

$$G_n = A^*_n g_{n+1} + B^*_n g_n + C^*_n g_{n-1} + D^*_n \quad (20)$$

where the coefficients $A_n$, $B_n$, $C_n$, $A^*_n$, $B^*_n$, $C^*_n$ depend on $f_0$, $f_1$, ..., $f_{v1}$, $g_o$, $g_1$, ... , $g_{v2}$. Therefore the sequence of two iterative sweeps for the solution of a set of non-linear algebraic eq. (18), (19) is used. The iterative scheme is constructed as follows. The initial values for $f_n$, $g_n$ at layer m+1 are assigned (they may be put equal to the values on previous layer m) and the coefficients $A_n$,...,$C^*_n$ are calculated. Then the eq. (18), (19) are solved by sweep method and the coefficients $A_n$,...$C^*_n$ are recalculated again and so on up to convergence condition is carried out.

The gas dynamic equations (13), (14) are written as

$$dh/dx = \phi/(\rho U),\ h = C_p T + U^2/2 + e, \quad (21)$$

$$dq/dx = PdS/dx,\ q = GU + PS. \quad (22)$$

Then the same semi-implicit difference scheme is applied to eq. (21), (22):

$$h^{m+1} - h^m = \Delta x[0.6(\phi/\rho U)^{m+1} + 0.4(\phi/\rho U)^m] \quad (23)$$

$$q^{m+1} - q^m = \Delta x[0.6(PdS/dx)^{m+1} + 0.4(PdS/dx)^m], \quad (24)$$

Bearing in mind the eq. (12), (15), (23), (24), the quadratic equation for $U^{m+1}$ is obtained. One of it's roots refers to supersonic flow, while the other one to subsonic flow. Then the values $P^{m+1}$ and $T^{m+1}$ are obtained. The calculation of line intensities was described above.

The similar numerical scheme may be applied to impulse CO lasers. It should be noted also that for two-dimensional gas flow the difference scheme becomes essentially complicated. Thus the splitting both on physical as well as on spatial directions must be carried out in this case.

## 4. RESULTS

The calculated laser efficiency versus input specific power W is presented in Fig. 1.

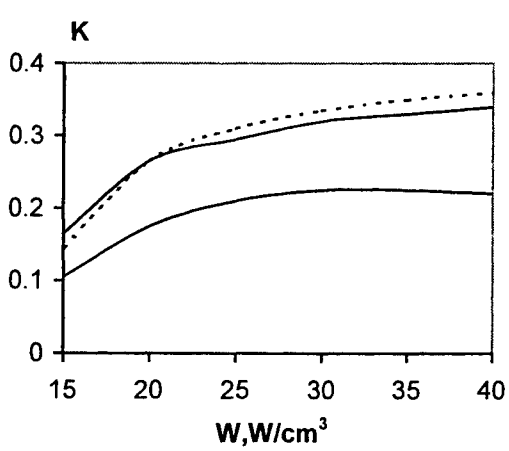


**Fig.1.** The calculated laser efficiency versus input specific power. The dotted curve corresponds to the method of constant amplification factor, the continuous neighbour curve - the constant intensity method. The lowest curve - the constant intensity method including de-excitation of vibrational levels by electrons.

The mixture $CO-N_2$ ( $\xi_1:\xi_2=1:9$) has been considered provided that $E/N = 2\cdot10^{-17}$ $V\cdot cm^2$ and P = 10 kPa, T = 90 K, U = 70 m/sec at entry of discharge region. The dashed line corresponds to the constant amplification factor method. The continuous neighbour line corresponds to calculations by the constant intensities method. The lowest continuous line – to the constant intensity method including de-excitation of vibrational levels by electrons. In the range of input specific powers applied the efficiency of the laser grows with increasing W.

The specific radiation energy $Q_{rad}$ versus input specific energy is presented in Fig. 2. The results correspond to pulse CO laser ($CO-N_2$ gas mixture, $\xi_1:\xi_2=1:6$, T = 100 K, P = 18.3 kPa at entry). It's evident that both numerical calculations as well as experiments[3] give the clear linear dependence.

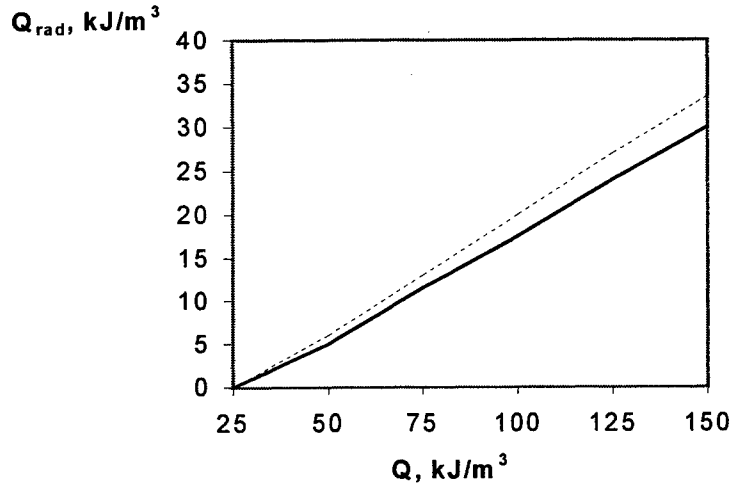


**Fig .2.** The specific radiative energy of pulse CO laser as a function of the input specific energy. The continuous curve corresponds to the experiment[3], the dotted line - the present calculations.

## ACKNOWLEDGMENTS

In conclusion the author should like to thank the Academy of Sciences of Republic Tatarstan for financial support and also to thank Dr. Sh. A. Araslanov for the help and useful discussions.

## REFERENCES

1. Sh. F. Araslanov, R. K. Safioulline, "Numerical simulation of gas discharge CO laser", *Proceedings of the 2-nd Inter national Symposium on Energy, Environment & Economics (EEE-2),* **II**, pp. 84-87, Kazan Power Engineering Institute, Kazan, 1998.
2. S. A. Losev, *Gas dynamics lasers,* Nauka, Moscow, 1977.
3. N. G. Basov, V. A. Danilychev, A. A. Ionin, V. S. Kazakevich, I. B. Kovsh, N. L. Poletaev, "Investigation of cooled electroionized CO laser. II. Generation on mixtures of CO with buffer gases", *Kvantovaya Electronica* (Russia), **6**, pp. 1215-1222, 1979.

* Correspondence: E-mail: bikchantaeva@ksaba.kcn.ru; Telephone: (8432) 684932; Fax: 7 (8432) 387972

# Comprehensive computer simulation on fundamental-band and first-overtone carbon monoxide lasers

Katsuhisa Takada*[a], Yoshitaka Maekawa*[a], Mitsuhiro Iyoda*[a],
Manabu Taniwaki**[b], Kouki Shimizu**[b], Shunichi Sato***[c]

[a]Chiba Institute of Technology, Computer Science, 2-17-1 Tsudanuma, Narashino, 275-8588 Japan
[b]Institute of Research and Innovation, Laser Laboratory, 1201 Takada, Kashiwa, 277-0861 Japan
[c]National Defense Medical College Research Institute, 3-2 Namiki, Tokorozawa, 359-8513 Japan

## ABSTRACT

Computer simulation codes for first-overtone CO laser have been developed. The codes are designed to be executed in distributed computing environment. Performance characteristics have been analyzed and compared with those of fundamental-band CO laser.

**Keywords:** computer, simulation, CO laser, fundamental-band, first-overtone

## 1. INTRODUCTION

More than ten tears ago the authors started the development of a series of computer models on discharge-exited continuous-wave (CW) CO lasers. The objectives of development were the analyses of experimental results and the estimation of a variety of performance characteristics. While the early codes were carried out by mainframe computers, successive codes were executed by engineering workstations and personal computers.[1-10] In the middle of 1990's the authors estimated the possibility of first-overtone (FO) CO laser by the modified computer code. The FO CO lasers are attractive due to shorter wavelength around 3 micrometers. Recently, detailed experimental and theoretical studies on pulsed FO CO laser were reported in Russia.[11] The authors have revised the computer code for CW FO CO lasers. New series of performance characteristics of CW FB and FO CO lines have been analyzed under the same condition.

## 2. KINETICS OF FB AND FO CO LASERS

For the typical discharge-excited gas lasers, fast direct pumping by electron-gas impact is active. As for CO lasers, however, slower indirect pumping by vibration to vibration (V-V) transfer is dominant. At lower gas temperature the rates of vibration to rotation and transition (V-R/T) transfer decrease and indirect pumping increases, as the V-V transfer process is exothermic in the pumping direction. Therefore, low temperature conditions by refrigeration were required for efficient CO laser operation. In order to maintain low temperature, the experimental apparatus was complicated and the control and operation were difficult. Various progresses in laser technology enabled the high power discharge excitation and CO laser operations at room temperature. The experimental devices, works, and operations were significantly simplified. Now, CO lasers are recognized as high power light source as well as $CO_2$ lasers.

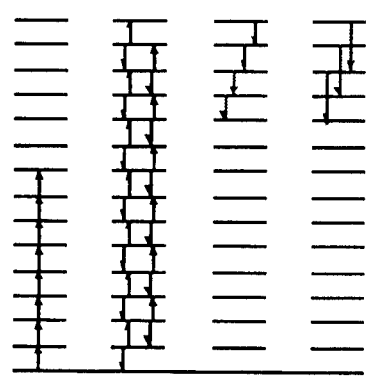

Fig.1. Transition of FB and FO CO.

*Email: takada@iyo.cs.it-chiba.ac.jp, maekawa@mae.cs.it-chiba.ac.jp, iyoda@iyo.cs.it-chiba.ac.jp
Telephone: +81 47 478 0530; Fax: +81 47 478 0549
**Email: taniwaki@iri.or.jp, kshimizu@iri.or.jp; Telephone: +81 471 44 8811; Fax: +81 471 44 8939
***Email: shunsato@ndmc.ac.jp; Telephone: +81 429 95 1211 Ext.2713; Fax: +81 0429 91 1757



XIII International Symposium on Gas Flow and Chemical Lasers and High-Power Laser Conference,
Antonio Lapucci, Marco Ciofini, Editors, Proceedings of SPIE Vol. 4184 (2001)

The total inversion, where the population in upper v-th vibration level exceeds that in lower (v-1)-th vibration level, is impossible for normal CW CO lasers. Only the partial inversion, where the partial population in upper (v,j-1)-th rotation level exceeds that in lower (v-1,j)-th rotation level, is realized for FB CW CO lasers. Recently in Russia[11], the importance of multiquantum V-V transfer processes was pointed out. For pulsed laser operation, where CO molecules are strongly pumped by discharge, multiquantum V-V transfer is not negligible. The gain of FO CO laser is much smaller than that of FB CO laser due both to the lower emission coefficients and smaller partial population inversion between (v,j-1)-th and (v-2,j)-th levels. These are the reasons why FO CO lasing is difficult.

## 3. COMPUTING PROCESSES

The computer simulation codes are divided into several modules those are corresponding to kinetic processes. The rate coefficients of direct discharge pumping are obtained by BOLTZ, which solves Boltzmann's transportation equations. The coefficients of V-R/T and V-V energy transfer are calculated by VRTVV, where the newer collision theories are taken into account instead of conventional SSH theory. The line factor is obtained by FLINE, where both of Doppler and collisional broadening are mixed. Rate equations for gas molecules are solved in EMPACT, VVXFER, and VRTXFER. The module GAIN calculates the optical emission process and gain of FB and FO lines. If any of gain lines exceeds the cavity threshold, LASE is also driven to obtain laser radiation. Along with these particle kinetics, FLOW updates the mass flow conditions.

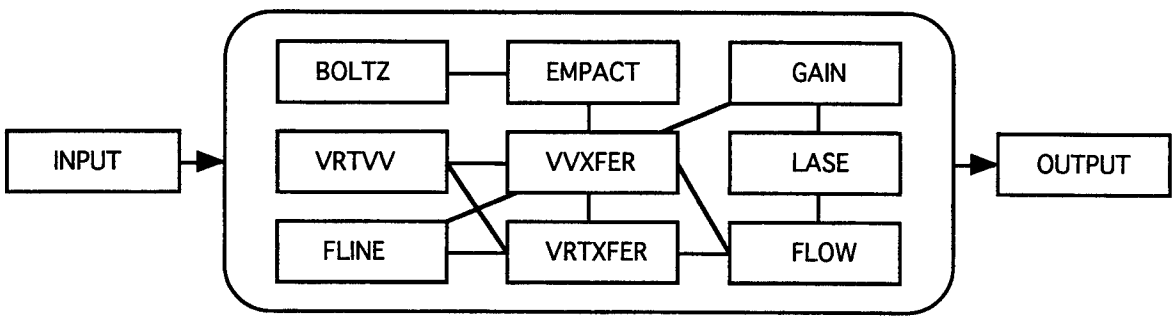


Fig. 2. Block diagram of computing modules.

## 4. IMPLEMENTATION OF CODES

Most of theese simulation modules described above were already implemented in personal computers (PCs), Apple Macintosh computers (Macs), and workstations (WSs). The dependence on conventional huge mainframe computers decreases rapidly. Under the common gateway interface (CGI), reported in GCL/HPL '96 in Edinburgh [8], the processes were executed mainly by the servers. In the Java programming environment, reported in GCL/HPL '98 in St. Petersburg [9], the processes were executed mainly by the clients. Now in the year 2000, to be reported in Firenze, the processes are partially distributed to the servers as well as partially distributed to the clients. The data and processes are transferred in TCP/IP (Transmission Control Protocol / Internet Protocol) in the internet and intranet. The operation is input and the results are output both by the clients.

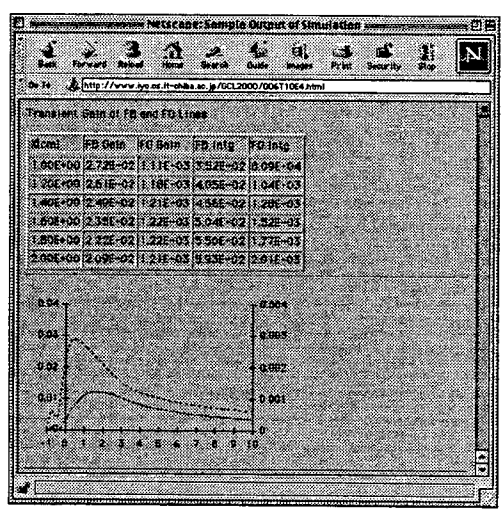

Fig. 3. Sample output of simulation results.

## 5. RESULTS OF SIMULATION

The data of GAIN, LASE, and FLOW are transferred from the server to the client, where the digital number formats are converted, visualized, and displayed as shown in Fig. 3. The simulation input parameters are set as follows; gas mixture ratio $CO/N_2/He/O_2$ = 6/16/78/0.2, 10/10/80/0.2, 12/26/62/0.2; gas pressure 20 - 60 [Torr]; gas flow velocity 20 - 60 [m $s^{-1}$]; gas temperature 100 - 300 [K]. The rate coefficients of direct discharge pumping are locally executed by BOLTZ and transferred to the server cluster with the other input parameters.

The results of BOLTZ show that more than 85% of discharge energy is converted to the vibrational energy of CO(v) and $N_2(v)$, $1 \leq v \leq 8$. Further indirect pumping processes to the upper vibrational levels are given by the collisional V-V energy transfer. The results of FLOW show that the gas temperature increase by 50 - 150 degrees while passing though the discharge section. When the laser action takes place the gas temperature decreases by 10 - 20 % in proportion to the laser power output.

## 6. COMPARISON AND DISCUSSION

The typical results of simulation are shown in Figs. 4 and 6. The horizontal and vertical axes correspond to distance along flow and optical gain, respectively. The transverse discharge section is set between x = -1 and 2 [cm]. Is is remarked that the gain values of FO are one order of magnitude smaller than those of FB. The FB gain rapidly increases upstream the discharge section. The peak gain around 0.03 [cm-1] is large enough to output laser power. The increase in FO gain is slower compared with FB gain. Downstream discharge section, FO gain reaches the peak around 0.001 [cm-1] which is poor to require the low loss FO cavity conditions. The reflectivity of output mirror for FO laser oscillation should be more than 96 %.

Several years ago, the authors carried out the experiments on CW FO CO lasers. Regrettably, the ideal mirrors for FO were not obtained at that time. The realistic mirrors had also the considerable reflectivity around 20 % for FB band. Although the experiments repeated with these realistic FO mirrors, several hundred watt strong FB laser output prevented us from the FO line observation. In order to analyze the reasons, the simulations have been executed by setting those experimental cavity conditions. The corresponding results are shown in Figs. 5 and 7. The other conditions are the same as those in Figs. 4 and 6, respectively. The FB gain is fixed to the cavity threshold while lasing. It is noted that the FO gain values decrease by 10 % due to the reduction of population inversion by FB laser transition. These results inform us that the accurate design of selective mirror is strictly required for CW FO oscillation.

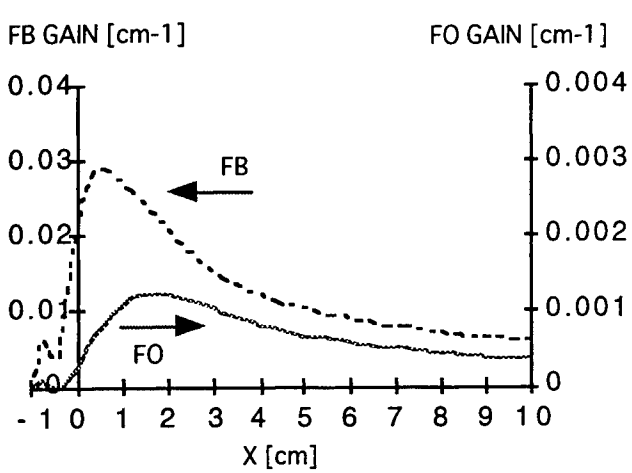


Fig. 4. Gain of FB and FO lines, $CO/N_2/He/O_2$ = 6/16/78/0.2.

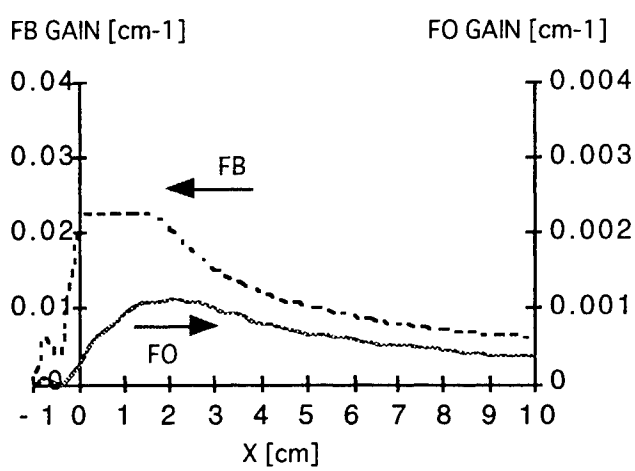


Fig. 5. Gain of lasing FB and FO lines, $CO/N_2/He/O_2$ = 6/16/78/0.2.

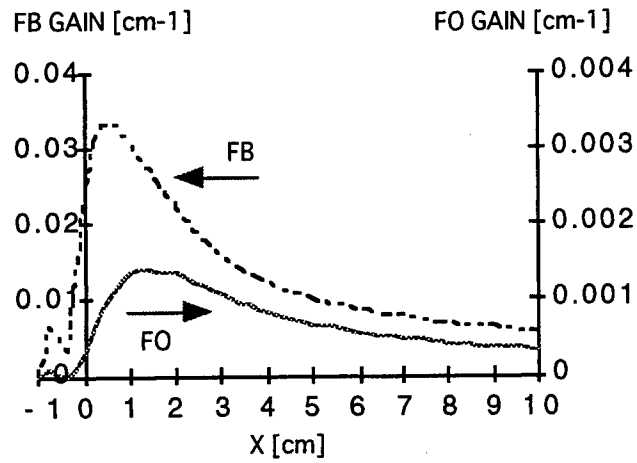


Fig. 6. Gain of FB and FO lines, $CO/N_2/He/O_2 = 10/10/80/0.2$.

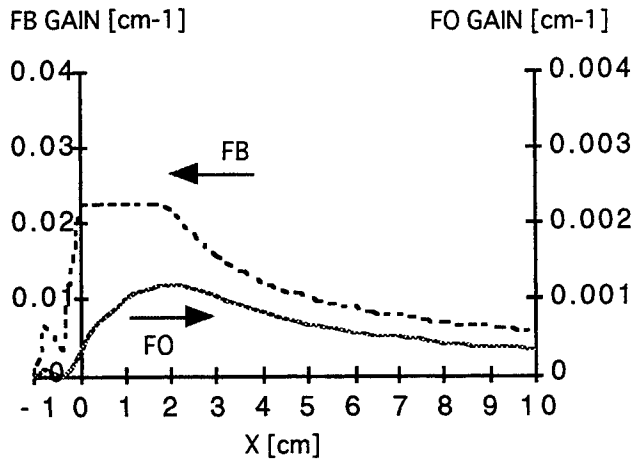


Fig. 7. Gain of lasing FB and FO lines, $CO/N_2/He/O_2 = 10/10/80/0.2$.

## 7. SUMMARY

The performance characteristics of FB and FO have been analyzed by distributed computer simulation. A series of calculations on FO CO transitions have been carried out under the same input conditions of FB CO transitions. The possibility and difficulty for FO CO lasing have been examined.

## REFERENCES


1. M.Iyoda, M.Hori, S.Sato, T.Fujioka, "Theoretical studies on subsonic flow transverse discharge CO laser," *5th International Symposium on Gas Flow and Chemical Lasers*, Oxford, 20-24 August, 1984.

2. M.Iyoda, K.Terunuma, S.Sato, and T.Fujioka, "Parametric analysis of a cw CO EDL by computer simulation," *6th International Symposium on Gas Flow and Chemical Lasers*, Jerusalem, 8-12 September, 1986.

3. M.Iyoda, S.Sato, H.Saito, T.Fujioka, T.Murota, and M.Akiyama, "Computer simulation for the efficient operation of a cw CO electric discharge laser," *7th International Symposium on Gas Flow and Chemical Lasers*, Vienna, 22-26 August, 1988.

4. M.Iyoda, S.Sato, T.Murota, and M.Akiyama, "Two-dimensional computer modeling of discharge-excited CO gas flow," *8th International Symposium on Gas Flow and Chemical Lasers*, Madrid, 10-14 September, 1990.

5. M.Iyoda, T.Murota, M.Akiyama, and S.Sato, "1D and 2D computer models of industrial CO laser," *Modeling and Simulation of Laser Systems II, SPIE International Conference on High Power Lasers*, Los Angels, 20-25 January, 1991.

6. M.Iyoda, Y.Yamaguchi, H.Okaya, M.Akiyama, M.Taniwaki, and S.Sato, "PC-based beam mode analysis of CO laser," *9th International Symposium on Gas Flow and Chemical Lasers*, Crete, 21-25 September 1992.

7. M.Iyoda, H.Okaya, M.Akiyama, M.Taniwaki, and S.Sato, "FFT analysis of CO laser beam mode based on PC and workstation," *10th International Symposium on Gas Flow and Chemical Lasers*, Friedrichshafen, 5-9 September, 1994.

8. M.Iyoda, M.Taniwaki, and S.Sato, "Network-based simulation of CO laser," *11th International Symposium on Gas Flow and Chemical Lasers and High Power Lasers*, 25-30 August, Edinburgh, 1996.

9. M.Taniwaki, S.Sato, Y.Maekawa and M.Iyoda, "Distributed computing for CO laser simulation," *12th International Symposium on Gas Flow and Chemical Lasers and High Power Lasers*, 31 August - 5 September, St. Petersburg, 1998.

10. M.S.Taylor, "High level, PC-based Laser System Modeling," *Modeling and Simulation of Laser Systems II, SPIE International Conference on High Power Lasers*, Los Angels, 20-25 January, 1991.

11. A.A.Ionin et. al., "Experimental and theoretical study of multiquantum vibrational kinetics in active medium of CO laser," Prep. Lebedev Physical Institute, No.70, Moscow, 1999.

# Slab $CO_2$ lasers excited by an all-solid-state 0.6 MHz generator

Stephan Wieneke, Stefan Born, and Wolfgang Viöl

Department PMF, University of Applied Sciences and Arts, von-Ossietzky-Str. 99,
D-37085 Göttingen, Germany •

## ABSTRACT

Sealed-off slab $CO_2$ lasers excited by a dielectric barrier discharge are studied. The laser output power is measured at excitation frequencies between 0.4 and 0.6 MHz; discharge gaps are in the range 1.6 – 6.0 mm. Due to the scaling laws of radio frequency excitation no laser activity should be possible for the laser under investigation. The use of high-frequency excitation (0.4 - 0.6 MHz) combined with a dielectric barrier discharge gives the possibility of creating a homogeneous and stable $CO_2$ laser gas discharge with high laser activity. The excitation efficiency of the all-solid-state generator reaches 90 %.

**Keywords:** Sealed-off slab $CO_2$ laser, dielectric barrier discharge, silent discharge, high-frequency excitation, all-solid-state generator

## 1. INTRODUCTION

Most of the $CO_2$ lasers operated today use the radio frequency (**rf**) excitation with frequencies between 10 and 150 MHz. One drawback is the high cost of the rf generators which have a relatively low efficiency of 60 %.

Therefore, low-cost, high frequency (**hf**), all-solid-state generators with frequencies of about 0.5 MHz are used in the laser systems under investigation. The use of a silent discharge with two dielectric ceramic walls enables excitation of such a laser with frequencies below 1 MHz. The excitation efficiency of the all-solid-state generator reaches more than 90 %. Up until now, hf high voltage was used only to excite fast axial flow $CO_2$ lasers.[1,2,3] This paper describes a high frequency excited sealed-off slab $CO_2$ laser which is a new candidate of low-cost, compact cw $CO_2$ lasers.

## 2. SIMILARITY LAWS FOR RF DISCHARGES

It is well known that the extrinsic properties of discharges are related according to the similarity laws.[4] Thus, in an rf discharge, the optimal gas pressure $p_o$ and the optimal generator frequency $f_o$ for a given $CO_2$ laser gas discharge gap $d$ are related according to the similarity laws:

$$p_o \cdot d \approx 240 \text{ hPa·mm} \quad (1)$$
$$f_o \cdot d \approx 280 \text{ MHz·mm} \quad (2)$$
$$p_o / f_o \approx 0.86 \text{ hPa·MHz}^{-1}. \quad (3)$$

For smaller excitation frequencies than the optimal generator frequency mentioned in equations 2 and 3, the specific laser output power decreases (see figure 3). For rf frequencies below

$$f_{min} = 80 \text{ MHz·mm} / d \quad (4)$$

no laser activity have been measured.[5] This is considered to be caused by ion losses in the sheath region of alpha rf discharge.

The thickness $d_s$ of this non-laser active sheath region increases with decreasing frequency [5,6] because

$$d_s \approx 15 \text{ mm·MHz} / \text{f}. \quad (5)$$

• Correspondence: E-mail: wolfgang.vioel@pmf.fh-goettingen.de; WWW: http://www.pmf.fh-goettingen.de; Telephone: 495513705218; Fax: 495513705101



XIII International Symposium on Gas Flow and Chemical Lasers and High-Power Laser Conference,
Antonio Lapucci, Marco Ciofini, Editors, Proceedings of SPIE Vol. 4184 (2001)

From equation 5 it follows that the non-laser active sheath should be $d_s \approx 25$ mm thick at an excitation frequency of 0.6 MHz, so the calculated sheath thickness $d_s$ is much higher than the discharge gap $d$ (for discharge gaps below 6 mm). At excitation frequencies below about 3 MHz, there is no rf discharge left. The laser is excited by a dielectric barrier discharge.

## 3. DESCRIPTION OF THE SEALED-OFF SLAB LASER

A schematic diagram showing the construction of the slab laser excited by a dielectric barrier discharge is shown in figure 1. The alumina plates between the electrodes are used as dielectric barriers.[7] For small discharge gaps, the dielectric barriers also provide waveguiding. Quartz glass sidewalls are used for photographic and spectroscopic monitoring of the laser gas discharge. The electrodes have an area of 540 × 12 mm$^2$; discharge gaps of 1.6 mm, 2.0 mm, 2.5 mm and 6.0 mm are investigated. The excitation frequency of the all-solid-state generator depends on the capacity of the electrode configuration and varies between 0.4 and 0.6 MHz. About 90 % of the source power is transformed into the discharge power. A silicon back mirror with a reflectivity of 99.7 % and a curvature of 2 m and a plane ZnSe output resonator mirror with 5 % transmission have been employed. The cavity is 0.703 m in total length including a mirror/waveguide separation of 1.5 mm on each side.

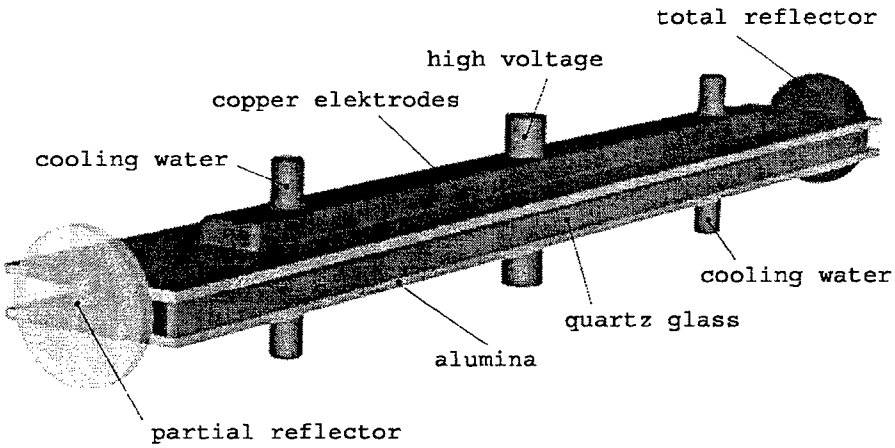


Figure 1: Schematic diagram of a hf excited slab $CO_2$ laser.

## 4. DIELECTRIC BARRIER LASER GAS DISCHARGE

Photographs of the laser gas discharge with an exposure time of 400 ns prove that the homogeneity of the discharge is excellent.[8] The electron temperature was determined by spectroscopic measurements of the laser gas discharge. The electron temperature is nearly constant versus discharge height. Average electron temperatures of 10.700 K for a discharge gap of 6 mm and 16.400 K for a discharge gap of 1.6 mm were measured.[8]

## 5. LASER OUTPUT POWER

The laser power was measured in a sealed-off operation and the power stability was determined to be between 2 and 4 % over an operation time of 1 h. The mean laser power did not decrease within 1 h, so that the dissociation of $CO_2$ seems to be constant over this time interval. A stable laser gas discharge can be created at remarkably high input power densities of more than 20 Wcm$^{-3}$ and 200 Wcm$^{-3}$ for a discharge gap of 6 mm and 1.6 mm, respectively. Figure 2 shows the laser efficiency of the slab $CO_2$ laser excited by an all-solid-state 0.6 MHz generator versus the electrical input power density for a discharge gap of 6 mm. In a comparable laser system with a discharge gap of 6 mm excited by an rf discharge, maximum electrical power densities of 4 Wcm$^{-3}$ at an excitation frequency of 13.6 MHz and 8 Wcm$^{-3}$ at 27.1 MHz have been reached. The specific power of the laser is only limited by thermal conductivity and not by the onset of discharge instabilities. Even the optimal gas pressure can be increased by high frequency excitation compared to radio frequency excitation (see equations 1 and 3).[7]

There is a potential to improve the laser efficiency of figure 2. Taking into account the high efficiency of the low-cost 0.6 MHz generator of about 90 %, the sealed-off slab $CO_2$ laser excited by a dielectric barrier discharge is a new candidate for an efficient $CO_2$ laser.

Compared to the $CO_2$ waveguide laser, the cooling of the slab laser (see figure 1) is only half as efficient because there are only two walls involved. The heat that can be extracted from the laser gas can be calculated from the heat diffusion equation. Assuming a laser efficiency of 10 % and a maximum gas temperature of 500 K, the specific laser power $P_L/A$ can be estimated for a discharge gap $d$ as[7]

$$P_L/A \approx 3 \text{ Wcm}^{-2} \text{ mm} / d . \tag{6}$$

In figure 6, the measured specific laser power for 1.6 mm, 2.0 mm, 2.5 mm and 6.0 mm are compared to the 1/d-scaling law (equation 6). The lasers with a discharge gap of 1.6 and 2.5 mm have been not optimized up to now. A higher laser output power and a higher laser efficiency can be expected by reducing the waveguide coupling losses, by using a better alignment of the optical axis relative to the waveguide, and by using additional mirror cooling. Therefore the specific laser power did not reach the calculated values of the 1/d-scaling law. A maximum laser output power of 49 W has been measured for a discharge gap of 6 mm corresponding to a specific laser power of 0.75 $\text{Wcm}^{-2}$. This value is a little bit higher than the value 0.5 $\text{Wcm}^{-2}$ calculated by equation 6. Therefore, the specific power of the laser is only limited by thermal conductivity and not by the onset of discharge instabilities.

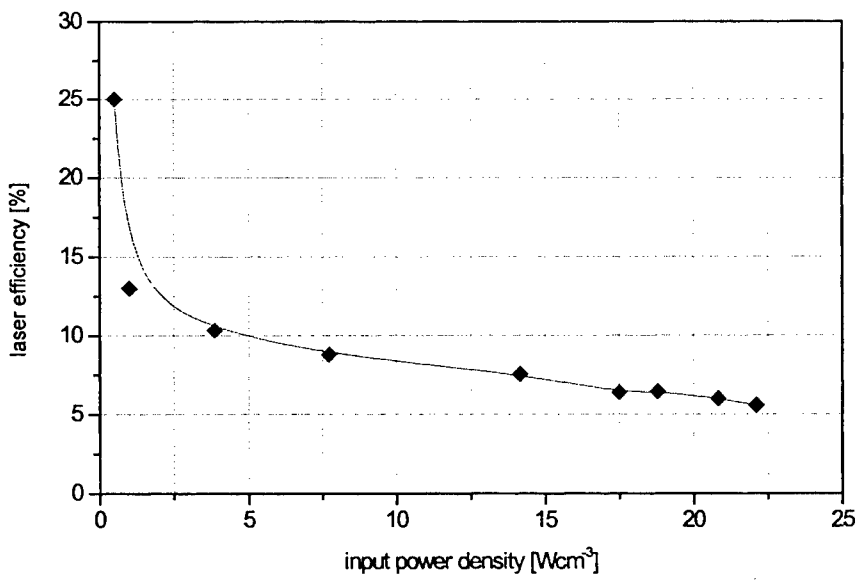


Figure 2: Laser efficiency as function of input power density for a 6 mm discharge gap at a gas pressure between 40 and 100 hPa ($He:N_2:CO_2$ = 60:34:6)

## 5. CONCLUSION

The use of hf excitation (0.4 – 0.6 MHz) combined with a dielectric barrier discharge gives the possibility of creating a homogeneous, stable $CO_2$ laser gas discharge. The optimal gas pressure and the input power density can be increased compared to rf excitation. The laser is only thermally limited and not by the onset of discharge instabilities. The efficiency of the all-solid-state generator used to excite the dielectric barrier discharge reaches 90 %.

Experimental results show that the sealed-off slab $CO_2$ laser excited by a hf dielectric barrier discharge is a promising candidate for a low-cost, commercial, high-power $CO_2$ laser for material processing.

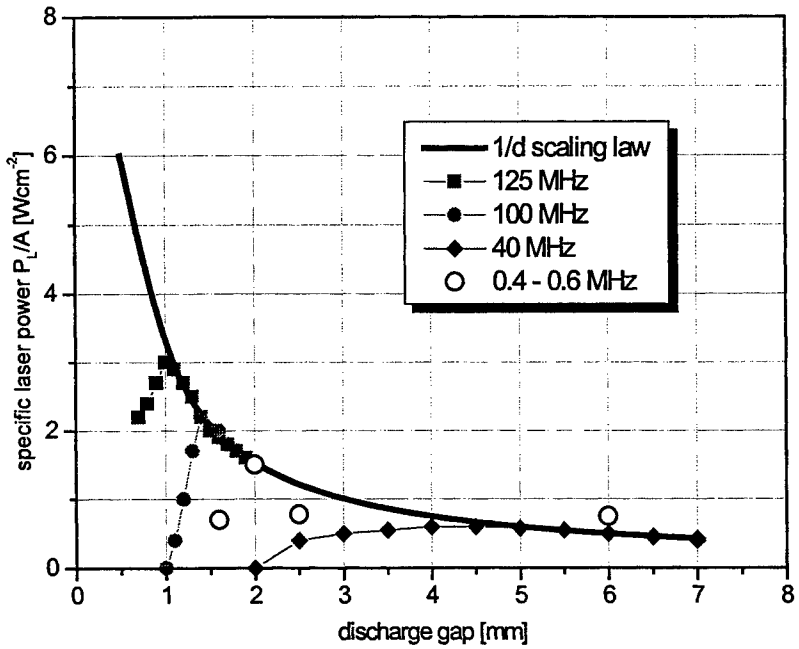


Figure 3: Specific laser power $P_L/A$ as a function of discharge gap $d$ (The results of hf excitation are compared to those of rf excitation with different excitation frequencies.)

## ACKNOWLEDGMENT

The authors wish to thank the Lower Saxony Ministry for Science and Culture for their support of this work.

## REFERENCES

1. M. Kuzumoto, S. Ogawa, M. Tanaka, and S. Yagi, "Fast axial flow $CO_2$ laser excited by silent discharge", *IEEE Journal of Quantum Electronics* **26**, pp. 1130-1134, 1990
2. H. Nagai, M. Hishii, M. Tanaka, Y. Myoi, H. Wakata, T. Yagi, and N. Tabata,"Cw 20-kW sage $CO_2$ laser for industrial use", *IEEE Journal of Quantum Electronics* **29**, pp. 2898-2909, 1993
3. J. Klein, G. Otto, U. Habich, and P. Loosen, "Mittelfrequenzangeregter $CO_2$-Laser mit axialer Gasströmung", *EuroLaser* **2**, pp. 48-50, 1994
4. A. D. Colley, F. Villarreal, A. A. Cammeron, P. P. Vitruk, H. J. Baker, and D. R. Hall, "High power cw molecular gas lasers using narrow gap slab waveguides", *Gas lasers – recent developments and future prospects*, Dordrecht: Kluwer Academic Publishers, pp. 89-103, 1996
5. S. Kobayyashi, T. Murata, K. Terai, and T. Tamagawa, "1 kW slab $CO_2$ laser excited by a self-excited RF generator, *SPIE Gas Flow and Chemical Lasers and High-Power Laser* **3092**, pp. 92-95, 1997
6. R. Nowack, H. Opower, K. Wessel, H. Krüger, W. Haas, and N. Wenzel, "Diffusion-cooled compact $CO_2$ high power lasers", *Laser und Optoelektronik* **23**, pp. 68-81, 1991
7. S. Wieneke, S. Born, and W. Viöl, "Sealed-off $CO_2$ lasers excited by an all-solid-state 0.6 MHz generator, *J. Phys. D: Appl. Phys.* **33**, pp. 1282-1286, 2000
8. S. Wieneke and W. Viöl, "Gas lasers excited by silent discharge", Proc. of the VIIth Int. Symp. HAKONE on High Pressure, Low Temperature Plasma Chemistry, 2000

# High peak power $CO_2$ planar waveguide lasers for direct high resolution machining

F. Villarreal, P.R.Murray, H.J.Baker, G.A.J Markillie,
R.J. Ramirez, Q. Cao, D.R. Hall

Department of Physics, Heriot-Watt University, Edinburgh EH14 4AS, United Kingdom

## ABSTRACT

The peak power and gain available from the RF excited planar waveguide $CO_2$ laser has been enhanced for pulses in the 10 to 100 μs range at pulse repetition rates up to 4 kHz. The specific peak power output for unit electrode area has been enhanced to a value of 240 kW.m$^{-2}$. Relative to cw, the small signal gain coefficient has been pulse enhanced by a factor of 7 to 2.5 m$^{-1}$.

**Keywords:** planar waveguides, carbon dioxide lasers, gain measurement, gas discharges.

## 1. INTRODUCTION

Conventional carbon dioxide lasers, either DC or RF excited, provide pulsed laser operation at high power for pulse lengths longer than 100 μs using pulsed modulation of the discharge. TEA $CO_2$ lasers readily produce much higher peak power in the 1 to 5 μs range. The pulse duration region between these two is of current interest, particularly for micro-machining applications of dielectric materials such as plastics, thermoset resins and glass where the material is naturally a strong absorber at the appropriately selected $CO_2$ laser wavelength. For such materials, the TEA laser generally has too much energy and peak power per pulse to be used in the direct writing mode, and often does not have the necessary beam quality. The high power density produced above the work-piece at the normal energy fluence for laser ablation creates a plasma in the ablation plume, modifying the coupling of power to the surface of the material. For pulses longer than 100 μs, heat conduction into the substrate produces much deeper melt and heat affected zones and reduces the peak surface temperature, so that the material ablation rate is lower. However in the pulse length $T$=20-50 μs region, the heat penetration depth $(4\kappa T)^{1/2}$, calculated with the typical values of thermal diffusivity κ for poor thermal conductors is often comparable to the absorption depth of the incident light. As an example of this, we have reported experiments on ablation of silica glass in which material removal by evaporation can be maximised at pulse lengths in the 20 to 30 μs range [1]. This avoids an explosive melt-ejection process caused by the higher ablation pressure with shorter pulses.

| | |
|---|---|
| **Temperature rise**<br>Low frequency pulsing<br><br>High frequency pulsing<br>(Pressure independent thermal conductivity) | Thermal mass $\propto p$<br>Input energy density $W.T \propto p$<br>Average power $\propto f.\,p$<br><br>Average power $W.T.f$ = const. |
| **Thermal response time**<br>(typically 1 to 2 ms for $a$ = 1.9 mm) | $\tau = a^2/4\kappa \propto p$ |
| **Oscillator response time**<br>(also depends on $W, T, f$ due to $CO_2$ dissociation) | $N_2$, CO → $CO_2$ energy transfer time $\propto 1/p$ |
| **Gain coefficient** | Stimulated emission cross-section $\propto 1/p$<br>Gain lifetime $\propto 1/p$ |

Table I. Scaling parameters for pulsed laser operation

Commercial RF excited planar waveguide lasers are commonly used in pulsed mode, offering a compact sealed-off laser source ideally suited to micro-machining processes, such as via drilling in pcb manufacture, but with pulse lengths currently ≥100 μs. In this paper, we report the extension of the capabilities of the planar waveguide $CO_2$ laser to produce greatly enhanced peak power pulses in the required time window, whilst maintaining high average power and high repetition rate [2]

## 2. SCALING PARAMETERS FOR HIGH PEAK POWER OPERATION

Planar waveguide $CO_2$ laser operating under long pulse and cw conditions optimise at pressures of typically $p$ = 80 torr with an average input power density $W$ = 40 to 50 W.cm$^{-3}$. These conditions represent the limitations on the power dissipation in



XIII International Symposium on Gas Flow and Chemical Lasers and High-Power Laser Conference,
Antonio Lapucci, Marco Ciofini, Editors, Proceedings of SPIE Vol. 4184 (2001)

the discharge channel, balanced by thermal conduction to the electrodes creating an axial temperature rise in the 300 K region. At higher temperatures the $CO_2$ gain medium becomes inefficient. In scaling the peak power of the laser, this temperature rise is the ultimate limiting factor, but technically, a lower limit may be set by discharge non-uniformity, instability and subsequent damage to the electrodes and optics.

Table I summarises the main variables of pressure $p$, power density $W$, pulse width $T$, and pulse frequency $f$ available for the scaling of peak power, and lists some of the interrelations. At low pulse rates, a RF excited laser behaves similarly to a TEA laser in that the thermal mass of the gas in the discharge channel, proportional to pressure, sets the maximum pulse energy input per pulse. Using high peak RF power, Brown *et al.* [3] have investigated this region for a large slab discharge cross section (6 x 11 $mm^2$) obtaining 150 mJ pulses with 50 μs duration, and 1.5 W average. Applying the same techniques to a planar waveguide laser, Dutov *et al.* [4] have reported similar pulse energies, again at limited pulse repetition rates and average power. In these experiments, the laser gas is cooled by conduction to the electrodes between pulses. The waveguide format of $CO_2$ laser has the advantage that the narrow gap gives a high rate of cooling, so that pulsing in the energy limit can be at high pulse rates, without the gas flow necessary for conventional TEA $CO_2$ lasers. The thermal response time $\tau = a^2/4\kappa$ for a slab shaped medium is $\tau \approx 1.5$ ms for the normal 80 Torr gas mixture, rising to ~2.2 ms for the higher pressure mixture used for enhanced pulsing, for $a$ =1.9 mm in our laser. For a pulse repetition period less than the thermal relaxation time, the gas temperature falls only a little between pulses, and the average temperature rise and average power input becomes the same as for cw operation. This limit is independent of pressure through the relatively fixed thermal conductivity of the gas mixture. In this paper we report reaching this average power limit for high peak power pulsing at pulse frequencies above 500 Hz.

Increasing the pressure of the gas can have an advantage at all pulse rates, in that the upper power density for discharge stability (the so-called α to γ transition) scales with pressure. In addition the rise and fall time of the laser pulse is shorter at high pressure, facilitating the production of short pulses. However, these advantages are balanced to some extent by the fall in the stimulated emission cross-section with pressure. However, as will be shown in section 4, gain can be maintained at a high value up >200 torr working pressure.

## 3. ENHANCED PEAK POWER LASER

The laser used for enhanced pulse operation is shown in Fig. 1. This is based on a standard, well-characterised design for a 100 W average power output laser, operating with a 2 kW peak, 1 kW average RF power supply at 81 MHz. In conventional operation, using an initial fill of 80 Torr of a 3/1/1 mixture of He, $N_2$, $CO_2$, plus 5% additional xenon, the laser can achieve peak powers of 300 W in 150 μs pulses. The resonator is the standard unstable type with a lateral magnification of 1.14, giving a beam quality after circularisation and clean-up of $M^2$ <1.2. By using this laser as baseline reference, a clear measure of the pulse enhancement can be obtained. For enhanced pulsing, the laser is adapted to run with a 25 kW cw power supply at 125 MHz, using pulse modulation capabilities to provide low duty factor operation with a maximum average power input ≤ 2 kW.

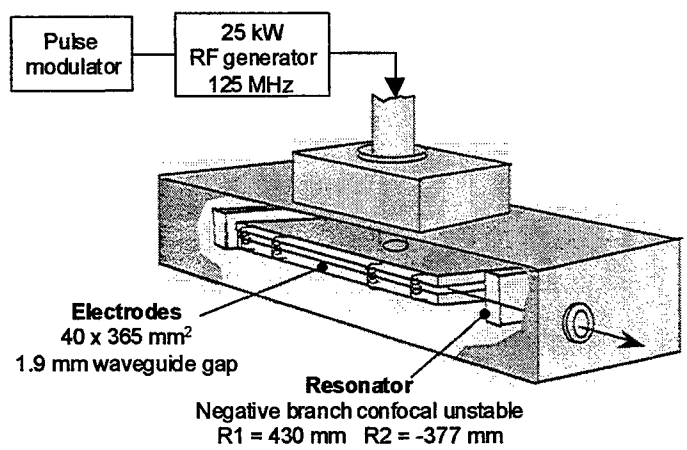


Fig.1. Details of laser structure used for enhanced pulse study.

The enhanced pulse experiments have covered the following parameter space: pressure up to 220 torr, mixture variations between 1:1:1 and 1:1:7, peak power to 23 kW, RF pulse width in the range 15 to 120 μs and pulse repetition frequency up to 4 kHz. Fig. 2 shows typical enhanced pulses [2] using a 200 Hz pulse rate and 20 kW peak power with 180 torr of 1:1:3 $CO_2$:$N_2$ ;He +5%Xe. A peak power of 3.5 kW is achieved in the 20 to 50 μs range. The discharge remains stable for these conditions up to an input power density of 860 $W.cm^{-3}$. The longest pulse in Fig.2 shows roll-over of the laser efficiency as the gas temperature approaches the maximum for $CO_2$ laser operation. However the efficiency remains high out to 120 μs.

The laser has been operated in the enhanced pulse mode over a wide range of conditions summarised in Table II at pulse rates up to 4 kHz. The results at 200 Hz are typical of the low frequency pulsing regime listed in Table I, in which the gas

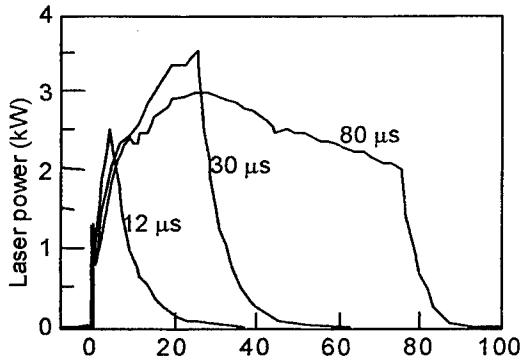


Fig.2. Laser pulses using 20 kW peak RF input power at 180 torr. The RF pulse widths are indicated.

cools nearly completely between pulses, with the energy limited by the temperature rise within a pulse. At 120 μs pulse width, this limit causes the efficiency to fall as is evident from Table II and Fig. 2. For 1 kHz pulsing, the laser operates in the high frequency limit set by thermal conduction, and an average power somewhat larger than the normal 100 W cw level is obtained. At 1 kHz and below, the thermal limit occurs before the α to γ instability at the presently available peak power. In the region of 2 kHz, the laser is subject to discharge instability, caused by the density variations in the acoustic standing wave generated by pulsing at a rate near the lateral resonant frequency of the gas in the discharge channel. Enhanced pulsing is possible, but at much more limited energy than at lower frequency. However, significant pulse enhancement can be obtained again at 4 kHz and above without discharge instability, but in this case the allowable input pulse energy is much reduced by the average power limit.

The minimum useful laser pulse width is determined by the rise and fall time of laser oscillation, as apparent in the 12 μs pulse in Fig. 2. We have measured the variation of the fall time with pressure and mixture for a static gas fill that has reached dissociation equilibrium [2]. As may be expected from the storage of vibrational energy in the $N_2$ and CO molecules followed by energy transfer to $CO_2$, the response time decreases in relation to the partial pressure of $CO_2$ in the mixture. At $p$=200 torr, the response time is fast enough for 10 μs FWHM laser pulses to be produced at high peak power.

| Pulse rep. rate and pressure | RF Pulse duration (μs) | Peak power input (kW) | Output peak power (kW) | Input energy (J) | Output energy (mJ) | Efficiency (%) | Average output power (W) |
|---|---|---|---|---|---|---|---|
| 200 Hz | 20 | 20 | 3.0 | 0.4 | 48 | 12 | 9.5 |
| 180 torr | 50 | 20 | 3.2 | 1.0 | 125 | 12.5 | 25 |
| | 120 | 20 | 3.0 | 2.4 | 235 | 9.8 | 47 |
| 1 kHz | 20 | 19 | 2.8 | 0.38 | 37 | 10 | 37 |
| 170 torr | 50 | 19 | 2.5 | 0.95 | 83 | 8.7 | 83 |
| | 120 | 19 | 1.7 | 2.28 | 133 | 6.6 | 133 |
| 4 kHz 170 torr | 40 | 19 | 1.35 | 0.76 | 35 | 4.6 | 140 |

Table II. Summary of high average power operating conditions.

## 4. ENHANCED PULSED GAIN COEFFICIENTS

The small signal gain coefficient of the $CO_2$ planar waveguide laser has been measured by Cao *et al.* [6] to be 0.35 $m^{-1}$ at 80 torr pressure, under the normal conditions of a *cw* laser oscillator. The gain is also found to *decrease* with increasing input power, partly as a result of the increasing gas temperature. In the enhanced pulse mode, conditions exist where the much higher peak discharge power can be used without significant gas temperature rise, and here the gain is expected to increase with input power. Higher gain relative to the fixed waveguiding loss and the loss associated with coupling between mirrors and waveguide will enhance power extraction in both amplifiers and oscillators. To illustrate this, a pulse gain measurement has been carried out on an identical structure to that in Fig. 1, but excited by a 10 kW, 81 MHz power source. The output of a line tunable, conventional $CO_2$ laser with ~1 W output has been mode-matched to the fundamental mode of propagation of the planar waveguide, and single-pass gain measured, using a fast thermopile detector with sub-microsecond response.

Fig. 3 shows measurements for 100 μs RF pulses, using varying pressures of the standard 3/1/1 mixture of He, $N_2$, $CO_2$, plus 5% additional xenon. The measurements are made under conditions where there is only moderate gas heating within the pulse and complete cooling between pulses. A peak gain coefficient of up to 2.4 $m^{-1}$ is obtained at 80 torr, approximately 7 times that of equivalent cw operation. Surprisingly, the gain does not fall as $p^{-1}$ as might be expected due to the scaling of the

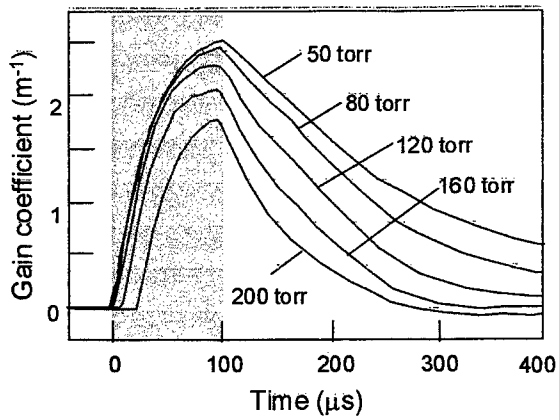


Fig. 3. Time-resolved small signal gain coefficient (10 P16 transition) for 10 kW peak, 100 µs pulses at 200 Hz rate.

stimulated emission coefficient, and high gain is available beyond $p$= 200 torr. However, the gain lifetime does behave as expected, in that the fall of gain is approximately a decaying exponential function after the end of the RF pulse, with a time constant inversely proportional to pressure. This reflects the increase quenching rate for stored vibrational energy with pressure. More work is needed to investigate higher pulse rates where increased $CO_2$ dissociation and gas temperature rise both will reduce the available gain.

## 5. CONCLUSIONS

The work reported here has extended the enhanced pulsing operating regime of the $CO_2$ waveguide laser to high pulse rates and an average power exceeding that of conventional operation. At 1 kHz, pulse energies similar to that in conventional operation is now available in the 10 to 100 µs range. Stable discharges have been obtained at power densities up to 860 W.cm$^{-2}$ and the specific power output of the 1.9 mm gap planar discharge is increased to 240 kW.m$^{-2}$. The "super-pulsing" ratio of peak to average power is increased from the conventional value of <3 to 35. As this performance is obtained under sealed-off conditions, there are good prospects for the adoption of this operating mode for many materials processing applications, particularly for polymers, glass and ceramic. The high gain coefficient under pulsed conditions may also make the technique useful for power amplifiers in coherent laser radar systems.

## 6. ACKNOWLEDGEMENT

Financial support from the Engineering and Physical Sciences Research Council, UK is gratefully acknowledged.

## 7. REFERENCES

1. F.Villarreal, P.R.Murray, Q.Cao, P.A.Field, G.A.J Markillie, H.J.Baker, D.R.Hall "Enhancement of the micromachining capabilities of $CO_2$ planar waveguide lasers" *ICALEO'99, LIA Proceedings* **88**, 20-28 (1999)
2. F.Villarreal, P.R.Murray, H.J.Baker, D.R.Hall "Enhanced peak power and short pulse operation of planar waveguide $CO_2$ lasers" *Submitted for publication.*
3. R.T.Brown, L.A.Newman, M.A.Murray, R.A.Hart, "Large volume pulsed-RF excited waveguide $CO_2$ lasers" *IEEE J. Quantum Electron.* **QE-28**, 404 (1992)
4. A.I. Dutov, I.Y. Evstratov, A.A. Kuleshov, S.A. Motovilov, N.A. Novoselov, V.E. Semenov, P.E.Smirnov, A.A. Sokolov, M.S.Yurev "Slab waveguide high-power pulsed rf-excited $CO_2$ laser", *XII GCL/HPL Symposium. SPIE Proc.* **3574**, 171 (1998)
5. Q. Cao, H.J.Baker, D.R. Hall "Transverse mode propagation and gain coefficients in a planar waveguide $CO_2$ laser amplifier" *Submitted for publication*

# Investigation of split-electrode configurations for high-power diffusion cooled annular $CO_2$ lasers

A. Lapucci[1*], M. Ciofini[1], R. Celli[1], S. Mascalchi[1], L. Roselli[2], G.L. Emili[2]
[1] - Istituto Nazionale di Ottica Applicata, Largo E. Fermi 6 – I50125 - Firenze – Italy
[2] - Dipartimento Ingegneria Elettronica ed Informatica – Università di Perugia, Perugia – Italy

## ABSTRACT

For a kW annular diffusion-cooled laser, we tested the possibility of using the electrodes directly as waveguide wall . We considered dielectric and metallic spacers. Electric field distribution calculations and preliminary experimental results are presented.
**keywords:** gas lasers, carbon dioxide lasers, diffusion cooled lasers, annular lasers.

## 1. INTRODUCTION

The annular geometry has always been representing a promising alternative to the slab format, already well established in the market of high-power diffusion cooled $CO_2$ lasers[1]. Eventually this solution leads to a higher cooling surface to global volume ratio. In spite of that, most attempts to adopt the annular format have, up to now, been frustrated by some construction difficulties inherent to this geometry. Problems are mainly related to two aspects: firstly the discharge system is more compact but less accessible putting some limits to the attainment of a uniform plasma excitation. Secondly, a reasonable optical resonator, capable of efficiently extracting a good beam from the annular gain region, has not yet been totally established.

Interesting solutions are now being found to both these kinds of problems. We already reported in the past conference of this same series, on the fruitful adoption of a Talbot resonator for the narrow annular gain region, together with the disclosure of a powerful method for re-shaping the extracted field distribution[2].

Talbot cavities have been mainly applied to diode laser arrays but they proved successful for $CO_2$ waveguide lasers as well, both in array or slab schemes. In this latter case, they consist in a conventional guided resonator with a periodic spatial filter inside the cavity, selecting a single lateral mode (or at least a frequency-degenerate reduced family of them). The selected mode is equivalent to a high order mode of the waveguide, i.e., a multilobed emission. We modified this concept to suit the annular geometry.

On the other hand the attainment of a uniform plasma generation has been approached in the past by means of electrodes sectioning, either longitudinal[3] or transversal[4]. We followed the first solution constructing some sample discharge units based on a split external electrode. In Ref.3 this solution brought to a pretty high multimode specific power extraction (16.8 kW/m$^2$), but it involved the use of a ceramic outer wall of the discharge channel. This construction appears hardly feasible for high power systems needing large electrode surfaces. Clearly in this case one should be able to machine large ceramic pipes with relatively tight tollerances, both for good waveguide optical properties and for a good thermal coupling with the cooled metallic electrode surfaces. We tested the possibility of having the metallic external electrodes directly acting as the outer wall of the waveguide. In this case the two split electrodes determine a discontinuous waveguide wall, but this effect can be maintained reasonably small. We considered both configurations with dielectric spacers between the external electrodes and configurations with metallic spacers. Two-dimensional electric field distribution calculations were performed to investigate the possibility of plasma generation also in the regions confined by the spacers. We report on the results of these numerical simulations and on the preliminary experimental results obtained on our discharge modules.

## 2. THE SPLIT ELECTRODE SCHEME

The longitudinal sectioning of the external electrode allows the adoption of established techniques devoted to the attainment of a uniform discharge excitation, such as those using terminating or resonating external inductors[5]. In this way the two halves of the external electrode are connected to the RF driver and the internal electrode is floating. As a consequence the external cylindrical surface must have an electrical discontinuity, while it is preferable from an optical viewpoint to maintain the guiding walls as uniform as possible. With these conditions in mind we experimented two solutions making use of different external electrode spacers.

* e-mail: lapo@ino.it


XIII International Symposium on Gas Flow and Chemical Lasers and High-Power Laser Conference,
Antonio Lapucci, Marco Ciofini, Editors, Proceedings of SPIE Vol. 4184 (2001)

In a first case we used dielectric spacers ( $Al_2O_3$ ceramic) and in a second case we adopted metallic spacers hold by ceramic blocks. In this case the metallic spacer must be kept a few tenth of millimeters away from the electrodes in order to allow only displacement currents to flow in the separation regions. A schematic drawing of this construction scheme is shown in Fig.1.

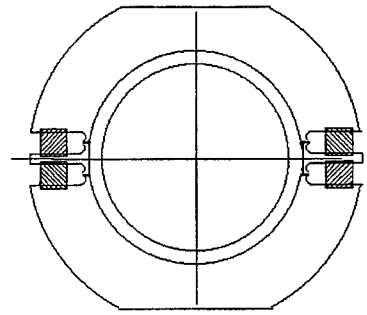

Fig. 1: Schematic drawing of external split electrode with metallic spacers.

## 3. NUMERICAL MODELING OF THE DISCHARGE

The design of the correct spacers presents some difficulties. Indeed the spacers shunt the discharge channel, thus their electrical behavior must be carefully evaluated. To do this we performed numerical computations of the discharge behavior making use of a two-dimensional finite difference electrostatic field simulator corrected to include the effect produced by electrodes sheaths regions, i.e. regions affected by electron depletion[6]. Following the results obtained in ref.[6] we assumed the effect of electron attachment as being mainly that of producing a higher electrostatic field in the charged regions. We took this effect into account considering a higher dielectric constant in the proximity of solid boundaries ( either metallic or dielectric).

The crucial points of our studies are related to the electric field behavior in the regions around the spacers . Here we have to obtain two conditions: firstly we do not want dark regions in the annular discharge channel, thus we need a reasonably high field intensity also in the volume between the spacers and the internal floating electrode. Secondly we do not want plasma spillover, that is the excitation of a discharge external to the annular channel. This means that we have to shape the spacers in such a way that the field equipotential lines are sufficiently spaced apart or that field lines close between solid boundaries with a long path in gas filled regions out of the annular channel. Fig.2 shows typical results of our simulations in the case of metallic and dielectric spacers.

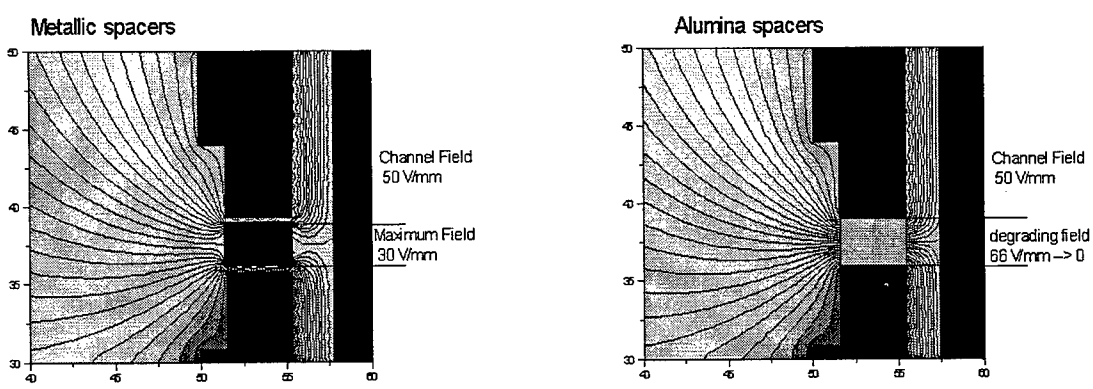


Fig.2 Electric field equipotential lines in the case of metallic spacers or ceramic spacers

Given this electrostatic field distributions and considering typical threshold condition for the stability of an RF alpha discharge we can mark sites in our simulations where the plasma exists and study its modifications consequent to electrodes or separators shape modifications.

Fig. 3 Reports examples of this functionality of our software . In this figure changes in the discharge spillover are evidenced correlated with changes in the shape of alumina spacers length.

Analogous considerations can be done for the case of metallic spacers. As well as the same parametric study can be done to find conditions for a reduced dark region in the separators vicinity inside the discharge annular channel.

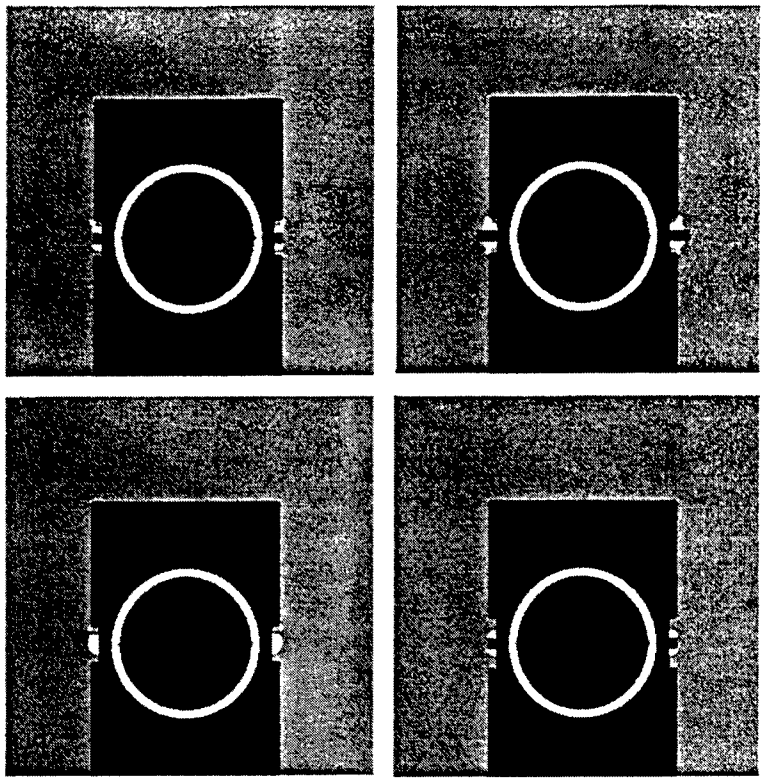

Fig.3: Numerical modeling of the plasma formation inside and outside the annular discharge channel varying the spacers geometry.

## 4. EXPERIMENTAL SYSTEMS AND RESULTS

Two test discharge modules, based on the two electrode formats numerically studied and presented in the previous sections, have been constructed and tested. The modules are characterized by a discharge channel external diameter of 49 mm and discharge gaps varying from 1.5 to 2.2 mm. Discharge gaps are easily changed in this geometry, simply changing the outer diameter of the inner floating electrode. For these experiments we limited the discharge length to 150 mm.

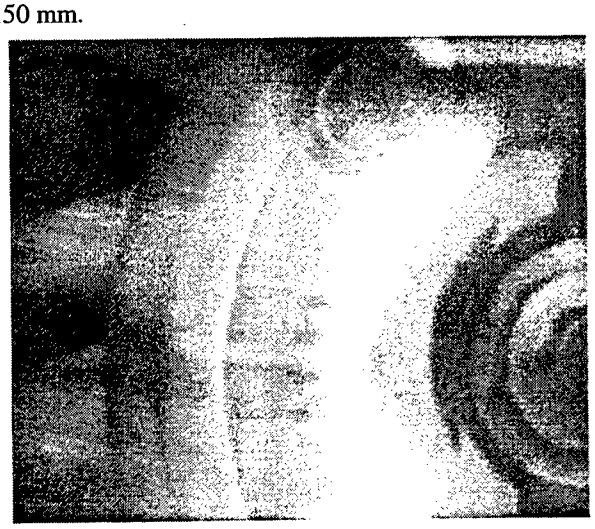

Fig.4: Experimental discharge module with metallic spacers. A reasonable discharge filling of the region between spacer and internal electrode is shown in coexistence with a limited discharge spillover in regions external to the annular channel.

We tested different discharge conditions always in a standard 1:1:3 $CO_2$,$N_2$,He gas mixture. Pressure varied between 30 and 120 mbar and RF power density between 7 and 55 W/cm$^3$ . Consistently with our expectations and with the predictions of our numerical modeling the dark region extension in the discharge channel varied with pressure, power density loading and spacer geometry. Precisely, we could reduce this extension reducing the gas pressure, rising the power loading or reducing the spacer-thickness to channel-gap ratio. Of course this last parameter cannot be lowered indefinitely since its excessive reduction brings to the discharge spillover and eventually to the localization of the discharge in the vicinity of the external electrodes separation only. Our preliminary parametric study brought us to the identification of geometries capable of maintaining a stable discharge with limited or even canceled dark regions in the annular channel at RF power density loading of interest for the construction of high power diffusion cooled

$CO_2$ lasers, as evidenced in Figs. 4 and 5. At the moment we have obtained uniform discharges at a 40 W/cm$^3$ power density level in a 1:1:3 mixture at 120 mbar using metallic spacers and at a 50 W/cm$^3$ in the same mixture at the same pressure using ceramic spacers. The discharge in a module with metallic separators is shown in Fig.4, whereas Fig.5 shows details of the ceramic-separated discharge module. In this figure a low pressure discharge is shown where significant plasma spillover is visible.

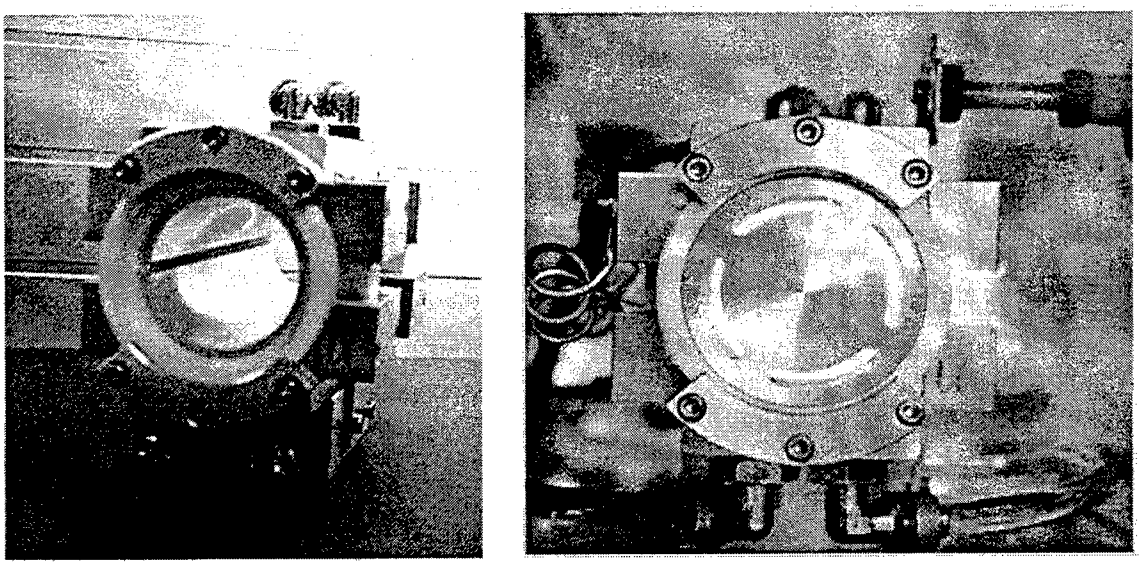

Fig.5: details of the discharge module with ceramic spacers.

## 5. CONCLUSIONS

In conclusion, we have shown the possibility of obtaining stable and uniform RF discharges in an annular channel with an external split electrode directly providing the waveguide outer wall. Reasonable results were obtained both in the case of metallic and ceramic spacers. We succeeded in obtaining working conditions in which the dark regions inside the annular channel were limited or totally canceled without producing large plasma spillover.

This solutions enable the construction of extremely compact and cost-effective high power diffusion cooled $CO_2$ lasers.

With the power density loading level we have obtained so far, the construction of a 1.5 kW laser is feasible with a discharge 70 cm in length and 6 cm in outer diameter.

## REFERENCES


[1] - D.R.Hall, H.J.Baker, " RF excitation of diffusion cooled and fast-axial flow lasers", VII GCL, SPIE Proc.**1031**, 60-67, (1988).

[2] - A.Lapucci, M.Ciofini, S.Mascalchi, "Beam properties of a waveguide annular $CO_2$ laser with a Talbot cavity"XII GCL-HPL, SPIE Proc.**3574**, 120- 127, (1998).

- A.Lapucci, "Laser source and filtering method for obtaining a good optical quality from beams of annular section" Intl. Pat. Appl. WO99/63633, (1999).

[3] - J.W.Bethel, H.J.Baker, D.R.Hall, " A new scalable annular $CO_2$ laser with high specific output power", Opt. Commun. **125**, 352-358, (1998).

[4] - R.Nowak, H.Bochum, T.Hall, K.Wessel, B.Grubert, " High power coaxial $CO_2$ waveguide laser", XI GCL-HPL, SPIE Proc.**3092**, 88-91, (1996).

[5] - A. Lapucci, F. Rossetti, M. Ciofini, G. Orlando, "On the longitudinal voltage distribution in Radio-frequency discharged $CO_2$ lasers with large area electrodes", IEEE J. Quantum Electron. **QE-31**(8), 1537-1542, (1995).

[6] - K.Schroeder, "Theoretical treatment of RF discharges in $CO_2$ waveguide lasers" , J. Appl. Phys. **68**(11), 5528-5531, (1990).

# High modulation rate, microsecond pulses for micromachining using a planar waveguide $CO_2$ laser amplifier

Qiusheng Cao, Howard J Baker, Denis R Hall

Department of Physics, Heriot-Watt University, Edinburgh EH14 4AS, United Kingdom

## ABSTRACT

A 7-pass, master oscillator and power amplifier $CO_2$ laser system is reported using planar waveguide structures. An acousto-optic modulator between oscillator and amplifier is shown to introduce thermal lens effects that modify the mode-matching. Amplification of pulse bursts at 50 kHz in cw gain is presented, and gain saturation and recovery effects are demonstrated to pulses at a modulation rate up to ~550 kHz.

**Keywords:** planar waveguides, carbon dioxide lasers, acousto-optic modulation, laser amplifiers, gain measurement, gas discharges

## 1. INTRODUCTION

$CO_2$ laser pulses at high repetition rates, in some cases in excess of 200 kHz, are required for fast, high resolution processing applications, such as engraving, scribing, perforating and so on. In addition, a combination of short laser pulses (1 to 20 μs) and enhanced peak power levels is preferred to achieve high processing efficiency with minimised heat-effected zone effects relative to conventional long pulse $CO_2$ lasers and reduced plasma screening effects relative to TEA $CO_2$ lasers. Laser pulses that satisfy such requirements are currently not achievable by direct modulation of DC or RF discharges. However, the master oscillator and power amplification approach has been shown to be appropriate by allowing the addition of a separate modulator between oscillator and amplifier. For example, Wheatley [1] has reported a MOPA system that uses a 12-leg, DC-excited, slow-flow amplifier and two AO modulators, producing microsecond pulses with full modulation depth at pulse rates in excess of 200 kHz and an average power up to 1 kW. This system is optimised for print roll engraving.

The planar waveguide format of $CO_2$ laser is attractive for MOPA systems because such devices operate in a true sealed-off mode at higher pressure than the slow-flow DC excited systems, enhancing the response time of the amplifier. The devices are compact and offer high power, near-diffraction limited beam quality and low running cost. Recently, we have carried out extensive development of MOPA systems using planar waveguide structures for both average and peak power enhancement and short pulse operation (<50 μs). A number of key issues have been studied, such as mode-matching between planar waveguides [2], control of parasitic oscillations [3], parametric gain characteristics [2] and so on. Here, we study acousto-optic modulation as the pulse forming mechanism, address the thermal effects in the AO modulator to laser beams passing through it, and discuss how to accommodate beam distortion in beam coupling to the amplifier. Then, we describe the configuration of a 7-pass, planar waveguide AOM/MOPA system and present the preliminary results on the amplification of high modulation rate pulses.

## 2. ACOUSTO-OPTIC MODULATION OF BEAM FROM A PLANAR WAVEGUIDE LASER

Acousto-optic modulators are ideal devices for fast switching (<1 μs) of laser beams with convenient intensity modulation capability through the control of RF drive power. At the 10.6 μm wavelength, current commercial AO modulators are made from germanium crystals and are limited in laser power to only 100 W because of the well-known thermal runaway effect in this material. Below this limit, thermal effects occur due to the non-uniform distribution of refractive index generated by absorption of the laser light, giving power dependent thermal distortion of the beam passing through the AO modulator. The beam distortion may be eased to some degree through the use of larger beam size in the AO modulator to reduce the power density. However, there is an upper limit to the beam size caused by the variation of the scattering efficiency as the beam exceeds the volume of the acoustic wave in the crystal, producing a second form of beam distortion. In addition, a large beam size lengthens the acoustic transit time and reduces the modulation bandwidth. In this section we consider these effects on the mode matching condition between oscillator and amplifier.

Fig. 1 is a schematic of the set-up used in the MOPA system reported here. The planar waveguide laser oscillator is a commercial device, producing an average output power up to 100 W in pulses with a peak power up to 300 W, dependent on the discharge conditions. The beam produced by the oscillator has a propagation parameter ($M^2$) ~1.1 in the transverse



XIII International Symposium on Gas Flow and Chemical Lasers and High-Power Laser Conference, Antonio Lapucci, Marco Ciofini, Editors, Proceedings of SPIE Vol. 4184 (2001)

direction and ~1.2 in the lateral direction (after beam clean-up). The germanium AO modulator, from NEOS, is water-cooled with an allowed incident power up to 100W, driven by a 27 MHz RF source giving a diffraction efficiency up to 75%. The AO modulator is positioned 350 mm from the laser exit, where the natural divergence of the oscillator beam gives a beam size of 4-5 mm in both directions within the germanium crystal. This leads to a transit time of 0.6~0.8μs for the AO modulator having an acoustic velocity of 5.5mm/μs, limiting the pulse duration of the diffracted beam to larger than ~1 μs (FWHM). The optical signal deflected by the AO modulator is frequency shifted by 27 MHz away from the natural line centre of the $CO_2$ laser line. However, this detuning has little effect on the subsequent amplification as the waveguide amplifier has a wide bandwidth of 400-500 MHz for typical pressures of 80-100 torr [4].

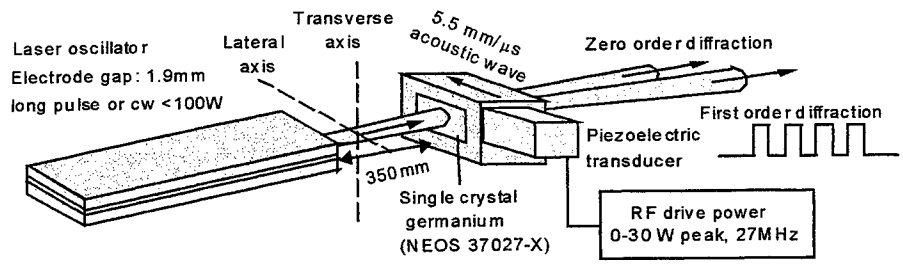


Fig. 1. The use of an acousto-optic modulator to produce high modulation rate laser pulses from a long pulse or cw incident beam

The zero order diffracted beam is blocked by a power dump and the first order diffraction is designated as the probe beam for the amplifier. As anticipated, thermal effects are observed, which result in beam distortion and complicate the beam coupling process to the amplifier. These thermal effects are seen to be dependent strongly on the laser power incident to the AO modulator, whilst the effects induced by the RF drive power are observed to be relatively insignificant. Fig. 2 shows the variation of the far-field beam profiles of the first order diffraction. In the transverse direction, the beam becomes less divergent in the far-field with increased laser power. For laser powers of 10 to 30 W, the equivalent focal power of the thermal lens is estimated as 1100-1200 mm and the beam quality degradation is measured to be ~10%. In the lateral direction, however, the thermal effects appear to be less significant, perhaps because of the larger lateral dimension of the crystal relative to the transverse dimension, leading to a smaller lateral temperature gradient. Consequently, the overall beam distortion corresponds to generation of an elliptical wavefront.

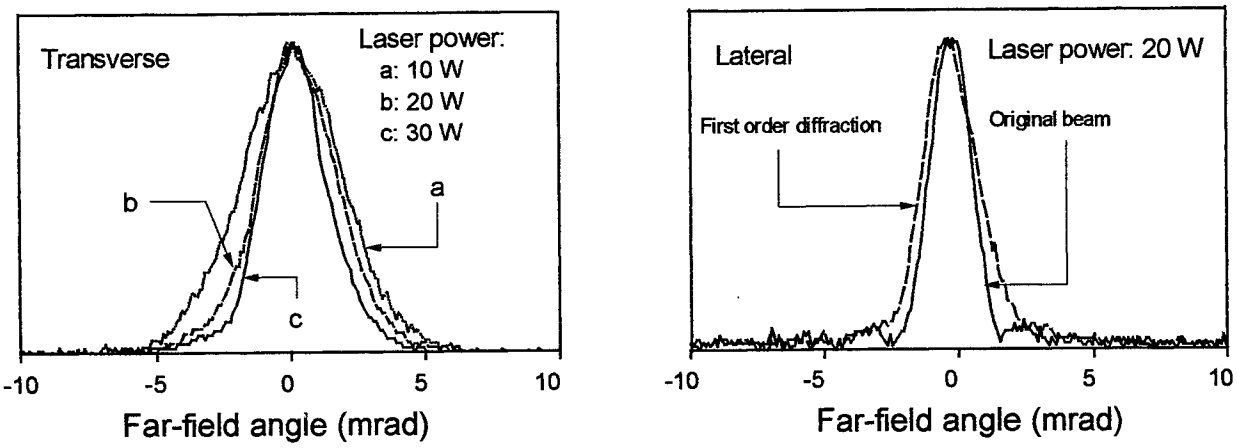


Fig. 2 Variation of far-field beam profiles due to thermal effects in the AOM dependent on laser power

## 3. CONFIGURATION OF THE AOM/MOPA SYSTEM

Fig. 3 shows a schematic of the MOPA system incorporating an AO modulator for pulse forming, which is positioned as in Fig. 1 relative to the laser oscillator. The power amplifier consists of a 95×770×1.75 $mm^3$ planar waveguide, and is driven by a 81 MHz RF power generator with variable duty factor pulsed discharges. A pair of mirrors from a positive branch unstable resonator, positioned off-axis, are used to give a 7-pass, multi-fold beam path within the waveguide, with a gain length of ~5.39 m. The amplifier vessel is filled with a standard gas mixture of $He(3):CO_2(1):N_2(1)+Xe(5\%)$. A fast thermopile of a response time <1 μs is used to measure the temporal laser pulse profiles. For some discharge conditions giving the highest gain, parasitic oscillation is observed. This has been eliminated by using two masks on the resonator mirrors [3] which match the desired beam path. The optical system in Fig. 3 has been developed to couple the beam to the

amplifier in the presence of the AOM thermal lens. An aperture near the focal plane between the two curved mirrors, both tilted vertically, cleans the beam in terms of side-lobes. The optical system is laterally telecentric, with a magnification of 1.66 to provide a suitable beam size and divergence to facilitate the 7-pass beam folding within the waveguide amplifier. In the transverse direction, it is designed to give the correct beam waist and position at the amplifier input to provide waveguide mode-matching. To cope with the thermally induced beam distortion, this optical system allows adjustments of the mirror positions and tilt angles to vary the beam parameters to some degree at the input of the amplifier to accommodate the variations of the beam parameters with different laser powers. In the experiments, near perfect mode matching has been achieved for an oscillator power of 40-50 W by setting a transverse beam waist of 0.60 mm at the input plane of the amplifier waveguide.

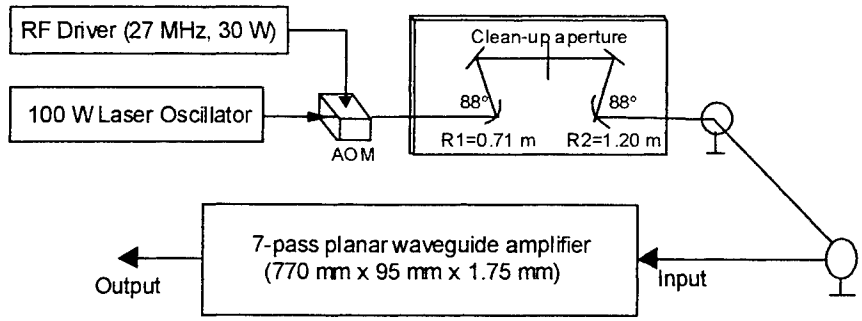


Fig. 3 Schematic diagram of the AOM/MOPA system

The passive power transmission in a single pass through the amplifier is ~ 98%, with over 95% of the power contained in the fundamental mode. Laterally, with a beam size of 3.4 mm measured at the amplifier input, the beam profiles on the resonator mirrors have been calculated for the 7-pass configuration using the real beam propagation theory [5] and the well-known ABCD law, giving a beam size of ~11.2 mm at the output port. With some degree of overlapping, the laterally expanding beam gives a filling factor of 81%. Because the non-guided spacing between the mirror and guide end varies from 1 mm to over 10 mm due to angular tilt of the resonator mirrors, significant coupling losses occur as the beam passes through the waveguide. In the 7-pass configuration, the passive transmission is 60~65%, and decreases to ~55% when two masks are included for the elimination of parasitic oscillations. The output beam quality has been examined by observing the beam profiles at the far-field as shown in Fig. 4, where the amplifier is operated with a pulsed discharge at a repetition rate of 1 kHz, amplifying 10 μs laser pulses. It is seen that the beam is very close to the fundamental mode in the transverse direction and laterally rather gaussian-like without side lobes.

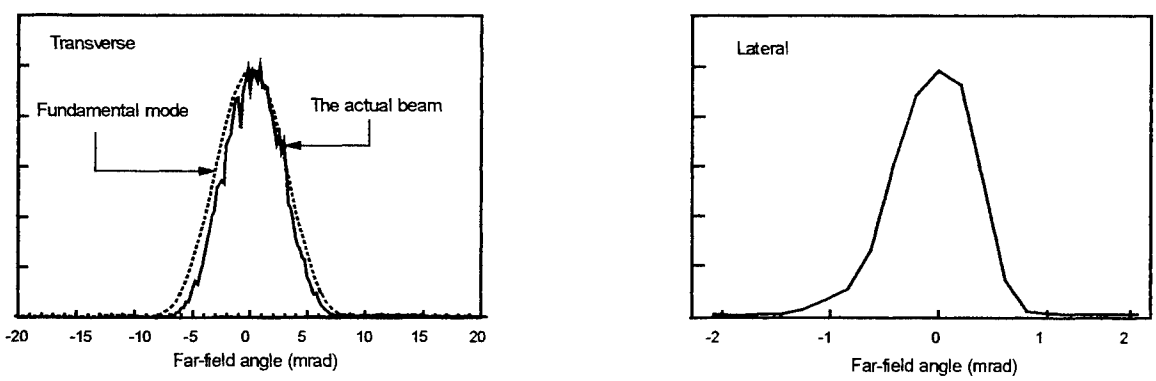


Fig. 4 Far-field profiles of the output beam (10 μs pulse width, 1 kHz pulse rate) from the 7-pass waveguide amplifier

## 4. PULSE AMPLIFICATION AT HIGH MODULATION RATE

Previously, the cw gain characteristics of the amplifier without AO modulation have been determined [2], and cw power amplification has been carried out in a 5-pass configuration, giving an amplified output power of 270 W at pressures in the range of 75-90 torr for an input power of 80 W [3]. Here, our main interests are to investigate the amplification characteristics of 1-20μs pulses at high modulation rates using the 7-pass amplifier system described above, with both the oscillator and amplifier operated with high frequency RF pulsing, producing effectively cw gain. This mode is required for the generation of continuous pulse trains needed for example in laser engraving. To allow powers which give some degree of gain saturation in the amplifier, whilst avoiding the thermal problems of the AO modulator, we have used bursts of pulses as the input, with a burst repetition rate of 1 kHz. For example, bursts of eight equal pulses at 50% duty cycle and 50 kHz modulation rate produce an average input power of 5.8 W with a peak power of 72.5 W. The amplifier has produced an

average output power of 34 W, corresponding to a peak power of 425 W, for a 10 kHz discharge at 50% duty cycle. This is equivalent to an output power of ~212 W if continuous input pulsing were to be used with an incident power of ~96 W to the AO modulator.

A problem associated with high pulse rate $CO_2$ amplifier operation is that a particular laser pulse may be affected by the gain saturation induced by the previous pulse, leading to a reduced pulse amplitude when the time between pulses is shorter than that required for gain recovery. As a result, in cases of varying pulse rate, for example in laser printers, pulses of random amplitudes may be produced. This phenomenon is more obvious using a pulsed discharge to produce higher gain than cw, as shown in Fig. 5. The oscillator signal passes through the amplifier immediately after the termination of the discharge. In Fig. 5(a), a 21 μs pulse is amplified both with and without additional modulation at 550 kHz. Both show loss of gain due to saturation on the 2 to 4 μs time scale, with the modulated pulse maintaining higher saturated gain due to a degree of gain recovery between individual pulses. We have used the AOM to generate pulse pairs as the input, to look into the gain recovery issue further as shown in Fig. 5(b). By varying the second pulse in time relative to the first one, the second pulse at the output appears to recover gain in about 8 to 10 μs at a pressure of 85 torr, about 3 times the resonance energy time between excited $N_2$ (or CO) and $CO_2$ ($00^01$) molecules [6]. However, the gain recovery time may be shortened at higher pressure or if the RF discharge is present. Fig. 5(a) shows that the AOM can usefully pulse modulate to near 100% depth at 500 kHz. However, Fig. 5(b) indicates that a lower pulse rate limit of about 200 kHz is needed to avoid unwanted pulse amplitude modulation effects by the gain saturation/gain recovery process.

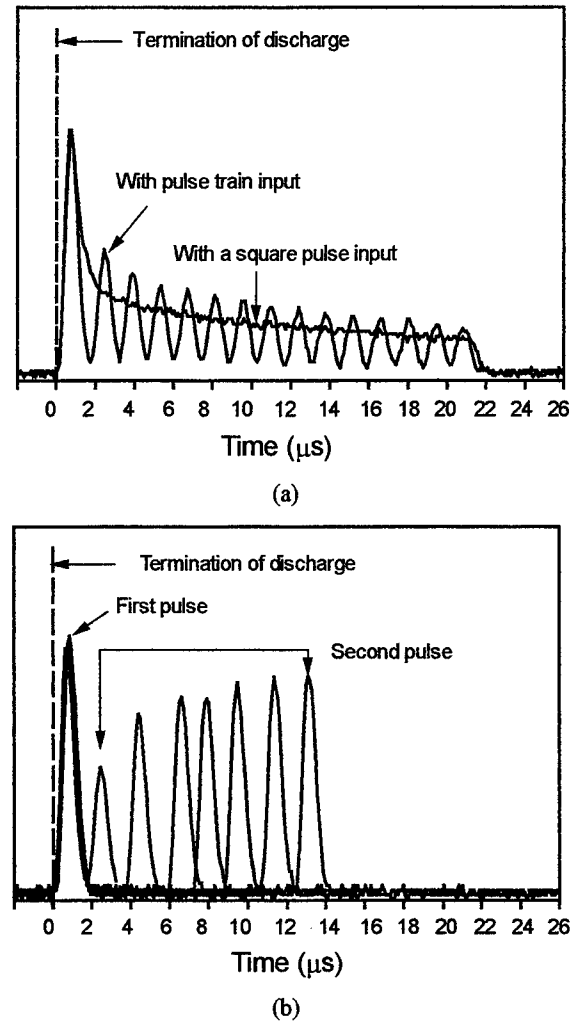


Fig. 5 (a) Demonstration of the gain saturation and recovery effects with a burst of 550 kHz pulses passing through the amplifier. (b) Observation of progressive gain recovery via amplification of separation-varying pulse pairs. Amplifier operating conditions: P = 85 torr, discharge duration = 180 μs, PRF = 1 kHz

## 5. CONCLUSION

The first planar waveguide AOM/MOPA system has been reported, which incorporates a beam coupling optical system accommodating some degree of beam distortion due to thermal effects occurred in AO modulation. The amplification of bursts of pulses at 50 kHz has been conducted in cw gain. Fast gain saturation and recovery time scales have been found, consistent with the operation of the waveguide amplifier at high pressure.

## 6. ACKNOWLEDGEMENT

The financial support from the Engineering and Physical Sciences Research Council, UK is gratefully acknowledged.

## 7. REFERENCES

1. D. Wheatley, "A High Power, High Modulation Bandwidth $CO_2$ Laser," GCL/HPL'96 Edinburgh, *SPIE Proc.* **3092**, pp.109-113, 1997
2. Q.Cao, H.J.Baker, D.R.Hall, "Transverse mode propagation and gain coefficients in a planar waveguide amplifier," Submitted for publication
3. Q.Cao, "Planar Waveguide $CO_2$ Laser Amplifiers," PhD thesis, Heriot-Watt University, UK, 2000
4. T. J. Bridges, H. A. Haus, and P. W. Hoff, " Small-signal Step Response of Laser Amplifiers and Measurement of $CO_2$ Laser Linewidth," *IEEE J. Quant. Electron.* **4**, pp.777-782, 1968
5. A. E. Siegman, "New development in laser resonators," *SPIE Proc.* **1224**, pp.2-14, 1990
6. P. K. Cheo, *$CO_2$ Lasers*, Chapter 2, Lasers, edited by Levine and Demaria, Marcel Dekker, Inc., New York, 1971

# Experimental study of small-signal gain and laser beam parameters in high-power pulse-repetitive RF-excited slab $CO_2$-lasers

A.I.Dutov, A.A.Kuleshov, N.A.Novoselov, N.L.Orlov, A.A.Sokolov

199034, Research Institute for Laser Physics, Birzhevaya, 12, St.-Petersburg, Russia.
Phone: (812) 328-10-93. Fax: (812) 328-58-91. E-mail: dutov@ilph.spb.su

## ABSTRACT

The paper presents the results of measuring of the small-signal gain $<g_0>$ in the active medium of the high-power pulse-repetitive RF-excited slab $CO_2$-laser. The measurements were carried out for the pumping pulse durations in the range 20..50 μs and pulse repetition rates 100..500 Hz. The maximal specific energy, delivered to the active medium, was 430 W/cm$^3$. In the experiment were measured the average output power of radiation, pulse energy and power and the output beam divergence.

**Keywords**: high power pulse-repetitive slab $CO_2$-laser, small-signal gain

## 1. INTRODUCTION

Laser processing of fragile materials, such as glass, ceramics, semiconductors, stones etc., and of materials with the high thermal conductivity, such as copper, aluminum etc., as well as the removal by laser radiation of dye or dirt from material surface, require the use of laser beams with the sufficiently high power and rather short pulse. Such pulses can provide the material cutting, drilling, scribing or surface cleaning (by evaporation) practically without any heat deposition.

For these purposes one can use the compact sealed-off RF-excited slab $CO_2$-lasers, providing pulse repetition rates from several hundred Hz to several kHz. One of the most important parameters of the active medium of lasers is the small-signal gain. One has to take it into account while designing and developing the laser of a kind.

Important experimental results in this direction were published in two papers. In the paper[1] there was provided the output pulse energy of 150 mJ and the maximal output pulsed power of about 3000 W. Its authors have used the RF excitation frequency of f=152 MHz, providing thus the possibility to deliver to the discharge the power density of ~ 700 W/cm$^3$. Pumping pulse duration was 50 μs, and the repetition rate - 50 Hz.

In our previous paper[2] we have studied the pulse-repetitive mode of pumping also for the excitation frequency of f=152 MHz. We have delivered to the medium up to 400 W/cm$^3$ at the pulse repetition rate F of up to 100 Hz.

This paper presents the results of measurements of small-signal gain and the output parameters of the laser for the pulse repetition rates of up to 500 Hz.

## 2. EXPERIMENTAL SETUP

Our investigations were carried out at the slab waveguide $CO_2$-laser with the planar configuration and with the sealed-off non-flow operation. The discharge channel was formed by two copper electrodes (80x600 mm), separated by the discharge gap with the height 2.4 mm. All internal surfaces of laser head were covered by the special aluminum coating.

The system of RF-power supply was based on the self-excitation scheme and operated at RF-frequency of 152 MHz. Peak RF power from generator equaled to 45-50 kW coming in RF pulses with the duration 20-50 μs and repetition rate of F=100..500 Hz. These values corresponded to the specific power density of 350..430 W/cm$^3$. The attempts to exceed the limit of F=500 Hz resulted in significant inhomogeneity of discharge distribution along the electrode length. Power, putting into the discharge, was measured by calorimetery method. All measurements were carried out for the active medium mixture of $CO_2$:$N_2$:He:Xe=1:1:6:0.4 and its pressure of 150 Torr.



XIII International Symposium on Gas Flow and Chemical Lasers and High-Power Laser Conference,
Antonio Lapucci, Marco Ciofini, Editors, Proceedings of SPIE Vol. 4184 (2001)

Small-signal gain $g_0(t)$ was measured in a double pass optical scheme under different modes of pumping. The probe beam was provided by frequency stabilized $CO_2$-laser LG-74, providing the CW output of ~ 1 W in the line 10P(20) ($\lambda$=10.59 μm). Its radiation passed through the active medium and was registered by the mercury-doped germanium-based photodetector with the time resolution of better than $10^{-7}$ sec. The value of small-signal gain was calculated according to the formula

$$g_0 = \frac{1}{L} \cdot \ln\left( {u_2}/{u_1} \right) \quad [cm^{-1}]$$

Here $u_1$ and $u_2$ are the amplitudes of the amplified and non-amplified signals at the photodetector and L is the length of the active medium. It is obvious that in the slab laser is thus measured the value of the small-signal gain $<g_0(t)>$, averaged both along the discharge gap and across the section. Laser output parameters were measured with the use of the confocal unstable resonator, formed by two concave spherical mirrors (negative branch of instability). Resonator magnification was equal to 1.17.

## 3. EXPERIMENTAL RESULTS

### 3.1. Small-signal gain in medium ($g_0$)

In Fig.1 is shown the dependence $<g_0(t)>$, measured for the pumping pulse duration of $\tau_p$=37 μs and repetition rate F=200 Hz. One can see that the maximal value of $g_0(t)$ reaches 1.5% $cm^{-1}$ to the moment of end of pumping pulse. In the same Figure are shown the oscilloscope records of the pumping and generation pulses (the latter was registered in another experiment with the use of laser resonator). The specific power density in this case was equal to 430 $W/cm^3$. Thus the value of $<g_0(t)>$, averaged along the pulse, was equal to 0.9% $cm^{-1}$.

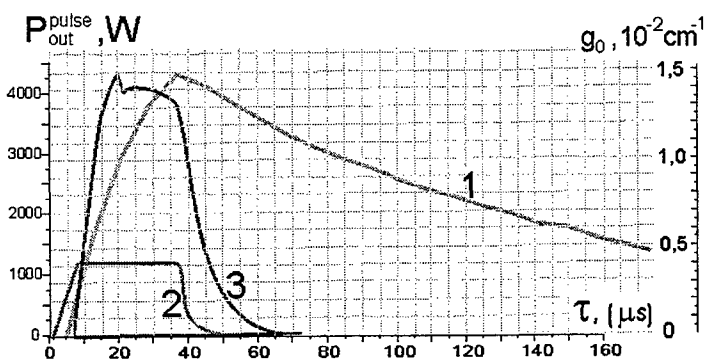


Fig.1. 1 - Time profile of $g_0(t)$, 2 and 3 – oscillograms of pumping pulse ($\tau$=37 μs) and generation pulse.

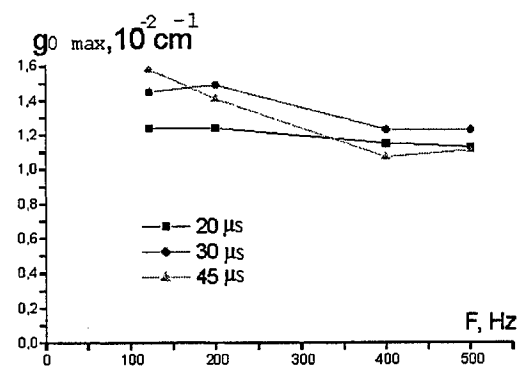


Fig.2. Dependence of maximal value $g_0(t)$ vs. pumping pulse duration and pulse repetition rate.

In Fig.2 is shown the dependence of the maximal values of $<g_0(t)>$, registered for various durations of pumping pulse in the range of pulse repetition rates from 120 to 500 Hz. One can see from this Figure, that with the heating of the active medium the value of $<g_0>$ reduces from 1.4-1.5%$cm^{-1}$ for F=120 Hz to 1.2%$cm^{-1}$ for F=500 Hz.

### 3.2. Laser generation parameters

The measurements of the laser parameters were carried out in the pulse-repetitive mode of operation. Repetition rate was varied within the range from 100 to 500 Hz. The output pulse energy was calculated from the measurements of the average output power. In Fig.3a,b are shown the dependencies of the output laser energy and maximal power in the pulse vs. the pulse repetition rate F.

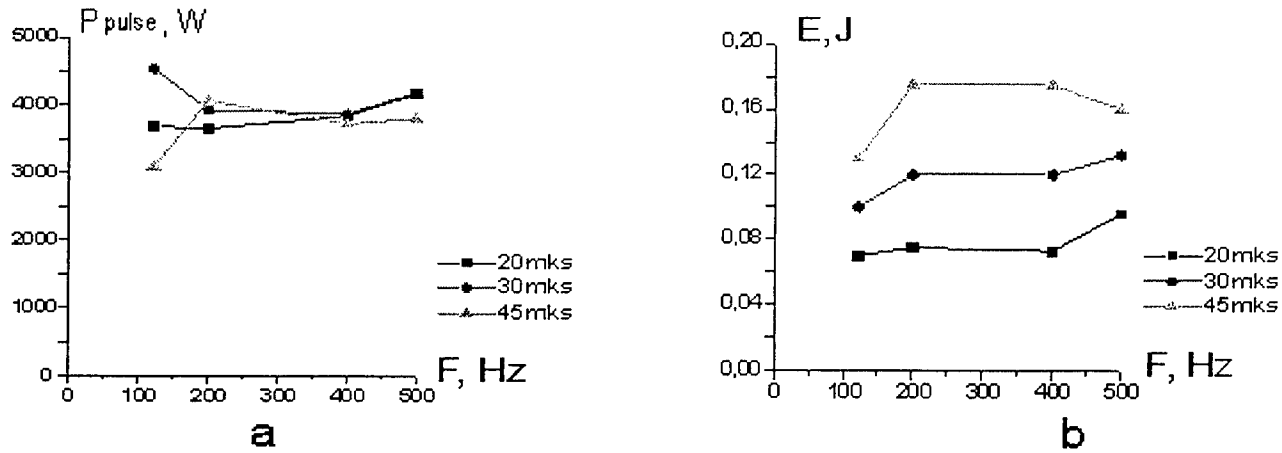


Fig.3. Dependencies of peak pulse power (a) and of pulse energy (b) vs. pumping pulse duration and pulse repetition rate.

One can see that the light power was reaching the value of 4000 W and more. Note, that the similar measurements, carried out for the gas pressure of 200 Torr have shown that the maximal pulsed light power is reached at $\tau_p$=20 μs and F=120 Hz; it was as high as 5000 W. However, in such case the gas pressure emphasizes the plasma instability and inhomogeneity, which prevent the normal performance of the laser for some pulse repetition rates.

In Fig.4 are shown the dependencies of the average output power of laser generation vs. pulse duration and vs. the pulse repetition rate. One can see that average power varied within the range from 10 to 100 W.

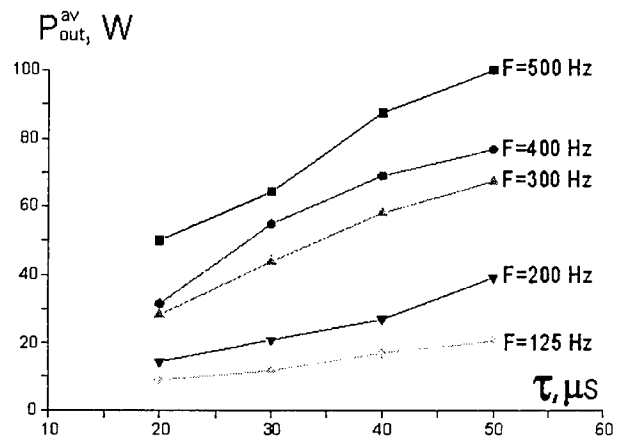


Fig.4. Dependencies of average output power of laser generation vs. pumping pulse duration and pulse repetition rate.

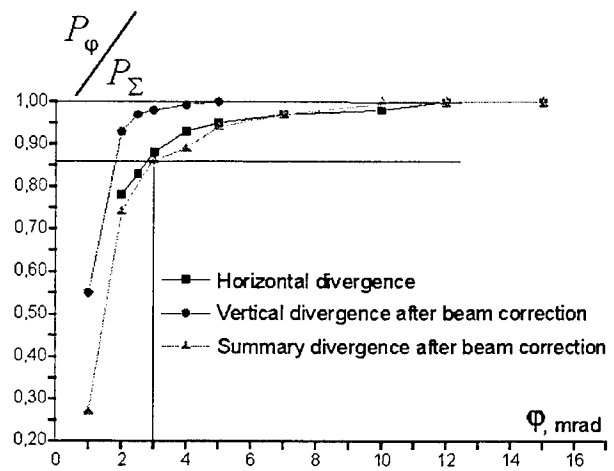


Fig.5. Angular distribution of radiation power (F=500 Hz, τ=45 μs, $P_{out}^{av}$=85 W).

Beam divergence was measured with the use of slot diaphragms in two sections - along the gap and across it. The measurements were done according to the calorimetery methodics. After correction of the divergence along the slab coordinate by the cylindrical lens, the divergence was measured by a round diaphragm. The corresponding dependencies are shown in the Fig.5. One can see that after correction 86% of radiation fills to the angle of 3 mrad.

## 4. CONCLUSIONS

The investigations of the slab waveguide RF-excited pulsed $CO_2$-laser with the active volume of 115 $cm^3$ were carried out. At the frequency of 152 MHz there was provided the specific pumping power density of ~ 400 $W/cm^3$. The

output pulsed power of 3-5 kW in the pulses with duration 20-50 μs with the repetition rate of 100..500 Hz was demonstrated. The measured maximum value of small-signal gain was about 1.2-1.5%$cm^{-1}$ for the typical pulse regime. The average output power of laser varied within the range of 10..100 W.

## ACKNOWLEDGEMENTS

The research was performed within the framework of the "Inco-Copernicus" Project No.ERB1C15CT960737.

## REFERENCES

1. R.T.Brown, L.A.Neuman, M.W.Murray, R.A.Hart, "Large volume pulsed RF-excited waveguide $CO_2$-lasers", IEEE J.Quant.Electronics, **28**, no.2, p.404-407, 1992.
2. A.I.Dutov, I.Yu.Evstratov, A.A.Kuleshov, S.A.Motovilov, N.A.Novoselov, V.E.Semenov, P.E.Smirnov, A.A,Sokolov, M.S.Yur'ev, "Slab waveguide high-power pulsed $CO_2$-laser", Proc.SPIE, **3574**, p.171-178, 1998.

# Experimental Investigation of Microwave-Enhanced Combustion of Methane-Air Mixture for Laser Application

Erwin F. Cabrido, Yoshinori Itaya and Shigekatsu Mori

Department of Chemical Engineering, Nagoya University
Furo-cho, Chikusa-ku, Nagoya, Japan

## ABSTRACT

A small signal gain was detected using a $CO_2$ laser during microwave-enhanced combustion of methane-air mixture in a quartz combustor suggesting perturbation of the Boltzmann distribution of molecular energy levels. A maximum value of $g = 0.69$ %cm$^{-1}$ was obtained when the combustion zone was irradiated by microwaves at 1000W sustaining the possibility of utilizing the system for laser applications.

**Keywords:** small signal gain, population inversion, Boltzmann distribution, combustion, microwave, $CO_2$ laser

## 1. INTRODUCTION

Combustion *per se* increases the vibration-rotation energy of molecules such as $CO_2$ and further addition of microwave energy might trigger the occurrence of population inversion when the assumed Boltzmann distribution of molecular energy levels is violated. In this condition, an incident photon will most likely cause a net emission of radiation and an enhancement of light intensity. Hence, it might be possible to exploit this non-equilibrium state for laser applications.

The classic work of Jaggers and von Engel (1971) on the effect of electric fields on the burning velocity of various flames paved the way for several researches into the interaction of electric fields and combustion[1]. Subsequent studies by Bradley and Ibrahim (1976) showed that the asymmetric vibration-rotation mode of $CO_2$ (001) becomes heavily populated during electrical enhancement of combustion[2]. Ward and Wu (1978) considered the feasibility of efficient microwave heating of flame-front electrons in internal combustion engines by means of a mathematical model[3]. Groff and Krage (1984) later examined the effects of microwave on premixed flames and concluded that the enhancement of burning velocity is caused by simple microwave heating of bulk gases in the flame zone[4]. Recently, Ogawa *et.al.* (1998) investigated the effect of microwaves (2.45 GHz) on methane-air flame and found that the electrons in the flame absorb the microwave energy attaining temperatures of up to 5000°C and 5700°C for premixed and diffusion flames respectively[5]. It is presumed that these hot electrons will transfer their energy to neutral species via collision.

In this research, the possibility of laser oscillation was verified by reactivating the gas molecules and chemical species by combustion and then irradiating them using microwave so that excitation will effectively occur. The small signal gain in the system was determined for infrared radiation at 10.6 $\mu$ m.

## 2. EXPERIMENTAL SETUP AND PROCEDURE

### 2.1 Ceramic Burner (One-Stage Combustion)

Figure 1 shows the quartz glass combustor (556 mm x 57 mm I.D. x 2.5 mm thick with a 5 mm aperture to allow the beam from a $CO_2$ laser to pass through) that was used in one-stage combustion experiments. A layer of 5 mm alumina balls ensured proper mixing of the air and $CH_4$ followed by a honeycomb ceramic burner (150 mm x 50 mm diameter with pore size of 1.5 x 1.5 mm) positioned less than 1 mm below the 5 mm hole. Methane-air mixture was introduced from the bottom of the combustor and primary flame was formed on the surface of the ceramic honeycomb. Combustion was carried out at several equivalence ratios, ranging from $\phi = 0.7$ to $\phi = 1.2$. Microwaves irradiated the combustion zone and the stub tuners were used to adjust the impedance of the system. The microwave generator used was the IMG-2502-SX, manufactured by IDX Corp. with a frequency of 2.45 GHz and maximum power of 1.3 kW.



XIII International Symposium on Gas Flow and Chemical Lasers and High-Power Laser Conference,
Antonio Lapucci, Marco Ciofini, Editors, Proceedings of SPIE Vol. 4184 (2001)

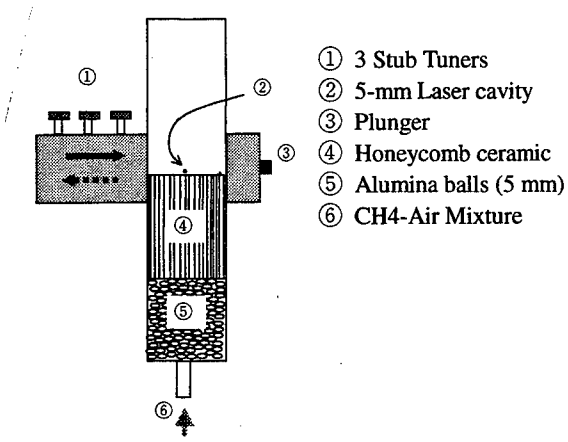


Fig. 1 One-stage combustion

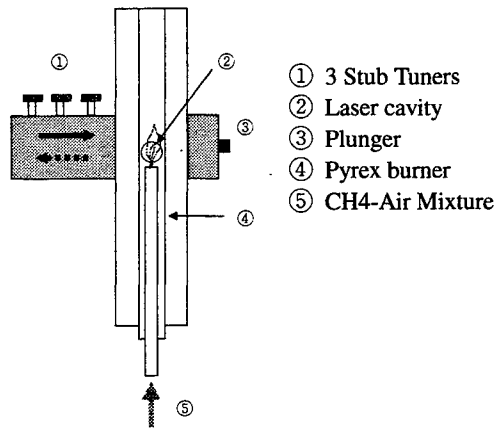


Fig. 2 Pyrex Burner

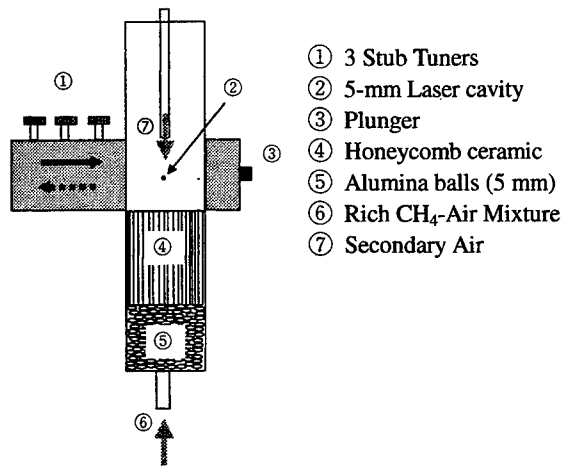


Fig. 3 Two-stage combustion

### 2.2 Pyrex Burner

A double tube Pyrex burner (1.5 mm thick, outer tube 20 mm O.D. and inner tube 10mm O.D), as shown in Fig. 2, was positioned inside the microwave cavity with the inner tube located about 2 to 3 mm below the cavity orifice (18 mm I.D.) in order to allow the laser beam to pass through the flame zone. Microwaves with power levels of 200, 400, 600, 800 and 1000 W were used to irradiate the premixed methane-air flame with $\phi$ = 1.05.

### 2.3 Ceramic Burner (Two-Stage Combustion)

In order to position the flame zone containing radicals and free electrons into the microwave field and into the path of the incident laser beam, two-stage combustion was carried out. The honeycomb ceramic was positioned 30 mm below the 5 mm aperture away from the path of the microwaves. The primary combustion gas was subsequently met by air flowing through a quartz glass tube (1.5 mm thick, 10 mm O.D., 30 mm above the path of the laser beam) from the top of the combustor producing secondary combustion. Combustion was carried out with a premixed equivalence ratio, $\phi$ = 1.14 and a final $\phi$ = 0.71. Microwaves irradiated the combustion zone at 200, 400, 600, 800 and 1000 W, after which the gain of the system was computed.

### 2.4 Optical Set-up

Figure 4 shows the optical system used to measure the small signal gain of the system. A $CO_2$ laser (10.6 $\mu$ m, $TEM_{00}$) that passes through a ZnSe beam splitter forms two beams – one beam reflected $90^0$ to a diffused mirror and another beam going straight through the combustion zone in the microwave cavity before being dispersed by another diffused mirror. The signals from the diffused mirrors were then detected by two MCT

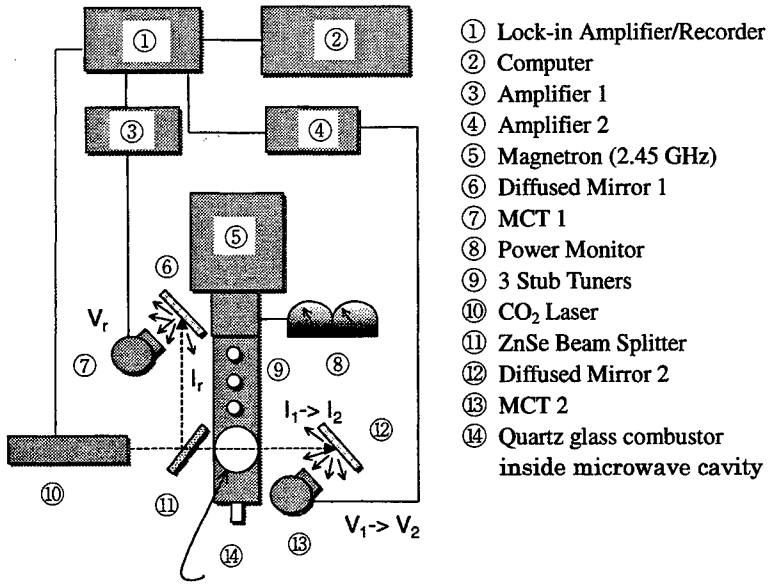


Fig. 4 Optical system to measure the small signal gain

photodetectors, amplified and then recorded. The data were then fed into a computer for analysis. The ratios of the MCT signals with microwave irradiation were compared to ratios without irradiation to determine an increase or decrease in the intensity of the incident radiation. Based on these ratios, the small signal gain of the system was computed as outlined in the Appendix.

## 3. RESULTS AND DISCUSSION

### 3.1 Ceramic Burner (One-Stage Combustion)

Experiments did not result into any signal gain, moreover melting of the ceramic burner was observed. Since the honeycomb ceramic became very hot during combustion, microwaves could have been drawn into it since it was located in the path of the waves themselves. It was believed that formation of hot plasma melted the ceramic burner as shown in Fig. 5 and caused cracking of the quartz combustor.

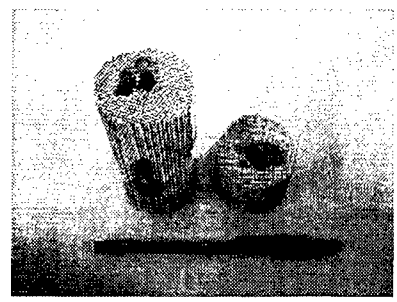

Fig.5 Melted Ceramic

### 3.2 Pyrex Burner

Figure 6 shows the negative signal gain obtained on all levels of microwave power except at 800 W. Thus, there was no amplification of radiation observed. Since the occurrence of population inversion depends to a large extent on the population of active chemical species in the flame, a limited flame volume in the Pyrex burner would mean less active chemical species present to absorb the microwave energy.

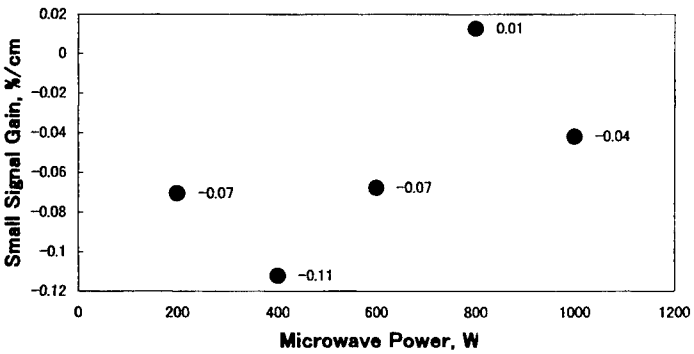


Fig. 6 Pyrex Burner Signal Gain

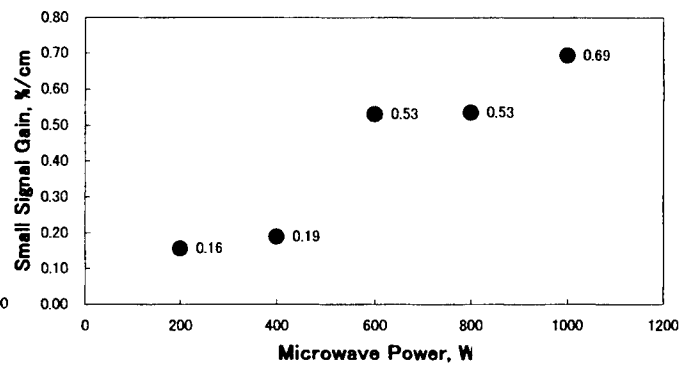


Fig. 7 Two-Stage Combustion Signal Gain

### 3.3 Ceramic Burner (Two-Stage Combustion)

The average values of the small signal gain obtained from experiments using two-stage combustion are shown in Fig. 7. Evidently, there is an amplification of infrared radiation on all levels of microwave power based on the positive value of the small signal gain. A maximum value of $g = 0.69$ %cm$^{-1}$ was obtained when the combustion zone was irradiated by microwaves at 1000 W. It is presumed that radicals and free electrons absorbed microwaves and the energy was transferred to $CO_2$ molecules via $N_2$ through collision. This is due to the fact that much of the energy in hydrocarbon-air flames is imparted to nitrogen[6]. The transfer of energy caused a depopulation of the lower energy levels and accumulation of molecules in the higher levels (e.g. 001 level) thereby prompting stimulated emission of radiation.

### 3.4 Statistical Analysis

Table 1 shows the Analysis of Variance (ANOVA) table. A completely randomized design (CRD) was used since the experimental units are homogenous. Varying level of microwave power represent the treatments. Definitely, a small signal gain was obtained for all levels of microwave power. However, since the computed F value is less than the tabular F value at 5% and 1% level of significance, the statistical analysis reveal that the effect of varying levels of microwave power on the small signal gain is not significantly different. In other words, the test failed to detect practical differences in different levels of microwave power. Nevertheless, a nonsignificant F test in the ANOVA does not in any way prove that all the treatments are the same. A very small numerical difference in the treatment means, as experienced in this experiment, is one reason why a nonsignificant F test would result from the ANOVA[7].

Table 1. Analysis of Variance in CRD

**ANOVA**

| Sources of Variation | degrees of freedom | Sum of Squares | Mean Square | F computed | F tabular 5% | F tabular 1% |
|---|---|---|---|---|---|---|
| Treatment | 5 | 3.5786 | 0.7157 | 0.1273 | 2.62 | 3.9 |
| Experimental Error | 24 | 134.8998 | 5.6208 | n.s. | | |
| Total | 29 | 138.4783 | | | | |

% c.v. = 5.68

F computed is not significant

## 4. CONCLUSION

Experiments involving one-stage combustion and use of a Pyrex burner did not produce an amplification of radiation. However, two-stage combustion experiments utilizing a ceramic burner in a quartz combustor yielded a small signal gain for all levels of microwave power for a premixed equivalence ratio, ø of 1.14 and a final ø of 0.71. A maximum value of g = 0.69%$cm^{-1}$ was detected when the combustion zone was irradiated with microwaves at 1000 W. Amplification of radiation suggests the occurrence of a non-Boltzmann distribution sustaining the potential of utilizing the system for laser applications. Statistical analysis however, failed to detect significant differences among the varying levels of microwave power.

## 5. APPENDIX

### 5.1 Computation of Gain

Based on Fig. 4, the laser intensity ratios, $I_1/I_r$ *(without microwave irradiation)* and $I_2/I_r$ *(with microwave irradiation)* were observed as voltage readings $V_1/V_r$ and $V_2/V_r$. From these ratios, we let $r_1 = V_1/V_r$ *and* $r_2 = V_2/V_r$, after which $r_2/r_1$ was computed. Gain was computed as: $g = (1/l)\ ln\ (r_2/r_1)$, where $l$ is the path length.[8]

## REFERENCES


1) H.C. Jaggers and A. von Engel, "The Effect of Electric Fields on the Burning Velocity of Various Flames", *Combustion and Flame*, **16**, pp.275-285, 1971.
2) D. Bradley and S.M.A Ibrahim, "Electron Energy Exchanges in ac Fields and their Relevance in Lasers", *Combustion and Flame*, **27**, pp.353-362, 1976.
3) M.A.V. Ward and T.T. Wu, "A Theoretical Study of the Microwave Heating of a Cylindrical Shell, Flame-Front Electron Plasma in an Internal Combustion Engine", *Combustion and Flame*, **32**, pp.57-71, 1978.
4) E. Groff and M.K. Krage, "Microwave Effects on Premixed Flames", *Combustion and Flame*, **56**, pp.293-306, 1984.
5) S. Ogawa, Y. Sakai, K. Sato, and S. Sega, "Influence of Microwave on Methane-Air Laminar Flames", *Japanese Journal of Applied Physics*, **37**, pp. 184-185, 1998.
6) D. Bradley, "Effect of Electric Fields on Combustion Processes", *Advanced Combustion Methods*, Felix Weinberg ed., pp.331-394, Academic Press Inc. London Ltd. 1986.
7) K. Gomez and A. Gomez, *Statistical Procedures for Agricultural Research*, John Wiley & Sons, New York, 1984.
8) Y. Itaya, Y. Kawamura, N. Kobayashi, C. Takami and M. Hasatani, "A Study on $CO_2$ Gas Dynamic Laser Driven by Methane-Air Combustion", *XI International Symposium on Gas Flow and Chemical Lasers and High-Power Laser Conference*, **3092**, pp.452-455, 1996.

# Time-Resolved Measurement of Gas Parameters inside Diffusion-Cooled $CO_2$ Lasers with NIR Diode Laser and UV-VIS Emission Spectroscopy

Rainer Engelbrecht[a] and Joachim Schulz[b]

[a]Lehrstuhl fuer Hochfrequenztechnik, Universitaet Erlangen-Nuernberg
Cauerstr. 9, 91058 Erlangen, Germany.

[b]Fraunhofer Institut fuer Lasertechnik, Steinbachstr. 15, 52074 Aachen, Germany.
currently with TRUMPF Lasertechnik GmbH, Johann-Maus-Str. 2, 71254 Ditzingen, Germany.

## ABSTRACT

Time-resolved gas dissociation inside diffusion-cooled RF excited $CO_2$ lasers was measured with NIR laser absorption spectroscopy and UV-VIS emission spectroscopy. Roto-vibrational temperatures were derived directly in the discharge region. Effects of gas additives on the plasma processes were studied.

**Keywords:** Carbon dioxide laser, diffusion-cooled, gas dissociation, diode laser, absorption spectroscopy, emission spectroscopy

## 1. INTRODUCTION: EXPERIMENTAL LASER SETUP

Diffusion-cooled RF excited $CO_2$ laser have the potential for compact, industrial high-power laser sources as sealed-off systems. Parameters to be optimized for high efficiency are the gas composition, the power loading, a proper material selection, the discharge geometry, and the resonator configuration. The dissociation of $CO_2$ into CO and O inside of the discharge volume changes plasma parameters and hence the laser power of such lasers. To study the temporal evolution of these effects with high resolution in the millisecond regime and without gas sampling, we used both NIR diode laser spectroscopy and UV-VIS spontaneous side-light emission spectroscopy of the discharge glow itself.

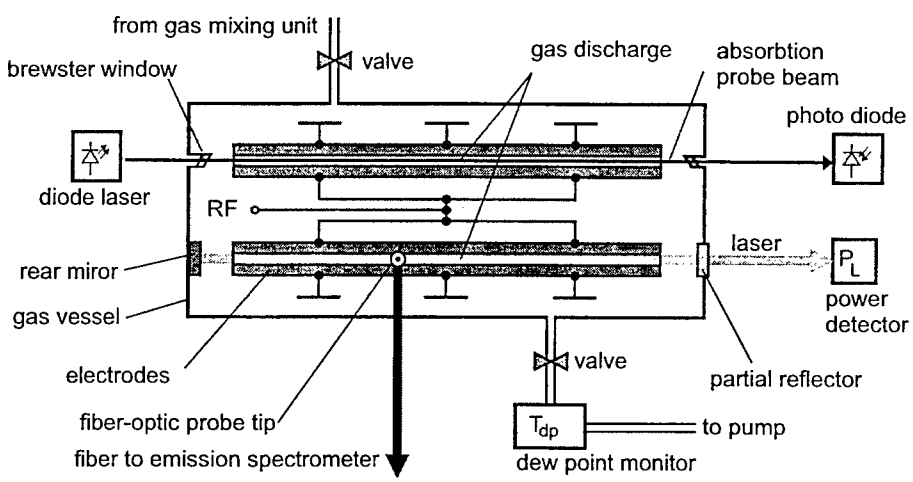


**Figure 1.** Experimental laser setup for discharge spectroscopy

Further author information: (Send correspondence to Rainer Engelbrecht)
Rainer Engelbrecht: E-mail: rainer@lhft.e-technik.uni-erlangen.de; http://www.lhft.de
Joachim Schulz: E-mail: joachim.schulz@de.trumpf.com; currently with TRUMPF Lasertechnik GmbH



XIII International Symposium on Gas Flow and Chemical Lasers and High-Power Laser Conference,
Antonio Lapucci, Marco Ciofini, Editors, Proceedings of SPIE Vol. 4184 (2001)

Two identical discharge volumes with dimensions of 6,5x17x900 $mm^3$ in the same laser gas vessel as shown in Fig. 1 each excited with an RF input power up to 1000 W at 27 MHz were used. One discharge volume was operated with resonator mirrors for fast measurement of the laser power with an atomic-layer thermopile. Emission spectroscopy of plasma sheaths was performed perpendicular to the long axis with a fibre-coupled CCD spectrometer. The other discharge volume was operated with Brewster windows for NIR absorption spectroscopy with an absorption path along the long axis. Both optical setups measured the concentrations of CO resp. $CO_2$ and CO with high temporal resolution. Comparing those time dependent data with a simple model summing up all reaction paths for dissociation ($k_d$) and recombination ($k_r$), the effects of different gas components were studied.

This set of differential equations was used to describe the temporal evolution of the number densities $n$ of $CO_2$, CO and O:

$$\begin{aligned} \dot{n}_{CO_2}(t) &= -k_d n_{CO_2}(t) + k_r n_{CO}(t) n_O(t) \\ \dot{n}_{CO}(t) &= +k_d n_{CO_2}(t) - k_r n_{CO}(t) n_O(t) \\ \dot{n}_O(t) &= +k_d n_{CO_2}(t) - k_r n_{CO}(t) n_O(t) \ . \end{aligned} \tag{1}$$

## 2. ABSORPTION AND EMISSION SPECTROSCOPY OF THE DISCAHRGE

The diode laser absorption spectrometer used a collimated beam from a tunable DFB diode laser chip emitting at 1567 nm[1,2] . Two closely adjacent absorption lines of $CO_2$ and CO were measured simultaneously in one wavelength scan. A 2f wavelength modulation setup and subtraction of a reference beam was used to achieve high sensitivity with short time constants[3] . 50 line scans per second were recorded with a PC leading to a temporal resolution of 20 ms. The gas concentrations and the vibrational/rotational gas temperatures were determined by fitting the measured spectra to a theoretical model of the setup and the molecular absorption properties.

The fiber-coupled CCD spectrometer for emission spectroscopy had a resolution of 1 nm. The main components in the reddish-blue discharge glow are $N_2$ lines with the strong $2^{nd}$ pos. system ($C^3\Pi_u$-$B^3\Pi_g$) and various CO bands[4] (Fig. 2). In the far UV region NO lines can be identified, but no $CO_2$ lines are in this spectral region. To quantify the CO content without much theoretical efforts, only the ratios of line intensities between time-dependent CO (519 nm) and almost time-independent $N_2$ (427 nm) lines are compared. Calibration is done with time-resolved spectroscopy and well-defined CO additions.

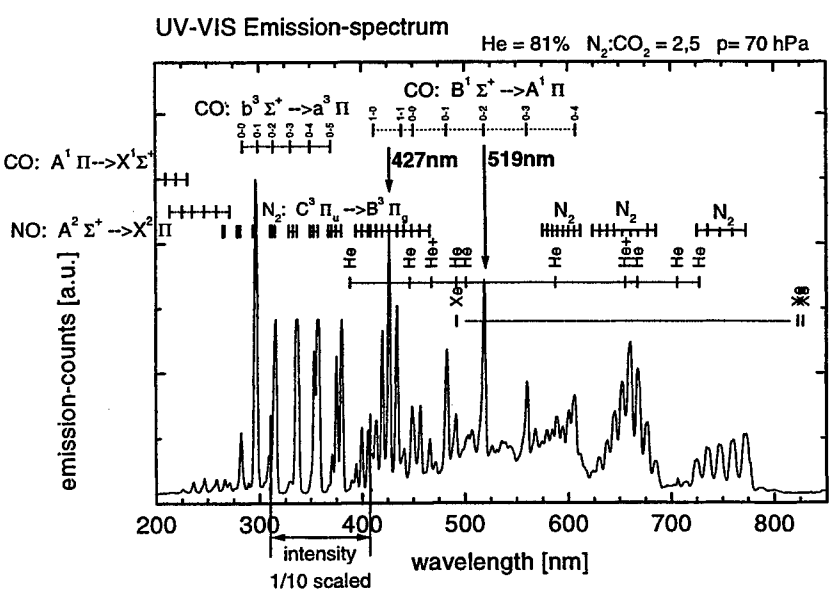


**Figure 2.** Emission spectrum of the discharge sheats

## 3. RESULTS: GAS TEMPERATURES AND DISSOCIATION DYNAMICS

In the discharge volume without laser activity all RF energy is transformed into heat (except dissociation and electronic excitation). The temperature profile can be calculated by solving the heat diffusion equation. Considering sheath losses near the electrode, less RF power reaches the gap center. These losses can be evaluated by comparing calculated and measured temperatures at given RF loads. The measured gas temperatures at the center of the gap are rather low even without laser activity. This can be explained when sheath losses[5] of the $\alpha$-discharge are considered. The more RF power has to penetrate those sheaths, the higher the loss. Evaluated sheath-losses for 27 MHz excitation are in the range of 25% up to 42%.

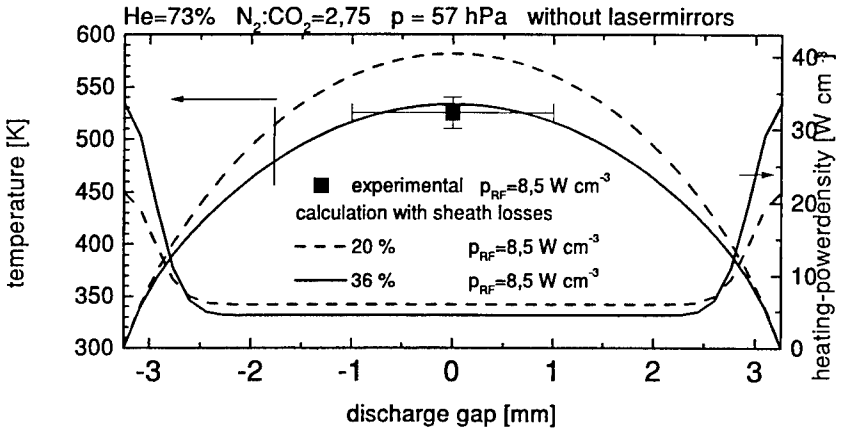


**Figure 3.** Calculated and measured gas temperatures

Fig. 4 shows that within 1 s an equilibrium of the laser power and dissociation is achieved. The time-slope can be fitted exponentially with a typical time constant of $t = 0.2$ s. The reaction coefficients that characterize the way of the reaction can be evaluated from these data: The equilibrium dissociation is only a function of the ratio $k_d/k_r$, the time constant is a function of the product $k_d k_r$.

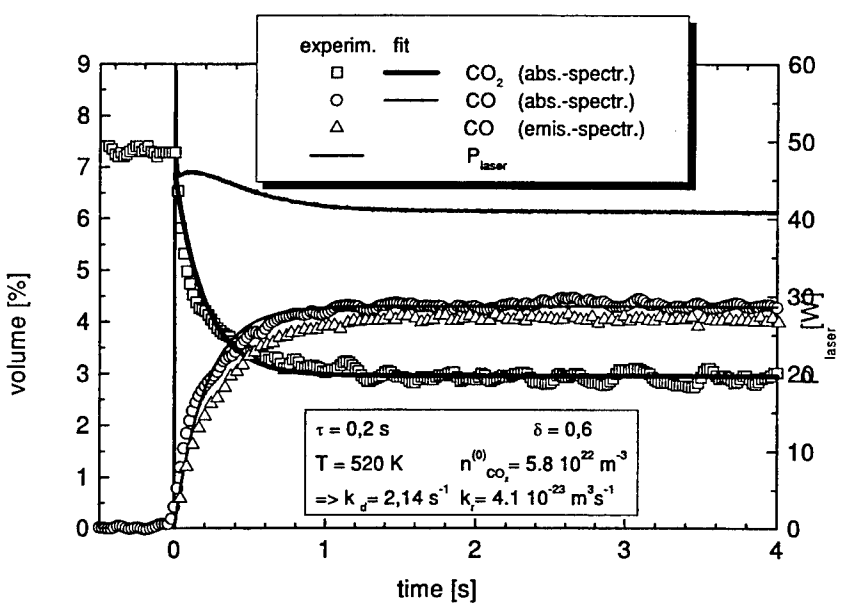


**Figure 4.** Measured dissociation dynamics and laser power

Table 1 compares different gas additions to the initial He:$N_2$:$CO_2$ gas mixture. While $H_2O$ highly increases the catalytic recombination rate coefficient and hence reduces the dissociation fraction, it also quenches the upper

laser level and reduces the laser power above a concentration of several thousand ppm (dew point above -40°C). Xe reduces the dissociation rate coefficients while keeping recombination nearly unchanged because of the reduction of the mean electron energy in the discharge. The addition of CO shifts the equilibrium state towards lower dissociation fractions, but keeps the reaction coefficients for recombination almost unchanged. Comparing rising power densities, both dissociation and recombination coefficients increase, keeping the ratio unchanged. This shows, that both reactions are electron- and volume-effects rather than catalytic surface reactions.

| | reaction rate coefficients | | dissociation | laser power |
|---|---|---|---|---|
| | $k_d$[ $s^{-1}$] | $k_r$[$10^{-23}$ $m^3s^{-1}$] | fraction[%] | [W] |
| $H_2O$-addition [ppm] | | | | |
| 400 | 1.64 | 3.3 | 60 | 42 |
| 2300 | 1.57 | 7.8 | 44 | 39 |
| 8300 | 1.60 | 18 | 31 | 30 |
| Xe-addition [%] | | | | |
| 0 | 1.64 | 3.3 | 60 | 42 |
| +2 | 1.15 | 4.0 | 49 | 45 |
| +4 | 0.83 | 3.9 | 45 | 45 |
| $N_2$:CO replacement | | | | |
| 2.0:0.0 | 1.64 | 3.3 | 60 | 42 |
| 1.5:1.5 | 0.9 | 3.1 | 31 | 38 |
| 1.0:1.0 | 0.6 | 2.6 | 20 | 33 |

| | reaction rate coefficients | | dissociation | temperature | calculated |
|---|---|---|---|---|---|
| RF-density [W $cm^{-3}$] | $k_d$[ $s^{-1}$] | $k_r$[$10^{-23}$ $m^3s^{-1}$] | fraction[%] | at center [K] | sheath loss [%] |
| 5,7 | 0.72 | 3.5 | 43 | 480 | 25 |
| 7,1 | 1.13 | 5.5 | 44 | 500 | 35 |
| 10,3 | 1.58 | 6.3 | 48 | 530 | 42 |

**Table 1.** Measured dissociation dynamics for various gas additives

## 4. CONCLUSIONS

Both spectroscopic methods have proved to be very valuable diagnostic tools for the development and optimization of diffusion-cooled sealed-off $CO_2$ lasers: Dissociation fractions of $CO_2$ can be measured fast and precisely. The temporal detection of the dissociation allows the calculation of the rate coefficients for dissociation and recombination. This gives further insight on how gas additions and catalytic surfaces influence the processes in the laser discharge.

## REFERENCES


1. R. Engelbrecht, R. Hocke, and H. Brand, "Measurement of trace gases in sealed-off $CO_2$ lasers with tunable diode lasers in the near infrared," in *8$^{th}$ ITG-Conference Displays and Vakuum Electronics*, ITG-Fachbericht 150, pp. 399–404, VDE-Verlag, Beuth, 1998.
2. L. Lorini, P. D. Natale, and A. Lapucci, "Accurate gas diagnostics for sealed-off $CO_2$ lasers using near-infrared DFB semiconductor lasers.," *IEEE J. QE.* **34**, pp. 949–954, 1998.
3. R. Engelbrecht, H. Brand, and L.-P. Schmidt, "Sensitive simultaneous detection of CO and $CO_2$ with commercial DFB diode lasers for optical communication systems," in *6$^{th}$ Conference on Infrared Sensors and Systems*, Proceedings, pp. 195–198, AMA Service GmbH, Erfurt, 2000.
4. S. D. Benedictis, G. Dilecce, and A. Raino, "Diagnostics of a $CO_2$ radiofrequency waveguide laser active medium," *J. Phys. D: Appl. Phys.* **26**, pp. 920–927, 1993.
5. P. Vitruk, H. Baker, and D. Hall, "Similarity and scaling in diffusion-cooled rf-excited carbon dioxide lasers," *IEEE J. QE.* **30**, pp. 1623–1634, 1994.

# Laser resonator with active mirror - generation of Q-switch regime in industrial CO2 laser

Alexis V. Kudryashov, Vadim V. Samarkin, Alexander M. Zabelin*

Russian Academy of Sciences, Institute on Laser and Information Technologies (IPLIT RAN),
Adaptive Optics for Industry and Medicine Group
Dm. Ulyanov 4, bld. 2, apt. 13, Moscow, 117333, Russia,[1]
*Technolaser Ltd., Svyatoozerskaya 1, Shatura, 140700, Russia.

## ABSTRACT

The results of the use of two types of adaptive mirrors to generate quasi Q-switch pulses of the $CO_2$ laser radiation are presented. The excess of the output power in peak above the average level in CW regime was more then 2.5 times. The power of the lasers that were used in the experiments was in the range of 1 – 3 kW CW. Also, the design of the different types of the active correctors used in the experiments is discussed.

**Keywords:** active corrector, intracavity laser beam control, Q-switch pulses.

## 1. INTRODUCTION

Adaptive optical elements are known to be used for the correction of various types of wavefront distortions of the light beam penetrated through some inhomogeneous media. In 80$^{th}$ and 90$^{th}$ adaptive technique was applied to control for the radiation of various industrial lasers – YAG, excimer, copper-vapor[1]. But usually authors were trying to influence on the output mode structure of the laser beam by means of the intracavity active mirror. For $CO_2$ laser there is also the necessity and the possibility to use active intracavity mirror to obtain quasi Q-switch regime of generation. The idea of application of active corrector is to change the parameters of laser resonator, the stability factor as well as lazing characteristics. Usually Q-switch pulses in $CO_2$ lasers is obtained by putting mechanical shutter inside laser cavity. To avoid undesirable beam transformations the beam is to be focused inside laser resonator and shutter is to be put exactly in the focal plane[2]. To overcome these problems we suggest to use active deformable mirrors as the modulating element – the bimorph one or/and "cylindrical".

## 2. ACTIVE MIRRORS FOR LASER BEAM MODULATION.

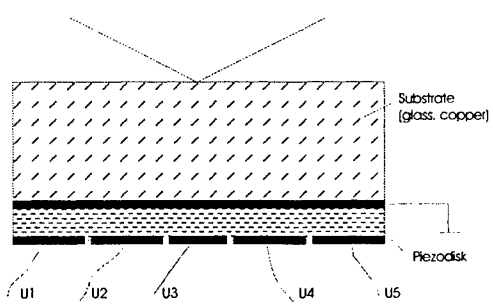


Fig. 1. Scheme of a semipassive bimorph corrector.

### 2.1. Bimorph active corrector.

The traditional semipassive bimorph mirror consists of a glass, copper or quartz substrate firmly glued to a plate actuator disk made from piezoelectric ceramic (lead zirconium titan, PZT) (see fig. 1). Applying the electrical signal to the electrodes of the piezoceramic plate causes, for example, tension of the piezodisc. Glued substrate prevents this tension, and this results in the deformation of the reflective surface. To reproduce different types of aberrations with the help of such corrector usually the outer electrode is divided in several controlling electrodes, that have the shape of a part of a sector. The size as well as the number of such electrodes depends upon the number and the type of the aberrations to be corrected. In our work we usually used the geometry of the electrodes

[1] Further author information –
Tel./Fax.: +7 095 1377136, E-MAIL: kud@laser.ru



XIII International Symposium on Gas Flow and Chemical Lasers and High-Power Laser Conference,
Antonio Lapucci, Marco Ciofini, Editors, Proceedings of SPIE Vol. 4184 (2001)

given on fig. 3.
For high average power $CO_2$ lasers there is the problem of constructing controllable cooled mirrors, production of which is rather complicated. A corrector of this kind should satisfy a number of technical requirements: it should have the necessary optical strength, its service life should be long (~ 1000 hours), and it should be easy to construct and use. The mirror surface should be continuously deformable and the amplitude of displacement of the corrector surface should be $\sim\lambda/2$ ($\lambda$=10.6 $\mu$ - is the wavelength of the corrected radiation).

In our Group we have developed water cooled mirrors based on semi-passive bimorph piezoelement. They consisted of a copper (or molybdenum) plate 2.5 mm thick and 100 mm in diameter. One side of the plate was polished and used as a mirror, whereas two piezoelectric ceramic disks 0.3 mm thick and 50 and 46 mm in diameter were glued on the other side (fig. 2). First piezodisk was used to control for the curvature of the mirror surface and 17 electrodes were evaporated on the outer side of the second piezodisk to compensate for different aberrations of the wavefront. The cooling system of the corrector was of the waffle type. A copper plate consisted of two solded disks in which channels of 0.5 mm deep were formed for the circulation of the cooling liquid. The size of the contact areas between the plates was 3x3 mm. Fig. 3 shows the sample of such a corrector.

The sensitivity of correctors was estimated from the displacement of the interference fringes at the center of the pattern when the voltage of 100 V was applied to all electrodes. It amounted to 1,7 $\mu$. The frequency of first resonance of our correctors was in the range of 3 - 4 kHz. An active mirror was tested under an optical load of $CO_2$ laser radiation with an average power

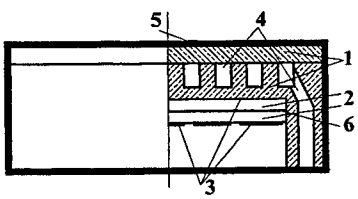


Fig. 2. Copper water cooled bimorph mirror. 1 - copper substrate; 2 - piezoceramic disks; 3 - control electrodes; 4 - canals for cooling water; 5 - reflecting surface; 6 - common electrode.

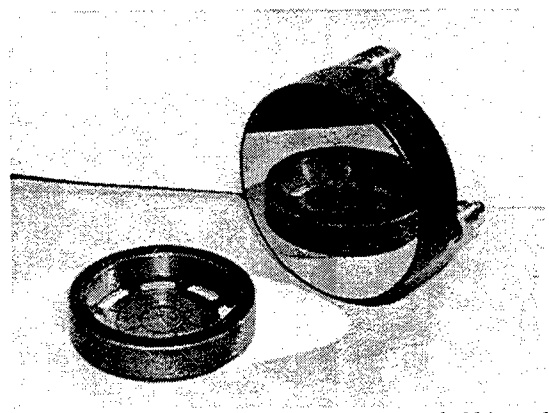

Fig. 3. A photo of a sample of a water cooled bimorph corrector

density of 2.5 kW/cm$^2$ [3]. The corrector surface profile was determined using a shearing interferometer. This optical load produced practically no deformation of the mirror surface, indicating that the cooling system was effective. The rate of flow of cooling water was 400 mliter/min.
*These bimorph correctors were successfully used as an intracvity mirrors to control for the radiation of a $CO_2$.*

### 2.1. "Cylindrical" active corrector.

Another type of the active mirror to be installed as one of the mirrors of the laser resonator was suggested to change the wavefront of the laser beam only in one direction by means of single actuator. The design of such mirror is given on fig. 4. The mirror itself is the rectangular copper plate. One side of this plate is polished to the optical quality. Piezoceramic column (actuator) is installed between the rib of rigidity (shown on fig. 4) and mirror support. The cooling system made of copper plate surrounded by the tube with cooling water is connected to deformable mirror through special thermo conductive pasta. Of course the deformation of the surface via applied voltage to piezoceramic column is not the spherical one, but has the shape close to cone in one direction. This is the main shortcoming of such a corrector. The amplitude of the deformation of the surface is 40 $\mu$, for the aperture of the mirror 55 mm (long side of the rectangular). Thickness of the reflecting plate of such corrector – 4 mm. First resonance frequency –

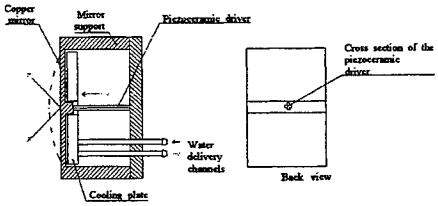


Fig. 4. Deformable "cylindrical" mirror.

15 kHz. Such a corrector was designed to be used in the scheme of the stable-unstable resonator to produce q-switch laser pulses.

## 3. RECEIVING THE Q-SWITCH REGIME OF $CO_2$ LASER GENERATION.

### 3.1. The use of the bimorph corrector.

To change some output parameters of the laser beam (for example get different output mode configuration or even change the regime of laser generation) you need to reconstruct all laser cavity or alter the block of power supply. Such operations are rather expensive and sometimes takes a long period of time. That is why the use of mirrors with controllable flexible surface in laser is of large interest. As for $CO_2$ lasers there is another interesting and promising field for active correctors – to obtain the Q-switch regime of generation of CW lasers. The problem here is that it is impossible to suggest some media that will change its transparency parameter on the wavelength of the $CO_2$ laser radiation (10.6 μ) and thus obtain Q-switch regime. So, the possible way of getting this regime is to use intracavity active corrector that will change the parameters of laser resonator ($g_1g_2$ parameter). In this case the time of change of the cavity should be about one order less then the time of the excited state of $CO_2$ gas (5 – 1.5 ms).

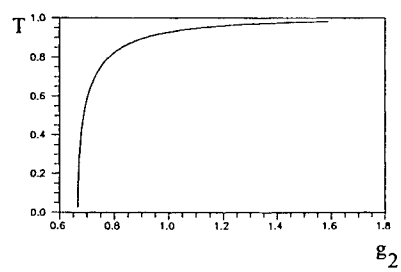


Fig. 4. Transmittance T of laser cavity vs $g_2$ in case $g_1$ =1.5.

In our work we installed active corrector inside the cavity of two types of lasers manufactured in Scientific Research Center for Technological Lasers Russian Academy of Sciences. The first type of cavity is unstable confocal one with magnification M=2, where we substituted one of the folding mirrors with bimorph water-cooled one. When a static voltage +300 V was applied to all electrodes of the flexible mirror radius of curvature of its surface R changed from plus to minus 200 m. The value $g_2$ of the resonator was changing correspondingly in the range of 0.69-0.82. In the dynamic regime of mirror action the cosine voltage with frequency in the range of 1 - 10 kHz was applied to mirror electrodes. At the mirror resonance frequency - 3.8 kHz the deformation of mirror increased up to R= +50 m and $g_2$ value was changed from 0.49 to 1.0. The magnification M of unstable non-confocal resonator could be given as : $M = \frac{g_1g_2 + \sqrt{g_1g_2(g_1g_2 - 1)}}{g_1g_2 - \sqrt{g_1g_2(g_1g_2 - 1)}}$. Fig.4 shows the dependence of resonator transmittance T= $1-1/M^2$ upon $g_2$ for $g_1$ =1.5. One can see that when $g_2$ changes from $g_2$ <0.67 (the case of stable resonator) to 1.0 the transmittance T varies from 0 and 0.93. So, changing the curvature of the flexible mirror surface by applying cosine voltage to the control electrodes one could change the transmittance of the telescopic unstable resonator with the same frequency and modulation of the laser output beam power could be obtained. The cosine voltage of frequency up to 10 kHz and amplitude up to 300V was applied for this purpose. Under control voltage of more than 1 kHz the period of the mirror surface oscillation could be compared with the life-time of the $CO_2$ laser active medium. Thus the Q-switch regime of laser generation was obtained. The periodical laser generation regime with 100% power modulation depth was obtained at near-resonance frequencies - 3.8 and 7.6 kHz. The pulse peak power exceeded the average power threefold[4]. The average power drop was insignificant (<10%).

### 3.2. The Use of the Cylindrical Corrector.

In our first experiments with bimorph corrector described above we used Russian TL-5 laser. The measurement of this laser focused beam profile showed that along with the narrow kern, there exists rather high energy-intensive environment (pedestal) that contains more than a half of the total beam power. The total divergence of the beam is approaching to 1 mrad. The beam quality parameter of such laser beam is rather poor (~ 4). That is why we have proposed and used a special scheme of the optical resonator[5,6]. It has the properties of an unstable telescopic resonator only in the plane perpendicular to the electrode walls, and it is stable in the plane parallel to these walls (Fig.5), as opposed to the known scheme of the stable - unstable resonator wherein the plane of the unstable resonator is parallel to the electrodes, and the plane of the stable resonator is perpendicular to the gas flow and electrodes. The resonator includes two end mirrors, one of them is spherical and another is cylindrical .The generatix of the cylindrical mirror is parallel to the electrode walls. This resonator allowed to increase the far-field beam intensity by a factor of 2-3 in comparison with an ordinary telescopic resonator. One of the very important

advantages of the «stable-unstable» resonator is a good space coupling of the resonator and GDC volumes. The geometry of the optical folding of this resonator takes into consideration the optimal utilization of gas discharge zones, being not included into the volume of the laser optical field. This became possible due to the flow of the excited gas.

Only the lowest gaussian mode of the stable resonator was selected by diaphragm installed inside the cavity. The principal mode size in our case was approximately 12 mm by $1/e^2$ level. The unstable resonator axis was located close to one of the electrode, the resonator caustic accounted for 50 mm, and the output beam size was 20 mm. As the practical applications require the compact beam, so we have to use the resonator with M=2 magnification. The output power of the laser employing the modified stable-unstable resonator was achieved to be 6 kW, i.e. no marked decrease in efficiency was practically observed. As it is shown on Fig. 5, we substituted one of the folding mirrors with the cylindrical corrector. Applying sine voltage to the actuator at the frequency 2 kHz we obtained the modulation of the output radiation and received quasi Q-switch regime of generation – for the CW power 2 kW output intensity of the beam was 5 kW. The duration of the pulses was 5 μc.

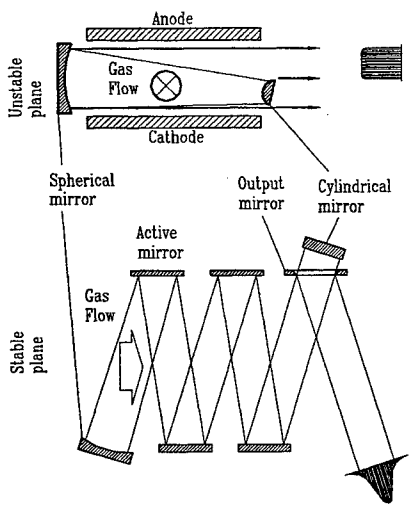


Fig. 5. Stable-unstable resonator with unilateral beam output. Modified scheme.

The quality of the output beam, beam size and beam phase in the case of this kind of laser resonator and the use of active cylindrical corrector does not change because the modulation of the cavity parameters takes place only in the stable plane: in stable resonator the wavefront of the output beam coincides with the surface of the output mirror. And this surface in our experiments was constant. Some changes of the size of the beam in the stable plane inside cavity leads to the modulation of the intracavity losses but does not lead to the increase of the size of the output beam. In the unstable plane of the resonator we did not change any parameters of resonator and so, no deformations of laser beam appear.

The use of the intracavity active mirrors do not require any significant modification of the whole laser. At the same time it broaden the possible spheres of technological lasers application and can improve different technological processes. The proposed method is characterized by simplicity, does not involve replacement of laser power supply and enables to obtain the pulse peak power higher than CW power level.

## ACKNOWLEDGMENTS

The authors would like to thank their colleagues A.Korotchenko and P.Romanov for the preparation of the experiment. This work was supported under the IPLIT-DERA Grant of Contract ELM1158 and NATO SfP Grant N974116.

## REFERENCES

1. *Laser Resonators: novel design and development.* Alexis Kudryashov, Horst Weber, editors, SPIE Press, 301 p. (1999).
2. J.Bae, T.Nozokido, H.Shirai et. all "High peak power and high repetition rate characteristics in a current-pulsed Q-switched $CO_2$ laser with a mechanical shutter", *IEEE Journal of Quantum Electronics* **30,** N4, 887-892 (1994).
3. M.A.Vorontsov, G.M.Izakson, A.V.Kudryashov, G.A.Kosheleva, S.I.Nazarkin, Yu.F.Suslov, and V.I.Shmalgauzen, "Adaptive cooled mirror for the resonator of an industrial laser", *Sov. J. of Quantum Electron.* **15**, 888 (1985).
4. A.V.Kudryashov, V.V.Samarkin, "Control of high power CO2 laser beam by adaptive optical elements", *Opt. Comm.* **118**, 317-322 (1995).
5. A.M.Zabelin, "Fast-transverse flow laser with stable- unstable resonator", Patent RU #2092947 Int. CL HO1S 308.
6. A.Borghese, R. Canevari, V. Donati and L. Garifo, « Unstable-stable resonators with toroidal mirrors», *Applied Optics*, **20**(20), pp.3547-3552 (1981).

# Mode selectivity using selective layered and combined metallic-dielectric electrodes in slab waveguide resonators

Thierry Teuma, Gerhard Schiffner
Dept. Electrical Engineering, Chair AEE0, Ruhr-University
Universitaetsstrasse 150, 44780 Bochum/Germany

## ABSTRACT

Using selective layered, and combined metallic-dielectric electrodes, the higher order mode selectivity of the slab waveguide resonator can be improved, reducing the sensitivity of the beam quality on small variations of the electrode gap by high power $CO_2$ lasers.

**Keywords:** $CO_2$ laser, resonator, slab waveguide, optical loss, electrode gap, fresnel number, interference, material

## 1. INTRODUCTION

One of the greatest problem by the operation of high power slab waveguide $CO_2$ lasers is to keep a long term stability of the achieved good beam quality. Due to slight misalignment or deformation of electrodes caused by mechanical vibrations or thermic stress, the effective electrode gap varied (in the range of some few microns), causing a slight change of the fresnel number which can have drastical effects on the beam quality like described by Gerlach, Hill or Abrams[1, 2, 3]. These effects are due to a change of the phase shift between propagating guide modes causing either constructive or destructive mode interference.
To reproduce such behaviour, the electrode gap of a slab waveguide was moved in steps of few microns and the resulting variation of optical losses was measured using a scanning Fabry-Perot-Resonator.
Resonator losses consist generally on attenuation (inside the guide) and coupling (between guide and mirrors) losses. Due to the slight beam divergence between guide and mirrors using near CASE I resonators, the losses are mainly dominated here by attenuation. Such a resonator will be used to compare the attenuation of different electrode configurations.
Using greater mirror-guide distances, the beam divergence on the path guide-mirror-guide causes increasing diffraction losses at the guide entrance. Additionally, after leaving the guide, free space interference between propagating modes causes the recombination of several guide modes to resulting resonator modes exiting the resonator. The influence of the attenuation through electrodes becomes limited.
The phase shift of the interfering modes depends beside the guide dimensions (fresnel number) also on physical properties of the electrodes like material and surface corrugation. One of the mostly used material by the design of slab waveguide is aluminium. Dielectric slab waveguide resonators have much higher losses then aluminum one, but are less sensitive to small variations of the electrode gap. Both materials should now be applied on the same electrode, trying to combine poor electrode gap sensitivity and smaller level of losses. Before discussing the results obtained, the principle of the measurement with the Scanning Fabry-Perot-Resonator will be shortly described.

## 2. PRINCIPLE OF MEASUREMENTS

The measurement setup used is the same like described in our last publication[4] using an hemispherical Fabry-Perot-resonator, whose length is varied periodically moving one mirror axially with piezo translators (fig. 1).
During the movement of this flat mirror, the resonance length of several propagating modes are crossed successively. At those resonance positions the transmitted intensity becomes maximal, causing a mode dependent peak in the output signal (fig. 2). The level of the optical losses for the light transmitting measured object between the mirrors is proportional to the width of those resonance peak's (fig. 2).


XIII International Symposium on Gas Flow and Chemical Lasers and High-Power Laser Conference,
Antonio Lapucci, Marco Ciofini, Editors, Proceedings of SPIE Vol. 4184 (2001)

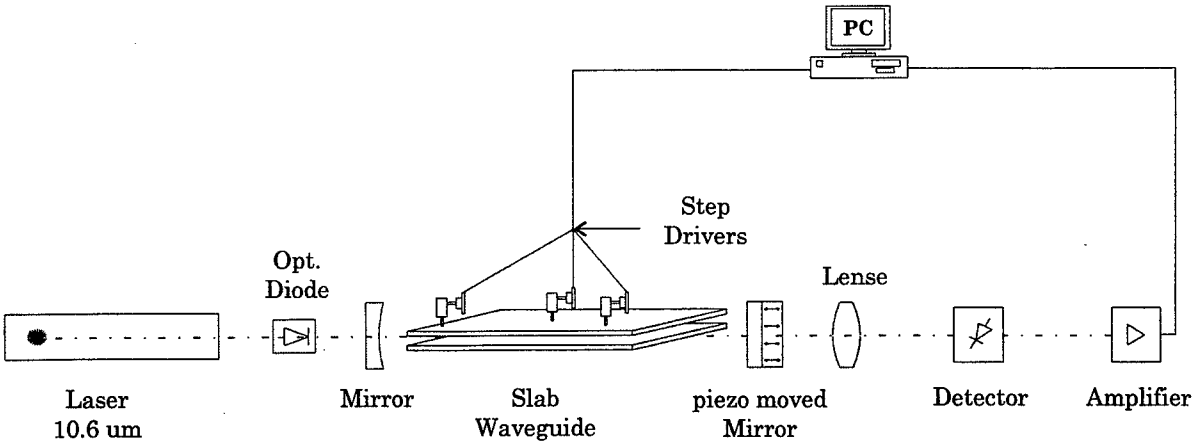


Fig. 1: Schematic of the experimental setup for measurement of optical losses

All the electrodes used during the measurements had a length of 400 mm. The radius of curvature of the curved mirror was 1.7 m. The mirror-guide distance by the near CASE I resonator configuration was 3 mm on both sides and 10 mm for the second applied resonator configuration.

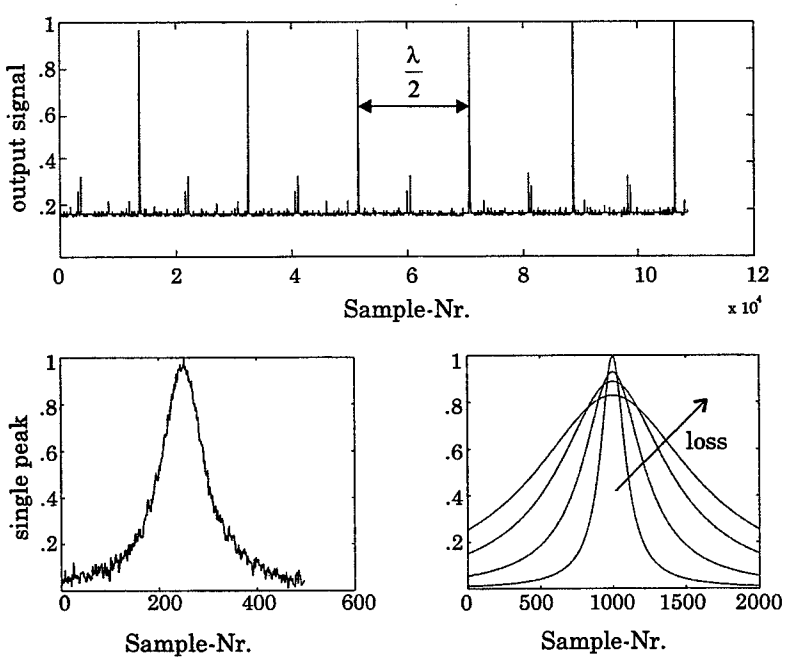


Fig. 2: Output signal of the scanning Fabry-Perot-Resonator

## 3. SELECTIVE LAYERED ELECTRODES

To combine metallic and dielectric propagation conditions on the same electrode, some electrodes were divided in sections. Using the anodizing method, some of the sections of the aluminium electrodes were coated like shown on fig. 3a. By all the three measured slab waveguides, the same top electrode was used. The three bottom electrodes shown on fig. 3a were applied one after another.

Due to the great heat absorption on the walls of the dielectric anodized electrodes by the grazing propagation inside the guide, the energy content for all propagating modes decreases. Simultaneously the attenuation losses, especially for those modes with large cross-sections increase. As consequence, the propagation inside such waveguides with high attenuation at their walls is dominated by one or very few modes, in which the greatest part of the energy is concentrated. Continuously varying the fresnel number, interference (within resonator free spaces between guide and mirrors) with much higher order modes causes only small local variations of the losses. This behavior can be observed by the

configuration with two full anodized electrodes (fig. 3c), where the losses decrease nearly continuously, superposed by only small local fluctuations.

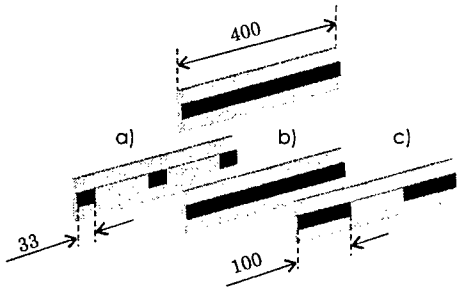


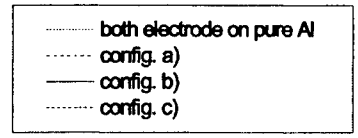


Fig. 3a: anodized electrodes

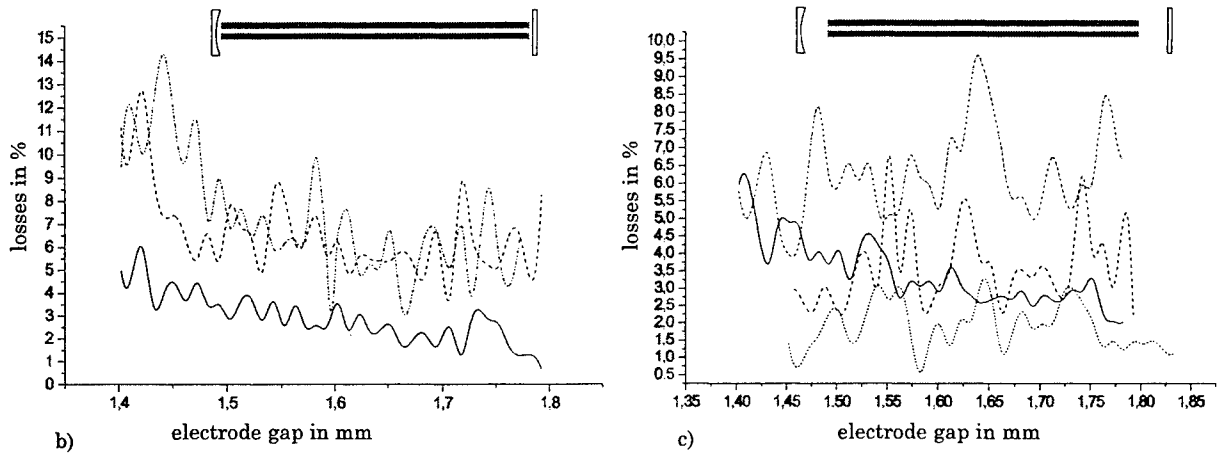


Fig. 3b and 3c: Losses versus electrode gap for the lowest-loss mode applying different mirror-guide distances

In contrast to the anodized one, aluminium electrodes are characterized through a great heat reflection on their walls. This feature supports the propagation of an great number of modes, because of the poor attenuation. The energy content of higher order modes is not more negligible like by anodized electrodes. Varying continuously the fresnel number, constructive and destructive interference between several modes within resonator free spaces between guide and mirrors leads to well pronounced minimum's and maximum's of optical losses (fig. 3c). In opposition to a nearly steady decrease of losses, characteristic for a near one mode propagation inside a resonator, the propagation inside a aluminium slab waveguide resonator is characterized through a pronounced multimode propagation.

Using now electrodes with metallic and dielectric sections, multimode propagation is favored within the metallic part. By interference between these guide modes within the resonator free spaces, the amount of the resulting minimum's and maximum's of losses increases with an increasing portion of the anodized sections. This is due on the one hand to the reduced energy inside the guide ground mode caused by the splitting of the available energy into several propagating guide modes within this metallic part. On the other hand the strong attenuation within the dielectric (anodized) sections, especially for those modes with large cross-sections leads to the absorption of an significant part of the remaining energy inside the higher order modes at the walls. The whole energy inside the resonator decreases. The qualitative behavior of the losses keep very similar to those for full aluminium electrodes, but with quantitative greater values. This is an indication for a similar mode composition inside the resonator configurations.

As conclusion it can be said that the propagation of higher order modes could be attenuated using selective layered electrodes compared with pure aluminium, but not suppressed. Due to the splitting of available energy, combined with the high local attenuation (within anodized sections), the energy in the guide ground mode is reduced causing a deterioration of the energy ratio between ground and higher order modes. This leads by interference between modes to considerable deviations in the loss curve varying the fresnel number.

## 4. COMBINED METALLIC-DIELECTRIC ELECTRODES

Another approach to obtain poor electrode gap sensitivity using less lossy metallic slab waveguide electrodes is to combine these with an additional much shorter dielectric slab waveguide with a fixed electrode gap like shown on fig. 4a. The macor electrodes operate as a both-sided spatial filter.

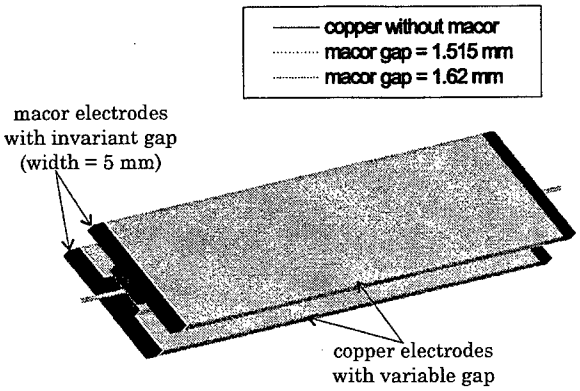


Fig. 4a: Combined macor-copper slab waveguide

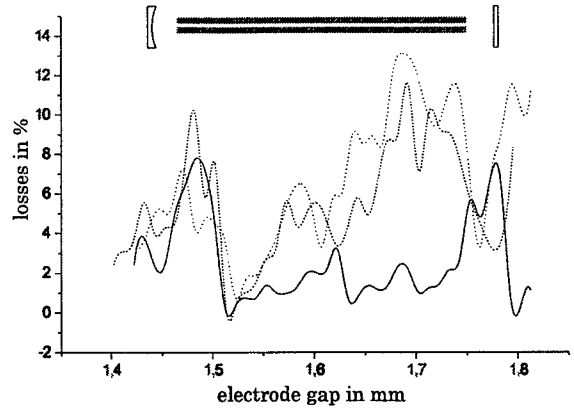


Fig. 4b: Losses versus electrode gap for the lowest-loss mode

By an increase of the gap of the copper electrodes, the difference between the electrode gaps of the metallic and dielectric slab waveguides rise continuously, causing an increasing diffraction of the beam formed inside the much longer metallic guide. Due to this diffraction, the losses rises steeply (fig. 4b) like expected for a one mode propagation with a diaphragm inside the resonator. But this steeply rise is interrupted by well pronounced local minimum's. These local minimum's characterise the constructive interference between at least two modes, expressing the fact that higher order modes could be attenuated but not completely suppressed through the spatial filters. The minimum's appear approximately at the same position like for the resonator without the macor part, what means that the mode composition inside the whole resonator kept mainly dominated by the longer metallic part and is qualitatively nearly not affected using the additional dielectric short slab waveguide. Outside the regions of constructive interference the influence of higher order modes decreases very fast, so that a laser operation there should deliver a good beam quality. Because of the steeply behaviour of the losses, the output power can vary sharply varying the fresnel number.

## 5. COMPARISON BETWEEN METALLIC ALUMINIUM AND COPPER ELECTRODES

A comparison between the most used materials for metallic slab waveguide (copper and aluminium) has shown that, because of higher heat absorption in copper, a part of modes energy is wasted at the electrode walls during propagation. Modes with enough energy are nevertheless able to continue their propagation inside the guide. Those with lower energy become critically decimate through the great amount of the accumulated losses by several round trips caused by successive absorption at the electrode walls.

Using aluminium as electrode material the number of modes able to propagate inside the guide is higher than by copper because of the lower mode attenuation due to lower heat absorption at electrode walls. The energy inside the guide is shared by more modes. Varying the fresnel number (e.g. electrode gap) the phase shift between these guide modes also varied, causing alternating interference within resonator free spaces between guide and mirrors. The losses for the resulting resonator ground mode, which can be represented as a linear combination of those interfering guide modes are then characterized through several well pronounced alternating minimum's and maximum's (fig. 5b).

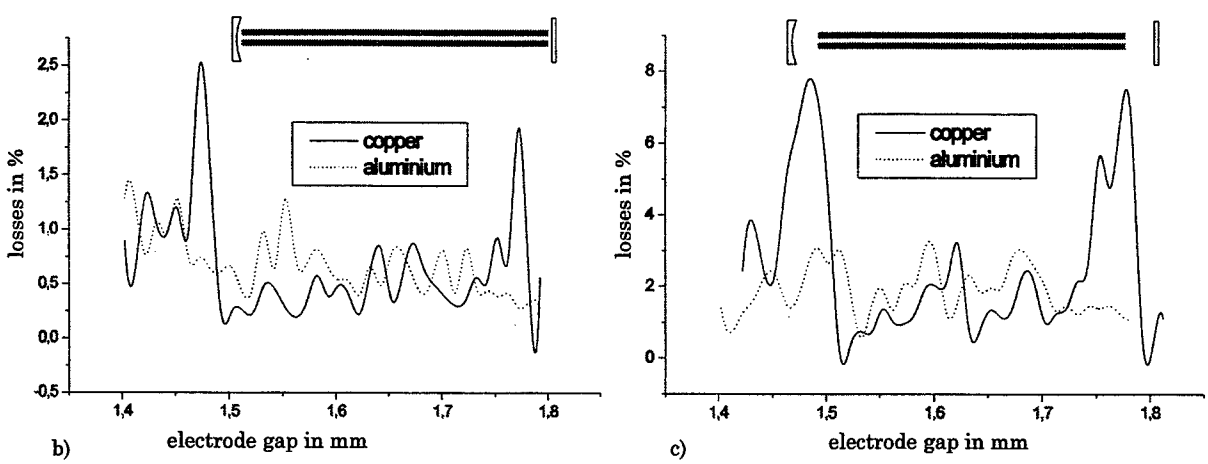


Fig. 5a and 5b: Losses versus electrode gap for the lowest-loss mode applying different mirror-guide distances

Using copper the number of these pronounced interference minimum's and maximum's decreases. Simultaneously these minimum's and maximum's become much more pronounced than by aluminium (fig. 5b) because of the splitting of the energy into only fewer guide modes. Through the synergy by constructive interference between these few modes, nearly the whole energy is concentrated into a single resulting resonator mode, which losses then become minimal like shown for 2a = 1.515 mm on fig. 5b. A laser operation at this position of the electrode gap is nevertheless very risky, because a slight variation is enough to move into the region of destructive interference with a much worse beam quality.

## 6. REFERENCES


[1] R. Gerlach, D. Wie and M. Amer, "Coupling efficiency of waveguide laser resonators formed by flats mirrors: analysis and experiment," J. of Quantum Electronics, Vol. QE-20, No. 8, August 1984, pp. 948-963

[2] C. A. Hill, "Transverse modes of plane-mirror waveguide resonators," J. of Quantum Electronics, Vol. 24, No. 9, September 1988, pp. 1936-1946

[3] R. L. Abrahms and A. N. Chester, "Resonator theory for hollow waveguide lasers;" Applied Optics, Vol. 13, No. 9, September 1974, pp. 2117-2125

[4] T. Teuma and G. Schiffner, "Fundamental- and High-Order-Mode Losses in Slab Waveguide Resonators for $CO_2$-Lasers", Proceedings of SPIE, Volume 3930, pp. 144-152

# Multikilohertz TEA $CO_2$ laser driven by an all-solid-state exciter

Stephan Wieneke, Stefan Born, and Wolfgang Viöl

Department PMF, University of Applied Sciences and Arts, von-Ossietzky-Str. 99,
D-37085 Göttingen, Germany *

## ABSTRACT

A multikilohertz operation of a transversely excited atmospheric $CO_2$ laser driven by an all-solid-state exciter has been demonstrated. The exciter consists of a long life time high-voltage pulse generator employing a transistor equipment working along the principle of fourier synthesis. High voltage pulses with a maximum voltage of 50 kV, 2 μs pulse duration, and a maximum pulse repetition rate of 17 kHz ignite the laser gas discharge. The electrodes have to be insulated by a dielectricum like glass, which homogenizes the laser gas discharge so that no preionization is necessary. A small device of this multikilohertz TEA $CO_2$ laser reaches an average laser power of 140 W and a laser efficiency of 11 % at a pulse repetition rate of 17 kHz.

**Keywords:** TEA $CO_2$ laser, dielectric barrier discharge, silent discharge, all-solid-state generator

## 1. INTRODUCTION

The high-power, high repetition rate, transversely excited atmospheric (TEA) $CO_2$ laser is very useful in a variety of application fields. Especially in the domain of industrial applications, a reliable, long-life, closed-cycle TEA $CO_2$ laser is highly desirable in view of operational cost, the simplicity of maintenance, and the compactness of the laser assembly. The maintenance interval of the thyratron driven commercial laser system with $4 \cdot 10^8$ laser pulses is very short, creating high running costs. The maximum pulse repetition rate of commercial TEA $CO_2$ laser is about 500 Hz.

Here we use a long-life all-solid-state generator in combination with a dielectric barrier discharge to excite a $CO_2$ laser at a pulse repetition rate of up to 17 kHz. In literature, fast axial flow cw $CO_2$ laser,[1,2,3] sealed-off cw $CO_2$ laser[4] and $N_2$ laser[5] pumped by dielectric barrier discharge are described.

## 2. DESCRIPTION OF THE MULTIKILOHERTZ TEA $CO_2$ LASER

Figure 1 shows a diagram of a closed-cycle and transversely excited atmospheric $CO_2$ laser driven by an all-solid-state exciter. The exciter consists of a long-life time high-voltage pulse generator employing a transistor equipment that works according to the principle of fourier synthesis. High voltage pulses with a maximum voltage of 50 kV, 2 μs pulse duration, and a maximum pulse repetition rate of $f_{rep}$ =17.3 kHz ignite the laser gas discharge. Both electrodes are insulated by quartz glass, which homogenizes the laser gas discharge, making preionization unnecessary. The electrodes have an area of $l \times b$ = 290 mm × 25 mm and $l \times b$ = 550 mm × 25 mm at discharge gaps of 11 and 26 mm, respectively. The optical resonator consists of a ZnSe output mirror with 0.5, 1 or 5 % transmission and a curvature of 5 m and a silicon back mirror with a reflectivity of 99.8 % and a curvature of 6 m. The cavity is 540 mm and 1000 mm in total length for the discharge gaps of 11 mm and 26 mm, respectively. The laser gas is cooled by an axial flow which has a mean velocity of $v$ = 1.25 m/s. The gas velocity was measured by a laser Doppler anemometer.

* Correspondence: E-mail: wolfgang.vioel@pmf.fh-goettingen.de; WWW: http://www.pmf.fh-goettingen.de; Telephone: 495513705218; Fax: 495513705101

XIII International Symposium on Gas Flow and Chemical Lasers and High-Power Laser Conference,
Antonio Lapucci, Marco Ciofini, Editors, Proceedings of SPIE Vol. 4184 (2001)

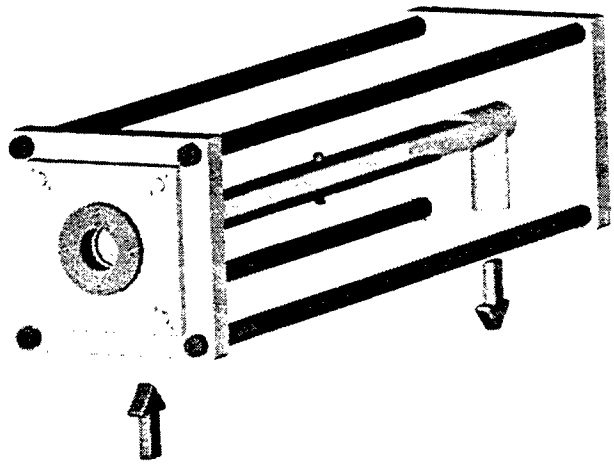

Figure 1: Schematic diagram of the multikilohertz TEA $CO_2$ laser

## 3. HOMOGENITY OF THE LASER GAS DISCHARGE

Figure 2 shows a photograph of laser gas discharge with an exposure time of 400 ns during the high voltage pulse. This photograph proves that the homogeneity of the discharge is excellent. The change of the laser gas between two laser pulses is described by the

$$clear\ ratio = v / (l \cdot f_{rep}). \tag{1}$$

The *clear ratio* should be above 1.0 to ignite a homogenous laser gas discharge.[6] Due to the dielectric stabilization of the gas discharge, no clear ratio is needed with a value above 1. The clear ratio of the laser system described here is only 0.00013.

Figure 2: Photograph of a pulsed laser gas discharge with an exposure time of 400 ns during the high voltage pulse

## 4. LASER OUTPUT POWER

A small device of the multikilohertz TEA $CO_2$ laser that is driven by the all-solid-state exciter reaches an average laser power of 140 W at a pulse repetition rate of 17 kHz using a discharge gap of 26 mm. Thus, the laser system delivers a pulse energy of 8 mJ. The output mirror with 1 % transmission delivers the highest average laser output power. The optimum ratio $He:N_2$ is about 1 and the best $CO_2$ concentration is 0.7 % as shown in figures 3 and 4. When using a laser gas mixture $He:N_2:CO_2 = 50.0:49.3:0.7$, the optimum gas pressure is 230 hPa and laser power can be measured up to a gas pressure of 400 hPa (see figure 5). When adding 10 % Xenon to the laser gas, the optimum gas pressure lies between 200 and 300 hPa and laser power can be measured up to 530 hPa. The laser efficiency reaches its maximum of 11 % at a gas pressure of 250 hPa (see figure 6). The laser pulse duration is about 20 μs due to the low gas pressure of about 200 hPa.

The laser device with 11 mm discharge gap can deliver laser power up to a gas pressure of 630 hPa, but the laser efficiency of about 4 % was relatively low compared to the 26 mm discharge gap. The optimum laser gas pressure was determined to be $He:N_2:CO_2 = 20:76:4$.

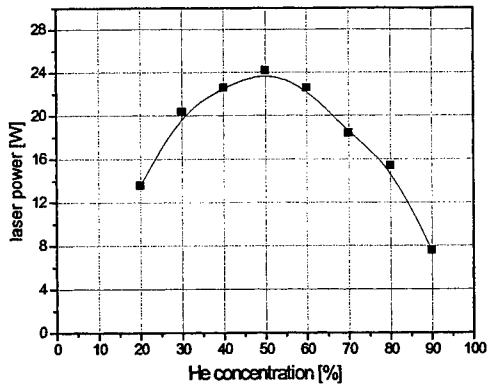


Figure 3: Laser power versus He concentration at a constant $CO_2$ concentration of 1 % (average electrical input power: 400 W, pulse repetition rate: 17 kHz, gas pressure: 200 hPa, discharge gap: 26 mm)

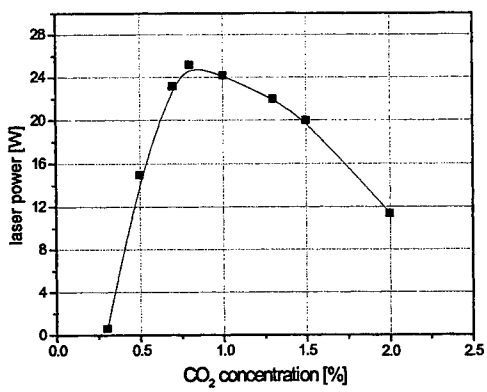


Figure 4: Laser power versus $CO_2$ concentration ($He:N_2$= 1:1, average electrical input power: 400 W, pulse repetition rate: 17 kHz, gas pressure: 200 hPa, discharge gap: 26 mm)

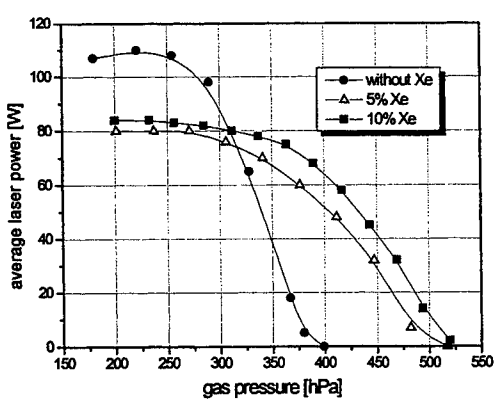


Figure 5: Laser power versus laser gas pressure at a pulse repetition rate of 17 kHz with a discharge gap of 26 mm

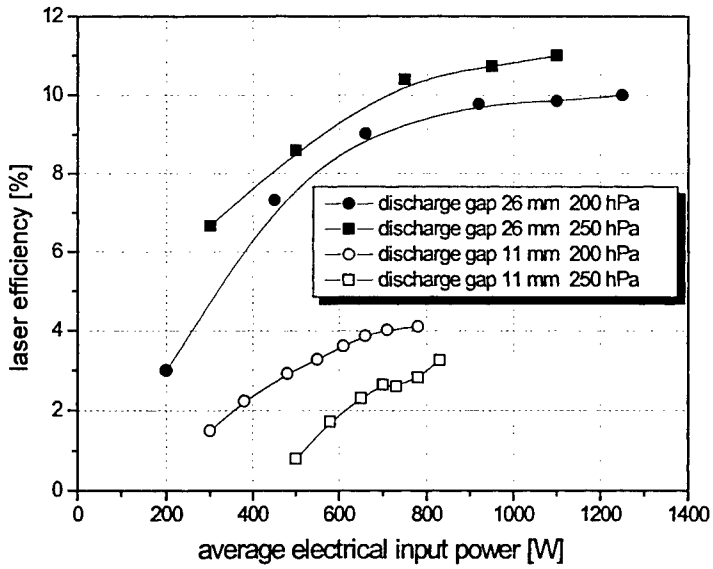


Figure 6: Laser efficiency versus average electrical input power at a pulse repetition rate of 17 kHz for 11 mm discharge gap ($He:N_2:CO_2$ = 20:76:4) and for 26 mm discharge gap ($He:N_2:CO_2$=50.0:49.3:0.7)

## 5. CONCLUSION

The multikilohertz TEA $CO_2$ laser excited by a dielectric barrier discharge driven by an all-solid-state generator is a promising candidate for low-cost, commercial, high-power $CO_2$ laser employed in material processing. The dielectric barrier discharge makes a preionization and a fast gas flow unnecessary to ignite a homogeneous laser gas discharge.

## 6. OUTLOOK

The described multikilohertz pulsed $CO_2$ laser has been optimized to reach high average laser power. Yet, optimization of the laser peak power will still have to be done to reach laser activity at atmospheric pressure.

## ACKNOWLEDGMENT

The authors wish to thank the Lower Saxony Ministry for Science and Culture for their support of this work.

## REFERENCES

1. M. Kuzumoto, S. Ogawa, M. Tanaka, and S. Yagi, "Fast axial flow $CO_2$ laser excited by silent discharge", *IEEE Journal of Quantum Electronics* **26**, pp. 1130-1134, 1990
2. H. Nagai, M. Hishii, M. Tanaka, Y. Myoi, H. Wakata, T. Yagi, and N. Tabata,"Cw 20-kW sage $CO_2$ laser for industrial use", *IEEE Journal of Quantum Electronics* **29**, pp. 2898-2909, 1993
3. J. Klein, G. Otto, U. Habich, and P. Loosen, "Mittelfrequenzangeregter $CO_2$-Laser mit axialer Gasströmung", *EuroLaser* **2**, pp. 48-50, 1994
4. S. Wieneke, S. Born, and W. Viöl, "Sealed-off $CO_2$ lasers excited by an all-solid-state 0.6 MHz generator, *J. Phys. D: Appl. Phys.* **33**, pp. 1282-1286, 2000
5. J. Köhler, "Dielectric barrier discharge pumped $N_2$ laser", *Applied Optics* **33**, pp. 3812-3815, 1994
6. Z. Guo, G. Gao, J. Wen, and D. Cai, "Compact sealed-off TEA $CO_2$ laser", *SPIE* **2118**, pp. 90-93, 1994

# Polarization state measurements of the industrial 1.2kW cw $CO_2$ laser beam

Sergei Labuda[a], Grażyna Rabczuk[*b]

[a] Heat & Mass Transfer Institute, Belarus Academy of Sciences Brovki 15, 220072 Minsk, Belarus
[b] Institute of Fluid Flow Machinery, Polish Academy of Sciences, Fiszera 14, 80-952 Gdańsk, Poland

## ABSTRACT

Results concerning the polarization state measurements of the beam emitted by an industrial cw $CO_2$ transverse-flow laser working at 1.2kW are reported in the paper. A measurement procedure with a rotating analyser and a quarter-phase retarder, designed for a $CO_2$ laser radiation is applied . The measurements prove that the optical beam transport system modifies the polarization of the laser radiation by increasing its ellipticity. The investigations of the temporal stability of the polarization show that polarization state of the investigated laser fluctuates considerably versus time.

**Keywords:** high power cw $CO_2$ laser, polarization measurements

## 1. INTRODUCTION

Polarization dependent effects during material processing with $CO_2$ laser are well known[1]. Any fluctuations of the polarization can influence the efficiency of certain industrial processes. At high processing velocities, the welding depth as well as the cutting quality depends on the polarization direction. Nevertheless, polarization properties of industrial $CO_2$ lasers are not widely studied. It can be connected with a difficulty of monitoring of the high power beams when special diagnostic equipment is required. Moreover, results received for one type of a laser generally can not be applied for another characterised by the different resonator properties and active medium parameters determined by excitation conditions and flow structure in the laser excitation region.

The results of the experimental investigations of the polarization of radiation emitted by an industrial cw $CO_2$ transverse –flow laser[2] excited by a self – sustained DC electric discharge and working at the output power range up to 1.2kW are reported in the paper.

## 2. PROCEDURE FOR THE POLARIZATION MEASUREMENTS

The laser under investigation works with a stable, semi-spherical resonator of three-pass configuration, which does not contain any additional polarization selective components. A flat total reflective mirror and a meniscus ZnSe output coupler of 10m radius of inner curvature and 50% of reflectivity form the laser cavity. Two additional flat reflectors folding the beam path across the working chamber are inclined at angles less than 5-deg to the beam optical axis. The cavity length is 3.9m. The laser working chamber is closed with an antireflection coated ZnSe flat window (99.5% transmittance at normal incidence). The laser output beam is transported to the processing region by a beam guiding system of a Π configuration composed by three flat mirrors inclined at angles of 45-deg to the beam axis. The polarization of the laser radiation has been tested at the laser output, and after the beam passing through the guiding system.

For the polarization analysis, the measurement procedure[3] have been was adopted in which the analysed beam is transmitted through an IR rotating polarization analyser. A time-varying signal of a sinusoidal shape, related to the angular orientation of the analyser, gives information on the polarization of the incoming radiation. Zero intensity at the signal minima indicates that incoming radiation is linearly polarized. For not linearly polarized beam, an additional polarization test is required through the measurements of the beam intensity after its transmission by both a quarter -wave retarder and a linear rotating polarizer.

The schematic arrangements of the experimental setup for the polarization tests are shown in Fig.1. The linear polarizer, used in our experiment, is composed by two Ge plates, oppositely inclined at Brewster angle and mounted on the holder that was rotated manually or by an electric engine. The anisotropic Ge crystal of electro-optic modulator of ML-8

* Correspondence: E-mail: rabczuk@imp.pg.gda.pl

XIII International Symposium on Gas Flow and Chemical Lasers and High-Power Laser Conference,
Antonio Lapucci, Marco Ciofini, Editors, Proceedings of SPIE Vol. 4184 (2001)

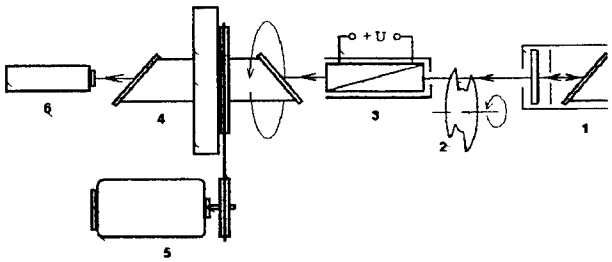


Fig.1 Experimental set-up for polarization analysis of the laser radiation: 1 – $CO_2$ laser generating radiation of linear polarization; 2 – mechanical chopper; 3 retarding crystal; 4 – rotating polarization analyser; 5 – electrical engine; 6 - IR detector.

type was used as a phase retarder. The operation modes of the crystal were tested for the linearly polarized beam of a probe $CO_2$ laser of power up to 100 W. NaCl Brewster window closing the discharge tube of the laser provides a linearly polarized output beam. The intensity of the laser beam transmitted through the retarding crystal and the rotating analyser was recorded for different values of the voltage applied to the crystal. It follows from the measurements that the crystal does not influence the polarization of the incoming radiation at zero voltage on its electrodes and that the phase retardation is linearly related to the applied voltage. As an example, the oscilloscope traces of the chopped laser beam intensity, transmitted through the retarding crystal and the rotating analyser, at different voltage applied to the crystal are shown in Fig.2. At zero voltage the rotating analyser produces modulation of the laser beam to zero intensity (Fig2 A) what indicates the linear polarization of the tested radiation. At the voltage of 1.7kV the recorded signal shows only modulation corresponding to the laser output fluctuations. It means that the radiation emerging from the retarder is circularly polarized. Hence at the voltage of 1.7kV the electro-optical cell with crystal of Ge introduces a phase retardation of $\pi/2$ between two orthogonal components of the linearly polarized radiation.

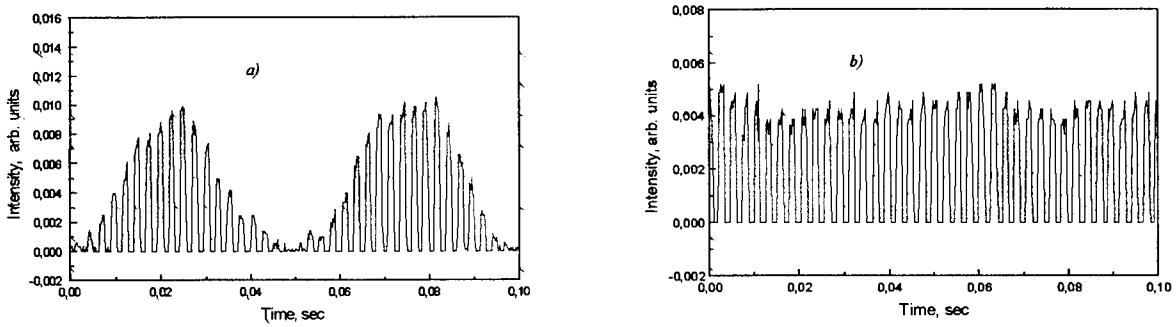


Fig.2. Intensity records of the output probe laser beam of linear polarization, transmitted through the retarding crystal and rotating polarizator: a) – at zero voltage on the retarding element; b) – applied voltage is 1.7 kV.

The polarization of 1 kW cw $CO_2$ laser beam was tested according to the described above procedure. First the beam was examined for the linear and than for elliptical or circular polarization. The small part of the laser beam, passing through the polarization test optics (see Fig.1) was monitored by the infrared Hg-Cd-Te detector and recorded by a digital oscilloscope. The main polarization characteristics like degree of polarization, azimuth and ellipticity angles [3] were found by recording the intensity transmitted through the analyser versus its angular position and comparing the maximum and minimum readings at the detector. The intensity ratio $I_{min}/I_{max}$ and the contrast defined as $Q = (I_{max}-I_{min})/(I_{max}+I_{min})$ were found and compared for the experimental arrangement without and with a quarter- phase retarder, respectively. The azimuth angle $\Phi$ of the ellipse is given by the direction of the main polarization component, corresponding to the maximum intensity, relatively to the horizontal axis. The ellipticity of the radiation is defined by the ratio of the minor and major semi-axes $I_{min}/I_{max}$ of the ellipse and ellipticity angle $\varepsilon$ is the angle equal to $\varepsilon = arctg(I_{min}/I_{max})$. Having the azimuth *and* ellipticity angles the Stockes parameters can be found [4]:

The temporal stability of the polarization state of the laser radiation was investigated by simultaneous monitoring the main polarisation components $I_P$, and $I_S$, versus time. They separated from the incoming radiation by the polarizer were directed to two fast infrared detectors. The detected intensities, polarized in the perpendicular planes, were recorded on a digital oscilloscope.

## 3. MEASUREMENT RESULTS

The signal of the laser intensity transmitted through the rotating analyser is shown on Fig.3a. The measured minimum and maximum intensity ratio is from the range 0.71-0.82 while the contrast is estimated to be between 0.1 and 0.16. The quarter wave retarder inserted in the optical path, in front of the analyser, leads to deeper modulation of the laser

intensity (Fig.3b). The intensity ratio and contrast are then from the range 0.54-0.6 and 0.25-0.3, respectively. Solid line in Fig.3 and in the following ones corresponds to the sine square function fitting to the experimental data while the dot line corresponds to the polynomial fit. The both fitting curves give the same values for the period of the intensity modulation as well as very close values for the average depth modulation. The slightly different values for $I_{min}$ and $I_{max}$ given by the following maximum and minimum of the polynomial curve indicate that the polarization characteristic of the investigated radiation vary versus time.

Applying the terminology suggested by ISO document [3] one can conclude that the laser radiation, examined at the laser output, is partially elliptically polarized, $\varepsilon$=35°-39° and $\Phi$≈50°.

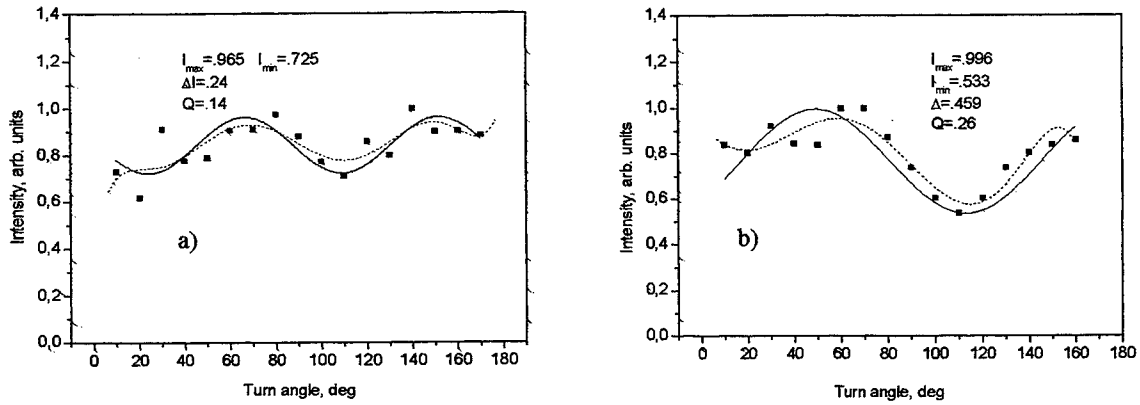


Fig.3. The laser beam intensity versus the angle position of the polarizer: a) – the laser beam is passing only through the rotating polarizer; b) – electro-optical wave retarder is inserted in the beam path in front of the polarizer

In order to investigate the influence of the three-mirror beam transport system on the polarization characteristics the intensity measurement procedure with the rotating analyser was repeated for the beam at the output of the optical duct (in the processing region). It follows from the data depicted in Fig.4,a that the transport optical system decreases the intensity ratio and increases the contrast, compared to the corresponding results recorded at the laser output. The oscilloscope traces obtained for the system with the quarter wave retarder are shown in Fig.4,b. The use of the retarder results in decreasing of the intensity ratio and increasing of the contrast. Corresponding values are equal to 0.18-0.25 for intensity ratio and 0.6-0.67 for contrast.

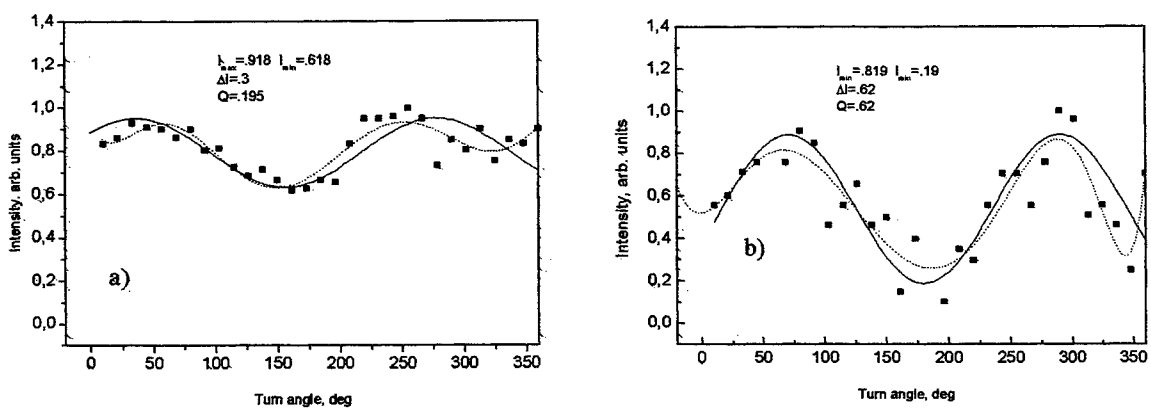


Fig.4. Laser radiation intensity measured at the output of the beam transport system: a) – the laser beam is passing only through the rotating polarizer; b) – the electro-optical qurter wave retarder is inserted in the beam path.

The observed shift of the minimum (maximum) intensity position recorded in the system without and with the retarder indicates [5] that the polarization state of the light can be characterised as a mixture of the linearly and elliptically polarized components. It can be concluded finally from the presented results that the optical beam transport system modifies the polarization of incoming radiation by increasing its ellipticity. From the measurements taken at the output of the transport system (Fig.4) it follows that $\Phi$≈50°, ellipticity $\varepsilon$ lies within the angle interval of 31°-35°.

The results concerning the temporal behaviour of orthogonal polarization components, $I_P$ and $I_S$, are gathered in Fig.5. In this figure, the time evolution of the total laser power and the intensities of p- and s- polarized components are compared for different time intervals (10 ms and 0.8 ms.). The laser beam was mechanically chopped at the laser output. The signals from both detectors corresponding to the polarization componens $I_P$ and $I_S$ show 'antiphase' variations. Minimum of $I_s$ corresponds to maximum $I_p$ and vice versa so the total power remains nearly constant. It is especially clear for the time interval of 0.8 ms, when the radiation, changes its polarization state two times e.g. from the only $p$-type to the $s$-type .

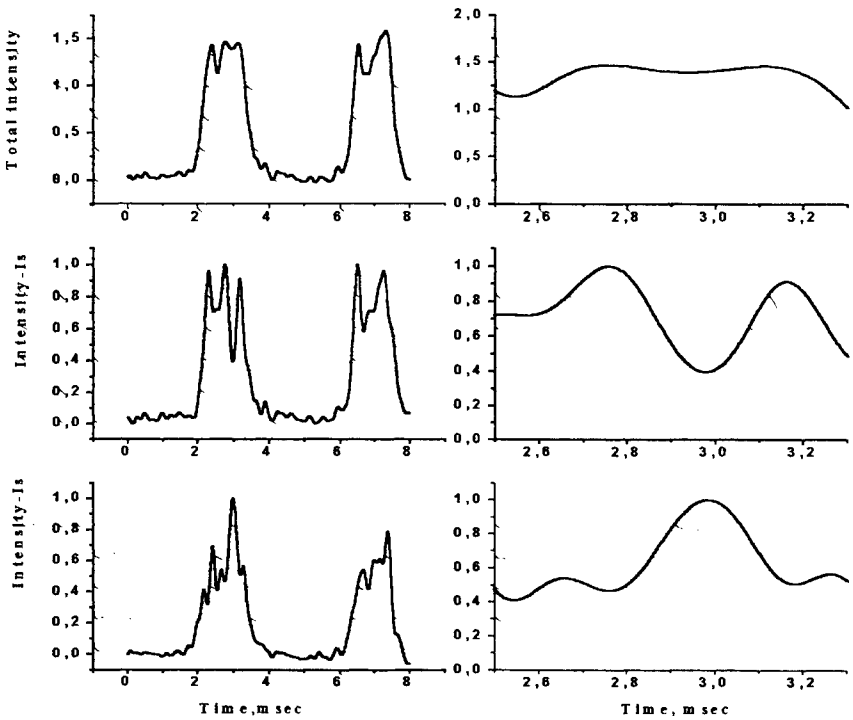


Fig.5. Temporal behavior of the laser power and intensities of orthogonal polarization components measured at different intervals of time

## 4. CONCLUSION

The polarization state measurements for the industrial 1kW cw $CO_2$ laser beam were performed according to the procedure in which the beam was tested for the linear and then for the elliptical or circular polarization. The beam polarization and its basic characteristics like the degree of polarization, azimuth and ellipticity angles were found. The detailed measurements show that the laser beam is partially elliptically polarized. The transport optical system modifies the polarization of the incoming radiation by increasing its ellipticity. It was discovered that the polarization state of the investigated laser fluctuates considerably versus time.

## ACKNOWLEGEMENTS

This work was sponsored by the National Scientific Committee within the Project PB1419/T11/98/14.

## REFERENCES

1. J.Franek, R.Kramer, "Measurement of Industry Laser Polarization", SPIE **1840**, pp. 637-641, 1993.
2. P. Kukiełło, G. Rabczuk, "High-power cw $CO_2$ Transverse Flow Laser with a Stable Multipass Cavity. Comparative Study", *Laser and Particle Beams* **10**, pp.865-870, 1992.
3. *ISO-DIS "Optics and Optical Instruments- Lasers and Laser Related Equipment- Test Methods for Laser Beam Parameters: Polarization "*, ISO/TC 172/S.C. 9, 1995.
4. M.Born, E.Wolf, *"Principles of Optics"*, Pergamon Press, Oxford, 1988.
5. J.R.Meyer-Arendt, *"Introduction to Classical and Modern Optics"*, Prentice-all, 1972.

# Modified overshoot mode of magnetic-spiker sustainer technology for multi-joule TEA $CO_2$ lasers

Y.X. Tang, R.G. Harrison

Physics Dept., Heriot-Watt University, Edinburgh EH14 4AS, U.K.

## ABSTRACT

A compact and efficient multi-joule TEA $CO_2$ laser using the modified overshoot mode (MOM) magnetic-spiker sustainer (MSS) excitation technique is described, giving an enhanced laser performance at a significantly reduced spiker switching energy (typically ~5% of total input energy) necessary for producing a stable discharge. A laser output energy of 7.1J was obtained with an overall efficiency of ~13.5%. The implementation of this technique in a dual module 10J TEA $CO_2$ laser is also successfully obtained, demonstrating the scalability of this technology to high pulse energy (≥10J) systems.

**Keywords:** TE/TEA $CO_2$ lasers, gas discharge, pulse power and switching technology

## 1. INTRODUCTION

Spiker sustainer excitation was originally introduced to sustain quasi-continuous-wave (cw) discharges for the production of efficient $CO_2$ laser operation at low pressure[1-3]. The essential idea of the spiker-sustainer approach for producing a stable high power density discharge is to operate the discharge in a sustained mode at low value of E/N and use some independent method (spiker) requiring only a small amount of energy to generate the current carriers in the plasma volume. The laser plasma control in this scheme is therefore one with two "knobs" - one controlling electron density, the other electron temperature. Consequently the dominant amount of energy is put into the gas by the sustainer exactly where it is desired, i.e., in vibrational excitation of $N_2$ and $CO_2$. Since its successful and widespread application to excimer lasers[4-7], in the last few years spiker sustainer excitation has been increasingly researched for application to TE/TEA $CO_2$ lasers, particularly as a means to overcome the long standing limitations of conventional systems, namely low efficiency and limited lifetime of the high power switch devices used. Results have demonstrated greatly enhanced laser performance[8-10] along with the notable feature of variable to long pulse operation[12-13]. However, in these systems a very high spiker pulse, and hence a relatively high switching energy (~20% of total input energy), is required for producing a uniform discharge in the magnetic switch operational mode[9,12]. Hence a large volume of magnetic material is needed and the magnetic switch in the form of a saturable pulse transformer, used to isolate the spiker and sustainer, tends to be rather bulky . This poses serious problems of reliability and stability of the discharge for high repetition rate operation, resulting from degradation of the quality and performance of magnetic material due to the temperature rise in the cores caused by high magnetic core loss which is directly proportional to the volume of magnetic material.

In this paper we report on the development of a new operational mode, i.e. modified overshoot mode (MOM), of magnetic-spiker sustainer discharge technology for multi-joule TEA $CO_2$ lasers that reduces the required spiker energy and volume of magnetic material used by more than 50%, providing an enhanced laser performance. As first described by Taylor *et al*[14], in the MOM mode operation the spiker pulse $V_{SP}$ is only required to be high enough to barely overcome the voltage $V_S$ applied to the sustainer capacitor, compared with the spiker pulse $V_{SP} \geq |V_S+V_{br}|$ required in the magnetic switch mode operation, where $V_{br}$ is the breakdown voltage. The spiker energy switched through a thyratron and the volume of magnetic material used are therefore greatly reduced since the voltage isolation capability of the magnetic switch is governed by $V\Delta t=\Delta BA$, where $\Delta t$ is the pulse duration, $\Delta B$ the magnetic flux swing and A the total cross section area of the core.

## 2. MOM MSS EXCITATION CONFIGURATION

The schematic of the new MOM operational mode spiker-sustainer discharge circuit along with the dual laser heads is shown in Fig. 1. As seen, the electrical circuitry consisted of a sustainer capacitor (main energy storage capacitor) $C_S$, connected across the laser head in series with the secondary winding of a saturable coupling pulse transformer $T_r$ and a spiker pulse generation circuit connected in series with the primary side of the transformer $T_r$. The saturable coupling pulse transformer $T_r$ was used to provide dc isolation between the spiker pulse circuit and the sustainer pulse circuit, and to impose a high voltage spiker pulsar onto the main discharge electrodes when the thyratron in the spiker circuit was fired.

XIII International Symposium on Gas Flow and Chemical Lasers and High-Power Laser Conference,
Antonio Lapucci, Marco Ciofini, Editors, Proceedings of SPIE Vol. 4184 (2001)

The sustainer capacitor $C_S$ was charged up by a high voltage power supply $PS_1$ to a voltage $V_S$ that was well below the self-breakdown level of the gas mixture in the volume between the main electrodes. The preionization and spiker pulse were generated when the capacitor $C_{SP}$ in the spiker pulse generation circuit, previously charged to a similar voltage $V_{SP}$ by another HV power supply $PS_2$, was discharged by a triggered thyratron into the primary winding of the pulse transformer $T_r$. The resulting negative high impulse voltage produced on the secondary winding of $T_r$ was imposed across the laser head causing the UV-preionizers connected across the main electrodes to breakdown through small ballast capacitors. However, the core was designated to be saturated when the voltage across the laser head reached zero or close, and hence no gas breakdown took place at this point. Then, the peaking capacitor $C_{PI}$ was rapidly resonantly charged up by the sustainer capacitor $C_S$ to a positive high voltage which was sufficient to cause gas breakdown in the volume between the main electrodes. This was followed by the main discharge current being rapidly drawn into the plasma from the main energy storage capacitor $C_S$ through the secondary winding of $T_r$, now saturated, resulting in a high energy volumetric glow discharge.

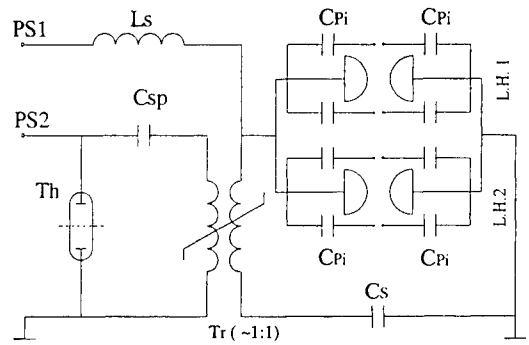


Fig. 1 Schematic of MOM MSS excitation for a dual discharge 10J TEA $CO_2$ laser

## 3. LASER PERFORMANCE

The laser head assembly used in this investigation was a traditional Lumonics TEA $CO_2$ laser model K-901. It consisted of a pair of Rogowski-profiled brass electrodes which were separated by 3.3cm, defining an active discharge volume of ~42cm x 3.3cm x 3cm (416cm$^3$). Ultraviolet (UV) preionization of the gas mixture was provided by an array of sparks created between pairs of pin electrodes on each side of the main electrodes. The pin electrodes were individually ballasted by small knob capacitors (570pF each) and connected across both sides of the main electrodes ( 7 x 2 on either side). The laser head was housed in a gas-tight Al drum with the laser cavity mounted directly on its flanges at both ends. The laser resonator consisted of a 10m radius of curvature, 2.5-inch diameter gold-plated copper mirror with a reflectivity of 100%, and a 3-inch plain Ge output coupler with a reflectivity of 65%, defining a cavity length of ~100cm. For measurement of laser output energy, a calibrated pyroelectric joule meter (ED500, Gentec) was used. The laser was operated at a fixed pulse repetition rate of 0.5 pps, limited only by the high voltage power supplies. A laser gas mixture of $CO_2 : N_2 : He = 12 : 14 : 74$ at atmospheric pressure was used in this investigation.

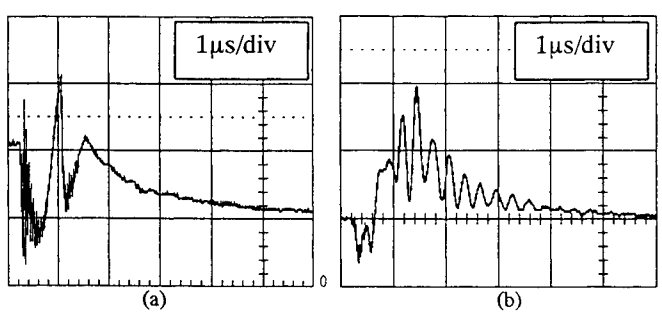


Fig. 2 Discharge waveforms of (a) voltage and (b) current.

In the MSS excitation scheme, the peak spiker voltage, $V_{SP}$, generation capability of the transformer $T_r$ is governed by

$$V_{SP}\Delta T/2 \approx \Delta B A N_P \qquad (1)$$

where $\Delta B$ and A are the maximum available flux swing and the total cross-section area of the cores, $N_p$ is the number of turns of the primary winding and $\Delta T$ the pulse duration in the spiker phase, respectively. $\Delta T$ may be estimated by:

$$\Delta T=\pi (L_L C)^{1/2}, \quad C=C_{PI}//C_{SP}//C_S \qquad (2)$$

where $L_L$ was the leakage inductance of the transformer $T_r$, and $C_{PI}$, $C_{SP}$ and $C_S$ the nominal preionizer capacitance, spiker capacitance and sustainer capacitance, respectively. The saturable coupling pulse transformer for MOM magnetic-spiker sustainer operation was designed and optimized based on Eqn (1) and (2) with $V_{SP} \approx V_S$. The transformer $T_r$ was constructed with 20 Siemens R58/N30 ferrite toroids, only ~50% of the core volume compared with the switch mode operation, and had three primary turns and three secondary turns of high voltage insulated cable. The entire saturable coupling pulse transformer assembly was put in a Perspex tank, filled with transformer oil, to avoid high voltage breakdown.

Initially, only a single laser head assembly was used in this study. It was observed that stable glow discharges could be obtained in the laser gas mixture at atmospheric pressure for various values of sustainer capacitance up to ~140μF over a wide range of charging voltages on the sustainer capacitor $C_S$, from 13kV to 32kV. The minimum spiker energy for generation of glow discharge was found to be ~2.7J, representing only ~5% of total input energy, which is about quarter of that required in the switch mode operation[9,12]. The typical discharge current and voltage waveforms across the laser head are shown in Fig.2. It should be pointed out that the polarity of the spiker pulse was opposite to that of the sustainer pulse ($V_S$). A stable glow discharge could be obtained only at a low energy loading over a very limited range of operating voltages of ~18kV - 22kV when the spiker and sustainer pulses have the same polarity.

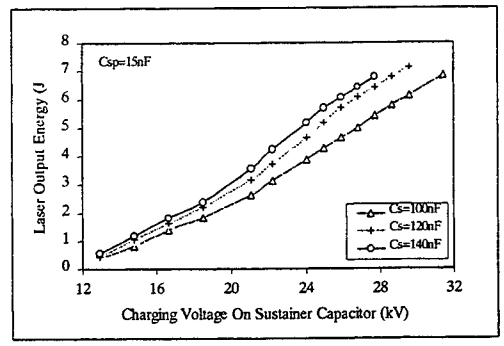


(a)

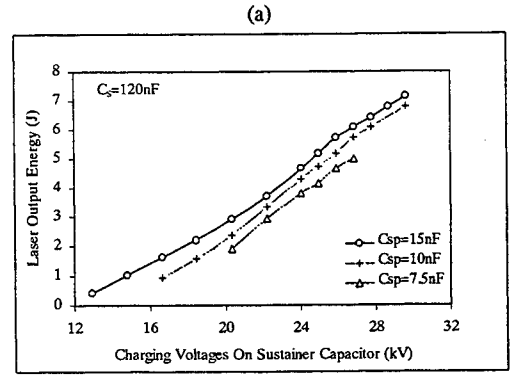


(b)

Fig. 3 Laser pulse energy as a function of charging voltage on $C_S$ (a) for different values of $C_S$ and (b) various spiker capacitances.

The laser pulse energies experimentally obtained are shown in Fig.3 as a function of charging voltages on the main storage capacitor $C_S$ for different values of capacitances, and for various spiker capacitances $C_{SP}$. As seen from these plots, a maximum laser output energy of 7.1J was obtained with an overall efficiency of ~13.5% when a 0.12μF sustainer capacitance was used at a charging voltage of ~29kV with a spiker capacitance of 15nF charged up to ~27kV. This corresponded a specific output energy of ~17.2J/l.atm. The maximum input energy that could be deposited into the plasma below arcing threshold was found to be ~55.6J giving an energy loading limit of 134J/l.atm. In addition, the laser system could be operated over a wide range of charging voltages on the main storage capacitor $C_S$ with the threshold voltage as low as 13kV. Nevertheless it was found that with the minimum spiker capacitance of 7.5nF the laser could only be operated for a sustainer capacitance up to 0.12μF at a maximum charging voltage of 27kV. It was also observed in the experiment that the energy stored in the sustainer capacitor $C_S$ could not be fully absorbed by the plasma at the end of discharge, and the voltage $V_f$ left on $C_S$ was found to be ~8kV. Hence the total input energy was calculated by $0.5(C_{SP}V_{SP}^2 + (C_S+C_{PI})V_S^2 - C_SV_f^2)$. The dependence of laser efficiency on input energies is shown in Fig.4(a) for different values of sustainer capacitance $C_S$ and in Fig.4(b) for various spiker capacitance $C_{SP}$, respectively. Fig. 5 shows the laser pulse shape for different gas mixtures, measured by the Ge photon drag detector. As seen, the gain-switched spike of the laser pulse is considerably reduced while the most of the laser energy is carried in the exponentially decayed laser pulse tail. This may have some advantages in laser surface treatment of materials where the air plasma, caused by a very high gain-switched spike of the laser pulse from a conventional system, prevents the laser energy from being efficiently coupled onto the work piece.

The MOM magnetic-spiker sustainer excitation scheme was further investigated to create a volumetric glow discharge for scaling up in high output energy (>10J) from TEA $CO_2$ lasers. Two identical 5J laser head modules described above were connected in parallel in this investigation to simulate a 10J TEA $CO_2$ laser, which was roughly equivalent to doubling the discharge length and hence the discharge volume. It was found that stable discharge could be obtained in this dual discharge system within a range of charging voltages on the main storage capacitor $C_S$ from 20kV to 26kV with the same pulse transformer $T_r$, a 0.22μF sustainer capacitance and a spiker

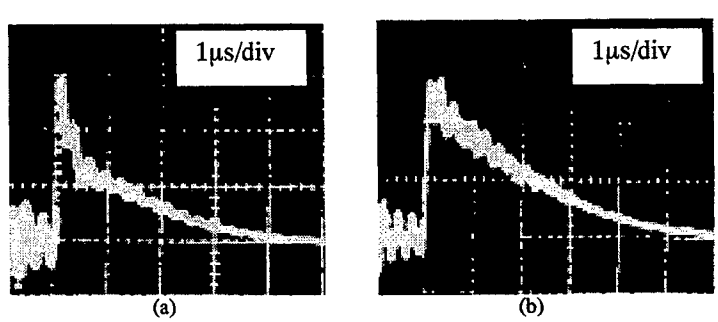


(a) (b)

Fig. 4 Laser pulse for different gas mixtures at atm pressure (a) $CO_2$:$N_2$:He=1:1:6, and (b) $CO_2$:$N_2$:He = 1:3:9

capacitor of 20nF charged up to 27kV. However the discharge was more sensitive to gas contamination mainly due to unbalanced energy distribution between the two modules. The experimentally obtained laser output energy and overall efficiency from this dual discharge laser system is depicted in Fig. 6 as a function of charging voltages on the sustainer capacitor $C_S$. As seen, maximum output energy of 9.7J was obtained at the maximum charging voltage of $V_S \approx 26$kV, representing an energy loading of 100.7J/l.atm, with an overall efficiency of 12.7%. It should noted that no attempt was made towards optimising the transformer $T_r$ for operation of this dual discharge laser system, and unbalanced input energy distribution between the two modules occurred resulting in the formation of hot filaments in either one of the modules at a large energy loading above 26kV; otherwise higher output energy should be obtained at higher energy loadings.

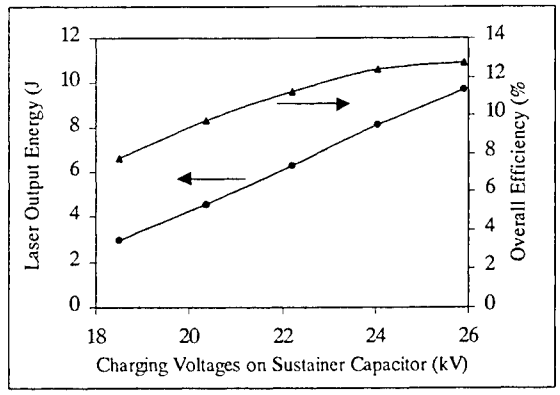


Fig. 5 Laser pulse energy and overall efficiency as a function of charging voltages on $C_S$ for a dual discharge TEA $CO_2$ laser.

## 4. DISCUSSION

The MOM magnetic-spiker sustainer excitation for TEA $CO_2$ lasers described in this paper has provided some important operational features. The very low minimum spiker energy (~2.7J) required for stable discharges offers a promising prospect for using low rating and inexpensive high voltage switch devices in these lasers. This also has important implication for the development of compact, lightweight and effective all-solid-state-switched multijoule laser systems utilizing magnetic pulse compression techniques. In addition, the magnetic material used in the MOM operational mode was reduced by ~50%, favouring operation at high repetition rate due to reduced thermal effect on the core. It should be noticed that in this investigation the magnetic core was operated in resetless mode with a maximum flux swing of $\Delta B \approx B_S$ because of the narrow B-H hystersis loop of the fast ferrite used, giving a pulse-to-pulse reproducibility better than 2%. Magnetic material with flatter B-H curve may be used with a maximum flux swing of $\Delta B \approx 2B_S$ to further minimise the core volume used, e.g. Metaglas. However, some sort of technique is needed to reset the core in this case, introducing extra complexity. Further the successful implementation of this technique in a dual module 10J TEA $CO_2$ laser has demonstrated the scalability of this technology to high pulse energy (≥10J) systems.

## ACKNOWLEDGEMENTS

The authors acknowledge the EPSRC for the support of these investigations (GR/L93690).

## REFERENCES

1 J.P. Reilly, J. Appl. Phys. **43**, 3411 (1973)
2 A. E. Hill, Appl. Phys. Lett. **22**, 670 (1973)
3 K.H. Nam, H.J.J. Seguin, and J. Tulip, IEEE J. Quantum Electron. **QE-15**, 44 (1979)
4 W.H. Long, M.J. Plumer and E.A. Stappaerts, Appl. Phys. Lett **43**, 735 (1983)
5 R.S. Taylor and K.E. Leopold, Appl. Phys. Lett. **46**, 335 (1985)
6 C.H. Fisher, M.J. Kushner, T.E. DeHart, J.P. McDaniel, R.A. Petr, and J.J. Ewing, Appl. Phys. Lett. **48**, 1574 (1986)
7 R.S. Taylor and K.E. Leopold, J. Appl. Phys. **65**, 22 (1989)
8 P.K. Bhadani, A. Sylvan, and R.G. Harrison, Rev. Sci. Instrum. **62**, 1404 (1991).
9 P.K. Bhadani, A. Sylvan, and R.G. Harrison, Rev. Sci. Instrum. **63**, 71 (1992).
10 P.K. Bhadani, Y.X. Tang, and R.G. Harrison, Rev. Sci. Instrum. **65**, 2175 (1994).
11 R.S. Taylor and K.E. Leopold, Rev. Sci. Instrum. **63**, 4467 (1992).
12 P.K. Bhadani and R.G. Harrison, Rev. Sci. Instrum. **63**, 5545 (1992).
13 M.R. Harris and D.V. Willetts, Opt. Commun. **83**, 227 (1991)
14 R.S. Taylor and K.E. Leopold, Appl. Phys. **B59**, 479 (1994).

# Effect of gas decomposition in multi-joule TE/TEA $CO_2$ lasers excited by magnetic-spiker sustainer technique

Y.X. Tang, R.G. Harrison

Physics Dept., Heriot-Watt University, Edinburgh EH14 4AS, U.K.

## ABSTRACT

Investigation of the effect of dissociation products on the discharge stability and laser performance of TE/TEA $CO_2$ lasers using magnetic-spiker sustainer excitation technology is presented. The tolerance of the discharge to $O_2$/CO concentration is determined, giving improved results to that found in conventional systems. Both solid state and gaseous catalyst are also investigated for extending operational lifetime of the laser gas mixture.

**Keywords:** TE/TEA $CO_2$ lasers, gas discharge, gas decomposition, catalysts, operational lifetime

## 1. INTRODUCTION

It is well known that the molecular gases in $CO_2$ lasers are decomposed by electron impact during the excitation discharge. The most important reactions of the molecular gas decomposition in the laser gas mixture are the neutral dissociation and dissociative attachment as follows:

$$CO_2 + e^- \rightarrow CO + O + e^- \quad (1)$$

$$CO_2 + e^- \rightarrow CO + O^- \quad (2)$$

$$O^- + O \Leftrightarrow O_2 + e^- \quad (3)$$

Together with the other constituents in the mixture, the reaction products CO, O, and $O^-$ cause many subsequent species as well as various negative or positive ions, which tend to destabilize the discharge and severely degrade the laser performance. This has long been recognized as the major limiting factor to the operational lifetime of closed-cycle high power TE/TEA $CO_2$ lasers, operated at high repetition rate, required in a wide range of industrial applications.

In the last few years, there is substantial interest in use of magnetic-spiker sustainer (MSS) discharge and switching technology to drive multi-joule TE/TEA $CO_2$ lasers for providing a reliable, infinite lifetime switching, and enhanced laser performance, notably high efficiency, variable pulse duration and tailored pulse shape.[1-4] Nevertheless, little attention has been paid to the effect of gas decomposition in these lasers on long term closed-cycle operation. It is known that the gas decomposition rate is proportional to the electrical energy deposited into the laser plasma, and the dissociation cross section depends strongly on the electron temperature $T_e$. Unlike the conventional TEA $CO_2$ lasers where the value of E/N is much higher than that required for efficient excitation of molecular gases, for lasers driven by MSS technology a high value of E/N is only applied with a small amount of energy in the spiker phase which is followed by the sustainer pulse depositing the main energy into the laser plasma with the electron temperature $T_e$ kept relatively low to the optimum value. It may be therefore anticipated that the gas decomposition in such lasers will be substantially lower than that found in conventional systems.

In this paper, we report on an investigation of the effect of molecular gas decomposition on the discharge stability and laser performance of a multi-joule TE/TEA $CO_2$ lasers using the magnetic-spiker sustainer excitation techniques, both switch mode and modified overshoot mode (MOM) operation. Both solid state and homogeneously gaseous catalysts were also investigated for extending the operational lifetime of the laser gas mixture for these lasers.

## 2. INVESTIGATION OF GAS DECOMPOSITION

### 2.1 Measurement of generation rate of dissociation products - $O_2$/CO

In this section TE $CO_2$ lasers driven by the switch mode magnetic-spiker sustainer excitation scheme[3, 4] were investigated for evaluating the suitability of this technology in regard to the generation rate of dissociation products with respect to that of conventional methods. The experimental set-up is schematically shown in Fig. 1. The laser head assembly was housed in a glass envelope with high vacuum integrity to minimize the problem of gas contamination caused by air leakage and degassing from the material of the laser chamber. A quadruple mass spectrometer (SuperVac) was used to analyze the laser

XIII International Symposium on Gas Flow and Chemical Lasers and High-Power Laser Conference,
Antonio Lapucci, Marco Ciofini, Editors, Proceedings of SPIE Vol. 4184 (2001)

gas mixture. The mass spectrometer head was placed in the gas flow loop for in-situ measurements of dissociation products, in particular $O_2$ and CO, along with leakage valves to control the amount of sample gas. A sputter ion pump or turbomolecular pump was used for pumping the mass spectrometer chamber down to ~$10^{-8}$ torr for accurate measurement. Before the actual measurement, the mass spectrometer was calibrated for $O_2$ with respect to He as He was the stable constituent in the laser gas mixture and its concentration did not change during the laser operation. It was not possible to measure accurately the concentration of CO by the mass spectrometer used in this investigation as the mass number of CO and $N_2$ were the same at 28. To do so, a mass spectrometer with a higher mass resolution was needed. However, as noted, even a small amount of $O_2$ in the laser gas mixture was most detrimental to producing a stable discharge, and hence its measurement provided sufficient information on the suitability of magnetic-spiker sustainer excitation method.

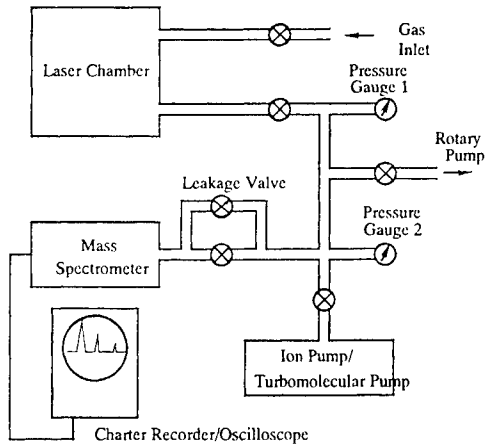


Fig. 1 Schematic of gas decomposition study

The laser was operated under both short and long pulse excitation at a repetition rate of ~ 0.5pps, using a helium-free gas mixture of $CO_2$+$N_2$ (1:3) = 300 torr with addition of 15torr $H_2$ at half atmospheric pressure. At the end of operation a small amount of the sample gas was introduced into the mass spectrometer chamber for analyzing. It was found that at the end of ~500 shots, ~1.2 torr (0.37%) $O_2$ was produced in the gas mixture, of which ~80% was contributed mainly from the (preionization + spiker) circuit while only 20% was contributed from the sustainer circuit. Comparing these findings with those obtained using a conventional excitation circuit for short pulse operation under similar conditions and for the same number of shots, $O_2$ produced in the discharge was ~1.5torr (0.46%), ~25% higher than that with magnetic-spiker sustainer circuit. This demonstrated that in regard to the generation rate of dissociation products, the magnetic-spiker sustainer excitation technology compared favourably with conventional methods. In addition, no oxide of nitrogen was detected in the experiments, nor ozone. Therefore, the dissociated products, $O_2$ and CO, were assumed to be primarily responsible for arc formation. Further investigation was undertaken for long pulse operation with addition of a small amount of CO to the laser gas mixture. Although arcing occurred at the end of ~7000 shots, analysis of the gas mixture revealed that $O_2$ could not be detected. This was in contrast to our expectation according to the reaction kinetics. It appeared that OH and H in the discharge reacted to form water vapor ($H_2O$) though this could not be confirmed by mass spectroscopy due to a significant background of $H_2O$ signal in the mass spectrometer.

### 2.2 Tolerance to dissociation products – $O_2$/CO

To determine the tolerance of the discharge to the dissociation products, $O_2$/CO, the multijoule TEA $CO_2$ laser using MOM magnetic-spiker sustainer excitation technique[1] was investigated for the laser gas mixture seeded with a small amount of $O_2$ or CO. The laser system was operated in the sealed-off mode at a repetition rate of ~ 1pps with the gas mixture of $CO_2$:$N_2$:He = 12:14:74 at atmospheric pressure.

To determine the effect of $O_2$ on the discharge stability, "contaminated gas mixtures" were used by deliberately adding a known small amount of $O_2$ to the laser gas mixture. Fig. 2 shows the input energy loading as a function of the oxygen concentration in the gas mixture for various values of sustainer capacitor $C_S$ and at different spiker energies. As seen from these plots, the input energy loading decreased with the $O_2$ concentration rise for all values of sustainer capacitance at a given spiker energy. It was found that the energy loading was dramatically reduced to only half of that found in the clean gas mixture when the $O_2$ concentration was increased to ~1.6%. Beyond

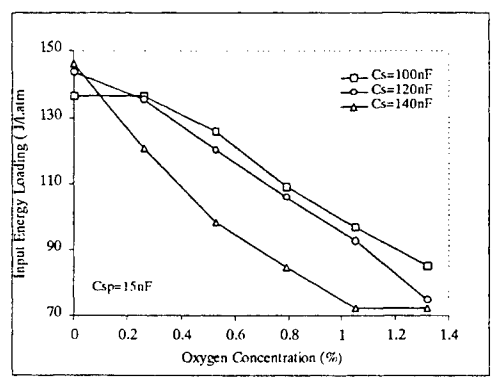


(a)

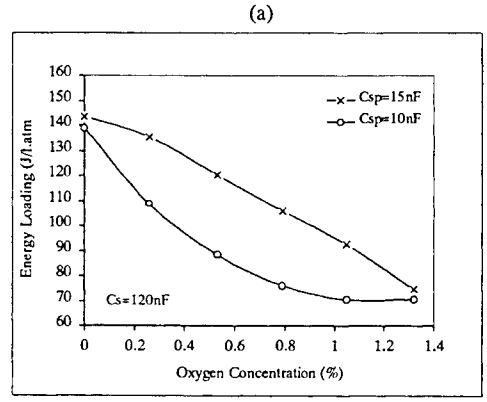


(b)

Fig. 2 Tolerance of discharge to $O_2$ (a) for various sustainer capacitances, and (b) different spiker energies

these limits, discharges always collapsed into hot filaments while the discharge of longer duration was more sensitive to the oxygen contamination. It was also observed experimentally that when the oxygen concentration reached a critical level $[O_2]_c$, the operating voltage on $C_S$ did not decrease further with increase of $O_2$ in the gas mixture. Nevertheless, the input energy loading was found to be only ~72 J/l.atm at $[O_2]_c$, independent of the sustainer capacitance and spiker energies, and the discharge unstable, hence of little practical significance. From these findings, it is concluded that an acceptable level of oxygen concentration was ~0.8% for a typical input energy loading of ~110J/l.atm in this laser, comparing well with that (~0.5%) obtained in conventional TEA $CO_2$ lasers of similar discharge volume[5].

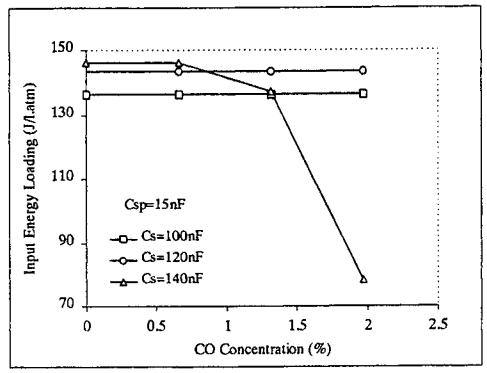


(a)

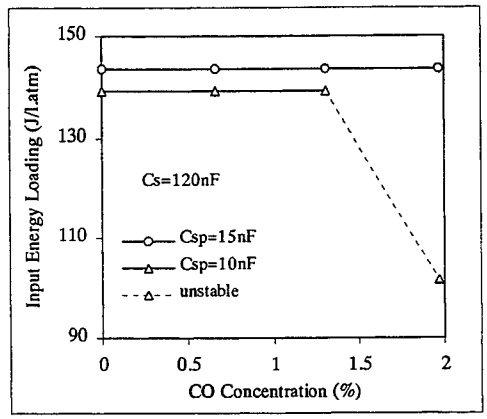


(b)

Fig. 3 Tolerance of the discharge to CO (a) for various sustainer capacitances, and (b) different spiker energies

The effect of CO on the discharge quality was also investigated in a similar way to that described above by adding a small amount of CO to the laser gas mixture. The dependence of the input energy loading as a function of the CO concentration is shown in Fig. 3 for various values of sustainer capacitance and at different spiker energies. The dashed lines in the figures denote the situation for which the stable discharge was difficult to maintain or accompanied by an increasing rate of arcing. As seen from these graphs, there was no significant effect on the discharge stability with CO in the gas mixture up to ~2% for the sustainer capacitor up to 0.12μF at a higher spiker energy, except the change of discharge colour from pink to white blue. However, the input energy loading decreased dramatically with increase of CO concentration for a larger value of sustainer capacitance, which implied that the discharge of longer duration was rather sensitive to CO. It was found that the tolerance of the discharge to CO degenerated enormously at smaller spiker energy. It was observed that with CO greater than 2% the discharge remained unaffected for the sustainer capacitance of 0.1μF at spiker energies above 3.4J. Nevertheless, a stable discharge could not be obtained for the larger sustainer capacitances at the same spiker energy with the concentration of CO in the mixture above ~0.7%. The findings may imply that with sufficiently high spiker energy the discharge ignores the presence of CO completely over a large concentration region of CO.

## 3. EFFECT OF SOLID STATE AND GASEOUS CATALYST

Gaseous additives have been used in conventional TEA $CO_2$ lasers resulting in remarkable improvement of the operational lifetime of the gas mixture. For example, the addition of a small quantity of CO, which we have seen does not have adverse effect on the discharge, was used to bias the dissociation reaction in the reverse direction, so that some of the oxygen produced could recombine with the CO and reform $CO_2$. Further a mixture of CO and $H_2$ added to the $CO_2$ laser gas mixture has been found to act as homogeneously gaseous catalysts in $CO_2$ lasers with a moderate $CO_2$ concentration. As proposed by Smith *et al*[6], in the presence of $H_2$ OH radicals are formed and the reformation of $CO_2$ occurs through the reactions:

$$CO_2 \Leftrightarrow CO + O \qquad (4)$$

$$O + H_2 \rightarrow OH + H \qquad (5)$$

$$H + O_2 \rightarrow OH + O \qquad (6)$$

$$CO + OH \rightarrow CO_2 + H \qquad (7)$$

Hence in effect $O_2$ and CO were recombined to form $CO_2$ with hydrogen made available to repeat the reaction cycle. The $CO_2$ reformation was, therefore, accelerated by the OH radicals derived from $H_2$ or $H_2O$ due to large kinetic rate coefficient of reaction (7).

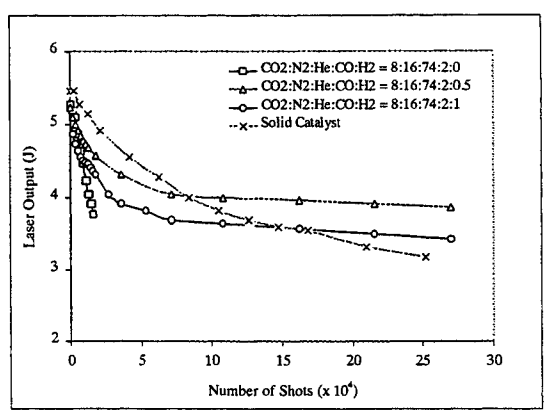


Fig. 4 Operational lifetime with gaseous/solid state catalysts

The effectiveness of the addition of a mixture of CO and $H_2$ to the laser gas mixture as a homogeneously gaseous catalyst was investigated for extending the operational lifetime of the laser medium in the TEA $CO_2$ laser using MOM magnetic-spiker sustainer excitation scheme. The laser system was operated in sealed-off mode at a pulse repetition rate of ~30pps with the sustainer capacitor $C_S$=0.1μF and spiker capacitor $C_{SP}$=15nF charged to a voltage of 27kV. The gas mixture of $CO_2$ : $N_2$ : He = 8 : 16 : 76 at atmospheric pressure was used in this investigation. In order to make a direct comparison the solid state catalyst Pt/Pb on $SeO_2$ in the form of honeycomb was also examined for restoration of dissociated $CO_2$ molecules in the discharge for extending the operational lifetime of the laser gas mixture. The overall dimensions of the solid state catalyst was ~ 48 x 6 x 2.5 $cm^3$, roughly as long as the discharge volume. The honeycomb was placed in the gas circulation loop in the laser chamber, in parallel to the main electrodes facing the gas flow. There was no significant degradation in the laser performance at repetitive operation observed due to the obstruction to the gas flow caused by the honeycomb. A typical result of the fall in the laser output energy with number of shots is shown in Fig. 4 for the gas mixture with and without the catalysts. As seen ~$2.7 \times 10^5$ shots in sealed-off operation within one gas fill was obtained with addition of 2% CO and 0.5% $H_2$ to the laser gas mixture. These plots explicitly indicate that though both types of catalysts resulted in a considerable improvement in extending the operational lifetime of the laser medium, homogeneous gaseous catalysts were more efficient than solid state catalyst at least by factor of 2 when a laser output energy at the level of ~ 80% of the initial laser output was to be retained. It should be pointed out that higher concentration of CO above 2% and $H_2$ above 0.5% did not result in any significant improvement in the operational lifetime of the gas mixture but dropped the laser pulse energy. The effect of addition of CO+$H_2$ mixture on the laser performance, in particular the laser output energy, was investigated. Fig. 5 shows the laser output energy as a function of the CO concentration and $H_2$ concentration in the laser gas mixture. It was observed that the laser output energy decreased with increase of CO and $H_2$. This is because in the presence of CO in the gas mixture, the resonant energy transfer from the vibrational levels of CO to the $CO_2$ upper laser level ($00^01$) is less efficient than that from $N_2$ due to a larger gap in vibrational levels between CO and $CO_2$ and the smaller vibrational excitation rate coefficient of CO. It is well known that the $CO_2$ upper laser level is rapidly depopulated by $H_2$ due to its large relaxation kinetic rate coefficient.

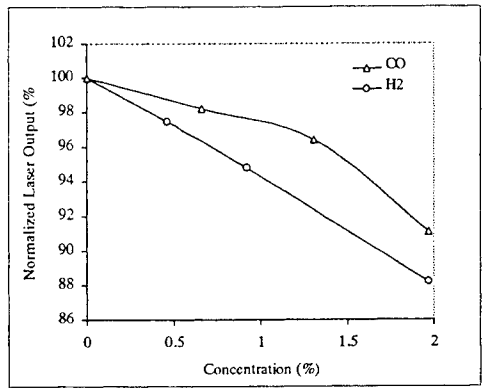

Fig. 5 Effect of gaseous catalysts on laser output energy

## 4. DISCUSSION

Our experiments have identified $O_2$ to have the dominant effect on the discharge stability, the spiker pulse and spark preionization giving the major contribution to the $CO_2$ decomposition since a very high E/N was applied to the discharge during the spiker phase which is well known to enhance the dissociation of $CO_2$. However, it was not possible to determine the individual contribution from preionization as the preionization and spiker circuit were tightly coupled. A mixture of CO and $H_2$ was demonstrated to be a superior catalyst to the solid state converter in extending the operational lifetime of the laser gas mixture. In general our findings show the operational lifetime of TEA $CO_2$ lasers using magnetic-spiker sustainer comparing favorably with that of conventional discharge systems.

## ACKNOWLEDGEMENTS

The authors acknowledge the EPSRC for the support of these investigations (GR/L93690).

## REFERENCE

1 Y.X. Tang and R.G. Harrison, "Modified overshoot mode of magnetic-spiker sustainer technology for multi-joule TEA $CO_2$ lasers", SPIE Proc. of XIII GCL/HPL'2000, Florence, Italy, Sep. 2000 (to be published).
2 P.K. Bhadani, Y.X. Tang, and R.G. Hrrison, , Rev. Sci. Instrum., **65**, 2175 (1994).
3 P.K. Bhadani, A. Sylvan, and R.G. Harrison, Rev. Sci. Instrum., **63**, 71 (1992).
4 P.K. Bhadani, and R.G. Harrison, Rev. Sci. Instrum., **63**, 5543 (1992).
5 Y. Uchida, S. Oukuma, S. Sato, and T. Goto, Jap. J. Appl. Phys. **29**, 1266 (1990).
6 A.L.S. Smith and P.G. Browne, J. Phys. D: Appl. Phys., **7**, 1652 (1974).

# Power stabilization of radio frequency excited slab laser using optogalvanic effect

**Jong-Woon Choi**
Dept. of Information and Telecommunication Engineering
Honam University, Gwansangu, Gwangju, Korea
E-mail: woon@honam.honam.ac.kr

## ABSTRACT

We stabilized an optical power of RF excited slab $CO_2$ laser on the pick of the Doppler broadened gain curves using an optogalvanic effect generated from the laser itself. The power stability is greatly improved to 2.9 %. We suggest that this method can be applied for frequency and power stabilization of other kinds of RF excited laser, for example, Xe and CO laser.

**Keywords:** slab laser, optogalvanic effect, power stabilization, radio frequency, $CO_2$ laser

## 1. INTRODUCTION

We report power stabilization method for RF excited slab $CO_2$ laser using optogalvanic effect. The optogalvanic effect is a change in the electric impedance of a discharge caused by illuminating the discharge with radiation having a frequency corresponding to an atomic or molecular transition in the discharge[1]. Optical output and frequency of a laser depends on an interval between two mirrors which constitute a cavity of the laser. Accordingly, the laser power and frequency is stabilized when the above interval, namely, cavity length, is stabilized to be constant. Many methods[2,3] were developed to stabilize an RF excited $CO_2$ laser. However, until now, the RF excited slab laser lacked a simple and reliable stabilization method. We stabilized the length of unstable resonator to the pick of the Doppler broadened gain curves using an optogalvanic effect generated from the laser itself, thereby stabilizing the optical power without requiring any specific unit to be arranged inside or outside of a laser cavity.

The optical output of a gas laser using a unstable resonator depends on an optical length of the cavity. For this reason, in order to stabilize the optical power and oscillating frequency of the laser, it is important to prevent the optical length of the cavity from being affected by the environment where the laser is used. Otherwise, a variation of the optical cavity length should be compensated. In other words, the optical length of the laser cavity, which may vary depending on the environmental temperature, mechanical vibrations, and variations of the pressure of laser mixture, should be kept constant.

A variation in laser radiation flux occurring in the laser cavity results in variations of laser beam intensity[4], spectrum distribution, gas pressure, discharge current, and discharge impedance. In this regard, when vibrations of a certain frequency (for example, 520 Hz) are applied to a piezo electric transducer mounted under one of unstable resonator mirrors, the optical length L of the laser cavity vibrates at the same frequency with the amplitude of $\Delta L$. The intensity of laser beam is modulated at the same frequency as that of the cavity length, along a laser gain characteristic. When the average mode frequency of the laser beam intensity is lower than the central frequency of the gain profile, the laser beam intensity has a phase opposite to that of the impedance variation $\Delta Z$. On the other hand, where the average mode frequency is higher than the central frequency, the impedance variation $\Delta Z$ increases correspondingly to a difference of the mode frequency from the central frequency. In such a way, a considerable variation in the radio frequency discharge impedance occurs even when a slight variation in laser beam intensity occurs in the laser cavity. For instance, an intensity variation of only 1 % results in a considerable variation in the radio frequency discharge impedance corresponding to about 0.1 % [3]. Based on such an impedance variation in the laser cavity, a variation in incident or reflected radio frequency energy is detected. Based on the detected signal, a frequency discriminator generates an error signal which is, in turn, fed back to the piezo electric transducer, carrying out a optical output and laser frequency stabilization by optogalvanic effect.

XIII International Symposium on Gas Flow and Chemical Lasers and High-Power Laser Conference,
Antonio Lapucci, Marco Ciofini, Editors, Proceedings of SPIE Vol. 4184 (2001)

## 2. EXPERIMENTAL APPARATUS

FIG. 1 shows the diagram of our laser optical power stabilization apparatus. The radio frequency excited slab $CO_2$ laser used is of an water cooled sealed off type. The laser cavity total length was of 646 mm, formed by the unstable confocal positive branch off-axis resonator. The electrodes of the radio frequency discharge tube were made of aluminum and had a width of 50 mm and a length of 380 mm. The output power and frequency of RF generator were respectively, 250 W and 125 MHz. The $\pi$-matching circuit serves to obtain an impedance matching between the radio frequency generator and laser cavity, thereby minimizing a reflection of high frequency energy. The output window was made of ZnSe. The piezo electric transducer assured a variation in the length of the laser cavity to a maximum of 15 $\mu$ m/150 V.

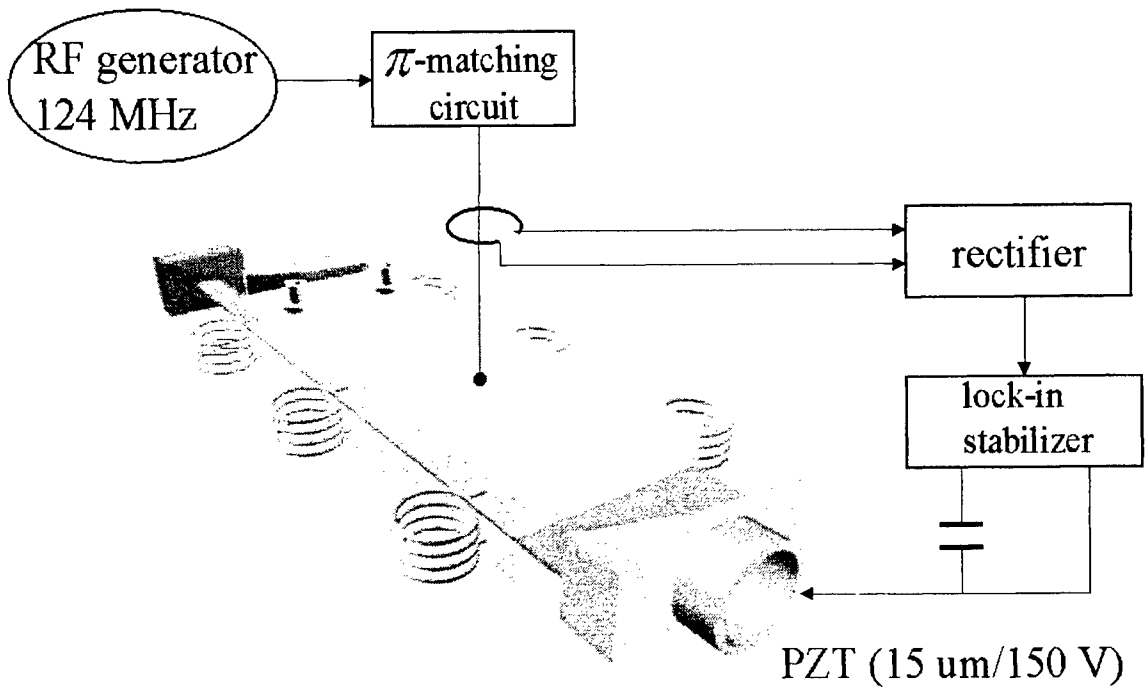


Fig. 1. Experimental setup for the stabilization of RF excited slab $CO_2$ laser.

A laser gas mixture of $CO_2$: $N_2$ : He was supplied, in a ratio of 1 : 1 : 3, to the radio frequency discharge channel to maintain a total pressure of 40 torr. In order to achieve a optical power stabilization of the laser, a lock-in stabilizer is coupled between the piezo electric transducer and detection circuit with a high-voltage amplifier adapted to directly drive the piezo electric transducer, and a signal generator adapted to generate a reference signal.

As mentioned above, when the piezo electric transducer drives, a modulation of the laser power is generated in accordance with vibrations generated by the piezo electric transducer. Such a variation in the laser power generates an optogalvanic effect in the laser cavity, thereby resulting in a variation in the impedance of the RF discharge tube. Accordingly, the RF energy applied to the RF discharge channel varies. In order to measure such a variation in the input RF energy caused by the optogalvanic effect, induction loop is coupled to the RF inlet of the RF discharge tube. The detector receives a part of RF energy induced through the capacitor and removes RF components from the received RF energy. The detector sends the resultant signal free of RF components to the lock-in stabilizer.

We performed an experiment to demonstrate the optogalvanic effect generated when the length of the laser cavity vibrates very slightly due to vibrations of the PZT. First, a sine wave signal (520 Hz) with a voltage of about 10 V p.p. from the lock-in stabilizer was applied to the PZT, thereby causing the vibrations of cav ty length. In order to measure the optogalvanic effect caused by the vibrations of the PZT, a part of the RF power picked up through the induction loop was sent to the detector, thereby removing RF components (125 MHz) from the signal The resultant signal free of RF components was then spectrum analyzed using a network signal analyzer (Stanford research system: SR-780) coupled to the

detector. After the analysis, as it is shown on Fig. 2, an optogalvanic signal (520 Hz) was observed. The optogalvanic effect was generated by a modulation of the optical flux circulating inside the laser cavity [5] from a variation in the cavity length caused by the vibrations of the PZT. Using such an optogalvanic signal, it is possible to measure a variation in the length of the laser cavity caused by a slight vibration of the PZT.

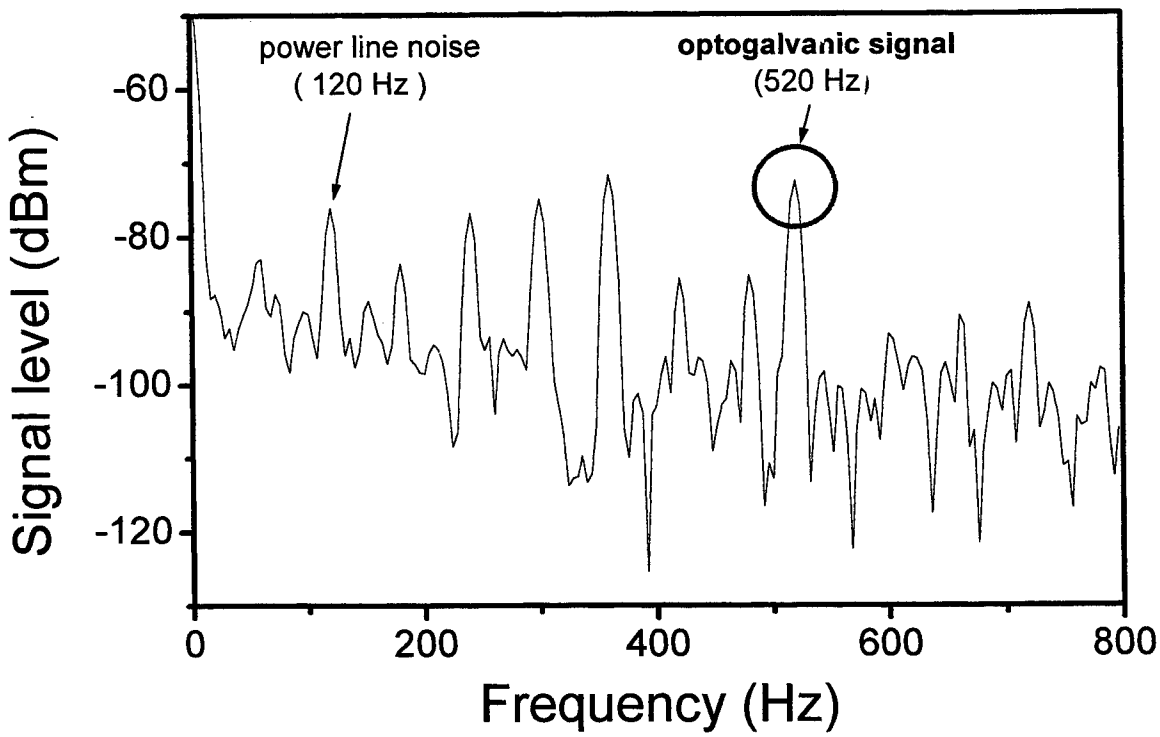


FIG. 2. Spectrum of optogalvanic signal (520 Hz), power line noise (60 Hz) with its harmonics, and laser discharge noise.

The laser is controlled to oscillate on the one of many picks of the gain curve by varying DC bias voltage applied to the piezo electric transducer. In this state, a feedback loop of the lock-in stabilizer is activated. In this case, three signals are applied to the piezo electric transducer. These signals include a DC bias voltage signal for finding an activation point, a sine wave signal of 520 Hz used as a reference signal for the lock-in stabilizer, and a compensation voltage signal obtained by integrating error signals generated and amplifying the resultant signal.

When the sine wave signal of 520 Hz is applied as a reference signal to the piezo electric transducer, the laser power is modulated in the form of a sine wave. Since an optogalvanic effect is generated in the laser cavity due to the modulation of the laser power, the impedance of the RF discharge tube is also modulated. In accordance with this impedance modulation of the RF discharge tube, RF energy introduced into or reflected from the discharge tube is also modulated to have the same frequency as that of the sine wave signal. When the resultant modulated signal passes through the detector, an optogalvanic signal free of RF components is obtained. The optogalvanic signal, which is derived by a detection based on a sine wave, is then applied to the lock-in stabilizer which, in turn, performs a synchronous detection for the optogalvanic signal. As a result, a voltage proportional to the gain curve is derived. Based on the derived voltage, it is possible to determine the position of the vertex of the gain curve. The signal derived by the synchronous detection is integrated and then converted into the form of a DC voltage. The resultant signal is then applied to the piezo electric transducer and serves to continuously vary the length of the laser cavity until the signal obtained by the synchronous detection has a zero level. In this moment the laser oscillates at the vertex of the gain curve. In accordance with this principle, the length of the laser cavity is kept constant and stabilization of the laser frequency is achieved.

## 3. RESULTS AND DISCUSSION

FIG. 3 shows the results obtained after stabilizing the optical output of the RF excited slab $CO_2$ laser using an optogalvanic effect. Referring to FIG. 3, it can be found that the optical power are stabilized by the lock-in stabilizer. The power variation occurring when the laser operates freely is expressed by "ΔP/P". Since a great power variation occurs in the case of a laser oscillating in multi longitudinal mode, the laser exhibits a power variation up to 100 %. When the laser is stabilized, a power variation of only 2.9 % is exhibited. We did not check the stability of optical frequency in this time, and we shell exepect that the stability of optical frequency was simultaneously improved with optical power. We suggest that this method can be applied for frequency and power stabilization of other kinds of RF excited laser, for example, Xe and CO laser.

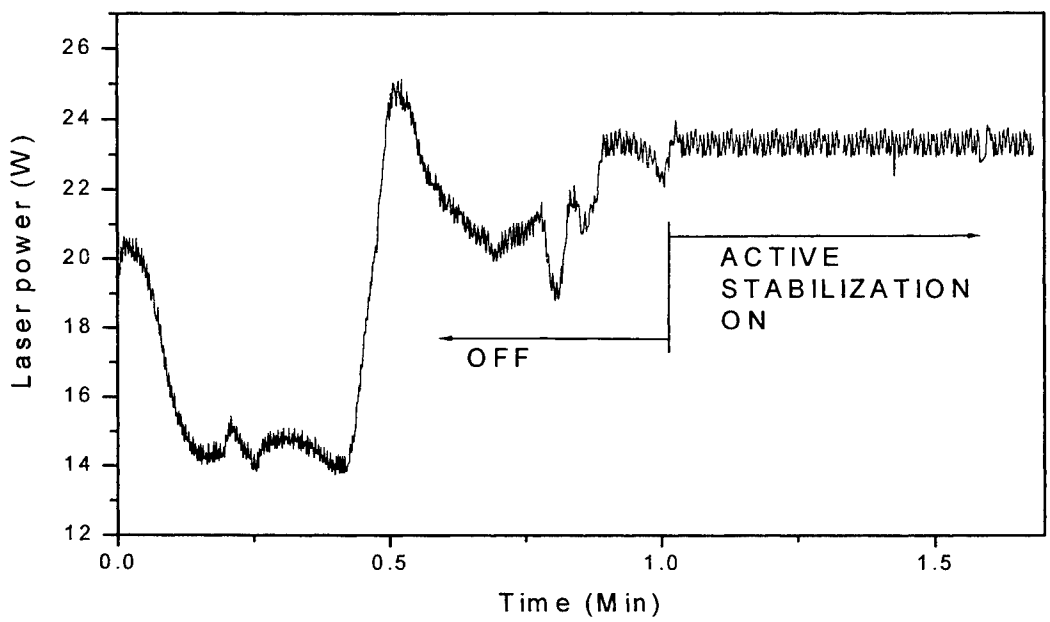


Fig. 3. Change of laser power before and after the laser is stabilized using optogalvanic effect. Here the laser line is P(20) and the power is 23 W at peak.

## 4. ACKNOWLEDGMENTS

Author gratefully thanks for supports of K.M. Abramski, E.F. Plinski in Laser & Fibre Electronics Group, Inst. of Telecommunication and Acoustics, Wroclaw Univ. of Technology, Wroclaw, Poland and Marek Strzelec, Mirek Kopiza in Military University of Technology, Poland.

## 5. REFERENCE

1. Beniamino Barbieri and Nicolo Beverini, "Optogalvanic spectroscopy," Rev. Mod. Phy., Vol. 62, No. 3, 1990.
2. Chin-Chun Tsai, Tyson Lin, Cherng-Yn Shieh, Tsu-Chiang Yen, and Jow-Tsong Shy, " $CO_2$ laser frequency stabilization using the radio-frequency optogalvanic Lamb dip," Appl. Opt., Vol. 30, No. 27, 1991.
3. A. L. S. Smith and S. Moffatt, "Opto-galvanic stabilized $CO_2$ laser," Opt. Comm., Vol. 30, No. 2, 1979.
4. William H. Thomason and Don C. Elbers, "An inexpensive method to stabilize the frequency of a $CO_2$ laser," Rev. Sci. Instrum., Vol. 46, No. 4, 1975.
5. J. W. Choi, Y. B. Chung, M. Strzelec and M. Kopica, Rev. of Sci. Inst. Vol. 69, No. 12, Dec. 1998.

# Modeling of injection seeding of a pulsed high pressure $CO_2$ laser

L. R. Botha*[a] and E. G. Rohwer[b]

[a]Scientific Development and Integration, Pretoria, South Africa

[b]Dept. of Physics, University of Stellenbosch, South Africa

## ABSTRACT

A computer model for injection seeding of a high pressure $CO_2$ laser is presented. A rate equation model is used to predict single longitudinal mode (SLM) operation through injection of a cw seed into the resonator cavity. The coupled non-linear differential equations are solved using a Runge-Kutta method. Predictions for the minimum injection power required to produce SLM pulses are made. Detuning off resonance and the effect of the output coupler reflectivity and small signal gain on SLM operation is also considered. Conditions for stable SLM operation through injection of a cw seed are suggested. Single mode operation, even in the detuned case, can be attained due to the homogeneous broadening of the gain, and the rapid growth of the pulse under high gain conditions.

**Keywords:** HP $CO_2$ laser, injection seeding, SLM pulses

## 1. INTRODUCTION

In order to obtain continuously tunable output from a $CO_2$ laser, it has to be operated at high pressure. Several techniques exist to obtain single longitudinal mode (SLM) pulses. Inserting frequency selective optics can provide SLM operation. Extremely high intensities inside the resonator can damage optics and these methods are sensitive to misalignment and require tuning and control mechanisms. In an industrial environment stability and ease of use is critical. Injection of a seed into the resonator has proven to be a very successful method to obtain SLM operation with TEA $CO_2$ lasers. Ease of use and good stability have been demonstrated, therefor the use of injection locking of a high pressure (HP) $CO_2$ laser was investigated.

## 2. INJECTION LOCKING MODEL

Injection locking is a well established technique. The principles of a mathematical model simulating the development of the output pulse of a HP $CO_2$ laser will be described. A rate equation model based on similar principles as described by Angelie et.al.[1], Lachambre et.al.[2] and Tashiro et.al.[3] is discussed. In this model electric fields are calculated, since the phase is of significance. Using the convention where $R$ is the intensity reflectivity loss, and $T$ intensity transmittance of the empty cavity per round trip, the electric field after one round trip ($2L$) can be written as

$$\mathbf{E}(t+2\tau) = E(t+2\tau)e^{i\omega(t+2\tau)} = E(t)\sqrt{RT}e^{\alpha(t)\ell}e^{i\omega t} + E_0'(t+2\tau)e^{i\omega t} \tag{1}$$

where $\alpha$ is the time dependent gain, $\ell$ is the length of the gain medium, $\omega = 2\pi\nu$ is the angular frequency, and $E_0'(t)e^{i\omega t}$ is the injected signal at frequency $\omega$. Introducing the photon lifetime $T_0$, such that $\sqrt{RT} = e^{-\tau/T_0}$, and using $\tau = L/c$, equation (1) can be written in terms of amplitudes as

$$E(t+2\tau) = E(t)e^{m_r(t)2\tau} + E_0'(t+2\tau). \tag{2}$$

where $m_r(t) = -1/2T_0 + c\ell\alpha(t)/2L$. If the injected signal with amplitude $E_0$ is off resonance, the phase difference has to be accounted for, when adding these amplitudes. The phase difference $\phi$ is given by $\phi = 2\pi\delta\nu \cdot 2L/c = 2\pi\delta\nu/\Delta\nu$, where $\Delta\nu = c/2L$ is the inter-mode spacing, $\delta\nu$ is the frequency difference. In this case $m(t) = -1/2T_0 + c\ell\alpha(t)/2L + i\phi \cdot c/2L$ has to replace $m_r$ in equation(2).

*Correspondence: Email: lourens.botha@sdi.co.za. Postal Adress: PO Box 1559 Pretoria 0001 RSA

XIII International Symposium on Gas Flow and Chemical Lasers and High-Power Laser Conference,
Antonio Lapucci, Marco Ciofini, Editors, Proceedings of SPIE Vol. 4184 (2001)

## 2.1. Photon rate equation

It can be shown[2] that equation (2) is a solution of the differential equation

$$\frac{\mathrm{d}E}{\mathrm{d}t} = m(t)E + \frac{m(t)E_0}{e^{2\tau m(t)} - 1} \tag{3}$$

assuming a slowly varying gain and constant value for $E_0$. Equation (3) has a real and an imaginary part. The real ($E_r$) and imaginary ($E_i$) parts are separated and each differential equation is solved separately. The intensity of the EM wave is determined using $I(t) = E_r^2 + E_i^2$. Clearly the solution of the differential equations depends on the behaviour of the small-signal gain $\alpha$. The small-signal gain $\alpha(t)$ is given by

$$\alpha(t) = \sigma[N_J(t) - N_{J'}(t)]l/2L \tag{4}$$

where $N_J(t)$ is the upper and $N_{J'}(t)$ is the lower level population, $\sigma$ is the effective radiative cross section for the transition.

## 2.2. Population rate equations

In a HP $CO_2$ laser the equations governing the populations of the $j^{th}$ rotational level of the upper vibrational state can be written as[5]

$$\frac{dN_j}{dt} = P_j - \gamma_j N_j - \sum_k \Gamma_{jk} N_j + \sum_k \Gamma_{kj} N_k - \sigma_J \frac{I}{h\upsilon}\left(N_j - N'_{j'}\right)\delta_{jJ} \tag{5}$$

where $\Gamma_{jk}$ is the rate for collisional transitions out of level $j$ to all other levels $k$ within the vibrational band. $P_j$ and $\gamma_j$ are the pumping and decay rates of the individual rotational levels. $\delta_{jJ}$ is the Kronecker delta and the primed quantities refer to the lower level. By detailed balance under equilibrium conditions $\Gamma_{jk} = \frac{z_k}{z_j}\Gamma_{kj}$, where $z_k$ and $z_j$ are the Boltzmann factors. Using this fact in equation 5 and then summing over $k$, the following equation is obtained

$$\frac{dN_j}{dt} = P_j - \gamma_j N_j - \frac{(N_j - z_j N_v)}{\tau_x} - \sigma_j \frac{I}{h\upsilon}\left(N_j - N_{j\pm1}\right)\delta_{jJ} \tag{6}$$

with $N_v$ the total vibrational population of the vibrational level given by

$$N_v = \sum_j N_j \tag{7}$$

By summing each term of equation 7 over $j$ an equation for the total population of the vibrational level is obtained and is given by

$$\frac{dN_v}{dt} = P - \gamma N_v - \sigma \frac{I}{h\upsilon}\left(N_J - N_{J'}\right) \tag{8}$$

where $P$ and $\gamma$ are the total pump and decay rates of the vibrational level. The pumping rate for a specific rotational level i.e. $P_j$ is given by

$$P_j = z_j P$$

An assumption was made that the time for the gain build-up is slow compared to the electrical discharge. The actual physics of the discharge excitation was ignored and an initial reservoir of vibrationally excited $N_2$ was assumed. The pumping $P$ was chosen to reproduce, in the absence of radiation, the small-signal gain. The maximum population inversion was calculated using a user specified small signal gain value.

## 2.3. Simultaneous solving of rate equations

The differential equations governing the populations and the photon numbers are coupled by the expression for the gain, equation (4). These coupled differential equations were solved simultaneously using a fourth order Runge-Kutta algorithm. The photon density was calculated separately for each longitudinal mode (using the same available gain) and finally the resultant intensity of all modes circulating in the cavity was calculated. The modes considered were: a) The mode related to the injection frequency with initial angular frequency $\omega_{inj} = \omega_c - \delta\omega$ where $\omega_c$ is the angular frequency of the longitudinal mode closest to the injected angular frequency and $\delta\nu$ is the so-called detuning frequency, and b) the modes at angular frequencies $\omega_n$ of the resonant longitudinal modes. For these modes the injection $E$-field $E_0$ was simply replaced by the background spontaneous emission $E$-field.

The output power $P(t)$ was determined using $P(t) = (1 - R_1)I_{\text{tot}}(t)A$,with $R$ the output coupler reflectivity, and $A$ the effective cross sectional area of the actual laser. The pulse energy $\mathcal{E}$ was calculated using $\mathcal{E} = \int_{t=0}^{\infty} P(t)\mathrm{d}t$.

## 3. EVALUATION OF MODEL

The model essentially requires only two starting values: The required small signal gain, and the injected intensity.

### 3.1. Gain and threshold.

In this model the time varying gain is calculated using eq. (4). In figure (1) the gain as a function of time was plotted for small signal gain of 3 $m^{-1}$. The threshold gain for a resonator mode ($\phi = 0$) is given by

$$\alpha_{\text{thres}} = L/(c\ell T_0) = \ln(1/RT)/2\ell \tag{9}$$

For values of $R = 0.65$; $T = 1$; $\ell = 0.4$ m, the threshold gain is 0.5 $m^{-1}$. In the presence of a photon field, the gain is reduced, coinciding with the output of the laser pulse.

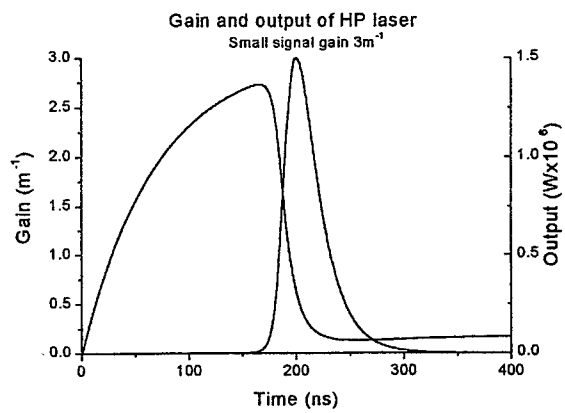


Figure 1.

### 3.2. Mode competition

The main purpose of this investigation is to determine effect of injection of a seed on the resulting mode beating. The cross section was assumed to be frequency independent, and it was assumed that the grating selects six modes to be above threshold. The background intensities of all the modes is chosen to be $3\times10^{-7}$ W/m$^2$. This value was obtained using the value of $4\times10^{-8}$ W/m$^2$ used by Lachambre et.al.[2] for one atmosphere and scaling according to the higher pressure of this 7 atm. laser. With a relatively small injection signal on resonance, mode beating is still observed, however the beating is reduced, as expected (figure (2)).

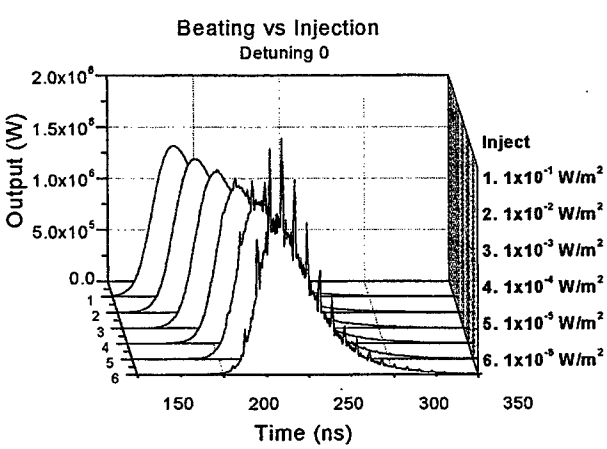


Figure 2.

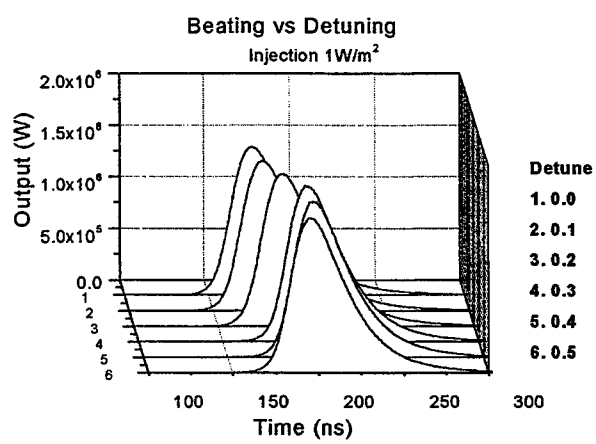


Figure 3.

For injection intensity $1 \times 10^{-1}$ W/m$^2$, the pulse is considered to be single mode. From the figure (2) it can clearly be seen that the gain switched pulse arrives sooner as the injected intensity is increased. This has to be taken into account when synchronizing the oscillators and amplifiers.

### 3.3. Detuning of injected signal

For practical stability considerations it is extremely important to investigate the effect of detuning on injection locking. In section (2) it was explained how detuning was taken care of in the model. This was investigated using a injection intensity (1 $W/m^2$) and 0.0 to 0.4 detuning (fraction of the intermode spacing). SLM operation can be achieved, even with larger detuning (figure (3)).

### 3.4. Output coupler reflectivity

The output coupler determines the threshold gain, as well as the photon lifetime in the cavity. The value of $R$ also determines the output energy. The output power of the pulses for different values of $R$ was calculated, using a detuning of 0.4 and an injection intensity of 1 $W/m^2$. The intensity inside the resonator was also calculated. These calculations show that the output can be optimized by choosing $R = 0.8$. Here the pulse energy is 60 mJ, which confirms that the model predictions are in the right order of magnitude regarding output energy. The intensity inside the cavity is about twice as much for the 0.8 output coupler, compared to the 0.65 case. There is not a marked decrease in the output energy moving from 0.8 to 0.65, hence a choice of $R = 0.65$ is a reasonable compromise, since it protects the optics in the resonator from very high intensities that could damage the optics, while sacrificing very little in terms of output.

## 4. DISCUSSION

The specific values for the parameters in the model, used to do the calculations, were chosen according to the design values for an oscillator running at 7 atm., with resonator length 1.1 m, gain length 0.4 m. The active volume was chosen according to the resonator design for $TEM_{00}$ mode output.

The modes compete for the same gain. Hence the situation where SLM is obtained through injection seeding may be realistic whereas, when locking is not obtained, the calculated pulses are optimistically smooth, and may not be realistic, since there could even be more modes competing than used in the calculation. The minimum injected intensity for SLM operation obtained here is 1 $W/m^2$. The value of 1 $W/m^2$ (0.1 $mW/cm^2$) is in the same order of magnitude as reported by Angelie et.al.[1] who reported results and experimental data using cw injection in the $mW/cm^2$ range to obtain SLM in a high pressure TE-$CO_2$ laser. The seed was injected through the output coupler (Ge, $R = 0.65$) and this gives effective injection in the 0.1 $mW/cm^2$ range. Sasaki et.al.[4] show, using a modified model of the Lachambre[2] version, that stable for injection locking over a wide detuning range, injection power of 1 $mW/cm^2$ is sufficient. It therefore seems reasonable to assume that a figure of between 0.1 and 1 $mW/cm^2$ (in the cavity) can be specified as the required power for effective injection.

## 5. CONCLUSION.

The mathematical model for injection mode locking was successful in predicting seed intensities required and detuning that can be tolerated for SLM operation. The model can be used to evaluate the effect of output coupler reflectivity and gain on the laser output. It has been shown, using this model, that injection power of 1 $W/m^2$ (0.1 $mW/cm^2$) is required inside the resonator for effective (SLM) locking. This required value is in the same order of magnitude as reported by Angelie et.al.[1] who reported using cw injection in the $mW/cm^2$ for a similar HP laser.

## REFERENCES


1. C.Angelie, R.Capitini, P.Girard: "Longitudinal mode selection by injection in a high pressure $CO_2$ laser." Applied Optics **Vol.** 26, No.6, 15 March 1987, pp. 1081-1088.

2. J-L. Lachambre, P.Lavigne, G.Otis, M.Noël: "Injection locking and mode selection in TEA -$CO_2$ laser oscillators." IEE Journal of Quantum electronics **Vol.** QE-12, No. 12, December 1976, pp. 756-764.

3. H.Tashiro, T.Shimada, K.Toyoda, S.Namba: "Studies on injection locking of a TEA-$CO_2$ laser for stable high power operation." IEE Journal of Quantum electronics **Vol.** QE-20, No. 2, February 1984, pp. 159-165.

4. K.Sasaki, H.Ohno, T.Tsukishima: "Theoretical model and numerical simulation of two-longitudinal-mode oscillation in an injection-locked TEA $CO_2$ laser." Japanese Journal of Applied Physics **Vol.** 29, No. 2, February, 1990, pp. 284-293.

5. O. Judd: " The interaction of pulsed optical radiation with an inverted medium" High Power Gas Lasers, Ed. E. R. Pike, Conference Series No. 20, The Institute of Physics, 1975, pp 45-57.

# Wide-aperture several THz bandwidth $CO_2$ laser amplifier with transverse pumping by the pulsed kJ power chemical HF laser

B.S.Alexandrov, A.V.Arsenjev, M.A.Azarov, V.A.Drozdov,

V.I.Mashendzhinov, V.E.Revich, G.A.Troshchinenko

Russian Scientific Centre "Applied Chemistry"

14, Dobrolubov ave., St.Petersburg, 197198, Russia

## ABSTRACT

For the grounding of the program of the wide-aperture several THz bandwidth $CO_2$ laser amplifier creation it was initiated the experimental investigation of a HF laser radiation transformation in a multiatmospheric $CO_2$/He medium. The $CO_2$/3He mixture (46×50×63 mm$^3$, 4 atm) was pumped by the 1P8 spectral line of the pulsed chemical HF laser (85 J, 1 μs). Transverse pumping geometry was used. Up to the power density of 2.7 MW/cm$^2$ an absorption saturation was not observed. At the deposited energy of 58 J and output coupling of 20% it was obtained $CO_2$ laser pulse of 2.7 J (quantum efficiency was about 18.6%). The estimated small-signal gain was of 0.05 cm$^{-1}$.

**Key words:** subnanosecond $CO_2$ laser amplifier, multiatmospheric laser medium, pulsed chemical HF laser.

## 1. INTRODUCTION

The project of the creation of a wide-aperture subnanosecond pulse $CO_2$ laser amplifier pumped by electric discharge [1] is known. In course of such project realisation there are certain difficulties connected to using of electronic or X-ray preionization and MV discharge voltage. It is proposed to use the optical kJ HF/DF laser pumping for creation of $CO_2$ laser amplifier medium with the amplification bandwidth of several THz and storage energy of several tens J. The idea to use a chemical HF/DF laser for pumping multiatmosphtric $CO_2$/He medium is offered and proved by results of small-scale experiments in the refined works [2,3]. Two ways of an optical excitation of $CO_2$ were investigated: the first is a direct pumping of the ($10^01$, $02^01$) levels $CO_2$ and, as consequence, creation of a population inversion for the $00^01$ and $10^00$ levels, and the second is a DF→ $CO_2$ transfer pumping by DF laser. There was a "bottle-neck" on the first way with the chosen spectral line (1P6) and longitudinal pump geometry. The main obstacles were the small absorption path for a pumping radiation in a lasing $CO_2$ medium due to high absorption coefficient (0.5 cm$^{-1}$ at 10 atm) for the pump transition and high saturation intensity, which was near to the damage threshold of the reflecting mirror coatings.

The goal of present work was to study a possibility of the optical pumping of a large volume multiatmospheric active medium with a gain bandwidth of 6 THz. The $CO_2$ output laser energy is considered as a measure of the efficiency of the amplifying $CO_2$ medium.

The transverse pumping and use of 1P8 spectral line with the less absorption coefficient have enabled to increase essentially the excited $CO_2$ laser volume. The use of spectral line (1P8) is more effective in comparison with the use of 1P6 line. The 1P8 single-line operated HF laser emitted about 30% of the multiline output energy. The 1P8 line has the less absorption coefficient in atmosphere than 1P6 line.

## 2. RESULTS OF EXPERIMENT

In the present work the transverse pump geometry of $CO_2$/He mixture was used as it is shown in the figure. The photoinitiated pulsed chemical chain HF laser [4,5] with a nominal output energy of 2 kJ per pulse operated both as single generator and in cascade "master generator – amplifier" and was used as a pump source. The main chemical reactor had a length of 5.5 m. The use of the cascade enabled to reduce the pulse duration two time. The 1P8 line was selected with use of a diffraction grating (300 lines/mm) which was set in the resonator cavity. A selected line output pulse was obtained with up to 350 J energy, about 1 μs FWHM, and 130 mm aperture. The $CO_2$ laser medium had a form of rounded box with maximal dimensions of 46×50×63 mm$^3$. The medium was illuminated through $CaF_2$ window (50×63 mm$^2$). The pumping radiation

Correspondence: Email: gtrosh@GT4631.spb.edu; Telephone: 812 238 9070; Fax: 812 238 9251

XIII International Symposium on Gas Flow and Chemical Lasers and High-Power Laser Conference,
Antonio Lapucci, Marco Ciofini, Editors, Proceedings of SPIE Vol. 4184 (2001)

was reflected from a copper mirror on the other side of the cavity for repeated pass through the medium. $CO_2$ laser was operated using a 45×50 $mm^2$ cross section resonator with inner copper and external dielectric (KCl) mirrors. The nominal parameters of the optical scheme are shown in the Figure.

The $CO_2$/3He mixture (4 atm) absorbed the pump radiation in accordance with Lambert-Beer's law (absorption coefficient was of 0.125 $cm^{-1}$). No absorption saturation was observed up to pumping intensity of 2.7 $MW/cm^2$. The deposited pumping energy was of 58 J at a 85 J, 1 μs FWHM pumping pulse. The larger part of pulse energy was lost due to absorption in atmospheric air (L=2.2 m). The $CO_2$ laser pulse energy $E_g$ was of 2.7 J, corresponding quantum efficiency was of 18.6% (in Ref. [2] - 14%), and the estimated small signal gain was of 0.05 $cm^{-1}$. The obtained value of the $CO_2$ laser pulse energy should be considered as a lower limit of the true output. The measured dependence of obtained output on coupling losses has shown an appreciable intracavity losses. The possible reasons for that may be the large divergence of $CO_2$ laser radiation and a deviation of the optical characteristics of the resonator elements from nominal values. The efficiency may be increased by using of a shorter but more powerful pumping pulse to decrease relaxation losses during the population inversion rise-time in $CO_2$ medium.

## CONCLUSIONS

The possibility of optical pumping of the great volume active medium was demonstrated. The $CO_2$ laser pulse energy of 2.7 J from the active medium volume of 140 $cm^3$ was measured. The physical efficiency was of 4.7%. The energy of HF laser was not used in full for the pumping of the $CO_2$ medium. The efficiency can be increased noticeably and the $CO_2$ laser pulse energy may be enlarged by one order of magnitude as a result of the modification of the experimental set-up.

## REFERENCES


1. V.A.Apollonov, K.Kh.Kazakov, N.V.Pletnyev, V.R.Sorochenko, "Wide aperture subnanosecond $CO_2$ laser system", in *XII International Symposium on Gas Flow and Chemical Lasers and High-Power Laser Conference*, Proc. SPIE Vol.3574, pp.140-148 (1998).
2. K.Stenersen, G.Wang, "Direct optical pumping of high-pressure $CO_2$ and $N_2O$ lasers with a pulsed HF pump laser", *IEEE J. Quantum Electron*, **QE-22**, pp.2236-2240, 1986.
3. K.Stenersen, G.Wang, "Continuously tunable optically pumped high-pressure DF→$CO_2$ transfer laser", *IEEE J. Quantum Electron*, **QE-19**, pp.1414-1426, 1983.
4. M.A.Azarov, B.S.Alexandrov, V.A.Drozdov, G.A.Troshchinenko, "Ways and conditions of achieving extreme characteristics of pulsed chemical DF and HF lasers", in *XI International Symposium on Gas Flow and Chemical Lasers and High-Power Laser Conference*, Proc. SPIE Vol.3092, pp.606-609 (1997).
5. B.S.Alexandrov, A.V.Arsenjev, M.A.Azarov, V.A.Drozdov, G.A.Troshchinenko, "Cascade scheme "master generator - amplifier" of the photoinitiated pulsed chain chemical HF/DF-laser", in *XIII International Symposium on Gas Flow and Chemical Lasers and High-Power Laser Conference*, this volume.


## EXPERIMENTAL SET-UP SCHEME

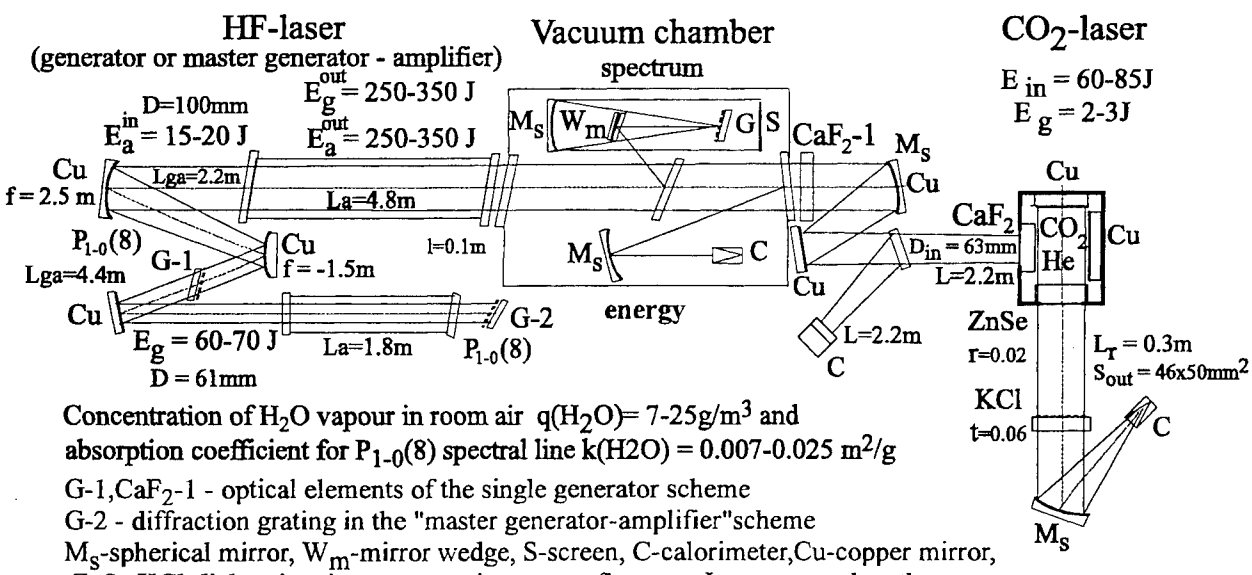


Concentration of $H_2O$ vapour in room air $q(H_2O)$= 7-25g/$m^3$ and absorption coefficient for $P_{1-0}(8)$ spectral line k(H2O) = 0.007-0.025 $m^2/g$

G-1,$CaF_2$-1 - optical elements of the single generator scheme

G-2 - diffraction grating in the "master generator-amplifier"scheme

$M_S$-spherical mirror, $W_m$-mirror wedge, S-screen, C-calorimeter,Cu-copper mirror, ZnSe,KCl-dielectric mirrors,t-tranmittance,r-reflectance,$L_r$-resonator length

# Superatmospheric X-ray preionized TE-$CO_2$ discharge unit

V.V.Apollonov, K.Kh. Kazakov, N.V.Pletnyev, V.R.Sorochenko

General Physics Institute of Russian Academy of Sciences,
38 Vavilova str., Moscow 117942, Russia

A.V.Astakhov, G.A.Baranov, A.A.Kuchinsky, V.P.Tomashevich

D.V.Efremov Scientific Research Institute of Electrophysical Apparatus, Laser Service Center
1 Sovetsky pr., Metallostroy, St.-Petersberg 189631, Russia

## ABSTRACT

$CO_2$ laser system generating the train of ~ 200 ps pulses with total energy up to 5 J was put in operation in General Physics Institute of Russian Academy of Sciences (IOFRAN) recently. Initial ~100 ps 10.6 μm laser pulse with energy ~ 10 μJ was regeneratively amplified in 5 x 5 x 5 $cm^3$ discharge volume X-ray preionized TE-$CO_2$ discharge unit developed and manufactured in D.V.Efremov Scientific Research Institute of Electrophysical Apparatus (NIIEFA) in cooperation with IOFRAN. The results on upgrade of this unit towards obtaining 10 atm volume self-sustained discharge in $CO_2$:$N_2$:He mixtures with reasonably high percentage of molecular gases are reported. Owing to this upgrade free running mode laser radiation energy $E_l$ (when the unit was equipped with unstable telescopic resonator) at 6 atm was increased up to 22.2 J, which corresponds to specific energy extraction 5.4 J/l/atm and efficiency 4.5%. The estimated value of $E_l$ from such a laser at 10 atm is 15 J. It corresponds to peak power of regeneratively amplified 2 ps 10 μm pulse formed in master oscillator of laser system ~ 1.5 TW. Prospective of further upgrade of laser system using new 10 x 10 x 100 $cm^3$ discharge volume 10 atm TE-$CO_2$ discharge unit which is under construction now in NIIEFA in the network of ISTC Project #1072 is discussed.

**Keywords:** picosecond pulse, $CO_2$-laser, high-pressure gas mixture, volume self-sustained discharge

## 1. INTRODUCTION

The creation of high-power 10 μm picosecond lasers opens new possibilities in fundamental investigations of laser radiation interaction with matter. One of potential and very efficient applications of high power ultrashort $\lambda$= 10 μm pulses is laser acceleration of charged particles. It was shown[1] that relative increase of electrons energy after interaction with laser field (averaged over electron bunch) is increased with laser radiation wavelength ~ $\lambda^2$. For the duration of laser pulse $10^{-11}$ s and its power $10^{12}$ W (laser pulse energy 10 J) the magnitude of accelerating gradient is ~ 1 GeV/m, that is substantially higher than for modern linear accelerators[2].

Another application is generation of high power and high repetition rate γ-beams by backward Compton scattering [3]. The γ-ray is planned to be applied to produce polarized positron beams for Japan Linear Collider (JLC). The temporal structure of e-beam of LINAC which is planned to be used in the experiments is a train of 85 bunches separated by period 1.4 ns. Train of the bunches comes every 6.7 ms corresponding to rep.rate 150 Hz. The estimated energy of the 10 μm laser pulse which will interact with every bunch in the train is 10 J (duration $\tau$= 10 ps). In this case about $10^{10}$ positron/bunch will be produced necessary for electron-positron experiments in JLC. In order to avoid nonlinear effects under high-intensity interaction it is proposed to divide each 10 J pulse into forty 250 mJ portions . In such a case forty 10 μm pulse trains each consisting of 85 pulses of 250 mJ energy (total train energy ≈21 J) are needed for the experiment.

Therefore for mentioned above experiments on interaction of laser radiation with e-beams an energy of 10 - 20 J in 10 ps 10 μm laser pulse or pulse train is needed. 10 ps duration of laser pulse in these experiments is connected with the duration of electrons bunch to be accelerated. At the same time the bandwidth of the high-pressure (~10atm) $CO_2$ discharge unit ($CO_2$ – HPDU) which is the principal element of picosecond $CO_2$ laser system enables to amplify the pulses with duration ~1 ps. In this case an order of magnitude higher power of laser radiation can be achieved in the given laser system.

XIII International Symposium on Gas Flow and Chemical Lasers and High-Power Laser Conference,
Antonio Lapucci, Marco Ciofini, Editors, Proceedings of SPIE Vol. 4184 (2001)

To our opinion besides mentioned above and many other fundamental applications high power picosecond 10 μm laser system can find some commercial applications. Between them is development of laser based lightning protection system, mid infrared laser lidars, laser plasma based source of X-ray with controlled temporal and spectral structure for use in microelectronics or medicine etc. Search and development of such an applications is the significant goal of ISTC Project.

At present time the methods of 10 μm picosecond laser pulses generation are well developed and enable production of pulses with $\tau = 1 - 10$ ps duration and 1 - 10 μJ energy [4-7]. In order to amplify these pulses up to energies ~ 10 J one have to utilize many-pass or regenerative amplification (RA) in $CO_2$ –HPDU with total gain exceeding $10^6$ - $10^7$ and gas pressure sufficient to provide necessary amplifier's gain bandwidth (≥ 10 atm for 9R or 10 R bands of $CO_2$ laser). The main factors determining maximum available energy of the amplified 10 μm laser pulse with duration 1 ÷10 ps are: aperture of the amplifier, saturation energy of typical high-pressure gas mixtures (~ 0.4 J/cm$^2$) , damage threshold of optical windows of the gas chamber (~ 0.7 J/cm$^2$)[8] and formation of electron density wave due to active medium avalanche ionization at very high intensities of radiation (~ 1 J/cm$^2$ )[7]. Simple estimates show that in order to exceed 1 TW peak power in maximum pulse of the train (containing in our case ≈15% of the total energy) it is necessary to use $CO_2$ –HPDU with aperture d ≥ 3 cm for $\tau$=1 ps and d ≥ 10 cm for $\tau$=10 ps.

The picosecond $CO_2$ laser system with output laser beam aperture 4 cm, discharge volume of $CO_2$ -HPDU 5 x 5 x 55 cm$^3$ (a prototype of further 10 x 10 x 100 cm$^3$ $CO_2$ -HPDU) and short pulse duration 2 ÷ 100 ps (tunable) is under construction now in IOFRAN. The system is intended to generate a pulse train with peak power up to 1.5 TW with present $CO_2$-HPDU and up to 15 TW with new one. Present status of the set up and the prospective of its upgrade are discussed in given report.

## 2. LASER SYSTEM CONFIGURATION

The main components of laser system are:
1. 10 μm picosecond master oscillator (MO), which produces a picosecond laser pulse with duration $\tau_i$ = 2 ÷ 100 ps (smoothly tunable) and power P = 0.1 - 1 MW by means of choppping a short transient from the 100 ns, 30 mJ radiation pulse of compact TEA-$CO_2$ laser ( method of chopping - semiconductor reflection/transmission switching[4-6]).
2. X-ray preionized $CO_2$ -HPDU developed and manufactured in NIIEFA under request of IOFRAN with 5 x 5 x 55 cm$^3$ discharge volume, 6 atm operational pressure and unstable telescopic resonator with aperture d= 4 cm, magnification M=2 and length L= 1.4 m to produce a train of picosecond laser pulses in RA regime.

The construction, principles of operation of MO as well as construction and parameters of $CO_2$-HPDU (for the case of 6 atm operation) were already reported[9]. The energy of laser radiation to the moment of publication[9] did not exceed 5 J and we were going to carry out the optimization of discharge pumping scheme in order to provide its better matching with the discharge. The results of this optimization will be discussed in the next section.

## 3. IMPROVEMENT OF $CO_2$-HPDU OPERATION.

### 3.1 Increase of preionization level.

In order to amplify 10 μm laser pulses as short as 2 ps it isnecessary to increase the pressure of the gas mixture in $CO_2$-HPDU up to 10 atm. To solve the problem we had to increase the concentration of initial electrons $n_{e0}$ produced in the active medium of $CO_2$-HPDU by X-ray preionizer. To realize it we made two independent steps. First, we decreased the distance between the source of X-ray photons (the foil) and discharge gap anode from 13 to 7 cm (taking into account high divergence of X-ray radiation). Second, we increased to the maximum the accelerating voltage $U_a$ on the e-beam vacuum diode (VD) (from 65 to 80 kV) since according to[10] in our case $n_{e0} \sim U_a^{4.2}$.

### 3.2 Optimization of $CO_2$-HPDU gas mixture for maximum radiation energy extraction.

After increasing of $n_{e0}$ due to mentioned above procedures we considerably increased the stability of volume self-sustained discharge (VSSD) at the previously used[9] $CO_2$:$N_2$:He= 2:1:17 gas mix with low ionizing additive (tri-n-propilamine) and got the possibility to use more "hard" gas mixtures that is the mixtures with higher absolute pressure $P_m$ of molecular gases ($CO_2$ and $N_2$). Attempts to increase absolute values of pressures of $CO_2$ and $N_2$ in the mixture $P_{CO2}$ and $P_{N2}$ while keeping constant $P_\Sigma = P_m + P_{He} = 6$ atm gave quite different results. In this experiments we controlled not only the volt-ampere parameters of VSSD but also a laser radiation energy in free running mode with the same resonator as in [9].

We did not succeeded to increase $P_{CO2}$ > 0.7 atm ( $P_{CO2}$ = 0.6 atm in initial $CO_2$:$N_2$:He=2:1:17 mix) with keeping high enough stability of VSSD. For $P_{CO2}$= 0.8 atm VSSD was very unstable, and practically we obtained very few "shots" without arcing after glow VSSD phase. There is an evident explanation of this - very high cross-section of electrons attachments to $CO_2$ molecules which probably even more severe for high pressure gas mixtures.

Absolute another picture took place for increase of $P_{N2}$. The stability of the VSSD was not changed when we increased $P_{N2}$ value in few times, but due to energy transfer from $N_2$ to $CO_2$ free running mode energy also increased and reached its maximum 22.2 J for the mixture $CO_2$:$N_2$:He= 12:21:67. Such energy corresponds to specific energy extraction 5.4 J/l/atm.. Scaling of radiation energy to full available for radiation area give us laser efficiency $\eta$= 4.5 % (relative to the energy ≈ 980 J stored in the capacitors of VSSD pumping generator, PG). Experiments with increasing of $P_{N2}$ value while keeping $P_{CO2}$ = 0.7 atm had shown that an optimum ratio of $N_2$ and $CO_2$ in the mix for maximum energy extraction is $P_{N2}/P_{CO2}$ = 1.7 ÷2.5. For higher $P_{N2}/P_{CO2}$ ratios some kind of $N_2 \rightarrow CO_2$ energy transfer saturation may take place.

It is interesting to note that using of mixtures with such relatively high ratio of $P_{N2}/P_{CO2}$ did not cause dramatic growth of the "tail" of laser radiation pulse typical for TEA-$CO_2$ lasers. The tail was totally absent for initial $CO_2$:$N_2$:He=2:1:17 mix while its energy did not exceed 30% of the total pulse energy for the mixtures with $P_{N2}/P_{CO2}$ = 2 ÷2.5 (see Fig.1). It is also seen from the figure that in the case $P_{N2}/P_{CO2}$ ≈ 2.4 the duration of pulse was shorter than for $P_{N2}/P_{CO2}$= 0.5 mixture (35 ns FWHM instead of 50 ns). It means that unlike the case of atmospheric pressure TEA-$CO_2$ -lasers for high pressure lasers nitrogen transfers the main part of stored energy to $CO_2$ during first gain switched spike of laser radiation. Dumping of "tail" can be also explained by the decrease of the gain lifetime in the active medium with gas mixture pressure as ~$1/P_\Sigma$. As a result in our case we increased more than in 4 times not only the energy but also a peak power of radiation. It is very promising result from the point of view of getting maximum peak power in the train necessary for generation of hard X-ray photons and high-amplitude currents in laser plasma[11,12].

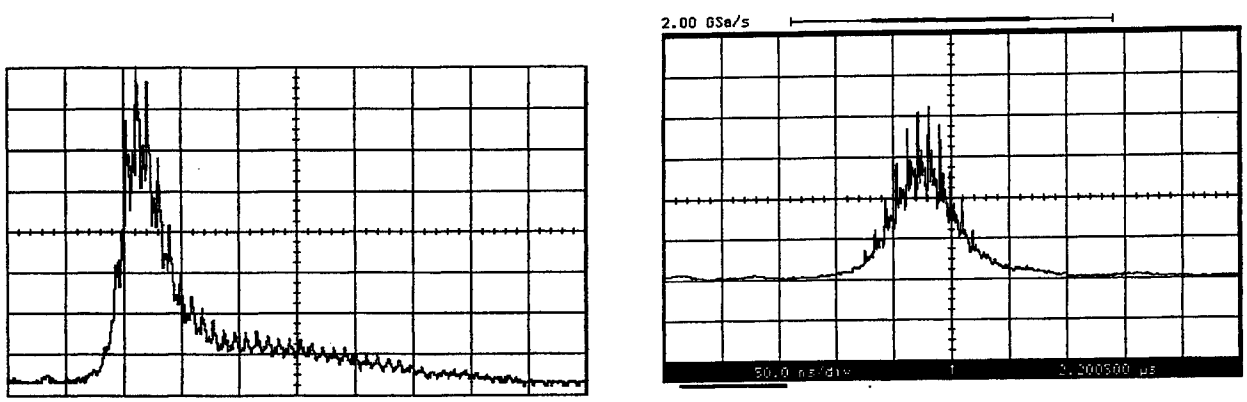


(a) (b)

Fig.1 Oscillograms of free-running mode radiation pulses for mixtures $CO_2$:$N_2$:He = 12:28:60 (a) and $CO_2$:$N_2$:He = 10:5:85 (b). Total mixture pressure 6 atm. Horizontal scale - 50 ns/div.

### 3.3 Optimization of VSSD pumping scheme parameters.

#### 3.3.1.The value of separating inductance.

During experiments on optimization of the gas mixture to get the maximum radiation energy we also varied the inductance $L_1$ which separated 8 -stage Fitch-Gowell generator and low inductance "fast" capacitance located maximally close to the discharge chamber(DC)[9]. Initially $L_1$ was 9.5 μH and energy 3.5 J on $CO_2$:$N_2$:He= 10:5:85 gas mix was obtained with this $L_1$ value. It turned out that increase of $L_1$ value lead to some increase of $E_l$ for fixed value of PG charging voltage $U_{ch}$. The oscilloscope traces of the voltage on the discharge gap $U_g(t)$ for $U_{ch}$ = 60 kV, two values of $L_1$ and the mixture $CO_2$:$N_2$:He= 10:10:80 are shown on Fig.2. It is seen from Fig.2 that increase of $L_1$ in 3 times did not influence the front of $U_g$ (t) as well as the breakdown voltage. Nevertheless, in the case $L_1$= 32μH this inductance in higher degree prevents the energy stored in the "fast" capacitance to go back into Fitch-Govell generator. It is illustrated in Fig.2 by the increase of both the duration of

quasistationary phase of $U_g(t)$ and total VSSD current duration (interval between the breakdown point and the point where $U_g(t)$ crosses zero line). As a result $E_l$ value increased from 5.5 to 9.5 J. The effect of $L_1$ increase on $E_l$ is stronger for lower values of $U_{ch}$. For more "hard" mixtures further increase of $L_1$ was shown to be efficient. Maximum $E_l$ value 22.2 J was obtained with $L_1$= 68 μH and $U_{ch}$ = 70 kV on the mixture $CO_2$:$N_2$:He= 12:21:67.

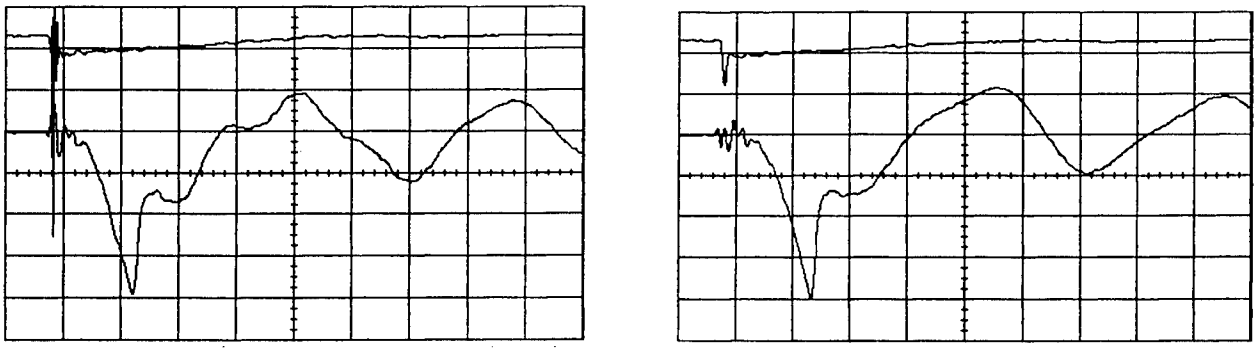

(a) (b)

Fig.2. Oscillograms of voltage on the discharge gap $U_g(t)$ (lower traces) for two values of "separating" inductance $L_1$: 9.5 μH (a) and 32 μH (b). Upper traces are voltage on the vacuum diode $U_{VD}(t)$. Horizontal scale - 1 μs/div.

### 3.3.2 The delay between X-ray preionization pulse and VSSD start.

Previously in[9] laser system operated with simultaneous triggering of the discharge gaps in PG and generator of pulsed voltages of VD. Such situation is illustrated on Fig.2. However when going to more "hard" mixtures it was established that VSSD stability increases when generator of pulsed voltages of VD was triggered with some delay to PG. This optimal delay value $\Delta t_{VD}$ (or the range of its variation) depended on the mixture and $U_{ch}$ value. For $L_1$ =68 μH the duration of $U_g(t)$ front was $T_{fr}$ = 2 ÷ 2.3 μs (depending on mentioned above parameters) and $\Delta t_{VD}$ was 0.6 ÷ 1.4 μs. The width of the $\Delta t_{VD}$ range decreased almost to zero when we tried to obtain VSSD at the mixtures with $P_{CO2}$= 0.8 atm.

While varying $\Delta t_{VD}$ value we had revealed very interesting fact: when $T_{fr}$ - $\Delta t_{VD}$ was less than some minimum value (it depended on $L_1$ and gas mixture, for example 300 ns for $L_1$ = 32 μH and $CO_2$:$N_2$:He= 10:10:80 mix) there were no glow VSSD phase at all (arcing took place just after gas breakdown). This fact corresponds to earlier obtained results on utilization of low-ionization additions in TEA-$CO_2$ lasers and is connected with significantly higher lifetime of initial photoplasma produced by ionization of organic additives than that produced by ionization of working mix components[13]. Therefore in our case due to the fact that photoplasma recombination rate is much lower that the rate of electrons production by X-ray ionization of tri-n-propylamine we have some kind of accumulation of electrons produced by ionization source.

It is well known that besides production of initial electrons in the discharge gap tri-n-propylamine stabilizes VSSD through depopulation of metastable levels of $N_2$ responsible for formation of VSSD contraction channels. Another and also very significant roles are: ionization of $N_2$ molecules via collisions with tri-n-propylamine molecules through Penning ionization process and decrease of $E/P_\Sigma$ parameter in VSSD causing optimization of electrons energies distribution function for more efficient pumping of laser levels[14]. It is Penning ionization that can explain the fact that at transition from $P_{N2}/P_{CO2}$ = 0.5 to $P_{N2}/P_{CO2}$ = 3.6 mixture (the most "hard" mixture in the experiments with $P_{N2}$ = 2.55 atm and $P_m/P_\Sigma$ = 54%) the breakdown voltage of the gas mixture increased only twice.

## 4. PROSPECTIVE OF PICOSECOND $CO_2$ LASER SYSTEM UPGRADE.

As a first step to 10 atm $CO_2$-HPDU operation we tried to obtain stable VSSD at $P_\Sigma$ >6 atm. The measurements were carried out in a condensed version at fixed values of some parameters: 1) energy stored in the PG = 720 J; 2) $P_{CO2}$ = 0.5 atm; $P_{N2}$ = 1.0 atm. As a result we succeeded to obtain VSSD at the mixtures with $P_\Sigma$ up to 9 atm. At $P_\Sigma$ =9 atm $P_m/P_\Sigma$ was 16.7% and W= 57 J/l/atm. In such version of experiment where $W \sim 1/P_\Sigma$ we did not detected any deterioration of VSSD with growth of $P_\Sigma$. We did not try to increase $P_\Sigma$ over 9 atm due to:1) sharp growth of the rate of gas mixture outlet from DC; 2) the fact that earlier at hydraulic tests of DC we observed few times the damage of Al foil at P = 11 – 12 atm.

At present time the new dielectric tube for DC of $CO_2$-HPDU is manufacturing which will have hermetic enclosure for $P_\Sigma \leq 15$ atm. After new tube manufacturing and reassembling of DC we plan to carry out investigations of possibility to increase the thickness of Al foil used up to 100 – 250 μm in order to make the VSSD investigations at $P_\Sigma \sim 10$ atm more safe.

In conclusion we look with optimism on getting 10 atm VSSD in our $CO_2$-HPDU but the concrete gas mixture will be determined only in experiments. In such a mixture we'll be able to regeneratively amplify laser pulses with wavelength corresponding to the top of $CO_2$ molecule 10R band (10.27 μm) and duration down to $\tau \approx 2$ ps. We will not be able to use 9R band of $CO_2$ laser due to substantial absorption of ≈ 9.3 μm radiation by the tri-n-propylamine.

Let's estimate the expected peak power of the train of 2 ps pulses which we are going to obtain. The temporal structure of free-running mode radiation pulse shown at Fig.1a may be differed by adding 4 atm of He to present gas mixture due to probable dumping of the pulse "tail" at further decrease of small signal gain lifetime with $P_\Sigma$. Therefore the expected radiation energy may be about 0.7 x 22 J ≈ 15 J. Our investigations of the temporal structure of the pulse train for $\tau = 200 \div 300$ ps [9] had shown that its envelope well correspond to free-running mode pulse. We can propose that for $\tau = 2$ ps this envelope will not be strongly changed since in both cases $\tau = 200$ and $\tau = 2$ ps the saturation energy densities of the gain medium are close to each other. It means that percentage of energy in the train's maximum pulse will be determined only by duration $T_{gen}$ of free-running mode pulse (FWHM) and $\Delta T = 2L/c$ parameter. For our case $T_{gen} \approx 35$ ns and $\Delta T = 9.3$ ns this percentage may reach 20%. Therefore the expected energy of the maximum train's pulse may be $E_m \approx 3$ J corresponding to train's peak power $P_m \approx 1.5$ TW.

Further increase of $E_m$ and $P_m$ values ( approximately on an order of magnitude) may become possible after manufacturing and putting into operation the new 10 x 10 x 100 $cm^3$ discharge volume $CO_2$-HPDU which is under construction now in NIIEFA in the network of ISTC Project #1072 (its putting into operation at IOFRAN test bench is planned at the end of 2001). The detailed discussion of the construction of this $CO_2$-HPDU exceeds the bounds of present report. Briefly, the main features and differences of the new unit relative to present one (except the discharge volume) are:

1. stainless steel body of the DC;
2. low inductance "fast" capacitance in the scheme of PG is an element of DC construction filled with deionized water: such an approach enables to realize minimum possible inductance of the discharge circuit (~ 200 nH) for given discharge volume and to provide the duration of energy input into discharge ~ 200 ns what is quite close to this parameter value of present $CO_2$-HPDU despite ~ 8 times higher discharge volume of the new unit;
3. the constructive features of the X-ray preionizer enable to realize two modes of its operation:
   - traditional one now used in the present $CO_2$-HPDU with $U_a = 70 \div 80$ kV, duration of current pulse of a few μs and utilization of 50 ÷ 100 μm thick Al foil;
   - nontraditional mode with $U_a = 40$ kV, duration of current pulse ~ 100 ns and utilization of thin (6÷10μm) foils from materials with high atomic weight, such as Ta, Au etc.

The main idea of the second variant is to use more soft part of the spectrum of X-ray (which is much more efficient for ionization of work gas mix) and to increase to the maximum the current of VD and correspondingly the X-ray flux. This variant may turn out to be more efficient when using gas mixtures without low ionizing organic additives where the mechanism of initial electrons accumulation discussed above will not work.

It will be very interesting to compare the volt-ampere and optical parameters of both $CO_2$ –HPDU in order to make a conclusions about possibility to scale $CO_2$-HPDU parameters with active volume (one of the goals of ISTC #1072 Project).

## 5. CONCLUSIONS.

1. Due to substantial increase of X -ray flux in the discharge volume of $CO_2$-HPDU we succeeded to dramatically increase percentage of molecular gases in 6 atm mixture (from 15 up to 54%) and free running mode radiation energy (from 5 to 22.2 J). The specific energy extraction reached 5.4 J/l/atm and laser efficiency (relative to the energy stored in the capacitors) reached 4.5%.

2. The optimal range of $N_2$ and $CO_2$ partial pressures ratio $P_{N2}/P_{CO2} = 1.7 - 2.5$ was determined which correspond to maximum extraction of radiation energy from $CO_2$ -HPDU when operating with unstable telescopic resonator.

3. The value of inductance separating Fitch-Gowell generator and "fast" capacitance located close to the DC can be optimized for maximum loading of energy to the discharge volume for given gas mixture and PG charging voltage.

4. Due to substantial more fast $N_2 \rightarrow CO_2$ energy transfer for $P_\Sigma = 6$ atm $CO_2$ -HPDU relative to TEA-$CO_2$ lasers increase of $P_{N2}/P_{CO2}$ in the 6 atm mixture from 0.5 to 2.5 did not cause dramatic growth of the "tail" of laser pulse. It means that peak

power of laser radiation in our case increased with $P_{N2}/P_{CO2}$. Moreover relative increase of peak power was close to that of laser radiation energy due to some shortening of laser pulse FWHM.

5. It was revealed that effect of accumulation of initial electrons produced by X-ray preionizer can take place. This effect is more pronounced at the mixtures with high relative concentration of molecular gases. Such accumulation can be associated with the features of photoplasma produced by X-ray ionization of tri-n-propylamine.

6. We have a real prospective to obtain VSSD in our present $CO_2$-HPDU configuration on 10 atm gas mixture with reasonably high $P_m/P_\Sigma$ value. The expected peak power of the train of 2 ps pulses obtained in RA regime in $CO_2$-HPDU with such a mixture is 1.5 TW. As a first step to realization of such a prospective a stable VSSD was obtained at 9 atm 16.7% molecular gases concentration gas mixture and a relatively low specific energy loading density 57 J/l/atm.

7. About an order of magnitude increase of 10 μm 2 ps laser pulse peak power (up to 15 TW) may become possible after putting into operation a new unique 10 l active volume 10 atm $CO_2$-HPDU now being under construction in the network of ISTC Project #1072.

## ACKNOWLEDGMENTS

The work was carried out in the network of ISTC Project #1072. The authors are grateful to Mr. J.-C. De Miscault, deputy director of CILAS, France and collaborator of ISTC Project for his constant interest in research.

## REFERENCES

1. V.V.Apollonov, A.I.Artemyev, Yu.L.Kalachev, A.G.Suzdaltsev, A.M.Prokhorov, M.V.Fedorov, "Electrons acceleration by intence laser radiation field in the presence of static magnetic filed",*JETF (in Russian),* **97**, No 5, p.1498-1510,1990.
2. J.Arnesson and F.K.Kneubuhl , "Future laser-driven particle accelerators",*Infrared Physics*, **25**, pp.121-130, 1985.
3. A. Tsumeni, A. Endo, M. Washio, T. Hirose, Y. Kurihara, T. Omori and J. Urakawa,"Picosecond $CO_2$ laser driven polarized positron source for Japan Linear Collider", *Proceedings of Int.Conf. on "Lasers'97"*, New Orleans, LA, December 1997, McLean, VA, 1998, pp. 839-844.
4. S.A.Jamison and A.V.Nurmikko ,"Generation of picosecond pulses of variable duration at 10.6 μm",*Applied Physics Letters*, **33(7)**, pp.589-600,1978.
5. P.B.Corkum ,"High-power, subpicosecond 10 μm pulse generation " *Optics Letters*, **8**, pp.514 -516,1983.
6. P.B.Corkum ,"Amplification of 10μm pulses in multiatmosphere $CO_2$ lasers", *IEEE,J.Quant.Electr.*,**QE-21**,pp.216 - 232,1985.
7. Z.A.Biglov, V.M.Gordienko, V.T.Platonenko, V.A.Slobodyanyuk, V.D.Taranukhin and S.Yu.Ten, "Generation and amplification of phazemodulated picosecond pulses of 10 μm range",*Izvestiya AN USSR, Seriya Fizicheskaya,* (in Russian), **55**, pp.337-341,1991.
8. P.B.Corkum and C.Roland ,"High Energy Picosecond 10 μm Pulses",*Proceedings of SPIE,* **664**,pp.212-2 16, 1986.
9. V.V.Apollonov, K.Kh.Kazakov, N.V.Pletnyev, V.R.Sorochenko, G.A.Baranov, A.A.Kuchinsky, V.P.Tomashevich "Wide aperture subnanosecond $CO_2$ laser system", *Proceedings of XII Int. Symp.on Gas Flow and Chemical Lasers*, St.-Petersberg,31 August-5 Sept 1998, SPIE v. **3574**, pp.140-148.
10. M.A.Vasilevsky, V.A.Rodichkin, I.M.Roife, E.G.Yankin " Creation of X-ray flux with utilization of large size explosive emission cathode" , *Sov.Journal of Technical Physics*, **55**, pp. 1118- 1122, 1985.
11. V.V.Apollonov, K.Kh.Kazakov, N.V.Pletnev and V.R.Sorochenko, " $CO_2$ laser system generating a train of subnanosecond pulses", *Proceedings of Int.Conf. on "Lasers'97"*, New Orleans, LA, December 1997, McLean, VA, 1998, pp.736-741.
12. V.V.Apollonov, K.Kh.Kazakov, N.V.Pletnev and V.R.Sorochenko, " Currents measurements in plasma produced by the train of 10.6 μm subnanosecond laser pulses", *Proceedings of AHPLA'99 HPL02 Conference "High-Power Lasers in Energy Engineering"*, Osaka, Japan, 1-5 Nobember 1999, SPIE v.**3886**, pp.198-206.
13. V.M.Borisov, G.G.Gladush, Yu.Yu.Stepanov, "Photoionization in pulsed $CO_2$ laser", *Kvantovaya Elektronika*,**4**, No 4,p.809,1977.
14. V.V.Apollonov, G.G.Baitsur, A.V.Ermachenko, K.N.Firsov, I.G.Kononov, O.B.Kovalchuk, V.V.Kralin, V.R.Minenkov, A.M.Prokhorov, S.K.Semenov, B.G.Shubin and V.A.Yamschikov,"High-power $CO_2$ and $N_2O$ lasers with volume self-sustained discharge pumping",*J.Opt.Soc.Am.B*, **8**, No.2,p.220,1991.

Invited Paper

# Excimer Laser as a Total Light Source Solution for DUV Microlithography

Palash Das

Cymer, Inc., 16750 Via Del Campo Ct., San Diego, CA 92127

## ABSTRACT

Excimer lasers are now being used in the manufacturing of ultra-large scale integrated devices that require feature widths of less than 0.25μm. The excimer laser for microlithography, since its introduction in 1987 has evolved from a laboratory instrument to a manufacturing tool. We will trace the history of the excimer laser in this industry and explain why it is and remains the total solution for the present and for many years in the future.

**Keywords**: Excimer laser, Deep Ultraviolet Microlithography, KrF, ArF, $F_2$, Hg lamp

## 1. INTRODUCTION

By 1996, the transition from an I-line (365nm) mercury lamp to deep-UV excimer laser – KrF (248nm) – as the illumination source for fabrication of ULSI had begun in earnest. The rapid transition is considered evolutionary and revolutionary. Evolutionary because the change in technology in the eyes of the IC maker was a mere reduction in UV wavelength. Revolutionary because of the complexity and the pulsed operation of the laser compared with the simple and continuous Hg lamp. However, we show that excimer lasers are optimally suited to meet the requirements for Deep-Ultraviolet microlithography as compared to Hg lamps at 248nm or solid state lasers at deep-ultraviolet wavelengths. The physics of excimer laser allows scaling to higher powers, narrower spectral widths and shorter wavelengths. The engineering of excimer lasers has kept pace with microlithography scanner requirements. New excimer products have maintained the performance trends set-up by the previous generation excimer products. In laboratory experiments, solid state lasers have shown promise. However, the scaling of a solid state to higher powers is still several years away, and has missed the opportunity to play a role in this very important semiconductor industry.

## 2. MICROLITHOGRAPHY – THE PROCESS

### 2.1 What is microlithography

Microlithography is a manufacturing process for highly precise microscopic 2-D patterns in a photosensitive resist material. These patterns are replicas of a master pattern on a mask, which is made from patterned layer of chromium on fused silica. At the end of the lithographic process, the resist is used to create a useful structure in the device that is being built such as trenches on silicon wafer (Fig. 1) or metal network on silicon. These structures then form the foundation for memory and processor chips that go into computers, cellular phones, PDAs, cars and about everything else. Microlithography is the technology and cost driver for semiconductor manufacturing.

### 2.2 Microlithography and microelectronics explosion

Progress is microlithography is evident due to continuous decrease in image sizes (Figures 1 and 2). A decrease in image size by X2 leads to a X4 increase in number of circuits per unit area, and significant improvements in switching speeds. Thus, a decrease in transistor size, and increase in chip size has resulted in rapid growth of number of transistors per chip. About half of the 4X increase per generation in DRAM capacity is due to reduced image size. The rest is from advances in design and increase in physical

XIII International Symposium on Gas Flow and Chemical Lasers and High-Power Laser Conference,
Antonio Lapucci, Marco Ciofini, Editors, Proceedings of SPIE Vol. 4184 (2001)

dimensions. Historically, it has taken about three years to advance from one generation of DRAM to the next. However, leading-edge microlithography started at 0.35mm in 1995.

### 2.3 The path to narrower images

Image Dimension is governed by Rayleigh's formula:

$$D = k1*\lambda/NA, \quad (1)$$

Where
D = Minimum Dimension printed on wafer, k1 = process constant, between 0.6 to 0.8,
$\lambda$ = Exposure Wavelength and NA = Numerical Aperture Of Lens (Fig. 3)

Thus, increasing NA may minimize the image dimension. But, the Depth of Focus (DOF) is related to NA via:

$$DOF = \pm k2*\lambda/NA^2, \quad (2)$$

Where:
k2 = process constant, ~ 0.5.
Despite DOF issues, increasing NA from 0.5 to 0.7 in the past few years (Fig. 4) has reduced image dimensions. By far, though, the greatest reduction in image size is achieved by reducing the wavelength. This is exactly where excimer lasers fit in!

## 3. MICROLITHOGRAPHY – THE ROLE OF LASERS

### 3.1 Excimer lasers and solid state lasers

Traditional light source for lithography has been Hg-Xe Arc Lamps. Its i line and g line are used for lithography below 256MB DRAM. Its emission centered on 248nm has also been used, but power is very low. On the other hand, excimer lasers, KrF at 248nm and ArF at 193 nm and F2 lasers at 157nm are sources of high power radiation. They have relatively narrow spectrum - thus optical filtering is not required. They provide tunable high power output at DUV, without wavelength conversion. They may be directly, efficiently spectral narrowed without external "injection" lasers. **Most importantly**, excimer lasers would act as sources for three generations of DRAM, at 248, 193 and then 157nm. They can be scaled in power and spectrally narrowed for the future microlithography. Excimer lasers are expected to meet the lithography requirements for 16Gbit DRAM and 10GHz microprocessors in the next ten years!

Solid State Lasers are other possible sources. Some examples are Alexandrite at 248 nm, and diode pumped lasers at 248 and 193 nm. But, considering the early lead by excimer lasers, it is **just too late** for solid state lasers!

### 3.2 Lasers and the microlithography process

The wafer exposure process involves the following systems: Laser, relay optics, homogenizer, illumination systems, lithography projection lens and wafer positioning system (Fig. 5). In terms of complexity, the lens is the most complex, the laser is the second most and the positioning system is the third.

The lithography projection lens is a large compound lens made up of over 20 simple elements mounted in a rigid barrel. The large number of elements corrects optical aberrations over a 30mm exposure field. The wavefront aberration must be less than $\lambda/10$ at every point in the exposure field. This lens produces the optical image of the mask, reduced by a factor of 4 or 5. A silicon wafer is exposed to this image, which is captured by the layer of photoresists. This image is eventually developed to leave the resist pattern on silicon. The lens at 248nm is not chromatically corrected. Hence, the narrow spectral width requirements. Thus for a lens of NA=0.7, the Full-Width-At-Half maximum requirement is about 0.6pm. At 193nm, there is some color correction otherwise the linewidths requirements are very low. The situation at 157nm is still

open. At 248nm, the lens material is fused silica, at 193nm is mostly fused silica and CaF2 and at 157nm it will be very likely CaF2.

The wafer positioning system is probably the most precise mechanical system in existence. It positions the wafer (200mm in diameter) under the lens by stepping or scanning to a precision of better than 20nm. The motion of the wafer positioning system coupled with the exposure technique determines two classes of microlithography systems - stepper and scanner.

Stepper exposes one chip at a time. The number of pulses the laser fires on each chip is equal to the total energy required to expose the resist. After each chip, the wafer positioning system moves the wafer to next. The field size depends on the lithography lens diameter. A scanner exposes the chip by painting a slit over the wafer. This is done by scanning the mask and the wafer through the slit. The field size is then limited by slit height and scan length. Since the slit is much smaller than the field size, the optical constraints on the litho lens are greatly reduced. Thus, all lithography equipment manufacturers have now switched to the design & development of scanner technology.

### 3.3 Impact of scanner based microlithography on laser performance

The scanner fundamental formula is given by:

$$\text{Time to expose the scanner slit} = s/V\text{scan}, \qquad (1)$$

where s is the slit width (typically 7 to 8mm wide) and Vscan is the scan speed of the scanner (100 to 250mm/sec). The time each point is within the slit should be at least equal to the time required to fire N pulses to expose the resist. Thus, if the resist requires Dr mJ/cm$^2$, and the laser provides $D_L$mJ/cm$^2$ per pulse, the number of pulses required to expose the resist is $Dr/D_L$. Thus, for a laser with repetition rate of f, the time to expose $Dr/D_L$ pulses is just $Dr/ D_L /f$. The goal of every litho equipment maker is to minimize exposure time. Thus, the laser **repetition-rate** must be maximized. The lithography process requires that the whole chip must be exposed uniformly. This means the energy of the laser, integrated over the exposure time must be constant. This forms the basis of **dose stability** requirement of the laser!

Excimer lasers today (20W KrF, 10W ArF) has kept up with scanner power requirements (Fig. 6). The "physics" allows scaling to higher powers without scaling laser physical size. In fact, the laser chambers used in CX2 product and ELS-6000 product have similar physical dimensions.

The "homogeneously" broadened KrF and ArF laser lines can be narrowed to 0.5pm FWHM at 248 and 193 nm without much loss in efficiency (Fig. 7). The line narrowing module used in first generation product and next generation product have similar physical dimensions.

Power stability of excimer laser is measured by the stability of the dose (integrated energy). Scaling the power of excimer laser without maintaining its stability will not help lithography. Power stability can be maintained by a combination of gas flow, pulsed power and software control technology.

The cost-of-operating a laser depends heavily on chamber life (~40% is due to chamber). The pulse life of a chamber has steadily improved, resulting in a huge decrease in cost-of-operation of the laser. While the cost-of-operation may not be as low as a Hg lamp, the reduction in past several years has been encouraging at 248nm. Similar improvements are required at 193nm.

A mix-and-match strategy will be followed by the chipmakers in integrating laser-based tools for lithography. For 256Mbit DRAM, approximately 70% of the layers would be exposed via Hg iline and the remaining via KrF. For 4Gbit DRAM, approximately 40% layers would use iline, 40% KrF and 20% ArF. Such mix-and-match strategy would keep iline technology alive. Likewise, this mix-and-match would keep excimer lasers arrive when microlithography reverts to EUV and E-beams.

## 4. MICROLITHOGRAPHY – FUTURE OF EXCIMER LASERS

The physics of excimer laser allows scaling to higher powers, narrower spectral widths and shorter wavelengths. Excimer lasers would provide a three-generation solution to microlithography. The engineering of excimer lasers has kept pace with stepper/scanner requirements of cost-of-operation, uptime and reliability. New excimer products have maintained the performance trends set-up by the previous generation excimer products. The economics has driven and will continue to drive the direction of microlithography. Excimer lasers have kept pace with that. This explains why a small excimer laser company in San Diego has experienced such rapid growth.


## ACKNOWLEDGEMENTS

The author thanks Oliver Sempreze for numerous discussions on this subject.


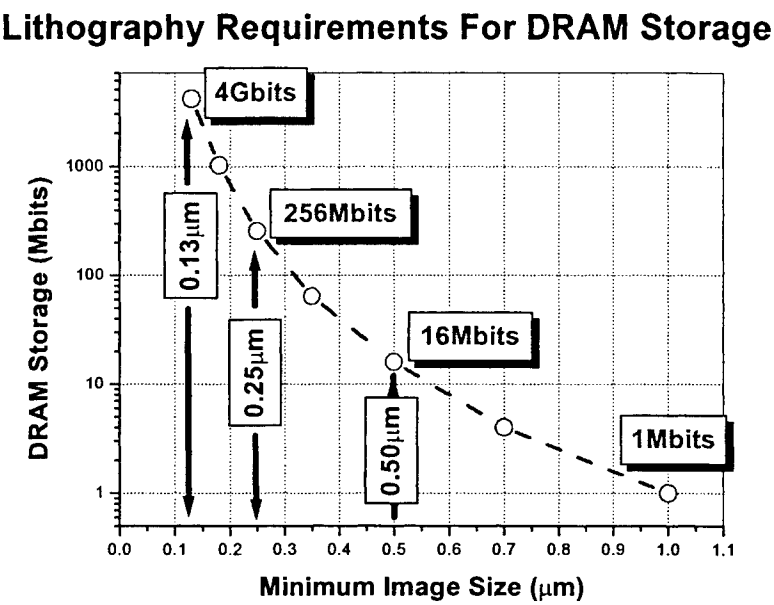


Figure 1. The increased DRAM capacity is associated with decreased image size

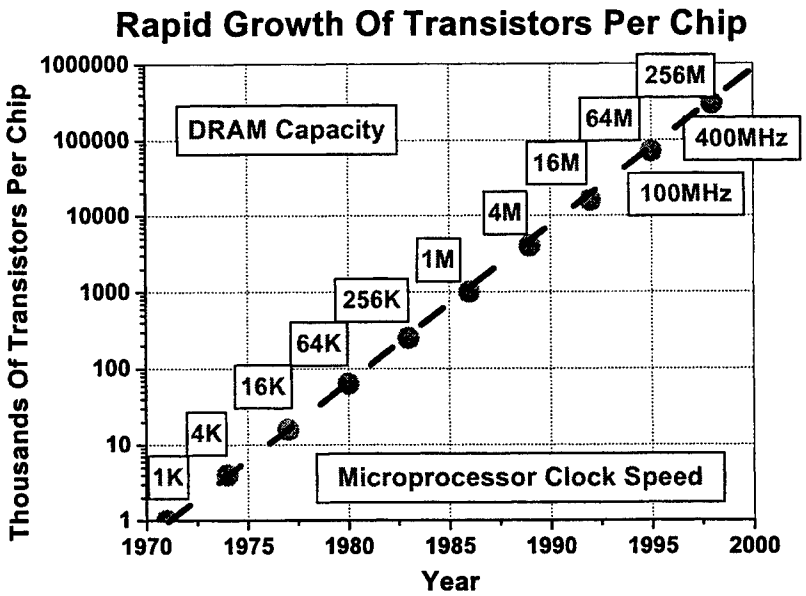


Figure 2. The relative increase in number of transistors per DRAM keeps pace with the increase in DRAM capacity.

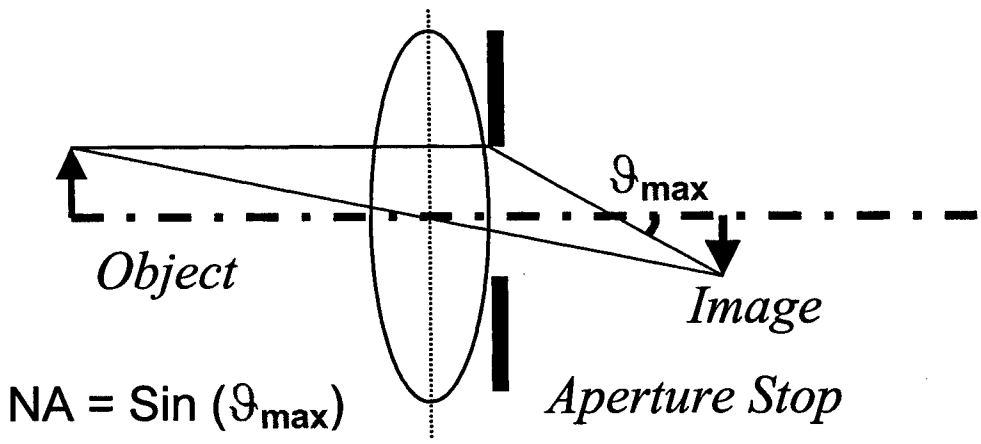


Figure 3. The properties that determine lens NA.

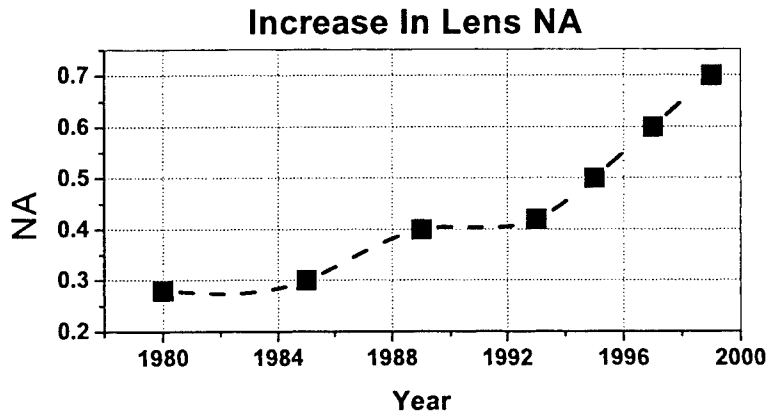


Figure 4. Lens NA has more than doubled in the past 20 years.

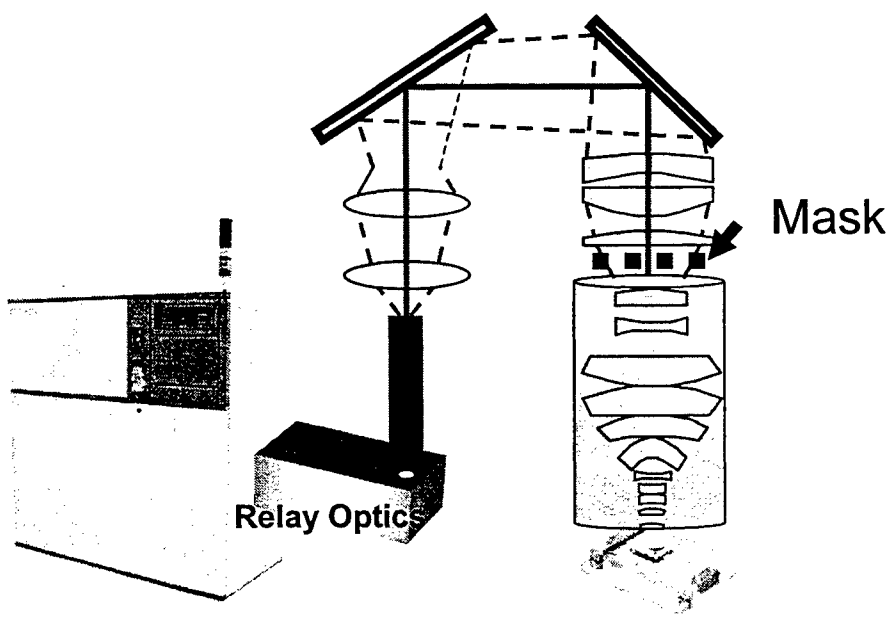


Figure 5. A laser based microlithography exposure system.

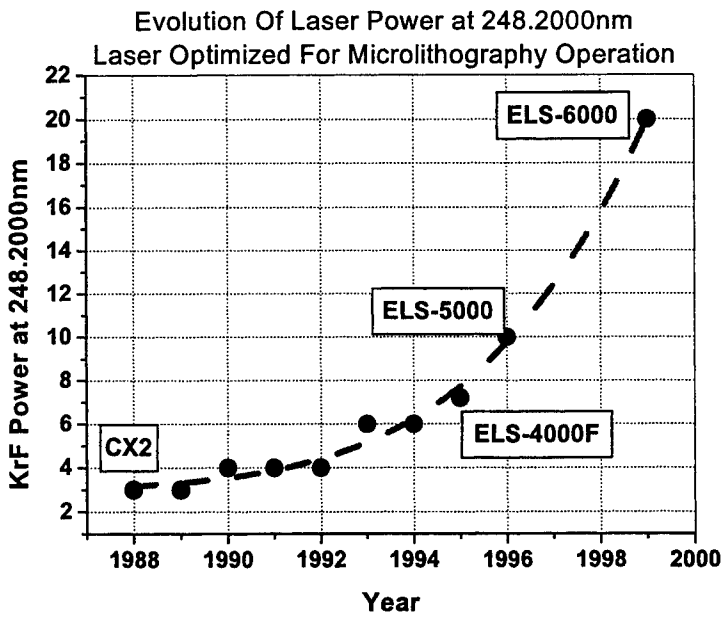


Figure 6. The evolution of laser power during the past ten years has kept up with scanner requirements.

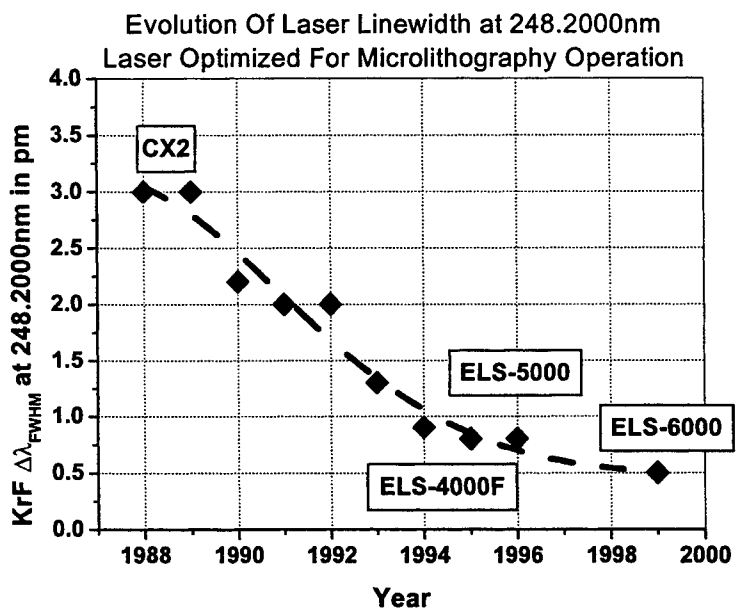


Figure 7. The decrease in linewidth in the past ten years has kept up with the lens requirements.

# High repetition rate 157 nm Mini - Excimer - Lasers

Andreas Görtler*, Claus Strowitzki, Stephan Geiger

TuiLaser AG, Lochhamer Schlag 19, 82166 Graefelfing, Germany

## ABSTRACT

For new industrial applications, mini excimer lasers with a wavelength of 157 nm were developed. The main goal was to extend the component lifetime. The laser tube is designed in metal-ceramic technology. An erosion-free corona preionization is installed. The pulsed-power module contains a solid state switch with additional compression stages to generate the high current rise at the electrodes of the laser tube. All of the modules in the laser system are designed for long lifetime. At 157 nm the mini excimer laser reaches a maximum single-pulse energy of 2 mJ up to a repetition rate of 1000 Hz. An overview of the results of long-term testing of these state–of–the–art mini excimer lasers at 157 nm will be given.

**Keywords:** 157 nm, $F_2$-laser, excimer laser, VUV, mini excimer laser

## 1. INTRODUCTION

Mini excimer lasers were developed in the recent years mainly for medical applications, especially in the field of ophthalmology. These mini lasers systems are used in a wide range of industrial applications at the normally used excimer wavelengths [1]. For some special applications in the telecommunication and semiconductor industry, besides the large excimer laser systems with several hundreds of mJ output energy, the mini systems with a maximum of 20 mJ [2] at 248 nm are advantageous. All components of the laser systems are developed for long lifetime. Therefore a solid state circuit replaces the formerly installed thyratron switch in the laser. Repetition rates up to 1000 Hz are now possible. New applications in material processing, especially in ceramics and optical materials, require a wavelength in the deep UV. Due to this trend to shorter wavelength a mini excimer laser system for 157 nm was developed. To achieve a commercially usable fluorine laser system some specific efforts had to be made. The fluorine laser is very sensitive to impurities in the gas. Therefore, all materials in the tube and all parts witch are in contact with the gas must be made of high-purity materials. The tube design itself must be specifically adapted for the fluorine laser system.

## 2. EXPERIMENTAL SETUP

For the fluorine laser some changes in the design of the standard laser tube were done. The electrode distance is reduced to 3 mm in order to use the standard pulsed-power module of the ExciStar S series. A thyristor is used as switching element in the pulsed-power module. Additional compression stages with magnetic switches generate the necessary high dI/dt at the laser electrodes. All components of the pulsed-power module are installed in insulating oil. The laser tube in general, and in particular the laser gas in the tube and the oil of the pulsed power module are cooled by water. The tube and the pulsed-power module is installed in the housing of an ExciStar S-1000. The maximum possible repetition rate is limited by the power supply and the cooling rate of the pulsed-power module. The laser tube itself is adapted for work at 157 nm. The gas circulation was optimized. The electrodes were also specially developed for the fluorine laser. $MgF_2$ windows with high reflective and partly reflective coatings are installed in the laser tube as an internal resonator. The emitted light at 157 nm is almost completely absorbed in air. Therefore the laser beam can be only delivered in a purged ( nitrogen or a rare gas) or in an evacuated beam path. Therefore the beam path can be connected to the optic by a standard Klein Flange (KF) vacuum

* Correspondence: Email: ag@tuilaser.com; WWW: http://www.tuilaser.com; Telephone: ++49 89 898169 14;

Fax: ++49 89 854 56 10



XIII International Symposium on Gas Flow and Chemical Lasers and High-Power Laser Conference,
Antonio Lapucci, Marco Ciofini, Editors, Proceedings of SPIE Vol. 4184 (2001)

sealing with 25 mm inner diameter. As power meter a thermoelectric sensor from Molectron (type PM10-19-C) with an adapter for the vacuum sealing of the purged beam path was used. In addition a pyroelectric sensor from Molectron (type J25HR9) was installed as energy meter with an adapter as well. The beam profiles and the divergence were measured with a Merchantek beam profiler system (type Vision 1024) adapted for the deep UV-radiation by an integrated fluorescence screen.

## 3. MEASUREMENTS

Long-term tests were done with the mini excimer laser system. During these test the output power of the laser is permanently monitored. Normally, after each change of optics the energy stability, beam profiles and pulse duration were measured. These intervals are determined by the optic lifetime of typically 100 million pulses. All power and energy measurements were done with argon as purge gas. The red emission of fluorine in the visible is about 4 % of the output energy in the deep UV. This additional power is corrected in all measured data. Figure 1 shows the dynamic gas lifetime obtained at the maximum applied voltage and the maximum repetition rate of 1000 Hz. After more than 6 million pulses half of the starting laser output power is reached.

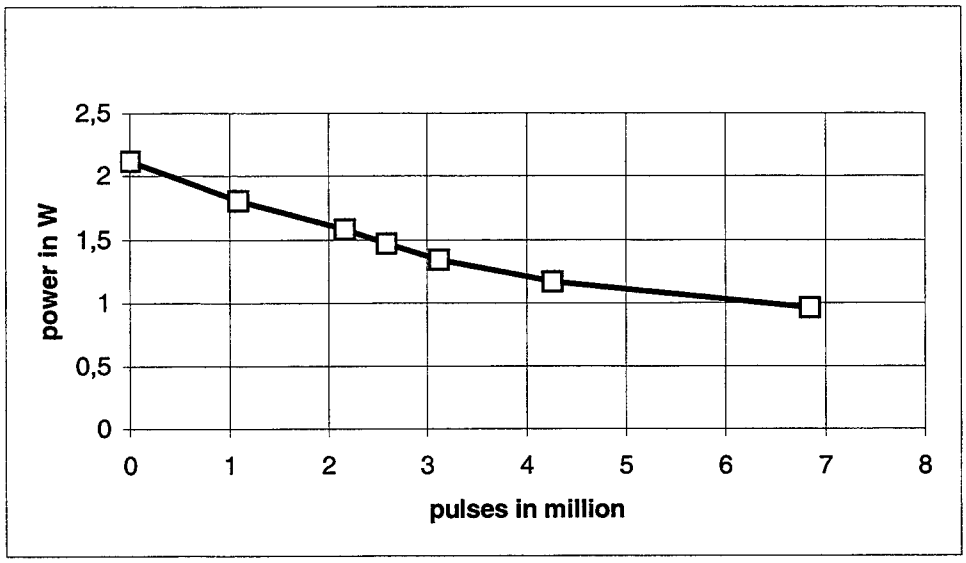


Figure 1: Dynamic gas lifetime at 1000 Hz and maximum voltage

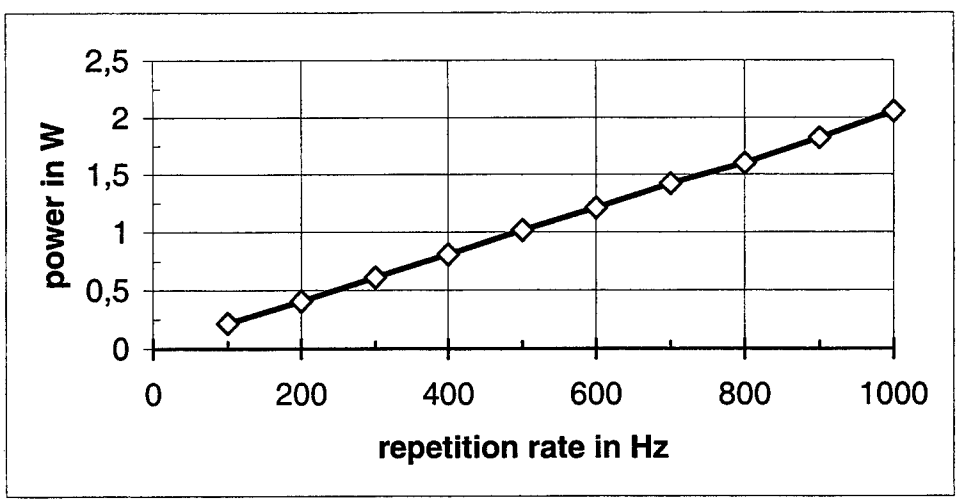


Figure 2: Output power at maximum voltage depending on repetition rate

Figure 2 shows the dependence of the output power at maximum voltage on the repetition rate. The output energy is independent of the repetition rate. The measurement was done with new optics installed. Therefore, a maximum output energy of 2 mJ was observed. The irradiation of the windows by the laser leads to a degradation of the transmission of the optical material and the reflective properties of the coatings. A second source of degradation is the pollution of the windows with dust. This dust is generated by the electrical discharge due to electrode erosion. Therefore, a decrease in the maximum pulse energy can be observed with increasing shot number. After typically 100 million pulses the maximum output energy is about 50 % of the energy measured with new optics.

Figure 3 shows the dependence of the pulse-to-pulse fluctuation sigma on the applied voltage. At low working voltages a rapid rise of the size of the fluctuations (sigma) can be observed. But in a wide range sigma is nearly constant. In figure 4 the dependence of the pulse-to-pulse fluctuation sigma on the repetition rate is shown. The measurements were done at maximum voltage. Additionally, the maximum and minimum value of the pulse energy are displayed.

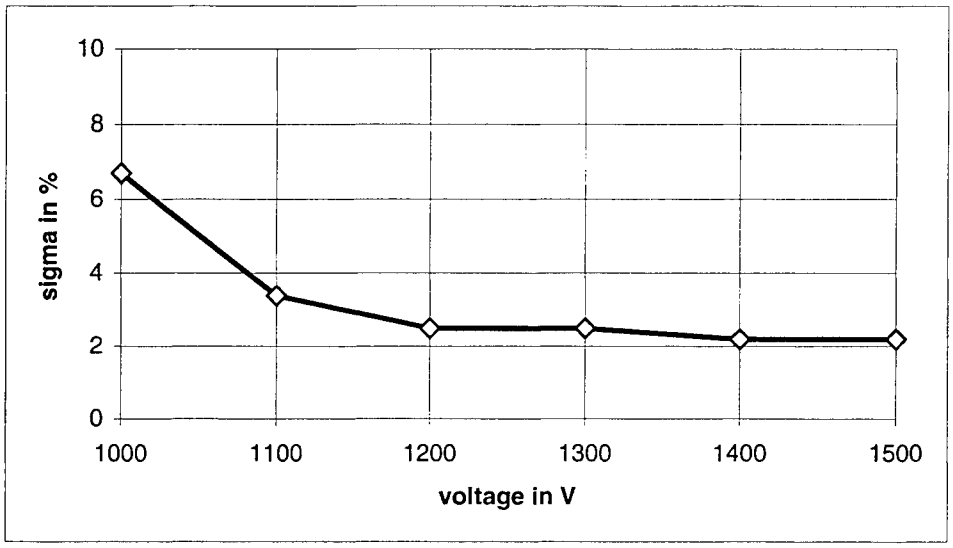


Figure 3: Pulse-to-pulse fluctuation at 500 Hz depending on the applied voltage

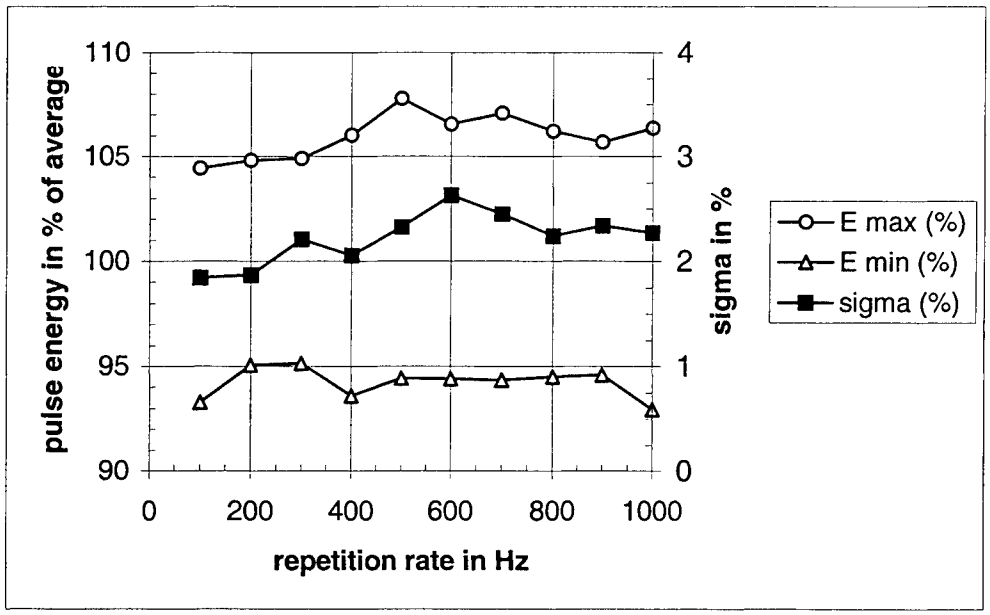


Figure 4: Pulse-to-pulse fluctuations and maximum respectively minimum pulse energy at maximum voltage in % of the mean value depending on the repetition rate

All curves show only a small increase with rising repetition rate. The laser energy is very stable and nearly constant up to 1000 Hz. The laser beam has a rectangular profile of 3 mm x 3.2 mm in the near field at 200 mm from the output coupler optic. The divergence is calculated from beam profiles in the near and far field at 1200 mm distance from the output coupler optic. The divergence is less than 2.5 mrad x 2.5 mrad. The pulse length is typically 16 ns (FWHM). The beam pointing stability is less than ± 0.5 mrad.

## 4. SUMMARY

The output data of the $F_2$-Laser at 157 nm are summarized in table 1. The maximum efficiency (electrical input energy to optical output energy) is 0.2 %. The long-term measurements showed that the laser output parameters (maximum power, pulse-to-pulse-fluctuations, divergence and pulse length) are nearly constant over the total lifetime of the tube of about 1 billion pulses. The mini fluorine excimer laser showed no decrease in the output data at repetition rates up to 1 kHz. The laser worked stable over hundreds of million pulses. After about 100 million pulses service intervals are necessary in order to change the laser optics. The lifetime of the mini excimer laser system is now distinctly increased and in a range for use in industrial applications like micro-machining and micro-lithography. Additional developments will be done to enlarge the maximum repetition rate and to increase the lifetime of the tube and the total system even further.

Table 1: Summary of the fluorine laser output parameters

| | |
|---|---|
| maximum pulse energy | 2 mJ |
| maximum repetition rate | 1000 Hz |
| pulse duration | 16 ± 3 ns (FWHM) |
| energy stability | < 3 % standard deviation |
| beam dimensions | 3.2 mm x 3 mm |
| beam divergence | 2.5 mrad x 2.5 mrad |
| pointing stability | < ± 0.5 mrad x ± 0.5 mrad |
| dynamic gas lifetime (at constant voltage, 100 % to 50 % of the output power) | 6 million pulses |
| optic lifetime | 100 million pulses |
| tube lifetime | > $10^9$ pulses |

## REFERENCES


1. Ch. K. Rhodes (Editor), *Excimer Lasers*, pp.87 – 134, Springer, Berlin Heidelberg New York, 1979
2. *Data Sheets "ExciStar S-200 S-500 S-1000"*, TuiLaser AG, Graefelfing, 2000

# Discharge Pumped Vacuum Ultraviolet $Kr_2$* Laser

Takahiro Shirai, Wataru Sasaki, Shoichi Kubodera*, Junji Kawanaka[a], and Tatsushi Igarashi[b]

Department of Electrical and Electronic Engineering and Photon Science Center,
Miyazaki University, Gakuen Kibanadai Nishi 1-1, Miyazaki, 889-2192 Japan
[a] Advanced Photon Research Center, Kansai Establishment/JAERI,
8-1 Umemidai, Kizu, Soraku-gun, Kyoto, 619-0215 Japan
[b] GIGAPHOTON Inc., 400 Yokokurashinden, Oyama, Tochigi, 323-8558 Japan

## ABSTRACT

We have realized a stable self-sustained discharge of high-pressure rare gases (Ar and Kr) using a compact discharge device. The glow discharge was obtained up to 10 atm of pure Kr. The vacuum ultraviolet emission intensity centered at 148 nm abruptly increased when the charging voltage exceeded a certain value. This "threshold" behavior indicates the onset of the stimulated emission at the wavelength. In addition to this threshold behavior, a considerable spectral narrowing was observed when the charging voltage exceeded the threshold value. The deconvoluted spectral width was 0.5 nm (FWHM), which was much narrower than that of 4 nm (FWHM) at the charging voltage below the threshold. This significant spectral narrowing also strongly indicates the onset of the stimulated emission at 148 nm.

**Keywords:** vacuum ultraviolet, rare gas excimer, self-sustained discharge, discharge pumped laser

There has been a considerable demand on the development of a practical laser in the vacuum ultraviolet (VUV) spectral region. Rare gas excimers are known to be one of the very few molecules that radiate in this spectral region. An electron beam excitation method has long been utilized to achieve the high power laser radiation in the VUV using these molecules [1]. In addition to this excitation method, compact discharge technique has been complementarily developed to realize practical VUV lasers. Such VUV lasers would open up various application fields, such as deep UV optical lithography and advanced materials processing. We have been studying and developing several new methods to realize compact VUV light sources using various compact discharge techniques, such as pulsed gas jet discharge pumping [2,3] and silent discharge excitation [4]. We also utilized soft x-ray emissions from a laser-produced plasma to ionize rare gases to produce the rare gas excimers by kinetics [5], and even used short pulse high intensity laser-produced electrons to initiate the rare gas production kinetics [6].

Many efforts have been pursued for the research and development of the discharge pumped rare gas excimer lasers. The group of the Clarendon Laboratory has made a pioneering work for the discharge pumped $Kr_2$* laser [7], however, no successful laser operation was reported mainly due to gas impurities and the low power deposition in the discharge. In 1990, the Kirov group reported the observation of the spectral narrowing of the $Kr_2$* emission using a microwave discharge technique [8]. The decrease of the spectral width from 13.5 nm to 4 nm at the Kr pressure of 5 atm indicates a positive result, however, a rather low deposition power (7 $MWcm^{-3}$) may have limited the lasing. Recently Kochetov and Lo reported a theoretical work of a discharge pumped $Xe_2$* laser [9]. Assuming a perfect self-sustained discharge, their result showed that one could obtain the gain duration of even hundreds of nanoseconds at 172 nm with high efficiency.

* Correspondence: e-mail kubodera@opt.miyazaki-u.ac.jp, phone: 81-985-58-7572, fax: 81-985-58-3899



XIII International Symposium on Gas Flow and Chemical Lasers and High-Power Laser Conference,
Antonio Lapucci, Marco Ciofini, Editors, Proceedings of SPIE Vol. 4184 (2001)

Their result may sound too optimistic from the experimental viewpoint, but indicates a promising conclusion for the possibility of the discharge pumped rare gas excimer laser. Using a traveling wave discharge excitation method, an optical gain of 0.6%$cm^{-1}$ has been reported for the $Ar_2$* emission at 126 nm [10]. The value of the gain seems to be reasonable but no other evidence of the lasing has been reported there. Despite these scientific efforts of various discharge pumping schemes, no discharge pumped rare gas excimer lasers have been reported to our knowledge.

Referring to these previous results [7-10], we have paid a special attention for the following two points throughout the development; the preionization configuration to obtain self-sustained discharge as long as possible and the gas handling system to minimize the impurities in the gas. Other improvements on the stability of the discharge have been done according to the discharge physics and our experience. As a result, we have realized a stable self-sustained discharge of the high-pressure rare gases using a compact discharge device. The glow discharge was obtained even up to 10 atm of pure Kr. The VUV emission intensity centered at 148 nm abruptly increased when the charging voltage exceeded a certain value. In addition to this threshold behavior, a considerable spectral narrowing was observed when the charging voltage was increased. The deconvoluted spectral width was 0.5 nm (FWHM), which was much narrower than that of the spontaneous emission (13 nm). The abrupt increase of the VUV intensity and the significant spectral narrowing show a direct evidence of the onset of the stimulated emission at 148 nm. We thus have made the first observation of the VUV $Kr_2$* excimer laser pumped by a compact transverse discharge technique.

Fig. 1 shows the schematic diagram of the experimental apparatus. The laser tube was originally designed and constructed for the $F_2$ and rare gas halide lasers [11]. The discharge tube contained a pair of electrodes. The distance of the electrodes was optimized at 5 mm. The widths of the cathode and anode were 3 cm and 5 cm, respectively. The electrode shape was thus asymmetric. The length of the electrodes was 110 cm. Fifty-one preionization pins in two parallel rows were placed near the cathode inside the tube. A pair of dielectric coated mirrors consisted of an optical cavity. A reflector had a reflectivity of 85% at 148 nm. An output coupler possessed the reflectivity of 85% with 6% transmission at 148 nm. The distance between the two mirrors was 135 cm. A threshold small signal gain evaluated from this optical cavity configuration was 0.1%$cm^{-1}$. High pressure Kr inside the laser tube was sealed with two $MgF_2$ windows.

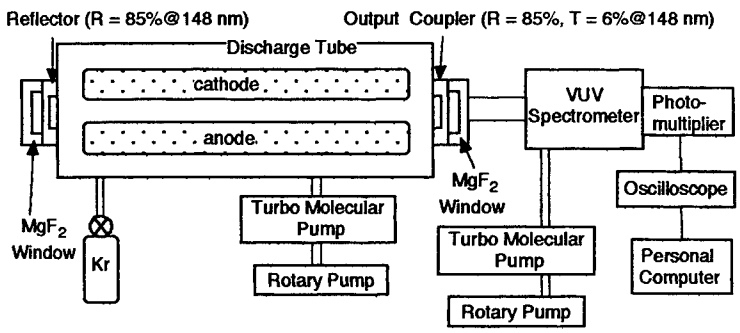


Fig. 1 Schematic diagram of the experimental apparatus.

The discharge circuit was a charge transfer type with automatic UV preionization. The stored charges in the primary capacitor (150 nF) were transferred into the 127 nF secondary capacitors placed inside the laser tube through 102 UV preionization pins. The ratio of the primary and secondary capacitance was optimized. The inductance of 10 nH in a main discharge loop was evaluated from a time-resolved voltage waveform, which leads to a static discharge impedance less than 1 Ω. The inductance of 1.7 $\mu$H was introduced in the primary discharge loop to ensure a good electrical contact between a high voltage feed-through and preionization pins inside. This inductance also regulated the timing between the switching and the gas breakdown. A mid-plane configuration was used as a gap switch. The discharge was operated at a single shot base.

The emission from the discharge region was detected with a solar blind VUV photomultiplier coupled to a 20 cm VUV spectrometer. The slit widths of the spectrometer were kept as narrow as possible to avoid any damage of optics caused by the intense VUV emission, resulting in the spectral resolution of the system to be 0.4 nm (FWHM). Time-resolved signals of the VUV emissions were recorded using a 2 GHz digital oscilloscope. All electronic devices were connected to a personal computer for data acquisition, storage and further data processing. In order to minimize the impurities inside the laser tube, a turbo molecular pump in addition to a rotary pump was used to evacuate the laser tube as low as

$10^{-6}$ Torr. A laboratory-grade Kr (99.999%) was used throughout the experiments.

Fig. 2 shows a time-resolved voltage signal, together with a time-resolved $Kr_2$* emission waveform. The spike at the time zero was caused by a switching noise. After the gas breakdown at 1.4 $\mu$s, the voltage signal started ringing with duration of 200 ns (FWHM), when the electrical power was deposited inside the discharge. The VUV emission evolved at the time of the breakdown and reached at the peak in 400 ns. The half width of the emission was 400 ns. This temporal behavior was much narrower than those observed at lower power deposition, which is described below. Note that no noise caused by arcing is shown in the afterglow regime after the onset of the discharge. The stored energy in the primary capacitor was calculated to be 70 J. When 80% of the energy was transferred inside the discharge, the estimated deposited energy was approximately 10 Jcm$^{-3}$. There is always an ambiguity about the estimate of an effective discharge volume, however, we evaluated the discharge width by inspecting the width of scars left on the electrodes. Although the measurement of the discharge current was not performed, the deposited power of more than 20 MWcm$^{-3}$ was estimated if assuming the current signal having a similar ringing behavior to that of the voltage signal.

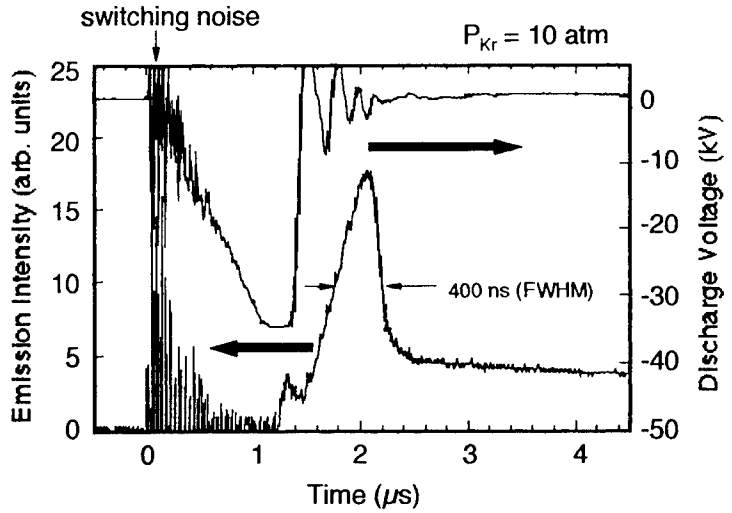


Fig. 2 Time-resolved voltage signal with a time-resolved $Kr_2$* signal.

The charging voltage dependence of the $Kr_2$* emission intensity is shown in Fig. 3. Time-resolved signals at two different charging voltages are also shown in inset. A spike at the time zero was caused by a switching noise. Stable self-sustained discharge was obtained even at 10 atm Kr at different charging voltages between 27 and 31 kV, which was verified from the time-resolved voltage waveforms. When the voltage exceeded 29 kV, the $Kr_2$* emission intensity abruptly increased. The peak intensity at 31 kV became almost one order of magnitude as high as that at 29 kV. The time-resolved signals also changed dramatically. At the voltage of 29 kV, the time-resolved signal had a 2.6 $\mu$s width (FWHM) with a rise time of 1.2 $\mu$s. On the other hand, the time-resolved waveform showed a width of 400 ns (FWHM) with a rise time of 400 ns at the voltage of 31 kV. The difference of the intensity and pulse shape represents the voltage threshold behavior of the VUV emission and indicates the onset of the stimulated emission.

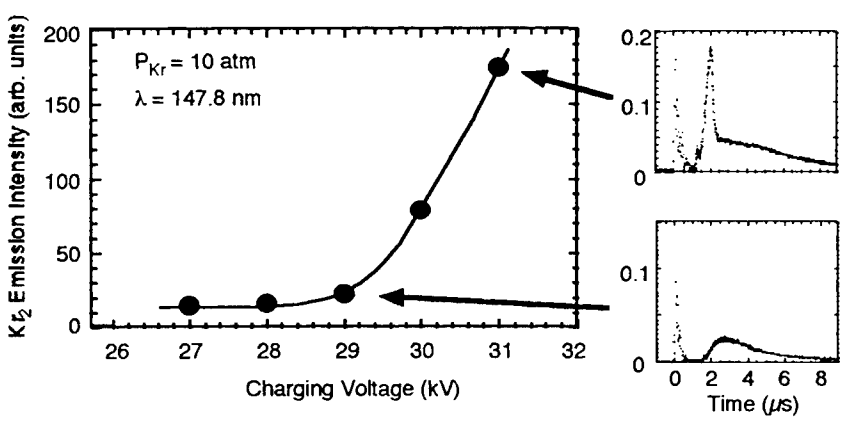


Fig. 3 Charging voltage dependence of the $Kr_2$* emission intensity.

In order to confirm this threshold behavior, the emission spectra were measured. The result is shown in Fig. 4. At the voltage of 27 kV, the spectral width was 4 nm (FWHM). In contrary to this, a considerable spectral narrowing down to 0.4 nm (FWHM) was observed when the charging voltage was increased to 31 kV. The deconvoluted spectral width was evaluated to be 0.5 nm (FWHM) by taking into account of the transmission function of the detection system. Note that

the spectral width of the spontaneous emission of the $Kr_2$* radiation was measured to be 13 nm (FWHM). This spectral narrowing is the direct evidence of the stimulated emission of the $Kr_2$* emission at 148 nm. Together with the voltage threshold behavior described above, we have concluded that we have demonstrated the stimulated emission of the $Kr_2$* excited by a compact discharge device for the first time to our knowledge.


## ACKNOWLEDGMENTS

This research was partially supported by a grant-in-aid for scientific research of the Ministry of Education, Science and Culture, Japan.


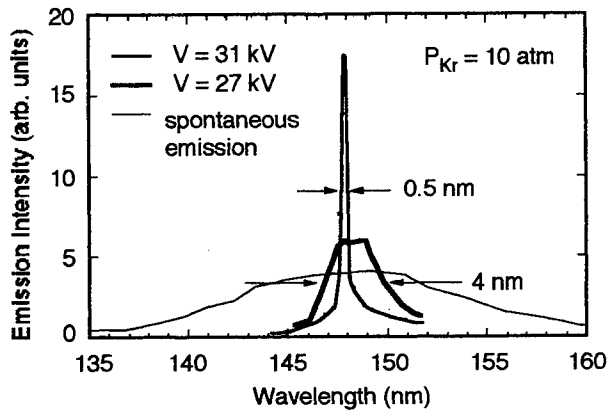


Fig. 4 Observed spectral narrowing at different voltages.

## REFERENCES


[1] Y. Uehara, W. Sasaki, S. Saito, E. Fujiwara, Y. Kato, M. Yamanaka, K. Tsuchida, and J. Fujita, "High-power argon excimer laser at 126 nm pumped by an electron beam," *Opt. Lett.* **9**, pp. 539-541 (1984).

[2] K. Mitsuhashi, T. Igarashi, M. Komori, T. Takada, E. Futagami, J. Kawanaka, S. Kubodera, K. Kurosawa, and W. Sasaki, "Xenon excimers produced from xenon clusters in a quasi-continuous-wave jet discharge," *Opt. Lett.* **20**, pp. 2423-2425 (1995).

[3] J. Kawanaka, S. Kubodera, W. Sasaki, K. Kurosawa, K. Mitsuhashi, and T. Igarashi, "New xenon excimer lamps excited by quasi-cw jet discharges," IEEE *J. Sel. Top. Quantum Electron.* **1**, pp. 852-858 (1995).

[4] S. Kubodera, M. Kitahara, J. Kawanaka, W. Sasaki, and K. Kurosawa, "A vacuum ultraviolet flash lamp with extremely broadened emission spectra," *Appl. Phys. Lett.* **69**, pp. 452-454 (1996).

[5] S. Kubodera, M. Ikeda, J. Kawanaka, and W. Sasaki, "Kr excimers produced by soft x-rays emitted from a laser produced plasma," *Appl. Phys. Lett.* **73**, pp. 1463-1465 (1998).

[6] S. Kubodera, J. Kawanaka, and W. Sasaki, "Vacuum ultraviolet Ar excimer emission initiated by high intensity laser produced electrons," *Opt. Commun.* **182**, pp. 407-412 (2000).

[7] T. Sakurai, N. Goto, and C. E. Webb, "$Kr_2$* excimer emission from multi-atmosphere discharges in Kr, Kr-He and Kr-Ne mixtures," *J. Phys. D: Appl. Phys.* **20**, pp. 709-713 (1987).

[8] O. A. Zakharenko, A. A. Kuznetsov, V, N, Slinko, and S. S. Sulakshin, "Experimental investigation of vacuum ultraviolet emission from Kr and Xe rare gases in a high-power high-pressure pulsed microwave discharge," *Sov. J. Quantum Electron.* **20**, pp. 813-815 (1990).

[9] I. V. Kochetov and D. Lo, "Kinetics of a self-sustained discharge-pumped $Xe_2$* laser at 172 nm," *Opt. Commun.* **113**, pp. 541-549 (1995).

[10] H. Ninomiya and K. Nakashima, "$Ar_2$* excimer emission from a pulsed electric discharge in pure Ar gas," *Opt. Commun.* **134**, pp. 521-528 (1997).

[11] K. Yamada, K. Miyazaki, T. Hasama, and T. Sato, "High-power discharge-pumped $F_2$ molecular laser," *Appl. Phys. Lett.* **54**, pp. 597-599 (1989).

Invited Paper

# Long pulse ArF and $F_2$ excimer lasers

**P.J.M. Peters*, L. Feenstra and H.M.J. Bastiaens**

Laser Physics Group, Faculty of Applied Physics
University of Twente
PO Box 217, 7500 AE, Enschede, The Netherlands

## ABSTRACT

For some specific application areas like (V)UV lithography or special processing of certain materials with high average power (V)UV lasers excimer lasers have to be developed further. In this contribution we will summarise the recent progress of our VUV excimer laser programme on the ArF and $F_2$ laser. Key point in our research programme is the production of long laser pulses in the order of 100 ns (FWHM).
An existing laser chamber was modified and optimised for the ArF laser research programme. Different excitation circuits have been tested. For long pulse operation the laser is operated in the ferrite switched resonant overshoot mode using 18 $cm^2$ of ferrite in the switch for a discharge volume of approximately 60 x 0,7 x 1,2 $cm^3$. Long optical pulses of up to 116 ns have been obtained with a lean gas mixture and a very low self-inductance of the electrical circuit of the packing capacitors.
For the $F_2$ laser a new discharge chamber and a new X-ray preionisation source was designed. With this set-up it was possible to produce a $F_2$ laser with a large optical cross-section of 1,5 x 2,4 $cm^2$ operating at an intrinsic efficiency of 0,1%. With a different electrical circuit the system produced long optical output pulses of 70 ns (FWHM) in a gas mixture of helium and 3 mbar $F_2$ at a total gas pressure of 2 bar.

**Keywords:** Excimer laser, long pulse, 157 nm, 193 nm, gas discharge, X-ray preionisation

## 1. INTRODUCTION

In general lasers are classified on basis of the employed lasing material. There are solid state, semi-conductor, dye, gas and free-electron lasers. Of these lasers, the gas lasers combine high (average) output power with high beam quality as the laser medium remains very homogeneous even at high input powers. Unsurpassed in high power is the $CO_2$ gas laser operating in the infra-red around 10 μm. A well established class of high power gas lasers operating in the ultraviolet (UV) part of the electro-magnetic spectrum are the excimer lasers of which the KrF and the XeCl laser are well-known representatives. The rapid progress in the field of diode-pumped solid state lasers has led to the development of compact laser systems with improved output power, efficiency and reliability. Therefore gas lasers operating in the visible to near-infrared are increasingly replaced by diode-pumped solid state lasers eventual in combination with non-linear frequency conversion schemes. However at high power levels the solid-state based laser systems still can not compete with gas lasers as thermal loading of the laser crystals and of the non-linear crystals prohibits operation at high output powers. The lack of transmitive materials limits also the accessibility of the vacuum ultraviolet (VUV) by solid state lasers down to 180 nm. The only reliable high power lasers operating in the (V)UV are ArF* and the molecular fluorine ($F_2$*) gas laser operating at 193 nm and 157 nm respectively.

* Correspondence: email: p.j.m.peters@tn.utwente.nl



XIII International Symposium on Gas Flow and Chemical Lasers and High-Power Laser Conference,
Antonio Lapucci, Marco Ciofini, Editors, Proceedings of SPIE Vol. 4184 (2001)

Excimer lasers can be very powerful lasers with large beam diameters at short wavelengths. A short wavelength means a high photon energy. These properties make excimer lasers ideally suitable for applications such as material processing and lithography.

Current lithographic techniques use KrF lasers to print 250-120 nm size features and ArF lasers for sizes as small as 90 nm. In the near future the $F_2$ laser emitting at 157 nm will allow feature sizes as small as 70 nm. The resolution is given by $k_1\lambda/NA$ while the depth of focus is given by $k_2\lambda/(NA)^2$. $k_1$ and $k_2$ depend on both the desired feature size and the manufacturing process. $k_1$ can be reduced by using resolution enhancement techniques such as off-axis illuminating, phase shift masks and optical proximity correction. In Fig. 1 the resolution as a function $k_1$ is given for various light sources. The area under the horizontal line in Fig.1 can be covered with resolution enhanced techniques.

The conventional optical lithography area will end with the $F_2$ laser. For wavelengths shorter than 157 nm no optical materials are available anymore. It is already a large challenge to develop good optical materials, resists and pellicle films for the $F_2$ laser wavelength. Introducing the $F_2$ laser is just at the edge of the possibilities as is stated by Will Conley[1]: "157 nm may be the most difficult optical technique; however, it is the least difficult post 193 nm technology".

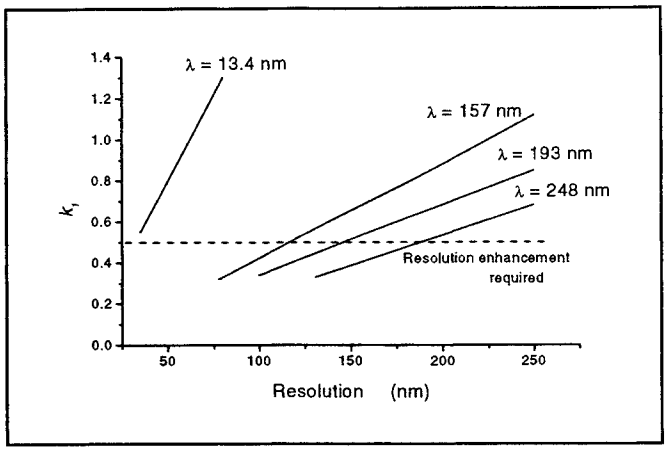


*Fig. 1 Dependency of resolution on $k_1$*

Future lithographic techniques will probably use EUV light sources. Currently in the USA subsystems are being developed which will be integrated into a lithographic tool referred to as the Engineering Test Stand (ETS). Various radiation sources are under development one of which is based on a laser produced plasma source. An intense laser beam is focused onto nano-clusters of Xenon that are produced in a supersonic jet. The heated plasma emits broadband radiation centred at 45 eV with discrete peaks due to atomic transitions [2]. Another source under consideration as a possible EUV source is a pulsed capillary discharge which yields a higher flux in the EUV [3]. A drawback of this technique is the erosion of the wall of the discharge tube. Also in Europe an EUVL test bench is under construction studying future lithographic techniques like laser plasma and synchrotron EUV sources [4].

In material processing the available sources are restricted to high energy lasers because of the flux requirements. In contrast to a lithographic application where a high-intensity per unit wavelength is required broadband light sources are allowed for material processing applications. The short wavelengths and consequently high photon energy of excimer lasers leads to special applications in material processing. Apart from the booming market in medical fields like eye surgery, with photorefractive-keratectomy (PRK) [5] and laser in situ keratomilensis (LASIK) [6], and micro-surgery, other promising fields are micro-machining [7,8], surface ablation and optical telecommunication where small scale structures can be made with these light sources [9]. On the other hand as stated before gas lasers can be designed to operate at high power levels which opens a new field for high speed, high volume processing applications. With the 1 kW (1 Joule/pulse, 1 kHz) XeCl excimer laser developed at NCLR bv, The Netherlands, it is for example possible to drill in a short time, a large numbers of tiny holes in aircraft wings [10]. By sucking off the boundary layer through these small holes the air turbulence across the wings can be reduced to a large extent during the flight of the airplane [11]. Another application is drilling numerous special shaped holes in turbine blades of jet engines. The cooling characteristics of the turbine blades can be improved considerably in this way [12,13].

However, most of these applications need a high beam quality, which means a low divergence of the beam and a well defined mode structure. The properties of the laser beam are mainly determined by the resonator properties. When the radiation field inside the resonator starts from the optical noise of the spontaneous emission it has a large number of degrees of freedom. After several round trips inside the resonator only those spectral and spatial modes that fit the resonator are amplified enough to sustain lasing, while the other modes die out. The result is a narrower bandwidth and a decreased divergence, which allows for better transportation of the beam over long distances and a better focusability of the beam for small-size applications. For pulsed lasers the combination of the resonator set-up and the pulse duration is a decisive parameter for the beam quality. Longer pulses can generate beams with improved optical quality [14] and

reduce the damaging of optics, since such processes as compaction and colour centre formation are related to the incident intensity. Long laser pulses equally facilitate the transportation of optical signals through fibers. It has also been shown that long excimer laser pulses are very interesting for the generation of long X-ray pulses for the study of bacteria. Furthermore, long pulse operation lowers stresses on the electrical components of the set-up. In the following paragraphs the ArF and $F_2$ long pulse excimer lasers will be discussed in more detail.

## 2. THE ArF LASER

The ArF excimer molecule has two very closely lying upper states, the B and the C state. The mixing between these two states is sufficiently fast to be treated as a single state with a lifetime of ~4 ns. The lower level A and X states are also strongly mixed. Therefore, the radiative transitions between the upper level states and the lower level can be seen as a continuum without a structure [15]. Lasing of this molecule was first reported in 1976 with e-beam excitation [16] of an $Ar/F_2$ gas mixture. Apart from e-beam excitation also discharge excitation [17] and e-beam sustained discharge techniques have been used in those days. For commercial applications only discharge pumped systems are interesting because they allow high repetition rate operation. In e-beam pumped systems the thin foil which separates the laser gas (pressure several bar) and the electron source (vacuum) will be heated too much at high repetition rates and foil problems will be unavoidable. Problems to be solved in discharge systems are a proper initiation of a volumetric gas discharge and once created, to keep the discharge stable for a longer period of time. A proper initiation can be achieved by using a pre-ionisation technique by which sufficient electrons in the laser gas mixture are created before the pumping pulse will be applied. Usually UV or X-rays are used as pre-ionisation source. Since X-rays have a large penetration depth large aperture systems can be homogeneously preionised with X-ray preionisation. The enhancement of the discharge stability of $F_2$ based laser gas mixtures is the subject of our current research.

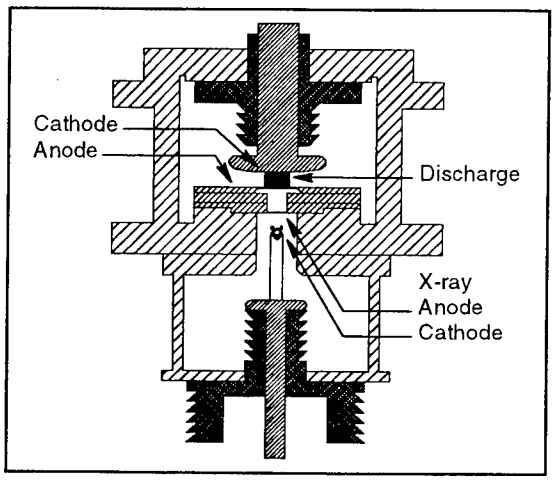


*Fig. 2 Schematic view of the laserchamber and X-ray source*

The laserhead used in our experiments was previously used for XeCl and XeF laser experiments at total gas pressures of up to 10 bar. The attached X-ray source was therefore modified producing 50 ns (FWHM) X- ray pulses generating an electron density of up to $2.10^8$ $cm^{-3}bar^{-1}$ in He and up to $5.10^9$ $cm^{-3}bar^{-1}$ in Ar (operating the X-ray source at a charging voltage of 28 kV). The X-rays are entering the laser chamber through the 1 mm thick aluminum anode. The laser head consists of a rectangular stainless steel vessel, fitted at opposite sides with uncoated $MgF_2$ windows. The cross-section of the laserhead is given in Fig. 2. The approximately 95 mm wide laser cathode is of the uniform field type, the grounded anode is flat (see Fig. 2). The discharge volume is approximately 60 x 1.5 x 1.2 $cm^3$ ($l$ x $w$ x $h$). Both electrodes are made of nickel plated aluminium. A typical gas mixture for the ArF laser is 6 mbar $F_2$, 100 mbar Ar, 200 mbar Ne and 3.7 bar He. The PFN and the peaking capacitors are mounted on top of the laser vessel, electrically separated by the rail gap or by a ferrite switch. The PFN capacitors are fastened in pairs between copper strips in the form of separate columns and with a variable number of rows. The middle conductor is charged, the outer conductors are grounded on the laser vessel, which is grounded externally. All other electrical components of the set-up are grounded on the laser vessel as well. The pre-pulse is generated by a

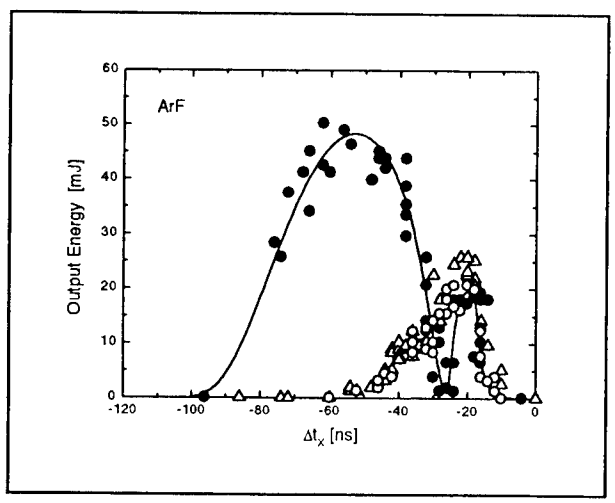


*Fig. 3 ArF laser output as a function of the pre-ionisation delay time O: Church, Δ: Resonant overshoot and •: Swing mode*

mini-marx generator, the same as the X-ray source driver. Both mini-marx generators are pressurized with nitrogen, just higher than the critical pressure for spontaneous breakdown. The nitrogen is flowed at a rate of 5 *l*/min. The PFN is pulse charged in a few μs from a separate circuit, consisting of a storage capacitor and an EEV CX1725 hydrogen-filled thyratron switch.

Several excitation circuits, each working with different switching schemes like the charge transfer mode, church mode, swing mode or resonant overshoot mode have been tested to pump the gas discharge. It appeared that for short pulse operation the swing mode was superior to the other modes. In the swing mode the polarity of the prepulse is opposite to that of the main pulse which causes a polarity reversal of the electrode voltage in the preionisation phase. From experiments with different delay times between the start of the X-ray pulse and the breakdown of the main discharge it can be seen that in the swing mode two timing windows exists [18]. In Fig. 3 the influence of the delay time on the laser output is shown. Especially the timing window for larger delay times (between 40 and 80 ns) shows very good results. Due to the fact that in two time intervals the voltage at the electrodes for two different polarities is much higher than the steady state voltage, so electron multiplication can take place here, a much better and more homogeneous preionisation is obtained resulting in a better laser performance.

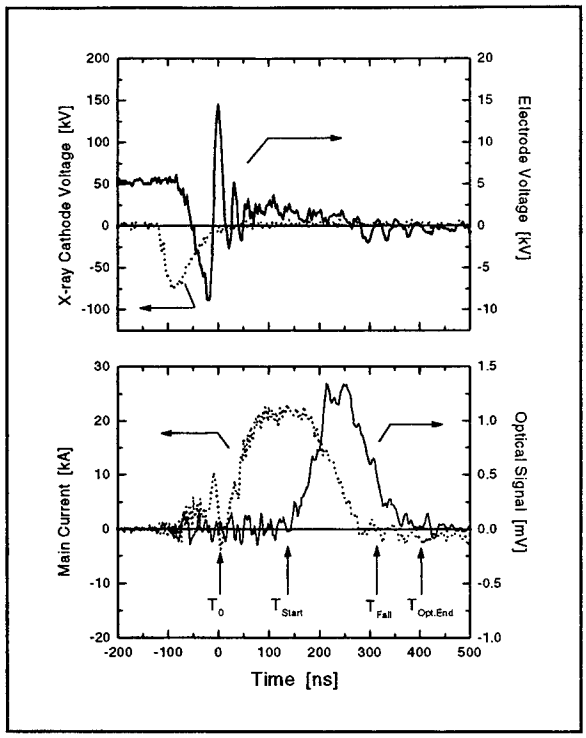


*Fig.4 Typical waveforms of the laser pulse*

In order to improve the results with this laser several hardware modifications have been made on the laserhead resulting in a lower self-inductance of the laserhead. At first additional current return paths on either side of the electrodes were mounted inside the laserhead thereby reducing the head inductance from 18 nH to 11 nH. It resulted in a higher specific laser output energy and slightly longer optical pulses.

As the next step the peaking capacitors were replaced from outside the laser vessel to the innerside equally distributed on either side of the electrode. With a different uniform field cathode placed at a distance of 12 mm from the flat anode a discharge volume of approximately 60 x 0.7 x 12 $cm^3$ is created with this configuration. Compared with the previous mentioned experimental configuration a significant increase in the performance of the laser is found. When using He as a buffergas in the modified setup the laser pulse length is found to be increased from 26 to 32 ns (FWHM). The maximum output energy is increased from 50 mJ (0.5 J/l) to 97 mJ (1.9 J/l). With the Ne buffered gas mixture the measured pulse length is up to 48 ns (FWHM) with an output energy per pulse of 181 mJ (3.6 J/l). These values for the specific output energy are in the same range as the figures reported in the literature for short pulse ArF lasers namely between 2 J/L and 5 J/l. However the average pulse lengths mentioned in these papers is approximately 12 ns [19,20].

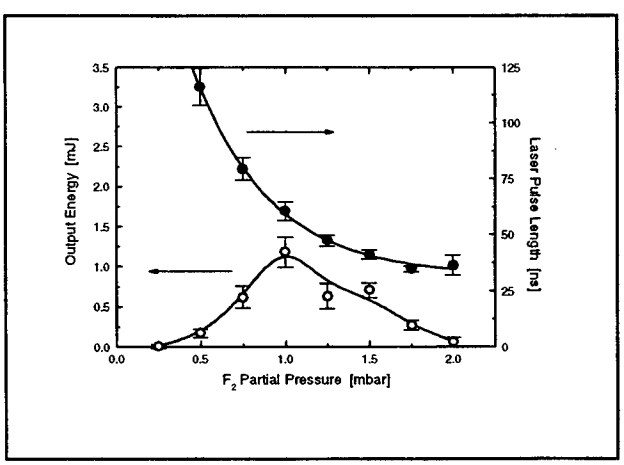


*Fig. 5 Laser pulse length (FWHM) and output energy vs $F_2$ concentration*

In order to obtain long excimer laser pulses the laser gas mixture should contain only low concentrations of the active gases especially of the halogen donor. Typically a lean gas mixture for a long pulse XeCl laser contains only ~0.7 mbar HCl and ~10 mbar Xe in a Ne buffered gas mixture at a total gas pressure of 5 bar [14]. With the unmodified experimental setup as described earlier ArF lasing could not be obtained with

such a lean gas mixture. The reduction of the self-inductance of the peaking circuit turned out to be the crucial step in order to obtain ArF lasing pulses with the lean laser gas mixtures.

Experiments with lean gas mixtures described below show that there is a clear trade-off between the laser gain and the discharge stability and therefore between the output energy and the pulse length. During the experiments the resonator is formed by a high reflecting concave mirror (R = 6 m) on one side and a plane output outcoupler with a reflection of 90 %. Both mirrors are placed outside the laser vessel. The standard gas mixture is 1.0 mbar $F_2$, 19.0 mbar He and 50 mbar Ar. Ne is added as buffergas up to a total gas pressure of 5 bar. The laser is operated in the ferrite switched overshoot mode using 18 $cm^2$ ferrite in the switch. The capacitance $C_{PFN}$ of the PFN is 427 nF and $C_P$ of the peaking capacitor is 4.6 nF. The laser is operated with a PFN voltage of 5.3 kV which is about twice the steady state discharge voltage. In Fig. 4 a set of typical wave forms is shown. The discharge voltage is calculated according to :

$$V_{Calc} = V_P - L_{Vess} \frac{dI_{Main}}{dt}$$

with $L_{Vess}$ = 8 nH and $V_P$ the voltage measured by the main voltage probe outside the laser vessel.

As in previous experiments the dependency of the laser output and the optical pulse length was measured as a function of the preionisation timing, the gas composition, the total gas pressure and pumping power[21]. In Fig. 5 a set of parametric measurements is shown. In this figure the optical pulse length and the laser output energy is given as a function of different $F_2$ partial pressures in the standard gas mixture. As can be seen in Fig. 5 the longest optical pulse of 116 ns (FWHM) was measured for 0.5 mbar $F_2$ in the laser gas mixture with a specific output energy of 4 mJ/l. By increasing the charging voltage of the PFN the output energy could be enhanced as is shown in Fig. 6. The gas mixture used in these experiments is the standard gas mixture ($F_2$ : Ar : He : Ne = 1.0 : 50.0 :19.0 : rest, [mbar]) at a total gas pressure of 5 bar.

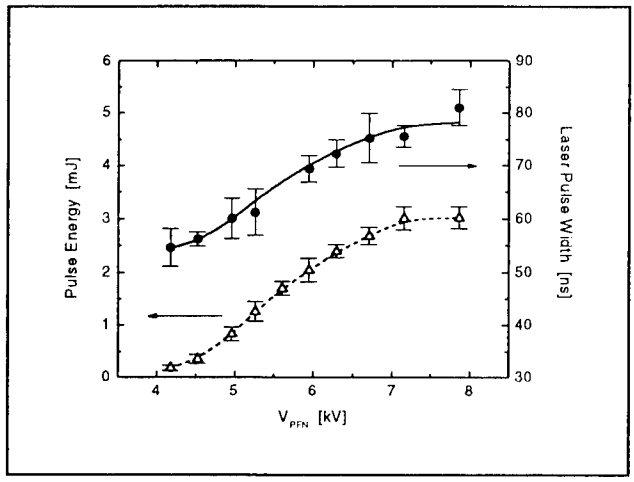


*Fig. 6 Laser pulse length (FWHM) and output energy vs energy stored in the PFN*

In conclusion it is shown that long optical ArF laser pulses can be obtained from a discharge pumped laser system. The discharge is made stable by the use of a proper preionisation, a lean laser gas mixture and a low inductance laserhead.

## 3. THE MOLECULAR $F_2$ LASER

The radiative transition of the $F_2$ laser is a bound-bound transition from the excited $D^1(^3\Pi_g)$ state to the $A^1(^3\Pi_u)$ ground state of the fluorine molecule. This transition is different from the usual excimer molecules in the sense that "normal" excimer transitions have an unbound ground state. Due to the bound-bound transition and the finite lifetime of the lower laser level of the $F_2$ molecule it has been suggested that the laser should be self terminating and no long pulse operation should be possible [22,23]. From our previous work on the e-beam pumped $F_2$ laser it appeared that the length of the laser pulse was only limited by the length of the pumping pulse. With our e-beam system a molecular $F_2$ laser output pulse width of 160 ns (FWHM) and an output energy of 1.8 J (11.3 J/l) has been realised [24]. Simulations on the $F_2$ lasers also suggest that depopulation of the lower laser level is fast enough to maintain gain during long pulse operation [25]. A further difference with the usual excimer laser is the spontaneous emission bandwidth of the molecular $F_2$ laser. Due to the bound-bound transition of the $F_2$ molecule the emission bandwidth is considerably smaller than from excimer transitions. Typical numbers are 1 nm for excimer transitions to 0.2 nm for the molecular $F_2$ transition. The laser linewidths are in the order of 1 to 5 pm [26].

The first discharge pumped $F_2^*$ laser, demonstrated by Pummer in 1979 [27], had an output energy that was limited to about 8 mJ. In the past decade considerable progress is made with regard to the output energy of the laser. The development of low inductance discharge devices operating at high pressures and delivering high specific pump powers in a short pulse has led to a major increase in the output energy of up to 240 mJ [28]. Typically laser pulses of 10 to 30 ns (FWHM) are obtained. The high peak intensity generated by these laser devices is however a disadvantage because it limits the lifetime of the beam optics. At 157 nm only two optically transparent materials are available: $MgF_2$ and $CaF_2$. These materials exhibit a strong absorption when exposed over extended periods to this short wavelength, high intensity laser beams. The absorption is attributed to the generation of crystals defects (color centers). Another problem is the

very high gain in the $F_2^*$ laser when it is operated at high pumping power densities. The laser beam is dominated then by amplified spontaneous emission (ASE) and shows a strong divergence up to several mrad resulting in a poor focusability [29]. A low beam divergence allows focusing to a smaller spot size and hence a higher brightness will be obtained which is important for applications like high resolution material processing.

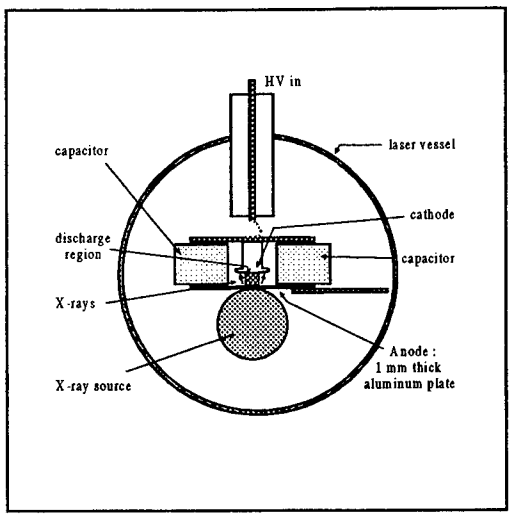


*Fig. 7 Cross-section of the laser head*

Our goal is to develop a long pulse, discharge pumped $F_2^*$ laser in which a high output energy can be combined with a high beam quality. An extension of the laser pulse duration offers also the possibility to maintain the energy extraction while reducing the laser peak intensity thus avoiding color center formation in the beam optics.

Recent advances in discharge technology have lead to the development of long pulse excimer lasers with a high average output power. A XeCl laser is demonstrated with a laser pulse duration of 200 ns and an average output power of 1 kW at a repetition rate of 1 kHz [10]. The performance of $F_2$ lasers that are commercially available is rather modest in comparison with the XeCl laser. For a repetition rate of 50 Hz an average output power of 3 Watt is obtained. The laser beam exhibits a large divergence due to the limited number of roundtrips possible within the short pulse length of 20 ns. Extension the laser pulse duration permits the improvement of the beam quality. We will discuss the successful operation of a discharge excited, long pulse $F_2$ laser in which key technologies for high repetition rate operation are implemented.

One of the key technologies is the design of a laser head with a very low self-inductance. The laser head with the capacitors and the discharge electrodes is mounted in a high pressure vessel as schematically illustrated in Fig. 7. The low inductance laser head is provided with a high voltage pulse $HV_{in}$ by a charge-transfer circuit from a double stage Marx generator with a total capacitance of 10 nF. The laser head consists of two metal plates holding two rows of capacitors in between. The lower plate is made of aluminum and forms the anode. The nickel plated, aluminum shaped cathode is attached to the upper plate. The capacitors (type TDK UHV 5A/7A) are placed along the cathode and are as close as possible to the discharge gap. This construction ensures a low inductance of the discharge circuit. It allows a rapid rise of the discharge current resulting in a high power deposition in the laser gas. The capacitance of the laser head can be easily varied and in this study amounts to 14 nF and 30.6 nF respectively. The inductance of the laser head is calculated from the oscillation period of the current in the discharge circuit. It amounts to 1.7 nH and 1.1 nH when the laser head is respectively equipped with a capacitance of 14 nF and 30.6 nF. The cathode has a length of 42 cm and a width of 2.2 cm. Setting the electrode spacing to 0.8 cm results in a discharge width of 1.4 cm and a excited volume of 46 $cm^3$. When the electrode spacing is set to 1.5 cm, the discharge has a width of 2.4 cm and an excited volume of 153 $cm^3$.

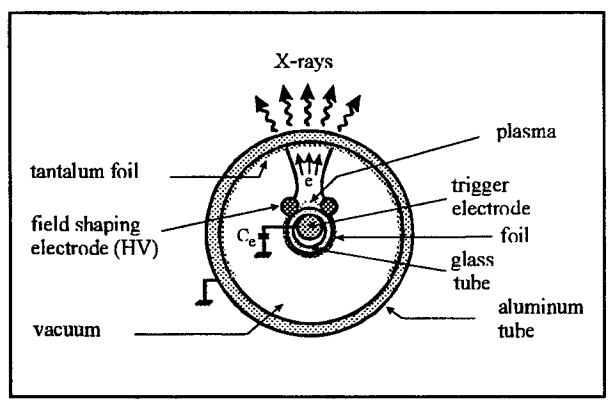


*Fig. 8 Cross-section of the X-ray source*

As the high pressure vessel has no entrance window for the X-rays, the X-ray preionisation source has to be placed inside the vessel. Because the space inside the vessel is limited the X-ray source is build very compact such that it fits in an aluminum tube with an outer diameter of 5 cm and a length 74 cm. The X-ray source is mounted directly under the anode. The X-rays have to pass the 1.5 mm thick wall of the tube and the 1 mm thick aluminum anode before reaching the laser gas. The low energy part of the X-ray spectrum is strongly absorbed in the aluminum causing a cut-off of the spectrum around 15 keV. The X-ray source is a revised version of a source developed earlier for the preionisation of a XeCl laser [30]. It employs a corona plasma cathode from which the electrons are emitted. The electrons are accelerated towards an anode with voltages ranging

from 40 kV up to 110 kV. The electrons produce Bremsstrahlung when they are decelerated in the high Z material of the anode which is attached to the vacuum housing of the X-ray source. In Fig. 8 the cross-section of the X-ray source is shown. The cathode consists of a pyrex tube with a metal foil wrapped tightly around it. In the metal foil a rectangular window is cut. A thin tungsten wire is wound around the tube with a pitch of several mm. Inside the tube a metal rod is placed serving as a trigger electrode for the initiation the corona plasma. With a small six stage mini-Marx generator a fast rising high voltage difference is applied between the trigger electrode and the metal foil. At the window in the foil, electrons are liberated from the wires by field emission. The electrons are accelerated towards the trigger electrode and hit the surface of the pyrex tube. They ionise surface material thereby creating a plasma that covers the window cut in the metal foil. A well defined plasma region is established from which easily electrons can be extracted and accelerated towards the anode (see Fig. 8). The anode consists of a 25 μm tantalum foil attached to the wall of the aluminum tube. The trigger electrode is connected via the capacitance $C_e$ to earth. This capacitance acts in series with the inherent capacitance ($C_{TF}$) between the trigger electrode and the metal foil to divide the applied voltage to about a third. This reduces the electrical stress on the pyrex tube and enhances its lifetime. With this X-ray source with a pulse width of 25 ns an electron density of $5.10^8$ $cm^3$ was produced at the location of the discharge in 5 bar He at a Marx load voltage of 20 kV/stage. The electron density was measured to be proportional to $V_{Load, Marx}^{7/2}$.

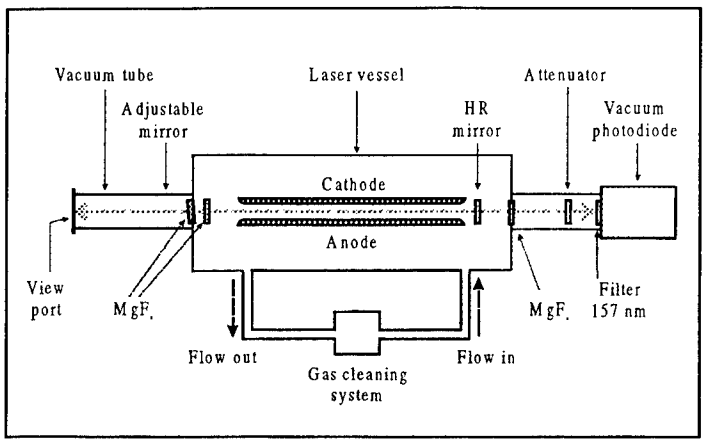


*Fig 9 Experimental setup*

With the high intensity X-ray source and the low-inductance laserhead it was possible to operate a molecular fluorine laser with a large cross-section of 1.5 x 2.4 $cm^2$ (electrode spacing x discharge width). The laser was operated with a resonator formed by a high reflectance dielectric mirror (R= 94 %, T≤ 1 %, Laser Optik GmbH) and an uncoated $MgF_2$ output coupler (R≈ 6%). The length of the resonator was 70 cm. The mirrors were placed inside the laser vessel close to the discharge section as shown in Fig. 9. The laser beam emerges from the left side of the vessel through a $MgF_2$ window. The window is tilted 5° to the axis of the laser to prevent back reflections into the laser medium. The laser energy is measured with pyroelectric a energy meter. The time history of the laser pulse is measured with a solar blind, vacuum photodiode (ITT F4115) in combination with an optical transmission filter for 157 nm. The optical paths to the detectors are evacuated to avoid strong absorption of the 157 nm laser light by the Schumann-Runge bands of molecular oxygen. The output energy of the red atomic fluorine emission which usually accompanies the 157 nm molecular fluorine emission is subtracted from the measured total energy. A cryogenic gas purification system is connected to the laser system to remove dust and absorbing impurities from the laser gas. It consists of a circulation pump, a liquid nitrogen cooled trap and a dust filter. The purification system is used during all laser experiments. The pressure of the laser gas is limited by the maximum operating pressure of the circulation pump which amounts to 5 bar.

An extensive laser performance study was done. The dependence of the laser output energy on the preionisation timing and strength, on the gas composition, the charging voltage of the main Marx generator was measured. Three different laser head configurations with varying capacitance and electrode spacing have been

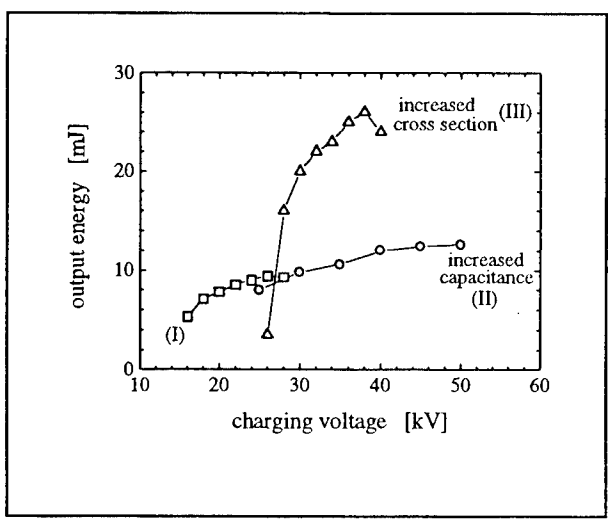


*Fig. 10 Output energy as function of the charging voltage of the Marx generator*

used. In Fig 10 the dependence of the output energy on the charging voltage of the Marx generator is shown for three different laserhead configurations and with a laser gas mixture containing 0.1% $F_2$ in He at a total gas ressure of 5 bar. In configuration I the capacitance $C_2$ of the laser head is 14 nF and the inductance is 1.7 nH. The electrode spacing is set to 0.8 cm which results in a discharge width of 1.5 cm. In configuration II the capacitance $C_2$ is raised to 30.6 nF, the inductance amounts to 1.1 nH. The electrode spacing and the discharge width are the same as in configuration I. For configuration III the capacitance $C_2$ is 14 nF and the inductance is 1.7 nH. The electrode spacing is raised to 1.5 cm which results in a discharge width of 2.4 cm. The maximum output energy increases from 9.4 mJ to 12.6 mJ when the capacitance is raised from 14 nF (config. I) to 30.6 nF (config. II). A much higher energy extraction can be reached by increasing the discharge cross section from $0.8\times1.5$ cm$^2$ (electrode spacing × discharge width : config.I) to $1.5\times2.4$ cm$^2$ (electrode spacing×discharge width : config.III). Consequently the discharge volume increases by a factor of three from 46 cm$^3$ to 153 cm$^3$. The maximum output energy scales nearly proportional with the discharge volume from 9.4 mJ to 26 mJ. With laser head configuration I a maximum a pump power density of 10 MW/cm$^3$ is obtained which results in a specific output energy of 0.2 J/l. For configuration II the electrode spacing is kept at 0.8 cm so that the breakdown voltage will not change. Although the capacitance is roughly doubled the pump power density increases less due to a less efficient energy transfer from the laser head to the discharge during the first power deposition pulse. The maximum pumping power density increases to 15 MW/cm$^3$ resulting in specific output energy of 0.3 J/l at an efficiency of 0.3 %. For configuration III the electrode spacing is raised by nearly a factor of two. This leads to a doubling of the breakdown voltage and an increase of the energy stored on the laser head by a factor of four. The discharge cross-section and with that the discharge volume increases by a factor of three. Accordingly, the pumping power density can increase with a factor of 1.3. The specific output energy is somewhat lower with an enlarged discharge cross section. For a peak pumping power density of 11 MW/cm$^3$ a specific output energy of 0.17 J/l is measured. The intrinsic efficiency amounts to 0.1 % which is comparable to values measured for discharge excited $F_2^*$ lasers with a small discharge cross section[31].

The charge transfer circuit is very well suited for pumping at very high power densities. In order to diminish the occurrence of discharge instabilities and to make long optical pulses a prepulse-mainpulse excitation circuit is a better choice. This type of excitation circuit has been shown its excellent pumping qualities in the production of homogeneous discharges for long pulse, high repetition rate $XeCl^*$ lasers[10,32]. The experimental setup is the same as shown in Fig 9. The outcoupling $MgF_2$ mirror is however replaced by another high reflecting mirror (R= 98 %, T≤ 0.2 %) thus forming a high Q resonator. The laser is excited with the prepulse-main pulse system operating in overshoot mode. Unless stated otherwise, a gas mixture of fluorine in helium is used at a total pressure of 2 bar. In Fig. 11 typical waveforms of the x-ray preionisation pulse, the voltage at the peaking capacitors, the current from the main capacitor, the power deposition calculated from the voltage and current signals and the laser pulse are shown. The main capacitor $C_m$ is slowly pulsed charged from the primary capacitor $C_T$. The charging voltage is also applied to the peaking capacitors and the laser electrodes. At the peak of the charging voltage a positive prepulse is applied to the peaking capacitors. This creates a large voltage difference across the magnetic switch driving it from a high to a low inductance state. The peaking capacitors are now resonantly charged by the main capacitor. The voltage reverses and rises fast until the laser gas breaks down. The low inductance of the laser head allows a fast rise of the current and thus a high power deposition from the peaking capacitors during the start of the discharge. The short risetime of the current leads to the formation of a dense hot-spot structure which enhances the homogeneity of the discharge and favours the generation of long laser pulses[33]. The high power deposition will reduce the ring-up time of the laser. A current from the main capacitor starts flowing through the low impedance discharge driving the magnetic switch deep into saturation. The resulting low

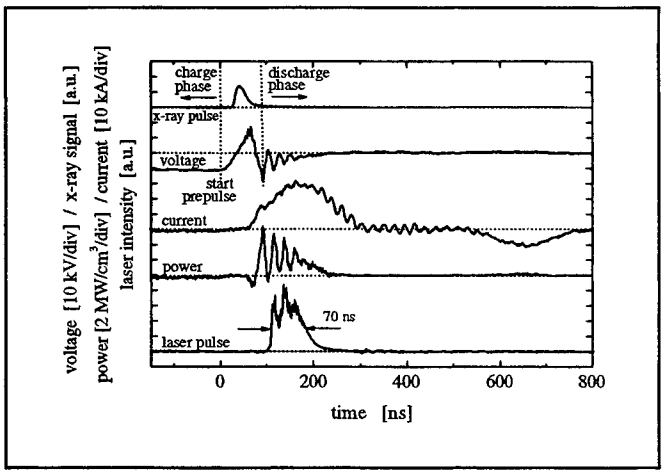


*Fig 11 Temporal behaviour of the x-ray preionisation pulse, voltage across the laser head, current from the main capacitor, power deposition from main capacitor in the discharge and the laser pulse in a gas mixture of helium and 3 mbar $F_2$ at a total pressure of 2 bar. Load voltages: on main capacitor $U_{Cm}$ =12 kV, on prepulse capacitance $U_{Cpp}$ = 20 kV, on the power supply for the X-ray source $U_X$ = 18 kV.*

inductance of the magnetic switch permits the main current to rapidly enter into the discharge as shown in Fig. 11. The oscillations on the voltage after the start of the discharge are induced by current oscillations in the circuit formed by the peaking capacitors, the laserhead inductance and the low impedance discharge. Near the peak of the main current the oscillations have damped out and the actual discharge voltage is measured ($L_H di/dt=0$). A specific peak power deposition in the order of 2 $MW/cm^3$ is calculated at the peak of the main current. After a build-up time of 20 ns a laser pulse of 70 ns (FWHM) is generated. The decay of the laser intensity proceeds at a much faster rate than given by the photon lifetime of the cavity (= 75 ns) indicating that the intracavity losses must be large. The modulation on the laser pulse reflects a modulation on the gain in the presence of large intracavity losses. The modulation on the gain results from oscillations in the power deposition caused by the current from the peaking capacitors. The laser pulse is seen to terminate before the end of the current pulse.

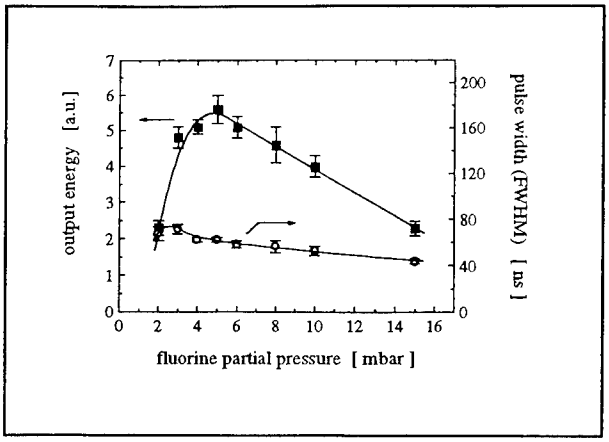


*Fig. 12 The output energy and the pulse width (FWHM) as a function of the $F_2$ partial pressure in a gas mixture with helium at a total pressure of 2 bar.*

In Fig 12 the output energy and the laser pulse width as a function of the fluorine partial pressure in a gas mixture with helium at a total pressure of 2 bar is plotted. The loading voltage on the main capacitor is kept constant at 12 kV. Each point in the graph is an average of 9 measurements. Load voltages: on main capacitor $U_{Cm}$ =12 kV, on prepulse capacitance $U_{Cpp}$ = 20 kV, on the power supply for the X-ray source $U_X$ = 18 kV. Power deposition ≈ 2 $MW/cm^3$. The output energy is proportional to the integral of the laser pulse. An optimum in the output energy is found at 5 mbar $F_2$. The laser pulse width reaches an optimum value of 70 ns (FWHM) at 3 mbar $F_2$ pressure.

In conclusion we have shown that the application of a prepulse-main pulse excitation scheme utilising a saturable magnetic switch in combination with x-ray preionisation has resulted in the generation of long optical pulses from a molecular fluorine laser. Optimum laser pulse durations of 70 ns (FWHM) have been obtained in a gas mixture of helium and 3 mbar fluorine at a total pressure of 2 bar. The laser pulse duration is found to decrease with increasing fluorine pressure and to saturate with increasing current density.

## ACKNOWLEDGEMENTS

The present work has been supported by the Netherlands Technology Foundation STW and by NCLR bv. Kinetic modelling of the discharge pumped ArF and $F_2$ laser and the effects of discharge filamentation has been studied by A.V. Demyanov and A.P. Napartovich at the Troitsk Institute of Innovative and Thermonuclear Research (TRINITI) Troitsk 142092, Moscow Province, Russia

## REFERENCES

[1] Conley, W. FSI Lithography Breakfast Forum, San Francisco, 1999. FSI Lithography Breakfast Forum, San Francisco
[2] Miura, E., Honda, H., Katsura, K., Takahashi, E., and Kondo, K., "Soft X-ray emission from noble gas clusters excited by an ultrashort KrF laser pulse," *Applied Physics B-Lasers and Optics*, vol. 70, no. 6, pp. 783-787, 2000.
[3] Rocca, J. J., "Table-top soft x-ray lasers," *Review of Scientific Instruments*, vol. 70, no. 10, pp. 3799-3827, 1999.
[4] Benschop, J. P. H., van Dijsseldonk, A. J. J., Kaiser, W. M., and Ockwell, D. C., "EUCLIDES: European EUVL program," *Journal of Vacuum Science & Technology B*, vol. 17, no. 6, pp. 2978-2981, 1999.
[5] Dierick, H. G., Van Mellaert, C. E., and Missotten, L., "Histology of rabbit corneas after 10-diopter photorefractive keratectomy for hyperopia," *Journal of Refractive Surgery*, vol. 15, no. 4, pp. 459-468, 1999.
[6] Farah, S. G., Azar, D. T., Gurdal, C., and Wong, J., "Laser in situ keratomileusis: Literature review of a developing technique," *Journal of Cataract and Refractive Surgery*, vol. 24, no. 7, pp. 989-1006, 1998.

[7] Endert, H., Patzel, R., and Basting, D., "Excimer laser: A new tool for precision micromachining," *Optical and Quantum Electronics*, vol. 27, no. 12, pp. 1319-1335, 1995.
[8] Behrmann, G. P. and Duignan, M. T., "Excimer laser micromachining for rapid fabrication of diffractive optical elements," *Applied Optics*, vol. 36, no. 20, pp. 4666-4674, 1997.
[9] Othonos, A., "Fiber Bragg gratings," *Review of Scientific Instruments*, vol. 68, no. 12, pp. 4309-4341, 1997.
[10] Timmermans, J. C. M., "1 kW Industrial excimer laser (308 nm)," *Proc.SPIE*, vol. 3343 pp. 687-691, 1998.
[11] Williams, S. W., Marsden, R. J., Roberts, N. C., Sidhu, J., and Venables, A., "Excimer laser beam shaping and material processing using diffractive optics," *Proc.SPIE*, vol. 3343 pp. 205-211, 1998.
[12] Brittingham, R. A. and Leylek, J. H., "A detailed analysis of film cooling physics: Part IV - Compound-angle injection with shaped holes," *Journal of Turbomachinery-Transactions of the Asme*, vol. 122, no. 1, pp. 133-145, 2000.
[13] Garg, V. K. and Rigby, D. L., "Heat transfer on a film-cooled blade - effect of hole physics," *International Journal of Heat and Fluid Flow*, vol. 20, no. 1, pp. 10-25, 1999.
[14] Hofstra, R. M., "On the optical performance of the long pulse XeCl excimer laser." ISBN 90 365 1241 7, Thesis, University of Twente, ISBN 90 365 1241 7, 1999.
[15] Michels, H. H., Hobbs, R. H., and Wright, L. A., "The electronic structure of ArF and $Ar_2F$," *Chem.Phys.Lett.*, vol. 48, no. 1, pp. 158-161, 1977.
[16] Hoffman, J. M., Hays, A. K., and Tisone, G. C., "High power UV noble gas halide lasers," *Applied Physics Letters*, vol. 28, no. 9, pp. 538-539, 1976.
[17] Burnham, R. and Djeu, N., "Ultra-violet preionized discharge pumped lasers in XeF,KrF and ArF," *Applied Physics Letters*, vol. 29, no. 11, pp. 707-709, 1976.
[18] Feenstra, L., Hoekstra, O. B., Peters, P. J. M., and Witteman, W. J., "On the performance of an ArF and a KrF laser as a function of the preionisation timing and the excitation mode," *Applied Physics B-Lasers and Optics*, vol. 70, no. 2, pp. 231-235, 2000.
[19] Zhupikov, A. A. and Razhev, A. M., "Excimer ArF laser with an output energy of 0.5 J and He buffer gas," *Quantum Electronics*, vol. 27, no. 8, pp. 665-669, 1997.
[20] Miayazaki, K., Hasama, T., Yamada, K., Fukatsu, T., Eura, T., and Sato, T., "Efficiency of a capacitor transfer type discharge excimer laser with automatic preionisation," *J.Appl.Phys*, vol. 60, no. 8, pp. 2721-2728, 1984.
[21] Feenstra, L., Bastiaens, H. M. J., Peters, P. J. M., and Witteman, W. J., "A long pulse discharge excited ArF laser," *IEEE Journal of Selected Topics in Quantum Electronics*, vol. 5, no. 6, pp. 1515-1521, 1999.
[22] Kakehata, M., Uematsu, T., Kannari, F., and Obara, M., "Efficiency characterization of vacuum ultraviolet molecular fluorine ($F_2$) laser (157 nm) excited by an intense electric discharge", *IEEE Journal of Quantum Electronics*, vol. 27, no. 11, pp. 2456-2464, 1991.
[23] Ohwa, M. and Obara, M., "Theoretical evaluation of high-efficiency operation of discharge pumped vacuum-ultraviolet $F_2$ lasers," *Applied Physics Letters*, vol. 51, no. 13, pp. 958-960, 1987.
[24] Lankhorst, F. T. J. L., Bastiaens, H. M. J., Botma, H., Peters, P. J. M., and Witteman, W. J., "Long pulse electron-beam-pumped molecular $F_2^*$ laser," *Journal of Applied Physics*, vol. 77, no. 1, pp. 399-401, 1995.
[25] Bastiaens, H. M. J., "On the long pulse operation of the molecular fluorine laser." Thesis, University of Twente, ISBN 90 365 141 69, 2000.
[26] McKee, T. J., "Optical cavity design for long pulse excimer lasers," *Applied Optics*, vol. 30, no. 6, pp. 635-644, 1991.
[27] Pummer, H., Hohla, K., Diegelman, M., and Reilly, J. P., "Discharge pumped $F_2$ laser at 158 nm," *Optics Communication*, vol. 28, no. 1, pp. 104-106, 1979.
[28] Hooker, S. M., Haxell, A. M., and Webb, C. E., "Influence of cavity configuration on the pulse energy of a high pressure molecular fluorine laser," *Applied Physics B-Lasers and Optics*, vol. 55 pp. 54-59, 1992.
[29] Kakehata, M., Yang, C. H., Ueno, Y., and Kannari, F., "Output characteristics of a discharge pumped $F_2$ laser (157 nm) with an injection seeded unstable resonator", *Journal of Applied Physics* , vol. 74, no. 4, pp. 2241-2246, 1993.
[30] vanGoor, F. A., "Fast rise time X-ray preionization source using a corona plasma cathode," *Journal of Physics D-Applied Physics*, vol. 26, no. 3, pp. 404-409, 1993.
[31] Yamada, K., Miyazaki, K., Hasama, T., and Sato, T., "High power discharge pumped molecular $F_2$ laser," *Applied Physics Letters*, vol. 54, no. 7, pp. 597-599, 1989.
[32] Taylor, R. S. and Leopold, K. E., "Magnetic-spiker excitation of gas discharge lasers," *Applied Physics B-Lasers and Optics*, vol. 59, no. 5, pp. 479-508, 1994.
[33] Makarov, M., "Effect of electrode processes on the spatial uniformity of the XeCl laser discharge," *Journal of Physics D-Applied Physics*, vol. 28, no. 6, pp. 1083-1093, 1995.

# Prospects for high power, high repetition rate industrial excimer lasers

V. Borisov., O. Khristoforov., Yu. Kirykhin., A. Vinokhodov., A. Demin., V. Vodchits, A.Eltzov

State Research Center of Russian Federation Troitsk Institute for Innovation
and Fusion Research (TRINITI)
142092 Troitsk Moscow reg. Russia

**Abstract**

Recent progress in excimer laser technology developed at TRINITI is reported. The key of the technology is a combination of simple reliable UV preionizer based on creeping discharge on surface of a sapphire plate and the compact highly efficient gas flow system. This technology allows to develop very compact, high power, high repetition rate models of excimer lasers capable to deliver stabilized average power up to 500W (XeCl, KrF), 250W (ArF) and realise pulse repetition rate of more then 5 kHz..

**Keywords**: excimer laser, power, high repetition rate

## 1. Introduction

The current and advanced industrial applications of excimer lasers are needed in various combinations of such laser parameters as wavelengths ($\lambda$), pulse energy(E), repetition rate($\omega$). In addition pulse to pulse energy stability, characterised by standard deviation ($\sigma$), is very important.

Today, highest level of a stabilized average power of industrial excimer (XeCl, KrF) laser is about 200W [1]. In principle, to realise higher throughput of process with use of laser an increase of output average power is desirable as the first requirement[1].Increasing the pulse repetition rate in KrF, ArF lasers more 2 kHz, available today [2], is potential need for DUV lithography.

Here we report the results of the development of two perspective models of excimer lasers for industrial application. The first model is oriented on high level of the stabilized average power (500 W for XeCl, KrF and 250W for ArF) and high output energy per pulse. This model is perspective for use mainly for polycrystalline-silicon TFT technology to provide next generation of large size Active Matrix Liquid Crystal Display (AMLCD). The other advanced applications are micromachining, shock hardening, cleaning of large surfaces contaminated with radionuclides.

The second model is intended for use in technology, which demands the high pulse repetition rate with moderate energy per pulse. DUF lithography can be the main application of this model today.

## 2. Model HPEL (High Power Excimer Laser)

In this model the discharge electrodes and gas-flow system are located in the tube with a diameter 0.5m and length 1.2m. The diametrical fan provides a gas velocity (V) of about 45m/s in the interelectrode gap D=3cm. The construction of the laser model allows magnification of D up to 7 cm. In this case V decreases down to 25m/s. The measurements demonstrated , that a fluctuations of a gas velocity along discharge length do not exceed 15 % from the average value.

Changing structure of a gas mixture, interelectrode gap D and discharge width B as well as use of various excitation systems, we could obtain various combinations $\lambda$, Å, $\omega$, with the request of max average power $P = E \times \omega$ for a selected wavelength $\lambda$.

An attractive feature of the created model is the simple and reliable UV preionizer based on creeping discharge on a dielectric surface developed by us earlier [3-4]. Different from corona discharge, which creates low level UV preionization [5], the creeping discharge provides homogeneous, high-power UV preionization, which allows to achieve the output energy in XeCl lasers up to 20 J[3] and the average power of 1kW (10J x 100Hz) [4,6].



XIII International Symposium on Gas Flow and Chemical Lasers and High-Power Laser Conference,
Antonio Lapucci, Marco Ciofini, Editors, Proceedings of SPIE Vol. 4184 (2001)

In case interelectrode gap D > 28 mm , the sapphire plate, on which surface creeping discharge develops, is placed under slotted, grounded electrode, as it was described in detail in [3,6], and for D < 28 mm sapphire plate is located on the side of solid grounded electrode.

The main combinations of parameters obtained for the model HPEL, are indicated in the table 1.

Table 1.

| Model HPEL, combination of possible parameters | | | | | |
|---|---|---|---|---|---|
| Radiating Molecule | XeCl | XeCl | KrF | KrF | ArF |
| Wavelength, nm | 308 | 308 | 248 | 248 | 193 |
| Maximum Pulse Energy, J | 4.6 | 3 | 1 | 0.2 | 0.08 |
| Max. Repetition rate, Hz | 150 | 200 | 620 | 4000 | 4000 |
| Stabilized Average Power, W | 500 | 500 | 500 | 500 | 250 |
| Pulse Duration(FWHM), ns | 67 | 62 | 36 | 28 | 24 |
| Beam Dimensions (typ.,FMHM), mm | 70 x 44 | 60 x 30 | 28 x 8 | 28 x3 | 28 x 2 |
| Pulse to Pulse Energy Stability (σ), % | 1.5 | 1.5 | 1.8 | 2.0 | 2.8 |

As it is seen from Table 1, the model HPEL allows to realise a high level of the average power with different wavelengths of laser radiation and is rather universal to meet requirements of various users of lasers. Modifying the combination of parameters is possible without changing cardinally the base structure of the model.

The model HPEL was tested in a multihour mode of laser operation for various combinations of laser parameters. In particular, the 500W test with XeCl was run continuously for 8 hour with 2,5J per pulse and 200 Hz without change of a gas mixture. The behaviour of output energy E and pulse to pulse energy stability during $10^5$ pulses is shown in Fig..1 with stabilized level of an average power 500W (λ=308nm).

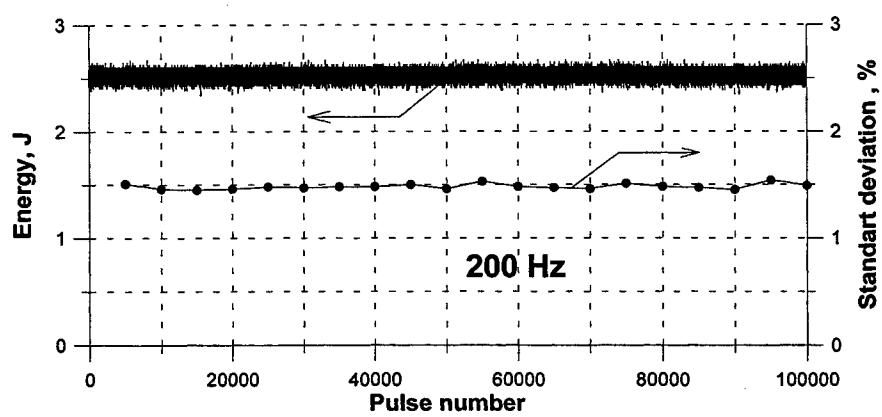


Fig.1 Output energy and pulse to pulse energy stability (σ) versus pulse number in the model HPEL

## 3. Model HRREL (High Repetition Rate Excimer Laser)

The feature of this model is a high gas flow velocity (up to ≈55m/s) at small interelectrode gap (D < 20мм). With this purpose we have been used in a model HRREL a diametrical fan, which could rotated with the velocity up to 4500 rev/min. The electrodes and gas flow system were located in the tube with diameter 0,4 м and length 0,8м. The electrodes have a profile, which provided a discharge width B=2÷3 mm for interelectrode gap 16 ÷ 18 mm.

If in the earlier variants of the module HRREL we used UV preionization by a number of spark gaps located on the side of the electrodes, in final variant of the model we use UV preionization by creeping discharge on a surface of the

sapphire plate. As it was mentioned above, in this model with D=16÷18mm the sapphire plate was located on the side of the solid grounded electrode.

Fig.2 shows the average power P (curves 1,3) and pulse to pulse energy stability σ(curves 2,4) versus the repetition rate in case of using UV preionization by a number of spark gaps( curves 1,2) and in case of using homogeneous along electrodes UV preionization by creeping discharge on a surface of the sapphire plate(curves 3,4) with KrF.

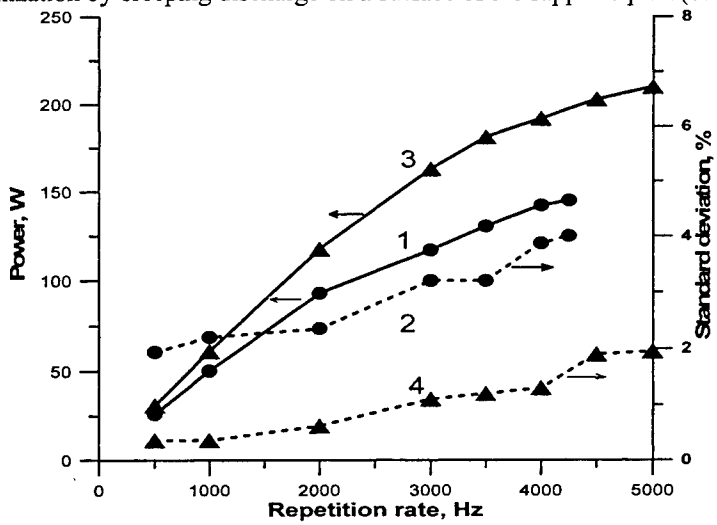


Fig.2. Average power and pulse to pulse stability in model HRRL with KrF

From the curve 2 follows, that with the use UV preionization by spark gaps σ (the curve 2) is changed from 2 % (for ω = 500Hz) up to 4 % (for ω = 4 kHz). The use of homogeneous along electrodes UV preionization by creeping discharge on a surface of the sapphire plate increases both the level of output average power(curve 3) and pulse to pulse energy stability (curve 4). As the curve 4 shows, with UV preionization , based on creeping discharge, σ is changed from 0.4 % (for ω = 500Hz) to 2% for ω= 5kHz).

The comparison of curves 2 and 4 is the evidence of importance of UV preionization homogeneity for reaching good (with less σ) pulse to pulse energy stability .

Fig.3 shows the behaviour of pulse to pulse energy stability(σ) versus repetition rate for various gas flow velocities through discharge.

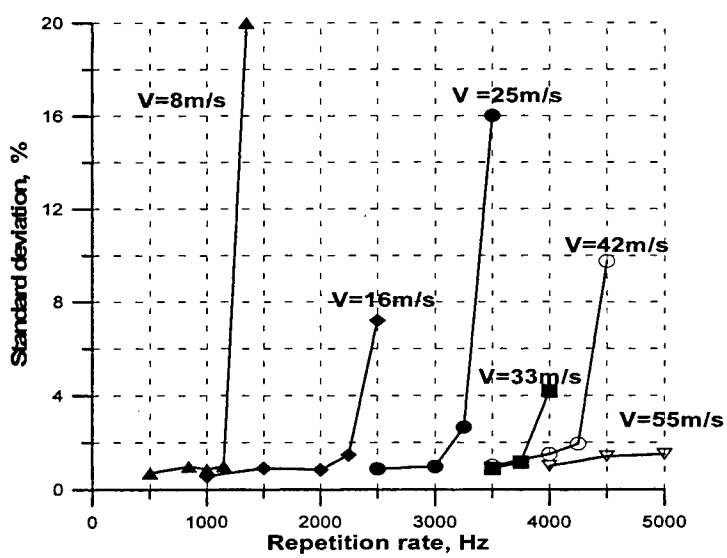


Fig.3. Pulse to pulse energy stability (σ) as function of repetition rate in model HRREL with KrF for various gas flow velocities in interelectrode gap.

Fig.3 demonstrates, that for each V there is a limiting repetition rate $\omega_{lim}$ and if $\omega > \omega_{lim}$, standard deviation ($\sigma$) sharply increases. The observations have shown, that if $\omega > \omega_{lim}$, discharge becomes less homogeneous. It means that the gas flow velocity is not sufficient to provide the needed pulse repetition rate. According to Fig.3, the higher pulse repetition rate $\omega$ is reached with magnification of V and $\omega$= 5kHz with KrF (Fig.2) is reached with the gas flow velocity of about 55m/s.

The average output power (curve 1) and pulse to pulse energy stability $\sigma$ (curve 2) for the case electrical energy storage in capacitor is about 1,9 J for model HRREL with XeF are shown on Fig.4.

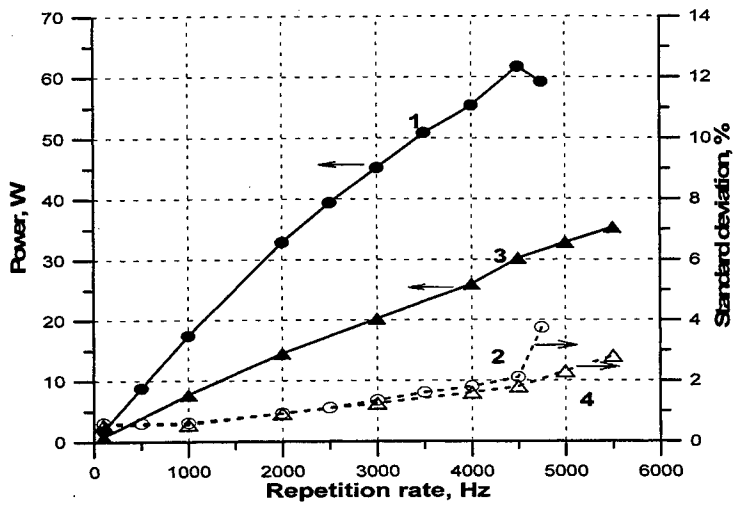


Fig.4. The average power(1,3) and pulse to pulse energy stability $\sigma$ (2,4) versus repetition rate in model HRREL with XeF at storage electrical energy in capacitor - 1,9J (curves 1,2) and 0.95J (curves 3,4).

It is necessary to notice, that the thyratron ТГИ-1000/25, used in the excitation scheme operates at high repetition rate ($\omega$>3kHz) in its extreme mode. To reduce a thyratron load we have reduced storage in condenser electrical energy by two, optimising conditions of generation so that the efficiency of model with XeF has remained constant (≈1%). The curves 3 and 4 on Fig.4 show the average power P and $\sigma$ for the reduced electrical energy(~0.95J)in the condenser by two. From the comparison of a behaviour of curves 1 and 3 on Fig.4 it is seen, that the reduction of the storage electrical energy allows reaching higher repetition rate ( up to 5.5kHz).

The operation with ArF is characterized by higher charging voltage in comparison with KrF and XeF. To reduce the thyratron stress in the excitation scheme, in case ArF we used two thyratrons, which were switched sequentially one after the other, so that repetition rate of laser radiation was twice as large as switching repetition rate for each thyratron.

The average power and pulse to pulse energy stability($\sigma$) as function of the repetition rate for ArF are shown on Fig.5.

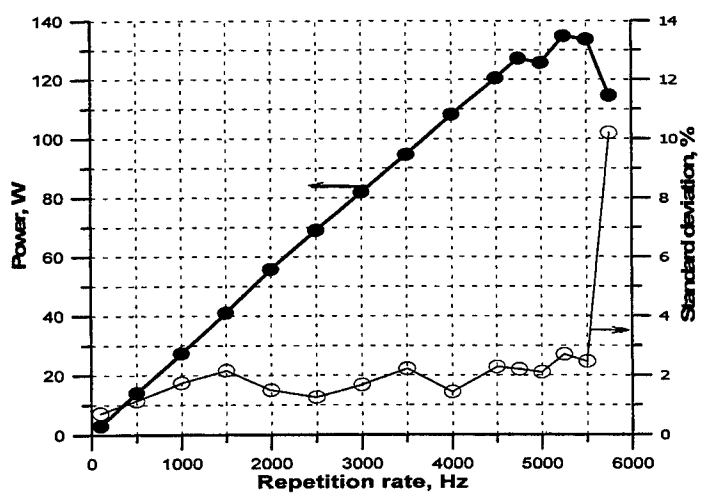


Fig.5.Average power and pulse to pulse energy stability ($\sigma$) in model HRRL with ArF.

It is seen, that model HRREL have allowed to achieve pulse repetition rate up to 5.5 kHz with ArF. The level of pulse to pulse energy stability $\sigma \cong 3$ % at 5.5kHz can be interpreted partially by unstability of operation of the thyratrons related each other and can be reduced with use of the solid state pulser, like as, for example, Lambda Physik used in 1÷2kHz lasers for lithography[2].

## 4. Conclusion

With the trend toward the achievement of higher average power and/or higher pulse repetition rate two model of excimer laser have be developed at TRINITI.

Tests have shown that these models can be brought to the level of the requirements for industrial excimer laser capable delivering stabilized average power of 500W or operating at pulse repetition rate more then 5kHz.

## References


1. M. Fiebig, R. Osmanov, U. Stamm, F.Voss, P. Oesterlin, N.Kobayaashi, B. Fechner, L.Uzuka, "High power excimer laser for high throughput poly-Si annealing", Proc. SPIE, **3888**, pp.464-469,2000.
2. U. Stamm, R. Paetzel, I. Bragin, V. Berger, I. Kleinschmidt, R. Osmanov, T. Schroeder, K Vogler, W.Zschocke, D. Basting, "High repetition rate excimer lasers for DUV lithography", *SPIE* **3679**, pp. 1050-1057,1999.
3. V.Y. Baranov. V.M. Borisov, O.B. Khristoforov, "Wide aperture electric discharge XeCl laser with UV preionization and 20J output energy", *Sov.J.Quantum Electronic*, **17**, pp.978-983 August.1987.
4. V.M. Borisov, O.B. Khristoforov, Yu.B. Kirykhin, S.G. Kuznetsov, Yu.Yu. Stepanov, A.Yu. Vinokhodov, "The kilowatt range high repetition rate excimer lasers". *Proc.SPIE*, **1503**, "Excimer Laser and Applications III", pp. 40-47, 1991.
5. Y. Sato, M. Inoue, S. Fujikawa, Y. Saito, A. Suzuki, K. Haruta and H. Nagai, "Development of a 2 kW XeCl laser with a Surface Corona Preionization Scheme and a Spiker-Sustainer Circuit" *IEEEE, J. of Selected Topics in Quantum Electronics*, **1**, №3, pp.811-824, Sept. 1995.
6. V.M. Borisov, O.B. Khristoforov, Yu.B. Kirykhin, A.Yu. Vinokhodov , A.I. Demin, A.V. Dem'yanov, "Theoretical and experimental investigations of the 1kW XeCl laser with UV preionisation", *SPIE* **2987**, pp.94-104, 1997.

# GARPUN laser experiments on e-beam transportation through Al-Be foil and optical window stability addressed to the NRL rep-rate e-beam-pumped KrF facility

V.D. Zvorykin*, S.V. Arlantsev, V.G. Bakaev, N.V. Morozov, O.V. Rantsev, P.B.Sergeev, G.V. Sychugov, A.Yu. Tserkovnikov

P. N. Lebedev Physical Institute, Russian Academy of Sciences, Leninsky Prospect 53, 117924 Moscow, Russia

S.P. Obenschain, J.D. Sethian

Plasma Physics Division, Naval Research Laboratory, Washington, DC 20375, USA

## ABSTRACT

Two key engineering issues in the development of a KrF laser driver for Inertial Fusion Energy are high transmitting and long life e-beam window and optical laser windows. We have performed experiments with e-beam-pumped KrF laser installation GARPUN on the transport of relativistic e-beams through Al-Be and Ti foils and compared them with Monte Carlo numerical calculations. It was shown that both 50-μm thick Al-Be foils and 20-μm thick Ti foils had equal transmittance of about 75% for ~300 keV, 50 A/cm$^2$, 100 ns e-beams. However in both cases the observed transmission was lower than calculated one. In contrast to Ti foil, whose surface was strongly etched by fluorine, no surface modification or fatal damages were observed for Al-Be foil after ~1000 laser shots and protracted fluorine exposure. It was shown that applied magnetic field of ~1kG significantly reduced electron scattering both across and along laser cell at typical pumping conditions with 1.5-atm pressure working gas. Without magnetic field irradiation of optical windows by scattered electrons resulted in additional transient and residual induced absorption of laser radiation. The analysis of different optical materials for KrF laser windows and coatings has also been done.

**Keywords:** e-beam-pumped high-power KrF laser, Aluminum-Beryllium foil transmittance and stability, e-beam scattering.

## 1. INTRODUCTION

Several physical and engineering issues should be addressed for high-energy large-scale (30-100 kJ) e-beam-pumped KrF lasers in order that they can meet the requirements for Inertial Confinement Fusion Energy power Plants[1]. These are efficient and reliable operation at 5-Hz repetition rate and up to $2*10^8$ laser shots between major maintenance intervals. To establish the key technologies for the IFE KrF driver a relatively small and manageable repetition-rate prototype ELECTRA is presently under construction and investigation at the Naval Research Laboratory (NRL) [2]. It has an active volume of 30*30*100 cm and is pumped by two counter-propagating 110 kA, 500 kV, 100 ns e-beams that are guided by a magnetic field. It will operate with 5 Hz, and have a 700 J output. Two problems to be solved at ELECTRA laser have been recently studied at single-pulse GARPUN [3-5] and EL-1 [6] KrF lasers at Lebedev Physical Institute (LPI) and are reported in this paper.

In KrF modules high-current relativistic e-beams of a large cross section are passed throughout vacuum-tight foil windows from vacuum diodes into a laser cell to pump a fluorine-containing working gas. This foil window, being arranged together with a foil-support structure (usually called as "hibachi") should have a transmittance of about 80-90%, high mechanical strength to withstand to a steady pressure difference and its sudden rise during e-beam energy release in a gas. Titanium foils or Kapton (polyimide) films typically have been used in single-pulse large KrF installations [7-11]. But they have a limited lifetime from several tens to hundreds shots. They are not suitable for a repetition-rate machine because of low heat conductivity and tend to allotropic transformation at elevated temperatures. Until recently only HOVAR foil based on Fe alloy was chosen for tests at repetition-rate KrF laser facility [12]. However, Aluminum-Beryllium (Al-Be) compounds might

* Correspondence: E-mail: zvorykin@sci.lebedev.ru; Tel.: (095)-132-6739; Fax: (095)-132-0425

XIII International Symposium on Gas Flow and Chemical Lasers and High-Power Laser Conference, Antonio Lapucci, Marco Ciofini, Editors, Proceedings of SPIE Vol. 4184 (2001)

be the best choice for the foil window due to high strength (compared with Ti), excellent heat conductivity, and low e-beam stopping [13]. Another key problem for the IFE KrF laser driver is the protection of output optical windows against fluorine etching, scattered energetic electrons and bremsstrahlung X-rays. The escapement of fast electrons onto optical windows could induce additional transient [14-17] and residual absorption of laser radiation [18], and thus decreasing total efficiency and durability of KrF laser driver operation.

## 2. E-BEAM TRANSPORTATION THROUGH Al-Be FOIL

Comprehensive investigation of Al-Be foil has been carried out with the e-beam-pumped large-aperture GARPUN amplifier (16*18*100 cm) and BERDYCH preamplifier (10*10*100 cm) modules. The Al-Be foil was manufactured by multi-stage hot rolling and then annealing samples of heterogeneous alloy. These foils are by weight 50% aluminum and 50% beryllium with an average density of 2.2 g/cm$^3$ and total thickness 50 μm. For safe handling a 2-μm aluminum layer is laminated its both sides. Direct comparison of transparency of 50-μm thickness Al-Be foil and the standard 20-μm Ti foil has been done with BERDYCH using Faraday cup measurements (Fig.1). An e-beam of ~50 A/cm$^2$ current density and ~100 ns pulse duration was generated in a vacuum diode and injected into laser chamber perpendicular to the axis. An external pulsed magnetic field of ~0.65 kG was applied to prevent e-beam pinching and scattering. The electron beam was produced by a 7-stage Marx generator with (3.0 kJ energy storage at 400 kV), which charged a water-filled 7.6 Ω Blumlein pulsed forming line. The output voltage was ~350 kV voltage. The foils were supported by the hibachi structure, which consisted of ribs 3-mm wide and 6-mm thick that were separated by free gaps of 27-mm width and 100-mm height. The measured transparency of the hibachi was 83%. It was less than 90% geometric transparency presumably due to transverse components of electron velocity [19]. Both Al-Be and Ti foils demonstrated equal transmittance of 75±2%.

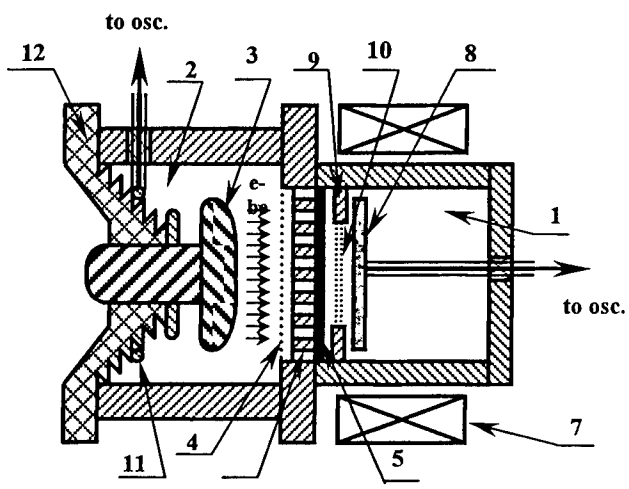


**Fig.1.** Cross section of BERDYCH module arranged for e beam transport measurements: 1-laser chamber; 2-vacuu diode; 3-cathode; 4-anode grid; 5-foil; 6-hibachi; 7-solenoid 8- Faraday cup; 9- stops; 10- additional foil; 11- Rogowsk coil; 12- bushing.

The Monte Carlo method, which has been used earlier in calculations of e-beam pumping of GARPUN laser [20], was applied to analyze the experiments. The calculated foil transmittance decreased rapidly from 100 to 91% when electron energy $\varepsilon_e$ was varied from 400 down to 200 keV. A wide energy distribution of electrons in the initial e-beam in the diode might be a cause of the discrepancy, as low-energy electrons would be absorbed by the foil. This was confirmed in experiments: transmitted e-beam current was measured as a function of the total thickness of additional Ti foils set between the main foil and the Faraday cup. The observed linear decrease in the transmitted current with foil thickness could not be explained if the electrons were assumed to be monoenergetic. On the other hand, the observed distribution could be explained if the electron energies were assumed to be distributed uniformly in the range $\varepsilon_e$=250-350 keV, having a mean value $\langle\varepsilon_e\rangle$=300 keV.

The durability of Al-Be foils was determined in a prolonged run of single-pulse experiments lasting up to 1000 shots. We didn't achieve foil's failure neither at preamplifier nor at amplifier modules. It is significantly higher than mean lifetime of usual Ti foils, which was at most 200 shots. After these series both foils have been examined visually with an optical microscope. In contrast to Ti foil, whose surface was strongly modified by fluorine etching, no noticeable changes were observed on Al-Be foil surface, even after a protracted fluorine exposure and laser operation. This evidenced that $AlF_3$ substance the most likely appeared in chemistry of laminating Al layer with fluorine-containing working gas mixture of KrF laser was stable enough to consequent fluorine action.

## 3. DISTRIBUTION OF SCATTERED ELECTRONS IN LASER CHAMBER

The main GARPUN module [19, 20] with dimensions of laser chamber 19×22×140 cm something bigger than an active volume was arranged to measure the distribution of scattered electrons in conditions typical for a large-aperture e-beam-pumped KrF laser amplifier. Two counter-propagating e-beams of area 12×100 cm and with current density 50 A/cm$^2$ were

coupled into the chamber from opposite sides throughout vacuum-tight 20-μm Ti or 50-μm Al-Be foils. The foils were supported by the hibachi structure having the ribs of 2-mm width, 10-mm thickness and 8-mm inter-rib gaps. The e-beams were guided by a pulsed magnetic field of inductance $B$~ 1 kG. The experiments have been also performed without magnetic field in order to understand its influence on e-beam scattering. The pulses of 350 kV accelerating voltage and 120 ns duration were delivered to a pair of cathodes in each vacuum diode by four water-filled Blumlein forming lines pulse-charged by Marx generator with 14 kJ storage energy. The energy fluence of the scattered electrons, as measured by calorimeters at two different distances along laser cell axis (Fig.2) revealed a great discrepancy with the numerical modeling

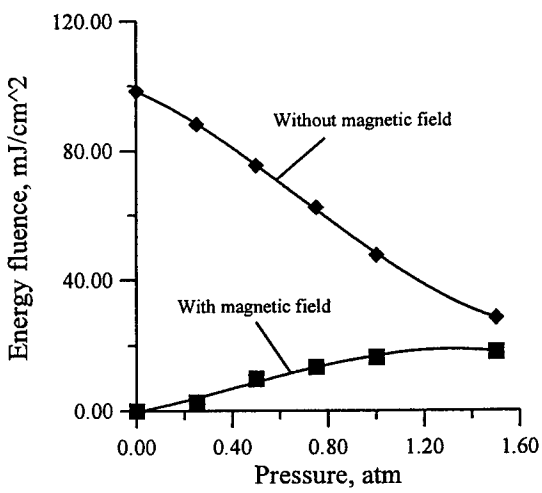


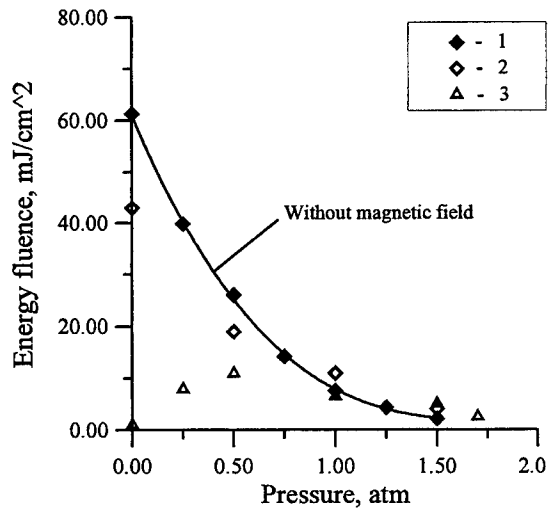


(2) that assumes the electrons are scattered only by the foils or the gas. Multiple passages of electrons from one vacuum diode into the laser chamber, then into another vacuum diode, and then once again in opposite direction were considered. Such regime would take place if electrons range in a gas will exceed the dimensions of laser chamber. It might be not only at low gas pressures, but if one makes electron energy too high in order to uniform a specific pumping power across laser chamber. In this multi-passage case a mean scattering angle would increase and additional significant heat loading of the foils would appear due to absorption of decelerated electrons. When additional e-beam scattering without magnetic field guiding was also taken into account by introducing an initial angular distribution of $\Delta\alpha$=45° to the electrons (3) good qualitative agreement with experimental results (1) was obtained in Fig.2. The same Monte Carlo code has been applied to simulate analogous distributions for the NRL ELECTRA repetition-rate laser. It was shown that the amount of scattered electrons fell down rapidly with increasing magnetic field. The laser gas pressure was varied over the optimal pumping range 1.2-1.8 atm and was found to affect not significantly the electron scattering.

## 4. OPTICAL MATERIALS FOR KrF LASER WINDOWS

Several materials transparent for UV laser radiation at λ=248 nm wavelength such as fused silica ($SiO_2$), calcium fluoride ($CaF_2$), magnesium fluoride ($MgF_2$), and synthetic leucosapphire ($Al_2O_3$) have been tested for either optical windows or AR coatings (see table 1).

**Table 1. Parameters of optical materials for KrF lasers**

| Optical material | Price, $/kg | Micro-hardness, GPa | $E_g$, eV | $\alpha$, $cm^{-1}$ | $\beta_1$, cm/GW | $\beta_2$, cm/GW | $\gamma$, $cm^2$/GW |
|---|---|---|---|---|---|---|---|
| $CaF_2$ | 400 | 1.68 | 10 | 0.02 | <0.008 [21] | <0.1 [24] | 136±27 [16] |
| $MgF_2$ | 600 | 4.5 | 11 | .007 | <0.001 [21] | 0.05±0.02 [24] | 150±20 [16] |
| $SiO_2$ (KU-1) | 200 | 7.4 | 7.6 | 0.01 | 0.045 [21] 0.08 [22] | 0.5±0.1 [24] | 4.6±1.2 [16] |
| $Al_2O_3$ | 600 | 20.0 | 9.4 | 0.01 | 0.27* [23] | 2±1 [25] | 0.25±0.07 |

$\alpha$ – absorption coefficient;
$\beta_1$ - two-photon absorption coefficient for ps laser pulses;
$\beta_2$ - nonlinear absorption coefficient for ~100 ns pulses;
* - was measured at 266 nm wavelength;
$\gamma$ - e-beam induced absorption coefficient.

Our experiments (see also [6, 14-17, 21-25]) confirmed that the most common synthetic fused silica might be the best material, provided one can establish an AR coating that will prevent substrate etching by fluorine. Being relatively low cost and available in large-size samples (≥1-m dia.), it demonstrated low absorption of UV light induced under simultaneous X-ray and e-beam irradiation. Although $Al_2O_3$ and $MgF_2$ are stable to fluorine, they are unlikely to be suitable for windows, because of their high cost, the difficulty of manufacturing and polishing of large-size samples, and birefringence. But they both are very attractive as coating materials [17]. Besides $SiO_2$, only $CaF_2$ is a promising material for the windows. It is absolutely resistant to fluorine, relatively cheap and might be manufactured of a large size. Transient and residual absorption in $CaF_2$ samples induced by fast electrons being measured in comparison with distribution of scattered e-beams revealed a linear dependence between induced optical thickness and specific power density of e-beam irradiation. It was shown that induced absorption of laser radiation in $CaF_2$ optical windows might be fully eliminated in e-beam pumping scheme with magnetic field guiding. Optimization of any e-beam-pumped KrF module will be a compromise between absorption of laser radiation in unpumped region by molecular fluorine and e-beam-induced absorption in optical windows.

## 5. CONCUSIONS

The experiments have been performed with single-pulse large-aperture e-beam-pumped GARPUN KrF laser installation to investigate Aluminum-Beryllium foil transmittance and stability to multiple high-current e-beam irradiations, as well as to protracted fluorine action. E-beam scattering in the laser chamber in typical pumping conditions with and without a guiding magnetic field was also investigated being a cause of additional losses of laser radiation in optical windows. Both problems are related to the development of the repetition-rate prototype of KrF laser driver for the Inertial Fusion Energy scheme. Such prototype, being constructed at the Naval Research Laboratory aimed at the research and development of key technologies, which would allow e-beam-pumped KrF laser to operate with output energy of tens kJ at 5-Hz repetition rate.

## ACKNOWLEDGEMENTS

We are grateful to E.V. Polyakov and S.I. Sagitov for assistance. This work was supported by Russian Foundation of Basic Research under Project No. 98-02-16993 and by the Naval Research Laboratory under Contract No. N68171-99-M-6338.

## REFERENCES

1. I.N. Svyatoslavsky, M.E. Sawan, R.R. Peterson, et al. *Fusion Technology*, **21**, p. 1470, 1992.
2. J.D Sethian, S.P. Obenschain, R.H. Lehmberg, M.W. McGeoch *Fusion Engineering and Design*, **44**, p. 371, 1999.
3. N.G.Basov, V.G.Bakaev, et al. *Sov.J. Quant. Electron.* **21**, p. 816, 1991.
4. N.G.Basov, V.G.Bakaev, et al. *J. Sov. Laser Res.* **14**, p. 326, 1993.
5. V.D. Zvorykin and I.G. Lebo *Laser and Particle Beams*, **17**, p. 69, 1999.
6. P.B. Sergeev *J. Sov. Laser Res.* **14**, p. 237, 1993.
7. L.A. Rosocha, K.B. Riepe *Fusion Technology*, **11**, p. 576, 1987.
8. Y. Owadano, et al. in *Plasma Physics and Controlled Nuclear Fusion Research 1994*, vol. **3**, p. 121, International Atomic Energy Agency, Vienna, 1996.
9. E.J. Divall, C.B. Edwards, G.J. Hirst, et al. *J. Mod. Opt.* **43**, p. 1025, 1996.
10. J.D. Sethian, S.P. Obenschain, K.A. Gerber, et al. *Rev. Sci. Instrum.* **68**, p. 2357, 1997.
11. J.D. Sethian, C.J. Powley, S.P. Obenschain, et al. *IEEE Transactions on Plasma Science*, **25**, p. 231, 1997.
12. E. Takahashi, I. Okuda, Y. Matsumoto, et al. in *Book of Abstracts of International Forum on Advanced High-Power Lasers and applications AHPLA' 99*, paper 3886-49, p. 71.
13. *Beryllium science and Technology*, Plenum Press, New York, 1979.
14. V.S. Barabanov, N.V. Morozov, P.B. Sergeev *J. of Non-crystalline Solids*, **149**, p. 102, 1992.
15. A.V. Amosov, V.S. Barabanov, et al. *Quant. Electron.* **23**, p. 939, 1993.
16. V.S. Barabanov, P.B. Sergeev *Quant. Electron.* **25**, p. 717, 1995.
17. E.N. Eliseev, E.I. Fadeeva, V.D. Zvorykin, et al. *J. of Optical Technology*, No. 2, p. 40, 1996.
18. E.J. Divall, G.J. Hirst in *Rutherford Appleton Laboratory Report RAL-93-031*, p. 143, 1993.
19. V.G. Bakaev, A.D. Vadkovskii, E.O. Danilov, et al. *Quant. Electron.* **24**, p. 5, 1994.
20. S.V. Arlantsev, E.A. Grigor'yants, A.D. Vadkovskii, et al. *Quant. Electron.* **24**, p. 223, 1994.
21. A.J. Taylor, R.B. Gibson, J.B. Roberts. *Opt. Lett.* **13**, p. 814, 1988.
22. T. Tomie, I. Okuda, M. Yano *Appl. Phys. Lett.* **55**, p. 325, 1985.
23. P. Liu, W.L. Smith, H. Lotem et al. *Phys.Rev.* **B17**, p. 4620, 1978.
24. V.S. Barabanov, N.V. Morozov., S.I. Sagitov., P.B. Sergeev. *J. Sov. Laser Res.* **14**, p. 294, 1993.
25. N.V. Morozov., V.M. Reiterov, P.B. Sergeev *Quant. Electron.* **29**, p. 979, 1999.

# Long-pulse Efficient XeCl Laser with Pre-pulse Formed by an Inductive Energy Storage

Aleksei N.Panchenko[1], Victor F.Tarasenko, and Evgenii H.Baksht

High Current Electronics Institute, Akademicheskii ave., 4, Tomsk, Russia, 634055

## ABSTRACT

An efficient electric-discharge XeCl laser is developed, which is pumped by a self-sustained discharge with a pre-pulse formed by a generator with an inductive energy storage and a semiconductor opening switch on a basis of SOS diodes. An output energy up to 800 mJ, total pulse length up to 450 ns, and a total laser efficiency of 2.2% were attained using a spark UV preionization.

**Key words:** inductive energy storage, XeCl laser, long-pulse, high-efficiency

## 1. INTRODUCTION

The development of efficient long-pulse discharge lasers on rare gas halide molecules is associated with solution of the following two problems. First one consists in formation and sustaining of an uniform volume discharge in a halogen containing gas mixtures. Second one is improvement of the efficiency of the energy transfer from a pumping generator to this volume discharge plasma.

First discharge XeCl-laser with pulse duration of ~200 ns was developed using a pulse forming line and X-ray preionization. Laser energy up to 2 J was obtained[1]. In 1984 we had demonstrated the possibility to extend pulse duration of discharge XeCl-laser up to 1 μs[2]. Non-steady-state excitation mode which involves specific build-up and decay rates of the discharge current had been suggested to improve discharge stability[3]. This pumping mode allowed us to obtaine 400 ns XeF-laser pulses and duration of spontaneous emission of KrCl* molecules up to 500 ns.

Double discharge pumping circuit[4] providing complete energy transfer to the discharge plasma is necessary for development of efficient discharge excimer laser. In this circuit a high-voltage generator with low stored energy ignites volume discharge while a low-voltage storage deposits main part of pumping energy in the impedance matched mode. This pumping technique with the use of a pulse forming line allowed to extend pulse duration of XeCl discharge laser up to 1,5 μs[5]. Radiation energy of 100 mJ and the laser efficiency of 0,44% were obtained. Besides a pulse length of ~ 800 ns was obtained for an energy of 500 mJ and an efficiency of ~ 2% (relative to the energy stored in the PFL). In addition, when the PFL was replaced by two 0.25-μF capacitors, the laser pulse length was ~ 500 ns for an energy of 600 mJ and an efficiency of 1.3%.

The aim of this work is to develop an efficient long-pulse XeCl laser with a spark preionization featuring high reliability and a long life expectancy. The laser is pumped using a double discharge with a pre-pulse formed by a generator with an inductive energy storage and semiconductor opening switch made on the base of industrial SOS-diodes. Notice that earlier[6-7], we used this method of forming a pre-pulse to pump a $CO_2$ laser, wherein the resistance of a discharge plasma was significantly higher than in a XeCl laser.

## 2. EXPERIMENTAL

The design of a long-pulse XeCl laser is shown in Fig. 1. The laser electrodes were located in a cylindrical chamber separated from the pump generator by a plastic insulator. The laser active volume was $V = 2.5 \times 4 \times 80\ cm^3 = 800\ cm^3$ for an inter-electrode gap d = 4 cm. The pre-ionization was accomplished by the radiation of 72 spark gaps evenly distributed on either side of the cathode. The pump generator consisted of a storage and a peaking capacitances assembled of the KVI type ceramic capacitors. Their capacitances were varied in the ranges 200-320 nF and 2.4 –3,5 nF, respectively. The storage

[1] Correspondence: Phone: (3822) 259-392; Fax: (3822) 259-410; E-mail: alexei@loi.hcei.tsc.ru

XIII International Symposium on Gas Flow and Chemical Lasers and High-Power Laser Conference,
Antonio Lapucci, Marco Ciofini, Editors, Proceedings of SPIE Vol. 4184 (2001)

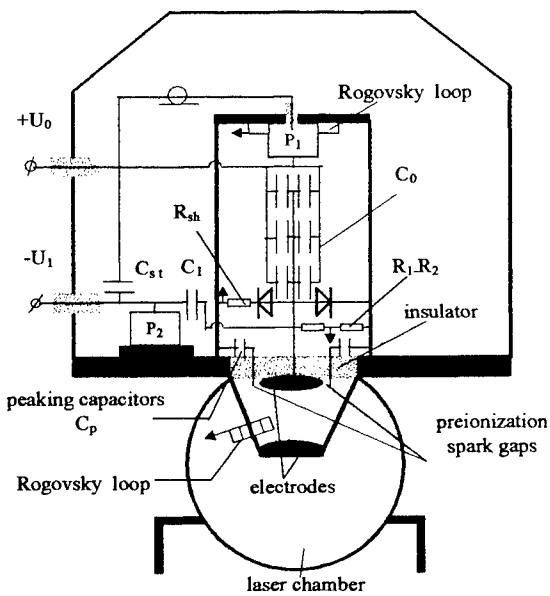


Fig.1
Schematic diagram of XeCl - laser with prepulse formed by an inductive energy storage with SOS-diodes. $C_0$ = 200-240 nF- storage capacitors, $C_1$ = 14 nF - the capacitof for pumping SOS-diodes in the forward direction, $C_{st}$ = 1,5 nF - switching capacitor, $R_1$-$R_2$ - voltage divider, $R_{sh}$ - shunt. $P_1$ - $P_2$ - spark gaps.

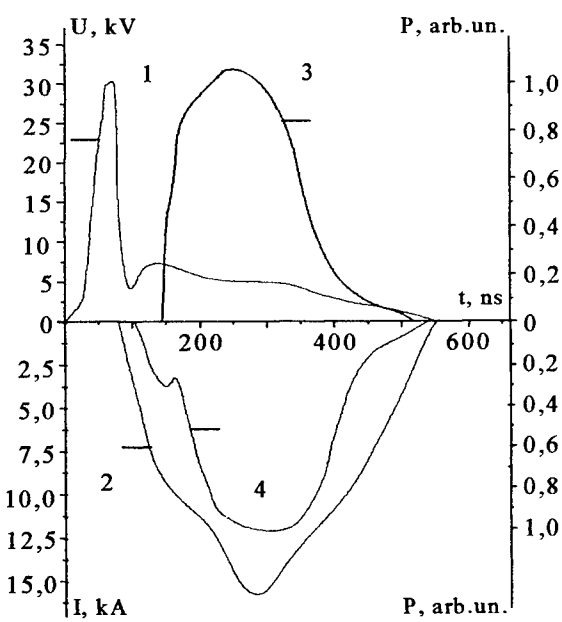


Fig.2
Waveforms of the voltage across the laser gap (1), discharge current (2) and laser radiation (3, 4). Gas mixture of the Ne : Xe : HCl = 3 Atm : 12 : 1,5 Torr composition is used. $C_0$ = 240 nF, $L_0$ = 100 nHn. $U_0$ = 16 kV, $U_1$ = 15 kV. Transmittance of the output mirror is 80% (3), 30% (4).

capacitor was charged to a voltage $U_0 \approx 2U_{ss}$ = 15 - 18 kV, where $U_{ss}$ is the voltage during the quasi-stationary phase of the discharge. Ten special-purpose semiconductor opening (SOS) diodes placed in parallel with the peaking capacitors were used as a semiconductor current interrupter. Maximal opening current of this SOS diode is as high as 2 kA, the response time is 10-20 ns, and the pulse repetition rate amounts to 1 kHz with oil cooling. To run the diodes as current interrupters, a current of 100 - 500 A was passed through each diode in the forward direction for 500 ns from a driving capacitor $C_1$ = 14 - 45 nF charged to the voltage $U_1$=10-30 kV and triggered by the spark gap $P_2$. The inductance of the $C_1$ capacitor circuit was 1.8 μHn. The minimum energy required to control the diodes did not exceed 5% of the energy stored in the $C_0$ storage capacitor. After triggering the $P_1$ spark gap, the reverse current from the $C_0$ storage capacitor began to flow through the diodes. The current attained the critical value[8] ~ 100 ns later and the diodes began to open and interrupted this current. At the instant of current interruption by the SOS diodes, across the laser gap there appeared a high voltage pre-pulse with an amplitude U = LdI/dt ~ 50 kV (where L = 0.11 μH is the inductance of the discharge circuit of the $C_0$ storage capacitor) which formed the volume discharge. Therewith inductance of the discharge circuit of the storage capacitor serves as the inductive energy storage element. The storage capacitor next discharged into the gas-discharge load in a nearly matched mode. Note that the SOS diodes can be placed both in parallel and in series to obtain the required break current and the pre-pulse amplitude. In this case, the triggering of the diodes is synchronized automatically.

The laser resonator was formed by a totally reflecting (100%) mirror and mirrors with dielectric coatings with the reflectivity from 20 to 80% at λ = 308 nm.

We measured the amplitude-time characteristics of voltage, current, and laser radiation pulses. An IMO-2N calorimeter was employed to measure the radiation energy. The shape of the radiation pulses was determined with a coaxial FEK-22SPU photocell. The pulses of the discharge current, the current through the SOS diodes, and the voltage across the laser discharge gap were recorded using a Rogowski loop, an ohmic shunt, and a voltage divider. S8-14 or TDS-220 oscilloscopes were employed to measure the parameters of the electric pulses.

## 3. EXPERIMENTAL RESULTS AND DISCUSSION

Mixtures with the neon buffer gas at pressures 1 - 3.5 bar were used in experiments. A maximum output energy was attained for the ratio Xe : HCl = 10 : 1 and a partial pressure of hydrogen chloride of 1.5 Torr. The increase in the content of HCl resulted in a quick discharge contraction and reduced the radiation pulse duration.

Fig.2 shows the oscilloscope traces of the pulses of the voltage across the discharge gap, discharge current of the storage capacitor $C_0$ through the laser gap, and the output laser power. The inductive storage provided a fast build-up of the voltage

across the laser gap, with the pulse rise time ~ 50 - 80 ns. The rate of rise of the voltage pulses and their amplitude were proportional to the forward current through the opening diodes determined by the charging voltage $U_1$ and the $C_1$ capacitance. In particular, as $U_1$ increased from 10 to 30 kV, the breakdown voltage increased from 30 to 36 kV, while the rise time decreased from 80 to 50 ns. Similar result was obtained with higher $C_1$. The increase in $U_1$ caused the increase in the diode opening current. As this takes place, a progressively larger fraction of the energy accumulated in the $C_0$ storage capacitor is spent to the formation of the high-voltage pre-pulse. On the one hand, this improves the conditions for the discharge formation and augments its stability, but on the other hand, the energy deposition from $C_0$ is reduced resulting in decrease of the laser output. A maximum energy and length of the laser pulse were obtained for $U_1$ = 15 kV. The length of the laser pulse at half maximum (FWHM) was 210 ns, and its total length was ~ 450 ns. Radiation pulse began 30-50 ns later the discharge gap breakdown and continued throughout the excitation pulse. This means that the discharge formed by the inductive energy storage is quite homogeneous.

The laser energy versus output mirror reflection is shown in Fig.3. When the resonator Q-factor was increased, the output pulse started earlier and its total duration increased. However, the laser energy began to fall as the mirror reflection coefficient R became higher than 30%.

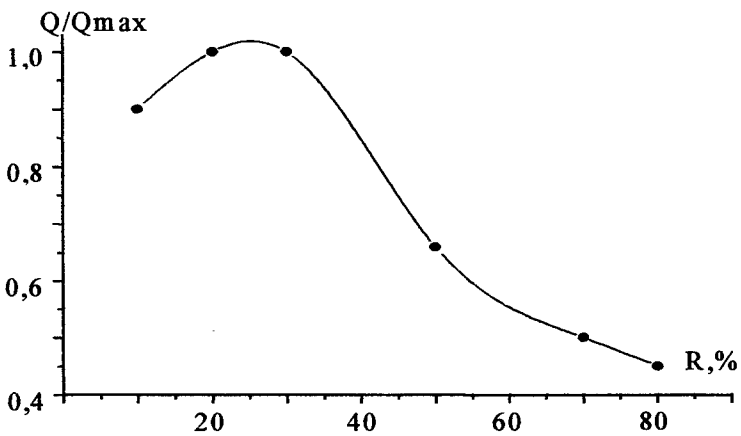


Fig.3
The laser energy as a function of the output mirror reflectivity

In our experiments, the charging voltage of the storage capacitor was varied from 15 to 18 kV. This is somewhat higher than the $2U_{ss}$ for the gas mixture in use. However, under optimal operating conditions, approximately 10% of the energy accumulated in the $C_0$ storage capacitor is spent to form the pre-pulse and laser discharge. For this reason the voltage across $C_0$ lowers by the time of breakdown of the laser gap, and the storage capacitor discharges in the regime close to the matched one. It is significant that the current of the storage capacitor flows, during the second half-period, through the SOS diodes rather than through the discharge gap. This precludes the formation of channels after change of polarity of the discharge current and reduces the erosion of the electrodes.

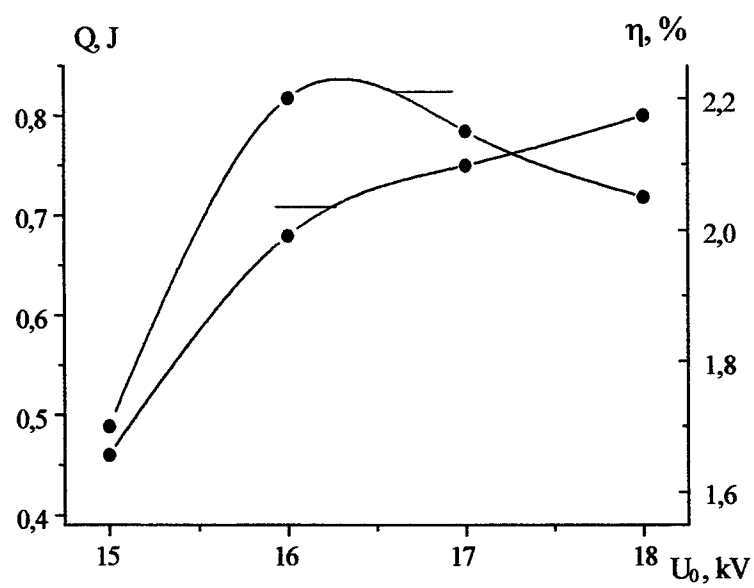


Fig.4
Output energy and total laser efficiency versus charging voltage of the storage capacitor $U_0$. $C_0$ = 240 nF, L = 100 nHn. Gas mixture of the Ne : Xe : HCl = 3 Atm : 12 : 1,5 Torr composition is used. $C_1$ = 14 nF, $U_1$ = 15 kV. Transmittance of the output mirror is 80%.

Output energy of 600 mJ and total laser efficiency of 2% were obtained with $C_0$ = 200 nF. Notice that in our experiments input electric power was about 100 kW/cm$^3$. So, an increase of the storage capacitor $C_0$ can result in better laser parameters. Increase of $C_0$ from 200 nF to 240 nF improved the laser energy and total efficiency. Output energy and the laser total efficiency versus the charging voltage of the storage capacitor $C_0$=240 nF are shown in Fig. 4. As the charging voltage increased, the output energy also increased to become as high as 800 mJ. The laser efficiency attained a maximum of 2.2% for $U_0$ = 16 kV. Then the efficiency began to fall because of higher impedance mismatching.

Further increase of $C_0$ to 340 nF did not give better laser efficiency. In that case pumping pulse duration became as long as 500 ns while total optical pulse duration was not longer 400 ns due to discharge constriction.

As was demonstrated earlier[6] inductive generator allows to short rise-time of the discharge current pulse and increase excitation power. This effect is achieved at high value of the diode opening current which is determined by the driving capacitor $C_1$ and its charging voltage $U_1$. Experiments were made with $C_1$ = 45 nF charged to 30 kV and the results obtained are shown in Fig.5. Leading peak of the current in the laser gap with very short rise-time is determined by joint discharge of the peaking capacitors $C_p$ and the circuit inductor L. Notice that after current interruption the opening current had to pass through the laser gap. In the first instant the circuit inductor L switches the opening current on the laser gap. That current can be higher than the discharge current of the storage capacitor. Besides peaking capacitor charged to high voltage gives short intensive current pulse. Significant sharpening of the pumping power was achieved during this current peak. In this case laser pulse had noticeable peak, as well and the laser oscillation starts within 20 ns after the one-set of the pumping pulse and lasts ~400 ns. Taking into account the peak the laser pulse duration (FWHM) is extended to 260 ns at $U_0$ = 16 kV and to 300 ns at $U_0$ = 12 kV.

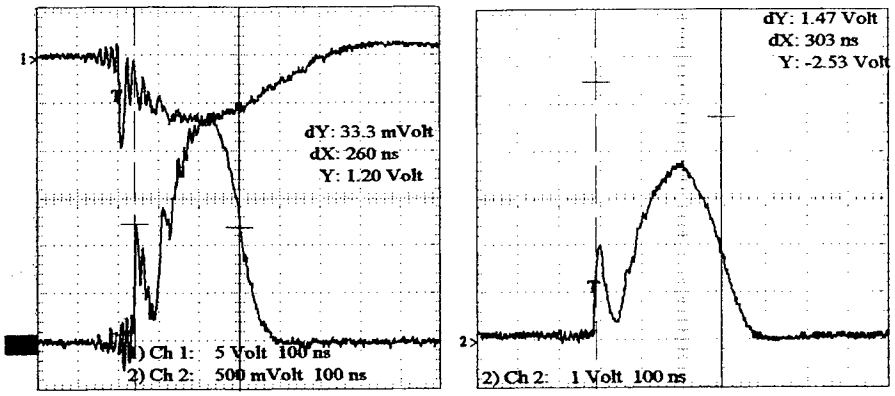


Fig.5
Oscilloscope traces of current through the laser gap (top) and laser pulses (bottom), $U_0$=16 kV (left) and $U_0$=12 kV (right). $C_1$=45 nF, $U_1$=30 kV, $C_0$=320 nF, $C_p$=3,45 nF. Output mirror reflectivity is 50%. Gas mixture of the Ne : Xe : HCl = 3 Atm : 12 : 1,5 Torr composition is used.

## 4. CONCLUSION

We have developed an efficient electric-discharge XeCl laser pumped by a double discharge, wherein the pre-pulse is formed by a generator with an inductive energy storage device and a semiconductor opening switch made on a basis of industrial SOS diodes. An output energy up to 800 mJ, a total pulse length up to 450 ns, pulse length (FWHM) of 210 ns, and a total laser efficiency of 2.2% were obtained. The laser pulse duration (FWHM) can be extended to 300 ns due to sharpening of input power by the inductive energy storage. These parameters were obtained using a reliable UV preionization from sparks. The elaborated inductive generator can also be applied to pump large-aperture and repetitively pulsed exciplex lasers.

## REFERENCES


1. J.I.Levatter, K.L.Robertson, and S.-C. Lin, "Long pulse behavior of the avalanche/self-sustained discharge pumped XeCl laser", *Appl.Phys.Lett.* **39**, pp.297-299, 1981.
2. S.V. Mel'chenko, A.N.Panchenko, and V.F. Tarasenko, "Discharge XeCl-laser with radiation pulse duration of 1 μs", Kvant. Electron. **11**, pp.1490-1492, 1984.
3. M.I.Lomaev, S.V. Mel'chenko, A.N.Panchenko, and V.F.Tarasenko, "Non-steady-state excitation mode of discharge excimer lasers", Izv. AN SSSR, Physics, 48, pp. 1385-1388, 1984.
4. W.H.Long, J.Plummer, E.A.Stappaerts, et.al., "Efficient discharge pumping of an XeCl laser using a high-voltage prepulse", *Appl. Phys. Lett.* **43**, pp. 735-737, 1983.
5. R.S. Taylor, and K.E.Leopold, "Ultalong optical-pulse corona preionized XeCl laser", *J.Appl.Phys.* **65**, pp.22-29, 1989.
6. E.H.Baksht, A.N.Panchenko, and V.F.Tarasenko, "Discharge lasers pumped by generators with inductive energy storage", *IEEE Journal of Quantum Electronics,* **QE-35**, pp.261-265, 1999.
7. E H.Baksht, V.M. Orlovskil, A.N.Panchenko, and V. F. Tarasenko, "Efficient discharge $CO_2$-laser with pre-pulse formed by a generator with inductive energy storage", *Tech. Phys. Lett.* **24** (2) pp.148-151, 1998.
8. S.N. Rukin, "Generators of powerful nanosecond pulses with semiconductor opening switches", *Prib. Tekh. Eksp.* No.4, pp. 5-36, 1999.

# Generation of nanosecond XeCl pulse trains

Olivier P. Uteza[1], Christophe Bonneville, Philippe C. Delaporte, Bernard L. Fontaine, Marc L. Sentis

Laboratoire Lasers, Plasmas et Procédés Photoniques (LP3)
FRE 2165 CNRS-Université Aix-Marseille II, C. 917, 163, av. de Luminy, 13009 Marseille, FRANCE

## ABSTRACT

High contrast nanosecond pulse trains are produced by an oscillator–amplifier XeCl laser system incorporating polarizing optics. The device is simple and flexible allowing to deliver nanosecond pulse trains up to 17 mJ and with adjustable characteristics mainly concerning the number of pulses (2 to 6 pulses) and the individual pulse peak power (0.2–2.3 MW).

**Keywords**: excimer laser, nanosecond, pulse train, polarization, oscillator–regenerative amplifier.

## 1. INTRODUCTION

Energetic nanosecond UV sources could be advantageously used in laser material processing[1], biomedicine and to create laser–produced plasmas emitting soft X-rays[2]. Unfortunately, the generation of energetic excimer nanosecond pulses (< 4 ns) is not an easy task due to the energy non-storage properties of the excimer laser media. Since many applications, as for instance in laser material processing and biomedicine, need moderate power but short pulse duration, the demand for a simple and flexible laser system delivering pulses of short duration and moderate energy still remains. This paper reports the results obtained with an oscillator–amplifier XeCl laser system able to deliver a pulse train of moderate total energy and of adjustable characteristics concerning the number of pulses, the inter-pulse delay and the individual pulse peak power. The system is based on a regenerative amplifier technique with off-axis amplification. Insertion of the seed pulse in the amplification loop and extraction of the laser pulse train are realized by controlling the polarization state of the seed pulse by means of a Brewster polarizing beam splitter (BPBS) and a half-wave plate (HWP).

The paper is organized as follows. The first section describes the developed oscillator-regenerative amplifier laser system. Afterwards, experimental results obtained through variable optical working conditions are discussed.

## 2. DESCRIPTION OF THE OSCILLATOR-AMPLIFIER LASER SYSTEM

The oscillator-regenerative amplifier excimer laser system is schemed on figure 1. The short duration pulse emitted by the laser oscillator (laser SOPRA-EXULT 2[3], see its characteristics in table 1) is initially not polarized. BPBS rejects the s component (perpendicular to the incidence plane) while the p component (parallel to the incidence plane) is transmitted. After two pass off–axis amplification in LUX test–bed[3] (see table 1 for a brief presentation of its performances), HWP rotates the pulse polarization of 90° to allow the s polarized pulse to enter again the two pass amplification loop along the same path after reflection on $M_3$ and BPBS ($R_{s,BPBS} \approx 99$ %). After bypassing HWP a second time, the four pass amplified laser pulse is p polarized and is then transmitted by BPBS. However, as $R_p \neq 0$, about 15 % of the energy of an incident p polarized pulse is reflected by BPBS while the remaining part of the energy (≈ 80 %) is transmitted. As a consequence, a significant amount of the four pass amplified laser energy is re-injected in the amplifier and will be amplified into two successive loops before to be extracted. As this self-injected amplification process is effective as long as the gain duration, a pulse train can be obtained in this way. Moreover, modification of the HWP neutral axes orientation allows to balance in different proportions, according to a $\cos^2\theta_{\lambda/2}$ Malus law, the reflected and transmitted energy by BPBS yielding to different amounts of the extracted energy and of the re-injected energy in the amplification loop. As a consequence, different pulse train characteristics (number of pulses, pulse energy, inter-pulse delay) can be obtained. So, two experiments have been carried out corresponding respectively to an incident plane-polarized radiation at an azimuth of $\theta_{\lambda/2} = 45°$ (Cases A) and $\theta_{\lambda/2} = 28°$ (Case B) to the direction of the HWP neutral axes angles.

[1] Correspondence : E-mail: olivier.uteza@lp3.univ-mrs.fr, Tél: 33 4 91 82 92 82; Fax: 33 4 91 82 92 89.

XIII International Symposium on Gas Flow and Chemical Lasers and High-Power Laser Conference,
Antonio Lapucci, Marco Ciofini, Editors, Proceedings of SPIE Vol. 4184 (2001)

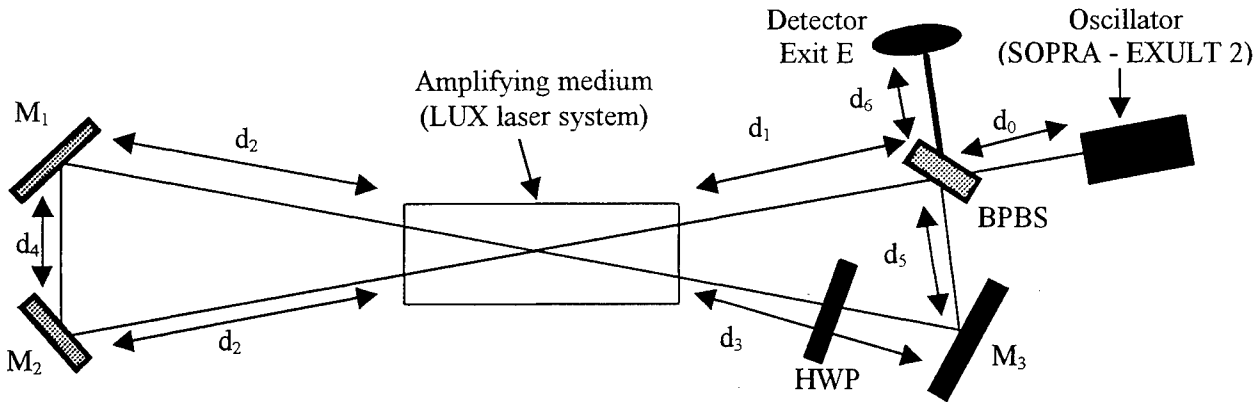


Figure 1. Scheme of the oscillator-regenerative amplifier laser system (not to scale). The off-axis angle is equal to ~ 1.8°. BPBS : Brewster polarizing beam splitter ($i_B$ = 56°). HWP : multiple order half–wave plate. $M_1$, $M_2$ and $M_3$ : $R_{max}$ at 45° incidence. $M_3$ is oriented for an incidence angle of ~ 30° ($R_{M3,30°}$ = 94 %). $d_0 \approx 1.8$ m, $d_1 = d_2 \approx 1$ m, $d_3 \approx 1.1$ m, $d_4 \approx 0.1$ m, $d_5 \approx 0.1$ m, $d_6 \approx 0.5$ m and $L \approx 0.56$ m.

| Laser system | $E_L$ | $\tau_{FWHM}$ | $P_L$ | Exit dimensions cm (X) x cm (Y) | Divergence mrad (X) x mrad (Y) | PRF |
|---|---|---|---|---|---|---|
| SOPRA-EXULT 2 | 0.6 mJ | 3.1 ns | 0.2 MW | 0.25 x 0.6 | 0.6 x 1.3 (near-field) | < 2 Hz |
| LUX (oscillator mode) | 200 mJ | 140 ns | 1.4 MW | 1.3 x 2.8 | 2 x 3 (far-field) | ≤ 1000 Hz |

Table 1. Main characteristics of the laser systems : SOPRA – EXULT 2 and LUX. In oscillator mode, the two AR coated windows closing the LUX cavity are removed and replaced by a high reflectivity rear reflector and a 60 % reflecting output coupler. The beam divergences have been measured with a CCD camera (Pulnix TM 745 E) connected to a beam analyzer (Spiricon LBA 100 A).

In Cases A ($\theta_{\lambda/2}$ = 45°), the incident radiation on HWP is plane-polarized at an azimuth of 45° to HWP neutral axes. So, HWP rotates by 90° (p ↔ s) the incident radiation during the successive amplification loops. In this configuration, the measured performances of BPBS are the following : $R_s$ = 98.5 %, $T_s$ = 1.5 %, $R_p$ = 15.5 %, $T_p$ = 80.5 %. Thus pulse trains with an inter-pulse delay equal to the time corresponding to the length of two amplification loops are obtained. In Case B ($\theta_{\lambda/2}$ = 28°), the incident radiation on HWP is plane-polarized at an azimuth of $\theta_{\lambda/2}$ to HWP neutral axes resulting in a transmitted radiation plane-polarized along a direction making an angle of $2\theta_{\lambda/2}$ with respect to the initial p-direction. So, the radiation incident on BPBS is reflected and transmitted in proportions related to the Malus law. In fact, the angle $\theta_{\lambda/2}$ has been chosen to extract a pulse train with an inter-pulse delay equal to the time corresponding to the length of one amplification loop. The selected angle is equal to $\theta_{\lambda/2} \approx 28°$ and the following performances of BPBS have been measured for a beam describing the first amplification loop : reflected energy ≈ 75 %; transmitted energy ≈ 25 %.

Finally, the length of the amplification loop fixes the delay between two successive extracted pulses. This parameter must be adjusted carefully by considering the gain recovery duration in the amplifier between two successive passes of an amplifying pulse ($\tau_{rec,gain} \approx 2$ ns[4]), the seed pulse total duration ($\tau_{seed} \approx 8$ ns), the amplifier gain duration ($\tau_{gain} \approx$ 140 ns) and the desired specifications of the pulse train. In the case described here, the length of the amplification loop is equal to ~ 5.4 m (see figure 1) representing an acceptable compromise between the previous requirements. In fact, this means that some photons of the amplifying beam travel permanently in the active medium preventing a complete gain recovery in the amplifier between two passes. However, the length of the amplification loop has to be kept small to minimize the losses related to the divergence of the seed pulse (see table 1) and to maximize the number of extracted pulses.

## 3. RESULTS AND DISCUSSION

The initial incident energy of the seed pulse (after BPBS) is equal to ~ 240 μJ and $\tau_{FWHM,osc}$ = 3.1 ns. Figures 2, 3 and 4 show the temporal evolution of the instantaneous laser power detected by a photodiode placed in E (see figure 1) in cases A1, A2 and B. The temporal evolution of the amplifier small signal gain is also reported on these figures to better analyze the experimental results. Cases A1 and A2 correspond to two different delays $\tau_{syn}$ between the beginning of the gain in the amplifier and the first detected pulse of the train. The energetic characteristics of each pulse of the trains are mentioned in the corresponding tables 2, 3 and 4. The pulse energy is obtained by integrating the amplitude of the signal related to each individual pulse detected by the photodiode. The pulse train total energy is averaged on ten shots (1 Hz). These values take into account the subtraction of the part of the energy initially reflected by BPBS (~ 300 μJ).

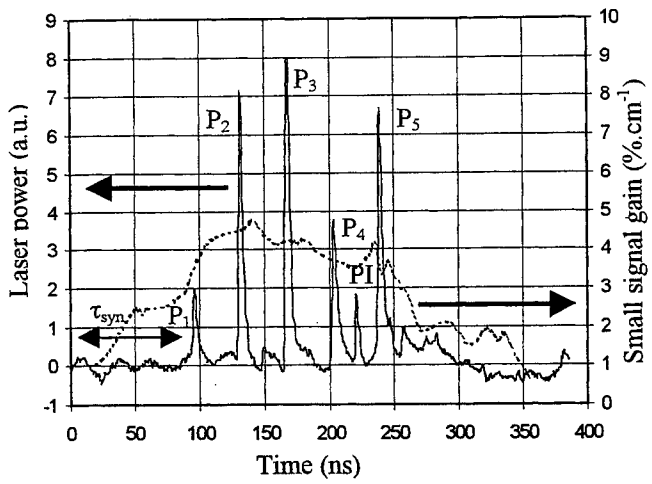


Figure 2. Temporal evolution of the laser instantaneous power (solid line) and of the amplifier small signal gain (dot line) in Case A1 ($\theta_{\lambda/2} = 45°$, $\tau_{syn} \approx 95$ ns, 6 pulses, $E_{total} \approx 16 \pm 0.5$mJ).

| Case A1 | $P_1$ | $P_2$ | $P_3$ | $P_4$ | PI | $P_5$ |
|---|---|---|---|---|---|---|
| Energy (mJ) | 0.8 | 3.6 | 4.9 | 2.1 | 0.55 | 3.95 |
| $\tau_{FWHM}$ (ns) | 3.5 | 3.6 | 3.7 | 3.85 | 3.15 | 3.6 |
| $P_{laser}$ (MW) | 0.23 | 1 | 1.32 | 0.55 | 0.17 | 1.1 |

Table 2. Energetic characteristics of each pulse composing the extracted pulse train in Case A1. These results correspond to the pulse train shown on figure 2.

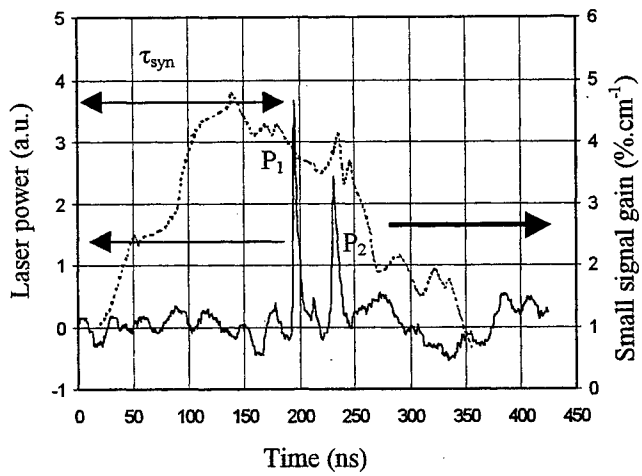


Figure 3. Temporal evolution of the laser instantaneous power (solid line) and of the amplifier small signal gain (dot line) in Case A2 ($\theta_{\lambda/2} = 45°$, $\tau_{syn} \approx 195$ ns, 2 pulses, $E_{total} \approx 17 \pm 0.5$ mJ).

| Case A2 | $P_1$ | $P_2$ |
|---|---|---|
| Energy (mJ) | 9.1 | 7.9 |
| $\tau_{FWHM}$ (ns) | 3.9 | 3.9 |
| $P_{laser}$ (MW) | 2.33 | 2.02 |

Table 3. Energetic characteristics of each pulse composing the extracted pulse train in Case A2. These results correspond to the pulse train shown on figure 3.

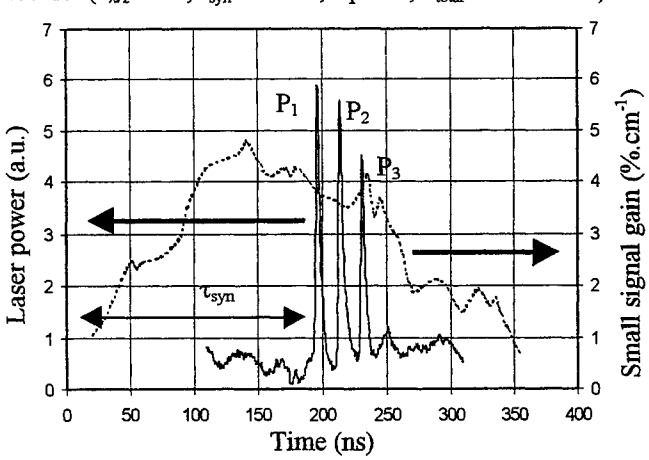


Figure 4. Temporal evolution of the laser instantaneous power (solid line) and of the amplifier small signal gain (dot line) in Case B ($\theta_{\lambda/2} = 28°$, $\tau_{syn} \approx 195$ ns, 3 pulses, $E_{total} \approx 9 \pm 0.5$mJ).

| Case B | $P_1$ | $P_2$ | $P_3$ |
|---|---|---|---|
| Energy (mJ) | 3.2 | 3.4 | 2.3 |
| $\tau_{FWHM}$ (ns) | 3.5 | 3.5 | 3.5 |
| $P_{laser}$ (MW) | 0.91 | 0.97 | 0.66 |

Table 4. Energetic characteristics of each pulse composing the extracted pulse train in Case B. These results correspond to the pulse train shown on figure 4.

Before to comment the peculiarity of each case, some general remarks can be expressed :

a- the peak power of each pulse is in the MW range (0.2–2.3 MW) which is comparable to the instantaneous power of the LUX test-bed working as a laser oscillator ($P_{LUX,osc} \approx 1.4$ MW, see table 1).

b- the slight increase of the amplified pulse FWHM duration (see tables 2, 3 and 4) with respect to $\tau_{FWHM,seed}$ (3.1 ns) is related to a significant amplification of the leading and trailing edges of the oscillator beam.

c- the contrast between the laser pulse train and the photon noise is high. No significant amplified laser signal has been detected and the maximum amplitude of the residual noise signal measured by the photodiode is limited to ± 0.5 a.u. (see figures 2-4). In fact, the low amplitude of the small signal gain, the off-axis design of the amplification laser system ($\alpha_{off\text{-}axis} \approx 1.8°$) and the use of polarizing optical elements prevent any ASE significant development.

As previously mentioned, it is possible to vary the characteristics of the extracted pulse trains according to the adjusting parameter $\theta_{\lambda/2}$. Synchronization between the two laser systems is also of major importance because this timing parameter $\tau_{syn}$ determines the amplification magnitude of the re-injected beam after two-pass amplification in the active medium. In figure 2 (Case A1), the obtained pulse train ($E_{total}$ ~ 16 mJ ± 0.5 mJ) is composed of five principal pulses ($P_1$ – $P_5$) separated of the duration of two amplification loops (~ 35 ns) and with an envelop roughly corresponding to the duration of the small signal gain. An intermediate sixth pulse of very low energy (PI, $E_{PI}$ = 0.5 mJ) appears between two principal pulses ($P_4$ and $P_5$). This pulse PI is related to the amplification of the s polarized residual part of the initial pulse transmitted by BPBS and resulting from a coefficient $T_{s,BPBS} \neq 0$ and from beam depolarizing effects mainly induced by its passage through BPBS. In fact, the amplification of this residual pulse becomes significant only when the gain is maximum. Energy of pulses $P_1$ and $P_4$ (0.8 mJ and 2.1 mJ respectively) are significantly lower than the others ($E_{P2}$ = 3.6 mJ, $E_{P3}$ = 4.9 mJ and $E_{P5}$ = 3.95 mJ) because $P_1$ experienced the beginning of the gain and $P_4$ had to share the gain with the intermediate pulse PI. Now, it is interesting to modify the delay between the oscillator and the amplifier in order to maximize the power of each individual pulse of the extracted train. The result, seen on figure 3 (Case A2), shows the extraction of two main pulses ($E_{P1}$ = 9.1 mJ, $\tau_{FWHM,P1}$ = 3.9 ns; $E_{P2}$ = 7.9 mJ, $\tau_{FWHM,P2}$ = 3.9 ns) separated of 35 ns. In particular, it can be noticed that the peak power of each principal pulse is superior to 2 MW therefore exceeding the instantaneous power of the single LUX test-bed ($P_{LUX,osc} \approx 1.4$ MW). In fact, as ASE does not develop in the amplification loop, delaying the trigger of the oscillator with respect to the amplifier allows the oscillator beam to enter the amplifier active medium when the gain is maximum and, as a consequence, to be strongly amplified. However, the lesser use of the duration of the gain results in a reduced number of extracted pulses. Finally, after recombination of this two pulses, as for instance with a delay line including a fast polarization switching optical element as a Pockels cell, one can expect a single pulse of ~ 4.2 MW laser power representing an increase by a factor three of the laser peak power obtained with the laser LUX ($P_{LUX} \approx 1.4$ MW).

In Case B ($\theta_{\lambda/2} \approx 28°$, figure 4), HWP neutral axes have been oriented to extract a pulse train with an inter-pulse delay equal to the time corresponding to the length of one amplification loop (≈ 17.5 ns). Afterwards, the synchronization between the two laser system has been adjusted to extract ~ MW pulses of roughly equal energy. The result of the combining effects of these two adjusting parameters is illustrated by figure 4 and table 4 showing that the obtained pulse train ($E_{total} \approx 9$ mJ) is composed of three main pulses of comparable energy and FWHM duration (3.5 ns) and separated of 17.5 ns. Moreover, the length of the amplification loop can be easily modified to vary in a larger range the inter-pulse delay to match very diversified application requirements.

## ACKOWLEDGMENTS

This work was supported by the laser company SOPRA in the frame of the EUREKA – 1182 EXULT program. The authors also thank Dr. S. Branly, Dr. M. Makarov and Dr. M. Pealat of SOPRA for valuable discussions.

## REFERENCES

1. U. Rebhan, B. Nikolaus, D. Basting, "Excimer lasers : current status and future developments," in *Excimer Lasers*, L.D. Laude ed., NATO ASI Series E: Applied Sciences Vol. 265, Kluwer Academic Publishers, 1-13, (1994).
2. A.L. Morsell, M. Powers, H. Shields, "Plasma soft x–ray source generated by 4 ns excimer laser pulses," *Appl. Phys. Lett.* **60** (4), 425-427 (1992).
3. O. Uteza, N. Destouches, Ph. Delaporte, B. Fontaine, M. Sentis, "Nanosecond high-energy oscillator : regenerative amplifier excimer laser system", in *Advanced High – Power Lasers*, M. Osinski, H.T. Powell, K. Toyoda, Editors, Proceedings of SPIE Vol. 3889 (2000), pp. 368-378.
4. P.B. Corkum, R.S. Taylor, "Picosecond amplification and kinetic studies of XeCl," *IEEE J. of Quantum Electron.* **18** (11), 1962-1975 (1982).

# Influence of floating particles on excitation discharge for TEA gas lasers

Go Imada*, Takahiro Shinkai[a], Wataru Masuda[a], and Kiyoshi Yatsui

Extreme Energy-Density Research Institute, Nagaoka University of Technology,
1603-1 Kamitomioka, Nagaoka, Niigata 940-2188, Japan

[a] Department of Mechanical Engineering, Nagaoka University of Technology,
1603-1 Kamitomioka, Nagaoka, Niigata 940-2188, Japan

## ABSTRACT

The floating particles produced by the excitation discharge for TEA gas laser have been visualized by the pulsed-laser reflection method. The double-pulse discharge experiments have also been carried out to study the effects of the floating particles on the discharge instabilities. Two kinds of gas mixture are used to simulate KrF excimer laser; $F_2$/Kr/He/Ne (gas A) and Kr/He/Ne (gas B). The particles with diameter of the order of 100 μm are observed in the discharge region. In both gas mixture, the number density of the particles increases to ~ 3 particle/cm$^3$ at 200 ms after the discharge, and then decreases to ~ 1 particle/cm$^3$ at 500 ms. On the other hand, the double-pulse discharge characteristics are very different between gases A and B. In the gas A, the second discharge tends to be an arc when the pulse interval decreases to 300 ms. However, the arc does not occur in the gas B. It is deduced that the floating particles of the order of 100 μm in diameter do not strongly affect the discharge instabilities.

**Keywords:** Glow discharge, Arc, Excimer laser, Floating particle

## 1. INTRODUCTION

The high-pressure, pulsed glow discharge has been studied for further understanding of the excitation discharge on TEA gas lasers. The excitation discharge causes various instabilities in subsequent discharge which collapse at the highly-repetitive operation. It has been suggested that the instabilities are induced by a gas density depletion,[1,2] shock wave,[3,4] residual ion,[5] electrode heating,[6] and floating particle generated in the discharge region. However, the influences of the respective factors on collapse of the highly-repetitive operation have not been clarified.

The purpose of this paper is to visualize the floating particles in the discharge region and to investigate the dependence of discharge characteristics on the number density of particle. The floating particles originate from the electrodes which are sputtered by the ions of discharge. The floating particles are visualized by the laser reflection method using a pulsed YAG laser and CCD camera. The double pulse discharge experiments are also carried out to study the influences of the floating particles on the discharge characteristics of the second pulse, where the gas density depletion, shock wave, residual ion, electrode heating, and floating particle are remained in the discharge region. The discharge properties in the gas mixture of $F_2$/Kr/He/Ne have been compared with those in the gas mixture of Kr/He/Ne to investigate which of the floating particle or the gas composition is influential for the discharge instabilities.

## 2. EXPERIMENTAL SETUP

Figure 1 shows the schematic of experimental setup. The main electrodes consist of half-cylindrical-type anode and cathode where the width, length, gap distance and radius of curvature are 40 mm, 400 mm, 20 mm and 100 mm, respectively. The $y$ axis indicates the discharge direction, and the origin of the $x$-$y$ plane corresponds to the center of the discharge region. The automatic UV preionization electrodes consist of 40-pin spark gaps which are set at the both sides of the cathode. The excitation circuit is a charge-transfer type circuit ($C_1 / C_p$ = 16 / 14 nF) where the storage capacitor is charged up to 30 kV. The preionization electrodes are directly connected to $C_p$. Two kinds of gas mixture are used in the present experiment in order to simulate KrF excimer laser. The gas composition and pressure are summarized in Table I. The gas A includes fluorine, it tends to create the negative ion having long lifetime which induces an arc instead of a stable glow discharge.

Figure 2 shows the schematic diagram of visualization system of the floating particles. After a certain time from a pulse excitation discharge, a pulsed YAG laser beam as sheet probe beam irradiates into the middle of the discharge region. Then, the reflected light from the floating particles is recorded by a CCD camera. To reduce the background light in

XIII International Symposium on Gas Flow and Chemical Lasers and High-Power Laser Conference,
Antonio Lapucci, Marco Ciofini, Editors, Proceedings of SPIE Vol. 4184 (2001)

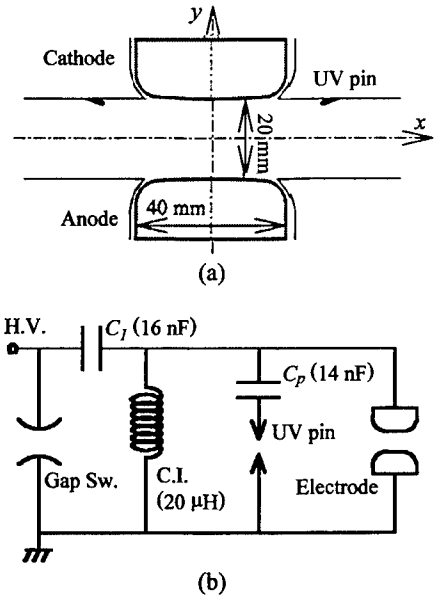


Fig. 1 Schematic of experimental setup. (a) Cross-sectional view of discharge electrode, (b) electrical excitation circuit.

Table I Gas conditions.

| | Gas A (with $F_2$) | Gas B (without $F_2$) |
|---|---|---|
| Composition | He/Ne/Kr/$F_2$ = 64.8/33/2/0.2 | He/Ne/Kr = 65/33/2 |
| Pressure | $p$ = 295 kPa | |

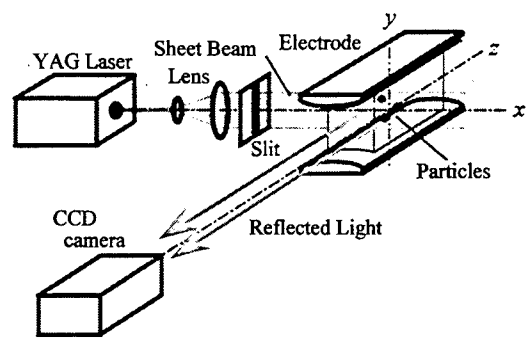


Fig. 2 Schematic diagram of visualization system of floating particles.

photographs, the exposure time of CCD camera decreases to 20 μs. The size of the sheet beam is 12.5 mm in height and 1.5 mm in width. The wavelength and pulse duration of YAG laser beam are 532 nm and 8 ns, respectively. The spatial resolution of this system has been experimentally found to be ~ 100 μm on the object plane.

## 3. RESULTS AND DISCUSSION

Figure 3 shows the photograph of reflected light by floating particles in the gases A and B, where $t$ indicates the time after the discharge. The white spots denote the reflected light from the particles. The probe beam does not always irradiate the floating particles because the number of particles is estimated to be few. Therefore, the photograph of reflected light is taken at multi-exposure of 100 times. To confirm the reliability of the laser reflection method, the comparison has been made on the distribution of particle diameter estimated by the laser reflection method with that measured by the microscopy. After the discharge, the particles covered on the electrodes are collected by the clean cloth, and then taken through the microscope. The number of particle as a function of diameter of particle estimated by the photograph of the laser reflection method and the microscopy are shown in Fig. 4. We found that the distribution of particle diameter estimated by the laser reflection method agrees approximately with that by the microscopy.

Figure 5 shows the energy spectra of EDX (Energy Dispersive X-ray spectroscopy) analysis of the floating particles generated by a single-pulse discharge in the gas A. We found that the particles mainly consist of Fe, Cr, and Ni. It becomes clear that the floating particles originate from the stainless steel electrodes.

Figure 6 shows the time evolution of discharge voltage ($V$), current ($I$), and power ($P = VI$). The single-pulse discharge occurs in the gases A and B. We found very little difference between the discharge properties in the gases A and B. It is also found from the visual observation of discharge that the single-pulse discharges in the gases A and B are a stable glow discharge.

Figure 7 shows the time dependence of number density of the floating particles generated by a single-pulse discharge in the gases A and B. The floating particles with diameter of the order of 100 μm are observed in the discharge region filled with the gases A and B. In both mixture gases, the particles appear just after the discharge and the number density of the particles increase up to ~ 200 ms. The number density of the particles increases to ~ 3 particle/cm$^3$ at 200 ms after the discharge, and then decreases to ~ 1 particle/cm$^3$ at 500 ms. The number density and diameter of the particles do not strongly depend on the kind of gas mixture.

Figure 8 shows the probability of arc at the second discharge as a function of time interval of double-pulse discharge. The second discharge in the double-pulse experiment occurs in a stable gas where the gas density depletion, shock waves,

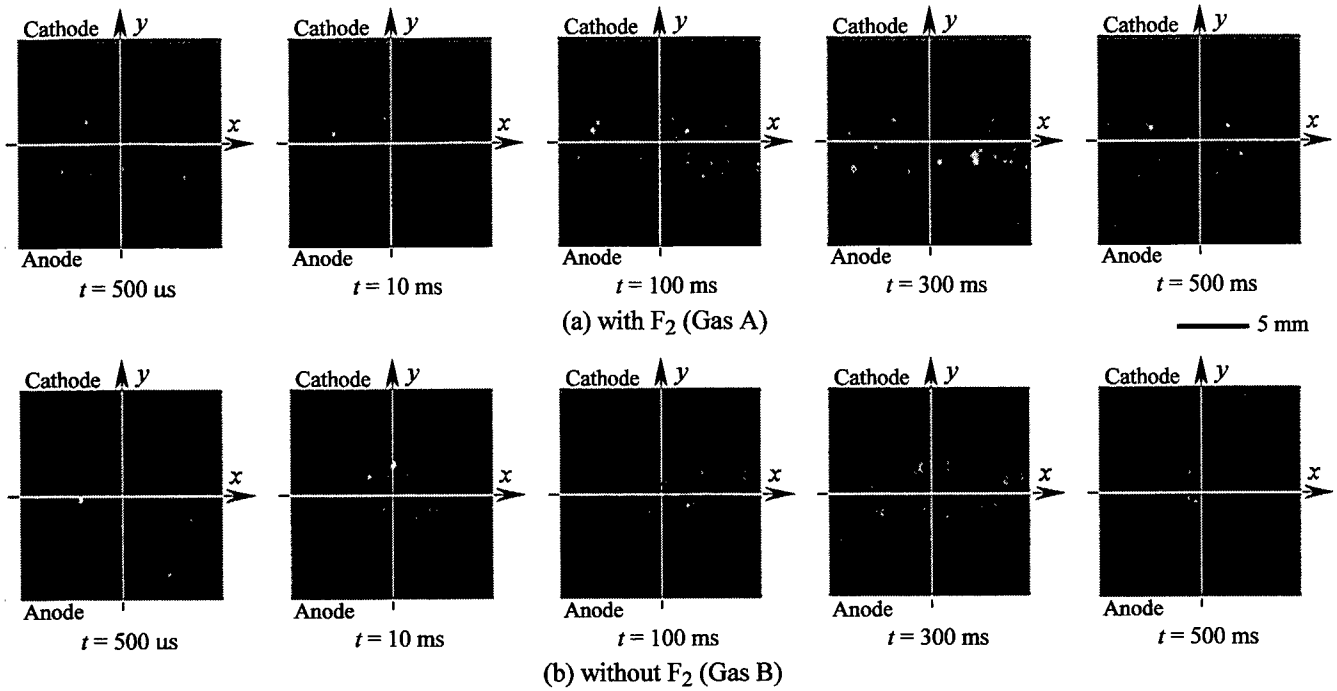


Fig. 3 Photograph of reflected light by floating particles.

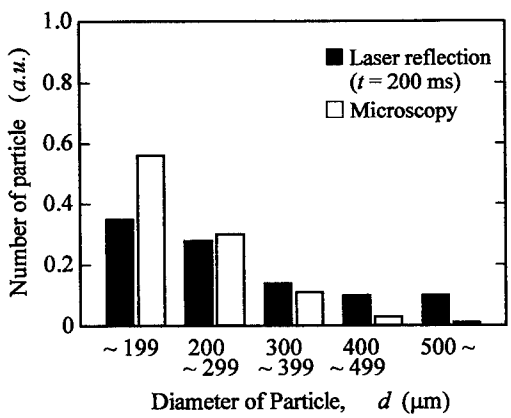


Fig. 4 Number of particle as a function of diameter of particle in gas A.

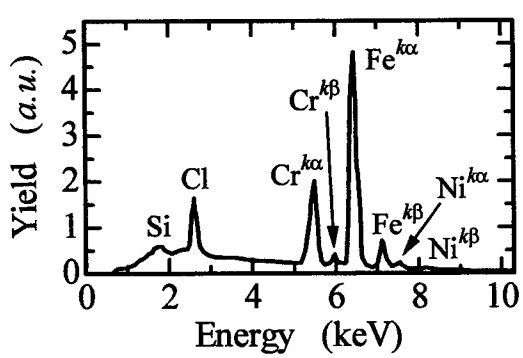


Fig. 5 EDX analysis of floating particles.

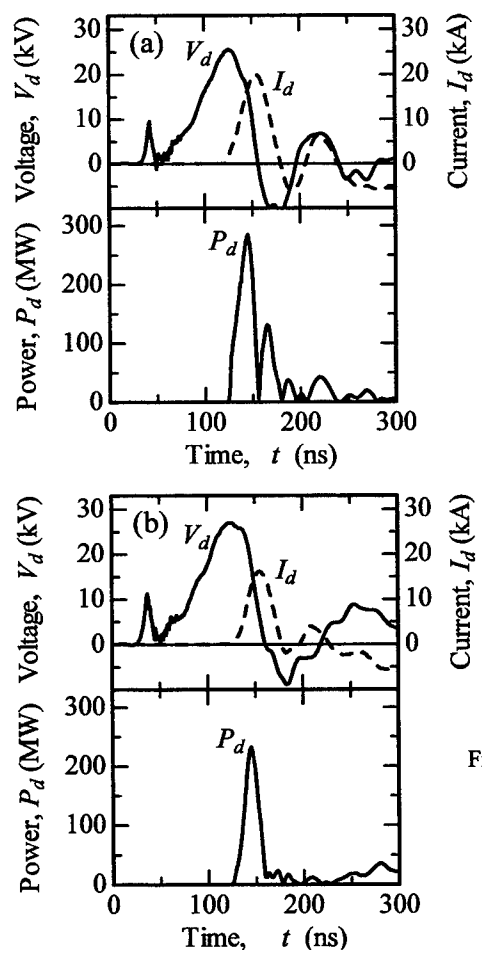


Fig. 6 Time evolution of discharge voltage, current, and power. (a) with $F_2$ (Gas A), (b) without $F_2$ (Gas B).

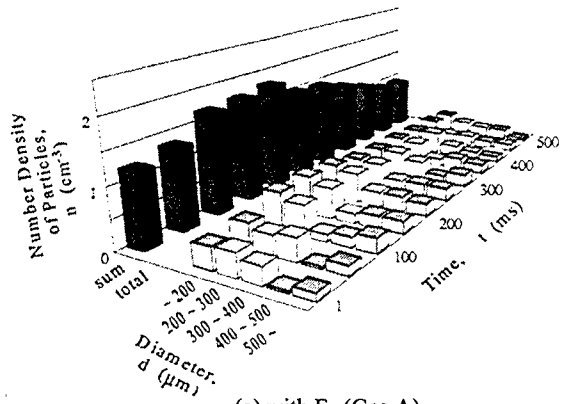


(a) with $F_2$ (Gas A).

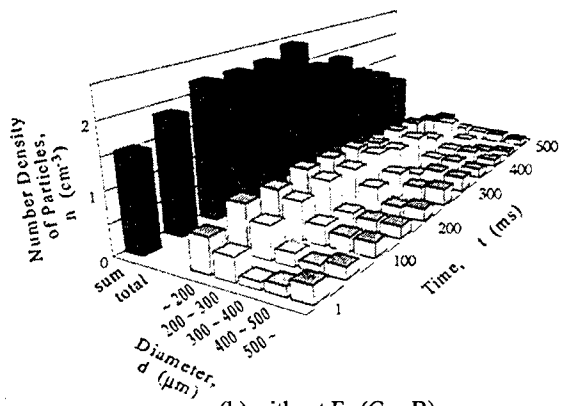


(b) without $F_2$ (Gas B).

Fig. 7 Time dependence of number density of particles.

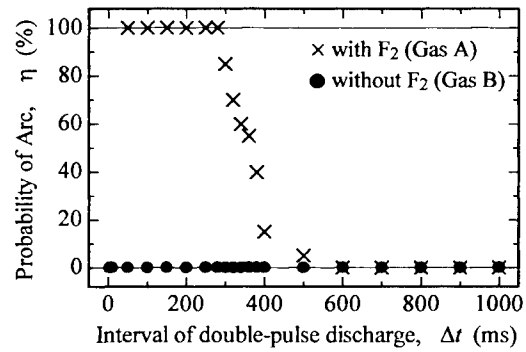


Fig. 8 Probability of arc as a function of time interval of double-pulse discharge.

residual ions, and discharge products generated by the first pulse discharge are remained. Twenty cycles of discharges are attempted and the probability of arc is calculated from the number of times in which the filamentary luminance is observed in the discharge. In the gas A, the second discharge easily tends to be arc within the time interval of 300 ms. However, the arc does not occur in the gas B. It has been clearly demonstrated that the floating particles of the order of 100 μm hardly affect the discharge characteristics. The present results show that some factor other than the floating particles, such as fluorine gas, strongly induce the transition form the glow to the arc.

## 4. CONCLUSION

The floating particles generated by the high-pressure, pulsed glow discharge in KrF excimer laser excitation have been visualized by the pulsed-laser reflection method. The particles are observed in the discharge region just after the discharge. The number density of the particles increases to ~ 3 particle/cm$^3$ at 200 ms after the discharge, and then decreases to ~ 1 particle/cm$^3$ at 500 ms. The floating particles with diameter of the order of 100 μm have little effect on the discharge instabilities.


## ACKNOWLEDGMENTS

This work was partly supported by Grant-in-Aid for Encouragement of Young Scientists from the Ministry of Education, Science, Sports and Culture in Japan. The authors would like to thank Mr. Y. Sekimoto for mechanical design and experimentation.


## REFERENCES


1. S. Kosugi, K Maeno, and H. Honma, "Measurement of Gas Temperature Profile in Discharge Region of Excimer Laser with Laser Schlieren Method", *Jpn. J. Appl. Phys.* **32**, pp. 4980-4986, 1993.
2. G. Imada, Y. Sato, H. Yoshida, W. Masuda, and K. Yatsui, "Observation of excitation discharge on excimer laser in non-uniform gas density distribution", *Proc. Int'l Symp. on Ultrahigh- and High-Speed Photography and Image-based Motion Measurement, San Diego*, **SPIE-3173**, pp. 124-131, 1997.
3. K. Yatsui, G. Imada, K. Masugata, and W. Masuda, "Generation and Propagation of Shocks in Discharge-Pumped Excimer Laser", *Proc. 10th Int'l Symp. on Gas Flow and Chem. Lasers, Madrid*, **SPIE-2502**, pp. 134-139, 1994.
4. M. Sentis, P. Delaporte, B. Forestier, and B. Fontaine, "Design and Characteristics of High Pulse Repetition Rate and High Average Power Excimer Laser Systems", *IEEE J. Quantum Electron.* **27**, pp. 2332-2339, 1991.
5. M. Osborne and J. Green, "Negative Ion Assisted Preionization for Excimer Lasers", *J. Appl. Phys.* **71**, pp. 3127-3133, 1992.
6. R. Arutyunyan, V. Borisov, A. Vinokhodov, Yu. Kiryukhin, and A. Morozov, "Electrode Effects in a Pulse-Periodic Excimer Laser", *Sov. J. Quantum Electron.* **16**, pp. 1589-1591, 1986.



*Correspondence: E-mail: imada@nagaokaut.ac.jp; Telephone: 81-258-47-9893; Fax: 81-258-47-9890

# One-dimensional model calculation of $F_2$ laser under high repetition rate operation

Takahiro Kamiya and Koichi Kasuya
Department of Energy Sciences, Interdisciplinary Graduate School
of Science and Engineering, Tokyo Institute of Technology
Nagatsuta 4259, Midori-ku. Yokohama, Japan 226-8502

## ABSTRACT

For discharge pumped $F_2$ lasers, the uniformity of the laser medium is important for the laser quality. So that, we developed a one-dimensional simulation code to investigate the effect of the inhomogeneity of the initial electron density. Only a few percent initial fluctuations affected the main-discharge electron number density largely.

## 1. INTRODUCTION

The $F_2$ laser is expected to have next generation applications including the laser lithography and so on. For discharge pumped lasers, the uniformity of the discharge affects to the quality of laser. So, we developed a one-dimensional $F_2$ laser simulation code, and investigated the effect of nonuniformity.

## 2. SIMULATION MODEL

Our simulation code is based on the one developed by Green and Brau.[1] This model is constructed with three blocks including the discharge circuit equation, Boltzmann equation and the rate equations.

### 2.1. Discharge circuit

Discharge circuit used in the simulation code is shown in Fig.1. This is a circuit of transfer capacity type and the circuit constants are $R_1$=0.15[Ω], $R_2$=0.1[Ω], $R_3$=$R_2$, $L_1$=140[nH], $L_2$=10[nH], $L_3$=$L_2$, $C_1$=20[nF], $C_2$=14[nF]

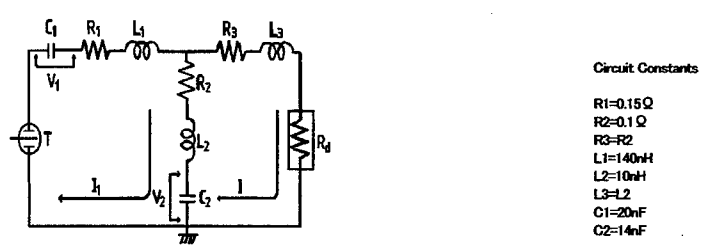


Fig.1 Discharge circuit

### 2.2. Rate equations and Rate Constants

The rate equations and Rate Constants used in this code are shown in Table-1.[2]

XIII International Symposium on Gas Flow and Chemical Lasers and High-Power Laser Conference,
Antonio Lapucci, Marco Ciofini, Editors, Proceedings of SPIE Vol. 4184 (2001)

Table-1 Main Reactions and Rate Constants

| Reactions | Rate Constants | Reactions | RateConstants |
|---|---|---|---|
| $He + e \rightarrow He^* + e$ | Boltzmann | $F_2 + e \rightarrow F^- + F$ | Boltzmann |
| $F_2 + e \rightarrow F_2^+ + 2e$ | Boltzmann | $F_2 + e \rightarrow (F_2(A)^* + e) \rightarrow 2F + e$ | Boltzmann |
| $F_2(A)^* + e \rightarrow F_2 + e$ | Boltzmann | $He^+ + F^- + M \rightarrow F^* + He + M$ | P-dependent |
| $F_2^+ + F^- + M \rightarrow F^* + 2F + M$ | P-dependent | $F^+ + F^- + M \rightarrow F_2(D)^* + M$ | P-dependent |
| $He^* + F_2 \rightarrow F_2^+ + He + e$ | $1.0\times10^{-19}cm^3/s$ | $He^+ + F_2 \rightarrow F_2^+ + He$ | $1.7\times10^{-9}cm^3/s$ |
| $F_2^+ + e \rightarrow F^* + F$ | $7.0\times10^{-8}\ cm^3/s$ | $F^* + F_2 \rightarrow F2(D)^* + F$ | $5.1\times10^{-10}cm^3/s$ |
| $F^* + 2He \rightarrow F + 2He$ | $1.0\times10^{-35}\ cm^6/s$ | $F_2(D)^* + He \rightarrow 2F + He$ | $1.0\times10^{-13}cm^3/s$ |
| $F_2(D)^* + 2He \rightarrow 2F + 2He$ | $1.0\times10^{-33}\ cm^6/s$ | $F_2(D)^* + F_2 \rightarrow 2F + F_2$ | $5.0\times10^{-9}\ cm^3/s$ |
| $F_2(D)^* + e \rightarrow 2F + e$ | $2.0\times10^{-7}\ cm^3/s$ | $F_2(D)^* + Ph \rightarrow F_2(A)^* + 2Ph$ | $6.8\times10^{-16}cm^3/s$ |
| $F_2(D)^* \rightarrow F_2(A)^* + Ph$ | $3.7\times10^{-9}$ s | $F_2(A)^* + M \rightarrow 2F + M$ | e-life time |
| $He^* + Ph \rightarrow He^+ + e$ | $2.2\times10^{-18}\ cm^2$ | $He_2^* + Ph \rightarrow He_2^+ + e$ | $1.9\times10^{-18}\ cm^2$ |
| $F^- + Ph \rightarrow F + e$ | $1.9\times10^{-18}\ cm^2$ | | |

| | | | |
|---|---|---|---|
| e: | electron | e-life time: | effective life time |
| $F_2(A)^*$: | low level excited state | $F_2(D)^*$: | high level excited state |
| Ph: | photon (157nm) | p-dependent: | pressure dependent constant |
| M: | Neutral gas | | |

### 2.3. Modification of the simulation code

As a space coordinate axis, we took X-axis which is perpendicular to the light axis and discharge direction. We assumed that the shape of the electrode was conical. The discharge volume was divided into small sections. The cross section of the electrode section is shown in Fig2. The minimum gap length is 22.5mm. The length and width of the electrode are 45cm, 2.6cm respectively.

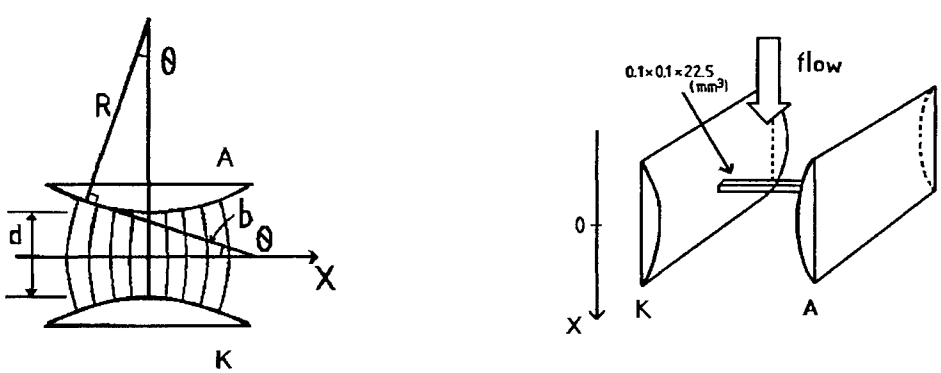


Fig.2 Discharge section
K: Cathode A: Anode

## 3. RESULTS AND DISCUSSION

The condition of the simulation is as follows. Gas mixture ratio is $He:F_2=99.85:0.15$, and the total pressure is 3[atm]. Charging voltage is 30[kV]. The initial electron number density is $10^8$[electorons/$cm^3$]. At this condition, the results of simulation are shown below. Fig.3,4 show the discharge voltage and current. Fig.5 shows the electron number density. Fig.6 shows the photon number density. Fig.7 shows the gas temperature.

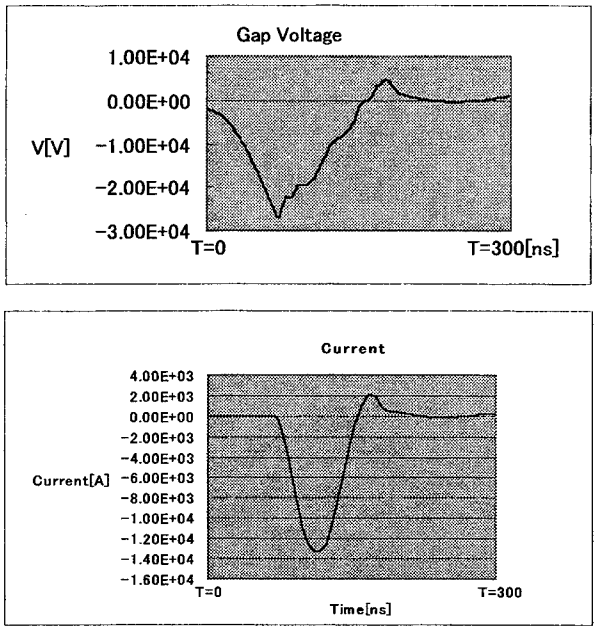


Fig.3, 4 Discharge gap voltage and current (Charging voltage is 30[kV])

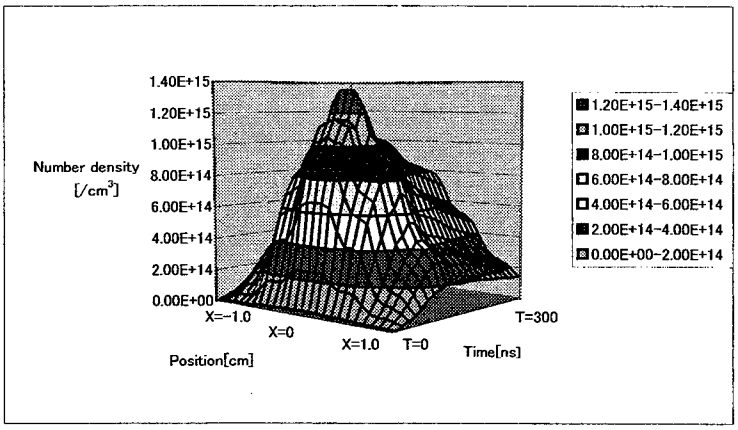


Fig.5 Electron number density

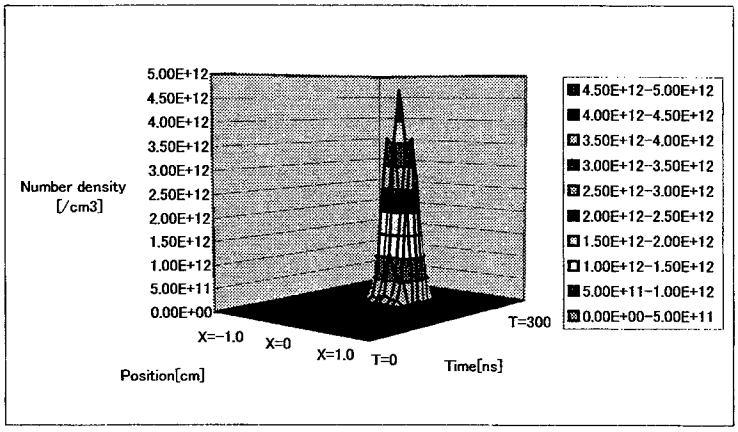


Fig.6 Photon number density

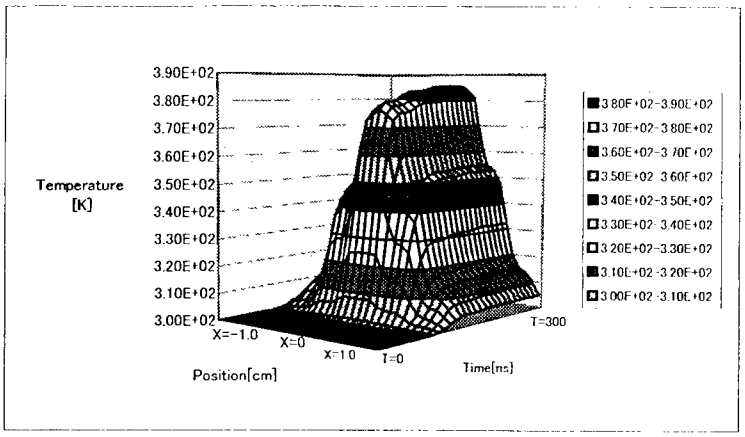


Fig.7 Gas temperature

To investigate the effect of the fluctuation of the initial electron density, we assumed the local density fluctuation in the initial electron density. Fig8 with +1% fluctuation and +10% fluctuation.

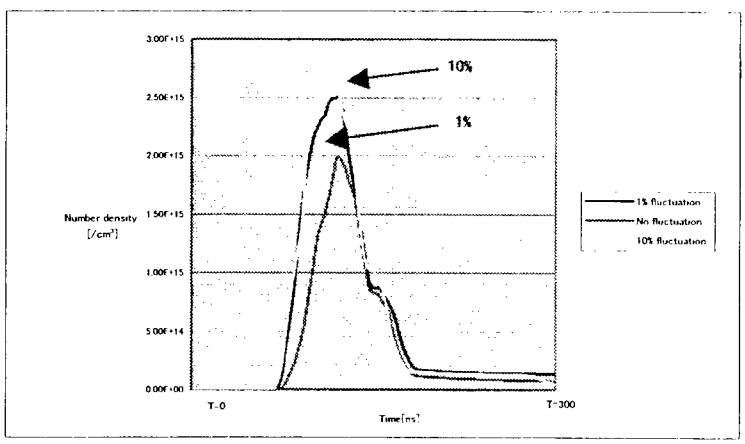


Fig.8 1%fluctuation and 10% fluctuation

From the Fig.6, we estimate the laser output energy is about 3[mJ]. From the Fig.8, electron density is affected by the initial electron fluctuation. Only 1% fluctuation, it affects the electron density.

## 4. SUMMARY

We developed a one-dimensional simulation code. Gas mixture ratio is $He:F_2=99.85:0.15$, and the total pressure is 3atm. Charging voltage is 30kV. We estimate the laser output energy is about 3[mJ]. Only a few percent initial fluctuations affected the main-discharge electron number density.

## 5. REFERENCES

1. A.E.Green and C.A.Brau, "Theoretical Studies of UV-Preionized Transverse Discharge KrF and ArF lasers," IEEE J.Q.Electronics **QE-14**, pp.951-957, 1978.
2. M.Kakehata, T Uematsu, F Kannari, and M.Obara, "Efficiency Characterization of Vacuum Ultraviolet Molecular Fluorine ($F_2$) Laser (157nm) Excited by Intense Electric Discharge," IEEE J.Q.Electronics **27**, pp.2456-2464, 1991.

# Highly efficient lasers using polycrystalline Nd:YAG ceramics

J. Lu[a], M. Prabhu[a], K. Ueda[a], H. Yagi[b], T. Yanagitani[b], A. Kudryashov[c]
[a]Institute for Laser Science, University of Electro-communications, Chofu, Tokyo 182, Japan.
Email: lu@ils.uec.ac.jp, Fax: 81-424-85-8960
[b]Takuma Works, Konoshima Chemical Co., Ltd., 80 Kouda, Takuma, Mitoyo, Kagawa 769, Japan
[c]Russian Academy of Sciences, Dm. Ulyanov 4, bld. 2. apt. 13 Moscow, 117333 Russia

## ABSTRACT

Highly efficient Nd:YAG ceramic laser at 1064 nm was demonstrated. Using 1 W LD end-pumping scheme, with 883 mW pumping, 499 mW 1064 nm CW laser output has been obtained corresponding to an optical to optical efficiency of 56.5%. High power CW Nd:YAG ceramic rod laser was also demonstrated for the first time. The maximum output power of 31 W with 18.8% slope efficiency was obtained at 1064 nm. The potential of Nd:YAG ceramic laser was also discussed.

**Key words**: Solid-state lasers, Ceramic laser, Nd:YAG ceramics,

## 1. INTRODUCTION

Ceramic Lasers appeared more than 30 years ago. The Hot-pressed $CaF_2$ doped with dysprosium appears to be the first reported polycrystalline material, which established laser oscillation.[1] Recently polycrystalline Nd:YAG ceramic laser material has received much attention since the quality of Nd:YAG ceramics has been improved greatly and highly efficient laser oscillation could be obtained that is comparable in efficiency with Nd:YAG single crystal lasers. Compared to growing technique of Nd:YAG single crystals, the fabrication of polycrystalline transparent Nd:YAG ceramics has a great potential of scaling. The large size ( now of about $\phi$400 mm×10 mm sample is available) and high concentration (>1%) neodymium doped samples can be fabricated. And also multi-layer active elements and multi-functional ceramics can be easily fabricated. These advantages give much more freedom in laser designs. For the fabrication of transparent ceramics, hot press method, wet chemical method and urea precipitation method had been used. In 1995, Akio Ikesue, et. al. fabricated highly transparent Nd:YAG ceramics. The scattering loss (0.009 $cm^{-1}$) for this sample was sufficiently low to obtain laser output for the very first time. Slope efficiency of 28% was reported. [2]

Recently Konoshima Chemical Co. Ltd. developed Nd:YAG ceramics successfully by a new method.[3,4] We prepared fine YAG particles of around 10 nm in diameter in the combination of liquid phase chemical reaction and pre-sintering technique. The ceramic formation process and sintering process have been optimized for fabricating highly transparent Nd:YAG ceramics. The average diameter of grain size is about 10 μm with grain boundary width less than 1 nm. The porosity in this kind of ceramics is only 1 ppm level. Such narrow grain boundary and very low porosity ensure very low scattering loss inside the ceramic samples. The optical properties, including absorption spectrum, emission spectrum and fluorescence lifetime, had been studied, almost identical optical properties with those of Nd:YAG single crystal was obtained.[5]

## 2. LASER EXPERIMENTS

### 2.1 End pumping laser experiment

1% and 2% Nd:YAG ceramic lasers were demonstrated using end-pumping scheme. The experimental setup for LD end-pumped Nd:YAG laser is shown in Fig. 1. A 1 W high brightness Hamamatsu 2901 LD with 1×50 $\mu m^2$ emission profiles was used as the pump source. When the LD output is 1 W, about 883 mW pump power can be focused on the end of sample. A 5 mm 1% Nd:YAG ceramic sample and a 2.5 mm 2% Nd:YAG ceramic sample were used in this experiment. One end of the ceramic samples was anti-reflection coated at 808 nm (R<5%) and high-reflection coated at 1064nm (R>99.8%) to act as a cavity mirror of the laser (input mirror), the other end was anti-reflection coated at 1064nm. Output mirror is a concave mirror with 250 mm radius and the reflectivity is 97% at 1064 nm. The cavity length is about 20 mm. A 5 mm 0.9% Nd:YAG single crystal sample procured from Litton-Airtron Inc. was used for comparison. The coatings are the

XIII International Symposium on Gas Flow and Chemical Lasers and High-Power Laser Conference,
Antonio Lapucci, Marco Ciofini, Editors, Proceedings of SPIE Vol. 4184 (2001)

same with that of ceramic samples.

Figure 2 shows the laser output versus input power for Nd:YAG ceramic lasers and single crystal laser, respectively. The slope efficiencies are 58.5%, 55.4% and 55.2% for 1% ceramic, 2% ceramic and 0.9% single crystal, respectively. With 883 mW maximum pump power, 499 mW, 465 mW and 474 mW laser output at 1064nm were obtained for 1% ceramic, 2%

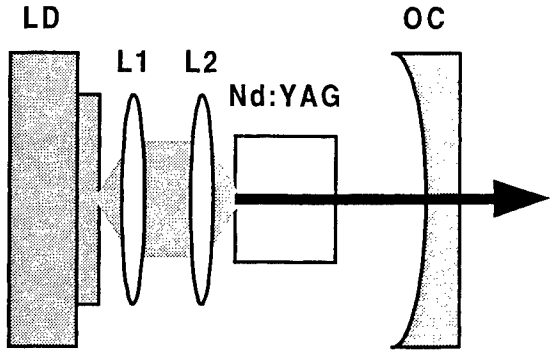


Fig.1. Schematic diagram of the end-pumped laser experimental setup. LD: laser diode; L1, L2: collimating and focusing lens; OC: output coupler.

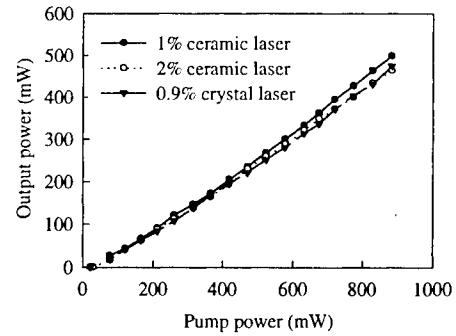


Fig.2. Nd:YAG Lasers output at 1064 nm versus pump power.

ceramic and 0.9% crystal lasers, respectively. The corresponding optical to optical conversion efficiency is 56.5% for 1% ceramic laser, 52.7% for 2% ceramic laser and 53.7% for single crystal laser.

Because the neodymium concentration and sample length are different, under the same maximum pump power of 883 mW, 840 mW, 842 mW and 795 mW pump power were absorbed by %1 ceramic sample, 2% ceramic sample and 0.9% single crystal sample, respectively. In order to have a reasonable comparison, absorbed pump power should be used to calculate the efficiencies. Table 1 lists all results calculated according to absorbed pump power for ceramic and single crystal lasers, respectively.

From Table 1, one can see, for 1% ceramic and 0.9% single crystal lasers, whatever on thresholds, Optical to Optical (O-O) conversion efficiencies or slope efficiencies, the two kinds of laser materials share almost identical laser properties. This is the first highly efficient Nd:YAG ceramic laser demonstration this is comparable to Nd:YAG single crystal lasers up to now.

The threshold of 2% ceramic laser (27 mW) is a little larger than that of 1% ceramic laser (20 mW). The slope efficiency is 57.6%, which is about 3% less than that of 1% ceramic laser. This is because of the quenching effect in high concentration Nd:YAG ceramics. The fluorescence lifetime of 1% and 2% ceramic are 234 μs and 174 μs, the difference is 60 μs, and the difference in lifetimes indicates the possibility of fluorescence quenching. But on the contrary, the absorption coefficient increases almost linearly with increasing the neodymium concentration. For end pumping scheme, the required thickness of laser materials is reduced because of high absorption coefficient. One of the advantages of high concentration Nd:YAG is that it can be used in microchip lasers to generate single frequency output efficiently. Since Nd:YAG has much better thermo-mechanical properties than Nd:$YVO_4$, high concentration Nd:YAG is a very good alternative in single frequency lasers.

Table 1. Laser parameters calculated according to absorbed pump power

| | Absorbed power | Output power | O-O efficiency | Threshold | Slope efficiency |
|---|---|---|---|---|---|
| 1% Ceramic | 840 mW | 499 mW | 59.4% | 20 mW | 60.8% |
| 2% ceramic | 842 mW | 465 mW | 55.2% | 27 mW | 57.6% |
| 0.9% crystal | 795 mW | 474 mW | 59.6% | 20 mW | 60.6% |

## 2.2 High power laser experiment

High power CW laser oscillation with Nd:YAG ceramic rod using virtual point source (VPS) pumping system was

obtained for the first time.

The pumping geometry used in this work is called virtual point source (VPS) which has been described previously.[7] In this setup, 32 sets of 10 W laser diodes (807 nm) were used to form a symmetrical ring-shaped pumping source so as to get

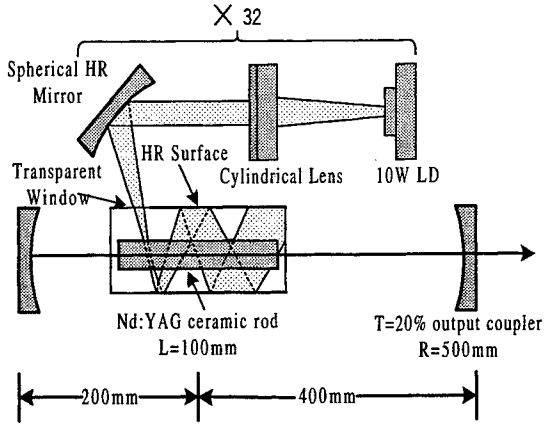


Fig. 3 Schematic diagram of Nd:YAG ceramics laser cavity and the virtual-point pumping source (VPS).

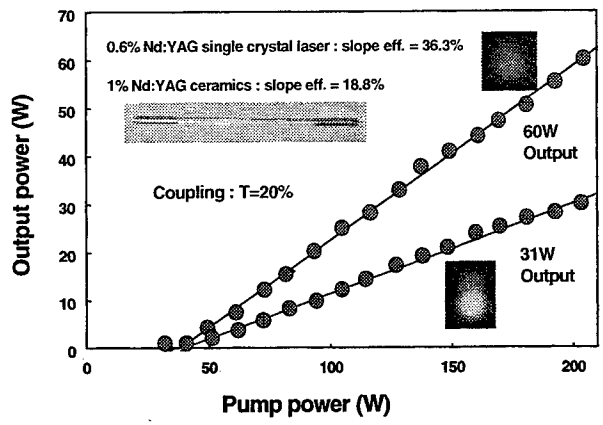


Fig.4 Laser output versus VPS pump power.

better angular uniformity. The outputs of the laser diodes were focused into a point (or line) at the rod axis by 32 set of optics. The axial illuminations completed by a coaxial cylinder with Ag-coated side surface and Au-coated end surfaces which, in all, act like a huge double-clad fiber. The point of focus, acting as a virtual point source, was imaged and re-imaged along the rod axis and reflected by the end surface, so that after multiple passes the whole of the laser rod was illuminated.

The schematic laser setup is shown in Figure 3. The sample used in this experiment is a $\phi 3\times 100$ mm 1% Nd:YAG ceramic rod. The end faces of the rod were flat and antireflection-coated at 1064 nm. Two concave mirrors both with 500 mm radius were used to form the laser cavity. One was HR coated at 1064 nm; the other mirror has a reflectivity of 80% at 1064 nm. The cavity length is about 60 cm. A $\phi 3\times 100$ mm 0.6% Nd:YAG single crystal rod with the same coatings was used to have a comparison.

Figure 4 shows the high power laser output at 1064 nm versus pump power. Laser threshold is 39.9 W, and when the pump power was increased to 214.5 W, 31 W multi-mode continuous laser output at 1064 nm was obtained corresponding to an optical-to-optical efficiency of 14.5%. The slope efficiency is 18.8%. For single crystal laser, the threshold is 34 W, and with 214.5 W pumping, the output is 65 W. The slope efficiency is 36.3% which is about 2 times larger than that of ceramic laser. When pump power was increased above 214.5 W, the ceramic laser output began to decrease because the very short thermal focal length (estimated 120 mm) make the resonator approach the stability edge. For such VPS system, low neodymium concentration Nd:YAG sample is better because at the same pump power, low concentration sample has longer absorption depth, longer thermal focal length and less thermal distortion loss, so that more pump power can be added and higher efficiency can be expected. High power low concentration (such as 0.6%) Nd:YAG ceramic laser will be investigated later.

## 3. FUTURE PROSPECTS

We reported the present status of YAG ceramic laser in this report. We understood the ceramic formation is the crystal growing process 10 nm nano-crystals to 10 μm micro-crystals. Growing speed of the crystal was approximately 2 μm/hr. Such a slow growing speed of crystals allows the new crystals difficult to be grown in the conventional crystal growth under high temperature. The crystal growth in ceramics is more natural.

The big advantage of ceramic lasers is the scaling. It is possible to fabricate a meter size laser material through a glass-like fabrication process. This gives us a new possibility of large size and low cost laser materials. In addition, the mixed ceramics allow the possibility of multi-color active material, which is important for the laser fusion driver for ultra-high homogeneous illumination on target. We already demonstrated the formation of 1m x 1m thin ceramic YAG. If we develop the multi-layered ceramics of such a large size as shown in Figure 5, the cost of microchip lasers with multi-functions should be drop drastically.

The modern technology of the ceramic formation and fabrication shows the great progress, recently. For example, the inc

jet printer contains the piezo-electric actuator with 10 μm thickness. The thickness of the ceramic layer in high capacitance ceramics is only 2 to 3 μm. To avoid the breakdown in such a high field strength the dielectric ceramics are pore-free and defect-free. The transparent ceramics for lasing materials are very similar to these ceramics. It means the mass productive process for the ceramic capacitance can be applied on to the ceramic laser fabrication. Figure 6 shows the future image of continuous fabricating process of multi-functional ceramic lasers which is similar to the iron and glass fabrications. The green-sheet of ceramics are combined in the multi-layered sheet in the rolling mill. If the thickness of layers is thin enough, the mismatching in the thermal expansion and volume reduction in the sintering process can be overcome.

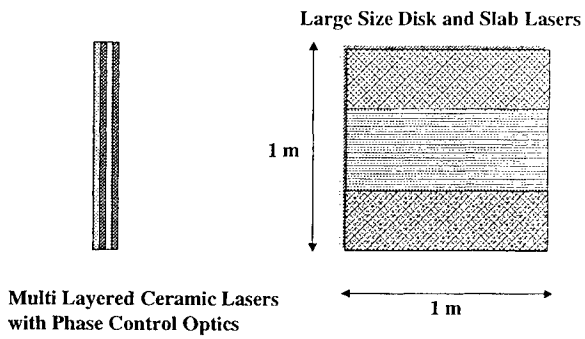


Fig.5 Multi-layered and large size ceramics

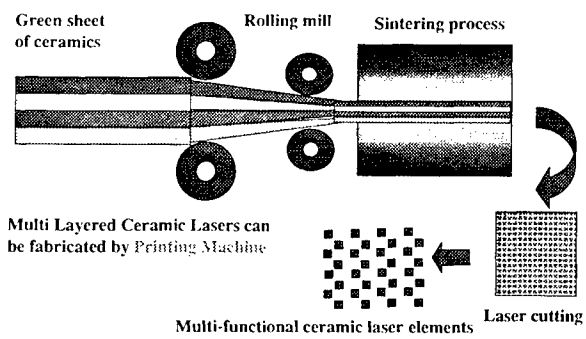


Fig. 6. Future image of ceramic laser fabricating process.

## 4. CONCLUSION

Optical absorption, emission spectra and fluorescence lifetime for Nd:YAG ceramics have been measured and compared to that of single crystal. Almost identical results have been obtained.

End-pumped laser experiment results show that the Nd:YAG ceramic lasers have almost the same laser efficiencies with that of single crystal. It means the scattering loss at the lasing wavelength of 1.064 μm is similar to that of single crystal. High power laser oscillation also was demonstrated using VPS pumping system. 31 W was obtained with 214.5 W pumping. Since Nd:YAG ceramics have their own advantages, for example, no expensive Ir crucible is required, large size and high concentration samples can be fabricated easily compared to single crystal growth method, and also mass production is possible. This kind of Nd:YAG ceramic is a very good alternative to Nd:YAG single crystals. The low cost and large-scale ceramic lasers can open the door to the new world of solid state lasers.

## ACKNOWLEDGEMENT

The authors would like to thank Prof. A. A. Kaminskii, the guest professors in our group from Russia, for very useful discussion. The authors would like to mention that the investigation was considerably enhanced due to collaboration with the Joint Open Laboratory for Laser Crystals and Precise Laser Systems.

## REFERENCES

1. E. Carnall, Jr., S. E. Hatch, and W. F. Parson, *Materials Science Research*, edited by W. Wruth Kriegel and Hayne Palmour III (Plenum, New York, 1966), vol. 3.
2. A. Ikesue, T. Kinoshita, K. Kamata et al., *J. Am. Ceram. Soc.* 78, 1033 (1995).
3. T. Yanagitani, H. Yagi, and M. Ichikawa, *Japanese patent*: 10-101333 (1998).
4. T. Yanagitani, H. Yagi, and Y. Hiro, *Japanese patent*: 10-101411 (1998).
5. J. Lu, M. Prabhu, J. Song, C. Li, J. Xu, K. Ueda, et al., accepted by *Appl. Phys B.*
6. A. A. Kaminskii, *Laser Crystals.* (Berlin, Heidelberg: Springer-Verlag, 1990).
7. N. Uehara, K. Nakahara, and K. Ueda, *Opt. Lett.*, vol. 20, 1707 (1995).

# Multi-wavelengths Z-scan $n_2$ measurements on crystal hosts for ultraviolet laser systems

Guido Toci [a], Matteo Vannini [a *], Renzo Salimbeni [a], Mark A. Dubinskii [b], E. Giorgetti [c]

[a] Istituto di Elettronica Quantistica (IEQ-CNR), Via Panciatichi 56/30, 50127 Firenze (Italy)

[b] Magnon, Inc. , 11710 Reisterstown Road S204A, Reisterstown MD 21136, USA

[c] Istituto di Ricerca sulle Onde Elettromagnetiche "Nello Carrara" (IROE-CNR) Via Panciatichi 64, 50127 Firenze (Italy)

## ABSTRACT

The nonlinear Kerr refractive index $n_2$ was determined in several crystal hosts, suitable for $Ce^{3+}$ doping to obtain tunable laser emission in the UV ($LiBaF_3$, $LiLuF_4$, LiCAF, $SrAlF_5$) and in the $KMgF_3$, suitable for $Yb^{2+}$ doping, a potential laser material in blue region. These parameters were measured by means of Z-scan measurements at 1064 nm and 532 nm, using picosecond laser pulses. The materials under test didn't exhibit two photon absorption effects, within the experimental sensitivity limits. The characterization of these new optical materials is important in view of the development of high peak power laser oscillators and amplifiers.

**Keywords**: Z-scan, nonlinear refraction, $LiBaF_3$, $LiLuF_4$, LiCAF, $SrAlF_5$, $KMgF_3$, Cerium laser, Ytterbium laser, blue-UV laser

## 1. INTRODUCTION

Solid state laser media obtained by doping wide band–gap dielectric crystals with rare earth ions for emission in the blue and ultraviolet (UV) region, and based on the dipole-allowed 5d↔4f transition were firstly proposed[1] , then experimentally demonstrated [2], and they are currently receiving increasing attention due to their wide range of potential applications (spanning environmental sensing, biology, semiconductor technology). These laser media could offer an alternative to the efficient but rather complicated and expensive excimer lasers and very complicated sources based on nonlinear frequency up-conversion of tunable lasers in the red and near infrared wavelength domain.

In particular $Ce^{3+}$ activated Colquiriites such as Ce:LiSAF and Ce:LiCAF are widely tunable (280-320 nm), highly efficient and capable to deliver nanosecond and subnanosecond pulses in the tens of mJ energy range [3 4 5]. Other Ce-based materials, such as $Ce^{3+}$:$LiLuF_4$ , $Ce^{3+}$:$LiBaF_3$ and $Ce^{3+}$:$SrAlF_5$ have shown similar laser properties [3 5 6 7]. The $Yb^{2+}$-doped $KMgF_3$ fluoroperowskite shows promising spectroscopic features for broadly tunable laser emission around 410 nm [8], although laser action is still to be demonstrated for this material.

In this paper we report the measurements of the bound electronic nonlinear refractive index $n_2$ of $LiBaF_3$ , $LiLuF_4$, LiCAF, $SrAlF_3$ and $KMgF_3$ measured on undoped samples at 1064 nm in the picosecond time scale, by means of the well-established Z-scan technique [9]. The $n_2$ value at 532 nm of some of these materials was already measured by us [10 11] and is reported here for completeness. The knowledge of the value of $n_2$ is important for the development of new, high-power laser oscillators and amplifiers. In particular, the refractive part of the nonlinearity gives rise to self-lensing, that must be taken into account in the optical design of the device, as it can affect the resonator operation, the output beam quality or even lead to catastrophic optical damage [12]. Furthermore self-phase modulation effects are important in the design of ultrafast laser systems (although this possibility has yet to be demonstrated for the materials under test).

To measure the non-linear refractive index of these materials, we employed the sensitive and relatively simple standard Z-scan technique [9]. This method is based on the self-focusing, or defocusing, of an optical beam induced by a nonlinear sample, which is moved along the propagation direction (Z axis) of a focused beam of known spatial structure.

* Correspondence: Email vannini@ieq.fi.cnr.it; Telephone: +39-055-416128; fax: +39-055-414612

XIII International Symposium on Gas Flow and Chemical Lasers and High-Power Laser Conference,
Antonio Lapucci, Marco Ciofini, Editors, Proceedings of SPIE Vol. 4184 (2001)

## 2. EXPERIMENTAL SET-UP

The experimental set-up is sketched in fig. 1. The laser that we employed to test the samples was a picosecond Nd:YAG oscillator/amplifier system, operating at 10 Hz, mode locked and frequency doubled (EKSPLA mod. PL2143A). Its emission parameters are reported in the table below. The pulse-to-pulse energy fluctuation is typically +-3% at 1064 nm and +- 5% at 532 nm (defined as standard deviation over 100 pulses). The pulse duration at the two wavelength was measured with the standard second-order autocorrelation method, and evaluated assuming a $sech^2$ pulse shape. We adopted the so-called trimmed Airy beam to perform the Z-scan measurements because this beam structure is easier to obtain than a gaussian beam from a real laser source, and it also provides higher sensitivity than this latter [13] .We obtained such a beam structure by first selecting the most uniform part of the laser beam with a 400 μm diameter pinhole and then, after a distance $d$ of free propagation ($d$ = 200 cm @ 532 nm, $d$ = 260 cm @ 1064 nm), by selecting the central lobe of the resulting Airy pattern with an iris (diameter 6.4 mm @ 532 nm, 16.9 mm @ 1064). This lobe is focused at a distance $f$ = 350 mm by a lens placed next to the iris. After the focus, the beam reached an aperture in the far field with a transmission T≈5%. The transmitted energy was measured by a silicon photodiode, and a beamsplitter placed between the iris and the lens sent part of the pulse energy to a reference photodiode. A 12 bit ADC board (National Instruments) simultaneously acquired a pulse sequence from the two photodiodes (both equipped with an integrating pulse-formation circuit, providing a peak voltage proportional to the light pulse energy), each at 10 ksample/sec of acquisition frequency. The signals were then stored and processed on a PC, which evaluates the time-averaged aperture transmission $\langle T\rangle = E_{aperture}/E_{total}$ for each laser pulse and averages this latter value over several laser pulses (typically 30) for each crystal position. The crystal was mounted on a motorized stage (Microcontrole) with 0.1 μm resolution, controlled by the same PC. For each sample, we acquired several Z-scan traces at various input pulse energies (measured with an Ophir NOVA energy meter equipped with a PE10 pyroelectric head), adjusted with rotating disk variable attenuators. The maximum pulse energy impinging on the sample was about 40 μJ for both wavelengths.

The fluctuations in the linear transmission of the sample, due to small surface and volume defects, were compensated by calculating the ratio between each scan and one acquired at low pulse energy, as reported in [9]. The overall sensitivity in the transmission variation thus achieved ranged from 0.25 % for the samples with better optical quality to 2 % for the worst ones.

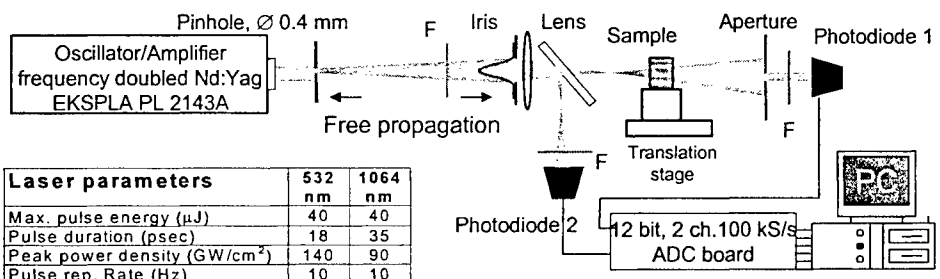


| Laser parameters | 532 nm | 1064 nm |
|---|---|---|
| Max. pulse energy (μJ) | 40 | 40 |
| Pulse duration (psec) | 18 | 35 |
| Peak power density (GW/cm²) | 140 | 90 |
| Pulse rep. Rate (Hz) | 10 | 10 |
| Pulse energy fluctuation | 5% | 3% |

Figure 1: The experimental setup

## 3. THEORY AND DATA ANALYSIS

The theory for the trimmed Airy beam, within the limit of thin samples, has already been reported by Rhee *et al.* [13]; in a previous work, we have extended this theory to the case of thick samples [11]. This enabled us to process and calibrate measurements obtained from samples having very different optical thickness. Neglecting the phase modulation effects of an order higher than the first, and the so-called self-action (that is, the perturbation due to the nonlinear beam refraction in the first portion of the sample, affecting the beam that crosses the remaining parts of the sample), one obtains the expression

$$\Delta T_{thick}(x,L) = kn_2^I I_0 z_d n_0 F_\Psi(x, L/n_0 z_d), \tag{1}$$

where $z_d=(\lambda f^2)/(\pi r_A^2)$ is a characteristic diffraction length, determined by the lens focal length $f$ and the radius of the first zero of the Airy intensity distribution at the lens plane $r_A$ ; $k$ is the vacuum wavenumber, $I_0$ is the beam intensity in the focus, $n_0$ is the linear refractive index , $n_2^I$ is the nonlinear refractive index. $F_\Psi$ is a function of $x=z/z_d$ (where $z$ is the distance of the crystal input face from the beam waist) and of the crystal length $L$ (measured in units of the beam diffraction length in the crystal , $n_0 z_d$ ). $F_\Psi$ can be calculated by properly integrating over the sample length the transmission variation obtained in the case of a thin sample, numerically calculated using the method described by Rhee *et al.* [13].

As pointed out before, our experimental set-up is capable to measure the transmission averaged over the pulse duration: $\langle T\rangle = E_{aperture}/E_{total}$, which is related to the instantaneous transmission described by eq. (1) via the following expression

$$\langle \Delta T_{thick}(x,L) \rangle = C\, F_{\Psi}(x, L/n_0 z_d)\,, \tag{2}$$

where $C$ is related to the laser pulse temporal shape and to the laser pulse energy through the formula

$$C = k n_0 n_2^I z_d \left(2/\pi w^2\right)\left[\int f(t)^2 dt \Big/ \int f(t) dt\right] E'_p \;=\; b E'_p \;, \tag{3}$$

with : $E'_p$ , pulse energy (corrected for the Fresnel losses at the crystal surface); $f(t)$, pulse temporal shape (so that $f(t)E'_p = P(t)$, instantaneous power); and $w$ , effective beam radius in the focus (so that the focal power density is $I(t)=2P(t)/\pi w^2$).

The value of the $n_2^I$ coefficients was determined by means of relative measurements calibrated with a reference material. As a calibrating sample we used a 5-mm-long sapphire ($Al_2O_3$) sample, whose $n_2^I$ value has been accurately determined at several wavelengths [14]. With this approach we avoided the needing of an accurate determination of the laser pulse shape and of the beam waist radius appearing in eq. (4), which are difficult to determine accurately in the picosecond or femtosecond pulse regime.

We fitted each Z-scan profile (corrected for the linear transmission as described above) with eq. (2). For each series of measurements taken on a given sample at different energy levels, we calculated the energy slopes $b$ defined in eq. (3). The $n_2^I$ value of the sample is given by (the subscripts *Sam.* and *Ref.* indicate the sample and the reference , respectively)

$$n_{2Sam.}^I = n_{2\mathrm{Ref}}^I \left[b_{Sam.} n_{0\mathrm{Ref.}}\right] / \left[b_{\mathrm{Ref.}} n_{0Sam.}\right] \;. \tag{4}$$

## 4. RESULTS AND CONCLUSIONS

Table 1 reports the values of $n_2^I$ obtained at 1064 nm ; the values previously obtained at 532 nm [10 11] are also reported for completeness. In addition to the previously uncharacterized materials, i.e. $LiLuF_4$ and $LiBaF_3$, we also report the measurements obtained with a LiCAF sample and a fused silica sample. This latter was added to the samples under test because it is a fairly well characterized material [14], thus providing validation for the measurement set up and the data processing technique that we adopted. The $n_2^I$ value for LiCAF was measured because, although this host appears in the literature as a suitable material for $Ce^{3+}$ doping for UV laser emission, its $n_2^I$ was previously measured only at 1064 nm [15]. It is reasonable to expect that this value of $n_2^I$ will increase at shorter wavelengths.

In table I, the error reported on the $n_2^I/n_2^I(Al_2O_3)$ ratio depends on the statistical error of the fits and on the determination of the energy slopes, whereas the error on the absolute values of $n_2^I$ also accounts for the error in the reported value of sapphire $n_2^I$. According to Table I, all the materials exhibit a $n_2^I$ value smaller than that of $Al_2O_3$ . No two photon absorption effects were observed within our sensitivity limits, as it is reasonable considering that for all the materials under test the energy band-gap is above the incident two-photon energy. For instance, the cutoff wavelength of $LiBaF_3$ and LiCAF is 112 nm , and for $KMgF_3$ is 115 nm [16 17]. For the same reason, all the materials under test exhibit a quite low dispersion of the $n_2^I$ value in the wavelength region under test.

In conclusion, we reported the measurements of $n_2^I$ nonlinearity at 1064 and 532 nm of important host crystals $LiBaF_3$ and $LiLuF_4$ . These materials have shown attractive characteristics as UV laser materials when doped with $Ce^{3+}$, and this characterization is useful in view of the development of high peak power UV laser devices. For example, the materials showing lower values of $n_2^I$, such as LiCAF, seem to be more appropriate for the development of an high power density

| Sample | L (mm) | $n_0$ | $n_2^I/n_2^I(Al_2O_3)$ | Measured $n_2^I$ ($10^{-16}$ cm$^2$/W) | Reported $n_2^I$ ($10^{-16}$ cm$^2$/W) | Ref. |
|---|---|---|---|---|---|---|
| 1064 nm | | | | | | |
| $Al_2O_3$ | 5.0 | 1.75 | - | - | 2.9±0.7 | 14 |
| $LiBaF_3$ | 9.0 | 1.544 | 0.70±0.03 | 2.0±0.5 | - | - |
| $LiLuF_4$ | 3.65 | 1.448 | 0.50±0.03 | 1.5±0.4 | - | - |
| LiCAF | | 1.39 | | | 0.4 | 15 |
| $KMgF_5$ | 3.65 | 1.4 | 0.22±0.04 | 0.6±0.3 | - | - |
| $SrAlF_5$ | 3.65 | 1.55 | 0.3±0.05 | 0.9±0.4 | - | - |
| 532 nm | | | | | | |
| $Al_2O_3$ | 5.0 | 1.76 | - | - | 3.3±0.7 | 14 |
| $LiBaF_3$ | 9.0 | 1.544 | 0.82±0.14 | 2.7±0.9 | - | - |
| $LiLuF_4$ | 1.0 | 1.47 | 0.45±0.04 | 1.5±0.5 | - | - |
| LiCAF | 12.6 | 1.398 | 0.16±0.02 | 0.73±0.25 | - | - |

Table 1: Experimental values of the nonlinear refractive indexes for the materials under test.

amplifier useful, because they determine smaller self-focusing effects (although this is not the only parameter determining the material choice)

The measurement of the $n_2^I$ value and the two-photon absorption coefficient of the above materials at shorter wavelengths, closer to the pump and lasing wavelength associated with $Ce^{3+}$-activation, will be the subject of future works.

## REFERENCES


1. K. H. Yang, J. A. De Luca, "UV fluorescence of cerium-doped lutetium and lanthanum trifluorides, potential tunable coherent sources from 2760 to 3220 Å", *Appl. Phys. Lett.* **31**, pp. 594-596, 1977

2. D. J. Ehrlich, P. F. Moulton, R. M. Osgood, Jr., "Ultraviolet solid-state Ce:YLF laser at 325 nm", *Opt. Lett.* **4**, pp. 184-186, 1979

3. Z. Liu, N. Sarukura, M. A. Dubinskii, R. Yu. Abduslabirov, S. L. Korableva, "All-solid-state subnanosecond tunable ultraviolet laser sources based on $Ce^{3+}$-activated fluoride crystals" *J. Nonlin. Opt. Phys. Mat.*, **8**, pp. 41-54, 1999

4. Z. Liu, K. Shimamura, K. Nakano, T. Fukuda, T. Kozeki, H. Ohtake, N. Sarukura, "High-pulse-energy ultraviolet $Ce^{3+}$:$LiCaAlF_6$ laser oscillator with newly designed pumping schemes.", *Jap. J. Appl. Phys.* Part 2 (Letters), **39**, pp. 466-467, 2000

5. N. Sarukura, M. A. Dubinskii, Z. Liu, V V. Semanshko, A. K. Naumov, S. L. Korableva, R. Y. Abdulsabirov, K. Edamatsu, Y. Suzuki, T. Itoh, Y. Segawa, "$Ce^{3+}$ Activated Fluoride Crystals as Prospective Active media for Widely Tunable Ultraviolet Ultrafast Lasers with Direct 10-ns Pumping", *IEEE J. Sel. Top. Quant. Electron.*, **1**, pp. 792-803, 1995

6. N. Sarukura, Z. Liu, S. Izumida, M. A. Dubinskii, R. Yu. Abdulsabirov, S. L. Korableva, "All-solid-state tunable ultraviolet subnanosecond laser with direct pumping by the fifth harmonic of a Nd:YAG laser", *Appl. Opt.* **37**, pp. 6446-6448, 1998

7. Z. Liu, H. Ohtake, N. Sarukura, M. A. Dubinskii, R. Y. Abdulsabirov, S. L. Korableva, "All-solid-state ultraviolet pulse generation from various cerium:fluoride lasers" Corcoran, V.J.; Goldman, T.A, *Proc. on the Int. Conf. On LASERS' 98*, STS Press, McLean (VA), pp. 421-427, 1999

8. M. A. Dubinskii, C. R. Prasad, A. K. Naumov, V. V. Shemansko, R. Y. Abdulsabirov, S. L. Korableva, "Laser spectroscopy of Yb-doped KMgF3 as a potential UV-Vis tunable material", Corcoran, V. J. and Corcoran, T. A., *Proc. on the Int. Conf. On LASERS' 99*, McLean, STS Press, pp. 407-412, 2000

9. Sheik-Bahae, M.; Said, A.A.; Wei, T.-H.; Hagan, D.J.; Van Stryland, E.W.," Sensitive measurement of optical nonlinearities using a single beam" 1990, *IEEE J. Quantum Electron.* **26**, pp. 760-769, 1990

10. G. Toci, M. Vannini, R. Salimbeni, M. A. Dubinskii, E. Giorgetti, "Z-Scan Measurements on Crystals Hosts for Ultraviolet Laser Emission", Corcoran, V. J. and Corcoran, T. A., *Proc. on the Int. Conf. On LASERS' 99*, McLean, STS Press, pp. 18-21, 2000

11. G. Toci, M. Vannini, R. Salimbeni, M. A. Dubinskii, E. Giorgetti, "First Z-scan $n_2$ measurements on crystal hosts for ultraviolet laser systems ", in press on *Appl. Phys. B*, 2000

12. W. H. Knox., "Femtosecond optical pulse amplification", *IEEE J. Quantum Electron.*, **24**, pp. 388-397, 1988

13. B. K. Rhee, J. S. Byun, E. W. Van Stryland, "Z scan using circularly symmetric beams", *J. Opt. Soc. Am. B*, **13**, pp. 2720-2723, 1996

14. DeSalvo, R., Said, A.A. , Van Stryland, E.W. , Sheik-Bahae, M. , "Infrared to ultraviolet measurements of two-photon absorption and $n_2$ in wide bandgap solids", *IEEE J. Quantum Electron.* **32**, pp. 1324-33, 1996

15. Beaud, P. , Richardson, M. C. , Chen, Y. F. , Chai, B. H. T., "Optical amplification characteristics of Cr:LiSAF and Cr:LiCAF under flashlamp-pumping", *IEEE J. Quantum Electron.* **30**, pp. 1259-1266, 1994

16. M. Sakai, Z. Liu, H. Ohtake, N. Sarukura, Y. Segawa, Y. Miyazawa, K. Shimamura, S.L. Baldochi, K. Nakano, N. Mujilatu, T. Fukuda, "*LiCAF crystal as a new vacuum ultraviolet optical material with transmission down to 112 nm.*", Technical Digest. CLEO/Pacific Rim '99. Pacific Rim Conference on Lasers and Electro-Optics, Piscataway, NJ, USA: IEEE p. 242-243 vol.2, 1999.

17 Shimamura, K.; Fukuda, T., "*[Fluoride single crystals for VUV optical applications]*" (in japanese) Oyo Buturi, **69**, pp.518-524, 2000.

# Energy extraction performance for a diode-pumped CPA system in Yb-doped materials at low temperature

Junji Kawanaka*[a], Hajime Nishioka[b], Norihiro Inoue[b], Yoshinori Kubota [c] and Ken-ichi Ueda[b]
[a] Advanced Photon Research Center, Japan Atomic Energy Research Institute (APR/JAERI)
[b]Institute for Laser Science, University of Electro-Communications (ILS/UEC)
[c]Chemical Research Center / Ube, Central Glass Co., Ltd.

## ABSTRACT

The observed absorption and emission spectra of Yb:YLF at low temperature show that energy extraction efficiency is improved drastically with the reduced saturation fluence of 9 J/cm$^2$ and the expanded spectral width of 38 nm. Yb:glass also shows a similar temperature dependence of the spectral characteristics to that of Yb:YLF.

**Keywords:** Yb-doped material, ultrahigh-peak-power laser, diode-pumping, low temperature, spectroscopy

## 1. INTRODUCTION

Since the first demonstration of a chirped pulse amplification (CPA) system,[1)] table-top ultrahigh-peak-power lasers have been developed utilizing an ultrashort pulse duration using a wide laser gain width of a Ti:Sapphire crystal.[2-4)] Using such ultrahigh-peak-power lasers, many novel phenomena in a high-field science have been shown experimentally.[5-6)] Nd:YAG lasers are one of the most major and verified pumping sources in such a Ti:Sapphire laser system, but occupy a comparably large space. Recently direct diode-pumped solid-state lasers with compactness and easy handling are in high demands and will advance many application fields. Yb:YLF and Yb:glass are one of the most promising laser materials for the diode-pumped ultrahigh-peak-power lasers due to a wide fluorescence spectral width and an absorption spectrum range matched to an emission wavelength of commercially obtainable high power laser diodes. We have demonstrated a diode-pumped oscillator with a Yb:YLF in a free running mode for the first time to our knowledge.[7)] A tunability measured with a birefringence filter shows the wide spectral width of 20 nm. In our free-running oscillator, the slope efficiency was high of 50%, which indicates the high ability for an efficient operation. But an optical-to-optical conversion efficiency was quite low of 13% in spite of an intense diode-pumping with more than 100 kW/cm$^2$. Our oscillator using Yb:glass also shows the low optical conversion efficiency of 10%. Because there was much re-absorption of the lower levels of the laser transition at room temperature, which are often found in the quasi-three-level system. As an energy splitting separation between the resolved ytterbium ground levels in both laser materials ($\Delta E_{max} < 800$ cm$^{-1}$) is comparable to room temperature (kT ~ 209 cm$^{-1}$ at 300 K), the population of the ground levels is very sensitive to the material temperature and the reabsorption of the laser lower levels can be controlled actively by changing the material temperature. By cooling the Yb-doped materials, therefore, much higher energy extraction efficiency must be obtained due to the reduction of the re-absorption, leading to a higher optical-to-optical conversion efficiency. In this paper, the high possibility of the drastic increase of the energy extraction efficiency by cooling

*Correspondence: E-mail: kawanaka@apr.jaeri.go.jp; Telephone: +81-774-71-3330; Fax: +81-774-71-3338

XIII International Symposium on Gas Flow and Chemical Lasers and High-Power Laser Conference,
Antonio Lapucci, Marco Ciofini, Editors, Proceedings of SPIE Vol. 4184 (2001)

the Yb:YLF and Yb:glass materials was shown based on our laser output characteristics and spectroscopic researches.

## 2. SPECTROSCOPIC RESEARCH AND PROSPECTS FOR ULTRAHIGH-PEAK-POWER LASERS

### 2.1. At Room Temperature

The absorption and emission spectra of Yb:YLF (60 at. %) and Yb:glass (19 wt. %, Kigre Inc., QX glass) were observed in a near-infrared region. In Yb:YLF at room temperature, the emission spectrum was overlapped with the absorption spectrum in the most of its spectral region for both π- and σ-polarization, shown in fig.1 (a) and (b), respectively. A spectral range without the re-absorption was at the longer wavelength than 1040 nm for π-polarization and than 1050 nm for σ-polarization, both of which were far from the wavelength of each emission peak. Our diode-pumped free-running laser was actually oscillated at 1040 nm for π-polarization, not for σ-polarization.[6] The slope efficiency was high of 50%, but the optical-to-optical conversion efficiency was low of 13%. If the pumping intensity could increase higher, the optical conversion efficiency would increase. That, however, can't be expected in diode-pumping because the pumping intensity in our oscillator was already enough high of 100 kW/cm$^2$ as an available high-brightness laser-diode. The oscillation wavelength could be tuned by putting a birefringence filter into the cavity. The spectral tuning width was wide of 20 nm, but much narrower than the emission spectral width. The effective saturation fluence at 1040 nm was numerically calculated at 114 J/cm$^2$. Even if a quite high pumping intensity can be obtained by diode lasers, the efficient energy extraction of an Yb:YLF crystal in a CPA system can't be technically achieved because the damage thresholds of any optics are much lower than the effective saturation fluence. Fig. 2 shows the absorption and emission spectra of the Yb:glass at room temperature. The overlap between them was observed in the almost whole observed spectral range. The emission spectral range without absorption was at the longer wavelength than 1040nm. A free-running laser oscillation with the Yb:glass was observed by changing the Yb:YLF crystal to the Yb:glass.[7] The oscillation wavelength was 1056 nm which is far from the emission peak wavelength as well as that in Yb:YLF. The observed tuning width was 26 nm between 1042 nm and 1068 nm. The slope efficiency was 23% and the optical conversion efficiency was 10%. The saturation fluence at 1060 nm was estimated too high of 251 J/cm$^2$.

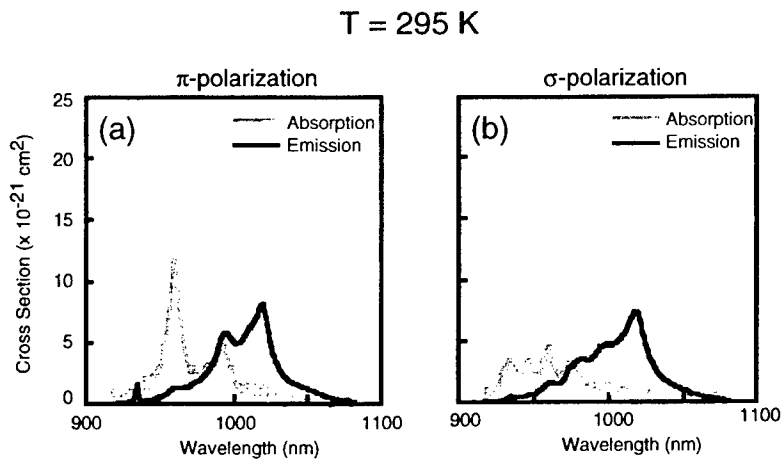


Fig. 1 Absorption and emission spectra for (a) π- and (b) σ-plarization of Yb:YLF at room temperature.

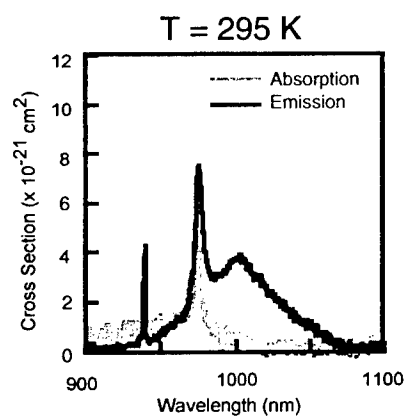


Fig. 2 Absorption and emission spectra of Yb:glass at room temperature.

### 2.2. At Low Temperature

Cooling the Yb:YLF crystal or Yb:glass leads to an efficient energy extraction. All resolved levels in the lower level ($^2F_{7/2}$) of the laser transition are populated at room temperature. As the energy seperation is comparable to room temperature, the population of each level changes at low temperature, that is, the upper levels among the resolved ground levels become empty and the lowest level becomes more enriched, shown in Fig. 3. The re-absorption of lower levels of the laser transition, therefore, will be reduced. The energy extraction efficiency will increase and the spectral width for the effective laser gain will be expanded. Fig. 4 (a) and (b) show the absorption and emission spectra at 8 K for π- and σ-polarization of an Yb:YLF crystal, respectively. The spectral overlap was completely vanished for both polarization. The energy extraction efficiency increases drastically even in diode-pumping without the re-absorption just like the four-level laser system. The spectral range with an effective laser gain is expected to be the same as the whole emission spectral range, that is about 38 nm for both polarization which corresponds to a 39 fs ultrashort pulse duration under the assumption of the Fourier transform limit of the gaussian profile. The peak emission cross section for π-polarization increased extremely to 2.3 x $10^{-20}$ $cm^2$ at 995 nm, which was about one-order higher than the effective emission cross section at 1040 nm at room temperature. The effective saturation fluence in a diode-pumping was decreased to 9 $J/cm^2$ (at 1015 nm) at 8 K from 114 $J/cm^2$ (at 1040 nm) at room temperature, which was comparable to the minimum damage threshold among various optics for a 1-ns pulse in a CPA system. For σ-polarization, the saturation fluence was low of 11 $J/cm^2$ (at 1013 nm) comparable to that for π-polarization. At low temperature, the efficient energy extraction can be achieved with commercially obtainable optics for both polarization. Fig. 4 shows absorption and emission spectra of Yb:glass at 30 K. The temperature dependence of the observed spectral characteristics were almost same as that of Yb:YLF. The spectral range for the efficient energy extraction will be expanded to 70 nm. The saturation fluence decreased to 56 $J/cm^2$ (at 1013 nm) at 30 K from 251 $J/cm^2$ (at 1056 nm) at room temperature. These spectral characteristics for Yb:YLF and Yb:glass were kept almost the same at the liquid nitrogen

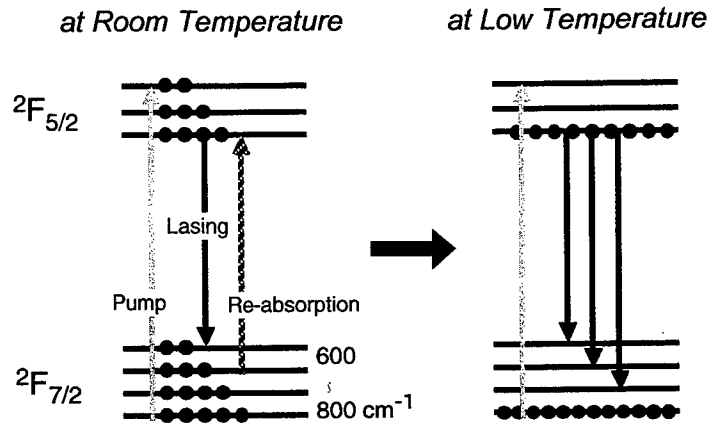


Fig.3 Populations in $Yb^{3+}$ doped in YLF and glass.

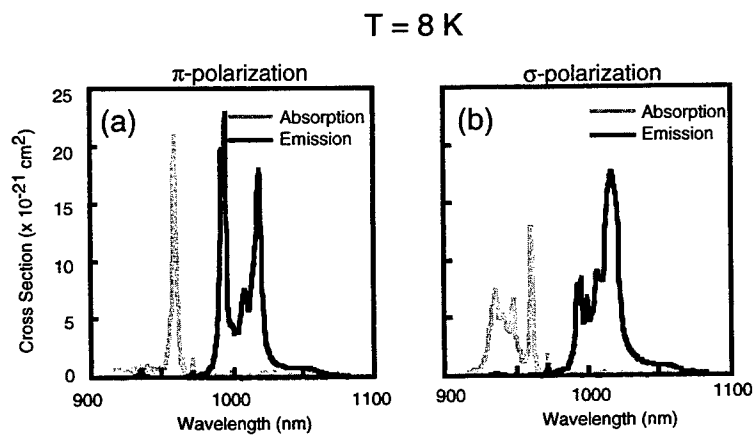


Fig. 4 Absorption and emission spectra for (a) π- and (b) σ-polarizaiton of Yb:YLF at 8 K.

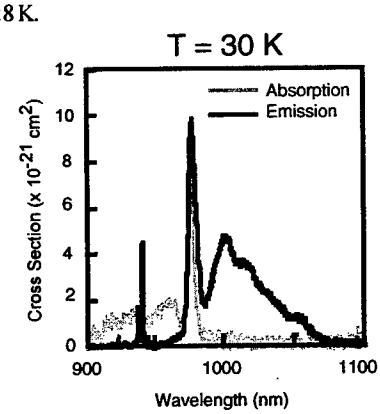


Fig. 5 Absorption and emission spectra of Yb:glass at 30 K.

temperature. That leads to a compact and low-cost cooling unit.

## 3. CONCLUSION

The absorption and emission spectra of Yb:YLF and Yb:glass were observed. At low temperature, there were no overlaps between them for both polarization of a Yb:YLF crystal and the optical-to-optical conversion efficiency is expected to increase drastically even at a diode-pumping intensity. The broadened spectral range with the effective laser gain was 38 nm for both $\pi$- and $\sigma$-polarization, which corresponded to a 39 fs ultrashort pulse duration. The effective saturation fluence was reduced below the damage thresholds of any optics used in a CPA system and the efficient energy extraction can be achieved with commercially obtainable optics. In Yb:glass, the similar temperature dependence of the spectral characteristics to that of Yb:YLF were shown qualitatively. The Yb:YLF and Yb:glass at low temperature will be used as the highly efficient laser materials for the diode-pumped ultrahigh-peak-power lasers.

## REFERENCES


1) D. Strickland and G. Mourou, Opt. Comm. **56**, 219 (1985).

2) J. P. Chambaret, C. Le Blanc, A. Antonetti, G. Cheriaux, P. F. Curley, G. Darpentigny, and F. Salin, Opt. Lett. **21**, 1921 (1996).

3) A. Sullivan, J. Bonlie, D. F. Price, and W. E. White, Opt. Lett. **21**, 603 (1996).

4) K. Yamakawa, M. Aoyama, S. Matsuoka, T. Kase, Y. Akahane, and H. Takuma, Opt. Lett. **23**, 1468 (1998).

5) K. W. D. Ledingham, I. Spencer, T. McCanny, R. P. Singhal, M. I. K. Santala, E. Clark, I. Watts, F. N. Beg, M. Zepf, K. Krushelnick, M. Tatarakis, A. E. Dangor, P. A. Norreys, R. Allott, D. Neely, R. J. Clark, A. C. Machacek, J. S. Wark, A. J. Cresswell, D. C. W. Sanderson, and J. Magill, Phys. Rev. Lett. **84**, 899 (2000).

6) J. Kawanaka, H. Nishioka, N. Inoue, and K. Ueda, submitted to Appl. Opt. (2000).

7) J. Kawanaka, H. Nishioka, and K. Ueda, Technical Digest of Conference on Lasers and Electro-Optics 2000, 250 (2000).

# Models for description of nonlinear dynamics and switching regimes in a laser with a saturable absorber

Liudmila A. Kotomtseva, Sergey G. Rusov
B.I.Stepanov Institute of Physics, National Academy of Sciences of Belarus, Minsk, Belarus

## ABSTRACT

Results of consideration of nonlinear dynamics and switching regimes in a solid state laser with a saturable absorber, which take into account spectral properties of both an active medium and saturable absorber with different resonant frequencies, give us multi-stability of their steady states and coexistence of two regular regimes with sequences of nanosecond sinusoidal pulses or picosecond high intensity pulses both with constant in time intensity regime in dependence on the beginning conditions. Switching regimes between coexisting steady states are demonstrated. Another model is proposed for consideration of the polarization of light in a isotropic cavity with crystal active medium and saturable absorber. Steady states both with two directions of linear polarization as result of self induced anisotropy effects are described.

**Keywords:** Laser with a saturable absorber, nonlinear dynamics, multi-stability, polarization of light

## 1. INTRODUCTION

Lasers with a saturable absorber (LSA) find wide application both in scientific research and practical applications in nonlinear optics, spectroscopy, optical communications and so on due to rich number of valuable properties. New high quality crystals and dyes are widely used as compact laser sources and nonlinear elements. Picosecond pulses are observed in microchip LSA[1,2] . That is why modifying of the basic equations to real new media, which permits us to find potential possibilities of the definite laser systems and predict their spectral and temporal properties is important.

We propose results of consideration of two models for description of dynamics in a solid state or dye laser with a saturable absorber. One of them accounts for the spectral properties for arbitrary resonant frequencies of the transition in an active medium, saturable absorber and the cavity in the isotropic system. Another model is proposed for description of polarization properties of a LSA with a crystal active medium and saturable absorber in isotropic cavity.

## 2. MULTISTABILITY AND SWITCHING REGIMES IN A LSA

Results of theoretical consideration of the steady states, their stability,switching regimes under change of the definite parameter and nonlinear dynamics of a single mode solid state laser with a saturable absorber on the basis of model[3-4] are proposed. The basic system of equations looks in the next way:

$$\dot{I} = 2a\left(\frac{k_a}{1+\Delta_a^2} + \frac{k_b}{1+\Delta_b^2} - 1\right)I, \quad (1)$$

XIII International Symposium on Gas Flow and Chemical Lasers and High-Power Laser Conference,
Antonio Lapucci, Marco Ciofini, Editors, Proceedings of SPIE Vol. 4184 (2001)

(GSGG, $GdVO_4$ and so on) and a saturable absorber $Cr^{4+}$:YAG or LiF:$F^-_2$ crystal, as for example in experiments[5,6] demonstrate us new polarization properties of laser radiation. There are phenomenological models for description of the experimental behavior of a $YAG:Nd^{3+}$ laser with a saturable absorber $Cr^{4+}$:YAG crystal and for a dye laser with a saturable absorber with anisotropy[5-9]. We propose model for theoretical description of a polarization properties of a solid state laser with a saturable absorber, which takes into account orientations of the dipole moments of crystals of the resonant transitions both in an active medium and in an absorber.

The basic system of equations is written for two orthogonal components of the complex amplitude of electric field of radiation $E_x$ and $E_y$ in the isotropic cavity with direction of light propagation along z-axis. For the same orientations of dipole moments in an active medium as cubic crystal with optical axes along $x,y,z$ directions there are written equations for the components of relative inversion of populations $n_{ax}$ and $n_{ay}$. We consider the $x$- and $y$- components of the relative difference of populations of the ground and excited level in an absorber $n_{b1}$ and $n_{b2}$, which take into account arbitrary directions of optical axes of crystal grating in an absorber. Namely angle $\theta$ between optical axes of an absorber and axes $x$, $y$ determines effective absorption. For nonlinear absorber withdifference of populationns following the field with small saturation parameters $s_{bx}$ <<1 and $s_{by}$ <<1 the basic system of equations is the next one:

$$\dot{E}_x = a\{n_{ax}(1-ib_{ax}) - [n_{b1}f_1[1-s_{bx}(f_1I_x + f_2I_y + \sqrt{f_1f_2}(E_xE_y^* + E_x^*E_y)) +$$
$$+ n_{b2}f_2(1-s_{by}(f_2I_x + f_1I_y - \sqrt{f_1f_2}(E_xE_y^* + E_x^*E_y))](1-ib_{bx}) - 1\}E_x,$$
$$\dot{E}_y = a\{n_{ay}(1-ib_{ay}) - [n_{b2}f_1(1-s_{by}(f_2I_x + f_1I_y - \sqrt{f_1f_2}(E_xE_y^* + E_x^*E_y)) +$$
$$+ n_{b1}f_2(1-s_{bx}(f_1I_x + f_2I_y + \sqrt{f_1f_2}(E_xE_y^* + E_x^*E_y))](1-ib_{by}) - 1\}E_y,$$

$$\dot{n}_{ax} = n_{ax}^0 - n_{ax} - s_{ax}n_{ax}I_x, \quad \dot{n}_{ay} = n_{ay}^0 - n_{ay} - s_{ay}n_{ay}I_y.$$

Here $f_1=cos^2\theta$, $f_2=sin^2\theta$ give us typical for cubic crystal dependence of absorption of the resonant dipoles[5,7] on the angle $\theta$ between optical axes of an active medium and absorber in the plane $(x,y)$. Then effective difference of populations in an absorber along axis $x$ or axis $y$ is written as

$$n_{bx} = n_{b1}f_1 + n_{b2}f_2, \quad n_{by} = n_{b1}f_2 + n_{b2}f_1.$$

Coefficient $a$ is equal to the ratio of the decay rate of inversion of populations in an active medium to the photon life time in the cavity, $b_{ax}$, $b_{ay}$, $b_{bx}$ and $b_{by}$ give us resonant addition to refraction[6], which for solid state medium is usually <<1, but for a semiconductor, which can be used as a saturable absorber, it can be sufficient. Parameters of saturation of an active medium for each of polarization $s_{ax}$ and $s_{ay}$ are of the order of unity. Unsaturated gain in an active medium $n_{ax}^0$ and $n_{ay}^0$ gives us ratio of the unsaturated inversion of populations to the laser loss.

There are three types of steady state solutions with nonzero intensity, namely two of them are linearly polarized with intensities $I_x>0$, $I_y=0$, and $I_x=0$, $I_y>0$ and can be determined as roots of square equation . Elliptically polarized solution with amplitudes of field $E_x=e_xe^{if_x}$ and $E_y=e_ye^{if_y}$ can be determined from the quartic equation. Trivial steady state with zero intensities of both polarizations exists for any parameters.

Figure 3 gives us example of the dependence of the intensity of the steady state $I_x$ (a), $I_y$ (b) with linear polarization of rotation of an absorber in plane $(x, y)$.

$$\dot{k}_{a,b} = d_{a,b}(q_{a,b} - k_{a,b} - s_{a,b}k_{a,b}\frac{I}{1+\Delta_{a,b}^2}), \qquad (2)$$

$$\dot{f} = -\Delta_c - ak_a\Delta_a/(1+\Delta_a^2) - ak_b\Delta_b/(1+\Delta_b^2), \qquad (3)$$

There are two kinds of multivalued steady states which correspond to two sets of roots due to action of nonlinear dispersion of both active and passive media when spectral width of an absorption line of absorber is more narrow than spectral width of the gain line of an active medium. Conditions for several such values of intensity and frequency, up to five, coexistence together with the zero intensity trivial state, can be given analytically and their stability is considered in dependence on the parameters of an active medium, absorber and the cavity with attraction attention to the role of the detunings of the resonant frequencies.

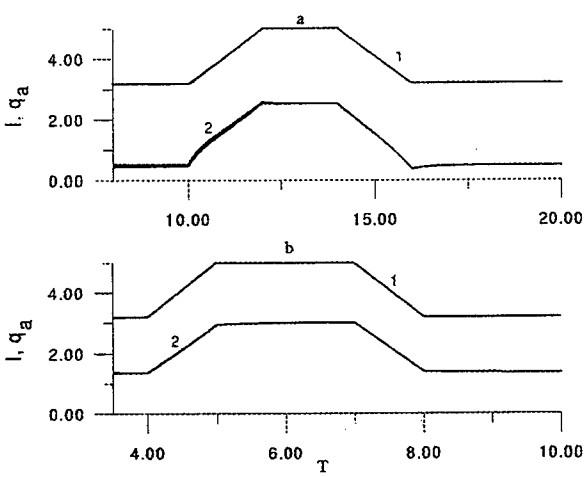


Figure1. Unsaturated gain (1) and intensity (2) vs time at $q_a(0)$=3.2,$d_b$=1, $I(0)$=0.48 (a), $I(0)$=1.367 (b), $g$=0.05, $\Delta_{ac}$=-0.01,$q_b$=-2.

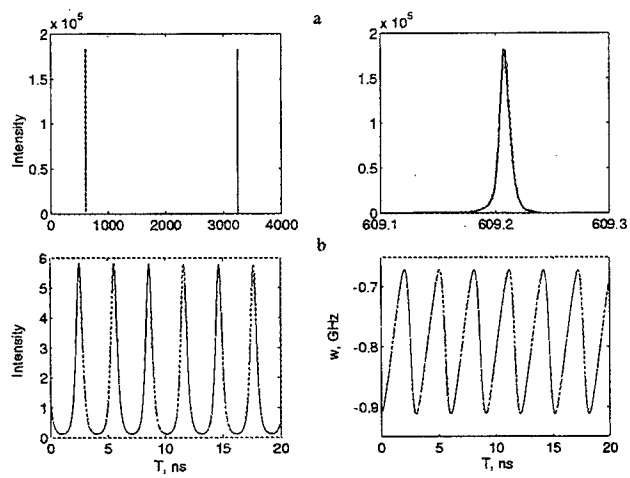


Figure 2. Intensity vs time at $q_a$=3.2,$d_b$=6, $I(0)$=0.48 (a), $I(0)$=1.367 (b), $g$=0.05, $\Delta_{ac}$=-0.01,$q_b$=-2.

Figure 1 gives us switching regimes during adiabatic change of pumping $q_a$ under the coexistence of three nonzero intensity steady states and shows us possibility to have several roads of the intensity and frequency change in the dependence on the beginning conditions and switching between some of states.

Two types of regular sequences of steady pulses with chirped frequency have been found: upper part of figure 2 gives us high intensity pulses with frequency of repetition ~ 0.1 *MHz* and duration of about 10 *ps*. Below there is sequence of sinusoidal pulses with four order less intensity and high frequency of repetition of about 10 *MHz* with duration of the definite pulse of about 10 *ns* and with chirped frequency of radiationn given in right part. Such regimes can coexist in the same LSA and develop in dependence on the beginning conditions. For the same parameters constant intensity light at the definite frequency can be found at the other beginning conditions. Conditions for the experimental observation of described regimes of LSA operation can fe fulfilled in typical solid state microlaser.

## 3. POLARIZATION PROPERTIES OF A LSA

Solid state lasers with anisotropy and nonlinear change of refractive index both in an active crystals doped with $Nd^{3+}$

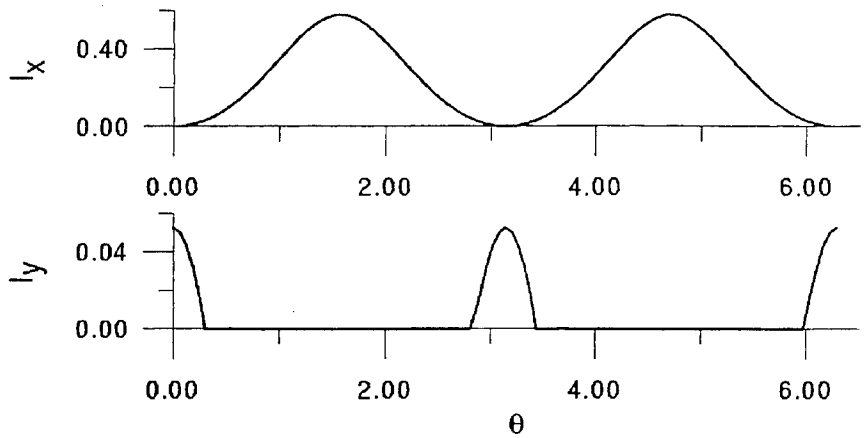


Figure 3. Intensities $I_x$ and $I_y$ vs $\theta$ at $n_{ax}^0=3$, $n_{b1}^0=2$, $n_{ay}^0=2$, $n_{b2}^0=0.9$, $s_{ax}=s_{ay}=1$, $s_{bx}=s_{by}=10^{-5}$, $b_{ax}=b_{ay}=10^{-5}$, $b_{bx}=10^{-6}$, $b_{by}=2\cdot10^{-5}$.

## ACKNOWLEDGMENTS

This work is supported by grant number F98-068 of Basic Research Foundation of Belarus republic.

## REFERENCES

1. B.Braun, F.Kartner, U.Keller, J.-P.Meyn and G.Huber, "Passively Q-switched 180-ps Nd:$LaSc_3(BO_3)_4$ microchip laser", *Opt. Lett.* **21**, pp. 381-383, 1996.

2. B.Braun, F.Kartner, G.Zhang, M.Moser and U.Keller, "56-ps passively Q-switched diode-pumped microchip laser", *Opt. Lett.* **22**, pp. 405-407, 1997.

3. L. A. Kotomtseva, "Solid state laser with a saturable absorber models for the tunable passive loss modulation and mode-locking regimes", *Laser Physics* **8,** pp. 254-258, 1998.

4. L.A.Kotomtseva, S.G.Rusov,"Multivalued steady states and their stability in a LSA", *Journ. Appl. Spectroscopy* **67**, pp. 322-326, 2000 (Rus).

5. N.N.Il'ichov, A.V.Kir'yanov, P.P.Pashinin, "Model of passive Q switching taking account of the anisotropy of nonlinear absorption in a crystal switch with phototropic centres", *Quantum Electron.* **25,** pp.155-159,1998 (Rus).

6. O.L.Antipov, A.S.Kuzhelev, D.V.Chausov, A.P.Zinov'ev, "Dynamics of refractive-index changes in a Nd:YAG laser crystal under excitation of $Nd^{3+}$ ions", *J. Opt. Soc. Am.* **B 16**, pp. 1072-1079, 1999.

7. A.Dement'ev, R.Navakas, "Generation simulation of a solid state microlaser with passive-active modulation Q-switching and continuous diode pump" in book *Lasers and Optical Nonlinearity*, pp.124-127, Minsk, 1999 (in Russian).

8. M.Wittman, F.Rotemund, R.Weigand, A.Penzkofer, "Saturable absorption and absorption recovery of indocyanine green J-aggregates in water", *Applied Physics* **B 66**, pp. 453-459, 1998.

9. S.V.Sergeyev, I.V.Brezgunova, "Light polarization symmetry breaking in a anisotropic dye laser with a saturable absorber for orthogonal dipole moments with emission and absorption", *Nonlinear Phenomena in Complex Systems* **2**, pp. 83-90, 1999.

# Interactions between DC plasma and HF fields

Adam Cenian*, Andrey Chernukho*#, Christophe Leys& and Annemie Bogaerts$

* Institute of Fluid-Flow Machinery, Polish Academy of Sciences, 80-952 Gda• sk, Fiszera 14, e-mail:cenian@imp.pg.gda.pl

& Ghent University, Department of Applied Physics, Rozier 44, 9000 Ghent, Belgium, e-mail: Christophe.Leys@rug.ac.be

$ University of Antwep (U.I.A.), Department of Chemistry, Universiteitsplein 1, 2610 Antwerp-Wilrijk, Belgium, e-mail: bogaerts@uia.ua.ac.be

## ABSTRACT

The influence of electromagnetic fields on a DC discharge in a $CO_2$:$N_2$:He mixture is studied by means of a Monte Carlo simulation. The HF fields polarised in parallel and perpendicular directions to DC are considered.

**Keywords:** $CO_2$ lasers, DC plasma, HF fields

## 1. INTRODUCTION

The high frequency (HF) fields may have a pronounced influence on the properties of a direct-current plasma. For example, it was observed that the plasma instabilities evolve much faster in a DC discharge when a resonator couples laser radiation. The influence of laser radiation on the plasma impedance (optogalvanic effect) has been studied extensively by Smith et al. [1,2]. The generation of sound waves due to the interaction of radiation and laser medium was discussed in ref. [3,4].

In some cases it may be interesting to use the coupled DC and HF fields for excitation of an active medium, e.g. the HF field can be used to trigger pulses in a DC discharge. The direct transfer of energy from the coupled electrical fields to electrons is studied here by means of a Monte Carlo simulation. The HF fields polarised in parallel and perpendicular directions to DC are considered.

## 2. MODEL DESCRIPTION

The simulations are performed using a Monte Carlo (MC) algorithm [5], which is a modified version of that described in ref. 6. The null collision method is applied ($v_{tot}$ = const), and so, the mean free time between collisions is given by the expression $t_f = -\ln(R) / v_{tot}$, where R is a random number. The model is applied to a DC+HF discharge in a $CO_2$:$N_2$:He mixture. The total collision frequency is calculated using cross-sections tabulated by Phelps et al. [7] for elastic collisions, ionization as well as rotational, vibrational and electronic state excitations. All the collision processes are treated in the isotropic approximation, and the scattering angle is given by a random number. The energy partition between the primary and secondary electrons (after ionization) is random as well.

The MC algorithm is checked using the results for a DC discharge in nitrogen. In the figure the results of the simulation (dots) are compared with a standard solution of the Boltzmann equation [8] in a 2-term spherical harmonics appr. (solid line). The agreement is

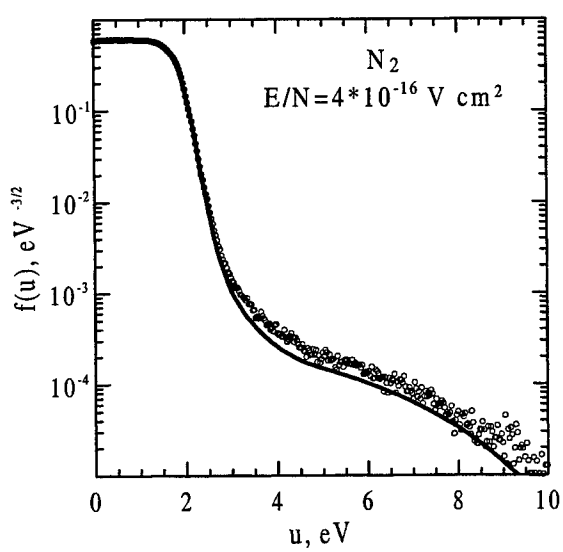


Fig. 1. EEDF in nitrogen plasma calculated using Boltzman equation (line) and MC (dots)

# on leave from: Belarus Academy of Sci., Heat and Mass Transfer Institute, 220072 Minsk, 15 P.Brovka Str., Belarus; e-mail: chern@itmo.by

XIII International Symposium on Gas Flow and Chemical Lasers and High-Power Laser Conference, Antonio Lapucci, Marco Ciofini, Editors, Proceedings of SPIE Vol. 4184 (2001)

satisfactory and the results agree well with the conclusion presented by Braglia et al. [9].

The stationary discharge conditions in the bulk plasma are considered. Electrons are accelerated in the coupled DC and HF fields, directed parallel or perpendicular to one another. The reduced electric field of a DC discharge is equal to that of the DC laser system [8]; $E/N = 4.5*10^{-20}$ $Vm^2$ and is kept constant for all the considered HF frequencies. The effect of increased ionization after the inclusion of the HF field is discussed shortly.

## 3. RESULTS AND DISCUSSION

Figure 2 presents the effectiveness of energy transfer from the HF field to electrons. The fields with frequencies higher than 100 GHz do not participate in energy transfer to electrons of laser plasma (at least as long as the quantum effects e.g. the inverse bremsstrahlung process, are not important). This results from the fact that as long as there is no collision (total frequency of electron collisions is in the range 10 – 100 GHz under the considered conditions) the electron oscillates in the HF field and does not gain any energy from the field. Then, the averaged energy of electrons, <u>, is constant - the same as for DC field alone. This is illustrated by saturation at high frequencies.

The maximum of the coupling between the HF field and electrons exists at frequencies ~ 1 GHz. The value $\langle u \rangle_{max}$ for the parallel field is higher than for the perpendicular one because of the vector summation rule. The very steep decrease at lower frequencies (in the case of the parallel arrangement of the HF field) can be related to the fact that the resultant field E falls periodically to null in this case. Eventually the averaged electron energy reaches saturation at lower frequencies. This is the frequency region where the stationary solution of the Boltzmann equation may be applied with the so-called 'effective field' approximation $E_{eff} = E_{HF}/\sqrt{2}$ [10].

For the $CO_2$ laser medium the more important than the electron energy is the vibrational excitation or

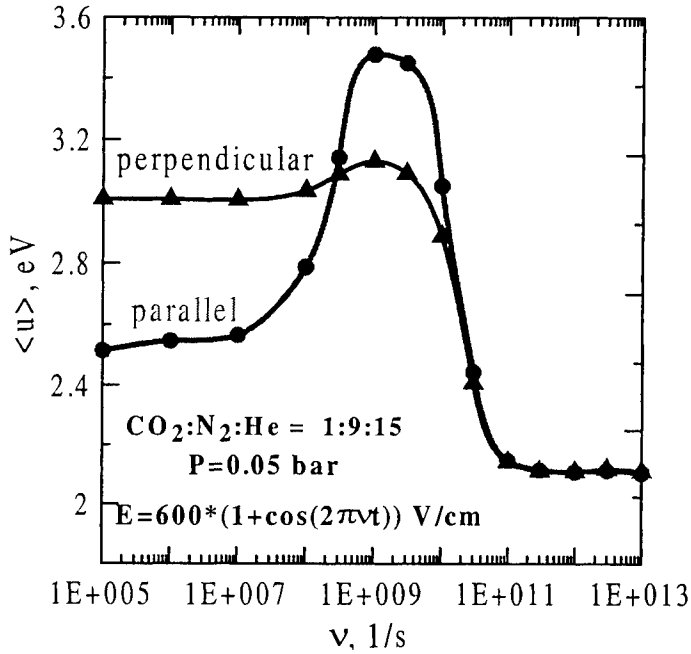


Fig. 2. Electron energy in a DC + HF plasma; HF electric field parallel and perpendicular to DC field

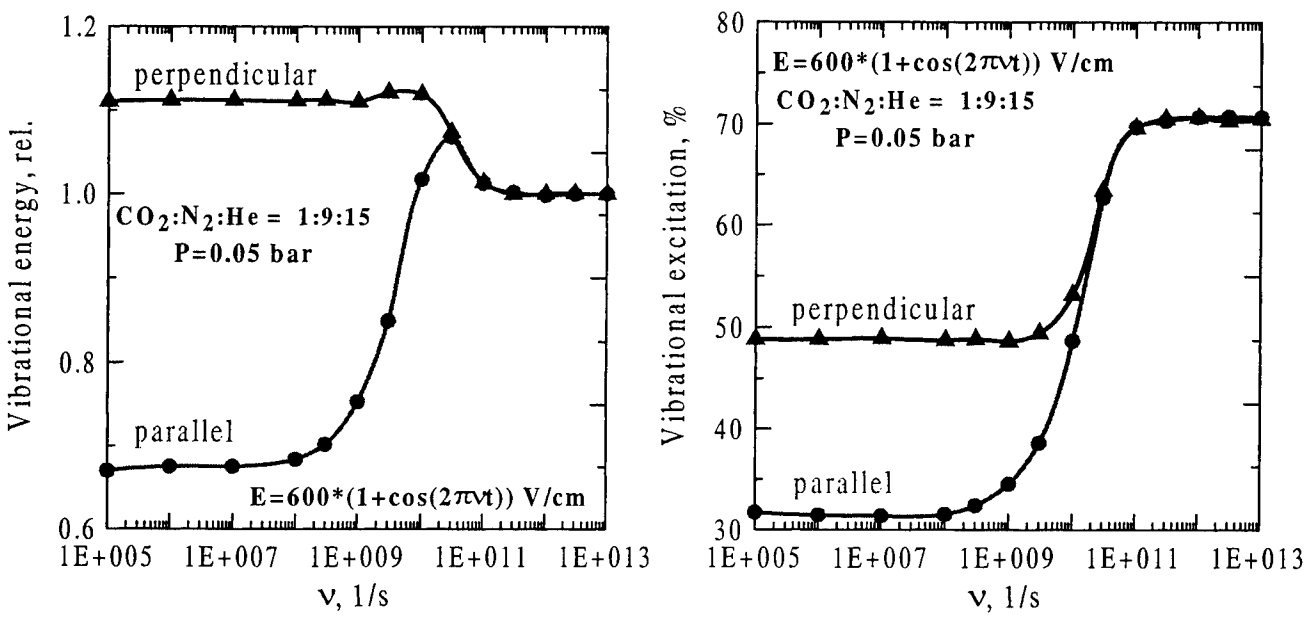


Fig. 3. (a) Energy transferred to the vibrational modes of nitrogen and (b) its ratio to whole absorbed energy in DC +HF plasma.

the energy transferred to the vibrational modes, especially to the oscillations of nitrogen molecules. Figure 3 (a) shows the energy transferred from the coupled DC+HF fields to the vibrational modes of $N_2$. One sees that the maximum energy transferred to the vibrations is only about 10% higher than that corresponding to DC field alone (value 1 in Fig. 3(a)).

The energy is not transferred to the vibrations very efficiently if compared with the pure DC case. This is resembled by the high frequency region in Fig. 3(b), where electrons do not absorb energy from HF. The main reason for this behaviour is that the average electron energy <u> is much too high. After the HF field is turned-on the ionization rates in the DC plasma increase rapidly. The significant increase of electron density will result in the fall of DC voltage of the current source. Figure 4 presents estimated $E_{DC}/N$ after the HF field is turned-on. In this case (current sources) the electron energy may be much closer to the optimal one (for the vibrational excitation).

Finally, we have considered the case of discharge generated by the HF field alone - Fig.5. Again, in the high frequency range, $\nu > 100$ GHz, the energy of the HF field is poorly absorbed by electrons; average electron energy <u> $\leq$ 0.1 eV - Fig.5.(a). One sees that the energy transferred to the electrons rapidly increases in the frequency region which is close to the total collision frequency i.e. 10 – 100 GHz. At lower frequencies <u> does not change with the field frequency, significantly.

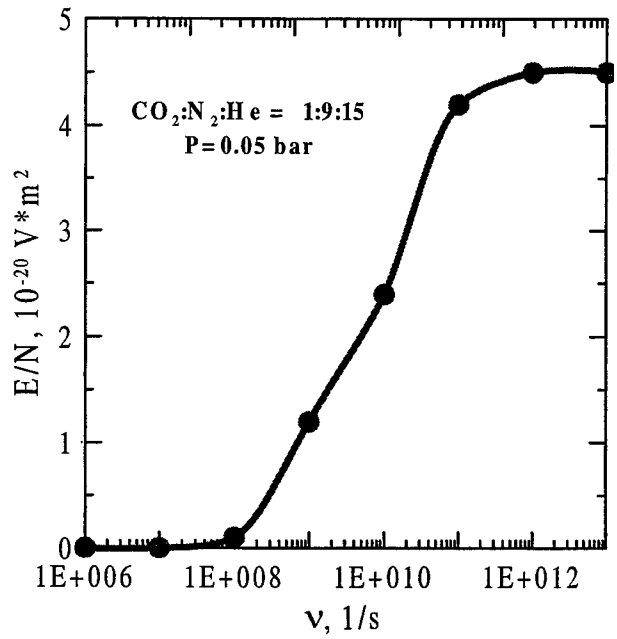


Fig. 4. E/N of DC field after HF is turned-on.

The energy transferred to the nitrogen vibration is related to the maximum value at $\nu_{max}$ = 3 GHz. The energy slightly decreases for lower frequencies but again there is no any significant dependence. For the frequencies higher than the $\nu_{max}$ the transferred energy falls quit rapidly. The ratio of energy transferred to vibrations to the total energy absorbed by electrons reaches its maximum at ~ 30 GHz, the value higher than $\nu_{max}$ . But this need to be related to the significant drop of the total energy absorbed by electrons from the HF field.

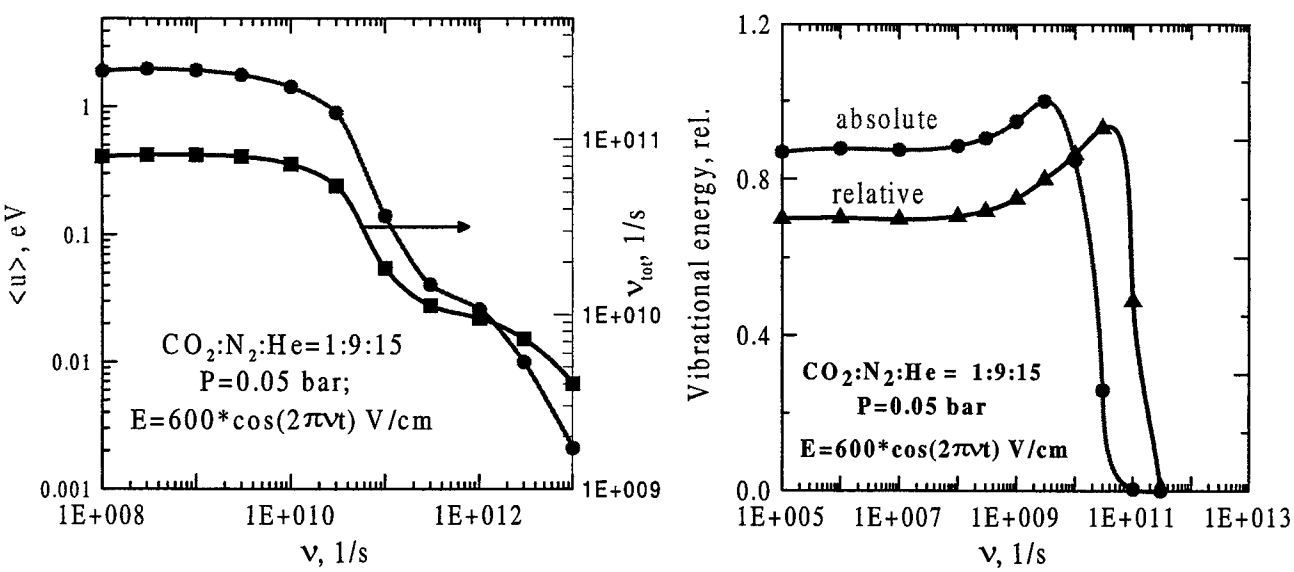


Fig. 5 (a) Electron energy, total collision frequency, (c) vibrational energy and excitation (ratio of energy transferred to vibrations to the total energy absorbed by electrons) in plasma of HF fields

## 4. CONCLUSIONS

It was shown that the HF field at frequencies lower than the total collision frequency of electrons in the plasma may significantly increase the electron temperature of the DC discharge. This lead to the increased ionization rates and the fall of the DC voltage in the case of a current source. When the DC voltage is constant, then the energy absorbed by electrons from the HF field is not transferred to the nitrogen vibrations very efficiently. The electron temperature, <u>, becomes too high.

The presented mechanism may be used to trigger the pulsed operation of DC discharges. In this case the optimal HF source should operate in the frequency range, $0.4 < \nu_{opt} < 4$ GHz, with $E_{HF}$ parallel to $E_{DC}$ . The perpendicular arrangement is better for the HF sources operating at the frequencies lower than 0.3 GHz.

## REFERENCES


1. A.L.S. Smith and M.Brooks, *J.Phys. D: Appl.Phys.* **12**, pp. 1237-48, 1979
2. S.Moffatt and A.L.S. Smith, *Opt.Comm.* 37 , 119-122, 1981, *J.Phys. D: Appl.Phys.* **17**, pp. 59 – 70 and 71 – 78, 1984.
3. P.F.Kellen, A.C.Mattsson, D.R.Ahouse and M.J.Yoder, *Opt. Eng.*, **18**, pp. 340-344, 1979.
4. A.A.Deryugin, V.V.Likhanskij and A.P.Napartovich, *Quant. Electr.* **13**, pp.950- 955, 1986 (in Russian).
5. A.Cenian, A.Chernukho, A.Bogaerts, R.Gijbels, V International School-Seminar "*Nonequilibrium Processes and their Applications*", Minsk, Belarus, Contr. Papers, pp.3-8, 2000.
6. A.Bogaerts, M.van Straaten and R.Gijbels, Spectrochim.Acta B **50**, pp.179 , 1995
7. A.V.Phelps et al., *Joint Institute for Laboratory Astrophysics (JILA) Information Center Report* No.26 (1985), (to be found on ftp://jila.colorado.edu/collision_data/).
8. A.Cenian, A.Chernukho, et al., *J.Phys.D:Appl.Phys.*, **30**, pp. 1103- 111, 1997 *Contr.Plasma Phys.*, **34**, 25-37, 1994; **35**, 273-296, 1995.
9. G.L.Braglia, et al., *Lett. Nuovo Cimento* **30**, pp. 459- , 1981; **35**, pp.193- , 1982; *Phys.Rev.A* **26** (1982) 3689.
10. T.Ledig and B.Schroeder, *J.Phys.D:Appl.Phys.*, **23**, pp. 1624-1632, 1990.

# Phase conjugation of long pulses at stimulated Brillouin scattering with feedback

Mikhail Galushkin, Konstantin Mitin
IPLIT, Russian Academy of Sciences, Svyatoozerskaya 1, Shatura, Moscow reg., 140700 Russia

## ABSTRACT

The theoretical investigation and numerical simulation of phase conjugation (PC) at stimulated Brillouin scattering (SBS) with feedback is carried out. A case of long pulse PC is considered. At this condition both running and standing phase gratings which responsible for the positive feedback are taken to account. The threshold of PC wave generation and PC reflectivity are calculated. The numerical solution for temporal behavior of PC intensity is obtained.

**Keywords:** Phase conjugation, stimulated Brillouin scattering

## 1. INTRODUCTION

Stimulated Brillouin scattering (SBS) is one of the main methods of phase conjugation (PC) of a laser radiation[1-3]. However it is implemented in a rather short range of pulse duration which usually not exceeds some hundreds of nanoseconds. The common cause of it is in great energy overloads taken place in a scattering medium because of a high threshold intensity of radiation at SBS of long pulses, in particular more than 1 μs. For attenuation of this factor the high degree of clearing of SBS matter calls. Thus the absorption is strongly reduced and by that the consequences of a specific (in a unit of volume) energy load raise are relaxed. However on this way there are some technical difficulties.

Other way of this problem solution consists in reduction of the SBS threshold. Its essential reduction is reached at use of the PC geometry with a feedback[4,5]. Therefore this method of PC represents great practical interest and allow to increase duration of conjugated pulses of radiation.

The method of a feedback arranging proposed and investigated in ref. 4. In this method the parametric feedback is used. In other words, the feedback results from scattering on a running phase grating arising at SBS. Such feedback can arise only at forward self-interception of a laser beam under a small angle.

Considered in ref. 4 version of a feedback formation is not unique. Except for running grating the standing phase grating arising because of an electrostriction at an interference of light beams of equal frequency can be utilized.

In the report a capability of realization of PC - mirror at SBS with a feedback forming due to a standing phase grating is theoretically considered.

## 2. CALCULATIONS AND THEIR ANALYSIS

At shallow angle of the laser beam self-interception the period of a standing phase grating appears rather big[6]. Therefore the time of its build up can considerably exceed pulse duration. At these condition such long spacing grating will not play essential role in process of PC at SBS with feedback. However at self-interception of a laser beam under a wide angle (backward self-interception) the standing phase grating can be a one of the kind of a feedback building at SBS. Therefore further we shall consider this geometry of PC at SBS (see fig. 1.).

The interaction of waves in this geometry can be considered in terms of nondegenerate four-wave mixing (FWM), at which the Stokes waves $E_2$ and $E_4$ are amplified with gain factor $g = g'J$, where $g'$ is the medium parameter and $J$ is the radiation intensity. In noise radiation always there is a weak PC wave $E_2$ (conjugated to probe wave $E_1$). The waves $E_1$ and $E_3$ interfering and as a result produce a standing phase grating on which the wave $E_2$ according to a Bragg's condition effectively scattered and gives rise to a wave $E_4$. By this way the feedback in the geometry of PC wave generation is carried out. The necessary gain at this is supplied by the wave $E_1$ for the Stokes wave $E_2$ and by the wave $E_3$ for a Stokes wave $E_4$.

Process of interaction of waves is described by the following set of equations for slowly varying amplitudes of coupled waves at the degenerated FWM

$$\frac{dA_1}{dz} = -\gamma_1 |A_2|^2 A_1, \tag{1}$$

XIII International Symposium on Gas Flow and Chemical Lasers and High-Power Laser Conference,
Antonio Lapucci, Marco Ciofini, Editors, Proceedings of SPIE Vol. 4184 (2001)

$$-\frac{dA_2}{dz}=\gamma_1|A_1|^2A_2+i\gamma_0\left(A_1^*A_3\right)A_4, \tag{2}$$

$$-\frac{dA_3}{dz}=-\gamma_1|A_4|^2A_3, \tag{3}$$

$$\frac{dA_4}{dz}=\gamma_1|A_3|^2A_4+i\gamma_0\left(A_1A_3^*\right)A_2, \tag{4}$$

$$\gamma_1=\frac{|q||k_1|\mathrm{Y}^2\beta_s}{32\pi n_0^2\alpha},\quad \gamma_0=\frac{k\mathrm{Y}^2}{8\pi n_0^2\rho_0 v^2},\quad q=2k\sin(\theta/2),\quad k_1\cong k=2\pi/\lambda,$$

where $A_j$ is the amplitude of the corresponding waves , $\lambda$ is the wavelength of a laser radiation, $\theta$ is the angle of interaction, $\mathrm{Y}=\rho\left(\frac{\partial\varepsilon}{\partial\rho}\right)_S$, $\beta_s=\frac{1}{\rho v^2}$, $\rho$ is the medium density, $v$ is the sound velocity, $n_0$ is the refractive index, $\alpha$ is the absorption coefficient of sound. The boundary conditions for geometry of interaction presented in a fig. 1. can be recorded as $A_3(l,t)=\sqrt{\eta_1}A_1(l,t)$, $A_2(l,t)=\sqrt{\eta_2}A_4(l,t)$, $A_4(0,t)=A_n$, where $\eta_1$ and $\eta_2$ are the coefficients of attenuation of intensity for the corresponding waves, $A_n$ is the amplitude of a noise component of a field, $l$ is the length of interaction.

It is necessary to mark that in the equations (1) - (4) only the gain of Stokes wave at SBS of single - mode beam (for example Gaussian beam) is taken into account (here and further). The multiplier 2 in the first term of right part of this equations corrects the mathematical model for the case of SBS of speckle - inhomogeneous beam.

For a calculation of a generation threshold it is possible to limiting by consideration of the equations (2) - (4). From the solution of these equations a threshold requirement is obtained

$$\left(\frac{\xi_1+\mu_1}{|\mu_0|}\sqrt{\eta_1}-1\right)\exp[(\xi_1-\xi_2)l]=\frac{(\xi_1+\mu_1)(\xi_2-\mu_1')}{\mu_0\mu_0'}+\frac{(\xi_1+\mu_1)}{|\mu_0|}\sqrt{\eta_2}, \tag{5}$$

here $\xi_{1,2}=\frac{\mu_1'-\mu_1}{2}\pm\sqrt{\frac{(\mu_1'-\mu_1)^2}{4}-\mu_0\mu_0'+\mu_1\mu_1'}$, were $\mu_0=\frac{i}{16}\gamma_0\left(A_1^*A_3\right)$, $\mu_0=\frac{i}{16}\gamma_0\left(A_1A_3^*\right)$, $\mu_1=\gamma_1|A_1|^2$, $\mu_1'=\gamma_1|A_3|^2=\eta_1\gamma_1|A_1|^2$.

From (5) with account of ratio $(\xi_1\mu_1)/|\mu_0|>>1$ is obtained following expression

$$\exp[(\xi_1-\xi_2)l]\cong\frac{4}{\sqrt{\eta_1\eta_2}}\frac{\gamma_1}{\gamma_0}\left[2(1+\eta_1)+2\sqrt{(1-\eta_1)^2+4\eta_1+\frac{1}{64}\frac{\gamma_0^2}{\gamma_1^2}\eta_1}\right], \tag{6}$$

were $\xi_1-\xi_2\cong\gamma_1|A_1|^2\sqrt{(1-\eta_1)^2+4\eta_1+\frac{1}{64}\frac{\gamma_0^2}{\gamma_1^2}\eta_1}$.

From (5) and (6) it is easily to see, that the threshold of the PC wave generation can be overcome at the sufficiently big intensity of Stokes waves.

The mathematical simulation of the PC wave generation according with the geometry presented in fig. 1 was carried out. The equations (1) - (4) were solved numerically. As nonlinear medium the liquid $CCl_4$ was used. The following values of parameters of medium and interaction were used: $n_0$ = 1.45, $\rho$ = 1.595 g/cm$^3$, Y = 1.35, $\beta_s$ = 6.014·10$^{-11}$ cm s$^2$/g, $l$ = 10 cm, $\theta$= 179°, resonator length $L$ = 50 cm, $\lambda$ = 1.064 μm.

In a fig. 2. the calculated dependence of PC intensity on time is shown. In a fig. 3. the dependence of PC reflectivity (on energy) on peak pulse intensity of a laser radiation is shown. It is follow from the obtained data that the dependence of the PC - mirror reflectivity have a threshold character and PC pulse is more shorter then probe one. These are characteristic properties of SBS and of scheme with a feedback in particular.

It is necessary to note, that the liquid $CCl_4$ chosen as nonlinear medium is not best for SBS. Therefore the comparison of the surveyed scheme with the classical scheme of PC at SBS in the same liquid may be useful. For $CCl_4$ gain parameter of a Stokes wave $g'$ = 0.006 cm s / MW [7]. So for the SBS (without feedback) in optical waveguide of 10 cm length the required threshold intensity of radiation is determined from equality $g'lJ$ = 20÷25 and $J\cong$ 400 MW/cm$^2$. It more than on the order is more than in a considered case of PC at SBS with a feedback.

Further for comparison we shall consider the geometry of PC with a parametric feedback at SBS, offered in ref. 4. This method also supposes interpretation in terms of nondegenerate FWM with a feedback if formally to consider a running phase grating as amplitude gain grating.

For the geometry of PC presented in a fig. 4., it is possible to record the following set of equations for slowly varying amplitudes of coupled waves which explain process of interaction:

$$\frac{dA_1}{dz} = -\gamma_1 |A_2|^2 A_1 - \gamma_1' |A_4|^2 A_1, \tag{7}$$

$$-\frac{dA_2}{dz} = \gamma_1 |A_1|^2 A_2 + \gamma_1' |A_3|^2 A_2 - \gamma_1 \left(A_1^* A_4\right) A_3, \tag{8}$$

$$\frac{dA_3}{dz} = -\gamma_1 |A_4|^2 A_3 - \gamma_1' |A_2|^2 A_3, \tag{9}$$

$$-\frac{dA_4}{dz} = \gamma_1 |A_3|^2 A_4 + \gamma_1' |A_1|^2 A_4 - \gamma_1 \left(A_3^* A_2\right) A_1. \tag{10}$$

In a linear approximation, when $|A_1|^2, |A_3|^2 = const$, the solution of equations (8) and (10) is obtained and is investigated in ref. 4.

In the terms of nondegenerate FWM the waves $E_2$ and $E_3$ interfering and produce a running phase grating on which the wave $E_1$ according to a Bragg's condition effectively scattered with Stokes frequency shift and forms a PC wave $E_4$. Formally this running phase grating shows itself as a grating on a gain.

The numerical solution of a set of equations (7) - (10) is found and the threshold of generation is determined. At calculation the same parameters as for the previous scheme of PC were utilized. With that the standing phase grating was not taken into account because its build up time is much more than for running phase grating and besides this $\gamma_0 < \gamma_1$. Both schemes of PC differ on a little to threshold values of intensity because the gain at SBS have exponential from of dependence on *J*.

## 3. CONCLUSION

The results of the carried out calculations and their analysis show that the standing phase grating arising due to electrostriction at an interference of beams of equal frequency and can be used for building a feedback in the scheme of PC wave generation at SBS. Thus, certainly, the conditions of phase matching in region of self-interception of a laser beam, as it is usually done at FWM, should be fulfilled. The tuning of the resonator to a resonant frequency is implemented on the same way as at use of a running grating for building a feedback[4].

The considered version of a feedback building extends capabilities of a method of PC wave generation at SBS because it has essential advantages such as rather short resonator, compactness of the scheme and lack of a stringent restriction on a angle of self-interception of a laser beam.

## REFERENCES


1. B.Ya.Zeldovich, V.I.Popvichev, V.V.Ragulskiy et al. Pisma v GETF, **15**, p.100, 1972.
2. I.M.Beldugin, M.G.Galushkin, E.M.Zemskov et al. Kvantovaya elektronika, **3**, p.2467, 1976.
3. N.G.Basov, V.F.Efimkov, I.G.Zubarev, S.I.Mikhaylov Formation of space - temporary structure of light waves at stimulated scattering on hypersound. Trudy FIAN, **172**, pp.10-115, 1986.
4. V.I.Odintsov, L.F.Rogachyova Pisma v GETF, **36**, p.452, 1982.
5. M.G.Galushkin, K.V.Mitin, K.A.Sviridov Izvestiya Akademii Nauk, seriya fizicheskaya, **59**, p.114, 1994.
6. D.Pohl, W.Kaiser Phys. Rev., **B1**, p.31, 1970.

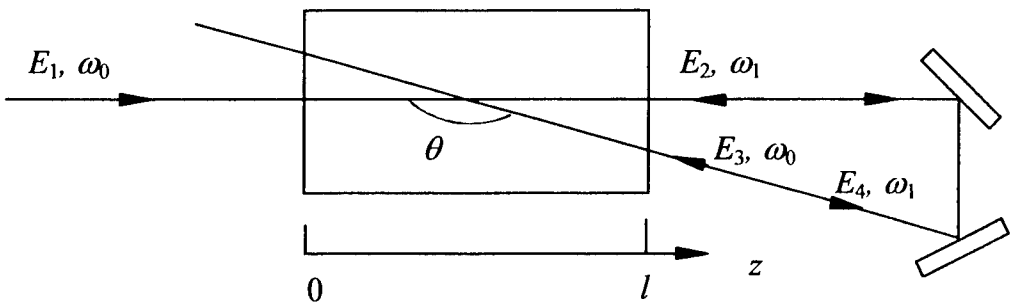


Fig. 1. Geometry of PC mirror on SBS with feed - back.

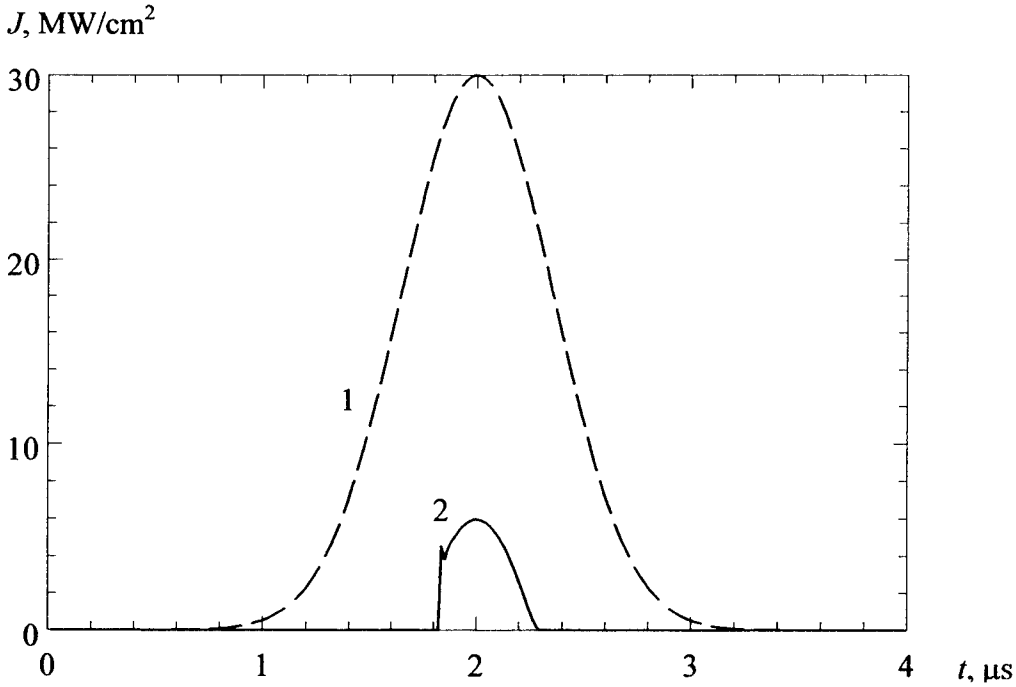


Fig. 2 Temporal behavior of probe (1) and PC intensities (2).

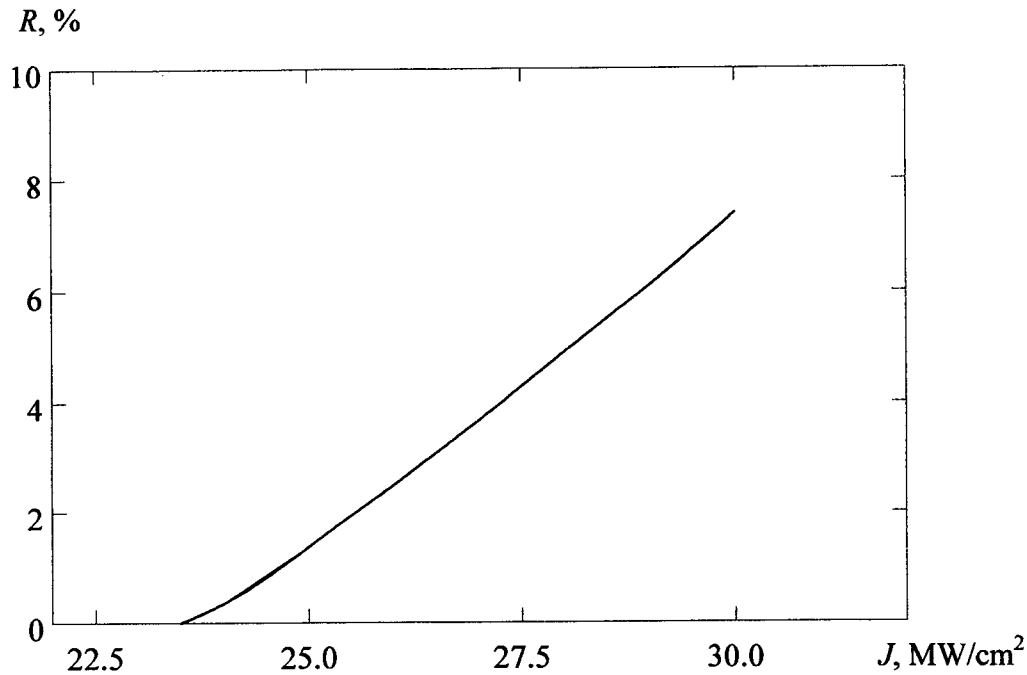


Fig. 3. Dependence of PC reflectivity (on energy) on maximum intensity of probe.

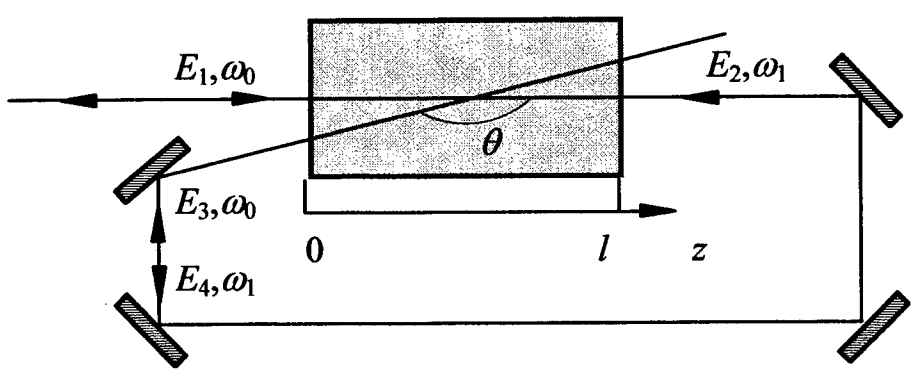


Fig. 4. Geometry of PC - mirror on SBS with a parametric feedback.

# Development of a Mobile High-Power Laser Module on the Basis of a Gas-dynamic $CO_2$-Laser, Intended for Cleaning Thin Oil Films from Large Water Areas

Apollonov V.V., Kijko V.V., Prokhorov A.M., Suzdal'tsev A.G., Vagin Y.S.,
General Physics Institute of Russian Academy of Sciences
Vavilov St. 38, Moscow, 117942, Russia

Guterman V.Y., Rachuk V.S., Zavision G.I., Zhuravlev P.D.
Chemical Automatics Engineering Design Corp.
Voroshilov St. 22, Voronezh , 394055, Russia

Fedotov V.B., Ivanov A.V., Koroteev A.S., Svirchuk Y.S.
Keldysh Research Center
Onezhskaya St., 8-10, Moscow,125438, Russia

## ABSTRACT

Considered is recent progress in development AMT GDL – a high power ~100 kW CW) CO2 highly mobile industrial laser of wide application. Substantiated are general composition scheme of AMT GDL and choice of prototype engine for power unit of AMT GDL.

**Keywords:** $CO_2$ laser, gas-dynamic laser, gas-turbine engine.

## 1. AMT GDL GENERAL SCHEME CHOICE

Discussed are three most promising schemes of GDL head, with respect to arrangement of combustion, mixing and expansion process. They are: GDL with a set of axially symmetric nozzles, one with separate heating and feeding of active medium components to the nozzle (mixing in a supersonic flow) unit and conventional one (homogeneous combustion of fuel and its expansion through flat supersonic nozzles).

Taking into account the whole complex of characteristics we have concluded that the most reasonable is to employ classical scheme. Relatively easy-to-manufacture board of axially symmetric nozzles can not provide gas mixture flow of satisfactory optical quality. Generator of active gas with mixing in a supersonic flow proves to be of insufficient power efficiency and/or gas optical quality. Although under other limitations, not like AMT GDL, such gas generators could demonstrate higher specific characteristics.

## 2. CHOICE OF POWER UNIT FOR AMT GDL SCHEMATIC OF THE POWER UNIT

As it is seen from our earlier considerations, for a operation of the laser module rated at 100 kW CW it is necessary to have the compressor with an air flow rate ~ 16 kg / s and compression >22÷23 atm.

The problem is to find the optimal solution ensuring the reasonable cost of power unit, reliability and convenience in operation.
Three possible schematics of power unit.

- Development and manufacturing specially intended power unit for the above mentioned parameters of the compressor.
- Attachment of a separate air compressor to an aviation engine shaft.
- Air feeding from high pressure section of airplane engine compressor


XIII International Symposium on Gas Flow and Chemical Lasers and High-Power Laser Conference,
Antonio Lapucci, Marco Ciofini, Editors, Proceedings of SPIE Vol. 4184 (2001)

All these three ways are absolutely technologically feasible. Omitting details, our decision is to employ an airplane engine with direct air feeding, after proper finishing works. As our estimations show such approach could be most economically reasonable, from one hand and could provide quite sufficient performance of power unit, after modification.

If it is decided to take an air bleed for GDL after a final section of the engine compressor, practically there is no necessity redesign the power unit equipping with new aggregates. Moreover, the dismantling from the engine of the free running turbine which provides driving the propeller shaft, considerably simplifies a design of the power unit as a whole. The engines not only will be used with minimum modification, but also all control systems are kept, including the use of the control panel which is taken off from a flight vehicle. Besides, from point of view of the power, dismantling of the free running turbine together with nozzle block allows to lower required power of the turbine of system of the compressor - free running turbine.

The decrease of required power of the system implies the possibility to reduce consumption of air and kerosene in the combustion chamber of the gas-turbine engine. With constant power rate of the turbine for the drive of the compressor and with fixed the compressor flow rate, probably, there exists a possibility to take off a part of the air and to direct it to the combustion chamber of gas dynamic laser. At the same time, utilizing the characteristics of the combustion products down the main turbine ($\rho$, m, T), it is possible to arrange ejection of GDL gases down the supersonic diffuser for improvement of the gas dynamic laser overall performance, especially at start.

## 3. CHOICE OF AIRPLANE GAS-TURBINE ENGINE

Aiming optimal choice of an aviation-engine for this task it is necessary to formulate the initial requirements.
1. To obtain air pressure in GDL inlet not less than 20 atm and taking into account losses in a flow channel the compressor of the engine should provide not less than 22-25 atm.
2. The GDL inlet air flow rate is to be 16,25 kg /s.

As for elimination of extreme engine power extraction the air bleeding from the compressor should not exceed 15-18 %, the total air flow rate through the engine should be not less than 100 kg /s.

3. The chosen aviation engine should be of wide use, that enables to utilize engines which are decommissioned from flight vehicles, having passed prescribed operational life limit, but still are operable for ground installation. To buy them is much cheaper, than to purchase new engines.
4. It is desirable to make a choice of domestic (Russian made) engines

| Engine | НК-12СТ | НК-14СТ | НК-14Э | НК-16СТ | НК-17 | НК-36СТ | ПС-90А | РД-33 |
|---|---|---|---|---|---|---|---|---|
| Compression | 8,8 | 9,5 | 9,5 | 9,68 | 9,68 | 23,12 | 19,6 | 22,0 |
| Total air floe rate (kg/s) | 56,0 | 37 .1 | 39,0 | 102,0 | 102,0 | 101,4 | 56,0 | 80,0 |

After comparison this basic data on the most popular domestic engines one concludes, that most reasonable for the laser power unit could fit the engine HK-36CT manufactured by Samara plant "Motorostroitel", which satisfies all requirements presented above. It is obvious, this is not the single engine, which can be put to use for this task, but in advantage of it would be desirable to note the following.

The high performance engine HK-36CT of the Samara industrial complex "Motorostroitel"," is developed in 1990 on the basis of an airplane engine HK-321 and is designed for the drive of the centrifugal supercharger of a gas pipeline pumping aggregate.

The modular design of the engine facilitates transport and assembly. The engine has the remote control panel and record of long life ground operation.

Other important data of the engine HK-29 is listed below.

| | |
|---|---|
| Fuel | Kerosene TC-1 |
| Power, MW | 25 |
| Air flow, kg/s | 107,2 |
| Compressor pressure ratio, Atm | 23,12 |
| Gas temperature, K | 1420 |
| Gas exit temperature, K | 698 |
| Fuel consumption, kg / s | 1,434 |
| Engine weight, with subframes, kg | ~ 5000 |

Thus, as a result of the fulfilled research work not only the optimistic predictions for possibility of adaptation of the gas-turbine engine for mobile GDL complex were obtained, but also engineering design activities on definition of general realization of such a module are executed in practice.

## 4. CONCLUSIONS

In conclusion, we would like to emphasize the following. At the present stage of AMT GDL project implementation, consideration of possible technical solutions, comparison of basic characteristics of airplane engines and further analysis have demonstrated that the chosen engine HK-39CT is an adequate basis for creation of key block - power unit of AMT GDL. Development of other necessary units and systems of AMT GDL may be fulfilled in compliance with general requirements on mobile industrial laser.

## REFERENCES

1. Technical Letter. Substantiation of laser type choice from specific parameters, weight and overall dimensions characteristics, mobility, self-contained design. Project ISTC 1099.
2. Technical report. Basic scheme of self-contained transportable $CO_2$ - GDL. Calculated justification of main power characteristics. Project ISTC 1099.
3. Technical report. Theoretical researches of processes of interaction laser beam with a thin oil film on a surface waters. Project ISTC 1099.
4. The technological report. Selection of power installation for gas dynamic laser (GDL). The principal diagram, main characteristics. Project ISTC 1099.
5. Plyer E.K., Acquista N. Infrared absorption of liquid water from 2 to 42 mkm. – JOSA, 1954, v.44, N6, p.505.

# Pressure Recovery Systems for High Power Gas Flow Chemical Lasers

A.S.Boreysho[a], V.M.Khailov[b], V.M.Mal'kov[c], A.V.Savin[a]
[a]Baltic State Technical University, St.Petersburg
[b]Central Institute of Aviation Motors, Moscow
[c]Institute of Theoretical and Applied Mechanics, Novosibirsk

## I. THE GENERAL APPROACH

Some important applications of High Power Gas Flow and Chemical Lasers (HPGCL) are aimed to ground level operations. HPGCL are understood here as open cycle machines. It means that after the laser cavity their exhaust gases run out to the ambient atmosphere. Exhaust gas products after resonator cavity cannot be evacuated directly to atmosphere. The atmosphere pressure on the sea level exceeds the cavity pressure by 10 – 20 times for $CO_2$ gasdynamic lasers (GDL) and by 150 – 200 times for chemical oxygen-iodine lasers (COIL).

Combustion Driven $CO_2$ GDL only can operate without energy additions, using ordinary "passive" diffusers. However, and in these cases, the whole HPGCL system scale is determined, by the diffusers' dimensions. Meanwhile, the ground operation of High Power HF/DF-CL and COIL requires already "active" Pressure Recovery Systems (PRS): large-scale complexes, including diffusers and high-energy ejectors.

Fig.1 demonstrates a correlation between scales of the HF/DF-chemical laser and it pressure recovery system. Even without component supply subsystems (balloons, tanks, pipes, accessories, etc.) the scales are non-compared. For COIL the difference becomes more significant. Approximate estimates confirm also, that the ejecting gas flow rate of ejector stations may exceed the laser components' summary gas flow rate by many tens times [1].

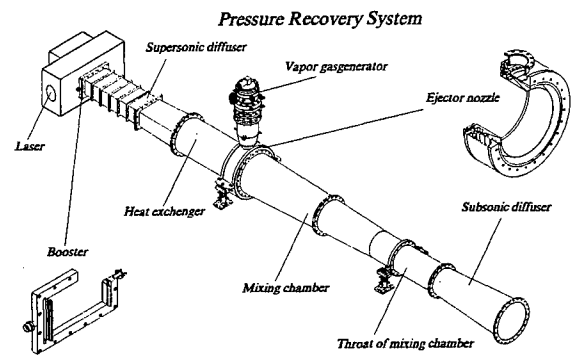


Fig.1

It changes seriously the general estimations the HPGCL effectiveness. There are some results of such calculations on Fig. 2. No doubt, that specific energetic effectiveness of the HF/DF-CL and COIL with and without the PRS components is to be very different.

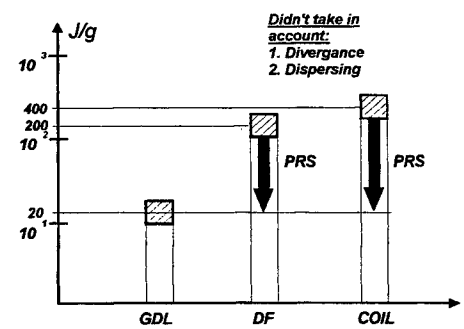


Fig. 2

The HPGCL and PRS have to be considered as indivisible, strictly integrated systems. Their combined analysis, aimed to a search of optimal technical solutions, has to take into account many links and interactions, except of the additional expenditures of energy and components.

The present papers contains a review of various technical concepts and schematic solutions aimed to practical uses for some real applications, meanwhile, physical processes in the diffusers and supersonic ejectors of the HPGCL PRS are considered more precisely in the [2, 3].

## II. DIFFUSERS

Independently on a pressure level into cavities, gas flows of all considered HPGCL are supersonic, therefore, the streams' kinetic energy may be applied for the PRS operation. However, this energy, is not enough for direct exhaust of the laser gases to ambient atmosphere. Hence, it is necessary providing of an energy addition to the stream with agency of ejector and compressor technologies. In spite of some known interest to supersonic mixing ejectors [4], all presented bellow data are related to traditional schemes.

Characteristics of the supersonic laser gas mixture flows after DF and COIL cavities are given in [2]. Parameters of the laser flows are close enough, so, at least, from constructive point of view, diffusers for both types of the lasers have to be similar. A supersonic flow slowdown process into diffusers' channel is occurred as a result of interactions of oblique shock waves, arisen into the stream under it geometric or gasdynamic (boundary layers growth) constriction effects. These interactions stimulate a separation of boundary layers from walls and a formation of subsonic ranges with intensive turbulence in the separation zones. A growth of these ranges along the channel, stimulated by intensive turbulence of the flow, leads to capture a core of the flow, transforming it in subsonic state. At this rate it is important to take into account such feature of the laser PRS operation, as a heat generation by exhaust laser gas mixtures in diffuser channels [2,5].

XIII International Symposium on Gas Flow and Chemical Lasers and High-Power Laser Conference,
Antonio Lapucci, Marco Ciofini, Editors, Proceedings of SPIE Vol. 4184 (2001)

The supersonic diffuser's (SD) main parameters: start ($P_s$) and breakaway – unstart - ($P_b$) pressures, and maximal magnitude of pressure recovery after SD - $P_{max}$. In details the SD operation and evaluation of SD performances are considered in [2, 5].

The main feature of diffusers is a strong relationship between the diffuser length and minimal $P_s$ [6]. A similarity relation for diffuser's flow is a ratio of it length to a special diameter [6,7]. The universal criterion that allowed generalization of experimental results obtained in different kinds of rectangular channels was offered in [6,7]. Using this criterion it is possible to find out recommendation dividing the SD channels – to design multichannel SD - more precisely. This approach - multichannel SD - is a main way for SD shortening (Fig. 3).

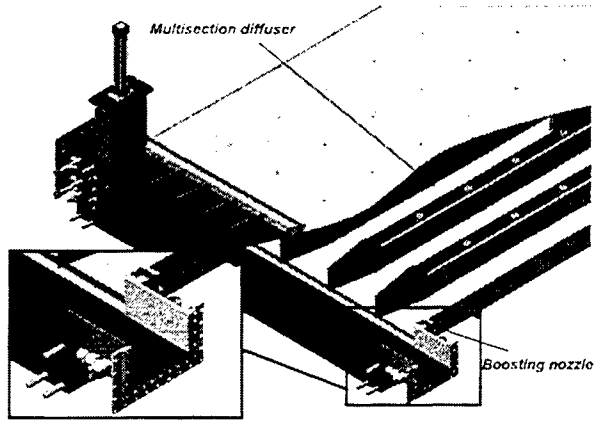

Fig. 3

In spite of similarity of the multichannel SD separate sections, exterior ones operate in different conditions. There are the particular intensive growth of the boundary layers along external narrow walls and the appearance of separation zone in the beginning of SD channel at the moment of start. This negative phenomenon makes troubles for the SD starts. Special devices – boosting nozzles, located just on the narrow sides of the exterior channels may aid to this process (Fig.1 and 3).

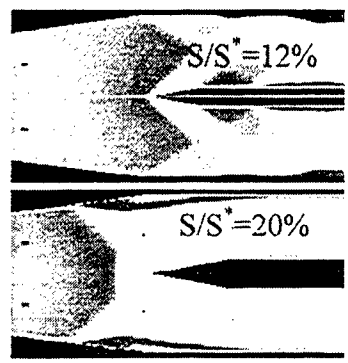

Fig. 4

One-dimensional evaluations of SD performances are a first approximation for chemical lasers. The professional design of large-scale PRS requires three-dimensional viscous calculations of the non-equilibrium laser media, since of the cavity output. As example, the flow structure in SD with a central pylon – the picture is based on three-dimensional calculations of the Navier-Stokes equations – is shown on Fig.4. (Model and details of these calculations are given in [3].) According to one-dimensional calculations, it is possible to have SD channel with 20% restriction. Meanwhile the data demonstrates that reducing of the restriction to 12% only transfers the flow at a normal mode.

## III. EJECTORS

Further increasing of the laser gas pressure may be provided by external energy addition. One of the most useful way for the laser gas pressure recovery is an ejector.

The ejecting gas inflow may be realized from channel walls as a "peripheral" scheme. Such scheme provides a minimal length of the ejector. An additional restriction of ejector mixing chamber promotes to raising of jet interaction efficiency [8].

As a rule, the peripheral injection applies in low-temperature aerodynamic tunnels, because of difficulties in keeping stable geometric dimensions of the ejector ring nozzles. Nevertheless, we could resolve this technical problem and build a minimal length high-temperature ejector with ring injection of the ejecting gas (Fig.5).

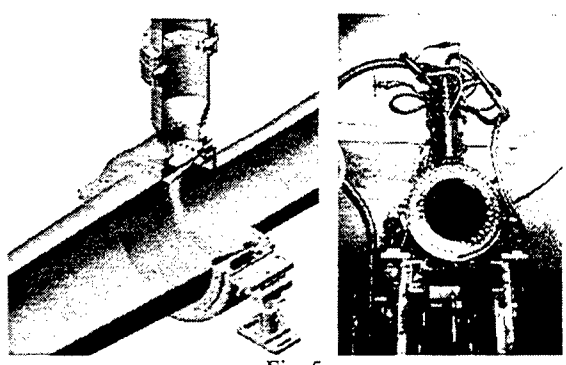
Fig. 5

Maximization of the ejection coefficient is considered usually as an optimization objective for ejectors and the whole PRS. The rest characteristics: dimensions, mass, applied equipment, materials are considered as limitations. The ejector diagrammatic work, determining limitations on duration both the separate starts and the whole operation period, is very important characteristic of optimization as well.

Similarly to supersonic diffusers, on prime of project development, calculations based on one-dimensional inviscid theory applying of conservative equations in an integral form are quite sufficiently [9]. Such approach allows finding out geometric dimensions, ejecting gas delivery pressure and recommendations on parameters of the gas.

After that, on the base of three-dimensional Navier-Stokes full equation calculations, real situations for the ejector start and it consequent operation, as well as all important work characteristics are determined finally. The most important ones are start and unstart pressures of the ejector. A difference between them (so-called "hysteresis") is a common thing for gasdynamic devices because of viscous real gas properties.

Applying of the suggested approach for the discussed above PRS of HF/DF-laser, we could reach a compression coefficient as much as 14. It allowed realizing one-stage ejector and thanking to this approach, to satisfy very strong gabarit limits of the project. We got an acceptable correlation between numerical results and experimental data [2].

Since the COIL pressure level is significantly lower then the same characteristics of HF/DF-lasers, a normal operation of the COIL ejectors based on ordinary technical schemes, depending on their design details, requires two- and even three-stage ejectors for their PRS. Multi-stage ejectors have been realized for the air-dynamic tunnels, however, start and checkout of such system remain extremely complicate procedure. Beside of that, dimensions of multi-stage ejectors are too big for their installation on mobile platforms.

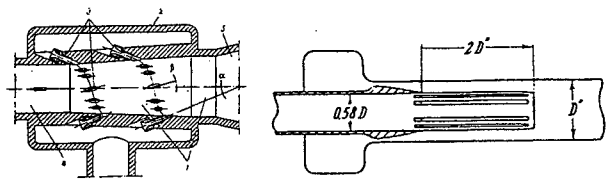

Fig. 6

There is an idea of so-called differential ejector, based on principle of critical regime pulling [10]. Some realizations of this approach – Arkadov's schemes [11,12]- are shown on Fig.6. The mixing process is controlled by dimensions and quantity of slots and arrangement of axisymmetrical nozzles, supplying the efficiency of mixing of high-pressure and low-pressure streams. Such approach allows to reach a compression degree as much as 300 (without ejected gas flow).

## IV. VAPOR GAS GENERATORS

The ejector effectiveness depends on high energetic parameters of ejecting gases: pressure and temperature, and minimal molecular weight of the gas mixture. Modern combustion driven gas generators on various fuels can provide practically unlimited volumes of high temperature gases under high pressure. Usually these parameters about 100 atm and 2000÷2500K.

Application of liquid components looks as very attractive idea especially for the PRS mass and scale minimization. However, some liquid components may be quite toxic, so they may make additional limitations for the whole laser system. Therefore, considering possible oxidizer-fuel combinations, it is necessary to take into account their use- and serviceabilities and safety. There are some results of calculation estimates of dependence's ejection coefficients on fuel and oxidizer options (Fig.7).

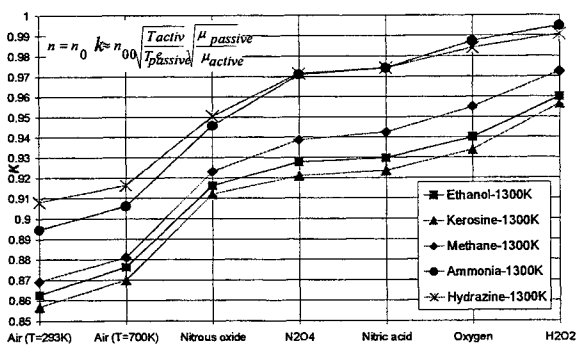

Fig. 7

Limitations on pressure and temperature depend, first of all, on materials of gasdynamic tunnels. Cooling of large-scale PRS vast surfaces does not look too reasonable. Therefore the ejecting gas temperature is kept usually within 900-1000K. Applying the modern aerospace materials, the reliable operation of the PRS may be provided within 1300-1400K working gas temperatures. It improves the ejecting coefficient as much as ~20%. Growth of the temperature removes a condensation limit and allows to increase the ejecting gas pressure and Mach number. The ejecting coefficient may additionally growth as much as ~30%. The acceptable temperature level is regulated by dilution of the combustion products by water. It may reduce the mixture's molecular weight aiding to growth of the ejection coefficient as well.

## V. GAS TURBINE ENGINES

At all their own advantages the vapor gas generators needs large consumption of the components, and all of them are to be stored beforehand. The save and inexpensive oxidizer – air – has to be stored within heavy high-pressure balloons. High-capacity axial compressors of aviation gas turbine engines (AGTE) may turn out to be an exception, sometime. The AGTE thank to energy efficiency, high pressure air flow rate characteristics, compactness of all subsystems, can be considered as the most powerful and compact sources of energy for PRS. Such PRS may be reasonable for some applications because of it autonomy and ejecting mass flow rate in comparison with the PRS gas generators.

Many possible design schemes of the PRS on AGTE have been considered. A feature of such analysis is necessity of continuous comparison between theoretical calculated results and characteristics of real aviation engines, which may be really applied. Estimates have been made for HF/DF-laser with gas flow rate about 2-3 kg/s (pressure after SD – 70-80 torr), and for COIL with flow rate of 0.3 – 0.4 kg/s (pressure after diffuser – 17-20 torr). Bellow there is presented some operation-integrated variants only from a number of discussed and investigated technical solutions.

*I. The laser gas with (or without) an ejecting backup on the diffuser outlet is pumped by the AGTE cycle compressor(Fig.8).*

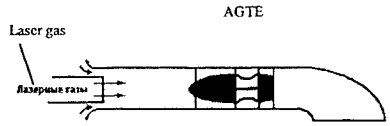


Fig. 8

*HF/DF-lasers* –This variant of the PRS is most advantageous from viewpoint of it reliability and fastest development rate as well as maintain- and usability. The same time such conversion is being made without changing of main subsystems and parts of the AGTE: starting, fuel feed, oil ones. Dependence of the required pressure recovery level on air effective flow rate through some real AGTE's compressors is presented in Fig. 9. The only RD-3651 engine meets such practical requirement for it effective flow rate level, while it compression is less then necessary. In this case the required combination of the air effective flow rate (G) and compression level ($P_k$) may be provided with two R-35 AGTEs array (Fig.9). Such scheme cannot provide suitable conditions for COIL operation.

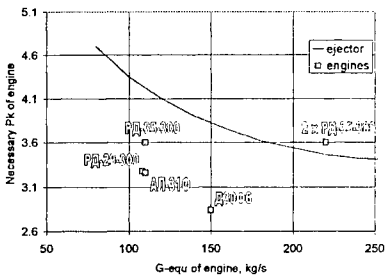


Fig. 9

*II. Pumping of the gases with water addition for a temperature reduction (Fig.10) is realized by a separate installed an axial (or radial) flow compressor of an aviation engine, driven by a powerful turbine of another turboshaft engine.*

*HF/DF-lasers* – The laser gas initial temperature is too high while it pressure is very low, therefore, the gas is to be very diluted by ambient air addition into a preliminary ejector section before the post-compression. The significant dilution of the input gas to tolerance temperature leads to big flow rate of the mixture incoming to the compressor. Therefore, realization of such schemes requests large discharge compressors with higher compression ratio (as much as 4 – 6) and, accordingly, extremely powerful turboshaft drive.

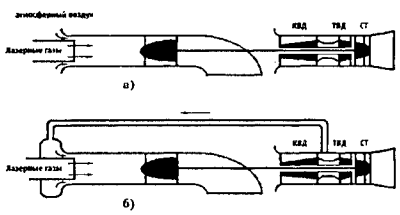


Fig. 10

A chance to select a reasonable combination of existing compressors and AGTEs which might satisfy of all above listed requirements, is too small. Meanwhile, modernization of the machines for the considered tasks looks very complicated and expensive. An alternative way for such scheme realization is the preliminary reduction of laser gas temperature by water injection into the gas jet.

The D-136 stock GTE of V-26 helicopters may be considered as a possible driven for compressor as well as gas turbine drives of D-336 and AI-336-8 AGTE. Unfortunately for COIL these technical solutions remain still unacceptable.

*III. Pumping of the laser gas with an ejector, where the ejecting gas is generated by AGTE. Two technical schemes look the most attractive:*

*a) – application of two R-35 AGTEs (Fig. 11);*

*b) –application of two RD-33 AGTEs or one R-35 with water injection into the after burner (Fig.12).*

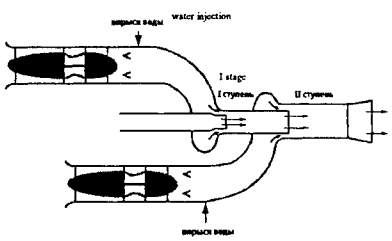


Fig. 11

*HF/DF-lasers* – In results of preliminary calculations, division of the summary gas flow rate as 12,5% of this flow coming to a first stage of the double stage ejector, while the rest flow rate of 87,5% running through the ejector's second stage. The best result of two AGTEs application without kerosene afterburning and water injection is presented on the Table. The output pressure after the PRS may reach $1{,}173 \cdot 10^5$ Pa, providing reliable exhaust of the laser gases.

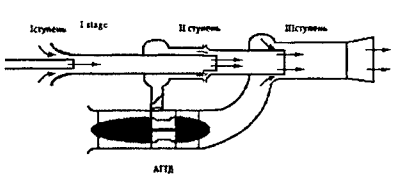


Fig. 12

Results of calculations of double stage compressors with additional afterburning of kerosene (in tables-Af-b) and water addition (in tables-W) are presented in the Table as well.

*COIL* – Two-stage ejector variant turned out to be fitted for the considered COIL PRS. The ejecting gases are: compressor bleed air of the AGTE RD-33 (powering MiG-29 fighters) - for the first stage, and exhaust gases of the same engine –for the second stage. Such PRS technical scheme can provide the required pressure on an outlet of two-stage ejectors for input laser gas pressure as $0{,}0293 \cdot 10^5$ Pa. The similar result may be obtained using one AGTE R-35 type.

*Table:*

| Characteristic | 2·R-35 | 2·(RD-33+Af-b +W) | R-35 + Af-b+W |
|---|---|---|---|
| First stage total input pressure of ejecting gas, Pa | $3{,}53 \cdot 10^5$ | $2{,}94 \cdot 10^5$ | $3{,}53 \cdot 10^5$ |
| First stage total output pressure of gas mixture, Pa | $0{,}389 \cdot 10^5$ | $0{,}387 \cdot 10^5$ | $0{,}375 \cdot 10^5$ |
| Second stage total output pressure of gas mixture, Pa | $1{,}173 \cdot 10^5$ | $1{,}107 \cdot 10^5$ | $1{,}047 \cdot 10^5$ |

## V. ADDITIONAL SUBSYSTEMS

Ejector systems are extremely powerful noise sources. It may make some problems for use of the HPGCL in real operational situations. There are two approaches for noise reduction:

1) stationary variants of the exhaust system silencer, intended for laboratory and/or experimental test facilities;

*2)* untethered variants of such a system, installed on a mobile vehicle.

The main requirement to silencers is reduction of the PRS exhaust jets to sanitary codes for the terrain. The level of noise reduction is about 30 – 40dB for stationary systems, and 15 – 20dB for mobile ones. Both systems have to foresee possibilities for deactivation (neutralization) of some toxic species (HF/DF, HF, iodine, etc.). As a rule a summary mass proportion of these species into the exhaust gases does not exceed ~ 1% of the whole gas flow rate.

The reduction of noise level for stationary is obtained by a «passive» way: coating of flow-through parts with «sound-absorbing» panels, cooling most heated surfaces of the panels with ambient air inflow. However, such approach does not allow simultaneous injection of water into the flow. A noise protection efficiency of the panels may be seriously impaired because of the cooling water condensation on these surfaces. So the stationary system is developed similarly to an "additional gas ejectors". The ejector flow-through parts are covered by the sound absorbing panels with minimal hydraulic resistance. Such approach is absolutely unacceptable for mobile systems, it leads to serious growth of the PRS dimensions and weight. In this case an " active" approach based just on water injection into the flow may be more reasonable.

## VI. CONCLUSION

In the present paper we intentionally do not touch one effective pressure recovery technology with agency of vapor ejector stations. This effective approach has been realized successfully in the USA for the ALFA HF-chemical laser test facility. Many published information [13] have described at great all technical details of this powerful PRS. In our turn we wanted to mention about some alternative ways which as well may turn out to be reasonable for some smaller, less powerful laser projects. One main result of the analysis is confirmation of real possibility to build the ground based HPGCL systems with application of known technologies, and today's equipment.

Aviation gas-turbine engines may be an effective base for the HPGCL operating in atmosphere meeting real civil industrial demands for such a kind of laser radiation. Mostly real practical tasks, like industrial applications for large-scale emergency operations, meteorological, environment protection, including the space debris cleaning require, at least, hours per day as a normal operational time. In this case the AGTE PRS only can provide reasonable effectiveness for the HPGCL.


## ACKNOWLEDGMENTS

The authors are grateful to "Laser Systems" Ltd., St-Petersburg, Russia for financial support.


## REFERENCES


1. A.W. Ratliff, A.J. McDanal, S.C. Kurzius, W.D. Martin "Power and pressure recovery analysis of chemical laser devices", AIAA Paper, №75-721.
2. V.M. Malkov, A.S. Boreisho, A.V. Savin, I.A. Kiselev, A.E. Orlov , "About choice of working parameters of Pressure recovery system for high power gas flow chemical laser" Proceedings of XIII International Symposium On Gas Flow & Chemical Lasers - High Power Laser Conference (GCL-HPL-2000), September 18th-22nd, 2000, Florence, Italy.
3. A.V. Savin, A.A. Ignatiev, A.V. Fedotov, "Numerical simulation of gas dynamic flows in pressure recovery systems of supersonic chemical lasers", Proceedings of XIII GCL-HPL-2000, September 18th-22nd, 2000, Florence, Italy.
4. J.C. Dutton, C.D. Mikkelsen, A.L. Addy, "A Theoretical and Experimental Investigation of the Constant Area, Supersonic-Supersonic Ejector", AIAA J, Vol.20, №10, 1981.
5. R.J. Driscoll, L.F. Moon, "Pressure recovery in Chemical lasers", AIAA J. -V.15. -№5. -P.665. -1977.
6. M.G. Ktalkherman, V.M. Malkov, N.A. Ruban, "Slowdown of supersonic flow in rectangular channel of constant cross-section", J. Appl. Mech. Tech. Phys., -№6, 854, November-December 1984, (in Russian).
7. M.G. Ktalkherman, V.M. Malkov, N.A. Ruban, "Experimental investigation of GDL diffusers", AIAA-paper №90-1512. -N.Y.: AIAA, 1990.
8. G.N. Abramovich, "Applied Gas Dynamics", Science, Moscow, 1976, (in Russian).
9. U.N. Vaselyev "Gas ejectors with supersonics nozzles" Proceedings of works on investigations of gas supersonic ejectors, TsAGI, 1961.
10. B.A. Urukov "Theory of differentuional ejector", J. Appl. Mech. Tech. Phys., -№5, 1963, (in Russian)
11. J.K. Arkadov, "Gas ejector with nozzle perforated by longitudinal slots", Fluid Mechanics J., -№2. –1968, (in Russian).
12. J.K. Arkadov, "Compact high compression gas ejector with nozzles along the spiral", Proceedings of TsAGI, Vol. 15, -№6. -1984. (in Russian).
13. D. Hook, K. Magiawala, D. Haflinger, H. Behrens, "An ejector system for space simulations of the ALPHA laser", AIAA-paper 92-2981, 1992.



Correspondence Email: boreisho@iltt.ru, office@iltt.ru; WWW: http://iltt.ru; Phone: 812-251 21 62, Fax: 812-251 22 57

# The Estimation of $C_n^2$ of Nonequilibrium Turbulent Gas Flow in $CO_2$- laser on Data of Luminescence Diagnostics

M.G. Galushkin, V.S. Golubev, V.Ya. Panchenko, Yu.N. Zavalov, R.V. Grishayev
Russia Academy of Sciences- Institute on Laser and Information Technologies (ILIT)
Svyatoozerskaya 1, Shatura, Moscow region, 140700, Russia
(fax: 7+09645-22532, tel: 7+09645-25995)
E-mail:panch@laser.nictl.msk.su

## ABSTRACT

The method of estimation of $C_n^2$ of laser mixture turbulent flow is proposed based on experimental dependencies of amplitude of gas pulsation on spatial pulsation scale. The connection between degree of nonequilibrium and $C_n^2$ magnitude is shown. The boundaries of inertial and viscosity ranges are determined. The estimation of $C_n^2$ is within $(3\ldots14)\cdot10^{15}$ cm$^{-2/3}$ as dependence of gas- discharge current.

## 1. INTRODUCTION

The deterioration[1] of output beam of high-power gas laser due to turbulent pulsation of active medium flow impels us consider the particularities of nonequilibrium turbulent gas flow. The progress of high-power gas laser technique leads to reducing the influence of other factors of deterioration of laser beam [2, 3] such as mode coupling or resonator axis vibration. But the turbulence pulsations are fundamental factor of decreasing of optical quality of laser beam. Why the turbulence is involved? In gas laser the energy of input source comes to (and stores on) upper energy levels of molecules and partially transfers to the coherent radiation. Remaining energy transfers to heat moving. The heat removing from active volume by convection is the principal scheme of high-power gas lasers [4]. As well the turbulence of flow allows to intensify the convection, because, on one side, the nonequilibrium energy temporally stores in whirlwind movements, on other side, these movements accelerate the viscose dissipation [5]. Moreover, to increase the laser power one needs to increase gas velocity, gas pressure and beam aperture. As a product of these parameters the Reynolds number has to increase. Another extensive method of enhancing the output power is to increase the active medium length, i.e. the length of turbulent intracavity trace. The intensive factor, i.e. to increase the specific input power, as shown below is the same way. We worked out this problem: the enhancement of turbulent pulsation of gas density in the condition of self-sustained gas discharge[6]. It is also be mentioned the turbulence flow could stabilize the gas discharge uniformity[7].

## 2. THEORETICAL BACKGROUND AND DIAGNOSTICS METHOD

As we studied earlier, the self-sustained discharge in FAF $CO_2$ laser is exist under fulfilment condition[8]. The discharge is a rather thin nonuniformly illuminating streamer. At the regime of quasi-stationary state the radial distribution of electron density of electro-negative discharge plasma between two nearby cross-sections of glow discharge may be written

$$\frac{1}{r}\frac{\partial}{\partial r}\left(r\left(D_a^+ + D_T\right)\frac{\partial n_e}{\partial r}\right) + \frac{\nu_i}{1+\chi}n_e - \left(\beta_r + \chi\beta_-\right)n_e^2 = 0, \qquad \beta_{rek}^{eff} \approx \beta_{rek}\left(1 + 2n^-/n_e\right) \tag{1}$$

where $n_{e0}$ is the stationary concentration of electrons, $n^-$ is the concentration of negative electrons, $k_{ion}$ is the constant of ionization rate, $D_a^e \approx D^+\left(1+2n^-/n_e\right)T_e/T$ is the coefficient of electron ambipolar diffusion, $\beta_{rek}$ is the coefficient of electron-ion recombination, $D_T \approx 0.09\cdot v\cdot d_{tb}$ is the coefficient of turbulent diffusion, $T$, $T_e$ are gas and electron temperatures, $v$ is the gas flow velocity, $d_{tb}$ is the tube diameter, $r_{dis}$ is the discharge channel radius.

The effect of enhancement of turbulent pulsation in condition of sustained gas discharge is shown schematically on Fig. 1A. For case of RF discharge (Fig.1B) the threshold of plasma instabilities is higher, and the enhancement of turbulent pulsations would be based on temperature relationship of kinetics constants, but this question is not investigated. Nevertheless, the threshold of enhancement due to nonequilibrium energy input could be estimated as: $\gamma\tau\approx1$, where $\gamma$-instability rate, $\tau$- time of dissipation or removing.

The use of the luminescent method is based on the fact that the local value of glow intensity of discharge plasma in the visible spectrum is proportional to molecule and electron concentrations[9], i.e. $\tilde{\rho}_e \cong \tilde{n}_e + \tilde{N}$, where $N$ is the concentration of neutral molecules, $\rho_e$ is the integrated emissivity of optically thin plasma, that is total for the lines of discharge visible glow; the sign "~" is used for relative fluctuation of the parameter: $\tilde{f} = \delta f/f$. The balance equation (1) gives the relationship for particle


XIII International Symposium on Gas Flow and Chemical Lasers and High-Power Laser Conference,
Antonio Lapucci, Marco Ciofini, Editors, Proceedings of SPIE Vol. 4184 (2001)

density pulsation in near-stationary condition: $\tilde{n}_e \cong -\hat{k}\tilde{N}$, $\hat{k} = \hat{k}_{ion} - \hat{k}_{rek} \approx 8...10$, $\hat{k}_i = \dfrac{\partial \ln k_i}{\partial \ln(E/N)}$, (2)

i.e. gas pulsation is accompanied by more intense relative pulsation of electron density and, respectively, by relative pulsation of $\tilde{\rho}_\varepsilon \cong \tilde{n}_e \cdot (1 - 1/\hat{k}) \approx \tilde{n}_e$. It is obtained that glow fluctuations are related to density fluctuations in the following way: $\tilde{\rho}_\varepsilon \cong \tilde{N} \cdot (1 - \hat{k})$. Thus, the registration of luminescent glow relative fluctuations permits even weaker pulsation of gas density to be determined.

## 3. EXPERIMENTAL SETUP

We used in the experiments a pilot model of the fast-axial flow $CO_2$ laser TLA-600 with output power 600 W, designed at the ILIT RAS. The set-up have 4 gas- discharge tube (GDT). The turbulizer on entrance of GDT is used to enhance the stabilization of gas discharge. Also the discharge current of each GDT is stabilized by electronic block with feedback. The maximum specific input power with relatively uniform discharge and acceptable laser efficiency is near 16 Wt/cm$^3$. Down stream from the entrance of GDT the gas fluorescences at the glow discharge. The temporal behaviour of local integral luminescence is measured as shown on Fig.2.

## 4. EXPERIMENTAL RESULTS

In the case spectral density of pulsation energy *S(k)* has been measured, the squared value of velocity pulsation $\tilde{v}^2$ (~to kinetic energy of turbulence whirlwinds) at the scale *k~1/l* and at shorter scales can be evaluated as $\int_k^\infty S(k)dk$ [10]. The physical values are founded from the experimental data based on the relationships: $\tilde{N} = -\gamma M_0^2 \tilde{v} - \tilde{T}$, $\tilde{N}^2 \sim \tilde{v}^2 \sim \int_k^\infty E(k)dk \sim \int_\omega^\infty E(\omega)d\omega$, (3)

where $\gamma$ is the adiabatic index, $M_0$ is the Mach number, $v$ is the flow velocity, $E(\omega)$ is the spectral density of luminescent glow fluctuations, averaged by several observations. The experimental results obtained by this method are illustrated in Fig. 3 as dependences of relative root-mean-square gas density pulsation on the size of turbulent fluctuations. The specific electric energy input into discharge is a parameter. The lower figure presents the data obtained in the absence of laser radiation (the resonator is misadjusted). The upper figure illustrates the case when laser radiation is present. Firstly, there is the influence of gas discharge on amplitude of turbulent pulsations. Secondly, the influence of gas discharge has a threshold nature. Thirdly, laser radiation lowers this threshold.

## 5. DISCUSSION

The obtained results (Fig.3) allow an estimation of the structure constant to be made. The $C_n^2$ value is conventionally calculated relying upon the results obtained for the ideal case of turbulent flow when homogeneity and isotropy of velocity pulsation exist not only at small scales, but generally at all scales. Such motion would be damped with time. In this case the structure function $B_{rr}$ ($B_{i,j} = \langle |\bar{v}_{2i} - \bar{v}_{1i}| \cdot |\bar{v}_{2j} - \bar{v}_{1j}| \rangle$, the angular brackets here and further denote averaging by many observations) is presented by: $B_{rr} = \varepsilon/_{15\nu} r^2$, $r << l_0$, ν is kinematics viscosity; $B_{rr} = 2C_1(\varepsilon r)^{2/3} = C_V^2 r^{2/3}$, $l_0 < r < L$; (5)

$C_1$ is Kholmogorov constant[10], the empiric evaluation $C_1$ =1.6±0.06. The amplitude of phase incursion fluctuation can be determined by calculating its dispersion value[11]: $D_S(r) = 2.92 C_n^2 \left(\dfrac{2\pi}{\lambda}\right)^2 L r^{5/3}$, $\{l_0, \sqrt{\lambda L}\} < r < L$, $L$ is the path length, (6)

$\lambda$ is radiation wavelength, $r$ is the distance between the beams. In this case, the evaluation of $C_n^{2'}$ given by Fig. 4A is based on the experimental data (Fig. 3B): $C_n^{2'} = \left\langle \dfrac{\delta n}{n} \right\rangle^2 r^{-2/3} = \Gamma^2 \left\langle \dfrac{\delta N}{N} \right\rangle^2 r^{-2/3}$, $\Gamma = \gamma_{GD} N/N_{norm} \approx 3 \cdot 10^{-5}$, $n \approx 1$ is the refraction index; (7)

$\gamma_{GD}$ is the Gladstone-Deule constant. It is obvious that the typical value $C_n^{2'} \approx (3...12) \cdot 10^{-15}$ $cм^{-2/3}$ is dependent on discharge energy. For comparison, the most probable value of $C_n^2$ for atmospheric paths varies[15] within $(10^{-16}...10^{-18}) \cdot cm^{-2/3}$ at the height of 3 to 15 *km*. The evaluation of r-m-s estimation of phase incursion difference at $r$=10 *mm*, $L$=1 *m*, $\lambda$ =0.63 $\mu m$ for the highest value of $C_n^{2'}$ used in the experiment follows from (6): $\langle \delta\varphi \rangle = \sqrt{D_S} \approx 0.2$ *рад*. (8)

Fig. 4B presents the $<\delta n>^2 \cdot r^{-2}$ value. The maximum of this value corresponds to the boundary $l_0$ of the viscosity and inertia intervals. The peculiarities of dissipation processes in the viscosity interval cause the dependences illustrated by Fig. 4C. The value $<\delta n>^2 \cdot r^{-3}$ is calculated here at different scales of $r$. It is supposed that in the case when $W<8$ $Wt/cm^2$ in the presence of laser generation (and $W<12$ $Wt/cm^2$ in the absence of it) and when the gas flow is not disturbed by heat releasing, as follows from Fig. 4, the dependence of the structure function in the viscosity interval increases as $r^2$. As energy input grows, the upper boundary of viscosity interval shifts to higher values (Fig. 4B), and at the scale of $r<l_0$ it varies as $r^3$.

## 6. ACKNOWLEDGEMENTS

The authors wish to thank the Russian Foundation for Basic Research for financial support of this work (grant number 99-02-16863).

## 7. REFERENCES


[1] V.V.Lyubimov- Bulletin of Russian Academy of Sciences, Physics, vl. **48**, p. 1477, 1979

[2] P.Loosen, V.Niehoff, U.Jarosch. Proceed. of SPIE, **2502**, pp. 536-541, 1995.

[3] Progress in Research and Development of High-Power Industrial $CO_2$ Lasers, V. Ya. Panchenko, V. S. Golubev, Editors, Proceedings of SPIE, **4165**, (2000)

[4] E.P. Velikhov, V.S. Golubev, V.S. Pashkin, Glow discharge in gas flow, Uspechi Fizicheskikh Nauk, **137**, p. 117, 1982.

[5] L.F.Richardson Proc. Royal Soc., **A110**, No.756, pp.709-737, 1926

[6] M.G. Galushkin, V.S. Golubev, V.Ya. Panchenko, Yu.N. Zavalov -High Temperature, **37**, N5, 1999, pp.676-684

[7] Yu.S. Akishev, A.P. Napartovich, Influence of gas-dynamic turbulence on discharge stability in gas flow, Fizika Plazmy, **4**, p.1146, 1978 (in Russian).

[8] M.G. Galushkin, V.S. Golubev, Yu.N. Zavalov et al., Quantum Electronics, **26**, p. 676-679, 1996.

[9] G.A. Garosi, G. Bekefi, M. Schulz, Phys. Fluids, **13**, N 11, pp. 2795-2809, 1970.

[10] L. D.Landau, E.M.Lifshits Theoretical Physics (in 10 vs.), v.IV, Hydrodynamics, M., Nauka.

[11] Laser Beam Propagation in the Atmosphere, Topics in Applied Physics Ed. by D.B. Strohbehn, **25**, Springer-Verlag, 1978.


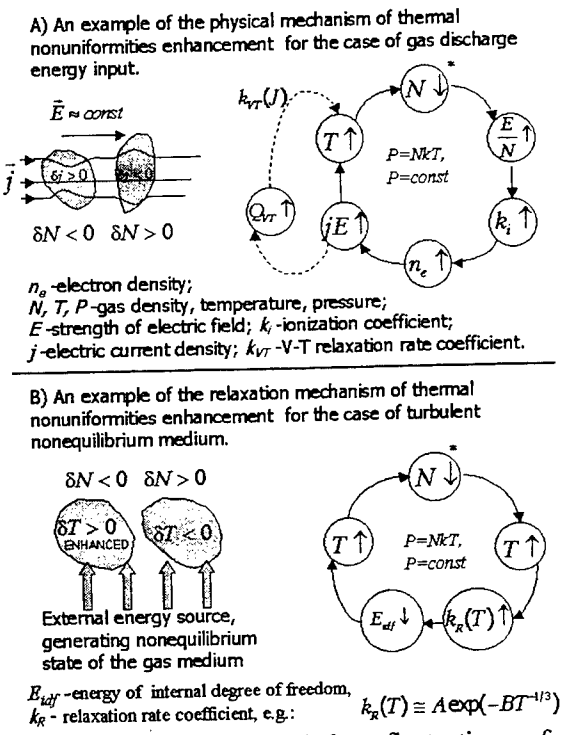


Fig. 1 The enhancement of turbulent fluctuations of gas refraction due to thermal instabilities of a nonuniform medium, induced by a non-thermal external energy input.

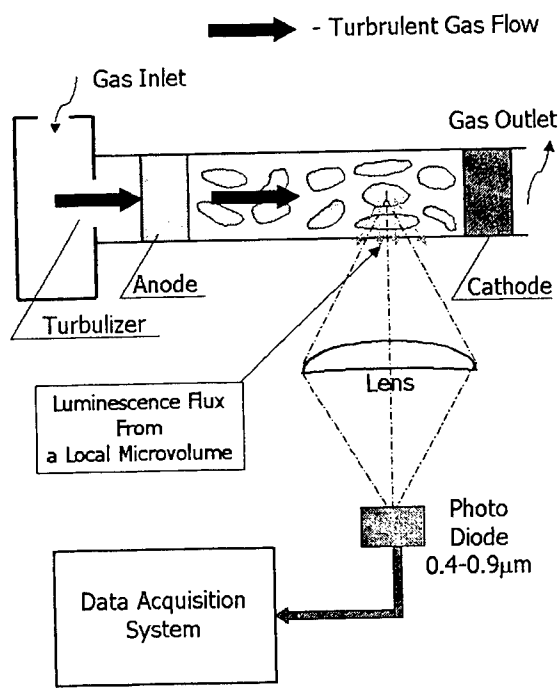


Fig.2 The scheme of experimental set-up

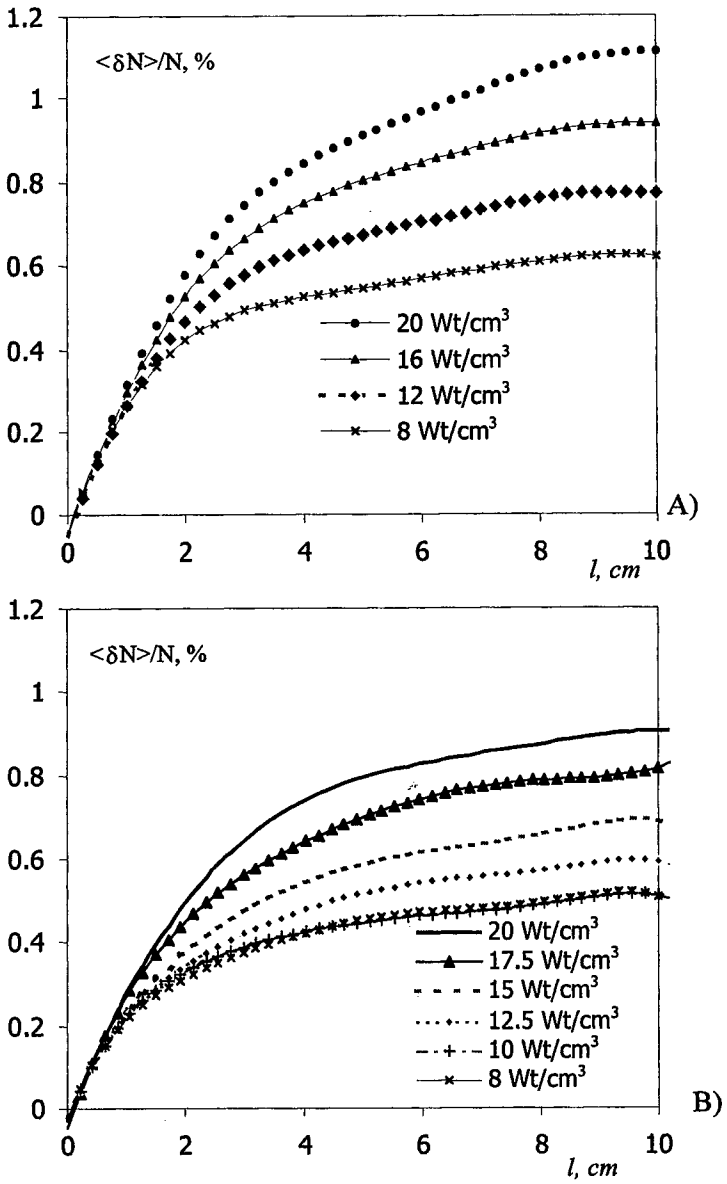


Fig. 3

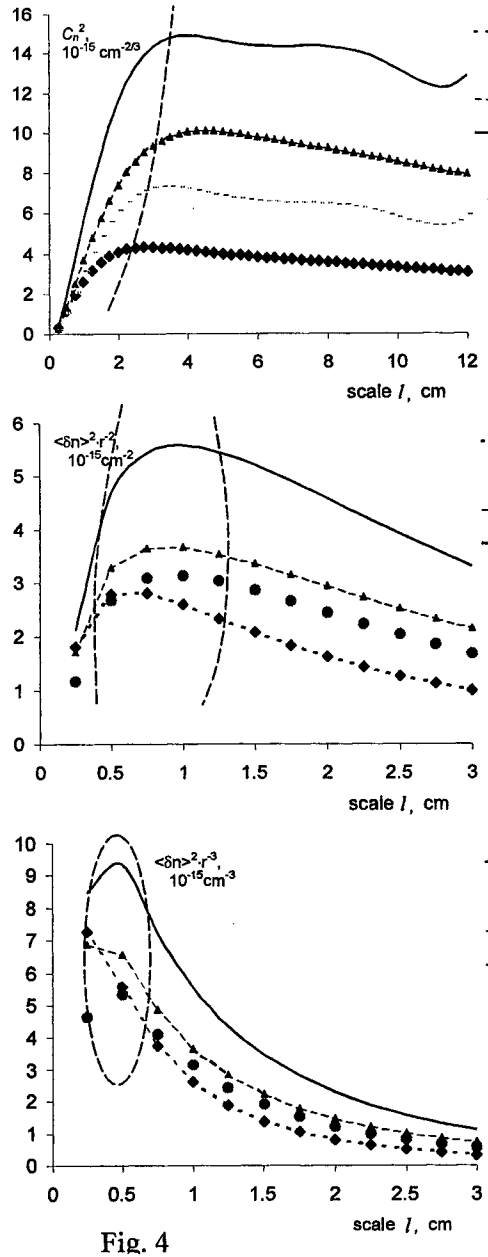


A) Dependence of estimation of structure constant $C_n^2$ on spatial scale of turbulent fluctuations. For $2<l<10$ cm there is the inertia range of Kolmogoroff- Obukhov turbulence.

B) The value $\langle\delta n\rangle^2 \cdot r^{-2}$ as a function of spatial scale of turbulent fluctuations. For $0.5< l <1.5$ cm there is the viscous range of Kolmogoroff -Obukhov turbulence.

C) The value $\langle\delta n\rangle^2 \cdot r^{-3}$ as a function of spatial scale of turbulent fluctuations. For $l <0.6$ cm there is non-Kolmogoroff -Obukhov turbulence.

Fig. 4

# NUMERICAL SIMULATION OF GAS DYNAMIC FLOWS IN PRESSURE RECOVERY SYSTEMS OF SUPERSONIC CHEMICAL LASERS

**A.V. Savin**
Baltic State Technical University, St.Petersburg, Russia
**A.A. Ignatiev, A.V. Fedotov**
Institute of High Performance Computing and Data Bases, St.Petersburg, Russia

## ABSTRACT

Technical parameters of powerful gas flow laser are substantially determined by pressure recovery systems (PRS). The computational simulation is the important tool for the design and improvement of PRS. Some features are reviewed and some results are shown concerning the computational simulation of PRS.

## I. Pressure recovery systems of HF/DF lasers

### A) Supersonic diffuser:

Gas flows in supersonic diffuser and ejector have a number of essential particularities as contrasted to conventional PRS of supersonic wind tunnels. Principal reasons of these particularities are: low Reynolds numbers, physical features of laser mediums and physicochemical non-equilibrium.

The Reynolds number in diffusers of HF/DF-lasers is of 1-2 order lower, than in diffusers of supersonic wind tunnels and GDL. As a consequence, three-dimensional boundary flows make essential displacing effect on a supersonic flow of laser medium. Non-equilibrium processes taking place in the medium (recombination of atomic hydrogen mainly) are the reason for some heat production, that, in turn, causes extra losses of total pressure in addition to usual shock losses. Operational mode with increased pressure in the resonator cavity (15-20 torr) is optimal for high power ground-based lasers from a point of view of weight-size optimization. On such increased pressure level non-equilibrium processes have time to be completed before entry of the medium into supersonic diffuser. Therefore when we investigate diffuser flows of such lasers there is no necessity to take into account the heat production in the medium. (Note, that the optimal operational mode for space-born lasers corresponds to essentially lower cavity pressure: 3-5 torr. In this case considerable heat release takes place in diffusers of ground-level test facility causing reduction of recovered pressure.) So, physical phenomena taking place in diffusers of high power ground-based HF/DF lasers are described by classical gas dynamics of non-reacting mediums.

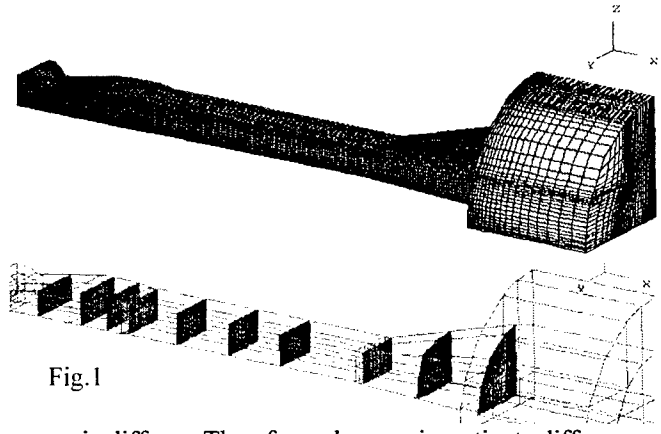

Fig.1

Computational simulation of flows in diffusers of such lasers based on non-stationary three-dimensional Navier-Stokes equations (3D NS) with appropriate turbulence model allows to describe in details flow patterns of 3D turbulent boundary flows on walls of channels. We use software CFDD (Computational Fluid Dynamics Desktop) and VICON (Viscous Computations based on Navier-Stokes equations). Splitting by physical processes and original implicit method for viscous terms allows applying modern high-resolution schemes (like ENO) for viscous flows [3]. This method is monotonic and stable, like usual high-resolution

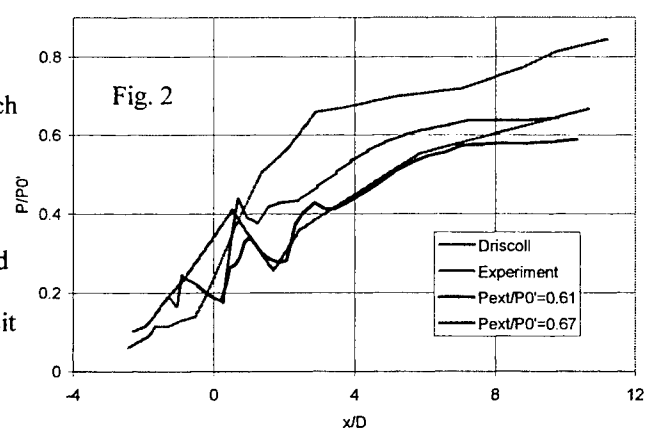




XIII International Symposium on Gas Flow and Chemical Lasers and High-Power Laser Conference,
Antonio Lapucci, Marco Ciofini, Editors, Proceedings of SPIE Vol. 4184 (2001)

scheme for non-viscous flow. Block-regular grids provide high efficiency for not too complex geometry. The model based on Lennard-Jones potential and Wilke formula are used for molecular viscosity. The turbulence is described by differential two-parametric k-ω model by Menter [4].

The start processes and stationary flow in the diffuser of the laboratory HF/DF-laser are investigated. Geometry of computational domain and overall design of grid are shown in Fig. 1. The channel of diffuser is of rectangular cross section. Two X-shaped vanes provide appropriate constriction. The subsonic part of a diffuser is made with transformation to round cross-section. Longitudinal profile of the resonator cavity is simulated by the equivalent $M_a$=2 nozzle. Symmetry allows selecting ¼ of cross-section. Matching condition of the diffuser and ejector is the following: the recovered pressure of diffuser and suction pressure of ejector should be equal. The suction pressure of ejector was simulated by backpressure in reservoir, attached to an exit of the diffuser.

The profiles of pressure along the diffuser for different magnitudes of backpressure are shown in a fig. 2. For comparison the experimentally measured profiles [1, 2] and also profiles in diffuser without constriction [5] are shown.

The flow pattern in the diffuser is shown in fig. 3. The pseudo-shock structure in supersonic diffuser of the HF/DF-laser essentially differs from the corresponding pattern observed in GDL or wind tunnel diffusers. This flow has tendency to formation of compact shock-wave pattern followed by an intensive three-dimensional separation. This effect should be taken into account at the selection of geometrical constriction, manner of sectioning of diffuser and its length.

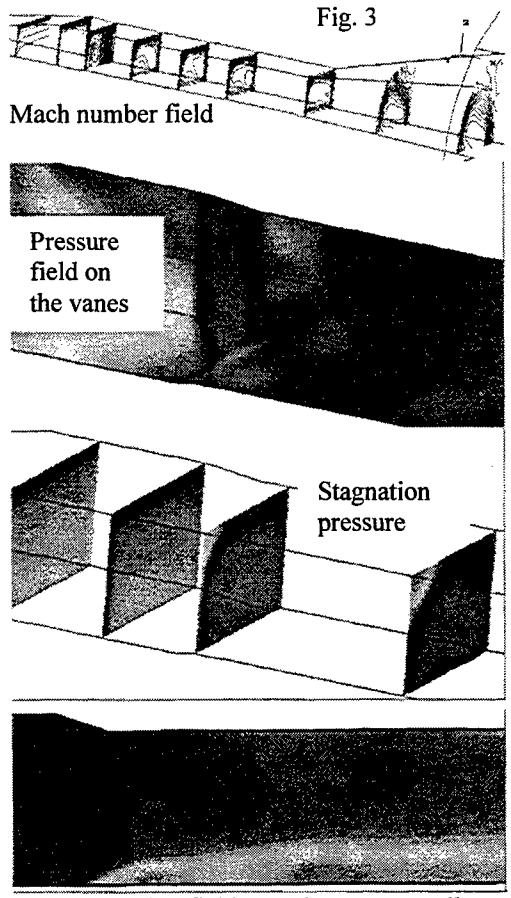

Fig. 3

Mach number field near the «upper wall»

## b) Ejector:

The ejector of the ground based HF/DF-laser should have compression ratio of about 13...15. Preliminary estimations of ejector parameters made on the base of integral conservation laws do not give any information on length of mixing chamber. The length should be sufficient for completion of mixing. At the same time too high length of mixing chamber leads to unnecessary increasing of overall length of PRS.

Optimal length of mixing chamber depends on the design of the ejector nozzle bank. As a basic variant the peripheral circular nozzle is selected. The axisymmetrical geometry of the ejector makes it possible to carry out parametric computational experiment on the basis of two-dimensional Navier-Stokes equations. So, we can select the length of mixing chamber by the optimization of start-up pressure and throttling characteristic of the ejector.

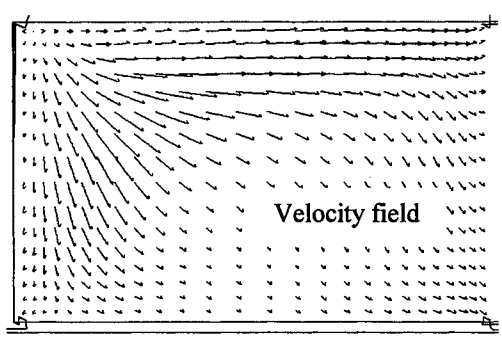


The example stationary flow pattern after reaching of maximal vacuum is shown in fig. 4. The supersonic flow is decelerated in narrowed mixing chamber and reaches the throat at transonic parameters. The separation and all gas dynamic phenomena related to pseudo-shock accompany this flow. The flow in diverging part of mixing chamber is non-stationary. The self-induced oscillations of surging type can take place sometimes.

Parameters of stationary flow calculated for the series of ejection coefficient $n=G_{passive}/G_{active}$ allows building throttling characteristics of ejector necessary for the accurate matching of the ejector and the diffuser. The set of calculated throttling characteristics is shown in the fig. 5.


Fig. 4

## II. COIL diffuser

Chemical processes in COIL mediums at flow in diffuser causes heat production, in turn owing to additional losses of total pressure. This effect can cause impossibility of diffuser start. Vice versa, the matching of the diffuser profile with kinetics of heat production allows to minimize losses and to increase recovered pressure. The analysis of chemical and gas-dynamic processes in COIL nozzle channel and resonator is carried out on the base of one-dimensional gas dynamic model. Analysis of such kind makes possible estimation of gas-dynamic and chemical parameters of laser gas at the inlet of supersonic diffuser. The active medium within the frame of a described model is formed instantly, and the amplification begins to fall down at once. However the effect of gas-dynamic cooling leads to positive influence on an amplification magnitude in supercritical area of nozzle. The analysis shows that it is necessary to take into account a dependence of reactions velocities on temperature and it is possible to not take into account suppression on the walls.

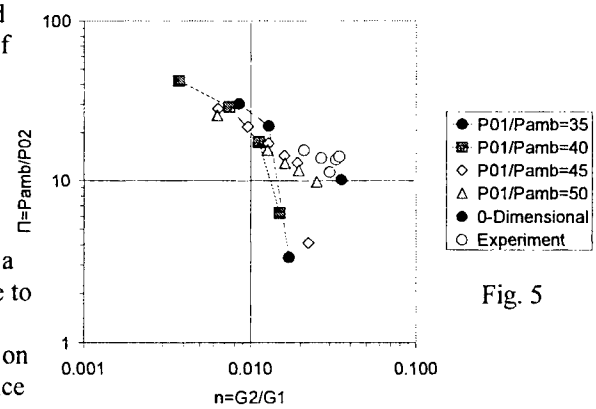


Fig. 5

Some results of such one-dimensional analysis are shown on Fig. 6. Pressure and temperature profiles show the essential influence of non-equilibrium heat production on gas dynamic features.

The next step is two-dimensional analysis. The most consistent way is to use Navier-Stokes equations and some appropriate kinetic scheme. But before this it seems useful to carry out more simple analysis within the framework of phenomenological half-empirical models of heat production.

The two-dimensional supersonic flow is considered in a channel of gas, which have nonequilibrium excited oscillatory-electronic modes. In N-S equations the full internal energy of gas is represented as the sum:

$$E_{int}=E_t+E_{ev},$$

Where $E_t$ - energy of translational moving of molecules and $E_{ev}$ - energy of oscillatory-electronic modes. Thus, there are two temperatures $T_t$ and $T_{ev}$, so temperature $T_t$ is evaluated as

$$T_t=f(E_{int}-E_{ev}).$$

The temporary variation of oscillatory-electronic energy are described by a relaxation equation of a kind:

$$\frac{dE_{ev}}{dt}=\frac{E_{ev}(T_t)-E_{ev}(T_{ev})}{\tau} \qquad (1)$$

Two simplifying assumptions are entered:

1. The equilibrium oscillatory-electronic energy is constant in the entire channel:

$$E_{ev}(T_t)=E_{ev}^{*}=\text{const}$$

2. The relaxation time is represented in Landau-Teller form:

$$\tau = A\exp\left[\left(\frac{T_h}{T_t}\right)^{1/3}\right]$$

with A and $T_h$ as parameters. So, equation (1) can be written in the form:

$$\frac{df}{dt}=-\frac{f}{\tau}$$

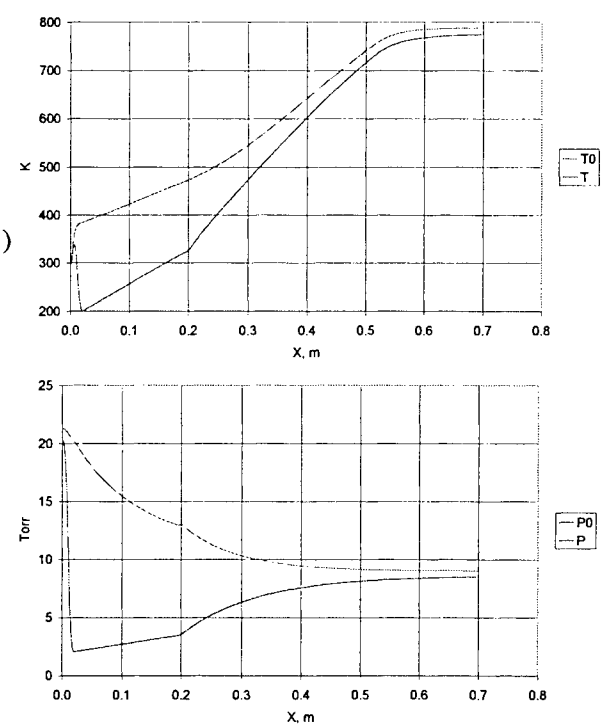


Fig. 6

where

$$f = \frac{E_{ev}(T_{ev}) - E^*_{ev}}{\left(E_{ev}(T_{ev}) - E^*_{ev}\right)_{init}}$$

The lower index "init" concerns to an inlet of the channel, so f=1 on an inlet. The example result of analysis is shown on Fig. 7.

## III. Conclusion

The computational experiment allows considering all particularities of non-stationary start processes in high compression ejector and supersonic diffuser characteristic for HF/DF and COIL pressure recovery system. The starting pressure of ejector, start time and compression ratio depend on constriction of mixing chamber and its longitudinal profile. This profile is selected on the basis of numerical simulation. For the ensuring of the successful diffuser start the time of this process should be matched with time of transformation of flow within the mixing chamber of ejector.

The modern techniques of computational simulation let us to understand complex nature of flows in PRS and allow reducing expenditures to experimental improvement of such complex systems, as PRS of HPCL.

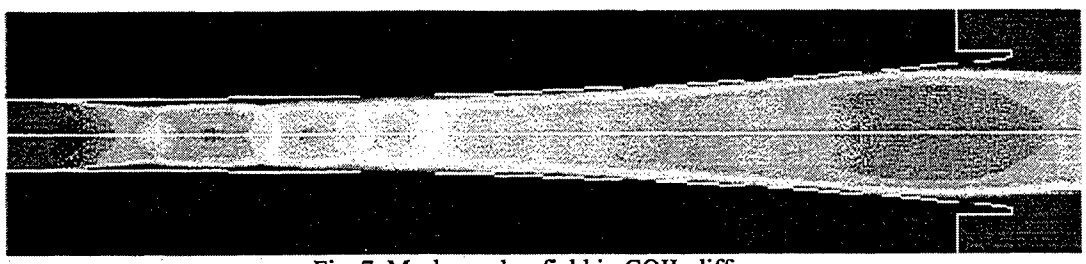

Fig. 7. Mach number field in COIL diffuser


## ACKNOWLEDGMENTS

The authors are grateful to "Laser Systems" Ltd., St-Petersburg, Russia for financial support.


## REFERENCES


1. A.S. Boreisho, A.V. Savin, V.M. Khailov, V.M. Malkov, "Pressure recovery system for high power gas flow chemical laser" Proceedings of XIII International Symposium On Gas Flow & Chemical Lasers - High Power Laser Conference (GCL-HPL-2000), September 18th-22nd, 2000, Florence, Italy.
2. V.M. Malkov, A.S. Boreysho, A.V. Savin, I.A. Kiselev, A.E. Orlov, "About choice of working parameters of Pressure Recovery Systems for high power gas flow chemical lasers" Proceedings of XIII International Symposium On Gas Flow & Chemical Lasers - High Power Laser Conference (GCL-HPL-2000), September 18th-22nd, 2000, Florence, Italy.
3. A.A. Ignatiev, "Building of regular grids by the mechanical analogy", Matematicheskoye modelirovanie, V. 12, No 2, 2000, pp. 101-105. (in Russian).
4. F.R.Menter, "Two-Equation Eddy-Viscosity Turbulence Models for Engineering Applications", AIAA J. - V.32, No. 8, 1994, pp. 1598-1605.
5. R.J. Driscoll, L.F. Moon, "Pressure recovery in Chemical lasers", AIAA J. - V.15, №5, 1977, p. 665.

# Industrial lasers of power up to 10 kW with high quality of radiation

A. P. Golishev A. I. Ivanchenko, A. M. Orishich, V. B. Shulyat'ev

Institute of Theoretical and Applied Mechanics,

Siberian Division, Russian Academy of Sciences, Novosibirsk, Russia

## ABSTRACT

In activity the device of the high-power electrodigit laser with optical system and the problem of pressure losses upon gas motion along a closed circuit containing channels in which heat is supplied to and removed from the gas is studied. The object where the pressure losses are studied is a $CO_2$ laser with a crossflow.

**Keywords:** laser, gas flow, pressure loss distribution, gas velocity, radiation power, resonator.

## 1. INTRODUCTION

With increasing power of electric-discharge lasers with a closed cycle of the flow, the role of the gas-dynamic circuit and optical system with high quality of radiation becomes more important. The gas-dynamic circuit of a powerful continuous-wave $CO_2$ laser with a crossflow and transverse discharge resembles a subsonic wind tunnel with a closed circuit but differs from the latter by configuration of the gas-discharge chamber wherein the electric energy is converted to radiation and thermal energy.

There are different approaches to designing the gas-dynamic circuit of the laser, and the choice of its schemes is based on contradictory criteria. The circuit has either a large specific volume (3 $m^3$ per 1 kW of generated power) and a low specific power for sustaining gas circulation over the closed circuit (1 kW per 1 kW) or a high (up to 2 kW per 1 kW) specific power and a comparatively small ($1 \div 1.5$ $m^3$/kW) specific volume [1-3]. Various approaches, which are often incompatible, are proposed to choose the pumping tools that ensure gas circulation over a closed circuit and aerodynamic schemes of gas-discharge channels wherein the pumping of the laser mixture of gases is performed. The results of papers devoted to the problem of calculation of pressure losses upon nonisothermal gas flow are contradictory.

There is a problem of high quality of output beam in high power $CO_2$ lasers. The requirement of high beam quality is in contradiction with requirements of high mode volume and high extraction efficiency. A variety if resonator schemes are used to overcome this tradeoff. As it has been shown in our prior works [4], self filtering unstable resonator (SFUR) [5] provides a high beam quality (close to $TEM_{00}$ mode one) in high power $CO_2$ lasers with several times larger mode volume as compared to $TEM_{00}$ mode of stable resonator.

In the present paper we study the self filtering unstable resonator (SFUR) with high quality of radiation with a level of power up to 10 kw and the problem of pressure losses upon circulation of a subsonic gas flow over the circuit of a device with a closed cycle, which contains channels wherein heat is supplied to and removed from the gas. The pressure losses are studied in a $CO_2$ laser with a crossflow.

The pressure losses are understood as the total pressure losses, which determine the power necessary for gas pumping. Nonisothermal motion is understood as a gas flow under conditions of changing stagnation temperature of the flow due to heat addition or removal. The effect of nonisothermality on pressure losses should be understood as the account of additional losses for gas acceleration upon heat addition (removal).

## 2. THERMOHYDRODYNAMICS OF A LASER WITH A CLOSED CYCLE OF THE FLOW

One of the possible configurations of the gas-dynamic laser circuit is shown in Fig.1. The velocity vector (is shown by arrows) of the flow in the gas-discharge chamber is directed perpendicular to the propagation of the laser beam and the discharge current, which decreases the Mach number necessary for changing the gas in the chamber. The flow velocity at the forefront of the gas-discharge channel is usually less than 60—70 m/sec [1-3].



XIII International Symposium on Gas Flow and Chemical Lasers and High-Power Laser Conference,
Antonio Lapucci, Marco Ciofini, Editors, Proceedings of SPIE Vol. 4184 (2001)

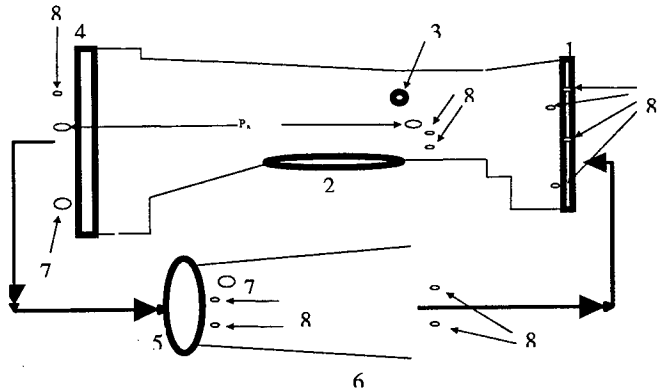


Fig.1. The scheme of the experimental installation:
1 - lattice, 2 - anode, 3 cathodes, 4 heat exchangers, 5 - fan, 6 - diffuser, 7 thermometers, 8 - sensors of pressure.

To verify the calculation results [6] we measured the difference in the total pressures P on a "load" containing channels wherein the heat is added and removed, for a constant fan capacity $\rho V'$, in two regimes: with heat addition and without it. This load in the gas-dynamic circuit of the laser is the section between the gas-discharge channel entrance and the heat-exchanger exit. Heat addition was ensured by a glow discharge. The discharge power was sufficient for the total pressure losses in the gas-discharge channel to be $(0.2-0.4)\rho_0 v_0^2$. Good homogeneity of the flow upstream of the gas-discharge channel entrance and a significant difference in cross-sectional areas upstream of the gas-discharge channel and behind the heat exchanger ensured correct measurements.

The experiments were conducted in the gas-dynamic circuit of the laser described in [3,4,6]. The layout of the experimental setup is shown in Fig. 1. The cross section of the gas path from the region ahead of the gas-discharge channel to the heat-exchanger exit and other elements of the circuit are shown conventionally (not to scale). The path width is 0.93 m. Grid 1, a gas-discharge channel containing anode 2 and cathode 3, and heat exchanger 4 are consecutively placed along the gas flow. The gap between the anode surface and the channel wall is 0.1 m. The characteristic length of the anode in the streamwise direction is 0.12 m. A cylindrical cathode 0.016~m in diameter is placed at a distance of 0.065 m from the anode. In the crossflow direction, the cathode and anode have a length of 0.86~m. The heat exchanger, 0.28~m high, is connected with the gas-discharge channel by a stepwise diffuser. A smooth expansion section begins immediately after the anode, the expansion angle is 12°, and the degree of expansion is 2. The section from the grid to the anode is constricting, and the degree of constriction is 2. The profile of the section was chosen so that the flows behind the anode were mainly nonseparated or separated depending on test conditions. Behind the heat exchanger, there was fan 5 with diffuser 6 at the exit. Thermometers 7 were located behind the heat exchanger and the fan. Probes of static and total pressure 8 were located in flow cross sections where physical conditions allowed it.

The discharge was ignited in the airflow at a pressure of 10.3 and 16 hPa or in a mixture of $CO_2$ and air with a ratio $(2.66 \div 13.3)$ hPa and $(2.66 \div 16)$ hPa. The gas-flow velocity at the forefront of the gas-discharge channel was $(60 \div 70)$ m/sec. The velocity non-uniformity over the channel cross section did not exceed 3%. The calculated pressure losses in the heat exchanger were about $0.6\rho_0 v_0^2$ in the regime without the discharge and less than $1.1\rho_0 v_0^2$ with the discharge. A variant of calculation of the heat exchanger is shown below. The calculated values of pressure losses at the section between the aft front of the discharge and the heat-exchanger entrance were about $0.2\,\rho_0 v_0^2/2$. The error in determining the value of P was less than $0.1\,\rho_0 v_0^2/2$.

Primary attention was paid to the measurement of the difference in total pressures P on the load using pressure probes mounted upstream of the gas-discharge channel and directly behind the heat exchanger (Fig.1). The fan capacity was controlled by total and static pressure probes located upstream of the gas-discharge channel. The increase in temperature ensured by the fan allowed us also to control the change in flow regimes at different sections of the circuit. For example, if the height of the heat exchanger was reduced by one quarter, the temperature produced by the fan increased by a factor of 1.4. Total and static pressure probes mounted at various points of the circuit performed additional control of the gas-flow regimes.

For the case of a nonseparated flow in the diffuser behind the gas-discharge channel, the experiments gave the following results.

1. The dynamic pressure at the forefront of the gas-discharge channel was $\rho_0 \upsilon_0^2/2 \approx p_0 \cdot 2.5 \cdot 10^{-2}$, which corresponds to a mean velocity of the gas $\upsilon_0 \approx 65$ m/sec.

2. The fan increased the gas temperature by the same value regardless of the pressure, for example, by 13.6°C for air.

3. The fan capacity in both regimes (with and without the discharge) was constant.

4. The difference in temperature between the gas exhausting from the heat exchanger and the water entering the heat exchanger was not greater than 12-13°C.

5. In both regimes (with and without the discharge), the pressure losses on the load $p_{xy}$ were roughly equal to $0.9\rho_0\upsilon_0^2$.

It should be noted that the experiments with air and laser mixtures gave identical results. From the experiment and thermodynamic calculation, we can conclude that nonisothermal processes do not introduce additional pressure losses for maintaining gas circulation over the circuit.

The absence of the effect of nonisothermality does not mean that heat addition should not be accompanied by an increase in pressure losses. Heat addition increases the mean temperature of the gas, hence, the physical parameters of the flow change, which should lead to an increase in pressure losses, for example, for overcoming the friction forces in the heat exchanger. The calculation of the heat exchanger is explained below. It was expected that heat addition would give an increase in pressure losses by $(0.3-0.5)\rho_0\upsilon_0^2$. An unexpected result of these experiments was that heat addition was not accompanied by an increase in pressure losses.

A set of experiments on gas-flow visualization was conducted. It was performed using light filaments attached to the surface of the lower wall of the diffuser and the anode surface in a staggered order. The glowing of the anode surface was inhomogeneous. It clearly reflected the flow pattern near the surface. The discharge glowing on the cathode surface was visually homogeneous.

The results of these experiments allowed the following conclusions. The flow in the diffuser behind the anode is three-dimensional. There are vortex regions on the diffuser walls. The vortices rotate in the plane of the wall and are located symmetrically relative to the side walls. A typical size of the vortices is 0.03-0.07m. The area of the surface occupied by the vortex increases with decreasing velocity and pressure of the gas. When the discharge is ignited, the flow is reconstructed: it becomes more stable, the regions with separated flows become smaller, and large vortices are split into smaller ones.

Depending on the path configuration ahead of the anode (stepwise entrance, constriction, straightening section, etc.), flow reconstruction occurred; in particular, globally separated flows were observed. In each experiment with air or laser mixtures of gases, the discharge reconstructed the flow pattern, but the value of $p_{xy}$ in both regimes (with and without the discharge) was identical. The reconstruction of flow regimes may be responsible for the fact that heat addition is not accompanied by an increase in pressure losses on the load.

## 3. RESONATOR

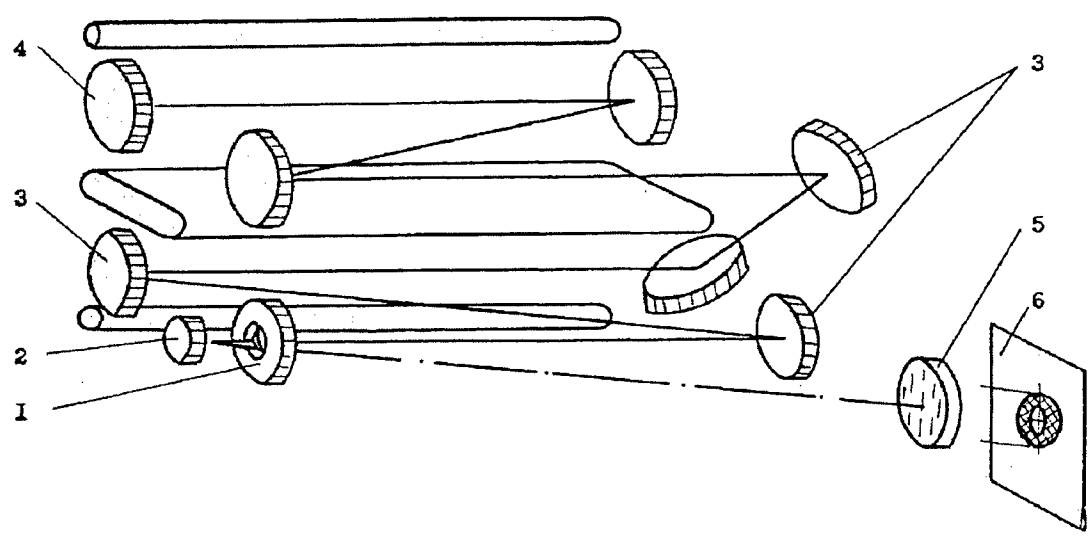


Fig. 2. The scheme of the unstable resonator (SFUR).
1 - output mirror, 2,4 - spherical mirror, 3,5 – plane mirrors, 5 – output window, 6 - radiation structure.

The self filtering unstable resonator (SFUR) scheme (fig. 2) comprises confocal spherical mirror 4 with focal length $f_1$ and mirror 2 with focal length $f_2$ and annular output mirror (1) in common focal point (3 – plane mirrors, 5 – output window). The annular mirror with hole radius $a = (0{,}61\lambda f_2)^{1/2}$ and spherical mirror with smaller focal length composes a spatial filter. The filter forms a smooth Gaussian–like intensity profile of low order mode [4]. Numerical calculations have been made to determine the dependence of output beam characteristics on resonator parameters. It has been established, that SFUR output beam is close to Gaussian one in terms of beam quality in the event that $M = f_1/f_2 \geq 4$ [2]. Spot radius R on the output mirror (1) is 1,5Ma [4], and Fresnel number of active medium arm is $N = R^2/\lambda f_1 \approx 1{,}37M$. Upper limit of M and N imposes by demand of high extraction efficiency, as feedback value of SFUR is approximately $2/M^2$. Achieving of the high extraction efficiency in CW $CO_2$ lasers is conjectural if M exceeds 5…6. That is, Fresnel number operation range is $\approx 5 \div 8$. Such a narrow range is the drawback of the scheme in conditions of CW $CO_2$ laser, but in operation range SFUR allows to generate a high power and high quality beam. As we believe, power level up to 10 kW or more is achievable. Following features of the SFUR also make it attractive for high power lasers. First, reflective optics only is used in this scheme. Second, low power (~ 0,1 of output power in operation range) and small beam diameter in feedback arm facilitates the control over the temporal characteristics of an output beam. For example, Q-switching may be easily realized.

## 4. CONCLUSION

From thermodynamic calculation follows that the actuation of electrical discharge should result in additional losses of pressure in a discharge channel on acceleration of gas. It is caused by presence of not isothermal processes in a discharge channel. At actuation of discharge there should be additional pressure losses and in the heat exchanger owing to change of the physical characteristics of a flow (speed and viscosity of gas), temperature, caused by increase, of gas. The resistance to motion of gas in a contour should essentially grow. From experiments, however, follows that the actuation of discharge does not accompany by increase of resistance to motion of gas. It, should be, connected that the actuation of electrical discharge results to improvement of the aerodynamic characteristics of a contour on a site from an input in a discharge channel up to an output for the heat exchanger.

By means of visualization, it was found that the flow in a two-dimensional diffuser could be three-dimensional, which is manifested in formation of large-scale vortices rotating in the plane of the diffuser wall.

The authors are unaware of any publications devoted to the problem of three-dimensional flows in two-dimensional diffusers. In experiments, three-dimensional flows were observed for very small angles of expansion (about 12°). However, there are publications on three-dimensional flows arising in the flow around a wing mounted at a certain angle of attack. Zanin [7] studied the three-dimensional structure of the flow around a wing and the changes in this structure induced by sequential increasing and decreasing of the flow velocity. The experiments [7] were conducted at an atmospheric pressure for flow velocities of 0-23 m/sec; the model span was 0.945 m and the chord length was 0.196 m. As a whole, similar flow patterns were observed under test conditions [7] and in our experiments. The flow structure under our experimental conditions could be reconstructed by placing steps in the vortex region or by mounting a flap (rotating blade) behind the diffuser near its wall. The physical mechanisms of three-dimensional flows and the effect of the discharge on them remain unclear yet.

In this paper shown, that self filtering unstable resonator (SFUR) may be use for production of high quality of output beam in high power $CO_2$ lasers. The requirement of high beam quality is in contradiction with requirements of high mode volume and high extraction efficiency. As it has been shown here and in our prior work [4], self filtering unstable resonator (SFUR) [5] provides a high beam quality (close to $TEM_{00}$ mode one) in high power $CO_2$ lasers with several times larger mode volume as compared to $TEM_{00}$ mode of stable resonator.

## ACKNOWLEDGMENTS

The authors are thankful to B. Yu. Zanin and V. V. Kozlov who helped in conducting the experiment on visualization of aerodynamic flows and comparison with the wind-tunnel results.

## REFERENCES


1. G. A. Abil'siitov, V. S. Golubev and F. V. Lebedev, "Problems of creation of industrial technological lasers with power 1--10 kW", *Izv. Akad. Nauk SSSR, Ser. Fiz.*, **47**, No. 8, pp.1507--1512, 1983.
2. A. I.. Ivanchenko, V. V. Krasheninnikov, A. G. Ponomarenko and A. A. Shepelenko, "Selecting gas-dynamic channel parameters for electrical discharge fast flowrate lasers", *Prikl. Mekh. Tekh. Fiz.*, **27**, No. 6, pp. 3--8, 1986.
3. V. K. Golov, A. I. Ivanchenko, V. V. Krasheninnikov, et al., "Technological $CO_2$ laser with power 2.5 kW", *Izv. Sib. Otd. Akad. Nauk SSSR, Ser. Tekh. Nauk*, **2**, No.10, pp.87--91, 1986.
4. A.I. Ivanchenko et al., Quantum Eelectronics, vol.24, pp. 591-594, 1994.
5. P.G. Gobbi, G.F. Reali, Opt.Com. vol.52,pp.195-198,1984.
6. A.I. Ivanchenko, A.M.Orishich, S. S. Woronsow. " Termogidrodynemik of $CO_2$ laser of continuous action with the closed cycle of a flow" *Prikl. Mekh. Tekh. Fiz•* (in Russian). 41, • 1• .3-13, 2000.
7. B. Yu. Zanin}, "Hysteresis of a separated variable-velocity flow about a straight-wing model," Prikl. Mekh. Tekh. Fiz., 38 No. 5, 80-84 (1997).

# About choice of working parameters of Pressure Recovery Systems for high power gas flow chemical lasers

V.M. Malkov Institute of Theoretical and Applied Mechanics, Novosibirsk
A.S. Boreysho, A.V. Savin, I.A. Kiselev, A.E. Orlov
Baltic State Technical University, St. Petersburg

## 1. INTRODUCTIONS

The general view of PRS is shown in the paper [1] of the present book. The PRS is known gasdynamic device consisting from the next main elements: supersonic diffuser and supersonic ejector. Traditionally it is utilized for providing of supersonic wind tunnels exhaust.

The scheme solution of PRS, the working parameters of system, the operating mode in many respects are determined by output parameters of gasdynamic installation, for which the PRS is designed. The features of PRS for continuous wave chemical lasers (CCL) HF/DF-CCL and COIL - in comparison with usual aerodynamic systems are connected with the particularities of laser flow gasdynamic parameters after a resonator. Some characteristic values of flow parameters on SD input for two these cases - wind tunnels and CCL - are represented in the table.

| | $T_0$ K | $\mu$, g/mol | $\gamma$ | $P_{st}$, torr | Re | M | Cross section |
|---|---|---|---|---|---|---|---|
| Wind tunnel | 300 | 29 | 1.4 | >40 | $10^6 \div 10^7$ | >3 | Circle |
| HF/DF | 1400-1900 | 8-10 | 1.5 | 15-20 | $10^4 \div 10^5$ | 2 | Rectangle |
| COIL | 300-400 | 8-10 | 1.5 | 5-7 | $10^3 \div 10^4$ | 2 | Rectangle |

Here $T_0$ - flow stagnation temperature $\mu$ molecular weight of gas, $\gamma$ - isentropic index, M -flow Mach number, Re - characteristic Reynolds numbers, $P_{st}$- approximate range of static pressure on input in SD.

In the paper some common statements concerning the rational selection of the working parameters of SD and EJ for PRS-CCL are represented. The condition of matching of SD and EJ parameters in a unified system is considering.

## 2. SUPERSONIC DIFFUSER

In PRS the diffuser is intended for slowdown of supersonic flow which is coming out of resonator cavity. The slowdown is necessary for effective mixing of subsonic laser flow (passive flow) with supersonic flow from EJ nozzle (active flow) in EJ mixing chamber. Such a mixing scheme is conventional, however there are proposals on providing of mixing by "supersonic + supersonic" scheme [2]. But there are not enough of data on lengths of mixing chambers today and are some starting problems for these EJ. Therefore the conventional scheme is considered in this paper only.

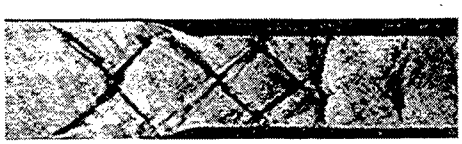

Fig. 1

Process of slowdown of supersonic flow in a channel is the interaction of oblique shocks originating in a flow with the boundary layer (Fig. 1). This interaction is reason of the boundary layer separation and of subsonic areas formation with intensive turbulence. Due to turbulence these areas increase along the channel, gradually catching a flow core. Slowdown of supersonic flow needs particular length, which depends on the flow velocity and on the shape of a channel [3-5]. A slowdown zone is named as area of pseudoshock.

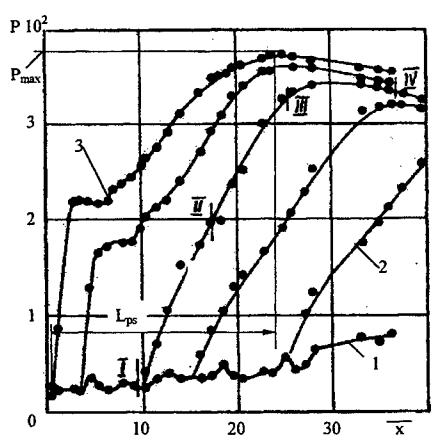


Fig. 2

Characteristic distributions of static pressure P(x) on a wall of rectangular cross-section diffuser are shown in Fig.2. Basic SD performances are : start and unstart pressure - $P_{st}$, and $P_{unst}$, and maximal pressure recovery in a flow after SD - $P_{max}$. The curve 1 corresponds to supersonic flow existing in a whole channel - at $P_{00}$ in nozzle prechamber that much bigger than pressure $P_{st}$. The curve 2 corresponds to $P_{00} = P_{st}$, when part of channel is occupied by pseudoshock. At decreasing of $P_{00}$ the pseudoshock shifts along the channel. Different curves are corresponding to different values of $P_{00}$. At last, at $P_{00} = P_{unst}$ they have the prestalling curve 3, when the regime with $P_{max}$ is realized (length of a pseudoshock is shown). At $P_{00}<P_{unst}$ supersonic flow is destroyed in a working section - P(x) increasing begins in the nozzle which works in off-design condition. $P_{st}>P_{unst}$ - it is characteristic case for viscous flows and such a phenomenon is named by hysteresis.

Values of $P_{max}$, $P_{st}$ and $P_{unst}$ for SD of sufficient length are easily evaluated with the help of the halfempirical one-dimensional theory based on relations for normal shock [6]. The experiments have shown - the minimum $P_{st}$, close to magnitude evaluated by normal shock relation, is reached when the SD length is equal to pseudoshock length ($L_{sd}=L_{ps}$). At $L_{sd}<L_{ps}$ the $P_{st}$ increases sharply [7,8]. So $L_{sd}$ is the main empirical parameter of the theory. Effective diameter,

XIII International Symposium on Gas Flow and Chemical Lasers and High-Power Laser Conference,
Antonio Lapucci, Marco Ciofini, Editors, Proceedings of SPIE Vol. 4184 (2001)

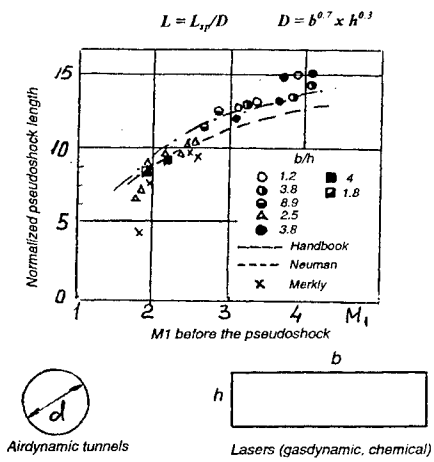


Fig. 3

allowing the generalization of experimental data obtained in the installations with different channels, at different Mach number, was offered in [8]: $D=b^{0.7}x\ h^{0.3}$ (where b - width, h - channel altitude). D - empirical parameter is offered on the basis of analysis of the large number of experiments. Both sizes of a cross-section go into it, since the flow in rectangular channels is three-dimensional. In Fig. 3 the universal curve $L= L_{ps}/D =f(M)$ for length of a pseudoshock in the different shape channels (for wind tunnels and GDL basically) is given.

In Fig.4 the results of tests for two HF/DF-CCL diffusers are compared. (Magnitudes of b/h are indicated in fig.). P(x) is related to the value of stagnation pressure behind normal shock (fig.4a). It is visible, that caliber D works in the field of CCL parameters (low Re numbers). In accordance with Fig. 3 magnitude of $L_{ps}$ is (8-9)D (M about 2). The difference of $P/P_0'$ from unit at the end of a subsonic diffuser is connected with friction losses. (At one-dimensional estimations of $P_{st}$ this effect can be taken into account with help of the empirical corrections [8]).

Absolute values P(x) differ strongly for two these tests, x'=x/l – relative magnitude (fig.4b). It is connected with the differences of flow parameters on SD input (point A). The data demonstrate how it is important to select the shape of cavity correctly. The analysis [9] shows a considerable degree of influence of the cavity extension and parameters in the generator of atomic fluorine (GAF) on parameters of flow before SD. In the CCL case the selection of SD performances starts with selection of GAF parameters. It is important to select profile of cavity wall. In the second case the profile was non-optimal. Moreover, the wall of cavity had a kink at SD input. The cavity wall should be shaped taking in account the heat generation in the flow to avoid appearance of shock from broad walls of a channel, because it results in the pressure start increase.

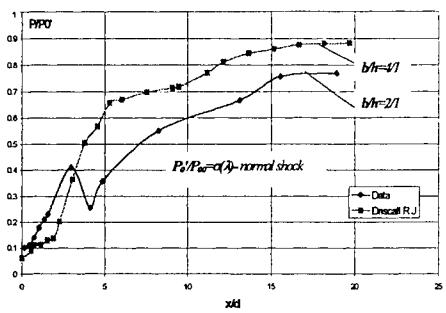


Fig. 4a

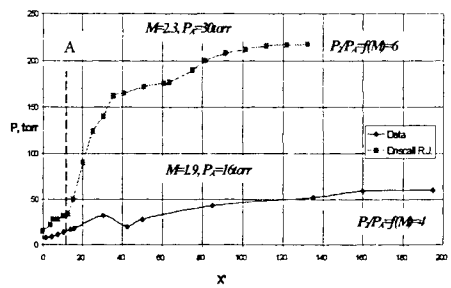


Fig. 4b

The choice of pylon site in a channel must be correct too. In case of big installations the multisectional SD is employed [1]: large distance between pylons and nozzle device carries on to increasing of $P_{st}$ [7,8].

Herewith, the start of multisectional SD and the reaching of design values of $P_{st}$- especially for channels with b/h>>1 - remains by a problem, which solution requires special efforts. At moment of start in such a channels the separation zones are shaped on narrow walls apart from a thick boundary layer [10]. It can lock the extreme channels and lead to unstart of a whole SD. To eliminate such phenomena the blow-downs along narrow walls from special small nozzles is applied. The size of blow-down nozzles, the place and the working parameters are selected empirically [11].

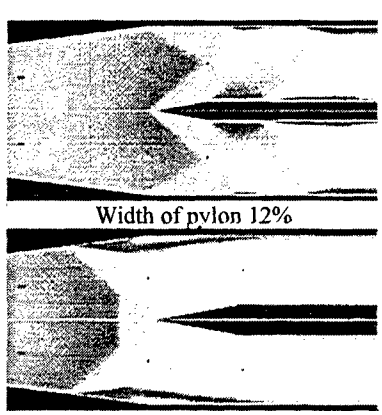


Fig. 5

For PRS SD the very important performance is $P_{max}$ that is a function of Mach number and of channel constriction degree - S/S*. At start the initial level of vacuum on SD exit exists set by a degree of ejector compression on zero load. In next moment the pressure on EJ input increases in accordance with the load. So another mode of SD - not start mode - is implemented - the curve 3 in Fig. 2. For the better PRS performance it is necessary to have the bigger of $P_{max}$. So it is demanded to define the maximum possible magnitude of S/S*. For GDL SD this magnitude is easily evaluated on a basis of the one-dimensional inviscid theory. In case of SD-CCL three-dimensional Navier-Stokes equations calculations is demanded -boundary layers are thicker (Re numbers are lower) [12]. Data of such calculation (Fig. 5) are showing that SD with a pylon width 20% - evaluation of one-dimensional inviscid theory - is not started: 12 % is maximum possible magnitude for pylon width.

Thus, on basis of the half-empirical one-dimensional theory the basic geometrical parameters are selected and the estimations of SD performances are made. These estimations are the first approximation for three-dimensional

calculations, on basis of which the final sizes are selected and the performances of diffusers are updated.

At calculation of SD performances and geometry for COIL it is necessary to take into account the heat generation as result of singlet oxygen thermolisation in SD channel. The influence of heat generation on SD shape can be considerable. Quantitatively influence of heat generation depends on particular kind of working process in the laser.

## 2. SUPERSONIC EJECTOR

The principle of coordination SD and EJ in unified PRS was already stated above qualitatively. To determine it in details, it is necessary to examine the operation of ejector. The dependence of $P_{02}$-total pressure before EJ on the $G_2$-passive gas mass-flow rate is shown in Fig. 6. There is a hysteresis for EJ with constricting mixing chamber, as well as for SD with constriction. There is the start performance at $P_0=P_{st}$, ($P_0$-pressure in ejector nozzle prechamber), and unstart characteristic at $P_0=P_{unst}$: $P_{st} > P_{unst}$. For a mode $P_0=P_{unst}$ the common level of pressure decreases along the PRS channel, but also the EJ operation area on a loading is restricted.

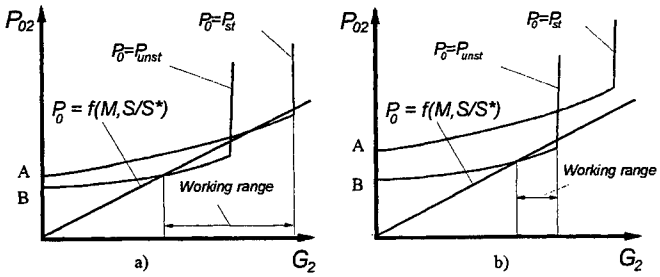


Fig. 6

The SD performance - pressure after SD on mass-flow rate - is given here. It is linear and slope angle depends on Mach number on SD inlet and on channel constriction ratio. PRS is started, when the EJ and SD performances are intercrossed - here different versions are possible. More economic regime is the EJ operation on prestalling performance (Fig. 6b). But in this case the gas-generator operation cyclogram should be double-regime: at first, shortly with $P_0=P_{st}$ - EJ is started, then on prestalling mode with $P_0=P_{unst}$, when laser with corresponding mass-flow rate is started. The positions of points A and B on the diagrams are determined by EJ parameters and first of all by Mach number. The higher Mach numbers allow reaching the higher degree of vacuum and the higher ejection coefficients.

The calculation of EJ parameters and its geometry begins from standard one-dimensional non-viscous technique, based on integral relations of conservation equation [13]. The mixing chamber length is the key empirical parameter again. For a peripheral scheme (injection of active gas along the walls) chamber length makes 4-5 caliber's, and for a central injection - 10-12 caliber's [13]. Geometry of mixing chamber can be either cylindrical, or conical - restricting. The constriction ratio is selected from different requirements: or keeping of pressure along the chamber, or achievement of flow crisis in a throat of the chamber. It is possible to choose constriction ratio on the basis of an optimum ratio of velocities: flow velocity after SD and outlet velocity from mixing chamber- $\lambda_3$. (At this rate the mixing chamber will be shorter, and the throat will be longer, than in case of ejector calculation for condition of crisis achievement in a throat.) The example of such optimization are given on Fig. 7

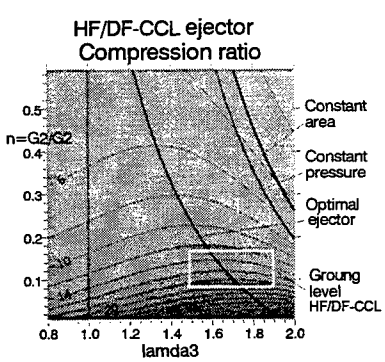


Fig. 7

EJ parameters and geometry chosen on the basis of non-viscous model, as well as in a case of SD, are considered as the first approach. Further for the previously chosen geometry the three-dimensional flow pattern is calculated on the basis of the complete Navier-Stokes equations. On the basis of these calculations the necessary changes in EJ geometry are done and EJ performances are determined.

The flow pattern in PRS channel on operating regime is shown in Fig. 8. The color shows fields of the Mach number. The ejector nozzle was designed on M=4,5. Gas-vapor mixture with $T_0$=1300K was used as a working medium. In figure the theoretical distribution of wall pressure along the whole PRS channel in comparison with experimental data is given. It is visible, that theoretical model (about it see [12]) reflects processes occurring in SD and EJ adequately. The model allows estimating the PRS performances enough precisely.

In the article the basic moments of PRS operation considered from the viewpoint of gas-dynamics. The main parameters of SD and EJ, influencing on a general efficiency of whole system are specified. However it is possible to influence on ejection coefficient of system with the help of perfection of channel gas-dynamics but by the choice of fuel and oxidizer in a gas-generator.

However thermodynamics questions lie behind frameworks of this article - briefly they are considered in [1]. Here we shall touch a question about a choice of EJ operating temperature only. As it is better to use a system without active cooling as more reliable system, the level $T_0$ in EJ is determined by constructional opportunities of used materials.

For usual stainless steels $T_0$ < 1000K. It is expediently to use the vapor-gas as active gas, when in combustion products the water is injected. By this mean decreasing of $T_0$ to a reasonable level and decreasing of a molecular weight of active gas is achieved. However there is a problem of condensation at vapor-gas expansion in an ejector nozzle. At

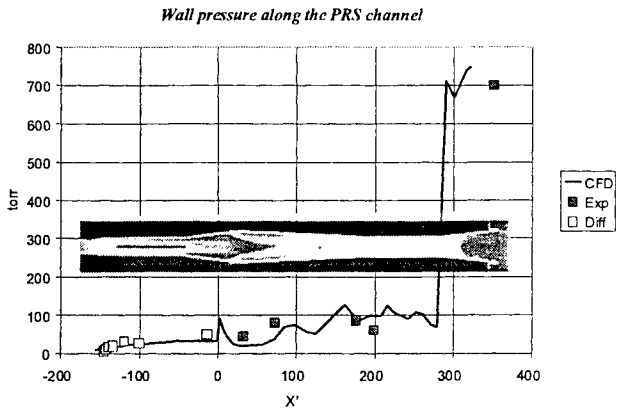

Fig. 8

$T_0$<1000K possible Mach numbers lie in region M≈3 (taking into account a pressures level in gas generators). Such Mach numbers do not allow the getting of high ejection coefficients.

The application of modern materials used in aero-jet industry allows one to choose operating temperatures $T_0$=1300K that considerably removes condensation limits. And then Mach numbers can be chosen in region M≈4,5. Use of EJ with such parameters allows one to realize the PRS for HF/DF CCL on the basis of one-stage scheme.

For COIL such compression ratio are not enough already. In this case it is necessary to consider the many-stage schemes of ejectors. Such systems are used for the wind tunnels designed for large Mach numbers. But these systems are not simple in operation, there are known some complexities of their start and achievement of their calculated performances. Besides PRS on the basis of many-stage EJ are resulting in a very long installation. Differential and slot-hole ejectors are alternative to many-stage systems [14, 15]. The principle of delaying of conditions for occurrence of critical regimes lies in a basis of these schemes. Such EJ are close to one-step systems from viewpoint of dimensions. However, the high compression ratio is realized at low ejection coefficients.

## ACKNOWLEDGMENTS

The authors are grateful to "Laser Systems" Ltd., St-Petersburg, Russia for financial support.

## REFERENCES

1. A.S. Boreisho, V.M. Khailov, V.M. Malkov, A.V. Savin, "Pressure recovery system for high power gas flow chemical laser" Proceedings of XIII International Symposium GCL/HPL-2000, September 18th-22nd, 2000, Florence, Italy.
2. J.C. Dutton, C.D. Mikkelsen, A.L. Addy, "A Theoretical and Experimental Investigation of the Constant Area, Supersonic-Supersonic Ejector", AIAA J, Vol.20, №10, 1981.
3. E.P. Neumann, F. Lustwerk, "Supersonic Diffusers for Wind Tunnels", J. of Applied Mechanics, 1949, V.16, .№2.
4. S.H. Hasinger, D.K. Miller, "Two-Dimensional Supersonic Diffuser Experiments'". AIAA J., V.13, №4, 1975.
5. M.G. Ktalkherman, V.M. Malkov, N.A. Ruban, "Slowdown of supersonic flow in rectangular channel of constant cross-section", J. Appl. Mech. Tech. Phys., №6, 854, November-December 1984 (in Russian).
6. L. Crocco, "One-dimensional Treatment of Steady Gas Dynamic" Fundamentals of Gas-dynamics. Vol. III, Princeton University Press, Princeton, N.J., 1958.
7. M.G. Ktalkherman, V.M. Malkov, N.A. Ruban, "Experimental investigation of GDL diffusers", AIAA-paper №90-1512. -N.Y.: AIAA, 1990.
8. M.G. Ktalkherman, V.M. Malkov, N.A. Ruban, "Influence of main parameters on efficiency of rectangular cross-section supersonic diffusers", Gas-dynamic of GDL flow channel: Proceedings of Siberian Division of USSR Academy of Sciences, ITAM. -Novosibirsk, 1987. -Pp.116-162 (in Russian).
9. R.J. Driscoll, L.F. Moon, "Pressure recovery in Chemical lasers", AIAA J. -V.15. -№5. -P.665. -1977.
10. V.A. Kuzmin, "Slowdown of supersonic flow in rectangular channel", Gas Dynamics of Aircraft Engine, Kazan', KAI, 1978 (in Russian)
11. N.A. Shushin, "Experimental investigation of Start of plane supersonic Aerodynamic tube with cavity in working channel", Trudy TsAGI, 2208, Moscow, 1984 (in Russian).
12. A.V. Savin, A.A. Ignatiev, A.V. Fedotov, "Numerical simulation of gas dynamic flows in pressure recovery systems of supersonic chemical lasers", Proceedings of XIII GCL/HPL-2000, September 18th-22nd, 2000, Florence, Italy.
13. G.N. Abramovich, "Applied Gas Dynamics", Science, Moscow, 1976 (in Russian).
14. J.K. Arkadov, "Compact high compression gas ejector with nozzles along the spiral", Proceedings of TsAGI, Vol. 15, -№6. -1984 (in Russian).
15. J.K. Arkadov, "Gas ejector with nozzle perforated by longitudinal slots", Fluid Mechanics J., -№2. -1968 (in Russian).

Correspondence Email: boreisho@iltt.ru, office@iltt.ru; WWW: http://iltt.ru; Phone: 812-251 21 62, Fax: 812-251 22 57

# Influence of shock waves on excitation discharge for TEA gas lasers

Go Imada*, Hiroshi Yamanoi[a], Masataroh Suzuki[a], Wataru Masuda[a], and Kiyoshi Yatsui

Extreme Energy-Density Research Institute, Nagaoka University of Technology,
1603-1 Kamitomioka, Nagaoka, Niigata 940-2188, Japan

[a] Department of Mechanical Engineering, Nagaoka University of Technology,
1603-1 Kamitomioka, Nagaoka, Niigata 940-2188, Japan

## ABSTRACT

The influence of shock waves on the excitation discharge for TEA gas laser have been investigated eliminating the other factors which may affect the discharge instabilities, such as gas density depletion, discharge products, residual ions and electrode heating. A shock wave of 1.2 in Mach number is produced by a shock tube with gas mixture of helium and argon in order to simulate the ArF excimer laser. The schlieren photographs of shock wave and direct images of light emitted from the discharge are recorded simultaneously by a high-speed image-converter camera. It is found that, if the shock wave does not reach to the discharge region, glow discharge occurs only in front of the shock wave. Even if the shock wave passes through the middle of discharge region, the glow discharge occurs only in front of the shock wave. However, an arc-like filament through the shock front is also produced. If the shock wave passes through the discharge region, the weak glow discharge can be produced again, however, a surface discharge is also produced between the main electrode and the pre-ionization electrode. It becomes clear that the discharge instabilities depend on the location of shock wave in the discharge region.

**Keywords:** Glow discharge, Arc, Excimer laser, Shock wave

## 1. INTRODUCTION

The high-pressure, pulsed glow discharge has been studied for further understanding of the excitation discharge on TEA gas lasers. The excitation discharge causes various instabilities in subsequent discharge which collapse at the highly-repetitive operation. It has been suggested that the instabilities are induced by a gas density depletion,[1,2] shock wave,[3,4] residual ion,[5] electrode heating,[6] and discharge product generated in the discharge region. However, the influences of the respective factors on collapse of the highly-repetitive operation have not been clarified.

The present paper inquires into the influence of the shock wave on the discharge instability eliminating the other factors. A shock wave of 1.2 in Mach number ($M$) is produced by a shock tube with gas mixture of helium and argon in order to simulate the ArF excimer laser.

## 2. EXPERIMENTAL SETUP

Figure 1 shows the schematic diagram of experimental setup. The setup consists of shock tube, electrical excitation circuits, discharge electrodes, schlieren system, and CCD camera. The $y$ axis indicates the discharge direction, and the origin of the $x$-$y$ plane corresponds to the center of the discharge region. The main electrodes consist of half-cylindrical-type anode and cathode where the width, length, gap distance and radius of curvature are 40 mm, 120 mm, 22.7 mm and 100 mm, respectively. The automatic ultra-violet pre-ionization electrodes consist of 6-pin spark gaps. To reduce the growth of perturbation in the shock wave, these gaps are set downstream of the main electrode. The excitation circuit is a charge-transfer type circuit ($C_1 / C_p$ = 5.3 / 4.2 nF) where the storage capacitor is charged up to 30 kV. The discharge voltage and current are measured by a resistive voltage divider and a current transformer, respectively. A gas mixture of helium and argon is used to simulate ArF excimer laser. The gas composition is Ar / He = 1 / 9 with a pressure of 178 kPa which corresponds to an initial gas density ($\rho_g$) of 0.57 kg/m$^3$. The ratio of specific heats ($\gamma$) and the sound velocity of the mixed gas are calculated to be 1.66 and 726 m/s (at 290 K), respectively. The gas density difference through the shock front is given as follows:

$$\rho_2/\rho_1 = (\gamma+1)M^2/[(\gamma-1)M^2+2], \tag{1}$$

XIII International Symposium on Gas Flow and Chemical Lasers and High-Power Laser Conference,
Antonio Lapucci, Marco Ciofini, Editors, Proceedings of SPIE Vol. 4184 (2001)

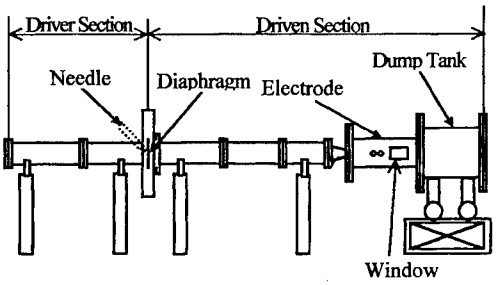


(a) Schematic of shock tube.

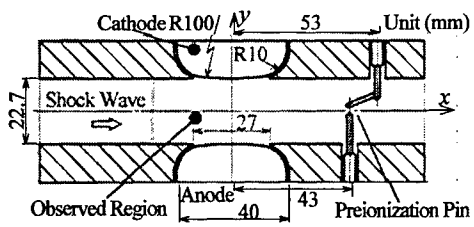


(b) Cross-sectional view of electrode (*x*-*y* plane).

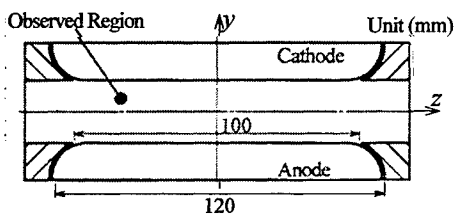


(c) Cross-sectional view of electrode (*y*-*z* plane).

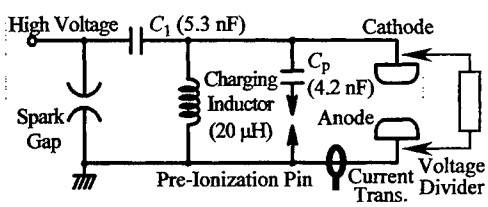


(d) Electrical excitation circuits.

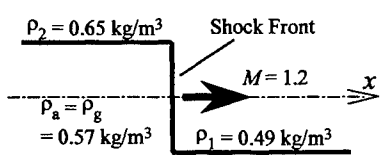


(e) Schematic diagram of shock wave.

Fig. 1 Schematic of experimental setup.

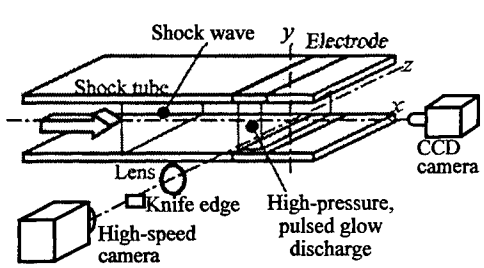


Fig. 2 Schematic diagram of observation system of schlieren photograph and discharge light.

where $\rho_1$ and $\rho_2$ are the gas density in front of and behind the shock front, respectively. In this experiment, $\rho_1$ and $\rho_2$ are determined to be 0.49 and 0.65 kg/m$^3$, respectively, where the gas density satisfies the following condition: $(\rho_1+\rho_2)/2 = \rho_a$.

Figure 2 shows the schematic diagram of the observation system of the schlieren photograph and the discharge light. An argon-ion laser ($\lambda$ = 514.5 nm) is used as a light source for the schlieren photograph. The schlieren photographs of shock wave and the direct images of light emitted from the discharge in *x*-*y* plane are recorded simultaneously by a high-speed image-converter camera. The schlieren photographs have been taken at an exposure time of 750 ns which is shorter than the characteristic time of the shock wave. The spatial resolution of this system has been experimentally found to be ~ 0.1 mm on the object plane. The time-integrated, direct images of light emitted from the discharge in *y*-*z* plane are taken by CCD camera, where the exposure time is estimated to be ~ 2 s.

## 3. RESULTS AND DISCUSSION

Figure 3 shows the typical time-integrated photograph of light emitted from glow discharge in a stationary gas with a gas density of 0.57 kg/m$^3$. The six spots of intense light indicated in *y*-*z* plane correspond to the preionization discharge. We found that the homogeneous glow discharge are obtained, however, the center of discharge locates at $x$ ~ 4.5 mm because the preionization gaps are set downstream of the main electrode.

Figure 4 shows the time-resolved schlieren photographs of the

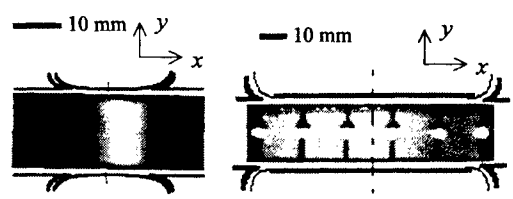


Fig. 3 Time-integrated photograph of light emitted from glow.

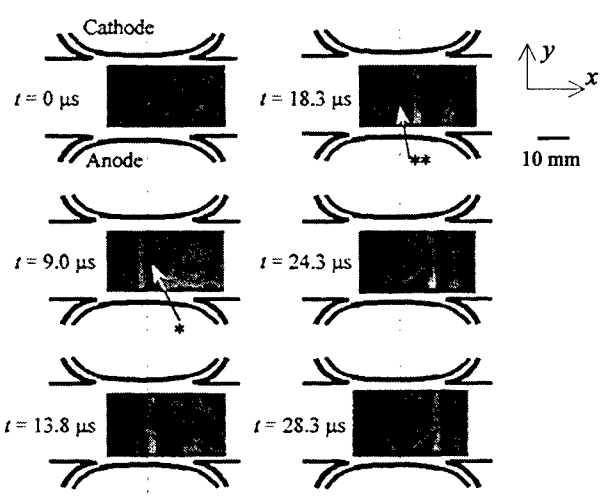


Fig. 4 Time-resolved schlieren photographs of shock wave. *: Shock wave propagating along *x* axis, **: shock wave reflected by main electrode.

shock wave in the *x-y* plane. It is found that the velocity of shock wave is estimated to be ~ 850 m/s which corresponds to the Mach number of 1.2.

Figure 5 shows the schlieren photographs of the shock wave in the *x-y* plane and the photographs of the direct image of light from the discharge in *y-z* plane. The shock waves propagate along the *x* axis. It is found that, if the shock wave does not reach to but close to the middle of the discharge region, glow discharge occurs only in front of the shock wave (mode 1). Even if the shock wave passes through the middle of the discharge region, the glow discharge occurs only in front of the shock wave, and an arc-like filament also exists through the shock front (mode 2). A lot of streamer exists through the shock front when the shock wave just reaches the edge of electrode (mode 3). If the shock wave passes through the discharge region, the weak glow discharge can be produced again behind the shock front, however, a surface discharge is also produced between the main electrode (cathode) and the pre-ionization pin electrode (mode 4).

Figure 6 shows the discharge mode as a function of position of the shock wave. It is clearly found that the discharge mode is classified into four modes according to the position of the shock wave.

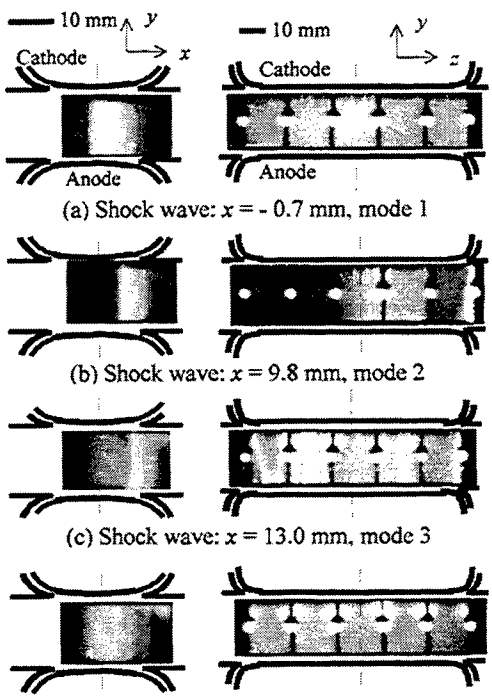


(a) Shock wave: $x$ = - 0.7 mm, mode 1

(b) Shock wave: $x$ = 9.8 mm, mode 2

(c) Shock wave: $x$ = 13.0 mm, mode 3

(d) Shock wave: $x$ = 15.6 mm, mode 4

Fig. 5 Schlieren photographs of shock wave (*x-y plane*) and direct images of light emitted from discharge (*y-z plane*).

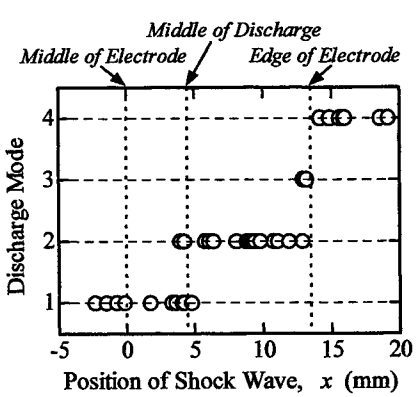


Fig. 6 Discharge mode as a function of position of shock wave.

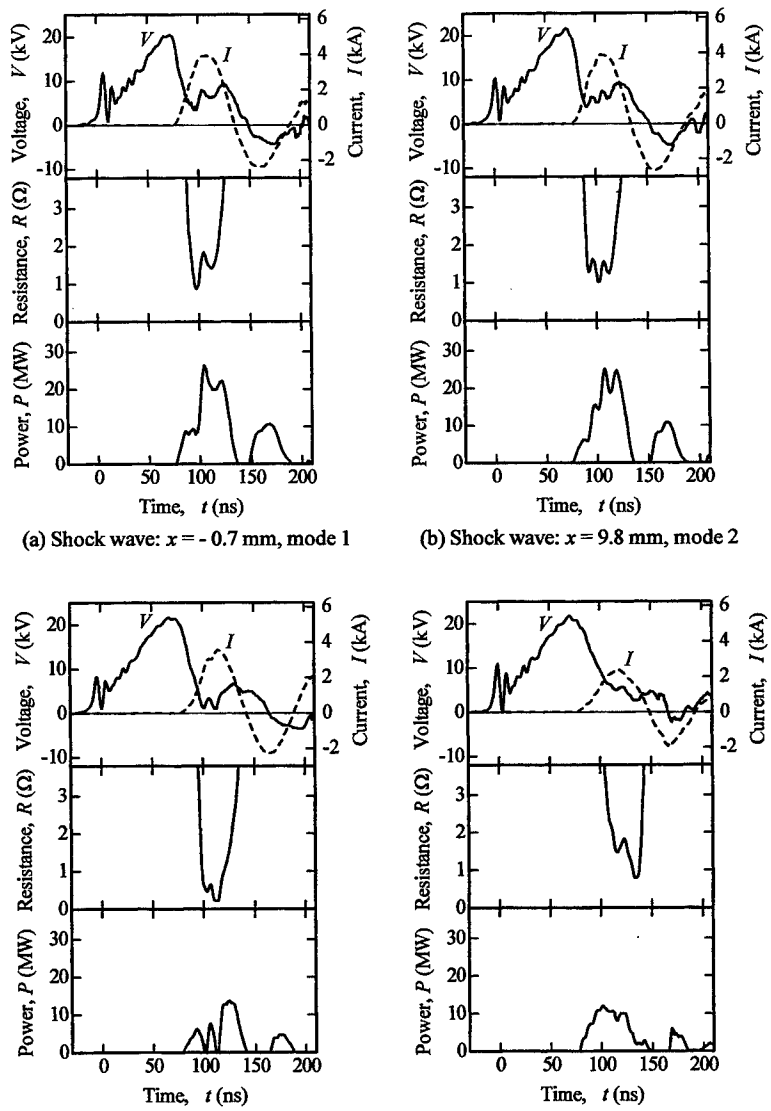


(a) Shock wave: $x$ = - 0.7 mm, mode 1

(b) Shock wave: $x$ = 9.8 mm, mode 2

(c) Shock wave: $x$ = 13.0 mm, mode 3

(d) Shock wave: $x$ = 15.6 mm, mode 4

Fig. 7 Time evolution of discharge voltage, current, resistance, and power.

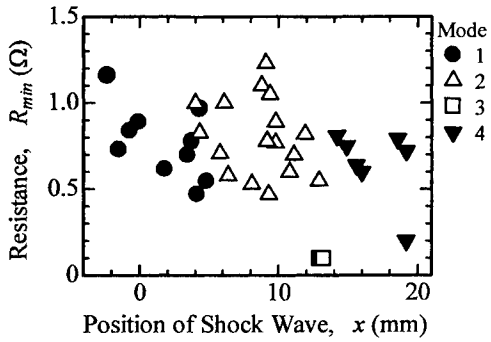


Fig. 8 Discharge resistance as a function of position of shock wave.

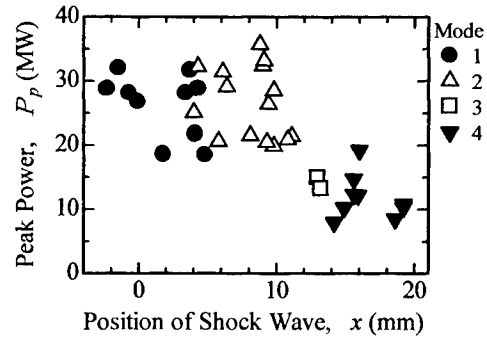


Fig. 9 Discharge power as a function of position of shock wave.

Figure 7 shows the typical waveforms of the discharge voltage ($V$), current ($I$), resistance ($R = V/I$), and power ($P = VI$). The discharge resistance ($R_{min}$) as a function of the position of shock wave is shown in Fig. 8 . Here, $R_{min}$ is defined as the minimum resistance in the discharge. In mode 3, $R_{min}$ decreases to ~ 0.1 Ω when the shock wave exists on the edge of electrode where the radius of curvature of the electrode changes into 10 mm. The peak discharge power ($P_p$) as a function of the position of shock wave is shown in Fig. 9. In mode 1 and 2, the discharges maintain $P_p$ of 20 ~ 35 MW. On the other hand, $P_p$ is reduced to 8 ~ 15 MW in mode 3 and 4.

## 4. CONCLUSION

The influence of shock wave on the excitation discharge has been investigated eliminating the other factors which may affect the discharge instabilities. The following conclusions can be drawn from the present investigation.

(1) The discharge is classified into four modes according to the position of the shock wave.

(2) The glow discharge occurs either in front of or behind the shock front. However, the glow discharge behind the shock front decreases in the discharge power.

(3) The shock wave ($M$ ~ 1.2) tends to induce the instabilities in the high-pressure, pulsed glow discharge without a halogen gas.

## ACKNOWLEDGMENTS

This work was partly supported by Grant-in-Aid for Encouragement of Young Scientists from the Ministry of Education, Science, Sports and Culture in Japan. The authors would like to thank Mr. Y. Sekimoto for mechanical design and experimentation.

## REFERENCES

1. S. Kosugi, K Maeno, and H. Honma, "Measurement of Gas Temperature Profile in Discharge Region of Excimer Laser with Laser Schlieren Method", *Jpn. J. Appl. Phys.* **32**, pp. 4980-4986, 1993.
2. G. Imada, Y. Sato, H. Yoshida, W. Masuda, and K. Yatsui, "Observation of excitation discharge on excimer laser in non-uniform gas density distribution", *Proc. Int'l Symp. on Ultrahigh- and High-Speed Photography and Image-based Motion Measurement, San Diego*, **SPIE-3173**, pp. 124-131, 1997.
3. K. Yatsui, G. Imada, K. Masugata, and W. Masuda, "Generation and Propagation of Shocks in Discharge-Pumped Excimer Laser", *Proc. 10th Int'l Symp. on Gas Flow and Chem. Lasers, Madrid*, **SPIE-2502**, pp. 134-139, 1994.
4. M. Sentis, P. Delaporte, B. Forestier, and B. Fontaine, "Design and Characteristics of High Pulse Repetition Rate and High Average Power Excimer Laser Systems", *IEEE J. Quantum Electron.* **27**, pp. 2332-2339, 1991.
5. M. Osborne and J. Green, "Negative Ion Assisted Preionization for Excimer Lasers", *J. Appl. Phys.* **71**, pp. 3127-3133, 1992.
6. R. Arutyunyan, V. Borisov, A. Vinokhodov, Yu. Kiryukhin, and A. Morozov, "Electrode Effects in a Pulse-Periodic Excimer Laser", *Sov. J. Quantum Electron.* **16**, pp. 1589-1591, 1986.

*Correspondence: E-mail: imada@nagaokaut.ac.jp; Telephone: 81-258-47-9893; Fax: 81-258-47-9890

# $CO_2$ Slab Laser with a Variable Reflectivity Grating (VRG) as Lineselective Element

Ralf Hocke[a]

[a]Lehrstuhl fuer Hochfrequenztechnik, Universitaet Erlangen-Nuernberg
Cauerstr. 9, 91058 Erlangen, Germany.

## ABSTRACT

A lineselective $CO_2$-laser with a 'Variable Reflectivity Grating' (VRG) instead of a 'Variable Reflectivity Mirror' (VRM) was realised. The binary grating has a constant grating-period and -depth and a modulated width of the grating-bars. Stable and unstable resonator designs were investigated.

**Keywords:** Carbon dioxide laser, diffusion-cooled, stable resonators, unstable resonators, binary gratings

## 1. INTRODUCTION

We have investigated the use of modified binary Littrow gratings in an rf-excited $CO_2$ slab laser setup for lineselective operation (Fig. 1). The slab laser setup leads, due to area power scaling, to a compact design of the whole $CO_2$ laser.[1] The main disadvantage of this system is the huge Fresnel number in the plane parallel to the electrodes ($x$-direction). Different resonator concepts have been investigated in the last years to solve this problem. One solution for a non-lineselective setup is a resonator with a 'Variable Reflectivity Mirror' (VRM).[2] Our approach has been to replace the VRM by a 'Variable Reflectivity Grating' (VRG) with the advantage of enabling lineselective operation.[3,4]

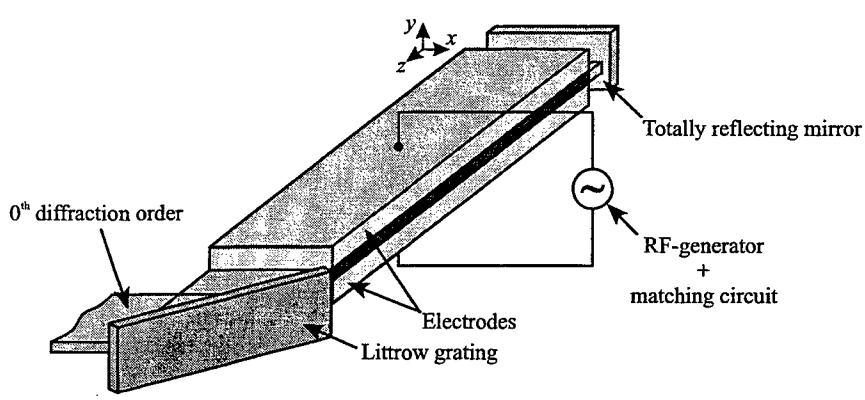


**Figure 1.** RF-excited lineselective slab laser.

## 2. BINARY GRATINGS

For reflection gratings with a period $p$ of about 7 $\mu$m, a wavelength $\lambda$ of about 10 $\mu$m, and an incident angle $\alpha$ of about $45^o$ only two diffraction orders appear. If the incident angle holds for the equation:

$$\sin(\alpha) = \sin(\alpha_L) = \frac{\lambda}{2p}, \tag{1}$$

the direction of the reflected wave of the -1$^{st}$ diffraction order is opposite to the direction of the incident wave (Fig. 2a). This diffraction order is coupled back into the resonator, whereas the 0$^{th}$ diffraction order is coupled out. The

Further author information: Send correspondence to Ralf Hocke, Taunusstr. 55, 91056 Erlangen, Germany
E-mail: hmr@gmx.de; http://www.lhft.e-technik.uni-erlangen.de

XIII International Symposium on Gas Flow and Chemical Lasers and High-Power Laser Conference,
Antonio Lapucci, Marco Ciofini, Editors, Proceedings of SPIE Vol. 4184 (2001)

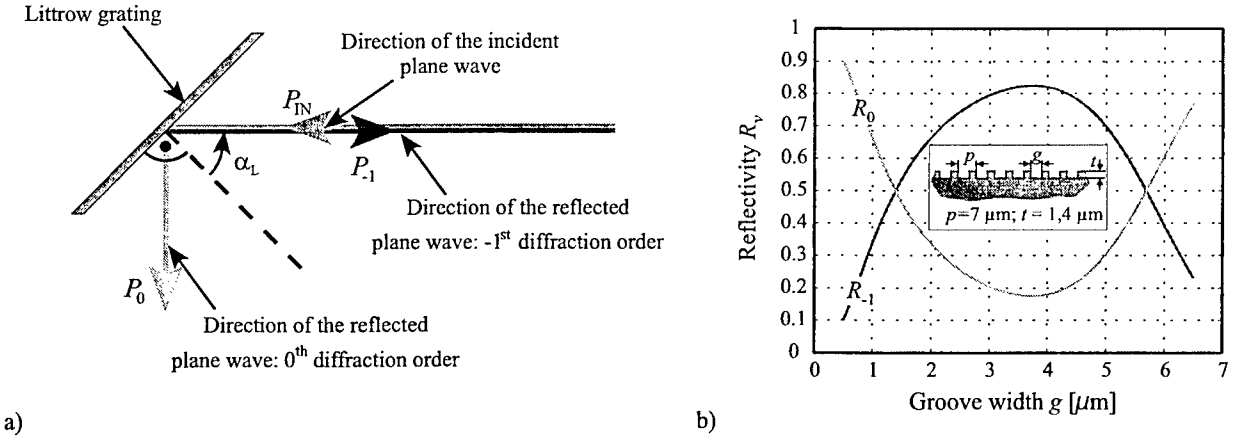


**Figure 2.** a) Littrow configuration of a diffraction grating.
b) Reflectivities of a binary Littrow grating of constant grating depth and period.

portions of power ($P_0$ and $P_{-1}$), which are coupled into the two diffraction orders, are called reflectivities $R_0$ and $R_{-1}$:

$$R_0 = \frac{P_0}{P_{IN}} \qquad R_{-1} = \frac{P_{-1}}{P_{IN}} \tag{2}$$

and depend on the individual parameters of the grating structure.[5] For a binary grating with a period $p = 7\mu m$ and depth $t = 1,4\mu m$, the dependence of the reflectivities on the groove width $g$ are shown in Fig. 2b for a lossless grating ($R_0 + R_{-1} = 1$).

As shown in Fig. 3, it is therefore possible to realize areas with different reflectivities by changing the groove width $g$, without changing the period or the grating depth. In Fig. 3b, two different areas (mid- and rim-region) of one realized grating are shown. We fabricated the gratings by a photolithographic/microgalvanic process on copper substrates.

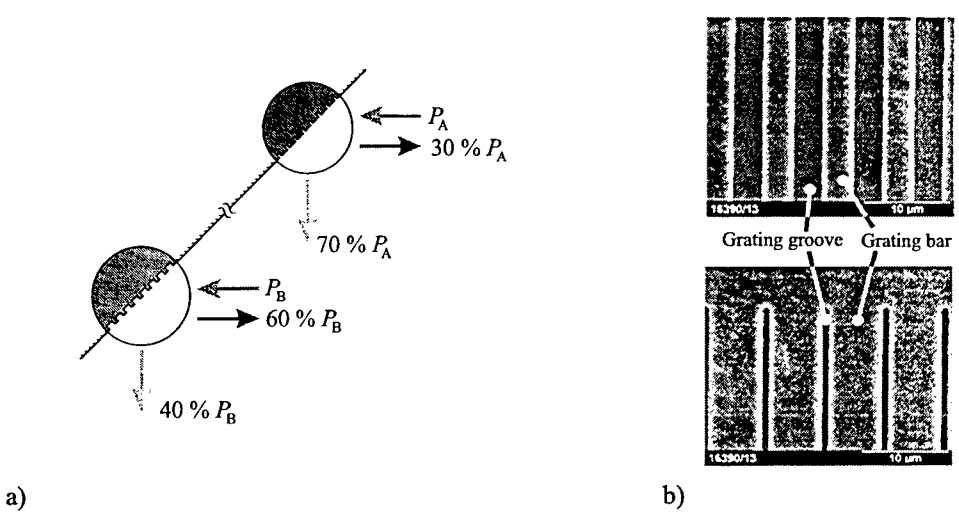


**Figure 3.** a) Binary Littrow grating with areas of different groove width.
b) Top view of the grating in the middle (top) and the edge (bottom) of the structure.

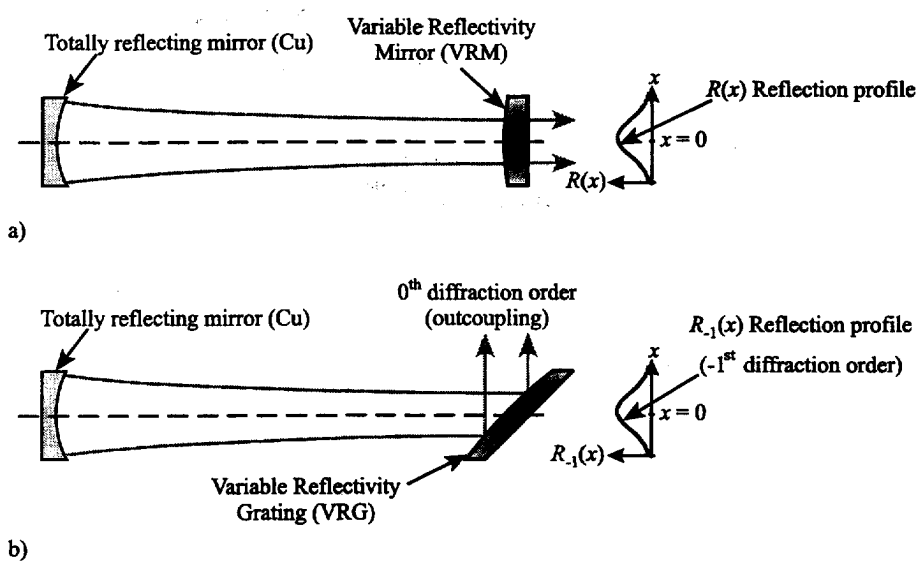


**Figure 4.** a) VRM resonator. b) VRG resonator.

## 3. RESONATOR WITH VARIABLE REFLECTIVITY GRATINGS

By changing continuously the groove width of the grating along the $x$-axis of the resonator, it is possible to realize a gaussian or supergaussian reflection profile of the grating for the -1$^{st}$ diffraction order. We can then substitute the VRM in a nonlineselective VRM resonator by such a grating, as is shown in Fig. 4. The reflection profile of the VRM is now represented by the reflection into the -1$^{st}$ diffraction order, whereas the 0$^{th}$ is used to couple out the laser beam. We have investigated this principle for a stable and an unstable resonator setup with gratings on plane and convex surfaces.

## 4. RESULTS

The overall efficiency of the gratings we realized always was better than 97 %. Fig. 5a is an example of a measured reflection profile of a VRG. It can be seen that the profile has a good symmetry, but also, that in the rim-region of the grating a difference in reflectivity of about 15 % appears. There are two reasons for this deviation. The first reason is that the angle of the grating-sidewalls is not 90$^o$, which means, that the realized structure not precisely has a binary shape, which may result in the measured difference between the measured and the expected profile. The

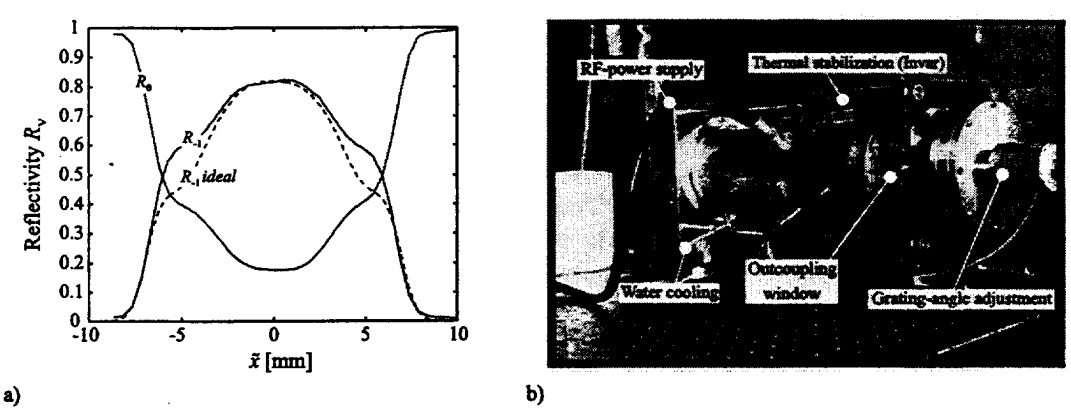


**Figure 5.** a) Measured reflection profile of the grating for the stable resonator.
b) Lineselective laser (9P36 line)

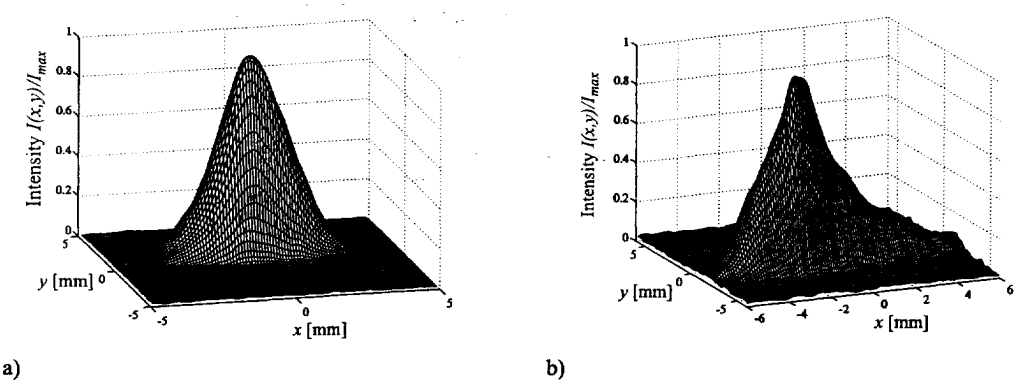


**Figure 6.** Measured beam profile of the stable (a) and unstable (b) resonator.

second reason is that the reflectivity has its maximum slope for small groove widths (Fig. 2), which occur in the rim-region of the grating. Due to technological tolerances it is therefore more critical to realize a certain reflectivity in the rim-region of the grating than in the mid of the grating.

To test the stable and unstable resonator setup, we used an rf-excited (40 MHz) $CO_2$ slab laser with slow gasflow (Fig. 5b).

The typical beam profile of the stable resonator is shown in Fig. 6a, which is in good agreement with the theoretically expected profile. For the grating substrates we used plane copper-mirrors. The unstable resonator we realized was a positive branch resonator with a concave totally reflecting mirror and a convex VRG as outcoupling element. As it was expected, this resonator was very alignment-sensitive. The typical beam profile for the unstable resonator is shown in Fig. 6b. It significantly deviates from the theoretically expected profile. The main reason for this discrepancy seems to be the fact, that we carried out our simulations for a passive resonator without any active medium.

## 5. CONCLUSION

The utilization of a VRG in a slab laser resonator has prooved to be a good possibility to realize a compact, lineselective slab laser. An unstable resonator is the best choice to extract a high brightness beam out of the wide active medium of a slab laser. For an alignment insensitive setup, a negative branch resonator has to be used. For this purpose, curved gratings on concave surfaces are necessary. The simulation results can be improved by including the parameters of the active medium in our simulation tool.

## ACKNOWLEDGMENTS

This work was supported by the DFG (Deutsche Forschungsgemeinschaft). I wish to thank Prof. H. Brand, Prof. J. Schwider, Prof. L.-P. Schmidt and all persons, who have been involved in this work, for the useful discussions and support.

## REFERENCES

1. K. Abramski, A. Colley, H. Baker, and D. Hall, "Power scaling of large-area transverse radio frequency discharge $CO_2$ lasers," *Applied Physics Letters* **54**, pp. 1833–1835, May 1989.
2. M. Morin and M. Poirier, "Graded reflectivity mirror unstable laser resonator design," *SPIE* **3267**, pp. 52–65, January 1998.
3. R. Hocke, *Linienabstimmbarer $CO_2$-Flachkanal-Laser mit räumlich inhomogen reflektierenden Littrow-Gittern.* PhD thesis, Lehrstuhl für Hochfrequenztechnik, Universität Erlangen-Nürnberg, 1999.
4. R. Hocke and M. Collischon, "Lineselective resonators with variable reflectivity gratings (VRG) for slab-laser geometry," in *Proceedings of the SPIE*, vol. 3930, (San Jose, California, USA), January 2000.
5. J. Andrewartha, J. Fox, and I. Wilson, "Resonance anomalies in the lamellar grating," *Optica Acta* **26**(1), pp. 69–89, 1979.

# Simple way for in-phase mode selection in laser with annular gain region

A. P. Napartovich*, N. N. Elkin, D. V. Vysotsky

Troitsk Institute for Innovation and Fusion Research, Troitsk,
142092 Moscow region, Russia

## ABSTRACT

Properties of laser cavity composed of two plane segmented mirrors placed at half-Talbot distance are considered theoretically in application to gas laser with annular active medium. Discrimination of in-phase mode against other supermodes is demonstrated. For saturable gain model, a critical small gain is found for which the in-phase mode become unstable.

**Keywords:** annular waveguide, Talbot effect, phase locking, in-phase mode, mode discrimination

## 1. INTRODUCTION

An attractive feature of a gas laser with annular shape of gain region is its compactness at high power level. A particular simple situation takes place when radial propagation of the wave field is limited by waveguide walls like construction of diffusion cooled $CO_2$ laser with radio-frequency (RF) discharge excitation.[1] Problems inherent to this construction are non-uniform plasma excitation and a large amount of transverse modes lasing simultaneously. In the case of RF discharge the voltage drop on the plasma uniformity can be improved by sectioning electrodes[2]. But the problem still remains how to arrange single-mode laser operation. Azimuth propagation properties of radiation field in cavity considered are very similar to lateral propagation of radiation in a cavity formed by infinite stripe mirrors. Diffraction losses in azimuthal direction are completely eliminated resulting in a plenty of modes with equal losses.

In ref.[3] it was proposed to introduce mode discrimination by placing a spatial filter in front of one of mirrors absorbing radiation incident on it. This filter was periodical in azimuthal direction. The length of the resonator $L$ and spatial period of the filter $\Delta$ satisfied to Talbot condition $L = \Delta^2/\lambda = L_T/2$, where $L_T$ is the so-called Talbot distance where self-reproduction of a periodical field takes place. For $L_T/4$ cavity the only collective mode selected was the out-of-phase mode. Placing an external phase-modulated mirror this out-of-phase mode was converted to the in-phase one (all beams with the same phase). Numerical simulations made in [4] have shown the existence of the fractional Talbot effect in a system of circularly positioned beams without annular waveguide. In ref.[5] the fractional Talbot effect (i.e. self-reproduction with image multiplication of the periodical field distribution at fractions of Talbot distance) was studied numerically in the guided Talbot resonator. It should be mentioned that the field distribution of the in-phase mode was expressed as a combination of several azimuthal modes, while in the radial direction only the fundamental mode of the waveguide was taken into account.

The inherent drawback of resonator geometry considered above results from the exact reproduction of two different modes: in-phase and out-of-phase ones [6]. For $L_T/4$ cavity the out-of-phase mode can be selected effectively, but additional phase rectification is necessary to improve output beam quality. We propose and analyze numerically a new version of Talbot cavity when both plane reflectors are segmented with reflecting parts positioned periodically along the ring and supplementing each other (see Fig. 1). Distance between reflectors is also $L_T/2$. Reflectors are identical except a turn around common axis onto half a reflectance modulation period. The out-of-phase mode is discriminated completely having high losses in this construction. The in-phase mode has diffraction losses close to zero because of property of the periodical field to form an image identical to the origin but turned onto a half a period [6]. An additional benefit of this cavity is anticipated: high laser energy extraction efficiency due to rather good amplifying space filling by the in-phase mode intensity in the middle of cavity. Numerical simulations of cavity modes including saturable gain medium were performed aimed to evaluate single-mode oscillation stability limit. It is expected that because of spatial hole burning effect the in-phase mode lose stability at some above threshold small-signal gain. The magnitude of this critical small-signal gain is an important characteristic of the cavity.

* Correspondence: E-mail: apn@triniti.ru

XIII International Symposium on Gas Flow and Chemical Lasers and High-Power Laser Conference,
Antonio Lapucci, Marco Ciofini, Editors, Proceedings of SPIE Vol. 4184 (2001)

## 2. PROBLEM STATEMENT AND NUMERICAL MODEL

Construction showed in Fig. 1 consists of annular waveguide (AWG) with internal and external radii $R_i$ and $R_e$ respectively and length $L_m$. The AWG is filled with $CO_2$ laser medium having gain $g=g_0/(1+I)$, $g_0$ is the small signal gain coefficient, and local intensity $I$ is scaled by saturation intensity. Two segmented mirrors (M1 and M2) are placed at equal distance $d$ from the ends of the AWG. Each of $N$ segments of M1 is totally reflected while segments of M2 have reflectance $r$ = 64%. The length of the AWG is to be found from condition: $L_m + 2d = L_T/2 = \Delta^2/\lambda$, where λ is a radiation wavelength, $\Delta = \pi(R_e + R_i)/N$ is the reflectance period. Width of segments in azimuthal direction is equal to Δ/2. Neglecting diffraction in radial direction, construction considered is equivalent to two infinite arrays of plane mirrors shifted to each other for a half of the period. Because after propagating over the half of Talbot distance the in-phase mode is reproduced exactly but with a half-period shift, this mode would not have any diffraction losses in the considered cavity for an arbitrary field profile on the mirror segment. The analysis has shown that the losses associated with incomplete field reproduction caused by annular waveguide curvature are much less than $(1 - R_i/R_e)^2$. Propagation over free space gaps introduces diffraction losses into the system and makes different losses for different modes.

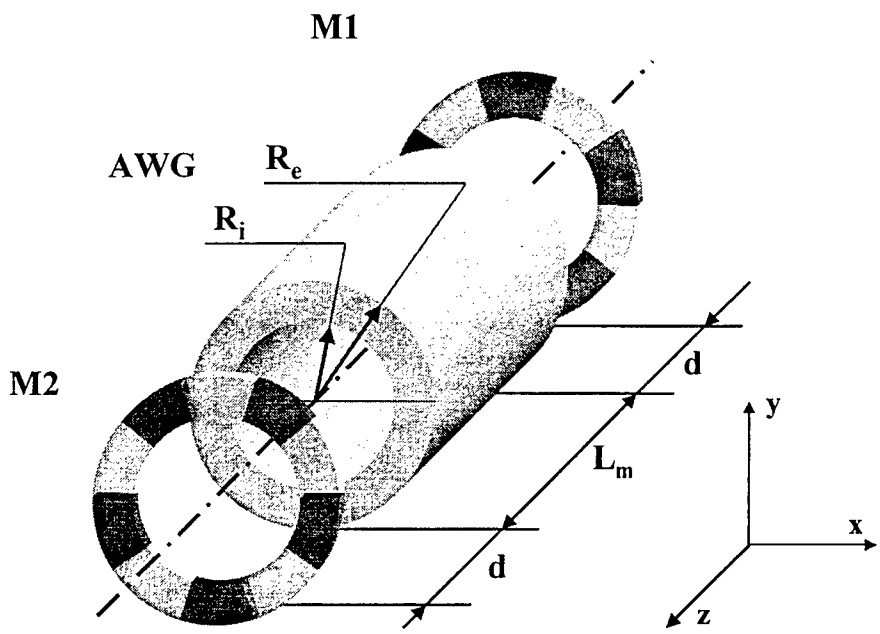


Figure 1. Schematic of the resonator consisting of annular waveguide (AWG) and two segmented mirrors: M1 with totally reflecting segments and M2 with semi-transparent segments

The numerical methodology applicable for adequate description of the laser radiation propagation was described in ref. [7]. The 3-D diffraction code is based on splitting into diffraction and gain operators after each propagation step. We employed the 2-D Fast Fourier Transformation technique (FFT) in calculations of diffraction effects using Cartesian mesh. Cavity modes were found by traditional iteration procedure. Using the fact that symmetry of some optical modes is quite different, it appeared possible to find numerically besides fundamental (in-phase) mode also some higher order modes. The calculations were made for the following values of parameters: $R_i$ = 1.25 cm, $R_e$ = 1.5 cm, $N$ = 17, λ = 10.6 μm; cavity length is $L_T/2$ = 243.6 cm. Generally, the distances between mirrors and waveguide faces (RF discharge) are subject to some restrictions, but can be varied within a wide range. Evidently, increasing these gaps results in growth of diffraction losses. From the other side, these losses produce stronger discrimination between modes. Therefore, a series of calculations for gain-loaded cavity was made to evaluate discrimination properties of the resonator for different gaps lengths.

## 3. RESULTS AND DISCUSSIONS

It was found that in-phase mode pattern is not too much sensitive to the spacing length variations and to increase of small signal gain coefficient. Therefore near- and far-field patterns shown in Fig. 2 for the in-phase mode are representative for a

wide range of $d$ and $g_0$. One can see that all beams are perfectly phase locked resulting in high summed beam optical quality. Fig. 3 shows near field pattern for the in-phase mode over one segment of the output mirror. It was found that this distribution in some degree varies with growth of $d$ and $g_0$ both: it's becoming broader in both azimuthal and radial directions. It is worth to note that the wave field at the azimuthal edges of the segment is much weaker than at the radial edges.

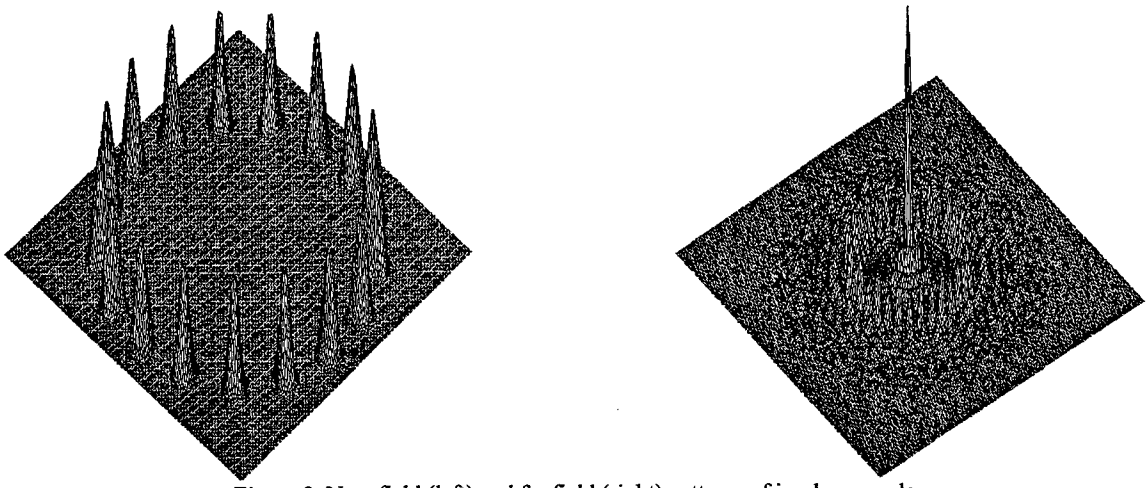

Figure 2. Near field (left) and far field (right) patterns of in-phase mode

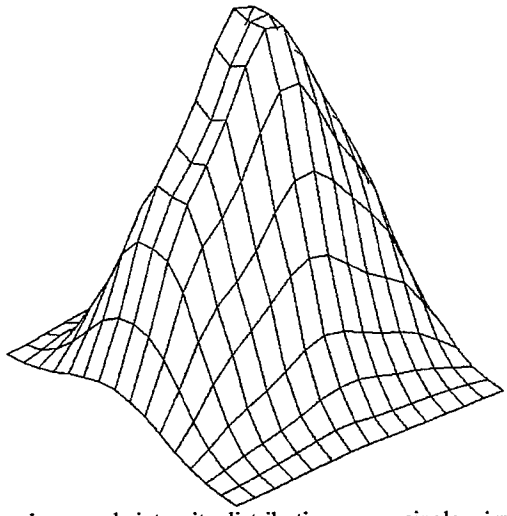

Figure 3. In-phase mode intensity distribution over a single mirror segment

This is a particular feature of the configuration considered. The constructive interference between laser beams results in rather good reproduction of the beam array in azimuthal direction, while in radial direction an irreversible expansion of radiation takes place. As it was mentioned above, the annular waveguide with closely spaced periodical mirrors is equivalent to an infinite 1D array. In this limit, any periodical wave field distribution is reproduced exactly. Fig. 4 demonstrates this effect. It was possible to calculate by iterations with an appropriate initial distribution two more in-phase modes differing by mode pattern within each segment: two peaks in azimuthal (right) and radial directions. As it is known from the theory [6], besides shown in Figs. 2 and 4 modes there exists a number of modes modulated in phase over the azimuthal direction. Generally, they have larger diffraction losses than the in-phase mode. However, they can also compete for the gain at further increase of gain over threshold. We have studied mode competition effect numerically for two free-space gaps length values. For short gaps it was found that the in-phase mode became unstable at rather small above threshold gain (about 1.05). This effect evidently is explained by a low discrimination of modes. For longer gaps radial diffraction is more important, and discrimination against higher-order modes should increase. Fig. 5a shows how the

threshold gain for the in-phase mode grows with $d$ in case of perfectly reflecting mirrors. Taking $d$ such that diffraction losses are comparable to output, the output power was calculated as a function of small-signal gain (see Fig. 5b).

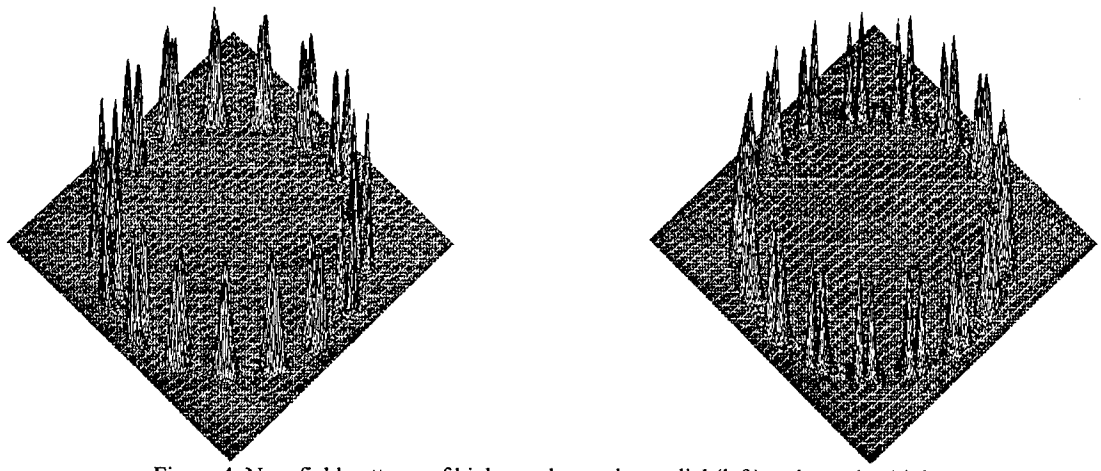

Figure 4. Near field patterns of higher order modes: radial (left) and angular (right)

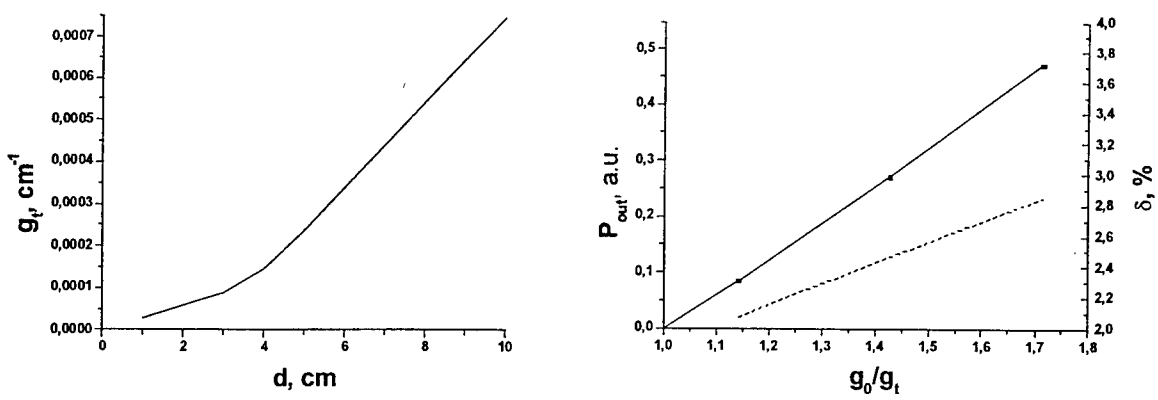


a) b)

Figure 5. a) Fundamental mode threshold gain in dependence on spacing width $d$ for perfectly reflecting mirrors; b) Output power and percentage of diffraction loss vs small-signal gain reduced to the threshold for $d = 10$ cm

It is seen that laser operates stable in single (in-phase) mode regime up to above threshold gain 1.7. Still percentage of diffraction loss is rather low (right axis). This demonstrates an opportunity to stabilize the in-phase mode in the cavity proposed up to high powers with simple means. Further studies are necessary to evaluate effects produced by refractive index gradients induced by gas heating. Authors acknowledge the financial support from the RFBR project 99-02-17469a.

## REFERENCES


1. J. G. Xin, D. R. Hall, *Appl. Phys. Lett.*, **51** 469 (1987)
2. J. W. Bethel, H. J. Baker, D. R. Hall, "A new scalable annular $CO_2$ laser with high specific output power", *Opt. Comm.*, **125** 352 (1998)
3. A. Lapucci, M. Ciofini, S. Mascalchi, E. Di Fabrizio, M. Gentili, "Beam quality enhancement for a radio-frequency excited annular $CO_2$ laser", *Appl. Phys. Lett.*, **73**, 2549, (1998)
4. A. Lapucci, M. Ciofini, "Extraction of a high quality beam from narrow annular laser sources", *Appl. Opt.* **38**, 4552 (1999)
5. M. Ciofini, A. Lapucci, "Guided Talbot Resonator for annular laser sources", to be published
6. V. V. Likhanskii, A. P. Napartovich, "Radiation emitted by optically coupled lasers", *Sov. Phys. Usp.*, **33**, 228 (1990)
7. N. N. Elkin, A. P. Napartovich, A. G. Sukharev, V. N. Troshchieva, D. V. Vysotsky, "Direct numerical simulation of radiation propagation in a multicore fiber", *Optics Communications*, **177**, 1-6, 207-217, 2000

# Dynamic correction of thermal lensing and birefringence in high-power solid-state lasers

Inon Moshe* and Steven Jackel

Non-linear Optics Group - Soreq NRC, 81800 Yavne, Israel

**Abstract**

Enhanced birefringence compensation together with dynamic thermal focus correction was demonstrated in a high-power, high-pulse-energy oscillator based on two flashlamp-pumped, 1x10cm Nd:YAG rods. Birefringence compensation was achieved by 90° polarization rotation with either a quartz rotator between the rods or with a Faraday Rotator between forward and backward resonator passes. An Imaging Variable Radius Mirror –IVRM composed of discrete optics was used as the resonator rear mirror. Imaging was required to re-image the rod principal plane onto itself so as to minimize the birefringence compensation's bifocal lensing sensitivity. Dynamic control of the IVRM radius of curvature was required to compensate thermal focusing variations. Integration into a Reentrant configuration, enabled average output power of 114W @ 20Hz with 3% overall efficiency in a polarized beam. Pulse energy dropped by only 3% compared to "cold" operation.

**Keywords:** laser resonators, thermal lensing, birefringence, bifocal lensing.

## 1. Introduction

Solid state laser materials are heated throughout their volume, by the absorbed pump power not converted to light, but are surface cooled, usually by a flowing fluid. This situation causes a temperature gradient with a maximum value at the center, and a minimum value near the periphery. In the case of laser rods, the temperature gradient causes the local index of refraction to quadraticly depend on radius. This behavior causes thermal focusing.[1] Temperature gradients, additionally, induce thermal stresses inside the rod that result in birefringence related phenomena. The rod's index of refraction tensor becomes radially and tangentially dependent.[2] Thermally induced birefringence causes two main problems in optical systems. First, a linearly polarized incident ray will accumulate different phase delay on its radial and tangential components, and will become elliptically polarized after exiting the birefringent laser rod. This distortion is angularly and radially dependent and cannot be corrected in single pass with waveplates or Faraday rotators (FRs). The second problem is bipolar lensing, where the radial and the tangential polarization components of the input beam are focused by different amount by the birefringent rod. This phenomenon reduces beam quality in two ways: first, it introduces an optical aberration with a circle of least confusion located between the two focal planes. Second, the bipolar focusing makes design of $TEM_{00}$ laser resonators much more difficult and even impossible (in case of large fundamental-mode size inside the rod)[3]. Thus, birefringence compensation is essential to produce efficient lasing with high beam quality.

One of the basic birefringence compensation techniques uses 90° polarization rotation between two laser rods. A quartz rotator (QR) can be used to average, to an equal value, the accumulated phase delay of both polarization components of the first rod by passage through the second rod.[4] This compensation technique is conditional on identical optical paths, experienced by both polarization components, through the two rods. Unfortunately, this condition cannot be met due to the bipolar focusing that always accompanies depolarization. In order to partially overcome bipolar focusing, relay imaging is used to couple the rod principal planes.[5] This compensation technique requires identical laser rods/pump heads/power supplies. When heat values and distributions are not identical and/or when the laser rod axis are not sufficiently aligned, the compensation will not be complete.

* Correspondence: Email: inon@ndc.soreq.gov.il , Tel: 972-8-9434779; Fax: 972-8-9434401

XIII International Symposium on Gas Flow and Chemical Lasers and High-Power Laser Conference,
Antonio Lapucci, Marco Ciofini, Editors, Proceedings of SPIE Vol. 4184 (2001)

A better solution should be to correct the polarization distortion in the same distorting media, even when multiple rods are used. Practically, a 45° FR, located between the second laser rod and the rear mirror, is used for 90° polarization rotation, and an "imaging mirror" is used for re-imaging the rod principal plane and to retrace the incident rays. An erecting imaging mirror consists of an imaging lens and a retroreflecting mirror. An adaptive mirror enables dynamic correction of unstable aberrations without affecting the re-imaging.

In this work, adaptive compensation of thermal focusing is achieved using a one degree of freedom Variable Radius Mirror (VRM).[6] An additional positive lens is used to form an inverted image of the rod principal plane on the VRM entrance/exit pupil and then an erect 1:1 reimage of the original rod principal plane at its original location. We call the imaging lens plus VRM combination an Imaging VRM or IVRM.[7]

## 2. Experiments

### 2.1 Birefringence compensation by 90° polarization rotation between laser rods

In this section, birefringence-compensated resonators based on 90° polarization rotation between laser rods were tested. The polarization distortion occurring in the first rod was compensated in the second identical rod. Resonator performance was measured in two configurations, using only a 90° QR, or using a 90° QR plus a relay-imaging telescope (figures 1 (a) and (b), respectively). In both configurations, the VRM was controlled to maximize output power while varying repetition rate. Proper operation of this compensation technique requires good equality of the laser rods/heads/pump-distribution, because the beam distortion generated in one rod should be corrected in an identical distorting distribution. Before operation in the oscillator, the PFN energies to the two heads were set to generate equal average heat loads.

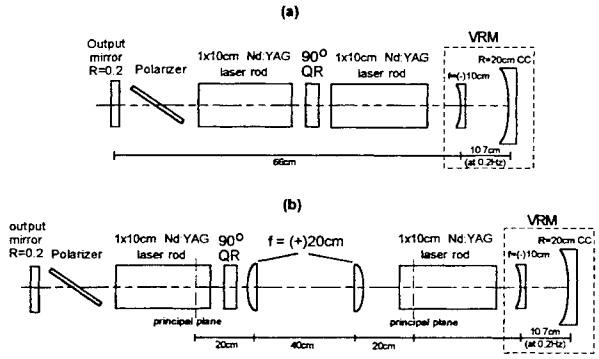


Figure 1: Birefringence compensated resonator schemes, with 90° QR (a), and with 90° QR plus relay-imaging telescope (b).

Output energy normalized by the output energy at single shot operation was measured as function of the average pump power using no birefringence compensation, and with 90° QR or 90° QR + relay imaging compensation (figure 2).

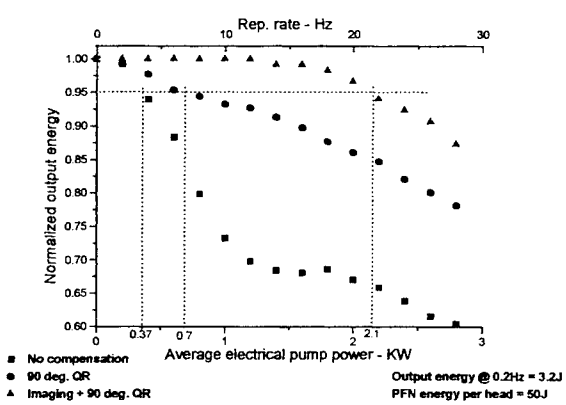


Figure 2: Normalized output energy without or with 90° QR or 90° QR plus relay-imaging telescope birefringence-compensation.

One can see that the simple configuration, without relay imaging, did not provide sufficient birefringence compensation, and strong depolarization induced energy reduction occurred. The operating range (5% loss) was extended by a factor of three using the enhanced configuration that also contained the relay-imaging telescope. Nevertheless, this configuration, that theoretically provides perfect bifocus insensitive birefringence compensation[5], was also found to be limited. A large, 13% loss occurred at 2.8KW pump power. This limitation could be due to nonequality of the heat distribution in both rods, and/or due to asymmetrical heat distributions around the optical axis. Thus, birefringence compensation failed at high pump power, although both rods were pumped to generate the same average heat load.

### 2.2 Birefringence compensation by 90°-polarization rotation between passes through the two rods.

For laser rods with nonidentical optical distortions and/or nonsymmetrical heat distributions, the birefringence compensation should be done by double-passing (with erect imaging) the same extended distorting media. The $E_r$, $E_\theta$ ray separation due to bifocal lensing should be eliminated. These considerations were implemented by using the resonator shown in Figure 3. A 45° FR, was placed between the second rod and the rear mirror, instead of the 90° QR located between the rods. This enabled correction after alternate resonator passes. The IVRM as the resonator rear mirror enabled erect imaging (in order to avoid asymmetry limitations) and dynamically corrected time-dependant thermal lensing. In order to retain the beam polarization on the polarizer axis, an additional FR was placed between the first rod and the polarizer. Figure 5 depicts the normalized output energy as function of the repetition rate, using an IVRM and a FR to correct for birefringence between passes. Figure 5 also provides a comparison with inter-rod 90° QR compensation. Less than 5% loss at pumping power of 4KW occurred with compensation between passes. These results demonstrate the advantage of birefringence compensation between passes using the IVRM and 45° FR, with depolarization correction between alternate passes through both distorting rods and with erect-imaging.

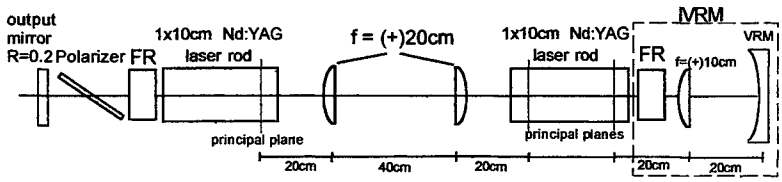


Figure 3: Birefringence compensated resonator using 45° FR and IVRM to 1:1 re-imaging and dynamic correction for thermal lensing.

A reentrant configuration[8], which acts as a three-mirror resonator, (figure 4) was used to prevent possible losses at the polarizer. This configuration replaces the polarization-plane retaining FR with a 0° HR mirror positioned to retroreflect the beam reflected by the polarizer. IVRM was integrated to eliminate bifocal lensing induce compensation failure. 5.7J @ 20Hz was achieved using this configuration. This configuration gave the best results.

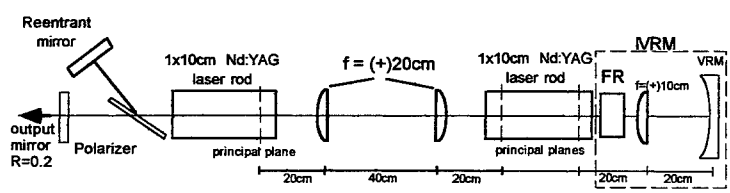


Figure 4: Birefringence compensated resonator scheme using IVRM in a reentrant configuration.

Average output power as a function of the electrical pump power, using a Reentrant plus IVRM, two FRs plus IVRM, and inter-rod QR plus VRM are presented in figure 6. The two configurations that used the IVRM depict a linear behavior, which means good birefringence compensation and low pump dependent losses. In contrast, birefringence compensation between the laser rods was insufficient, and depolarization losses increased with pump power to flatten the output power curve. At pump power of 3.9KW, 114W polarized output power (overall efficiency of about 3%) was extracted through the reentrant resonator with IVRM, in contrast to only 90W extracted from the resonator with inter-rod 90° QR (overall efficiency of 2.3%). These results demonstrate the superiority of the IVRM + FR+ relay-telescope Reentrant resonator. Replacing the IVRM with a VRM (no re-imaging) yielded inadequate compensation.

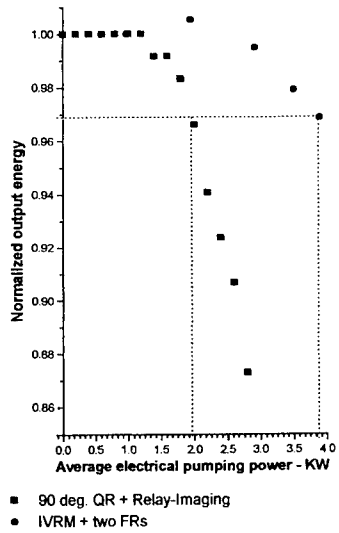


Figure 5: Normalized output energy from birefringence compensated polarized resonators using either an inter-rod 90° QR + relay imaging or two FRs + IVRM + relay-imaging.

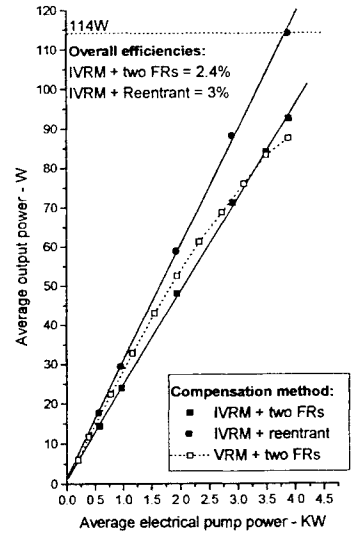


Figure 6: Average output power as function of the average electrical power from two 1x10cm Nd:YAG laser rods in polarized output resonators.

## 3. Conclusions

Birefringence compensation was tested in pulsed power oscillators based on two 1x10cm Nd:YAG flashlamp pumped rods. Two basic methods were tested, compensation in the second rod for depolarization generated in the first rod with a $90^0$ QR, and compensation in the second resonator pass for the distortion generated by both rods in the first pass using a FR. Both compensation methods used rod principal-plane relay-imaging to eliminate free-space bifocusing errors. Birefringence compensation without relay imaging was effective only at low powers. Significant depolarization loss occurred, with inter-rod birefringence compensation. In contrast, less than 5% losses @ 3.9kW pumping power occurred with birefringence compensating between resonator passes through both rods. In the inter-pass configuration, a 45° FR was placed between the second rod and the rear mirror. An IVRM was used as the resonator adaptive rear mirror and relay imaging optic. This compensation method was tested in two configurations, linear and Reentrant. The Reentrant scheme proved to be more efficient, resulting in 114W of polarized output power (PRF= 20Hz) @ 3% overall efficiency.

## 4. References


1. J. D. Foster and L. M Osterink, "Thermal effects in Nd:YAG laser" J. of Applied Physics, **41** 3656 3663 (1970).
2 W. Koechner, D. K. Rice, "Effect of birefringence on the performance of linearly YAG:Nd lasers", IEEE J. Q. Elect., **QE-6** 557 566 (1970).
3. G.Cerullo, S. De Silvestri, V. Magni, and O.Svelto, " Output power limitation in CW single transverse mode Nd:YAG lasers with a rod of large cross-section", Opt. Quant. Elect. 25 489 500 (1993).
4. W. Koechner, Solid-State Laser Engineering , 3rd ed., (New York: Springer Varlag,1996).
5. Q. Lü, N. Kugler, H. Weber, S. Dong, N. Müller, U. Wittrock, "A novel approach for compensation of birefringence in cylindrical Nd:YAG rods", Opt. Q. Elect. **28,** 57 69 (1996).
6. I. Moshe, S. Jackel, and R. Lallouz, "Working beyond the static limits of laser stability by use of adaptive and polarization-conjugation optics", Appl. Opt. **37** 6415 6419(1998).
7. I. Moshe, and S. Jackel "Correction of birefringence and thermal lensing in non-reciprocal resonators using a dynamic imaging mirror" Appl. Opt. **39** 4313 4319 (2000).
8. S. Jackel, A. Kaufman, and R. Lallouz, "High-repetition rate oscillators based on athermal glass rods and on birefringence correction techniques," Opt. Eng. **33**, 3008 3017 (1994).

# An Improved Virtual Confocal Unstable Resonator Suitable for COIL

Du Xiangwan, Wang Taichun, Fu hanqing
Institute of Applied Physics and Computational Mathematics
P.O. Box 8009 Beijing 100088, China

## ABSTRACT

By analysing the advantages and disadvantages of the unstable resonator with phase-unifying output coupler, An improved unstable resonator is designed. The numerical simulation results indicate, that the fat-field intensity focusing of the improved resonator is better than the conventional resonator.

**Keywords:** unstable resonator, improved resonator, numerical simulation

## 1. Description of the Improved Resonator

The idea of the improved resorator is to increase the magnification and guarantee the extraction efficiency simultaneously. For this purpose we devide the convex output mirror into two parts: the central part with full reflectivity $R_i = 1$ and the outer circle part with partial reflectivity $R_0 = \eta < 1$.

When $\eta \to 1$, the improved resonator degenerates into the conventional unstable resonator; When $R_i \to \eta < 1$, the improved resonator becomes the unstable resonator with a phase-unifying output coupler(Yasui K, et. al.).

The magnification of conventional unstable resonator is

$$m_1 = a_1 / a_3$$

Where $a_1$ and $a_3$ is the radius of concave and convex mirror respectively.

The effective magnification of improved resonator is

$$m_2 = a_1 / a_2, \quad m_2 > m_1$$

Where $a_2$ is the radius of central part of convex mirror.

XIII International Symposium on Gas Flow and Chemical Lasers and High-Power Laser Conference,
Antonio Lapucci, Marco Ciofini, Editors, Proceedings of SPIE Vol. 4184 (2001)

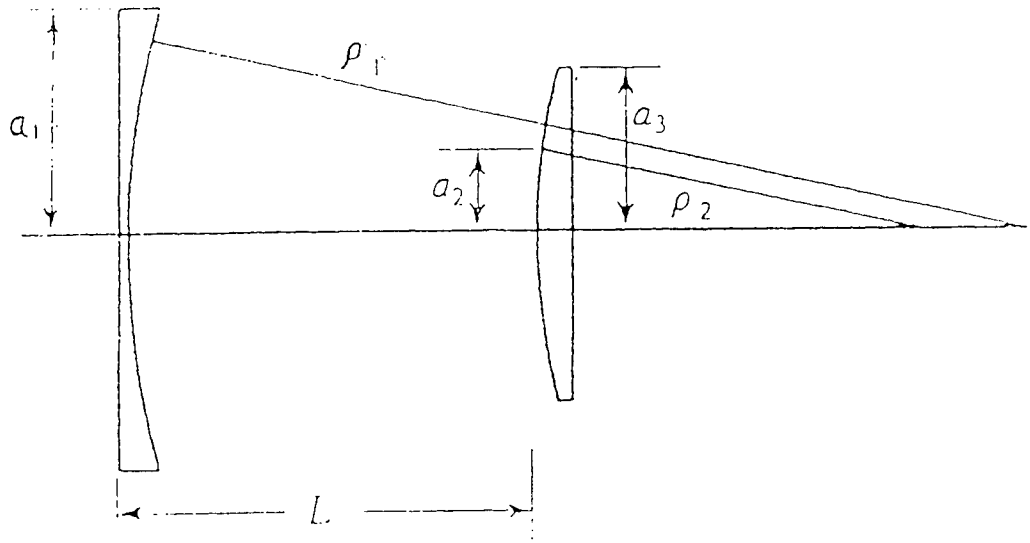


Fig.1 Schematic of the improved unstable resonator.

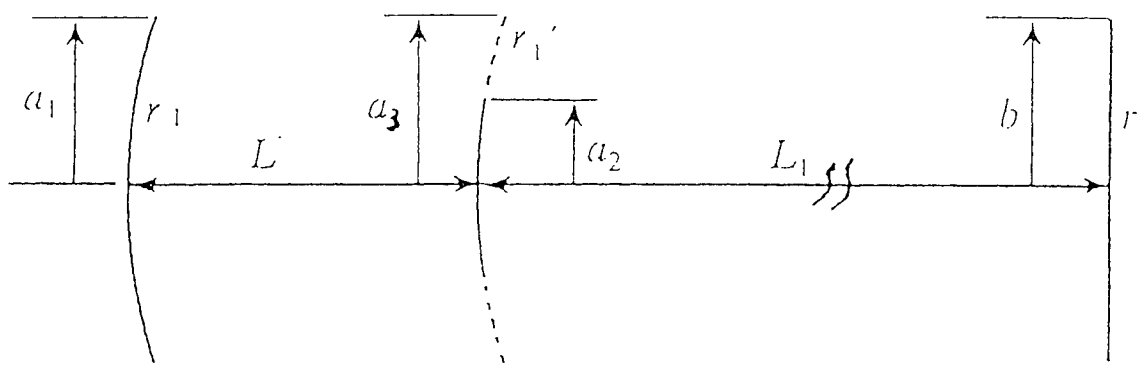


Fig.2 Coordinate system of the ner-and far-field for the unstable resonator with circular mirrors of spherical surfaces

b-radius of laser spot in far-field

$L_1$-distance between output mirror and focal plane

The step function distribution of reflectivity:

$$R(r_1'/a_1)=\begin{cases}1, & 0\le(r_1'/a_1)\le 1/m_2\\ \eta<1, & 1/m_2\le(r_1'/a_1)\le 1/m_1\\ 0, & 1/m_1\le(r_1'/a_1)\le 1\end{cases}$$

The Gaussian distribution of reflectivity:

$$R(r_1'/a_1)=\begin{cases}1, & 0\le(r_1'/a_1)\le 1/m_2\\ \exp\left[-2(r_1'/a_1-1/m_2)^2/\tau^2\right], & 1/m_2\le(r_1'/a_1)\le 1/m_1\\ 0, & 1/m_1\le(r_1'/a_1)\le 1\end{cases}$$

## 2. Results of Numerical simulation

By solving Fresnel integral equation numerically we can obtain the near-and far-field distribution of laser intensity.

### 2.1 Results for conventional unstable resonator (see Tab.1 and Fig.3)

Table 1 The computational results of normalized far-field intensity I and integral intensity $I_t$: for the conventional unstable resonator

| r/b | 0 | 0.1 | 0.2 | 0.6 | 1.0 |
|---|---|---|---|---|---|
| I/r.u. | 1 | 0.033 | 0.062 | 0.573(-4) | 0.333(-5) |
| $I_t$ /r.u | 0 | 0.485 | 0.815 | 0.983 | 1.0 |

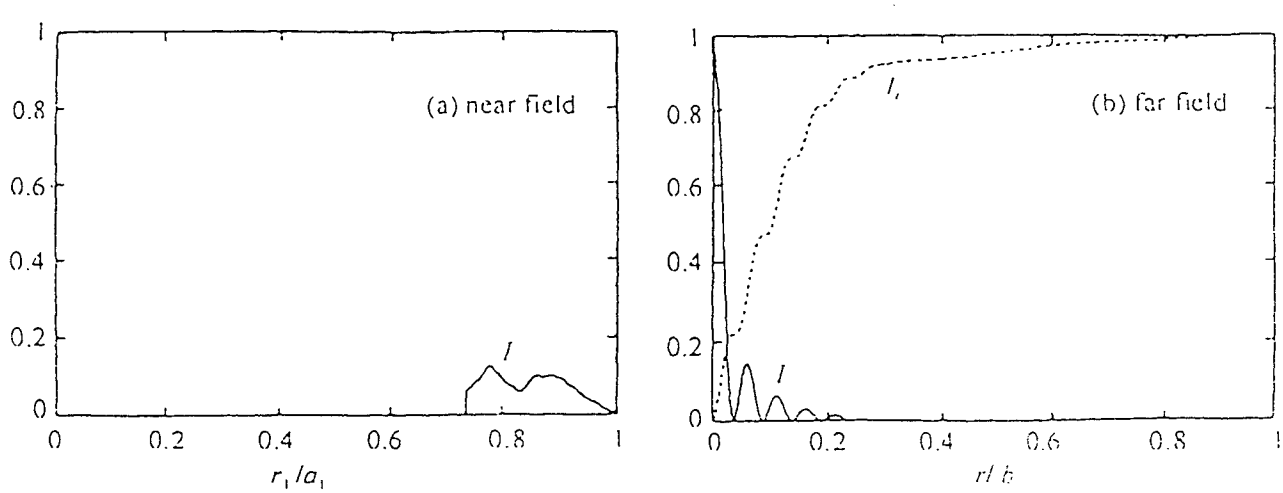


Fig3. The laser intensity distribution of near-and far-field for conventional unstable resonator.

## 2.2 Results for Improved Resonator(see Tab.2 and Fig.4,5)

Table 2 The computational results of normalized far-field intensity and integral Intenaity for the improved unstable resonator ($\eta = 0.5; 1/m_2 = 0.5\, and\, 0.3$)

| r/b | 0 | 0.1 | 0.2 | 0.6 | 1.0 | $m_2$ |
|---|---|---|---|---|---|---|
| I/r.u. | 1 | 0.858(-2) | 0.134(-2) | 0.485(-4) | 0.894(-5) | 2.0 |
| $I_t$/r.u | 0 | 0.745 | 0.907 | 0.988 | 1.0 | |
| I/r.u. | 1 | 0.0155 | 0.135(-2) | 0.168(-5) | 0.135(-4) | 3.33 |
| $I_t$/r.u | 0 | 0.752 | 0.895 | 0.987 | 1.0 | |

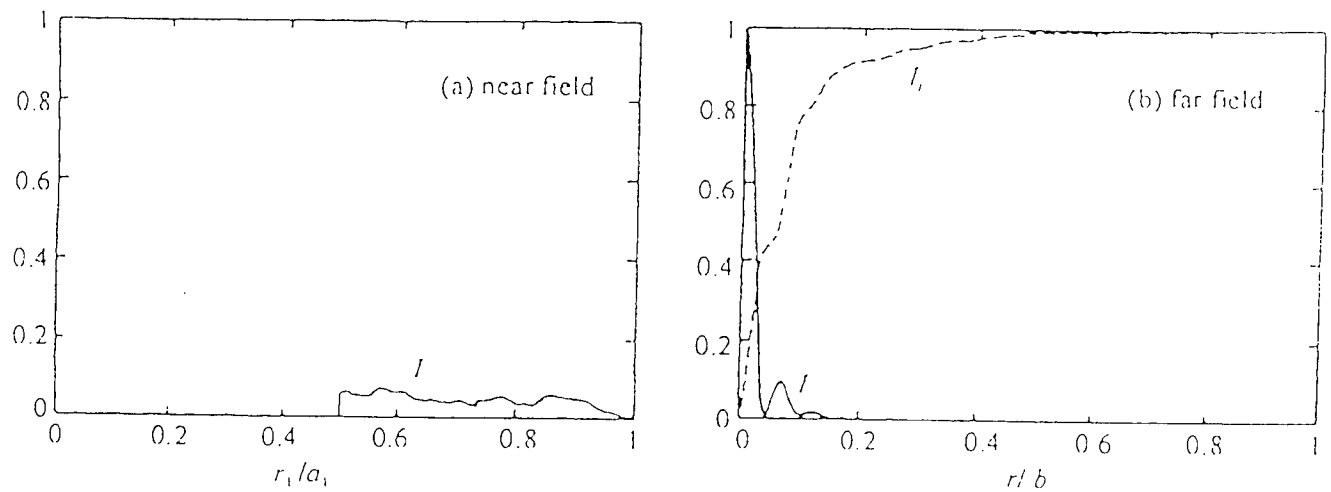


Fig.4 The laser intensity distribution of near-and far-field for the improved unstable resonator for $\eta = 0.5$ and $1/m_2 = 0.5$

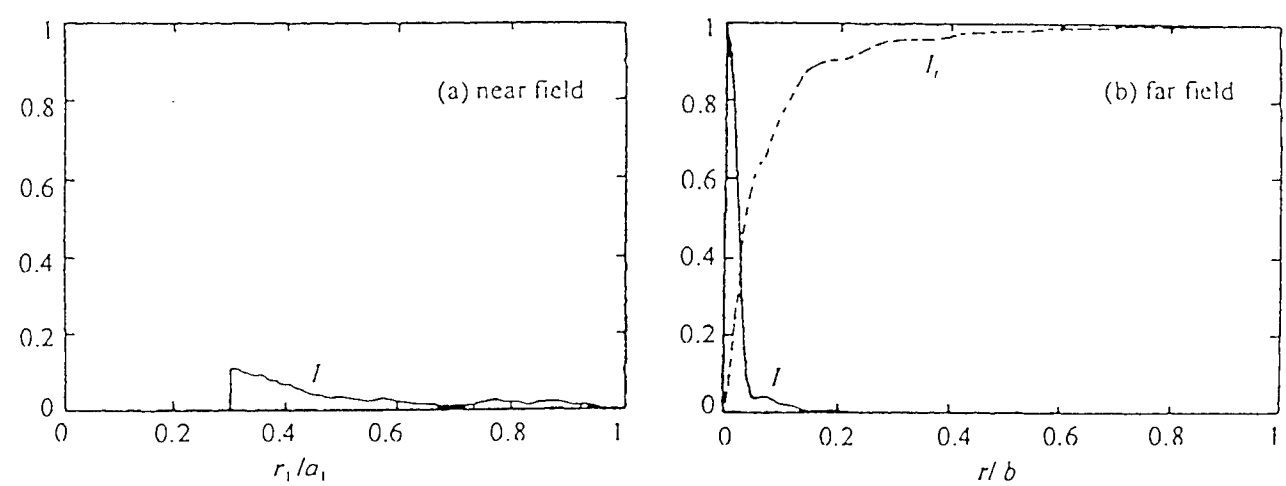


Fig.5 The same for $\eta = 0.5$, $1/m_2 = 0.3$

## 2.3 Results for Resonator with Gaussian distribution of Reflectivity (see Tab.3 and Fig.6,7)

Table 3 The computational results of normalized far-field intensity and integral intensity for the unstable resonator with Gauss distribution ( $1/m_2 = 0.5$, $\tau = 0.237$; $1/m_2 = 0.3$, $\tau = 0.437$ )

| r/b | 0 | 0.1 | 0.2 | 0.6 | 1.0 | $m_2$ | $\tau$ |
|---|---|---|---|---|---|---|---|
| I/r.u. | 1 | 0.0107 | 0.140(-2) | 0.734(-4) | 0.103(-4) | 2.0 | 0.237 |
| $I_t$/r.u | 0 | 0.689 | 0.815 | 0.979 | 1.0 | | |
| I/r.u. | 1 | 0.0153 | 0.201(-2) | 0.654(-5) | 0.195(-4) | 3.33 | 0.437 |
| $I_t$/r.u | 0 | 0.690 | 0.861 | 0.985 | 1.0 | | |

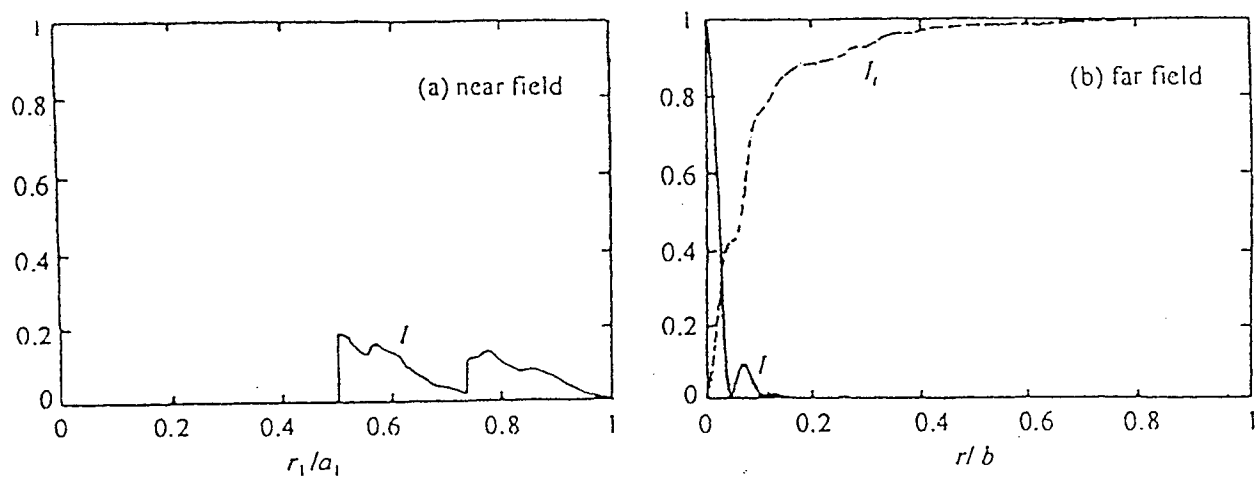


Fig.6 The laser intensity distribution of near-and far-field for the unstable resonator with Guass distribution $R(r/a_1)$ of $1/m_2 = 0.5$ and $\tau = 0.237$

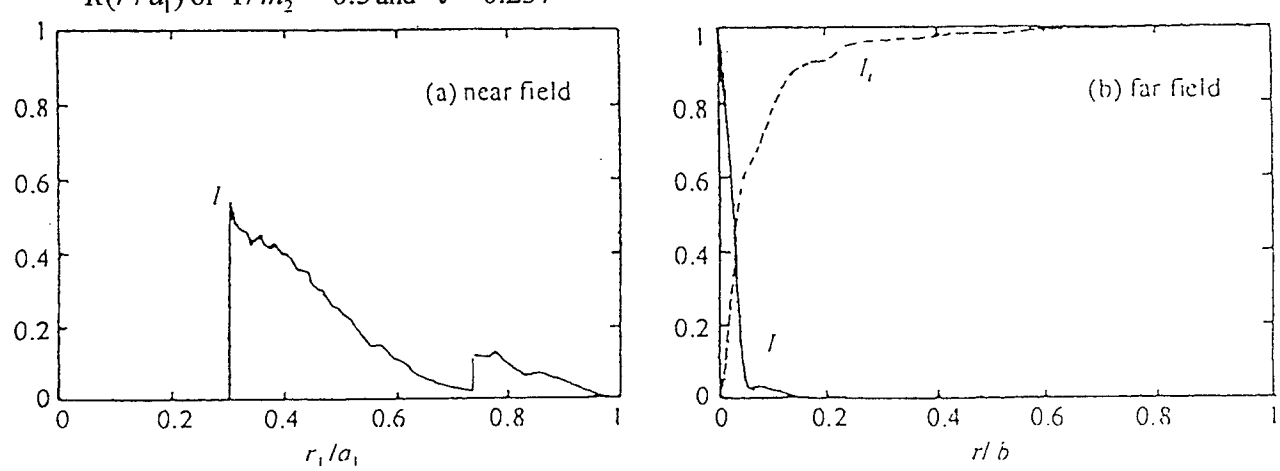


Fig.7 The same for $1/m_2 = 0.3$ and $\tau = 0.437$

## 3. Conclusion

The numerical simulation results indicate that far-field laser focusing of improved resonator is better than the conventional resonator and the resonator with Gaussian distribution of reflectivity.

We can change the parameters $m_1$, $m_2$ and η to optimize the design of the improved resonator.

## REFERENCES


1. 周炳昆，高以智，陈家烨等。*激光原理（第五章）*。北京：国防工业出版社， 1984
2. Yasui K, Tanaka M, et al. *J Applphys*, 1989,65(1):17
3. Mccarrthy N. and Lavigne P. *Opt lett,* 1985, 10:552
4. Silvestri S. De, Lavigne P, et al.J *Opt Soc Am,* 1987, A4:1413
5. Takenaka Y, Kuzumoto M, et, al. IEEE *J QE*, 1991, 27(11):2482
6. 李斌颖，天线原理与应用（第十二集）.兰州：兰州大学出版社， 1993
7. 王泰春，付汉清. 强激光与粒子束， 1998， 10（3）：
8. 桑凤亭，杨柏龄等. 强激光与粒子束， 1996， 8（增刊）

# Superhigh quality of phase conjugation at SBS

F. A. Starikov, Yu. V. Dolgopolov, S. A. Kovaldov, G. G. Kochemasov, A. V. Kopalkin, S. M. Kulikov, V. K. Ladagin, S. A. Sukharev, N. N. Gerasimenko

Russian Federal Nuclear Center – Institute of Experimental Physics
607190 Sarov (Arzamas-16), Nizhny Novgorod Reg., Russia

## ABSTRACT

As a result of experiments and numerical simulation of phase conjugation (PC) in the SBS-mirror with an ordered raster of small lenses, its optimal configuration is determined that has unique properties as compared with the current SBS-mirrors. In current SBS-mirrors in the focused beams the high PC quality takes place at high reflection coefficients only that is often unachievable. The presented SBS-mirror fixedly yields the PC quality that is near to an ideal at any level of SBS saturation, i.e. any reflection coefficient. The simulation results are in good agreement with the experimental data obtained for pulsed Nd laser radiation with using a super-clean SBS-cell and multi-level raster of small Fresnel lenses.

**Key words:** phase conjugation, stimulated Brillouin scattering

## 1. INTRODUCTION

In phase conjugation (PC) mirrors based on stimulated Brillouin scattering (SBS) it was a usual way to use a random phase plate located ahead of SBS-cell.[1-4] But there are a few experimental investigations of double-pass amplifiers where the aberrated laser beam experience ordered spatial distortions at the use of a raster of Fresnel lenses in the PC-mirror scheme [5-8] or at an amplifier in the form of an ordered fibre bundle.[9] We have recently carried out a numerical investigation[10] of PC at SBS in the case of the ordered raster of small lenses. An arrangement optimisation of such PC-mirror has allowed to find a new effect of extremely low noising of Stokes beam. Its essence is in the fact that the angular selection of Stokes radiation leads to the nearly perfect PC when the input window of SBS-cell is placed in a certain intermediate region between the focal plane of rasher's lenses and the focal plane of main lens. Calculations[10] have been performed in an approximation of steady-state linear (unsaturated) SBS but in the experiments the SBS saturation shows itself in any event. For modeling the experiments on PC at SBS of pulsed laser beams, a physical and numerical SBS model has been developed.[11] It allows for SBS saturation and non-steady-state processes related to the finite time of hyper-sound relaxation in the SBS-medium. Here the model is applied to PC quality study in PC-mirror with the raster of small lenses. Experiments have been carried out at second harmonics of a pulsed Nd laser with energy of 0.3 J.

## 2. TRANSIENT SBS MODEL

The SBS is described by the set of equations:[11]

$$\frac{n_0}{c}\frac{\partial A_L}{\partial t}+\frac{\partial A_L}{\partial z}-\frac{1}{2ik}\Delta_\perp A_L+\frac{ik}{2}\left(\frac{n^2}{n_0^2}-1\right)A_L=-\frac{i}{2}pA_S, \tag{1}$$

$$\frac{n_0}{c}\frac{\partial A_S}{\partial t}-\frac{\partial A_S}{\partial z}-\frac{1}{2ik}\Delta_\perp A_S+\frac{ik}{2}\left(\frac{n^2}{n_0^2}-1\right)A_S=-\frac{i}{2}p^*A_L, \tag{2}$$

$$\frac{\partial^2 p}{\partial t^2}+2\left(\frac{1}{\tau}+i\Omega\right)\frac{\partial p}{\partial t}+\frac{2i\Omega}{\tau}p=\frac{2g\Omega}{\tau}A_LA_S^*+2i\Omega S, \tag{3}$$

where $A_L$, $A_S$ and $p$ are slowly varying laser, Stokes and hypersonic complex amplitudes, respectively, $g=\omega_0\tau\Omega/[4\beta_S n_0^2c^2]$ is the SBS gain coefficient, $\tau=2/(q^2\Gamma)^2$ is the hyper-sound relaxation time, $\Omega=\omega_L-\omega_S$ and $q\cong 2k_L$ are the frequency and wave number of hyper-sound, $n_0$ is the mean refractive index defined by the relationship $k=n_0\omega_0/c$, $\beta_s=1/(\rho^0 v_s^2)$ is the compressibility of the medium, $v_s$ is the adiabatic hyper-sound speed, $\Gamma=(4\eta/3+\eta')/\rho^0$ is the damping constant, $\eta$ and $\eta'$ are the shear and bulk viscosity, $\rho^0$ is the mean density. The field amplitudes are normalized so that the radiation density fluxes are equal to $J_L=|A_L|^2$, $J_S=|A_S|^2$. The fluctuation Langevin force $S$ in (3) is delta-correlated in time. Linear as well as nonlinear refraction is neglected here. The model is described in detail in Ref.11. To evaluate the PC quality in the plane $z$=const we introduce the PC coefficient $h=|\iint A_LA_S d\mathbf{r}|^2/[P_SP_L]$, where $P_L$ and $P_S$ are the laser and Stokes powers.

XIII International Symposium on Gas Flow and Chemical Lasers and High-Power Laser Conference,
Antonio Lapucci, Marco Ciofini, Editors, Proceedings of SPIE Vol. 4184 (2001)

## 3. EXPERIMENT AND CALCULATIONS

The scheme of SBS-mirror is shown in Fig.1. Laser beam with a half-width $a$ and angular divergence $\theta_L$ is coupled into the angular selector with transmission angle $\theta_{sel}>\theta_L$. Then the laser beam goes through the ordered raster of small lenses with a focal length $f$ and a size $d$. The main lens with focal length $F$ focuses the laser beam into the SBS-cell of length $L$. The distance between the main lens and the input window of the SBS-cell is $L_1$. The laser intensity after passing through the raster has the specific distributions in the zones I and II, where the laser beam is broken up into the ordered arrays of beamlets. One of them, zone I, is the focal region of main focusing lens. An ordered spotted picture is formed in zone I. Each peak of this picture has a structure of angular distribution of the laser intensity incident on the raster. The angular interval between the peaks is equal to $\theta_d=\lambda/d$. The smooth envelop of the peaks depends on $d^2/f$ only. The other specific distribution of the intensity is in zone II, i.e. focal region of the raster's small lenses.

The steady-state linear SBS calculations[10] have shown that the distribution of Stokes intensity in the pinhole plane consists of a discrete set of peaks or diffraction orders that is consistent with experiments.[5-8]. The angular separation between them equals $\theta_d$. A perfect PC requires only the central Stokes order of diffraction conjugated to the laser beam. Angular selection in the pinhole plane removes the non-zero orders of diffraction, thereby increasing the PC fidelity. A novel encouraging effect of extremely low noising of the Stokes field was found.[10] Its essence is in the fact that the angular selection of central Stokes mode allows achieving a nearly perfect PC when the input window of the SBS-cell is placed in a certain region between the zone I and zone II, where the quasi-lightguide mosaic zones with the periodical distribution of the laser intensity are formed. If the arrangement of PC-mirror is optimal, the PC coefficient is more than 90-95% whereas the PC coefficient before the selection does not exceed the value of 30%. The selector transmission coefficient $k_{sel}$ is not maximal at optimal arrangement. To increase it, the SBS-cell should be moved towards the main focusing lens so that the zone II would be put within the SBS-cell. However, this increase of selection coefficient is accompanied by a noticeable decrease of PC fidelity after the selection.

To carry out experiments on exciting SBS in gaseous mixtures, special gas-filled cells have been manufactured. Mechanical and electrical polishing permits to obtain the surface roughness of the inner walls and separate parts of the cell is less than 0.3 μm. Separate parts in the cell are joined by of copper and indium gaskets; welding works are carried out by means of electron beam welding. Design philosophy and technology of the cell manufacture permit to keep the initial purity of the gas introduced into the cell.

The PC fidelity is significantly affected by competitive with SBS non linear optical processes, in particular heating and optical breakdown of SBS-medium. Since both these processes are considerably determined by the degree of the impurities removal from the gas, a special system for gas cleaning from dispersed micro-impurities and filling it into the cell has been manufactured. The main part of this system is a filtering system designed for the treatment of working gas (xenon). The treatment system enables not only remove solid impurities from gases, but filling in SBS-cells with gaseous mixtures with a component content at given partial pressures. Two stages of gas cleaning are used in the system (after the gas cylinders in front of the cell). The second stage of treatment is equipped with special fine filters. As a filtering element in the fine filter nickel powder of the given particle size is used. Depending on the pore size of the filtering element specific degree of gas cleaning can be attained. Filters of the system developed allow to clean gases from particles with the size of more than 0.1 μm with the efficiency of ~99.9999%. In order not to pollute filter during the evacuation, the latter and filling in SBS-cell are carried out by different routes.

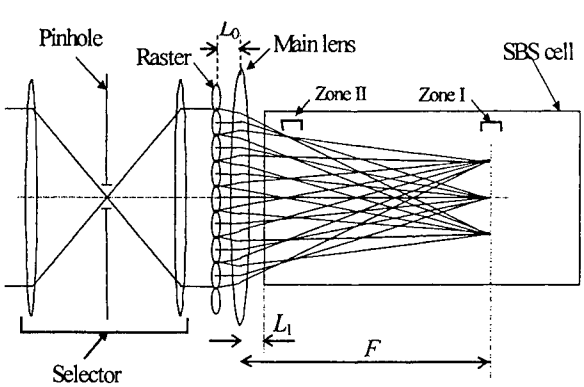


**Fig.1.** Schematic of the SBS-mirror

The experiments have been carried out at the Nd laser facility consisted of master oscillator and two amplifiers.[12] At the output of the second amplifier a practically diffraction-limited laser beam is formed with $\lambda$=1.06 μm, energy 1.5 J and pulse duration 25 ns. The laser radiation is sent to a KD*P crystal where its frequency is doubled. Energy of the second harmonic radiation is ≤300 mJ, the pulse duration is 25 ns, the divergence is $3\cdot10^{-4}$ rad. On going to the second harmonic, the laser setup is isolated from the back-scattered SBS component. SBS is excited in a superclean cell filled with a mixture of $SF_6$ and Xe. The $SF_6$ partial pressure is 1.5 atm and the total mixture pressure is 28 atm. The SBS gain coefficient is $g$=0.023 cm/MW, and $\tau\approx$5 ns. We use an eight-level kinoform raster of closely packed diffraction Fresnel lenses with the diffraction efficiency of 95% and $d$=0.5 mm, $f$=6 cm.

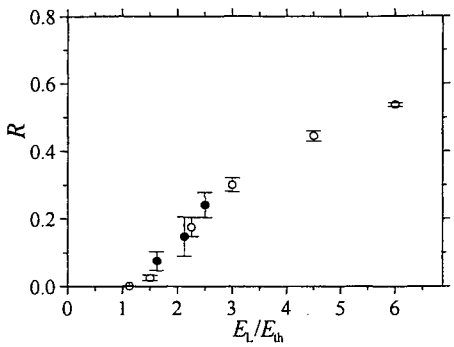


**Fig.2.** The dependence of the reflection coefficient $R$ in experiment (●) and calculations (o) on the laser energy at the arrangement of the zone I within the SBS-cell. $E_{th}$=80 mJ.

For simulating and optimizing the experiment, we conduct calculations of (1)-(3) in 2D approximation, which describes all features of operation of PC-mirror considered.[10] In this case the $h_{sel}$ and $k_{sel}$ values for 3D medium are close to the squared corresponding values obtained in the 2D approximation. The transverse profile of $A_L$ and temporal behaviour of laser power correspond to experiment. The calculations with different realizations of the hyper-sound noise are analogous to a series of laser flashes in the experiment.

Two configurations of SBS-mirror have been considered. In the first, which is typical for experiments, [5-8] in the SBS-cell the both bright zones are situated in the sequence II+I as in Fig.1. In the second, SBS-cell is moved away of the lens and in the SBS-cell the only zone I is situated so that the region of quasi-lightguide zones is close to input window of SBS-cell that has to highest PC fidelity.[10] Experimental dependency of reflection coefficient $R$ is shown in Fig.2. It is in agreement with the results of calculations.

Figs 3(a) and 3(b) give the experimental and numerical dependencies of the time-integrated selection coefficient $k_{sel}$ on the laser energy $E_L$ for two arrangements of the SBS-mirror. In the case when only zone I is put into the SBS-cell, mean value of $k_{sel}$ equals 0.3 and the great spread of $k_{sel}$ takes place as there is no complete diffraction mixing of the Stokes field in the transverse section of the beam.[11] Putting into SBS-cell of zone II leads to a significant increase of $k_{sel}$ and to a decrease of spread in its value. The results of calculations are in good agreement with the experimental data.

In Fig.3(c) is shown numerical dependence of PC coefficient of selected radiation $h_{sel}$ on laser energy for two PC-mirror configurations. Here are given the $h_{sel}$ values, which have been averaged over the pulse (i.e. the values time-integrated with a weight of the output Stokes power and divided by the Stokes energy). In accordance with theory,[10,11] at situating zones II+I in SBS-cell the PC quality is not satisfactory whereas in the presence of the only zone I in the cell it is close to an ideal under any level of SBS saturation. The last is very important since in conventional PC-mirrors the near-to-ideal PC fidelity in focused beams can be obtained at great reflection coefficients only.[11] But often it results in considerable light loads and the growth of parasitic competitive non-linear processes in the SBS-medium.

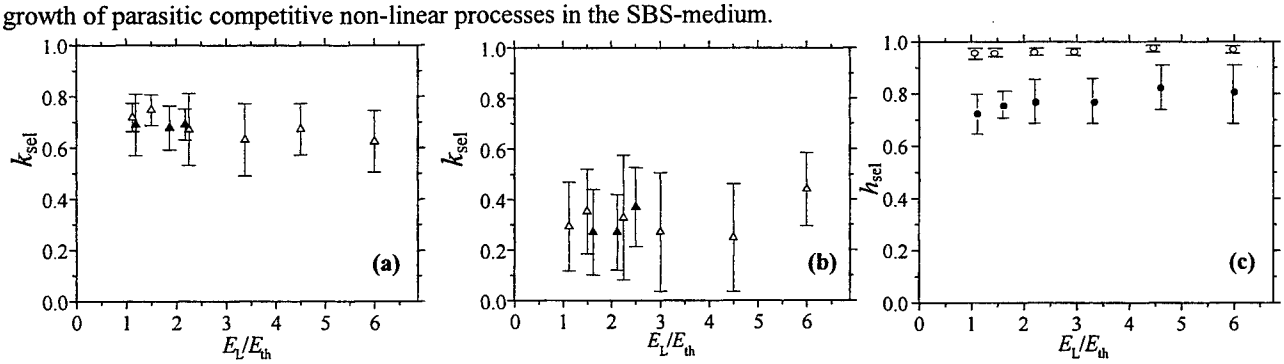


**Fig.3.** (a, b) The dependence of the time-integrated selection coefficient $k_{sel}$ in experiment (▲) and calculation (Δ) on the laser energy at the arrangement of the zone II+zone I (a) and the zone I (b) within the SBS-cell. (c) Numerical dependence of the time-integrated PC coefficient after selection $h_{sel}$ on the laser energy at the arrangement of the zone II+zone I (●) and the zone I (o) within the SBS-cell.

It is impossible to conduct the comparison of calculations with experiment on parameter $h_{sel}$ in view of impossibility of its direct measurement. There has been conducted the detailed measurement and comparison of laser and Stokes energy distributions in front of the raster, i.e. in near field. In Fig.4 are shown the experimental dependencies of energy part in the circle of radius $r$ for laser and Stokes beams at both configurations of SBS-mirror. Under processing CCD-camera images the optical axis ($r$=0) is referred to "center of gravity" of the beam. At each SBS-mirror geometry 5-10 experimental curves are presented for laser and Stokes signals, from which conclusions can be done about the spread of experimental data from flash to flash. It is seen that the configuration with zones II and I in the SBS-cell results in narrower distribution of Stokes energy in near field that is intrinsic for PC, which is far from the ideal.[10] At SBS-mirror configuration with the only zone I in the SBS-cell, closer agreement of laser and Stokes energy distributions takes place. It conforms to calculations of PC coefficient shown in Fig.3(c).

For the purpose of increasing and stabilizing $k_{sel}$ at keeping the high PC quality we propose to modify the SBS-mirror configuration. We must fulfil two conditions. First, the input window of the SBS-cell should be set in the field of quasi-

waveguide zones for achieving the high PC quality. Second, the zones I and II should be within the SBS-cell for reaching more high and stable values of $k_{sel}$. Both the conditions can be satisfied at placing the zone II in the SBS-cell behind the zone I. In order to realize this, we move the raster away the main lens so that $L_0$ exceeds the distance $(F+f)$. Calculations show [11] that it allows to obtain $h_{sel}$~0.95 at $k_{sel}$~0.6-0.7 with small spread in its value.

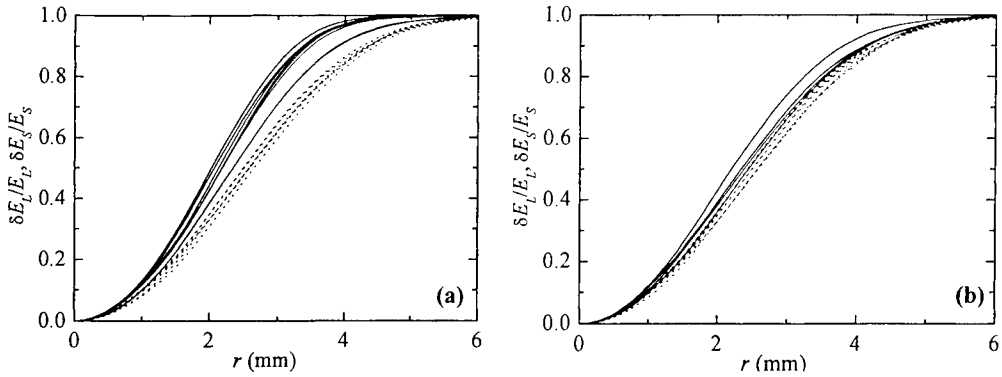


**Fig.4.** Experimental dependence of energy fraction in the circle of radius $r$ in the near field for laser (dotted curves) and Stokes (solid curves) beam at the arrangement of zone II+zone I (a) and zone I (b) within the SBS-cell.

## 4. CONCLUSIONS

PC has been experimentally and numerically studied of the focusing laser beam with the pulse duration about $4\tau$, where $\tau$ is the hyper-sound relaxation time, in the SBS-mirror that includes the ordered raster of small lenses and the angular selector. The raster allows to perform the effective angular filtration of non-conjugated Stokes component, to reduce the local light loads in the SBS-medium and to avoid the influence of undesirable nonlinear effects. Unlike the random phase plate, in the case of using the raster there are more possibilities to controllably change its characteristics. As a result of the calculations, an optimal arrangement of the SBS-mirror has been found with the unique properties. It gives PC fidelity that is more than 90-95% at any laser power (beginning from the threshold one), i.e. at any reflection coefficient, whereas in conventional PC-mirrors the near-to-ideal PC in focused beams is obtained at great reflection coefficients only. The experimental data obtained at the Nd laser facility have shown the validity of the simulation results. Measured reflection and selection coefficients are in a good agreement with calculations. Measured near-field laser and Stokes energy distributions are very close to each other in the case when calculations give near-to-ideal PC fidelity.

## ACKNOWLEDGEMENT


The present work was financially supported by ISTC (project #591-98).


## REFERENCES


1. *Optical Phase Conjugation*, R. Fisher, ed., Academic Press, N.Y., 1983.
2. B.Ya. Zel'dovich, N.F. Pilipetskii, V.V. Shkunov, *Principles of Phase Conjugation*, Springer-Verlag, Berlin, 1985.
3. V.I. Bespalov, G.A. Pasmanik, *Nonlinear Optics and Adaptive Laser System*, Nauka, Moscow, 1985.
4. V.V. Ragul'skii, *Wave Front Reversal at Stimulated Scattering of Light*, Nauka, Moscow, 1990.
5. S.T. Bobrov, K.V. Gratsianov, A.F. Kornev et al., "*Investigation* of possibility of phase conjugation fidelity improvement of SBS-mirrors at smooth aberrations", *Optics Spectrosc.* **62**, pp. 402-406, 1987.
6. K.V. Gratsianov, A.F. Kornev, V.V. Lyubimov, V.G. Pankov, "Phasing of laser beams at phase conjugation by SBS", *Optics Spectrosc.* **68**, pp. 617-619, 1990.
7. Yu.V. Dolgopolov et al, "Iodine laser with SBS-mirror" *Proc. SPIE*, **1980**, pp. 23-30, 1992.
8. Yu.V. Dolgopolov, A.M. Dudov, L.I. Zykov et al., "High power iodine laser with high quality phase conjugation" *Izv. AN USSR ser. fiz.* **58**, pp. 35-40, 1994.
9. H.J. Eichler, B. Liu, M. Duelk, Z. Lu, J. Chen, "Phase conjugation behind an ordered multimode fibre bundle", *Optics Communications* **123**, pp. 412-422, 1996.
10. G.G.Kochemasov, F.A.Starikov, "Novel features of phase conjugation at SBS of beams passed through an ordered phase plate ", *Optics Communications* **170**, pp.161-174, 1999.
11. F.A.Starikov, Yu.V.Dolgopolov, G.G.Kochemasov, S.M.Kulikov, V.K.Ladagin, S.A.Sukharev, "Phase conjugation at SBS of pulse laser radiation with using the kinoform optics", *Proc. SPIE* **3930**, pp. 12-23, 2000.
12. Yu.V. Dolgopolov, G.G. Kochemasov, A.V. Kopalkin et al., *Proc. of Int. Conference on LASERS'99*, Quebec, Canada, December 11-16, 1999 (ed.V.J.Corcoran&T.A.Corcoran, STS Press, McLean, VA, 2000), pp.466-473.

# $CO_2$ and Iodine lasers with SBS mirrors
## (Experimental investigation and aspects of COIL with phase conjugation development)

S.M.Kulikov, S.A.Buyko, V.N.Novikov, and S.A.Sukharev

Russian Federal Nuclear Center (RFNC-VNIIEF) 607190 Sarov, Russia

E-mail: kulikov@otd13.vniief.ru

**ABSTRACT**

Phase conjugation of $CO_2$ and iodine laser radiation in SBS cell placed into resonator of this same laser has been demonstrated experimentally. The first experimental results on simulating of operation of iodine-oxygen laser with SBS-mirror with the help of photolytic iodine laser are presented. The possibilities of creation of COIL with phase conjugation are discussed.

## 1. INTRODUCTION

Nowadays $CO_2$ lasers find a wide application for manufacturing. Investigation directed on technological iodine-oxygen laser creation is being carried out actively. However, the quality of radiation of such gas lasers in a number of cases leaves much to be desired. Phase conjugating SBS-mirrors for aberration compensating are not practically used to present day. The reasons of that are following. When the wavelength increases, the influence of competitive with SBS processes (absorption, breakdown) grows up catastrophically and finally it does not allow SBS accomplishing in usual schemes with relatively high SBS threshold. Resolving the problem of SBS mirror creating for $CO_2$ lasers requires the development of new purification technologies for SBS-media and development of low threshold schemes of SBS-mirror /1/. In the powerful iodine photolytic lasers the SBS-mirrors are used for a long time /2/. So it seems very attractive to determine the directions of development of iodine-oxygen lasers with phase conjugation on SBS- nonlinearity using the results achieved in the development of photolytic iodine lasers with SBS-mirrors and low threshold scheme of SBS mirror, which we have approved in case of $CO_2$ laser. The main difficulty for SBS-mirrors in existent iodine-oxygen lasers is that amplification line width of iodine-oxygen laser medium is narrow as compared to SBS Stocks frequency shift.

## 2. $CO_2$ LASER WITH SBS MIRROR

The optical scheme of experiments is shown in Fig.1. In experiments the chemical $CO_2$ laser with excitation transfer from DF* to $CO_2$ molecules was used as laser radiation source. As SBS mirror we use a cell with Xe (59 atm, $21^0$C), located in the $CO_2$ laser resonator. The decrease of the SBS threshold was obtained due to the increase of intensity of the input Stokes signal when nonlinear medium was pumped by focussed opposing polychromatic beams with the frequency difference between monochromatic components equal to Stokes frequency shift $\delta\nu_S$. The optical resonator length $L_R$ (the length of round trip) required for effective SBS excitation was determined from the condition of equality of the frequency difference between the longitudinal modes of the resonator and the sound wave frequency, i.e., $L_R = L_{SBS} = c/\nu_s = (931 \pm 1)$ cm. In the case of SBS excitation, the number of modes increases over the laser pulse duration (from 4 to 10), and the

XIII International Symposium on Gas Flow and Chemical Lasers and High-Power Laser Conference,
Antonio Lapucci, Marco Ciofini, Editors, Proceedings of SPIE Vol. 4184 (2001)

modes are phased in gradually up to complete synchronization (Fig 2). Mode locking via SBS non-linearity is advantageous from the energy point of view since all modes in this case participate in the creation of acoustic grating, which increases the Q-factor of the resonator. As a result the radiation power and laser pulse duration increase (Fig.2,3). The energy of radiation emitted by the $CO_2$ laser was doubled in the case of SBS excitation. SBS excitation and the presence of phase conjugation are manifested most clearly in the change in laser beam divergence (Fig.1a). While the beam divergence in the absence of SBS was equal to eight diffraction limits, the laser beam divergence in the case of SBS excitation and PC realization was reduced almost to the diffraction limit and the brightness of laser radiation increased by a factor of 64.

## 3. IODINE LASER WITH SBS MIRROR

The experimental results on $CO_2$ laser demonstrate the possibility of low threshold SBS-mirror application as a part of the resonator. They show also that the amplification line width must exceed the value of SBS Stocks shift of frequency $\delta\nu_S$ to make the operation of laser with SBS-mirror successful. To be more accurate it is necessary to provide conditions for SBS pump radiation at the frequency of $\nu$ and Stokes radiation at the frequency $\nu - \delta\nu_S$ to have the same amplification in the laser medium and for the radiation frequencies of both waves to coincide with the center of the amplification line. This condition is possible to be fulfilled in iodine laser with longitudinal supersonic laser medium flow along resonator axes /3/. Using small admixtures of buffer gases for increasing the velocity of supersonic flow it is possible to change the value of the distance between maximums of split amplification line $2\Delta\nu_D$ (see Fig.4) and make this value equal to the SBS Stokes shift of frequency. It is especially attractive to use the SBS-mirrors for maximization of the brightness of a iodine-oxygen laser with radiation output through a fibers assembly. A laser with fiber radiation output has the following peculiarity: laser beam in the fibers assembly splits into a number of beams, which must to be phased in the output beam (Fig.5). The photolytic iodine laser with beam splitting with the help of kinoform element and following radiation phasing in the SBS-mirror (see Fig.6) was investigated earlier in the work /2/. Now we are presenting the first results on simulating the operation of iodine-oxygen laser with low threshold SBS-mirror on the base of counter propagating beams with the help of photolytic iodine laser (Fig.7). In the present experiments we have registered SBS excitation inside the iodine laser resonator (resonator length was equal to $L_R=10L_{SBS}=10c/\nu_S$) and have got laser radiation divergence decreasing to 1-2 diffraction limits.

## REFERENCES


1. S.M.Kulikov, S.A.Buyko, V.N.Novikov, et.al, in *Gas, Chemical, and Electrical Lasers and Intense Beam Control and Applications*, Proceeding of SPIE Vol. **3931**, pp.193-199, 2000

2. Y.V.Dolgopolov, G.A.Kirillov, G.G.Kochemasov, et. al, in *Third International Workshop on Iodine Laser and Applications*, Proceeding of SPIE Vol.**1980**, p.23-30, 1992.

3. L.I.Zikov, S.B.Kormer, S.M.Kulikov, S.A.Sukharev, and A.F.Shkapa, , in *Gas and Metal Vapor Lasers and Applications*, Proceeding of SPIE Vol. **1412**, pp.258-266, 1991.

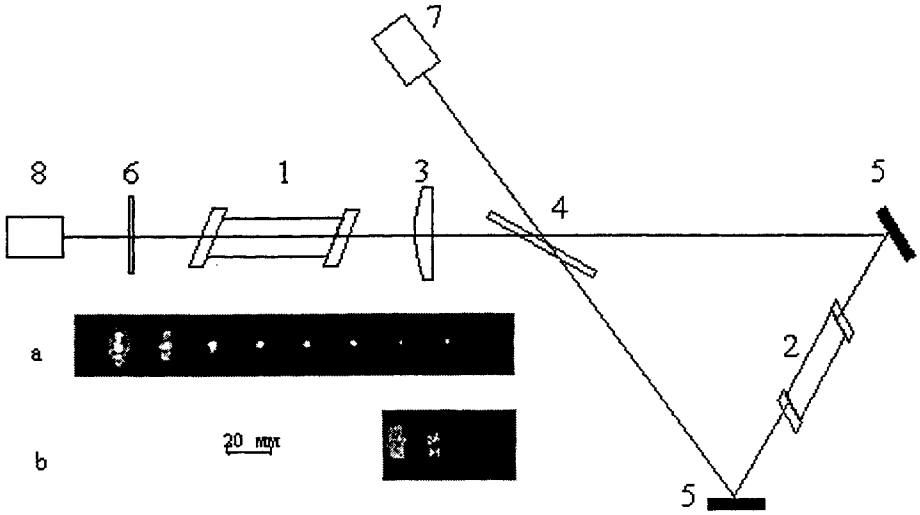


Fig.1. Optical scheme of a $CO_2$ laser with SBS non-linearity in the resonator: 1 - laser medium; 2 – SBS cell, 3 – lens with a focal length of 146 cm; 4 – $BaF_2$ plane-parallel plate; 5 – copper mirrors; 6 – plane resonator mirror; 7 – detectors of radiation power and energy; 8 – detector of power, energy, divergence, and spectral composition of the radiation. a) – far field zone recorded with the help of a 50% wedge in the case of SBS excitation. a) – far field zone recorded in the absence of SBS excitation.

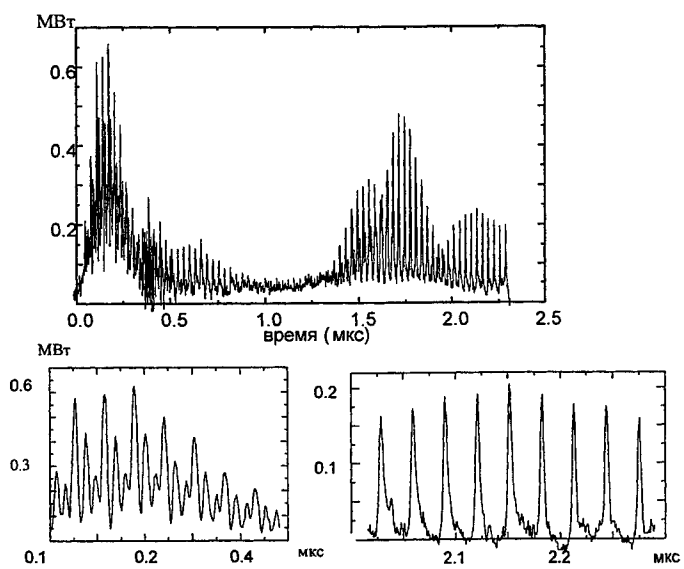


Fig. 2. Time dependent profile of $CO_2$ laser radiation power in the case of SBS excitation and fine structure of the pulse at the beginning and end of oscillation.

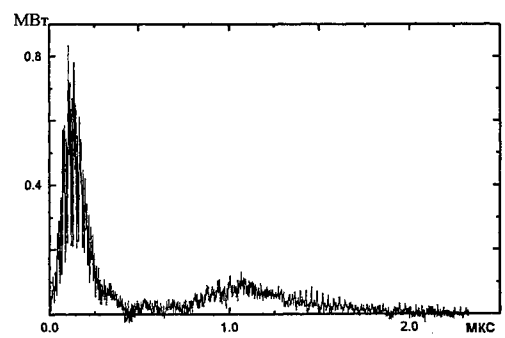


Fig.3. Time dependent profile of $CO_2$ laser radiation power in the absence of SBS excitation.

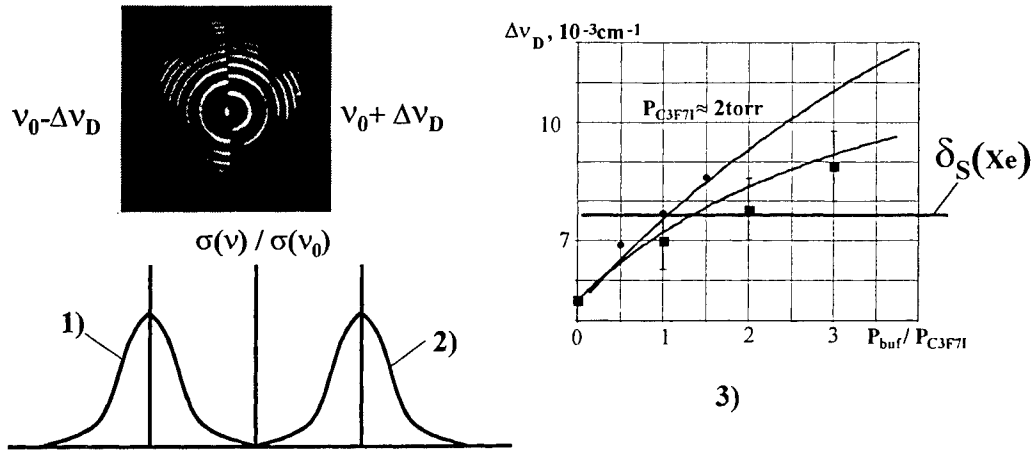


Fig.4. Demonstration of amplification line splitting in iodine laser with longitudinal supersonic gas flow. 1-amplification line for radiation passing with gas flow. 2-amplification line for radiation in opposite direction. 3-amplification line splitting in supersonic gas flow in the iodine laser resonator for various composition of laser medium.

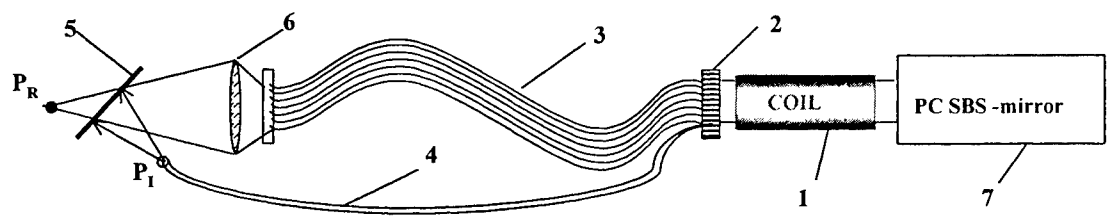


Fig.5. Concept of COIL with SBS mirror and fiber assembly.1 - longitudinal gas flow COIL, 2 - kinoform lenses array , 3 - fibers assemble, 4 - feedback fiber, 5 - feedback mirror, 6 - focusing lens, 7 -phase conjugation SBS mirror with kinoform array, $P_R$ - real focal point of high power beam, $P_I$ - image of focal point

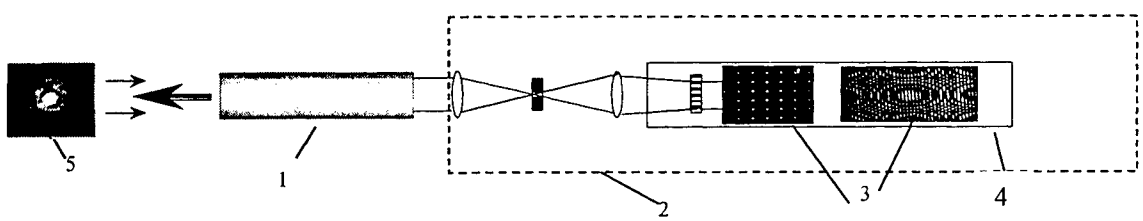


Fig.6. Demonstration of radiation phasing in iodine laser with SBS mirror and beam splitting by kinoform array. 1 - iodine laser, 2 - SBS mirror with kinoform array, 3 - pump beam picture at array focal plane, 4 - SBS cell, 5 - far field picture of output beam

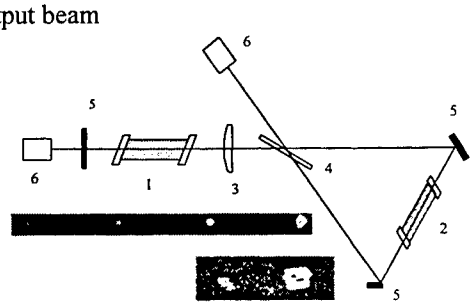


Fig.7. Optical scheme of a iodine laser with SBS non-linearity in the resonator: 1 - laser medium; 2 – SBS cell, 3 – lens; 4 – R =0.13 mirror; 5 – R=0.99 mirrors; 6 – detectors of radiation power, energy, and divergence.

# Slab laser mode control

K. M. Abramski, E. F. Pliński, J. S. Witkowski

Institute of Telecommunications and Acoustics
Laser and Fiber Electronics Group
Wrocław University of Technology
Wybrzeże Wyspiańskiego 27, 50-370 Wrocław, Poland
tel.:(+48) (71) 320 25 05, fax: (+48) (71) 320 31 89, e-mail: kma@zr.ita.pwr.wroc.pl

## ABSTRACT

Each mode inside a rectangular slab-waveguide laser consists of four quasi plane waves propagating at small angles to its axis and inducing specific grating of the refractive index in the slab medium. Multimode operation of such laser is a superposition of single modes. Each mode can be spatially separated into two high quality lobes with $M^2$ parameter near 1. When geometry of the slab is controlled, high stability of a mode pattern can be obtained. This effect is particularly strong when extra single mode selection (for example Talbot filtering) is applied. The experimental evidences were performed on a RF excited $CO_2$ slab-waveguide laser.

**Keywords**, slab lasers, four-wave mixing, $CO_2$ lasers, laser modes

## 1. INTRODUCTION

The planar-waveguide geometry of the laser, so called slab or large area laser, is currently of great interest through their potential for the development of ultra-compact, high power lasers. This concept has been developed for basic types of: gas lasers [1], solid-state lasers [2], and semiconductor lasers [3]. The slab laser of the length $L$ has a

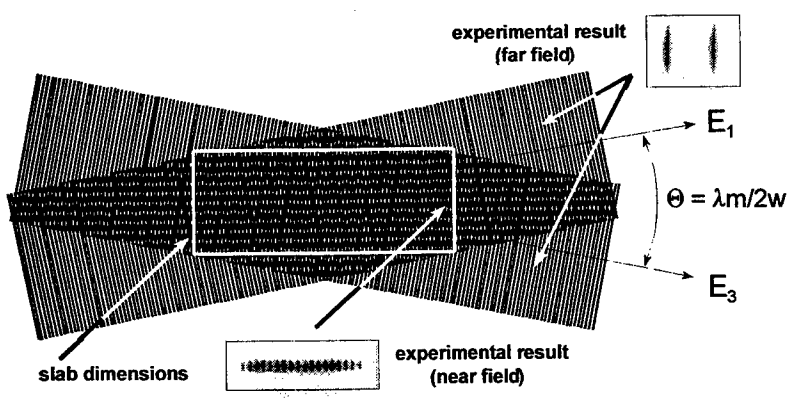


Fig. 1. Two standing wave model of waveguide $EH_{20,1}$ mode forming in a slab laser.

box-like shape were the transverse dimension $a$ is much smaller compare to the lateral dimension $w$. As a result of it the large difference between lateral $N_x = w^2/\lambda L >> 1$ and transvere $N_y = a^2/\lambda L \geq 1$ Fresnel numbers occurs. We will refer to this configuration simply as a slab-waveguide one. The lasers with slab-waveguide resonators have the advantages of attaining high uniformity of gain saturation and consequently highest output powers. The slab-waveguide resonator is characterised by its own oscillations or modes. The ideal, unperturbed amplitude profile of these modes is given by:

$$E_{mn}(x,y) = E_0 \begin{matrix}\cos\\ \sin\end{matrix}\left(\frac{m\pi x}{w}\right)\begin{matrix}\cos\\ \sin\end{matrix}\left(\frac{n\pi y}{a}\right), \qquad \text{where } \left.\begin{matrix}\cos\\ \sin\end{matrix}\right\} \text{ for } m, n \left\{\begin{matrix}\text{odd}\\ \text{even}\end{matrix}\right\} \text{integers}, \tag{1}$$

This waveguide mode is called $EH_{mn}$. In general case the output of the laser can be a mixture of a few $EH_{mn}$ modes. The number and the order of modes depend on the gain spectrum of the laser medium. The consequence of the small Fresnel

XIII International Symposium on Gas Flow and Chemical Lasers and High-Power Laser Conference,
Antonio Lapucci, Marco Ciofini, Editors, Proceedings of SPIE Vol. 4184 (2001)

number for the transverse dimension is the fundamental waveguide mode propagation ($n$=1). The lateral dimension with the large Fresnel number is responsible for propagation of high order waveguide modes ($m$.>>1). One selected mode $EH_{m1}$ formed in the slab-waveguide structure can be imagine as the picture of two standing plane waves interfering at the angle $\Theta=\lambda m/2w$, in a way shown in Fig.1 [4]. The rectangular frame on the interference pattern indicates the borders of the slab. As can be seen from the model in Fig. 1 the interference pattern on both mirror planes consists of 10 interference maximums and 10 minima, creating the $EH_{20,1}$ mode.

## 2. INDUCED GRATINGS IN SLAB LASERS

Four-wave mixing (FWM) is the one of the main techniques of non-linear optics. The interaction of coherent waves in optical media can be understood as a forming of an optical grating due to interference in a mixing region [5]. Crossing of two running waves $E_1$ and $E_2$ (pumping waves) and the third one $E_3$ (probe wave) induces a periodic spatial modulation of optical nonlinear material (Fig.2) as a grating (phase or amplitude) of refractive index. When all waves have the same frequency (degenerate mixing), the grating is static. It looks like a "frozen" ultrasound wave. The $E_1$ and $E_3$ waves induce a grating of refractive index with a period $\Lambda$ given by formula

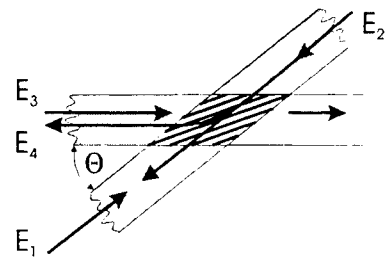


Fig. 2. The illustration of degenerate four-wave mixing

$$\Lambda = \frac{\lambda}{2n_r \sin(\Theta/2)}, \tag{2}$$

where: $\Theta$ - angle between $E_1$ and $E_3$ waves, $\lambda$ - light wavelength, $n_r$ - refractive index of medium. The grating of length $L$ fulfils conditions for the Bragg or thick holographic grating when the Klein-Cook parameter $Q$ [6]:

$$Q = \frac{2\pi L\lambda}{\Lambda^2 n_r} >> 1. \tag{3}$$

For this condition the grating created by the $E_1/E_3$ waves is thick enough to diffract in Bragg manner the part of $E_2$ into the $E_4$ wave, so called a phase conjugate reflected wave. The reflection coefficient $R$ defined as the ratio of the diffracted wave intensity $I_4$ to the probe wave intensity $I_3$ takes the form [7]:

$$R = \frac{I_4}{I_3} = tan^2\left(\frac{\pi}{\lambda}\Delta nL\right), \tag{4}$$

where: $\Delta n$ is the amplitude of refractive index changes induced by $E_1/E_3$ Bragg grating. One can see the full analogy between the model of wave structure in the slab laser (see Fig.1) and a diffraction grating structure created in the four-wave mixing process (Fig.2). Four wave crossing itself introduces interference in the frame of nonlinear medium. The gain and absorbing media are good candidates for the four-wave mixing. The dominant role in the process of four-wave mixing plays so called the large period grating illustrated in Fig.1 with the period given by formula (2). Depending on the nature of nonlinear medium described generally by a complex refractive index $n_r(I,\nu)$, ($I$ is the intensity of radiation and $\nu$ is the frequency of the light), we can distinguish three kinds of gratings. The amplitude gratings, when the wave interference induces only the modulation of an imaginary part of a refractive index (absorptive/gain media), or the phase gratings, when only a real part of a refractive index is modulated (typical for ultrasound waves). The mixed grating can also appear, when both above effects occur.

Assuming a homogeneously broadened laser gain transition as it is for waveguide $CO_2$ lasers under the experimental conditions used, the general form of the medium susceptibility, $\chi$, is given by [8, 9]:

$$\chi(I,\Delta) = \frac{2g_0}{k}\frac{i+\Delta}{1+\Delta^2+I/I_S}, \tag{5}$$

where: $k=2\pi/\lambda$, $g_0$ is the small signal gain, $I_s$ is the saturation intensity, $I$ is the intracavity intensity, $\Delta$ is the normalised frequency detuning from the line centre $\omega_0$, given by $\Delta=2(\omega-\omega_0)/\Delta\omega$, where $\Delta\omega$ is the width of emission line. The change of refractive index $\Delta n_r(I,\Delta)$ induced by the wave with the intensity $I$ is given by:

$$\Delta n_r(I,\Delta)=\frac{1}{2}\chi(I,\Delta)=\frac{g_0}{k}\left(\frac{i+\Delta}{(1+\Delta^2)^2}\frac{I}{I_S}\right)=\Delta n_r'+i\Delta n_r''. \tag{6}$$

In the case of two intersecting standing waves, eq. (6) may be used to define either a system of two phase gratings (real part $\Delta n_r'$ responsible for the phase grating) or two amplitude gratings (imaginary part $\Delta n_r''$ responsible for the amplitude grating):

$$\Delta n_r'=\frac{g_0}{k}\frac{\Delta}{\left(1+\Delta^2\right)^2}\frac{I}{I_S}, \qquad \text{and} \qquad \Delta n_r''=\frac{g_0}{k}\frac{1}{\left(1+\Delta^2\right)^2}\frac{I}{I_S}. \tag{7}$$

For the case of $CO_2$ slab-waveguide lasers, laser oscillation is usually quite close to the line centre ($\Delta<<1$) because of the phenomenon of line hopping. Bellow, we consider only the case of the amplitude grating formed in the laser medium. Assuming typical conditions of RF excited slab-waveguide $CO_2$ laser operation (the saturation parameter $I/I_s \approx 1$, the small signal gain $g_0 = 0.3$ m$^{-1}$, $\lambda = 10.6$ μm., [10]), the estimated changes of the refractive index $\boldsymbol{\Delta n_r'' \approx 0.5\ 10^{-6}}$.

## 3. SELF-PHASE-LOCKING EFFECT OF MODE CONTOL

According to the discussion presented above sepatate single mode induces an amplitude grating with the Klein-Cook parameter $Q$ depending on the mode $EH_{nl}$ order. Assuming that the grating fulfils the Bragg condition there will be four elementary Bragg diffractions at the common grating formed inside the slab resonator. The Fig.3 explains this phenomenon, for example: $E_1'$ is a part of the wave $E_4$ (diffracted at the common Bragg grating) running in phase with $E_2$. Three more similar coupling patters can be recognised similarly, as is shown in Fig. 3. All above effects are responsible for i nternal mutual coupling between all mentioned waves. This phenomenon should cause self-stabilisation of the laser mode. It means that such self-sustained laser mode with the internal coupling should be more resistive to the lateral distortion of the refractive index.

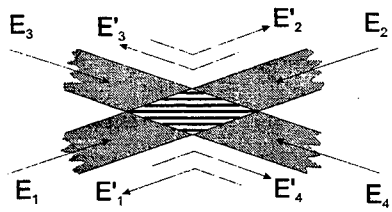


Fig. 3. Explanation of four elementary Bragg diffraction effects in the slab laser.

We have investigated this effect in the RF excited slab-waveguide $CO_2$ laser operating on $\lambda = 10.6$ μm. with the slab dimensions: $L = 400$ mm, $w = 20.7$ mm, $a = 2$ mm [4]. According to (3), the Klein-Cook parameter $Q$ depends on the period $\Lambda = w/m$. of the grating. The length $L$ of the slab is an equivalent of the Bragg grating length (see Fig .1 and Fig. 2). The main requirement for the mode order $m$, which ensures effective Bragg diffraction, can be written as:

$$m >> w\sqrt{\frac{n_r}{2\pi\lambda L}} \tag{8}$$

The Bragg condition requires smaller $\Lambda$. For our slab waveguide geometry the condition $Q>1$ is satisfied for $m=5$, $Q(m=5) = 1.7$. To estimate the Bragg reflection of one diffracted beam (see Fig.2) as the result of the four-wave mixing process under our experimental conditions in slab $CO_2$ laser, we consider only the amplitude induced Bragg grating ($\Delta n_r = \Delta n_r''$). The elementary estimation from formula (4) reflection $\boldsymbol{R \approx 7\ 10^{-3}}$, which is the measure of the internal coupling. To say more clear, for our slab laser with the output power of 100W, with 10% transmission of the output coupler mirror, we can estimated the internally oscillating power in the slab resonator approximately 10 times higher, it means 1kW shared in two waves. This allows estimating the power of each wave as high as about 500W. According to (4) the power of 0.35W is diffracted in the Bragg manner.

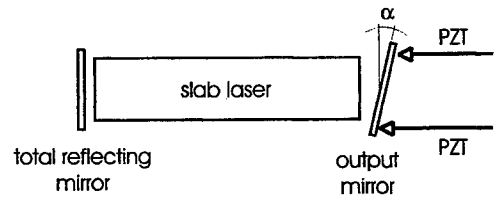


Fig. 4. The scheme of pure mirror tilting.

To find the evidences of coupling caused by the mutual leaking of the Bragg diffracted waves in the slab we observed the mode structure of the laser, multi-mode and single-mode operation. The number of gratings appearing is equal to the number of oscillating modes. For multi-mode case they overlap and saturate the gain inside of the total slab volume washing-out any induced grating. For this case we can not expect any effect of FWM. For single-mode operation, when the induced grating is very well defined, we can expect the mutual coupling of the Bragg diffracted waves. Because the internal coupling improves the self-stabilisation of the waveguide mode, one can expect higher resistance to the lateral disturbances of the laser resonator. As a measure of the coupling effect we introduce the angle

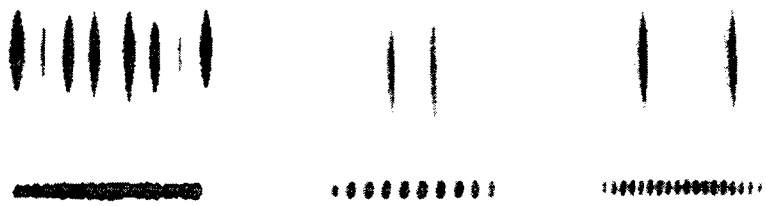

$\alpha_{lock} \approx 20$ μrad $\alpha_{lock} \approx 60$ μrad $\alpha_{lock} \approx 70$ μrad

Fig. 5. Three cases of the output mode pattern from the slab-waveguide laser: multimode (left), single $EH_{10,1}$ mode (middle), single $EH_{20,1}$ (rigth), registered at near-field plane (lower pictures), and the far-field plane (upper pictures).

$\alpha_{lock}$ of mirror tilting throughout which the single mode is still kept. The continuation of the tilting causes jumping of laser operation into the new mode. The Fig. 4 explains the measurement procedure. The pure mirror tilting was obtained by precise PZT mirror driving. Three cases of the laser operation registered for near and far field planes (Fig. 5). The Fig. 5a illustrates the multi-mode operation of the slab laser. As can be seen, the near field for this case is almost totally filled up with the laser radiation and any grating structure can be identified. In that case the laser operated in four modes which are better recognised in the far field. The locking angle $\alpha_{lock}$ of the laser mode, did not exceed **20 μrad** for this structure (for each mode). Forcing the laser to the single-mode operation, in the $EH_{10,1}$ (Fig. 5b) or $EH_{20,1}$ (Fig. 5c) modes, we found the locking angles $\alpha_{lock}$ = **60 μrad** and $\alpha_{lock}$ = **70 μrad**, respectively. So, the single mode operation accepts much higher lateral tilting. It can be explained by self-stabilising mechanism caused by the internal Bragg FWM coupling between the running waves inside the slab resonator. For the $EH_{10,1}$ mode the Klein-Cook parameter was $Q = 6.7$ and for the $EH_{20,1}$ mode $Q = 24.8$, and they fulfil conditions for the Bragg diffraction.

## CONCLUSIONS

The effect of four-wave mixing in the nonlinear lasing medium in the slab-waveguide laser has been demonstrated. We emphasised the analogy between four-wave mixing and the mode structure inside the slab-waveguide resonator. As a result of it the self-control of high order slab-waveguide modes was observed. The effect is not very strong in gas media. One can, however, expect much more effective four-wave mixing process in solid state and semiconductor lasers, because of their high gain. The Bragg induced gratings formed in such slab structures can have larger contrast and should be more stable.

## REFERENCES


[1]. K.M.Abramski, A.D.Colley, H.J.Baker, D.R.Hall, "Power scaling of large-area transverse radio frequency discharge $CO_2$ lasers", Appl.Phys.Lett. 54, pp. 1833-1835, 1989, No. 19.

[2]. T.J.Warburton, D.P.Shephard, A.C.Tropper, D.C.Hanna, "A thermally bonded Nd:YAG planar waveguide laser and amplifier", CLEO/Europe'96, Hamburg, paper CFH6, p. 347, 1996.

[3]. A.Larsson, M.Mittlestein, Y.Arakava, A.Yariv, "High efficiency broad area single quantum well lasers with narrow single-lobed farfield pattern prepared by MBE", Electron Lett. 22, 79-81, 1986, No. 2.

[4]. E.F.Plinski, K.M.Abramski, J.S.Witkowski, "Optical resonators for slab-waveguide lasers" in *Optical Resonators – Science and Engineering*, ed. Ram Kossowski, Miroslav Jelinek and Josef Novak, Kluwer Academic Publishers, Dordrecht, Boston, London, 1998.

[5]. H.J.Eichler, P.Gunter, D.W.Pohl, *Laser-Induced Dynamic Gratings*, Springer-Verlag, Berlin, 1986.

[6]. W.R.Klein, B.D.Cook, W.G.Mayer, "Light diffraction by ultrasonic gratings", Acustica, **15**, 67-74, 1965, No. 2.

[7]. A. Yariv, *Optical Electronics*, Holt, Reinhart and Winston, New York, ch. 16, 1985,.

[8]. A.Yariv, *Quantum electronics*, Wiley, New York, p. 149, 1975.

[9]. K.M.Abramski H.J.Baker, A.D.Colley, D.R.Hall, „Phase-locked operation of intersecting $CO_2$ waveguide lasers by four-wave mixing", Opt.Commun. 90, pp. 61-64, 1992.

[10]. K.M.Abramski, "Methods of analysis, control and locking of gas laser frequencies", Monograph No. 36 of Wroclaw University of Technology, ch. 6, 1993, in Polish.

# Spatial and temporal characteristics of an industrial cw $CO_2$ laser beam

G. Rabczuk*, M. Sawczak, G. Śliwiński

Institute of Fluid Flow Machinery, Polish Academy of Sciences,

Fiszera 14, PL 80-952, Gdańsk, Poland,

## ABSTRACT

The spatial and temporal characteristics of the laser beam extracted from the industrial high power cw $CO_2$ laser are investigated experimentally and analysed. The beam properties are compared for two optical stable cavity configurations characterised by the different values of the Fresnel number. It is found that the beam shape fluctuations, observed for both cavities, are mainly due to the mechanical vibrations of the laser construction. The cavity of the lower Fresnel number emits the beam of better quality and provides better focussing condition in the processing zone.

**Keywords:** High power cw $CO_2$ laser, measurements, laser beam properties

## 1. INTRODUCTION

Increasing requirements for a high quality material processing stimulate investigations of the space and temporal behaviour of the laser radiation. It is known that in the case of a high power, transverse-flow, DC excited $CO_2$ lasers the fluctuations of the active medium parameters and resonator properties produce variations in the laser output beam characteristics. Mechanical vibrations of the optical cavity elements, fluctuations of the active medium density and the gain and saturation intensity variations are considered to be the main factors responsible for the instabilities of the laser beam parameters [1-3]. They can influence strongly the quality of the industrial processes accomplished by the laser devices.

The purpose of this paper is to analyse the stability of the output beam characteristics for the industrial, transverse-flow, cw $CO_2$ laser [4] excited by a self-sustained DC electric discharge and working at the output power range up to 1.2 kW. The laser serves as a processing tool for cutting, hardening and surface treatment so the analysis of the factors influencing the stability of the laser output parameters is essential. Parameters characterizing the output beam are investigated for two resonator configurations described by the different optical and active medium length. Results concerning the laser power stability, temporal behaviour of the beam intensity distributions and beam propagation characteristics are discussed.

## 2. EXPERIMENTAL PROCEDURE AND RESULTS

### 2.1. Laser resonator characteristics.

Measurements of the beam parameters were performed for a transverse flow cw $CO_2$ laser source used for industrial purposes and operating typically at 500 – 1000W. The laser output characteristics are controlled by the pressure of the working mixture ($CO_2$:$N_2$:He =1:9:15) in the range of 30-40 Torr and the excitation current of 7 –10 A. The optical cavity is a half-symmetric, stable resonator folded in the flow direction in order to cover the whole cross-section of the active medium with the field radiation. The resonator optics comprises mirrors of circular symmetry with the effective diameter of 20 mm. In the three-pass configuration (n=3), two flat folding reflectors are used while in the four-pass configuration (n=4) three reflectors fold the beam path across the discharge chamber. The resonator length of the three-and four-pass configuration is 3.9 m and 5.2m, respectively. The radius of curvature of the inner concave-convex ZnSe output coupler of 50% reflectivity equals 10 m. The Fresnel numbers of considered resonator configurations are $N_f$ = 2.42 for a three-pass cavity and $N_f$ = 1.81 for n = 4. The resonator is mounted inside the chamber, and the beam is extracted through the antireflection-coated flat window (ZnSe) of 99.5% transmittance. The laser output beam is guided to the processing region

* Correspondence: E-mail: rabczuk@imp.pg.gda.pl

XIII International Symposium on Gas Flow and Chemical Lasers and High-Power Laser Conference,
Antonio Lapucci, Marco Ciofini, Editors, Proceedings of SPIE Vol. 4184 (2001)

by the optical train of 4.3m in length, composed by three flat mirrors. The beam measurements were performed for the laser working at 1kW, in the region close to the focal plane of a focusing lens (ZnSe, f = 127 mm.) incorporated into the processing head closing the beam guiding system.

### 2.2. Beam shape and output beam power stability measurements

The temporal behavior of the laser beam was investigated by the detailed analysis of the power density distributions recorded at the different time instants. They were measured with the use of a diagnostic system[5] developed at IF-FM for monitoring the laser beam properties. The instrument uses a hollow rotating needle with a pinhole of a diameter chosen respectively to the size of the analysed beam. The recorded spatial beam profiles are represented by a two-dimensional, 60x60 array of values corresponding to the local power densities, which are measured versus the pinhole location in the beam zone by the IR detector. Recording time of the two-dimensional beam profile amounts to 1.6 s.

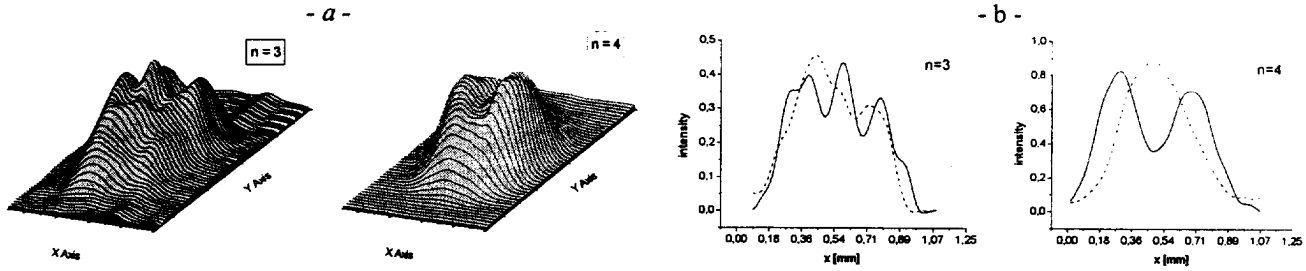


Fig. 1. Average beam power density distribution for 3- and 4-pass cavity (*a*), and typical beam profiles between the beam oscillates (*b*)

The examples of the laser power density distributions across the laser beam recorded for three- and four- pass cavity are shown in Fig. 1a. Although the values of the Fresnel numbers of the investigated resonators are not so much different (1.8 and 2.4), the differences in the beam shape are distinct. The four-pass cavity characterised by the less value of $N_f$ and thus higher diffraction losses, produces the beam of a simpler spatial structure, determined by the superposition of the lower order modes (e.g. $TEM_{00}$ and $TEM_{01}$). In the case of three-pass resonator, the mode structure is more complex and it can be ascribed to the superposition of $TEM_{00}$, $TEM_{01}$ and $TEM_{02}$.

The beam symmetry is determined by the symmetry of the optical system as well as by the symmetry of the active medium parameters. A non-uniform gain profile, typical for $CO_2$ transverse-flow lasers, is responsible for symmetry distortions of the recorded power density distributions. It is also the reason for the different mode structure of the field distributions measured in the directions orthogonal to the beam axis. Different level of the symmetry distortions observed for the four and three-pass cavity is due to the differences in the aligning accuracy related to the different optical lengths of the cavities under consideration.

In order to detect the beam shape changes faster than those described above, the option of the scanner operation allowing for the fast recording of 1D cross-sectional profiles was used. In the experiment 1200 profiles through the fixed cross-section of the beam were recorded during 30s as a single 1200x60 matrix. Each row of 1200x60 matrix represents the beam profile given by 60 measurement points corresponding to 60 different locations of the rotating pinhole in the radiation field. One cross-sectional profile is recorded during 0.3 ms. Successive rows give the beam profiles recorded at time intervals of 28 ms. Reading the 1200x60 matrix by "columns" gives the temporal variations of the local value of the beam intensity corresponding to the same position of the rotating pinhole in relation to the beam gravity center.

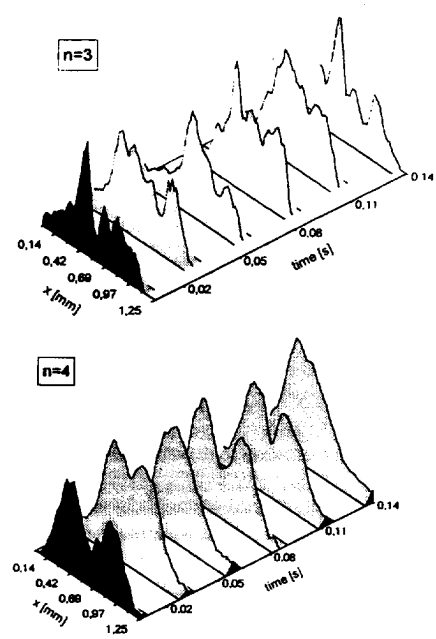


Fig. 2. 1D profiles registered in the x-direction for 3- and 4-pass resonator. Profiles recorded during 0.14s at time intervals of 28 ms

The detailed analysis of 1D profiles shows that for both considered cavity configurations the beam shape fluctuates between characteristic profiles, which are depicted in Fig.1b This conclusion is supported by the profile records given in

Fig.2. For the three-pass cavity the beam profile fluctuates between the double lobes mode and the one with a central maximum surrounded by two lobes of lower intensity. In the four-pass cavity case, the beam profile changes from the double lobes mode to a single one of $TEM_{00}$ type and then it attains its former shape. The observed fluctuations of the beam profiles occur periodically with the period of about 80 ms what corresponds to the oscillation frequency of 12 Hz.

*a)* *b)*

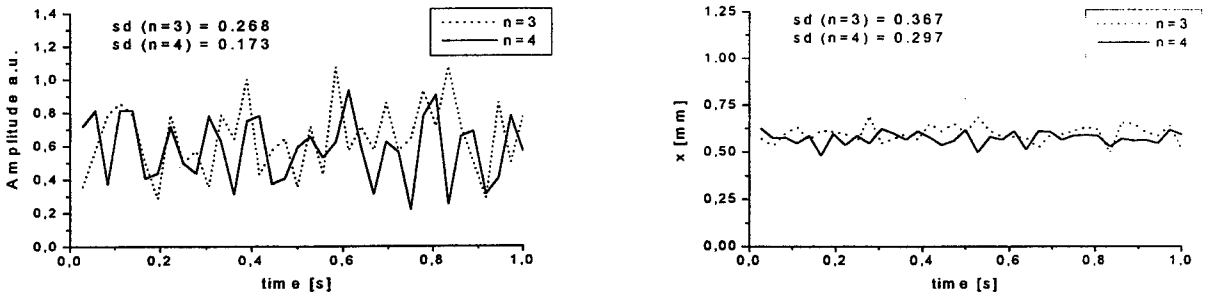


Fig. 3. Time variations of the local value of the beam intensity (*a*) and the position of the beam gravity centre calculated as the first moment of the recorded field distributions (*b*) - for two resonators configuration. The '*sd*' parameter indicates the standard deviation of the field intensity and position of the first moment, respectively.

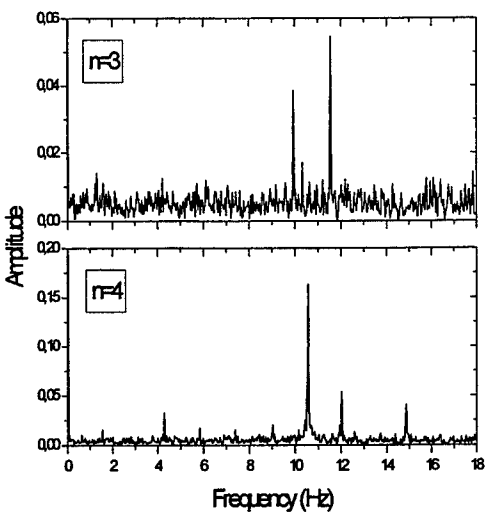


Fig. 4. Comparison of FFT spectra characteristic for 3- and 4-pass resonator

Time variations of the local value of the beam intensity, corresponding to the same position of the rotating pinhole, close to the beam center, are compared for both investigated resonators in Fig.3a. Fluctuations of the position of the beam gravity centre calculated as the first moment of the recorded distributions are depicted in Fig 3b. For three- pass cavity the local value of the beam intensity as well as the beam gravity centre are subject to the fluctuations of higher amplitude compare to those recorded for the four–pass cavity. It indicates that the mode structure of the beam from the four–pass cavity is more stable in time than the one with higher content of the higher order modes produced by three-pass cavity.

The FFT frequency spectra of the beam intensity oscillation for both cavity configurations are presented in Fig. 4. The components corresponding to the frequencies from the range of 10 – 16 Hz can be identified as the oscillations due to the mechanical vibrations of the laser construction[6]. Note that the frequency of abt. 12 Hz was also found as a frequency of the beam shape fluctuations (Fig.2). Higher amplitude values of the FFT components, found for the four–pass cavity prove its higher sensitivity to the mechanical vibrations.

### 2.3. Beam propagation characteristics

In order to determine the beam quality factor and the far field divergence the beam power density distributions were recorded at several locations in relation to the focal plane of the focusing lens. At each location, the beam diameters were calculated on the base of the second moments of the recorded spatial power distributions. The characteristic beam parameters were determined from the propagation law of the laser beam. The hyperbolic fit to the data following the beam profiles measurements allows to find the beam quality parameter $M^2$, size of the beam waist and its location. The results concerning the beam diameters measurements, performed for the considered cavities, are gathered in Fig.5 and Table 1. In the case of three-pass resonator the beam quality parameter $M^2$ was estimated to be in the range 3.5 -4.1 while for the four-pass resonator the value of $M^2$ concluded from the measurements was abt 2.1-3.2. These results confirm our previous conclusions concerning the different mode content of the beam from the cavities of n=3 and n=4. The cavity of the lower Fresnel number emits the beam of the better quality and provides condition for the smaller size of the focused beam waist and thus for the higher power densities in the processing zone. The beam asymmetry ($d_x \neq . d_y$) is noticeably higher for the four pass cavity and is described by differences observed for the beam waist as well as for the divergence values measured in two transverse directions. It is mainly the result of the different mode content of the beam profiles along the x- and y-directions, especially noticeable for the four-pass cavity case.

Tab. 1. Parameters of the 1kW laser beam focused by a lens of 127 mm focal length

| | focus diameter [mm] | divergence [rad] | $M^2$ |
|---|---|---|---|
| 3-pass resonator | $d_x = 0{,}36$ / $d_y = 0.33$ | $\theta_x = 0.16$ / $\theta_y = 0.15$ | $M_x^2 = 4.11$ / $M_y^2 = 3.53$ |
| 4-pass resonator | $d_x = 0{,}31$ / $d_y = 0.25$ | $\theta_x = 0.15$ / $\theta_y = 0.11$ | $M_x^2 = 3.18$ / $M_y^2 = 2.09$ |

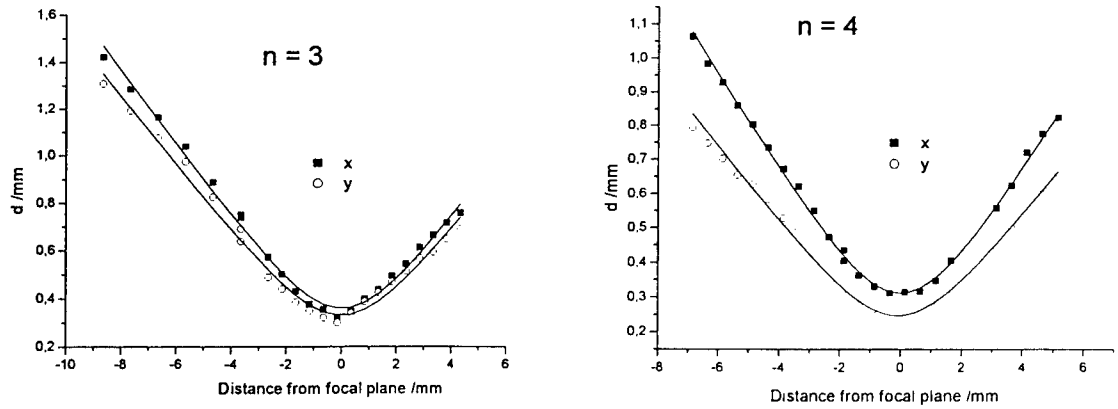


Fig. 5. Beam diameters vs distance from the focal plane of the focusing lens (f=127mm) for the 1kW $CO_2$ laser, measured for the three- and four- pass cavity

## 3. CONCLUSIONS

The aim of the performed analysis was to compare the spatial and temporal characteristics of the radiation beam from the industrial transverse-flow cw $CO_2$ laser for two different stable resonators configurations, characterised by the different Fresnel numbers. The analysis of the temporal behaviour of the laser beam profiles recorded at different instants of time proved that the beam shape fluctuates between characteristic profiles corresponding to the different contents of the lower order modes. From the FFT analysis performed for the intensity signals measured at the fixed point of the beam profiles follows, that the mechanical vibrations of the laser construction are mainly responsible for the observed beam profiles fluctuations. Values of the beam quality parameter and beam divergence calculated from the propagation characteristics confirm the fact that the cavity characterised by the lower Fresnel number emits the beam of the better quality and provides condition for the smaller size of the focused beam waist and thus for the higher power densities in the processing zone.

## ACKNOWLEDGEMENTS

This work was sponsored by the National Scientific Committee within Project PB1419/T11/98/14.

## REFERENCES

1. V. S. Golubev, F. V. Lebedev, "Stability of the emission from fast-glow discharge industrial $CO_2$ laser", Kwantowaja Elektronika 12, 663, (1985)
2. J. L. Neira, J. Delgado, G. Calvo, M. Sanchez, "Influence of active medium fluctuations on high power laser amplifier performances, SPIE 1276 (1990)
3. G. Śliwiński, G. Rabczuk, "Characterization of the temporal behaviour of a high power $CO_2$ laser radiation properties IF-FM Report 262/98 (1998)
4. P. Kukiełło, G. Rabczuk, "High-power cw $CO_2$ transverse flow laser with a stable multipass cavity. Comparative study" *Laser and Particle Beams*, Vol.10,no. 4, pp.865-870,1992
5. G. Rabczuk, M. Sawczak, G. Śliwiński," Diagnostic instrument for measurements of a high power $CO_2$ laser beam", SPIE Proc. of VI STL, Szczecin, (1999) (in print)
6. G. Rabczuk, S. Labuda, M. Sawczak, "Experimental study of the high power $CO_2$ laser beam stability" SPIE Proc. of VI STL, Szczecin, (1999) (in print)

# Unstable Resonator for COIL

Wolfgang O. Schall, Thomas Hall, Jürgen Handke
DLR – Institut für Technische Physik, Stuttgart, Germany

## ABSTRACT

An unstable double-pass resonator of the hybrid, confocal type has been designed for outcoupling the radiation of a 10 kW chemical oxygen-iodine laser (COIL) with optimum beam quality. The single pass gain length is 20 cm and the measured small signal gain is 1.1 $m^{-1}$. The near and far field mode distributions have been calculated by solving the Kirchhoff-Fresnel integral for optimum mirror alignment as well as for a misaligned resonator. A particular problem is the provision of glass mirrors with large radii of curvature for the preferred resonator of the positive branch. These radii are a consequence of the low total round trip gain of smaller COILs. The problem has been solved by using one-element adaptive mirrors. A second problem has been identified in the high sensitivity in angular adjustment of the resonator mirrors.

**Keywords**: COIL, unstable resonator, hybrid resonator, adaptive resonator

## 1. INTRODUCTION

At its Lampoldshausen site DLR (German Aerospace Center) operates a supersonic chemical oxygen-iodine laser (COIL) of the 10 kW-class. The flow cross-section in the laser cavity is only 20 x 2.5 $cm^2$ wide. The radiation is coupled out with a conventional stable resonator. For maximum power the optimum coupling mirror transmission is 8%. The resonator has a length of 90 cm, a cross-section of 37 x 25 mm and extracts more than 95% of the power available for output coupling. Rigrod-type measurements with various degrees of coupling have shown a maximum permissible coupling fraction of 30% for the extraction of power[1]. This value corresponds well with direct measurements of the maximum small signal gain coefficient of 1.1 $m^{-1}$ [2].

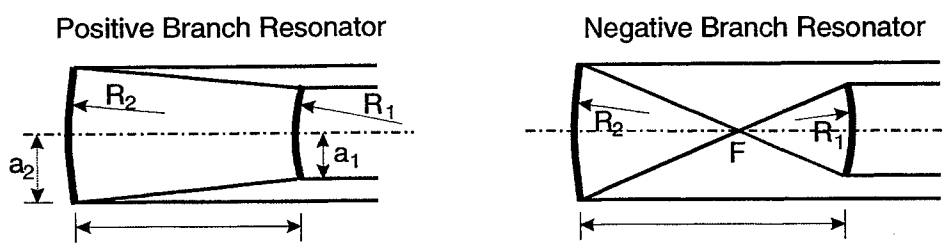


Fig. 1 Principle of unstable confocal resonators with external focus of the mirrors (left) and internal focus (right).

A stable resonator of reasonable dimensions runs in a high multimode and has a large mode volume. It is therefore well suited for the extraction of high powers and it is also easy to align. However, this advantage is associated with a large beam divergence and thus with a beam quality that is far from what is required for the general applications of such a laser. It is well known, that this problem can be overcome with a resonator of the unstable type. As shown in Fig. 1 two basic types of a confocal unstable resonator can be distinguished, one having an external common focus of the mirrors (positive branch resonator) and one with internal focus (negative branch) [3]. The so-called magnification is equal to the ratio of the radii of the two (spherically symmetric) mirrors $M = a_2/a_1$ and describes the outcoupled fraction of the mode volume by simple geometry. M is a measure for the amount of power (intensity) that can be concentrated in the central peak of the far-field mode pattern. Minimum power in the side maxima is obtained only for large M. It is the dilemma of small and medium sized COILs that only a small percentage of the intracavity power can be coupled out without a serious loss in total laser power. This implies a small M and hence a small fraction of power in the central peak, as well as a thin and difficult to adjust output coupling ring for conventional unstable resonators with spherical mirrors [4]. One way for improving this situation has been suggested first by Anan'ev et al. [5] in 1979 and investigated for a COIL by Latham et al. [6] in 1990.

Correspondence: Wolfgang Schall, DLR-Institut für Technische Physik, Postfach 80 03 20, D-70503 Stuttgart, Germany. E-mail: Wolfgang.Schall@dlr.de Fax no. +49 711 6862 715. Internet: www.coil.dlr.de

XIII International Symposium on Gas Flow and Chemical Lasers and High-Power Laser Conference,
Antonio Lapucci, Marco Ciofini, Editors, Proceedings of SPIE Vol. 4184 (2001)

This resonator utilizes an oblique roof top reflector to turn the phase by 90° with each pass. It is relatively elongated, complex and cumbersome to install and to adjust. Nevertheless, this type of resonator has been used successfully by the Dahlian group [7] more recently.

## 2. HYBRID UNSTABLE RESONATOR

For spherically symmetric resonator mirrors the magnification is defined as $M = 1/(1-T^2)$, the transmission T entering with squared power. However, for a one-dimensional, cylindrical mirror the relation is $M = 1/(1-T)$, giving a higher magnification for the same degree of transmission. While being unstable in the curved direction it is of indifferent type (Fabry-Perot) in the other direction. Stability in this direction could be enforced by introducing a slightly focusing element into the resonator. Using only one half of the symmetric arrangement of Fig. 1 doubles the relative size of the now rectangular output coupling aperture. This type of resonator in both configurations according to Fig. 1 has been successfully applied in different versions of $CO_2$ slab lasers [8]. The rectangular cross-section of a COIL cavity, bound by the duct walls on top and bottom and having some extension in flow direction, naturally lends itself for the application of a hybrid resonator. In addition, the setup of such a resonator is rather simple.

For the 10 kW COIL a hybrid, unstable resonator has been considered with the following geometrical characteristics: A double pass configuration in vertical direction is utilized to increase the gain length. The resonator width in the flow direction is equivalent to that of the stable resonator. Under these conditions a simplified numerical analysis of the laser kinetics and an outcoupling of radiation with various degrees of transmission results in an optimum coupling fraction in the range of 13 to 18%, depending on the assumed resonator losses, and the laser stops oscillating at a coupling rate of more than 55%. Hence, an outcoupling with a transmission of 14.5% has been selected for a more detailed numerical inspection. This value corresponds to a magnification of $M = 1.17$. A resonator length of 3 m, basically determined by the given laser geometry, then requires the following mirror radii (definition see fig.1): positive branch resonator $R_1 = -36$ m (convex coupling mirror) and $R_2 = 42$ m (total reflector – back mirror), negative branch resonator $R_1 = 2.77$ m and $R_2 = 3.23$ m. Although the radii of the negative branch resonator seem to be much more conventional, this type has been set aside for a first test because a) of the potential danger of a breakdown at the internal focal point and b) for the necessity of very precise mirror radii. Fig. 2 shows the chosen arrangement schematically. On one side of the cavity the beam is folded and returned by a roof-top reflector. The aperture of the emitted beam has a size of 6 x 11mm. The two passes are separated by 2 mm to reduce mode interference between the two passes.

The two-dimensional near-field distribution of the resonator with the given dimensions has been analyzed numerically in the following manner: Starting with an arbitrary field distribution, for instance on the coupling mirror, the distribution on the total reflector is calculated by solving the Kirchhoff-Fresnel integral. In an iterative procedure this distribution is then used to find the distribution on the first mirror and the procedure is continued until the distribution on one mirror differs between two consecutive runs only by a constant complex factor and is therefore identical in shape. This is the stationary mode distribution of the resonator. The loss of the resonator can be inferred from the complex factor. The calculated near-field mode distribution is shown in Fig. 3. As marked in the figure the fraction of the distribution between 3.2 cm and 3.8 cm leaves the resonator. The actual percentage of outcoupled power is 15.4 % and the losses from radiation escaping in vertical direction amount to 1.7 %. In the far field the distribution assumes the profile shown in Fig. 4. As before it is found from transformation of the de-coupled near field by solving the Kirchhoff-Fresnel integral. More than 95% of the power is contained within a peak of 0.5 x 0.3 mrad divergence (power in the bucket).

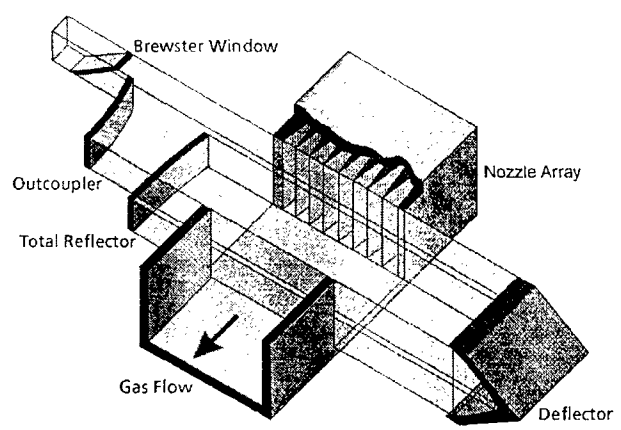


Fig. 2 Principal arrangement of the hybrid double-pass resonator

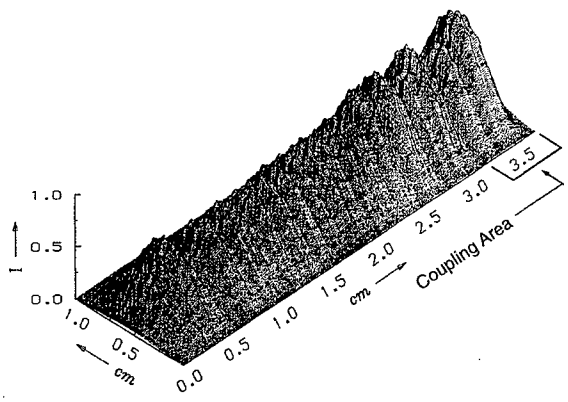


Fig. 3 Calculated Near-field mode distribution

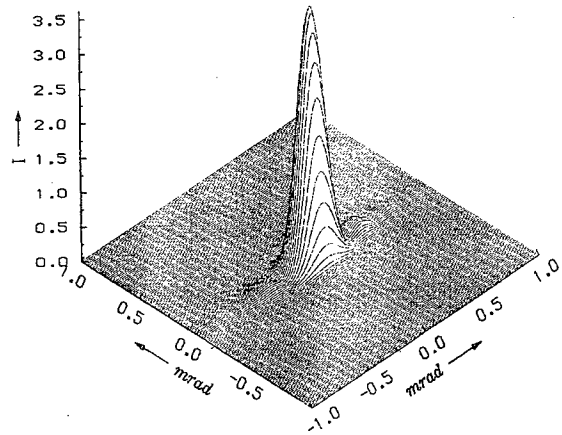


Fig. 4 Calculated far-field mode distribution

## 3. EXPERIMENTAL SETUP

No manufacturer of glass mirror substrates is able to produce mirrors without undue effort with the specified large radii of curvature and sufficient accuracy in a cylindrical geometry. This problem has been overcome by using 4 mm thick glass slabs. If the slabs are securely fixed on one side and a force is exerted on the free side, the slabs are bent to a parabolic shape. In order to match the bending curve most closely to a circle for the mirror shape, the bending force has to be selected such that the free end point of the mirror has the same displacement as a circular mirror surface with the desired radius. The maximum separation of the two curves, and hence the maximum phase difference, is less than one wavelength. The adjustment of the correct bending radius is done in an interferometer by increasing the displacement at the outer edge of the mirror until the correct number of stripes is obtained. As the pushing element a piezo driven "Picomotor" is used from New Focus. The mirror with adjustable displacement at the end point has the feature of a 1-element adaptive mirror. A certain difficulty in adjustment to the correct number of stripes arises from the fact, that the fixture of the mirror slabs is not totally solid. Therefore, with increasing load a tilt is superimposed to the bending, resulting in the appearance of additional stripes. However, since the distances between the stripes from the two sources follow different laws (the stripes from the tilt are equidistant) they can be separated numerically and the loading adjusted accordingly in an iterative procedure. The finite number of stripes, as well as some difficulties to count the correct number limit the accuracy for matching the desired radius of the mirrors to a value of approximately +/-2 m of the nominal radius. Fig. 5 is a photograph of the laser with attached box for the two reflection mirrors.

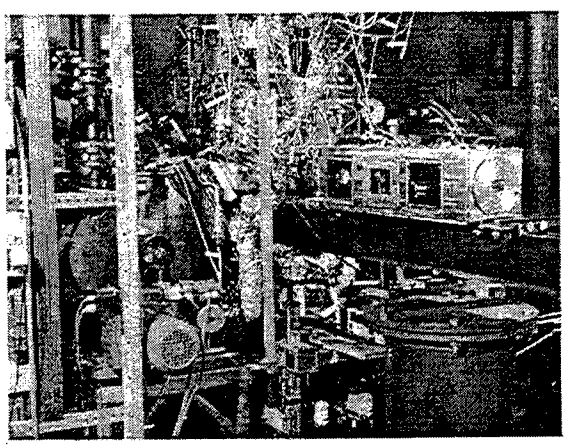

Fig. 5 COIL with attached mirror box

## 4. ALIGNMENT SENSITIVITY CONSIDERATIONS

The resonator is aligned with the aid of two HeNe lasers. The fundamental alignment of each mirror is possible with an accuracy of 0.1 mrad. A basic adjustment can be made by reflecting the HeNe spot on the optical axis back onto itself. If the reflection of the laser mirrors for the HeNe wavelength is sufficient to observe several passes of the beam, then the alignment can be improved. For this purpose the alignment beam is introduced through the coupling opening. Geometric ray tracing calculation tells the necessary offset of the beam spot on the mirrors after each round trip through the resonator. It is expected, that the initial accuracy of the adjustment may not be sufficient for an instantaneous onset of the laser oscillation, i.e. upon flowing the inverted medium into the laser cavity. Therefore, the calculation of the mode distribution has been performed for the situation if one of the mirrors is offset from the ideal alignment angle by a certain degree in order to

determine the resulting coupling and total losses. One result is shown in Fig. 6 for a tilt of one mirror in flow direction. A tilt in outward direction basically increases the outcoupled fraction of power, while a tilt in inward direction quickly results in the loss of power. The situation is further impaired if a tilt in vertical direction is superimposed as well. The scatter of the data is a consequence of a shift in the mode distribution by the tilt. A mismatch of both mirrors at the same time is less significant if the two mirrors maintain a certain parallelity. It can be achieved by adjusting one of the mirrors only. The domain of acceptable angular mismatch is smaller than 100 µrad. Therefore, as suspected, it is unlikely that the laser starts oscillating instantaneously. A computer controlled search strategy will be applied in order to first find laser power at all and later for its optimization. Due to the basic principle of the setup even an adaptive control of the mirror radii is possible.

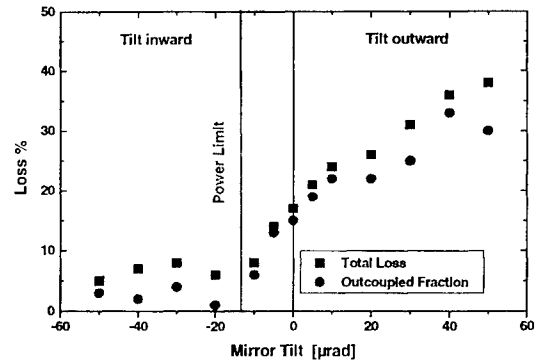


Fig. 6 Alignment sensitivity to mirror tilt in flow direction .

## 5. CONCLUSIONS

A geometrically simple resonator has been designed for extracting a large percentage of power at maximum beam quality from a COIL with small total round trip gain. This resonator is of the hybrid, unstable, confocal type. Computation of the mode field distribution shows excellent beam quality in the far field with over 95% of the outcoupled power within the central peak with 0.3 x 0.5 mrad divergence. One drawback of the resonator in the positive branch configuration with an external focus of the mirrors is the need for cylindrical mirrors with very large radii of curvature. This difficulty has been solved by designing one-point adaptive mirrors with adjustable radius of curvature. The radius of curvature is set in an interferometer prior to the insertion into the resonator. Another difficulty of the resonator is the high accuracy required for the mirror alignment. Since it is higher than achievable by conventional ray adjustment with a HeNe laser beam, a computer controlled mirror alignment will be implemented.

## ACKNOWLEDGEMENTS

The authors wish to express their gratitude to G. Spindler for his valuable advice in the computation of the resonator performance and to F. Duschek for his important contributions with the interferometer.

## REFERENCES

1. J. Handke, K.M. Grünewald, W.O. Schall and L.v. Entress-Fürsteneck, "Power Extraction Investigations for a 10 kW-Class Supersonic COIL", XII GCL/HPL '98, Proc. SPIE Vol. 3574 pp.309-314, 1998.
2. K.M. Grünewald, J. Handke, F. Duschek, "Small Signal Gain and Temperature Profiles in Supersonic COIL", XIII GCL/HPL 2000, paper no. Proc. SPIE this volume.
3. W.F. Krupke and W.R. Sooy, "Properties of an Unstable Confocal Resonator $CO_2$ Laser System", J.Quantum Electronics, Vol. QE-5, no. 12, pp. 575-586, Dec. 1969.
4. Yang Bailing, "Latest advances in COIL at Dalian", XII GCL/HPL '98, Proc. SPIE Vol. 3574 pp.281-289, 1998
5. Yu.A. Anan'ev, V.I. Kuprenyuk and V.E. Sherstobitov, "Properties of unstable resonators with field rotation", Sov. J. Quantum Electron. 9(9) p.1105-1110, Sept . 1979.
6. W.P. Latham, A.H. Paxton and G.C. Dente, "Laser with 90-degree rotation", SPIE Vol.1224, pp.265-282, 1990.
7. Jin Yuqi, Yang Bailing, Zhou Dazheng, Sang Fengting, Duo Liping and Zhuang Qi, "Experimental investigation on a novel unstable resonator for chemical oxygen iodine laser", XII GCL/HPL '98, Proc. SPIE Vol. 3574 pp.564-568, 1998.
8. R. Nowack, H. Opower, U. Schäfer, K. Wessel, Th. Hall, H. Krüger and H. Weber, "High Power $CO_2$ Waveguide Laser of the 1 kW Category", ECO3, Proc. SPIE Vol. 1276, pp.18-28, 1990.

# Adaptive system of laser energy transport with OA LC SLM correction element

Vladimir A.Berenberg, Alexey A.Leshchev, Leonid N.Soms,
Michael V.Vasil'ev, Vladimir Yu.Venediktov
199034, Research Institute for Laser Physics, Birzhevaya, 12, St.-Petersburg, Russia.
Phone: (812) 328-10-93. Fax: (812) 328-58-91. E-mail: vened@ilph.spb.su

## ABSTRACTS

We discuss the system of laser energy delivery to a remote object using joint action of high-sensitive phase conjugation mirror and of dynamic hologram in optically addressed liquid crystal spatial light modulators. This scheme (the scheme of "frozen" phase conjugation) makes it possible to use the advantages of phase conjugation application in laser systems, whose radiation can be hardly subjected to standard methods of phase conjugation.

**Keywords**: adaptive optics, phase conjugation, dynamic holographic correction, Brillouin-enhanced four wave mixing, BEFWM, liquid crystal spatial light modulator

It is well known that application of phase conjugation[1,2] makes it possible to solve numerous tasks of laser optics, such as compensation for laser amplifier distortions, self-delivery of radiation to an object etc., and thus to create sophisticated laser systems of various kinds. However, realization of traditional approaches to phase conjugation, such as stimulated Brillouin scattering (SBS), four-wave mixing in thermal, Brillouin or other media etc. imposes very strict limitations onto the coherent properties of laser radiation, its temporal profile and absolute intensity. Fulfillment of these requirements is often in a contradiction with provision of high efficiency of laser systems, and in many cases the designer of laser system has to reject the use of phase conjugation and to substitute it by more expensive and less efficient tools, such as traditional adaptive optics etc.

Last several years have brought fast progress in development of a little bit different approach to application of nonlinear-optical analogous methods in adaptive optics. It is based on the use of dynamic holographic correction of distortions. The coherent radiation from an auxiliary source, which has passed through the optically inhomogeneous area or optical system, records the hologram together with the undistorted reference wave. This hologram can work as the corrector for distortions. Illuminated by distorted waves, it reconstructs the non-distorted wave.

The use of dynamic holograms has made it possible to provide the real-time correction. Especially interesting and promising are the dynamic holograms in optically addressed spatial light modulators (LC OA SLM)[3] (see Fig.1). Such sandwich-like devices are comprised by several layers. The key layers are that of photoconductor (semiconductor) and of the liquid crystal (LC). The interference pattern illuminates the photoconductor layer The photo-induced charge carriers are accumulated on the boundary of the LC layer, modifying thus the optical properties of the latter. So the efficient thin dynamic hologram can be recorded. To this moment there were realized the values of diffraction efficiency of such holograms, close to its theoretical limit (35-40%)[4]. Recently there was also proposed special approach to such holograms record (blazed holography), promising nearly 100% diffraction efficiency to the working order of diffraction[5,6]. Standard value of sensitivity of such devices fills to the range $10^{-4}..10^{-6}$ J/cm$^2$ (pulsed record). The hologram can be renewed with the repetition rate of 10..1000 Hz and more.

Very important advantage of such device is the thin (plain) nature of the recorded dynamic hologram. It means that the hologram can be efficiently reconstructed in rather wide spectral range and can be thus applied to correction in incoherent and non-monochrome radiation. For example, in the paper[7] the appropriate quality of correction of distortions was observed in the system, working in the overall visible spectral range.

XIII International Symposium on Gas Flow and Chemical Lasers and High-Power Laser Conference,
Antonio Lapucci, Marco Ciofini, Editors, Proceedings of SPIE Vol. 4184 (2001)

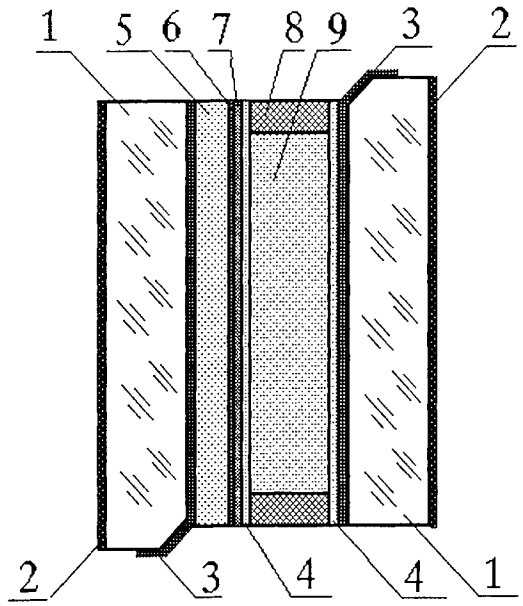


Fig.1. OA LC SLM design: 1 - flat glass substrate, 2 - AR coatings, 3 - transparent electrodes, 4 - alignment layers, 5 - photoconductor, 6 - opaque blocking layer, 7 - dielectric mirror, 8 - spacer, 9 - liquid crystal.

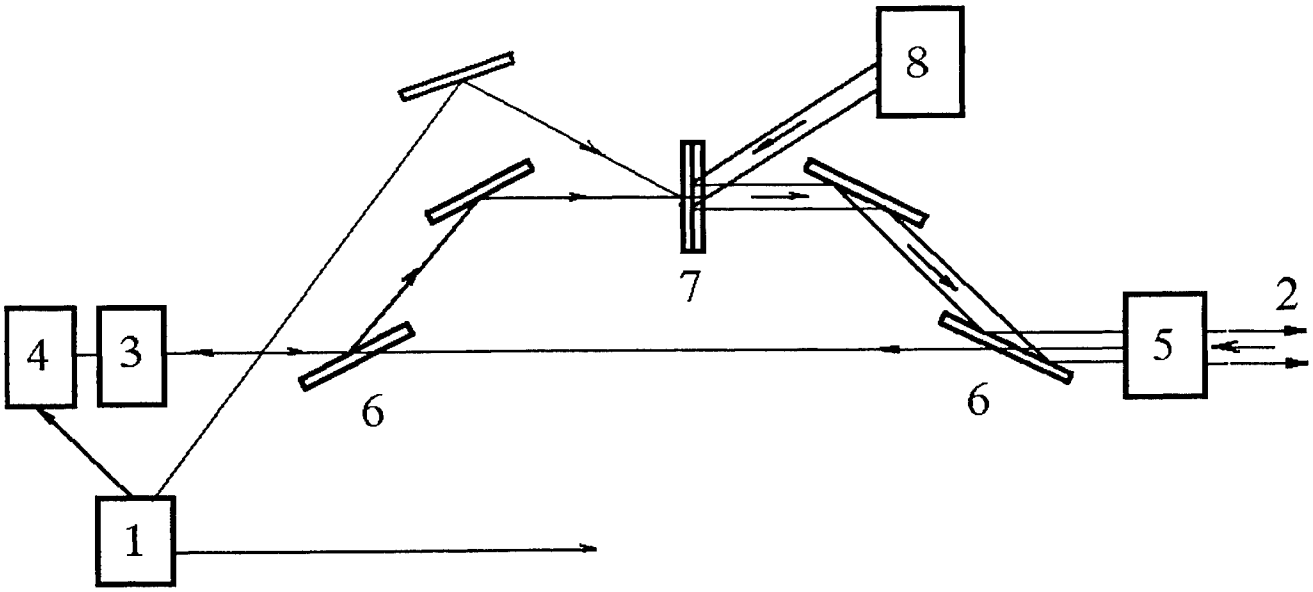


Fig.2. "Frozen" phase conjugation application to radiation delivery to remote object. In the Figure: 1 - laser source of radiation with nanosecond pulse duration, 2 - remote object, 3 - brightness amplifier of nanosecond radiation, 4 - high-sensitive (BEFWM) phase conjugation mirror, 5 - power amplifier, 6 - beam-splitters, 7 - OA LC SLM with internal mirror, 8 - long pulse or CW laser. Direction of radiation propagation is shown by arrows, single line corresponds to propagation of nanosecond pulse radiation and double line - to radiation with long pulse or CW.

The primary goal of developing this technique was caused by possible applications in imaging systems, such as astronomy and Earth surveillance telescopes (see, for example, paper[8], where this technique was applied to the primary mirror of model telescope), microscopes etc. However, the same schematics can be readily applied to correction in various kinds of lasers and lasers systems. The dynamic hologram, recorded in OA LC SLM can successfully replace the four-wave mixing cell (i.e., in fact, the same dynamic hologram) in traditional scheme of phase conjugation. Of course, the damage threshold for such devices is slightly lower than that for traditional phase conjugation media; however, it can be rather high; for example, in the paper[9] was shown the damage threshold for LC SLM of ~0.5 J/cm$^2$ for the Q-switched laser radiation (1.06 μm). Several papers[10-11] already discussed application of such devices to correction of distortions in laser systems, for example, in high-energy picosecond and femtosecond laser systems.

However, direct substitution for traditional phase conjugation mirror is not the only possible application of dynamic holograms in OA LC SLMs in adaptive optics. We describe here more sophisticated approach - the so-called scheme of "frozen" phase conjugation. The essence of the idea is as follows.

One of the most interesting application of phase conjugation is self-delivery of intense laser radiation to remote objects. One can illuminate the zone, containing the scattering or reflecting object, by radiation of auxiliary laser source. Some part of this radiation can be collected by poor-quality telescope, amplified in laser amplifier, phase conjugated, amplified further and sent to the object. In this case the intense radiation is delivered only to the object but not to the other objects. Such schematics is very interesting for the purposes of free-space and atmospheric communications, for various ecology monitoring and for some other tasks. It is well known that for these purposes among all the schematics of phase conjugation there exists one, which is out of any competition - the so-called Brillouin-enhanced four-wave mixing phase conjugation[12,13] technique. Due to some special features of this effect, it is practically insensitive to any sources of noise and can thus reflect (provide phase conjugation) of very weak (down to quantum level of sensitivity - some dozen of photons per resolution mode) signals. It provides not only selection of the weak signal on the intense noise background and its phase conjugation, but also high ($10^6$-$10^{10}$ times) gain of conjugated signal. However, this effect can be realized only with the use of pulses of highly-coherent radiation with nanosecond duration, and hence its direct application to delivery of really intense radiation from efficient laser sources is hardly possible.

We suggest combining two effects - BEFWM phase conjugation and dynamic holography in OA LC SLM - so as to solve this contradiction. One can illuminate the remote object by nanosecond pulse of weak radiation from auxiliary laser, collect scattered radiation, phase conjugate it in BEFWM cell and amplify it up to the level of OA LC SLM sensitivity ($10^{-6}$-$10^{-4}$ J/cm$^2$). Then the conjugated signal can be used for the record of dynamic hologram in OA LC SLM. Such dynamic hologram has much longer lifetime and lacks spectral selectivity. So one can reconstruct it by radiation of low-coherent and efficient lasers source (long pulse, pulse-repetitive or CW), amplify it (if necessary) and then send to the object is in above described scheme. In the Fig.2 is shown one of possible variants of such a scheme realization.

Such a scheme can be realized in the nearest future. Note only one obstacle of technical nature. The specified above parameters of the LC OA SLM are realized in the visual range with wavelength of about 500-700 nm. Information on obtaining such high parameters of the LC OA SLM in the near IR range (about 1 μm) is absent in the literature. However, modulators with the PCL on base of GaAs, amorphous, or crystalline silicon can be used for the range of 1 μm also[14]. There are no any significant physical or technical limitations on the parameters in the near IR range.

The LC OA SLM for the near IR spectral range with sufficiently high parameters can be created, if we use monocrystalline Si as the PCL. Its maximum sensitivity is at wavelength of about 1 μm and not less than the sensitivity of the a-Si:C:H PCL at wavelength of 0.5 μm. The PCL must be fabricated as a mosaic of Schottky diodes with sizes of about 5×5 μm$^2$ and gap of 1-2 μm between them that is necessary for the spatial resolution achievement. The ferroelectric LC with the DHF effect can be used as the modulating medium. The mirror reflectivity, as estimates show, must be 95-99% and transmission of the blocking layer must be about $10^{-4}$. The damage threshold in this case is not less than 50 W/cm$^2$.

## REFERENCES


1. B.Ya.Zeldovitch, N.F.Pilipetsky, V.V.Shkunov. Phase conjugation. Moscow, Nauka, 1985 (in Russian).
2. Optical Phase Conjugation, Ed.by R.A.Fisher. Acad press, USA, 1983.
3. C.Warde, A.D.Fisher, In "Optical Signal Processing", J.L.Homer, ed., Academic Press, NY, 1987, 477.
4. D.V.Wick, Ty Martinez, M.V.Wood, J.M.Wilkes, M.T.Gruneisen, V.A.Berenberg, A.P.Onokhov, L.A.Beresnev, M.V. Vasil'ev, Deformed-helix ferroelectric liquid-crystal spatial light modulator that demonstrates high diffraction efficiency and 370-line pairs/mm resolution. Applied Optics, 1999, Vol. 38, No. 17, pp. 3798-3803.
5. H.Toyoda, Y.Kobayashi, N.Yoshida, Y.Igasaki, T.Hara, M Ishikawa, M.H.Wu, High effisiend electrically-addressable spatial light modulator for reconfigurable optical interconnection, OSA Snowmass Meeting, SLM'99 technical digest, SMB3.
6. I.Percheron, J.T.Baker, M.Gruneisen, Ty Martinez, D.Wick, Blazed holographic optical aberration compensation. Proceedings of the 2nd International Workshop on Adaptive Optics for Industry and Medicine, 1999, pp. 384-387.
7. V.A.Berenberg, A.A.Leshchev, L.N.Soms, M.V.Vasil'ev, V.Yu.Venediktov, A.P.Onokhov, L.A.Beresnev, "Polychromatic dynamic holographic one-way image correction using liquid crystal SLMs," *Opt. Comm.*, v.166, p.181-188, 1999.
8. V.A.Berenberg, A.A.Leshchev, P.M.Semenov, M.V.Vasil'ev and V.Yu.Venediktov. Large numerical aperture imaging bypass system with dynamic holographic correction for primary mirror distortions. Proc.of SPIE, v.3353, p.889, 1998.
9. F.L. Vladimirov, N.I. Pletneva, I.E. Morichev, V.P. Pokrovskiy, L.N. Soms. Liquid Crystal Modulators with Improved Laser Damage Resistance. Proceeding of SPIE, vol.3682, p. 176-182, 1998.
10. S.S.Oliver, M.W.Kartz, B.J.Bauman, J.M.Brase, C.G.Brown, D.M.Pennington D.A.Silva, High-resolution wavefront control using liquid crystal spatial light modulators. Proceedings of SPIE, v.3760, 1999, pp. 47-51.
11. V.Y.Venediktov, V.A.Berenberg, A.V.Leshchev, M.V.Vasil'ev, M.Gruneisen. Novel advances in laser beam directors with nonlinear optical correction, Proc.SPIE, v.4065, p.939-444, 2000
12. V.I.Bespalov, A.Z.Matve'ev, G.A.Pasmanik, The study of maximal sensitivity of the SBS amplifier and Brillouin enhanced four-wave mixing, Izvestiya vuzov, Radiophisics, v.29, n.9, pp.1080-1094, 1986 (in Russian).
13. A.M.Scott, K.D.Ridley, "A Review of Brillouin-Enhanced Four-Wave Mixing", IEEE J. Quantum Electronics, v.25, n.3, .438-459 (1989).
14. K.Sayyah, U.Efron, Optically addressed spatial light modulator with a high photosensitivity and intensity adaptation range, Opt. Lett., 1996, Vol. 21, pp.1384-1386.

# Sol-gel technology for french inertial confinement fusion laser driver

Philippe Belleville, Philippe Prené

CEA - Le Ripault, BP 16, 37260 Monts - France

## ABSTRACT

The French Commission for Atomic Energy is currently involved in a project which consists of the construction of a 2 MJ/500TW (351-nm) pulsed Nd:glass laser and which will be devoted to Inertial Confinement Fusion (ICF) research in France. With 240 laser beams and almost 10,000 $m^2$ in coated area required, the proposed megajoule-class laser will be the largest laser system ever built in the world. Room temperature and atmospheric pressure deposited coatings such as sol-gel for antireflective (AR) applications and silicone for environmental protective coatings, with high optical and laser-included damage performance, can be applied at a low cost compared to conventional vacuum deposition processes. Today, we are using such a technology to AR-coat prototypes of lenses, windows, blast-shields, debris-shields, flashlamps and harmonic converters required by our proposed megajoule-class laser. This technology has also been selected for the preparation of multilayer highly reflective (HR) coatings for use as cavity-end deformable mirrors in the laser system. Due to their suitability to ensure appropriate deposited optical thickness, room-temperature deposition techniques such as dip-, spin- or laminar-flow-coating have been optimized for such laser coating production.

**Keywords :** Sol-gel, optical coatings, composites, liquid-medium deposition techniques, laser damage threshold.

## 1. INTRODUCTION

The French Commission for Atomic Energy (CEA) megajoule-class pulsed Nd:glass laser devoted to Inertial Confinement Fusion (ICF) research will focus 240 beams on a target. The approved laser design of the LMJ (MegaJoule-class Laser) is based on a fourpass laser cavity in which neodynium doped-glass is pumped using cylindrical flashlamps. Because of the power of such a laser (2 MJ/500TW @ 351 nm), the architecture involves large-area square or rectangular glass substrates (from 400 × 400 $mm^2$ for optical components such as windows, lenses, harmonic converters or cavity-end deformable mirrors up to 1800 × 635 $mm^2$ for blastshield component). 10,000 $m^2$ in coated area is required with various coating functions such as antireflective (AR), broadband antireflective (BBAR), high-reflective (HR) or environmentally protective one. Sol-gel technology has been selected to coat optical LMJ components because coatings have high optical and laser-incluced damage performances. It can be applied at a low cost compared to conventional vacuum deposition processes using room temperature and atmospheric pressure deposition techniques such as dip-, spin- or laminar-flow-coating. Today, deposition methods have been optimized for such laser coating production and sol-gel AR, BBAR and HR-coatings have been successfully applied onto optical prototypes.

## 2. SOL-GEL OPTICAL COATING AND DEPOSITION TECHNIQUES

Oxide coatings have been the most widely investigated and, therefore, are the best oppportunity for the promotion of the sol-gel technology in the modern industry[1]. Two different kinds of sol-gel solutions could be chosen for their preparation : the polymeric and the colloidal systems. These coating solutions are prepared by the hydrolysis and the condensation of metallic precursors (salts or alkoxides) : the inorganic polymerization reaction (nucleation and growth) is controlled by varying the chemical conditions (pH, hydrolysis ratio, .....) and allow to prepare colloidal particles (1 to 1,000 nm diameter) or polymeric species dispersed in liquid medium. The colloidal route is a good way to prepare unstressed thick films or multilayer coatings and consequently preventing crazing and peeling phenomena using a room-temperature deposition technique. Moreover, it generally produces high laser damage resistant optical coatings, but their abrasion resistance after deposition remains poor[2]. Depending of the coating use, these colloids may be combined with binders, fillers or coupling agent in order to improve mechanical properties. With the polymeric route, a densification step (UV irradiation or thermal curing) is necessary to obtain a dense layer which shows generally a good abrasion resistance and a high refractive index.

XIII International Symposium on Gas Flow and Chemical Lasers and High-Power Laser Conference,
Antonio Lapucci, Marco Ciofini, Editors, Proceedings of SPIE Vol. 4184 (2001)

Because of the important internal stress induced by the shrinkage during densification step, the polymeric materials are not used for preparing thick films or multilayer stacks.

Today, three liquid coating methods are available to lay down very thin layers with accurate and uniform thickness : the dip- and spin-coating[3] which are the most widely used and comparatively a new technique, the laminar-flow coating[4] (or meniscus-coating). The choice of the coating methods depends on the size, the shape and the geometry (plane or curved surface) of the substrate, the number of side coated, the optical stack structure, the nature, the cost and the lifetime of the sol-gel coating solution. Dip-coating necessitates to use a large coating solution amount, but allows to coat simultaneously both sides of large-area components. With the spin-coating, a small sol-gel solution volume is necessary, however only one side is coated and the substrate must be preferably circular. For the laminar flow-coating, the multilayer coating process is very simple and no coating solution is lost after deposition : the component surface needs to be planar and only one side is coated. In all cases, the layer thickness is controlled by the deposition speed and both colloidal and polymeric sol-gel solutions can be equally deposited.

## 3. ANTIREFLECTIVE COATING

There are basically three types of antireflective coatings : the first and simplest one is a single-layer coating in which the refractive index is ideally equal to the square root of the substrate index, assuming air as the external medium. The other two types are multilayer stacks (two or more layers of different refractive index) and graded-index systems where the index is uniformly and continuously graded from the substrate, to the external medium. For le LMJ project, we have developed three kinds of antireflective coatings, all based on single-layer or multilayer designs : the standard single-layer antireflective coating (SAR) for the windows, lenses and debris-shields, the two-layer antireflective and environmentally protective coating (AREP) for Potassium Dihydrogen Phosphate (KDP) crystals used as harmonic converters or in Pockel's cells and the two-layer broadband antireflective coating (BBAR) for the blast-shields flat glass component.

### 3.1. Standard single-layer antireflective coating (SAR)

This coating is a single-layer system made of nanosized spherical particles (10-nm average diameter) of amorphous silica and deposited from a colloidal suspension. The coating solution we are routinely using is prepared from a Stöber silica sol[5]. This silica sol synthesis is based on the base-catalysed (ammonium hydroxide catalyst) hydrolysis of tetrahydroxysilane in ethanol with a $Si/H_2O$ molar ratio of 1/2.2 at room temperature. In basic conditions, hydrolysis followed by formation of insoluble silica colloidal particles is favoured over condensation to soluble polymers. After deposition and solvent evaporation, the silica nanoparticles do not pack perfectly together and give rise to a porous film (~ 57 % porosity). Air present within the space between particles allow to decrease of the coating refractive index to a value of 1.22. Deposited onto both sides of a silica substrate (refractive index : 1.45), this standard single-layer antireflective coating allows to reach practically a transmission value of 100 % at a single wavelength which can be shifted by varying layer thickness (fig. 1). The silica coating is of highly pure and this contributes to a UV cut-off as low as 200 nm and to a very high laser damage threshold (> 50 J $cm^{-2}$ @ 1,053 nm wavelength, R/1 mode and 3 ns pulse duration). The single-layer antireflective coating scratch-resistance is poor because no chemical bond exists between independant silica particles and with the substrate. A treatment of this porous silica coating with ammonia vapors results in a consistent strengthening of the coating with no loss in optical performance[6]. A suitable explanation of this observation consists of a particle-to-particle surface base-catalysed condensation. This generates a shrinkage of the coating thickness (~ 20 % of the original thickness), but the antireflective function is

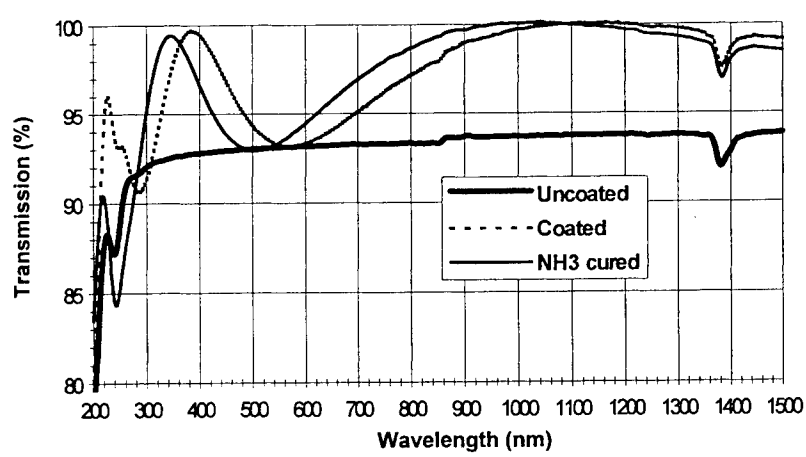


Figure 1. Transmission spectra of two-side SAR-coated silica substrate before and after ammonia curing.

retained : this induces that the porosity and hence the refractive index remain unchanged. The ammonia hardening post-treatment enables us to alcohol drag-wipe and physically touch SAR-coated glass substrates. However, the resulting coating can not be considered as a scratch-resistant product. This improvement is now routinely used for SAR sol-gel coatings since it allows more convenient handling of coated parts and if required still allows an easy removal of the coating by a soft scrubbing without damaging the optical form of the surface beneath.

### 3.2. Two-layer antireflective and environmentally protective coating (AREP)

The crystals of KDP used as harmonic converters for the Phebus laser were originally antireflective coated with the standard single-layer porous sol-gel coating which has been described previously. While optically very good, this coating did not provide environmental protection for the KDP surface which can show scattering effect by atmospheric moisture. Use of transparent organic-inorganic materials (ORMOSILs) is investigated as a protective coating on KDP crystals. The methyl silicone used is $(CH_3SiO_{1.5})_m$, with a refractive index of 1.41. This hybrid material is a high purity product prepared by the hydrolysis of methyltrimethoxysilane and is supplied as a soluble prepolymer in ethanolic solution. It is applied by dipping and, after 16 hours curing at 150°C, gives a dense and insoluble coating of optical quality. When applied onto KDP (index 1.49-1.51), this coating is sufficient to reduce reflection from 4 % to 2 % per surface. This residual reflection can be enhanced by simply overcoating with the standard porous silica quarterwave antireflective thin film from an ammonia-free coating solution. This two-layer system gives a broad transmission increase which is adjusted to cover both harmonics by a suitable choice of coating thickness. The Phebus laser was routinely using silicone-sol AR coated SHG-crystals (for use at 526.5 and 1,053-nm) and THG-crystals (for use at 351-nm). Typically, the gain in transmission is ranging 6.5-7.5 % at the wavelengths of interest.

### 3.3. Two-layer broadband antireflective coating (BBAR)

The blast-shields component is a float glass placed between the flashlamps and the laser disk amplifiers to prevent damage of the costly amplifiers by possible explosion of a flashlamp. An antireflective coating is essential to avoid light reflection loss between flashlamp and amplifier medium induced by the two sides of blast-shields components. Based on both flashlamp and LHG-8 laser disk absorption spectra (fig 2), a two-layer broadband antireflective coating made from tantalum and silicon oxide has been developed[8]. The choice of materials to prepare BBAR coating was directed to the selection of sol-gel polymeric layers rather than colloidal-based ones because of the mechanical requirements including abrasion-resistance and durability. Sol-gel synthesis have been carried out starting from cheap precursors in order to produce metallic-based solutions, each one suitable for liquid-deposition technique use such as dip-coating because of the blast-shields large size (1811× 635 $mm^2$). Baking step temperature does not exceed 150°C during 30 minutes allowing to coat various substrates and to offer scratch-resistance properties in compliance with US-MIL-C-0675C severe test. The antireflective properties of this optical stack made of a halfwave high index layer deposited onto Schott glass substrate followed by a quarterwave thickness low-index thin film were optimized to increase the amplification yield, taking into account the optical and geometrical parameters of the multipass amplification laser cavity. Good agreement over the range of interest is obtained between experimental and calculated spectra (taking into account both dispersions of coating index, fig. 2). The transmission increase due to sol-gel coating will enhance laser amplification step and using the experimental data, gain calculations have predicted a 6.3% amplification gain.

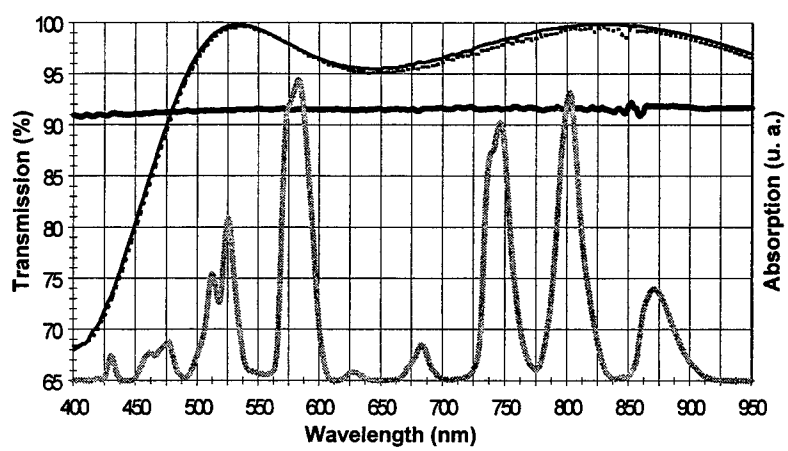


Figure 2. LHG-8 laser-glass absorption (gray line) and experimental transmission spectrum of the 2-layer BBAR-coated blastshield (solid line) in comparison with calculation (dotted line) and bare substrate tranmission (bold line).

## 4. HIGH-REFLECTIVE COATING

For le LMJ laser, we have developed a highly reflective coating consisting of alternating layers of quarterwave-thick high and low refractive index materials. In order to prevent crazing and peeling phenomena, the colloidal route has been selected. Moreover, the HR coating has to be deposited onto the deformable surface of the cavity-end mirrors in the laser system, so mechanical induced-stresse could damage coating structure if too rigid. To prepare multilayered HR coatings we have selected $ZrO_2$-PVP as the high index material and colloidal $SiO_2$ as the low index material (with a refractive index of 1.72 and 1.22 respectively @ 1053 nm)[8]. In such a system, for a reflectance of 99 %, generally up to 20 total quarterwave layers of alternating high and low optical indexes are necessary. $ZrO_2$-PVP component is a mixture of $ZrO_2$ colloidal particles (plate-like with the longest dimension around 30 nm) dispersed in methanol with polyvinylpyrrolidone polymer (PVP) used as binder. $ZrO_2$ particles were prepared by the hydrothermal treatment of a $ZrOCl_2/H_2O/(NH_2)_2CO$ precursor mixture. The refractive index of $ZrO_2$ coating made of colloidal particles increases from 1.57 to 1.72 by addition of 0 % to 20 % by weight of PVP compared to zirconia. This corresponds to the maximum refractive index value we have achievied : a further addition results in increasing interparticle distance and the packing density will decrease as the refractive index does. After each $ZrO_2$-PVP layer deposition, a UV-curing ($\lambda$ = 195 nm) is necessary for complete reticulation of the polymer and to make it insoluble. HR coatings were produced by spin coating, dip coating and also laminar-flow coating. This last deposition technique has been considered as the most appropriate method to coat cavity-end deformable mirrors of LMJ laser. Moreover, using laminar-flow coating deposition method, the laser damage threshold of sol-gel $SiO_2/ZrO_2$-PVP HR coatings is in compliance with LMJ requirements (~ 18 J $cm^{-2}$ @ 1,053 nm wavelength, R/1 mode and 3 ns pulse duration).

## 5. CONCLUSION

The sol-gel coating technology appears to be an appropriate process to produce the coatings needed for building the french mega-joule class laser. Room temperature and atmospheric pressure deposited coatings have high optical and laser damage performances and can be applied onto large-size substrates at a low cost compared to conventional vaccum deposition processes. Today, we are using such a technology to AR-coat the lenses, windows, blast-shields, debris-shields, and harmonic converters required for the LMJ laser. Moreover, this technology allows to prepare multilayer highly reflective coating for the cavity-end deformable mirror of the laser. Sol-gel replication process is under development to produce the phase plates used for smoothing the laser beam wave surface.

## ACKNOWLEDGMENTS

We are very grateful to L. Beaurain, C. Bonnin, P. Pégon and J.-J. Priotton for the scientific and technological support.

## REFERENCES

1. L. C. Klein, *Sol-Gel Optics : Processing and Applications*, Kluwer Academic Publishers, Dordrecht, 1994.
2. H. G. Floch, P. F. Belleville, J. J. Priotton *et al.*, "Sol-gel Optical Coatings for Lasers, I, II, and III", *Am. Ceram. Soc. Bull.* **74**, No. 10 p. 60, No. 11 p. 84, and No. 12 p. 48, 1995.
3. L. E. Scriven, "Physics and Applications of Dip Coating and Spin Coating", *Mat. Res. Soc. Symp. Proc.* **121**, p. 717, 1988.
4. H. G. Floch, P. F. Belleville, "Procédé de Fabrication de Couches Minces Présentant des Propriétés Optiques", French Patent No. 92 08524, assigned to CEA.
5. W. Stöber *et al.*, "Controlled Growth of Monodisperse Silica Spheres in the Micron Range", *J. Colloid Interface Sci.* **26**, p. 62, 1968.
6. P. F. Belleville, H. G. Floch, "Procédé de Fabrication de Couches Minces Présentant des Propriétés Optiques et de Résistance à l'Abrasion", French Patent No. 93 03987, assigned to CEA.
7. P. Prené *et al.*, "Preparation of a Sol-Gel Broadband Antireflective and Scratch-Resistant Coating for Amplifier Blast-Shields of the French Laser LIL", *Sol-Gel'99 10th International Workshop on Glasses, Ceramics, Hybrids and Nanocomposites from Gels*, paper No. 92.
8. P. F. Belleville *et al.*, "Room-Temperature Mirror Preparation Using Sol-Gel Chemistry and Laminar-Flow Coating Technique", *Sol-Gel'99 10th International Workshop on Glasses, Ceramics, Hybrids and Nanocomposites from Gels*, paper TS38.

# Microimpurities effect on bimodal radiation of aerosol microparticle

Ludmila G. Astafieva, Andrey V. Korzhov, Liudmila A. Kotomtseva, Galina P. Lednyeva
Institute of Physics of the National Academy of Sciences,
Minsk, Belarus
Tel.: 375 172 842521 Fax: 375 172 840879 E-mail: kotomts@dragon.bas-net.by

## ABSTRACT

Results of consideration for bimodal laser regime in aerosol micro particle under the action of the second harmonic of a Nd-doped power glass laser as a pumping source for the mixture of an active substance and a saturable absorber as micro impurity in a spherical micro particle are proposed. Bimodal radiation in aerosol microparticle as spherical cavity is considered. Interactions of modes in presence of impurity as absorber both and enlargement and inhibition effects are described to enlarge sensitivity to impurity.

**Keywords:** microsphere. aerosol, saturable absorber, microimpurity, whispering gallery mode.

## 1. INTRODUCTION

Nonlinear interactions and laser oscillations in dielectric aerosol micro droplet with weak absorption attract attention due to extremely high quality of quasi normal modes in such meso-cavities. High sensitivity of modal radiation to absorbing permits us to found reliable method for detection of pollution in atmosphere and enviromental medium as micro impurities in an aerosol micro droplet.for practical application in information processing systems due to their fitting to other optical elements and concentration of high energy in small volume, what permits us to preserve energy and materials. It is known from experiment that multimode emission is typical in a microlaser based on a spherical microparticle. Spectral measurements of lasing reveal the existence of quasi periodic peaks which are likely to be identified with morphology-dependent resonances or whispering gallery modes of spherical microparticle[1,2].

Results of consideration for bimodal laser regime in aerosol micro particle under the action of the second harmonic of a Nd-doped power glass laser as a pumping source for the mixture of an active substance and a saturable absorber as micro impurity in a spherical micro particle are proposed in our report. Basic system of equations is modified to describe an electric and magnetic field, and inversion of populations in an active medium and absorption in a saturable impurity in micro sphere. Interaction between two modes and effects of spatial short wave grating of populations of about half of the length of the light wave due to self-action of one mode during it's counter propagation inside cavity and of the long wave grating of populations at the difference of the lengths of waves of modes as result of interaction of two modes in micro droplet and their role in laser action of micro droplet are considered.

Conditions which permit us to get two orders more high sensitivity to impurities due to effect of enlargement or inhibition for the probability of stimulated emission of radiation in the presence of detuning between the resonant modal frequency, the resonant frequency of the gain line and the resonant frequency of the absorption line of impurity are determined.

## 2. BASIC SYSTEM OF EQUATIONS AND STEADY STATES OF BIMODAL LASER WITH A SATURABLE ABSORBER

We consider microparticle as $N$ independent two-level atoms with gain under action of pumping. The electrical field is a sum of the morphology-dependent resonances of spherical microparticle and counter running waves create coupling between the complex modal amplitudes of two consecutive modes and self-coupling of the complex modal amplitudes via created with standing wave population grating. For the amplitudes of modes $q_1$ and $q_2$ slowly varying in time and difference between their phases $\phi=\phi_2-\phi_1$and components of inversion of populations $y_{11}, y_{22}$ and $y_{12}$ the next system of equations is obtained

$$\frac{dq_1}{dt} + (2\pi\sigma + k_1/(1+\alpha q_1^2))q_1 = \frac{v}{4Nh}[q_1 y_{11}\,\mathrm{Re}\,\kappa_1 + q_2 y_{12}(\mathrm{Im}\,\kappa_1 \cos\varphi + \mathrm{Re}\,\kappa_1 \sin\varphi)] = 0,$$

$$q_1 \frac{d\varphi_1}{dt} + \frac{v}{4N\hbar}\left[q_1 y_{11}\,\mathrm{Im}\,\kappa_1 + q_2 y_{12}\left(\mathrm{Im}\,\kappa_1 \cos\Delta\varphi - \mathrm{Re}\,\kappa_1 \sin\Delta\varphi\right)\right] = 0$$

$$\frac{dq_2}{dt} + 2\pi\sigma_2 q_2 - \frac{v}{4N\hbar}\left[\mathrm{Re}\,\kappa_2 q_2 y_{22} + q_1 y_{12}\left(\mathrm{Re}\,\kappa_2 \cos\Delta\varphi - \mathrm{Im}\,\kappa_2 \sin\Delta\varphi\right)\right] = 0$$

$$q_2 \frac{d\varphi_2}{dt} + \frac{v}{4N\hbar}\left[q_2 y_{22}\,\mathrm{Im}\,\kappa_2 + q_1 y_{12}\left(\mathrm{Im}\,\kappa_2 \cos\Delta\varphi + \mathrm{Re}\,\kappa_2 \sin\Delta\varphi\right)\right] = 0$$

$$\frac{dy_{11}}{dt} = D(y_{11}^0 - y_{11}) - \frac{v\mu_{11}}{4\pi\omega N\hbar}\left[\mathrm{Re}\,\kappa_1 q_1^2 y_{11} + q_1 q_2 y_{12}\left(\mathrm{Re}\,\kappa_1 \cos\Delta\varphi + \mathrm{Im}\,\kappa_1 \sin\Delta\varphi\right)\right] -$$

$$-\frac{v\mu_{12}}{4\pi\omega N\hbar}\left[\mathrm{Re}\,\kappa_2 q_2^2 y_{22} + q_1 q_2 y_{12}\left(\mathrm{Re}\,\kappa_2 \cos\Delta\varphi - \mathrm{Im}\,\kappa_2 \sin\Delta\varphi\right)\right]$$

$$\frac{dy_{12}}{dt} = D(y_{12}^0 - y_{12}) - \frac{v\mu_{12}}{4\pi\omega N\hbar}\left[y_{12}\left(\mathrm{Re}\,\kappa_1 q_2^2 + \mathrm{Re}\,\kappa_2 q_1^2\right) + q_1 q_2 y_{11}(\mathrm{Re}\,\kappa_1 \cos\Delta\varphi -\right.$$

$$\left.\mathrm{Im}\,\kappa_1 \sin\Delta\varphi) + q_1 q_2 y_{22}(\mathrm{Re}\,\kappa_2 \cos\Delta\varphi + \mathrm{Im}\,\kappa_2 \sin\Delta\varphi)\right]$$

$$\frac{dy_{22}}{dt} = D(y_{22}^0 - y_{22}) - \frac{v\mu_{12}}{4\pi\omega N\hbar}\left[\mathrm{Re}\,\kappa_1 q_1^2 y_{11} + q_1 q_2 y_{12}\left(\mathrm{Re}\,\kappa_1 \cos\Delta\varphi - \mathrm{Im}\,\kappa_1 \sin\Delta\varphi\right)\right] -$$

$$-\frac{v\mu_{22}}{4\pi\omega N\hbar}\left[\mathrm{Re}\,\kappa_2 q_2^2 y_{22} + q_1 q_2 y_{12}\left(\mathrm{Re}\,\kappa_2 \cos\Delta\varphi + \mathrm{Im}\,\kappa_2 \sin\Delta\varphi\right)\right]$$

Here

$$\Pi = \sum_{n}^{n+1} q_n(t) d_n \psi_n(kmr) Y_n(\theta,\varphi) e^{i\omega t}$$

where $k=\omega/c$, $Y_n(\theta,\varphi)$ are spherical harmonics. The coefficients of the resonance magnetic waves of the field inside the particle $d_n$ are

$$d_n = i^n \frac{2n+1}{n(n+1)} \frac{m}{m\xi_n(ka)\psi_n'(mka) - \xi_n'(ka)\psi_n(mka)}$$

where m are the complex refraction index, $\xi_n$ and $\psi_n$ are the Ricatti-Bessel functions, a are the radius of the particle, the superscript prime indicate the spatial derivative.

$$\mu_{11} = \int_v \psi_1^4(kra)\left[S_1^2(\theta)+Q_1^2(\theta)\right]^2 dv, \qquad \mu_{22} = \int_v \psi_2^4(kra)\left[S_2^2(\theta)+Q_2^2(\theta)\right]^2 dv,$$

$$\mu_{12} = \int_v \psi_1^2(kra)\psi_2^2(kra)\left[S_1(\theta)S_2(\theta)+Q_1(\theta)Q_2(\theta)\right]^2 dv$$ are integrals that are characterized as mode self- and cross-saturation.

Dependence of a bimodal steady state on the spatial overlapping of the modes is considered. The linkage coefficients $a_{12} \sim \mu_{12}$ determine the degree of spatial overlapping for modes of the same polarization. Dependence of the intensity of the first mode on the unsaturated gain $y^0_{11}$ is given in the right part of the figure 1. Upper line corresponds to the absence of saturable absorption $k_1=0$ , lower line – for $k_1=0.001$ from loss of the first laser mode. The right side of figure 1 shows us dependence of the intensity of the first mode on the overlapping value $a_{12}$ of the first and the second modes for the same values of $k_1$. For more high linkage between modes the steady state disappears, it means that generation of light disappears. So, we can consider action of different factors of selfaction and interaction of two modes in our model.

Figure 2 gives us spatial distribution of the intensity of a single mode with the quality two orders more high than in traditional cavity.

## ACKNOWLEDGMENTS

This work is supported by the Belorussian Republician Foundation for Fundamental Research (GRANT f98-068).

## REFERENCES

1. J. Popp, M.H. Fields and R.K. Chang, "Q switching by saturable absorption in microdroplets: elastic scattering and laser emission", *Opt. Lett.* **22,** pp. 1296-1298, 1997.
2. A.N. Oraevsky, "Spontaneous emission in the cavity", *Uspekhi Fiz. Nauk,* **164,** pp. 415-427, 1994.
3. L.G. Astafieva, L.A. Kotomtseva and G.P. Lednyeva, "Microparticles as laser sources and bistable elements", *Laser Physics.* **8,** pp. 34-37, 1998.

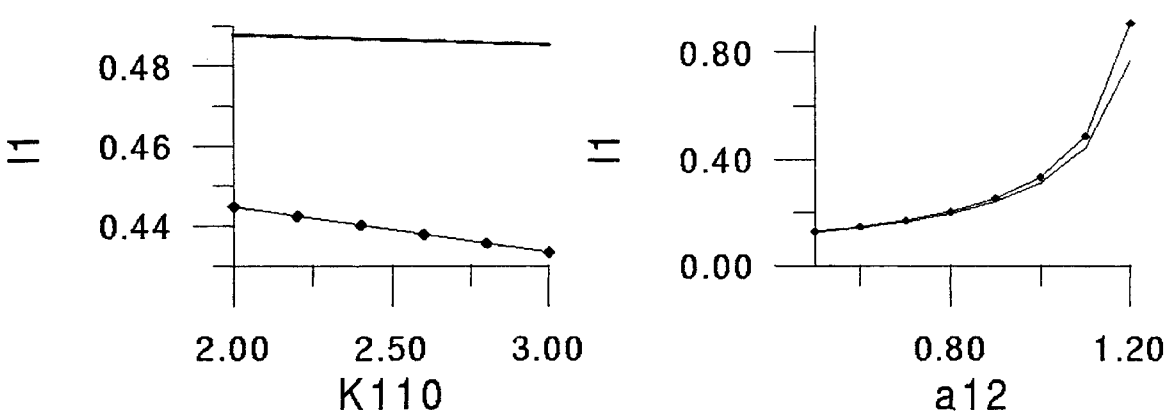


**Figure 1.** Dependence of the intensity of the first mode $I_1$ on the unsaturated gain $y^0_{11}$ ( at left) and coupling coefficient $a_{12}$ (at right) at the absence of a saturable absorption (upper lines) and for $k_1=0.0001$.

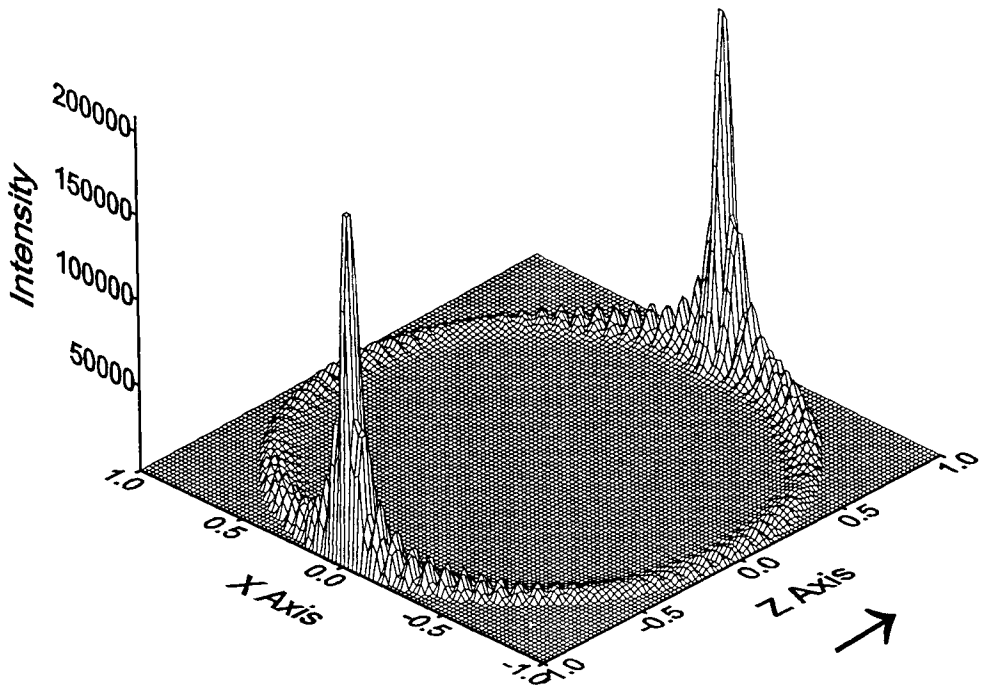


**Figure 1.** Distribution of the internal intensity in equatorial plane of spherical microparticle for TE polarization resonance mode with n=46, s=1, m=1.53-i10$^{-7}$ and size parameter $r$=33.99873497.

# Flattened Gaussian beams and their general propagation properties

Baida Lü Shirong Luo

Institute of Laser Physics & Chemistry, Sichuan University, Chengdu 610064, China

## ABSTRACT

The general propagation equation of flattened Gaussian beams passing through a paraxial optical ABCD system, where the amplifying and absorbing media with a linear gain and absorption are included, is derived and the applications are illustrated with numerical examples.

Keywords: Flattened Gaussian beam(FGB), general propagation equation, ABCD system, linear gain and absorption.

## 1. INTRODUCTION

The concept of flattened Gaussian beams(FGBs) was introduced by Gori in 1994. Since then, a growing interest has developed in the propagation, focusing and beam quality of FGBs owing to their advantages in simulation of beams with a flat-top spatial profile in comparison with super-Gaussian beams[1]-[8]. As usual, FGBs can be expanded into a finite sum of Laguerre-Gauss modes in the cylindrical coordinate system, or Hermite-Gaussian modes in the Cartesian coordinate system[1]-[3], so that their propagation was treated by using the well-known propagation law of Gaussian beams. Another method is based on the generalized Huygens-Fresnel diffraction integral, and the FGB is regarded as a whole beam, thus the propagation of FGBs through a paraxial optical ABCD system were treated by means of the diffraction integral[6]. On the other hand, the propagation of partially coherent beams in amplifying and absorbing media was studied by Palma et. al.[9][10]. This paper is aimed at studying the general propagation properties of FGBs passing through a paraxial ABCD system including amplifying and absorbing media. The general propagation equation is derived and numerical results are given to illustrate its applications.

## 2. THE GENERAL PROPAGATION EQUATION OF FGBs

The field distribution $E_0(r,z)$ of FGBs at the plane of $z=0$ in the cylindrical coordinate

XIII International Symposium on Gas Flow and Chemical Lasers and High-Power Laser Conference,
Antonio Lapucci, Marco Ciofini, Editors, Proceedings of SPIE Vol. 4184 (2001)

system is written as[1][2]

$$E_0(r,0) = A_0 \exp\left[-\frac{(N+1)r^2}{w_0^2}\right]\sum_{n=0}^{N}\frac{1}{n!}\left[\frac{(N+1)r^2}{w_0^2}\right]^n \tag{1}$$

where $w_0$ and $N$ ($N = 0,1,2,\cdots$)denote two characteristic parameters of FGBs, namely, the waist width and beam order, respectively, $A_0 = E_0(0,0)$ is the amplitude at the central position of $r = z = 0$. The propagation of FGBs passing through a paraxial optical system parametrized by a transfer matrix $\begin{pmatrix} \mathrm{A} & \mathrm{B} \\ \mathrm{C} & \mathrm{D} \end{pmatrix}$ is described by the generalized Huygens-Fresnel diffraction integral of the form

$$E(r,z) = \frac{\mathrm{i}k}{\mathrm{B}}\exp(-\mathrm{i}kz)\int_0^\infty E_0(r',0)J_0\left(\frac{krr'}{\mathrm{B}}\right)\exp\left[-\frac{\mathrm{i}k}{2\mathrm{B}}(\mathrm{A}r'^2 + \mathrm{D}r^2)\right]r'dr' \tag{2}$$

where $k$ is the wave number in the medium, which is generally complex, if the amplifying or absorbing media are considered, and $k$ is expressed as[9][10]

$$k = k_r + \mathrm{i}k_i \tag{3}$$

$k_r, k_i$ are the real and imaginary parts of $k$, $k_i > 0$ and $k_i < 0$ account for the amplifying and absorbing media, respectively. The matrix elements A,B,C,D are assumed to be real-valued. On substituting from Eq.(1) into Eq.(2) and after tedious integral calculations we obtain

$$E(r,z) = A_0 \frac{\mathrm{i}k/2\mathrm{B}}{\left(\frac{N+1}{w_0^2} + \frac{\mathrm{i}k\mathrm{A}}{2\mathrm{B}}\right)}\exp(-ikz)\exp\left(-\frac{\mathrm{i}k\mathrm{D}r^2}{2\mathrm{B}}\right)\exp\left[\frac{-(kr/2\mathrm{B})^2}{\frac{N+1}{w_0^2} + \frac{\mathrm{i}k\mathrm{A}}{2\mathrm{B}}}\right]$$

$$\times\sum_{n=0}^{N}\left(\frac{N+1}{w_0^2}\right)^n\left(\frac{N+1}{w_0^2} + \frac{\mathrm{i}k\mathrm{A}}{2\mathrm{B}}\right)^{-n} L_n\left[\frac{(kr/2\mathrm{B})^2}{\frac{N+1}{w_0^2} + \frac{\mathrm{i}k\mathrm{A}}{2\mathrm{B}}}\right] \tag{4}$$

Eq.(4) is the general propagation expression for FGBs passing through an optical ABCD system, where the media with a linear gain and absorption are considered. If we let $k$ be real, Eq.(4)

becomes the propagation of FGBs through an ABCD system without gain and absorption. For the case of FGBs propagating in linear gain and absorption media with effective length $l$, Eq.(4) reduces to

$$E(r,l) = A_0 \frac{\frac{\mathrm{i}k_r - k_i}{2l}\exp(k_i - \mathrm{i}k_r)l}{\frac{N+1}{w_0^2} + \frac{\mathrm{i}k_r - k_i}{2l}} \exp\left[\frac{(k_i - \mathrm{i}k_r)r^2}{2l}\right] \exp\left\{\frac{-[(k_r + \mathrm{i}k_i)r/2l]^2}{\frac{N+1}{w_0^2} + \frac{\mathrm{i}k_r - k_i}{2l}}\right\}$$

$$\times \sum_{n=0}^{N} \left(\frac{N+1}{w_0^2}\right)^n \left[\frac{N+1}{w_0^2} + \frac{\mathrm{i}k_r - k_i}{2l}\right]^{-n} L_n\left\{\frac{[(k_r + \mathrm{i}k_i)r/2l]^2}{\frac{N+1}{w_0^2} + \frac{\mathrm{i}k_r - k_i}{2l}}\right\} \tag{5}$$

The condition for the transverse field convergence in the gain medium can be derived from Eq.(5), and is given by

$$l \le \frac{w_0^2|k|}{2\eta(N+1)} \tag{6}$$

where

$$\eta = \frac{k_i}{|k|} \tag{7}$$

which is similar to Eq.(15) in Ref.[10] for the case of partially coherent beams. In addition, it follows readily from Eq.(5) that for the absorption media ($\eta < 0$), the field is always convergent.

## 3. NUMERICAL EXAMPLES

Numerical calculations were performed by using Eq.(5), typical examples are given in Fig.1(a)-(c), where the calculation parameters are $N = 12, w_0 = 1\text{mm}, |k| = 6000\text{mm}^{-1}$, and $\eta = \pm 10^{-6}$ for the gain and absorption media, respectively. Fig.1(a) showes the intensity distribution of a FGB at the initial plane of $l = 0$. From Fig.1(b)($l = 600\text{mm}$) and 1(c)($l = 7\text{m}$) we see that the shape of FGBs can not remain unchanged upon propagation in free space, linear gain and absorption media for the Fresnel and Fraunhofer cases. The power amplification (absorption) defined as the output power divided by the input power at the $z = 0$ position are $\exp(7.2)$ and $\exp(-7.2)$ for $l = 600\text{mm}$,

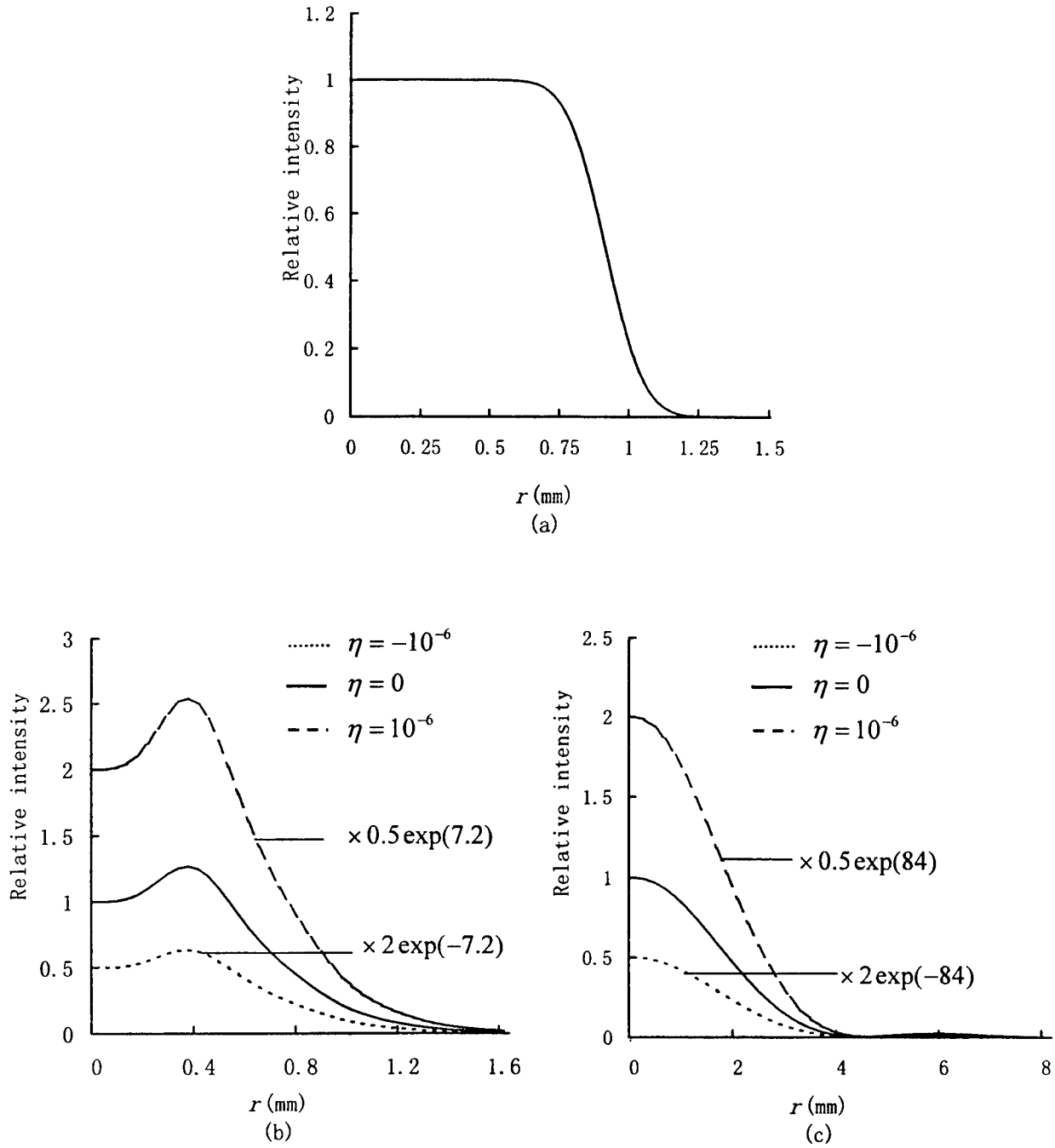


Fig.1 Relative intensity distributions of a FGB propagating in (———) free space, (– – –) linear gain and (····· ) linear absorption media.(a) $l = 0$, (b) $l = 600\text{mm}$, (c) $l = 7\text{m}$.

and $\exp(84)$, $\exp(-84)$ for $l = 7\text{m}$, respectively.

## 4. CONCLUSION

In this study the general propagation equation of FGBs passing through a paraxial ABCD

system, where the linear gain and absorption media are included, has been derived, and their propagation properties have been illustrated with numerical examples. The main advantage of our approach is that the propagation of FGBs through ABCD systems with or without aperture, with or without amplifying and absorbing media can be treated in a unified way. The results obtained in this paper would be useful for the optical system design and optical beam propagation, where the flat-top beam profile is required.

## 5. ACKNOWLEDGEMENT

This work was supported by the National Hi-Tech Project of China and the Foundation of the State Key Laboratory of Laser Technology.

**REFERENCES**

[1] F. Gori, "Flattened gaussian beams", Opt. Commun. **107,** 335-341 (1994).

[2] V.Bagini, R.Borghi, F.Gori, A. M. Pacileo and M.Santarsiero, "Propagation of axially symmetric flatted Gaussian beams", J. Opt. Soc.Am. A **13**, 1385-1394(1996).

[3] S.-A. Amarande, "Beam propagation factor and kurtosis parameter of flattened Gaussian beams", Opt. Commun. **129**, 311-317(1996).

[4] M. Santarsiero, D.Aiello, R.Borghi and S.Vicalvi, "Focusing of axially symmetric flattened Gaussian beams", J. Mod. Opt. **44**, 633-650(1997).

[5] B. Lü , S. Luo, B. Zhang, "A comparison between the flattened Gaussian beam and super-Gaussian beam ", Optik. **110,** 285-287 (1999).

[6] B. Lü , S. Luo, B. Zhang, "Propagation of flattened Gaussian beams with rectangular symmetry passing through a paraxial optical ABCD system with and without aperture", Opt. Commun. **164**, 1-6 (1999).

[7] B. Lü , B. Zhang, S. Luo, "Far-field distribution, $M^2$-factor, and propagation of flattened Gaussian beams", Appl. Opt. **20**, 4581-4584 (1999).

[8] B. Lü , S. Luo, B. Zhang, , "Propagation of three-dimensional flattened Gaussian beams ", J. Mod. Opt. **46**, 1753-1762(1999).

[9] C. Palma, P. De Santis, G. Cincotti, and G. Guattari, "Propagation of partially coherent beams in absorbing media ", J. Mod. Opt. **42**, 1123-1135(1995).

[10] C. Palma, P. De Santis, G. Cincotti, and G. Guattari, "Propagation and coherence evolution of optical beams in gain media ", J. Mod. Opt. **43**, 139-153(1996).

# High-power CW Raman fiber laser using phosphosilicate fiber pumped by Yb-doped double-clad fiber laser

Mahendra PRABHU*[a], Nam Seong KIM[b], Lu JIANREN[a], Ken-ichi UEDA[a]

[a]Institute for Laser Science, University of Electro-communications, 1-5-1 Chofugaoka, Chofu, Tokyo 182-8585, Japan.

[b]Nortel Networks, 6800 Broken Sound Parkway N.W., Boca Raton, FL 33487, U.S.A.

## ABSTRACT

A high-power Raman fiber laser (RFL) with maximum output power of 4.11 W/1239 nm and 2.24 W/1484 nm is obtained using a continuous wave (CW) 8.4 W/1064 nm Yb-doped double-clad fiber laser (DCFL) as a pump, phosphorous-doped fiber (PDF) and cascaded cavities made with fiber Bragg Gratings (FBG). RFL performance for the 300, 700 and 1150 m PDF lengths and output mirror reflectance was experimentally investigated by observing maximum output power, slope efficiency, threshold power, and full-width at half maximum at both the first and second Stokes wavelength.

**Keywords:** Raman fiber laser, phosphosilicate fiber, stimulated Raman scattering, Raman fiber amplifier, Optical fiber communications

## 1. INTRODUCTION

Raman fiber amplifiers (RFA)[1-3] and lasers (RFL)[4-6] have been actively studied by different groups since discovery of Raman effect in optical fiber in 1972[1]. A resurgence of research in the field of RFAs and RFLs started with recent advances in the construction of practical high-power pump lasers sources like narrow-stripe lasers diodes (LD) with maximum output power of 150 mW to 200 mW at 1484 nm, and Yb-doped double-clad fiber lasers (DCFL) with an output power in tens of watts at wavelengths ranging from 1040 nm to 1120 nm and are now commercially available[7]. These lasers have been used as pump sources in RFL. There is great demand for very high-output power RFL to be used distributed Raman amplifiers and for remote pumping of Er-doped fiber amplifiers (EDFA) in very long distance repeaterless wavelength division multiplexing (WDM) transmission systems. These applications stress the need for very high-power RFL at 1239 nm and 1484 nm.

The stimulated Raman scattering (SRS) in the RFL and the RFA involves a frequency-conversion process in which light traveling down a fiber interacts with the vibrating molecules in silica material[8]. This interaction triggers a spectral shift that transfers the energy from a shorter-wavelength pump beam to a longer-wavelength signal. Though the Raman gain can be obtained for any silicate fiber, the value of Raman gain coefficient is about eight times higher for germanosilicate fiber than for silicate fiber[9]. Hence, the germanosilicate fiber is used extensively in the RFL and the RFA. Using the germanosilicate fiber with a peak Raman shift of 440-490 $cm^{-1}$, the third and the sixth Stokes orders produce outputs at 1239 nm and 1484 nm, respectively, with a 1064 nm pump source. However, the low-loss phosphosilicate ($P_2O_5$-$SiO_2$) fiber which we will herein call P-doped fiber (PDF) has a peak Raman shift of 1330 $cm^{-1}$, and when pumped with 1064 nm pump source, the first Stokes ($S_1$) and the second Stokes ($S_2$) orders occur at 1239 nm and 1484 nm, respectively[4,6]. To make an RFL at 1484 nm, one would need six cascaded cavities if GDF were used as the gain medium, whereas with PDF only two cascaded cavities would be required, thereby greatly increasing the RFL efficiency. This paper focuses on the output characteristics of RFL at 1239 nm and 1484 nm.

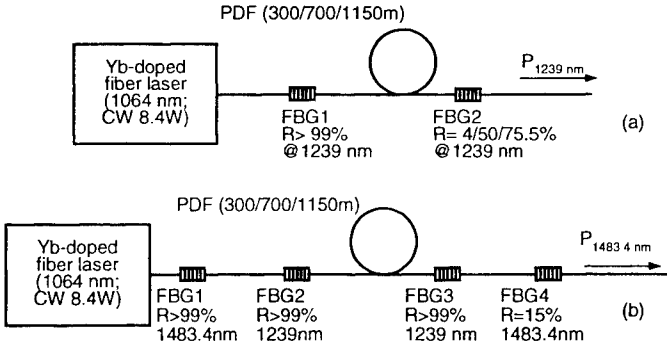


Figure 1 Raman fiber laser setup (a) first Stokes RFL (b) second Stokes RFL

* Correspondence: Email: praboo@email.com ; WWW: http://www.homeofprabhus.com; Telephone: 81 424 891958; Fax: 81 424 858960



XIII International Symposium on Gas Flow and Chemical Lasers and High-Power Laser Conference, Antonio Lapucci, Marco Ciofini, Editors, Proceedings of SPIE Vol. 4184 (2001)

## 2. EXPERIMENTAL SETUP

The experimental setup for the first Stokes RFL (FSRFL) at 1239 nm and second Stokes RFL (SSRFL) 1484 nm is shown in Fig. 1. The pump source is the Yb-doped DCFL with Flexcor-1060 singlemode fiber (SMF) output with maximum output power of CW 8.4 W at 1064 nm, and was manufactured by IRE-Polus. The Yb-doped DCFL SMF output was spliced with low loss to the Raman cavity, which consists of a pair of FBG mirrors. As in Fig.1(a) FSRFL consists of a HR FBG at $S_1$ and an output coupler FBG with reflectivity of either 4%, 50% or 75.5% at $S_1$ was used. In SSRFL (Fig. 1(b)), the reflectivities of the HR FBG mirrors at $S_1$ and $S_2$ are more than 99%. A 15% output coupler FBG at $S_2$ was used to extract the 1484 nm output from the SSRFL. The FBG mirrors for the $S_1$ and the $S_2$ cavities were fabricated on the Flexcor-1060 SMF using an excimer laser. The presence of HR FBG at 1239 nm in SSRFL ensured an efficient conversion of $S_1$ order to $S_2$ order. Since the DCFL output and the FBGs are made of the same Flexcor-1060 fiber, a very low loss splicing is achieved between them. The PDF lengths of 300, 700, and 1150 m are used for Raman gain medium. The PDF has 12 mol% of $P_2O_5$ with a refractive index difference of 0.0107. The propagation loss of the PDF at 1064, 1239, and 1484 nm is 1.84, 1.23, and 1.00 dB/km, respectively. The mode-field diameters (MFD) of the PDF at 1064 nm and 1239 nm wavelengths are 5.96 and 7.05 μm, respectively, whereas the corresponding MFD for the Flexcor-1060 is 6.16 μm and 7.13 μm, respectively. The mismatch in the MFD of the Flexcor-1060 and PDF results in a splicing loss between them, the average splice loss being 0.22 dB. The average insertion loss due to the four FBG mirrors in the setup is 0.6 dB at 1064 nm. This is measured after configuring the RFL and before the generation of the $S_1$ or $S_2$ orders. The PDF and the FBGs were obtained from General Physics Institute, Russia. The output spectrum was measured using an AQ-6315B optical spectrum analyzer manufactured by ANDO Co. The output power was measured using a LaserMate optical power meter manufactured by Coherent Inc.

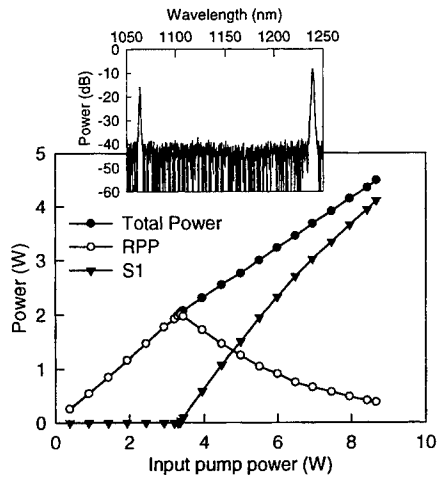


Figure 2 Power evolution of Total power, Residual pump power (RPP) and first Stokes (S1) power in the FSRFL.

## 3. EXPERIMENTAL RESULTS

The experimental results for FSRFL with different PDF lengths and output coupler FBG reflectivities are reported. Similarly the output characteristics of SSRF for different PDF lengths are reported.

### 1. First Stokes Raman Fiber Laser

Figure 2 shows the variation of the first Stokes power and the residual pump power for change in the input pump power for 700 m PDF length and 4% output mirror reflectivity. For that RFL configuration, the laser threshold, the PCE efficiency, and the slope efficiency were 3.36 W, 47.40%, and 76.87%, respectively. The full width at half maximum (FWHM) is 1.46 nm and the first Stokes power at the output 4.11 W. The inset of Fig. 2 shows the output spectrum of the RFL, which includes the residual pump power and the first Stokes power.

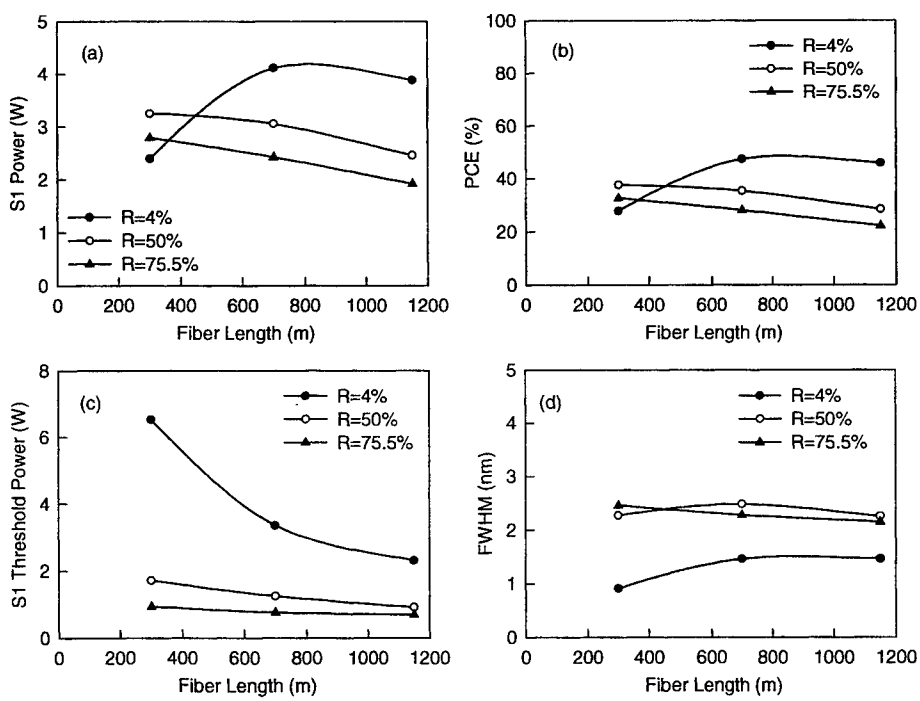


Figure 3 Experimental results for different PDF lengths and output coupler reflectivity: (a) maximum first Stokes (S1) output (b) Power conversion efficiency (c) S1 threshold power (d) FWHM

The consolidated results of the experiments are shown in Fig. 3. Maximum PCE was achieved for the output coupler reflectivity of 4% and the 700m PDF length. This result is very similar to the theoretical simulation wherein, for the 700m PDF length, maximum first Stokes output occurred for 4% output coupler reflectivity.

Figure 3 (a) and (b) show the variation of maximum $S_1$ power and power conversion efficiency (PCE) of $S_1$ power from the input pump power (IPP) as a function of the PDF length and the output mirror reflectivity. The maximum output of 4.11 W from the RFL is obtained for the length of 700 m and 4% output coupler reflectivity with maximum PCE of 47.4%. The variation of the $S_1$ threshold with respect to the fiber length as shown in Fig. 3 (c). The S1 threshold decreases with increase in fiber length. Figure 3 (d) shows the FWHM of $S_1$ as a function of fiber length. For the 4% output coupler reflectivity case, we have used the cleaved facet of the fiber as the output coupler and as the power reflected into the cavity is smaller compared to other cases, the $S_1$ FWHM increases with increase in fiber length upto the FBG bandwidth (HR FBG used at the input). The FWHM of outputs for 50% and 75.5% remains almost identical and this is because large amount of $S_1$ power is reflected back into the cavity and this results in broadening of the $S_1$ spectrum upto the Raman gain spectrum.

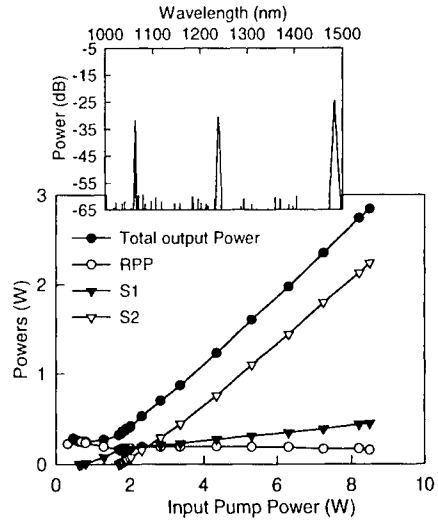


Figure 4 Power evolution of Total power, Residual pump power (RPP) and first Stokes (S1) and second Stoke (S2) power in the FSRFL. Inset shows the total output spectrum

The maximum $S_1$ of 4.11 W at 1239 nm with slope efficiency of 76.9% and threshold of 3.36 W for 700 m of PDF using 4% output FBG coupler is obtained in FSRFL. The full width at half maximum (FWHM) at 1239 nm is 1.46 nm.

## 2. Second Stokes Raman Fiber Laser

The output characteristics of the RFL cavities for the fiber lengths of 300, 700, and 1150 m are reported. Figure 4 shows the variation in total output power, $S_1$ and $S_2$ power and residual pump power (RPP) for change in the IPP for the 700 m PDF length and the 15% output mirror reflectivity. For this RFL configuration, the $S_1$ threshold is 0.57 W. Increasing the IPP to 1.70 W results in generation of $S_2$ order. The maximum output power and slope efficiency of the $S_2$ orders are 2.24 W and 32.8%, respectively. The FWHM of the $S_2$ order is 1.49 nm. The inset of Fig. 4 shows the output spectrum of the RFL, which shows the RPP, the $S_1$ and the $S_2$ wavelengths. As far as we know, the output power of 2.24 W is the largest reported for the PDF RFL.

The consolidated results of the RFL experiments with 300, 700, 1150 m of PDF are shown in Fig. 5. As seen in (a), the maximum $S_2$ output power occurs for a PDF length of 700 m when compared to the case of 300 m and 1150 m. Correspondingly, the $S_1$ power for 700m was small compared to 300 m and 1150 m. The same trend was observed for the RPP, but the power level is smaller than the $S_1$ case. At the output end of the RFL,

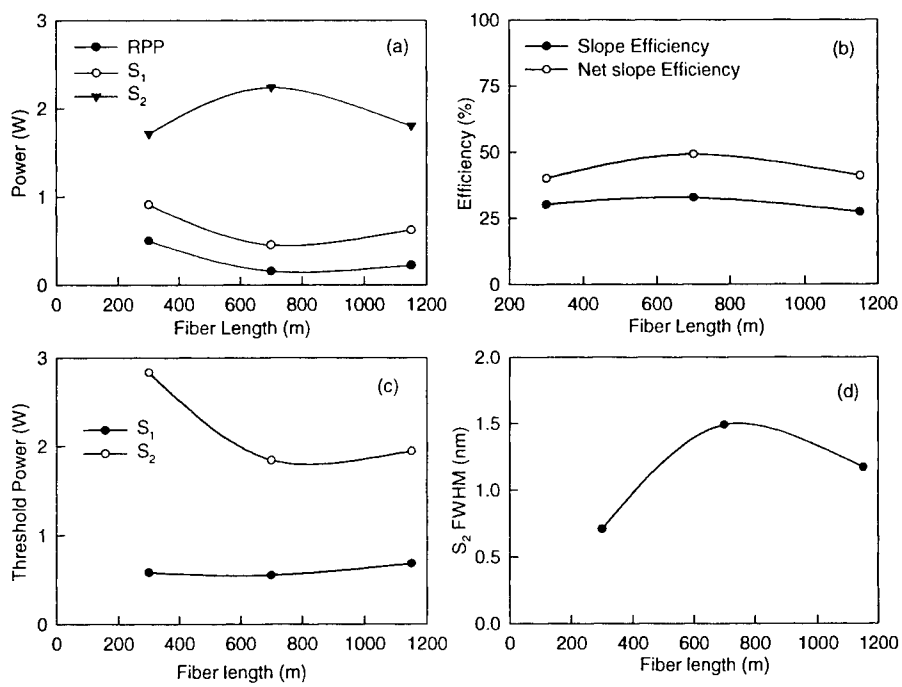


Figure 5 Experimental Results for different PDF lengths: (a) maximum Stokes, first Stokes and residual pump powers (b) slope and net slope efficiencies of second Stokes output (c) first Stokes and second Stokes threshold powers (d) FWHM of second Stokes RFL output

all the PDF lengths generated more than 2.6 W for the total output power and 1.7 W for the $S_2$ power. Figure 5 (b) shows the variation of the slope efficiency and net slope efficiency of the $S_2$ power as a function of PDF length. The total slope efficiency is calculated by measuring the rate of generation of $S_2$ power for the change of IPP. The net slope efficiency is for the convertible input pump power which excludes the non-conversion loss due to splice loss, total cavity loss for the FBG mirrors, and the RPP from the IPP that can be converted to the $S_2$ power through the $S_1$ one. The net slope efficiency is a measure of the system performance and indicates how much the slope efficiency can be improved if we can reduce the non-conversion loss. The slope efficiencies at the $S_2$ wavelength are 30.2%/32.8%/27.3% for 300/700/1150 m, whereas the net slope efficiencies at $S_2$ wavelength are 40%/49%/41% for 300/700/1150 m. Figure 5 (c) shows the variation of the $S_1$ and $S_2$ threshold power as a function of PDF length. The $S_1$ threshold powers for 300/700/1150 m are 0.6/0.57/0.61 W, respectively. The variation in the $S_1$ threshold is very small, whereas the $S_2$ threshold powers for 300/700/1150 m of PDF are 2.83/1.7/2.0 W, respectively. Figure 5(d) shows the variation of the FWHM of the $S_2$ output as a function of fiber length. The maximum FWHM of $S_2$ output for 300/700/1150 m of PDF length is 0.71/1.49/1.17 nm, respectively.

## 4. CONCLUSION

The maximum first Stokes power of 4.11 W at 1239 nm with slope efficiency of 76.9% and first Stokes threshold of 3.36 W for 700 m of PDF using 4% output FBG coupler is obtained in first Stokes RFL. The full width at half maximum (FWHM) at 1239 nm is 1.46 nm. In the second Stokes RFL, maximum second Stokes output of 2.24 W at 1484 nm with a slope efficiency of 32.8% for 700 m of PDF using 15% output FBG coupler at 1484 nm is achieved. The FWHM of the second Stokes RFL output is 1.49 nm.

## 5. ACKNOWLEDGMENTS

The authors would like to thank the Japan Space Forum for financial support. The authors acknowledge PDF, FBG mirrors, and WDM couplers supplied by E. M. Dianov, V. M. Mashinsky, S.A.Vasiliev, M. Yu. Tsvetkov, from the Fiber Optics Research Center at the General Physics Institute, Russia, and the supply of Yb-doped DCFL from IRE Polus. They would also like to mention that the investigations were considerably enhanced due to collaboration with the Joint Open Laboratory for Laser Crystals and Precise Laser Systems.

## 6. REFERENCES:

1. R. H. Stolen, E. P. Ippen, and A. R. Tynes, "Raman oscillation in glass optical waveguide," *App. Phys. Lett.* **20**, pp. 62-64, 1972.
2. E. M. Dianov, M. V. Grekov, I. A. Bufetov, V. M. Mashinsky, O. D. Sazhin, A. M. Prokhorov, G. G. Devyatykh, A. N. Guryanov, and V. F. Khopin, "High efficient 1.3μm Raman Fiber Amplifier," *Electron. Lett.* **34**, pp. 669, 1998.
3. D. V. Gapontsev, S. V. Chernikov, and J. R. Taylor, "Fiber Raman amplifiers for broadband operation at 1.3μm," *Opt. Commun.* **166**, pp. 85-88, 1999.
4. M. Prabhu, N. S. Kim, L. Jianren, and K. Ueda, "Output Characteristics of High-Power Continuous Wave Raman Fiber Laser at 1484 Using Phosphosilicate Fiber," *Opt. Rev.* pp. 2000.
5. E. M. Dianov, I. A. Bufetov, M. M. Bubnov, M. V. Grekov, S. A. Vasiliev, and O. I. Medvedkov, "Three-cascaded 1407-nm Raman laser based on phosphorous-doped silica fiber," *Opt. Lett.* **25**, pp. 402-404, 2000.
6. N. S. Kim, M. Prabhu, C. Li, J. Song, and K. Ueda, "Output characteristics of P-doped Raman fiber laser at 1484 nm with 2.11 W maximum output power pumped by CW 1064 nm Yb-doped double-clad fiber laser," *Jpn. J. Appl. Phys.* pp. 2000.
7. L. Zenteno, "High-power double-clad fiber lasers," *IEEE J. Lightwave Technol.* **11**, pp. 1435-1446, 1993.
8. G. P. Agarwal, *Nonlinear Fiber Optics*, 2nd ed. Academic Press, San Diego, 1995.
9. A. Bertoni, "Analysis of the efficiency of a third order cascaded Raman laser operating at the wavelength of 1.24μm," *Opt. Quantum Electron.* **29**, pp. 1047, 1997.

# Beam perturbations through a MOPA chain

A. Forbes, L.R. Botha, H.J. Strydom, F.J. Prinsloo and E. Ronander

Scientific Development and Integration, PO Box 1559, Pretoria 0001, South Africa
www.sdi.co.za

## ABSTRACT

A theoretical and experimental study investigated beam perturbations on propagation through a MOPA chain, including both optical and medium influences. Analytical models are presented to explain the influence of thermal aberrations on the beam, and these effects are related directly to the change in $M^2$(quality factor) of the beam.

**Keywords:** beam quality, aberrations, thermal lensing, beam propagation, gain, MOPA

## 1. INTRODUCTION

In a commercial high pressure carbon dioxide laser oscillator and amplifier pair, the possible beam distortions need to be addressed in order to be able to offer consistently good beam quality ($M^2 \leq 1.1$), on a shot for shot basis, over a range of repetition rates. The system investigated consists of a high pressure (10 Bar) oscillator and a single amplifier. The input energy into both is more than 30 J per pulse. The MOPA (master oscillator power amplifier) chain can be operated at pulse repetition rates of up to 300 Hz. The lasers are operated as closed loop systems, with internal room temperature catalysts. The measured $M^2$ of the oscillator output pulse is less than 1.1, with 400mJ per pulse. The time jitter between pulses is less than 4 ns (1 sigma value). In this paper, we consider influences resulting in distortions in both the spatial and temporal field. Spatial distortions in MOPA chains are of interest because of the associated beam degradation (higher divergence), and the possible optical damage due to high intensity values when the beam shows irregular structure (intensity spikes). Spatial distortions can be introduced through non-uniformity in the lasing medium, gain saturation, diffraction effects, acoustic disturbances and thermal distortions. Temporal distortions resulting from varying population inversions across the pulse will also influence the propagation of the beam, although more so when dispersion plays an important role. In this paper we will address the influence of thermal distortions following propagation through transmission elements, and gain related distortions. Throughout this paper, the $M^2$ factor[1] is used as a measure of laser beam quality. Aberrations are described using Zernike polynomials,[2] which can be related directly to the primary aberrations of Seidel.[3] Unless otherwise stated, beam size is defined as a half width $1/e^2$ intensity value and divergence as a half width value. Where the beam deviates significantly from Gaussian, the beam size and divergence are defined as second moment values.

## 2. THERMAL DISTORTIONS

The finite absorption of laser beam energy on propagation through a transmission element results in a thermal gradient across the optic, distorting the wavefront by introducing a spatially and temporally dependent phase term. Most attempts at solving the thermal lensing problem have been successful only numerically, with some closed form solutions found for single pulse or cw conditions.[4,5] Some of the present authors have reported previously[6,7] on a multiple pulse model under cylindrical symmetry, assuming semi-infinite substrates.

In the case of Cartesian co-ordinates, without the assumption of infinite width substrates, the temperature distribution in the substrate will be the solution to the heat diffusion equation

$$\rho C_p \frac{\partial u(x,y,t)}{\partial t} - \nabla\kappa.\nabla u(x,y,t) = Q(x,y,t). \tag{1}$$

Here $u(x,y,t)$ is the substrate temperature, $Q(x,y,t)$ is the heat source due to the absorption of beam energy, $\kappa$ is the thermal conductivity, and $\rho$ and $C_p$ are the density and specific heat capacity of the material respectively. Surface heat loss is ignored, and we note that since the optical holders act as very good heat sinks, the boundaries can be assumed to be at constant temperature. The absorption is significant, but nevertheless small compared to the



XIII International Symposium on Gas Flow and Chemical Lasers and High-Power Laser Conference,
Antonio Lapucci, Marco Ciofini, Editors, Proceedings of SPIE Vol. 4184 (2001)

transmitted energy, thus the beam parameters remain constant within the sample and the resulting temperature rise is small. This suggests that $\kappa$ and $C_p$ can be considered constant.

To find the temperature distribution in the optic, we consider what the effect of a single pulse of laser light would be. Because the heat transfer is small, we write the contribution of $Q(x,y)$ as a *Dirichlet* boundary condition for $u(x,y,t)$ on the surface, and solve the heat diffusion equation with no source term. To keep the solution as general as possible, an elliptical Gaussian beam is transmitted through a rectangular optic. The optic has widths $2l_x$ and $2l_y$ in the $x$ and $y$ axes respectively. The origin is at the centre of the optic, so that the co-ordinate system extends from $x \in [-l_x, l_x]$ and $y \in [-l_y, l_y]$, with the Gaussian beam centred at $(0,0)$. The beam is assumed to have a total energy of $E_o$, and beam radii of $\omega_x$ and $\omega_y$ in the $x$ and $y$ axes respectively. The thickness of the optic is small compared to the surface dimensions, and is given by $l$.

Equation (1) then reduces to a linear homogeneous heat diffusion equation, and can be solved by separation of variables. The series coefficients are determined by assuming an initial temperature rise on the surface (after each pulse) due to an elliptical beam given by:

$$u(x,y,0) = \frac{\alpha E_o}{\pi \rho C_p \omega_x \omega_y} \exp\left(-2\left(\frac{x^2}{\omega_x^2} + \frac{y^2}{\omega_y^2}\right)\right). \tag{2}$$

One can extend the above to multiple pulses by considering the decay in temperature during the time between pulses, and the introduction of heat from each subsequent pulse. A difference equation can be derived, giving the temperature profile in the optic after $i$ pulses as

$$\begin{aligned} u^{(i)}(x,y,t) &= \sum_{j=1}^{i} \sum_{n,m=0}^{\infty} a_{nm} \exp\left(-D(t+(j-1)T)\left(\left[\frac{(2n+1)\pi}{2l_x}\right]^2 + \left[\frac{(2m+1)\pi}{2l_y}\right]^2\right)\right) \\ &\quad \times \cos\left(\frac{(2n+1)\pi x}{2l_x}\right) \cos\left(\frac{(2m+1)\pi y}{2l_y}\right), \end{aligned} \tag{3}$$

with $a_{nm}$ given by

$$a_{nm} = \frac{\alpha E_o}{2l_x l_y \rho C_p} \exp\left(\frac{-\pi^2}{32}\left[\frac{\omega_x^2}{l_x^2}(2n+1)^2 + \frac{\omega_y^2}{l_y^2}(2m+1)^2\right]\right). \tag{4}$$

Here $D = \kappa/\rho C_p$ is the diffusivity, and $t$ now denotes elasped time after the $i$th pulse.

Equation (3) is the first analytical expression that the authors are aware of for the solution to the heating due to optical absorption with a pulsed source in Cartesian co-ordinates.

Knowing the temperature profile, it is possible to calculate the change in refractive index, and therefore the induced focal length in the optic. The phase term can be written in the standard form for a focusing element as $\phi = -k(x^2+y^2)/2f$, where $k$ is the wavenumber, and $f$ is the focal length. Also, the phase difference across the wavefront on passing through the lens is $\phi = k \triangle n(x,y)l$, where $l$ is the propagation distance through the substrate. By expanding the refractive index in a two variable Taylor expansion about the optical centre, and equating like powers of $x$ and $y$ in the above phase expressions, we find that the general expression for the focal length after the $i$th pulse is given by

$$\begin{aligned} \frac{1}{f_x(i)} &= \sum_{j=1}^{i} \sum_{n,m=0}^{\infty} \frac{\alpha l E_o \pi^2}{2l_x l_y \rho C_p} \frac{\partial n}{\partial u} \left(\frac{2n+1}{2l_x}\right)^2 \exp\left(\frac{-\pi^2}{32}\left[\frac{\omega_x^2}{l_x^2}(2n+1)^2\left(1+\frac{2(j-1)T}{t_x}\right)\right.\right. \\ &\quad \left.\left. + \frac{\omega_y^2}{l_y^2}(2m+1)^2\left(1+\frac{2(j-1)T}{t_y}\right)\right]\right), \end{aligned} \tag{5}$$

where $t_x$ and $t_y$ are relaxation times, given by $\omega_x^2/4D$ and $\omega_y^2/4D$ respectively. $f_y(i)$ can be obtained from the above equation by replacing the term $((2n+1)/2l_x)^2$ with $((2m+1)/2l_y)^2$. A comparison between the analytical models and a numerical model is shown in Figure (1). The numerically generated points are found by solving the heat diffusion equation for the temperature with a finite element analysis routine. This is then used in

the Rayleigh–Sommerfeld diffraction integral to establish the resultant beam propagation after the window. By looking at the change in focal position after a known lens, the focal length of the thermal lens can be deduced. For the correlation test, the focal length as a function of the pulse energy was investigated. Clearly there is very good agreement between the analytical models and the numerical calculations. For very strong thermal lensing, the deviation is in the order of 7%, while for weak thermal lensing, the deviation is around 1%. A full derivation of a generalised version of the above analysis will appear shortly.[8]

The Zernike coefficients can be obtained by writing the phase as $\phi(x,y,t) = k\triangle n(x,y,t)l = k\partial n/\partial u \triangle u(x,y,t)$ and expanding this function as a series of Zernike polynomials. Figure (2) shows the change in coefficient values as a function of the thermal strength in the optic.

It is clear that in addition to the defocus (curvature) term, spherical aberration is also introduced to the wavefront. This degrades the beam quality, so that the $M^2$ factor is higher, and the propagation constants change. Figure (3) shows the beam propagation with and without thermal aberrations.

## 3. GAIN DISTORTIONS

A multilevel rate equation model (including rotational thermalization) based on that of Judd[9] was used to calculate the oscillator output energy as well as to calculate the pulse amplification and distortion through the high pressure amplifier. The controlling difference equations can be written as

$$\frac{d\delta_r}{dt} = P_j - \frac{(\delta_r z \Delta_v)}{\tau_x} - 2\sigma\frac{I}{hv}\delta_r, \tag{6}$$

$$\frac{d\Delta_v}{dt} = P - 2\sigma\frac{I}{hv}\delta_r, \tag{7}$$

$$\frac{\partial I}{\partial t} + c\frac{\partial I}{\partial x} = c\sigma\delta_r - \frac{I}{\tau_c}, \tag{8}$$

with $\delta_r$ the population difference between the rotational levels, $P_j$ the pumping term of a rotational level, $z$ the Boltzmann factor, $\Delta_v$ the total population difference of the vibrational levels, $\sigma$ is the cross section, $P$ is the total pumping term, $\tau_x$ is the rotational thermalization time, $I$ is the intensity of the pulse and $\tau_c$ is the calculated photon life time inside the resonator.

The above set of equations were solved numerically using code written in C++. Figure (4) shows the calculated beam distortion through a high pressure amplifier. The small signal gain in the amplifier was 3%/cm, the gain length was 0.4 m and the radius of the Gaussian beam propagating through the amplifier was 4 mm. The input energy of the pulse was 178 mJ and this was amplified to 477 mJ after a single pass through the amplifier. The beam is amplified more on the sides than in the centre, thus distorting the beam shape, and changing its waist value. This can be expected since the centre of the beam will saturate the laser gain medium first. The beam radius ($1/e^2$) value changes from 4mm to approximately 4.4 mm. It is also evident that the pulse shape changes, and thus a change in the $M^2$ value is expected. The resulting propagation of this beam will not be that of a perfect Gaussian.

## 4. CONCLUSION

We have considered a few sources of beam degradation on propagating through an oscillator–amplifier pair. For the repetition rates and energies of our lasers, thermal distortions are minimal, while spatial and temporal distortions due to the gain appear to dominate.

## 5. ACKOWLEDGEMENTS

We would like to thank S.P. van Heerden for useful discussions, and for the availablility of his Rayleigh–Sommerfeld diffraction code.

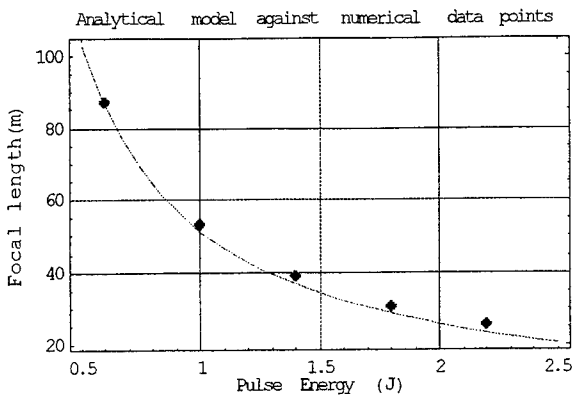


Figure 1: The numerical data points are in good agreement with the analytical model

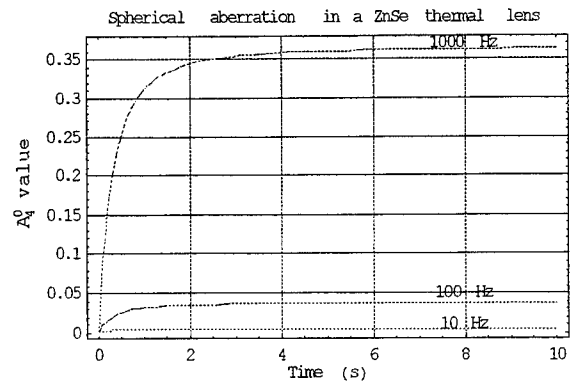


Figure 2: Spherical aberration is introduced to the wavefront, and shows a transient nature, due to the changing refractive index.

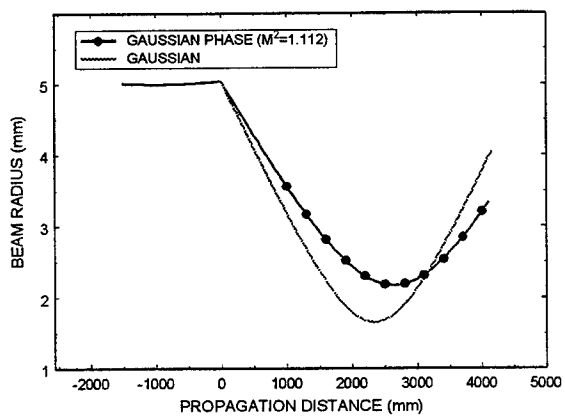


Figure 3: The introduction of spherical aberration increases the $M^2$ of the beam, altering the propagation.

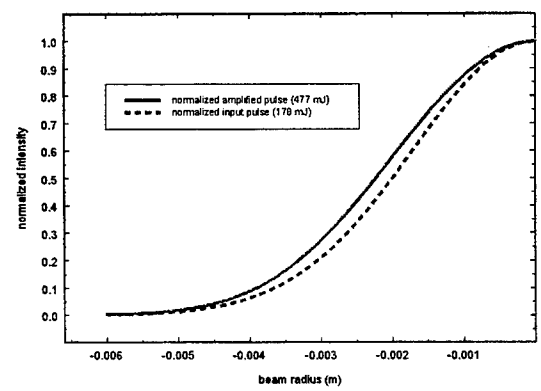


Figure 4: Gain distortions change both the pulse size and shape.

## REFERENCES


1. A. E. Siegman, "New developments in laser resonators," in *Optical Resonators, Proc. SPIE* **1224**, pp. 2–14, 1990.
2. V. N. Mahajan, "Zernike cirlce polynomials and optical aberrations of systems with circular pupils," Eng. Lab. Notes, in *Opt. and Phot. News* **5**, 1994.
3. V. N. Mahajan, "Zernike Polynomials and Optical Aberrations," Eng. Lab. Notes, in *Opt. and Phot. News* **6**, 1995.
4. B. Haba, B. W. Hussey, and A. Gupta, "Temperature distribution during heating using a high repetition rate pulsed laser," *J. Appl. Phys.*, **69**, pp. 2871–2876, 1991.
5. Y. Han, Z. L. Wu, J. S. Rosenshein, M. Thomsen, Q. Zhoa and K. Moncur, "Pulsed photothermal deflection and diffraction effects: numerical modeling based on Fresnel diffraction theory," *Opt. Eng.*, **38**, pp. 2122–2128, 1999.
6. S. P. van Heerden, W. Klopper, F. J. Prinsloo, and A. Forbes, "The influence of finite absorption in transmission optics on the propagation of high average-power pulsed $CO_2$laser beams," in *Laser Beam Characterisation, Proc. SPIE* **2870**, pp. 515–520, 1996.
7. A. Forbes, "Thermal lensing," in *Photothermal refraction and focussing*, Ph.D dissertation, University of Natal, 1997.
8. A. Forbes, S. P. van Heerden and M. M. Michaelis, "Beam degradation due to thermal aberrations," *in preparation*.
9. O. Judd, "High power gas lasers," in *Conference Series, The Inst. of Physics* **20**, pp. 45–53, 1975.

# Stimulated Brillouin Scattering in Multi-Mode Optical Fibers

Kazuyoku Tei*[a], Yasuhiko Tsuruoka[a], Taro Uchiyama[b] and Tomoo Fujioka[a]

[a]Dept. of Physics, Tokai Univ., 1117 Kitakaname, Hiratsuka, Kanagawa, Japan

[b]Dept. of System Design Engineering, Keio Univ., 3-14-1 Hiyoshi, Kohoku-Ward, Yokohama, Kanagawa, Japan

## ABSTRACT

In high power applications of multimode optical fibers such as high power beam delivery and optical phase conjugation, the estimation of critical power of stimulated Brillouin scattering is important. Nevertheless, the estimations have taken no account of mode dispersion effect to date. In this paper we show that the critical power in a multimode fiber depends on the numerical aperture (NA) of fiber, i.e. mode dispersion, and find out the analytical solution taking account of the effect. The critical power increases as the fiber NA increases.

**Keywords:** stimulated Brillouin scattering, optical multimode fiber, beam delivery, phase conjugation

## 1. INTRODUCTION

Multimode optical fibers have been widely used for high-power beam delivery 10-100m long in processes such as welding and cutting. The optical power deliverable has reached the multi-kilowatt level [1,2]. Such high power induces stimulated Brillouin scattering (SBS) in fibers when the bandwidth of laser light is comparable to or narrower than the bandwidth of Brillouin scattering. Such backscattering is an obstacle to high-power beam delivery. On the other hand, because such backscattering (stokes wave) is the phase conjugate wave of pumping wave, multimode fibers turn to be useful devises as optical phase conjugators[3].

The equation used to estimate the critical power of SBS in single-mode fiber was derived by Smith[4]. The observed critical powers in single-mode fibers are in good agreement with those estimated from Smith's equation. In the experimental work of Murata et al. [5], it was shown that the critical powers in multimode fibers are higher than those in single-mode fibers having the same diameter and the same length. Moreover, Their experimental results and our experimental results, described below, show that the critical powers in multimode fibers depend on the numerical apertures of fibers. This indicates that the critical powers are influenced by the mode dispersion in multimode fibers, and therefore, for multimode fibers, the Smith's equation should be rewritten by taking account of that effect.

In this work, we derive a simple equation to estimate the critical powers of SBS taking account of the mode dispersion in multimode fibers. The critical powers estimated from the equation are in good agreement with the experimental results.

## 2. CRITICAL POWER OF SBS

Critical powers of SBS excited by CW laser light in single-mode fibers are given by [4]

$$\frac{g_{\max} K P_{cr} L_{eff}}{A_{eff}} \cong 21, \qquad (1)$$

where $g_{max}$ is the peak value of Brillouin gain. Its value is $4.6\times10^{-11}$m/W. $K$ is the factor of polarization. $K$=1 for unchanging polarization, $K$=1/2 for polarization scrambling. $P_{cr}$ is the critical power, $L_{eff}$ is the effective interaction length and $A_{eff}$ is the effective core cross section. We regard the mode dispersion in multimode fibers as reduction effect on Brillouin gain:

$$g_B = b \times g_{\max}, \qquad (2)$$

$b$ is the factor of gain reduction due to mode dispersion. If we assume that $L_{eff}/A_{eff}$ is invariable, $P_{cr}$ is inversely proportional to $b$. Brillouin gain is proportional to the coupling constant of the coupled-wave equations that describe the energy transfer from a pump wave to a Stokes wave. Therefore, the $b$-factor is derived from the ratio of the coupling coefficient of a multimode fiber to that of a single-mode fiber.

*Correspondence: Email: tei@keyaki.cc.u-tokai.ac.jp; Telephone: +81 463 58 1211; Fax: +81 463 50 2013



XIII International Symposium on Gas Flow and Chemical Lasers and High-Power Laser Conference, Antonio Lapucci, Marco Ciofini, Editors, Proceedings of SPIE Vol. 4184 (2001)

Each transverse mode in a multimode fiber traverses at a corresponding phase velocity. A mode (m) of the Stokes wave interacts with a mode (m') of the pump wave that corresponds to the following phonon frequency:

$$\Omega_{mm'} = \omega_0 (V_a / c)(n_m + n_{m'}). \qquad (3)$$

$\omega_0$ is the pump wave frequency, $V_a$ is the acoustic velocity, $c$ is the light velocity in vaccum, and $n_m$ and $n_{m'}$ are the effective mode indices of refraction. We assume the cross-interactions $(m \neq m')$ occur when the phonon frequencies of eq. (3) are within the bandwidth of the phonon produced through a direct interaction ($m = m'$). Therefore, we consider the gain reduction in a multimode fiber is due to the limitation of the number of pump modes affecting each mode of the Stokes wave. We have derived a set of coupled wave equations for stimulated Brillouin Scattering in multi-mode optical fibers [6]. From the coupling coefficients the $b$-factor is dereived:

$$b \cong 2\left(\frac{2\Gamma}{\Omega_1 - \Omega_2}\right)\arctan\left(\frac{1}{2}\frac{\Omega_1 - \Omega_2}{2\Gamma}\right) . \qquad (4)$$

Here, $\Gamma = (\alpha_P/2)V_a$, and it is related to the phonon bandwidth $\Delta\nu_{FWHM}$, $\Gamma = \pi\Delta\nu_{FWHM}$. $\Omega_1$ $(=2N_1\omega_o V_a/c)$ and $\Omega_2$ are the phonon frequencies when the fiber core and clad materials exist as a bulk mass. $N_1$ and $N_2$ are the refraction indices of core and clad respectively. Equation (4) shows that the $b$-factor depends not on core diameters or total number of modes, but on $N_1$-$N_2$, that is, NA, and $\Gamma$.

## 3. EXPERIMENTS WITH IODINE LASER

Murata et al. employed a pulsed iodine photodissociation laser ($\lambda$=1.315 $\mu$m) [5] as a pump source. The pulse width was about 4 $\mu$ sec. The linewidth of laser light was narrower than 20 MHz. In the experiments they used two different multimode fibers. The specifications are shown in Table.1. The observed critical powers are different from the values estimated using the Smith's equation (Eq.1). Figure.1 shows the NA dependence of $P_{cr} / P_{min}$ $(=b^{-1})$. $P_{min}$ is the critical power predicted from only Eq. (1). The curves are drawn using the value of $\Gamma$ for silica [7] and $K$=1/2 for polarization scrambling. Squares (■) in Fig.1 represent the experimental results from ref. 5. Equations (1) and (4) yield the critical powers within an error of 25%.

Table. 1 Fiber specifications in ref. 5 and the observed values of critical power

| Diameter ($\mu$m) | Length (m) | NA | $P_{cr} / P_{min}$ |
|---|---|---|---|
| 100 | 260 | 0.25 | 4 |
| 200 | 100 | 0.4 | 10 |

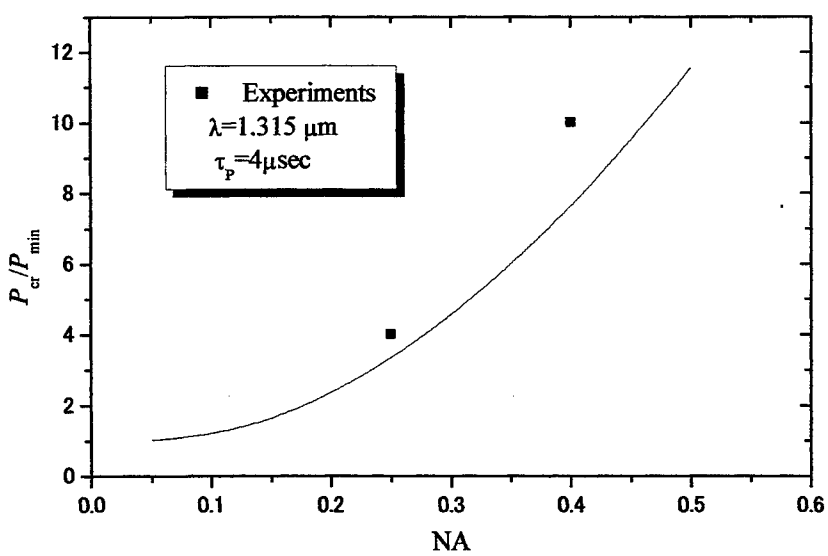


Fig.1 Critical power versus fiber NA ($\lambda$=1.315 $\mu$m)

## 4. EXPERIMENTS WITH Nd:YAG LASER

We have also employed a Q-switched Nd:YAG laser ($\lambda$=1.064 $\mu$m) as a pump source. The linewidth of laser light was narrower than 30 MHz The laser pulses have a width of 60 nsec and generate at a repetition rate of 100Hz (Fig.2). Although the SBS process with the pump pulse duration of 60 nsec is a transient regime, the difference of critical power between this case and the stationary (CW) regime is small. If we assume the phonon lifetime of 10 nsec, the difference is estimated to be about 8%[8]. We have measured the critical powers of two fibers while the bending radius changes. The fibers have relatively short length ($L$=1.15m and 5.105m) as using as phase conjugators and have the same fiber NA (NA=0.22). The fiber core diameter is 320 $\mu$m. All over the experiments, NA of launching optics is 0.008. The focus spot diameter was 140 $\mu$m at the end of fibers. The coupling efficiency was about 90%. Through changing of the bending radius the output NA changes within a range: 0.05~0.14. Figure3 shows the products of critical power and fiber length for different values of the output NA. $E_{cr}$ is the critical energy, which is calculated with the critical power $P_{cr}$ and the laser pulse width $\tau_P$: $E_{cr} = P_{cr} \cdot \tau_P$. The experimental data split into two groups. This is probably caused by the polarization scrambling for the group of $L$=5.105m. It is supported from the fact that the data of $L$=5.105m are on the theoretical curve for $K$=1/2. The curves are drawn by making compensation for the transient regime.

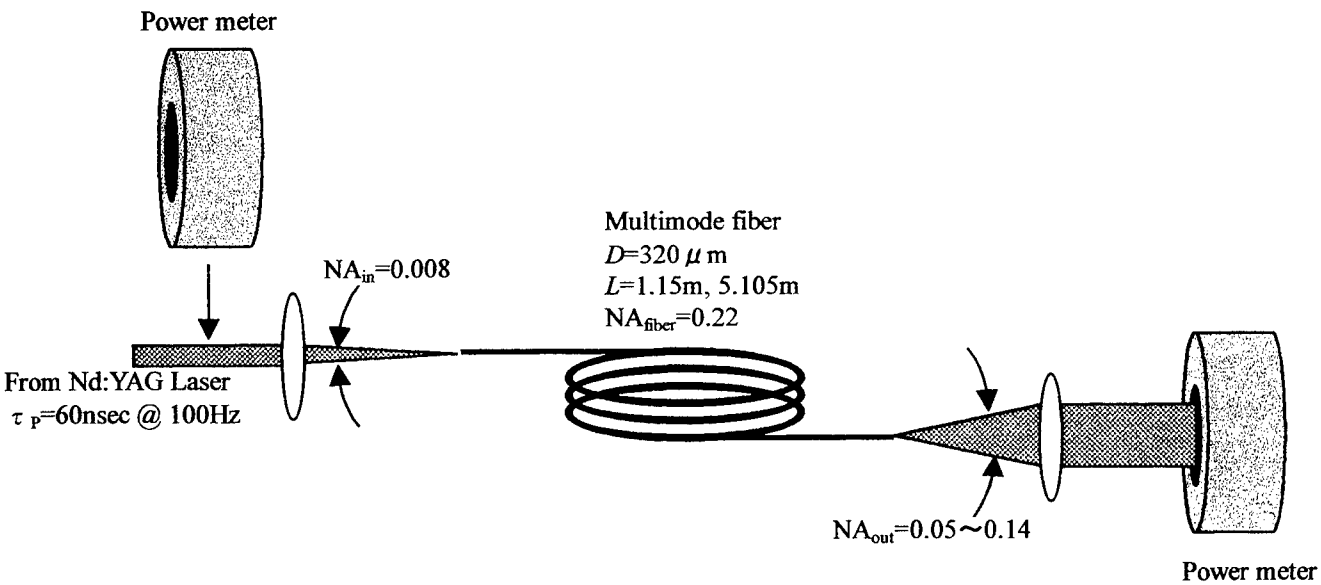


Fig.2 Measurements of SBS critical power in multimode fibers with a Q-switched Nd:YAG laser

## 5. COCLUSION

We derive the analytical solution to estimate the critical powers, taking account of mode dispersion in multimode fibers. The ratio of critical power for a multimode fiber to that for a single-mode fiber having the same diameter and the same length depends on the NA of the fiber and the phonon bandwidth. For a large NA, the critical power for a multimode fiber is much different from that for a single-mode fiber. It is expected that the critical powers of commercially available multimode fibers (NA≃ 0.2) will be about twice as much as values estimated by only Eq.(1) if the output NA is close to the fiber NA. The relatively short ($L$<5m) multimode fibers have recently been used as the optical phase conjugators[3]. The pump power diffusion between inter-modes in such short fibers takes place in the limited range of mode number. This fact is found out through the effect that the output NA of transmitted pump wave is less than the fiber NA. Therefore the SBS critical power of such the short multimode fiber increases the output NA increases due to various causes, i.e. bending, coupling optics, etc.

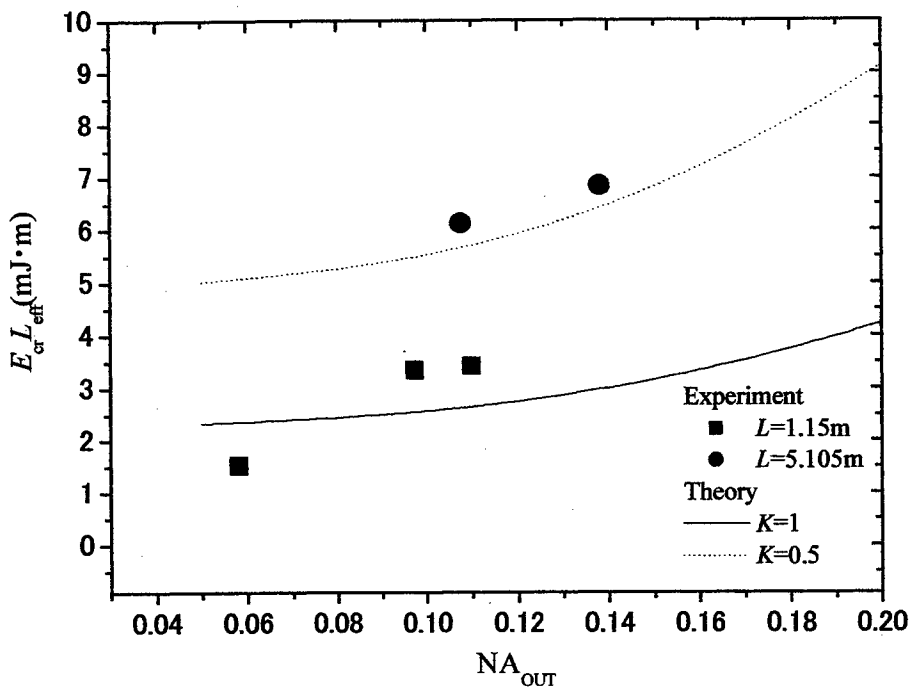


Fig.3 Critical power versus output NA( $\lambda$ =1.064 $\mu$ m)

## REFERENCES


1. T. Sakurai, K. Yasuda, T. Osaki, E. Tada, K. Koizumi and M. Nakahira, "Study on material processing and fiber transmittance of COIL," Proceedings of ICALEO '96, **81**, Section-E, 28-37 (1996).
2. P. M. Noaker, "Laser delivers 7.36kW via fiber," Laser Focus World, **December**, 22-23 (1998).
3. H. J. Eichler, J. Kunde and B. Liu, "Quartz fibre phase conjugators with high fidelity and reflectivity," Opt. Commun., **139**, 327-334 (1997)
4. R. G. Smith, "Optical power handling capacity of low loss optical fibers as determined by stimulated Raman and Brillouin scattering," Appl. Opt, **11**, 2489-2494 (1972).
5. H. Murata, A. Otsuka, K. Serizawa, T. Uchiyama and T. Fujioka, "Chemically-pumped iodine laser and its application to optical power transmission," Proceedings of the 5th GCL Symp., (Inst. Phys. Conf. Ser. No. 72) 163-168 (1984).
6. K. Tei, Y. Tsuruoka, T. Fujioka and T. Uchiyama, "Critical power of stimulated Brillouin scattering in multimode optical fibers", Appl. Opt (submitted)
7. D. Cotter, "Observation of stimulated Brillouin scattering in low-loss silica fibre at 1.3μm," Electron. Lett., **18**, 495-496 (1982).
8. V. I. Bespalov and G. A. Pasmanik, *Nolinear Optics and Adaptive Laser Systems*, Chapter 1, Nova Science Publishers, Inc., New York, 1993.

# Slow components of solitonic wave of change in reflection and conduction excited by $CO_2$ laser pulse in plexiglas: experiments with IR detector

E.M.Kudriavtsev*[a], S.D.Zotov[a], M.Autric[b]

[a]Lebedev Physical Institute of RAS, 117994 Moscow, 53 Leninsky Pr., Russia.

[b]IRPHE Institute for research on nonequilibrium phenomenon, University of Marseille/CNRS, Marseille, France.

## ABSTRACT

Experimental results of investigation in plexiglas support previously published our groups data of IR laser and e-beam excitation in solids of solitonic Wave of Change in Reflection and Conduction (WCRC). Method of single IR detector WCRC registration was applied in addition to IR thermovision method used before (there were used also ~5 other different methods). Results of slow WCRC components investigations showed that solitonic heat transfer play additional role to usual diffusive heat transfer. This role could be important at some conditions. As the control, the measured in this work WCRC component velocity ~ 0.26 cm/s does not depend from sample thickness which was equal 1.5 and 2.0 mm. Analysis of records treatment by help of (x-t) diagram permit to show many features of studied solitonic excitations lived in the solid sample during many minutes. Irradiation of the front surface by single laser pulse produced WCRC components; in experimental conditions of this work one can see pair components of the same velocity which were born as on front as on rear sample surface. They moved in different directions and reflects from sample surfaces many times with small energy losses. This work was sponsored by RFBR (Russia), project 97-02-17954-a) and 00-02-17249 a).

**Keywords**: solitonic wave; IR laser excitation; light reflection, heat transfer; plexiglass.

## 1. INTRODUCTION

Since 1992 we study experimentally and theoretically the Wave of Change in Reflection and Conduction (WCRC)[1,2,3,4]. WCRC characteristics were measured from variation: 1) of the optical constants (by reflection on the surface or absorption in the bulk); 2) of the temperature (by thermovision camera or thermocouples) en the sample surfaces; 3) of the pressure (by pressure pick up); 4) of the conduction on the surface and in the bulk (in the case of conducting samples).

WCRC shows an universal character: it can translate the pulse of energy through the samples of any of 4 main crystal types, some amorphous solids (glasses ) or condensed matter samples in the manner different from usual diffusion. Also WCRC could be excited by pulse beam as of laser (electromagnetic) as of electron (particle) [5] emissions with neighboring thresholds (about 5÷10 kW/cm$^2$).

WCRC can present solitonic mechanism of heat transfer in condensed matter and could be important in many laser / surface interaction studies. As example, it could be important for investigation of processes in the materials exposed to pulse laser irradiation, especially in the case of pulse - periodic irradiation, where it is possible to get some new regimes of laser - matter interaction.

The point is that even the WCRC which was excited by single IR pulse laser consist from the whole series of more than 30 solitary kind waves (which velocity drop twice starting from speed of sound to less then cm/s). Each WCRC wave structure component keeps the velocity, measured signal variation sign and pulse shape in the process of propagation through the material and reflection from the sample surfaces. Each WCRC component can be reflected many times (20-30), so the whole wave process in the sample could be seen during many minutes as a very complex one.

* Correspondence: Email: kudri@x4u.lebedev.ru ;Telephone:(095)132-64-55



XIII International Symposium on Gas Flow and Chemical Lasers and High-Power Laser Conference, Antonio Lapucci, Marco Ciofini, Editors, Proceedings of SPIE Vol. 4184 (2001)

The present article will show the results of one more method of WCRC registration by help of single IR detector on the example of plexiglas sample investigations.

## 2. EXPERIMENT

### 2.1. Schema of experiments

Schema of measurements is very simple in principle [6]. The plexiglass samples of different thickness (2.0 and 1.5 mm) are irradiated through the IR lens (~10kW/cm$^2$) by single 10.6 μ $CO_2$ laser pulse (~0.3 s; ~0.1 J) from one side. The temperature variation of rear side of the sample is registered by IR detect
or equipped by appropriate scheme of signal amplification and treatment (description in more details of this part of experimental installation see in [6]).

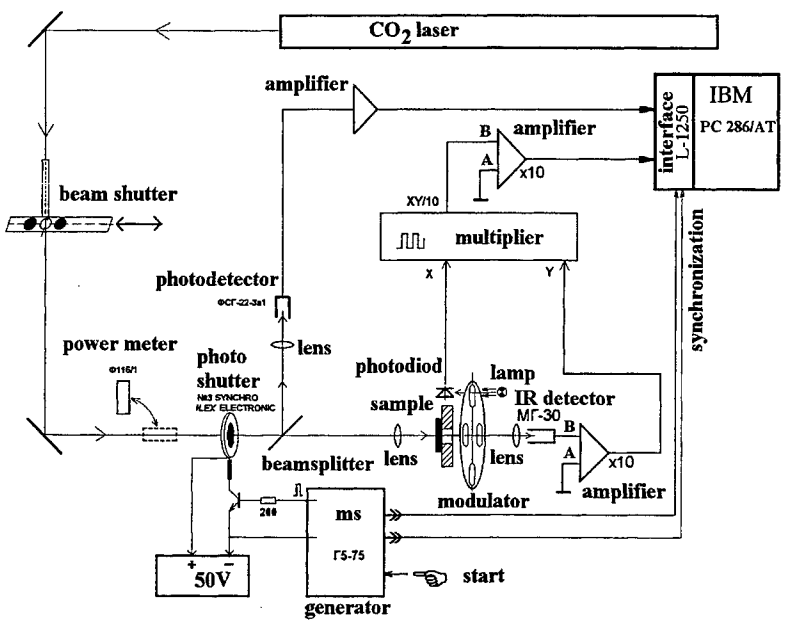


Fig.1 Optical scheme of experiment

### 2.2. Experimental data

Fig.2a)b), 3a)b) presents a) **typical** results of the record treatment for 2.0 and 1.5 mm thickness, ***d***, of plexiglas samples and b) - correspondent (x-t)- diagrams of WCRC reflection process. Excitation laser impulse (0.32 ms) region on t-scale is marked on Fig.2a)b), 3a)b) by vertical hatched column.
Mostly we experienced with ***d***=2.0 mm and for that case it is possible to present here many (~30) records treatment with the same features discussed later. It was fulfilled ~100 experiments separated in 7 series.

#### 2.2.1. Usual diffusion heating

As one can see, the main common feature of both Fig. 2a),3a) (which could be seen at different curves smoothing) is a slowly increased IR emission intensity of rear side of the samples. (Curves 1,2 come through the maximum and then slowly falls down at the end of 10 sec display time). This IR emission intensity is proportional generally speaking to the surface sample temperature, ***T***, and coefficient of light reflection by surface sample, ***R***. One can suppose that ***R*** – value is constant in the process of usual slow heat diffusion flow from the front side of the undisturbed plexiglas sample. Then all the curves 1,2 on Fig. 2a),3a) correspond to the slow temperature variation of the rear sample surface, $\Delta T$, with maximum value $T_{max}$. Calculations of heat propagation through the sample (thin dashed curves 5) for two different thickness support this conclusion. The $T_{max}$ for ***d***=1.5mm sample correspond to ~3.4 sec, in rather good agreement with both experimental curves on Fig. 3a). The $T_{max}$ for ***d***=2.0 mm is remarkably later ( ~5.5 sec). This agrees also well with experimental data of Fig. 2a).

#### 2.2.2. Solitonic wave

There is one more common feature on the curves 1,2 of both Fig. 2a),3a) (curve 1 is shifted relatively curve 2 by ordinate for reader convenience). It is clearly pronounced periodicity of registered IR emission variation, $\Delta I$. We interpret this variations as the results of WCRC influence. As one can see from Fig. 2a),3a), the time variations of zero-lines 3,4 (registered before or after group of experiments) are each less in amplitude; and else diminished in amplitude after averaging of them. Besides, there is no clear periodicity for zero-lines as it must be for the noise curves.
As the opposite to this character of zero-lines, the curves 1,2 of Fig. 2a),3a) are periodically disturbed and this periodicity is clearly reproducible in different experiments made in the same conditions. Following to our interpretation of such a data, each WCRC component change periodically and locally thermodynamic parameters and optical characteristics of the

sample surface each time when it appears there in the process of running between sample surfaces with many reflections and nearly constant velocity.
For each specified time display and experimental point smoothing one can distinguish on the curves 1,2 mainly one WCRC component. It is periodically running back and forth between the front and rear sides of the sample and so produce periodical disturbance of IR emission intensity which are seen as variations $\Delta I$.

### 2.2.3. Process of soliton reflections

The correspondent (x-t)-diagram of WCRC reflection process is shown on Fig. 2b),3b). As one can see on Fig.2b), minims $C_2$,$D_2$,$E_2$ are nearly equidistant. Their positions on (x-t)-diagram at X=2 mm (rear side of the sample) marked by oblique crosses. The correspondent WCRC component velocity $U_i$ = 0.28cm/s. The (x-t)-diagram being extrapolated two more steps (to the minimum $B_2$ and to the very beginning where measurements are not trustworthy) fit exactly to the start of experiment at t=0. It gives one more proof to our data interpretation. It is important to note that this WCRC component was generated *on the rear side* of the sample (what was usually happened also in experiments with massive metal sample [5] ).
One can go to more detail for better agreement of minims $B_2$,$C_2$,$D_2$,$E_2$,$F_2$ with (x-t) diagram. It needs suppose that after some reflections the $U_i$ –value start to drop (on ~2.5% after 5$^{th}$, ~12% after 7$^{th}$, and ~13% after 9$^{th}$ reflection).
Looking ones more on Fig.2a) one can note that minims $d_2$,$e_2$ (marked by circles on X=2 mm line of (x-t)-diagram) separated for the same distance as $C_2$,$D_2$,$E_2$. In our interpretation and in agreement as example with [5] it means that $d_2$,$e_2$ are "footprints" of another WCRC component moving with the same velocity but generated on the front sample surface (dashed line on (x-t) diagram). Also one can note that the same kind of analysis for curve 1 of Fig. 2a) which is periodically disturbed in less pronounced shape gives velocity $U_i$ about 4% less.

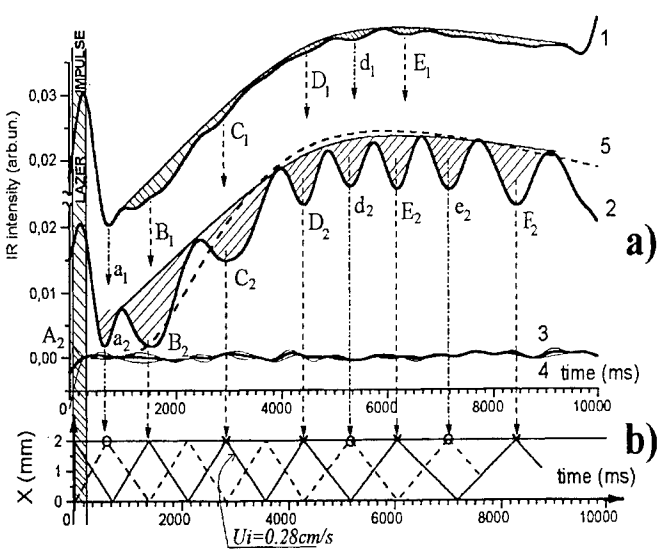


Fig 2a),b)

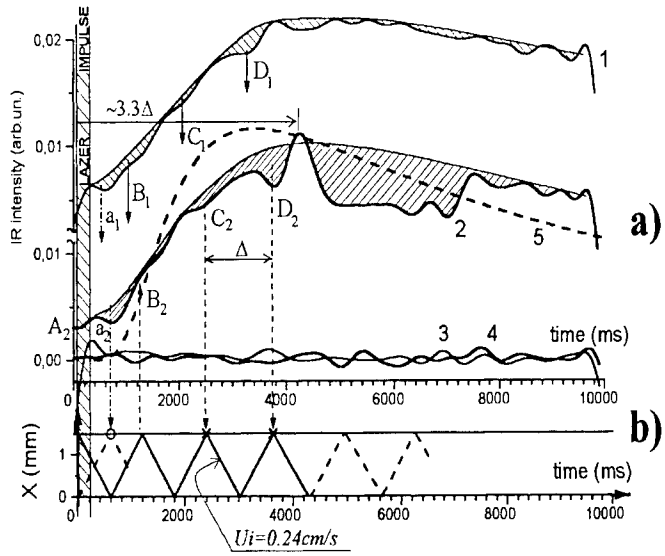


Fig. 3a),b)

### 2.2.4. Control WCRC velocity measurements

Fig. 3a),b) presents the same records treatment as on Fig 2a),b) but for the thickness of the sample $d$ = 1.5 mm. The same kind of analysis shows that velocity measured here from curve 2 is $U_i$ = 0.24 cm/s and value measured from curve 1 is higher on 17%. (Between many reasons of that could be uncontrolled difference in the damage of sample surface which change the sample thickness and so one). The mostly important that velocities $U_i$ measured in the same conditions for two different sample thickness ($d$ = 2.0 and 1.5 mm) are well agree in the limits of errors ($U_i$ = 0.28 and 0.24 cm/s).

### 2.2.5. Soliton reflections from sample walls

One can note the sharp drop down of the curve 2 on Fig. 3a) behind the minimum $D_2$. It starts at the time ~3.3 times longer then period of WCRC component moving back and forth trough the distance 1.5 mm. As it was found, the place of sample excitation by laser pulse was in this experiment only situated 5 mm from both side walls of the plexiglass sample. The

WCRC component reflected from both side walls must come to place of measurements after time which is 5.0 mm :1.5 mm = 3.3 times longer then reflected from rear side of the sample. This proofs again that studied WCRC reflects as solitonic wave. Besides it proofs that light reflection variation $\Delta R$ has negative sign in WCRC, what was used in the (x-t) diagrams of Fig. 2b),3b) construction.

### 2.2.6. Variations of light reflection or temperature?

It is reliable to suppose that mentioned WCRC disturbances of experimental curves 1,2 of Fig. 2a),3a) correspond mostly to $\Delta R$ variations of sample surfaces. Change of reflection produce quick variation of IR intensity, $\Delta I$, that could exist at constant value of $T$. Increased $R$-value in this conditions correspond to decreased IR emission intensity (which could be interpreted as local surface *cooling* at WCRC arrival. Theory of Frenkel and Kontorova' soliton permit it [7].).

### 2.2.7. Effect of sample "saturation" by solitons

It is very interesting preliminary find of this investigation that the first experiment on WCRC excitation in the sample has the record treatment which contains much more pronounced disturbances, "footprints" of WCRC in comparison with the following experiments of the same series fulfilled later with the intervals 2-3 minutes. This situation shown on Fig. 2a), where curve 2 corresponds to the first experiment and curve 1 – to the third experiment fulfilled ~4 minutes later in the same series. As one can see the minimum deepness differs for this curves in many times. Nearly analogous situations could be seen in 3-5 other series experiments on plexiglas.
The explanation of this could be in solitonic features of WCRC. Namely, classical solitons propagate trough the media without interaction with each other (see, as example [8] ). So there exists during minutes [5, 9] in the investigated sample after repetition of WCRC excitations by laser pulses a lot of solitonic components which are slowly moving in different directions without interaction. Because each of them produce his own local influence on the sample it diminish the grade of disturbance pronunciation (saturation process). The same situation could be noted for the zero-lines registration which could include solitonic waves still living in the sample after previous experiments.
We plane to control this facts in father experiments.

## ACKNOWLEDGEMENTS

Authors express their gratitude to A. M. Baldin (JINR, Dubna) for interest to investigation and support; to V. I. Emel'yanov (Moscow State University), E. E. Godik (USA), A. Feldman (NIST, USA) for interest and discussion; to E. N. Lotkova, B. G. Makeev for their help in experiments. This work was sponsored by RFBR (Russia), project 97-02-17954-a) and 00-02-17249 a).

## REFERENCES

1. E.M.Kudriavtsev, S.D.Zotov, V.V.Krivov, M.Autric, *Physica C*, vol. 234-240, p.1439, 1994.
2. E.M.Kudriavtsev, S.D.Zotov, V.V.Krivov, M.Autric, *Physica C*, 282-287, p.1145, 1997.
3. E.M.Kudriavtsev, "Thermal solitons in the laser-surface interactions", in: *High-Power Laser Ablation*, Claude R.Phipps, Editor, Proceedings of SPIE Vol.3343, pp.411-422, 1998.
4. E.M.Kudriavtsev, «Solitonic type excitations in laser- condensed matter interaction: additional proof by independent publications», invited paper, in: *High-Power Laser Ablation-III*, Claude R.Phipps Editor, *.Proc.of SPIE,* Vol. **4055,** pp. 411-424, 2000.
5. E.M.Kudriavtsev, A.N.Varava, A.V.Dedov, A.T.Komov, "Observation of slow components of solitonic-tipe wave structure excited by e-beam in massive copper sample", *JINR Rapid Communications*, N. 5,6[97]-99, pp.13-21, 1999.
6. С.Д.Зотов, Е.М.Кудрявцев, Э.Н.Лоткова, Б.Г.Макеев, Разработка оптической методики обнаружения солитоно-подобной составляющей теплопереноса в твердых телах. *Препринт ФИАН* № 10, стр.26, Москва, 2000.
7. Y.Frenkel and T. Kontorova, *Zh. Eksp. Teor. Phys.* **8,** 89, 1938; 1340, 1938; *J.Phys. (Moscow)* 1, 137, 1939.
8. А.Т.Филиппов, *Многоликий солитон,* Наука, Москва, 1990.
9. E.M.Kudriavtsev, S.D.Zotov, M.Autric, «Slow components of wave of reflection and conduction (WRC) in plexiglas irradiated by single pulse of $CO_2$ laser for damage threshold study (Abstract only) », in: *Laser -Induced Damage in Optical Materials: 1997*, Gregory J.Exarhos, Arthur H.Guenther, Mark R.Kozlowski, M.J.Soileau, Editors, Proceedings of SPIE Vol.**3244**, p. 314, 1998.

Invited Paper

# INDUSTRIAL APPLICATIONS OF LASERS

Maichi Cantello, Cristina Rivela, Mauro Penasa

RTM SpA, 10080 Vico Canavese TO – Italy

## ABSTRACT

Lasers have reached a relevant importance as production means, and are integrated in the manufacturing cycles of the most diversified industrial sectors, ranging from micromachining to heavy industry. This memory gives a short account of the state of the art of laser application in industrial production.

## INTRODUCTION

In the landscape of industrial production, the fields of laser application are numerous and range from micromachining of silicon chips to shipbuilding: because of the countless number of applications there are obvious difficulties to produce a deep uniform analysis. In this memory we will try to give a picture as accurate as possible of the situation of laser based production and applications in Italy, with attention to general developments and to new industrial opportunities.

Of clear relevance are all the applications of high power laser systems in industrial production, involving mainly cutting, some special drilling processes, few applications of treatments and cladding (prototyping) and welding at an increasing extent. Industrial sectors like automotive, aerospace, shipbuilding, energy and electromechanics will be briefly examined, with special regards to the situation in Italy and attention to the general state of the art and future developments which are expected in the next years.

Laser micromachining is also a processing operation of basic importance for several sectors (biomedics, electronics, silicon chips production, brazing and joining of terminals); surface preparation and cleaning is another field relatively new in which laser processing is finding its niche of special industrial application.

## CUTTING

Laser cutting is the dominating industrial application of the laser technology. As far as investments are concerned, laser cutting is involved for more than 60% of total of laser applications, covering a rough 85-90% of the technical market for high power lasers. The main reasons lay in the large degree of flexibility and in a noticeable productivity (rendering laser cutting a strong competitor of punching for medium size batches), as well as in the quality of the results achieved and in a relatively simple and robust procedure, at least in the general acception of 2-D cutting, which is the most diffused application. Applications range from 2-D cutting of metal sheets (sometimes coupled with punching systems) and pipes, to 3-D cutting (trimming of formed sheets, beveling of pipes for subsequent welding), with processed thickness mainly in the range 1-6 mm, but with cutting capability up to 25 mm and even more. $CO_2$ and Nd:YAG lasers are the sources involved in high power cutting applications. Application to plastics may however be pursued with other sources.

Laser cutting is produced by a beam focused on the material surface at a sufficient power density to cause heating, melting (combustion on non metallic materials), and vaporization. For small thickness the molten layer may reach the boiling point and vaporization prevails, otherwise melting is the relevant aspect which requires a gas flow in order to remove the liquid parts.

The assist gas flow, coaxial with the beam, removes the molten material. Depending on material requirements, the gas can be active or inert. The main process parameters for laser cutting of metallic materials are: laser power, travel speed, type and flow of assist gas, laser spot dimension, nozzle distance from the material.

A distinction between strong (> 6 mm) and precision (< 6 mm) cutting is usually made. Most applications may be found in this second field, since with increasing thickness the productivity changes dramatically. On metal sheets virtually every sector of industrial production benefits from lasers cutting.

However the enhanced optical quality of modern laser sources allows high power lasers (3-6 kW) to be applied in cutting applications. Thus the productivity and resulting economical convenience of heavy section cutting is more evident (i.e. in shipbuilding).

On the market there are numberless laser cutting systems, in particular for plane or tubes cutting applications, Fig. 1. However also 3-D laser systems have high diffusion as in the trimming of body car parts for prototypes and pre-series.

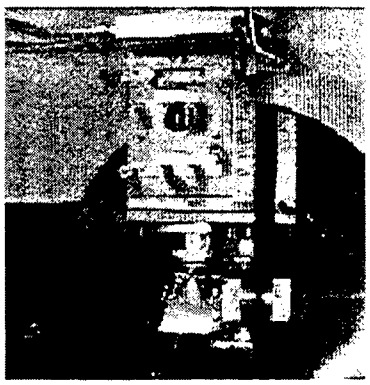

**Fig. 1 - Laser cutting system**



XIII International Symposium on Gas Flow and Chemical Lasers and High-Power Laser Conference,
Antonio Lapucci, Marco Ciofini, Editors, Proceedings of SPIE Vol. 4184 (2001)

As a brief conclusion laser cutting has to be considered a mature technology, widely used and generally accepted as a standard. Performance of existing commercial systems are of great relevance, for what concerns speed and dynamic stability, and few items have remained for applied research.
The main objects for R&D at present days are related to quality and/or productivity increase in high power heavy section cutting, as well as to closed loop process control (a general objective of laser applications). From the technical point of view chamfering (inclined cutting) is getting more and more relevance in the landscape of industrial applications.

## LASER BEAM WELDING

Laser welding technology shows advantages of considerable importance in several industrial applications, in particular for its high energy concentration which makes the welding process extremely innovative in comparison to conventional techniques. The laser beam can in fact be focused to a few tenths of a millimetre and can reach energy concentrations of as much as $1 \cdot 10^5$-$1 \cdot 10^7$ W/cm$^2$ (on spots which typically range between 0.04 and 0.4 mm, depending on the laser source, on the specific application and on the focusing optical system) which produce high penetration depths with a narrow molten and heat affected zone.
The main feature of high power density laser welding is keyholing. The keyhole permits a deep penetration with high aspect ratios (weld bead depth to width ratio) much improved with respect to conventional techniques, and partly traps laser energy in the cavity, increasing absorption.

### Industrial Application of Laser Beam Welding

The survey of industrial applications of laser welding has been organised by sectors. Some of these are already making an extensive use of LBW, as in automotive production, while in other sectors laser welding is under study as a possible competitor of existing production technologies, as is for riveting in the aerospace fuselage assembly.

### Automotive

This is the first industrial sector which involved laser as a standard production welding technique. LBW of synchronizer on gears surpassed brazing techniques since the beginning of the '80s, with obvious advantages on process related distortion, allowing laser operations on finished parts. LBW is used in several components of the transmission chain, in the assembly of clutch elements, vibration damping components, and in general on cylindrical couplings used to connect spindles and gears (axels, steering boxes, etc.). In most situations weldability of such materials is not an easy task, and pre-heating may be necessary to reduce the chance of solidification cracking.
Other special applications are in the field of motor parts, involving mainly the competition sector, with laser assembly of hollow structures as piston pins and rods, engine sodium cooled valves, all components made by special materials, from improved steels to titanium alloys and superalloys.
Of relevant importance and wide diffusion, the LBW based production of semifinished elements for the car body-in-white assembly has somehow revolutionised the sector of car bodies manufactury. Since 1986 the laser beam welding process has been used for producing flat formable sheets made of sections of different thicknesses joined by laser, called tailor-blanks.
In the field of car body assembly, several applications exist on industrial production lines. The most diffused is the joint between the roof and the side rails, although many others developments are already under exploitation to assembling front/rear rails which support the windscreens, to several parts of various hoods. At last, relatively new application is laser brazing of joints, where requirements force towards high surface quality standards. As far as new tendencies are concerned, the deep interest in space-frame design made up of tubular elements, and in the use of the related hydroforming technology, makes LBW a precious technique capable of tackling joining problems by a single side process, and a powerful substitute of spot welding processes.
Other components welded for the auto-motive industry range from small tanks to parts of the exhaust system, from airbag elements to a large number of sensors widely used in automotive. A large number of new applications involve laser welding of plastics, using differential absorption of various polymeric materials to perform joining at their interface. Diode lasers are used to this purpose.

### Energy

The energy sector is extremely diversified and usually characterised by components from relatively small up to huge dimension, in this case produced in small numbers. Power generation plant components (conventional, nuclear fissile and fusion), conventional heat exchangers, turbine components, high temperature parts of furnaces, may all be tackled by laser beam welding, as long as thicknesses involved are in the range of up to 15 – 20 mm.
Investigated applications are in the construction of parts for nuclear fissile power plants, where accuracy of preparation for joint edges is not typically an additional requirement. In the '80s studies have clarified the possibility to use LBW for the

assembly of tubes to plate for steam generators, and of connection tubes inside the cooling circuits. The results have shown the small distortion and high quality which characterise the laser process.
A recent production of few functional modules of toroidal field magnets as shown the capability of controlling distortion even when relevant weld lengths are involved.
Other applications in nuclear power plants range from dismantling (sealing/cutting), to assembly of special parts as spacing grids for tube bundles or fuel elements. Inflating spacers have been produced to avoid displacements in magnet batteries, and lasers have been tested for welding of resonating cavities, employed in physics.
Conventional applications are far more easily driven to the technology with industrial objectives. In addition to applied researches on butt welding of pipe coils, and on laser assembly of membrane panel walls, as well as on pipeline elements (all on Cr-Mo steels often requiring pre-heating to avoid solidification cracks), many interesting components as panel walls for heat exchangers may be manufactured by overlap welding of flat sheets to drawn channels to form sealed ducts. This technique of composition is extremely relevant in the design of structures involving laser beam welding, and a typical example of product innovation related to manufacturing techniques.
In conclusion, in the energy sector, laser beam welding is taken into high consideration for the low distortion – high quality joints produced. However the production volume, often limited to small series, is not sufficient to fully benefit of the particular features of the technique. Thus, more than real dedicated production systems, lasers are used on laboratory facilities applied to special cases.

**Aerospace**
Laser welding applications in the aerospace sector are widely encountered although at a limited extent, mainly for the competitiveness of electron beam welding. Two typology of componentes may be involved: aeroengines and airframes.
In fact any production based on laser beam welding has been so far related to parts of engines, typically made in various superalloys (high temperature stages) or titanium alloys (compressor stages), with welded thickness limited to few mm. Lots of producers are using lasers to reduce distortions on finished parts, in general rings and casing, pocket closures or blade inserts. Productivity is of secondary concern while the required quality is often difficult to be achieved, depending on the processed material, due to defectivity like microporosity or microcracks. A widely adopted configuration is butt welding on 2-3 mm thickness, even if also heavy sections are of interest.
The repair and replacement of worn parts (laser cutting and rewelding) is another field that can grow in importance.
Regarding airframes ( fuselage panels, wings special sections, box-type flaps...),the kind of material (aluminium alloys with high performances, series 2xxx, 6xxx, 7xxx) has up-to-now made difficult the welding technology. Traditionally obtained by riveting, aeronautical structures are highly exposed to corrosion. Moreover the increasing request of lighter structures makes the riveting not fit to obtain high performances.
Nowadays a process of laser welding of skins is being studied. These skins are the external part of the fuselage and they are welded to reinforcement stringers: this is possible because of the development of new sources (high focalisation), the intensive use of weld wires and the study of new materials.
The laser is also used to weld boxes for inboard electronic devices (avionics), made of aluminium alloy, for EM isolation.

**Shipbuilding**
Another possible sector in which laser technology is capable of leading to important savings is the shipbuilding industry. In the construction of internal decks and substructures of ships, materials and geometries involved in welding operations and suitable for laser welding as well as for automation are common standards. Carbon and low alloyed steels, although primerised with zinc base paints, are normally used in commercial ships while lower thickness stainless steels are mainly involved in military ships and aluminum alloys in fast transportation.
Welding configurations are typically butt joints and T butt double sided joints, with thickness ranging from 5 to 30 mm, but mainly around 12-15 mm. Of course only a fraction of this production can be welded from one side only in a single pass; most welds starting from 15 mm are to be performed via opposite side or by chamfer filling multipass.
A recent industrial application regards the stake welding of reinforcements through the external plate. It is an efficient method to complete closed structures from the outside. The thickness of panels may be up to 10 mm or more.
The laser is also used in the production of special elements, such as the welding of cable guides in austenitic, ferritic-martensitic or duplex steels. Also various sandwich panels are actually produced by laser beam welding.

**Mass Production (house appliances, electromechanical components)**
Information technology is an important sector in which laser is profitably used. Printer components are laser cut and subsequently spot welded using solid state Nd:YAG sources. Solid state and diode laser sources are also used for brazing electrical components or mechanical elements such as print needles. Laser welded boxes for PC also have wide diffusion.

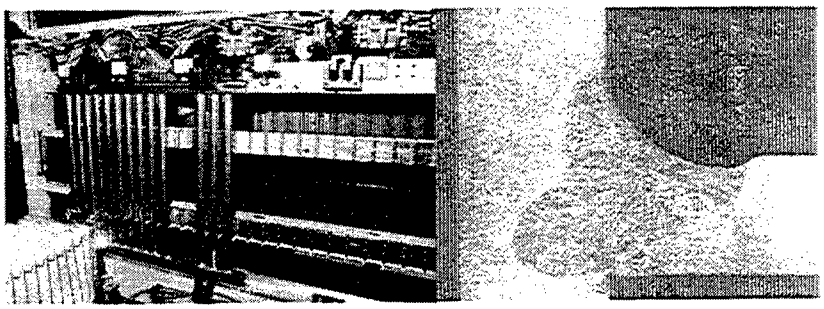

**Fig. 2 - $CO_2$ laser welding of radiators**

There are also several applications in the electro-mechanical sector, generally on metal sheet. The greatest diffusion is in the field of electrical household appliances.
In the production of the washing-machines, the laser welding of stainless steel drums has permitted a reduction in sheet thickness down to 0.4 mm, with high productivity and remarkable savings. This component can be welded in few seconds.
The assembly of cooking plates, featuring special aesthetical requirements, is another interesting application, involving Nd:YAG sources, and wide diffusion of laser welding can be observed in the production of steel radiators for domestic use, Fig. 2.
The $CO_2$ laser is also used for welding solenoid valves, a delicate process because of the materials involved and the required fatigue performance.
A recent application is the welding of brass ball-valves: the bad answer of the material can be cause of difficulties but an appropriate joint design and Nd:YAG laser sources of high power solve the problems.
Laser is used in producing circular saws for cutting granite: sintered diamond charged cobalt base sectors are welded to steel disks as a cost effective and high quality alternative to brazing, preventing disk deformation and improving resistance, particularly at high temperatures.
Finally, solid state sources are used for spot welding of jewels and goldsmith's wares, as well for razor blades.

## HEAT TREATMENT

The laser heat treatment is a solution to improve surface metallurgical qualities of metals (resistance to wear, to fatigue, to corrosion) in specific parts strongly stressed, with the maintenance of the base material properties in the core zone. Surface treatments can be subdivided in thermal processes, such as hardening and remelting, and thermo-chemical processes such as cladding and alloying.
The main features of a laser treatment are: localized thermal input and limited distortion, no structural change in the non treated zone, treatment of difficult zones by means of specific optics, selectivity of application (not suitable for wide surfaces) and high cooling rate, related to high performance.
The use of an appropriate coating (graphite, metallic oxides, colloidal suspensions) is required to achieve sufficient absorption of laser energy. In laser hardening, cooling rates of 1000 K/s and more occurs and are generally high enough for martensitic transformation. The short period in which the layer is above austenization temperature can lead to incomplete austenization as the time for carbon diffusion may be insufficient. Therefore the carbon distribution in the substrate has an essential influence on the generated spatial sequence of microstructures and the resulting hardening profiles. The phase transformation during heating causes a change of the grain size of the material. Compared to other techniques the hardness values are similar and metallurgic structures are finer.
For the heat treatment of metallic materials, $CO_2$ laser sources are mostly used, but good results can be obtained with Nd:YAG lasers. A great number of components have been heat treated by laser technology: the first application was the hardening of the housing of the steering-gear in 1973. At present, laser treatments have been tested in many industrial fields as automotive, energy, aerospace. However most research results were not transferred to production, due to the strong competition of traditional techniques and high investments required by lasers.
To supply a brief list of laser heat treated components, a mention is deserved by valve seats, pistons and valves for power stations, valve stems, crankshafts, camshafts, gears, gearshafts, gearshaft forks, turbine blades, knife blades. Laser processes have also been performed on printing-machine rollers and on components of measurement-machines, again without industrial success.
By laser treatment it is also possible to change the chemical composition of the surface by adding other materials. During the coating process, melting of the base material may occur or not.
Compared to what previously underlined for treatments, other parameters influence the process: form of additional material and method of adduction (with related entities).
To increase the absorbed energy and the efficiency of the laser process, the use of powder coating materials is preferred. The appropriate way of adduction and dosage of powders is very important and influences the thickness and composition of coating layers.

Since the first industrial application, the laser coating technology has taken great strides: nickel and cobalt base alloys, titanium, tungsten, chromium, molybdenum carbide, iron-chromium-nickel-boron alloys, nickel-chromium-boron-silicon alloys, copper and aluminum alloys, as well as ceramic powders can be all adducted, at present.
A different kind of coating a material is surface alloying using a gas: a chemical reaction occurs between gas and base material when laser radiation strikes the surface. A typical example is the nitriding of titanium alloys for improving surface properties: a thin yellow nitrided layer with very high hardness can be obtained.
For laser coating the fields of possible application are many: automotive, energy, aerospace, forging, equipment and rolling sectors are the most commonly involved; coating treatments on knife edges, valves, dies, fire arms, flap guide, torsion bars have been carried out as experimental tests. Yet, despite the interesting results obtained, little relevance of this techniques has been evidenced in industrial production.

## CLEANING

Presently several technologies are used to clean industrial objects and electronic devices: chemical, mechanical or a combination of both (chemical removers, water jet, sandblasting, etc.). The upcoming European environment directive will require to protect the environment against solvents. Laser cleaning can satisfy this requirement. It has also other advantages, for example it is possible to apply the technology on critical materials and parts and on extremely adhesive paints.
Several areas are interested by problems of surface cleaning. The most important are civil and military aircrafts, trains and buses, small ships, automobiles, moulds and dies, electronics and microelectronics devices, semiconductor wafers, medical equipments, monuments and stone buildings.
Different laser sources can be used ($CO_2$, Nd:YAG),depending on the application.
The comparatively large spot of $CO_2$ lasers make them fit for applications such as paint removing from aircrafts, trains and wide metal surfaces in general. High power levels are involved (about one kW or more) and this is why the surface material can be directly vaporised by the laser beam. Usual paint thickness are: 20-25 μm for the primer, 20-25 μm for the surface paint. In this application $CO_2$ lasers can work both in continuos and in pulsed mode. When working in CW, the substrate can reach high temperatures and permanent deformations may be induced. The problem is avoided in pulsed processing.
The applications of Nd:YAG lasers differ from the previous ones. Very often the surface paint is transparent to the laser beam, that is absorbed by the primer; this one vaporises, creating a pressure sufficient to scatter or detach the particles of the surface paint. In this way the cleaning action due to Nd:YAG is both linked to vaporisation and to mechanical phenomena.
The beam power is relatively low: there are usually no problems of deformation and it is also possible to use Nd:YAG to clean wood or paper surfaces because they are not burnt.
The application of Nd:YAG are disparate: paint removal from walls (graffiti), cleaning of monuments, cleaning stone in general but also wood, paper, metal... Regarding stone cleaning, the laser is often preferred to sandblasting because it leaves the surface less porous, that's to say stronger against atmospheric attacks.

## MARKING

As far as plastic materials are concerned, the marking process can be used to create stencils on proper components, to recognise parts (quality control, recycling) and to personalise devices.
Laser marking has a high esthetical quality for its sharpness and contrast, excellent functional properties, superior flexibility and little environmental impact because of limited and controlled evolution of toxic byproducts.
Most applications involve $CO_2$ lasers though also Nd:YAG are widely used. Plastics may also be marked with excimer lasers, producing a chemical reaction: the UV radiation, properly absorbed by the substratum, interacts with some components of the plastic, for example titanium dioxide, dispersed in the matrix. The UV radiation absorption causes molecular changes and creates new not stoichiometric compounds that absorb light, thus looking dark.
There are two kinds of marking: extended imaging marking and plotter marking.
In the extended imaging marking, the whole mark is projected on the component: an objective reproduces the image of a mask which is lighted up by the laser. The process is fit particularly for symbolise and defined marks (for example trade-marks) because complex handling systems are avoided. Excimer lasers involve this solution.
In the plotter marking, micrometrical control tables or piezoelectric scanners move the laser spot along a prefixed path; with this technique complex masks construction is not needed but the productivity is lower because of the relative movement between beam and component. Plotter marking is generally accomplishes by $CO_2$ or Nd:YAG lasers.
Nowadays plastics marking is used to mark wires with excimer lasers for the aeronautical field, to mark PC-keyboards and to produce and personalise cards (both with Nd:YAG lasers). However marking applications are countless and $CO_2$ lasers still retain supremacy.
Regarding painted metal marking, laser advantages are similar to the ones for plastic components: in comparison the printing and other mechanical techniques, laser marking is faster, flexible and apt to be inserted in production lines.

The metal process marking is different from plastic marking because the contrast is not due to the colour change of the material but to the creation of surface oxidation and/or nitrided layers.
In most cases the kind of marking used is plotter marking with Nd:YAG laser in Q-Sw mode; this laser is particularly fit because its high repetition frequency and short impulse period let the superficial marking be realised with a limited thermal input reducing the material restructuration to only a few microns of thickness. In particular cases such as marking of big metal pieces with big and low quality stencils, Nd:YAG lasers are used in free running conditions: they melt the material and leave the print on the piece.

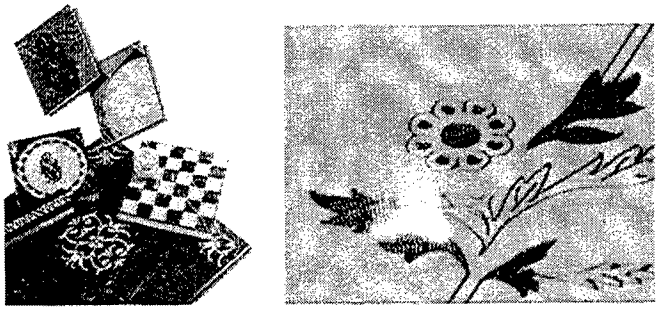

**Fig. 3 – Stone and wood laser treatment**

## MICROMACHINING

Micromachining generally refers to drilling and cutting operations on dimensions in the range of tens of micron. In comparison with traditional techniques, the laser has many advantages; the most important is the possibility to reach far smaller dimensions than the ones got mechanically and to work in areas with a difficult access. The absence of contact with the piece and the process nature make possible to reach relevant accuracies. The process can be easily automated using numerical control systems: great positioning accuracy, high working speed and flexibility can thus be obtained.
The removal process consists either in material vaporisation, obtained with high power density, or in molten material ejection in the shape of particles because of the great pressures developed. The intensity required is obtained using super-impulsed lasers, such as Nd-YAG Q-Sw, CVL, excimer, whose beams are focalised in very small areas.
In these last years there is an increasing interest in Ti:sapphire laser in the micro-drilling field: its ultra-short pulses make possible to obtain excellent results both in efficiency and above all in quality.
Regarding cutting, it is very similar to high pressure cutting. In the microworking field, the material is cut in presence of a neutral gas maintained in high pressure (15-20 bar); it expels the molten material which has not been completely vaporised by the laser, carrying out very precise processing. Laser micromachining is used in a wide range of fields (aerospace, micromechanics, microelectronics).

## CONCLUSION

The industrial diffusion of laser technology seems conditioned by inertia to invest, traditional project criteria and manufacturing modality employed at present. Regarding productivity and quality, the advantages are enormous, sometimes superior to specific industrial requirements but the technology diffusion is limited by the installation and management costs of a laser plant.
However recent improvements of the solid state sources with high power for which fibre optics beam delivery is feasible open up new horizons and partially revolutionize the laser perspectives in some industrial sectors, since most of the problems of beam management are reduced to a minimum.
Regarding industrial production, during the last years, the laser system installations have increased in a considerable way, first of all due to laser cutting systems. Marking and cleaning applications are also very important while welding manufacturing systems are growing. In the heat treatment sector, potentialities are not yet exploited, however the first industrial systems are making their appearance on the market.
Future developments are mainly expected in micromachining. Nevertheless most new industrial applications will be seen in the field of laser welding.

# Computational Simulation of the Laser Cutting Process

M.S. Groß, I. Black and W.H. Müller

MASTRMAN - The Materials and Structures Modelling and Analysis Group

Department of Mechanical and Chemical Engineering

Heriot-Watt University, Riccarton, Edinburgh EH14 4AS, UK

## ABSTRACT

This paper describes the implementation and numerical evaluation of a transient three-dimensional computer simulation of the $CO_2$ laser cutting process. Utilising Crank-Nicolsen-Finite-Difference equations for the solution of the Fourier heat transfer equation with Newtonian convection, the temperature distribution is predicted. For high accuracy the mesh is of non-equidistant nature, following a Weibull Distribution for the grid spacing. A parallel computation solver will be used, based on Aztec (a parallel iterative library for solving linear systems - www.sandia.gov), to calculate the nodal temperatures using a cluster of two HP J5000 workstations. Included in the solution is the behaviour of the material during phase change, whilst the open structure of the developed software allows incorporation of effects such as surface oxidation, radiation and limited convective flow. The main area of interest is the cutting capability with respect to varying material thickness (e.g. tailored blanks), cutting speed, power of the laser, laser mode, focal spot diameter and material properties, as well as the effect of these parameters on the quality of the cut. Further developments will also be outlined in this paper.

**Keywords:** Laser cutting, parallel computation, finite difference methods

## 1. INTRODUCTION

A considerable proportion of laser processing modelling work in the academic literature has been directed at understanding the physics of the interactions between the various processes involved. Such modelling, based on first principles, is a necessary long-term contribution to the field, and has clearly provided stimulating challenges to a large number of scientists. However, only some of this work has been taken to a point where the results can be usefully extracted by those whose aims are towards the *development and control of industrial processes.* In common with many sophisticated modelling activities in other fields, provision of useful modelling tools for the industry is far more frequently cited as an objective than practised in reality.

It can be expected that the laser industry will have a high level of integration with computers in the future. So far computer-based models are rarely found at a laser facility. Typically operating parameters are selected from data handbooks and based on operator's experience. Consequently, while modelling efforts in laser processing have been very extensive, this activity has not really led to the development of much software that can be used on-line.

## 2. INTRODUCING CONVECTION AND PHASE CHANGE AS BOUNDARY CONDITIONS

### 2.1. Finite Difference Equation (FDE) Involving Change of Phase

To apply the phase change to the FDE's developed, Croft and Lilley[1] suggest that the temperature fall $\Delta T$ should be calculated that would occur if the latent heat were extracted from unit mass of material of specific heat. For the approach taken, whenever a node temperature exceeds the transformation temperature during the solution procedure of the FDEs, the temperature is reset to the transformation temperature, and the difference between the predicted temperature and the transformation temperature noted. During subsequent iterations this adjustment procedure continues until the cumulative total of the adjustments is equal to $\Delta T$. At that point the temperature will be allowed to continue to increase in the normal manner. Due to this procedure an amount of energy equivalent to $\Delta T$ is extracted from the model. A matrix to store the accumulated temperature difference can be used, which acts as storage for the case where phase change occurs due to the transition from solid to liquid during heating, and the transition from liquid to solid during cooling.

Further author information e-mail:
M.S.Groß: m.s.gross@hw.ac.uk, I. Black: i.black@hw.ac.uk, W.H.Müller: w.h.muller@hw.ac.uk



XIII International Symposium on Gas Flow and Chemical Lasers and High-Power Laser Conference,
Antonio Lapucci, Marco Ciofini, Editors, Proceedings of SPIE Vol. 4184 (2001)

## 2.2. The Implicit 3D Crank-Nicolson Method with Surface Convection

Crank and Nicolson[2] developed a numerical method that can be used for the solution of the heat conduction equation. The time differential is expressed by a central difference operator. The partial differential equation is satisfied at the midpoint and therefore $\partial T/\partial t$ is substituted by the difference approximations at the $k$th and the $(k+1)$th time step, i.e.:

$$\frac{\partial T^{k+1}_{x,y,z}}{\partial t} = \frac{T^{k+1}_{x,y,z} - T^{k}_{x,y,z}}{\Delta t} + O(\Delta t^2).$$

The derivative of temperature, $T$, with respect to position is expressed by the arithmetic average with respect to time of the second central differential operator, i.e. for example in $x$-direction:

$$\frac{\partial^2 T^{k+1}_{x,y,z}}{\partial x^2} = \frac{1}{2}\left(\frac{T^{k+1}_{x-1,y,z} - 2T^{k+1}_{x,y,z} + T^{k+1}_{x+1,y,z}}{\Delta x^2} + \frac{T^{k}_{x-1,y,z} - 2T^{k}_{x,y,z} + T^{k}_{x+1,y,z}}{\Delta x^2}\right) + O(\Delta x^2).$$

Consequently, the FD formulation for 3D heat conduction with internal heat production becomes:

$$\frac{T^{k+1}_{x,y,z} - T^{k}_{x,y,z}}{\alpha \Delta t} = \frac{1}{2}\left(\frac{T^{k+1}_{x-1,y,z} - 2T^{k+1}_{x,y,z} + T^{k+1}_{x+1,y,z}}{\Delta x^2} + \frac{T^{k}_{x-1,y,z} - 2T^{k}_{x,y,z} + T^{k}_{x+1,y,z}}{\Delta x^2}\right) + \ldots + E_{Vol}. \quad (1)$$

In order to introduce convection into this model, "ambient" nodes have to be defined which, in the end, will not appear in the equation matrix and, therefore, are substituted using the equation for Newtonian convection.

$$T_{x-1,y,z} = 2\Delta x \frac{\alpha_s}{\lambda}(T_{x,y,z} - T_0) + T_{x+1,y,z}. \quad (2)$$

# 3. VARYING GRID SPACING ACROSS THE DOMAIN

To obtain more accurate discretisation, a varying mesh size was employed in $(x, y)$-direction. Consequently, the heat conduction equation in 3D is discretised as follows:

$$\begin{aligned}
\frac{T^{k+1}_{x,y,z} - T^{k}_{x,y,z}}{\alpha \delta t} = {} & \frac{1}{2}\frac{\frac{T^{k}_{x+1,y,z}-T^{k}_{x,y,z}}{\delta x_2} - \frac{T^{k}_{x,y,z}-T^{k}_{x-1,y,z}}{\delta x_1}}{\frac{1}{2}\delta x_1 + \frac{1}{2}\delta x_2} + \frac{1}{2}\frac{\frac{T^{k+1}_{x+1,y,z}-T^{k+1}_{x,y,z}}{\delta x_2} - \frac{T^{k+1}_{x,y,z}-T^{k+1}_{x-1,y,z}}{\delta x_1}}{\frac{1}{2}\delta x_1 + \frac{1}{2}\delta x_2} + \\
& + \frac{1}{2}\frac{\frac{T^{k}_{x,y+1,z}-T^{k}_{x,y,z}}{\delta y_2} - \frac{T^{k}_{x,y,z}-T^{k}_{x,y-1,z}}{\delta y_1}}{\frac{1}{2}\delta y_1 + \frac{1}{2}\delta y_2} + \frac{1}{2}\frac{\frac{T^{k+1}_{x,y+1,z}-T^{k+1}_{x,y,z}}{\delta y_2} - \frac{T^{k+1}_{x,y,z}-T^{k+1}_{x,y-1,z}}{\delta y_1}}{\frac{1}{2}\delta y_1 + \frac{1}{2}\delta y_2} + \\
& + \frac{1}{2}\frac{T^{k+1}_{x,y,z-1} - 2T^{k+1}_{x,y,z} + T^{k+1}_{x,y,z+1}}{\delta z^2} + \frac{1}{2}\frac{T^{k}_{x,y,z-1} - 2T^{k}_{x,y,z} + T^{k}_{x,y,z+1}}{\delta z^2}.
\end{aligned} \quad (3)$$

This formulation can now easily be broken down into individual factors and programmed in matrix fashion as was previously done for a constant grid spacing. However, a procedure that allows a suitable non-equidistant grid spacing had to be set up. To achieve higher accuracy in representing the gradient of the temperature change, the grid spacing has to be small close to the laser. Far from the laser source the mesh can be coarse, since no rapid change in temperature will occur there. This has to be incorporated in an algorithm that computes the grid. This algorithm will modify the mesh according to the error norm as frequently used in computational mechanics.

A suitable formulation for such a grid can be based on the Weibull function, since it allows change from a very small grid spacing with a programmable gradient to a coarser one. The number of grid points left and right of the laser needs to be computed by fitting the Weibull function according to the position of the laser on the domain.

## 3.1. Programming the Heat Input

The laser beam was modelled as a heat production term in the set of linear equations. The intensity is modelled using the expression used by Miyamoto *et al.*[3] :

$$w(r) = \frac{W}{\pi a^2} \exp\left(\frac{-r^2}{a^2}\right) \quad (4)$$

assuming a $TEM_{00}$ mode (Gaussian) beam, where $r = \sqrt{x^2 + y^2}$ and $a$ is the beam radius at the 1/e cut-off point. This heat input is applied to surface nodes which therefore represents a surface load. Since the laser does not penetrate significantly below the surface in the solid and due to the lack of liquid phase this is considered accurate.

| Material | time until "burn-through" $\times 10^{-2}$[s] | kerf width $\times 10^{-4}$ [m] | cutting speed [m/s] |
|---|---|---|---|
| Aluminium oxide | 0.84 | 7.44 | 0.023 |
| Soda-Lime-Silica | 0.57 | 7.88 | 0.023 |
| Silicon oxide - Quartz | 0.21 | 8.36 | 0.023 |
| Silicon oxide - Cristobalite | 0.12 | 8.62 | 0.023 |
| PMMA | 0.57 | 9.12 | 0.160 |

**Table 1.** Comparison of results for materials considered

### 3.2. Material Removal

The material removal is based on the shear cutting, i.e. all liquid is immediately ejected by the shield gas jet. This is incorporated in the mathematical model as follows. Once the system of equations has been solved, a routine scans through the results and identifies nodes that have undergone a phase change. From this information it can be determined how the matrix of linear equations needs to be altered, i.e. for the removed element the whole row is set to 0 and the element $A_{i,i}$ is set to 1. The right hand side is set to an arbitrarily high value to identify the removed material in later post-processing. To remove the conductive links to the neighbouring elements of the bulk material, the kind of element, i.e. corner or edge, produced at this point has to be identified and their row and right hand side is altered accordingly to remove the conductive link and substitute a convection term.

### 3.3. Solution Procedure

Previously the solution procedure was a divide-and-conquer Gaussian elimination method for banded matrices based on the parallel routine library ScaLAPACK (www.netlib.org/scalapack). The solution method was concerned with the solution of banded linear systems of equations $Ax = b$, where the matrix $A$ is of order $n \times n$.

The key parameter for choosing between algorithms is the bandwidth. For small bandwidths, dense methods are very inefficient. Reordering methods behave the opposite way: the smaller the bandwidth, the greater the potential level of parallelism. However, reordering methods have an automatic penalty that reduces the spectrum over which they are the methods of choice: because of fill-in, they incur an operation count penalty of approximately four compared with sequential algorithms. They are therefore limited to an efficiency of no greater than 25%.

The disadvantage of this routine was the fact that it did not cater for the specific structure of the matrix. A matrix resulting from a 3D discretisation of the Fourier equation on a $n \times n \times m$ domain consists only of seven bands with a bandwidth of $2 \times n \times m + 1$. Hence a solver that solves the whole band, irrespectively of the zeros within the band suffers a fill-in penalty, which in this order of magnitude proves unacceptable. This is overcome by using a iterative solver, which computes only on the non zeros. Aztec is a parallel iterative library for solving linear systems, which is both easy-to-use and efficient. Simplicity is attained using the notion of a global distributed matrix. The global distributed matrix allows a user to specify pieces (different rows for different processors) of his application matrix exactly as he would in the serial setting (i.e. using a global numbering scheme). The authors are currently in the process of implementing this library into the simulation code.

## 4. CASE STUDIES

Several case studies were performed. These case studies analysed the behaviour of three different types of material under laser cutting: glasses, ceramics and polymers (refer to Table 1). The results obtained correlate well with experimental evidence (for example see Black[4]). A fringe plot is reproduced in Fig. 1 and 2, removed material is indicated by the highest temperature shown. Within this plot, a close-up of the laser penetration zone is shown, sliced along the direction of movement. The domain is $8 \times 8$ cm and the dimensions shown are in metres, degrees centigrade and seconds, respectively. The workpiece moves to the left with a steady-state laser source impinging upon it. It is expected that a finer overall mesh would increase the resolution of these results but not neccesarily the qualitative result.

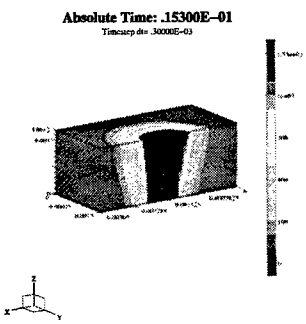


**Fig. 1.** $t = 0.153s$

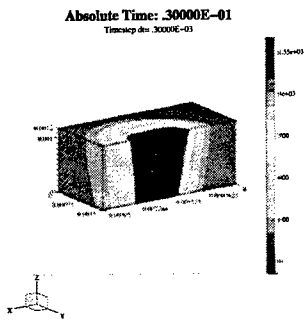


**Fig. 2.** $t = 0.3s$

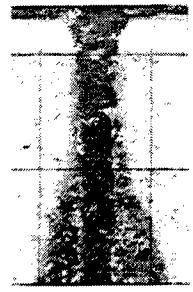

**Fig. 3.** Melt profile

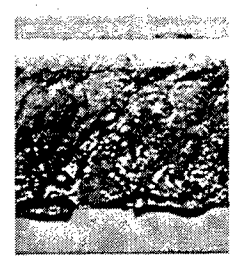

**Fig. 4.** Cut-front showing dross

## 5. CONCLUDING REMARKS

For the given materials the model developed enables the estimation of the burn through time, validation of cutting speeds, prediction of kerf-width, estimation of the temperature distribution in the bulk material, inclusion of focal-spot characteristics and laser beam intensity distribution and power level and influence estimation of convective environments.

So far the simulation considers temperature independent values for $c_p$, $\lambda$ and $\alpha_s$, which represents a constraint on the validity of the result. The practical relevance of the results would certainly benefit from the incorporation of temperature-dependent material properties. In the future a temperature dependent $c_p$ will be introduced based on the Shomate equation. The fluid flow of the molten material is of major significance to the cutting process. The incorporation of this into the simulation model would describe the physical behaviour of the cutting process with increased accuracy and enhance the validity of the results obtained through the numerical simulation. This will be achieved by expanding the underlying physical description of the model to a full description based on a coupled momentum and energy balance. This will provide vital information about liquid velocities at the liquid/solid interface which leads to a significantly higher heat exchange between the overheated liquid and the solid. This will explain the cut profile given in Fig. 3 (which is not captured by the simulation so far). Furthermore this will enable us to compute residual stresses in the material which is of importance to the process and the geometrical distortion of the work piece.

Furthermore it is planned to capture the dross (re-solidified material at the lower cut edge) as shown in Fig. 4 and a more precise representation of the HAZ. It is obvious that a model for the laser/matter interaction itself on a microscopic level is needed in order to flexibly assess and analyse the cutting of different materials, since it is still difficult to find a concise description covering the different phenomena and materials encountered during the process (see Mazhukin and Samarskii[5]). Knowing the temperature history of the HAZ (heat affected zone) is also important, particularly for high load bearing structures, as well as memory alloys.

## REFERENCES


1. Croft, D.R. and Lilley, D.G. *'Heat Transfer Calculations Using Finite Difference Equations'* . Applied Science Publishers LTD, London (1977).
2. Crank, J. and Nicolson, P., *'A practical method for numerical evaluation of solutions of partial differential equations of the heat conduction type'*. P. Proc. Camb. Phil. Soc. **43** (1947), 50-67.
3. Miyamoto, I., Maruo, H. and Arata, Y. *'Intensity Profile Measurement of Focused $CO_2$ Laser beam Using PMMA'*. Proceedings of ICALEO '84 (1984), 313 - 320.
4. Black, I. *'Laser cutting of perspex'*. Journal of Materials Science Letters, **17** (1998), 1531-1533.
5. Mazhukin, V.I. and Samarskii, A.A. *'Mathematical modeling in the technology of laser treatments of materials'*. Surv. Math. Ind., **4** (1994), 85-149.

# FORMATION OF LARGE VOLUMINAL DEFECTS IN TANTALUM Nd:YAG LASER WELDING

J.M.JOUVARD[(1)*], K.GIRARD[(1,2)],
D. NORE[(2)], J. NADAL[(2)], G. PASCAL[(2)], Ph. NAUDY[(2)]

[(1)] Laboratoire Laser et Traitements des matériaux, IUT Le Creusot, F71200 Le Creusot, France
[*] E-mail: jmj@iutlecreusot.u-bourgogne.fr
[(2)] CEA, F21120 Is sur Tille / CEA, F51420 Pontfaverger, France

## ABSTRACT :

The purpose of this work is to study and model the formation of voluminal defects in laser spot weld on tantalum. Formation of these defects has been studied by radiography X-flash and modelled with FLUENT software.

**Keywords:** Welding, defects, radiography, tantalum

## 1. INTRODUCTION

For specific application, we have to join tantalum pieces by laser welding. A pulsed laser is used to minimise heat input and consequently reduce tensile strains in the workpiece. This is particularly important for tantalum material, which has a high thermal conductivity. However, the optimum parameters often lead to the generation of voluminal defects within the molten zone. The objective of this investigation is to identify and understand the formation of these defects.

The effect of a laser pulse on the material can be split into three consecutive stages [1,2]. During the first stage, the metal surface locally melts and vaporizes. Then a deep and narrow keyhole appears and traps the laser beam inside the material itself. During the second stage, the keyhole grows vertically and is surrounded by the molten metal. But due to both an excess of energy and to convective effects, the molten metal is ejected from the bottom to the top of the keyhole, where it gathers in a crown shape [3]. Finally, the last stage occurs at the end of the laser pulse. At this moment, the surrounding molten metal collapses into the keyhole and solidifies. The purpose of this work is to study and model the formation of voluminal defects during the solidification in laser spot weld on tantalum.

An analysis of spot weld by Scanning Electron Microscope allows to observed voluminal defects (fig.1). Large voids consist in empty zones delimited by the melted zone boundary as if the molten metal had solidified before collapsing into the keyhole entirely. These voids seem to be the result of a lack of metal filling up the keyhole at the end of the laser pulse, associated to a very fast solidification. The study of the melt flow back into the keyhole should help to understand the voids forming mechanims.

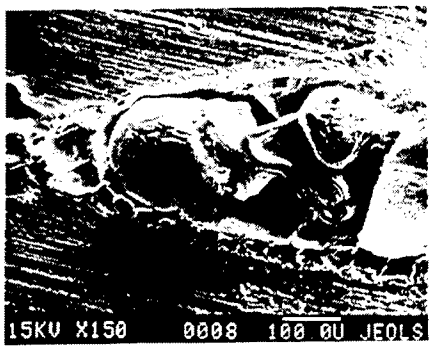


*Figure 1 : Detail of the large void*

## 2. OBSERVATION BY X-RAY RADIOGRAPHY

In order to complete these observations, we studied the solidification stage by radiography with an X-ray flash generator [4] and high sensitivity photographic films. The aim of this experiment is to visualize in a front face view, the matter behavior during and after a Nd:YAG laser pulse.

A photodiode detects the beginning of the laser pulse and triggers the flash X-ray generator with a programmed delay. To one X-ray pulse, shot with a fixed delay, corresponds one laser pulse. Laser pulses are all performed with a peak power of 7 kW, and a pulse duration of 15 ms. The laser beam is tilted (10°) to avoid



XIII International Symposium on Gas Flow and Chemical Lasers and High-Power Laser Conference,
Antonio Lapucci, Marco Ciofini, Editors, Proceedings of SPIE Vol. 4184 (2001)

reflections back on the welding device; the beam diameter is 1000 μm. The plume was drawn up. X-ray pulses are 30 ns long. The sample is a tantalum plate which is slided after each pulse. All the films have been digitized with a pixel size of 50 μm x 50 μm. The contrast is enhanced by image processing (reversal and histogram spreading). In spite of a bad resolution (300 μm approximately), the images give some information about creation stage of the keyhole and solidification stage [5,6]. Figure 2 shows results obtained in case of study of solidification stage. We can see images released with different delays after the end of the laser pulse. To one picture released with a precise delay, corresponds one picture, placed on the right hand side, showing the same spot weld which has been solidified. Dark parts absorbed X-rays so they stand for dense matter (solid or liquid metal) and bright parts did not absorb X-rays so they square with the gaseous phase (keyhole).

The main results of this experimental study are :

- We observe the keyhole formation during the impulse duration (15 ms). The keyhole appears between 3 ms and 4 ms. Then it grows until being stabilised around 12.5 ms.
- At the end of laser pulse (figure 2), metal collapses rapidly into the keyhole which is occluded between 1 ms and 1.5 ms. The mode of filling depends on the movements of the liquid, which can be different from one impulse to another. However, these movements tend to bring the liquid to the top of the keyhole and to trap gas inside. Also, we have formation of a cavity trapped during solidification. Furthermore, we can compare a picture released at a given time with the corresponding picture showing the same spot weld that has been solidified. There is an evolution between both images untill 5.0 ms, which is no more true from 7.0 ms. However, we cannot make the difference between strongly viscous liquid and the solid. One cannot deduce the solidification time.

## 3 . MODEL OF LARGE VOIDS FORMING

In order to simulate the process of voids forming, we used FLUENT software [6]. This problem corresponds to the flow of the molten metal, initially rejected outside the keyhole and constituting the crown, through the keyhole. The driving forces are capillarity and gravity effects, which are quickly counteracted by the increasing viscosity of the cooling metal.

Our example corresponds to the case of a laser impact realised with a peak power of 20 kW, and a pulse duration of 10 ms. The keyhole corresponding has a depth of 4.3 mm and a diameter of 0.8 mm. However we have simplified the geometry: The system has a cylindrical symmetry. The interfaces liquid-gas and solid-liquid are approximated by half-ellipses. The volume of liquid is assumed equal to the volume of the keyhole. Typically 75% of the molten metal constitute the crown, the remainder corresponds to a fine layer of liquid covering the walls of the keyhole. This crown has an elliptical toric shape. Its cross section is rather complicated due to dynamical effects induced by the melt flow and to physical properties fluctuations with temperature.

Main results are presented on figure 3. Initial conditions, at the end of the laser pulse, are shown on the first picture (instant 0.0 ms). On each image, the left hand part shows the calculated thermal field and the liquid/gas interface (black curve). On the right hand part, different phases appear (solid or liquid metal and vapour). The fusion isotherm allows to discern solidified metal from liquid metal.

At the beginning, because of surface tension effects, molten metal tends to gather on the top of the keyhole. The metal lying on the keyhole walls is solidified (instant 2.7 ms). At 3.5-3.7 ms, the keyhole is occluded and some air is trapped inside. Then the geometry of liquid volume evolves under the action of surface tensions. On the top, the liquid mass gathers and forms a shape of warhead (5.1 ms), then becomes round (15.1 ms), and finally the solidified metal takes the shape of a "Chinese hat". Inside the hole, the gas pocket takes a spheroid shape. At 29.1 ms, only the upper part of the metal is still liquid. Consequently, the liquid can not flow down anymore and the void is trapped within the welded zone definitively.

## 4 . CONCLUSION

Large voids forming was modeled owing to the study of melt flow back into the keyhole. Main assumptions concerned the definition of the system geometry. According to the results, the melt gathers at the top of the keyhole and collapses while cooling. Consequently, some vapor is trapped inside the weld preventing the keyhole from being filled up entirely. The study was made in the case of an isolated laser spot weld which is the most unfavourable case, thus.

The experimental validation of simulation is not easy because of many difficulties for the observation of phenomena during and after welding: speed of the phenomena, too small dimensions to be visualised (a

resolution of less than 100 μm is needed) and intense radiance induced by high temperatures. However, these results can be correlated with various observations.

This model is in good agreement with observations made by X-ray radiography. At the end of the laser pulse, the melt flows back into the keyhole and traps some vapor inside. It solidifies before refilling entirely the hole and a large void is left within the welded zone.

The X-ray starts at the end of the laser pulse. They prove that the keyhole refilling mode is at the origin of the formation of cavities. Indeed, on X-ray, we do observe that the molten metal obstructs the keyhole at the top and traps some vapour inside. Thus, it is difficult to correlate the results precisely. In particular, we cannot correlate the refilling durations.

In order to compare the results of simulation with observations, we present, a micrography of the weld on figure 3. One notices a cavity similar to calculation, as well as a dome at the top of the weld in the shape of a " Chinese hat ".

Finally, we carried out a visualisation with high-speed video solidifying molten pool. We used a camera CCD Ektapro with 1000 images per seconds. At the end of the laser pulse, one can see an emissive zone, which makes it possible to locate hot metal. However, the images do not enable us to locate the isotherm of solidification and, consequently, to determine the duration of metal solidification on the surface of the workpiece. Moreover, the shape of the emissive zone changes in time. One can suppose that metal remains liquid at least up to 27 ms. This hot zone clearly takes the shape of a dome above surface. This observation confirms the results of simulation, which show that the liquid gathers above the keyhole and goes up high compared to the surface of the piece. Then, as in simulation, one notices that metal subsides little by little inside the keyhole by forming a dome characteristic of this type of welding.

Thus this study enabled to note that, although the phenomena are not reproducible from one pulse to another, one can find rather clear tendencies, that show formation of cavities arises from the keyhole refilling mode.

Two parameters are determining in the formation of the voluminal defects: the keyhole geometry and weld solidification time. The keyhole geometry influences the mechanism of filling. More keyhole is narrow and liquid layer is weak, more liquid forming the crown has difficulty to flow and gathers to form a stopper. The melt cooling is also very important, since the shorter the solidification time is, the more possible it is to trap voluminal defects. In cooling, the viscosity increase and the voids can not go up.

A short duration allows reduce metallurgical transformations, but forms voluminal defects. The suppression of voluminal defects thus results from a compromise between optimization of these parameters which are induced by mostly the energy deposit mode. In particular, we can use a spatial or temporal pulse shaping.

## REFERENCES


[1] **V.V. Semak, J.A. Hopkins, M.H. McCay, T.D. McCay**, A Concept for Hydrodynamic Model of Keyhole Formation and Support During Laser Welding, ICALEO 1994, pp. 641-650.

[2] **J.T. Liu, D.C. Weckman, H.W. Kerr**, The Effects of Process Variables on Pulsed Nd:YAG Laser Spots Welds: Part I. AISI 409 Stainless Steel, Metal. Trans. B, Vol. 24B, pp. 1065-1076.

[3] **J.S. Kim, T. Watanabe, Y.Yoshida**, Investigation of the Porosity Formation Mechanism in Laser Spot Welding, ICALEO 1995, pp. 1011-1017.

[4] **G.Pascal, D.Noré, K.Girard, O.Perret, Ph.Naudy**, Analysis of induced effects in matter during pulsed Nd:YAG laser welding by flash radiography, Quant. Non Destr. Evaluat., Montréal, Jul. 1999.

[5] **K.Girard**, Etude de la création de défauts volumiques générés pendant la solidification de soudures laser Nd:YAG impulsionnel, Thèse de doctorat, Université de Bourgogne, 1999.

[6] **K.Girard, J.M.Jouvard, Ph.Naudy**, Study of voluminal defects observed in laser spot welding of tantalum, J. Physics D: Applied Phys. (accepted)

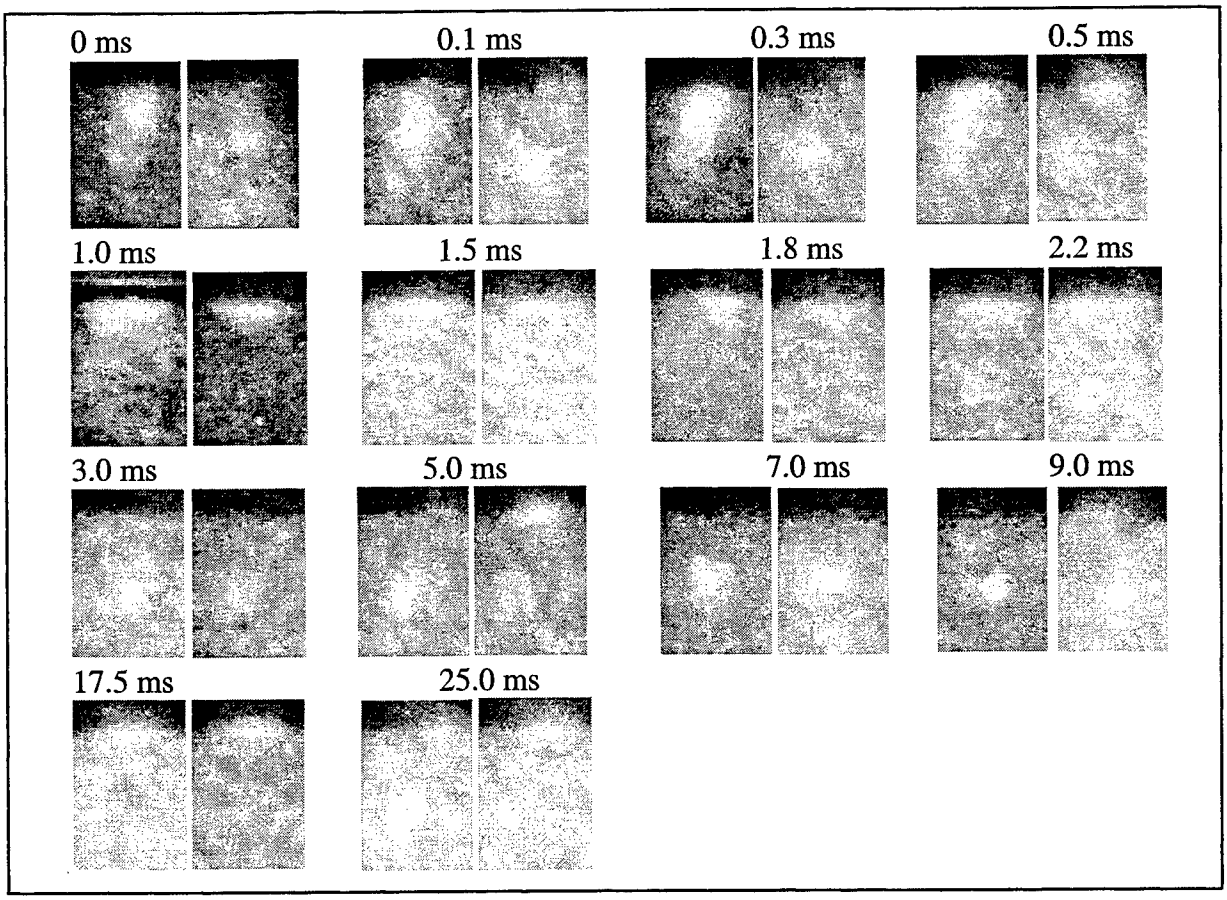


*Figure 2 : Images obtained at different delays after a laser pulse*

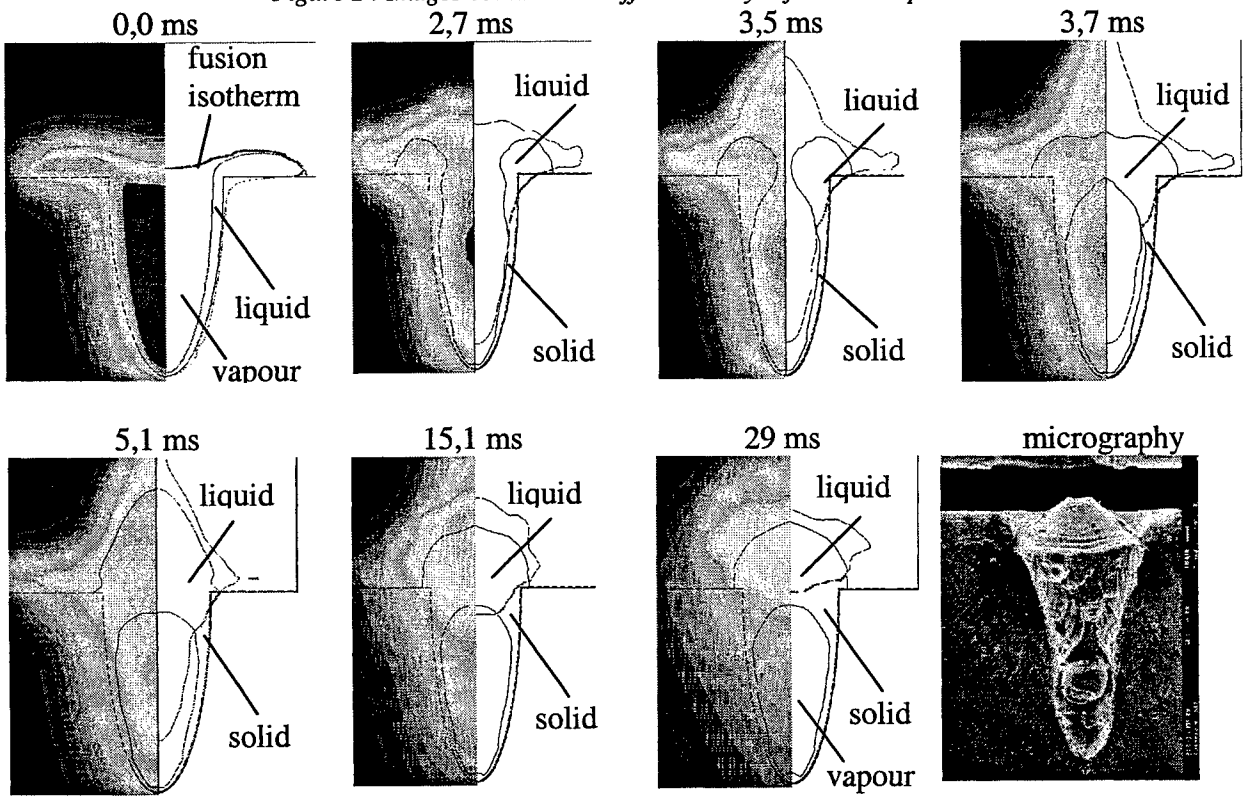


*Figure 3 : Simulation of the flow of molten metal inside the keyhole*

# Laser surface micro-texturing on the mechanical seal rings for enhancing the tribological properties

D. Allegretti *, G. Daurelio ** , F. Guerrini *

* Meccanotecnica Umbra S.p.A., Via G. Agnelli, 7 / 9 - 06042 Campello sul Clitunno, Italy
e-mail: *rd@mail.meccanotecnica.it*
* * Centro Laser S.c.r.l. - Centro Ricerche, Str. Prov. per Casamassima, Km.3 - 70010 Valenzano, Italy
e-mail: *dau@centrolaser.it*

## ABSTRACT

Laser texturing was performed on the sliding surface of silicon carbide sealing rings, in order to investigate the surface modification in relationships with the laser processing parameters and the tribological performances of the mechanical face seals. As no graphs or data sheets were found in literature on the surface absorption (or reflection) properties of the SiC versus the laser wavelengths, it was necessary to execute a series of screening tests using different laser sources, wavelengths (0.532 μm, 0.810 μm, 1.06 μm and 10.6 μm) and modes (Normal and Q – Switch) to verify the surface absorption properties of the SiC seal faces. So far, only the pulsed $CO_2$ laser irradiation was proved to be efficient in producing regular shaped holes. Hole size and microstructural modification were related to laser power, pulse duration and spot size. Under selected processing conditions, seal faces were regularly textured producing microholes (80 to 100 μm diameter) at a distance of about 200 μm (center to center of the holes). Tribological performances of these mechanical seals under specific proof tests evidenced the increase of the fluid film stiffness and seal life and the reduction of friction coefficient and torque values.

**Keywords:** laser texturing, silicon carbide, mechanical seals, microstructure

## 1. INTRODUCTION

The potential of improving seal performances and increasing seal life by using laser texturing techniques, to form regular surface structures on the mating rings, was estimated experimentally on hardened steel mechanical seals [1]. The laser introduced modifications of the metal sliding ring surfaces were efficient to reduce friction and eliminate leakage [1,2].
No data are available on the possibility to apply these surface modifications to ceramic seals, although several studies concern the surface modification of ceramics by laser irradiation [3-7]. Lasers are ideal tools for fabricating small diameter high aspect ratio holes at designated locations, for cutting, for surface scribing, etc., thereby allowing flexible machining when other methods cannot be employed. Amongst the different types of laser, the $CO_2$ laser has become a popular tool for machining sintered ceramics because it offers the recognized advantages of accuracy and speed.
The principal aim of this investigation is to study the effects of using different laser sources to produce a regular micro-surface structure in the form of micropores on the face of silicon carbide mechanical seals. Several sets of preliminary experiments were conducted to investigate the surface microstructure modification depending on variables as laser energy, pulse duration and focused spot size. On the basis of these results, using a number of selected conditions, seal rings of internal diameter 18 mm, external diameter 28 mm, were textured with regularly distributed holes, in a number of 1200 per ring. Tribological performances of these mechanical seals were compared under specific proof tests to evaluate seal life, friction and torque.

## 2. EXPERIMENTAL

### 2.1. Experimental

Commercial silicon carbide ceramic rings were used for laser testing. The density of the material is about 95%, an example of the material morphology is shown in Fig. 1: some pores and voids up to 10 μm are observed. The surface roughness is 0.4 ±0.1 μm.
Several sets of experiments were carried out by using different laser sources: a Portable pulsed Nd – YAG, a Portable continuous High Power Diode 98 W, a Portable continuous and pulsed 25 W $CO_2$, a continuous 50 W $CO_2$, a continuous and pulsed 1500 W $CO_2$). Individual, single-pulse, blind holes were drilled on the ceramic surface. The beam angle of incidence


XIII International Symposium on Gas Flow and Chemical Lasers and High-Power Laser Conference,
Antonio Lapucci, Marco Ciofini, Editors, Proceedings of SPIE Vol. 4184 (2001)

was 90° and the beam was focused on the sample surface. Each specific set of experimental conditions is reported in the next section, along with the related results.
The microstructure and microchemistry of the treated areas were analyzed before and after a mechanical polishing in order to remove the debris areas around each hole. After laser treatment and after polishing the hole diameter and depth were measured by optical and SEM microscopy.
After the screening tests, rings textured with 1200 holes were produced using the pulsed $CO_2$ laser with different hole mean diameters: 80, 100, 130 and 150 μm. In order to evaluate the influence of microporosity on the friction coefficient and torque of the mechanical seals, room temperature wear tests were performed with a columnar tribometer "disk on disk". The ceramic ring was mated with a carbon ring. The tests were carried out in a wet environment, with a load of 32 Kg and with two rotating speeds: 1000 and 3000 rpm. The tests were carried out also on untreated ceramic rings for comparison.

## 3. RESULTS AND DISCUSSION

### 3.1. Preliminary tests

As previously mentioned, several sets of experiments were carried out varying the laser source, the wavelengths and modes. In the following some considerations are pointed out, relatively to the effects related to the laser processing conditions:
- *Diode Laser Array Source*: the 0.81 μm wavelength is poorly absorbed by the SiC surface in spite of long exposition time (5 to 10 sec). The surface of the specimen reached a very low temperature (about 40°C), even when 16 W and 98 W, in continuous wave regime, were employed. In addition, as the outcoming laser beam is rectangular shaped, after a focusing lens (f = 55 mm), a rectangular spot (0.3 x 0.4 mm) was obtained; which is not acceptable for the microdrilling applications.
- *Nd–YAG Laser*: with a multi–articulated arm, operating both in 1st armonic (1.064 μm, in N–Mode or Q–Switch regimes) and in 2nd armonic (0.532 μm, in Q–Switch Mode), interesting results were obtained, although photo–thermal and/or photo–mechanical effects cannot be excluded. Moreover, as the multi-articulated arm (with 7 mirrors) strongly affects the final results, further tests are necessary to assess the suitability of this laser equipment.
- *25 W, 50 W and 1.5 kw $CO_2$ laser sources*: in the continuous wave regime, with power level ranging from 1 to 25 W and from 10 to 50 W, no effects were produced on the SiC surface even under very long exposition times (up to 20 sec). These power levels were considered not sufficient for laser texturing. Similarly, the series of tests executed in pulsed and super–pulsed regimes, by using 1 to 50 Hz repetition rates, different values of $T_{ON}$ and $T_{OFF}$, different pulse widths (0.1 to 8 ms), diverse $T_{ON}$ / $T_{OFF}$ ratios, diverse medium power levels (0.5 to 10 W), produced no positive results. This was probably due to the low medium power and energy per pulse that this source provides.
These preliminary tests evidenced that only the pulsed $CO_2$ laser (λ = 10.6 μm, maximum continuous wave power ($P_{cw}$) 1.5 kW) is suitable for texturing the ceramic surface.

### 3.2 $CO_2$ pulsed laser tests: influence of the laser parameters on the hole characteristics

A test program was formulated to determine the effect of varying the following parameters individually: laser power, pulse duration and lens focal length. The pulse duration was varied in the range 0.5 to 2 ms, whilst maintaining a constant laser power and lens focal length. The same series of trials with variable pulse duration were then repeated for two levels of $P_{cw}$ laser power (0.5 and 1 kW) and three lens focal lengths (31.75, 63.5 and 95.25 mm).
The values of the hole depths and diameters plotted against the pulse duration, for two values of laser power (0.5 and 1 kW) and for three values of lens focal length (95, 64 and 32 mm) (i.e. at decreasing values of spot size) are shown in Figs. 2a-b. The penetration depth is affected by many factors, i.e.: pulse duration (ms), pulse energy (J), depth of focus (mm), energy density at the sample surface (kJ/cm$^2$).
So, at the end of the test experiments, it is possible to underline the following final considerations :

- To obtain the minimum ( the lowest one ) hole diameter ( about 80 to 100 μm ) it is necessary to adopt the shortest *f* ( 31.75 mm ) and the lowest $P_{cw}$ value ( 0.5 KW ), indipendently from all the other working parameters .
- To obtain the maximum ( the highest one ) hole depth ( about 250 to 300 μm ) it is necessary to adopt

f 31.75 mm - $P_{cw}$ 1 KW - Pulse Duration 1.5 ms to 2 ms or

f 63.5 mm - $P_{cw}$ 1 KW - Pulse Duration 1.2 ms to 1.7 ms or

f 63.5 mm - $P_{cw}$ 0.5 KW - Pulse Duration 1.7 ms to 2 ms

- Once that $f$ and $P_{cw}$ are fixed ( 31.75 or 63,5 mm - $P_{cw}$ 0.5 or 1 KW ), when the pulse duration ( energy per pulse ) increases from 0 sec to 10 sec, $M\ H\ D_e$ ( Medium Hole Depth ) always increases for pulse duration from 0 to 1 ms . This is due to the contributions of the

  ***Depth of Focus , Energy Density , Energy per Pulse and Pulse Peak Power*** parameters .

After 1 ms value and till to 1.5 ( or 2 ms ) pilse duration , the Peak Power parameter ( having reached its maximum value to 1 ms ) cannot strongly partecipate to the process ;so that only

***Depth of Focus , Energy Density and Energy per Pulse*** parameters

can partecipate to increase $M\ H\ D_e$ values . Into this range ( 1.5 to 2 ms ) these last three parameters reach also their individual maximum value ( different according to $f$ and $P_{cw}$ pair cosidered ), so that $M\ H\ D_e$ does not more increases ( the process has been saturated ) , that is , even it begins to decrease .

After 2 ms till to 10 ms pulse durations $M\ H\ D_e$ lightly decreses and the surplus of the energy, furnished to the process , makes only to widely to enlarge the surface entry diameter of the micro - hole on SiC .

- If the $f$ is still increased ( e,g, 95,25 mm ) as setted , at the first, on the range 0 to 1 ms , there are two opposite contributions of $Z$ and $D_e$; this last one becomes more important respect to $Z$, so that the increasing of $Z$ is not anymore able to compensate the decreasing of $D_e$ . All this makes to the lowest values of $M\ H\ D_e$ , compared with ones obtained by using $f$ 31.75 or 63.5 mm ( at $P_{cw}$ 0.5 or 1 KW ) .
- After 1 ms and till to 2 ms , $M\ H\ D_e$ is strongly increased and it is due to the contributions of

  ***Depth of Focus , Energy Density and Energy per Pulse*** parameters .

Finally into the range 2 to 10 ms , the system saturates and the behaviour is similar to the one already and just referred above as regarding the other focal lengths .

- Even if , from fig.2 , the *MHDi ( Medium Hole Diameter )* seems not to be constant for each setting of $f$ and $P_{cw}$ pair , this is only apparent and due to an experimental error . In fact, from examination of the experimental and measured data, it is evident that the difference among the *MHDi* values and the other single measurements, for each $f$ and $P_{cw}$ pair , is only a tenth or some tenths of micrometers , acceptable as scattering values .

### 3.3 General features of the holes: morphology and microstructure

The general shapes and profiles of the drilled holes are revealed in Figs. 3a and 3b at lens focal lengths 31.75 mm and $P_{cw}$ laser power levels of 1 kW for different values of pulse duration.
When the laser beam irradiates the ceramic surface very high temperatures are reached in a short time, which cause melting and vaporization of SiC. The laser beam produced cone or cylinder-shaped holes depending on the extent of penetration. Holes produced by a pulse duration of 1 ms are conic shaped, but subsequent penetration resulted in parallel bores. The build-up of debris and melted material around the holes, caused by heat, increased with increasing the pulse duration and decreasing the laser spot (i.e. increasing the energy density). Moreover, heat caused material adjacent to the scribe to be fused into a glassy-like phase. The heat affected zone extended beyond the crater: around the hole an area of melted material was always present. Inside the crater wall droplets of silicon were observed resulting from the decomposition of SiC. Along the crater walls inside the hole, a subtle porous scale of about 7 to 8 microns is present with a morphology completely different from the bulk. The porosity of such scale is probably due to emission of gaseous species during the decomposition of SiC. No or little oxygen amount was observed inside this scale, i.e. no oxidation occurred of the chemical species although the tests were carried out in air. The tests carried out showed that for pulse duration < 0.5 ms and $P_{cw}$ = 0.5 kW no appreciable material removal was observed. In this case there was not enough energy absorption to cause vaporization. However the heat transmitted to the material caused melting and formation of glassy phases. Presence of cracking due to thermal spalling was also observed on the melted material. Microcracking is always present in the samples treated, which is again an effect of heat. Thermal shock caused microfractures which extend radially from the hole as well as along the cone profile. The series of tests performed showed that it is possible to use a pulsed $CO_2$ laser to produce micro-holes in silicon carbide. However, the dimensions of the holes and their surface and subsurface characteristics are strongly affected by the processing parameters.

**Seal rings textured with 1200 holes**

In the case of mechanical seals, according to previous results [1], positive results were demonstrated for pore dimensions around 100 μm. Therefore, for silicon carbide, this study evidenced the possibility to obtain holes having diameter and depth in the range 80 to 150 μm, using a pulsed $CO_2$ laser, with $P_{cw}$ of 0.5 kW, and lens focal length of 31.75 mm and 63.5 mm. The pulse duration were 1, 1.2 and 2 ms. Higher laser power induces more evident undesirable effects on the microstructure of the area affected by heating.

All the seal surface was textured with about 1200 holes (see an example in Fig. 4a and 4b ).

The laser treated surfaces were polished for a short time (30 s) and the thickness of the layer removed was about 13 to 14 micron. The final roughness in the region far from holes was 0.070 to 0.078 μm. In the micrograph of Fig. 4b some holes resulting from treatment at focal length 31.75 mm and pulse duration 2 ms are reported before and after polishing. Despite the removed layer, radial cracks are still present around the hole. Radial cracks are present in almost all the samples examined and their extension increases with increasing pulse energy. In some cases radial cracks extended from one hole to the adjacent ones, creating a network of cracks. In this case brittle areas are generated on the ring surface that may deteriorate the seal performance. During polishing, spalling around the holes was observed. These phenomena of crack formation and spalling were found to increase as the pulse duration increased, so that short pulses seem to be preferable.

**3.2. Tribological tests**

We carried out the tests on 4 sliding rings made of Silicon Carbide laser textured. The medium measured diameters of the micro-bores were 80, 100, 130 and 150 μm.

Each sliding ring worked against a carbon sliding ring, leaving the same surface finishing on each ring.

The tests were performed in water under atmospheric pressure and room temperature conditions . During the tests we imposed an axial load of about 32 Kg and two different speeds of 1000 and 3000 rpm.

The goal of these tests was to have showed the influence of the micro-bores on friction ratio and torque.

We controlled the percentage difference of these two parameters, changing the speed and comparing the last ones with the same tests performed on rings not textured.

From the results analysis it was clear that the best working condition was obtained with the 80 μm micro-bore medium diameters , because there is a decreasing of the friction ratio and the torque even at the lower speed ( 1000 rpm ) in comparison with the SiC rings non textured.

With the micro-bores until 130 μm diameter and at 3000 rpm speed value a similar behaviour was observed . At the lower speed ( 1000 rpm ) an increasing of torque was noticed : this fact can explain the hypothesis that, with diameters of the micro-bores higher than 80 μm, the hydrodynamic lift decreases, favouring a closer contact between the rings.

This phenomenon was more evident when some rings, on which micro-bores with diameters higher than 130 μm, were tested .

This effect , already known as *mixed friction,* is a consequence a fluid film formation with a variable thickness between the two sliding rings. Generally, the variability of this thickness is a function as of the test conditions as the surface finishing.

Till to now the influence of the micro-bores depth on the tribological tests has not been yet verified .

**3.2.1 Bench Tests**

We carried out some *life tests* on three different SiC sliding rings . The medium measured diameters of the micro-bores are 90, 100 and 135 μm.

We mounted these SiC vs. Carbon sliding rings as seals, assembled on pumps, used for automotive appliances so that to simulate an automotive engine cooling circuit .

The tests had a standard duration of 1000 hours. The cooling fluid temperature (water plus antifreeze at 50%) was hold at 90°C temperature while some sliding rings, that rotate at 7000 rpm, were employed .

At the end of all these test series , we did not notice any leakage . The surfaces of Carbon and SiC showed a good final finishing without scratches.

The micro-bores, textured by laser , are partially filled by deposits , composed by some fluid and carbon powder , which enhance the lubricant characteristics of the fluid film at the interface.

The increasing of the fluid film thickness, due to the effects of hydrodynamic lift as supposed on the previous tests, did not evidence some leakage.

## 4. CONCLUSIONS

Silicon carbide mechanical seals surfaces were laser-treated to produce micro-pores of various dimensions and shape. An extensive study was carried out using different laser sources. After a series of preliminary tests it was assessed that the most suitable laser source to produce regular shaped holes is a pulsed $CO_2$ laser. Several sets of experiments were performed to determine the relationships between the laser processing parameters and dimensions and surface characteristics of the blind holes. Hole diameters as low as 100 μm and scarce undesirable effects were obtained using a $P_{cw}$ laser power of 0.5 kW and a lens focal length of 31.75 mm.

In the second part of the work, the whole surface of the seals was textured with 1200 micro-pores with diameters in the range 80 to 150 μm. The microstructure of the as-laser treated surface was compared to that of polished surface, in order to observe the extent of surface defects and cracks.

The best tribological performances were achieved by using some sliding rings on which 1200 micro-bores with a diameter of 80 μm were been produced . The following life test results confirmed that there is no leakage by adopting this surface laser texturing .

All the bench test series furnished positive results and any leakage or wear on the carbon sliding rings was apreciated. On the ligth of all just referred the best laser working parameters are :

31.75 mm focal length - 1 ms pulse duration - 1 KW $P_{cw}$ or

31.75 mm focal length - 1 ms pulse duration - 0.5 KW $P_{cw}$

We are planning to carry out some other tribological tests to verify which is the best diameter of micro-bores for each rotating speed value ( on the range 4000 to 7000 rpm) and also to carry out other life tests , on the sliding rings with micro-bores diameters higher than 130 μm, to verify a possible different behaviour.

## 5. ACKNOWLEDGEMENT

This work was carried out under the aegis of the National Programme PF MSTA II (Progetto Finalizzato Materiali Speciali per Tecnologie Avanzate) of the National Research Council - CNR.

The Authors are gratefull to Dr.ssa A. BELLOSI and Dr.ssa D. SCITI of the C.N.R. – Research Institute for Ceramics Technology ( located in Faenza – Italy ) for their experimental work , support , results evaluation and discussion

## 6. REFERENCES

1. Etsion, G. Halperin, Y. Greenberg, "Increasing mechanical seals life with laser textured seal faces", *Proc. 15th International Conference on Fluid Sealing*, BHR Group, pp. 4-11, 1997

2. B. Antoszewski, J. Rokicki, "Tribological aspects of the laser treatment for mechanical seals", *Proc. 15th International Conference on Fluid Sealing*, pp. 27-34, 1997

3. K. J. Schmatjko, E. Endres and H. Durchholz, "Surface modification of ceramics by excimer laser irradiation" *Proc. 5th Conf. Laser in Manufacturing*, IFS ltd, pp.145-154, 1988

4. T. R. Jervis, M. Natasi, K. M. Hubbard and J. –P. Hirvonen "Excimer Laser Processing of Ceramics:Process and Properties" *J. Am. Ceram. Soc.* **76** [2] (1993) 350-55

5. P. Crosby, W. Shiner "Improving performance of ceramic scribing", *Am. Ceram. Soc. Bull.*71 [1] (1992) 1631-37

6.L. Y. Sadler, M. Shamsuzzoha "Response of silicon carbide to high intensity laser irradiation" *J. Mater. Res.* **12** [1] (1997) 147-160

7. G. Daurelio, A. Bellosi, D. Sciti, D. Allegretti, F. Guerrini, "U.V. laser ablation of silicon carbide ring surfaces for mechanical seal applications", Proceedings of SPIE, Vol. 4070 (2000), pp. 300-305.

8. L.I.A. – Laser Institute of America : " Guide for material processing by lasers " - 1977

9. G . Daurelio, L. Cento, C. Esposito : " Saldatura al laser $CO_2$ da 2KW di acciai al carbonio e inossidabili " , Monografia del P.F. – LASER di POTENZA del C.N.R. , pp. 1 – 164, Settembre 1982

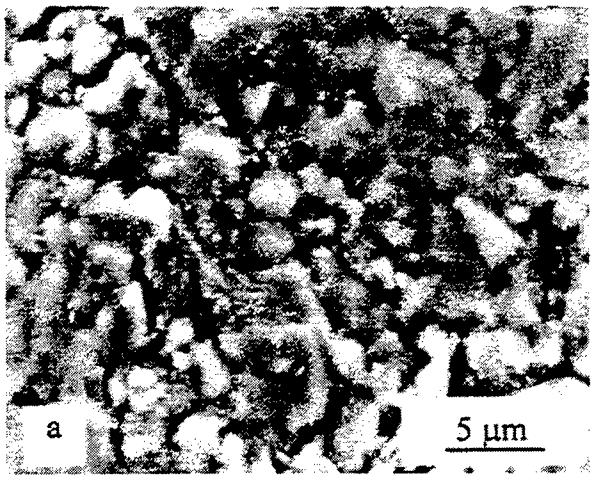


**Fig. 1**

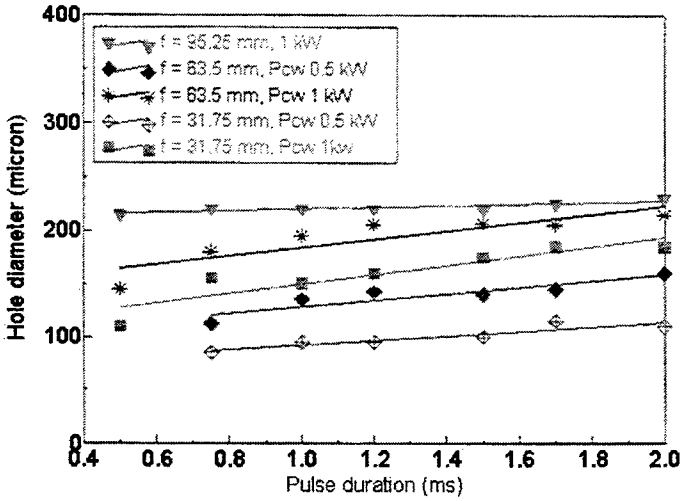


**Fig. 2a**

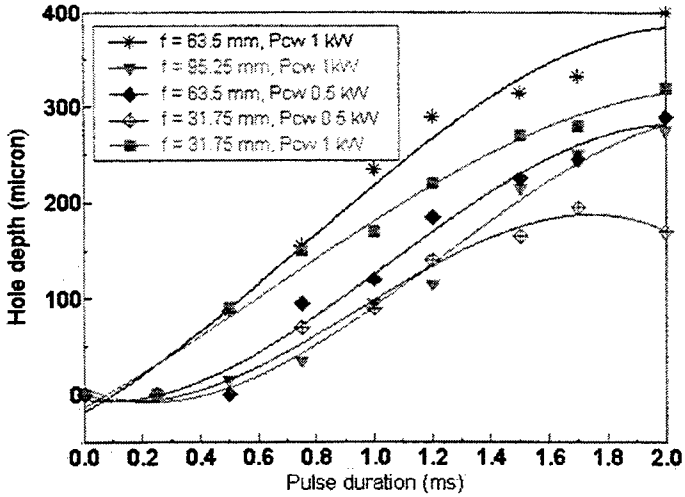


**Fig. 2b**

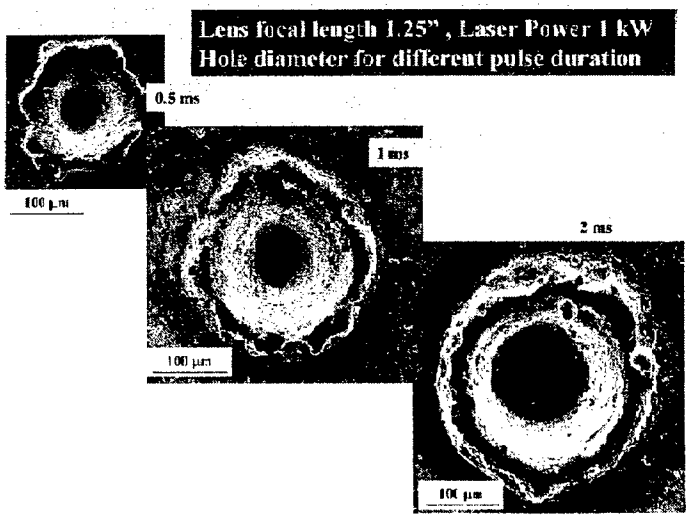


Fig. 3a

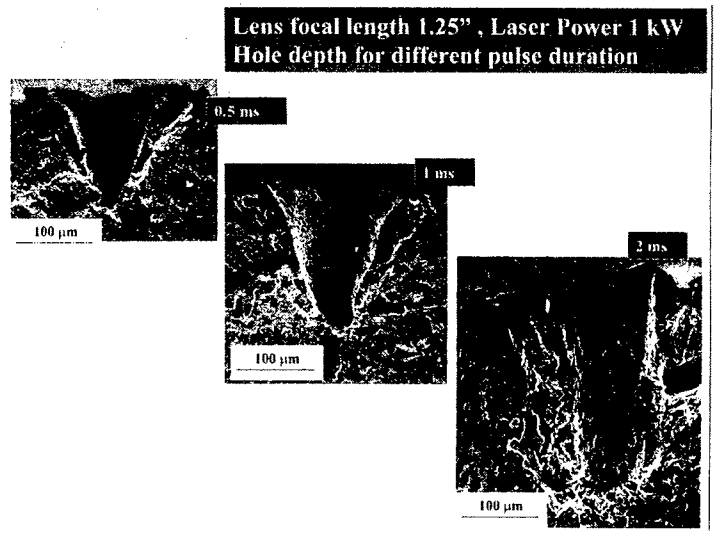


Fig. 3b

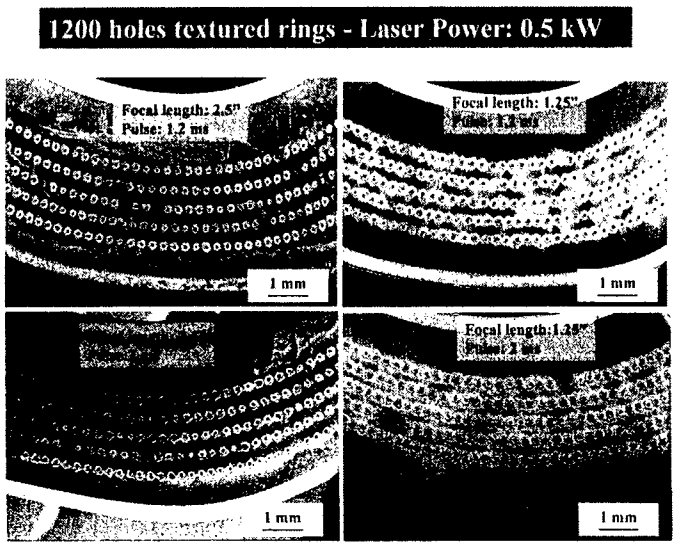


Fig. 4a

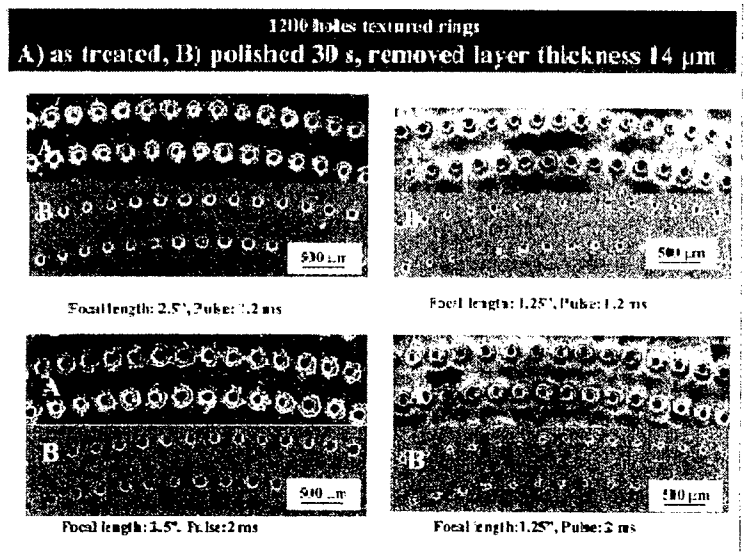


Fig. 4b

Invited Paper

# Laser Drilling with Short Pulses

Friedrich Dausinger*
Institut fuer Strahlwerkzeuge (IFSW), University of Stuttgart
Stuttgart, Germany

## ABSTRACT

The paper summarizes drilling results obtained in the pulse regime from milliseconds to several hundred femtoseconds. A new drilling procedure for unprecedented accuracy and a model explaining experimental results will be presented.

**Keywords:** drilling, diode-pumped solid-state lasers

## 1. INTRODUCTION

Lamp pumped Nd:YAG lasers with pulse lengths of several tenths of milliseconds are well established tools for drilling technical materials. A well-known example is the drilling of airfoil cooling holes in components of aircraft engines. Recently, a new application was published showing the entrance of laser drilling into the automobile manufacturing. A fuel filter is produced by perforating a nozzle holder with 540 holes of 80 μm diameter[1]. Both applications have in common that the desired function is achieved by a multitude of holes and that a certain degree of inaccuracy of diameter and shape as well as a thin recast layer can be tolerated. In cases when higher accuracy is required, laser drilling with millisecond pulses could not meet the requirements, however.

Even in well established applications a lot of problems are not solved satisfactorily:

- Recast layers cause cracks,
- the protection of walls opposite to hole exits necessitates additional process steps,
- insufficient process stability leads to the need of exhaustive control,
- ceramic coatings tend to chip off around the hole,
- shaped hole cross sections and higher aspect are out of reach, still.

Recent attempts to overcome these problems have been published in the U.S., mainly. For instance, Chen showed the advantages of shorter pulse duration[2] (several hundreds of nanoseconds) and visible light instead of infrared[3]. In that case, green light was obtained by frequency doubling, whereas Chang[4] used a similar wavelength of a copper vapor laser and demonstrated the potential of this laser type for precise machining.

## 2. MEANS TO INCREASE PRECISION

### 2.1 Reduction of Pulse Length

In classical machining processes, the shape of the cutting edge and its programmed path determine the machined geometry directly. When a laser is taken as tool, however, this is not the case, see figure 1[5]. There is an influence of the intensity distribution, certainly. The changes in hole shape at given materials could be attributed to variations of the intensity profile. But obviously other factors play an important role, additionally. The initial intensity distribution is altered by its effect on the workpiece, i.e. the hole it produces. The response of the workpiece is determined by materials properties such as absorptivity, temperatures of melting and boiling, density and specific heat. This explains the obvious systematic differences between hole shapes obtained in different materials as shown in figure 1.

* Correspondence: Email: dausinger@ifsw.uni-stuttgart.de; http://www.ifsw.uni-stuttgart.de; Telephone: +49-711-685-6844; Fax: +49-711-685-7244

XIII International Symposium on Gas Flow and Chemical Lasers and High-Power Laser Conference,
Antonio Lapucci, Marco Ciofini, Editors, Proceedings of SPIE Vol. 4184 (2001)

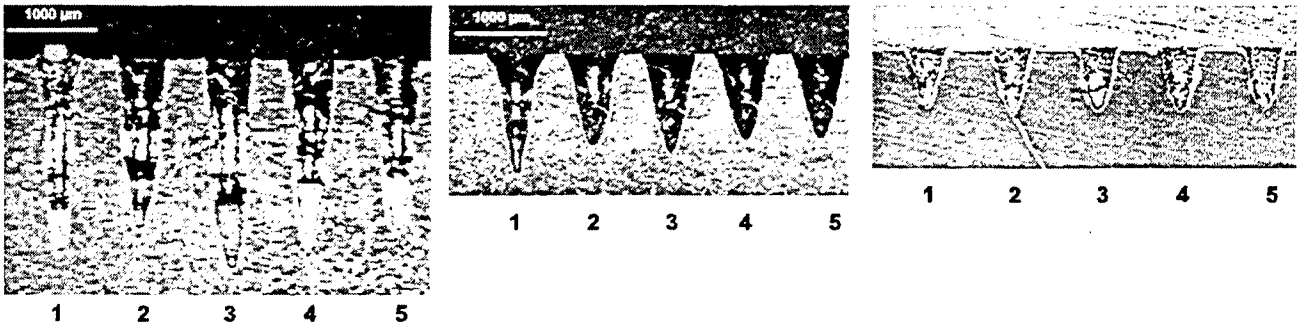


Fig. 1: Shape of holes drilled in different materials with single pulse drilling (0,4 ms, 5 J)

In laser drilling, material is removed as a mixture of melt and vapor, the distribution of which depending on materials properties and laser intensity: A large amount of melt is advantageous for process efficiency, but causes a destabilization of the process, on the other hand. The thicker a layer of melt is, the less is defined its surface geometry, the more the reshaping effect of the hole geometry fluctuates. The thickness of a layer molten during a laser pulse can be reduced by shortening the penetration depth l which is composed of an optical ($l_\alpha$) and a thermal ($l_{th}$) contribution:

$$l = l_\alpha + l_{th} \ . \tag{1}$$

In metals, $l_\alpha$ is smaller than a tenth of the wavelength, generally, and can be neglected in equation (1), therefore. For dielectric materials, this is not the case in visible and near IR wavelength range. If irradiated with high enough intensity, however, ceramics decompose and produce metallic surface layers limiting optical penetration depth[6], [7]. In both material groups of technical interest, metals and ceramics, penetration depth is determined by the thermal one, therefore. This thermal penetration is given by the thermal diffusivity $\kappa$ and the pulse length $\tau_H$

$$l_{th} = 2\sqrt{\kappa \cdot \tau_H} \tag{2}$$

provided $\tau_H$ is longer than the electron/photon relaxation time being in the order of 10 ps.

The expectation to increase drilling accuracy by shortening the pulse duration was not fulfilled in a first attempt, however. Figure 2 shows massive recast layers on a hole wall after percussion drilling of 1 mm thick steel with a nanosecond laser. From this it was concluded, that the reduction of pulse duration had to be accompanied by the development of adequate processing techniques.

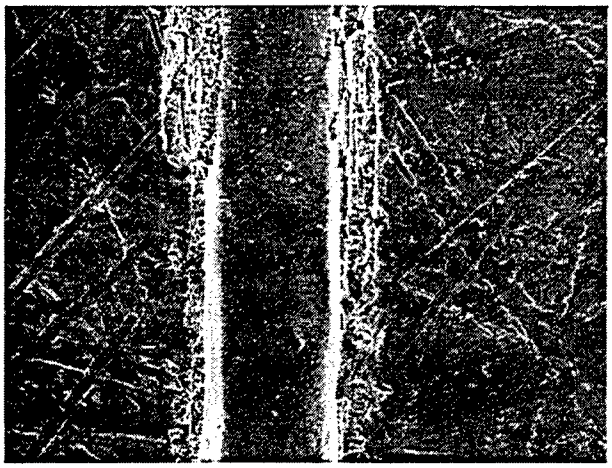

Fig. 2: Typical recast layers in percussion drilling of 1 mm thick steel with ns lasers. The total recast with thickness up to several tens of micrometers is composed of about 1 µm thick layers

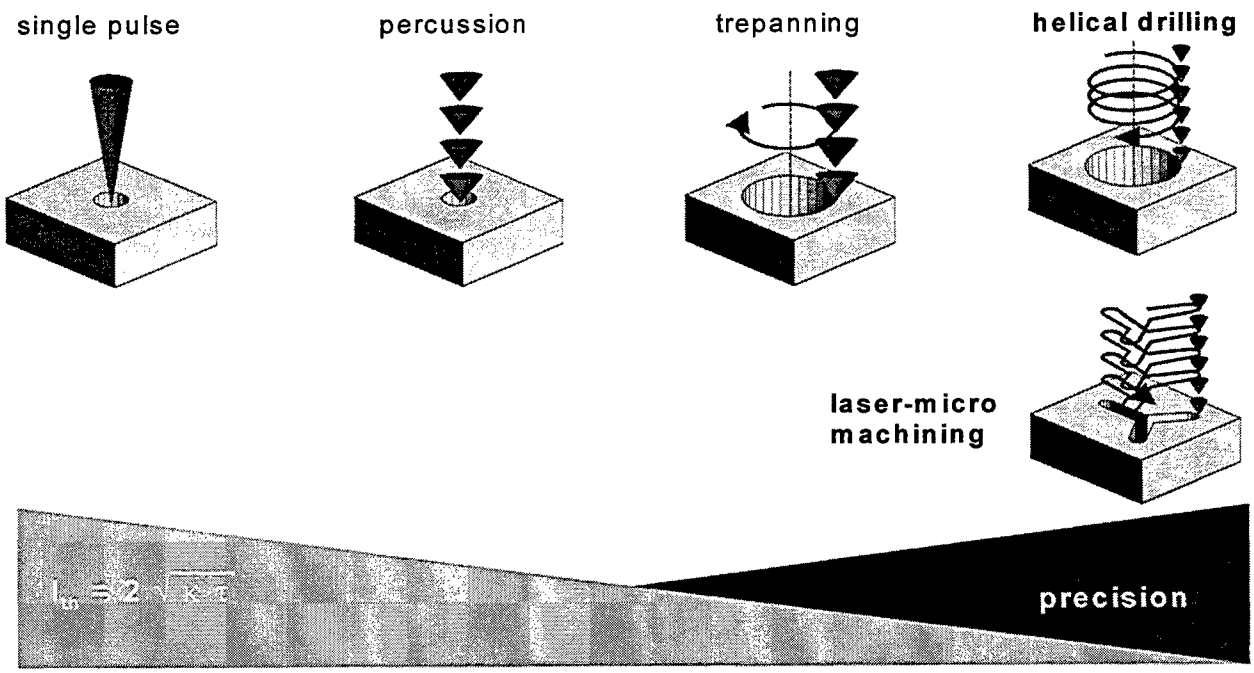


Fig. 3: Processing techniques in laser drilling

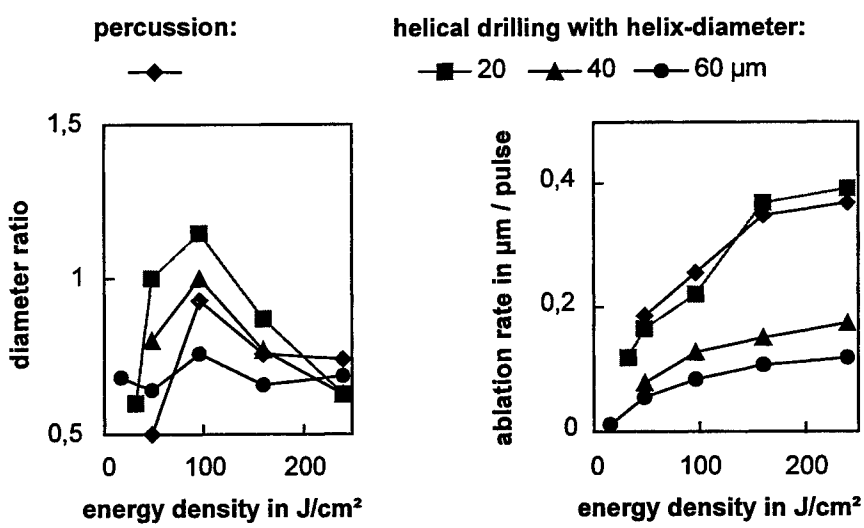


Fig. 4: Percussion ($d_h = 0$) and helical drilling of 1 mm thick ceramic $Si_3N_4$ with variation of the helical diameter $d_h$ from 0 to 60 µm. The ratio of exit through entrance diameter (left) and the average drilling rate determined by the number of pulses necessary to drill through are shown.

## 2.2 Processing Techniques

In industrial applications of laser drilling three techniques are used, up to now (see figure 3):

- single pulse drilling,
- percussion drilling,
- trepanning.

In this sequence the required number of pulses increases. This can be used to increase the machined volume, on one hand. If, on the other hand, the total volume is kept constant and the volume per pulse is reduced (by shortening the pulse duration, e.g.) the accuracy of the process can be increased.

Trepanning is the standard technique for large hole diameters, e.g. 500 µm holes in turbine blades. It is essentially a percussion drilling process followed by a cutting procedure. Start and end of drilling path are often visible as deviations from circularity[8]. The application of nanosecond pulses to trepanning allows to increase hole quality. The load on walls opposite to hole exits is reduced, especially if a sensor is used to detect break-through[9]. Furthermore, the chipping-off of ceramic layers can be avoided[10].

A new technique, the so-called helical drilling, makes use of the breaking up of the process into a multitude of ablation steps in order to enhance the accuracy. In contrast to trepanning, the helical drilling reaches the breakthrough only after many turns of a spiral describing the path of the ablation front. This has favorable effects on drilling accuracy:

- The described deviation from circularity caused by the cutting path's start and end in trepanning does not occur,
- the load on opposite walls is minimized.

Furthermore, and this is the main advantage, recast layers as observed in percussion with ns-lasers (figure 2) are greatly reduced or completely avoided. While penetrating the workpiece, the focal position, the pulse energy and to some extend the helix radius can be varied.

Depending on the application a certain shape of the hole is required. The most simple geometry, a cylinder, turned out to be a challenging task for laser drilling. A measure for cylindricity is the ratio between exit and entrance diameter. This ratio is shown in figure 4 together with the average drilling velocity calculated from material thickness divided by number of pulses for breakthrough[11]. The helix diameter $d_h$ is varied from 0 to 60 µm. Figure 4 shows that for the given plate thickness of 1 mm, wavelength of 539 nm and pulse duration of 220 ps an energy density of about 100 J/cm$^2$ is required to approach cylindricity if percussion drilling ($d_h = 0$) is applied. Using helical drilling with $d_h = 20$ µm, a diameter ratio of 1 is achieved at 50 J/cm$^2$, already. The drilling velocity is nearly the same in both cases. In helical drilling the removed volume is larger, however, so this indicates a better efficiency of this technique. If the helical diameter is chosen too large - the optimum value being near the focal diameter - it is no longer possible to achieve cylindricity, however, see figure 4.

The following figures 5 and 6 exhibit some examples of successful applications of the helical drilling method on ceramics[8] and steel[12]. The bores in the ceramic material $Si_3N_4$ demonstrate a diameter and aspect ratio range which has not been accessible before for these materials. The cross section through steel shows high cylindricity, no visible recast layer and sharp entrance and exit edges. The little recast on top of the plate around the hole entrance can be avoided by additional technical measures.

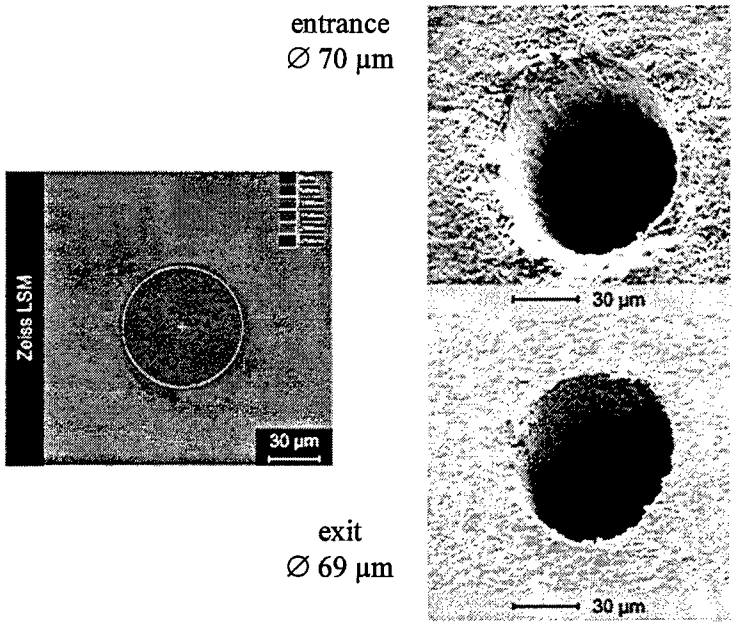


Fig. 5: Microhole in 1 mm thick $Si_3N_4$ (helical drilling, $\lambda = 532$ nm, $\tau_H = 10$ ns, $d_f = 11$ µm). Left: profile obtained with laser scanning microscope, right above: entrance, right below: exit

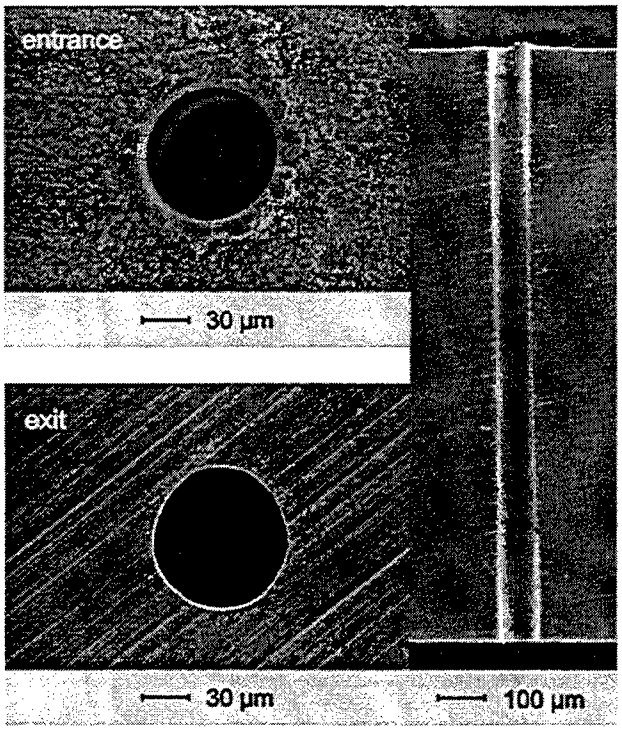


Fig. 6: Microhole in 1 mm thick steel plate (helical drilling, $\lambda = 1{,}06$ µm)

## 3. CONCLUSIONS AND OUTLOOK

Newly developed diode pumped solid state lasers offering pulse energy values beyond several mJ at pulse duration near to 10 ns allow to drill microholes of high aspect ratio and unprecedented accuracy in steel and ceramics. A further increase in accuracy is expected by using pulses in the ps and fs range. Stable turn-key lasers with high focussability, adequate processing techniques and suitable systems have to be developed, however, before the potential of ultrafast pulses can be exploited for industrial applications. These are the tasks of a new joint BMBF project called PRIMUS which started at the end of 1999.

## ACKNOWLEDGEMENT

The author wishes to thank the Federal German Ministry of Education and Research (BMBF) for funding of the underlying projects in the framework of PRABO.

## REFERENCES

1. A. De Paoli, and J. Rapp, "Laseranwendung in der Kraftstoffeinspritztechnik", *Proceedings of Stuttgarter Lasertage (SLT '99)*, In: F. Dausinger, H. Hügel, and H. Opower (Ed.), pp. 8-11, Stuttgart: Forschungsgesellschaft für Strahlwerkzeuge, Stuttgart, 1999.
2. X. Chen, W.T. Lotshaw, A.L. Ortiz, P.R. Staver, C.E. Erikson, M.H. McLaughlin, and T.J. Rockstroh,. "Laser drilling of advanced materials: effects of peak power, pulse format and wavelength", Journal of Laser Applications, **Vol. 8**, pp. 233-239, 1996.
3. X. Chen, A.L. Ortiz, P.R. Staver, W.T. Lotshaw, T.J. Rockstroh, and M.H. McLaughlin, "Improved hole drilling using a high peak power Nd:YAG laser at the second harmonic wavelength", Journal of Laser Applications, **Vol. 9**, pp. 287-290, 1997.
4. J.J. Chang, B.E. Warner, E.P. Dragon, M.W. and Martinez, "Precision micromachining with pulsed green lasers", Journal of Laser Applications, **Vol. 10,** p. 285, 1998.
5. J. Bahnmüller, *Charakterisierung gepulster Laserstrahlung zur Qualitätssteigerung beim Laserbohren*, Dissertation Universität Stuttgart, 2000.
6. A. Raiber, *Grundlagen und Prozeßtechnik für das Lasermikrobohren technischer Keramiken*, B.G. Teubner, Stuttgart, 1999.
7. T. Abeln, J. Radtke, and F. Dausinger, "High Precision Drilling with Short-Pulsed Solid-State Lasers", *Proceedings of the Laser Materials Processing Conference (ICALEO 99)*, In: P. Christensen. (Ed.), Proceedings of LIA Vol. 88, p. 195, Orlando (FL): LIA, 2000, San Diego (CA), 1999.
8. A. Giering, M. Beck, and J. Bahnmüller,. "Laserbohranwendungen im Luftfahrtbereich", *Proceedings of Stuttgarter Lasertage (SLT '99)*, In: F. Dausinger, H. Hügel, and H. Opower (Ed.), p. 32, Stuttgart: Forschungsgesellschaft für Strahlwerkzeuge, Stuttgart, 1999.
9. X. Chen, "Method and Apparatus for Laser Drilling", United States Patent 6,054,673, September, 1997.
10. T. Beck, R. Motzkus, S. Seidel, and K. Richter, "Präzisionsbohren mit aktiv gütegeschalteten Festkörperlasern mit hoher mittlerer Leistung". Laser in der Materialbearbeitung, Düsseldorf: VDI-Technologiezentrum, **Vol. 12,** pp. 15-26, 2000.
11. F. Dausinger, T. Abeln, D. Breitling, J. Radtke, V. Konov, S. Garnov, S. Klimentov, T. Kononenko, and O. Tsarkova, "Drilling of ceramics with short-pulsed solid-state lasers", LaserOpto 31, **Vol. 3,** pp. 78-85, 1999.
12. G. Callies, and T. Wawra, "Verfahrensstrategien zur effizienten Erzeugung von Durchbrüchen und Bohrungen hoher Präzision für die Mengenfertigung". Laser in der Materialbearbeitung, Düsseldorf: VDI-Technologiezentrum, **Vol. 12**, 2000.

# Amorphous silicon crystallisation by a long-pulse excimer laser

P. Di Lazzaro[1], S. Bollanti, F. Bonfigli, F. Flora, G. Giordano, T. Letardi, D. Murra, C.E. Zheng[§], A. Baldesi[§]

ENEA, Division FIS-LAC, C.P. 65, 00044 Frascati (Roma, Italia)
[§]El.En. via Baldanzese 17, 50041 Calenzano (Firenze, Italia)

## ABSTRACT

In this paper we summarise the results of the annealing of a-Si films done at ENEA Frascati by the XeCl laser facility Hercules and the preliminary results of the characterisation work done on the first Italian industrial high-energy excimer laser, named Hercules L. Some information will be also given on a novel process to obtain homogeneous, large grain poly-Si and on a new homogeniser with zoom.

**Keywords:** Excimer laser, homogenizer, silicon annealing, super lateral growth, TFT, flat panel display.

## 1. INTRODUCTION

The transformation of amorphous silicon (a-Si) into polycrystalline silicon (poly-Si) is an important process in microelectronics, since poly-Si films are used for the fabrication of high-mobility Thin-Film-Transistors (TFT) which are a key-component of flat-panel displays. The preferred light source for the transformation a-Si into poly-Si is the excimer laser, because its high-power UV pulse may increase the temperature of the silicon film up to the melting point without heating the substrate. In this way, the substrate can be made by glass instead of the expensive quartz used in the traditional high-temperature oven annealing process.

ENEA co-ordinates the EU-funded Project *FOTO* [1], aiming at the construction of a 200 $m^2$ clean room for the production of high-mobility TFT. In this frame, the task of our laboratory was twofold: 1) Find the optimum working point for crystallising (10×10) $cm^2$ a-Si panels by using the XeCl laser facility Hercules ($\lambda$ = 308 nm, E = 8 J / pulse, $\Delta t$ = 160 ns) and a line-step homogenizer; 2) Design, construct and test a new industrial prototype XeCl laser, similar to Hercules, in collaboration with the Company El.En.

## 2. ANNEALING a-Si FILMS

### 2.1. The laser facility Hercules

The XeCl laser Hercules is operative in our laboratory since 1987, and it has been used as a laser-facility for high-intensity/large-area irradiation experiments (e.g., laser-plasma, material processing) since 1992. Details about the Hercules performance can be found in [2, 3, 4, 5] and references therein. In the configuration chosen for these experiments, Hercules delivers 8 J per pulse within 160 ns FWHM in a spot size of (10×5) $cm^2$ at a repetition rate of 2 Hz. In this working point, the shot-to-shot output energy fluctuation over a typical 100-shots burst is less than 4%.

### 2.2. Grain size vs. laser fluence

In order to find the optimum working point for crystallising a-Si panels, the first action was measuring the size of poly-Si grains as a function of the laser energy density. This is a crucial point, because the field-effect mobility of TFT is proportional to the grain size. We irradiated a 50-nm-thick a-Si film deposited on glass by a single-shot of Hercules focused by a cylindrical lens, as shown in Fig. 1. In this way, we annealed the a-Si film with fluence ranging up to 0.5 J/$cm^2$, and measured the poly-Si grain size by Scanning Electron Microscope. Then, we removed the poly-Si and scanned a photo-tube with a 50-μm pinhole, clamped on the motorised slide, for the measurement of the fluence profile. To achieve a one-to-one correspondence between grain size and laser fluence, we used two markers (namely, a screen and a copper wire put on the a-Si film, see Fig. 1) as detailed in [6]. In fact, the distance between the shadows of the screen and of the wire unambiguously determines the position of the track where the measurements of grain-size/fluence are made. The final result is summarised in Fig. 2. Thanks to the two-markers, the experimental fluence uncertainty was reduced to less than 10%. From Fig. 2, we can identify three regions: 1) Low fluence region: the poly-Si grain size ranges between (100 - 200) nm. 2) Critical fluence: the poly-Si grain size increases with a steep slope of 0.5 μm/(mJ/$cm^2$) up to a maximum of 2 μm, then falls down. 3) Over critical fluence, where the silicon is totally melted and the poly-Si grain size is about 100 nm. Clearly, it is not convenient working in the region 2), the so-called Super Lateral Growth (SLG) region, because its highly non-linear behaviour may cause a large spread in the size of the poly-Si grains when the local laser energy density fluctuates more than 1%.

[1] Correspondence: Email: dilazzaro@frascati.enea.it; fac-simile: 0039 06 94005334

XIII International Symposium on Gas Flow and Chemical Lasers and High-Power Laser Conference,
Antonio Lapucci, Marco Ciofini, Editors, Proceedings of SPIE Vol. 4184 (2001)

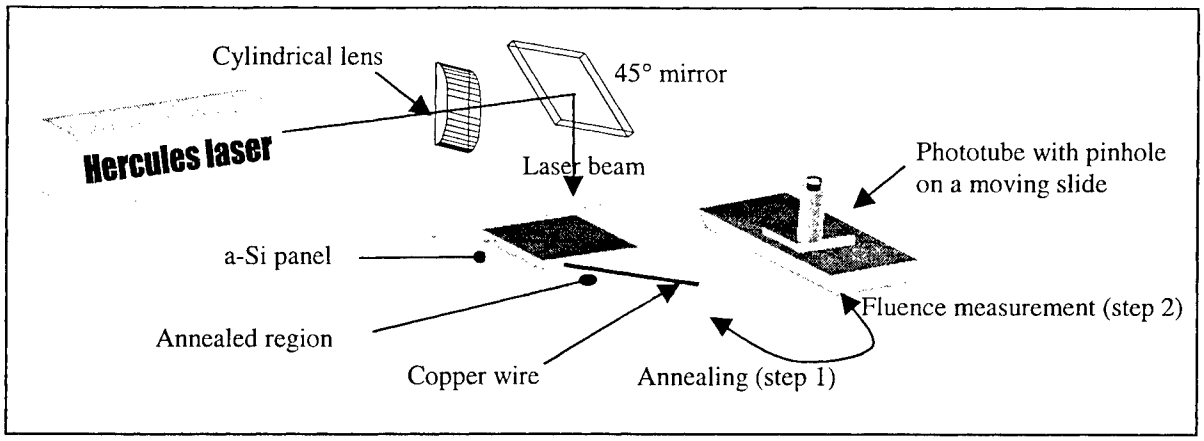


**Fig. 1**: Experimental set-up during the grain-size measurement. During the second step of the measurement, the silicon panel is replaced by the photo-tube on the motorised slide

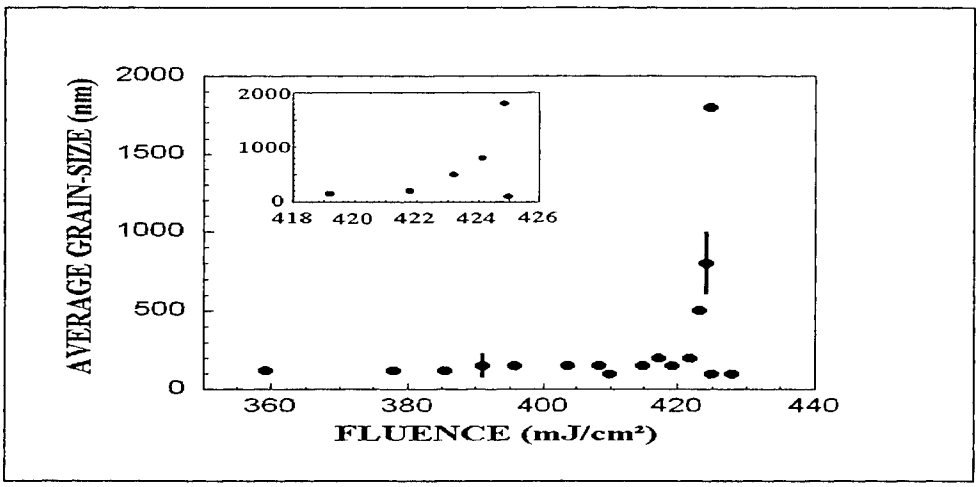


**Fig.2**: Poly-Si grain size vs. laser energy density.

### 2.3. Laser beam homogeniser

In order to achieve TFT having uniform device characteristics, we need a uniform poly-Si grain size, that is a uniform laser energy-density distribution incident on the a-Si film. This is done by a beam homogeniser. The working principle of a line-step homogeniser is schematised in Fig. 3. A lens array D divides the incoming beam in a number of secondary beams, each one spread over the focal plane by a condenser lens C. In this way, all the secondary beams are perfectly overlapped on the focal plane, forgetful of their different energy content, and the spatial energy distribution is integrated. The beam homogeniser shown in Fig. 3 transformed the $(10 \times 5)$ cm$^2$ near-field of Hercules into a $(13 \times 1)$ cm$^2$ beam, with a 3% r.m.s. energy fluctuations and a sharper steepness, as shown in Fig. 4.

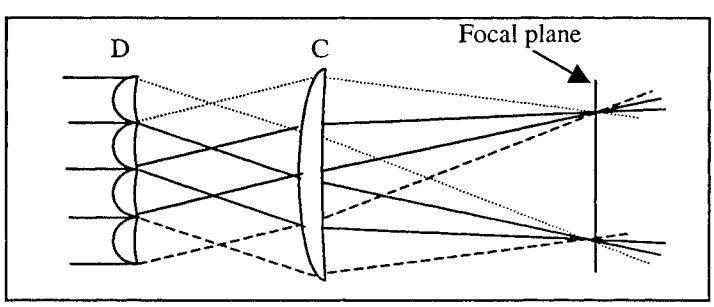


**Fig. 3**: One-dimensional scheme of the line-step homogeniser used in these experiments.
D = array of divider lenses.
C = condenser lens.

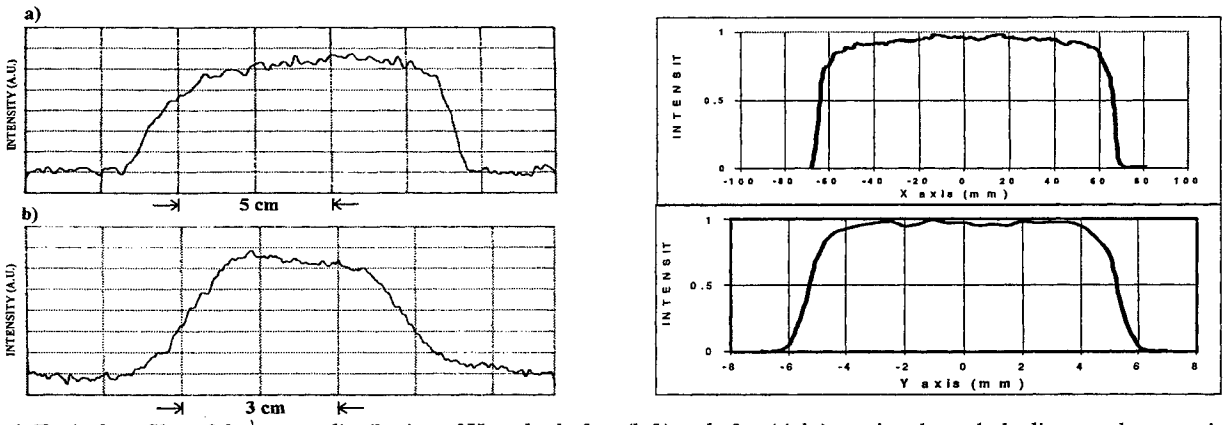


**Fig. 4**: Typical profiles of the energy distribution of Hercules before (left) and after (right) passing through the line-step homogeniser of figure 3. Note the different horizontal scales of the homogenised beam on the right.

### 2.4. Annealing results

We have re-crystallised many (10×10) $cm^2$ a-Si films having different thickness, in vacuum, in air, in a controlled He atmosphere, with and without heating the glass panel substrate. This huge amount of work is detailed in [7]. Here we have room only to point out a couple of relevant results: 1) a longer laser pulse duration allows a larger poly-Si grain size, in average. This is because the longer the trailing edge of the pulse, the slower the cooling rate of the melted Si, and the longer the time available to the growth of the grain. We found that the average grain size is roughly proportional to the square root of the FWHM laser pulsewidth. 2) The spatial overlap the laser pulses is beneficial to both poly-Si grain size and to the roughness of the poly-Si film at the grain boundary caused by the material transport during the melted period. In our case the best results were obtained by using an overlap percentage between 90% and 95%.

## 3. IMPROVEMENTS (WORK IS IN PROGRESS...)

### 3.1. Novel two-step process to obtain homogeneous, large grain poly-Si

The SLG region is the more effective to have very large size poly-Si grains, but it is the less workable due to the narrow window of acceptable laser fluence (see Fig. 2). The non linearity of SLG can be explained as follows. There is a critical laser fluence that melts the whole a-Si films but some residual seeds at the interface film-substrate. Each seed can laterally grow expanding into the melted Si until it meets another seed growing in the opposite direction. Lower than critical fluence allows a higher density of residual seeds (smaller room to expand means smaller grains). Higher than critical fluence melts the whole film at all, and the crystallisation occurs during the film cooling, starting from seeds randomly distributed in the bulk of the film (too many seeds generate very small grains). How can we control the SLG artificially creating cold seeds? For example, by using a periodic mask put on the a-Si [8]. After a first laser irradiation, the mask modulates a grating made by adjoining strips of poly-Si (irradiated zone) and a-Si (shadowed zone). After removing the mask, a second irradiation with laser fluence adjusted to melt the a-Si strips and partially melt the poly-Si strips allows the growth of pencil-like grains aligned perpendicular to the poly-Si strips, as wide as half the period of the grating, see Fig. 5.

### 3.2. Homogeniser with a variable focal length

Films with different thickness require different laser fluence to optimise the crystallisation results. Also, we found it may be convenient irradiating the a-Si by more shots having different laser fluence values, like in the above case of a two-step process. Unfortunately, homogenisers are stiff systems: once fixed their geometry and lens power (and the input laser energy), the laser fluence on the focal plane can be hardly changed. We solved the problem designing and testing a line-step homogeniser with zoom [9], which can modulate almost continuously the spot size of the homogenised beam along one or both axes. Preliminary results achieved by a prototype gave a zoom factor of up to 1200% along each side of the rectangular beam, corresponding to an energy density variation on the focal plane of a factor 144. These results did affect neither the beam homogeneity nor the overall length of the homogeniser. Simulation results show that there are no limits in the maximum zoom factor achievable, and only practical reasons (e.g., a lower limit to the f-number of the lenses, the damage thresholds of lens coatings) may limit the maximum zoom factor.

### 3.3. The new laser Hercules L

Concerning our second task in the frame of *FOTO* (see introduction), ENEA and El.En. have designed, realised and tested a new XeCl laser system, named Hercules L, see Fig. 6. Like Hercules, Hercules L is excited by an X-ray triggered discharge delivered by a LC-inversion circuit, and electrodes are profiled according with the "mixed" solution proposed in [4]. The

ionising X-rays are emitted by a double X-ray diode similar to that detailed in [10]. The table below summarises the main characteristics and performance of Hercules L.

| | | | |
|---|---|---|---|
| **Active medium** | XeCl ($\lambda$ = 308 nm) | **Near-field beam size** | 10 cm x 7 cm |
| **Gas mixture pressure** | 5 bar (absolute) | **Pulsewidth FWHM** | (100 – 150) ns |
| **Gas flow** | Longitudinal | **Energy output** | ≥ 10 J |
| **Ionisation** | 80 keV bremsstrahlung X-rays | **Repetition rate** | (0.01 – 10) Hz |
| **Discharge voltage** | 50 kV | **Average power (in burst)** | 100 W |

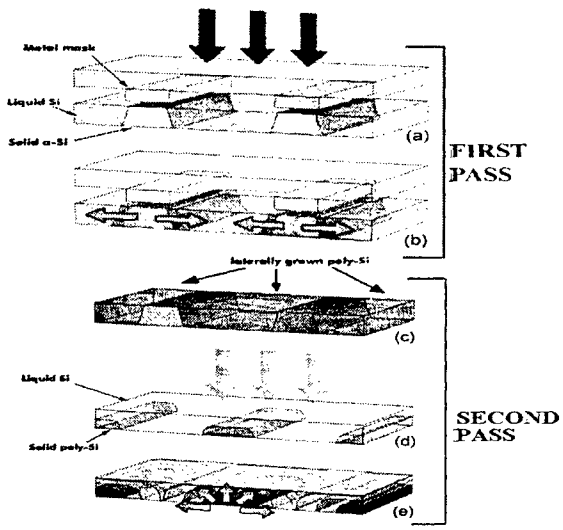


**Fig. 5**: Scheme of the two-pass technique to achieve large and self-aligned poly-Si grains (see [8]).

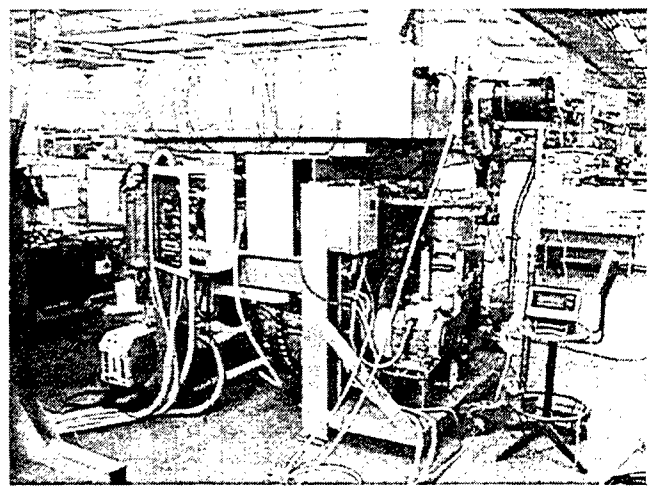

**Fig. 6**: Photo of Hercules L during the average power measurement. The overall size is (l × w × h) = (2.5 × 1.5 × 2) $m^3$.

## 4. CONCLUSIONS

In the frame of the European Project FOTO[1], we made some experiments to determine the optimum parameters for a-Si annealing by a long pulsewidth excimer laser. By using a 160-ns XeCl laser pulse and a scanning device we obtained a precise relation between grain-size and laser-energy-density which allows a correct choice of the working point (see Fig. 2). By using a line-step beam homogeneizer we reduced the laser spatial fluctuations down to 3% r.m.s. (see Fig. 4) and irradiated 10x10-$cm^2$ a-Si films (having different thickness) deposited on glass panels [7]. When the fluence is less than the critical one the grain sizes are uniform but smaller than those achieved in the SLG region. When the fluence is close to the SLG region, fluence fluctuations larger than 1% create a large spread of the poly-Si grain size.

To overcome the SLG problem, we are testing a new process (patent pending) [8] to obtain large and homogeneous poly-Si grains (see Fig. 5). To allow the irradiation of a-Si films with different fluence by the same homogeniser, we designed and tested a new homogeniser with variable focal length (patent pending) [9].

Based on the experience gained operating the laser facility Hercules, we made a new XeCl laser system named "Hercules L" (10 J/p, 120 ns, 10 Hz). The final goal is the accomplishment of a line for the production of high-mobility TFTs suitable for flat panel displays.

## REFERENCES


1. D. Della Sala, C. Privato, P. Di Lazzaro, G. Fortunato: "Microelettronica gigante" E.A.I. **4**, 52 (1999).
2. S. Bollanti, P. Di Lazzaro, F. Flora, G. Giordano, T. Hermsen, T. Letardi, C.E. Zheng, "Performance of a ten-liter electron avalanche discharge XeCl laser device" Appl. Phys. B **50**, 415 (1990).
3. T. Letardi, S. Bollanti, P. Di Lazzaro, F. Flora, N. Lisi, C.E. Zheng: "Some design limitations for large-aperture high-energy per pulse excimer lasers", Il Nuovo Cimento D **14**, 495 (1992).
4. P. Di Lazzaro, G. Giordano, L. Mezi, C.E. Zheng: "Field uniformity of discharge lasers: electrode profiles and current return path effect", Opt. & Laser Techn. **26**, 15 (1994).

5. P. Di Lazzaro: "Hercules, an XeCl laser facility for high-intensity irradiation experiments" Proc. 2nd GR-I Int. Conf. on New Lasers, Technologies and Applications, A. Carabelas, P. Di Lazzaro, A. Torre, G. Baldacchini Eds., SPIE vol. 3423, pp. 35 - 43 (1998).
6. D. Murra, S. Bollanti, F. Bonfigli, D. Della Sala, P. Di Lazzaro, T. Letardi: "Experimental results on silicon annealing by a long pulse XeCl laser", Int. Conf. on Advanced Laser Technologies ALT '99, V.I. Pustovoy, V.I. Konov Eds., Proc. SPIE vol. 4070, pp. 345 - 350 (2000).
7. S. Bollanti, P. Di Lazzaro, D. Murra, A. Imparato, C. Privato, R. Carluccio, G. Fortunato, L. Mariucci,: "Cristallizzazione di silicio amorfo via laser: rapporto degli esperimenti a Frascati **RT/INN/00/** (2000).
8. ENEA patents n° RM99A000182, March 1999, and n° RM99A000381, June 1999. See also L. Mariucci, R. Carluccio, A. Pecora, V. Foglietti, G. Fortunato, D. Della Sala: "A novel two-pass excimer laser crystallization process to obtain homogeneous large grain polysilicon" Jpn. J. Appl. Phys. **38** L907 (1999).
9. ENEA patent n° RM2000A000229, April 2000.
10. S. Bollanti, P. Di Lazzaro, F. Flora, G. Giordano, T. Letardi, D. Murra, G. Schina, C.E. Zheng: "X-ray diode with spark-plug plasma cathode", XII Int. Symp. on Gas Flow and Chemical Lasers and High Power Laser Conf., A. Boreisho, G. Baranov Eds., SPIE vol. 3574, pp. 84 - 92 (1998).

# Fabrication of $Nd:Gd_3Ga_5O_{12}$ and self Q-switched $Nd,Cr:Gd_3Ga_5O_{12}$ laser waveguides by pulsed laser deposition method

Yoshihisa Ishida, Sachiyo Fukaya, Tomoyuki Shimoda and Minoru Obara*
Department of Electronics and Electrical Engineering, Keio University,
3-14-1 Hiyoshi, Kohoku-ku, Yokohama, 223-8522, Japan

## ABSTRACT

In this paper, we report the fabrication of a neodymium-doped $Gd_3Ga_5O_{12}$ (Nd:GGG) film and neodymium, chromium-codoped $Gd_3Ga_5O_{12}$ (Nd,Cr:GGG) film to realize a self Q-switched laser grown upon $Y_3Al_5O_{12}$ (YAG) substrate by pulsed laser deposition (PLD) method. Consequently, epitaxial films have been grown.

Keywords: Laser ablation, pulsed laser deposition, waveguide laser, co-doping, optical thin film

## 1. INTRODUCTION

The PLD method has attracted much attention for the growth of electronic thin films such as semiconductor and high-temperature superconducting films, because the PLD is a simple and affordable method to fabricate highly crystallized films. Recently, this method is applied to the fabrication of optical waveguides, because this method is suitable to deposit high quality epitaxial films in order to reduce optical propagation loss.

In optical planar waveguide, which has a structure of the higher refractive index film on the low refractive index substrate, the laser beam is confined in the micrometer-order thick core layer. This structure is useful for waveguide lasers, because waveguide structure leads to highly efficient laser oscillation by the high optical power densities with a short laser length and the effective heat removal by heat sink adjacent to the core layer. The high efficiency and low threshold waveguide laser fabricated by PLD was indeed reported for Nd:GGG[1].

In this paper, we would like to report on the fabrication of $Nd:Gd_3Ga_5O_{12}$ and self Q-switched $Nd,Cr:Gd_3Ga_5O_{12}$ laser waveguides by pulsed laser deposition method. Since GGG crystal has a low misfit factor with YAG crystal and has higher refractive index than that of the YAG substrate, leading to the compatibility with coupling to highly divergent laser diode.

## 2. FABRICATION OF Nd DOPED GGG AND Nd, Cr CO-DOPED GGG THIN FILM BY PLD

The experimental setup for PLD method is shown in Fig. 2. For the fabrication of Nd:GGG thin films, Nd:GGG ([Nd] = 2 at.%) sintered target is ablated by one KrF excimer laser pulse (LPX150 LAMBDA PHYSIK, 248 nm, 20 ns, laser ablation

*Correspondence: Email: obara@obara.elec.keio.ac.jp;
Telephone: +81 45 563 1141 ext. 42226; Fax: +81 45 566 1529



XIII International Symposium on Gas Flow and Chemical Lasers and High-Power Laser Conference,
Antonio Lapucci, Marco Ciofini, Editors, Proceedings of SPIE Vol. 4184 (2001)

fluence: 0.5-1.2 J/cm$^2$, 20pps) in vacuum chamber containing oxygen gas (10 mTorr). Nd doped GGG are deposited on the YAG (111) single crystal substrate placed several centimeters apart. This substrate is heated at 350 ℃ to stimulate the migration. The GGG crystal has a garnet structure like YAG and has a low misfit factor of 2.9 %. As as-deposited films are found amorphous, epitaxial films are achieved by post-annealing at 1100 ℃ for 4hours. Fabricated films are epitaxially grown. These epitaxial thin films are successfully deposited up to a thickness of 8 μm.

For Nd, Cr:GGG, The laser beam is divided into two beams by beam splitter to simultaneously ablate two targets, i.e. Nd:GGG and Cr,Ca:GGG ([Cr] = 1.6 at.%, [Ca]/[Cr] = 2) sintered targets in vacuum chamber. In the case of Nd,Cr:GGG thin films, another sintered target for Cr was also simultaneously ablated with divided beam from KrF excimer laser beam(see Fig. 1). The concentrations of Nd and Cr ions in Nd, Cr:GGG thin films are adjustable by changing laser ablation fluences independently for Nd:GGG and Cr, Ca:GGG targets. As the laser ablation fluence onto Cr, Ca:GGG target were reduced, the concentration of Cr in Nd, Cr:GGG thin films were also reduced. This was confirmed by the shift of the X-ray diffraction (XRD) spectrum of the Nd, Cr co-doped GGG epitaxial thin films as shown in Fig. 2.

## 3. OPTICAL PROPERTIES

### 3.1 WAVEGUIDE STRUCTURE

The refractive index of Nd:GGG and Nd, Cr:GGG epitaxial films on the YAG substrate was measured by bright m-line method with a 633 nm laser and rutile prism. The incident angles of the prism for $TE_0$ and $TE_1$ were measured, and then the reflective index was calculated. As a result, the refractive index of Nd:GGG and Nd, Cr:GGG was estimated to be 1.97 and 2.00, respectively. The Nd, Cr:GGG films on the YAG substrate show a waveguide structure due to the refractive index of substrate(YAG 1.82). These waveguides have high numerical aperture(NA) of 0.75. Such a high-NA waveguide is compatible with coupling to highly divergent laser diode.

### 3.2 FLUORESCENCE SPECTRUM

The fluorescence spectrum of the $Nd^{3+}$ ions in the Nd:GGG thin film is shown in Fig. 3. The Nd:GGG thin film was pumped by laser diode at 808 nm corresponding to the $Nd^{3+}$ absorption band. Fluorescence around 1.06 μm was observed, which corresponds to the $^4F_{3/2} \rightarrow {}^4I_{11/2}$ transitions of $Nd^{3+}$ ions. Hence, $Nd^{3+}$ ions in the Nd:GGG thin films will serve as laser active ion at 1.06 μm. From these data, it is acticipated that the $Nd^{3+}$ ions doped in a 8 μm thick Nd:GGG waveguide are active as laser active ions at 1.06 μm.

In order to estimate the laser performance of Nd:GGG waveguide, we theoretically analyzed small signal gain of waveguide. Thus, the optimum focal length for pump beam and waveguide length was determined by this calculation. Now, we try to test waveguide lasers. We cut a Nd:GGG waveguide to 1 × 4 mm$^2$ and both ends of the shorter length were polished flat and parallel each other to be optically flat by diamond polisher and form a plane-parallel laser resonator by placing dielectric-coated mirrors with a high reflectivity at 1.06 μm near the end faces of the waveguide. The output coupler had a 2 %

transmission at the expected laser wavelength (1.06 μm). The waveguide is end-pumped by a 1 W diode laser emitting at 808 nm.

### 3.3 OPTICAL PROPERTIES OF Nd, Cr CO-DOPED GGG THIN FILMS

The Cr ions doped in garnet crystal are mainly $Cr^{3+}$ ions which do not act as a saturable absorber. However, a fraction of Cr ions can be oxidized into $Cr^{4+}$ which acts as a saturable absorber by adding $Ca^{2+}$ ions as a charge compensator to the target under proper oxygen pressure. It is confirmed that $Cr^{4+}$ ions are present in Nd, Cr:GGG thin films. Fluorescence of $Cr^{4+}$ ions in Nd, Cr:GGG thin films was also observed around 1.4 μm when pumped by a LD at 940 nm as shown in Fig. 3. This spectrum was similar to that of Cr, Ca:GGG thin films.

In order to make clear that $Cr^{4+}$ ions in Cr, Ca:GGG thin films act as a saturable absorber at 1.06 μm for Q switching, we measured the relationship between $Nd^{3+}$ laser (Nd:KGW 1067nm) fluence and optical transmission through thin film. Saturable absorption and the loss due to the excited sate absorption (ESA) were measured. These experimental results are fitted. As a result, fluence $F_s = 0.023$ J/cm$^2$, $\sigma_{es} = 2\times10^{-19}$ cm$^2$ were obtained, and these data are equivalent to the values of $F_s = 0.032$ J/cm$^2$, and $\sigma_{es} = (13\pm5)\times10^{-19}$ cm$^2$ of bulk crystal[2].

Therefore it is fully expected that $Cr^{4+}$ ions in Nd, Cr:GGG thin films will act as a saturable absorber as well as that of Cr, Ca:GGG thin films.

## 4. SUMMARY

Epitaxial GGG thin films on the YAG substrate have been deposited by PLD method. It is confirmed by m-line method that the structure of these thin films on YAG substrate is a planar waveguide structure. The fluorescence spectrum and lifetime of $Nd^{3+}$ ion in Nd doped GGG waveguide have been measured. And the concentrations of Nd and Cr ion in Nd,Cr co-doped GGG thin films were controlled by changing laser ablation fluences independently for Nd:GGG and Cr, Ca:GGG sintered targets. It is shown that $Cr^{4+}$ ions are present, which are saturable absorbers for Q-switching. Actually, the bulk crystal laser of Cr ,Nd: YAG was successfully operated with LD pumping and showed a self-Q-switched output[3].

## REFERENCES


1. D. S. Gill, A. A. Anderson, R. W. Eason, T. J. Warburton, and D. P. Shepherd, "Laser operation of an Nd:$Gd_3Ga_5O_{12}$ thin-film optical waveguide fabricated by pulsed laser deposition," *Appl. Phys. Lett.*, **69**, pp. 10-12, 1996.
2. Z. Burshtein, P. Blau, Y. Kalisky, Y. Shimony, and M. R. Kokta, "Excited-State Absorption Studies of $Cr^{4+}$ Ions in Several Garnet Host Crystals," *IEEE J. Quantum Electron.*, **34**, pp. 292-299, 1998
3. J. Dong, P. Deng, Y. Lu, Y. Zhang, Yupu Liu , J. Xu and W. Chen, "Laser-diode-pumped $Cr^{4+}$,$Nd^{3+}$:YAG with self-Q-switched laser output of 1.4 W," *Opt. Lett.*, **25**, pp. 1101-1103, 2000.

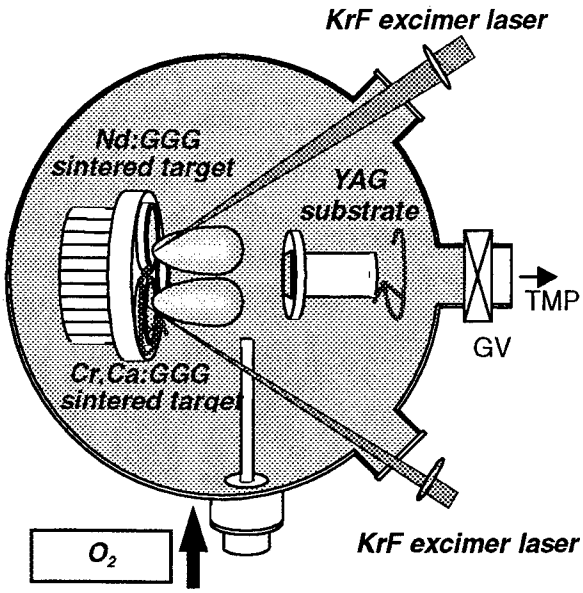


Fig. 1 Schematic of experimental setup of two-target PLD method for fabrication of Nd,Cr co-doped GGG thin film.

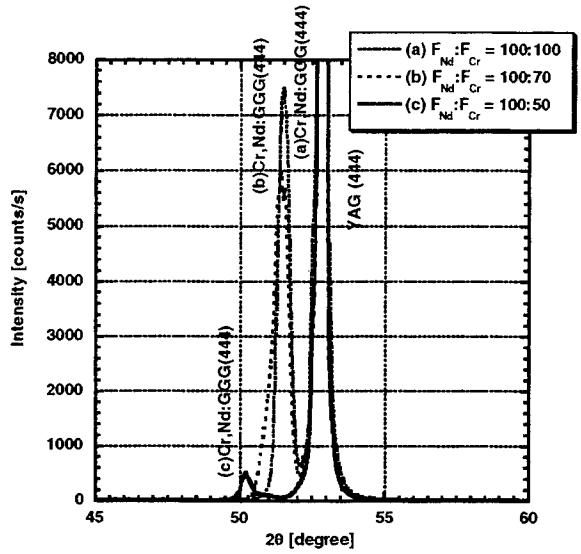


Fig. 2 X-ray diffraction patterns of Nd:GGG thin films grown on YAG(111) substrate and X-ray diffraction patterns of Nd, Cr:GGG thin films grown on YAG(111) substrate when $F_{Nd}:F_{Cr}$ is (a) 100:100, (b) 100:70, (c) 100:50.

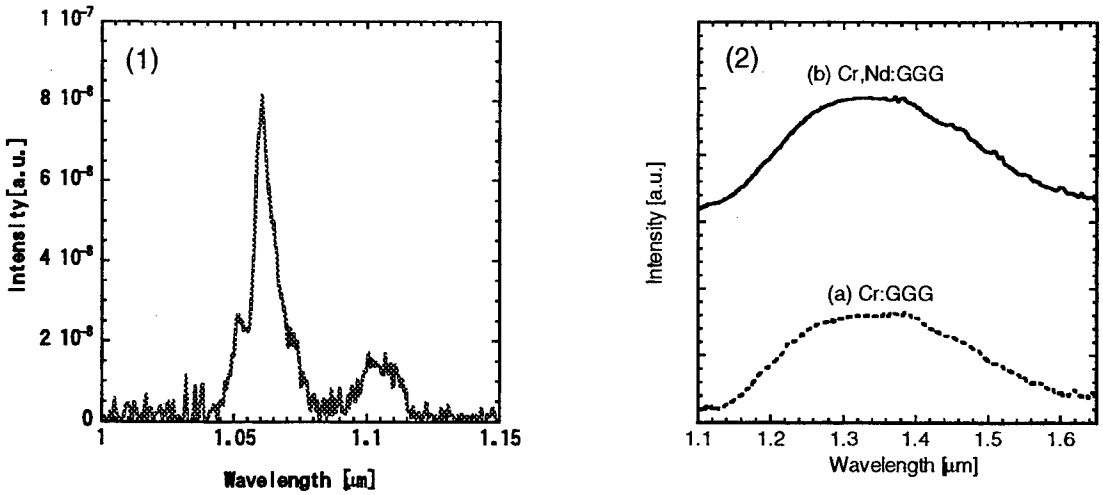


Fig. 3 Fluorescence spectra of (1)$Nd^{3+}$ ions ($^4F_{3/2} \rightarrow {}^4I_{11/2}$ transition) in Nd:GGG thin film grown on YAG(111) substrate pumped at 808 nm and (2) $Cr^{4+}$ ions ($^3T_2 \rightarrow {}^3A_2$ transition) (a) in Nd,Cr:GGG thin film and (b) in Cr:GGG thin films grown on YAG(111) substrate pumped at 940 nm.

# Shadowgraphic and interferometric investigations on Nd:YAG laser-induced vapor/plasma plumes for different processing wavelengths

D. Breitling*, H. Schittenhelm, P. Berger, F. Dausinger, and H. Hügel

Institut für Strahlwerkzeuge (IFSW), Universiät Stuttgart,
Pfaffenwaldring 43, 70569 Stuttgart, Germany

## ABSTRACT

Shadowgraphic and interferometric analysis of vapor/plasma plumes generated by pulses of a ns-Nd:YAG laser display a distinctive morphology for each of three different processing wavelengths (1064 nm, 532 nm, and 355 nm). Analytical models of shock wave expansion can be applied to determine the total energy stored within the plumes. Electron density distribution measurements reveal the regions of absorption and, using a simple model of inverse bremsstrahlung and photoionization, allow us to estimate absorption coefficients.

**Keywords:** Laser induced vapor/plasma plumes, shock waves, laser supported detonation (LSD) waves, plasma absorption, shadowgraphy, interferometry

## 1. INTRODUCTION

In micro-machining and micro-structuring ablation and drilling using short pulsed solid state lasers are becoming increasingly important technologies. Meanwhile power densities well above $10^{11}$ W/cm$^2$ are achieved even by commercially available nanosecond solid state lasers, leading to laser-induced vapor/plasma plumes which interact strongly with the processing laser beam. There is growing interest in the fundamental interaction mechanisms between the laser-induced plumes and the radiation field during the various stages of ablation and while it is widely accepted that material vapor/plasma plumes impair the quality and efficiency of ablation processes, recent studies in deep hole drilling reveal that structure quality may even be improved by plasma formation.[1]

## 2. EXPERIMENTAL SETUP

The experimental setup for the shadowgraphic and interferometric investigations is depicted in Fig. 2. The collimated beam of a pulsed diode-pumped Lambda Physik StarLine Nd:YAG laser operating at 1064 nm, 532 nm, or 355 nm wavelength was focused onto a $Si_3N_4$-target. The laser data are summarized in Tab. 1. The interaction zone, located in the object beam of a Mach-Zehnder interferometer, was illuminated by a nitrogen laser pumped dye laser pulse (LTB MSG 800/UDL 301, $\lambda = 633$ nm, $\Delta\lambda = 0.05$ nm). A plane close to the interaction zone (shadow plane) was imaged onto a fast ICCD camera (PCO DICAM). By simply blocking the reference beam a common shadowgraphic setup was obtained. A bandpass filter ($\lambda = 633$ nm, FWHM = 1 nm) was used to suppress plasma luminescence. Thus, the temporal resolution of the frames was determined only by the pulse duration of the dye laser pulse (FWHM = 500 ps).

*Corresponding author: Fax: +49-711/685-6842, E-mail: breitling@ifsw.uni-stuttgart.de

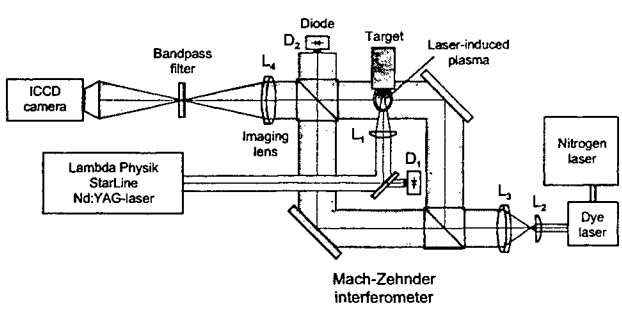


**Figure 1.** Setup for shadowgraphy and interferometry.

**Table 1.** Data for the Lambda Physik StarLine laser.

| Wavelength (nm) | 1064 | 532 | 355 |
|---|---|---|---|
| Max. pulse energy (mJ) | 7.5 | 3.8 | 2.8 |
| Pulse duration FWHM (ns) | 12 | 12 | 12 |
| Focal diameter ($\mu$m) | 23 | 15 | ≈11 |
| Max. energy density (J/cm$^2$) | 1800 | 2150 | 2950 |
| Max. power density ($10^{11}$ W/cm$^2$) | 1.5 | 1.8 | 2.5 |



XIII International Symposium on Gas Flow and Chemical Lasers and High-Power Laser Conference,
Antonio Lapucci, Marco Ciofini, Editors, Proceedings of SPIE Vol. 4184 (2001)

## 3. SHADOWGRAPHY ON LASER-INDUCED SHOCK WAVES

Figure 2 shows the temporal evolution of the shock wave expansion for the three different processing wavelengths. The dark shadow to the left is caused by the $Si_3N_4$-target and the processing laser beam is incident perpendicularly from the right hand side. The shadowgraphs clearly show a strong dependence of the shock wave expansion on the wavelength. Whereas processing in the UV region leads to a shock front with primarily spherical symmetry, at 532 nm processing wavelength a bulge becomes visible at the tip of the shock front which is accelerated in a direction towards the incident laser beam. Changing from 532 nm to IR processing, the bulging increases even further leading to a strongly directional expansion similar to an LSD-wave with a noticeably higher velocity in the direction towards the incident Nd:YAG-laser beam while the laser pulse is present. The distinct shapes associated with the shock waves for each of the processing wavelengths show clearly that the shock fronts are driven by energy being released in different regions of the vapor/plasma plumes, thereby indicating absorption of the incoming laser beam in different regions of the plumes. The formation of the spherical base of the plumes for 355 nm and 532 nm wavelength must be driven by strong absorption near the target surface. On the other hand, the LSD-wave like bulge at the very tip of the shock waves is caused by an additional absorption region right behind the shock front traveling forward with the shock front as the plume expands and accelerating it even further. This interpretation is further confirmed by Fig. 3 displaying a strong growth of the LSD-wave shaped bulging at 532 nm-generated plumes with increasing power density or increasing energy deposition in the second absorption zone, respectively. Eventually after the end of the laser pulse (> 20 ns) the shock wave expansion for 1064 nm and 532 nm wavelength becomes more uniform in all directions (Fig. 2), similar to the case of 355 nm processing. With no further absorption taking place the energy deposited within the plumes leads to an increasingly isotropical expansion.

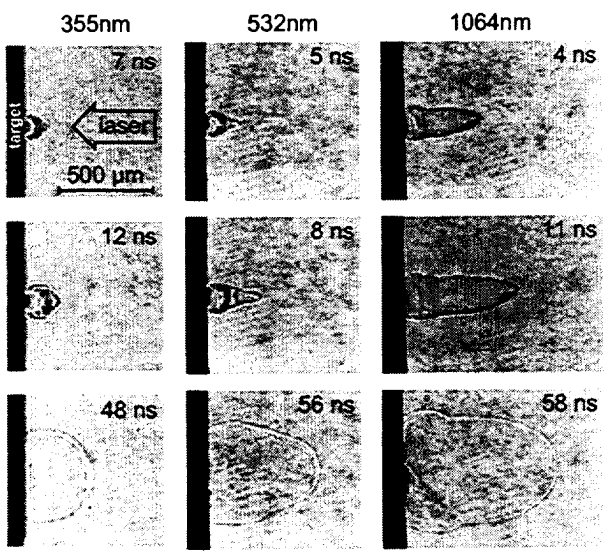


**Figure 2.** Shadowgraphs displaying the temporal evolution of shock wave expansion for three different processing wavelengths of a Nd:YAG-laser. Target material $Si_3N_4$; ambient gas: air, 0.1 MPa; 355 nm: 1.1 mJ/pulse, 1160 J/cm$^2$; 532 nm: 2.0 mJ/pulse, 1130 J/cm$^2$; 1064 nm: 5.0 mJ/pulse, 1200 J/cm$^2$.

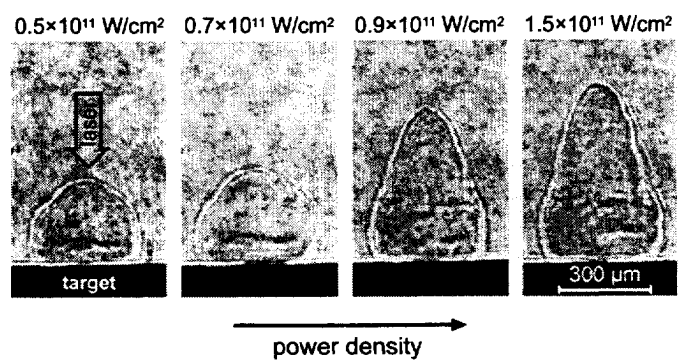


**Figure 3.** Power density dependence of shock front expansion at 532 nm wavelength about 30 ns after pulse beginning. Nd:YAG-laser on $Si_3N_4$ target; ambient gas: air, 0.1 MPa; 1.0 mJ/pulse, 570 J/cm$^2$; 1.5 mJ/pulse, 850 J/cm$^2$; 2.0 mJ/pulse, 1130 J/cm$^2$; 3.1 mJ/pulse, 1750 J/cm$^2$.

## 4. ANALYSIS OF SHOCK FRONT EXPANSION WITH ANALYTICAL MODELS

In order to determine the amount of absorption in the laser-induced vapor/plasma plumes associated with different processing wavelengths the axial distances traveled by the shock fronts have been studied. Hemispherical propagation of laser-induced shock waves has been found to agree excellently with the Sedov-theory[2] of gasdynamic blast wave expansion.[3]

On the other hand, LSD-waves have been studied originally for one-dimensional plane waves.[4] Based on a detailed model of two-dimensional LSD-wave propagation,[5] which is more suitable for many applications involving

tightly focused laser beams, an axial shock front velocity $c$ has been proposed[6] as an extrapolation of numerical simulations[7] which happened to amount to exactly half of the value obtained for the one-dimensional case.

Experimental data on the axial shock front expansion for the three different processing wavelengths is displayed in Fig. 4. As the morphology of the corresponding shadowgraphs in Fig. 2 suggests already, the pure blast wave and LSD-models are not applicable to describe the entire propagation of the shock waves. Nonetheless, an attempt to determine the energy deposited within the laser-induced plumes has been undertaken using the 2D-LSD model during the first 15–20 ns of the expansion and Sedov-theory for longer delay times. Thus, including the temporal pulse shape, the shock front distance $r$ becomes

$$r_{\mathrm{2D-LSD}}(t) = \int_0^t c_{\mathrm{2D-LSD}}(t')\,dt' = \frac{1}{2}\int_0^t \left[2(\gamma^2-1)\frac{I(t')}{\rho}\right]^{\frac{1}{3}} dt' \,, \quad t \le t_0 \,, \tag{1}$$

with $\gamma$ and $\rho$ denoting the adiabatic exponent and the density of the surrounding atmosphere (1.4 and $1.293\,\mathrm{kg\,m^{-3}}$ for air) and $I(t)$ being the (absorbed) power density of the laser irradiation. The latter is given by the absorbed energy density $H$ and the empirical laser pulse form function $f(t)$:

$$I(t) = H\,f(t)\,, \quad \int_0^\infty f(t)\,dt = 1\,, \quad f(t) = \left(\frac{t}{2.06938\,\mathrm{ps}}\right)^{2.5} \exp\left(-\frac{t}{3.2\,\mathrm{ns}}\right)\mathrm{s}^{-1}\,. \tag{2}$$

In order to ensure continuity for the traveled shock front distance for the expansion in the blast wave regime ($\gtrsim$15 ns) the formula derived by Sedov[2] has been adapted:

$$r_{\mathrm{Sedov}}(t) = \Lambda_0\left(\frac{E_0}{\rho}\right)^{\frac{1}{5}}\left(t^{\frac{2}{5}} - t_0^{\frac{2}{5}}\right) + r_{\mathrm{2D-LSD}}(t_0)\,, \quad t > t_0\,, \tag{3}$$

where $E_0$ is the energy contained within the shock wave and for hemispherical expansion in ambient air the dimension-free constant becomes $\Lambda_0 = 1.1863$.

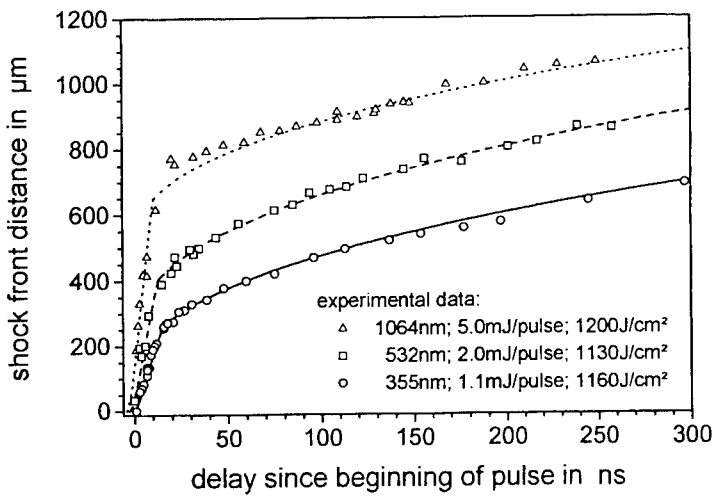


**Figure 4.** Axial shock front expansion for three different processing wavelengths of a Nd:YAG-laser. Target material $Si_3N_4$; ambient gas: air, 0.1 MPa. The experimental data has been analyzed by modified models of 2-dimensional LSD-wave propagation ($\lesssim$15 ns) and of gasdynamic blast wave expansion ($\gtrsim$15 ns).

Table 2 displays the values for the energy contained in the blast wave according to the Sedov-theory and the absorbed power density determined by the LSD-model. Since the respective energy transfer for LSD-wave and blast wave formation takes place at different locations as the morphologies of the shock waves reveal, the fractions of energy transferred into the plumes according to the two models have been added to determine the total fraction of energy deposited in the plumes. As could be expected according to common plasma absorption mechanisms, the energy deposition increases with increasing wavelength. Furthermore, in good agreement with the morphological analysis of the shock waves, for the UV-wavelength the major portion of the absorbed pulse energy is transferred into a blast wave of spherical symmetry and only a minor part into LSD-wave formation and the opposite is revealed for IR-processing. For the intermediate green wavelength the blast wave still dominates but a considerable amount of energy is already transferred via LSD-wave absorption.

**Table 2.** Energy deposition in the laser-induced shock waves.

| Processing wavelength (nm) | 1064 | 532 | 355 |
|---|---|---|---|
| Pulse energy $E_p$ [mJ] | 5.0 | 2.0 | 1.1 |
| Energy content of blast wave (Sedov) $E_0$ [mJ] | 0.5±0.3 | 1.1±0.4 | 0.6±0.2 |
| Energy density (laser focus) $H_f$ [J/cm$^2$] | 1200 | 1130 | 1160 |
| Modeled energy density (LSD) $H_f$ [J/cm$^2$] | 1000±400 | 200 (+300/-100) | 50 (+50/-20) |
| Fraction of energy contained | | | |
| – in blast wave $E_0/E_p$ [%] | 10±6 | 55±20 | 55±18 |
| – in LSD-wave $H/H_f$ [%] | 83±30 | 17±27 | 4±4 |
| – in total plume [%] | **93±31** | **72±34** | **59±19** |

## 5. PLASMA DIAGNOSTICS BY INTERFEROMETRY

The existence of distinct absorption regions in the vapor/plasma plumes has been confirmed by interferometric frames of the plumes that have been analyzed with respect to the refractive index and free electron density distributions.[8] Figure 5 displays electron density plots obtained shortly after the pulse maximum for the three processing wavelengths. The distributions clearly show that high electron densities are found where strong absorption was assumed according to the shock wave morphology. Figure 6 compares shadowgraphic frames for each of the processing wavelengths with schematics of the discontinuities found in the laser-induced shock waves. The outer discontinuity $US_1$ (according to the terminology[3,9]) can be identified as shock front separating the undisturbed atmosphere from a region of compressed atmospheric gas. This region is bounded by $US_2$ denoting the ionization front with rapidly increasing free electron densities towards the inside of the plume. Furthermore the schematics indicate the identified regions of absorption for each of the processing wavelengths.

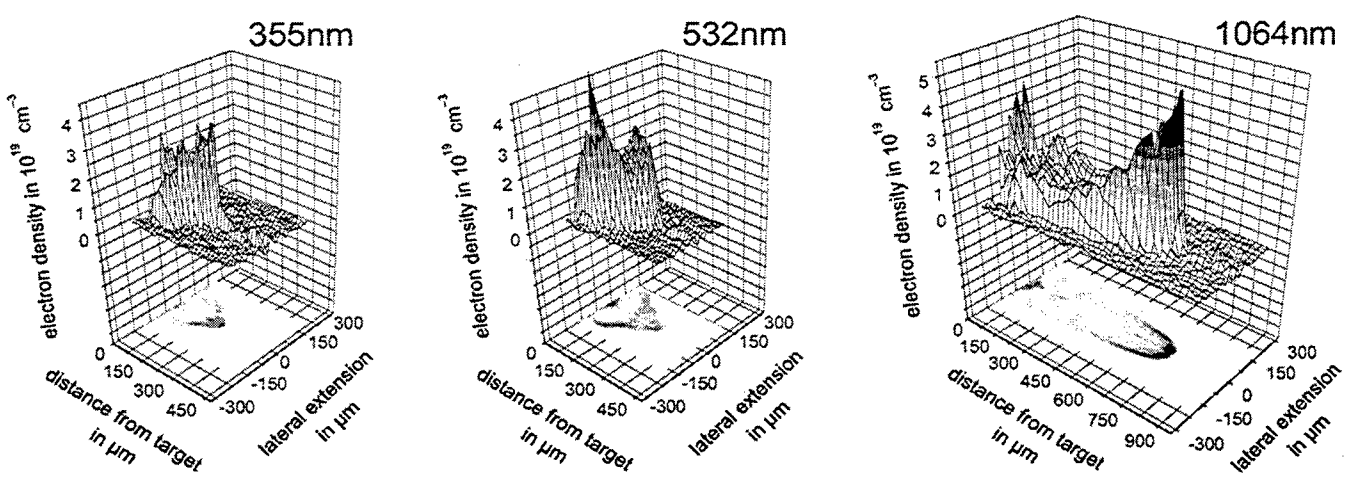


**Figure 5.** Wavelength dependence of the free electron density shortly after the pulse maximum (15 ns) for plasma plumes generated on a $Si_3N_4$ target at three different processing wavelengths. Ambient gas: air, 0.1 MPa; 355 nm: 1.1 mJ/pulse, 1160 J/cm$^2$; 532 nm: 2.0 mJ/pulse, 1130 J/cm$^2$; 1064 nm: 5.0 mJ/pulse, 1200 J/cm$^2$.

## 6. INTERACTION MECHANISMS

Based on the experimentally obtained values for the electron densities, absorption coefficients have been estimated[8] using simplified models of inverse bremsstrahlung (IB) and photoionization (PI) of excited states.[10] The results are displayed in Tab. 3 and the values indicate that both inverse bremsstrahlung and photoionization absorption increase dramatically with the wavelength. While IB exceeds PI at 1064 nm it decreases more significantly towards shorter wavelengths and PI can be assumed to be the dominant absorption mechanism at 532 nm. However, while the combined PI and IB absorption coefficients at 1064 nm and 532 nm account for more than 63 % or 50 %, respectively,

of the total absorption estimated from the energy contents of the plumes (which is a reasonable agreement considering the large margins of uncertainty associated with the data in Tab. 2), at 355 nm wavelength they are by far too low to explain the total absorption occuring in the UV-laser induced plume. Since extensive research on excimer-laser induced plasma plumes[9] suggests that Mie-absorption at small particles can play a dominant role in the UV range we have strong reason to believe that it accounts for a significant amount of absorption in 355 nm processing as well.

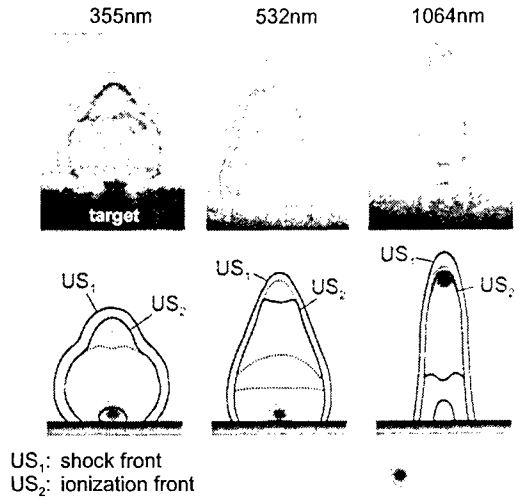


**Figure 6.** Discontinuities and absorption regions identified within laser-induced vapor/plasma plumes at each of the processing wavelengths.

**Table 3.** Modeled absorption coefficients for the main absorption regions at 15 ns after pulse beginning, and a comparison with total coefficients estimated from the energy content of the shock waves assuming an absorption layer of 200 $\mu$m. Qualification of main absorption mechanisms.

| Wavelength [nm] | 355 | 532 | 532 | 1064 |
|---|---|---|---|---|
| Main abs. region | near target | near target | tip of wave | tip of of wave |
| Electron density [$10^{19}$ cm$^{-3}$] | 2.0 | 3.5 | 2.2 | 4.5 |
| abs. coefficients: | | | | |
| $\alpha_{IB}$ [cm$^{-1}$] | 1.0 | 5.9 | 3.8 | 61.3 |
| $\alpha_{PI}$ [cm$^{-1}$] | 2.4 | 14.0 | 8.8 | 23.0 |
| estimated total abs. coeff. [cm$^{-1}$] | **45** | **64** | | **133** |
| Dominant abs. mechanism | Mie-abs. | PI Mie-abs. | PI IB | IB |

## 7. CONCLUSION

The investigations on Nd:YAG-laser induced vapor/plasmas reveal distinct plume morphologies for different processing wavelengths which can be interpreted in terms of dominant absorption regions. Analytical models of LSD- and blast wave expansion have been successfully applied to describe the shock wave propagation which allowed to calculate the total fraction of the pulse energy stored within the plumes. Interferometrically measured electron density distributions confirm the identified regions of absorption and allow to estimate IB and PI absorption coefficients. While there is reasonable agreement with the data for total absorption at the longer wavelengths, at 355 nm further mechanisms of absorption (such as Mie-absorption at particles) need to be considered.

## REFERENCES


1. T. Abeln, J. Radtke, and F. Dausinger, "High precision drilling with short-pulsed solid-state lasers," in *Proc. Laser Microfab. Conf. ICALEO '99*, P. Christensen, P. Herman, and R. Patel, eds., LIA **88**, pp. 195–203, 1999.
2. L. I. Sedov, *Similarity and Dimensional Methods in Mechanics*, Cleaver–Hume Press, London, 1959.
3. G. Callies, P. Berger, and H. Hügel, "Time-resolved observation of gas-dynamic discontinuities arising during excimer laser ablation and their interpretation," *J. Phys. D: Appl. Phys.* **28**, pp. 794–806, 1995.
4. Y. P. Raĭzer, "Heating of a gas by a powerful light pulse," *Sov. Phys. JETP* **21**(5), pp. 1009–1017, 1965.
5. A. N. Pirri, "Theory for momentum transfer to a surface ...," *Phys. Fluids* **16**(9), pp. 1435–1440, 1973.
6. C. Prat, T. Sarnet, M. Autric, and G. Inglesakis, "Dynamics of 248 nm-laser produced plasmas ...," in *Gas Flow and Chemical Lasers GCL '94*, W. L. Bohn and H. Hügel, eds., *Proc. SPIE* **2052**, pp. 701–705, 1995.
7. A. L. Edwards and J. A. Fleck, Jr., "Two-dimensional modeling ...," *J. Appl. Phys.* **50**(6), pp. 4307–4313, 1979.
8. D. Breitling, H. Schittenhelm, P. Berger, F. Dausinger, and H. Hügel, "Shadowgraphic and interferometric investigations on Nd:YAG laser-induced vapor/plasma plumes ...," *Appl. Phys. A* **69**, pp. S505–S508, 1999.
9. H. Schittenhelm, G. Callies, A. Straub, P. Berger, and H. Hügel, "Measurements of wavelength-dependent transmission in excimer laser-induced plasma plumes ...," *J. Phys. D: Appl. Phys.* **31**, pp. 418–427, 1998.
10. Y. B. Zel'dovich and Y. P. Raĭzer, *Physics of Shock Waves ...*, vol. 1, Academic Press, Inc., New York, 1966.

# Dynamics of laser-induced cracking in glasses at a picosecond time scale

A. Horn,[a*] R. Weichenhain,[a] E.W. Kreutz,[a] and R. Poprawe[a,b]

[a] Lehrstuhl für Lasertechnik, Rheinisch-Westfälische Technische Hochschule Aachen
[b] Fraunhofer-Institut für Lasertechnik
Steinbachstraße 15, D-52074 Aachen
Germany

## ABSTRACT

The interaction of picosecond pulsed laser radiation with BK7 glass has been investigated. Focusing laser pulses with 40 picosecond pulse duration in BK7 glass leads to plasma and crack formation by evaporation and induced stress. The plasma dynamics is measured by pump and probe techniques using the speckle method with a time resolution of 50 ps and a spatial resolution of 1 $\mu m$. Plasma transmission and refractive index changes are measured during and after irradiation on a picosecond time-scale. The plasma emission is investigated on the time scale of 10 ps - 500 ns by high-speed photography and by time-resolved spectroscopy. The morphology of the cracks is evaluated using Nomarski microscopy.

**Keywords:** microstructuring, glass, cracking, spectroscopy, ultrafast phenomena

## 1. INTRODUCTION

The interaction of laser radiation with dielectric materials has been investigated since the beginning of the laser era. Puzzling effects of optical breakdown, avalanche ionization, multiphoton ionization or laser-induced colour center formation claim research until now. Many reports about breakdown threshold measurements of different dielectric materials, especially glasses, have been performed in the last years.[1] Heat conduction in material depends on pulse duration of laser radiation. For pulse durations $\tau > 10$ ps the heat conduction is proportional to $\tau^{1/2}$. The deviation of the thermally driven $\tau^{1/2}$-rule for pulse durations $\tau < 10$ ps was found for dielectrics.[2] In order to understand the reaction of the material during and after irradiation with laser radiation pump and probe experiments have been performed.[3] By time resolved interferometry the time resolved phase shift and the absorption coefficient of MgO, $SiO_2$ and diamond have been measured using as pump pulse with $\tau = 120$ fs pulse duration.[4] These investigations were done in the time range from 100 fs to 6 ps. A positive phase shift results from an increase of the refractive index by the Kerr effect and a negative phase shift by the plasma formation. Time-resolved laser-induced plasma emission spectroscopy has been used largely.[5] A dependence of the emission spectra on the pulse number by colour center formation using time resolved optical spectroscopy of excimer laser induced plasmas in bulk has been shown.[6] This behaviour can be seen also when glasses are irradiated by high energy particles.[7]

Pump and probe experiments are performed in BK7 glass measuring plasma transmission and refractive index change during and after irradiation with laser radiation on a picosecond time-scale. The spatial-temporal evolution of the plasma is measured in order to show e.g. the formation of a plasma within the focal region. By high-speed photography the temporal and spatial evolution of the plasma intensity has been investigated and by time resolved spectroscopy of the plasma the decay time and spectral distribution of the emission has been measured. Plasma-induced cracks formed in BK7 glass are evaluated using Nomarski microscopy.

*Correspondence: Email: a_horn@llt.rwth-aachen.de; WWW: http://www.llt.rwth-aachen.de; Telephone: +49-241-8906-205; Fax: +49-241-8906-121

XIII International Symposium on Gas Flow and Chemical Lasers and High-Power Laser Conference,
Antonio Lapucci, Marco Ciofini, Editors, Proceedings of SPIE Vol. 4184 (2001)

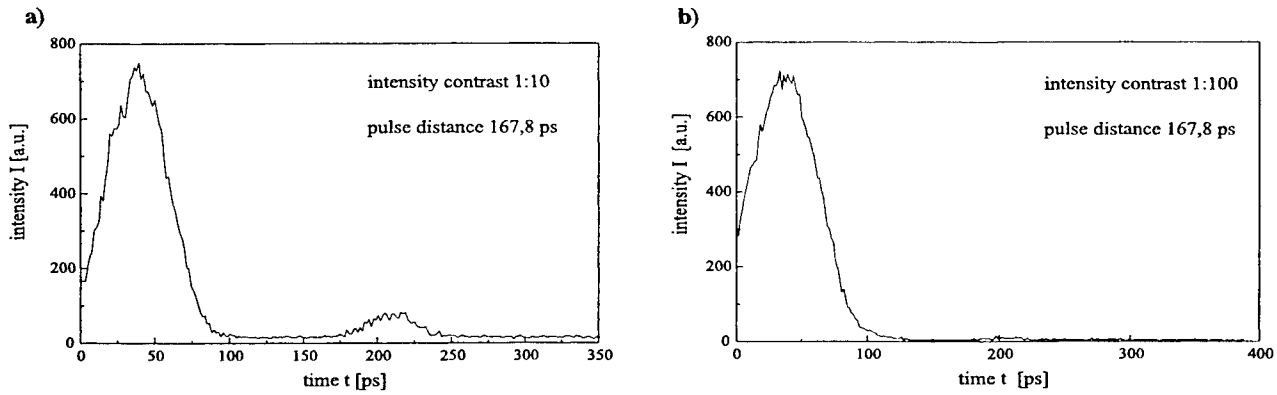


**Figure 1.** Autocorrelation (intensity versus time) for a) misaligned and b) aligned laser ($\lambda = 1064\,mm$, P $= 200\,mW$, $f_p = 500\,Hz$, $t_p = 40\ ps$).

## 2. EXPERIMENTAL SETUP

### 2.1. Laser

For all investigations a diode pumped, active mode locked and regenerative amplified Nd:YAG laser has been used as described elsewhere.[8] This laser system working as MOPA (Master-Oscillator Power Amplifier) has a repetition rate $f_p = 500$ Hz and a pulse duration $t_p = 40$ ps at $\lambda = 1064$ nm wavelength. Working with MOPA the laser system needs a precise control of the resonator length of seeder and amplifier. Differences in the resonator length of the laser can cause additional pre/post pulses. Machining with pre/post pulses can change the conditions of the material before the main pulse reaches the interaction region. The post pulses may interact with the material by absorption in the plasma formed from the interaction of main pulse with the material. Additionally a misaligned $\lambda/4$-voltage of the Pockels cell (PC) can cause pre/post pulses. By this misfit of the laser system pre/post pulses have a time delay of 167.8 ps to the main pulse. Using an autocorrelator with long measurement range this pre/post pulses can be measured (figure 1). This pulses have intensities up to 35 % of the main pulse possibly influencing the material properties. For example colour center, pre-ionization, shallow-trap or free electrons can be formed.[9] Well aligned Pockels cell and MOPA give a contrast ratio of pre/post pulses of 1:100 (figure 1). By aligning the MOPA and making the rising time of the Pockels cell as fast as possible changes the shutting time of the Pockels cell also. This gives rise to leaking pre/post pulses with a distance from the main pulse equal to the seeder repetition rate ($f_p = 120$ MHz). This pre/post pulses have a contrast ratio up to 1:25 to the main pulse and can influence irradiated material too. By an additional Pockels cell the intensities of the pre/post pulses can be reduced increasing the contrast ratio up to 1:100. The intensities of the pre/post pulses are for the investigations well below the plasma formation threshold intensity giving the possibility to investigate the interaction of the main pulse only with material.

### 2.2. Conversion efficiency of KTP

For pump and probe experiments the second harmonic (SH) of the laser beam (GH) is needed. The SH is generated by a KTP crystal (3mm x3mm x5mm) using the ground harmonic of the laser beam (beam diameter d= 1 mm, beam divergence $\Theta = 0.84$ mrad, beam quality $M^2$ =1.6). The pulse duration of GH and SH were measured with an autocorrelator. The dependence on the pulse duration of GH and SH is shown in figure 2. Because of saturation effects of the KTP crystal the pulse duration of SH increases with the pulse energy $E_p$ of GH linearly.[10] The conversion efficiency $P_p^{532}/P_p^{1064}$ is independent of the peak power of GH (figure 3).

### 2.3. Measurement tools

For pump and probe experiments the pulse duration of SH was set to $t_p = 40$ ps as for GH. The setup for pump and probe experiments uses a pump beam ($\lambda = 532$ nm) orthogonal oriented to the probe beam ($\lambda = 1064$ nm). The delay time between pump and probe pulse can be varied in the range 0-7 ns. Within the bulk material the pump beam is focused 200 $\mu m$ below the surface, whereas the probe beam was prepared by focusing it into a quartz glass fiber (diameter 600 $\mu m$, length 5 cm). The exit of the fiber was etched in order to get a rough surface. Doing so, the probe laser beam intensity at the exit is homogeneous distributed and has speckles with diameter about 1 $\mu m$.

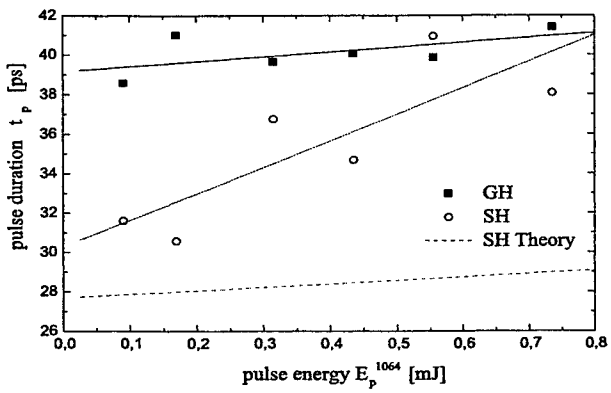


**Figure 2.** Pulse duration of GH and SH as function of pulse energy ($\lambda = 1064\,mm$, $f_p = 500\,Hz$).

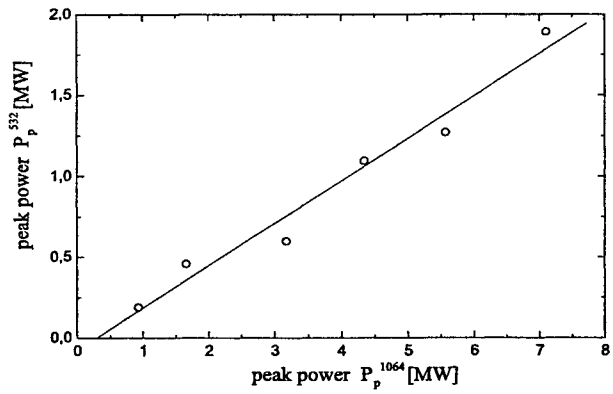


**Figure 3.** Peak power $P_p^{532}$ as function of peak power $P_p^{1064}$($\lambda = 1064\,mm$, $f_p = 500\,Hz$).

The probe beam is then focused tightly within the bulk material to 400 $\mu m$ diameter and monitored with a CCD camera (738x416 pixel). To separate pump and probe beam an interference filter with 1 nm FWHM was used. The probe pulse energy was $< 0.1\ \mu J$ getting intensities $< 2\ GW/cm^2$. By knife edge method a pump beam diameter of 7 $\mu m$ was measured.[11] A picture was taken by getting first one reference picture of the probe pulse without the pump pulse. A second picture, the measurement picture, was then taken with one pump pulse. One gets a final picture by dividing each pixel of the reference picture with the measured ones. In order to reduce noise two pictures were taken and averaged (figure 4). The transmission $T = \sum_i a_i^{ref} / \sum_i a_i^{meas}$ can be calculated by the fraction of the summarized pixel intensities $a_i^{ref}$ of the reference picture with the summarized pixel intensities $a_i^{meas}$ of the measurement picture.

The change in refractive index can be measured with speckles similar to interferometry pump and probe experiments. This can be achieved by calculating the displacement $D = \sum_i a_i^{ref} / a_i^{meas}$ of the speckles.

The spatial time-dependent evolution of the plasma intensity has been measured by high-speed photography in the streak mode operation (Imacon 500, Hadland Photonics). The used streak time was about 100 ns (time resolution 10 ps, spatial resolution 10 $\mu m$).

Time resolved spectroscopy was achieved by focusing the laser beam ($\lambda = 1064$ nm) within the bulk material. A spectrometer (S500I, Chromex ) with a 300 lines/mm graiting was used in the range from 200-650 nm with 1 nm resolution. The plasma intensity was detected by a ICC (4PICOS, Soliton) with a shutter time of 1 ns. Using a tungsten band lamp the spectrometer has been calibrated.

The morphology of the interaction region has been investigated by Nomarski-Differential-Interference-Contrast microscopy (Zeiss Axiophot). By this method changes of the refractive index in the interaction range by laser radiation can be made visible giving a 3 dimensional impression.

## 3. RESULTS AND DISCUSSION

### 3.1. Pump and Probe Experiments

The plasma is formed along the beam waist getting denser until 100 ps (figure 5). The corresponding falling time of transmission is about 50 ps in agreement with the electron-phonon relaxation time $\tau_{e-p} = 0.6$ fs.[3] After 2.5 ns the transmission T begins to increase slowly (figure 5).

The displacement D increases by the Kerr-effect as fast as the pump laser pulse (figure 5). The displacement drops down after 100 ps by plasma formation passing a minimum. After 1 ns the density of the plasma drops down and the displacement increases again getting positive and subsequently going down after passing a maximum. This change is due to a change of the refractive index caused by stress and densification within the interaction region. The displacement drops down again after 2 ns by relaxation of the glass via crack formation. Because of the formed cracks the displacement does not reach unity again.

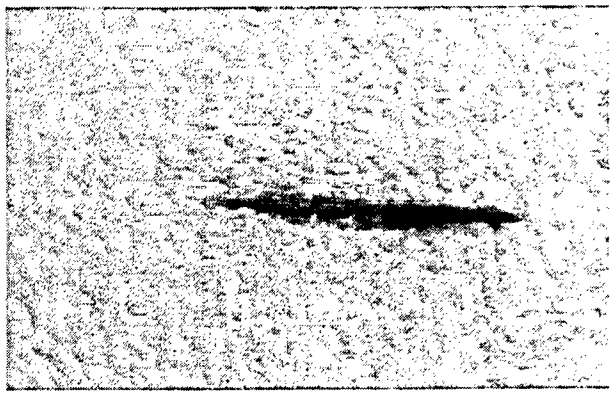

**Figure 4.** Plasma in BK7 ($\lambda = 532\,nm$, $I = 11{,}7$ TW/$cm^2$, delay time = 260 ps).

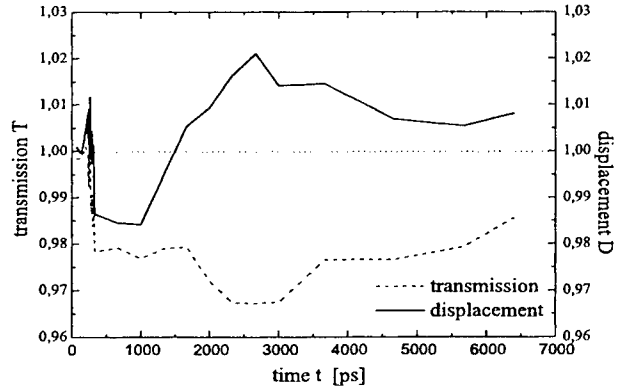


**Figure 5.** Transmission T and displacement D as function of time ($\lambda = 532\,nm$, $I = 11{,}6$ TW/$cm^2$).

### 3.2. High-speed photography

The spatially integrated intensity increases within 50 ps to a maximum decreasing then with a exponential behaviour (figure 6). The threshold intensity of plasma formation (figure 7) can be calculated by spatial and temporal integration of the plasma intensities. A linear dependence of the plasma intensity to the pulse intensity is found in agreement with investigations for metals and semiconductors.[12] The threshold intensity can be found to be $(66,7 \pm 0,1) GW/cm^2$. The plasma intensity decays exponentially. The decay time $\tau_d$ has a logarithmic behaviour with the pulse intensity (figure 8).

When the pulse intensities at the surfaces are above threshold for plasma formation a plasma can be detected at the bottom and the rear side of the material (thickness 1 mm) additionally to the plasma within the bulk material (figure 9).

### 3.3. Time resolved spectroscopy

Without delay time the plasma emission of BK7 glass shows for different pulse intensities a spectral continuum with peaks at 310 nm, 360 nm, 400 nm and at 600 nm (figure 10). With increasing delay time the intensity of the peaks decreases without changing their position. The peaks at 360 nm, 400 nm and 600 nm decrease faster in intensity than the peak at 310 nm. After a delay time t = 222 ns only the peak at 310 nm is detectable (inlet of figure 10).

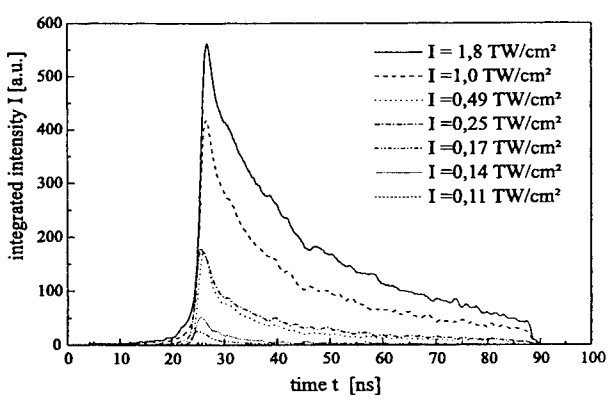


**Figure 6.** Spatially integrated plasma intensity as function of time and pulse intensity ($\lambda = 1064\,nm$, $t_p = 40$ ps).

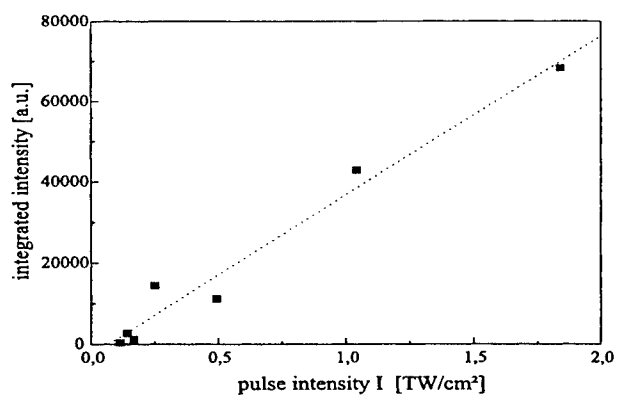


**Figure 7.** Spatially and temporally integrated plasma intensity as function of pulse intensity ($\lambda = 1064\,nm$, $t_p = 40$ ps).

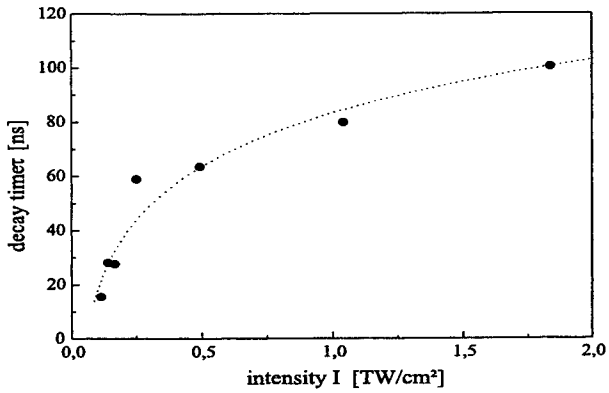


**Figure 8.** Decay time of spatially integrated plasma intensity as function of pulse intensity ($\lambda = 1064\,nm$, $t_p = 40$ ps).

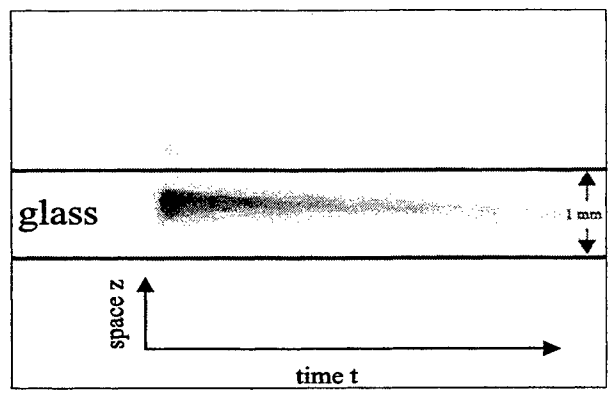


**Figure 9.** High-speed image of plasma emission in BK7 ($\lambda = 1064\,nm$, $t_p = 40$ ps).

### 3.4. Crack Morphology

The formed cracks and bubbles show a thickening towards the incident laser beam. The plasma formed initially absorbs the major part of the laser pulse energy (figure 11 a). Measurements by Nomarski microscopy show an abrupt change in refractive index seen as cauliflower structures with 200 $\mu m$ extension. Cracks and bubbles along the beam waist are visible, too. With decreasing intensity the size of the cracks becomes smaller (figure 11 b). Reducing the pulse intensity two separated cracks are formed. The crack averted to the incident laser beam is caused by self focusing (figure 11 c).

## 4. CONCLUSION

The temporal and spatial evolution of the plasma expansion during irradiation of BK7 glass with picosecond pulsed laser radiation have been investigated by speckle pump and probe experiments, high speed photography and time-resolved spectroscopy. The crack morphology has been photographed using Nomarski microscopy.

The plasma intensity, detected by high-speed photography in the streak mode operation, has a linear dependence on the pulse intensity. The threshold intensity for plasma formation has been measured to $(66,7 \pm 0,1) MW/cm^2$. The plasma decay time increases with pulse intensity. With pump and probe experiments the plasma transmission was found to drop down within 50 ps by absorption in the bulk plasma and to increase slowly in the ns time scale. The measured change in refractive index shows an initial increase by the Kerr-effect caused from the incident laser

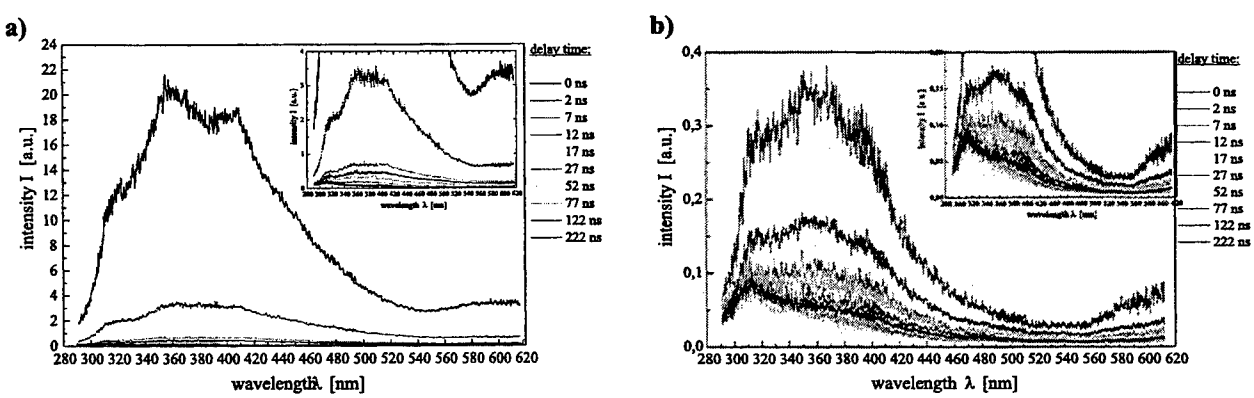


**Figure 10.** Spectral intensity for different delay times after irradiation a) I = 5,7 $TW/cm^2$ and b) I = 1,0 $TW/cm^2$($\lambda = 1064\,nm$, $t_p = 40$ ps).

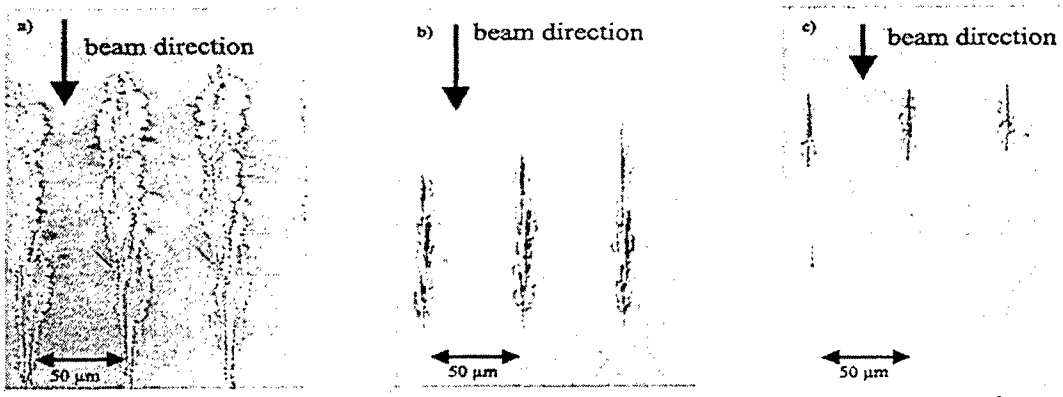


**Figure 11.** Cracks within BK7 glass at different pulse intensities a) I = 5,7 $TW/cm^2$, b) I = 1,9 $TW/cm^2$ and c) I = 1,0 $TW/cm^2$($\lambda = 1064\,nm$, I = 5,7 $TW/cm^2$, $t_p$ = 40 ps).

radiation followed by plasma formation with a decrease in the refractive index. The plasma-induced stresses cause cracking changing the refractive index to positive values. Within the interaction region a large spectral continuum peaking around 400 nm has been detected by time resolved spectroscopy. No emission lines of Si or O are observed. With increasing delay time the spectral intensity of the plasma drops down but the peak locations sustain at 400 nm. Emission via recombination and Bremsstrahlung are the underlying processes. For intensities above 2 $TW/cm^2$ additional cracks are formed by self-focusing of the laser pulse. Working with small pulse intensities yields symmetric cracks with 20 $\mu m$ extension.

## ACKNOWLEDGMENTS

The authors are grateful to Dipl.-Phys. P. Russbüldt for stimulating discussions and technical assistance.

## REFERENCES

1. R. Alfano and S. Shapiro, "Observation of self-phase modulation and small-scale filaments in crystals and glasses," *Phys. Rev. Lett.* **24**, pp. 592–594, 1970.
2. B. Stuart, M. Feit, S. Herman, M. Rubenchik, B. Shore, and M. Perry, "Nanosecond-to-femtosecond laser-induced breakdown in dielectrics," *Phys. Rev. B* **53**, pp. 1749–1761, 1996.
3. P. Martin, S. Guizard, P. Daguzan, G. Petite, P. D' Oliveira, P. Meynadier, and M. Perdrix, "Subpicosecond study of carrier trapping dynamics in wide-band-gap crystals," *Phys. Rev. B* **55**, pp. 5799–5810, 1997.
4. F. Quere, S. Guizard, M. Ph., G. Petite, O. Gobert, P. Meynadier, and M. Perdrix, "Subpicosecond studies of carrier dynamics in laser induced breakdown," *Proc. SPIE* **3578**, pp. 10–19, 1998.
5. K. Yoshida, N. Umemura, N. Kuzuu, H. Yoshida, T. Kamimura, and T. Sasaki, "Wavelength-dependence of laser-induced damage in fused silica and fused quartz," *Proc. SPIE* **3244**, pp. 164–175, 1998.
6. X. Mao, A. Fernandez, and R. Russo, "Behavior of laser induced emission intensity versus laser power density during breakdown of optical materials," *SPIE* **2428**, pp. 271–280, 1995.
7. E. Friebele and P. Higby, "Radiation effects in amorphous $SiO_2$ for windows an mirror substrates," *Damage in Laser Materials* **756**, pp. 122–132, 1997.
8. J. Jandeleit, P. Rußbüldt, G. Urbasch, D. Hoffmann, H.-G. Treusch, and E. Kreutz, "Investigation of laser-induced ablation processes and production of microstructures by picosecond laser pulses," *LIA* **81E**, pp. 83–91, 1996.
9. O. Efimov, K. Gäbel, S. Garnov, L. Glebov, S. Grantham, M. Richardson, and M. Soileau, "Color centers generation in silicate glasses exposed to ir femtosecond pulses," *JOSA B* **15**, pp. 193–199, 1998.
10. J. Diels and W. Rudolph, *Ultrashort Laser Pulse Phenomena*, Academic Press, San Diego, 1996.
11. Y. Suzaki and A. Tachibana, "Measurement of the $\mu$m sized radius of Gaussian laser beam using the scanning knife-edge," *Appl. Opt.* **14**, pp. 2809–2810, 1975.
12. F. Billmann, "Zeitaufgelöste Plasmauntersuchungen beim Festkörperabtrag mit Pikosekunden Laserpulsen," Master's thesis, RWTH-Aachen, 1996.

Invited Paper

# Fundamental aspects in the laser restoration of painted artworks

D. Anglos, A. Athanassiou, L. Antonnucci, E. Andreou, A. Bonarou, S. Georgiou, V. Tornari, V. Zafiropulos, C. Fotakis*

Institute of Electronic Structure and Laser, Foundation for Research and Technology-Hellas, P.O. Box 1527, 71110 Heraklion, Crete, Greece

## ABSTRACT

Chemical and mechanical modifications are expected to be the two major types of side effects in the UV laser ablation-based processing of strongly absorbing molecular substrates. For the systematic characterization of these effects, studies on model polymeric systems are presented. As far as photochemical effects are concerned, UV ablation is shown to promote chemical pathways over the ones observed in the sub-ablative regime. However, the extent of these effects can be limited by an optimal etching depth vs. effective optical penetration depth in substrates of high absorptivity. Concerning mechanical effects, UV ablation is similarly shown to result in structural defects that are not observed in the irradiation at low energy fluence values. In practice, these may be limited by the inhomogeneous and stratified structure of the substrates encountered in real-life applications. The applicability of the results to the implementations of UV laser ablation is exemplified using the procedures that have been defined in laser restoration of painted artworks as a study case. Besides their implications for laser material processing implementations, the present results indicate that UV ablation introduces new physical and chemical paradigms that are of scientific importance in their own right.

**Keywords:** UV ablation, molecular substrates, polymers, photochemistry, shock waves, restoration of artworks

## 1. INTRODUCTION

Ultraviolet ablation constitutes the basis of a number of diverse techniques aiming at the analysis and material processing of molecular substrates. These range from matrix-assisted laser desorption of biopolymers,[1] to the patterning of polymers[2] and removal of microparticles in microelectronic industry,[3] to photorefractive keratectomy in medicine.[4] By now, the potential of excimer laser ablation for the restoration of painted artworks has also been amply demonstrated.[5-6]

In all these applications, UV ablation offers the advantage of limited thermal "load" to the substrate. On the other hand, chemical and mechanical modifications would be expected to be significant. First, high intensity UV laser pulses are employed to irradiate molecular substrates (f.e. painted artworks) that include a wide variety of chromophores. Upon photoexcitation, several of the included chromophores dissociate into highly reactive fragments, which can subsequently react with nearby units and/or form oxidation products. Thus, photochemical modifications in the substrates would be expected to be extensive with detrimental effects on their integrity. Second, UV ablation has been shown[7] to result in the development of high amplitude stress waves within the irradiated materials. As the processed substrates tend to be mechanically rather fragile, they would be expected to suffer various mechanical deformations under the influence of these stress waves.

In practice, in each implementation, appropriate conditions can be found for the minimization of these side-effects. However, the previous discussion clearly illustrates that optimisation of the treatment parameters is critical for the success of the UV ablation-based processing schemes. The previous discussion also indicates that key elements of the phenomenon are still not fully understood. Elucidation of these factors is important in guiding the systematic optimisation of the present applications and the development of novel new ones. In an attempt to characterize these effects in a systematic way, studies on model polymeric systems appropriate for each type of effect are presented. Furthermore, for the photomechanical effects, a new approach of their characterization on the basis of holographic interferometric techniques is employed[8-9]. We show that for both types of effects, UV ablation results in modifications that deviate much from the ones observed at low fluences. However, for both types of effects, parameters can be defined

* corresponding author: e-mail: fotakis@iesl.forth.gr, tel: 0030-81-39/ 1315, 1318 fax

XIII International Symposium on Gas Flow and Chemical Lasers and High-Power Laser Conference, Antonio Lapucci, Marco Ciofini, Editors, Proceedings of SPIE Vol. 4184 (2001)

for their minimization. The importance of these findings for the implementations of UV ablation is illustrated using the procedures adapted in the laser restoration of painted artworks as a study case.

# 2. PHOTOCHEMICAL EFFECTS

## 2.1 Methodology

Our approach for modelling the photochemical effects of UV ablation relies on the use of simple, prototype photodissociable chromophores embedded within polymeric films. Various organic chromophores have been employed, with the work focussed on the halo-derivatives (bromo- and iodo-derivatives) of the aromatics naphthalene and phenanhthrene. Given the chemical simplicity and the well-known solution photochemistry of the dopants, their modifications can be monitored and elucidated in much greater detail than those that the polymer chromophores undergo.

Upon excitation, these derivatives undergo homolytic dissociation to aryl (naphthyl-Nap, and phenanhthrenyl-Phen-) and halogen radicals with near unity quantum yield in solution[10]. Thus, they constitute highly sensitive probes of the photochemical modifications induced by the laser irradiation. Furthermore, the aryl radicals that are formed by the photolysis of precursors form naphthalene-like (NapH) or phenanhthrene-like (PhenH) photoproducts, which are generally highly fluorescing. Thus, the chosen dopants offer the additional experimental advantage that their photoproducts can be conveniently probed via laser-induced fluorescence (LIF).

## 2.2 Experimental

The employed experimental procedures have been described in detail elsewhere [11-12]. Briefly, films (50-100 μm thick) of highly purified PMMA ($M_w$ ~120000) and polystyrene (PS) doped with the small chromophore are cast on quartz substrates. The films are irradiated (in air) with the perpendicularly focussed (≈6-10 $mm^2$) UV beam of an excimer laser at 193, 248 and 308 nm. Photoproduct fluorescence is induced by using the same beam configuration, but with the laser fluence attenuated to $F_{LASER} \leq 5$ $mJ/cm^2$. A relatively long delay (≥ 1min) between the pump and probe pulses is employed for ensuring nearly quantitative reaction of the photoproduced radicals and formation of stable photoproducts The induced emission is collected by an optical fiber and spectrally analyzed in a 0.2 m grating spectrograph, interfaced to an optical multichannel analyser (OMA III system, EG&G PARC Model 1406)

## 2.3 Results and Discussion

The spectrally resolved probe spectra recorded after irradiation of the NapX (X=Br, I)-doped PMMA (1.2% wt) with a single pump laser pulse at 248 nm is shown in Fig. 1. At low laser fluences, the spectra, at least for low dopant concentrations (≤2 % wt), are seen to be dominated by the NapH-type $^1B_{3u} \rightarrow {}^1A_{1g}$ emission at 320-340 nm (Fig. 1(A))[13]. Since the precursors NapX are characterized by negligible fluorescence[10], the observation of this emission band demonstrates the exclusive formation of NapH-like photoproducts at these fluences. In sharp contrast, the spectra recorded after irradiation of NapX/PMMA samples (of ≥ 1%wt concentration) above the threshold are (Fig. 1(B)) much broader and exhibit distinct peaks at ≈440 nm and ≈470 nm. Such broadening is not observed in the irradiation of NapH-doped films. Consequently, these features represent products that are characteristic of the NapX (X=I, Br) reactivity. On the basis of solution examination, these can be ascribed to $Nap_2$, emitting in the 320-400 nm range, and $Nap_2X$ products, where X is some polymer fragment/chain. As discussed in detail elsewhere, the formation of $Nap_2$-type products demonstrates that radical mobility is highly enhanced in UV ablation with nanosecond pulses. Preliminary spectral examination indicates that $Nap_2$-type product formation is observed at all examined wavelengths (193 nm, 248 nm and 308 nm), although its relative intensity versus the NapH-photoproduct emission appears to differ.

For the purposes of our present study, much more important are the implications of the quantitative characterization of the photoinduced effects. To this end, Fig. 2 depicts the fluence dependence of the NapH-like photoproduct fluorescence following a single pump pulse on virgin polymer. This intensity reflects essentially the amount of the fluorescing naphthyl species that remains in the substrate after irradiation. Interestingly, aside for quantitative differences, two general types of dependences are observed. At 248 nm and 308 nm, the linear increase of the photoproduct yield at low laser fluences is followed by a sharp rise above the threshold (Fig. 2 (A)). In contrast, in the irradiation at 193 nm, the yield is found to reach a limiting value near the threshold (Fig. 2(B)).

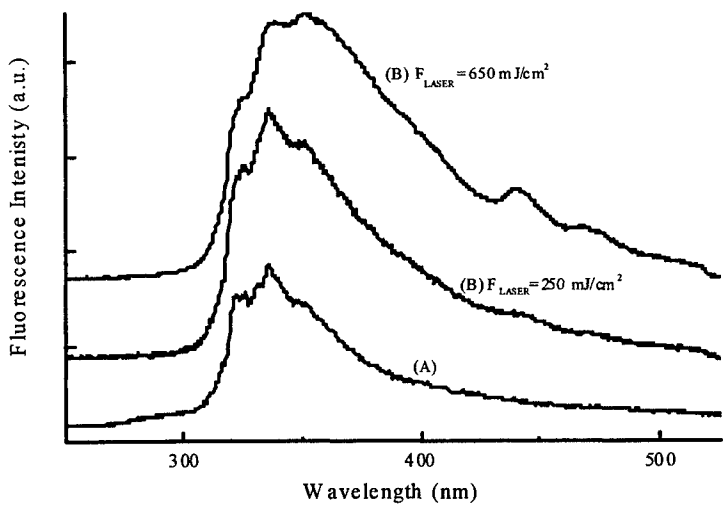


*Fig. 1 Spectrally-resolved probe fluorescence spectra recorded following irradiation of NapX/PMMA*

Since the spectral examination does not indicate any major qualitative differences between the three wavelengths, the difference in the $F_{LASER}$-dependence must relate mainly to the much higher absorptivity of PMMA at 193 nm (≈2000 $cm^{-1}$) vs. that at the other two wavelengths (≤300 $cm^{-1}$) [14]. To demonstrate this, similar experiments with polystyrene doped with iodo-phenanthrene (so that dopant emission is not swamped by the strong polymer emission) were undertaken. In this case, curve (B) is observed for the PhenH-type photoproduct in the irradiation at 193 nm and 248 nm, whereas the dependence at 308 nm is described by curve (A). The absorption coefficient of PS decreases much from 193 nm to 308 nm.[15] Thus, for both polymers, there appear to be a close correlation between the absorption coefficient and the $F_{LASER}$-dependence of the photoproduct yield. This dependence can be understood by the fact that the absorption coefficient determines the relative ratio of etching depth vs. optical penetration depth and thus the depth over which any photoproducts formed with increasing laser fluence remain in the substrate.

There are two major and significant mechanistic implications of the previous results. First, the observation of $Nap_2$-type product formation demonstrates that new photochemical pathways are promoted in the ablative regime. This aspect is discussed in greater detail elsewhere. Second, as far as photochemical modifications are concerned, no qualitative difference between the various UV wavelengths is observed, with the changes being limited to quantitative ones. The main determinant for these quantitative differences is indicated to be the value of the absorption coefficient at the irradiation wavelength.

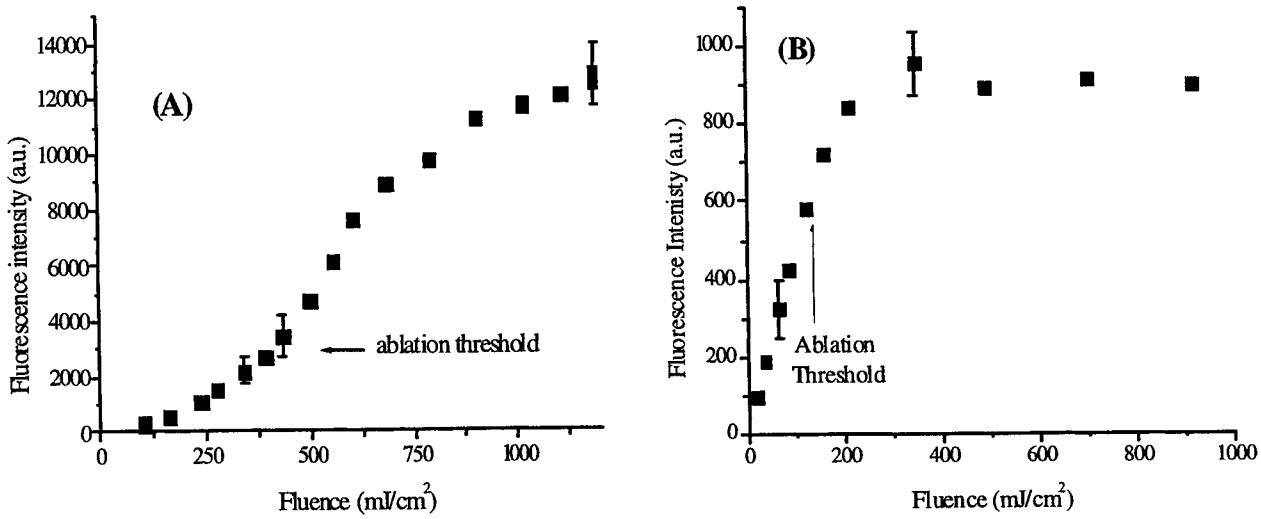


*Fig. 2 $F_{LASER}$-dependence of the fluorescence intensity of the NapH-like photoproduct that remains in the substrate following irradiation of NapI/PMMA (0.4% wt) at: (A) 248 nm and (B) 193 nm.*

Concerning the various implementations of UV ablation, the previous conclusion indicates that a key factor for their success relates to the high absorptivity of the processed molecular substrates. This is for example the case in the laser-restoration of painted artworks. In this application, irradiation with excimer laser pulses is employed to effect removal of the outer degraded layers of varnish.. Varnish is a mixture of strongly UV-absorbing organic substances and is applied on the top of the paintings for aesthetic and protective purposes. However, with time it undergoes photooxidation at its outer layers, with detrimental effects in the appearance and even for the integrity of the painting. The high absorptivity ($\varepsilon \approx 10^5$ $cm^{-1}$) of varnish ensures, on one hand, that excimer laser irradiation effects efficient etching and material removal, and on the other, that photochemical effects are localized within $d < 1\text{-}5$ μm, at most, from the surface. To this end, a thin layer (5 -10 μm) of varnish is left on the painting, thereby ensuring negligible effects on the pigments in the underlying painting medium.

For modelling this procedure, experiments have been performed on polymer bilayer systems in which the NapI/PMMA film is covered by a PMMA film of varying thickness. The existence of the overlayer is indeed found to result in a significant reduction of the photoproduct formation in the underlying layer. Interestingly, the reduction (i.e., the extent of the "photochemical protection") is higher than that expected on the basis of the (linear) absorption coefficient of PMMA. At present, it has not been possible to establish the exact factor responsible for this effect. One possibility includes the operation of multiphoton processes that decrease substantially the transmitted light from that expected on the basis of linear absorption coefficient. Independently of the exact factors, the results illustrate the subtlety of the factors that may be operative in the UV ablation and which may be critical for the optimisation of the various implementations of the phenomenon.

## 3. PHOTOMECHANICAL EFFECTS

### 3.1 Experimental

For the characterization of the mechanical effects of UV laser ablation, the experimental set-up was designed to enable the parallel irradiation of the polymer substrates and the recording of the holographic interferograms. The set-up includes an excimer laser (Lambda Physik model LPX210) emitting at 248 or at 193 nm for the irradiation of polymer samples and a TEM00 laser for the recording of holograms. The holographic setup is aligned in an off-axis two-beam geometry for phase media[16]. Two consequent exposures of the polymers were made on the same hologram plate before and after irradiation of the sample with a certain number of excimer laser pulses. Refractive index and/or transmittance changes between successive exposures of the polymer result in phase and/or intensity changes generating optical path differences recorded in the interferogram.

### 3.2 Results

A double exposure holographic interferogram recorded in the UV laser ablation of polymer films (PMMA and PS of 50-100 μm thickness) cast on a suprasil window is illustrated in Figure 3. The photograph is the interferogram between the reference hologram of the polymer target before irradiation and the hologram recorded after irradiation with 15 excimer laser pulse. The figure clearly shows that defects are developed at various distances from the irradiated spot. Most interestingly, formation of structural defects is observed far from the ablation spot, even close to the edges of the substrate (d=50 mm). In sharp contrast, no such changes are detected in the irradiation of samples with the same number of pulses at fluences below the threshold. Thus, the development of these modifications relates directly to the UV ablation process. It appears that the stress waves generated by the process can propagate all over the sample with an energy high enough to create defects.

With continuing irradiation, the deformations are observed to grow and additional ones are formed. A quantitative assessment of the evolution of the defects with number of successive laser pulses is illustrated in figure 4. Initially, a gradual increase in the deformed area is observed, indicating an accumulative effect of the stresses developed in each laser pulse. However, in many cases, after extensive irradiation (100-150 pulses) a sudden increase is observed. This observation may indicate that repeated laser irradiation results in extreme mechanical "fatigue" of the substrate, with an irreversible change in its response to any subsequent strains.

Concerning the morphology of the deformations, two main types can be distinguished, namely dendrites and "dot"-like (i.e. circular structures of small diameter) structures. These are discrete features that must correspond to different structural deformations. Tentatively, the dendrite structure is ascribed to local fracture/slippage, while the isles are more indicative of local delaminations. Preliminary examination by scanning electron microscopy supports this assignment.

The morphology and extent of the induced defects has been found to depend sensitively on a number of parameters such as on the nature of the polymer, its molecular weight, etc. However, even for a given polymer, the morphology and the extent of the defects depend sensitively on the mode of preparation of the film and in particular on the degree of annealing. Generally, for polymer films irradiated shortly after preparation, the deformations were observed to be mainly of the "isle" type, whereas dendrites is the predominant form of defect in the irradiation of well-annealed films. It is reasonable to suggest that the degree of film annealing affects its adhesion strength to the quartz substrate and as a result, the lowest-energy deformations that can be induced. Thus, even for these simple polymeric systems, the induced mechanical deformations depend sensitively on a number of parameters. This indicates the importance of careful optimisation of irradiation parameters in the implementations of UV laser processing of molecular substrates.

For stratified media, propagation of stress waves between the different layers depends on the relative acoustic impedances of the two media. Furthermore, in real-life substrates, attenuation of the propagating stress waves will also depend on the structural inhomogeneities that are present in each medium. The presence of such pre-existing defects can severely limit the propagation of the induced waves to the sublayers, thereby limiting the extent of inadvertent effects to the substrates. Indeed, in experiments on bilayer polymer films, we have observed defect formation in the lower layer to depend on the degree of adhesion between the two layers. Extending these observations to the laser-based restoration of artworks, the presence of several layers of widely different acoustical impedances and properties may be eventually crucial for the success of the technique.

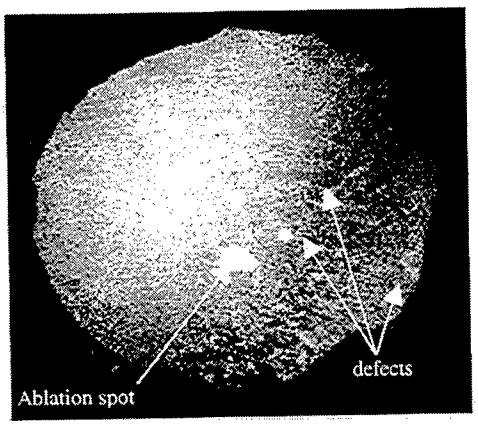


*Fig.3. D.E holographic interferogram of a polymer sample after 15 pulses, arrows shown defect formation in respect to the ablation spot*

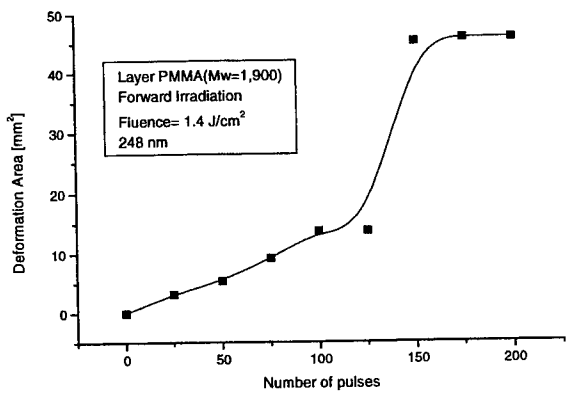


Fig.4. *Deformation area (dot-morphology) in the irradiation of PMMA (Mw=1,900) film on quartz 248 nm.*

## 4. CONTROLLED LASER CLEANING OF ARTWORKS

In a laser cleaning workstation, a holographic interferometric system is adapted for evaluating the structural sate of the artwork. The layers removed during a cleaning application may be aged varnish in the case of paintings, dark encrustation on sculptures or even environmental attack on calcite reliefs[17]. The study of interferograms before laser treatment reveals, amongst other things, the irregular detachments of these surface layers from the underlying layers that have to be conserved. After each laser cleaning trial, the post-evaluation by holographic interferometry guides the laser cleaning operation[18] by monitoring the remaining detachments and verifying the proper removal of the unwanted layers.

Laser induced breakdown spectroscopy is used to control the extent of laser ablation[19]. To provide on-line control during the laser cleaning process, LIBS spectral data is continuously recorded within a pre-selected spectral range. This pre-selection is based on the results of a preliminary study, prerequisite at the beginning of each project. The data acquisition processor is programmed to calculate certain peak intensity ratios, which are subsequently used to compute the value of an algorithm designed for each specific case. When this value is not found within certain boundaries, the laser stops firing and the motorized X-Y stage moves the artwork to a new position with respect to the laser beam. The cleaning process is again initiated. At this new position, laser pulses are delivered until the same threshold condition is attained and the process continues similarly thereafter. The distance that the sample is moved in every step is determined by an overlapping protocol for the sequential sample movement in both X and Y directions. This parameter is introduced in the computer program and is directly dependent on the laser parameters and the experimental arrangement. Therefore, the LIBS algorithm, the overlapping parameters, the energy fluence, the pulse

repetition rate and the laser wavelength are all crucial for an optimized cleaning process. Their careful selection and optimization is assumed.

## 5. CONCLUSIONS

In conclusion, the interaction of high intensity UV laser pulses with molecular substrates can result in significant chemical and mechanical modifications. The nature and the extent of these modifications/effects cannot be anticipated on the basis of the ones observed at low laser fluences. Thus, essentially UV ablation introduces new physical and chemical paradigms. Besides their scientific importance, these paradigms are important in any implementation of UV laser processing of molecular substrates. As shown, irradiation conditions can be defined under which potentially damaging side effects to the substrate are minimal or at least inconsequential. Herein, we have exemplified the applicability of these concepts in reference with the laser restoration of painted artworks.

The application of modern laser technology in the field of art-conservation is providing exciting possibilities and new prospects both in the context of unwanted surface layer removal as well as diagnostic methods. The successful cleaning of various types of artworks is dependent on the appropriate choice of laser cleaning parameters and on-line monitoring techniques.

## ACKNOWLEDGEMENTS

The work was supported by the Large Installations Plan DGXII (Project G/89100086/GEP) and by the TMR Programme (No. ERB FMRX-CT98-0188).

## REFERENCES

1. F. Hillenkamp, M. Karas, R. C. Beavis and B. T. Chait, "Matrix-Assisted Laser Desorption/Ionization Mass Spectrometry", *Anal. Chem.*, **63**, 1193A-1202A, 1991.
2. I. A. Boyd (Ed.): *Photochemical Processing of Electronic Materials*, Academic Press, London 1992.
3. J. C. Miller (Ed.): *Laser Ablation. Principles and Applications*, Springer Ser. Mater. Sci. **28**, Springer-Verlag , Berlin 1994.
4. P. Homolka, R. Biowski, S. Haminski, T. Barisani, W. Husinsky, H. Bergmann, and G. Grabner, *Phys. Med. Biol.*, **44**, 1169-1180, 1999 and references therein.
5. V. Zafiropulos, C. Fotakis, "Lasers in the Conservation of Painted Artworks" (chapter 6), M. Cooper (Ed.): *Laser Cleaning in Conservation: an Introduction,* Butterworth Heinemann, Oxford 1998.
6. S. Georgiou, V. Zafiropulos, D. Anglos, C. Balas, V. Tornari, C. Fotakis "Excimer laser restoration of painted artworks: procedures, mechanisms and effects", *Appl. Surf. Sci.* **127-129**, 738 -745, 1998
7. D. D. Dlott, S. Hambir, and J. Franken, "The new wave in shock waves", *J. Phys. Chem. B*, **102**, 2121-2130, 1998.
8. V. Tornari, D. Fantidou, V. Zafiropulos, N. A. Vainos, and C. Fotakis "Photomechanical effects of laser cleaning: a long-term non-destructive holographic interferometric investigation on painted artworks", SPIE vol. 3411, pp.420-430, (1998)
9. V. Tornari, V. Zafiropulos, D. Fantidou, N. A. Vainos and C. Fotakis. "Discrimination of photomechanical effects after laser cleaning of artworks by means of holographic interferometry" in *Optics and Lasers in Biomedicine and Culture – Series of the International Society on Optics Within Life Sciences - Vol. V*, Series Ed. G. von Bally, Springer-Verlag, Berlin, 2000, pp. 208-212
10. E. Haselbach, Y. Rohner, P. Suppan, *Helv. Chim. Acta* **73**, 1644, 1990.
11. M. Lassithiotaki, A. Athanassiou, D. Anglos, S. Georgiou, and C. Fotakis, *Appl. Phys. A* **69**, 363, 1999.
12. A. Athanassiou, E. Andreou, D. Anglos, S. Georgiou, , C. Fotakis, manuscript in preparation
13. J. B. Birks: *Photophysics of Aromatic Molecules*, (John Wiley & Sons, London, 1970) p. 232
14. R. Srinivasan, B. Braren, D. E. Seeger and R. W. Dreyfus, *Macromolecules*, **19**, 916-921, 1986.
15. J. F. Rabek, *"Mechanisms of photophysical processes and photochemical reactions in polymers",* John Wiley, Great Britain, 1987
16. C. H. Vest, *"Holographic Interferometry"* 1971, Academic Press
17. Maravelaki P.V., Zafiropulos V., Kylikoglou V., Kalaitzaki M., and C. Fotakis, "Laser induced breakdown spectroscopy as a diagnostic technique for the laser cleaning of marble", Spectrochimica Acta B, **52,** 41-53 (1997).
18. V. Tornari, A. Bonarou, V. Zafiropulos, and C. Fotakis, "Holographic Applications in evaluation of Defect and Cleaning Procedures", LACONA III, *3rd International Conference on Lasers in Art Conservation-April 1999,* J. Cult. Heritage, Elsevier, 2000.
19. Zafiropulos V. and Fotakis C., "Lasers in the Conservation of Painted Artworks", *Laser Cleaning in Conservation: an Introduction*, M. Cooper ed. 79-90 (Butterworth Heinemann, Oxford, 1998) Chap. 6.

# High quality cleaning in conservation of cultural heritage by optimized Nd:YAG laser induced ablative effects

R. Salimbeni, R. Pini, S. Siano
Istituto di Elettronica Quantistica-CNR, Florence, Italy

**Abstract**

The achievement of high quality cleaning of encrusted stone and metals manufacts by optimised laser ablation processes was demonstrated for several deterioration typologies. Here we present some representative cases were intermediate pulse duration Nd:YAG lasers we developed allowed to achieve specific restoration goals.

## 1. Introduction

Laser cleaning applications in the conservation of cultural heritage have shown in recent years an increasing interest by the conservation community. Important laser restoration studies and interventions [1-4] pointed out the necessity of appropriate laser technologies and methodologies in order to achieve selective removal of deterioration layers which affect the conservation of the manufact and its aesthetic value. For stones and metals, this problem is in a more advanced level of investigation, since several physical optimisation studies have demonstrated excellent results based on suitable laser parameters. These studies put in evidence a favourable use of Nd:YAG lasers as the optimum choice for its optical and practical characteristics for a large variety of restoration problems. Nevertheless typical operating regimes may intrinsically induce undesired photothermal and photomechanical effects [5-6]. To avoid these side effects we have devised and developed intermediate pulse duration Nd:YAG laser systems, between Q-Switching and Free Running pulse-widths, devoted to cleaning applications of different materials and deterioration typologies. Non standard operating regimes beside specific intervention methodologies provided restoration goals not allowed by conventional techniques as well as by common Nd:YAG lasers.

Tasks and strategy of the restoration intervention are defined for each specific case through the characterisation of the conservation state of the manufact. Various conventional diagnostic techniques are employed in this investigation phase, which belong to the standard approaches for the characterisation of the materials under investigation. In particular for stones and metals, petrographic, mineralogical and metallographic studies allow a detailed description of the deterioration features. That allows defining the main objectives of the cleaning intervention and further conservation treatments such as for consolidation and protection.

Before the demonstration of the capability of the laser techniques, optimum cleaning results with low invasivity methods were achieved just in case of simple stratigraphies or where the deterioration was not so advanced. Whereas for example the controlled removal or the safeguard of mineral films arising from ancient treatments was often impossible. Thus, chemical cleaning, microsandblasting and other conventional approaches typically involve compromises that are hard to be accepted in view of the detailed characterisation provided by diagnostic analysis.

For stones and metals, the proper choice of the laser source and the optimisation of the laser ablation regime can provide the achievement of the optimum cleaning goal in a large variety of cases. Here we report the concept of high quality laser cleaning to fine discrimination in the removal of layers and/or sub-layers within the encrustation, as well as to the finishing of the exposed surface in terms of "readability", surface parameters, colour and other measurable properties.

In the present paper we discuss briefly some examples of cleaning problems for stones and archaeological metals that were encountered during important restoration interventions.

## 2. Intermediate pulse duration Nd:YAG lasers

On the basis of the laser ablation modeling that was developed along the last two decades, and many experimental investigation on cases of interest for the conservative restoration we retained intermediate pulse-widths, in the range 100-10 μs, very interesting for the precise material removal. This pulse duration range can realize a good compromise between very explosive material removal associated with irradiation by a few nanoseconds pulse duration and too slow vaporization regimes generated by hundred of microseconds pulses. The lack of commercial sources in the cited pulse range, led us to develop Nd:YAG laser system prototypes based on Short Free Running (SFR) and a Long Q-Switching (LQS) regimes. In

XIII International Symposium on Gas Flow and Chemical Lasers and High-Power Laser Conference,
Antonio Lapucci, Marco Ciofini, Editors, Proceedings of SPIE Vol. 4184 (2001)

the first case, a pulse duration of 20 μs was achieved by shortening the pumping pulse of the flashlamp driver, while a 40 ns was achieved by increasing the switching time of the Q-Switching electro-optical device.

## 3. Application cases

After the optimisation of the intervention methodologies on a large variety of standardised and original samples, the laser cleaning approach was applied on important manufacts. Thus, cleaning trials of large areas aimed at achieving specific cleaning goals were performed on monuments and statues in Florence, Siena and Ravenna. Furthermore we performed the laser cleaning of about 30 archaeological metal findings from Tuscany excavation sites. Some of the restoration problem we investigated are reported in the following.

### 3.1 *Santa Maria del Fiore* (cathedral of Florence)

The façade of Florence cathedral, completed in the XVIII century, is in a very advanced state of deterioration because of the high pollution of the downtown environment. In particular, extended sulphation phenomena involve the Carrara marble columns, which call for urgent controlled cleaning, consolidation, and protection interventions.

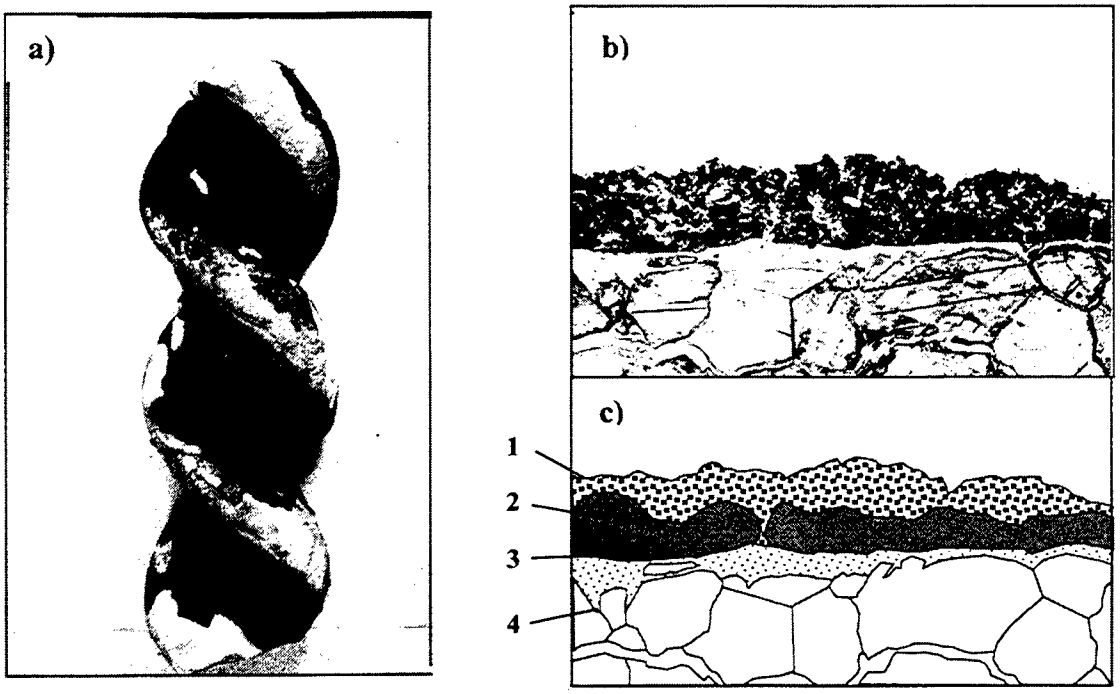


Fig. 1. a) Column sample from Santa Maria del Fiore, Florence. b) Stratigraphy of the deterioration horizon observed by an ultrathin section. c) Descriptive scheme: 1) black crust, 2) sulfated Ca-oxalates film, 3) surface pseudomorphic sulphation layer i.e. reproducing the shape of the original surface, 4) calcite crystals with intergranular decohesion.

Figure 1 shows one of the samples employed to test different cleaning approach and its typical stratigraphy. Because of the high sulphation and darkness of the Ca-oxalates film in this case the restoration task was the complete removal of the film, without damage the fragile surface pseudomorphic gypsum, that represents the "memory" of the original sculptured surface. Ammonium carbonate poultices, microsandblasting and laser ablation were compared in order to achieve this restoration goal.

### 3.2 *Mausoleo di Teodorico*

During the cleaning operations of the Mausoleo di Teodorico in Ravenna, built with biocalcarenite (*Pietra di Aurisina*), some problems were encountered in the cleaning of the sculptured monolithic dome. It presented a hard and thick encrustation (up to 1 mm) over a coherent and not sulphated brown Ca-oxalates film (100 μm). The optimum cleaning result in this case, was the removal of the black crust and the thinning of the Ca-oxalate film up to achieve a clear "readability" of the denticulate decoration. The laser ablation approach was suggested after not satisfactory cleaning trials by EDTA

chemical poultices and microsandblasting. Actually, these methods do not allowed the controlled removal required and they also showed low effectiveness, probably because of previous consolidation treatments performed in the past.

### 3.3 *Palazzo Rucellai*

The façade of Palazzo Rucellai was built in XV century with a Florentine calcareous matrix sandstone (*Pietra Forte*). Present chemical cleaning with ammonium carbonate poultices was unable to clean the capitals and other sculptured elements because of the small gypsum content. These elements presented a thick (several hundred microns) and dark Ca-oxalates film, originated by ancient treatments with linseed oil. Laser ablation, EDTA poultices, and microsandblasting were compared in order to thin the Ca-oxalates films up to achieve a clear readability of the sculptures without the complete removal of the *patina* layer for esthetical purposes similarly to the previous case.

### 3.4 Archaeological metal findings

The laser cleaning of a collection of small archaeological metal findings, including bronze, iron and silver objects coming from Tuscany excavation sites was also investigated. After the preliminar analyses of substrate and encrustation materials by conventional diagnostics, different cleaning tasks were defined. For example, for the typical encrustation stratigraphy of bronze manufacts the cleaning action should be stopped at the copper oxide layer which typically represent the trace of the original surface.

## 4. Results

The SFR Nd:YAG laser allowed to achieve the cleaning goals for all the three cases of stones cited above with a final quality significantly higher with respect to classical cleaning approaches and standard Nd:YAG lasers. Figure 2 shows details of the ultra-thin section at a cleaning transition on the column sample from Santa Maria del Fiore façade. As it can be observed, the sulphated Ca-oxalates film was finely removed while the underlying pseudomorphic sulphation was safeguarded, according to the restoration aim. This result was achieved in water-assisted conditions at operative fluences of 2-4.5 J/cm$^2$ and a pulse frequency rate of 10 Hz.

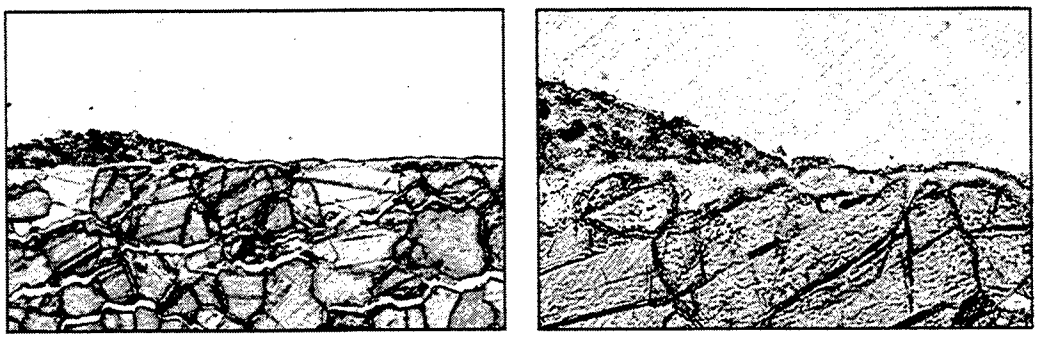

Fig. 2. Marble column from Santa Maria del Fiore, Florence. Details of a transition between laser -treated and untreated regions.

A detail of the Ca-oxalates film thinning achieved on the Mausoleo di Teodorico is showed in Fig. 3. The operative fluences were slightly higher with respect to the previous case (3-5 J/cm$^2$). Similar high quality results were achieved in the case of Palazzo Rucellai. It must be underlined that this controlled thinning of Ca-oxalates films are impossible with

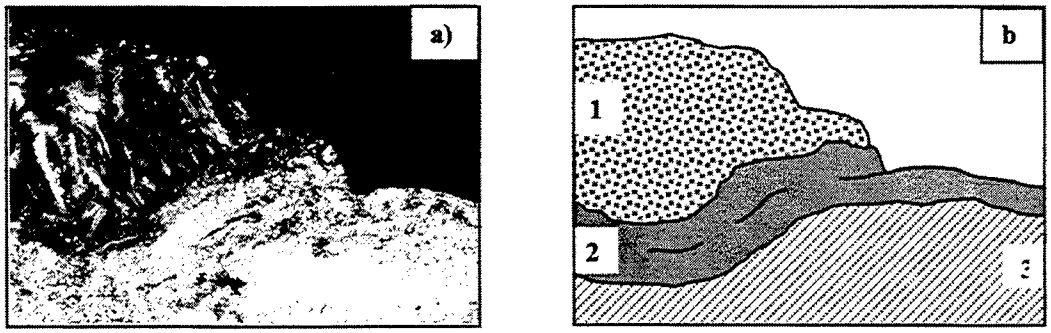


Fig. 3. Mausoleo di Teodorico. Detail of a transition between laser-treated and untreated regions: a) ultra-thin section, b) scheme of the previous figure (1: black crust, 2: lime-Ca-oxalate film, 3: stone substrate).

conventional techniques and they are quite difficult or impossible by standard QS Nd:YAG lasers because of the intense photoacoustic generation and non linear optical absorption phenomena associated with the very high operative intensity.
The SFR Nd:YAG laser was successfully employed also for the cleaning of archaeological bronze findings. As it can be seen in Fig. 4 the readability of the laser cleaned area resulted much better than the one provided by scalpel ablation. Conversely the 20 μs pulse duration laser was not suitable for cleaning of tin, silver and gold films on bronze substrates. In fact, the ablation fluence also generated metalization and melting phenomena which substantially altered the texture of the film surface. For these cases high quality cleaning (Fig. 5) was achieved by LQS Nd:YAG laser cited above, whereas typical QS pulse duration (1-10 ns) can affect the surface texture of low melting point metals because of the high peak temperature risen by high operative laser intensity.

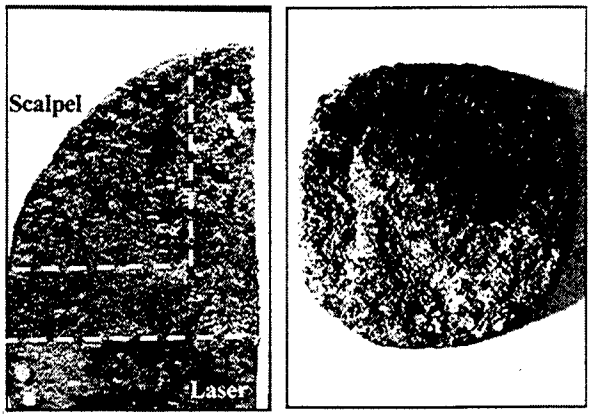


Fig. 4. Examples of laser cleaning of bronze findings by SFR Nd:YAG laser.

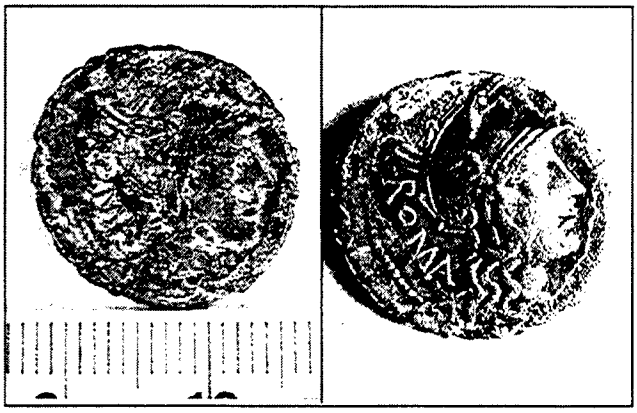

Fig.5. Example of laser cleaning of silver film on bronze by LQS Nd:YAG laser.

## 5. Conclusions

Our experience in the application of the laser ablation in the conservative restoration led us to select and realise optimised Nd:YAG laser sources to overcome intrinsic limitations of the typical commercial systems. Furthermore, after a long experimentation aimed at the parametrization of the interaction processes, we defined specific operative methodologies aimed at achieving restoration tasks not allowed before. We demonstrated for various restoration problems that high quality material removal can be achieved with negligible side effects. In particular we presented the good results in stone cleaning by a SFR Nd:YAG laser, especially designed for stone sculpture restoration. The systems resulted suitable also for cleaning of archaeological bronze findings, whereas for low melting temperature metals the risk of thermal damages was avoided by a LQS Nd:YAG lasers.

## ACKWNOLEDGEMENTS

This research has been supported by Special Project "Cultural Heritage" of Italian National Research Council.
The authors wish to thank G. Sabatini and M. Giamello of IGACPCL of Siena University for the petrographic analyses.

### References

[1] J. F. Asmus, More ligth for art conservation, IEEE, Circuits and Device Magazine, March 1986.

[2] S. Siano, F. Margheri, P. Mazzinghi, R. Pini, R. Salimbeni, G. Toci, M. Vannini, "Laser ablation in the artworks restoration: benefits and problems", LASERS 95, STS Press McLean, VA 1996, 441-444.

[3] Weeks C., The portail del la mere dieu' of Amiens Cathedral: its polychromy and conservation, Studies in Conservation 43 (1998), 101-108.

[4] *Proceedings of Lasers in the Conservation of Artworks, LACONA III*, in Journal of Cultural Heritage, **1** – Supplement 1 (2000).

[5] S. Siano, F. Margheri, P. Mazzinghi, R. Pini, R. Salimbeni Cleaning processes of encrusted marbles by Nd:YAG lasers operating in Free Running and Q-switching regime, Appl. Opt. **36** (1997), 7073-7079.

[6] S. Siano, R. Pini Analysis of blast waves induced by Q-S Nd:YAG laser photodistruption of absorbing targets, Opt. Commun. **135** (1997) 279-284.

# Laser-assisted generating of three-dimensional parts by the blown powder process

M. Resch, A.F.H. Kaplan, D. Schuöcker

Department of Non-Conventional Processing, Forming and Laser Technology
Vienna University of Technology, Arsenal, Objekt 207, A-1030 Vienna, Austria

## ABSTRACT

Laser-assisted generating by the blown powder process is investigated, both, experimentally and theoretically, with respect to layer cross section, grain growth, mechanical testing, track remelting and wall surface roughness compared to post-remelting.

**Keywords:** rapid prototyping, rapid tooling, high power lasers, blown powder process, laser generating, laser cladding

## 1. INTRODUCTION

As Rapid Prototyping (RP) and Rapid Tooling (RT) are two new technologies, the definitions of RP and especially of RT are not clearly defined and often discussed by experts and users[1,2]. Most of the RP models are used as design models and for assembling tests, whereas RT is used for the direct production of tools and moulds. There are two categories of RT: the indirect and the direct approach. All methods related to indirect tooling generate a master prototype for finally production of the desired mold. Direct approaches do not require the creation of a pattern in advance, the mold can directly be produced[3]. This new technique is very promising for industry as a lot of time and money for design and production can be saved. Right now there are some different ways of direct RT. DTM and EOS, two of the leading RP-companies, offer processes for the direct production of metal parts, both are based on the Selective Laser Sintering[4,5]. For another method of direct production of metal parts several different names exist: Optomec called it Laser Engineered Net Shaping[6], some research centers named it 3D-cladding or laser-generating[7], the present publication presents this technique as Blown Powder Process (BPP).
Figure 1 shows the process mechanism and the experimental setup. Similar to laser cladding[1] metal powder is blown by a lateral or coaxial nozzle into a melt pool induced by a $CO_2$-laser. A motion system moves the workpiece horizontally but also the powder nozzle and the focusing system vertically layer by layer in order to create a wall. This method can be compared to repair welding, as in contrast to cladding the previous layer is substantially remelted by the scanning laser beam, thus producing dense metal parts free of spaces or holes.

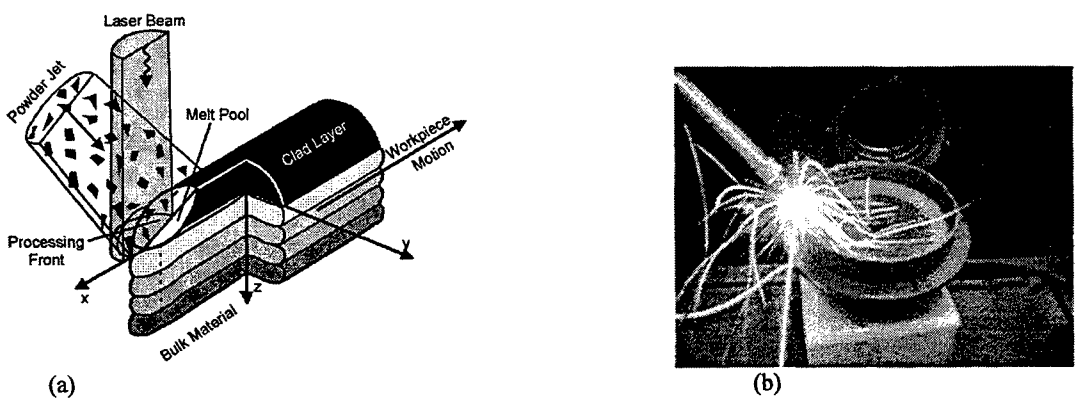


*Fig. 1: (a) process-scheme, (b) experimental setup*

As the technology of the BPP is new and relies upon complex physical mechanisms, rather few theoretical investigation about track geometry, grain growth and powder efficiency rate can be found in literature[8]. Almost all models for the BPP are derived from cladding models[8] as is done in the present study where a recently developed analytical model[9] is applied. This model is based on a local energy balance that determines the width $w_m$ of the remelted track of the previous layer by deriving a melting threshold from the laser beam intensity distribution. Based on the width a mass balance is stated according to the powder feeding rate creating due to surface tension a circular cross section of the generated new layer, see Fig. 2(a), with a corresponding track width $w$, height $h_0$, $h$ and surface roughness $R_z$. The amount $A_m$ of remelting of the previous layer is then estimated by an overall energy balance. The model is described in more detail by Kaplan et al[10].

XIII International Symposium on Gas Flow and Chemical Lasers and High-Power Laser Conference,
Antonio Lapucci, Marco Ciofini, Editors, Proceedings of SPIE Vol. 4184 (2001)

## 2. BASIC INVESTIGATIONS

Experiments were performed with a Co-base-alloy powder 45 C-NS from Sulzer-Metco: Co 25,5Cr 10,5Ni 7,5W 0,5C, the grain size ranging from 40 to 125 µm. The beam power of the $CO_2$-Laser is 1050 W, focal plane position + 2 mm, beam diameter at the workpiece 1,4 mm. The nozzle of diameter 1,5 mm and stand-off distance 10 mm is 30° inclined. The process setup is shown in Fig.2(a). Two powder feeding rates are compared: 5 and 10 g/min, processing speed is varied between 5 and 20 mm/s.

The height and width of the processed tracks is shown in Fig. 2(b) as a function of the processing speed for two powder feeding rates. The values computed by the mathematical model are in good agreement with the experiments. Width and height increase for decreasing speed and increasing powder delivery. At low speed the track is wider than the laser beam diameter, but drops below it at high speed which can be explained by the melting threshold intensity compared to the beam profile that lowers the width of the remelted track at the top of the previous layer. The powder catchment efficiency $\eta_p$ is derived by relating the track cross section of the added layer $wh$ to the powder feeding rate and the processing speed. $\eta_p$ ranges from 30 % to 45 %, increasing with speed. For the model a constant value $\eta_p$ = 40 % was applied.

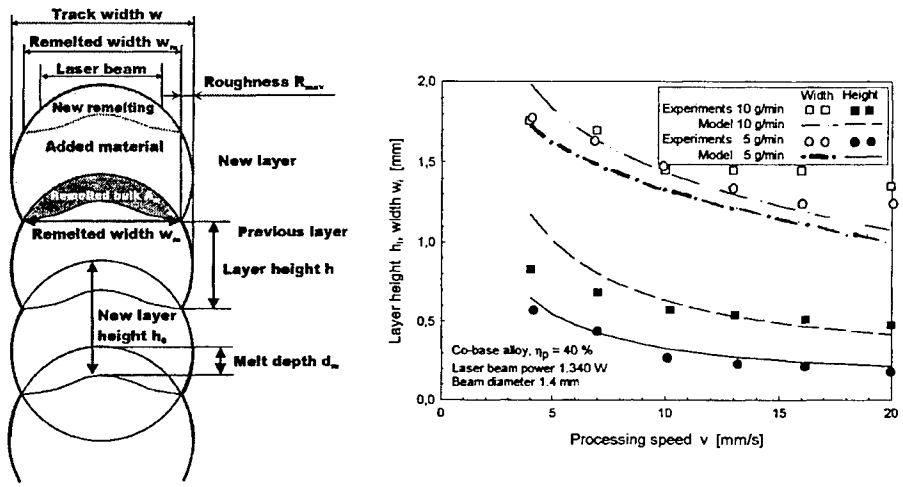


*Fig. 2: (a) schematic description of the cross section, (b) experimental and calculated track height and width as a function of the processing speed for two powder feeding rates $m_v$*

Cross sections of the generated tracks, prepared by polishing and etching, are shown in Fig. 3(a) for different values of processing speed and powder feeding rate. The trend of height and width from Fig. 2(b) can be clearly seen. For all shown walls the bottom layer is the first layer that was generated on a steel sheet, similar to laser cladding. As can be seen the tracks can become wider layer by layer, while in some cases the width decreases. This behavior is caused by a change from three-dimensional heat conduction in the substrate to heat flow constrained to the vertical wall in the generated wall, thus altering the width of the remelted track as base of the next layer. This mechanism is theoretically confirmed by applying an extended model of a moving Gaussian source of heat[11].

A magnified view on the track cross section is given in Fig. 3(b) for three significant cases. The cross sections predicted by the mathematical model that are in good agreement with experiments are shown above for comparison. Low powder feeding rate ($m_v$ < 5 g/min) corresponds to the deposition of thin layers, while several previous layers are substantially remelted, causing a very smooth wall surface, but low building rate. The height $h_0$ of the entire melted track is much higher than the height $h$ of the added layer, thus $h_0 >> h$.

In case of medium powder delivery (5 g/min < $m_v$ < 20 g/min) the depth remelted in the previous track ($d_m = h_0 - h$) is of similar extent compared to the deposited layer ($h_0 \sim 2h$, $d_m \sim h$), while roughness increases slightly. This case is the most common case for laser generating and can be recommended for application. The characteristic shape of the remelted track is governed by increased heat conduction and absorption at the side walls compared to the center.

At high powder feeding rate ($m_v$ > 20 g/min) the building rate is very high and remelting of the previous track is limited to a thin layer ($h_0 \sim h$, $d_m << h$). The circular cross section creates a geometry of undesirably high surface roughness. In addition the height varies significantly layer by layer and defects are likely to occur, as can be seen in Fig. 3(a) for $m_v$ = 20 g/min and $m_v$ = 30 g/min.

These three process modes are almost unaffected by the processing speed that mainly alters height and width. As can be seen, the track cross sections are almost circular. Detailed investigation reveals a slightly elliptic shape with the lateral main axis being merely 10-20 % larger than the second elliptical axis over the whole parameter range.

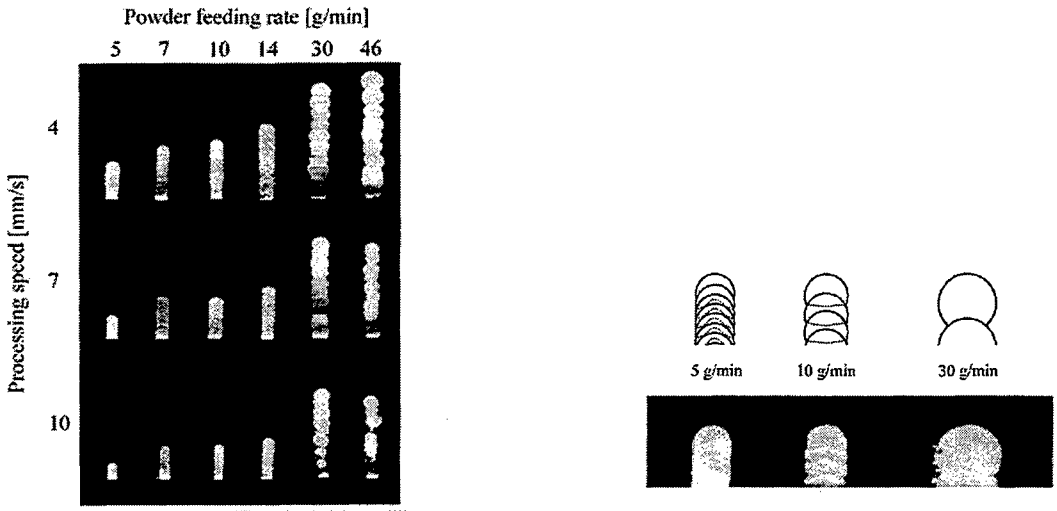


*Fig. 3: (a) cross sections of generated walls for varying speed and powder feeding rate, (b) three distinct building modes for low, medium and high powder delivery: experiments (lower) and model results (upper)*

Due to the layered construction method of the BPP only anisotropic parts are produced. Thus specimen for tensile testing have to be examined in two directions: parallel to the direction of processing speed and perpendicular to this direction. Results of tensile testing for powder 45C-NS can be found in Table 1.

| | Tensile strength $R_m$ (N/mm²) | Yield stress $R_{p0,2}$ (N/mm²) | Elongation after fracture (%) |
|---|---|---|---|
| Parallel | 1046,0 | 711,8 | 11,4 |
| Perpendicular | 864,7 | 640,0 | 2,4 |

*Table 1: Characteristic values of tensile testing parallel and perpendicular to the processing direction*

The tested Vickers hardness varied between 340 and 360 HV(30). As can be seen from the cross sections in Fig. 3, no cracks, holes or any other defects occur in the material except for very high powder rate and speed. Moreover, density of the welded material is 100 %, i.e. the same as for the base material. All the above stated features clearly demonstrate the feasibility of BPP with respect to mechanical properties for the production of heavy-loaded parts as moulds and tools for deep drawing.

## 3. APPLIED IMPROVEMENTS

No doubt the rough surface is a disadvantage of the BPP. Main reason for the roughness is the circular shaped cross section as mentioned above. Fig. 4(a) shows the experimentally measured and the calculated surface roughness $R_{max}$ as a function of processing speed for two powder feeding rates. Particularly in the low speed regime the model overestimates the roughness, but the qualitative trend permits to explain the experimental behavior. Roughness decreases for decreasing powder feeding rate as explained in Section 2.2. Moreover, increasing speed lowers the roughness due to reduced layer height and in turn finer structures.

For low values of $R_{max}$ a rectangular-shaped melt pool would be ideal for building the next layer, as no ruggedness would occur. The above conditions of high speed and low powder feeding rate provide a flat, almost rectangular melt pool[11]. Of course, for these parameters building-rates are rather low, thus a compromise has to be found. Roughness can be reduced from 30 µm to 15 µm by this measure as to be seen in Fig 4(a). A further promising way to improve the surface quality is remelting of the surface with a laser beam. This can either be done with a $CO_2$-laser with line-shaped focus or with a semiconductor laser. During first experiments $R_{max}$ was reduced from 40 to about 13 µm.

A fundamental condition for the creation of 3D-parts is the creation of inclined walls. With a linear three-axis motion system this can only be done by a lateral offset after each layer. Due to this offset the melt pool of a new track only partially overlaps the former track. If the ratio of the width of the new track to the previous track exceeds a certain limit building-up fails because the melt pool has no opportunity to stick on the former track. Experimental investigations reveal a maximum inclination between 40° and 45°. Fig. 4 (b) shows another interesting aspect of inclined prototyping: as the tracks become larger for rising inclination angles, the width increases and the depth decreases. Moreover, the powder catchment rate slightly decreases compared to building of straight walls with the same parameters due to a reduced interaction-cross-section between the powder jet and the melt pool.

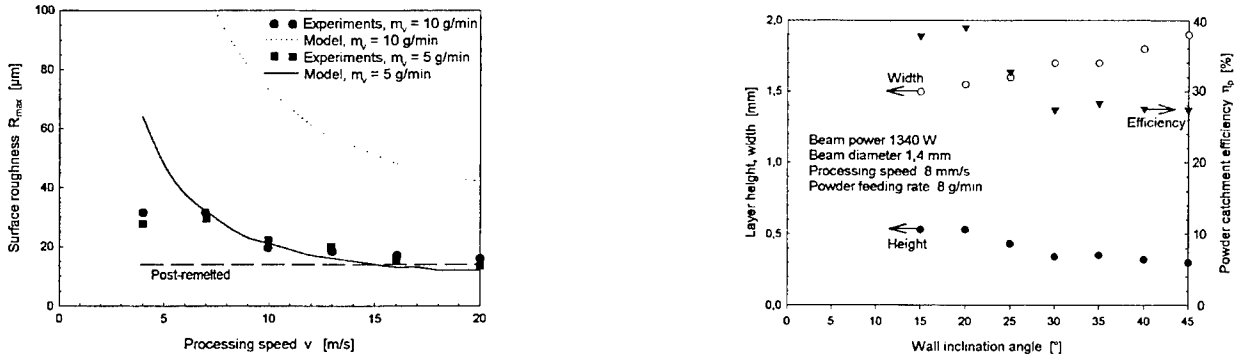


*Fig. 4: (a) Surface roughness as a function of processing speed for two powder feeding rates, (b) powder catchment efficiency, width and depth of the track as a function of the wall inclination angle*

Another technique for building of 3D-parts is handling of the workpiece by a 5-axis-gantry or articulated robot in order to keep the melt pool horizontal for any wall inclination without limiting angle, the only restriction is the minimum wall thickness. Most important is a powerful CAD-system and a fitting post-processor in order to create a correct slicing-model of the part to be built. There are several post-processors on the market for five-axis motion systems, but currently no applications demand for a horizontal melt pool.

## 4. CONCLUSIONS

(i) Laser rapid prototyping by the blown powder process has been studied experimentally and theoretically
(ii) For Co-base alloy powder the influence of powder feeding rate and processing speed were studied
(iii) A mathematical model based on balances of mass and energy well predicts and explains the experiment
(iv) Roughness and layer width and height decrease for increasing speed and decreasing powder feeding rate
(v) Depending on powder delivery three modes can be distinguished
  1: Low powder feeding causes smooth surfaces but little building rates
  2: Medium powder feeding (5-20 g/min) creates tracks of reasonable roughness and building rates
  3: High powder delivery causes high roughness and minimum substrate remelting, defects can occur
(vi) The mechanical properties of the generated walls are anisotropic but satisfactory, density is 100 %
(vii) The track cross section is almost circular and determines the roughness when intersecting the next layer
(viii) Surface smoothening can be achieved by post-remelting of the generated wall surface yielding Rz = 13µm
(ix) For 3D-processing the wall inclination limit was identified to be 40-45°, except for robot handling
(x) BPP is a suitable method for rapid tooling, the present study is a first step to state limits and potential

## 5. REFERENCES


1. Schuöcker, D, "High power lasers in production engineering", *Imperial College Press*, London and World Scientific Publishing, Singapore, 1999.
2. Gebhardt, A, "Werkzeuge für die schnelle Produktentwicklung", *Hanser Verlag*, 1999.
3. Wohlers T.: Wohlers report 2000, *Wohlers Associates*, Inc., 2000.
4 DTM Corporation, Austin, TX 78754, *www.dtm-corp.com*
5. EOS GmbH, D 82152 Planegg/München, *www.eos-gmbh.de*
6. Optomec Design Company, Albuquerque, NM 87107, *www.optomec.com*
7. Fraunhofer Institut für Werkstoff- und Strahltechnik, D-01277 Dresden, *www.iws.fhg.de/ext/infonew/lm.htm*
8. Lin, J., Steen, W.M., "Powder flow and catchment during coaxial laser cladding", *SPIE Vol. 3097*, pp 517-528, 1997.
9. Kaplan, A.F.H., Groboth, G., "Process analysis of laser beam cladding", *Trans. ASME: Journal of Manufacturing Science and Engineering* (to be published in February 2001), 2001.
10. Kaplan, A.F.H., "Mathematical model of laser-assisted rapid prototyping", submitted to *Applied Physics Letters*, 2000.
11. Kaplan, A.F.H., Resch, M., "Analysis of Rapid Prototyping with Co-Base Alloy Powder", *Proc. M⁴PL15*, Eds.: A.F.H. Kaplan, D. Schuöcker, 19-20.01.2000, Igls/Innsbruck (A), E345, TU Vienna, 2000.

# Transient processes under the interaction between gas laser lights and various targets

Koichi Kasuya*, Takahiro Kamiya, Masato Funatsu, Chunlei Wu and Satokazu Saitoh

Department of Energy Sciences, Interdisciplinary Graduate School of Science and Engineering, Tokyo Institute of Technology, Nagatsuta 4259, Midori-ku, Yokohama, Kanagawa, Japan 226-8502

## ABSTRACT

Recent research results concerning lasers and the laser ablation of solid and liquid targets are described briefly. The main laser for experiments was KrF laser pumped by an electron beam. The model calculations were performed for the high rep-rate $F_2$ lasers in mind. An infrared laser and X-ray were taken into account for the model calculations of a space re-entry program and the wall material ablation of an inertial confinement fusion implosion.

**Keywords:** KrF laser, $F_2$ laser, X-ray, Target ablation, Carbon, SiC, 1D model calculation, Re-entry probe, Implosion

## 1. INTRODUCTION

Solid and liquid targets were irradiated by focused high power UV and VUV lasers to investigate the accompanied fundamental processes which are interesting from the point of view of transient fluid dynamics. When the targets are irradiated with intense pulsed laser lights, the surface layers of the targets are ablated. In some cases, mists of the target materials are produced and remain for rather long time. In other cases, macro-particles are produced and degrade the quality of thin films on the substrates. If the duration of the mists is too long, the next coming laser light is disturbed by the mists and may not be able to arrive at the targets. So that, in these cases, we can not irradiate the targets with repetitively operated laser lights. These kinds of situations are not preferable for the lasers to be applied to the material processing or the inertial confinement fusion. We must suppress the formation of the mists and macro-particles, or make the mist duration as short as possible. To solve these problems in the near future, we made some experiments and calculations as the preparatory works. Two kinds of excimer lasers were considered in this paper. One was a short pulse KrF laser, and the other was a VUV laser. Temperature controlled target holder was designed and built. Various solid or liquid targets were used to simulate some practical situations.

## 2. EXPERIMENTS OF UV LASER INTERACTION WITH TARGETS

Various kinds of targets were irradiated with KrF lasers to investigate the basic ablation processes. The preliminary results are shown in our former publications.[1] The continued experiments were performed recently, which are shown here. An electron beam pumped KrF laser (248nm, ~1J, ~10ns) was focused on targets and the produced ion flow was measured with a biased ion collector. The schematic diagram of experimental setup is shown in Fig.1 of Reference 1 or Fig.10 of Reference 2. When we used solid carbon target, we could observe the quantity of produced plasma as a function of the laser fluence (Fig.1). Solid aluminum or liquid welding solder was used as the target in place of carbon. Produced thin films on substrates were observed with a microscope. In some cases, we could observe macro particles on the films. More experiments are necessary to discuss our results in more details.

## 3. MODEL CALCULATION OF VUV LASER CHARACTERISTICS

We have reported some experimental results of UV (KrF) lasers under high repetition rate operation[3-5]. To make same experiments under VUV laser irradiation, we must shorten the laser wavelength in our laboratory. Before we revise our UV laser to VUV laser, it is necessary to estimate the UVU laser characteristics. Although some numerical results concerning

* Correspondence: Email: kkasuya@es.titech.ac.jp; WWW:http://www.es.titech.ac.jp/~kkasuya/intro1.html; Telephone:81 45 924 5662; Fax:81 45 924 5575

XIII International Symposium on Gas Flow and Chemical Lasers and High-Power Laser Conference, Antonio Lapucci, Marco Ciofini, Editors, Proceedings of SPIE Vol. 4184 (2001)

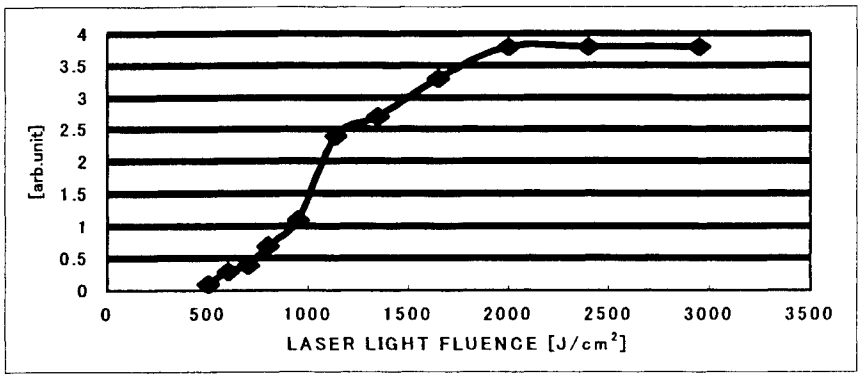


Figure 1. Quantity of ablated plasma as a function of KrF laser fluence.

UVU lasers are published, all of them are zero dimensional calculations. As we have experiences of one dimensional calculation for UV laser[6], we extended our former computations to the UVU region. Some of our most recent results in the case of $F_2$ laser are shown here, which details are described in our accompanying paper[7]. The cross sectional view of the two dimensional discharge-electrode space is shown in Fig.2 of Reference 7. The gas flow axis is denoted with X in the same figure, while the optical axis of the laser cavity is vertical to the page. The shape of the both electrodes was assumed to be a part of cylinder. The width, length and separation of the electrodes were 26mm, 450mm and 22.5mm. The numerical results of the discharge current and the photon density profile at the laser wavelength are shown in Fig.2 and Fig.3. Although these results are for the case of discharge-pumped laser, we would like to extend our calculation also to our electron beam pumped laser case (if possible, in the near future).

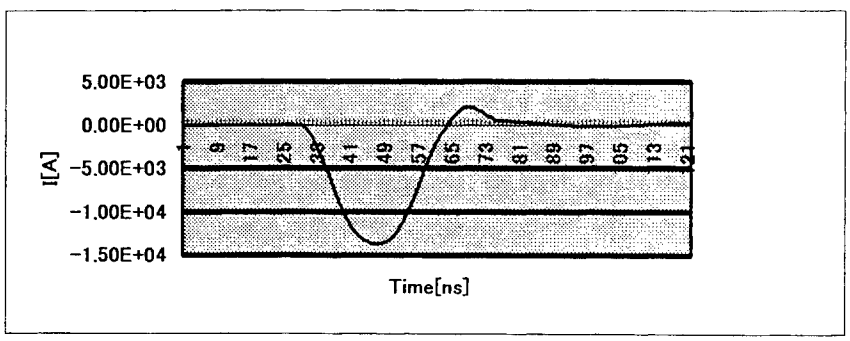


Fig.2 Discharge Current as a function of time

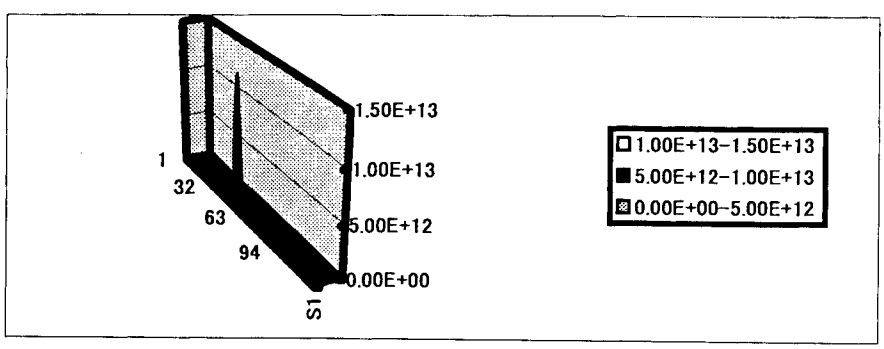


Fig.3 Three dimensional plot of photon-density profile

## 4. MODEL CALCULATION OF UV LASER ABLATION

A sample calculation of solid target ablation was performed here. A graphite target was irradiated with a KrF laser light (248nm, 100mJ, 20ns, flat top with time, 1mm$^2$ diameter and $5\times10^{12}$w/m$^2$). A CIPRIS (Cubic Interpolated Propagation for Research Ingenious Software) computer code was borrowed and used. The simulation results are shown in Fig.4. Only a

small restricted region of the whole target is shown here (5mm vertical and 1mm horizontal, the scales are not same for the both directions). The left ones are the number density contours, while the right ones are the temperature contours. In the same figures, "time" is the delay time in nanosecond from the start of the laser light. The center vertical line is the interface between the solid (on the left side) and the vacuum (on the right side). When the ablated plasma expands, the temperature also drops rapidly. With these results, we can see that the ablation does occur with a time delay after the laser irradiation. The ablation time scale is between some tens of nanosecond and some hundreds of nanosecond. The density contour does not change any more after 250ns and then begins the solidification. The depth of crater in the target is about 0.3mm.

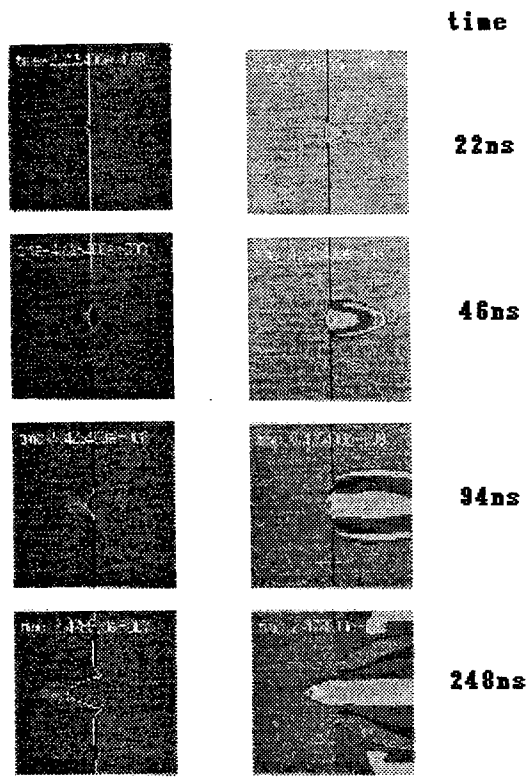


Fig.4 Density (left) and temperature (right) contours of ablated graphite with short pulse KrF laser light.

## 5.MODEL CALCULATION OF RE-ENTRY FLOW FIELD WITH HIGH RADIATION FLUX

To estimate the extreme conditions accompanied with a Jupiter entry probe[8] in the field of space sciences, a model calculation was performed. The equilibrium composition and spectral absorption coefficient of SiC ablation layer plasmas were calculated for temperature of 5,000 to 7,000K, layer thickness of 0 to 7.5mm, and pressure of 0.1 to 1.0Mpa. The included radiation species were molecular bands, atomic lines, and continuum processes. The absorption coefficient thus calculated was applied to a simplified model of the ablation layer. In Fig.5, the sample results of total radiation intensity are shown as a function of the shock standoff distance, where the notations are same with the ones in Reference 9. It was found that the molecular carbon bands were very effective in reducing the high-temperature radiation flux from a stagnation shock layer at low ablation-layer temperature, and the photo-ionization process in atomic elements (carbon, silicon) at high ablation-layer temperature.

## 6.SIMPLE CALCULATION OF WALL ABLATION WITH X-RAY

The last subject in this paper is a simple numerical estimation of the wall material ablation with X-ray under an inertial confinement target implosion. We obtained preliminary results for the quantity of the wall-materials which was ablated by the implosion. We gathered the necessary data for X-ray absorption as a function of radiation wavelength. Taking into

account of the spectral distribution of the implosion X-ray and the absorption data, the absorbed X-ray energy to estimate the evaporated wall thickness was calculated[9].

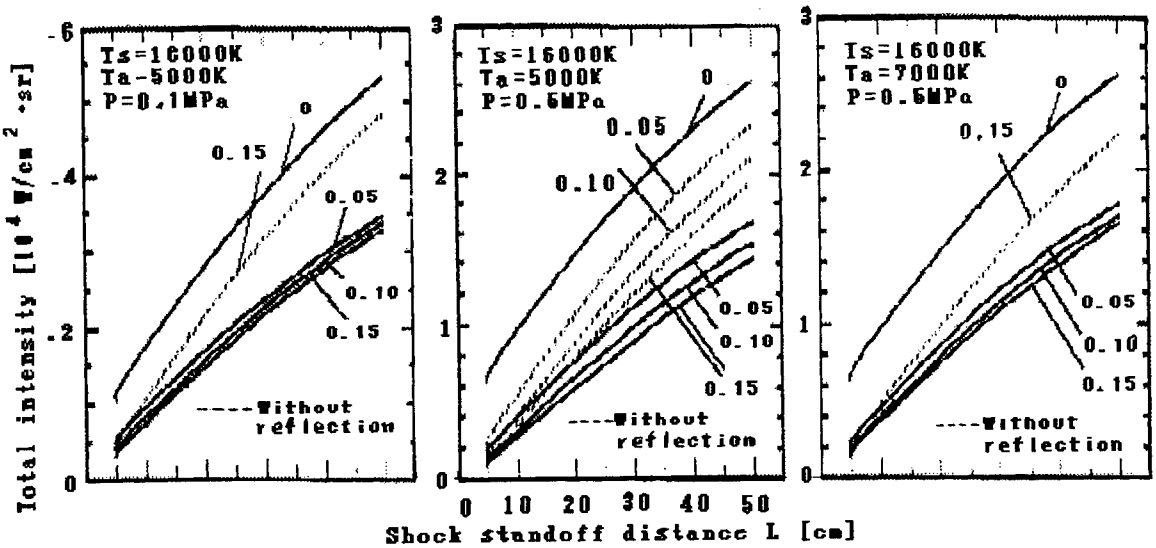


Fig.5 Numerical results of intense radiation from hydrogen-SiC shock layer.

## ACKNOWLEDGMENTS

This work was supported by the Ministry of Education, Science, Culture and Sports in Japan together with the Japan Society for Promotion of Sciences. The authors acknowledge also to the supports by Sandia National Laboratories (Albuquerque), USA and Institute of Laser Engineering, Osaka University, Japan.

## REFERENCES

1. K. Kasuya et al., "Characteristics of laser produced plasmas and lasers for pulsed ion sources," *AIP Conference Proceedings*, **369**, pp. 1054-1059, 1996.
2. K. Kasuya et al., "Diagnostics of KrF, CO laser modes and laser plasmas produced by the lasers," *Proceedings of 10th IEEE International Pulsed Power Conference*, pp. 634-39, 1995.
3. K. Kasuya et al., "Measurements of gas flow and gas constituent in a wind-tunnel type excimer laser under high repetition rate operations," *Proceedings of 8th International Symposium on Gas Flow and Chemical Lasers*, **SPIE-1397**, pp. 67-70, 1991.
4. K. Kasuya et al., "Highly sensitive diagnostics of particle density relaxation process in KrF laser," Proceedings of 9th *International Symposium on* Gas Flow and Chemical Lasers, **SPIE-1810**, pp. 388-391, 1993.
5. K. Kasuya et al., "Quality measurements of KrF laser beams under high repetition rate operation with advanced high speed photography: Preparatory experiments," Proceedings of 10th *International Symposium on* Gas Flow and Chemical Lasers, **SPIE-2502**, pp. 450-457, 1995.
6. K. Kasuya et al., "One-dimensional computation of the discharge-pumped excimer lasers under repetitive operations," *Laser and Particle Beams*, **12**, pp. 647-679, 1994.
7. T. Kamiya et al., "One-dimensional model calculation of $F_2$ laser under high repetition rate operation," in this Proceedings, 2000.
8. M. Funatsu et al., "Numerical simulations of viscous shock layer with carbon ablation: Preparatory research works for future reentry experiment with high-power laser and target," *Proceedings of 11th International Symposium on Gas Flow and Chemical Lasers and High-Power Laser Conference*, **SPIE-2502**, pp. 651-654, 1996
9. K. Kasuya et al., "Probable approaches to develop particle beam energy drivers and to calculate wall material ablation with X-ray radiation from imploded targets," Proceedings of the 18th Fusion Energy Conference, to be published, 2000.

# Enhancement of laser absorptivity properties of HEX

F. Lacroix, B. Gautier
French-German Research Institute of Saint-Louis, ISL
P.O. Box 34, 68301 Saint-Louis Cedex, France

## ABSTRACT

In this paper we report measurements ($0.3 < \lambda(\mu m) < 2$) of the diffuse reflectivity and absorptivity of TNT obtained from different manufacturing processes (cast or compressed) and HMX. Particular emphasis is placed on the Nd:YAG laser ($\lambda = 1.064$ µm). It has been found that the diffuse reflectivity of TNT increases from about 50% for the cast material to 97% for the compressed one; furthermore, liquid TNT (T > 81°C) appears to be quite transparent. The laser beam volume absorption has been computed according to the Kubelka-Munk (KM) semi-empirical model including our own measurements. This diffusion model has been incorporated into a 2D numerical code of heat conduction of reactive materials in order to predict thermal ignition. Numerical applications of this model are in agreement with the concept of "critical laser intensity", providing material phase changes are taken into account. Otherwise, the same numerical model has been used in order to optimize the dopant (CB) concentration in HMX to enhance its thermal ignition. It has been shown that a very low CB concentration (<1%) has a dramatic effect on the optical properties of doped HMX.

**Keywords:** HEX laser ignition, Optical properties, TNT, HMX, $CO_2$, Nd:YAG, Diode lasers.

## 1. INTRODUCTION

The first part of this paper deals with laser neutralization of land mines (or UXO). We consider here the case of explosives embedded in a plastic casing (PVC). As opposed to a metallic casing where the laser energy is transferred to the explosive only by heat conduction, the plastic wall is soon burnt through by pyrolysis leaving the explosive directly irradiated by the laser beam. The rate of energy transfer is then strongly dependent on the optical properties of the explosive material at the laser wavelength. The second part of this paper deals with the modification of the absorption properties of HMX by dopant addition (carbon black = CB), its purpose is to optimize laser diode ignitors (LDI).

## 2. MEASUREMENT OF THE OPTICAL PROPERTIES OF TNT

Two test set-ups have been used in order to measure the reflection and the transmission of slices of explosive materials: a) a spectrophotometer equipped with mirrors allowing diffuse radiation measurements ($200 < \lambda < 2000$ nm); b) a specific test set-up including an Nd:YAG laser and integrating spheres to collect the reflected and transmitted radiation. The two-step operating mode used on this test bench is described in fig. 1. The system calibration is done with a totally reflecting mirror and the measurements of reflection and transmission are performed by placing the sample at the bottom and in the sphere aperture respectively.

### 2.1. TNT Transmission Measurements at $CO_2$ Laser Wavelength ($\lambda$=10.6 µm)

The device used is the spectrophotometer. Due to a rather short absorption length (a few µm), the TNT powder has been mixed and pressed with KBr in thin pellets. From the effective mass of TNT contained in these pellets one computes an equivalent thickness $E_{eq,}$. Assuming that the Lambert-Beer absorption law holds it can be written as:

$$I_{tr} = (1-R) I_0 \exp\left(-\alpha E_{eq}\right). \tag{1}$$

One can extract a value of the absorption coefficient $\alpha$ from a couple of measured transmission values $\tau_1$ and $\tau_2$ corresponding to two different equivalent thicknesses $E_{eq1}$,$E_{eq2}$:

$$\alpha = \mathrm{Ln}\left(\tau_2/\tau_1\right) / \left(E_{eq1} - E_{eq2}\right). \tag{2}$$

The slope of the straight line fitting the measured data points provides a value of $\alpha = 220\ \mathrm{cm}^{-1}$ for the TNT analyzed at the $CO_2$ laser wavelength (fig. 2).

### 2.2 TNT Diffuse Reflection and Transmission at Nd:YAG Laser Wavelength ($\lambda$ = 1.064 µm)

The absorption coefficient computation used for the $CO_2$ laser is no longer valid for the Nd:YAG laser: i.e. the absorption length is greater than for the $CO_2$ laser (a few mm), TNT exhibits a semi-transparent behavior; the grain structure of this material (dependent on the manufacturing process) induces light scattering. Two types of material have been tested: cast TNT and the pressed one. The measured values of diffuse reflection and transmission are reported in table 1 for different sample thicknesses.

XIII International Symposium on Gas Flow and Chemical Lasers and High-Power Laser Conference,
Antonio Lapucci, Marco Ciofini, Editors, Proceedings of SPIE Vol. 4184 (2001)

## 3. LIGHT SCATTERING MODEL

| Material | Thick (mm) | Reflect. ρ | Trans. τ |
|---|---|---|---|
| Cast TNT | 2 | 0.424 | 0.37 |
| « | 3 | 0.435 | 0.29 |
| « | 4 | 0.436 | 0.23 |
| Pressed TNT | 2.1 | 0.935 | 0.064 |
| « | 3 | 0.948 | 0.043 |
| « | 4 | 0.956 | 0.028 |

Table 1. Measured values of diffuse reflect./transm. for TNT at $\lambda = 1.064$ µm.

The laser beam absorption in the bulk material can be described by the semi-empirical KM model[1] based on an analytical solution of the Hamaker[2] equations and fully described in ref.[3]. The basic differential equations have been written in terms of two parameters: $a$ as the diffuse absorption coefficient ($a \neq \alpha$) and $s$, the scattering coefficient:

$$dI(x)/dx = -(a+s)I + sJ \quad (3)$$

$$dJ(x)/dx = (a+s)J - sI \quad (4)$$

with the following boundary conditions:

$$I(x=0) = (1-\rho_0)I_i + \rho_i J(x=0) \quad (5)$$

$$J(x=D) = \rho_i I(x=D), \quad (6)$$

where $I$ and $J$ are the light fluxes propagating in the incident beam direction and in the backward direction, respectively. $I_i$ = incident flux, $\rho_0$ = reflectivity of incident energy ($x = 0$), $\rho_i$ =reflectivity of radiant energy emerging from the solid, $D$= sample thickness. An analytical solution of this set of equations can be found, providing one knows experimentally the reflection ρ and the transmission τ of at least two samples of different thickness $D$. It results in a set of implicit algebraic equations whose solution yields the required values of the $a$ and $s$ coefficients defining the absorption law for a given sample thickness. The computed values of $a$ and $s$ for the two kinds of TNT investigated and a thickness of 4 mm are reported in table 2. Using the above-computed values $a$, $s$ of table 2, the local relative light intensity $(I-J)/I_i$ and its derivative $d[(I-J)/I_i]/dx$ have been plotted vs. the depth inside the sample (fig. 3). This graph refers to both kinds of TNT at $\lambda = 1.064$ µm.

| Material | Thick (mm) | Ref. index n | a ($cm^{-1}$) | s ($cm^{-1}$) |
|---|---|---|---|---|
| Cast TNT | 4 | 1.413 | 0.6216 | 4.322 |
| Pressed TNT | 4 | 1.413 | 0.0579 | 113.1 |

Table 2. Computed values of diffuse absorption and scattering coefficients from the KM theory.

## 4. NUMERICAL MODEL FOR THE THERMAL IGNITION OF HEX

A numerical model solving the heat conduction equation of reactive materials has been developed[4,5]. The basic assumptions included are the following: a) the optical and thermo-physical properties of the material are temperature dependent; therefore, for applications presented here $C_p$, $K$, $\alpha$ are kept constant; b) phase changes, i.e. melting and vaporization, are taken into account; c) HEX exothermic reactions are included as internal heat source, expressed by an Arrhenius type law; d) the light volume absorption is computed according to the KM model; e) the heat conduction equation is solved numerically by an explicit integration method based on a 2D spatially variable step grid.

### 4.1. Thermal Ignition of TNT with $CO_2$ Laser Beam

Prior to running numerical codes, one can compute a critical laser intensity $I^*$ [6,7] defined by a balance between the surface temperature gradient due to laser heating and those due to chemical reactions. The critical conditions are met when the surface temperature reaches vaporization at time $t^*$:

$$[\partial T_s/\partial t]_{chem} = [\partial T_s/\partial t]_{las} \text{ and } T_s(\alpha, t^*) = T_v. \quad (7)$$

The computed values of $I^*$ for cast and pressed TNT at both $\lambda$=10.6 and 1.064 µm are reported in table 3, assuming constant thermo-optical properties and neglecting phase changes.

### 4.2. Numerical Applications

Several numerical applications using numerical codes have been attempted. The laser intensity of 63.6 W/cm² is higher than the computed critical value for the $CO_2$ laser, but lower than that of the Nd:YAG laser. For the latter, measured values of table 2 have been introduced into the KM model. Fig. 4 is a plot of the centerline front and back temperature rises of the TNT sample (Φ = 20 mm, thick = 4 mm) in the three successive cases: 1) cast TNT/$CO_2$ laser; 2) cast TNT/Nd:YAG laser; 3) pressed TNT/Nd:YAG laser. It can be seen that for $CO_2$ irradiation, surface vaporization is reached very soon and that the target is entirely burnt through after 8.3 s without ignition. The situation is different with the Nd:YAG laser; it can be seen that a complete melting of the sample occurs, the liquid TNT being heated up to sudden vaporization (≅12 s) and critical conditions are met for $t^* \cong 10$ s. A similar phenomenon is observed for pressed TNT; critical conditions are met at $t^* \cong 120$ s. Fig. 5 is an assembly of successive sample sections showing the melting front

| Material | Laser | Surf.absorp.(1-R) | $\alpha_{eq}$.($cm^{-1}$) | I* (W/cm²) |
|---|---|---|---|---|
| Cast TNT | YAG | 0.56 | 2.25 | 310 |
| Pressed TNT | YAG | 0.06 | 2.1 | 2700 |
| Cast TNT | $CO_2$ | 0.9 | 220 | 24 |

Table 3. Computed values of critical intensities $I^*$

recession in the last case 3). The difference in behavior between the two TNT samples lies in the fact that diffuse reflection on the surface of cast TNT is close to 50%, whereas it reaches 95% for pressed TNT, yielding an extremely low heating rate. As a conclusion, the ignition conditions are obtained in the melting phase.

## 5. EXPERIMENTAL RESULTS

Qualitative results have been obtained by irradiating TNT with a CW $CO_2$ laser ($P_{max}$ = 500 W) and an RP Nd:YAG laser ($P_{max}$ = 600 W). The different behavior of TNT towards both lasers can be summarized as follows: using the $CO_2$ laser, an encapsulated charge of TNT (30 g) in a 3 mm thick PVC casing has been irradiated under 300 W/cm², the plastic skin is burnt through after 40 to 60 s irradiation; then the combustion of vaporized TNT starts on the heated residues of the envelope, the combustion is self-sustained and may last several minutes. Fig. 6 shows the two halves of the cut cylinder after irradiation. Experiments performed with the Nd:YAG laser on TNT contained in a transparent vessel (glass) show a low melting of the whole TNT followed by spontaneous ignition of the emitted vapor. Although, no quantitative comparison has been attempted, the experimental observations are in good agreement with our theoretical predictions.

## 6. ENHANCEMENT OF HMX ABSORPTIVITY FOR CONTROLLED LASER IGNITION

The model developed to describe the thermal ignition of scattering materials has been used to optimize a laser diode ignitor (LDI) made of HMX carbon black (CB) doped irradiated by diode laser ($\lambda$ = 830 nm). The fine CB powder ($\Phi$ = 40 nm) is mixed in low concentration (< 3% in mass) with HMX powder ($\Phi_{mean}$ = 3 µm) and pressed together. The diffusion coefficients $a_m$ and $s_m$ of the mixture can be computed from both the values for pure products and the specific surfaces of the dopant $\Sigma_d$ (CB) and the powder $\Sigma_p$ (HMX) according to:

$$a_m = a_p \Sigma_p + a_d \Sigma_d . \tag{8}$$

$$s_m = s_p \Sigma_p + s_d \Sigma_d . \tag{9}$$

The specific surfaces $\Sigma_p$ and $\Sigma_d$ are usually given by the manufacturer ($\Sigma_d$ = 61m²/g) or computed assuming spherical joined grains with a given diameter, thus $a_m$ and $s_m$ (coefficients of the mixture) are a function of the dopant concentration. Measurements of reflection/transmission on pure HMX pellets (1mm thick) at $\lambda$ = 830 nm give values of $a_p$ = 108 cm$^{-1}$, $s_p$ = 1446 cm$^{-1}$ (highly scattering medium). Similar measurements on CB doped HMX pellets provide values of $a_d$ = 1670 cm$^{-1}$, $s_d$ = 170 cm$^{-1}$ (quasi-opaque material). Using the KM model described in chapter 3, on can compute the surface diffuse reflection which can be compared to measured values as shown in fig. 7 as a function of CB concentration. It appears that the effect of a very small addition of CB to HMX may change considerably the laser absorption and enhances the ignition probability of HMX.

## CONCLUSIONS

From measurements of both diffuse reflection and absorption of HEX at current laser wavelengths ($CO_2$, Nd:YAG, diodes) a theoretical model has been established in order to study the thermal ignition of several HEX (TNT, HMX). It has been shown that TNT irradiated with a $CO_2$ laser exhibits a behavior governed by an ablation phenomenon which may prevent the ignition even at low flux (≈ 60 W/cm²), whereas irradiation by an YAG laser induces a total melting and heating of the liquid phase which may lead to thermal ignition. It has been shown that the addition of CB, at a very low concentration, to HMX considerably changes the optical properties of the explosive, thus enhancing the laser absorptivity and the probability of thermal ignition.

## REFERENCES


1. P. Kubelka & F. Munk, «Ein Beitrag zur Optik der Farbenstriche», Z. Tech. Physik 12, 539, 1931.
2. H.C. Hamaker, «Radiation and heat conduction in light scattering materials», Philips Research Rpts, Vol. 2, pp. 55-67, 103-125, 420-425, 1947.
3. R.C. Folweiler, «Thermal radiation characteristics of transparent, semi-transparent and translucent materials under non-isothermal conditions», AFML ASD TDR 62-719, Lexington Lab. Inc., Cambridge/MA, USA, April 1964.
4. B. Gautier, «Neutralisation laser des mines : I : Approche théorique de l'interaction laser/explosifs», ISL Rpt. R 104/99.
5. B. Gautier, «Neutralisation laser des mines : II : Irradiation laser d'explosifs nus, caractérisation optique des explosifs», ISL Rpt. R 119/2000.
6. R.J. Harrach, «Estimates of the ignition of high explosives by laser pulses», J. Appl. Phys., Vol. 47, No. 6, June 1976.
7. L.G. Strakovkii, E.I. Frolov, «Properties of the ignition of semi-transparent volatile explosives by monochromatic light flux», Trans. Fizika Goreniya Vzryva, Vol. 16, No. 5, pp. 140-147, Sept.-Oct. 1980. In: Combustion, Explosion and Shock Waves, March 1981.

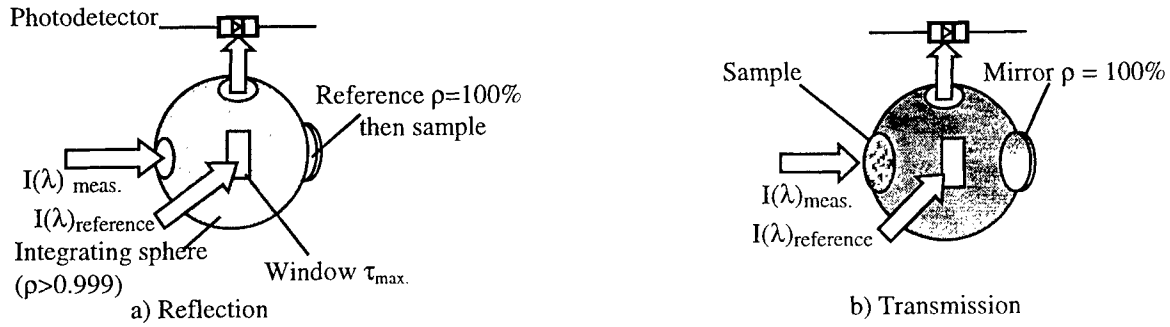


**Fig. 1 Diffuse reflection / transmission measurement principle**

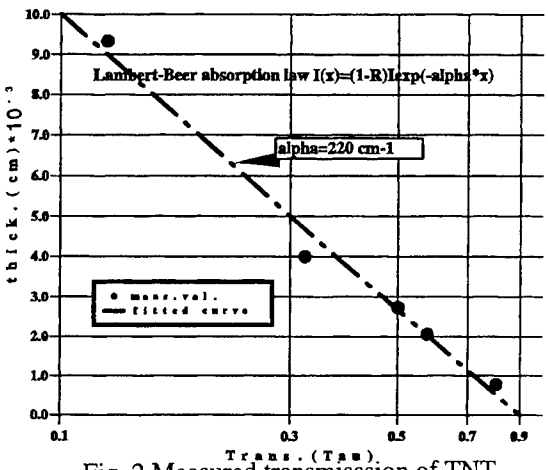


Fig. 2 Measured transmisssion of TNT samples with $CO_2$ laser

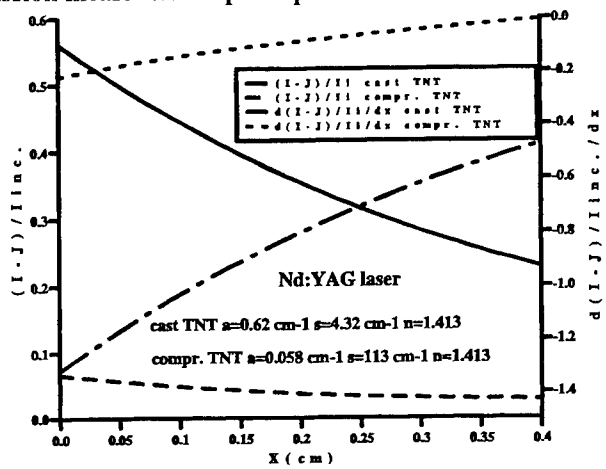


Fig. 3 Computed bulk absorption of different TNT samples

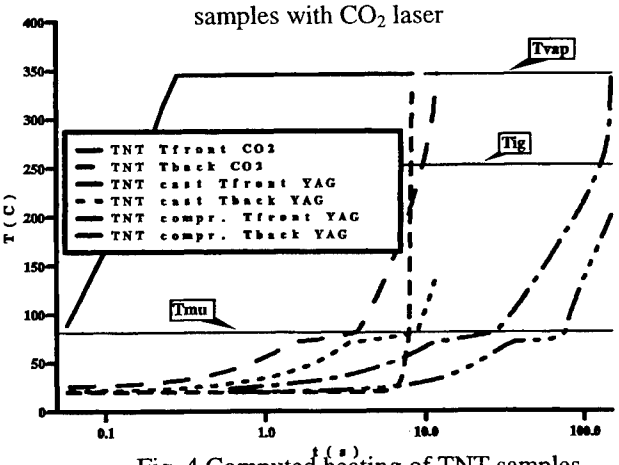


Fig. 4 Computed heating of TNT samples with $CO_2$, Nd:YAG lasers

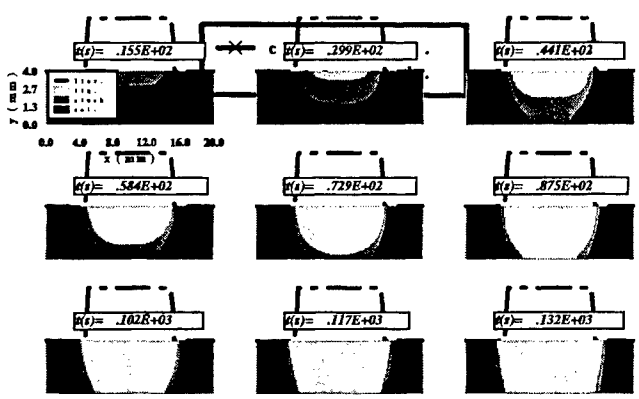


Fig. 5 Computed melting front of pressed TNT with Nd:YAG laser

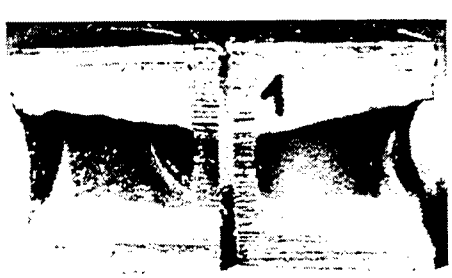

Fig. 6 Cut of TNT sample in PVC casing with $CO_2$ laser: I = 75 W/cm²

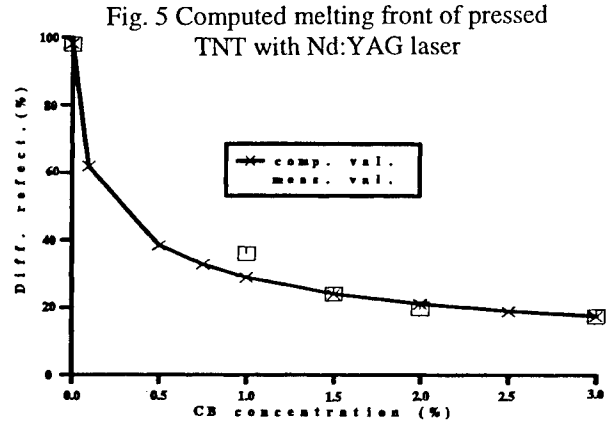


Fig. 7 Effect of CB concentration on diffuse reflectivity of HMX

# Industrial Iodine Lasers: An Untapped Military Resource

Marc R. Hallada[a], Stephen L. Seiffert[a], Robert F. Walter[a], John Vetrovec[b]
[a]Schafer Corporation, 2903 Renard Place SE, Suite 300, Albuquerque, NM 87106
Tel 505-242-9992 Fax 505-242-9975
[b]The Boeing Company - Rocketdyne, 6633 Canoga Avenue, Canoga Park, CA 91309

## ABSTRACT

The Chemical Oxygen-Iodine Laser (COIL) has been studied for several industrial applications. Recent demonstrations have shown that lasers can be highly effective for size-reduction cutting of radioactively-contaminated structures.

## 1. INTRODUCTION

The dismantlement of obsolete nuclear weapon production facilities and nuclear power reactors is a major challenge for the U.S. Department of Energy (DOE) and commercial nuclear power utilities. It is also a festering international problem, with dangerous reactors and Cold War weapon facilities endangering the environment and people's health and increasing the threat of proliferation. The DOE has over 3700 old facilities in need of dismantlement and other nuclear nations undoubtedly have similar numbers of facilities. It is also estimated that the republics of the former Soviet Union have over 400 military nuclear reactors, many on naval vessels, which should be decommissioned as soon as possible. A similar number of commercial power reactors will need to be decommissioned in the next 30 years. Existing tools are inadequate to deal with tasks of this magnitude and urgency in an expeditious, safe, and cost-effective manner. New tools are needed to accelerate decommissioning schedules and to efficiently segregate wastes so that materials can be reutilized and long-term storage requirements minimized. More effective dismantlement and reutilization would reduce the dangers of accidents and proliferation and simplify the monitoring and control of the remaining facilities.

## 2. WHY LASERS FOR DISMANTLEMENT?

Conventional dismantlement technologies (plasma arcs, water jets, oxygen-gas torches, diamond wires, etc) have a number of limitations. They are often labor intensive and expensive, they usually generate significant secondary waste streams, they sometimes require bulky equipment that cannot be used in confined areas, and many of them cannot expeditiously cut through the thickest components or through certain materials. As a result, multiple tools are required to conduct dismantlement operations, even for similar tasks. Although these conventional tools are able to accomplish many of the dismantlement tasks, they require extensive worker interaction for setup and maintenance. Shortcomings in these techniques can usually be compensated for, but at the expense of increased exposures, secondary wastes, and times. As a result, it is difficult for such techniques to provide the rap[id and versatile sectioning needed to efficiently segregate different waste streams, minimizing the volumes required for long-term storage and maximizing the recycling of low-level activity materials.

A number of recent experiments have shown that laser systems can be highly effective tools (and perhaps the only feasible tools) for certain dismantlement tasks.[1,2] The Nuclear Power Engineering Corporation of Japan demonstrated the use of a 20 kW carbon monoxide (CO) laser in doing single-pass cutting of large arrays of stainless steel pipes and in cutting through a twelve-inch thick stainless steel core support plate.[3] However, a CO laser beam cannot be conveniently and efficiently delivered to remote and confined areas since it operates at wavelengths (4-8 microns) that are not transmitted by standard fiber optics. Thus, articulated, hard optics delivery systems are required, which are prone to misalignment and have high losses from beam spillover, absorption, and reflections at each relay optic interface. $CO_2$ lasers, at 10.6 microns, suffer from the same losses. These far infrared wavelengths do not couple as well as near infrared wavelengths into many materials, especially aluminum alloys. As a result, a laser beam near 10 microns cuts at about a third of the rate for a beam near one micron. However, current industrial laser systems that

XIII International Symposium on Gas Flow and Chemical Lasers and High-Power Laser Conference,
Antonio Lapucci, Marco Ciofini, Editors, Proceedings of SPIE Vol. 4184 (2001)

can be delivered via standard fused silica fiber optics (restricted to wavelengths from about 0.4 microns to about 1.6 microns) are not capable of the high average powers needed for practical dismantlement systems. Neodymium YAG (Nd: YAG) lasers, at1.06 microns, can be transmitted by fiber optics, but they have not been demonstrated at average powers beyond 10 kW (and will not exceed this threshold for the forseeable future). Nd: YAG systems have been used to cut a variety of reactor and weapon production components, including fuel rod support assemblies and plutonium-processing glove boxes.[4] However, in all cases, the off-the-shelf industrial Nd:YAG lasers were limited to cutting of relatively thin sections (0.5 cm or less). In addition, in many instances the tasks were simple and repetitive and the objects to be cut had to be delivered to a laser cutting station. Although the cutting generated little secondary waste, the beam quality of the devices used was at least several hundred times diffraction limited, requiring the laser cutting heads to be precisely positioned, within about a millimeter of the objects being cut, to keep the beam focus on the surface.

## 3. FULL ADVANTAGES OF LASERS NOT REALIZED

Low average power and poor beam quality lasers have also prevented the full capabilities of robotic systems from being demonstrated in dismantlement. (The same case may be made for many other applications of lasers in industry, where the speed and accuracy possible with may robotic systems is hampered by underpowered lasers and poor beam quality.) Because of the relatively poor beam quality, robotic systems must adapt precisely to object contours and to any relaxation of the structures as they are cut. Thus, auto focus systems are critical and cutting routes must be carefully planned to avoid sections which are too thick to cut easily. In past demonstrations, when off-the-shelf robotic control systems were used, complex cuts, as for glove boxes, were meticulously preplanned and often took many minutes to accomplish. More advanced robotics control systems, such as those developed by Sandia National Laboratory's Intelligent Systems and Robotics Center, allow such route planning to be done much more rapidly. However, the full capabilities of these advanced robotic control systems are limited by the low average laser powers, which reduces cutting rates below practical levels for thick structures. (A 3 kW Nd: YAG is limited to cutting materials no thicker than ~ 1 cm.) A 3 kW Nd: YAG laser was used recently by the Intelligent Systems and Robotics Center to cut a glove box made of .125-inch stainless steel. However, the 3 kW system was not used to cut through the glove flanges or support structures and it had to precisely follow the box contours because of the laser's relatively poor beam quality and short depth of focus. In addition, many glove boxes are often much thicker, constructed of half-inch stainless steel, and are laminated with lead plates in certain sections. Thus, to enable narrow-kerf, single-pass cutting of complex, thick objects, a high average power, high quality beam is needed.

Direct laser cutting of such laminates has not been demonstrated in the U.S. However, Russian researchers recently reported the laser cutting of lead plate and reactor fuel elements, constructed of a variety of materials, using a 3 kW $CO_2$ laser.[5] Currently available Nd: YAG systems would probably require manual removal of any lead laminates before laser cutting could be done. (Note: Plasma arc cutting of the plutonium-processing glove boxes at DOE's Rocky Flats site is the current baseline approach, though such cutting generates relatively large volumes of secondary wastes and requires significant manual intervention. Laser cutting options for such contaminated structures are being investigated by a few groups, however.)

The full benefits of using lasers in decontaminating and dismantling nuclear facilities can only be realized with high average power beams (~20-30 kW) that can be delivered by standard industrial fiber optics to remote and/or confined work areas. Fiber optics delivery, especially with high beam quality, also allows the full benefits of robotics systems (rapid, precise operations) to be realized. High powers are critical to enable the cutting of even the thickest components (up to twelve-inch thick reactor vessels), rapid cutting of thinner components, rapid scabbling of contaminated surfaces, or the simultaneous use by multiple work stations. There are no commercial lasers that can provide a fiber-transmitted beam at such powers. While a $CO_2$ laser can be scaled to high average powers, it cannot be fiber delivered. Conversely, a Nd: YAG beam is fiber deliverable, but it cannot be scaled to 20-30 kW. Fiber delivery to remote locations could reduce worker exposures and thus labor turnover costs. No-wear laser end effectors would require only minimal maintenance, again reducing labor hours and exposures. High beam quality allows small laser spot sizes and narrow kerfs, reducing secondary wastes. In addition, high beam quality allows the beam to have a large depth of focus, creating an extended range over which the laser beam will maintain a high

enough intensity to cut effectively. This allows the beam to cut more uniformly, for a greater depth, without rigid control of the spacing between the cutting head and the work surface.

A laser system to satisfy dismantlement needs could be produced by modifying a military weapon laser to operate more economically and for longer times. The Chemical Oxygen-Iodine Laser (COIL) was invented and developed by the U.S. Air Force, beginning in 1977, as a weapon system. As a gas-transfer laser, the COIL concept is scaleable to very high powers without loss in beam quality. It has been demonstrated at over a hundred kiloWatts and an airborne version is now being built, at even greater powers, to shoot down ballistic missiles from hundreds of kilometers. An industrialized COIL, with power to spare and a wavelength (1.315 microns) that is easily transmitted by standard fused silica fiber optics, would be an extremely versatile tool for dismantlement and recycling operations. It would not be a single-task tool. It could be used for cutting, scabbling, and welding of a variety of materials and components. It's high average power would also allow the simultaneous use of multiple workstations. Industrialization of COIL is straightforward. A 20-30 kW device capable of running for extended times could be built and deployed

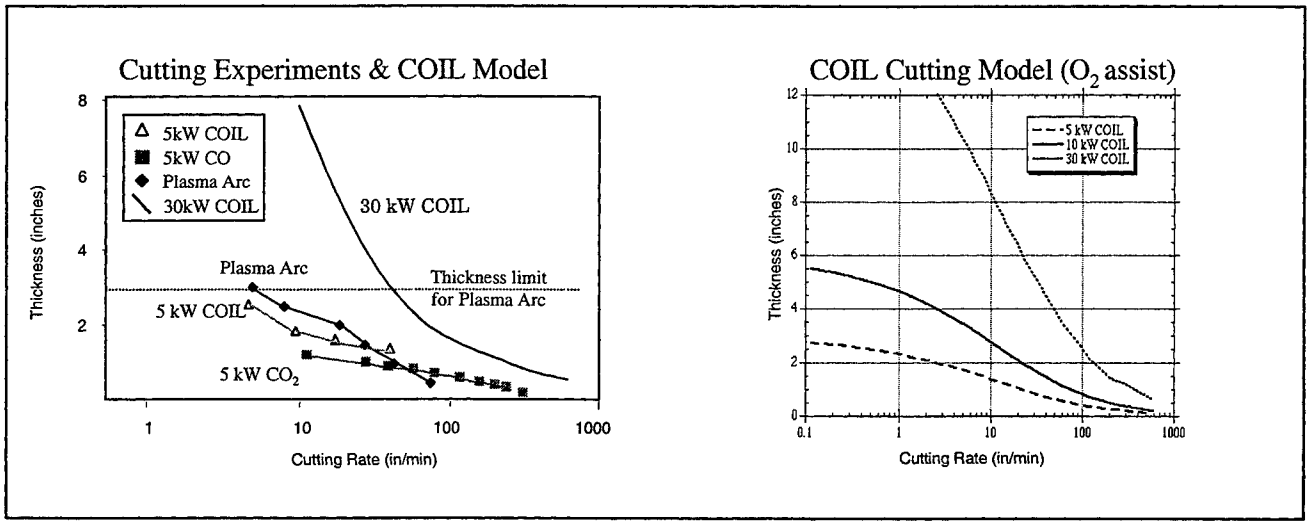


Figure 1 COIL Cutting Experiments and Models

in less than two years. Reductions in capital and operations costs could be achieved by developing more refined industrial subsystems and controls. These refinements could be made while the performance of a prototype is tested at a variety of tasks and locations. In fact, a number of achievements in this area have already been made, as reported by others at this conference and by groups in Japan, Germany, Russia, and the United States.

The combination of high beam quality of a COIL and efficient coupling into a variety of materials makes a COIL system very attractive for cutting thick sections rapidly. Because of the wavelength difference, a COIL cuts about three times faster than a $CO_2$ laser of comparable power. Also, while standard plasma arc cutting is apparently limited to structures no thicker than about 3 inches, computational models of COIL cutting indicate that a 30 kW system could cut even foot-thick stainless steel at over 2 cm/min. (See Fig 1.)

The construction and deployment of an "industrial" COIL at a nuclear facility, perhaps as shown in Figure 2, would probably cost $5-10 M. The deployment cost would depend upon whether a high or low operating cost system is built. The capital costs of these two general options are, in general, inversely related to their operating costs. Thus, potential users of such a system must decide on what type of industrial system would best satisfy their objectives. Although there is a large market for dismantlement and recycling services in the US and overseas, the actual profitability of using COIL for dismantlement is uncertain, preventing potential industrial sponsors from independently supporting it's development. It seems that a large portion of the profits in DD&R are a result of the huge amount of labor required. An industrial COIL system could potentially break the paradigm of such labor-intensive operations and enable dismantlement schedules to be accelerated and costs to be reduced dramatically. Thus, an industrial COIL

could be of great benefit to the U.S. Department of Energy and to U.S. nuclear power utilities, and for similar groups overseas. With mortgage costs of some nuclear weapon production sites, such as Rocky Flats, approaching a million dollars a day, the cost of a COIL prototype could easily be justified if an industrial COIL accelerated the closure of such a site by even a couple of weeks!

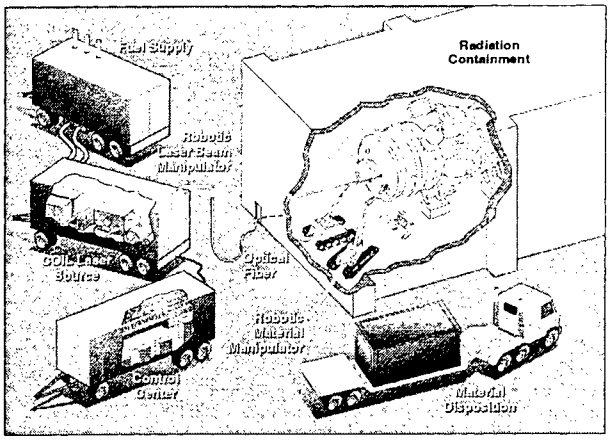


Figure 2 In-Situ Dismantlement with High Power COIL

Fiber delivery of the high power COIL beam is also a critical area for an industrial or dismantlement COIL system. The Air Force has demonstrated delivery of a 7.2 kW COIL beam through a standard industrial 600-micron fiber about a meter long for nearly a minute. Kawasaki Heavy Industries has delivered a 7.0 kW beam through a similar fiber for over 10 minutes.

Schafer has collaborated with Brookhaven National Laboratory to set up a COIL optical fiber beam delivery and cutting test project, under the auspices of the Department of Energy International Proliferation Prevention (IPP) program. This program, which provides funding to former Russian weapon scientists, will provide funds to the Russian Sarov facility to use an existing COIL system to investigate optimal fiber optics beam delivery techniques and do a variety of cutting demonstrations relevant to dismantlement tasks.

Schafer is also working closely with the Intelligent Systems and Robotics Center at Sandia National Laboratory. They have developed robotics systems for dismantlement that can use a variety of end effectors. However, the full advantages of their sophisticated robotic control systems can only be realized with high average power laser beams that can be delivered via fiber optics. Fiber optics delivery is critical for such robotic systems to reduce the moments of inertia of the robotic arms and allow rapid and accurate movements. In addition, the fiber core diameters must be less than 1 mm so that the fiber is flexible enough to withstand small radii of curvature and thus allow more compact robotic systems. Although the robotic systems being developed at Sandia can use a variety of end effectors, high quality, high average power laser beams delivered via optical fiber would allow the rapid, precise cutting that is one of the key advantages of robotics. Many conventional tools would limit those natural advantages of robotics.


1. Perrin, J., "Advanced Cutting Technologies," Proceedings of European Conference on Decommissioning of Nuclear Power Plants, Luxembourg, May 1994.
2. Rocketdyne/ETEC, Canoga Park, CA, "Remote Laser Processing of Radioactive Components," TTP: SF3-5-20-03, U.S. DOE, 1995.
3. NUPEC, Tokyo, Japan, "Verification Tests on Decommissioning Technology for Commercial Nuclear Power facilities," brochure, 1994.
4. Hohman, Edward, "Oversize TRU Waste Laser Cutting Project," DOE National Technology Information Exchange workshop, Las Vegas, NV, Oct 1999.
5. Kosyrev, F.K., et al., "Laser Technology in Atomic Industry," Lasers '99, Quebec, Canada, Dec 1999.

# Requirements for Launching Payloads into Low Earth Orbit with a Ground-based Laser

Claude R. Phipps*[a], James P. Reilly[b] and Jonathan W. Campbell[c]
[a]Photonic Associates, 200A Ojo de la Vaca Road, Santa Fe, New Mexico 87505 USA
[b]Northeast Science and Technology, 117 Northshore Blvd., East Sandwich, MA 02537 USA
[c]NASA Marshall Spaceflight Center, AL 35812 USA

## ABSTRACT

We present results of computer simulations of the launch through the atmosphere of a cone-shaped flyer which demonstrate that laser ablation rockets, using a 1MW ground-based laser, can lift 6kg payloads into low earth orbit. We discuss optimization of delivered mass, mass ratio and energy cost.

**Keywords:** Laser propulsion, pulsed lasers, laser-produced impulse, laser ablation

## 1. INTRODUCTION

The way we now send things to space is very expensive. Present day costs of raising mass from the Earth's surface into low Earth orbit (LEO) with chemical rockets is at least $10,000/kg [Table 1]. This cost dominates all other considerations relating to spaceflight, limiting what we consider to be possible today. But it need not be so. In 1972, Kantrowitz[4] suggested using a remote laser to heat a propellant and produce an ablation plasma jet for thrust, which is the principle of laser ablation space propulsion.

**Table 1:** Present Day LEO Launch Costs

| Launch System | Minimum Cost (k$/kg) | Ref. |
|---|---|---|
| Rockot | 10 | 1 |
| Shuttle | 12 | 2 |
| Athena 2 | 12 | 3 |
| Taurus | 20 | 1 |
| ISS, commercial | 22 | 3 |
| Pegasus XL | 24 | 1 |
| Long March CZ-2C | 30 | 1 |
| Athena 1 | 41 | 1 |

Myrabo and Raizer[5] and Myrabo *et al.*[6] described an air-breathing, laser-driven aerospike flyer or "Lightcraft". This flyer has a very specific design featuring light concentration near the rim of a frisbee-like shape that provides thrust from laser supported detonations in air. A pure-ablation version of this flyer has flown to altitudes of 39m using a ≈20kW laser[7]. Bohn[8] has reported flying a wire-guided parabolic device to a height of a few m in the laboratory. Phipps and Michaelis[9] showed that there is an optimum set of parameters for laser space propulsion which can reduce the cost of lifting mass to LEO 100-fold. This paper is a review of the problem of optimizing the performance of laser-driven Earth-to-LEO spacecraft. Our approach to the problem is to consider the three basic functions of light collection, light concentration and steering to be conceptually and physically separate, so that each can be optimized without arbitrary limits arising from coupling to the other functions, rather than from basic physics.

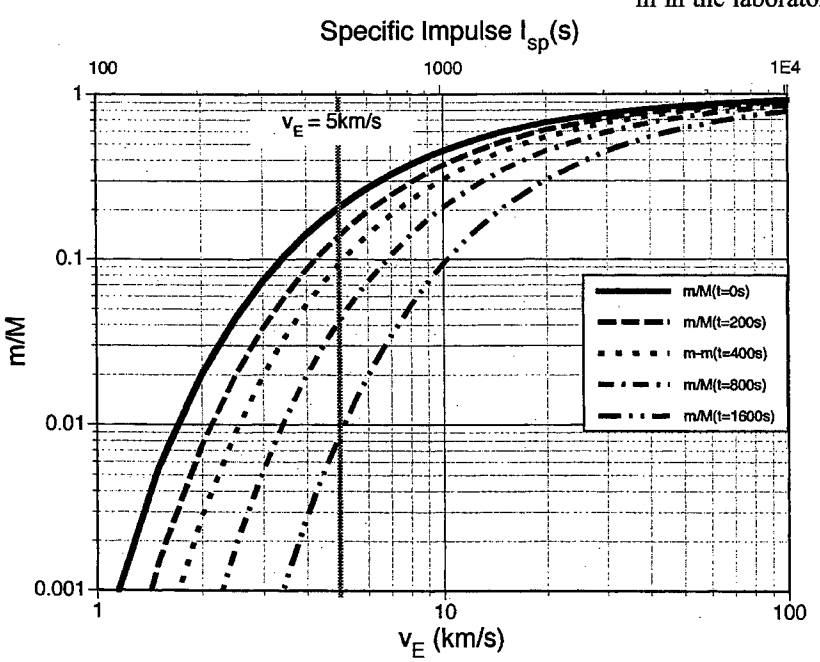


**Figure 1.** Ratio of mass m delivered to low Earth orbit (LEO) to initial mass M, vs. exit velocity $v_E$ or specific impulse, in vacuum. For chemical rockets with $I_{sp} \approx 500$s, long flights are disastrous for this ratio,but, for a very hot exhaust, such as is available with laser ablation, flight time doesn't matter very much.

## 2. LASER ABLATION PARAMETERS

The momentum coupling coefficient $C_m$ is defined as the ratio of target momentum $m\Delta v$ produced as the ratio of target momentum to incident laser pulse energy W during the ejection of laser-ablated material (the photoablation process). By convention, this ratio is expressed in mixed units:

$$C_m = \frac{m\Delta v}{W} \quad \text{dyn-s/J} \qquad (1)$$

In the ablation process, Q* joules of laser light are consumed to ablate each gram of target material:

$$Q^* = \frac{W}{\Delta m} \quad \text{J/g} . \qquad (2)$$

*Correspondence: email: crphipps@aol.com;Phone/Fax 505-466-3877

XIII International Symposium on Gas Flow and Chemical Lasers and High-Power Laser Conference,
Antonio Lapucci, Marco Ciofini, Editors, Proceedings of SPIE Vol. 4184 (2001)

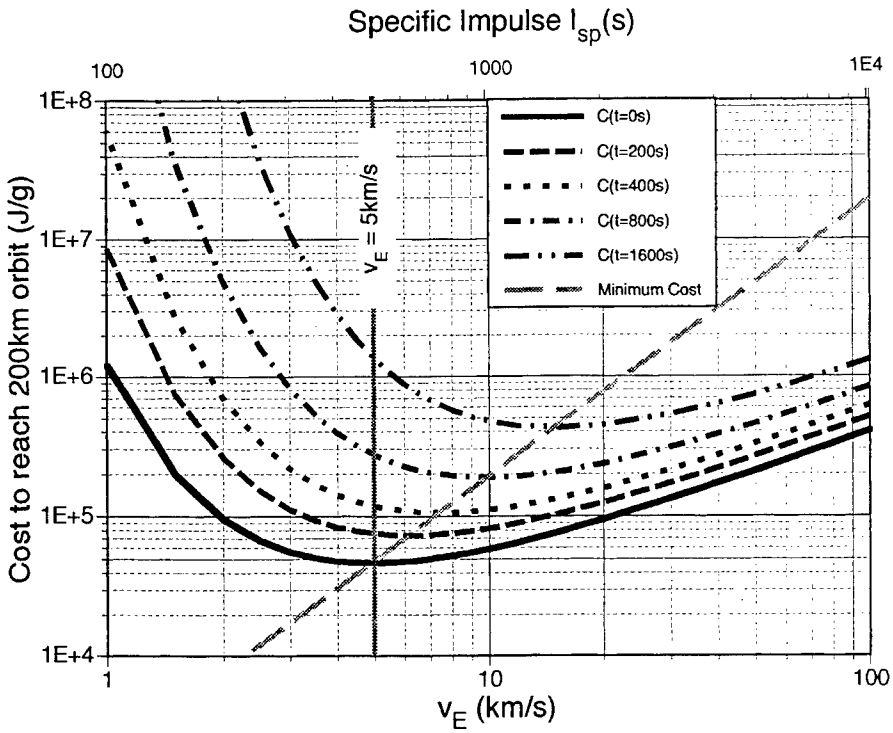


**Figure 2.** Cost in joules per gram delivered from the ground to a 200km altitude orbit against gravity in vacuum, versus exit velocity $v_E$ for various flight times. Long-duration flights to LEO require high exit velocity to be cost-efficient.

For a monoenergetic exhaust stream, given these definitions, and since

$$m\Delta v = \Delta m v_E , \qquad (3)$$

momentum conservation requires that the product of $C_m$ and $Q^*$ is the effective exhaust velocity $v_E$ of the laser rocket, independent of the efficiency with which laser energy is absorbed. This is simply related to the specific impulse $I_{sp}$:

$$C_m Q^* = v_E = g I_{sp} \quad \text{cm/s.} \qquad (4)$$

In the following, we will describe a monoenergetic exhaust stream with velocity $v_E$. Real exhaust streams have a velocity distribution, but the error associated with the monoenergetic approximation does not introduce large errors for laser-produced plasmas.[6] Energy conservation of energy prevents $C_m$ and $Q^*$ from being arbitrary. Increasing one decreases the other. Using Eqs. (2) – (4), we see that several constant product relationships exist:

$$2E7\ \eta_{AB} = \Delta m v_E^2/W = C_m^2 Q^* = g C_m I_{sp} = C_m v_E. \qquad (5)$$

In Eq. (5), $\eta_{AB} \leq 1$ is the efficiency with which laser energy W is converted into exhaust kinetic energy, and the factor 1E7 occurs only because of the units in which the quantities are defined. Choosing combinations of $C_m$ and $Q^*$ which exceed the limit expressed in (5) violates physics, since the errors involved in the monoenergetic approximation underestimate $\eta_{AB}$. The rate of mass usage is

$$-\dot{m} = \frac{P}{Q^*} \quad \text{g/s} \qquad (6)$$

where P is laser power in watts, so, when considering $C_m$ and $Q^*$ as design variables it is important to realize that the lifetime of the ablator increases with $Q^*$ and decreases very rapidly with increasing $C_m$:

$$\tau_{AB} = \left|M/\dot{m}\right| = \frac{MQ^*}{P} = \frac{2E7\,\eta_{AB} M}{P C_m^2} = I_{sp}/\beta \qquad (7)$$

and increasing $C_m$ to get more initial lifting power through the relationship

$$F \equiv -\dot{m} v_E = -\dot{m} g I_{sp} = P C_m \equiv \beta M g \qquad (8)$$

at launch from a given laser entails a serious penalty for ablator lifetime, because, from Eq. (7), $\tau_{AB} \propto 1/C_m^2$. Although a lot of mass can be lifted with high $C_m$, the ablator will be used up before reaching orbit (or the end of the mission). In Eqs. 7 and 8, $\beta$ is the acceleration at liftoff. Since the maximum specific impulse of ordinary chemical rockets is about 500 seconds, limited by temperatures available in chemical reactions, exit velocity $v_E > 5E5$ ($I_{sp} > 5000$s) is accessible only by laser ablation or some other non-chemical process such as ion acceleration. Specific impulse $I_{sp}$ up to 8000s has been measured in KrF-laser ablation of aluminum[6]. It is clear that there may be optimum values of $C_m$, $Q^*$ and their product $v_E$ for launch into LEO, given a desired outcome. The three outcomes evaluated are: a) Lowest possible cost C=W/m (J/g) of mass delivered to LEO, b) Maximum mass m delivered to LEO independent of cost C and ground mass M, and c) Maximum ratio m/M of mass surviving to LEO to ground mass M, regardless of cost.

**Table 2.** Comparison of Three Laser Wavelengths
[Strehl = 0.5, range = 800km, 95-cm spot at range]

| Laser λ | 1MW Available? | Coupling | Aperture dia. Db(m) | Adaptive Optics |
|---|---|---|---|---|
| 11.1μm | Yes | Good | 30 | Minimal |
| 1.32μm | Maybe | Good | 3.7 | Substantial |
| 530nm | No | Good | 1.5 | Difficult |

## 3. OPTIMIZATION INCLUDING VACUUM AND GRAVITY

For a laser ablation rocket, the rocket equation is

$$\frac{m_I}{M} = \Gamma \exp\left[-\left(\frac{\Delta v + g t_I}{v_E}\right)\right] \tag{9}$$

where M is the initial mass, $m_I$ is the mass inserted into orbit, g the acceleration of gravity (constant near Earth), $t_I$ the time from launch to insertion, $v_E$ is exhaust velocity, $\Delta v = v_I$ is the net change in velocity required for the flight, and $\Gamma$ is a factor related to insertion efficiency which is never larger than 1.02 in practical cases. Eq. (9) shows that, in vacuum, optimizations (a) – most mass delivered to orbit and (b) – the best ratio of mass in orbit to mass on the ground is achieved for $v_E = \infty$, or $C_m = 0$ [Figure 1]. To treat optimization (c) – the energy cost optimization in vacuum – we note that the laser energy W expended in the flight is, by definition,

$$W = \Delta m Q^* = \Delta m\, v_E / C_m \tag{10}$$

Energy cost for a laser-driven flight in space is defined as joules per gram of mass delivered at the end of mission:

$$C = \frac{W}{m_I} = \left[\frac{(1 - m_I/M)}{(m_I/M)}\right] Q^* = \frac{v_E}{C_m}\left[\exp\left(\frac{\Delta v + g t_I}{v_E}\right) - 1\right] \tag{11}$$

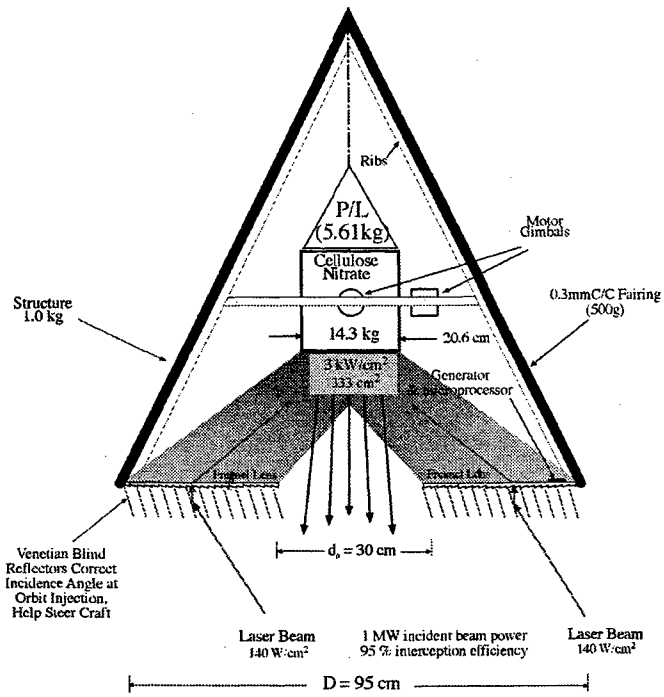


**Figure 3.** Flyer concept requires 3kW/cm$^2$ (average) on ablator for takeoff thrust. "Venetian blind" reflectors correct incidence on Fresnel lens during flight, help steer craft by shifting illumination on ablator. Some steering provided by gimbals. "P/L" is 5.61kg true payload. Maximum 140W/cm$^2$ on Fresnel lens with a 1MW laser beam sets 95cm diameter. "Heavy" 20-kg, flyer is illustrated.

There is an optimum exhaust velocity $v_E$ for which the cost C is minimized. To find it, let $x = v_E$, $b = 2E7\ \eta_{AB}$, and $a = (\Delta v + gt)_2$ so that Eq. (11) becomes

$$C = \frac{x}{b}\left[\exp(a/x) - 1\right] \tag{12}$$

Then setting dC/dx = 0 gives an optimum value of a/x:

$$\frac{a}{x} = -\ln\left[1 - \frac{a}{2x}\right] \tag{13}$$

a transcendental equation for which the solution is:

$$\frac{a}{x} = \left(\frac{\Delta v + gt}{v_E}\right) = 1.59362 \tag{14}$$

Eq. 14 is a result obtained for standard rockets by Möckel[10] in 1975. In the absence of gravity or for short flights to LEO such that t<<800 seconds [$\Delta v$ = 7.8E5 cm/s], the optimum exhaust velocity $v_E = 0.6275\Delta v$ = 4.9 km/s. Given Eq. (5), the corresponding coupling coefficient for optimum energy cost in this circumstance is $C_{mopt} = 41\eta_{AB}$ dyn-s/J. Plasma temperature adequate to produce this $v_E$ are achievable by pulsed lasers and, with difficulty, by CW lasers. From Eq.(9), the payload ratio at this optimum a/x is m/M = 0.203, however long the flight takes, so long as ($\Delta v$+gt)>0 and bearing in mind that $v_E$ and energy cost both have to adjust upward as t increases to maintain a/x at its optimum value. For comparison, m/M for the Shuttle is 0.0479, considering the entire Shuttle plus a 55,000 lb. payload to be the mass m. Figure 2 shows the predictions of Eq. (11), illustrating how steeply the cost penalty rises on the low side of the optimum value for $v_e$, and how the optimum shifts to larger $v_E$ for longer flights. Figure 2 shows that low velocity to orbit entails a penalty for mass delivery and energy cost. On the other hand, high velocity in the atmosphere leads to unacceptable drag losses. There is an additional optimum to find – for velocity – in the lower atmosphere. We developed an analytical solution for this optimization. We also developed a computer code to simulate flights through the atmosphere using the optimum velocity profile.[12]

## 4. THE FLYER

Figure 3 shows the cone-shaped flyer design we employed for simulations. A cone shape was chosen for the flyer because drag coefficients are well known for that shape. This choice also facilitated optimization of diameter to length (D/L) ratio. The need

**Table 3.** Launch Procedure

1. Start at 30 – 35km
2. Initial acceleration 1 – 2G's – not more– to avoid unnecessary drag and approximate the conditions on $\alpha$ and $\beta$ dictated by the optimization.
3. Start at 90° elevation angle (vertical flight) until radial velocity $v_r \approx 0.3$ km/s, then gradually roll over to 50 – 60°until $v_r \approx 1.2$ km/s.
4. Turn off the laser, coast down to $v_r \approx 0.8 - 0.2$ km/s, the magnitude depending on $C_m$.
5. Rotate flyer to horizontal
6. Reapply laser to reach orbit insertion with $v_r = 0$.

for this optimization arises from the competing interests of reducing drag – minimized for a slender flyer – and maintaining the center of thrust ahead of the center of drag, a choice which leads to a short, squat shape.

## 5. FLIGHT SIMULATIONS

We simulated flights of a 20-kg "heavy" flyer and a 10-kg "light" flyer. The heavy flyer is very efficient but requires more than one laser station along its route because of unfavorable elevation angle with respect to a single station at the end of powered flight. The light flyer is less efficient but gets to LEO quickly with good elevation angles. Dramatic advantages accrue from launching laser driven rockets bound for LEO from an initial altitude of 30 – 35km as illustrated in Figure 4. One relatively inexpensive way of doing this is to use a high altitude balloon as a launch platform. Reaching 35km altitude in this way is not difficult. Table 3 shows the launch procedure used in flight simulations. Figure 4 (upper) shows how the collection of simulated flights support the theory for optimizations a), b) and c) – that is, mass, mass ratio and cost. Mass delivered to orbit independent of cost optimizes at $C_m$ = 20 in air. This is somewhat different from results of vacuum theory [see discussion at Eq. (15), in that the optimum $C_m$ has shifted to a lower value, corresponding to the requirement for a higher Q* to permit taking more time to move through the lower atmosphere so as to avoid unacceptable drag losses. As predicted by theory, the ratio m/M is optimized for the lowest possible $C_m$ [corresponding to the highest exhaust velocity or $I_{sp}$]. Figure 4 (lower) shows that the results of simulated flights compare well to vacuum cost predictions.

## 6. CONCLUSIONS

We have shown that a 1MW laser can deliver 6kg to low Earth orbit in about 700 s. With optimum flight profiles, it costs about 100kJ/g to put mass in LEO. Other work supports this statement[9].


## ACKNOWLEDGMENTS

The authors are grateful for useful discussions and ideas from Mike Lander, Anteon Corporation, Dayton, OH; Prof. Max Michaelis, University of Natal; and especially Prof. (Emeritus) Arthur Kantrowitz, Dartmouth College, founder of AVCO Research Laboratory. Support was provided, in part, by NASA Marshall Spaceflight Center.


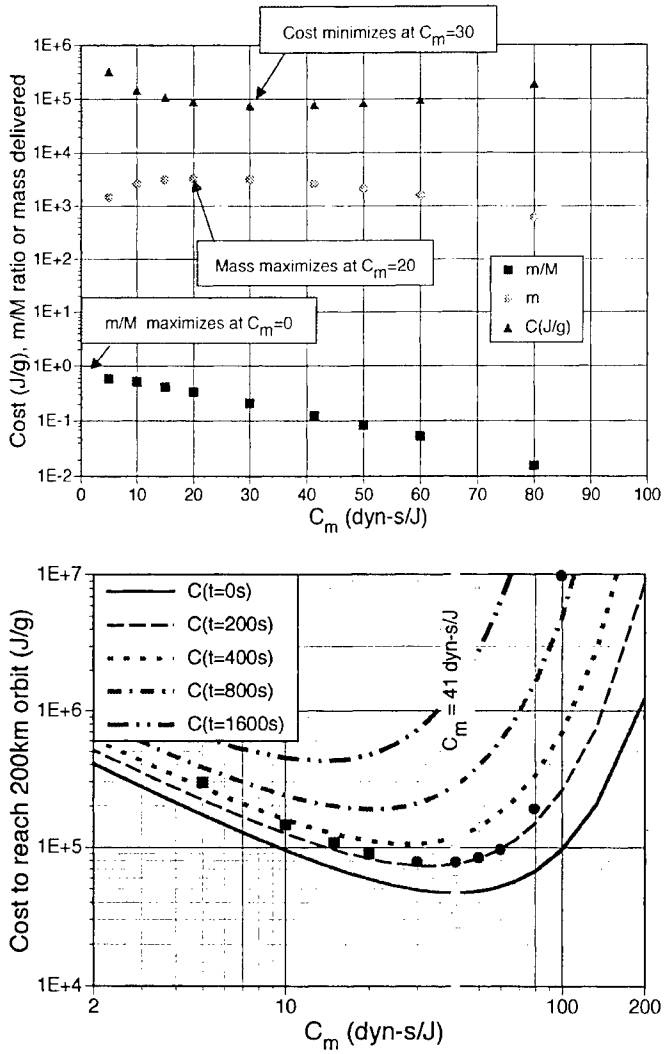


**Figure 4. (Upper plot)** Results of simulated flights confirm analysis, showing that mass, mass ratio and cost optimize at different values of $C_m$. As theory predicts, m/M maximizes at $C_m$=0 ($v_E$=∞), m maximizes at $C_m$=20 ($v_E$=10km/s) and energy cost C minimizes at $C_m$=30 dyn-s/J. Here, we assume $\eta_{AB}$=1, so exit velocity is then $v_E$=2E7/$C_m$. Laser power was 1MW. **(Lower plot)** Shows how well simulated flight efficiency with elevated launch altitude matches optimum theoretical cost to orbit in vacuum. Round spots: flight times t≈200s, square spots: t≈400s. Launch mass M ranged from 2.5 to 51 kg to match the $C_m$ chosen. Launch altitude =35km, D=95 cm.

## REFERENCES


1. CORNARA, *et al.* , "Satellite Constellation Launch, Deployment, Replacement and End-of-life Strategies", paper SSC99-X-1, *Proceedings of AIAA Conference on Small Satellites Utah State University* (1999)
2. U.S. CONGRESSIONAL BUDGET OFFICE, *Analysis of Shuttle Launch Costs* (1993)
3. *Spaceviews,* 6 March, 2000
4. Kantrowitz, *J. Aeronaut. Astronaut.* **10,** 74 (1972)
5. Myrabo, L.N. and Raizer Yu. P., *AIAA Plasmadynamics and Lasers Conference, Colorado Springs, Paper 94-2451* (1994)
6. Myrabo, L. N., Raizer, Yu. P. and Schneider, M. N., *High Temperature* **36** no. 2 pp. 287-292 (1998)
7. Myrabo, L. N., *Proc. Santa Fe High Power Ablation Conference 2000* **SPIE 4025** (2000)
8. Bohn, W., *Proc. SPIE Symposium on Advanced High Power Lasers and Applications, Institute for Laser Engineering, Osaka* **SPIE 3885** (1999)
9. Phipps, C.R. and Michaelis, M. M. *J. Laser and Particle Beams* **12** no. 1, pp. 23-54 (1994)
10. Möckel, W.E. *J. Spacecraft and Rockets* **12,** pp. 700-1 (1975)
11. Kantrowitz, A., *Proc. Santa Fe High Power Ablation Conference* **SPIE 3343** (1998)
12. Phipps, C. R., Reilly, J. P. and Campbell, J. W., "Optimum Parameters for Laser-launching Objects into Low Earth Orbit", *J. Laser and Particle Beams,* **18** no. 4 (2000) to be published

# Artistic processing on acrylic materials using a segmented pixel drawing method with a slab, RF excited $CO_2$ laser

Hajime EBISUTANI *, Noriyo SAKURADA *, Yoshio ISHII,
Kazuhiro WATANABE, and Yuzuru KUBOTA

Department of Information Systems Science, Faculty of Engineering, SOKA University, Tokyo, Japan.
Mailing Address: 1-236, Tangi-cho, Hachiouji-shi, Tokyo 192-8577, JAPAN.

## ABSTRACT

There have been various processing methods such as marking, masking, and rapid prototyping system have been typically known as an attractive application of high power laser based on single stroke drawing.

We have proposed a segmented pixel drawing (SPD) method which creates a surface by laser in a segmented pixel-base, in which various surface effects can be given such as fluent, opaque, and rugged tones. This can be referred to as a digital way of display.

Experiments of SPD method were performed on acrylic surfaces by the pixel processing base with a pixel size of 2mm×2mm. The pixel patterns in this study were variously demonstrated by means of the varied density of the dot-matrix. From the degree of transparency of produce SPD pixels, visual effects of surfaces were analyzed to evaluate gray-scaled tones of produced pixels. The proposed method based SPD would offer a new possibility to realize more sophisticated sculpture on acrylic surfaces supported by visual effects using image information.

In addition to the SPD, coloring on acrylic surfaces has been successfully made using the $CO_2$ laser. This coloring process was performed based on a heat effect due to $CO_2$ laser irradiation on acrylic materials, the surface of which was exposed with a dye-containing liquid sheet flow.

**Keywords:** Slab $CO_2$ laser, Scanning system, Laser processing, Artistic sculpture, Pixel drawing, Coloring for acrylic board, SPD method

## 1. INTRODUCTION

Many methods of sculpture using a laser which are based on marking, masking[1], and rapid prototyping system[2] are presently well known. These have some features such as a processing capability of the large area and high accuracy, high efficiency of the processing time, and the processing of three dimensions. These methods have an inconvenience to handle pixel data of images. In this study, we propose a method named segmented pixel drawing[3]. The segmented pixel drawing method is an attractive processing method which can demonstrate image expression corresponding to pixels of the image data. In this method, a sculpture surface to be presented is created by laser in a segmented pixel-base in which various surface effects are given such as fluent, opaque, and rugged tones. This can be referred to as a digital way of display. A coloring method for acrylic board surfaces using a $CO_2$ laser has also been proposed.

## 2. THE SEGMENTED PIXEL DRAWING METHOD

Segmented pixel drawing (SPD) method has been proposed in our laboratory to produce a variety of surface presentation effects for sculptures. For this method, a high speed x, y, and z-beam scanner has been introduced with a slab, RF excited $CO_2$ laser to produce focused / defocused beam conditions. The operational mode of the slab laser producing about 30～100 W of the averaged powers are also controlled in terms of the frequency and duty cycle together with the scan speed of the scanner system. The laser beam is scanned in such a way to produce a pixel consisting of dots pattern on a processing field. Using these systems, various shapes and tones of surfaces have been successfully explored to make more artistic sculptures.

## 3. COLORING ON ACRYLIC BOARDS

It has been interestingly found that acrylic surface can be colored with $CO_2$ laser irradiation. When the laser beam is scanned with a proper scanning condition on an acrylic material surface on which a thin liquid layer containing a dye is flown, only a laser irradiated region can be interestingly colored by the heat effect due to laser beam. Acrylic materials can be usually colored by being immersed in a heated dye-containing liquid bath whose temperature is more than about 50°c. With the aid of laser heating proposed in this study, flexible color printing would be demonstrated when more detailed coloring conditions are found associated with the scanning parameters and dye liquid flow.

Correspondence: E-mail address: hebisuta@edu.t.soka.ac.jp; Telephone: +81(426) 91-8030; Fax: +81(426) 91-9312
*Graduate student

XIII International Symposium on Gas Flow and Chemical Lasers and High-Power Laser Conference,
Antonio Lapucci, Marco Ciofini, Editors, Proceedings of SPIE Vol. 4184 (2001)

## 4. EXPERIMENTAL SETUP AND PROCEDURE

### 4.1. Experimental setup of laser process

Figure.1 represents an experimental setup. A personal computer controls the RF power supply, Z axis lens, and X-Y axis mirrors through a scanning controller. The RF power supply can be controlled in terms of the duty cycle and the frequency. The averaged power of laser is affected by these parameters. The Z-axis lens controls focus / defocus conditions, whereas X-Y axis mirrors controls the scanning pattern and speed. We used an RF excited, slab carbon dioxide laser which is a very compact laser medium with a very good beam quality developed in our laboratory[4]. The attractive features of the slab $CO_2$ laser can be found in the capability of producing a moderate power level of 100-200 W with a high beam quality from a compact laser head. The laser system using our experiment consists of an RF power supply which is capable of producing a maximum RF power of 2 kW at 100 MHz, an laser head made by aluminum, a gas handling system that pump out an air and supply a mixed gas of $CO_2$, $N_2$ and He in a rate of 1:1:3 in the laser head, a cooling system using water, and personal computer with a control electronics which measures and controls for these above mentioned systems.

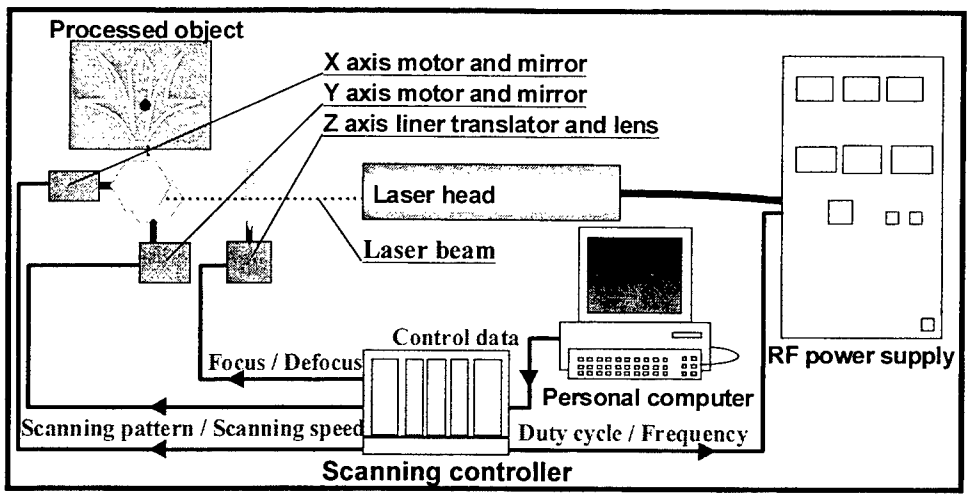


**Figure 1.** Experimental setup for laser processing

### 4.2. Optics

Optics and the focus / defocus conditions are illustrated to Fig.2. Laser beams from the laser head pass through a beam splitter, cylindrical lens, Z axis convex lens, objective convex lens, X axis mirror, and Y axis mirror, toward target object to be processed. The Z axis lens, which moves along the optical axis in the range of 10 mm at maximum so as to controls diameter of laser beam on the target. The beam waist of the focus varies in the position of the z axis lens. The maximum is 0.34mm, and the minimum is 0.17mm.

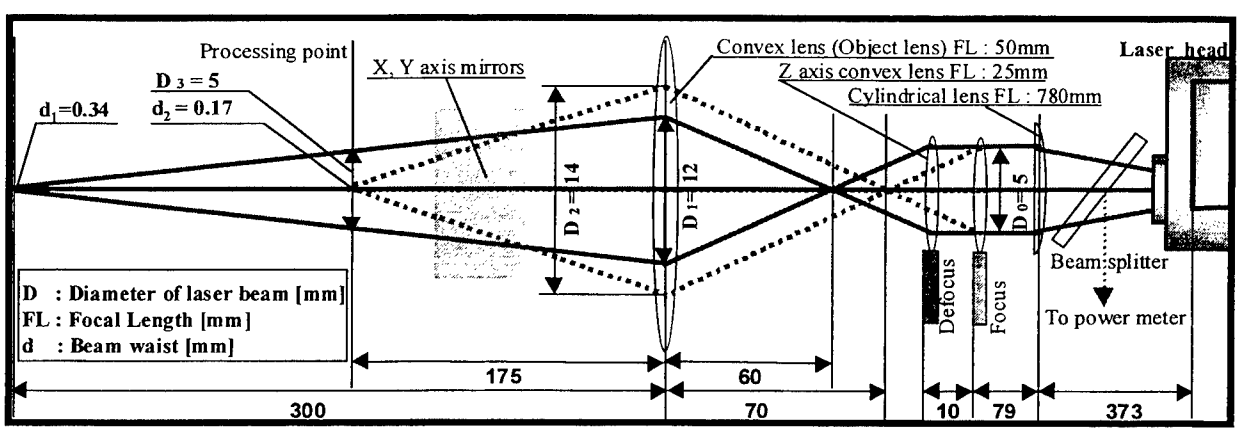


**Figure 2.** Optical concept of focus and defocus

### 4.3. Preliminary experimental setup of coloring on acrylic boards

Figure.3 represents an experimental setup of coloring for acrylic boards. Temperature of the dye liquid was set up at about 40°c. The concentration of the dye was about 15%. A pump was used to circulate the dye containing liquid on an acrylic material to be colored in the form of a thin liquid sheet. The dyes used in this experiment were of blue and black colors. A defocused beam with about 23W/cm$^2$ of the total laser power was scanned with the defocused beam spot of a 7mm×9mm oval shape. This beam was scanned along a 9×9mm-square with having a proper heating condition for the preliminary coloring experiments. In this experiment, coloring has been obtained with the laser exposures of 2, 4, and 6 min. during which many of the square scanning was repetitively performed with a scanning speed of 2.1 second per one square.

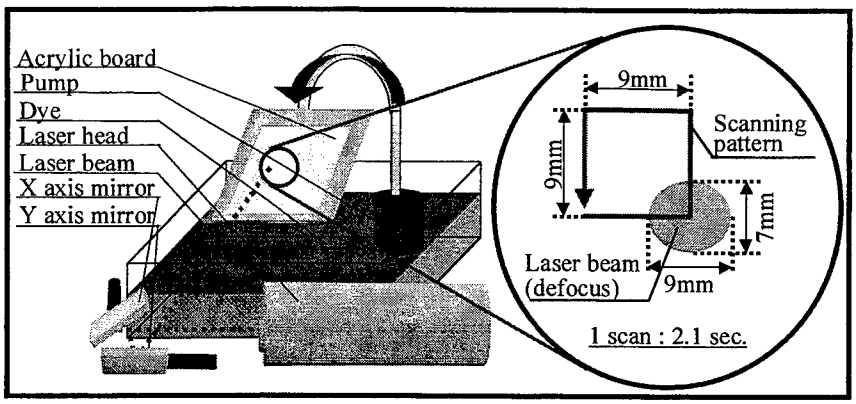


**Figure 3.** Preliminary experimental setup of coloring on acrylic boards using a $CO_2$ laser

## 5. RESULTS AND DISCUSSIONS

### 5.1. Gray-scale of pixel patterns

A 10-gray-scaled pixel representation by the SPD method is shown in Fig.4. The experiments method were performed on acrylic surfaces by the pixel processing base with a pixel size of 2mm×2 mm. From the degree of transparency of produce SPD pixels, visual effects of surfaces were analyzed to evaluate gray-scaled tones of produced pixels. The pixel patterns in this study were variously produced by means of the varied density of the dot-matrices which are 7×7, 9×9, 13×13, and 17×17. A distance between the dots in one pixel is uniform. The power of one dot is varied by the pulse frequency and the duty cycle of the laser. The processing time of a single pixel was less than 1.2 seconds. The degree of transparencies were demonstrated as a 10-gray-scale, depending on the combination of such pixel parameters as the number of dots, the power of one dot, and the processing time.

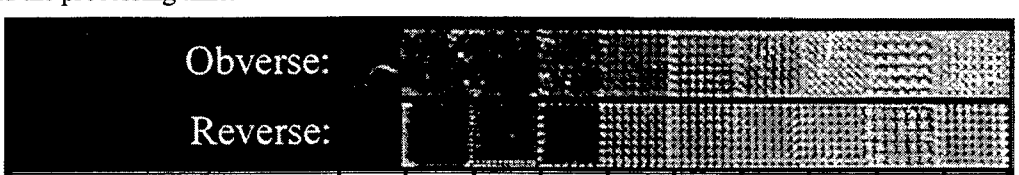


| | | | | | | | | | | |
|---|---|---|---|---|---|---|---|---|---|---|
| Degree of transparency [%] | 100 | 98 | 96 | 93 | 90 | 87 | 84 | 79 | 73 | 71 |
| Number of dots | 0 | 289 | 169 | 81 | 81 | 81 | 81 | 81 | 49 | 81 |
| Power of one dot [J] | 0 | 0.014 | 0.016 | 0.02 | 0.03 | 0.05 | 0.07 | 0.14 | 0.33 | 0.24 |
| Processing time [second] | 0 | 0.3 | 0.2 | 0.1 | 0.2 | 0.4 | 0.4 | 1.2 | 0.9 | 1.2 |

**Figure 4.** Experimental results of SPD method

### 5.2. Processing sample

Figure.5 shows a processed sample which was processed using a 10-gray-scale of SPD method. The 10-gray-scale picture is created based on an original image of 256-gray-scale image data. The picture of SPD results is sculptured by 28×28 pixels. In this way, SPD method can make visual effects that might be difficult to be made by conventional processing method.

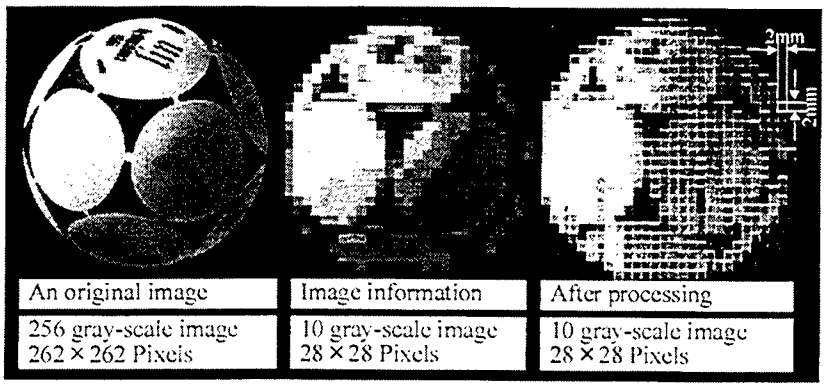


**Figure 5.** Sample of the SPD method

### 5.3. Results of coloring on acrylic boards

Figure.6 shows preliminary experimental results of coloring for acrylic boards. From these results, it is understandable that the longer the laser exposure time on the acrylic boards, the deeper they were colored. In this experimental condition, coloring in black seems to be more efficiently made than in blue. The surface of acrylic boards was not abraded but was colored by laser beam. Because of the use of the defocused beam and the non-uniform liquid layer in its thickness, the obtained results of the coloring shown in Fig.6 shows the lack of coloring uniformity. These problems will be improved by finding a proper condition for the preparations of uniform this liquid layer and the laser irradiation techniques. Using this coloring principle, flexible laser coloring will be realized.

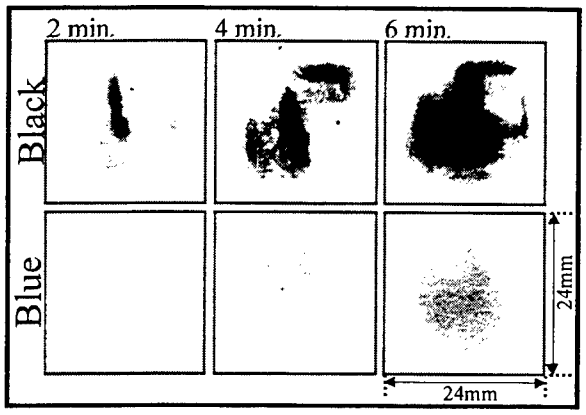


**Figure 6.** Preliminary experimental results of coloring on acrylic boards using the $CO_2$ laser

## 6. CONCLUSIONS

In this study, we proposed the new methods of the sculpture using a $CO_2$ laser. With the SPD method, the processing which directly uses the image data is possible. The proposed method based on the SPD would offer a new possibility to realize more sophisticated sculpture supported by visual effects using image information. Coloring process was successfully performed based on a heat effect due to $CO_2$ laser irradiation on acrylic materials. It is interesting that the acrylic boards were colored on their surfaces without surface abrasion. It will be possible that the acrylic boards could be colored in a more impressive way by laser scanning corresponding to the color data of pictures. Combining the SPD method and the coloring technique, more sophisticated acrylic sculpture could be demonstrated which is one of exploitation of laser processing application.

## REFERENCES

1. The Laser Society of Japan ed., LASER HANDBOOK, OHMSHA, 1982.
2. P. F. Jacobs, Rapid Prototyping & Manufacturing, Society of Manufacturing Engineers, 1992.
3. N. Sakurada, Y. Ishii, H. Ebisutani, K. Watanabe, and Y. Kubota, "A segmented pixel drawing method using a slab, RF excited $CO_2$ Laser for artistic sculpture," Proceedings of SPIE Vol.3887, 1999, pp.349-356.
4. K. Watanabe, "Performance Characteristics of a Slab RF-Excited $CO_2$ Laser," the Review of Laser Engineering, Vol. 21, No. 12, pp.1245-1254, 1993.

# Thin stainless steel sandwich structural panels all welded by laser technology: Residual Stresses Measurements by the Hole - Drilling Strain - Gage Method

G. Daurelio [1*], V. La Tegola [2**], C. Pappalettere [3**], E. Valentini [4***]

* CENTRO LASER S.c.r.l. - Centro Ricerche, Str. Prov. per Casamassima, Km. 3 - 70010 Valenzano (BARI), ITALY

** DIP. DI PROGETT. E PRODUZ. IND., Politecnico di Bari, V.le Japigia, 182 - 70126 BARI, ITALY

*** SINT Technology S.r.l., Via Giusti, 243 - 50041 Calenzano (FIRENZE), ITALY

## ABSTRACT

This paper reports the results obtained by using a measuring system concerned automatically residual stress by Hole-Drilling Strain Gage Method, in depth, on thin stainless steel sandwich structural panels all laser welded. Different corrugated cores, core geometries (usually trapezoidal ones), face thickness, welding parameters and methodologies (spot or continuous ones) have been carried out.

**Keywords:** sandwich structural panels, laser welding technology, metal sandwich technology, welded steel panels, all laser welded honeycomb structures, corrugated cores steel panels, residual stresses, hole-drilling method.

## 1. INTRODUCTION

This paper reports the results obtained by employing materials such as austenitic stainless steel (AISI 304) sheets, with different face thickness and core geometries, usually some trapezoidal ones.
A ROFIN SINAR C.W.$CO_2$ laser has been used as a fast axial flow source and a continuous wave 1500 W max power level to weld the many bases of the corrugated cores to the external faces has been utilised.
Four different constructional solutions, for the preparation of some new modular structural elements, with one or two beads for each welded base, have been experimented.
Each modular structure has sizes 300 mm wide, 700 mm length and 60 mm height.
After studying many different mechanical clampings, the best one has been realised. So, eight different constructional solutions and different operative sequences of the welds have been made.
All this for evaluating the effect of the weld sequence on the distortion of the panel and for obtaining different localisation of the residual stresses on the structural element. A measuring system concerning the automatically evaluation of residual stress distribution in depth by Hole-Drilling Strain-Gage Method is presented. The system makes it possible to use innovative test procedures, that allows measuring errors to be reduced, more complete results and test repeatability.

## 2. EXPERIMENTAL APPARATUS

### 2.1 Restan system

The system represents an evolution in the equipment available today for evaluation of residual stresses with The Hole-Drilling Strain Gage Method. It is a semi-destructive technique, in which residual stresses are evaluated by measuring the relaxation in the inspected area, which take place consequent to the drilling of a blind or a trough hole. The objective achieved with this system is that of simplifying, automating and computerizing a certain number of operations employed in the strain gage rosette method for which operator action was previously indispensable, and thus providing easy and

XIII International Symposium on Gas Flow and Chemical Lasers and High-Power Laser Conference,
Antonio Lapucci, Marco Ciofini, Editors, Proceedings of SPIE Vol. 4184 (2001)

complete control of testing. In particular, the operations having the greatest impact on accuracy and reliability of evaluation of residual stresses have been taken into considerations, among them:

- centring of the drilling axis with the centre of the strain rosette
- automatic identification of the dimension of the hole at the start of drilling and measurement of the depth of the hole at each drilling step
- automatic drilling of the hole with specified increments and measurement of the relaxed strains
- measurement of the diameter of the hole and its eccentricity, if any.

The automation and simplification of these operations offers significant advantages, the most important of which is that it enables numerous strain readings to be made with great precision, in the depth of the hole. This requisite is indispensable for measuring the behaviour of residual stresses through the thickness of the specimen.
Another innovative characteristic is the "overhung" architecture of the system, allowing it to be utilized on components or structures where access to all sides is impossible.

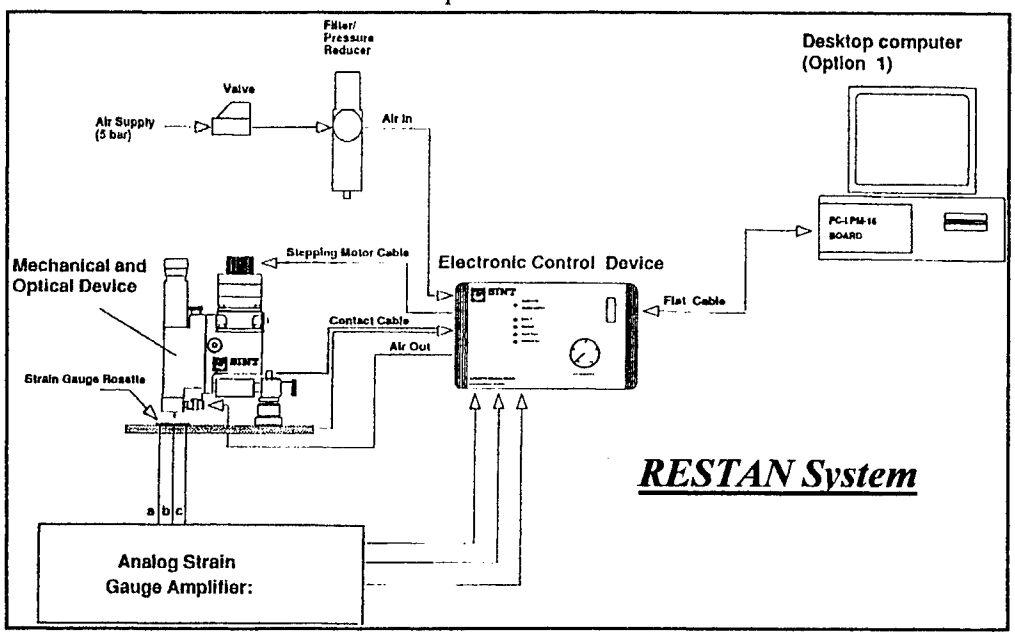


Fig.1 Instrumentation layout

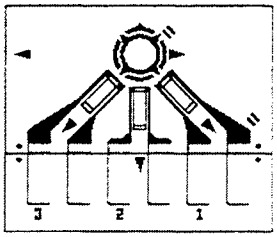


Fig.2 Strain gage adopted

The system consists of:

- Equipment for positioning and drilling (Mechanical and Optical Device)
- Control unit (Electronic control unit)
- I/O card PC-LPM-16 produced by National Instrument
- Three channel analog strain gage amplifier
- Filter /Pressure reducer

### 2.2 Strain gage

For strain relaxation measuring during drilling step, a Micro Measurement strain-gage rosette has been chosen. Its designation is: CEA-06-062UM-120. It is a specific for residual stresses measuring rosette, with three grids disposed at 0° 45° 90° and 0.62" long. The grids centreline diameter is 0.202". The 0° 45° 90° rosettes are more sensible to eccentricity of the hole, if any and as a consequence can give more measuring errors. However, it has been chosen to adopt this kind of rosettes, because it was necessary to measure at proximity of very narrow welding beads.

## 3. THE MATERIALS: ALL LASER WELDED SANDWICH MODULAR PANELS

These are sandwich modular panels realized with austenitic stainless steel AISI 304, all laser welded with structural properties, realized under the growing demand of structural elements which combine strength and lightness. In particular these panels were designed and realized to be utilized principally in civil and high speed transports field, in naval offshore platform field and for the production of railway wagon flatcars. The laser welding of thin ferrous rolled sections seems to be of higher quality than conventional ones (TIG, MIG, arc welding, etc). The welding process is of autogenously kind with a limited and localized specific thermal supply. So it allows obtaining weldments with high quality and dimensional control without any next finish machining. At first, some different geometrical solutions have been set, in any case panels was formed by two external steel plates, with different thickness and by an internal element, always a steel plate, with trapezoidal geometry. Then, actual arrangement has been reached. About the assembling process, all the parts of the panel are joined through laser welding. Also in this case, many alternative solutions have been set.

Panel dimension are: *width - 300 mm, length - 700 mm, height - 60 mm.* About the internal element, the trapezoidal shape is obtained by knife-forming.

For the panel welding, a $CO_2$ laser source has been utilized. It emits an infrared radiation with 10.6 mm wavelength. The interaction between the focused laser beam and the metal surface produces melting and a partial and very low material vaporization originating a welding bead with a section similar to a "nail". Welding of this kind need no weld material and generally show a limited Heat Affected Zone. In this case the HAZ does not exist at all, because the material is an austenitic stainless steel.

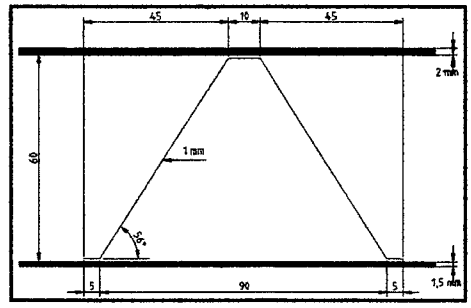

Fig. 3 Geometrical shape of the panels

Eight different constructive-technological solutions have been set, and as many prototypes have been carried out, in order to minimize mechanical strain induced by residual stresses, due both to welding process and panel geometry. Principal differences between the different prototypes are due to the welding kind (continuous or spot, single or double bead). Other is due to welding process parameters (penetration speed and depth), at the end to the welding sequence. So flat modules with on sight welding (full penetration) and modules with not on sight welding (partial penetration) have been produced.

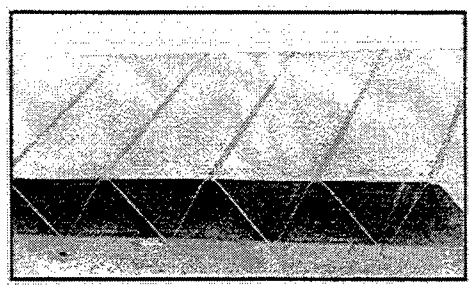
Fig. 4 Example of sandwich panel

## 4. EXPERIMENTAL TESTS

The residual stress analysis regarded a part of a panel (figure 5). Ten strain-gage rosettes have been applied on the 2mm thick surface, 7 in proximity of the 7 beads and the others between the first beads. The rosettes have been positioned in such a way that hole was tangent to the bead (figure 6).

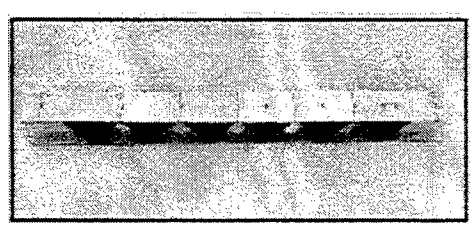
Fig. 5 Specimen used for measurements

### 4.1 Test execution

First of all, it is necessary to provide to the precise positioning of the drilling device with reference to the rosette. This step is very important, in order to minimize eccentricity that can affect experimental errors. It is carried out through a monocular microscope of which the device is equipped. The precision adjustment is carried out through two slides. The automatic setting of the end mill on the piece surface completes the positioning. At this point regulations on strain gage amplifiers have to be done. An half bridge configuration has been used, which presupposes the presence of a strain gage rosette to compensate for. Therefore a rosette equal to the others has been applied on a panel of the same material, positioned in the proximity and, when possible, in contact with the specimen which have been tested, just to eliminate any possible errors due to the difference of temperature. In this phase, on each of the three channels, the gain must be set and it goes on to a rough balance by the potentiometers positioned on the front panel.

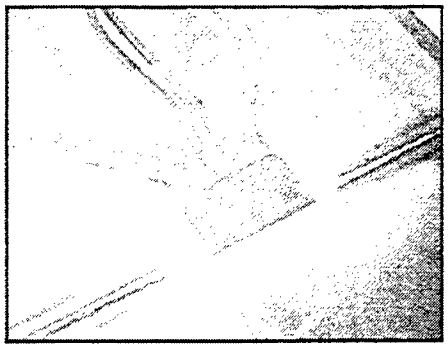

Fig. 6 A rosette on the specimen

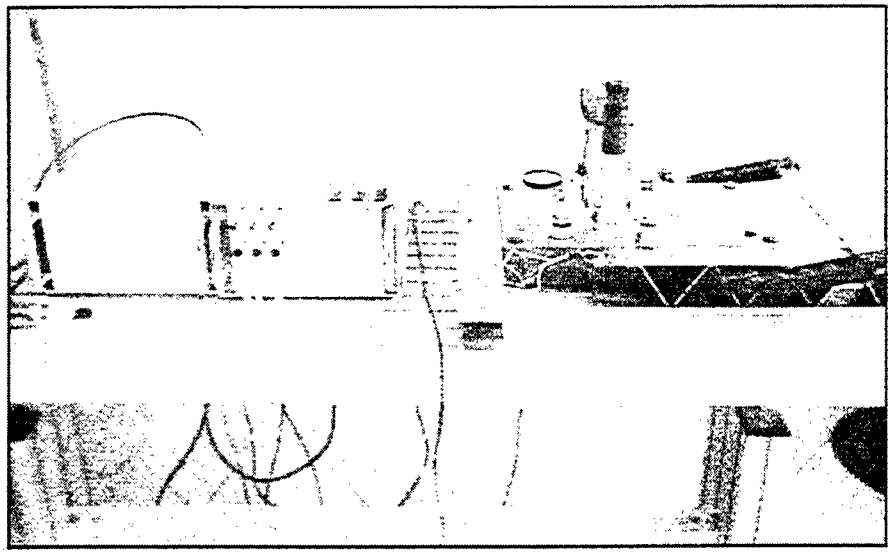

Fig. 7 A view of the Restan system

Once the test parameters have been set, via software, (hole depth, number of steps and feed speed), the programme automatically requires the balance and launches the specific routines, at the end of which, the test starts. It is also possible to choose an automatic procedure and in this case, at the end of each drilling step, after a proper delay reading of the strain of the three strain gages is done.
The parameters used for the execution of all the tests are:

- Hole depth: 2 [mm]
- Number of steps: 40
- Steps distribution: constant
- Feed speed: 0,1 [mm/min]

Throughout the test, a file is continuously updated with the values of the measured strains. At the same time, on the screen, a diagram, which sketches the trend in real time of the strain values, is visible too. After the last drilling step, the system stops automatically. At this point to complete the experiment, it is necessary to measure with the microscope the dimensions of the hole, thank to which the programme calculates automatically the value and the angle of eccentricity.

**4.2 Determination of residual stresses**

At the end of the test, it is necessary to launch the programme, which evaluates the strains, and then call back the file generated during the test. Different methods are available for calculating residual stresses: ASTM E837, Integral and Power Series. For what concerns the ASTM method, it presupposes the constancy of the stresses along the thickness. Selecting this method, the programme determines automatically the two curves $(\varepsilon_3 + \varepsilon_1)$ e $(\varepsilon_3 - \varepsilon_1)$ on the base of the values measured, and compares them with those expected by the standard ASTM, if the difference is greater than ±3 % the message *non uniform stress field* appears, which means that the method is not applicable. In all our tests, it hasn't been possible to use this method because the stresses were variable along the thickness. So that Integral Method and Power Series Method have been used. To be able to use these two methods, it is necessary to define the number of the calculation steps, the calculation depth and the order of the interpolating polynomial. About the order of the interpolating polynomial, it has always been used the option *optimised* that selects automatically the optimal order of the polynomial. Instead, about the number of calculation steps, with the Integral Method, 4, 5 or maximum 6 steps have been used depending on the different case, in fact the method results badly conditioned for greater number of steps. Using the Power Series Method, we have always considered 20 steps. For what concerns the maximum depth of calculation the Integral Method doesn't permit to overcome the value of 1 mm, while the Method of Power Series, in the specific case, has permitted to calculate the stresses along the whole depth of the hole.

## 5. RESULTS AND DISCUSSION

The results have been reported as a comparison between Integral and Power Series methods. In particular the graphs report the values, at 1 mm in depth, of the longitudinal, transversal and ideal stresses. Under the graphs a sketch of the specimen has been represented, in order to make easier its comprehension. The BETA angle values are reported too. Observing the vectors of the principal stresses, it appears that for all tests the BETA angle revealed is of about ± 45 ° refers to the grid 1 of the rosette. This means that the directions of principal stresses are practically parallel or perpendicular to the bead direction, with the only exception of the bead III. The stress values existing near the beads appear to be high. In particular the longitudinal stress values, assumed near the beads IV, V and VII*, reach the yield stress value, that for this kind of steel is about 250 MPa.

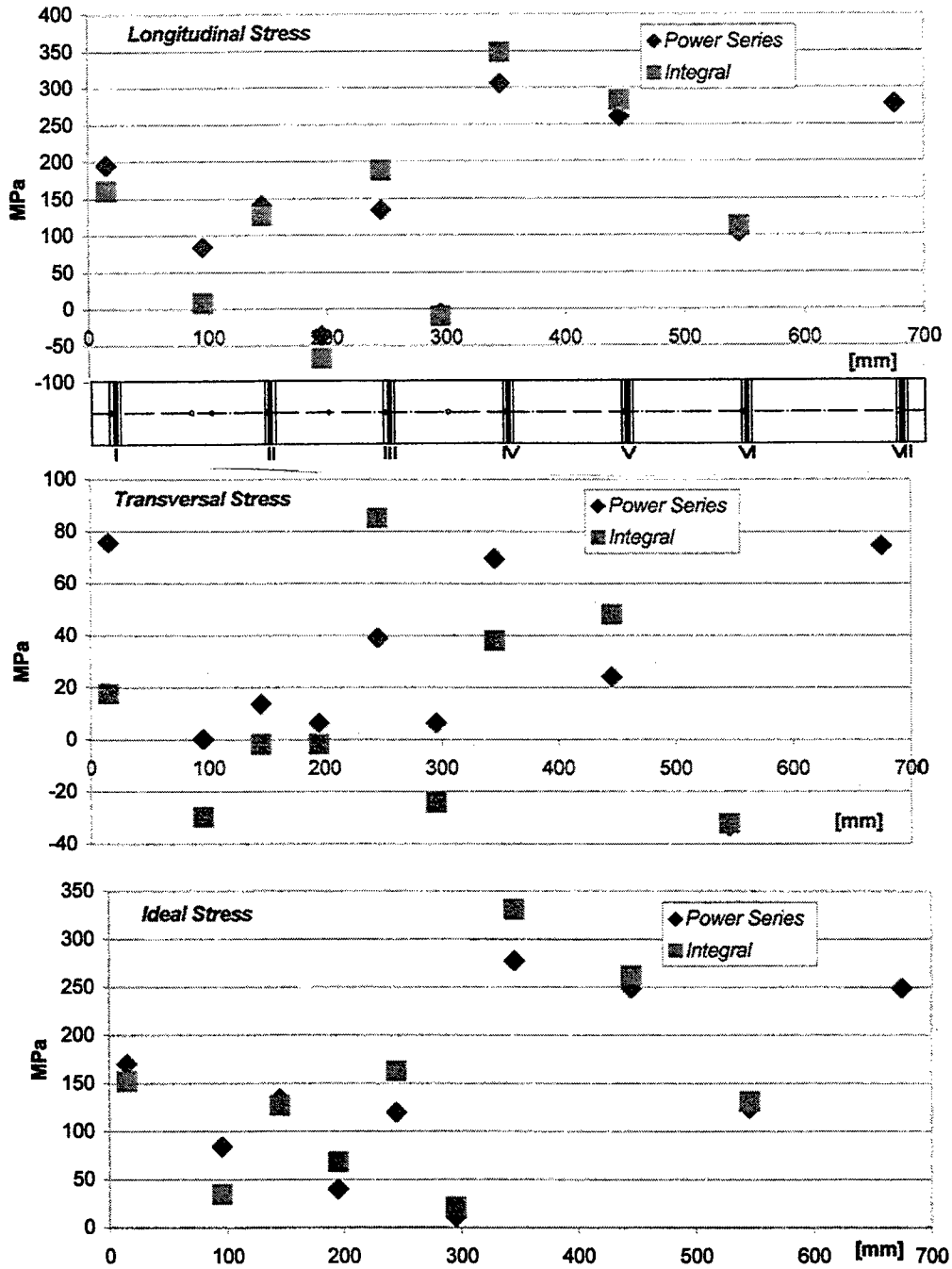


* For bead VII only the processing through the Power Series method has been carried out.

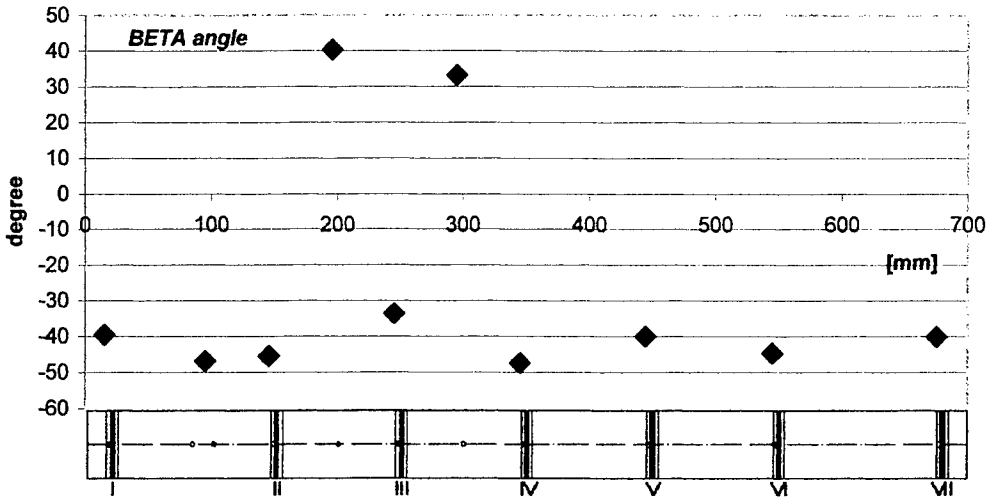


In the figure 8, the strain measured and Beta angle as a function of the hole depth are reported. The figure 9 then, shows the graph of the stress calculated as a function of the hole depth. The figure 10 shows the vectors $\sigma_{max}$ and $\sigma_{min}$ and the Beta angle they form with the direction of the grid 1 of the strain gage at the depth of 1,50 mm for example. All the figures represent an example of the outputs of the RESTAN System.

## 6. CONCLUSIONS

On conclusion, at the end of this work, the test of this sandwich panel, type TETA, has demonstrated that on this panel high residual stresses are present. As residual stresses assume different values along the material thickness, then the stress evaluations were carried out by using both the Integral and the Power Series Methods that have shown no particular differences. On the light of the all above referred, it is necessary to realize the TETA panels by using some other different constructional method and laser welding sequences.

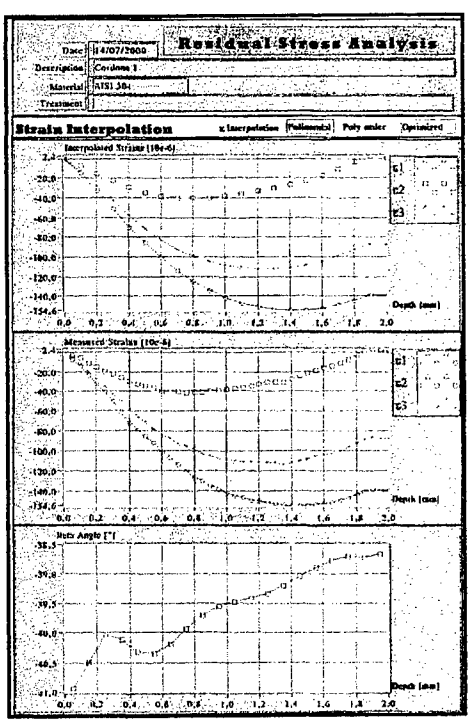


Fig. 8

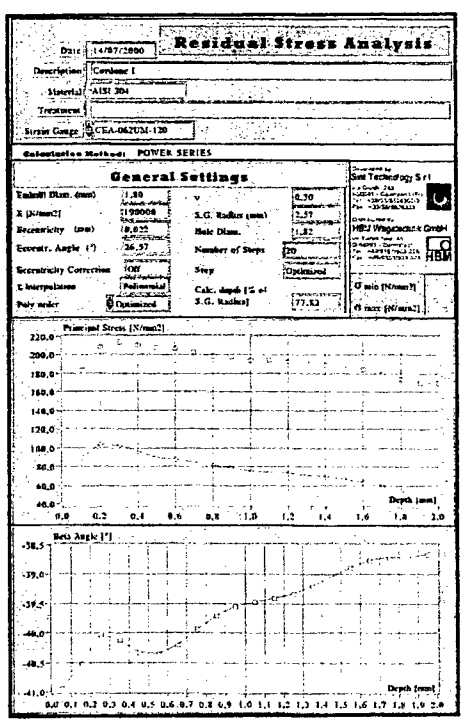


Fig. 9

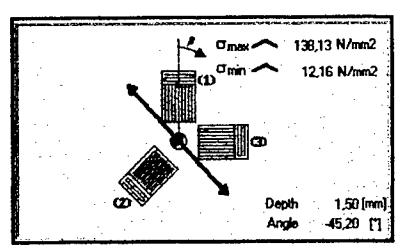


Fig. 10

## ACKNWOLEDGEMENTS

The authors are grateful to Dr. Olga De Pascale, director of Centro Laser, for help, discussion and support during this work.

## REFERENCES

1. Augusto Ajovalasit, "Rassegna del metodo del foro per tensioni costanti" AIAS - Studi per una proposta di raccomandazione sull'Analisi Sperimentale delle Tensioni Residue con il Metodo del Foro, Marzo 1997, Quaderno n. 3, pp. 3-11.
2. ASTM E 837 – *"Standard Test Method for Determining Residual Stresses by the Hole-Drilling Srain-Gage Method"* 1995.
3. A. Ajovalasit; G. Petrucci: *"Influenza dell'eccentricità sulla determinazione delle tensioni residue con il metodo del foro."* AIAS - Studi per una proposta di raccomandazione sull'Analisi Sperimentale delle Tensioni Residue con il Metodo del Foro, Marzo 1997, Quaderno n. 3, pp. 13-19.
4. G. S. Schajer: *"Measurement of Non-Uniform Residual Stresses Using the Hole-Drilling Method. Part I – Stress Calculation Procedures"* Journal of Engineering Materials and Technology, October 1988, vol. 110, pp. 338-343.
5. G. S. Schajer: *"Measurement of Non-Uniform Residual Stresses Using the Hole-Drilling Method. Part II – Practical Application of the Integral Method"* Journal of Engineering Materials and Technology, October 1988, vol. 110, pp. 344-349.
6. D. Vangi: *"Distribuzione non uniforme della tensione nello spessore."* AIAS - Studi per una proposta di raccomandazione sull'Analisi Sperimentale delle Tensioni Residue con il Metodo del Foro, Marzo 1997, Quaderno n. 3, pp. 31-41.
7. C. Esposito; G. Daurelio; A. Cingolati: *"On the cutting and penetration welding process with high power lasers"* Optic & Laser in Engineering 1985.
8. E. Valentini; M. Ferrari; S. Ponticelli: *"Metodologie di misura"* AIAS - Studi per una proposta di raccomandazione sull'Analisi Sperimentale delle Tensioni Residue con il Metodo del Foro, Marzo 1997, Quaderno n. 3, pp.53-67.
9. SINT Technology: *"System for measuring residual stresses by the hole drilling method (RESTAN)"* Manual of use and maintenance.
10. D. Vangi; B. Zuccarello: *"Scelta ottimale dei passi nel calcolo delle tensioni variabili nello spessore utilizzando il metodo dell'equazione integrale"* AIAS - Studi per una proposta di raccomandazione sull'Analisi Sperimentale delle Tensioni Residue con il Metodo del Foro, Marzo 1997, Quaderno n. 3, pp. 21-30.
11. G. Daurelio; A. Ludovico; F. Nenci; A. Zucchini: *"Studio e realizzazione, con tecnologia di saldatura a laser $CO_2$, di elementi strutturali modulari per pianali ferroviari"* Rivista Italiana della Saldatura, Gennaio-Febbraio 1998,pp. 31-41.
12. G. Daurelio; A. Ludovico; F. Nenci; A. Chiasera; M. Gaudio: *"Thin stainless steel sandwich structural panels all welded by laser technology."* European Symposium on Laser and Optics in Manufacturing 16-20 June 1997 Fairground, Munich FR Germany – paper # 3097 – 23 pp. 184 – 211.

[1] Correspondence Email : dau@centrolaser.it ; Phone : +39 080 46 74 314 ; Fax : +39 080 46 74 457
[2] Correspondence Email : latenzo@tiscalinet.it ; Phone : +39 080 35 19 790
[3] Correspondence Email : carpa@poliba.it ; Phone : +39 080 59 62 706 ; Fax : +39 080 59 62 777
[4] Correspondence Email : sint@fi.flashnet.it ; Phone : +39 055 88 26 302 ; Fax : +39 055 88 26 303

# Ablation of BN ceramics by femtosecond and picosecond laser pulses

Yoichi Hirayama, and Minoru Obara*
Department of Electronics and Electrical Engineering,
Faculty of Science and Technology,
Keio University
3-14-1 Hiyoshi Kouhoku-ku Yokohama 223-8522, JAPAN

## ABSTRACT

Ablation of cubic-boron nitride (c-BN) and hexagonal-boron nitride (h-BN) ceramics irradiated with Ti:sapphire laser (110fs) and Nd:YAG laser (100ps) pulses is studied. The relationship between ablation rate and laser fluence for the Nd:YAG laser shows a semi-logarithmic formula for c-BN and h-BN, and also the ablation rate of h-BN by Ti:sapphire laser is observed similar to that by the Nd:YAG laser, except that of c-BN. It is found that there are two different regimes of ablation rate for c-BN as same as metals by Ti:sapphire laser ablation. In addition, it is found from XPS analysis and SEM observation that the area ablated with Ti:sapphire laser shows the BN surface unchanged and has no evidence of melting. These results are different from the ablated surface with the Nd:YAG laser. In short, the microscopic processing of BN ceramics using femtosecond Ti:sapphire laser shows little heat effect and keeps the chemical composition of the ablated surface unchanged.

Keywords: Laser ablation, cubic-boron nitride, hexagonal-boron nitride, nitride ceramic, Ti:sapphire laser, Nd:YAG laser, femtosecond laser pulse, non-thermal ablation

## 1. INTRODUCTION

Boron nitride (BN) ceramics is an excellent electric insulator. In addition, it is a thermally and chemically stable material. The BN system is analogous to the carbon system in many aspects. For example, there are cubic-boron nitride (c-BN), and hexagonal-boron nitride (h-BN). The former has a hard *zincblende* structure with cubic symmetry, and the latter is breakable because of its structure like graphite. Thermo-physical properties of c-BN and h-BN ceramics are listed in Table 1. The c-BN and h-BN have larger thermal conductivity than aluminum oxides ($Al_2O_3$), which is generally used as a heat sink material in electrical industry. Moreover, these have thermal expansion constants close to silicon, high resistivity and low dielectric constant. Therefore, if microscopic processing of c-BN and h-BN is possible, these materials can be applied to heat sink for high power devices.

Table 1 Thermo-physical properties of ceramics.

| | c-BN | h-BN | AlN | $Al_2O_3$ |
|---|---|---|---|---|
| Thermal conductivity [W/cmK] | 6.0 | 0.8 | 2.2 | 0.3 |
| Expansion constant [$\times 10^{-6}$ $K^{-1}$] | 3.7 | 5 | 4.5 | 10 |
| Dielectric constant [at 1MHz] | 6.5 | 3.1 | 8.5 | 9~11 |

There are many papers about laser ablation of BN, but most of those are to fabricate BN thin film by physical vapor deposition (PVD) and pulsed laser deposition (PLD) using $CO_2$ laser, KrF excimer laser and Nd:YAG laser.[1-3] In addition, the fabrication of thin film BN ceramics[4] and the ablation of BN ceramics with $CO_2$ laser[5] are reported. In this paper, we report the ablation characteristics of c-BN and h-BN ceramics irradiated with Ti:sapphire laser (110fs) and Nd:YAG laser (100ps). Comparison of c-BN and h-BN ceramics ablated with between fs-laser and ps-laser is mainly investigated.

The BN chemical decomposition process can be described as bellow:

$$BN(s) \rightarrow B(g) + N(g) + \Delta H \text{ (303.4 kcal/mol)}, \quad (1)$$
$$BN(s) \rightarrow B(g) + 1/2N_2(g) + \Delta H \text{ (190.9 kcal/mol)}, \quad (2)$$
$$BN(s) \rightarrow BN(g) + \Delta H \text{ (172.3 kcal/mol)}, \quad (3)$$
$$BN(s) \rightarrow B(s) + 1/2N_2(g) + \Delta H \text{ (59.3 kcal/mol)}. \quad (4)$$

* Correspondence: Email: obara@obara.elec.keio.ac.jp;
Telephone: +81-45-563-1141 ext. 42226; Fax: +81-45-566-1529



XIII International Symposium on Gas Flow and Chemical Lasers and High-Power Laser Conference,
Antonio Lapucci, Marco Ciofini, Editors, Proceedings of SPIE Vol. 4184 (2001)

Here, (s) and (g) represent solid and gas phase, respectively. If decomposition process (3) can be induced, the chemical composition on the ablated surface will be unchanged. Hence, the characteristics of BN on the ablated area can remain. If reaction (4) is prevailing, the chemical nature of the ablated surface will change.

## 2. EXPERIMENTAL SETUP

In our experiments, we use two kinds of lasers as femtosecond (110fs) and picosecond (100ps) pulsed laser source. One is a commercially available Ti:sapphire laser (Tsunami, Spectra Physics), with a chirped pulse amplification (CPA) system (Split-fire, Spectra Physics) pumped by a second harmonic of Nd:YLF laser at a 1 kpps repetition rate (Merlin, Spectra Physics). This laser system finally delivers pulses with a pulse energy of 0.46 mJ/pulse, a pulsewidth of 110 fs, a center wavelength of 790 nm and a repetition rate of 1 kpps. The pulsewidth and energy are measured to use the intensity autocorrelator and the power meter, respectively. The number of laser pulses for ablation is controllable with a mechanical shutter. Another is a commercially available Nd:YAG laser (Model AML OSC, Lumonics), with amplification systems (Model AML AMP1 and AMP2, Lumonics). The obtainable energy, a pulsewidth, a wavelength and a repetition rate are 13.8 mJ/pulse, 100 ps, 1064 nm, and 10 pps, respectively. The pulse counter in the laser system and the joule meter are used in order to measure the number of laser pulses and the pulse energy.

In both experiments of Nd:YAG laser and Ti:sapphire laser ablation, we use neutral density filters to control the pulse energy. For all experiments of laser ablation, the c-BN and h-BN ceramics are ablated in air with a given fluence, which is focused by the 500 mm or 80 mm focal-length fused silica convex lens. The ablated surface is observed with FE-SEM (field emission-scanning electron microscopy, Hitachi Ltd. Model S-4700) and analyzed by XPS (x-ray photo-electron spectroscopy, JEOL Ltd. Model 9000-MC).

## 3. EXPERIMANTAL RESULTS AND DISCUSSION

First, we measure the depth of the ablated hole with several fluences in order to determine the ablation rate of c-BN and h-BN ceramics. Shot number averages the ablation rate per pulse using over 300 shots. Figure 1 shows the laser fluence dependence of ablation rates for c-BN and h-BN ceramics with Nd:YAG laser. In case of Ti:sapphire laser, the ablation rates of c-BN and h-BN ceramics are similarly measured, as shown in Fig.2 It is seen from Figs.1 and 2 that the laser fluence logarithmically increases with the ablation rate of h-BN ceramic in both cases of Nd:YAG laser and Ti:sapphire laser. While, the ablation rate of c-BN ceramic is similar to that of h-BN ceramic for Nd:YAG laser, but not for Ti:sapphire laser. In the case of Ti:sapphire laser, the two ablation regimes have previously been found in metal ablations[6, 7] because the thermal conductivity of c-BN ceramic is as high as those of metals. On the other hand, two ablation rate regimes of h-BN ceramic are not found presumably because the thermal conductivity of h-BN ceramic is not as high as that of c-BN ceramic. The ablation threshold fluence of h-BN ceramic by Ti:sapphire laser and Nd:YAG laser estimated from the experimental results are 0.0489 J/cm$^2$ and 0.104 J/cm$^2$, respectively. In addition, that of c-BN ceramic for Ti:sapphire laser in the two regimes is estimated to be 0.0158 J/cm$^2$ and 0.182 J/cm$^2$, respectively, and it is 0.0815 J/cm$^2$ for Nd:YAG laser.

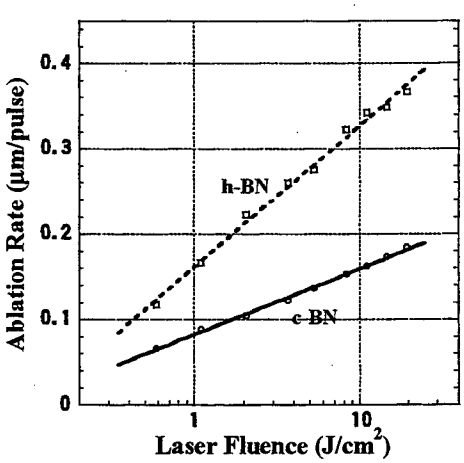


Fig.1 Plots of ablation rate per pulse as a function of 100 ps Nd:YAG laser fluence for c-BN and h-BN ceramics.

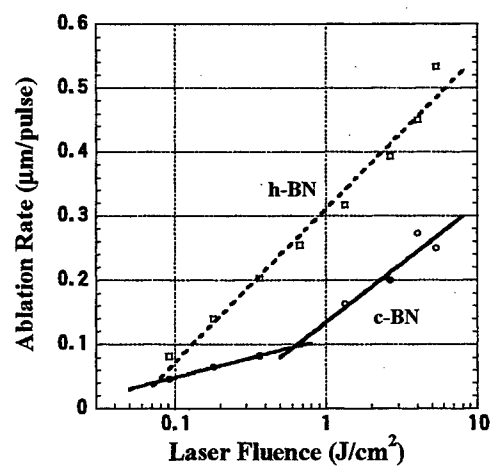


Fig.2 Plots of ablation rate per pulse as a function of 110 fs Ti:sapphire laser fluence for c-BN and h-BN ceramics.

Next, we perform the SEM observation of the surface ablated with Nd:YAG laser and Ti:sapphire laser. Figures 3 (a) and (b) show the SEM photographs of h-BN ceramic surface ablated by Nd:YAG laser and Ti:sapphire laser with laser fluences of 14.6 J/cm$^2$ and 5.32 J/cm$^2$, respectively. And c-BN ceramic surface ablated by Nd:YAG laser and Ti:sapphire laser with laser fluence of 14.6 J/cm$^2$, 0.183 J/cm$^2$ (low fluence regime of Ti:sapphire laser) and 5.32 J/cm$^2$ (high fluence regime of Ti:sapphire laser) is observed by SEM, as shown in Fig.4 (a) ~ (c), respectively. As can be seen in the both cases of c-BN and h-BN, while the melted trace around the hole ablated with Nd:YAG laser is observed, however, there is no evidence of the molten area or no direct ripple structure on the ablated surface is observed for Ti:sapphire laser. As be seen in Figs.3 and 4, in both cases of Nd:YAG laser and Ti:sapphire laser ablation, very pure ablation and sharp well-defined hole can be ablated on the c-BN and h-BN ceramics. In this way, the melted trace is found in case of Nd:YAG laser which has a pulsewidth of 100 ps, but not found with 110 fs-Ti:sapphire laser ablation. This difference depends on the relationship between laser pulsewidth and the electron-lattice relaxation time.

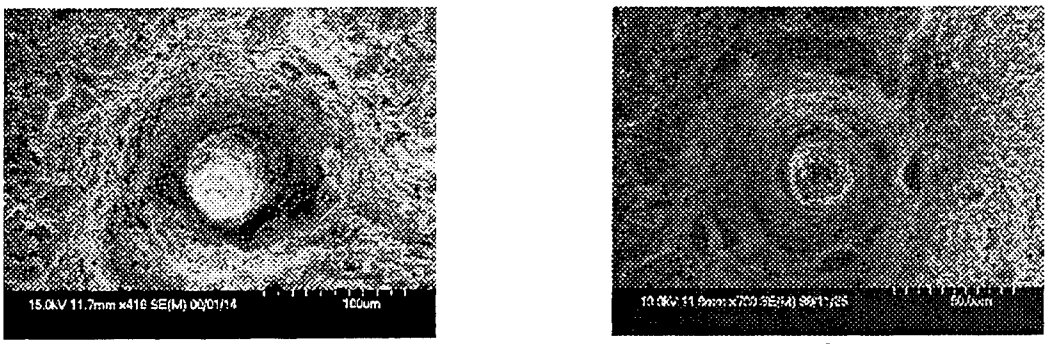


(a) (b)

Figure 3 SEM photographs of the ablated surface of the h-BN ceramic with (a) 100 ps Nd:YAG laser and (b) Ti:sapphire laser. The laser fluence is (a): 14.6 J/cm$^2$ for Nd:YAG laser, and (b): 5.32 J/cm$^2$ for Ti:sapphire laser.

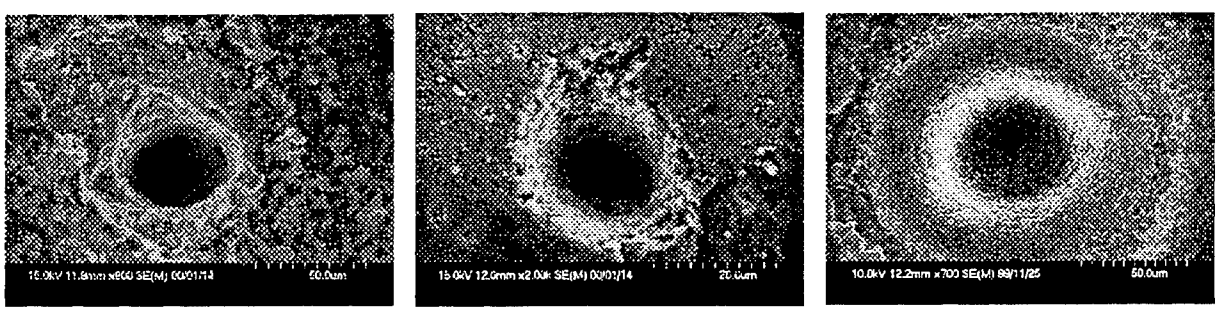


(a) (b) (c)

Figure 4 SEM photographs of the ablated surface of the c-BN ceramic with 100 ps Nd:YAG laser and 110 fs Ti:sapphire laser. The laser fluence is (a): 14.6 J/cm$^2$ for Nd:YAG laser, (b): a low fluence of 0.183 J/cm$^2$, and (c): a high fluence of 5.32 J/cm$^2$ for Ti:sapphire laser.

Finally, we perform the XPS analysis of the ablated area of c-BN and h-BN ceramics to investigate whether the boron layer is formed or not in the three fluence cases of Nd:YAG laser and Ti:sapphire laser (low and high fluence regimes). The three laser fluence of Nd:YAG laser and Ti:sapphire laser (low and high fluence regimes) are 4.88 J/cm$^2$, 0.183 J/cm$^2$ and 5.32 J/cm$^2$, respectively, in both cases of c-BN and h-BN ceramics. Figs.5 (a) and (b) show the binding energy of B(1*s*) on the h-BN ceramic surface ablated with Nd:YAG laser and Ti:sapphire laser, respectively. It is observed from Fig.5 that while the B(1*s*) peak spectrum of the h-BN ceramic surface ablated with Nd:YAG laser shifts from 190.3 eV (BN) to 187.9 eV (a simple boron), the B(1*s*) peak signal for Ti:sapphire laser corresponds to the binding energy of BN in both low and high fluence regimes. The result shows that a simple boron is formed on the area ablated with 100 ps Nd:YAG laser, however, the chemical composition of the area ablated with 110 fs Ti:sapphire laser remains unchanged and the thermal decomposition process does not occur. It is also seen that the ablation results of c-BN ceramic are similar to the h-BN ceramic.

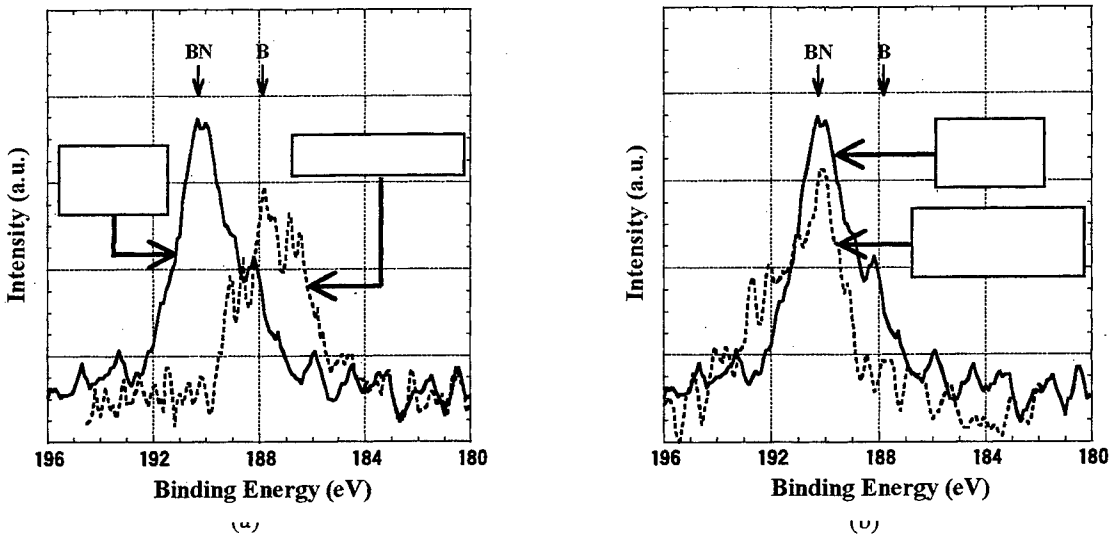


Figure 5 XPS spectrum of B(1s) of the ablated h-BN ceramic surface with (a) 100 ps Nd:YAG laser and (b) Ti:sapphire laser. The laser fluence is with (a): 4.88 J/cm$^2$ for Nd:YAG laser, and (b): 0.183 J/cm$^2$ for Ti:sapphire laser.

## 4. CONCLUSION

In summery, the picosecond and femtosecond laser ablations of c-BN and h-BN ceramics with Nd:YAG laser and Ti:sapphire laser are demonstrated. As a result of the c-BN ceramic ablation with Ti:sapphire laser, there are two regimes of ablation rate depending on laser fluence similar to metal ablation. This is not found in the h-BN ceramic ablation with Ti:sapphire laser, or in either case of c-BN and h-BN ceramics ablated with Nd:YAG laser. From the results of XPS analysis it is found that a simple boron is formed on the ablated area with Nd:YAG laser, but the surface ablated with Ti:sapphire laser is observed to remain as BN. Therefore, the chemical composition of the ablated surface remains unchanged and it is evident that the thermal decomposition process does not occur. Therefore, material processing of BN ceramics using a fs-Ti:sapphire laser can be demonstrated to prevent the attractive properties of BN ceramics from changing the chemical composition.

## ACKNOWLEDGEMENTS

The authors gratefully acknowledge the partial support on Development of High-Density Optical Pulse Generation and Advanced Material Control Techniques by Special Coordination Funds for Promoting Science and Technology from STA.

## REFERENCE

1. S. Mineta, M. Kohata, N. Yasunaga, and Y. Kikuta, "Preparation of cubic boron nitride film by CO2 laser physical vapour deposition with simultaneous nitrogen ion supply," *Thin Solid Films*, **189**, pp. 125-138, 1990.
2. G. L. Doll, J. A. Sell, C. A. Taylor II, and R. Clarke, "Growth and characterization of epitaxial cubic boron nitride films on silicon," *Phys. Rev. B*, **43**, pp. 6816-6819, 1991.
3. T. A. Friedmann, K. F. McCarty, E. J. Klaus, D. Boehme, W. H. Clift, H. A. Johnsen, M. J. Mills, and D. K. Ottesen, "Cubic boron nitride formation on Si (100) substrates at room temperature by pulsed laser deposition," *Appl. Phys. Lett.*, **61**, pp. 2406-2408, 1992.
4. E. W. Kreutz, "Pulsed laser deposition of ceramics – fundamentals and applications," *Appl. Surf. Sci.*, **127-129**, pp. 606-613, 1998.
5. T. Sumiyoshi, H. Tomita, A. Takahashi, M. Obara, and K. Ishii, "Wavelength dependence of boron nitride ablation by TEA CO2 lasers," *AIP Conf. Proc.*, **369**, pp. 1291-1296, 1996.
6. S. Nolte, C. Momma, H. Jacobs, A. Tünnermann, B. N. Chichkov, B. Wollegehausen, and H. Welling, "Ablation of metals by ultrashort laser pulses," *J. Opt. Soc. Amer.*, **B14**, 2716 (1997).
7. K. Furusawa, K. Takahashi, H. Kumagai, K. Midorikawa, and M. Obara, "Ablation characteristics of Au, Ag, and Cu metals using a femtosecond Ti:sapphire laser," *Appl. Phys.* **A69**, pp. S359-S366, 1999.

# High power laser rock cutting and drilling in mining operations: initial feasibility tests

Marc R. Hallada, Robert F. Walter, Stephen L. Seiffert,
Schafer Corporation, 2309 Renard Place SE, Albuquerque, NM 87106
Tel 505-242-9992 Fax 505-242-9975

## ABSTRACT

The interaction of a high power (infrared) laser beam with samples of rock encountered in hard-rock metal mining operations was experimentally investigated. These tests were intended to explore the feasibility of using high power lasers to improve the speed, performance, accuracy, and safety of rock cutting and drilling in mining operations. The current results were compared to similar tests, performed with the same laser, of materials typically encountered in gas and oil well drilling.

## 1. INTRODUCTION

Rock drilling and cutting operations have experienced a number of evolutionary developments over the last hundred years. However, these operations could be dramatically changed by the use of new technologies to augment traditional drilling techniques. In particular, high power lasers, with beams delivered via fiber optics, could provide a number of benefits in a variety of rock drilling and cutting applications, including disaster relief. For example, compact laser cutting systems, which can access confined areas, cut a wide range of materials regardless of their hardness, and do not generate large reaction forces, would be extremely valuable in unstable environments, such as for rock slides or earthquake-damaged structures. A variety of innovative laser rock drilling and cutting concepts have been proposed over the years.[1] Although many of these concepts seem to be quite impractical, advances in laser devices and fiber optics delivery systems in the last twenty years could make similar concepts quite feasible and enable direct laser or laser-augmented rock drilling and cutting to be the first revolution in this field in over a hundred years.

The removal of rock in production drilling and cutting operations requires huge energies. Although a laser can melt and/or vaporize the materials encountered, regardless of their hardness, it is not an efficient way to remove the large volumes of rock required in such operations. Thus, because the energies required are large and laser efficiencies are on the order of ten percent or less, extremely high average power lasers are needed for drilling/cutting rates that are competitive with conventional approaches. However, the unique characteristics of lasers, especially their ability to precisely deliver high energy intensities, via fiber optics, to remote and confined areas, could be extremely valuable in combination with other drilling techniques. Such hybrid combinations could potentially produce systems which require less manual intervention and maintenance (especially when extremely hard materials are encountered), provide more predictable and accurate guiding, enable dynamic sensing of the materials being penetrated (from the emission spectra of the gas/plasma generated by the laser), eliminate the need for drill casings, increase penetration rates, and, for all of these reasons, make such systems more reliable, faster, and cheaper to use.

## 2. ROCK CUTTING AND DRILLING TEST

A continuous wave (CW) infrared (IR) laser beam, operating at an average power of 6-7 kW, and at a wavelength of 1.315 μm, was used in the tests. The US Air Force Research Laboratory Directed Energy Directorate provided a Chemical Oxygen Iodine Laser (COIL), as well as the supporting infrastructure, for the tests. Three rock samples from a typical hard-rock mining operation were investigated: *waste rock*, *low-grade ore*, and *high-grade ore*. The sample compositions were:

| | | | | |
|---|---|---|---|---|
| *High-Grade Ore* | Massive Sulfide (9.60% Ni, 8.75% Cu, 0.13% Co) | | | |
| | Pyrrhotite | 55-65% | Pentlandite | 10-15% |



XIII International Symposium on Gas Flow and Chemical Lasers and High-Power Laser Conference,
Antonio Lapucci, Marco Ciofini, Editors, Proceedings of SPIE Vol. 4184 (2001)

| | | | | |
|---|---|---|---|---|
| | Chalcopyrite | 25-30% | Silicate&Oxides | <2% |
| *Waste Rock*: | Quartz Diorite | | | |
| | Plagioclase | 30-40% | Hornblende | 25-35% |
| | Quartz | 5-10% | Augite | 5-10% |
| | Biotite | 5-15% | K-Feldspar | 1-10% |
| *Low-Grade Ore:* | Disseminated Quartz Diorite (0.60% Ni, 0.50% Cu, 0.01% Co) | | | |
| | Plagioclase | 30-40% | Hornblende | 20-30% |
| | Quartz | 5-10% | Augite | 5-10% |
| | Pyrrhotite | 10-15% | Pentlandite | 1- 5% |
| | Chalcopyrite | 5-10% | | |

The laser beam was directed approximately perpendicular to the rock surfaces and focused to a spot of diameter 0.589 cm (~.25 inch) at each test location. A gas purge of the holes/kerfs, using nitrogen at 50-60 psi, delivered through 0.125 inch stainless steel tubing, was employed in each test. The purge was directed nearly perpendicular to the surface for stationary drilling. For the tests in which the sample was translated through the beam, the purge gas jet was directed at approximately 60° to the surface, measured from the surface opposite the direction of translation of the sample.

## 3. RELATED LASER CUTTING AND DRILLING TESTS

The stationary drilling tests were conducted using experimental parameters similar to those used in previous rock drilling tests, with the same laser system.[2] These results. as well as results from other drilling tests with lasers at other wavelengths, were presented in October 1999.[3] Their tests focused on rock types typically encountered in oil or gas well drilling operations: sandstone, limestone, shale, salt, and granite.

One of the key conclusions of that study was that a high power laser became very inefficient at drilling a narrow (0.25 inch diameter) hole when the depth exceeded the distance that the purge jet was able to effectively clear of ablation products. Beyond that depth, which varied from one material to another, the partially-ionized gas produced by the laser interaction with the rock could not be effectively removed and it absorbed the laser beam. Thus, the gas and the surrounding rock became hotter, but the gas shielded the virgin rock surfaces from the direct effects of the laser beam.

The energy needed to remove a cubic centimeter of material, the specific energy (kJ/cm$^3$), was the figure of merit used to compare the cutting performance in these cases and in a variety of other experimental conditions. (A small value of this parameter is desirable, indicating a higher efficiency for the removal of the rock by the laser.) To determine this value, the beam intensity (kW/cm$^2$) on the surface was first estimated. Since the radial intensity profile of the COIL beam is approximately Gaussian, the average intensity over the beam profile is lower than the peak power at the center of the beam. The average laser beam intensity on the surface of the rock samples was determined by assuming such a Gaussian radial intensity distribution and calculating the average value over the effective cross-section of the beam, to a radius at which the beam intensity was reduced to 1/e of the on-axis value. The specific energy was then calculated by multiplying this average beam intensity (kW/cm$^2$) by the laser pulse duration (sec) and dividing by the volume of material removed, approximated as the product of the depth (cm) of the hole and the effective diameter (cm) of the beam.

The inefficiency of laser drilling stationary holes beyond a certain depth was dramatically demonstrated by a series of holes this previous investigation drilled in a particular sandstone sample, for beam times which ranged from 3 to 15 seconds. In those tests, the specific energy was approximately constant, at about 37.5 kJ/cm$^3$, for beam times from 3 to 9 seconds. (The penetration depth for an 8-second illumination, by a beam with approximately the same parameters, was 4.3 cm.) However, for longer beam times, the hole depth did not increase substantially and the specific energy rapidly increased, indicating that the rock was increasingly shielded from direct laser interaction with the rock.

## 4. RESULTS OF ROCK CUTTING AND DRILLING TESTS

The specific energy was also calculated for the COIL cutting and drilling tests of the mining samples. However, cutting rates, both depth per unit time (cm/sec) and volume per unit time ($cm^3$/sec), were also determined. For the stationary holes, the values for depth per unit time were calculated directly from the measured depths and times. The volume per unit time for the stationary holes was calculated by assuming the volume removed was equal to the hole depth multiplied by the laser beam's cross-sectional area, out to a radius at which the intensity was 1/e of the on-axis value (in this case, 0.2945 cm). The volume per unit time for the scanned laser cuts was estimated by assuming the volume removed was equal to the greatest depth of the cut, multiplied by twice the effective beam radius (0.2945 cm), and multiplied by the length of the kerf.

In the tests of the hard-rock mining samples, two eight-second illuminations of both *waste rock* and *low-grade ore* were done. At an average laser power of about 7.6 kW (23.7 kW/$cm^2$ incident on the rock), the depth of the holes in the *waste rock*, produced by an illumination of ~8.22 seconds, was an average of 4.7 cm (tests 4 and 5). (See Table 1.) Thus, the average energy required to remove a cubic centimeter, the specific energy, was approximately 41.5 kJ/$cm^3$ (which is slightly more than the 37.5 kJ/$cm^3$ reported for sandstone). For the *low-grade ore* sample, the average laser power was 7.435 kW, during beam times of ~8.21 sec. This created stationary holes which were nearly identical in depth, at ~5.765 cm (tests 6 and 7). The specific energy in this case was only 33 kJ/$cm^3$, indicating that the drilling of the *low-grade ore* sample was more efficient than drilling the *waste rock* sample. Although no holes were drilled in the *high-grade ore* sample for times of ~ 8 sec, the specific energy for drilling this length of time can be interpolated from the drilling tests which were done, at 6 and 10 seconds (tests 8 and 9). Thus, the specific energy for an 8-second drilling of *the high-grade ore* sample should have been approximately 36.1 kJ/$cm^3$, intermediate between the *waste rock* and *low-grade ore* values.

However, it is probably not appropriate to compare the specific energies for drilling different rock samples a set length of time. The rock composition greatly affects the rate at which the laser can ablate material in such deep holes. Thus, a material that can be penetrated more easily (partially because the ablation by-products do not absorb the incident beam as readily) will more rapidly reach a depth at which the gas purge system can no longer even partially clear the hole of these by-products. In order for a specific energy to be characteristic of the material alone, and not the hole geometry or purge system, the specific energies must be compared for relatively short drilling times.

A series of stationary holes were produced in the *high-grade ore* sample, as mentioned previously, for beam times of 6, 10, and 14 seconds. The penetration depths were, respectively, 4.95, 5.84, and 7.70 cm, with corresponding specific energies of 30.41,41.78, and 41.12 kJ/$cm^3$. In the previous sandstone drilling series, the specific energies for the same times were approximately 37.5, 38.0, and 42.0 kJ/$cm^3$, illustrating that the laser drilling rapidly became less efficient for illumination times beyond 10 seconds (for a depth of penetration of about 5.3 cm). In the current experiments, the efficiency dropped off even more rapidly and sooner after the illumination started (beyond ~6 sec - corresponding, again, to penetrations of about 5 cm). Thus, it seems that the depth of the penetration, rather than the time for the laser illumination, is more indicative of the onset of reductions in drilling efficiency. Since the same gas purge system and drill hole diameters were used in both the current experiments and those of the previous tests, this drop in efficiency could simply be due to the inability of the jet to clear the holes of ablation products beyond these depths. In both cases, the 50-60 psi nitrogen purge gas was delivered through an untapered, 0.125 inch diameter tube. However, it should be noted that high energy laser industrial cutting systems often use gas purge pressures of up to 400 psi, through tapered nozzles, to efficiently clear deep kerfs. In recent rock drilling experiments by Japanese researchers, several purge jet options were investigated.[4] They concluded that a gas purge was actually detrimental in deep drilling since it was not able to remove the viscous molten material and actually made the situation worse by increasing the rate of cooling of the material.

The effect of hole depth on drilling efficiency in the current experiments can also be seen by comparing the depth-drilling speeds, in cm/sec, for the various stationary holes, as well as the volume-drilling speed ($cm^3$/sec), for both the stationary holes and linear kerfs. Comparing the depth-drilling speeds (cm/sec), it is seen that one of the shallowest holes (in the high-grade sample, test 8), produced by a laser pulse slightly

longer than 6 seconds, had the highest rate (0.8 cm/sec). The drilling rate in the *high-grade ore* sample, for an 8-second test, can be estimated from the tests at ~6 and ~10 sec (tests 8 and 9). Thus, the interpolated drilling rate is about 0.7 cm/sec, the same as for the *low-grade ore* sample (tests 6 and 7). The same

Table 1. COIL Rock Cutting and Drilling Test Results

| Test Number | Laser Beam Power (avg) (kW) | Laser Beam Intensity (avg) ($kW/cm^2$) | Sample | Laser Pulse Duration (sec) | Penetration Depth (cm) | Penetration Length (cm) | Sample Speed (cm/s) | Specific Energy ($kJ/cm^3$) | Drilling Speed (cm/s) | Drilling Speed ($cm^3/s$) | Comments |
|---|---|---|---|---|---|---|---|---|---|---|---|
| 1 | 7.652 | | Plexiglass | 3.17 | | | | | | | |
| 2 | 6.128 | 19.0 | Rock | 20.16 | 2.96 | 3.3 | 0.16 | 23.50 | | 0.285 | SE assuming kerf~5.5 beam diameters long |
| 3 | 6.225 | 19.4 | Rock | 30.04 | 7.43 | 1.3 | 0.04 | 35.70 | | 0.189 | SE assuming kerf~2.2 beam diameters long |
| 4 | 7.685 | 24.0 | Rock | 8.24 | 4.58 | | | 43.18 | 0.56 | 0.153 | |
| 5 | 7.532 | 23.5 | Rock | 8.21 | 4.83 | | | 39.95 | 0.59 | 0.161 | |
| 6 | 7.441 | 23.2 | Lo Grade | 8.22 | 5.77 | | | 33.05 | 0.7 | 0.191 | |
| 7 | 7.429 | 23.2 | Lo Grade | 8.19 | 5.76 | | | 32.99 | 0.7 | 0.191 | |
| 8 | 7.752 | 24.2 | Hi Grade | 6.22 | 4.95 | | | 30.41 | 0.8 | 0.218 | |
| 9 | 7.657 | 23.9 | Hi Grade | 10.21 | 5.84 | | | 41.78 | 0.57 | 0.155 | penetration cut, sample cracked |
| 10 | 7.150 | 22.3 | Hi Grade | 14.20 | 7.70 | | | 41.12 | 0.54 | 0.147 | penetration cut, sample cracked |
| 11 | 6.878 | 21.4 | Hi Grade | 30.13 | 11.10 | | | | | | intermittent translation, from edge, cracked |
| 12 | 6.668 | 20.8 | Hi Grade | 30.15 | 6.58 | | | | | | intermittent translation, from edge, cracked |
| 13 | 6.484 | 20.2 | Rock | 30.14 | 3.54 | 5.0 | 0.17 | 20.23 | | | smooth translation, opposite direction, cut from edge, videos from two perpendicular vantage points SE assuming kerk-8.5 beam diameters long |

conclusion can be reached by comparing the volume removal rates from the *low-grade ore* sample, 8-second illuminations (tests 6 and 7), with an estimate of the removal rate from the *high-grade ore* sample for 8 seconds (interpolated from tests 8 and 9). For both the high and low-grade samples, the volume removal rate was about 0.19 $cm^3$/sec, for an 8-second illumination. In contrast, the linear and volume drilling speeds (for stationary drilling) in the *waste rock* sample (tests 4 and 5) were about 20% slower. Thus, the ablation products from the *waste rock* sample, composed nearly entirely of quartz diorite, seem to be somewhat more effective at absorbing the incident laser beam and protecting the virgin material.

An improvement in volume drilling rates occurs when the laser beam is scanned along the rock surface. The volume drilling rates for these kerfs were determined by estimating the volume of material removed in the measured times as the product of cut depth, cut length, and cut (beam) width. Two "plunge" cuts (tests 2 and 3) and one "edge-entry" cut (test 13) were made in the *waste rock* sample. For the plunge cuts, quadrupling the scan rate increased the volume cutting rate by 50%. By increasing the scan rate another 50% and entering from the edge of the sample, however, the volume cutting rate increased by over 20%. The "edge-entry" kerf seemed to allow the gas purge to more easily expel the ablation products from the kerf and permit more efficient cutting. However, the gas purge was not strong enough to keep the kerf open during the entire cut. Some ten seconds into the "edge-entry" cut (test 13), the melted diorite blocked the kerf that had just been created, limiting the value of the kerf in efficiently eliminating the cutting by-products.

## REFERENCES


1. W.C. Maureer, *Advanced Drilling Techniques*, Chapter 17, Laser Drills, pp. 421-462, Petroleum Publishing Company, Tulsa, OK, 1980.

2. D.G. O'Brien, et al., "Laser-Rock-Fluid Interactions - Application of Free-Electron Laser in Petroleum Well Drilling and Completions," Free Electron Laser Challenges II, Proceedings of the International Society for Optical Engineering (SPIE), **3614**, pp. 168-176, San Jose, CA, Jan 25-29, 1999.

3. D.G. O'Brien, et al., "Star Wars Laser Technology for Gas Drilling and Completions in the 21st Century," Society of Petroleum Engineers Annual Meeting, October 1999, Houston, TX.

4. D. Sugimoto, et al., "Performance of high power lasers for rock excavation," Advanced High-Power Lasers and Their Applications, SPIE International Symposium, 1-5 Nov 1999, Osaka, Japan.

# Search for $CO_2$ laser beam parameters affecting the process of the laser elevating of cavitation resistance of steels

Bolesław G.Gireń[a], Grażyna Rabczuk[a*], Marek Szkodo[b],

[a]Institute of Fluid-Flow Machinery Polish Academy of Science, 80-952 Gdańsk, Fiszera 14, Poland

[b]Technical University of Gdańsk, Faculty of Mechanical Engineering, 80-952 Gdańsk, Narutowicza 11

## ABSTRACT

The influence of high power $CO_2$ laser beam parameters on the process of the laser elevating of cavitation resistance of steels was investigated. The samples of structural carbon steel and corrosion resistant chromium steel were melted superficially with the laser beam and subsequently subjected to the cavitation loading. It was discovered, that the power distribution in the cross section of the laser beam was of the great importance for the elevating of the cavitation resistance of the steel surface subjected to the multipath scan processing. The dependence of the erosion resistance of the tested materials on the frequency of the laser pulses as well as on the power of the beam was also discussed.

**Keywords.** Cavitation erosion, Laser processing of steels, $CO_2$ laser beam.

## 1. INTRODUCTION

Cavitation resistance of materials is unique for any specific intensity and structure of the erosion impingement and depends on the structural and mechanical features of both the surface layers and core material. The problem of the protection of materials against cavitation during the incubation period of the erosion consists in the manufacturing of the surface layer of the appropriate properties, and hence on the method and parameters of its processing. Transformed and hardfacing structures created by the laser techniques leads, in most cases, to considerable increase of the cavitation erosion resistance of the processed materials (see e.g. [1-4]). Any variations of the laser beam characteristics entail significant changes in the temperature field within the material and eventually induce the developing of various kinds of microstructure and residual stresses distributions [5].

**1.1 Subject and scope.** In the paper, the influence of the high power $CO_2$ laser beam parameters on the process of the laser elevating of cavitation resistance of steels was investigated. The samples of structural carbon steel (45 - normalized at 860 $^0$C) and corrosion resistant chromium steel (2H13 – hardened and low annealed) were melted superficially with high power $CO_2$ laser beam and subsequently subjected to the cavitation loading.

Laser processing was completed for various levels of the beam power (up to 8700 W), for both continuous and pulse laser operation modes. The dependence of the processing efficiency on the power distribution in the cross section of the beam was also tested.

## 2. PERFORMED EXPERIMENTS

The investigations reported in the paper were carried out in the Institute of the Fluid-Flow Machinery of Polish Academy of Science in Gdańsk and in the Technical University of Kielce. The laser treatments of the investigated material surfaces were accomplished with cw $CO_2$ lasers of 10 kW [6] (LPP10) and 1.2 kW [7] (MLT1.2) and with the $CO_2$ laser of 6.5 kW (LK) which worked optionally in cw or pulse operating modes. The main parameters of the applied devices are gathered in Tab. 1.

In order to process materials along 10 mm and 20 mm width paths, the additional optics was employed for the beam shaping. Methods of samples processing were described in detail previously [8].

Cavitation destruction of the prepared samples surfaces was completed at the rotating disk facility [9] in the Institute of the Fluid-Flow Machinery in Gdańsk. The tests were performed in 2 - 3 min long periods following one another. The total time of cavitating equalled 19 min. Some samples destined for residual stress investigations (subjected to multipath processing)

* Correspondence:E-mail:rabczuk@imp.pg.gda.pl



XIII International Symposium on Gas Flow and Chemical Lasers and High-Power Laser Conference,
Antonio Lapucci, Marco Ciofini, Editors, Proceedings of SPIE Vol. 4184 (2001)

were destroyed in 5 – 7 min long periods. Total time (56 min) of exposure of the samples to cavitation did not exceed the incubation period of the erosion of tested materials, specific for the applied cavitation device.

Table 1. The main parameters of the applied lasers.

| Laser | LPP10 | MLT1.2 | LK |
|---|---|---|---|
| Resonator | unstable | stable | Stable |
| Laser beam wavelength [μm] | 10.6 | 10.6 | 10.6 |
| Laser beam power [W] | 9800 | 1000 | 6500 |
| Laser beam mode | Multimode | TEM 01 + TEM 00 | TEM 01 |
| Laser beam diameter [mm] | 28 | 12 | 16 |
| Laser beam divergence [mrad] | | 2 | 1.7 |

The rate of surface pitting (the quantity (Nr-N)/Nr as a function of the cavitation time) was used as an indicator of the erosion resistance of the investigated materials. Nr means the number of pits within the reference – not processed zone, and N stands for the number of pits on processed area. Quantifying the cavitation damage of the materials by the pits counting is the method applied also by many other authors (e.g.[10]).

## 3. SELECTED RESULTS AND BRIEF DISCUSSION

The picture of an exemplary eroded sample of material is presented in Fig. 1 Herein the smooth surface of the remelted area could be compared to the developed surface of not processed part of the sample. The enhanced damage at the boundary between the processed region and the region of not transformed material is probably caused by the residual stresses of tensile nature.

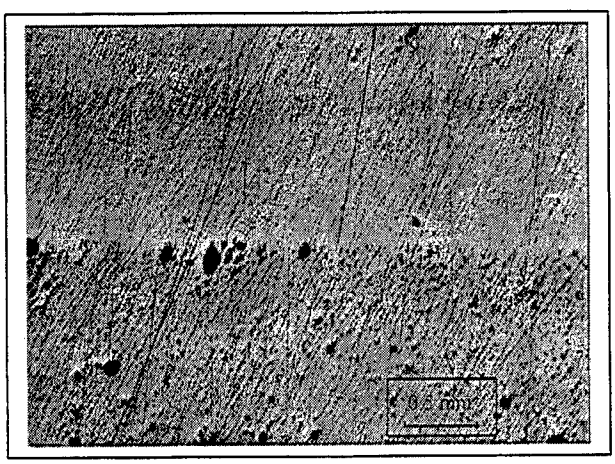

**Figure 1.** Steel 45; after 8 minutes of cavitation. Upper strip – the zone transformed with laser beam.

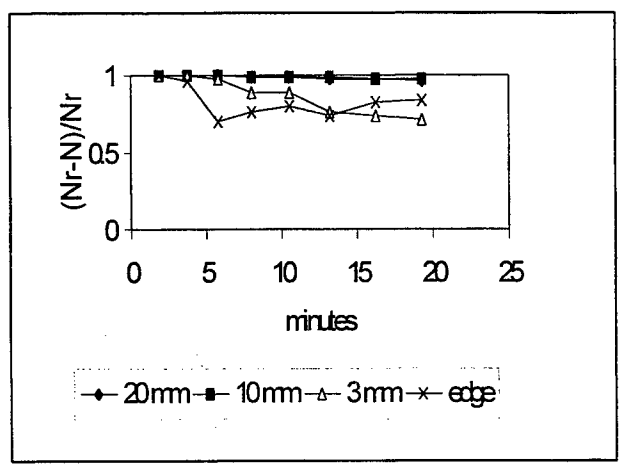


**Figure 2.** Rates of pitting found on steel 45. The curves refer to the remelted paths of 20 mm, 10 mm, 3 mm width and to the spots at the edge of the path of 10 mm.

It follows from the results presented on Fig. 2 that an increase of the cavitation resistance of steel 45, due to its remelting by the broad laser beam (of 10 mm or 20 mm width), was higher than an increase of the cavitation resistance obtained for the steel samples processed by the narrow beam (3 mm). Moreover, an increase of the cavitation resistance in the middle of the broad (10 mm) path significantly exceeds an increase detected at the edge of that path. The latter effect could be linked to the presence of the residual stresses fields of tensile nature. The results related to the investigations of the samples processed along the multiplied parallel paths (Fig.3) - with heat affected zones attached or separated - are coherent with the above results. It was found that for steel 45 the cavitation erosion resistance of the samples remelted along the separate paths exceeded the one referred to the samples transformed along the attached paths.

The results presented in Fig. 4 prove that the cavitation resistance of the steel 2H13 achieved on any remelted path was the same for nine initial min of cavitation. In the later stage of cavitation, an increase of the resistance observed on the

surface layer of the narrow remelted path of 3 mm was higher than an increase of the resistance detected on wider paths (of 10 and 20 mm). It happened probably because of the presence of the 1-dimensional dendritic structure (not very resistant) formed within the broad, shallow melting pools, as well as due to high hardness of core material. It is worth underlining that in the case of steel 45 the reversed relationship is observed: for the wider remelted path the higher resistance was obtained (see Fig.2). The highest resistance at the edge of the remelted path in the case of steel 2H13 seems to be also linked to the structural features of the material but not to the presence of the residual stresses. It results directly from the fact, that mentioned differences in cavitation resistance were not detected before the ninth minute of cavitation as it was shown in Fig.4.

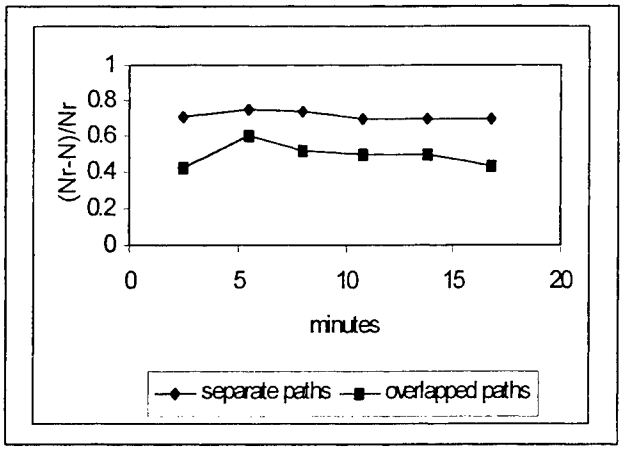


**Figure 3.** Rates of pitting found on steel 45 subjected to the cavitation loading at the rotating disk facility. The curves refer to the remelted paths of 3-mm width separated and attached.

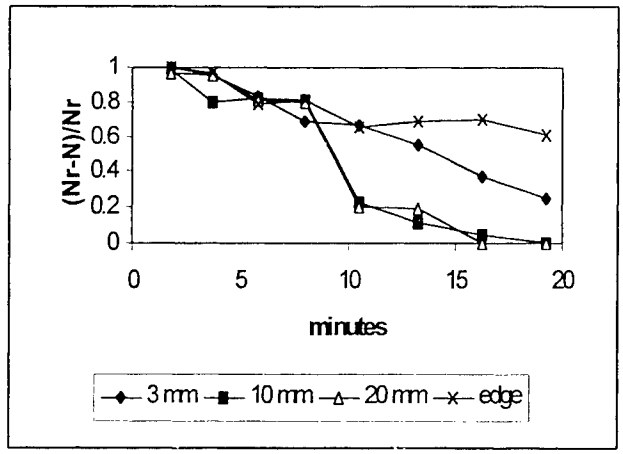


**Figure 4.** Rates of pitting found on steel 2H13 subjected to cavitation loading at the rotating disk facility. The curves refer to the remelted paths of 20 mm, 10 mm, 3-mm width and to the spots at the edge of the path of 10 mm.

Any distinct influence of the laser beam instabilities taking place during the surface processing on the response of the materials to the cavitation loading was hardly detected. However, the random creation of the optical breakdown – optical discharge plasma – at the solid state surface can cause the enhancing or weakening of the energy coupling between the laser beam and the material. It could affect the effectiveness of the processing (see Fig. 5) as well as the resistance to cavitation erosion. It follows from the performed investigations that the modulation of the laser beam power may deteriorate the efficiency of the process leading to the elevation of the cavitation resistance. At some frequencies of the laser pulses, the repeated cycle of heating during the processing contributes to reducing of the presence of the unstable hard material structures formed in the preceding moment. This leads to considerable decrease of the cavitation resistance, as it is shown in Fig. 6 for the laser repetition pulses frequency of 100 Hz.

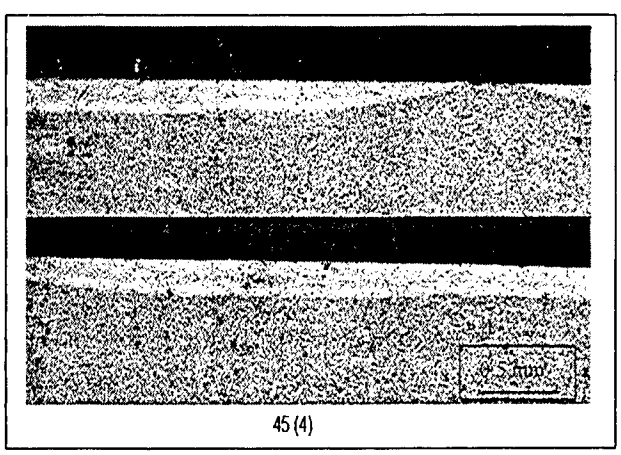


**Figure 5.** Cross-section of the steel 45 sample along the path of the laser beam processing with the presence of the optical discharge plasma.

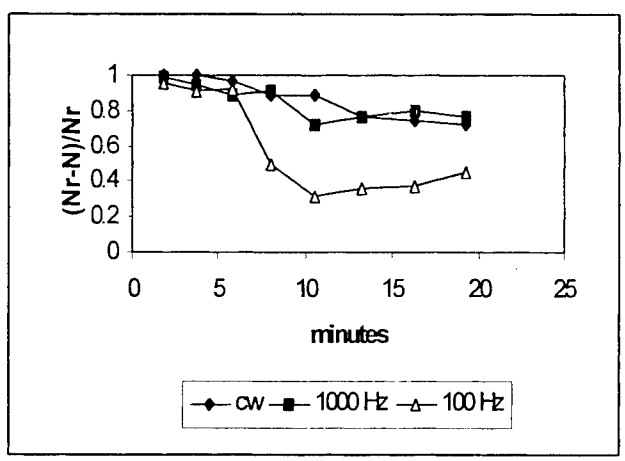


**Figure 6.** Rates of pitting found on steel 45. The curves refer to the paths remelted by the beam operating at various frequencies of the pulses.

It was found that amount of the laser beam energy absorbed within the surface layers of the material per unit of time was of great significance for the increase of its cavitation resistance in the initial stage of erosion. Therefore, the power of the beam should be regarded as the main parameter determining the processing efficiency with respect to the protection of the cavitation erosion. For example, the cavitation resistance of steel 2H13 processed with 1.9 kW laser beam increased 3.2 times (measured after 40 minutes of cavitation), whereas cavitation resistance of the samples melted with 8.7 kW increased 11.5 times. In the advanced stage of cavitation the dependence of the material erosion resistance on the laser beam power was less noticeable due to the limited possibility of the energy accumulation in the hardened, brittle structures.

## 4. CONCLUSIONS

4.1. Power distribution in the cross section of the laser beam is of the paramount significance for the generation of the residual stress fields in the processed material. Hence the laser beam parameters should be carefully selected, especially when the increase of the cavitation resistance of the steel surface is to be obtained by the multipath scan processing.

4.2. The frequency of the laser pulses should not be too low in order to avoid the repetition of the thermal cycle within the material in the course of the processing.

4.3. The power of the beam should be regarded as the main parameter determining the processing efficiency with respect to the protection of the cavitation erosion.

## ACKNOWLEGMENTS

This work was sponsored by the Polish National Scientific Committee within the Project PB1419/T11/98/14.

## REFERENCES

1. W.J.Tomlinson, J.H.Megaw, A.S.Bransden, M.Girardi, *The effect of laser surface melting on the cavitation wear of grey cast iron;* Wear **116,** p.249, 1987
2. Rao D.R., Ventakaraman B., Asundi M.K., Sundararajan G., *The effect of laser surface melting on the erosion behaviour of a low alloy steel;* Surface and Coatings Technology **58,** p. 85, 1993
3. Gireń B.G., *Cavitation erosion of steels processed with a laser beam and an optical discharge plasma,* Surface Engineering **14,** p.325, 1998
4. Gireń B.G. *On the increase of cavitation resistance of A1 structure alloys processed by laser beam*, Journal of Technical Physics, **XL,** 277, 1999
5. B.G.Gireń, M.Szkodo, J.Steller; *The influence of residual stresses on cavitation resistance of metals;* Wear, **233-235**, p. 86-92, 1999
6. Stańco J. et al., *A high power transverse flow $CO_2$ laser;* Appl.Phys.B, **41**, p.245, 1986
7. G.Rabczuk, P.Kukiełło, G.Śliwiński, *Experimental investigations of the output beam properties from a high power cw $CO_2$ laser*, NATO ASI Series, 3 High Technology, **7,** pp 449-454, Kluwer Acad. Pub.,1996
8. Gireń B.G. *Steel surface processing by a continuous optical discharge plasma,* Plasma Chemistry and Plasma Processing **13**, p.133, 1993
9. Steller K., Krzysztofowicz T., Reyman Z., *Effects of Cavitation on Materials in Field and Laboratory Conditions;* American Society for Testing and Materials, Special Tech. Pub. **567** p.152, 1975
10. Belahadji B., Franc J.P., Michel J.M., *Analysis of the Cavitation Erosion Pits;* Trans. ASME J.Fluid Eng. **113,** p. 700, 1991

# CUBR LASER SYSTEM FOR PRECISION MICROMACHINING OF THE MATERIALS

M. Kocik, A. Dąbrowski, T. Kasperkowicz, J. Mizeraczyk

Centre of Plasma and Laser Engineering, Institute of Fluid Flow Machinery,
Polish Academy of Sciences, 80-952 Gdańsk, Fiszera 14, Poland
tel: + 48 (58) 341 12 71 ext. 152, fax. + 48 (58) 341 61 44, e-mail: kocik@imp.pg.gda.pl

## ABSTRACT

In this paper the possibility of applying the new-generation high-power CuBr laser in precision micromachining is presented. Several industrial applications of the presented CuBr laser set-up are shown.

**Keywords:** Laser Micromachining, CuBr laser

## 1. INTRODUCTION

Laser micromachining, based on the microablation of materials, is an increasingly important production method used in the automotive, aerospace, electronics, telecommunications and medical device industries.
A variety of laser types are used in the laser micromachining. The lasers that are most commonly used are copper vapour lasers, excimer lasers and Nd solid state lasers and recently ultra-short pulsed from titanium sapphire lasers. It is clear that the laser type must be matched to the application and that no single laser type will be optimum for all applications.
The copper vapour lasers (CVL), including CuBr lasers, have been at the forefront of laser micro-machining technology for some years [1].
Principal applications of these lasers are in micro-hole drilling and precision cutting. In number of applications it has been demonstrated that the copper laser is the only viable tool because of the excellent results achieved with its combination of high power, short pulses, visible radiation, diffraction-limited beam quality, high reliability and low cost of ownership.
In this contribution 50 W CuBr laser advanced system for high-precision processing (cutting, drilling, trimming) of various materials is presented.

## 2. CuBr LASER SET-UP FOR MICROMACHINING

The experimental set-up for material processing (fig. 1) consists of a 50 W CuBr laser in MOPA (Master Oscillator – Power Amplifier) system, MTS (Master Timing System), XYZ rotary table, fast optical scanner head, optics for transmitting and focusing the laser beam, PC computer, microscope for direct observation of the laser machining process and video system.
The CuBr laser is composed of two CuBr laser tubes working as a MOPA system (fig.2); discharges in both tubes are steered by MTS – high frequency and voltage switch. This configuration allows higher power, better quality of laser beam and also full control of laser generated pulses compared to a single tube. An average output power of CuBr laser is 50 W in two wavelenghts - green (510.6 nm) and yellow (578.2 nm) (green/yellow ratio is 3:1), pulse frequency of 20 kHz and high beam quality ≈1,3 diffraction limit [2].

The optical scanner head with achromatic lenses of 16 cm focus was employed for very fast (up to 100 cm/s) and precision (1 μm) beam spot positioning. The scanner is equipped with plane-field objective that minimizes divergence of the spot. Maximal working area of the scanner is 10 x 10 cm. In order to proceed machining covering larger area it is necessary to combine scanner and XYZR table (resolution 4 μm, speed range 0.1 - 20 mm/s) movement. Z axis of the table is used to focuse the laser beam and operate with the spot on non-flat entities. Rotary table allows to perform


XIII International Symposium on Gas Flow and Chemical Lasers and High-Power Laser Conference,
Antonio Lapucci, Marco Ciofini, Editors, Proceedings of SPIE Vol. 4184 (2001)

trepanned holes of high quality and curve shape cuttings.
The optics in the set-up allows to achieve two modes of operation (fig. 1): **a**. the movement of the XYZR table assisting scanner, **b**. micromachining with the use of XYZR table without scanner.
Scanner and XYZ rotary table are controlled by a PC computer. An auto focusing system and MTS controlling to the computer software have been planned for the set-up.

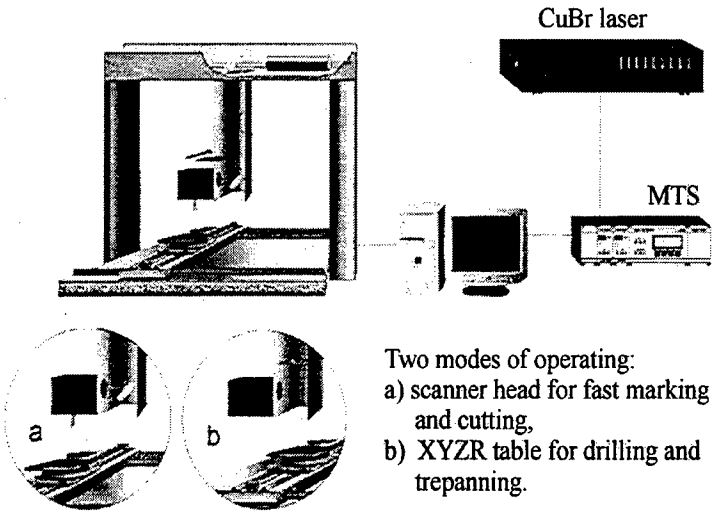


Fig.1 CuBr laser set-up for micromachining

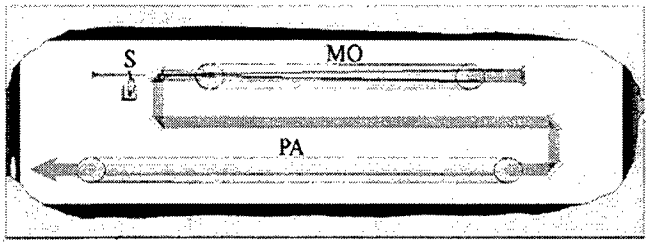


Fig.2 CuBr laser in MOPA configuration (MO – Master Oscillator, PA – Power Amplifier)

## 3. CuBr LASER BEAM OPTIMIZATION

Beam quality is crucial in micromachining. A relatively low peak power of the CuBr laser may have a negative effect on the laser processing materials. When used for the material drilling, the low peak power of the CuBr laser may not „ignite" the material wall developed plasma, and the ejection velocity of the vaporised material may prove too low to prohibit its solidification around the entrance hole. As a result debris or burr can form around the entrance hole, and spoil thus quality of drilling. When considering the laser material processing, the low peak power of the CuBr laser can be compensated with a good laser beam quality (proper laser beam profile and small divergence) which may significantly increase the laser beam fluence (laser pulse energy per unit area). The high quality laser beam can be focused to a very small spot whereby the laser beam fluence increases. Usually the quality of the laser materials processing increases with increasing laser beam fluence.
We aimed at investigating performance of the CuBr laser with negative-branch confocal self-filtering unstable resonator (SFUR) (Fig. 3b) configuration, and compared it with performances of the CuBr laser operating with the negative-branch confocal unstable resonator (UR) (Fig. 3a) and stable resonator (SR) (Fig. 3c). Comparison the performances of the CuBr lasers operating in the UR, SFUR and SR configurations of a 10 W CuBr laser (having the same laser tube inside) allowed to apply the most appropriate resonator to 50W MOPA configuration laser.
The 10 W CuBr laser was composed of a discharge tube placed in a UR formed by fully reflective concave mirrors $M_1$ and $M_2$ of a focal length of $f_1$ = 1200 mm and $f_2$ = 40 mm, respectively. The mirrors $M_1$ and $M_2$ were both set confocally so that the distance between them was 1240 mm. In the common focus of both mirrors $M_1$ and $M_2$ another

mirror $M_3$ was placed with a laser beam transmitting hole. The mirror $M_3$, called a scraper mirror was used to extract the laser radiation outside the resonator. The diameter of the transmitting hole in the scraper mirror $M_3$ was 0.5 mm.

In the second configuration CuBr laser was operating with a SFUR. The main property of the self-filtering unstable resonator, in which a self-filtering intracavity aperture is employed [3], is the achievement of a diffraction limited laser operation with high-efficiency power extraction from the laser cavity. SFUR resonators are particularly suited for high gain lasers and have been tested on Nd:YAG [4], $CO_2$ [5] and excimers lasers [6]. Efficient operation of the conventional copper vapour laser with SFUR, demonstrated by its diffraction limited emission with high-efficiency power extraction depends on the gain build-up in the resonator during the excitation pulse. In contrast to the conventional metal vapour laser, the build-up of the laser gain in CuBr lasers starts on the optical axis whereby the CuBr lasers provide a favourable condition for efficient operation of the SFUR resonator. This may be the advantage of using the CuBr laser instead of a conventional metal vapour laser.

The basic concept of operation of a laser with the SFUR configuration is as follows. The SFUR is a negative-branch confocal unstable resonator with concave mirrors $M_1$, $M_2$ and an aperture A of a diameter 2a set in a focal plane of the resonator, as shown in fig. 3b. When the laser gain starts to build-up on the resonator optical axis, the aperture A is illuminated by the emission of the active medium and transmits the radiation of the top-hat flat distribution resulting from a relatively high component of the amplified spontaneous emission (ASE). The mirror $M_2$ reflects the top-hat flat distribution radiation and focuses it on the aperture plane, producing the typical Airy pattern consisting of a central disk surrounded by rings. If the diameter 2a of the aperture A matches the central disk of the Airy pattern, only the central lobe is transmitted through the aperture to reach the laser medium, where it is amplified, becoming a diffraction-limited progressively amplified diverging laser beam. The mirror $M_1$ reflects this beam and collimates it towards the aperture A and mirror $M_2$. However, only a small part of the collimated back laser beam reaches the aperture A and mirror $M_2$. A major part of the laser beam is reflected from a scraper mirror $M_3$ (with a central hole) extracting the laser radiation from the laser resonator. The part of the laser beam which reaches the aperture A starts the selection process again. The selection process is then iterated whereby the laser oscillation establishes as far as gain duration allows the laser pulse to build up. For efficient selection filtering the aperture diameter 2a should be equal to the diameter of the first Airy disk defined by

$$2a = 2.44\frac{f_2}{2a}\lambda, \tag{1}$$

where $f_2$ is the focal length of the mirror $M_2$, and $\lambda$ is the laser radiation wavelength.

In our SFUR configuration the mirrors $M_1$ and $M_2$ with a focal length of $f_1$ = 1500 mm and $f_2$ = 25 mm, respectively, were used. From the SFUR condition (1) one can find that the diameter of the self-filtering aperture for both CuBr laser lines, $\lambda$ = 510.6 nm and $\lambda$ = 578.2 nm should be equal to 176.5 μm and 187.8 μm, respectively. The calculated diameters of the diffraction lobes on the mirror $M_1$ are 10.6 mm and 11.3 mm for $\lambda$ = 510.6 nm and $\lambda$ = 578.2 nm, respectively.

The actual diameter of the aperture A drilled in a ceramic substrate was 200 μm. The 1500 mm focal-length mirror $M_1$, coated with aluminium had a reflectivity of 95%. The 25 mm focal-length mirror $M_2$, coated with aluminium had a reflectivity of 70%. The scraper flat mirror $M_3$, used as an output coupler was also coated with aluminium. It was set at an angle of 45% in respect to the optical axis. The diameter of the transmitting hole in the scraper mirror $M_3$ was 1.8 mm.

In the third configuration, the 10 W CuBr laser was operating with a SR (Fig.3c). It was formed by two plane-parallel glass plates $M_1$ and $M_2$ inserted between the laser tube and the scraper mirror $M_3$. The output laser beam was outcoupled with the scraper mirror $M_3$, like in the SFUR.

During investigation we measured the profile (light intensity distribution in the cross section of the laser beam) and divergence of the beam of the CuBr laser with three types of resonators.

The investigation of 10 W CuBr laser showed that:

- the CuBr lasers with UR and SFUR generate the laser beams having the divergence (120 μrad) only 1.2 times larger than the diffraction-limited divergence,
- no difference in the power extraction coefficient or beam divergence was observed for the UR and SFUR configurations,
- the divergence of the CuBr laser with SR is about 1 mrad, This makes the laser with the SR useless for the most cases of the laser micromachining,
- superiority of the SFUR configuration over the UR was not found. The laser beam profile and laser gain rise-time were not studied in detail for both cases. It is obvious that the UR configuration is simpler than the SFUR.

Fig. 3. a) Negative-branch confocal unstable resonator (UR): $M_1$ - mirror ($f_1$ = 1200 mm), $M_2$ - mirror ($f_2$ = 40 mm), $M_3$ - scraper mirror for output coupling (diameter of the transmitting hole - 0.5 mm); b) - Self-filtering confocal unstable resonator (SFUR): $M_1$ - mirror ($f_1$ = 1500 mm, R = 95 %), $M_2$ - mirror ($f_2$ = 25 mm, R = 70 %), $M_3$ - scraper flat mirror for output coupling (diameter of the transmitting hole - 1.8 mm), A - pinhole aperture (diameter 200 μm); c) - Stable resonator (SR): $M_1$ - mirror ($f_1$ = 1500 mm), $M_4$ - plane-parallel glass plate (T = 92 %), S – shutter. 4. Set-up for beam measurements

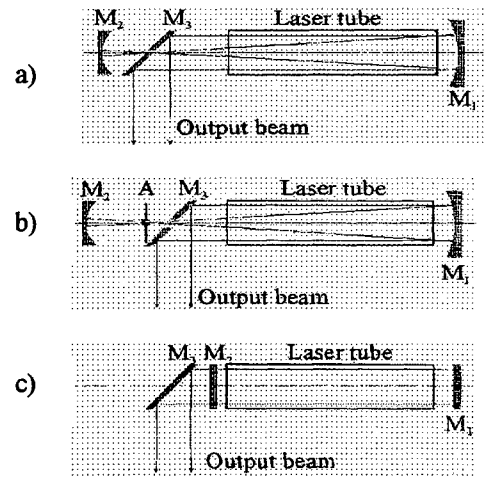


## 4. SET-UP FOR THE CUBR LASER BEAM PROFILE MEASUREMENT

The experimental set-up for the CuBr laser beam profile measurement (Fig. 4) consists of an optical system for transmitting, attenuating and collimating the laser beam, a CCD camera Pulnix 745 and a laser beam analyzer LBA-300 PC manufactured by the Spiricon Co. The CCD camera active element (8.5 mm x 6.4 mm in size) has 768 x 493 pixels (each 11 μm x 13 μm) [8].

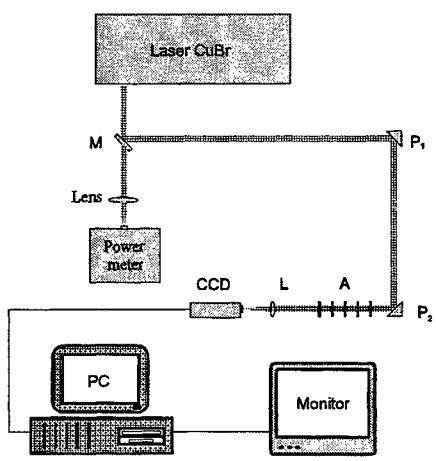


Fig. 4. The experimental set-up for CuBr laser beam measurement.

The laser beam from the CuBr laser is directed by a high-quality mirror M and two prisms $P_1$ and $P_2$ towards the CCD camera. The prisms $P_1$ and $P_2$ play a double role. First, by they reflect the laser beam towards the CCD camera without double reflection that occurs when using parallel-plane plates. Second, by they attenuate the laser beam (the intensity of the laser beam reflected on the prism surface is about 10% of that of the incident beam). The intensity of the laser beam attenuated by the prisms $P_1$ and $P_2$ is about 1% of the initial laser beam intensity. When such attenuation occurs not sufficient, the laser beam passes through the set-up of neutral filters A. The number of the filters in the set-up depends on required level of the final attenuation of the laser beam. Then, the laser beam is collimated by a lens L on the CCD active element. The optimum diameter of the laser beam collimated on the CCD element is set by adjusting the distance between the lens and the CCD element. All the optical parts used for transmitting, attenuating and collimating the laser beam did not distort the laser beam profile.

## 5. EXAMPLES OF LASER MICROMACHINING

Obtained results show the system that we inteded to present may be competitive in wide range of micromechanics and electronics.

Fig. 5.Drilling (30-270 μm holes) in pressurecontainer covers (0.4 mm thick aluminium) in order to test the leak detectors.

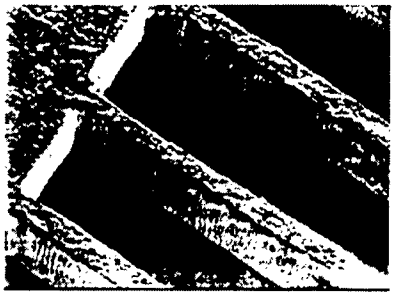

Fig. 6. Cutting of graphite shells used as an electrodes in thyratrons (magnification of 500 times – upper picture, and 250 times – lower picture).

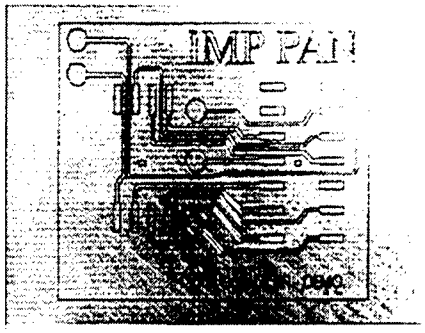

Fig. 7. Cutting of electrical circuit on PCB (track width of 100 μm).

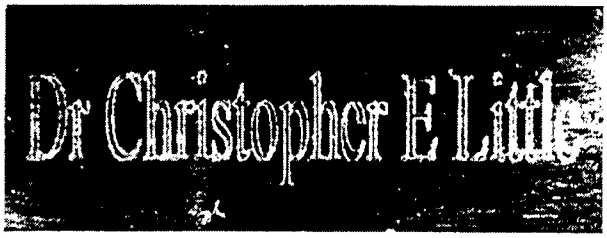


Fig. 8. Carving

## ACKNOWLEDGEMENT

This work was supported by the NATO SfP project 972685 and IMP PAN project O3Z3T1
The authors wish to thank SPIRICON Co. for LBA-300 PC donation.

## REFERENCES

1. M.R.H. Knowles, A.I. Bell,.G. Rutterford, G. Foster-Turner and A.J.Kearsley, *„Advances in copper lasers for micromachining," Proceedings of ICALEO 97* 82, 1997
2. M. Kocik, A. Dąbrowski, J. Mizeraczyk, *„Application of CuBr laser to precisemicromachining of the materials"*, VI Symposium of Laser Technique, Świnoujście, pp. 300-302, 1999
3. P.G. Gobbi, S. Morosi, G.C. Reali, Optics Comm., 52, 195, 1984
4. P.G. Gobbi, S. Morosi, G.C. Reali anid A.S. Zarkasi, Appl. Optics, 24, 26, 1985
5. R. Barbini, A. Ghigo, M. Giorgi, K.N. Iyer, A. Palucci and S. Ribezzo, Optics comm., 60, 239, 1986
6. V. Boffa, P. Di Lazzaro, G.P. Gallerano, G. Giordano, T. Hermsen, T. Letardi and C.E. Zheng, IEEE J. Quantum Electron, QE-23, 1241, 1987
7. M. Kocik, M. Mohamed-Seghir, J. Mizeraczyk, „Set-up for measuring the CuBr laser beam parameters", SPIE (USA) to be published.
8. N. V. Sabotinov, J. Mizeraczyk, I. K. Kostadinov, E. S. Livingstone, C. E. Little, „A 100 Watt Copper Bromide Laser for Materials Processing", CLEO/ Europe, Conference on Lasers and Electro-Optics Europe, 1998.
9. R. Pini, R. Salimbeni, G. Toci, M. Vannini, "High efficiency diffraction limited operation of copper vapour laser", Opt. Commun. 81, pp. 138-144, 1991.

# Experimental study of a laser processing head with integrated jet of metal powder for rapid prototyping and production of protective coatings

R. Jendrzejewski*[a], A. Conde[b], J. de Damborenea**[b] and G. Śliwiński[a]

[a] Polish Academy of Sciences, Institute of Fluid Flow Machinery, Fiszera 14, 80-231 Gdańsk, Poland
[b] Spanish Council for Scientific Research, National Center for Metallurgical Research (CENIM)
Avenida de Gregorio del Amo 8, Madrid, 28040, Spain

## ABSTRACT

A controllable, homogeneous stream of metal powder particles is remelted by a focused, coaxial $CO_2$ laser beam at the outlet of a multi-stream nozzle and applied for production of the protective coatings and volumetric structures for prototyping. For the stellite SF6 layers the optical, chemical, and metallographic tests show the fine-grained and chemically homogeneous structures with only a minor presence of the Cr/C precipitates and local micro-defects.

**Keywords:** laser processing head, $CO_2$ laser, laser cladding, rapid prototyping, protective coatings

## 1. INTRODUCTION

The laser remelting of metal powders applied for protective coatings and also for the rapid prototyping of models, manufacturing, and reparation of machine parts is extensively studied in the last decade [1-6]. Quality surfaces can be obtained by this method while achieving the required mechanical properties and microstructure of the final product. For the prototyping a significant reduction of the time between the design stage and manufacturing is achieved due to the effective combination of the CAD/CAM design techniques with the CNC controlled laser workstations [1]. The cw and pulsed laser sources allow for an optimised choice of the interaction parameters for a given material (base + powder) in several iterative steps. The optimisation can be supported by calculations of these parameters based on semi-empirical models where physical constants of materials and data characterising the process are applied [4]. Recently, an interest in the relevant experimental data growths rapidly despite of the fact, that in many cases they refer to specific applications, materials and interaction geometries [3-6]. It is stimulated by the need of the process control, which can be supported by a verified model of the process and a collection of appropriate data.

In this work an investigation of the volumetric structures consisting of a single and multilayer clads obtained by means of an experimental device for laser remelting of metal powders is reported for the case of Stellite SF6. Characteristics of the process are reported and results of sample examination obtained by the optical and scanning microscopy and also by the EDS chemical analysis and corrosion test are presented and discussed. The data characterising the microhardness, corrosion and also wear resistance are analysed.

## 2. EXPERIMENTAL

An experimental cw $CO_2$ laser stand of the output of 1.5 kW equipped with the numerically controlled XYZ manipulator was used for the experiments. The laser beam of 18 mm in dia was focused by means of a lens optics (ZnSe, f = 127 mm) integrated into the processing head - Fig. 1. The beam spot of 1 mm in dia measured on the processed surface has been kept constant. The applied beam intensities were equal to about $10^5$ W/cm$^2$ and the laser output was controlled with an accuracy of ±2%. For the powder injection into the processing zone, a multi-stream, water-cooled nozzle mounted co-axially with the focussing optics was applied. A gravitational powder feeder together with the nozzle assured a homogeneous flow of the powder at a feed rate controllable in the range of 0.05-0.33 g/s. The visualisation of the powder jet confirmed a uniform distribution of the metal particles in a conical volume corresponding to the flow expansion at the jet outlet and their velocities in the range of 2-6.5 m/s were measured - Fig. 2. Ar gas was applied for the powder transport. Two additional Ar streams were used for shielding of the focussing lens and of the interaction zone in order to prevent the production of oxides and avoid contamination due to the contact with surrounding. The processing head (see Fig. 1) was tested for several powder materials. However, the best results were obtained with powders of the bronze B10 (10% Sn) and of Stellite SF6

* Correspondence: e-mail: rafj@imp.pg.gda.pl, tel.: +48 58 341 12 71, fax: +48 58 341 61 44
** Correspondence: e-mail: jdambo@fresno.csic.es, tel. +34 1 5538900, fax: +34 1 5347425

XIII International Symposium on Gas Flow and Chemical Lasers and High-Power Laser Conference,
Antonio Lapucci, Marco Ciofini, Editors, Proceedings of SPIE Vol. 4184 (2001)

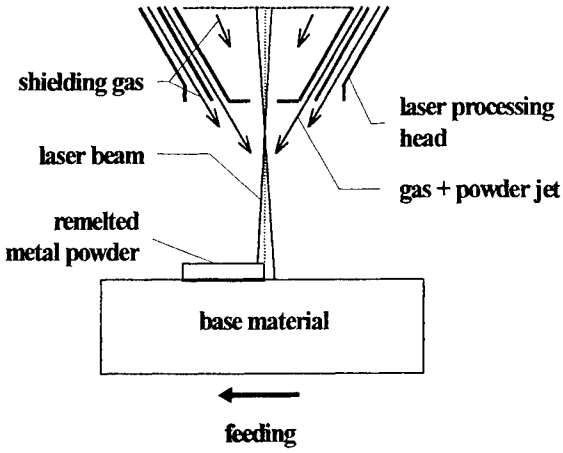


**Fig. 1.** Scheme of the laser cladding process with a metal powder used as an original material.

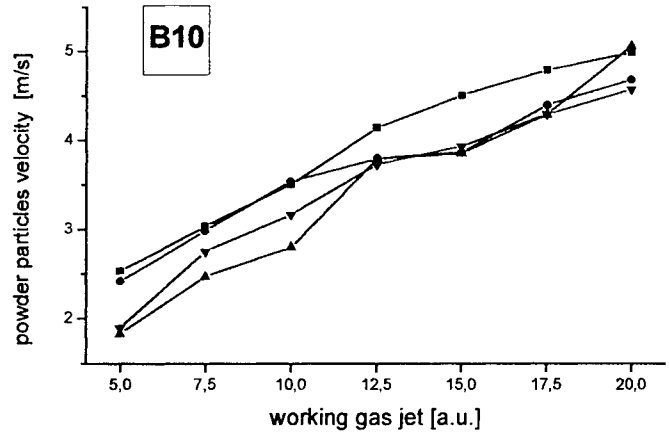


**Fig. 2.** Average velocity of the B10 powder particles vs. flow rate of the working gas for different nozzle geometries.

(51.5% Co /bal./, 19% Cr, 13.5% Ni, 7.5% W, max 3% Fe, 2.3% Si, 1.6% B, max 1% Mn, 0.7% C) of the grain size up to 60 μm. On Fig. 3 a relationship between the powder jet expansion coefficient ($\Delta d/\Delta z$) of the gas+Stellite stream and the powder feed rate is shown. Plates of the carbon steel and of a high-temperature resistive alloys (12% Cr, 1% Mo, 0.6% Ni, max 0.6% Mn, max 0.6% Si, 0.2% C, bal. Fe) were used as the base material. The horizontal feed rate used to produce the structures did not exceeded 25 mm/s, and the vertical one was controlled stepwise and steps equal to the layer height were applied. Traces of the remelted powder material of dimensions of 1 mm x 0.3 mm (width x height) were applied for a surface coatings by a partial trace overlap and also as volumetric structures by the trace-on-trace remelting as well.

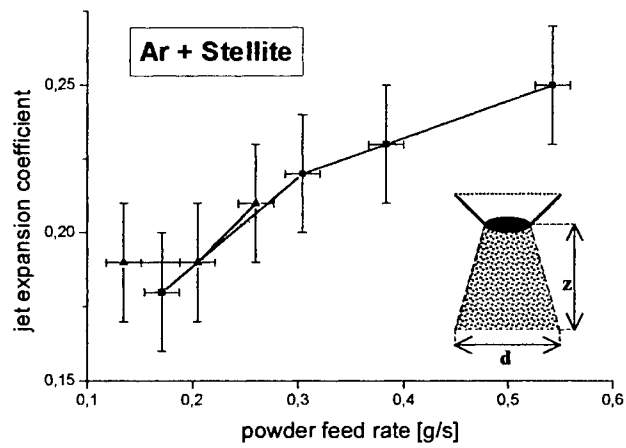


**Fig. 3.** Jet expansion coefficient vs. powder feed rate for two different nozzle geometries.

In order to conclude on the processing quality and reproducibility of results for a given set of parameters the samples were examined by means of the optical, chemical, and metallographic methods. After cutting, polishing and etching of the samples an inspection of the microstructure of the respective cross sections was performed by means of the optical and electron scanning microscopes (SEM) of the types PME-3 (Optimus) and JXA-840 (JEOL), respectively. The EDS (Energy Dispersive Spectroscopy) was applied for chemical analysis of the laser remelted layers. For characterisation of the mechanical properties of the cladded SF6 coatings the microhardness was measured by means of the Vickers method using a load of 300 g. Measurements were carried out at different distances from the coating surface in several, arbitrarily chosen, vertical cross sections of the clads. In order to obtain a quantitative data on corrosion resistance the potentiodynamical curve has been measured for the representative samples. The electrochemical tests were carried out in a standardised solution of 3.56% NaCl. The tested area was $1cm^2$ and the rest of the surface was masked by means of an anticorrosion tape. Once the samples were immersed in the electrolyte and the corrosion potential has been stabilised, a potential sweep was applied beginning at a level of -1000 mV/SCE at a scan rate of 1 mV/s until the current density of $1mA/cm^2$ was achieved.

## 3. RESULTS AND DISCUSSION

### 3.1 Microstructure and chemical composition of the laser clads

For a laser cladded layer of a thickness of 0.5mm the EDS analysis revealed a relatively uniform content of the original components at different depths of the coating, indicating that after the deposition and remelting no changes were induced in the chemical composition. Effects of dealloying or oxidation were not evidenced, too. Only in the stellite zone close to the base material a slight differences in composition can be observed with respect to the layer. This is demonstrated by the EDS

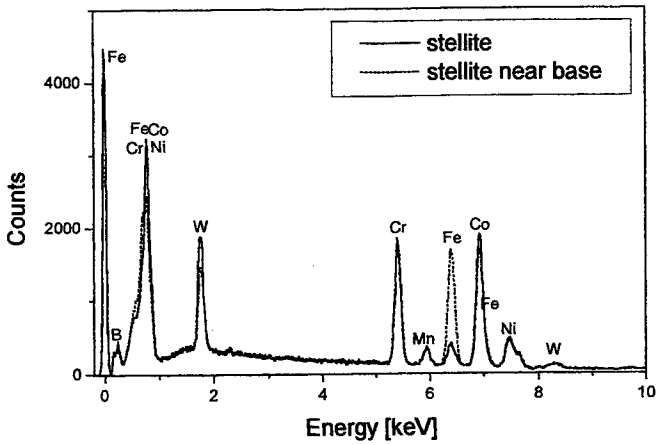


**Fig. 4.** The EDS analysis of the bulk stellite (full line) and its area close to the base (dashed line).

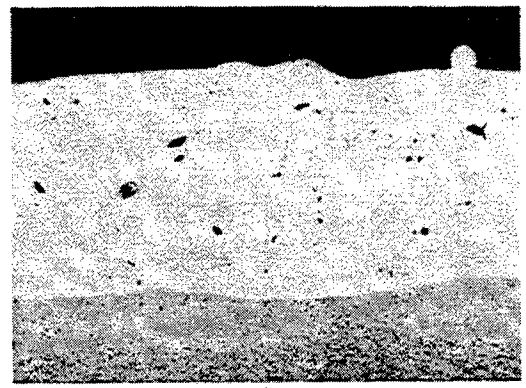

**Fig. 5.** The laser cladded stellite SF6 layer: a cross section of the coating - upper part, and base - lower part, magnification 30x.

results obtained for this area, which indicate a higher content of Fe in comparison to the Fe concentration in the bulk of the stellite. It allows to conclude that some diffusion of iron from the substrate has taken place - see Fig. 4.

A general view of the coating can be observed in Fig. 5. The layer is homogeneous and exhibits a good adherence with the substrate. The SEM micrograph in Fig. 6 reveals the presence of the white precipitates in the base steel as well as different structures of both zones. The upper part (Fig. 6) corresponds to the stellite clad and shows a dendritic structure growing from the interface. This fine-grained and homogeneous structure is characteristic for a fast sequential heating and cooling of the sample. At higher magnifications it is possible to distinguish more clearly that between the cladded layer and the base metal there is a metallurgical bond rather than an interface. This assures a good adherence of the coating. On the other hand, in the areas along the internal part of the interface towards the base steel there is an array of precipitates, for which the EDS analysis revealed that they contain mainly Cr. This is interpreted as precipitation of chromium carbides as a result of an enrichment of the local carbon promoted by melting of the carbon steel used as substrate.

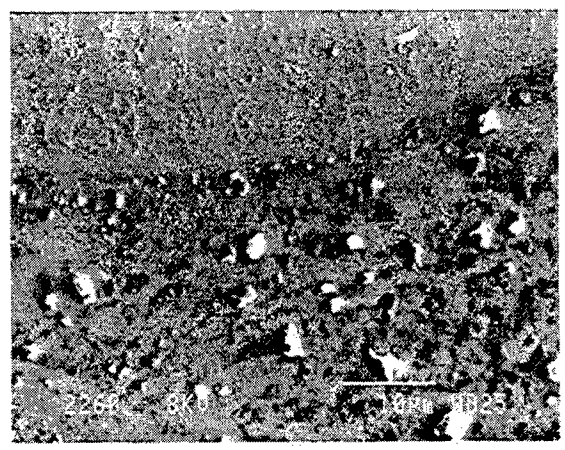

**Fig. 6.** SEM photograph of the dendritic structure of the stellite (upper zone) and the structure of the base steel.

### 3.2 Microhardness

Measurements of the Vickers microhardness were carried out at different depths of the cross section of the sample. Values obtained for the stellite are equal to about 750 HV (load 300 g) which is considerably higher than those measured for the base steel of 198 HV and values corresponding to the remelted track of the base metal are equal to about 400 HV. It is still higher than these of the core steel but half of the values measured for the stellite. This difference can be due either to a lower concentration of the elements of the alloy in that area or to the laser scanning of the surface prior to cladding. This initial scanning results in a rapid melting of the surface and leads to a dissolution and distribution of the included precipitates. The observed effect promote a finer structure of better mechanical and corrosion properties and confirms the results reported in the literature[6].

### 3.3 Corrosion resistance

Results of the corrosion tests are presented as the potentiodynamic curves in Fig. 7 for the base material (doted line) and the laser cladded sample (full line). The corrosion potential obtained for the cladded layer is of the same order of magnitude as that of the uncoated steel. Although for the coated sample a presence of a nearly vertical stage typical for passive material

can be observed. Its length is quite short and the current density corresponding to the passivity is similar to the corrosion current density of the non-cladded material. Unfortunately, this behaviour suggests the presence of defects in the form of micro-cracks in the coating which expose the base material locally to the aggressive environment. The corrosive agents may reach the substrate through these defects launching the corrosion attack, which can extend in the base in subsequent steps.

The occurrence of micro-cracks is most probably due to the residual, thermal tensions induced in the sample during the cladding. A similar effect was observed for the laser alloying by means of coatings containing the Fe, Cr, Mn and C and a marked improvement of the final effect was obtained for a selected clad composition and under conditions of preheating of the base material to a given temperature[6].

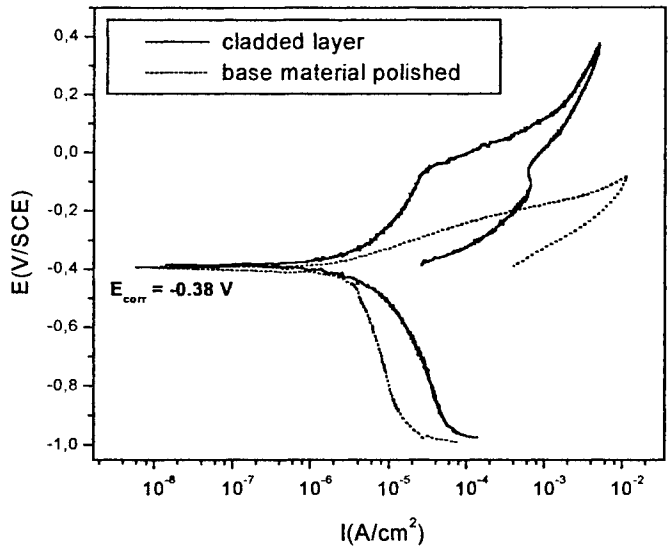


**Fig. 7.** The potentiodynamic curves of the base material and cladded layer.

## 4. CONCLUDING REMARKS

A laser processing head equipped with the water-cooled, multi-stream nozzle was applied for the production of protective coatings and for fast prototyping. Coatings and also volumetric structures were produced by remelting of metal powders by means of a $CO_2$ laser at intensities of about $10^5$ W/cm$^2$. The results of the optical, chemical, and metallographic examinations made for stellite SF6 layers confirmed that the process parameters can be controlled for a given material. For the fine-grained and chemically homogeneous structures showing the required adhesion to the base material only a minor presence of the Cr/C precipitates was observed. However, the corrosion tests indicated on a local structure defects (micro-cracks). An increase of microhardness of the remelted track of the base up to 400 HV compared to the core value of about 200 HV was measured and ascribed to the combined effect of diffusion and high temperature gradients under interaction of intense laser beam. Results allow to conclude that the investigated processing head can serve as an efficient tool for laser cladding and production of volumetric structures for protective coatings and fast prototyping.

## 5. ACKNOWLEDGEMENTS

This work was sponsored by the State Committee for Scientific Research (KBN) under contract No. 7 T08D 019 15 and by the bilateral agreement between Polish Academy of Sciences and Spanish Council for Scientific Research (CSIC). Authors appreciate the technical support of M. Piskulski (IFFM).

## 6. REFERENCES

1. G.K. Levis, E. Schlienger, "Practical considerations and capabilities for laser assisted direct metal deposition", *Materials&Design* **21**(4), pp. 417-423 (2000).
2. J.M. Yellup, "Laser cladding using the powder blowing technique", *Surface & Coatings Technology* **71**(2), pp. 121-128 (1995).
3. R. Jendrzejewski, G. Rabczuk, R. Zaremba, G. Śliwiński, "Laser stereolithography by multilayer cladding of metal powders", *Proceedings of SPIE* **3423**, pp. 348-352 (1998).
4. R. Jendrzejewski, T. Klimczuk, W. Sadowski, G. Śliwiński, "Multilayer laser cladding of metal powders for fast prototyping", *Proceedings of SPIE*, Vol. **3571**, pp. 383-387 (1998).
5. R. Jendrzejewski, R. Zaremba, P. Kukiełło, G. Śliwiński, "Multilayer sintering and cladding of metal powders for fast prototyping", *Proceedings of 6th International Conference on Welding and Melting by Electron and Laser Beam CISFFEL6, Toulon, France*, pp. 511-518 (1998).
6. R. Vilar, "Laser alloying and laser cladding", *Materials Science Forum* **301**, pp. 229-252 (1999).

# In-line thermal monitoring of acrylic surfaces processed by a segmented pixel drawing method using a slab-RF excited $CO_2$ laser

Noriyo SAKURADA *, Masashi IWAMOTO *, Hajime EBISUTANI *, Yoshio ISHII **
Kazuhiro WATANABE **, and Yuzuru KUBOTA **

* Graduate student
** Department of Information Systems Science, Faculty of Engineering, SOKA University.

## ABSTRACT

Visualization of thermal surfaces has been used in various fields. In this study, thermal monitoring of acrylic surfaces has been performed which were processed by a segmented pixel drawing (SPD) method using a slab-RF excited $CO_2$ laser. The SPD method has been newly developed to make an artistic sculpture. In this method, it is possible to obtain various effects on processed surfaces by controlling processing parameters. This method demands uniform processing shapes in a pixel and reproducibility of results. The purposes of this study are to evaluate the processing results and to investigate the causes of unfavorable processing shapes by capturing thermal phenomena. Thermal distribution on laser processed surfaces obtained by this study can be useful to correct some important data for acrylic laser sculptures. The causes of unfavorable processing can be improved so as to obtain uniform processing shapes.

**Keywords:** Thermal monitoring, Infrared thermography, Slab-RF excited $CO_2$ laser, Segmented pixel drawing method

## 1. INTRODUCTION

Visualization of thermal surfaces has been used in various industrial fields.[1] [2] These visualization has currently been introduced in field of laser processing.[3] [4] Laser processing is one of the most attractive methods in a field of processings, and has been widely used for various applications. Among various types of lasers for processing, $CO_2$ lasers with different excitation schemes have been commercially available for the processings not only of metals but also of non-metals such as acrylic, epoxy glass, ceramics, and glass due to the demands of industrial applications. [5] [6]

In this study, thermal monitoring of acrylic surfaces has been performed which were processed by a segmented pixel drawing (SPD) method using a slab-RF excited $CO_2$ laser. This method demands uniform processing shapes in a pixel and reproducibility of results, and so thermal monitoring is useful to analyze thermal phenomena of processed surfaces. Infrared thermography and an image analysis system have been introduced to capture these phenomena. Infrared thermography is a two-dimensional, non-contact technique of temperature measurement and can be used in various heat transfers found in not only research fields but also industrial applications.

Thermal phenomena occurred in processed surfaces have complex structures and variation in time with resulting in various processed structures. The purposes of this study are to evaluate the processing results and to investigate the causes of unfavorable processing shapes by capturing thermal phenomena.

## 2. A SEGMENTED PIXEL DRAWING (SPD) METHOD

In this study, we use a slab-RF excited $CO_2$ laser developed in our laboratory[7] and an acrylic board as processed materials. Conventional methods of laser processing are typically of marking and masking. Shortcomings of these methods are small processing area and few tones. The SPD method has been newly developed to cover shortcomings of these methods.[8] [9] Since this method has the characteristics that materials were processed in a pixel-base using focus/defocus beam, processing area can be large and it is possible to get various effects on processing surfaces. Using this method, processing surfaces are created by a laser in a segmented pixel-base in which various surface effects are given such as fluent, opaque, rugged tones and so on.

Figure1 shows a processed sample image using the SPD method. Figure2 shows the pixel samples. As one can see from Fig.1, processing surfaces are made of the combination of some pixels with the SPD method.

Correspondence: E-mail: miwamoto@edu.t.soka.ac.jp; Telephone: +81(426) 91 9312; Fax: +81(426) 91 9312

XIII International Symposium on Gas Flow and Chemical Lasers and High-Power Laser Conference,
Antonio Lapucci, Marco Ciofini, Editors, Proceedings of SPIE Vol. 4184 (2001)

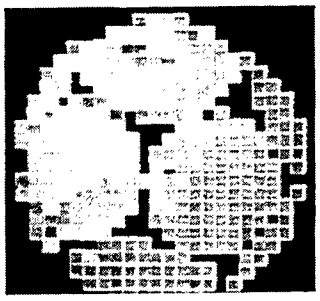

Fig.1 A processed sample image using the SPD method

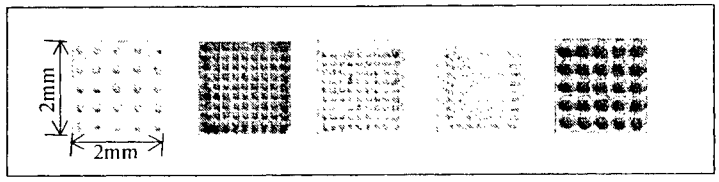


Fig.2 The pixel samples

## 3. PLANCK'S LAW OF THERMAL RADIATION

Plank's law of thermal radiation is shown in equation (1) and the relationship between wavelength and radiation energy is shown as Fig.3,

$$W_\lambda = \frac{2\pi hc^2}{\lambda^5} \cdot \frac{1}{e^{hc/\lambda kT} - 1}, \qquad (1)$$

where $W_\lambda$, $\lambda$ and T are the radiation energy per unit area and per unit wavelength [W/(cm$^2$ · $\mu$ m)], the wavelength[ $\mu$ m] and the absolute temperature[K], respectively. h, c and k are the Planck's constant[$6.626 \times 10^{-34}$W·s$^2$], the light velocity [$2.998 \times 10^{10}$cm/s] and the Boltzmann's constant [$1.380 \times 10^{-23}$W/ ( s · K ) ], respectively.

As one can see from Fig.3, in the case that the temperature of material is 3000K, the radiation distributes over the wavelength region of ultraviolet, visible and infrared. Decreasing the temperature, the radiation becomes dominated mainly with infrared region. Since the temperature at processed target areas using the SPD method are ranged about 390~520k, an infrared thermography enable us to observe such low temperature phenomena.

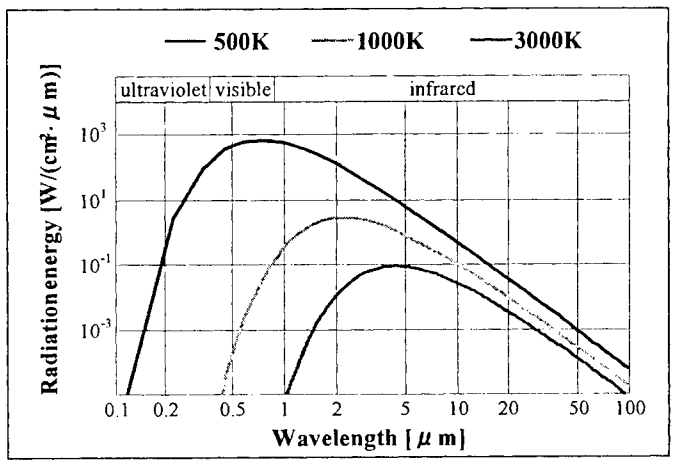


Fig.3 Plank's law of thermal radiation

## 4. EXPERIMENTAL SETUP AND ANALYSIS

### 4.1 Experimental setup

Figure4 shows experimental setup. The laser system consists of (1) an RF power supply which is capable of producing a maximum RF power of 2kW at the frequency of 100 MHz and can be controlled in terms of the duty cycle and the frequency, (2) a laser head made by aluminum, (3) a gas handling system that pump out an air and supply a mixed gas of $CO_2$, $N_2$, and He in a rate of 1:1:3 in the laser head, (4) a cooling system using water, and (5) a personal computer with a control electronics which measures and controls these above mentioned system.

The optical system consists of a scanner system with x-axis, y-axis mirror and z-axis lens, and a personal computer which controls this system through the scanning controller.

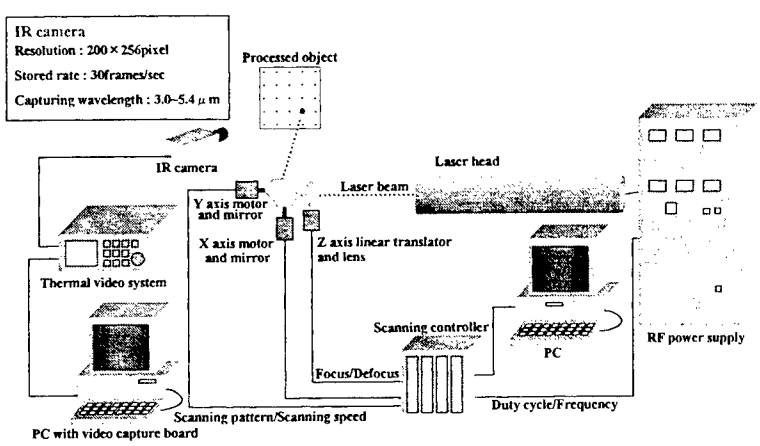


Fig.4 Experimental setup

The infrared thermography system consists of an infrared camera, a thermal video system and a personal computer. Through a video capture board, the images were captured and stored in a personal computer at a rate of 30 frames/sec. Infrared thermography have a capturing the wavelength ranged 3.0~5.4 $\mu$ m and an image resolution of 5.6image-pixel/mm. In this experiment, a SPD pixel pattern of $3 \times 3$ dots was observed under the use of focused beam operated with 50% of the duty cycle and 0.15 kHz of the frequency.

### 4.2 Analyzing method

In this study, several images were captured by the infrared thermography system during processing a pixel. These images have data of temperature in 45 × 45 pixels for the observed area. Maximum temperature was calculated using the temperature data of these images per each image-pixel. The maximum temperature obtained in a pixel was represented as a contour map and a 3-D histogram, with which we evaluate the causes of unfavorable processing.

## 5. RESULTS AND DISCUSSIONS

### 5.1 Maximum temperature map (1)

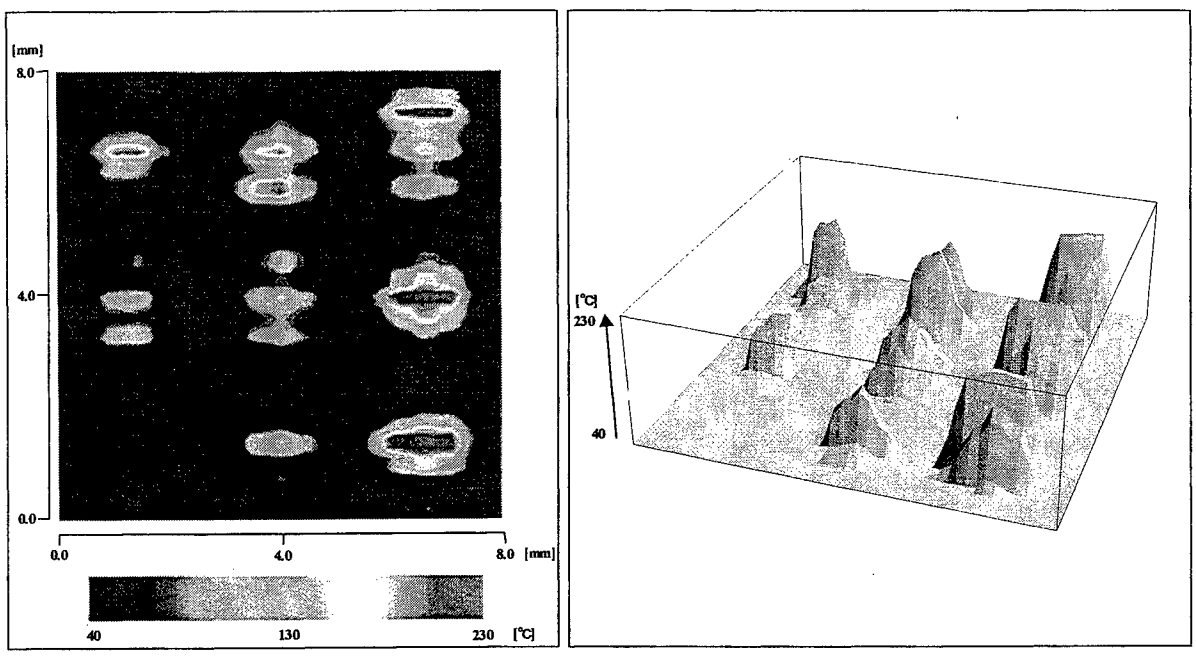


Fig.5 Maximum temperature contour map and 3-D histogram (1)

Figure5 shows the contour map and the 3-D histogram indicating the maximum temperature. As one can see from Fig.5, the thermal distribution in a pixel is found to be non-uniform in this processing. This means that laser beam irradiation at the lower left position in this pixel is not enough in it power level. Therefore it is evaluated that these operations are unfavorable in pixel-base processing.

The causes of unfavorable processing are probably due to the unstable power of laser beam and controllability of x-y scanner.

### 5.2 Maximum temperature map (2)

As experimental conditions, the initial value of jump delay and stroke delay about x-y scanner (500 $\mu$ s) are changed into 5000 $\mu$ s. The jump delay is defined as a waiting time after jumping. The stroke delay means a waiting time before jumping. Figure6 shows the maximum temperature map and 3-D histogram after changing x-y scanner setting. As one can see Fig.6, it is found that the uniformity of thermal distribution in a pixel was improved since laser beam scanning was uniformly made than in Fig.5. Therefore this processing is success.

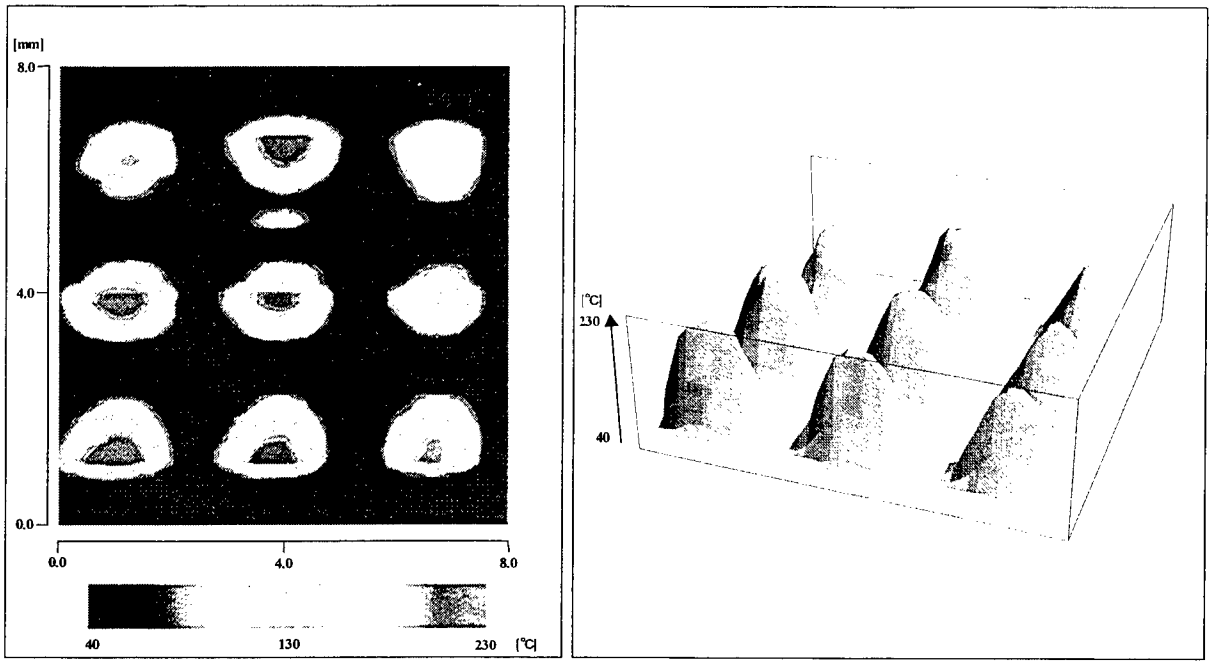


Fig.6 Maximum temperature contour map and 3-D histogram (2)

## 6 CONCLUSIONS

In this study, it is confirmed that infrared thermal monitoring system is useful to capture and analyze thermal phenomena of surfaces processed by the SPD method using slab-RF excited $CO_2$ laser. It is found the causes of unfavorable processing can be closely related the obtained thermographical information. Although the SPD pixel can be observable through the visual inspection by eyes, it is very difficult that such a visual inspection provide quantitative reasons for unfavorable pixel production. This thermal monitoring method would be very helpful to understand better the detailed production mechanisms of the SPD pixels.

## REFERENCES


1. Carlomagno,G.M., Cardone,G, Meola,C, and Astarita,T : Infrared Thermography as a Tool for Thermal Surface Flow Visualizations, Journal of Visualization, Vol.1, No1(1998) 37-50
2. Jian HUANG, Tatsuo TOGAWA, Kiichi TSUCHIYA : Visualization of skin thermal properties by successive thermographic measurements, Fifth Triennial International Symposium on Fluid Control, Measurement and Visualization,1997,899-904
3. Yoshio ISHII, Noriyo SAKURADA, Tadayuki SUGIMORI, Kazuhiro WATANABE, Yuzuru KUBOTA, and Katutoshi NAGANO : Visualization of infrared high power laser beam for in-line monitoring using an ultraviolet CCD camera, 8th International Symposium on Flow Visualization, CD Rom, No.249. (9 pages)
4. Noriyo SAKURADA, Yoshio ISHII, Hajime EBISUTANI, Kazuhiro WATANABE, Yuzuru KUBOTA: Visualization of thermal phenomena on acrylic surface processed by a SPD method using a slab-RF excited $CO_2$ laser, Proceeding of The Millennium 9th International Symposium on Flow Visualization, CD Rom, No.261. (9 pages.)
5. K. Bondelie : Sealed carbon dioxide lasers achieve new power levels, Laser Focus World, August, pp.95-100, 1996.
6. G. Ogura, J. Angell, and D. Wall : Applications test potential of laser micromachining, Laser Focus World, June, pp.117-123, 1998.
7. K.Watanabe.: Performance Characteristics of a Slab RF-Excited CO2 laser, the Review of Engineering ,Vol.21, No.12, pp.1245-1254, 1993.
8. Noriyo SAKURADA, Yoshio ISHII, Hajime EBISUTANI, Kazuhiro WATANABE, Yuzuru KUBOTA; A segmented pixel drawing method using a slab, RF excited CO2 laser for artistic sculpture, Proceeding of SPIE, Vol.3887, pp.349-356, 1999.
9. Hajime EBISUTANI, Noriyo SAKURADA, Yoshio ISHII, Kazuhiro Watanabe, Yuzuru. KUBOTA; Artistic processing on acrylic materials using a segmented pixel drawing method with a slab, RF excited CO2 laser, Proceeding of GCL-HPL 2000, Florence, 18-22.Sep., in press.

# Neural networks optimisation of laser welding process

F. Caiazzo[*a], G. Daurelio[**b], A. D. Ludovico[***c], F. Memola Capece Minutolo[****d], V. Sergi[*a]

[a]Dip. Ing. Meccanica – Univ. di Salerno - Via Ponte Don Melillo – 84084 Fisciano – Salerno (Italy)

[b]Centro Laser S.c.ar.l. – Str. Provinciale per Casamassima km 3 – 70010 Valenzano Bari (Italy)

[c]Dip. di Progettazione e Produzione Ind. – Politecnico di Bari – V.le Japigia, 182 – 70126 Bari (Italy)

[d]Dip. Ing. Materiali e Prod. – Univ. di Napoli "Federico II" – P.le Tecchio, 80 – 80125 Napoli (Italy)

## ABSTRACT

The employment of laser systems for completely automated welding processes needs an analysis of physical mechanisms by means of mathematical models to correlate the characteristic quality indexes of welding to working parameters. In this paper we describe the application of neural networks method in order to correlate, for different kinds of stainless steel, the melting area and the welding efficiency to working parameters, leaving out of account the knowledge of the chemical and thermo-physical properties of working materials. The results are quite satisfactory even if a direct search of the optimal process conditions is not possible.

**Keywords:** Laser welding, Neural network, Stainless steel, Parameter selection

## 1. INTRODUCTION

Optimisation of laser welding means, generally, to select the laser source and the variables or parameters affecting the process and to find analytical correlation between these parameters in order to produce an objective function of one or more variables to maximize or minimize. Usually this problem, when applied to technological processes, turns out to be analytically non-resoluble if the process parameters are not independent and if there are constraints to respect. In these cases it is only possible to obtain approximate solutions of some sub-problems and we are only able to find some conditions of relative minimum or maximum.

Regarding the laser welding process, we can infer that a leading role on the quality of weld bead is played by: power of the incident laser beam, laser beam diameter, speed of the workpiece, laser beam depth of focus, type of converging lens, type of covering gas, beyond obviously the physical and chemical properties of welding materials[1-3]. The welding quality can usually be evaluated directly by means of mechanical and technological properties and metallographic examinations of welded joints or alternatively by means of the welding efficiency, measured as the ratio between the melting volume per second (MV, $mm^3/s$) and the laser power (LP, kW), the former being the product between the welding speed (WS, mm/s) and the melting area (MA, $mm^2$); the melting area can be easily evaluated by image analysis of cross section of weld bead. The authors demonstrated that the welding efficiency (WE, $mm^3/kJ$), for acceptable welding joints, falls in the range $20 \div 55$[4]. In this paper we will consider the melting area and the welding efficiency, as the characteristic parameters of the welding process, and their dependence on internal and external process parameters will be examined.

Starting with the consideration that each experimental data, characterized by process and material variables, can be thought as a point in an n-dimensional space and that each experimental data can be linked to some output parameters, namely melting area and welding efficiency, we have carried out research in order to test a new method of classification, by means of Artificial Intelligence Techniques, namely Neural Networks with guided learning.

## 2. NEURAL NETWORKS BACKGROUND

The neural networks model is a highly parallel complex system built by interconnecting several computational elements or nodes. The computational elements are typically non-linear and are interconnected via weights that can be iteratively

* Telephone +39 089 964321 – Fax +39 089 964037 – E-MAIL: f.caiazzo@unisa.it – sergi@unisa.it

** Telephone +39 080 4674314 – Fax +39.080.4674457 – E-MAIL: dau@alien.claser.tno.it

*** Telephone +39 080 5962755 – Fax +39.080.5962788– E-MAIL: ludovico@poliba.it

**** Telephone +39 081 7682375 – Fax +39 081 7682362 – E-MAIL: capece@unina.it

XIII International Symposium on Gas Flow and Chemical Lasers and High-Power Laser Conference,
Antonio Lapucci, Marco Ciofini, Editors, Proceedings of SPIE Vol. 4184 (2001)

adapted to improve performance. Each simple node performs a weighted sum of the $N$ inputs and transform the sum to an output signal that is a non-linear function of the result.

The simplest neural network analysed in depth is the perceptron[5]; the linear algorithm and the iterative version of Widrow-Hoff procedure both advocate finding through the following rules:

$$\mathbf{w}_{p+1} = \mathbf{w}_k + \eta\left(\mathbf{t}^p - \mathbf{w}_p^T \cdot \mathbf{x}_p\right)\mathbf{x}_p \quad \text{with } \mathbf{w}_1 = \text{ arbitrary} \tag{1}$$

In the above equation **w** represents a column vector of synapses, **x** a column vector of characteristics or patterns, **t** the true output value specified by the training-set examples, the index p indicates the sequence of pattern presented to the net, and $\eta$ is the learning rate. We can write (1) also in the form $\Delta\mathbf{w} = \eta\delta x$, so-called DELTA RULE, where the vector $\delta$ represents the difference between the desired output and the actual output produced by the net.

One of the problems with the perceptron is that, when the classes are not linearly separable in the feature space, the algorithm will not converge. In most practical situations, the classes are seldom linearly separable, particularly when multiple categories are involved. Consequently, the nonlinear decision boundary can be generated by using a multi-layered structure, along with nonlinear transfer function of weighted sum of input. The intermediate layers extract the higher orders of correlation in the signals and in general can generate any arbitrary decision surface.

The multi-layered network proposed, as illustrated in the example, is a two-layered feed-forward network with a layer of $m$ input units at the bottom, which is only a buffer and doesn't perform any operation, a hidden layer of $j$ units in the middle, connected, in turn, to a layer of $k$ output units, fig. 1.

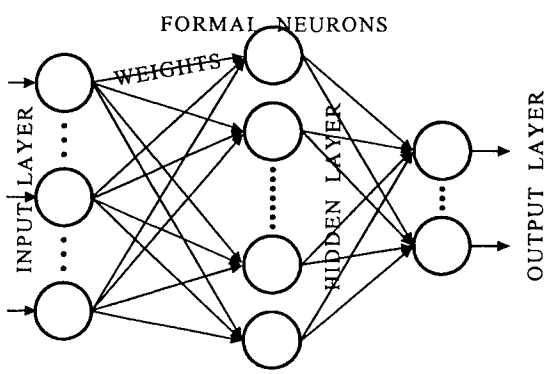


Fig. 1 – Neural Network Diagram

Using a superscript in square brackets to indicate which layer of the networks is being considered ($i$ = input, $h$ = hidden, $o$ = output), the input to node $j$ of first hidden layer is:

$$\text{in}_j^{[h]} = \sum_m w_{jm}^{[h]} x_m \tag{2}$$

while the output of this node is:

$$\text{out}_j^{[h]} = f\left(\text{in}_j^{[h]}\right) \tag{3}$$

where $f$ is the activation function, which is traditionally the sigmoid function, but can be any differentiable function. Therefore the input to the $k$ node of the output layer is:

$$\text{in}_k^{[o]} = \sum_j w_{kj}^{[o]} \cdot \text{out}_j^{[h]} = \sum_j w_{kj}^{[o]} \cdot f\left(\text{in}_j^{[h]}\right) \tag{4}$$

and finally the output of this node is:

$$\text{out}_k^{[o]} = f\left(\text{in}_k^{[o]}\right) = f\left(\sum_j w_{kj}^{[o]} \cdot f\left(\text{in}_j^{[h]}\right)\right) \tag{5}$$

In general, the calculated output $\{o_{pk}\}$ will not be the same as the target or desired values $\{t_{pk}\}$. The square errors for each pattern and the average system error are:

$$E_p = \frac{1}{2}\sum_k \left(t_{pk} - o_{pk}\right)^2 \quad \text{and} \quad E = \frac{1}{2P}\sum_p \sum_k \left(t_{pk} - o_{pk}\right)^2 \tag{6}$$

where the factor of one-half is inserted only for mathematical convenience.

The back-propagation algorithm relies on a recursive procedure to estimate the weights on the basis of error in response at each layer[6-8]. The weights are estimated using the gradient descent method for minimizing the error. To calculate them, we use the chain rule to express the partial derivative in term of two factors, one expressing the rate of change of error with respect to the output, and the other expressing the rate of change of the output of the node $k$ with respect to the input to that same node. In order to estimate the weights we can use the same formal expression of DELTA RULE, where the components of $\delta$ vector have the following values:

$$\begin{aligned} \delta_{pk} &= \left(t_{pk} - o_{pk}\right) \cdot o_{pk} \cdot \left(1 - o_{pk}\right) && \text{for the output layer} \\ \delta_{pj} &= o_{pj} \cdot \left(1 - o_{pj}\right) \cdot \sum_k \delta_{pk} w_{kj} && \text{for the hidden layer} \end{aligned} \tag{7}$$

## 3. MATERIALS, EXPERIMENTAL PROCEDURES AND NEURAL NETWORKS APPLICABILITY

In this first application stage of the neural networks method, the results relevant to welding laser processes in stainless steels (austenitic, ferritic and martensitic on a wide thickness range) have been worked out. For evaluating the melting area and the laser welding efficiency, about 300 experimental data have been collected; these joining (lap and butt) were carried out by different $CO_2$ laser sources[9-12]. The system variables and the variables relevant to the different welded materials, summarized in tab. I with the relative variation range, have been investigated.

Tab. I – Variables analysed

| Variables | Values |
|---|---|
| **Materials: AISI** | 304 – 316 – 420 – 430 |
| **Laser power level [kW]** | 0.35 ÷ 13 |
| **Welding speed [m/min]** | 0.10 ÷ 9 |
| **Covering gas** | He – $N_2$ |
| **Focal length [in]** | 3.75 – 5 |
| **Converging lens** | ZnSe – KCl |
| **Thickness [mm]** | 0.40 ÷ 15 |

We made use of a multi-layered neural network with supervised learning, simulated on a PC with Linux as operating system by means of Stuttgart Neural Network Simulator (SNNS Group©), a free software based on standard backpropagation paradigm. However, the learning algorithm has been modified, including a sort of momentum term, which attenuates the rate of change of synapses after each iteration. Really, a large learning rate corresponds to rapid learning but might also result in oscillations. This modification slows down the reduction of system error and therefore we must subsequently modify again the DELTA RULE by adding the error in the previous layer to the activation value, prior to doing the weight update.

For the stability of networks it is opportune to normalize the experimental data so that they vary in the range [0, 1]:

$$\text{normalized value} = \frac{x_i - \bar{x}}{6\sigma} \quad \text{where } \bar{x} \text{ is the average value and } \sigma \text{ the standard deviation.}$$

This type of normalization allows the employment of the neural network also for steels having composition very different from the ones analysed in this paper. The 293 experimental data are separated randomly in two sets: the learning set with 218 data and the checking set with 75 data. The selection was made so as to maintain the ratio between the kinds of steel.

A first attempt in order to obtain a continuous output at the same time for the melting area and for the welding efficiency did not furnish satisfactory results for the latter, partly because of limited data points and partly because of different layout necessary for the two outputs. Therefore, we preferred to construct two different nets, one relevant to the melting area and the other relevant to the welding efficiency. In all cases the input layer contains 7 units: 3 continuous units for the laser power, welding speed and steel thickness and 4 discrete units for the other conditions.

The neural net layout for the melting area that gave the best results was formed by one hidden layer with 21 units; the global error on the training set decreases decidedly in the first 200 iterations and asymptotically reaches the zero. When we stopped the learning, it is closely linked to the problem, the mean square error on the validation set was 0.18, if we eliminate two outlier data, fig. 2. However, 25000 iterations are, in general, sufficient to obtain stable results. We need to pay attention to the trend of error decreasing, because it is possible that the net might get trapped in some local minimum or even at some stationary point and, therefore, the only solution is to repeat the learning with a new set of initial weights.

The dependence of welding efficiency on system and material parameters is very complex. Even if the welding efficiency is a simple function of melting area, welding speed, and laser power:

$$WE = \frac{MV}{LP} = \frac{MA \cdot WS}{LP} \tag{8}$$

we obtained scarcely acceptable results with a previous neural network layout.

Results quite satisfactory were obtained with a neural network formed by 2 hidden layers of 21 and 7 processor units and an output layer with one continuous unit in order to forecast the welding efficiency. The results are reported in fig. 3. The industrial application of the proposed method presupposes a series of manual iterations, because the system is able only to answer to questions of the type WHAT-IF; for instance, if it is desired to realize a welding joint, it is necessary to enter, as input of the second neural network, the system known parameters and two trial values for the laser power and the welding speed. Using this neural network layout, we can verify if such conditions bring to an acceptable value of the welding efficiency. If it is true, taking into account that the same welding efficiency can be obtained with different pair of welding speed and melting area, the first neural network layout can help to select the optimal welding speed with a suitable melting area or form factor of weld bead. It is extremely opportune to verify with the new welding parameters that the welding efficiency still falls in the zone of acceptability.

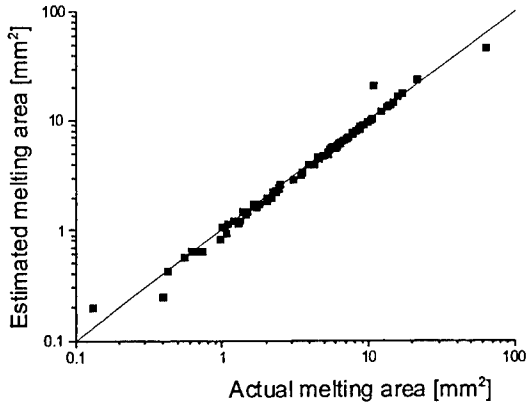


Fig. 2 – Estimated melting area vs. actual melting area

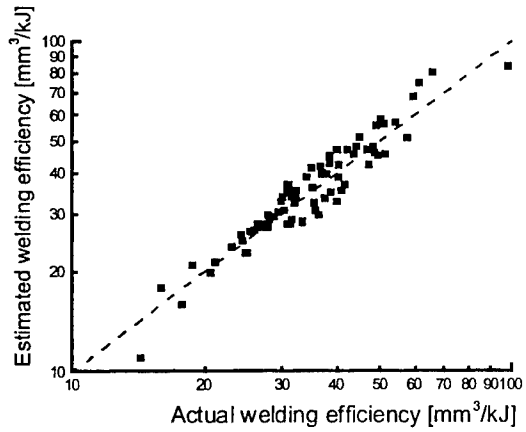


Fig. 3 – Estimated welding efficiency vs. actual welding efficiency

## 4. CONCLUDING REMARKS

In this paper we have demonstrated the applicability of Artificial Neural Networks technique in order to estimate the laser welding quality indexes, particularly the melting area and the welding efficiency. The results are quite satisfactory and we would like to carry on this research with implementation of many different neural network paradigms, like BAM (Bi-directional Associative Memory) or Kohonen. The first one permits, selected material to weld, the introduction, like input pattern, of the kind of steel, the sheet thickness, the system parameters, the desired range for melting area, and two trial values for laser power and speed, in order to recall the closest pattern which satisfies the process conditions with a good welding efficiency, but in this case we must also proceed by trial and error. On the other hand, the Kohonen's neural networks consider the operation of self-organized clustering to be a map, through which points in n-dimensional pattern space are mapped into a small number of points in an output space. The mapping is achieved autonomously by system without external supervision. Therefore, if the unit with the maximum response to a particular event is regarded as the image of the latter, it is possible to obtain a satisfactory response, near the true one, even if the input pattern is incomplete or noise affected. Unfortunately, both these methods need binary input and output and it is indispensable to transform the experimental data into a virtual image with a suitable number of pixels.

## REFERENCES


1. Schuöcker D., "Modeling of high power laser welding", *Proc. 8th Int. Symp. on Gas Flow and Chemical Laser*, pp. 745-751, 1990
2. Lankalapalli K., "Model-based laser weld penetration depth estimation" *Welding in the World*, **39**, pp. 304-313, 1997
3. Moon H.S., Na S.J. "Optimum design based on mathematical model and neural network to predict welding parameters for fillet joints", *Journal of Manufacturing Systems*, **16/1**, pp. 13-23, 1997
4. Ludovico A.D., Daurelio G., "A easy method for a quantitative evaluation of the laser welding process efficiency on austenitic, ferritic and martensitic stainless steel", *Proc. Eur. Symp. on Laser and Optics in Manufacturing*, pp. 80-96, 1997
5. Rumelhart D.E. et al., "Learning internal representation by error propagation" in *Parallel Distributed Processing*, M.I.T. Press, Cambridge, 1986
6. Hecht-Nielsen R., *Neurocomputing*, Addison-Wesley, New York, 1990
7. Haykin S.S., *Neural Networks: A Comprehensive Foundation*, Prentice Hall, 1998
8. Skapura D.M., Gordon P.S. (Ed.), *Building Neural Networks*, Addison-Wesley, 1996
9. Daurelio G., Dionoro, G, Memola Capece Minutolo F., "Lap and butt joints of dissimilar stainless steel welded by $CO_2$ Laser, *Proc. 8th Int. Symp. on Gas Flow and Chemical Laser*, pp. 658-663, 1990
10. Daurelio G., Dionoro, G, Memola Capece Minutolo F., "Ottimizzazione nella saldatura laser di acciai inossidabili", *Lamiera*, **10**, pp. 178-188, 1990
11. De Iorio I., Rossi F., Sergi V., "Steel sheet laser welding optimization with neural networks", *Proc. 9th Int. Symp. on Gas Flow and Chemical Lasers*, pp.787-790, 1992
12. Dilthey U., Risch A. "Laser welding of stainless steel and stainless/low-alloy material combination", *Welding in the World*, **36**, pp. 135-142, 1995

# KEYHOLE FORMATION AND POWER DEPOSIT LAW IN Nd:YAG LASER WELDING

J.M.JOUVARD[(1)*], O.PERRET[(1, 2)], Ph. NAUDY[(2)]

[(1)] Laboratoire Laser et Traitements des matériaux, IUT Le Creusot, F71200 Le Creusot, France

[*] E-mail: jmj@iutlecreusot.u-bourgogne.fr

[(2)] CEA, F21120 Is sur Tille, France

## ABSTRACT

The purpose of this work is to understand keyhole formation observed during pulse Nd:YAG laser welding. We determine the power deposit law during laser pulse. We present a calculation of the energy deposit law by Fresnel reflections. The aim is to calculate the ray trajectory in keyhole to deduce the local absorption. A previous study allows to observe keyhole formation using flash X-ray radiography, and determine evolution of keyhole geometry. These results are compared with a previous experimental determination of the interaction efficiency.

**Keywords:** Welding, keyhole, Fresnel reflection, radiography

## 1. INTRODUCTION

This work is part of study of the thermal modelling of Nd:YAG laser welding. In most welding processes, the energy is deposited on the surface, then transferred by conduction into the material, but this is not generally the case for laser welding. When the laser beam power density is sufficient to evaporate a thin layer of material, a narrow and deep keyhole is created inside the melting pool. It constitutes a trap for the beam [1,2]. The energy is deposited via the keyhole to the interior and this increases the welding penetration. The objective of this study is to model the energy deposited through Fresnel's reflections inside the keyhole in the case of a Nd:YAG laser impact on metal. We suppose that we know the geometry of the keyhole, and we model the quantity of energy deposited in this one during a laser pulse. The principle is to simulate the way of the rays inside the keyhole, and to calculate for each reflection the quantity of energy deposited. The study was carried out in the case of welding by pulse laser on a Titanium alloy (Ti-6Al-4V).

## 2. MODELLING OF THE FRESNEL REFLECTIONS

The energy deposition inside the keyhole is generated by multiple reflection of incident ray inside the keyhole wall. The rays are trapped in this cavity. For each reflection, part of energy is transferred to material. According to the Fresnel's law, considered energy is proportional to the energy of the incident ray and the angle of incidence on the wall.

To model rigorously the energy deposit law, we must, from keyhole geometry gives, calculate the rays trajectories in order to deduce the local absorption. We have developed a simulation procedure of the energy deposit by Fresnel reflection on the surface of the keyhole [3]. The principle is to simulate the way of the ray inside the keyhole (three-dimensional), and to calculate for each reflection the energy deposited for each point.

We start from a defined geometry of keyhole and a distribution of the incidental laser beam energy (beam collimated and homogeneous distribution). The laser beam is discretized in rays. For each ray, for which we associated a weighting function of the energy distribution of the beam, we determine the trajectory inside the keyhole. For each intersection with the keyhole wall, we calculate the angle of incidence, the reflection coefficient, and the reflection direction. The reflection coefficient is defined from the Fresnel's laws. The flow

XIII International Symposium on Gas Flow and Chemical Lasers and High-Power Laser Conference,
Antonio Lapucci, Marco Ciofini, Editors, Proceedings of SPIE Vol. 4184 (2001)

transferred to the wall is then stored in a file of absorptive flows. This program defines the absorptive part of the incidental laser beam, as well as the part that escapes by the opening of the keyhole after several reflections.

The Fresnel reflection coefficient is calculated by using the relation (with N = 3.38 and $\chi$ = 3.33 with $\lambda$ = 1.06 µm) :

$$R(\theta) = \frac{1}{2}\left\{\frac{1-2N\cos\theta+(N^2+\chi^2)\cos^2\theta}{1+2N\cos\theta+(N^2+\chi^2)\cos^2\theta}+\frac{(N^2+\chi^2)-2N\cos\theta+\cos^2\theta}{(N^2+\chi^2)+2N\cos\theta+\cos^2\theta}\right\}$$

The aim of this calculation is to determine the absorption coefficient by Fresnel's reflection in a keyhole that geometry varies during the laser pulse. For that, we calculate the absorption coefficient for a set of keyholes geometry. By making assumptions on the evolution of keyhole shape, we can determine the average absorption of material during the laser pulse. Thus, we obtain the energetic efficiency during the laser impact.

## 3. CALCULATION OF ABSORPTION COEFFICIENT

In a previous study, O.Perret [4] developed a measurement technique of the absorption coefficient using a differential microcalorimeter of Calvet type. It shows that laser-matter efficiency varies from 32% to 80% when the peak of power of the laser varies from 0.5 to 2 kW. Laser-matter efficiency is low in conduction mode and grows with peak power, when the keyhole volume increases.

Now, we consider the case of a laser pulse with 1.5 kW power peak, 5 ms pulse duration 7.5 J energy and 0.45 mm beam diameter. A micrographic observation of molten zone allows to determine the keyhole geometry. It can be characterised by a depth of 1.6 mm and a diameter of 0.96 mm.

However during the pulse, the keyhole geometry evolves. We made the assumption that the keyhole geometry increases linearly: depth of 0 to 1.6 mm and upper diameter of 0.45 to 0.96 mm. We calculated the absorption coefficient for a set of geometry (figures 1). By making an average, we obtain the energetic efficiency of A = 72 %. The measurement obtained by microcalorimetry [4] is 70 %. These results are similar, although we don't know the real geometry evolution of the keyhole.

## 4. STUDY OF THE KEYHOLE FORMATION

### 4.1. Observation by radiography X flash

An analysis of the evolution of the keyhole geometry during laser impact, was carried out by radiography X flash [5]. A series of radiography was carried out using a pulse X of 30ns, started with a variable delay compared to the beginning of the laser pulse. The study on a titanium alloy sample (Ti-Al-4V) was carried out with a power peak of the laser of 8.7 kW and a duration of 5 ms pulse, for a beam with a diameter 450 µm. From the images obtained, it was possible to determine the evolution of the characteristics of the keyhole during the laser pulse (figure 3).

The keyhole can be characterised [6] by a maximum depth of 3.2 mm and a maximum diameter on the surface of 1.5 mm. We consider that the keyhole follows laws versus time (figure 2):

- depth of the keyhole: $h = 0$ for $t < 0.5$ ms and $h = 3.21\,(t - 0.5) / 4.5$ for $0.5 < t < 5$ ms
- diameter on the surface varies from 1 to 1.5 mm for $0.5 < t < 5$ ms

### 4.2. Calculation of the energetic efficiency

We calculated the absorption coefficient for a set of keyholes whose geometry is defined like a similarity of the final keyhole (figure 3.a). The law of evolution of the absorption coefficient according to the depth is given on the figure 3.b. One notes the absorption coefficient strongly varies when there is formation of the keyhole. There is trapping of energy well. When we studies the evolution of irradiance in each point of the keyhole note that the deposit is primarily at the bottom of the keyhole. The rays are guided through the successive reflections towards the bottom. After one or two reflections, the rays end to the bottom with an absorption coefficient increasing (incidence angle decreasing). This explains why, the absorption coefficient, increases when the keyhole becomes deeper.

We can calculate the total absorption coefficient (energetic efficiency) during the interaction by an average of absorption during duration the laser pulse. For that, we integrate the composition of the evolution of absorption according to the depth and the evolution of depth versus the time.

$$\overline{A} = \frac{1}{5}\int_{0.0ms}^{5.0ms} A(h(t))\,dt = \frac{1}{5}\int_{0.0ms}^{0.5ms} A(0)\,dt + \frac{1}{5}\int_{0.0mm}^{3.21mm} A(h)\,\frac{4.5}{3.21}\,dh$$

We obtain energetic efficiency during the interaction equal to $\overline{A} = 74.9$ %. We verify that efficiency increases when keyhole becomes narrow and deeper.

## 5. CONCLUSION

The purpose of this work is to understand keyhole formation observed during pulse Nd:YAG laser welding. We present a calculation of the energy absorbed during laser pulse. This method is based on a calculation of absorption coefficient by Fresnel reflection in a keyhole whom geometry varies during the laser pulse. We calculate energetic efficiency by an average of this absorption coefficient during duration of the laser pulse. Thus, we can study evolution of energetic efficiency (figure 4) when the laser pulse duration increases. We note that, at the beginning energy is transferred by conduction into the metal (conduction stage), then energetic efficiency is weak (44 %). When the keyhole appears, energetic efficiency increases rapidly with the deep. The beam is trapped in the weld.

## REFERENCES


[1] E.DUMORD, J.M.JOUVARD, D.GREVEY, Modelling of deep penetration laser welding: Application to the cw Nd:YAG laser welding of X5Cr.Ni.18-10, Las. Eng. Vol. 9, 1999, p1-21

[2] V.V.SEMAK, J.A.HOPKINS, M.H.McCAY, T.D.McCAY, A concept for hydrodynamic model of keyhole formation and support during laser welding, ICALEO 1994, p. 641-650

[3] J.M.JOUVARD, N.HORNY, Modelling of Fresnel reflections in a keyhole formed in cw-Nd:YAG laser welding, J.Phys.D: Appl.Phys. (submit)

[4] O.PERRET, M.BIZOUARD, A.LAILLE, Ph.NAUDY, Laser-matter efficiency measurement - Application to the Ti-6Al-4V titanium alloy, submit to J. Laser Appl.

[5] G.PASCAL, D. NORE, K.GIRARD, O.PERRET, Ph. NAUDY, Analysis of induced effects in matter during pulsed Nd:YAG laser welding by flash radiography, Quant. Non Destr. Evaluat., Montréal, Juil. 1999.

[6] O.PERRET, M.BIZOUARD, Ph.NAUDY, G.PASCAL, D.NORE, Y.HORDE, Y.DELAISSE, Characterisation of the keyhole formed during pulse Nd:YAG laser interaction with a Ti-6Al-4V metallic target, submit to J. Appl.Phys.

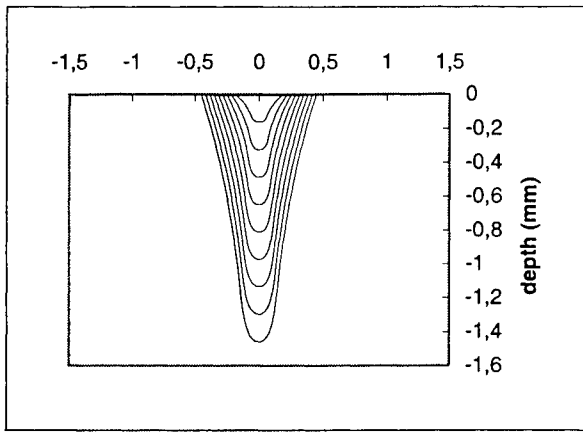


*Figure 1.a: Variation of keyhole geometry (1.5 kW, 5 ms)*

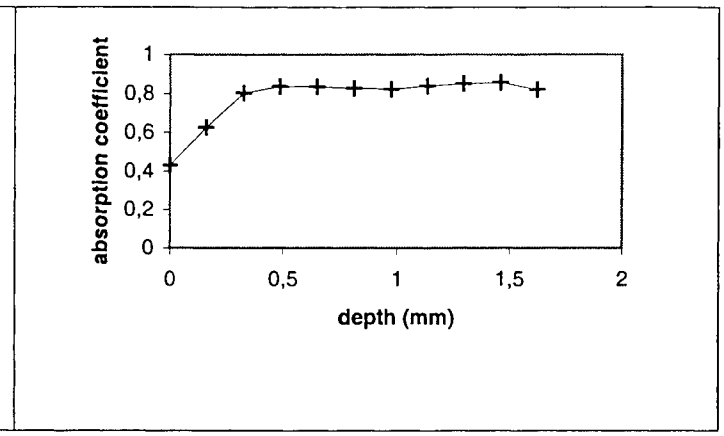


*Figure 1.b: Absorption coefficient versus depth*

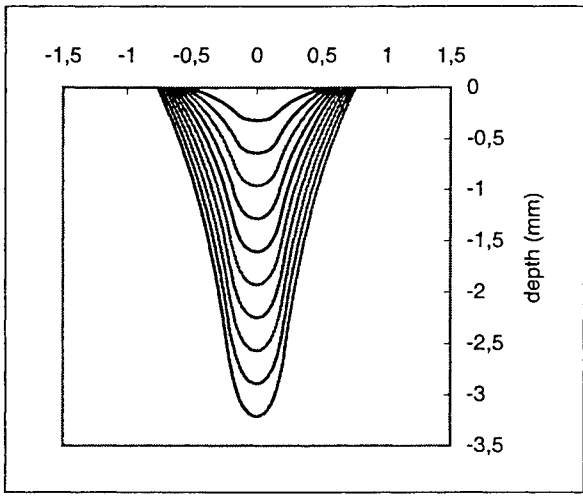


*Figure 3.a: Variation of keyhole geometry (8.7 kW, 5 ms)*

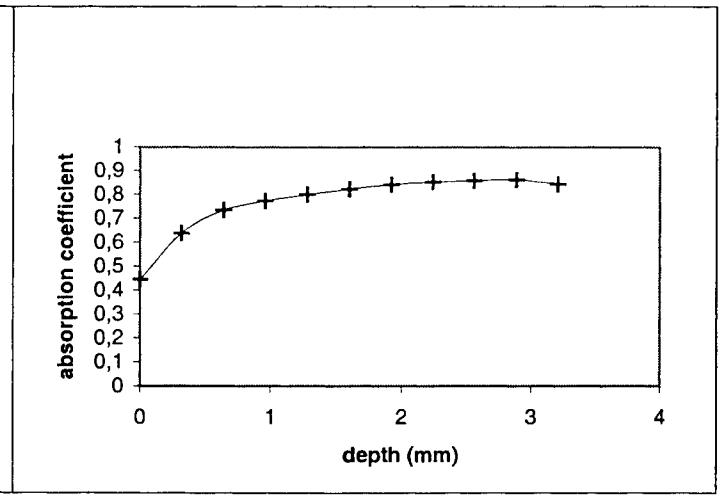


*Figure 3.b: Absorption coefficient versus depth*

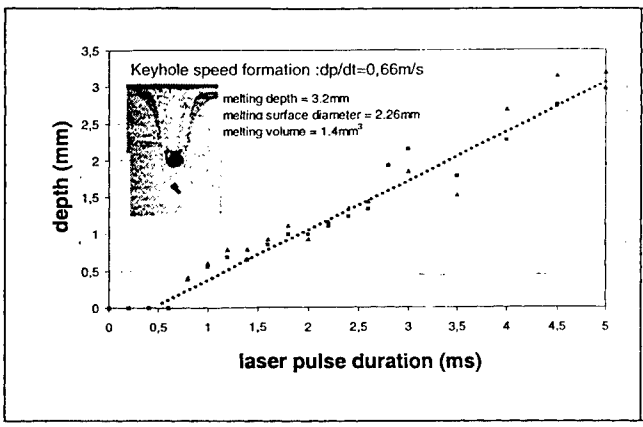


*Figure 2: Variation of depth versus time [6] (8.7 kW, 5 ms)*

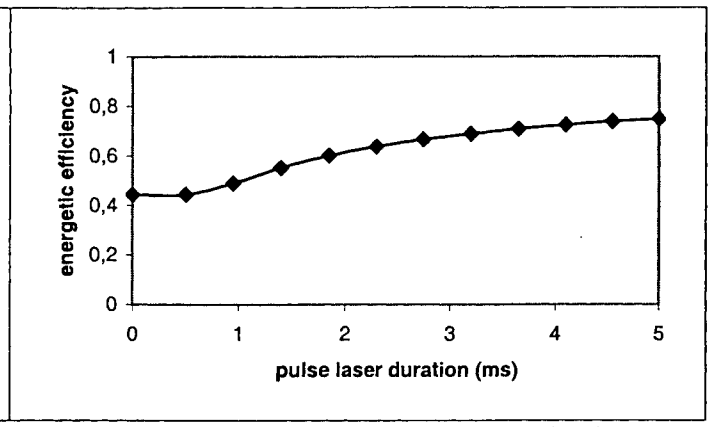


*Figure 4: energetic efficiency versus laser pulse duration (8.7 kW)*

# Control of molecular ion generation with high intensity femtosecond laser and nanosecond laser pulses

K. Toyoda, N. Morimoto, H. Kamada and Y. Takahashi
Department of Applied Electronics, Faculty of Industrial Science and Technology, Science University of Tokyo/2641 Yamazaki, Noda, Chiba 278-8510, Japan

## ABSTRUCT

Recently, much attention has been focused upon generation of ionized particles from solid target by coulomb explosion using high intensity and ultrashort pulse laser since the high intensity electric field can easily ionize to the maximum charge of the element. This paper reports the generation of molecular carbon ions and decrease of multiple charged ions in case of irradiation of low power nanosecond laser pulse prior to femtosecond laser pulse. The changes in the ion current waveform have been analysed by time of flight measurement with 76.4cm of drift section. This observed waveform was interpreted using energy conservation law.

**Keywords:** cluster ion, Ti:sapphire laser, TOF measurement

## 1.INTRODUCTION

Simultaneous irradiations of high intensity and ultrashort pulse of Ti:sapphire laser and fourth harmonics of Q-switched nanosecond pulse of Nd:YAG laser to carbon target were found to generate molecular ions of carbon. In case of single femtosecond pulse of Ti:sapphire laser, multiply charged ions such as $C^{6+}$(amu=12) were observed. Double pulse irradiations of femtosecond pulse of Ti:sapphire laser and nanosecond pulse of Nd:YAG laser to carbon target reduced generation of multiply charged ions and produced cluster ions such as $C_2^+$ (amu=24) and $C_3^+$ (amu=36). This measurement was made by time of flight (TOF) measurement using mass spectroscopic method.

## 2.THE EXPERIMENT

### 2.1. Experimental setup

Experimental setup for TOF measurements is given in Fig.1. Ti:sapphire laser of pulse width of 130fs was incident at an angle of about 30 degree onto a flat carbon target mounted on rotary rod. The laser energy was 8mJ/pulse, which was focused to a corresponding intensity of about 8.6PWcm$^{-2}$. Fourth harmonics of Q-switched Nd:YAG laser (HOYA-Continuum ML-2) of pulse width of 5ns was about 30 degree of opposite side of the direction of femtosecond laser. The laser energy of nanosecond pulse was 2.7mJ/pulse. Time of separation of double pulse irradiation were controlled by digital delay pulse generator (Stanford Research Systems DG535) which was triggered by a pulse of flash lamp of GCR of Nd:YAG laser (Spectra-Physics) used for pumping of chirped pulse amplification system (Spectra-Physics TSA). In this experiment, delay time was varied from -400ns to +2000ns.

Ionized particles which were ablated by coulomb explosion from carbon target fly to the pinhole via drift region in constant velocity and were decelerated in the region of pinhole-slit assembly. These decelerated ions were into the electro static energy

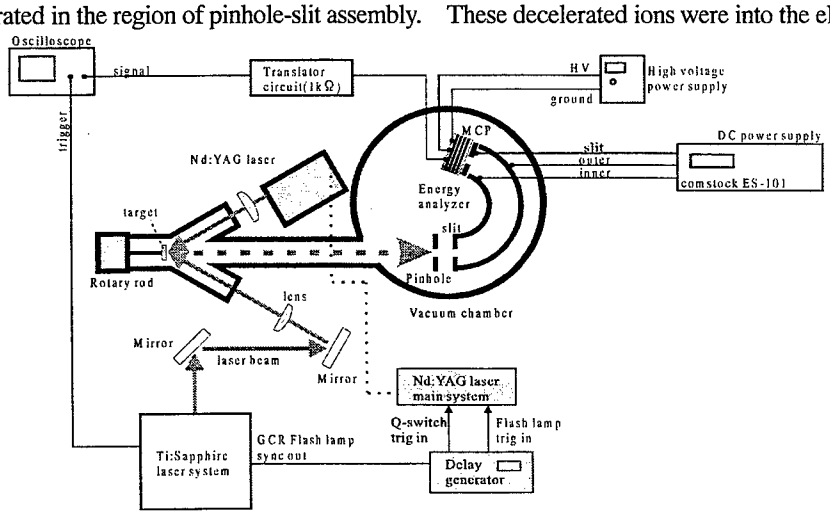


Fig.1 Experimental setup for TOF measurements using Ti:sapphire laser and Nd:YAG laser.

XIII International Symposium on Gas Flow and Chemical Lasers and High-Power Laser Conference,
Antonio Lapucci, Marco Ciofini, Editors, Proceedings of SPIE Vol. 4184 (2001)

analyzer (Comstock AC-901). The transmission energy of this energy analyzer was kept constant during changing slit voltage. Particles which have selective kinetic energy were detected by MCP (Comstock CP-602B). TOF signal was obtained from MCP.

### 2.2. Calculation of time of flight

Fig.2 shows time of flight of respective region. Particles which have selective kinetic energy were obtained by changing slit voltage of energy analyzer. So, time of flight from target to MCP was calculated as follow equation.

$$T = t_1 + t_2 + t_3 = \sqrt{\frac{m}{Z}}\left(\frac{L_1}{\sqrt{2e(TE+V_{slit})}} + \frac{2L_2}{\sqrt{2e(TE+V_{slit})}+\sqrt{2eTE}} + \frac{L_3}{\sqrt{2eTE}}\right) \quad (1)$$

where, $Z$ is ionic charge, $TE$ is transmission energy of energy analyzer and $V_{slit}$ is slit voltage.

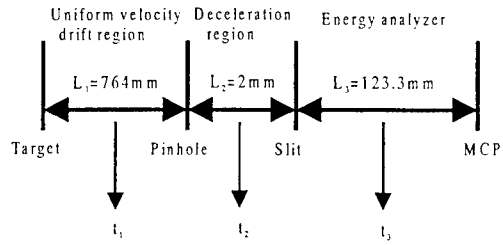


Fig.2 Time of flight of respective region

## 3.RESULTS

### 3.1. Preirradiation of femtosecond pulse

In case of irradiation of ultrashort pulse of Ti:sapphire laser into carbon target prior to Q-switched Nd:YAG laser, generation of the highest charge of $C^{6+}$ was observed. TOF waveform was identical with single pulse of T:sapphire laser, that is, interaction between Ti:sapphire laser and Nd:YAG laser was not observed.

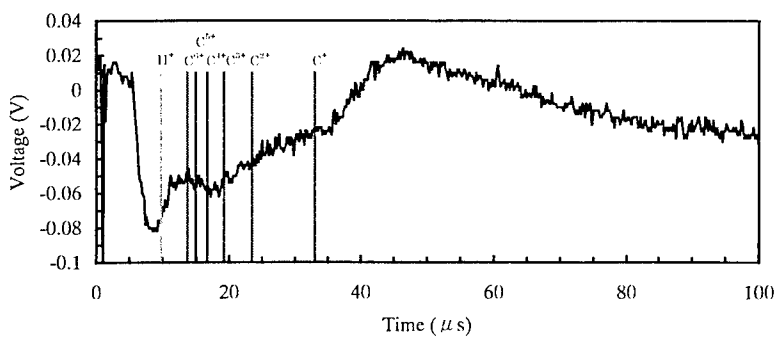


Fig.3 TOF waveform of preirradiation of femtosecond laser. Delay time = -400ns.

### 3.2. Coincident with Q-switched nanosecond pulse

In case of irradiation of ultrashort pulse of Ti:sapphire laser coincident with Q-switched Nd:YAG laser, ion current waveform of multiply charged ions such as $C^{6+} \sim C^{2+}$ decrease and enhancement of signal of $C^+$ and $C_2^+$ was observed. In this irradiation timing, interaction between Ti:sapphire laser pulse and excitation of target surface by Q-switched Nd:YAG laser was considerably observed.

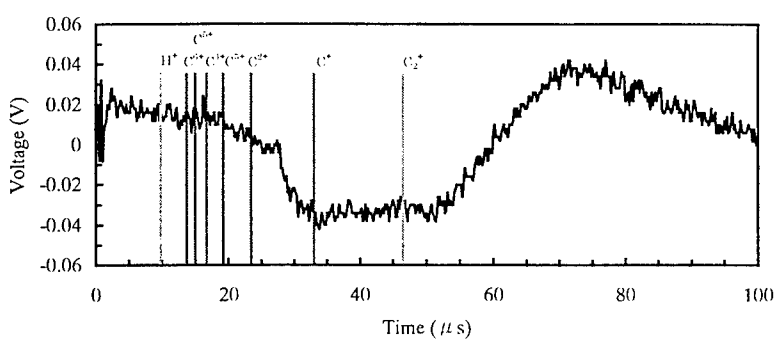


Fig.4 TOF waveform of coincident with Q-switched nanosecond pulse. Delay time = 0.

### 3.3. Preirradiation of Q-switched nanosecond pulse

In case of irradiation of Q-switched Nd:YAG laser prior to Ti:sapphire laser, signal of molecular ions was observed and gradually decreased according as separation between femotosecond pulse and nanosecond pulse was to be larger. The effect of preirradiation of Q-switched Nd:YAG laser remains within the thermal relaxation time of 1600ns.

Ion species vs. delay times were observed as shown in Table 1. In the delay time of larger than 2000ns, Ti:sapphire laser was irradiated into the target out of the thermal relaxation time of excitation by Q-switched Nd:YAG laser, therefore, ion current waveform was same to the one of single pulse of Ti:sapphire laser.

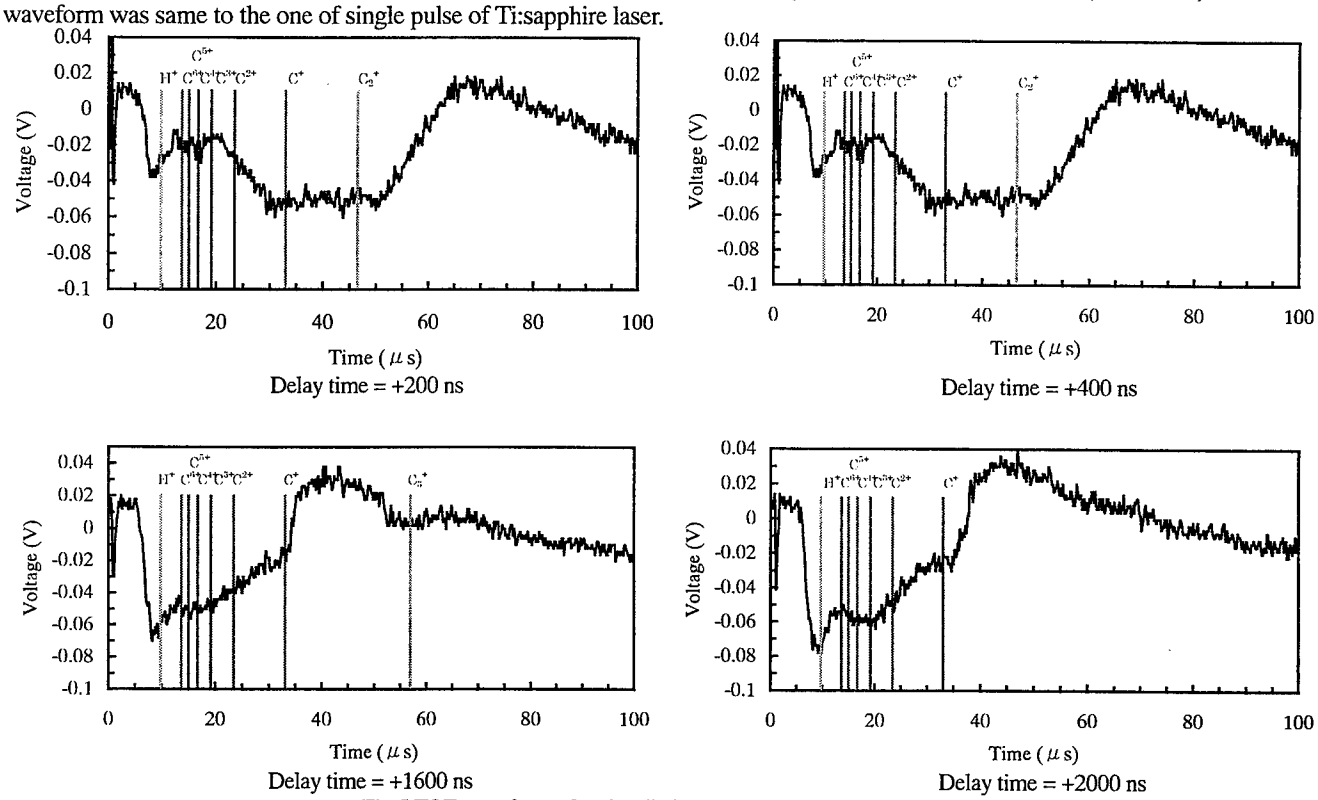


Fig.5 TOF waveform of preirradiation of Q-switched Nd:YAG laser

Table 1. Ionized species vs. delay times in preirradiation of Q-switched nanosecond laser

| Delay time | Ion species |
|---|---|
| +200 | $C^+$, $C_2^+$ |
| +400 | Multiple charged ion, $C_2^+$ |
| +900 | Multiple charged ion, $C_2^+$ |
| +1600 | Multiple charged ion, $C^+$, $C_3^+$ |
| +2000 | Multiple charged ion, $C^+$, |

## 5. DISCUSSION

The above observations demonstrate that molecular ions such as $C_2^+$ and $C_3^+$ have been observed in irradiation of Ti:sapphire laser within the thermal relaxation time of carbon target caused by Q-switched Nd:YAG laser pulse. To explain this, energy conservation law is considered using following model.

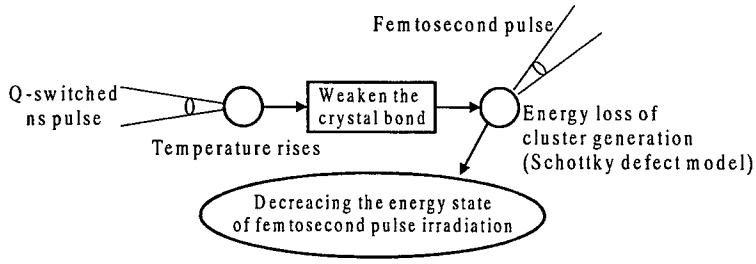


Fig.5 Effect of simultaneous irradiation

Fig.5 explains the effect of simultaneous irradiation. Irradiation of Q-switched ns laser pulse heated the surface of carbon target. Due to the temperature rise, energy of crystal bond becomes weak before fs laser pulse was irradiated.

From energy conservation law, energy state of femtosecond pulse irradiation is

$$\frac{E_L}{V} = \frac{C_V \rho}{M} \Delta T + \sum \varepsilon_i N_i \ . \tag{2}$$

Thus, temprature rise $\Delta T$:

$$\Delta T = \left( \frac{E_L}{V} - \sum \varepsilon_i N_i \right) \frac{M}{C_V \rho} \tag{3}$$

where,

$E_L$: Laser energy [J]
$V$: Irradiated volume
$C_V$: Specific heat at constant volume [$Jmol^{-1}K^{-1}$]
$M$: Atomic weight [$g\ mol^{-1}$]
$\rho$: Density [$g\ cc^{-1}$]
$\Delta T$: Rise of temprature [K]
$\varepsilon_i$: Energy required to cluster formation of cluster i [J]
$Ni$: Number of cluster in unit volume [$cc^{-1}$]
$N$: Number of atom in unit volume [$cc^{-1}$]

Fig.6 (a) shows that $\Delta T$ is calculated as the function of $N_i/N$. In this calculation, three different values of $\varepsilon_i$ are assumed. Temperature rise $\Delta T$ decreases with increase of number of cut of chemical bond. Temperature $\Delta T$ is sufficient to produce $C^+$ but not enough to produce multiply charged ions during $\Delta T$ is decreasing. In addition to energy conservation model, calculation of Boltzmann distribution of Schottky defect model[1] was performed. Using Boltzmann distribution leads to

$$\frac{N_i}{N} = \exp\left( -\frac{\varepsilon_i}{k\Delta T} \right). \tag{4}$$

$\Delta T$ increase with number of cut of chemical bond increase Ni. Temperature $\Delta T$ is obtained from cross point of the curve of energy conservation model and Schottky defect model as shown in Fig.6 (b). Introduction of these two models is found to correspond to experimental results. Decrease of $\varepsilon_i$ due to irradiation of Q-switched Nd:YAG laser results in decrease of energy state $\Delta T$ to lower state which, however, is enough to ionize $C^+$.

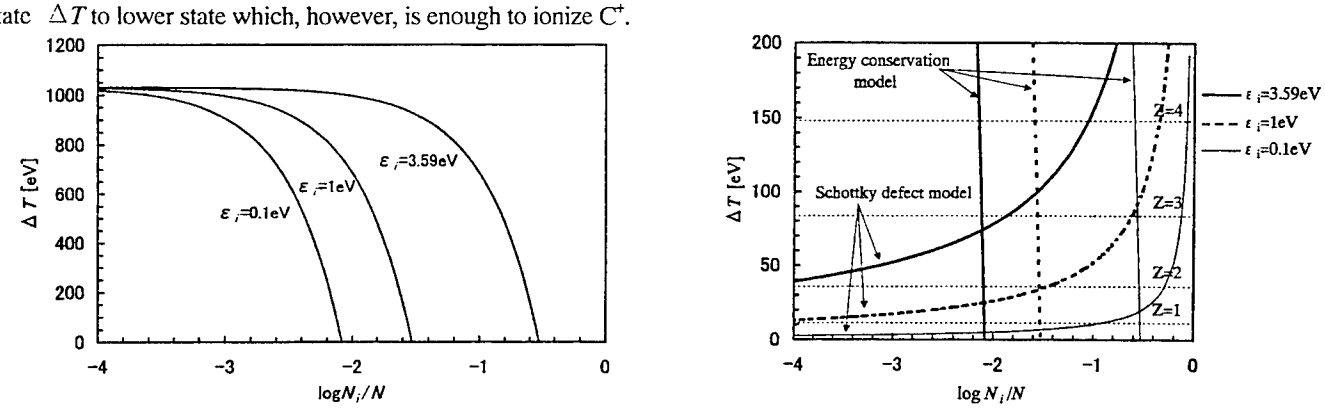


(a)energy conservation model (b)Schottky defect model and energy conservation model

Fig.6 Calculation of $\Delta T$ vs. $N_i/N$.

## 6. CONCLUSION

A novel method to control the cluster ion generation has been developed. Clusters are interesting for many reasons because they have potential to form novel materials with new chemical and physical properties.[2] Simultaneous irradiations of ultra high intensity laser pulse and Q-switched nanosecond laser pulse was found to be an effective method to control cluster ions.

## REFERENCES


1. F. Mandl, *Statistical Physics*, p48, John Wiley & Sons, Chichester, 1988.
2. Th. Lill, W. F. Calaway, M. J. Pellin, "Cluster emission during sputtering of liquid gallium-aluminum eutectic alloy", J. Appl. Phys., Vol. 78, No. 1, 1 July 1995.
3. N. Morimoto, H. Sano, H. Kamada, Y. Takahashi and K. Toyoda, "Cluster ion control by simultaneous irradiations of high intensity femtosecond laser and nanosecond laser pulse", 13th International conference on high-power particle beams, BEAMS 2000, Nagaoka, Japan, June25-30, 2000.

# HgCdTe energy gap modification due to laser irradiation

Moeglin J.P., Gautier B., Boffy A.

French-German Research Institute of Saint-Louis (ISL)
P.O. BOX 34 - 68301 SAINT-LOUIS - FRANCE

## ABSTRACT

Experimental investigations of the effects of laser irradiation on the response (sensitivity) of HgCdZnTe photoconductors (p type) working at ambient temperature have been performed. In-band (band III) irradiation of these devices has been carried out with two collinear $CO_2$ laser beams: a CW probe laser (beam diameter $\Phi$ = 60 $\mu$m) modulated by an acousto-optical modulator at a frequency of 500 kHz with a low energy output level giving the reference signal of the tested detector, and a second pulsed laser (named pump laser with $\Phi$ = 300 $\mu$m) used as the irradiation source. The pulse characteristics are a maximum energy of 200 mJ and a pulse duration of 2.5 µs. These two $CO_2$ lasers are part of an IR detector test bench design for experimental studies in IR band II (3-5 µm) and band III (8-12 µm) but only the experiments in band III are described herein. The irradiation densities range from 20 µJ/cm² to 6.6 J/cm². Both reversible effects, when the morphological damage threshold is not reached, and irreversible ones above this threshold have been observed. Moreover, it has been shown that irradiation produces a dramatic sensitivity decrease due to alloy concentration redistribution and thus causes a modification of the initial gap energy.

**Keywords:** laser, detector, MCT, countermeasure

## 1. INTRODUCTION

The detailed study of the effects of an «in-band» irradiation of mercury cadmium tellurium (MCT) photodetectors presents two interests. The primary one is to determine how long such a device is unable to transmit the measured low-level signal to the electronic system. The second one concerns the design of an intrinsic protection system (hardening) which requires a knowledge of the process involved by the laser irradiation of semiconductors. We will describe herein the tested devices and the experimental test bench used in order to measure the electronic parameters of the irradiated detector. Some theoretical considerations will also be reported in order to explain, at least qualitatively, the main features of the observed effects.

## 2. TESTED PHOTODETECTORS

Figure 1. MCT photoconductor

All the devices tested herein work at ambient temperature and are based on a new quaternary semiconductor HgCdZnTe (fig. 1) in which Zn has been introduced in order to reduce mercury defects ($10^4$-$10^5$ cm$^{-2}$). The sensitive area is covered with a Ge AR coating. The MCT wafer (active area = 1 mm²) is fixed on copper and encapsulated in a cylindrical aluminum cap. It must be noticed that no window is provided above the sensitive area. The field of view (FOV) is 60°. The entire bandwidth of these detectors extends from 2 to 12 µm, the useful bandwidth is 8-12 µm, the maximum detectivity is $D^* = 3 \cdot 10^7$ cmHz$^{0.5}$/W at $\lambda$ = 10.6 µm and the response time is 10 ns. The dynamic impedance is very low (10 Ω). The detectivity at $\lambda$ = 10.6 µm and at ambient temperature is $D^* = 10^7$ cmHz $^{0.5}$/W and the response time is less than 1 ns.

## 3. EXPERIMENTAL TEST BENCH

The complete test bench designed for photodetector irradiation studies is presented in Fig. 2. Four lasers can be used simultaneously; two of them working in IR band II (3-5 µm) and the two remaining ones working in band III (8-12 µm). The probe CW laser beams are frequency modulated at 500 kHz through a Bragg cell. They emit a low-intensity reference signal

XIII International Symposium on Gas Flow and Chemical Lasers and High-Power Laser Conference,
Antonio Lapucci, Marco Ciofini, Editors, Proceedings of SPIE Vol. 4184 (2001)

when directed toward the tested photodetector. The pulsed (pump) lasers are a $CO_2$ laser used exclusively for the experiments described herein (instantaneous power 80 kW, pulse duration 2.5 μs and pulse maximum energy 200 mJ) and a pulsed DF laser ($\lambda = 3.8$ μm), not used for the present experiments. In order to carry out accurate measurement tests, the probe and pump laser beams must be exactly superposed on the active area of the photodetector. The pump laser beam goes through a telescope and a vacuum cell, in order to prevent the plasma breakdown. The pressure is decreased below $5 \cdot 10^{-5}$ torr in order to remain below the breakdown threshold in the pump laser beam. Another MCT cooled detector mounted on an integrating sphere is used for the CW probe laser beam power measurement; thus, the signal variation on the tested detector cannot be attributed to the energy level fluctuation of the probe laser, but only to the effect of the pump laser irradiation. The different energy density levels applied to the tested detector can be adjusted through an incident beam attenuator composed of a stack of $CaF_2$ plates. In the test bench, a pyroelectric camera is used as a beam profiler and gives the spatial intensity distribution of the pump laser. This intensity distribution has been assumed to be gaussian and the fluence on the center line is: $F_0 = 2E_p/S_{spot}$, where $E_p$ is the pulse energy and $S_{spot}$ the irradiated area defined at $1/e^2$ [1]. All the reported experiments have been carried out with a spot area $S_{spot} = 7 \cdot 10^{-4}$ cm² ($\Phi = 300$ μm). The time-dependent intensity pulse shape is assumed to be roughly stepwise and the pulse duration is 2.5 μs.

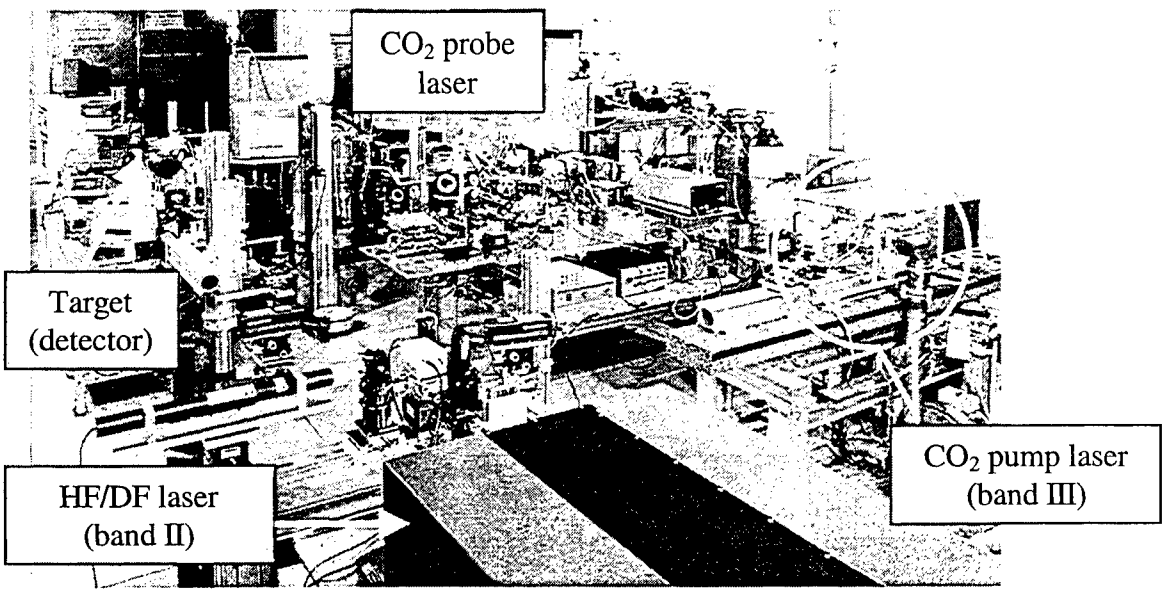


Figure 2. Experimental set-up

## 4. EXPERIMENTAL RESULTS AND DISCUSSION

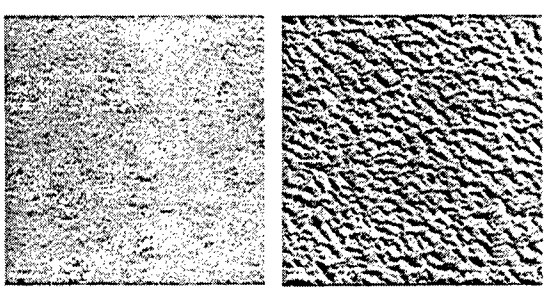

Figure 3. SEM pictures.
Left: No. 3138. Right: No. 3950

A different damage threshold has been measured, ranging from 33 to 104 mJ/cm². This damage threshold scattering for nominally identical devices can be explained by differences in the sensitive area, therefore yielding a variable surface reflectivity. In fig. 3 two SEM pictures of the undamaged detector surface are presented, displaying large differences in the apparent roughness of the sensitive surface. Figure 4 shows SEM pictures of the irradiated surface of the detector ($F_0 = 105$ mJ/cm², $I_0 = 42$ kW/cm²). Figure 4a presents the damaged area with a melting zone, while figure 4b and c show droplets of liquid material ejected from the center of the impact, and characteristic of the «splashdown» phenomenon. A species concentration analysis of undamaged and damaged detectors has been done using a classical X-ray diffraction method coupled to mass spectroscopy. Two of the spectra obtained on undamaged and damaged detectors are presented in figure 5. One can notice a disappearance of the mercury on the spectra related to the damaged detector, very probably due to surface vaporization. Moreover, the species concentration analysis along the droplet path exhibits a 13 % decrease in Cd concentration. Using the test bench capabilities, the local sensitivity of the damaged detectors has been measured. It has been done by scanning the whole laser impact area ($\Phi = 300$ μm) with an attenuated CW $CO_2$ probe laser beam whose spot diameter ($\Phi = 60$ μm) is smaller than the swept area. Figure 6 presents the results of this local sensitivity

measurement in the case of a fluence $F_0$ = 400 mJ/cm² ($I_0$ = 160 kW/cm²). Along the z-axis the measured relative detectivity $D_r$ is plotted, defined as: $D_r = S_{local}/S_{min} - 1$. Along the x-axis, the plotted values are distances from the edge of the scanned area, while distances from the center of the impact are plotted along the y-axis. The minimum value at point A (center of the

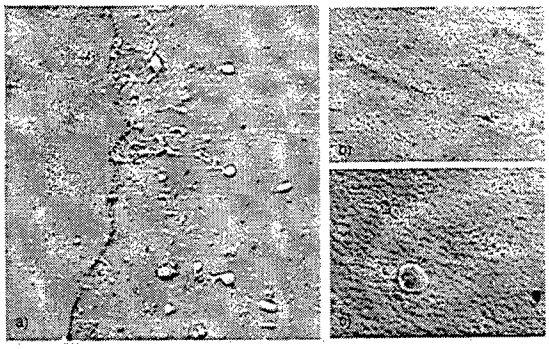

Figure 4. SEM pictures of the damaged detectors

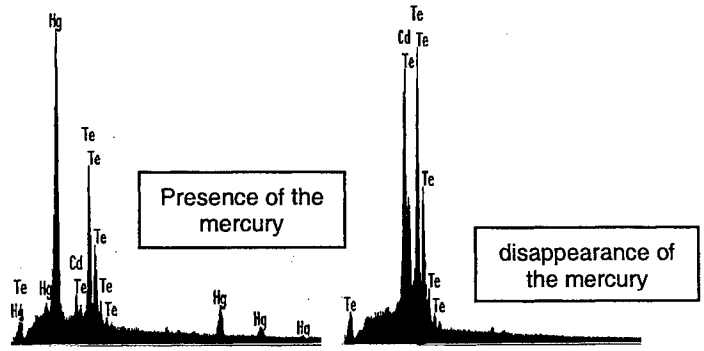


Figure 5. X-ray diffraction. Left: before laser irradiation. Right: after laser irradiation

impact) results from the local surface melting and vaporization due to a locally high power density. The maximum value at point B, slightly off the center, indicates an increase in detectivity which can be explained as follows: at this distance from the center line, the power density is relatively low (gaussian power density distribution), thus inducing melting without vaporization and a local «annealing» phenomenon. The crystal lattice is rearranged, due to the defects, which were able to diffuse in that liquid phase. This effect is indeed impossible to obtain at the center of the laser impact where material ablation through vaporization takes place. The symmetry of point B with respect to the centerline can be induced by defect diffusion along the privileged axis of the crystal (<111>)[2]. Integrating this measured sensitivity on the whole scanned surface, one gets an overall device detectivity decrease of only 20 %. The detectivity remains unchanged outside the laser. As already mentioned, a decrease in the Cd atoms concentration (-13%) has been measured at the impact center; the material becomes $Hg_{0.856}Cd_{0.144}Te$ while it was initially $Hg_{0.835}Cd_{0.165}Te$. The species concentration analysis has been done between the impact center (point A) and the edge (point B), showing a decrease of the molar fraction x; i.e. from 0.361 (center) to 0.010 (edge) (fig. 7). Elsewhere, the expression giving the band gap energy is[2]:

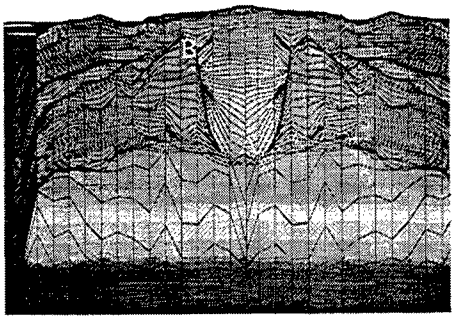

Figure 6. Local sensitivity measurement

$$E_g = -0.302 + 1.93x - 0.818x^2 + 0.832x^3 + 0.535(1-2x)T/1000 \quad [\text{eV}]. \tag{1}$$

According to the molar fraction decrease, the gap energy $E_g$ drops from an initial value of 0.37 eV to a negative value showing a semi-metal or metal behavior (fig. 7). Figure 7 shows the molar fraction x and the band gap energy $E_g$ variations

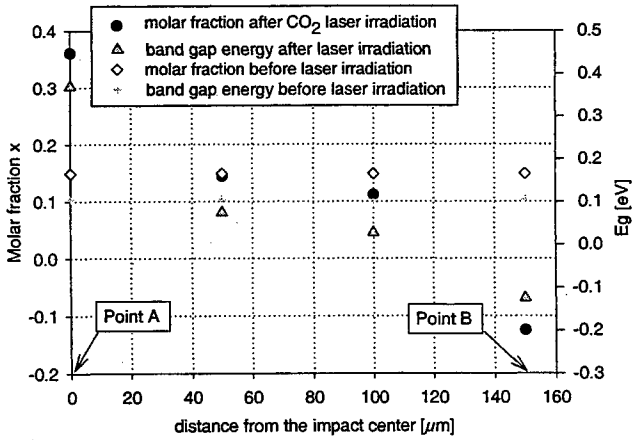


Figure 7. Measurement of the molar fraction x vs. distance from the impact center.

before and after a $CO_2$ laser irradiation. The molar fraction x has been measured while the gap energy has been calculated from the equation (1). At point A (center of the impact), the gap energy $E_g$ (0.37 eV) is higher than the photon energy at $\lambda = 10.6\ \mu m$ (0.117 eV). Therefore, the MCT material is locally more transparent to the laser beam and the detectivity decreases[3]. From the point A to the point B, the band gap energy $E_g$ drops and becomes lower than the photon energy, inducing an increase of the intrinsic carrier density and therefore, a detectivity increase[3]. As mentioned before, the maximum value at point B results from a local annealing phenomenon and the MCT material behaves such as a semi-metal or metal. At this point, the defect density decreases and therefore, a detectivity increase.

## 5. CONCLUSIONS

This work describes the capabilities of the multiwavelength test bench designed to study the transient irradiation effects on MCT photodetector performances in IR bands II (3-5 μm) and III (8-12 μm). Results show that the local detectivity drop is not only due to vaporization, induced by the laser beam, but to the molar fraction x decrease. If the damaged area is smaller than the sensitive area, the global detectivity of the device is only slightly affected by such laser irradiation. Finally, it is believed that the knowledge of the physical process involved in photodetector irradiation will allow to design new intrinsic hardening devices.

## REFERENCES

1. J.P. Moeglin, PhD thesis : "In-band laser irradiation of the silicon photodetectors. Measurements of the photoelectrical and semiconducting parameters" (1998, Mulhouse-France), ISL report R 102/99.

2. J. Brice, P. *Capper, Properties of Mercury Cadmium Telluride*, emis Datareviews series No. 3, INSPEC publication (1987).

3. M.S. Tyagi, *Semiconductor materials and devices*, ed. John Wiley & Sons (1991).

# Influence of the X-rays preionization on the performance of a HF phototriggered laser

S. Pasquiers, C. Postel, V. Puech

Laboratoire de Physique des Gaz et des Plasmas
Université Paris XI, Bât.210, 91405 Orsay cedex, France

## ABSTRACT

The influence of the X-rays preionization on the performance of a 312 $cm^3$ active volume phototriggered HF laser has been studied for $Ne/SF_6/C_2H_6$ and $SF_6/C_2H_6$ mixtures at a fixed $SF_6$ partial pressure (78 mbars). Parameters are the X-rays dose (0.1-10 mR), the pumping current pulse duration (60-155 ns), the electric charge deposited in the medium (< 3 mC), and the ethane partial pressure (< 10 mbars). It is shown that, without ethane in the mixture, arcs develop close to the discharge peak current as soon as the pumping pulse duration exceeds 100 ns at a fixed deposited charge value, in the whole range of X-rays dose values studied. An efficient discharge stabilisation effect can be obtained by addition of ethane, even without X-rays preionization and with a pumping pulse duration value as high as 155 ns. Nevertheless a low ethane concentration in the mixture is required in order to optimise the laser performance. In such conditions an arc free discharge, and correlatively high output laser energy and efficiency values, can be obtained only with use of the preionization. Optimum laser performance can be achieved with a low X-rays dose.

**Keywords:** HF laser, pulsed electric discharge, X-rays preionization, high pressure $SF_6/C_2H_6$ plasma.

## 1. INTRODUCTION

Discharge-pumped non-chain HF/DF chemical lasers have been widely studied since the end of the sixties[1], and it has been early recognised that $SF_6$ allows to achieved highest laser performance, i.e. output energy and electrical efficiency, than other F-atom donors. Preionization of the gas mixture, $SF_6$ with an hydrogenated compound RH (or RD), by VUV-photons[2,4,5] or X-rays[3,6] are now currently employed. Moreover the high laser performance achieved using the phototriggering technique[2,3] have stimulated the development of large aperture lasers in order to increase the output energy[7]. However the influence of the amount of preionization on the laser performance has not been yet precisely determined. The present work deals with the influence of the X-rays dose on the performance of a 312 $cm^3$ active volume laser, named « X525 ».

We have previously reported on the X525 performance[8], i.e. a specific output energy of 9.6 J/l at an electrical efficiency of 4.7 %, achieved with a $Ne/SF_6/C_2H_6$ mixture and a dose of 10 mR per shot. Such performance follows from the stabilisation of the discharge when $C_2H_6$ is added to the $Ne/SF_6(1/1)$ mixture[9]. The discharge dynamic in $Ne/SF_6$ mixtures or pure $SF_6$, as well as the stabilisation effect of $C_2H_6$ and consequences for the output energy and efficiency values, are now investigated for a large range of X-rays dose values. Other important parameters of this study is the pumping current pulse duration and the total electric charge deposited in the plasma.

## 2. EXPERIMENTAL DEVICES AND MEASUREMENTS

Both experimental devices and measurements have been detailed elsewhere[8], so that they will not be revisited in detail here. The discharge cell of the X525 laser has an electrode gap d=2.5 cm. Two electrode geometries have been used: firstly, a profile cathode and a flat anode, and secondly, a flat cathode and a profiled anode. The profiled electrode is 50 cm in length and is flat over 2.5 cm width. The laser cell has been filled with a $Ne/SF_6$ (1/1) mixture at a total pressure of 156 mbars, or with $SF_6$ at 78 mbars, with addition of ethane at a partial pressure ranging from 0 up to 10 mbars. The charging voltage value of the energy storage line can be chosen as high as 35 kV. The value of the capacitance, C, ranges from 36 up

XIII International Symposium on Gas Flow and Chemical Lasers and High-Power Laser Conference,
Antonio Lapucci, Marco Ciofini, Editors, Proceedings of SPIE Vol. 4184 (2001)

to 144 nF, and the circuit inductance L from 9.25 up to 40.5 nH. It gives a pumping pulse duration, $\tau_p$, between 60 and 155 ns.

The preionization is achieved by a short X-rays burst (12 ns) generated from a cold cathode diode powered by a low inductance Marx generator. X-rays are injected in the inter-electrodes space through the flat grounded electrode, and the dose can be chosen in the range 0.1 up to 10 mR. Variation of the X-rays dose in that range allows to vary the value of the primary electron density, $n_{eo}$, achieved from photoionization processes, from about $10^6$ up to $10^9$ $cm^{-3}$. For $SF_6$, $n_{eo}$ has been estimated from measurements in Xe taking into account that the absorption cross section of $SF_6$ is about twice the cross section of Xe in the photon energy range of the present study[10] (20-50 keV). Ne atoms and $C_2H_6$ molecules provide less primary electrons than $SF_6$.

## 3. DISCHARGE IN $SF_6$ AND IN Ne/$SF_6$ MIXTURES

As a first step, the influence of the X-rays preionization on the discharge dynamic has been examined in the Ne/$SF_6$ (1/1) mixture, and in pure $SF_6$. On figure 1 are displayed typical temporal evolutions of the current and of the voltage for a X-rays dose value of 0.2 mR, for C=72 nF and a charging voltage $V_o$=25 kV, for a flat cathode, and for two values of the pumping pulse duration, $\tau_p$=80 ns and $\tau_p$=155 ns. At a low $\tau_p$ value, 80 ns, the discharge is characterised by a single current pulse, followed by a very long afterglow during which a residual voltage remains across the electrodes and the capacitor bank. CCD camera measurements have shown that the discharge is homogeneous[11]. Arcs appear at a time of at least several hundreds nanoseconds. For the conditions of the figure the deposited electric charge and energy, Q and $E_d$, in the plasma during the current pulse are respectively equal to 0.8 mC and 50 J/l.

The increase of $\tau_p$ does not change the value of Q, at fixed C and $V_o$ values. However it leads to the decrease of the delay time, $\tau_{arc}$, between the peak current of the main discharge and arcs. At $\tau_p$=155 ns in figure 1, plasma inhomogeneities (localised current channels in the inter-electrodes space) develop at the end the pumping pulse and, thereafter, both the current and the voltage oscillate. As a general trend, at a constant Q value, the increase of the pumping pulse duration above 100 ns is detrimental for the discharge stability and homogeneity. Similar results than those displayed in figure 1 have been obtained when $\tau_p$ increases from 60 ns up to 115 ns at Q=0.8 mC, which corresponds to C=36 nF and $V_o$=30.7 kV. It has also been obtained both in the Ne/$SF_6$ (1/1) mixture and in pure $SF_6$. Moreover the increase of the X-rays dose value up to 10 mR does not change the discharge behaviour, i.e. the appearance time of plasma inhomogeneities is unchanged. The discharge in Ne/$SF_6$, or $SF_6$, cannot be stabilised by the increase of the electron preionization density, even by two orders of magnitude from about $10^7$ $cm^{-3}$ (0.2 mR) up to $10^9$ $cm^{-3}$ (10 mR). We have also established that the decrease of $n_{eo}$ down to about $10^6$ $cm^{-3}$ (0.1 mR) induces a decrease of the delay time between the peak current and arcs, even at a pumping pulse duration less than 100 ns.

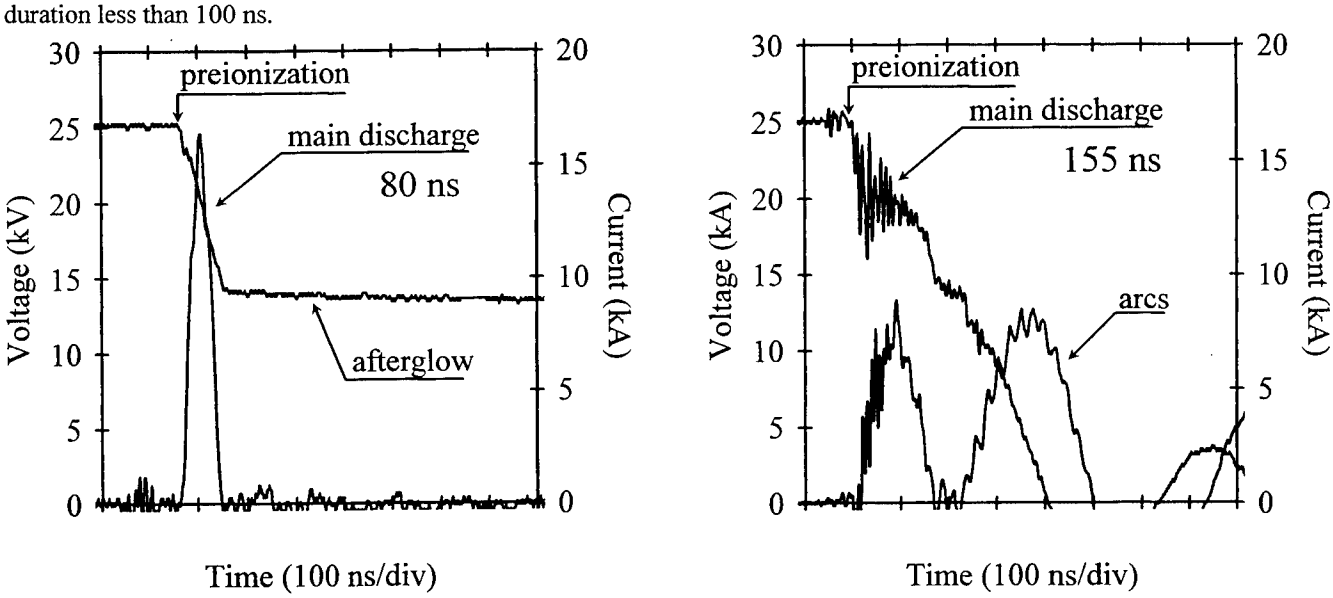


Fig. 1 - Temporal evolution of the discharge current and voltage for the Ne/$SF_6$ (1/1) mixture at C=72 nF, $V_o$=25 kV, X-rays dose of 0.2 mR, flat cathode. Values of the pumping pulse duration are given on the diagrams.

In figure 1, the current goes to zero before appearance of arcs at $\tau_p$=155 ns and $V_o$=25 kV, but experiments performed at higher charging voltage values have shown that higher is Q, shorter is the delay time $\tau_{arc}$ at a fixed pumping pulse duration. Thus arcs appear very close to the current maximum ($\tau_{arc}$ values of about 20 ns or less), when the $V_o$ value is equal to twice the self-sustaining discharge voltage value. As a result only a fraction of the stored energy is put in a homogeneous medium.

On the other hand, the discharge homogeneity in $Ne/SF_6$, or $SF_6$, depends much more on the X-rays dose (or on $n_{eo}$) when the cathode is profiled, as compared with the discharge obtained with a flat cathode. However plasma inhomogeneities always appear at high deposited charge, whatever the cathode shape is, and even at the high dose value of 10 mR. Consequences for the discharge dynamic in mixtures with ethane, and the consecutive effects on the HF laser performance, are examined in the followings with respect to the parameters ($\tau_p$, Q, dose) values.

## 4. DISCHARGE IN MIXTURES WITH ETHANE

It is known[9] that addition of ethane to the $Ne/SF_6$ (1/1) mixture, or to pure $SF_6$, inhibits the development of inhomogeneities during the discharge. Figure 2 illustrates this stabilisation effect for C=72 nF, $V_o$=26.35 kV, a flat cathode, a very low X-rays dose of 0.1 mR, and a pumping pulse duration of 155 ns. The displayed measurements correspond to a $C_2H_6$-pressure, $p_{C2H6}$, equal to 2.5 and 4.5 mbars. For such low pressure values the deposited charge Q and energy $E_d$ are almost unchanged at a fixed $V_o$ value, equal to 1.0 mC and 62 J/l for the conditions of figure 2. For same parameters values, arcs appeared before the end of the discharge in case of a $C_2H_6$ free medium.

In figure 2, at $p_{C2H6}$=2.5 mbars, the current of the main discharge goes to zero before appearance of arcs. However the arcs delay time $\tau_{arc}$ is lower than the pumping pulse duration $\tau_p$. The further increase of $p_{C2H6}$ up to 4.5 mbars leads to an afterglow duration higher than $\tau_p$.

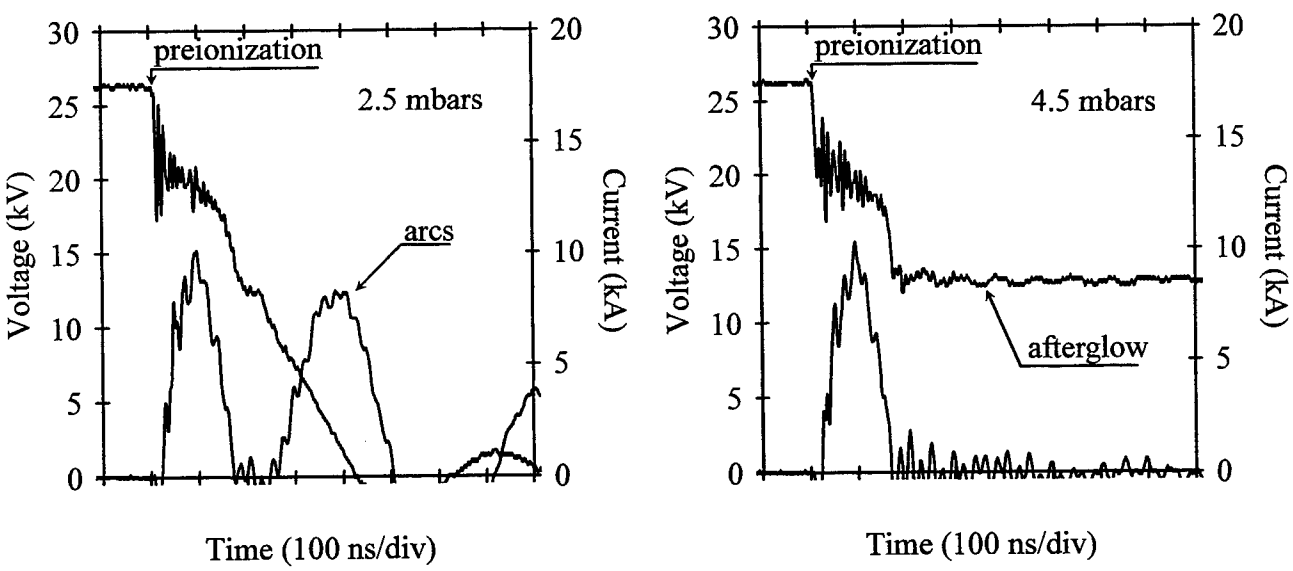


Fig. 2 - Temporal evolution of the discharge current and voltage for $Ne/SF_6/C_2H_6$ mixtures at C=72 nF, $V_o$=26.35 kV, X-rays dose of 0.1 mR, pumping pulse duration of 155 ns, flat cathode. Values of the $C_2H_6$-pressure are given on the diagrams.

Figure 2 emphasises that an homogeneous active medium can be obtained at an electron preionization density estimated to be as low as about $10^6$ $cm^{-3}$. However the minimum $C_2H_6$-pressure, $p_{min}$, which is required in order to obtain an efficient discharge stabilisation effect (long afterglow) depends on: i/ the X-rays dose, ii/ the pumping pulse duration, iii/ the deposited charge, and iv/ the cathode shape. The following table gives the $p_{min}$ values for some values of these parameters.

| X-rays dose (mR) ---> | | | 0.1 | 0.2 | 0.45 | 10 |
|---|---|---|---|---|---|---|
| cathode shape | Q (mC) | $\tau_p$ (ns) | | | | |
| flat | 0.8 | 80 | 0 | - | - | 0 |
| flat | 0.8 | 155 | 4.5 mbars | 1.0 mbars | - | 1.0 mbars |
| flat | 1.6 | 125 | 3.0 mbars | - | 1.0 mbars | 1.0 mbars |
| flat | 3.0 | 125 | 7.0 mbars | - | 3.5 mbars | 2.0 mbars |
| profiled | 3.0 | 125 | - | - | - | 5.0 mbars |

It follows from this table that: i/ higher is the X-rays dose at fixed Q, $\tau_p$ values, lower is $p_{min}$; ii/ higher is $\tau_p$ at fixed X-rays dose and Q values, higher is $p_{min}$; iii/ higher is Q at fixed X-rays dose and $\tau_p$ values, higher is $p_{min}$; iv/ $p_{min}$ is lower for a flat cathode than for a profiled one, at fixed values of the X-rays dose, Q, and $\tau_p$.

## 5. IMPORTANCE OF THE PREIONIZATION

The above results show that the reduction of the X-rays dose down to 0.1 mR has no effect on the discharge dynamic at $p_{C2H6}$ higher than 7 mbars, for a flat cathode. Moreover an arc free discharge can be obtained as the homogeneous X-rays preionization is suppressed at high ethane pressure. Without X-rays, the discharge self-breakdown is believed to follow from the preionization of the mixture by UV-photons emitted by accidental, random in time and position, corona discharges near the high voltage electrode. In figure 3 are displayed measurements in the self-breakdown mode, for $SF_6/C_2H_6$ mixtures at $p_{C2H6}$=2.5 and 10.4 mbars at Q=0.8 mC and $\tau_p$=155 ns.

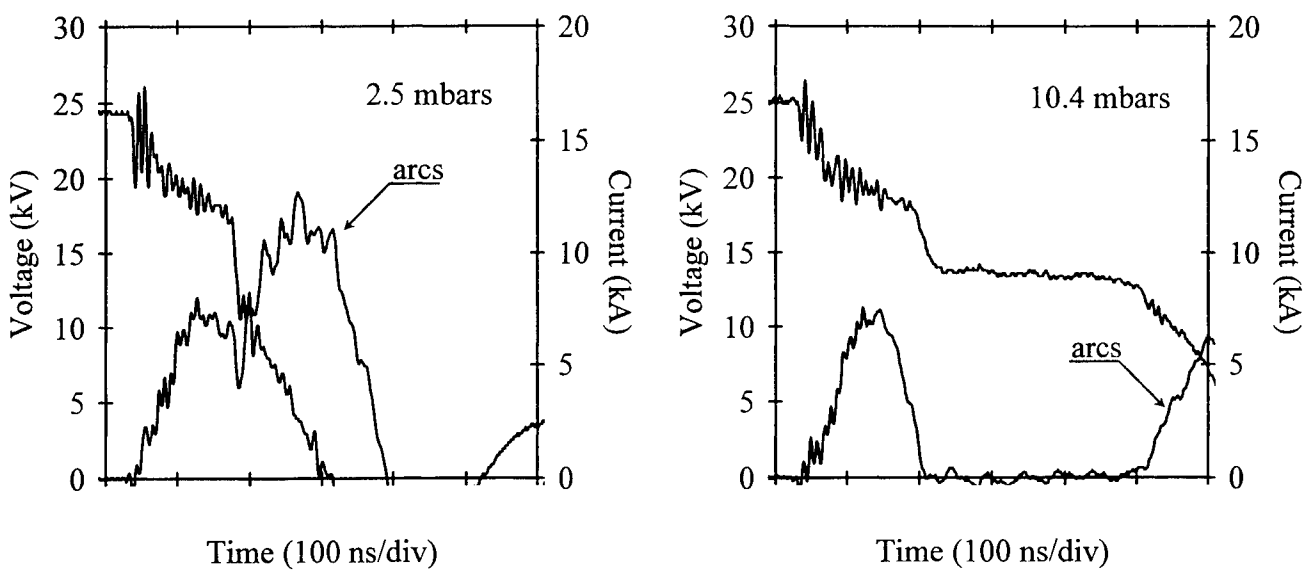


Fig. 3 - Temporal evolution of the discharge current and voltage for $SF_6/C_2H_6$ mixtures at C=72 nF, $V_o$=24.5 kV, pumping pulse duration of 155 ns, flat cathode. No X-rays preionization. Values of the $C_2H_6$-pressure are given on the diagrams.

Arcs appear close to the current maximum at 2.5 mbars of ethane, whereas a residual voltage is well established after the main discharge at 10.4 mbars. Consequences for the laser performance are displayed in figure 4. The laser energy is plotted against the charging voltage for the same parameters values than in figure 3, with or without X-rays preionization. At a fixed $V_o$ value, the laser energy $E_L$ decreases as X-rays are suppressed at $p_{C2H6}$=2.5 mbars owing to the rapid development of plasma inhomogeneities in the discharge volume (figure 3). This is not the case at $p_{C2H6}$=10.4 mbars, for which $E_L$ values obtained with or without preionization are equal. However lower laser performance are achieved at 10.5 mbars than at 2.5 mbars, for a X-rays dose of 10 mR. This is explained by the decrease of the F-atom production rate as soon as the ethane concentration in the mixture is increased[12]. Thus, for non-chain discharge pumped HF/DF laser using $SF_6$ with $C_2H_6$ (or $C_2D_6$), the optimisation of the laser performance, i.e. achievement of the highest output energy at the highest efficiency, can

be hardly obtained without preionization of the gas mixture. However the required X-rays dose is rather low, as discussed in the followings.

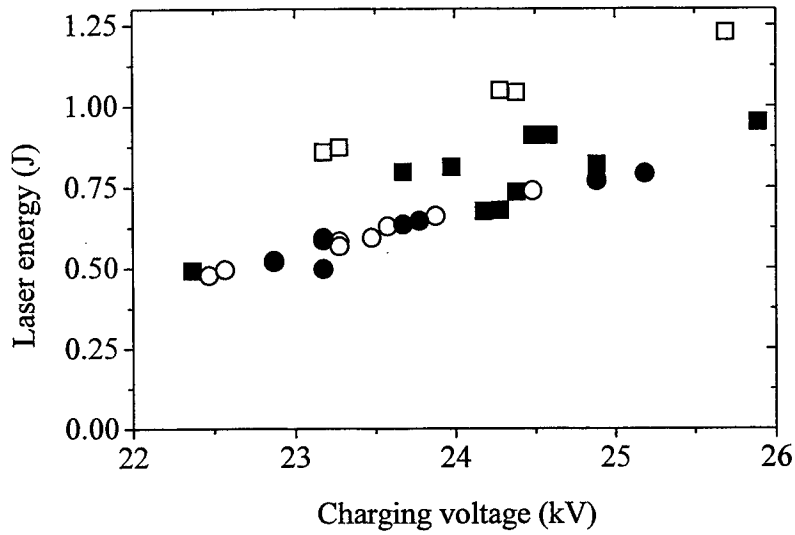


Fig. 4 - Laser energy plotted against the charging voltage. $SF_6/C_2H_6$ mixtures at C=72 nF, pumping pulse duration of 155 ns, flat cathode. Squares: $p_{C2H6}$=2.5 mbars, circles: $p_{C2H6}$=10.4 mbars. Open symbols: X-rays dose of 10 mR. Closed symbols: self-breakdown mode.

## 6. INFLUENCE OF THE PREIONIZATION ON LASER PERFORMANCE

In figure 5 is plotted the laser energy, in relative unit, against the X-rays dose in conditions of high specific deposited energy in the active medium and high pumping current pulse duration: $E_d$=200 J/l, Q=3.0 mC, $\tau_p$=125 ns, for a $Ne/SF_6/C_2H_6$ mixture at $p_{C2H6}$=2.5 mbars, and for a flat cathode. The arrow on the diagram indicates the laser energy value obtained in the self-breakdown mode. In that condition the temporal evolutions of the current and of the voltage are very similar to those plotted on the left diagram in figure 3.

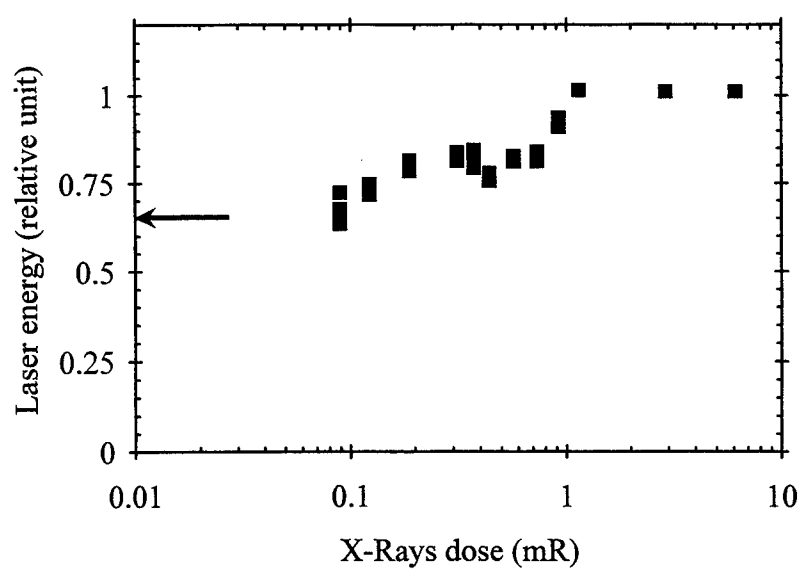


Fig. 5 - Laser energy plotted against the X-rays dose. $Ne/SF_6/C_2H_6$ mixture at $p_{C2H6}$=2.5 mbars. C=144 nF and $V_o$=31 kV, pumping pulse duration of 125 ns, flat cathode.

Figure 5 shows that $E_L$ increases when the dose increases from 0 up to 0.2 mR. It is correlated to the increase of the delay time between the peak current and appearance of arcs. The discharge current goes to zero at the end of the discharge at 0.2 mR, as measurements plotted in the left diagram in figure 2, and arcs are located just after. Thus the discharge dynamic is unchanged and the laser energy is almost constant for a dose between 0.2 and 0.8 mR. Arcs are throw away from the main discharge when the dose increases from 0.8 up to 1 mR, and correlatively $E_L$ increases in figure 4. Above 1 mR, the laser energy does not depend on the X-rays dose because the discharge is stabilised, with a long afterglow. Thus, for the conditions of figure 5, the required X-rays dose for the optimisation of the laser performance does not exceed 1 mR, which corresponds to an estimated electron preionization density of $2.5 \times 10^8$ $cm^{-3}$.

Keeping same values for $\tau_p$, Q and $E_d$ than in figure 5, we have studied the influence of the ethane pressure on the laser performance in correlation with the influence of the X-rays dose. Results are displayed in figure 6, in which is plotted $E_L$ against $p_{C2H6}$ for $Ne/SF_6/C_2H_6$ mixtures and a flat cathode, and two values of the X-rays dose, 0.1 and 10 mR.

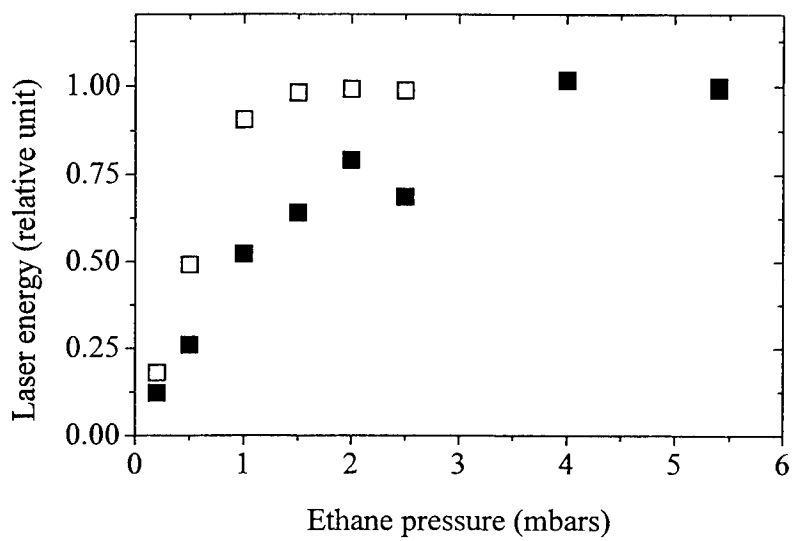


Fig. 6 - Laser energy plotted against the ethane pressure. $Ne/SF_6/C_2H_6$ mixture at C=144 nF and $V_o$=31 kV, pumping pulse duration of 125 ns, flat cathode. Open symbols: X-rays dose of 10 mR. Closed symbols: 0.1 mR.

At 10 mR, the increase of the ethane pressure from 0 up to 1 mbar induces a rapid increase of the laser energy. At $p_{C2H6}$ higher than 1.5 mbars, $E_L$ saturates but does not decrease until the pressure value increases above 6 mbars (not shown on the figure). On the other hand, the growth of $E_L$ when $p_{C2H6}$ increases at 0.1 mR is slower than at 10 mR. As a result the maximum laser energy, $E_L^{Max}$, is reached at only 4 mbars at 0.1 mR, instead of 1.5 mbars at 10 mR. Correlatively the discharge stabilisation by ethane is more difficult to achieve at 0.1 mR than at 10 mR, as discussed in part 4. However, at 0.1 mR, $E_L^{Max}$ is reached at a $p_{C2H6}$ value which is 3 mbars smaller than the minimum pressure required for a complete stabilisation of the discharge, 7 mbars (see table). Reasons for this difference should be understand looking at the relative temporal positions of the laser emission and of the plasma inhomogeneities onset.

## 7. CONCLUSIONS

The main result of this work is that the optimum performance of discharge pumped HF/DF lasers, using $SF_6$ with $C_2H_6$ ($C_2D_6$), cannot be reached without preionization of the active medium. A high specific laser energy value is obtained in the self-breakdown mode of the discharge. However it is about 25% lower than the energy achieved with preionization.

The optimum performance of the phototriggered lasers can be reached using a very low X-rays dose value, 0.1 mR, at the condition that the ethane concentration in the mixture is high enough to ensure that the laser emission appears before the development of high current channels in the inter-electrodes space. Two phenomena contribute to obtain this result when one increases the ethane pressure at a constant $Ne/SF_6$ (or $SF_6$) pressure: i/ the increase of the HF ro-vibrational levels

production frequencies, which leads to the decrease of the delay time between the peak current and the laser power growth, ii/ the very efficient stabilisation effect of the discharge induced by ethane. Combination of these two phenomena allows to keep $p_{C2H6}$ as low enough to avoid a decrease of the F-atom production rate.

## 8.ACKNOWLEDGMENTS

The authors wish to thank the DSP/STTC (DGA) for its financial support.

## 9. REFERENCES

1. S. Suchard and J. Airey, « Handbook of Chemical Lasers », chapter 6, John Wiley, New York, 1976, and references therein.
2. H. Brunet, M. Mabru, J. Rocca-Serra, and C. Vannier, "Pulsed HF chemical laser using a VUV photo-triggered discharge", *Proc. SPIE* **1397**, 273-276 (1991).
3. V. Puech, P. Prigent, and H. Brunet, "High-efficiency, high-energy performance of a pulsed HF laser pumped by phototriggered discharge", *Appl. Phys. B* **55**, 183-185 (1992).
4. G. Tsikrikas, A. Serafetinides, and A. Papayannis, « Performance studies of a pulsed HF laser with a sliding discharge plasma cathode », *Appl. Phys. B* **62**, 357-365 (1996).
5. Y. Kalisky, K. Waichman, S. Kamin, and D. Chuchem, « Plasma cathode preionized atmospharic pressure HF chemical laser », *Opt. Comm.* **137**, 59-63 (1997).
6. N. Anderson, T. Bearpark, and S. Scott, « An X-ray preionised self sustained discharge HF/DF laser », *Appl. Phys. B* **63**, 565-573 (1996).
7. B.Lacour, C. Gagnol, P. Prigent, and V. Puech, « High average power HF/DF laser », *XII GCL/HPL, St. Petersburg, Russia, 31 August-5 September 1998.*
8. F. Doussiet, M. Legentil, S. Pasquiers, C. Postel, V. Puech, and L. Richeboeuf, « Investigations of a phototriggered HF laser », *Proc. SPIE* **2702**, 179-190 (1996).
9. L. Richeboeuf, S. Pasquiers, F. Doussiet, M. Legentil, C. Postel, and V. Puech, « Dynamic and correlated performance of a phototriggered discharge pumped HF-laser using $SF_6$ with hydrogen or ethane », *to appear in Appl. Phys. B.*
10. J. Berkowitz, « Photoabsorption, photoionization, and photoelectron spectroscopy », chapter 5, Academic Press, New York, 1979.
11. M. Makarov, L. Ménager, S. Pasquiers, C. Postel, and V. Puech, « Time resolved imaging study of phototriggered discharges in $SF_6$ and Ne/$SF_6$ mixtures », *to appear in IEEE Trans. Plasma Science.*
12. L. Richeboeuf, S. Pasquiers, M. Legentil, and V. Puech, « The influence of $H_2$ and $C_2H_6$ molecules on discharge equilibrium and F-atom production in a phototriggered HF laser using $SF_6$ », *J. Phys. D* **31**, 373-389 (1998).

# Author Index